IAHR 2017

37th IAHR WORLD CONGRESS

13-18 August, 2017

Kuala Lumpur, Malaysia

Supported by Spain Water and IWHR, China

THEME 3: ENVIRONMENTAL HYDRAULICS AND INDUSTRIAL FLOWS

Editor: Junaidah Ariffin

IAHR AIRH
Supported by Spain Water and IWHR, China

IAHR 2017

37th IAHR WORLD CONGRESS
13-18 August, 2017
Kuala Lumpur, Malaysia

ECOHYDRAULICS

NUMERICAL SIMULATION STUDY ON EFFECTS OF WATER DEPTH ON TURBULENT IMPINGING JET DIFFUSION

WANGRU WEI [1] & JUN DENG [2]

[1,2] State Key Laboratory of Hydraulics and Mountain River Engineering, Sichuan University, Chengdu, China
wangru_wei@hotmail.com; djhao2002@scu.edu.cn

ABSTRACT

The objective of this study is to investigate turbulent characteristics of two-dimension impinging jet for different water depth. Numerical simulations of turbulent impinging jet are performed based on a standard k-ε turbulent model. It is found that jet core length does not change for different water depth, while the mean centerline velocity along relative flow direction decays faster in both established region and impact region for deeper water depth, and development of jet entrainment improves in deeper water depth. At a certain transverse section in established region, mean turbulent kinetic energy grows from centerline, reaches a peak, and then gradually falls. This process gets smoother and the distance between centerline and peak gets greater at the transverse direction as jet develops downstream in established region, which is much more notable in deeper water depth. In development region, mean turbulent kinetic energy decreases along the flow direction due to the sudden transition of boundary conditions, and the trends are not affected by water depth. In established region, mean turbulent kinetic energy increases rapidly with flow distance, reaches peak and then falls gradually until the end of this region. In jet impact region, mean turbulent kinetic energy rises steeply and drops sharply in the near-wall region. This is because the streamline direction of impinging jet changes drastically in this region. For deeper water depth, the variation range of mean turbulent kinetic energy in established region is larger, while in jet impact region near wall, mean turbulent kinetic energy changes much more drastically in shallow water.

Keywords: Impinging jet; velocity; turbulence; water depth; numerical simulation study.

1 INTRODUCTION

It is well known that the unsteady imping jet has important engineering applications, such as ski-jump flows scouring on river channel in hydraulic engineering, impact process of vertical take-off and landing for the lifting equipment and hydraulic coal mining technology. Impinging jet flows have been extensively studied experimentally in the past (Tani and Komatsu, 1964; Cola, 1965; Wolfshtein, 1970; Donaldson and Snedeker, 1971; Gutmark et al., 1978). Most studies are about the properties of velocity and heat transfer (Goldstein and Franchett 1988; Button and Jambunathan, 1989; Jambunathan and Button, 1994; Viskanta, 1993). With the development of turbulence theory and computer technology recently, numerical studies for jet flows are being performed. Chung et al. (2002) studied momentum and heat transfer characteristics of an unsteady impinging jet with direct numerical simulations (DNS). Reichert and Biringen (2007) studied two- and three- dimensional DNS of a compressible plane jet and stated that streamwise and spanwise turbulence intensities exhibit no change with increased compressible. Rembold et al. (2002) studied a jet flow at a Reynolds number of 2000 based on the narrow side of the nozzle with DNS. Ashforth and Jambunathan (1996) studied a turbulent impinging jet at a Reynolds number of 20000, and the numerical simulation results showed that the mean velocity profile is good agreement with experimental data and standard k-ε turbulent model could predict qualitatively turbulence profile in developed region well. Hirofumi and Yasutaka (2004) investigated the structures and characteristics of flows and heat transfer for plane turbulent imping jets. He stated that the Nusselt number increases with a decrease in the distance between the impingement wall and the upper wall. This indicated that water depth may have effects on the inside structure of impinging jet flow.

For better understanding of impinging jet, the turbulent properties associated with water depth are important. In present study, the two-dimension standard k-ε turbulent model is used and numerical simulations of a turbulent submerged impinging jet are performed to study the impingement turbulence properties.

2 FLOW PATTERN OF SUBMERGED IMPINGING JET

The submerged impinging jet diffusion is divided into three flow regions: development region, where the jet potential core persists, established region, and jet impact region, as is shown in Figure 1. In this article, section at the outlet of jet perpendicular to the jet travel distance and jet centerline distance were chosen as the *x* and *y* coordinate axis. While *h* is the water depth defined by the distance from the jet outlet to the impingement wall surface. The section at the end of flow development region was defined as the initial section of centerline velocity attenuation, and $2b_0$ is the initial flow thickness of jet and V_0 is the initial velocity at outlet. L_0 is the length of development region. The internal boundary is defined as lines from edge at the jet exit sidewall to the end of development region. The convergence angle α is the angle between internal boundary and jet centerline. For a special transverse section, V_m is the value of mean centerline velocity, and the b_r is the width of the jet defined by the points at the external boundary where the mean local velocity is 1/e of the mean centerline value.

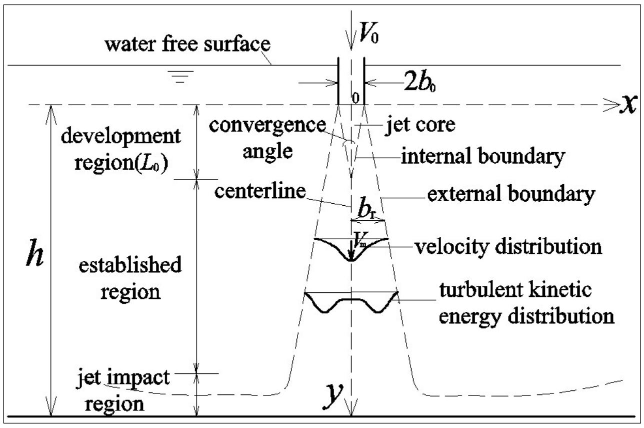

Figure 1. Impinging jet flow conditions and coordinate system.

3 RESULTS AND DISCUSSIONS

The initial velocity V_0 at the nozzle exit is 3.18m/s, under condition of R_e=48550. Simulation are performed at five water depths of 40, 60, 90, 110 and 260 cm (i.e. dimensionless downstream distance, h/b_0=40, 60, 90, 110 and 260). Figure 2 shows the mean velocity field of the numerical simulation results for different water depth. It is clear that the numerical calculated results are consistent with the pattern of jet flow. There is a triangle core near the outlet where the value of mean centerline velocity does not decay. As the jet develops along the flow direction, jet width grows and average velocity decays at both transverse and longitudinal direction. In comparison, for the cases with different water depth the flow behavior is markedly different. The flow velocity field shows that with the decreased water depth, there is a clear trend that the development of impinging jet is suppressed. It clearly indicates a different jet structure due to the suppression of jet development. And this will be discussed further below.

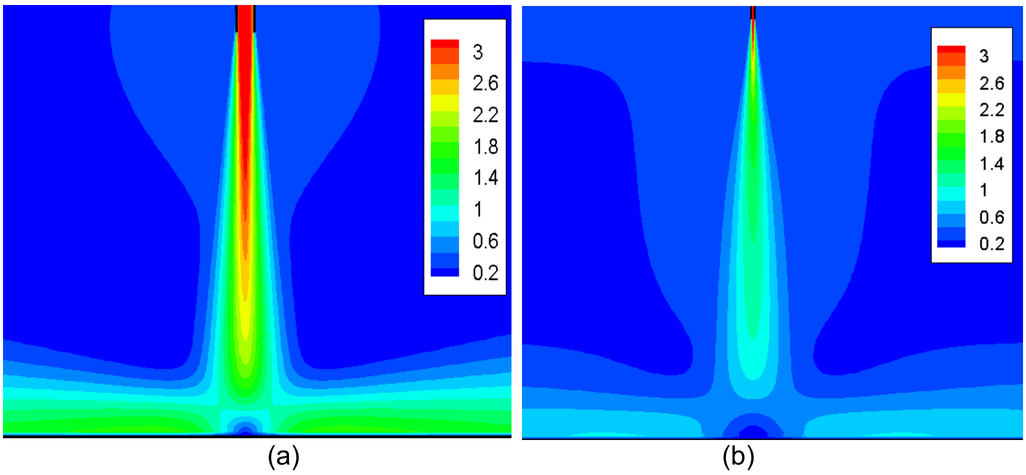

Figure 2. Velocity field contours for different water depth: (a) h/b_0=40; (d) h/b_0=260.

3.1 Velocity analysis

The numerically calculated mean centerline velocity profile along the way at h/b_0=110 is shown in Figure 3, with theoretical data obtained by Rajaratnam and Pani (1973) for comparison. The attenuation law and data of numerical simulation results are approximately consistent with the theoretical data. The mean velocity profile at different transverse sections in established region of jet at h/b_0=110 are obtained by numerical simulation which is shown in Figure 4(a). It can be seen that the curve of mean velocity attenuation along the transverse direction becomes much smoother as the section far from the outlet, due to the development of jet entrainment. The relative transverse distance is scaled by the vertical distance to the jet centerline and jet width b_r as x/b_r. Figure 4(b) shows the results, comparing with the theoretical data obtained from the equation:

 ©2017, IAHR. Used with permission / ISSN 1562-6865 (Online) - ISSN 1063-7710 (Print)

$$\frac{V}{V_{\mathrm{m}}} = \exp(-0.834 \times \frac{x^2}{b_r^2}) \qquad [1]$$

At different transverse sections, the velocity distributions show good self-similarity and are good consistent with theoretical data.

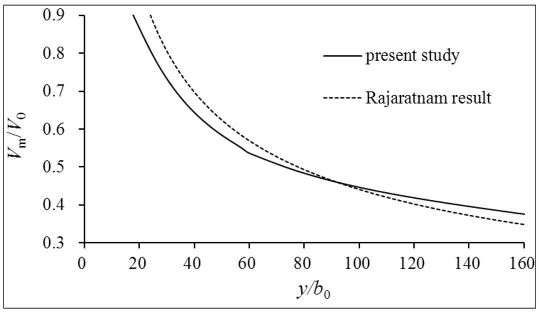

Figure 3. Comparison of axial velocity profiles.

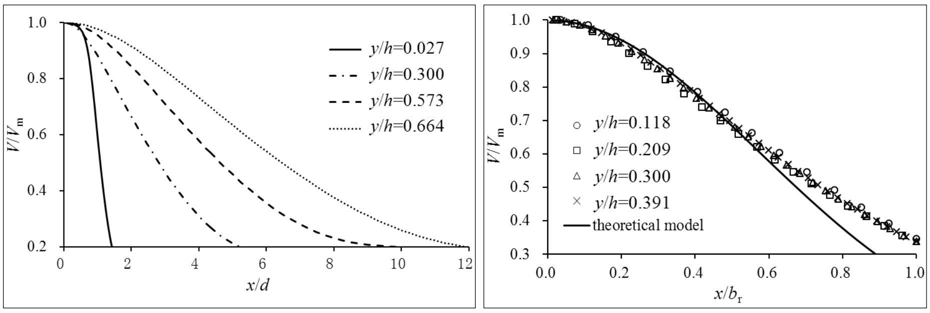

(a) (b)

Figure 4. The variation of velocity at transverse section for h/b_0=110.

In this study, the jet core length is defined as the longitudinal distance between outlet transverse section and the position where the velocity is $0.99V_0$ along the centerline direction. The calculated results indicate that the core length is about $3.25\times2b_0$ and does not change for different water depth. This is in agreement with the Ervine et al. (1997) given, who give an estimate of core length at about $3\times2b_0$. The convergence angle is about 7.6º. The computed mean centerline velocity attenuation along the flow direction is shown in Figure 5. It can been seen, as a whole, the values of V_m/V_0 decay faster along relative flow direction y/h with the increased values of relative water depth h/b_0 in both established region and jet impact region. The impact region is about 20% of water depth, and it does not change much for different water depth. In jet impact region, the mean velocity along the axial way decays much more notably than that in established region. In Figure 6, as the impinging jet develops downstream in established region, the value of b_r gets greater, and this process can be considered as a process of velocity expansion due to jet entrainment. The process develops much more sufficiently for deeper water depth, as the rate of relative transverse direction b_r/b_0 gets grater with the increased water depth. The improvement of relative width of b_r/b_0 with the increased water depth indicates that the process of jet entrainment develops much more sufficiently in deeper water depth. And the jet entrainment can be suppressed under the shallow water condition. It illustrates that in terms of mean velocity, impinging jet for deeper water depth develops much faster and fully.

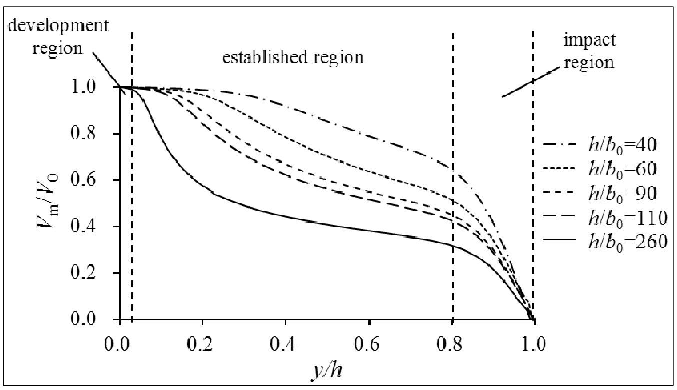

Figure 5. Comparison of mean centerline velocity profiles of jet for different water depth.

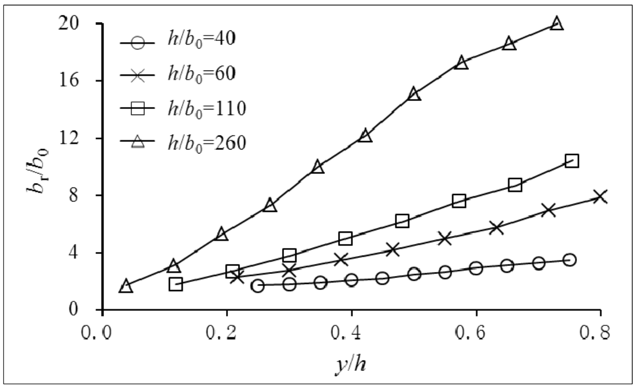

Figure 6. Comparison of velocity expansion jet flow for different water depth.

3.2 Turbulence properties analysis

As the jet develops transversely, maximum mean turbulent kinetic energy appears symmetrically between centerline and external boundary. Figure 7 plots distributions of mean turbulent kinetic energy at various streamwise sections at relative water depth h/b_0=110. As evident from this figure, the mean turbulent kinetic energy k grows with transverse distance from the centerline to external boundary, reaches a peak, and then gradually falls asymmetrically toward a fully developed value. This indicates that the maximum shearing intensity appears at the peak position, affected by the lateral gradient of mean velocity. As the jet develops downstream, this trend declines due to the smoother for mean velocity diffusion at transverse direction. In development region (y/h=0.027), the mean turbulent energy is quiet low and does not change remarkably at transverse direction in jet core region. The reason for this is that in the core region, mean velocity hardly decays in transverse direction, and the lateral gradient of mean velocity is quiet small, thus the jet flow is not affected by the shearing notably.

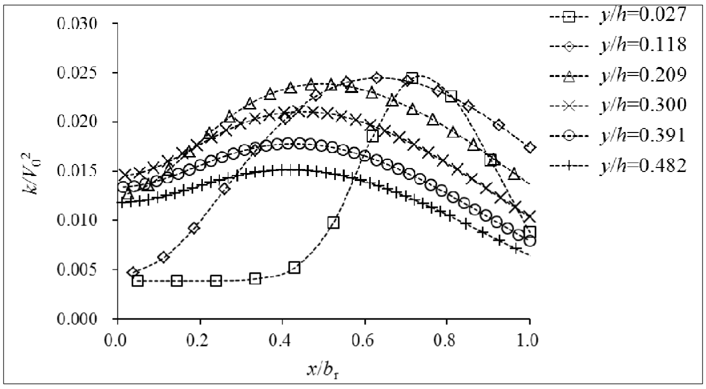

Figure 7. Mean turbulent kinetic energy profile for h/b_0=110.

A comparison of maximum mean turbulent energy k_m distributions downstream for different water depth is given in Figure 8. It is found that k_m declines along the flow direction and water depth has a strong effect on the distribution of turbulent energy. For deeper water depth h/b_0=260, the attenuation of mean turbulent kinetic energy k_m gets much more noticeable. The reason is that with increased water depth, the rate of jet width growth gets higher and the lateral gradient of mean velocity is smaller than that for lower water depth. Then the shearing intensity is relatively lower. The change of the k_m attenuation supports the hypothesis that with decreased water depth the jet development is suppressed. For a certain transverse section, b_{km} is the mean turbulent kinetic energy width defined by the distance between centerline and mean turbulent kinetic energy peak. In Figure 9, the b_{km} of impinging jet is documented. It can be seen clearly that the transverse distance of mean turbulent kinetic energy peak gets greater at the transverse direction as jet develops downstream. This process can be considered as a width growth of mean turbulent kinetic energy. In deeper water depth, the b_{km} increases rapidly and under a shallow water condition, this trend is suppressed. The ratio of b_{km} and b_r decreases as jet develops downstream for different water depth, as is shown in Figure 10. The width of mean turbulent kinetic energy does not grows synchronistically at the transverse direction as same as the width growth of mean velocity, and the rate of width growth of mean turbulent kinetic energy is significantly lower than that in velocity expansion. This indicates that the development of shearing due to the lateral gradient develops transversely lower than the process of jet entrainment as the jet develops along flow direction.

 ©2017, IAHR. Used with permission / ISSN 1562-6865 (Online) - ISSN 1063-7710 (Print)

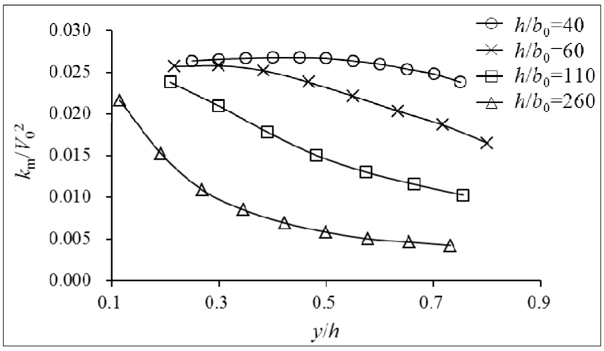

Figure 8. Comparison of mean streamwise turbulent kinetic energy peak for different water depth.

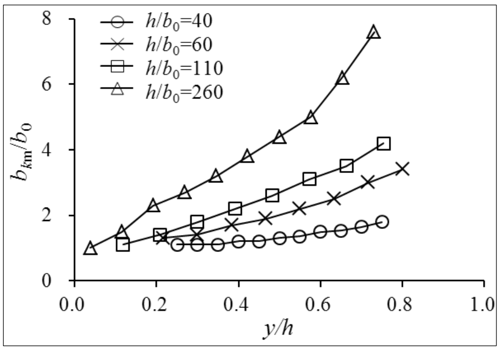

Figure 9. Comparison of mean turbulent kinetic energy width growth for different water depth.

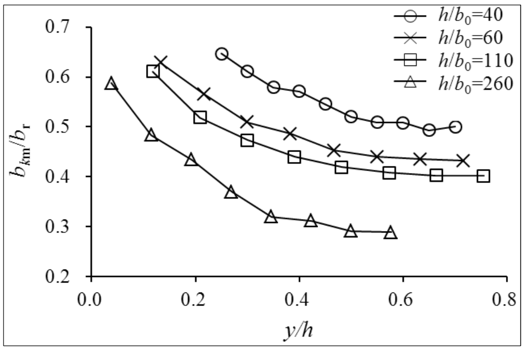

Figure 10. Comparison of jet diffusion for different water depth.

Figure 11 shows the distributions of mean turbulent kinetic energy at jet centerline in *y* direction. It can be observed that there are mainly three processes for the development of mean turbulent kinetic energy. Firstly, the mean turbulent kinetic energy decays in the development region of jet. This process is not affected by the water depth, as is shown in Figure 12. This is because the solid surface strengthens the turbulent intensity inside the jet flow, compared to flow shear. As turbulent jet is in the pressure conduit, the turbulence is affected by solid surfaces of conduit, while the turbulence is affected by flow shear after the jet into surrounding water (in Figure 13). This sudden transition of boundary condition results in the decrease of mean turbulent kinetic energy at the jet centerline. Besides, the attenuation trends of mean turbulent kinetic energy for different water depth are almost coincidental. The reason for this is that the process of boundary condition transition is quite relatively short and after the mean centerline velocity begins to decay the flow shear is the main factor affecting the turbulence of jet, so the decrease of mean turbulent kinetic energy at centerline is only in development region and is not affected by water depth. In the established region, due to the flow shearing caused by variation of gradient velocity, the mean turbulent kinetic energy increases rapidly with stream wise distance, reaches peak and then falls gradually until the end of this region. Finally, in the impact region, the mean turbulent kinetic energy increases steeply and a sudden drop occurs immediately. The reason is that due to the influence of impingement solid surface, the streamline direction of impinging jet changes drastically in the near-wall region, and this can improve the turbulent intensity of jet. At the solid wall surface where the stagnation point of impingement jet exist (in Fig. 2), both the mean velocity gradient and changes of jet streamlines are much lower, and this causes the decrease of mean turbulent kinetic energy.

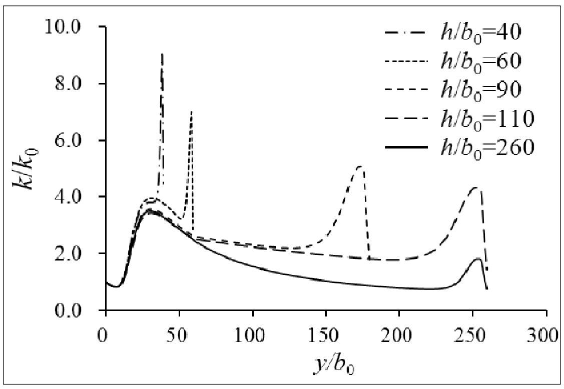

Figure 11. Comparison of mean turbulent properties at axial direction for different water depth.

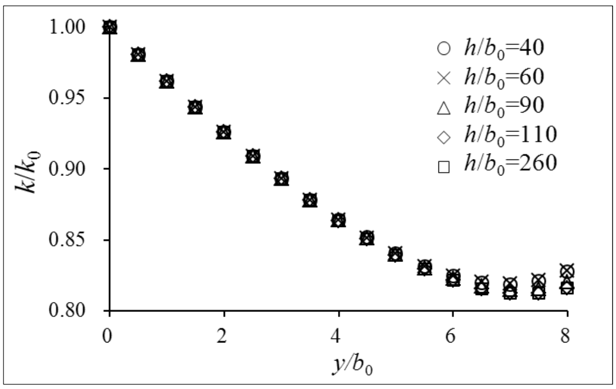

Figure 12. Comparison of mean turbulent properties in jet core for different water depth.

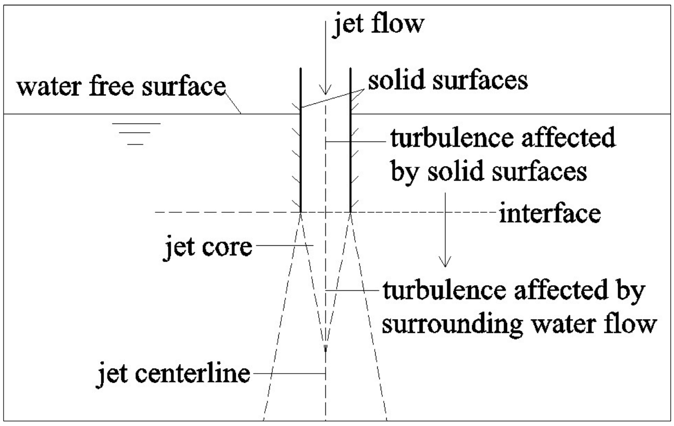

Figure 13. Transition of boundary condition in near outlet region.

These processes above can be observed more clearly when the *y* direction is scaled by the jet travel distance *y* and water depth *h* as *y*/*h*, as is shown in Fig. 14. Water depth has notable effects on the mean turbulent kinetic energy distribution in both established region and jet impact region. For deeper water depth, the variation range of mean turbulent kinetic energy in established region is larger than that in shallow water depth, while in jet impact region near wall, mean turbulent kinetic energy change much more drastically in shallow water depth. This results show that with increased in shallow water depth, the suppression for impinging jet decreases and energy disperses much more sufficiently. Thus, the mean turbulent kinetic energy fluctuation decreases in the near-wall region.

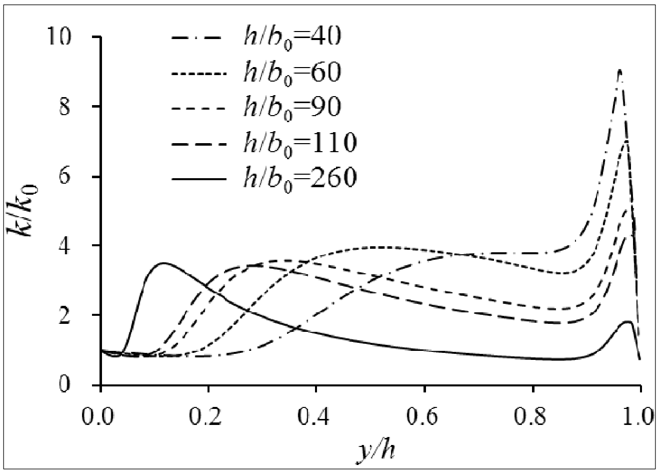

Figure 14. Comparison of mean turbulent properties at centerline direction for different non-dimensional in water depth.

4 CONCLUSIONS

This investigation has employed two-dimensional models to simulate the mean velocity and turbulent characteristics of impinging jet for different water depth. The following summarizes the central observations taken from these simulations.

Both of jet core and impact region do not change for different water depth. For deeper water depth, the mean centerline velocity along the relative flow direction decays faster in both established region and impact region, and jet entrainment improves, suggesting that in terms of mean velocity, the development of impinging jet is suppressed in shallow water depth.

At a certain transverse section in established region, the mean turbulent kinetic energy grows from the centerline to external boundary, reaches a peak, and then gradually falls toward a fully developed value. As jet develops downstream in established region, this process gets smoother and the peak gets away from the jet centerline at the transverse direction, which is much more notable for deeper water depth. However, the movement of peak is lower than the development of jet entrainment along the flow direction.

There are three processes for the development of mean turbulent kinetic energy at the centerline as the jet develops downstream. In development region, mean turbulent kinetic energy decreases along the flow direction due to the sudden transition of boundary conditions, and the trends are not affected by water depth. In the established region, the mean turbulent kinetic energy increases rapidly with streamwise distance, reaches peak and then fall gradually until the end of this region. In jet impact region, mean turbulent kinetic energy rises steeply and drops sharply in the near-wall region. For deeper water depth, the variation range of

 ©2017, IAHR. Used with permission / ISSN 1562-6865 (Online) - ISSN 1063-7710 (Print)

mean turbulent kinetic energy in established region is larger than that in shallow water depth, while in jet impact region near wall, it changes much more drastically in shallow water depth.

ACKNOWLEDGMENTS

The research reported herein is funded by the National Natural Science Foundation of China (Grant No. 51609162, 51379138), and the National Program on Key Research Project (Grant No. 2016YFC0401901).

REFERENCES

Ashforth, F.S. & Jambunathan, K. (1996). Numerical Prediction of Semi-Confined Jet Impingement and Comparison with Experimental Data. *International Journal of Numerical Methods in Fluid*, 23, 295-306.

Button, B.L. & Jambunathan, K. (1989). Impingement Heat Transfer-a Bibliography 1976-1985. *Prevention Heat Mass Transfer*, 15, 149.

Chung, Y.M., Luo, K.H. & Sandham, N.D. (2002). Numerical Study of Momentum and Heat Transfer in Unsteady Impinging Jets. *International Journal of Heat Mass Transfer*, 23, 592-600.

Cola, R. (1965). Energy Dissipation of A High Velocity Vertical Jet Entering A Basin. *Proceeding of 11th IAHR Congress*, Leningrad, USSR, 13.

Donaldson, C. & Snedeker, R.S. (1971). A Study of Free Jet Impingement. Part 1: Mean Properties of Free and Impinging Jets. *Journal of Fluid Mechanics*, 45, 281-319.

Ervine, D.A., Falvey, H.T. & Withers, W. (1997). Pressure Fluctuations on Plunge Pool Floors. *Journal of Hydraulic Research*, 35, 257-279.

Gutmark, E., Wlofshtein, M. & Wygnanski, I. (1978). The Plane Turbulent Impinging Jet. *Journal of Fluid Mechanics*, 73, 465-495.

Goldstein, R.J. & Franchett, M.E. (1988). Heat Transfer from a Flat Surface to an Oblique Impinging Jet. *Journal of Heat Transfer*, 110, 84-90.

Hirofumi, H. & Yasutaka, N. (2004). Direct Numerical Simulation of Turbulent Heat Transfer in Plane Impinging Jet. *International Journal of Heat Mass Transfer*, 25, 749-785.

Jambunathan, K. & Button, B.L. (1994). Impingement Heat Transfer-A Bibliography 1986-1993. *Prevention Heat Mass Transfer*, 20, 385.

Reichert, R.S. & Biringen, S. (2007). Numerical Simulation of Compressible Plane Jets. *Mechanics Research Communications,* 34, 249-259.

Rembold, B., Adams, N.A. & Kleiser, L. (2002). Direct Numerical Simulation of A Transitional Rectangular Jet. *International Journal of Heat Mass Transfer*, 23, 547-553.

Rajaratnam, N. & Pani, B.S. (1973).Three-Dimensional Turbulent Wall Jets. *Journal of Hydraulic Division*, *ASCE,* 100, 69-83.

Tani, I. & Komatsu, Y. (1964). Impingement of a Round Jet on a Flat Surface. *Proceeding of 11th International Congress on Applied Mechanics*, Munich, 672.

Viskanta, R. (1993). Heat Transfer to Impinging Isothermal Gas and Flame Jets. *Experimental Thermal and Fluid Science*, 6, 111-134.

Wolfshtein, M. (1970). Some Solutions of the Plane Turbulent Imping Jet. *Journal of Basic Engineering, ASEM*, 92, 915-922.

Proceedings of the 37th IAHR World Congress
August 13 – 18, 2017, Kuala Lumpur, Malaysia

SMALL EAVES ON FISH PASSAGE FACILITIES IMPROVE STABILITY AND MIGRATION OF SCULPIN

KEIKO MURAOKA(1) & YUICHI KAYABA(2)

(1,2) Water Environment Research Group, Public Works Research Institute, Tukuba, Japan
muraoka@pwri.go.jp; y-kayaba@pwri.go.jp

ABSTRACT

Most fish passages without natural fishways have been developed for strong-swimming species, such as salmonids. Although these passages have been designed to also accommodate weak swimmers, such as larval migrators, they create insufficient flow for the free migration of various species, especially bottom-swimming fishes such as sculpin. We propose including a cloister in fishway designs to facilitate the free movement of these weak swimmers. The scale of the cloister will depend on the body height of the targeted weak swimmer, but using an inclined ceiling would accommodate multiple fish sizes. In this study, small eaves have been installed along the lengthwise corner of the flow pipe to restrict sculpin from lifting their heads, and sculpin behavior in the flow was observed. Our results show that it is possible to optimize sculpin upstream movement by restricting head-raising movement using a design component such as small eaves. Although a maximum interior angle is effective for efficient sculpin migration, a 7.5–25° interior angle and increased roughness on the eaves' surface is suitable for migration of both sculpin and goldfish. For sculpin to remain in the flow without drifting downstream, a 10° interior eave angle, flow velocity of 0.5 m/s, and slippery acryl resin eave surface is the most effective combination. With slight roughness on the bottom, flow velocity of 0.5 m/s, and no eaves along the corner, all the sculpins drifted down without migrating to the upper side. This result is also consistent with natural river bed conditions.

Keywords: Fish passage; bottom-swimming fish; sculpin; ultra-high-speed camera; swimming physiology.

1 INTRODUCTION

Because river fragmentation has significant environmental impact on a local scale (Santos et al., 2012; Perkin et al., 2013), structures to facilitate the passage of fish around obstacles for multiple species and life stages are required (Ghimire and Jones, 2014). Given that swimming performance is variable across species, body size, and growth, such a fish passage should be designed to create a flow suitable to permit the target species to pass. This is especially important if the chosen species is a weak swimmer. Swimming velocities measured using swimming flumes provide us information for designing the maximum velocity of flow that a fish passage should allow (Rodríguez et al., 2006; Cheong et al., 2006). The jumping abilities of fish also need to be considered when designing the maximum drop of a fish passage (Rajartnam and Katopodis, 1994).

The development of investigative methods and equipment has provided the opportunity to collect data at unprecedented temporal and spatial scales. Image analysis methods of fish passage experimental models permit us to study the swimming behavior of fish in response to turbulent flow (Silva et al., 2012). Additionally, bio-logging systems can provide knowledge of the behavior and biological responses of fish moving along actual fish passages (Cooke and Hinch, 2013). Advances in biologically oriented fishway research over the last several decades have helped to optimize fishway designs. However, efforts have mainly focused on anadromous fish species, such as those of the Salmonidae family (Baras et al., 1994; Katopodis, 2005), and few data exist concerning small freshwater fish and bottom-swimming fish (Kerr et al., 2013; Santos et al., 2014). The established fish passage does not always allow the free movement of weak swimmers (Foulds, 2013). As freshwater biodiversity, will be increasingly severely reduced almost everywhere (Jenkins, 2003), there is no time to be lost in designing and implementing conservation efforts for freshwater species (Moyle et al., 2011). Simple methods to improve fish migration in established fish passages are required for rapid, economical, and wide-ranging improvement. In this study, we propose the inclusion of a cloister in fish passage designs to facilitate the migration of weak swimmers.

2 METHODS

2.1 Experimental setup

A translucent rectangular experiment pipe 0.2 m wide and 0.1 m high on the inner side was used for this study. The upper and lower ends were each connected to a water tank, and two controllable water pumps were connected to the upper water tank; these allowed a maximum flow velocity of 1.0 m/s. In addition, both water tanks had a spillway to control the velocity in the experiment pipe without turbulence, which impinges on

 ©2017, IAHR. Used with permission / ISSN 1562-6865 (Online) - ISSN 1063-7710 (Print)

fishes' swimming performance. Eaves 1.3 m long with internal angles of 7.5, 10, 12.5, 15, 20, and 25 degrees were installed respectively along the lengthwise corner of the experiment pipe. There was a cylindrical port for input of experimental fishes on the downstream end of the eaves.

2.2 Experiment

Sculpin (body length 32.9 ± 1.29 mm) which is a weak bottom swimming fish and goldfish (body length 39.29 ± 2.75 mm) which habitat are low velocity area such as pond, were the main fish used for the experiment. The behavior of each fish was observed by using ultra-high-speed cameras to observe their movement. The velocities were measured on the upstream end of the experiment pipe.

For the first step of our study, smooth-surface eaves with internal angles of 10, 12.5, and 25 degrees were installed in the experiment pipe to determine a suitable angle at which sculpin would remain without drifting downstream. These were installed individually in the experiment pipe with no flow inside it, and the fishes' behavior (remaining or being washed away) was observed as the flow was increased to a maximum velocity of 0.5 m/s. Second, several grades of roughness were installed on the inner surface of the eaves or on the bottom in cases of eaves having internal angles of 7.5, 10, 12.5, 15, 20, and 25 degrees to determine a suitable design that would allow free movement of the fish. Several sculpins or goldfish were fed into the experiment pipe, and their upstream movement in the flow was observed.

3 RESULTS

3.1 Suitable inner angle for fish to remain in the flow

Sculpin could not remain in 0.5 m/s of flow when the internal angle of the eaves was 12.5 or 25 degrees. In the case of 10-degree eaves, they fit their bodies between the eaves and the pipe bottom. An eave with an inner angle of 10 degrees or less seems suitable for enabling sculpin to remain.

3.2 Roughness for free movement

Roughness on the inner side of the eaves improved the migration of both sculpin and goldfish. A combination of roughness both under the eaves and on the bottom of the experiment pipe (*i.e.*, a V-shaped roughness), gave the best results for the sculpin and goldfish to remain and migrate goldfish. Eaves at angles of 7.5 and 10 degrees and having a small amount of roughness on the bottom brought about upstream movement of sculpin in 0.5 m/s flow, but it was passive. The V-shaped roughness improved the upstream migration activity of sculpin in 1.0 m/s flow and of goldfish in 0.3 m/s flow. The corridor consisting of roughed bottom and roughed eaves with internal angles of 7.5, 10, and 12.5 degrees were suitable for their migration. Artificial lawn worked as a means of providing roughness for this range of internal angles, but the 25-degree eave did not give good results in terms of sculpin movement and their ability to remain.

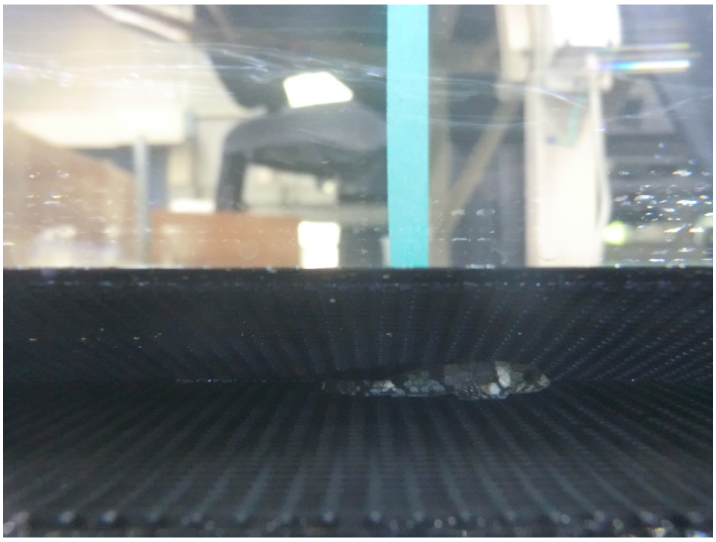

Figure 1. Sculpin staying on the corner of eave with internal angles of 12.5 degree.

4 DISCUSSIONS

Eaves with internal angles under 12.5 degrees improved the activity of sculpin and goldfish. A cloister consisting of such eaves could be installed not only in fish passages but also in existing facilities such as channels, the slanted faces of artificial facilities, and under the gates of dams. It is a simple method to improve fish migration in established fish passages and meets the objectives of being rapid, economical, and wide-ranging in its effectiveness.

Additionally, these results seem consistent with natural conditions. Our field survey has shown that juvenile sculpin use a habitat consisting of pebbles whose diameters are similar in size to their body length. Assuming the pebbles are spherical in shape, the inclination of the line tangential to the pebble and the head of the sculpin is almost the same as the internal eave angle found to be most suitable. The roughness on a narrow area of the eave works as a device to prevent fish from slipping and decreases flow velocity over it, thus acting to improve sculpin activity. Therefore, a juvenile sculpin possibly chooses a pebble similar in size to its body size to stabilize against flow until it grows large enough to swim strongly. Thus, variation of pebble size in habitats may be necessary for effective sculpin growth.

ACKNOWLEDGEMENTS

Many thanks the staffs of the Public Works Research Institute. Thanks are extended to Fukuda, Kikuchi and Kanazawa for their support of the experiment and data analysis.

REFERENCES

Baras, E., Lambert, H. & Philippart, J.G. (1994). A Comprehensive Assessment of the Failure of Barbus Barbus Spawning Migrations through a Fish Pass in the Canalized River Meuse (*Belgium*). *Aquatic Living Resour*ce 7, 181-189.

Cheong, T.S., Kavvas, M.L. & Anderson, E.K. (2006). Evaluation of Adult White Sturgeon Swimming Capabilities and Applications to Fishway Design. *Environment Biology Fisheries,* 77, 197-208.

Cooke, S.J. & Hinch, S.G. (2013). Improving the Reliability of Fishway Attraction and Passage Efficiency Estimates to Inform Fishway Engineering, Science, and Practice. *Ecological Engineering,* 58, 123-132.

Foulds, W.L. & Lucas, M.C. (2013). Extreme Inefficiency of Two Conventional, Technical Fishways used by European River Lamprey (*Lampetra fluviatilis*). *Ecological Engineering*, 58, 423-433.

Ghimire, S. & Jones, G. (2014). Restoration of a Gauging Weir to Aid Fish Passage. *Journal of Hydrological Environment Research,* 8(1), 43-49.

Jenkins, M. (2003). Prospects for Biodiversity. *Science*, 302(5648), 1175-1177.

Katopodis, C. (2005). Developing a Toolkit for Fish Passage, Ecological Flow Management and Fish Habitat Works. *Journal of Hydraulic Research,* 43, 451-457.

Kerr, J.R., Karageorgopoulos, P. & Kemp, P.S. (2015). Efficacy of a Side-Mounted Vertically Oriented Bristle Pass for Improving Upstream Passage of European Eel (*Anguilla Anguilla*) and River Lamprey (*Lampetra Fluviatilis*) at an Experimental Grump Weir. *Ecological Engineering*, 85, 121-131.

Moyle, P.B., Katz, V.E. & Quiñones, R.M. (2011). Rapid Decline of California’s Native Inland Fishes: A Status Assessment of *Biological Consevation.* 144, 2414–2423.

Perkin J.S., Gido, K.B., Táani, O. & Scoglio, C. (2013). Simulating Fish Dispersal in Stream Networks Fragmented by Multiple Road Crossings. *Ecological Modelling* 257, 44-56.

Rajaratnam, N. & Katopodis, C. (1994). *Fish Protection, in; Hino (Ed.) Water Quality and its Control.* International Association for Hydraulic Research, Hydraulic Structure Design Manual 5, Chapter 9: 243-255.

Rodríguez, T.T., Agudo, J.P., Mosquera, L.P. & Gonzalez, E.P. (2006). Evaluating Vertical-Slot Fishway Designs in Terms of Fish Swimming Capabilities. *Ecological Engineering* 27, 37-48.

Santos, J.M., Branco. P., Katopodis, K., Ferreira, T. & Pinheiro, A. (2014). Retrofitting Pool-and-Weir Fishway to Improve Passage Performance of Benthic Fishes: Effect of Boulder Density and Fishway Discharge. *Ecological Engineering* 73, 335-344.

Silva, A.T., Katopodis, C., Santos, J.M., Ferreira, M.T. & Pinheiro, A.N. (2012). Cyprinid Swimming Behaviour in Response to Turbulent Flow. *Ecological Engineering* 44, 314-32.

 ©2017, IAHR. Used with permission / ISSN 1562-6865 (Online) - ISSN 1063-7710 (Print)

FISH GUIDANCE STRUCTURES: NEW HEAD LOSS FORMULA AND FISH GUIDANCE EFFICIENCIES

ROBERT M. BOES[(1)] & ISMAIL ALBAYRAK[(2)]

[(1,2)] Laboratory of Hydraulics, Hydrology and Glaciology (VAW), ETH Zurich, Zurich, Switzerland
boes@vaw.baug.ethz.ch; albayrak@vaw.baug.ethz.ch

ABSTRACT

The installation of hydropower plants (HPP) and dams may cause problems for the fish fauna, such as blocking or delaying up- and downstream fish migration, injury or mortality of fish when passing turbines or spillways, and mortality due to predation by fish or birds. As a result, species population can decline. To counter these negative impacts for the downstream migration, fish protection systems and downstream migration facilities have recently been focused on the framework of re-establishing river continuity for the fish fauna. Etho-hydraulic research results on angled fish guidance structures (FGS) with vertical bars indicate that the modified version of conventional louvers and angled bar racks, i.e. modified angled bar racks (MBR), is a viable option and potentially applicable at prototype HPP. This paper presents the results of two experimental investigations on such FGS conducted at VAW of ETH Zurich.

Keywords: Downstream fish migration; fish guidance efficiency; fish guidance structure; head loss; modified angled bar rack.

1 INTRODUCTION

Hydropower plants (HPP) and dams in rivers may cause blocking or delaying up- and downstream fish migration and injury or mortality of fish when passing through turbines or spillways (Larinier and Travade, 2002). As a consequence, species populations can decline. To mitigate the negative impacts of HPP on fish migration, new fish passage facilities and connections to adjoining waterbodies must be erected, and existing structures must be reviewed and may have to be adapted if they do not function properly. Among downstream fish protection technologies for run-of-river hydropower applications, fish guidance structures (FGS), i.e. louver and angled bar racks, are successfully used to protect anadromous fish and guide them to a bypass (Bates and Vinsonhaler, 1957; Taft et al., 1976; EPRI, 1998; Amaral et al., 2003). FGS are classified as mechanical behavioral fish protection barriers, which may also function like physical barriers, depending on fish size and bar spacing (EPRI & DML, 2001).

Louvers consist of vertical bars placed at a bar angle β = 90° to the flow direction, mounted in a rack (Figure 1a). The main rack angle to the flow direction typically varies between α = 15° and 45°. Classical angled bar racks differs from louvers with a variable bar angle $\beta = 90°-\alpha$, since their bars are placed at 90° to the rack axis (Figure 1b). In addition to the former, a new FGS with an independent variation of α and β was investigated (Kriewitz-Byun, 2015; Albayrak et al., 2017). These FGS with $\beta \neq 90°-\alpha$ are termed modified angled bar racks (MBR) hereafter (Figure 1b). These three different FGS function similarly but differ from each other with resulting head loss and up- and downstream flow fields. In general, they create highly turbulent flow zones, flow separations around the bars, and changes in flow velocities and directions so that fish can sense them and react with behavioral avoidance (Amaral, 2003). The main angle α (15°- 45°), clear bar spacing b (25 -100 mm) and bypass design are important basic parameters of a FGS (Amaral, 2003; Amaral et al., 2003) (Figure 1). For an improved FGS design, biological parameters such as target fish behavioural patterns, swimming capabilities and size classes must also be considered (OTA, 1995; Amaral et al., 2003).

On the one hand, fish protection and guidance efficiency of FGS is of prime importance for the fish fauna. On the other hand, their effects on hydropower production due to head loss and change in turbine approach flow field have to be considered for sustainable use of HPP. To this end, Raynal et al. (2013) studied head losses caused by angled bar racks for a range of rack parameters in a 1:2 Froude scale model. These are: (I) rectangular and hydrodynamic bar shapes, (II) bar spacings ranging from b = 10 to 30 mm at prototype scale, and (III) α = 30, 45, 60 and 90°. Based on a regression analysis between the parameters, they developed a head loss prediction formula. Recently, Kriewitz-Byun (2015) and Albayrak et al. (2017) investigated not only angled bar racks but also louvers and MBR with b = 50 to 230 mm and a wide range of parameters under various flow conditions in a 1:2 Froude scale model and introduced a new head loss formula. The present study reports their results and formula, and expand its parameter range by including the effect of bypass flow and bottom overlay (BO) on the head loss. For the latter, a 1:1 Froude scale model study was conducted at VAW of ETH Zurich (Moretti, 2015). In addition, this study briefly reports the fish guidance efficiencies (FGE) of the selected FGS tested with five fish species, namely barbel, spirlin, grayling, eel and brown trout.

©2017, IAHR. Used with permission / ISSN 1562-6865 (Online) - ISSN 1063-7710 (Print)

The overarching goal of the present study was to improve the sustainable and efficient usage of hydropower by providing detailed geometric and hydraulic information on FGS for optimum engineering solutions accounting for head loss, safe fish guidance and project cost-benefit ratio.

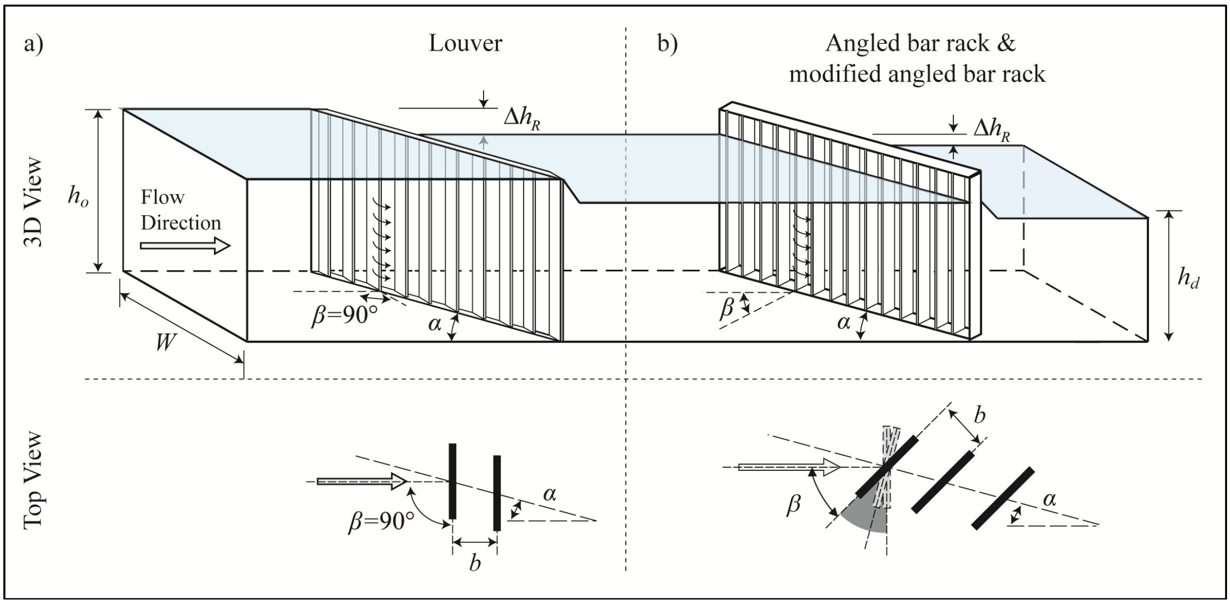

Figure 1. Detailed geometric view of louver, angled bar rack and modified angled bar rack (MBR).

2 EXPERIMENTATION

2.1 Test set-ups

Hydraulic head losses were systematically investigated for louvers, angled bar racks and MBR. The experiments were conducted at Froude models of scale (1) 1:2 in a 0.5 m wide, 0.6 m deep and 12 m long glass-sided laboratory flume without bypass ('small flume', Figure 2a) and (2) 1:1 in a 1.5 m wide, 1.2 m deep and 30 m long etho-hydraulic flume with a bypass ('large flume', Figure 2b) for a wide range of rack configurations and hydraulic conditions. Note that in contrast to the small flume there was a bypass (subscript *b*) with a width $W_b \approx 0.13W$, with W = width of the approach flow channel, in the large flume. Moreover, in the latter the FGS were tested with/without a bottom overlay (BO) with a height of 11% of the maximum water depth, i.e. 0.10 m. The discharges in both flumes were regulated with a frequency-controlled pump and measured with a magnetic inductive discharge meter (MID) of ±0.5% accuracy. The water depth h was measured using ultrasonic distance sensors (UDS) of ±0.5% accuracy along three longitudinal tracks. Two tracks were $0.10W$ away from the respective flume wall, while the other track was at the flume center axis. The average up- and downstream water depths h_o and h_d were determined by three individual measurements while the bypass water depths h_b were determined by one-point measurements (large flume).

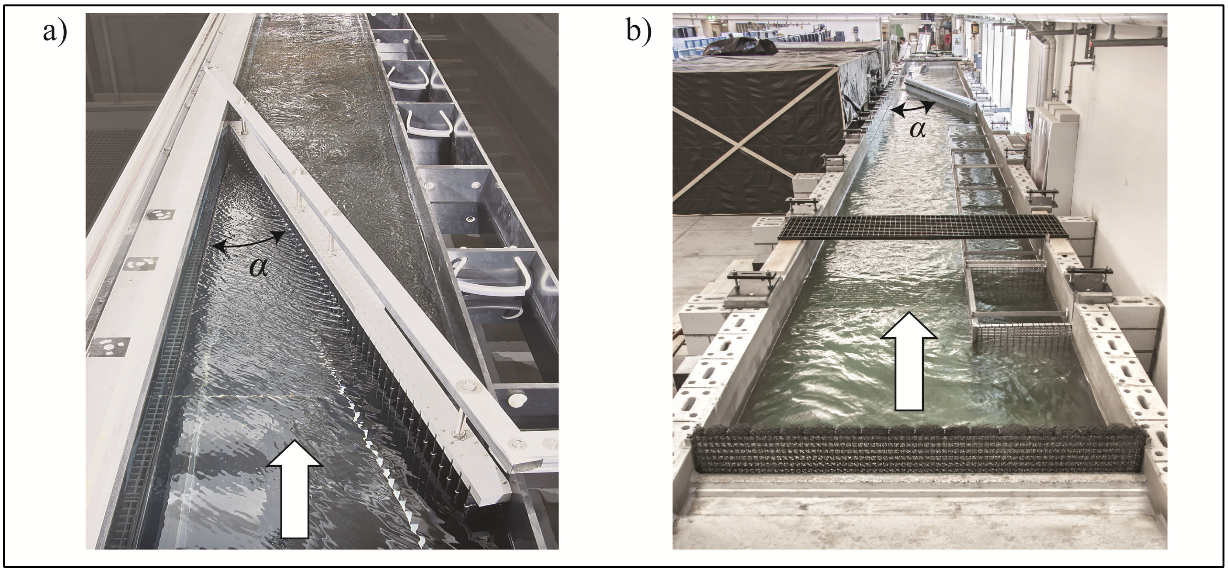

Figure 2. Photos of (a) small and (b) large scale flumes with louver placed at α = 15° to flow direction.

 ©2017, IAHR. Used with permission / ISSN 1562-6865 (Online) - ISSN 1063-7710 (Print)

2.2 Parameter range and test program

The main geometric rack characteristics are: α = 15, 30 and 45°, β = 45, 67.5 and 90° and b = 5, 11, and 23 cm or axial bar spacing $B = b + s$ = 6, 12 and 24 cm, and the secondary parameters are: bar thickness s = 1 cm, bar depth l = 7.5, 10 and 12.5 cm, bar shape K and rack submergence depth h_s (Figure 3). The rectangular and rounded bar shape coefficients are denoted by K_s and K_r, respectively (Figure 3b). The non-dimensional axial distance between the bars is $\sigma = s/B$ = 0.042, 0.083 and 0.167, and the non-dimensional bar depth is $\varepsilon = l/L$ = 0.75, 1 and 1.25, receptively, with L = 0.10 m as the reference bar depth. The relative rack submergence $\kappa = h_s/h_o$ = 0.33, 0.67 and 1 is a further non-dimensional parameter (Figure 3c). All dimensional parameter values refer to the 1:1 Froude-scaled model tests and thus they were scaled accordingly for the 1:2 Froude-scaled model tests.

The upstream, bypass and FGS discharges are denoted by Q, Q_b and $Q_F = Q - Q_b$, respectively, and $\theta = Q_b/Q$ denotes the relative bypass discharge. The depth-averaged upstream flow velocity is $U_o = Q/(h_oW)$ and the depth-averaged downstream velocities for the small and large flume tests are $U_d = Q/(h_dW)$, and $U_d = Q_F/(h_d(W - W_b - 0.10)) \approx Q_F/(h_d(0.87W - 0.10))$, respectively (Figure 3). The depth-averaged bypass velocity is $U_b = Q_b/(h_bW_b) \approx Q_b/(0.13h_bW)$ (Figure 3). The bar Reynolds number R_b based on the bar thickness s, the Reynolds number R based on the hydraulic radius R_h and Froude number F are defined as (Table 1)

$$\mathsf{R}_b = U_o s / \nu \quad [1]$$

$$\mathsf{R} = 4U_oR_h / \nu \quad [2]$$

$$\mathsf{F} = U_o / \sqrt{gh_o} \quad [3]$$

where ν is the kinematic viscosity of water ($\nu = 1\times10^{-6}$ for T = 20°C, with T = water temperature) and g = gravity acceleration.

Detailed information on the experimentation and the entire results has been published by Kriewitz-Byun (2015) and Albayrak et al. (2017) for small scale tests and by Moretti (2015) and Boes et al. (2016) for the large scale tests. Therefore, only selected rack configurations from those tests are presented in this paper. The hydraulic and rack parameters of selected configurations from small and large scale tests are listed in Table 1. In the tests, the rectangular bars K_s were used and the bar lengths were l = 5 and 10 cm for the small and large scale tests, respectively. The test series are denoted as "S" for the former and "L" for the latter, respectively.

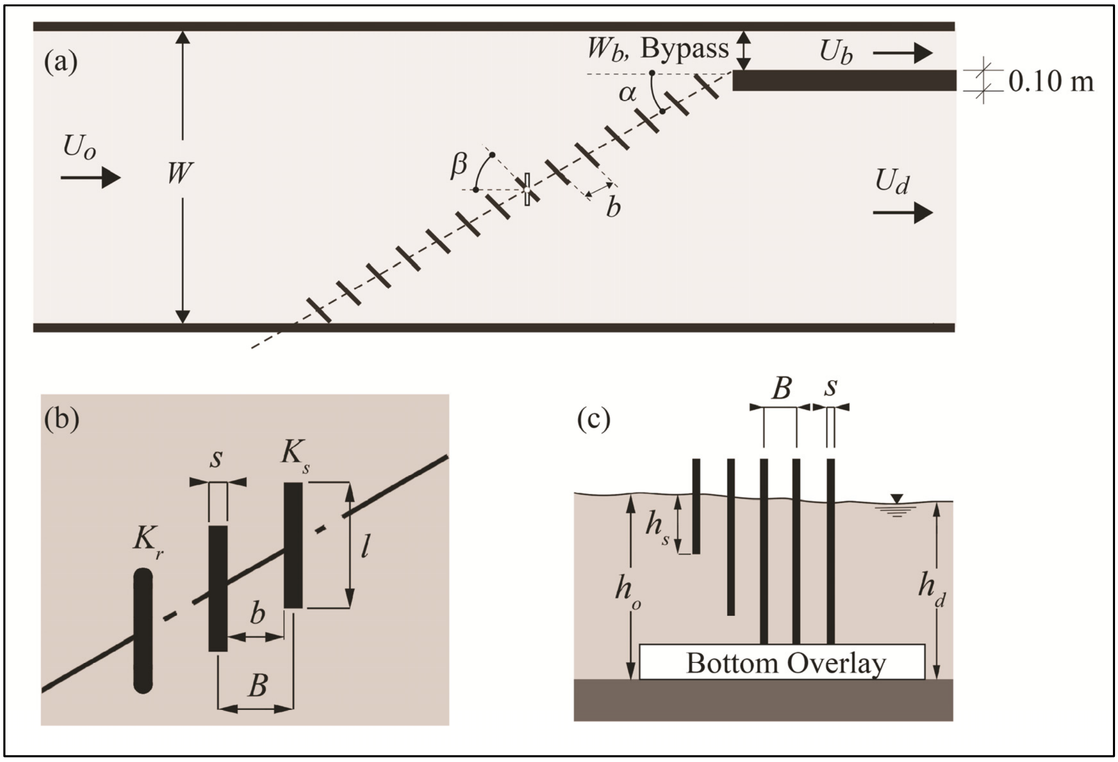

Figure 3. Geometric and hydraulic rack parameters: (a) top view, (b) rack detail, (c) side view.

Table 1. Hydraulic and rack parameters of the experiments (Kriewitz-Byun, 2015; Moretti, 2015; Boes et al., 2016; Albayrak et al., 2017).

Test	α (°)	β (°)	h_o (m)	σ (cm)	U_0 (m/s)	Q_o (m^3/s)	BO	R (10^5)	R_b (10^3)	F	Q_B (m^3/s)	Q_F (m^3/s)	θ
S1	15	90	0.46	0.167	0.38	0.087	-	2.46	1.9	0.18	-	0.087	0
S2	30	90	0.43	0.167	0.29	0.062	-	1.83	1.4	0.14	-	0.062	0
S3	45	90	0.47	0.167	0.34	0.080	-	2.21	1.7	0.16	-	0.080	0
S4	15	45	0.44	0.167	0.59	0.130	-	3.76	2.9	0.28	-	0.130	0
S5	30	45	0.44	0.167	0.55	0.121	-	3.50	2.7	0.26	-	0.121	0
S6	45	45	0.44	0.167	0.40	0.088	-	2.55	2.0	0.19	-	0.088	0
S7	15	45	0.43	0.083	0.59	0.127	-	3.73	2.9	0.28	-	0.127	0
S8	15	45	0.43	0.042	0.59	0.127	-	3.73	2.9	0.28	-	0.127	0
L1	15	90	0.90	0.167	0.60	0.810	-	9.82	6	0.20	0.113	0.697	0.140
L2	15	90	0.90	0.167	0.60	0.810	X	9.82	6	0.20	0.108	0.702	0.133
L3	15	45	0.90	0.167	0.60	0.810	-	9.82	6	0.20	0.118	0.692	0.146
L4	15	45	0.90	0.167	0.60	0.810	X	9.82	6	0.20	0.123	0.687	0.152
L5	30	45	0.90	0.167	0.60	0.810	-	9.82	6	0.20	0.112	0.698	0.138
L6	30	45	0.90	0.167	0.60	0.810	X	9.82	6	0.20	0.126	0.684	0.156

2.3 Live-fish experiments

In addition to the head loss experiments, live-fish experiments were also conducted in the large flume in collaboration with Eawag for the rack configurations L1-L6. Five fish species typically found in Swiss plateau rivers, i.e. barbel, spirlin, grayling, eel and brown trout, were tested. Some results from L3-L6 are presented in this study (Table 2), while the results of other configurations and a detailed description of the tests and fish species are reported by Kriewitz-Byun (2015) and Flügel et al. (2015).

Table 2. Rack parameters and tested fish species of the MBR configurations L3 to L6.

Test	Tested fish species
L3	barbel, spirlin, eel and brown trout
L4	barbel, eel and brown trout
L5	barbel, spirlin and grayling
L6	barbel, spirlin, eel, brown trout and grayling

3 RESULTS AND DISCUSSIONS

3.1 Head loss equation

The rack (subscript R) head losses Δh_R were experimentally determined for a large number of rack configurations tested in the 1:2 and 1:1 Froude-scaled models with and without bottom overlay (BO, Figure 3). Each rack configuration was tested at steady flow conditions with the approach flow velocities varied within $0.035 \le U_o \le 0.68$ m/s at 1:2 model scale, resulting in $0.05 \le U_o \le 0.96$ m/s for prototype conditions according to Froude's model similarity. In order to avoid scale effects, only the rack configurations with $R_b > 1500$ and relative depths of $h_o/s \ge 40$ with bar thicknesses $0.5 \le s \le 1$ cm and upstream water depths $0.4 \le h_o \le 0.9$ m were included to determine the rack head losses.

The rack head loss coefficient ξ_R was computed from:

$$\xi_R = \Delta h_R / (U_o^2 / 2g) \quad [4]$$

A formula for the total rack head loss coefficient ξ_R was developed from a regression analysis (Kriewitz-Byun, 2015; Moretti, 2015; Boes et al., 2016; Albayrak et al., 2017):

$$\xi_R = \xi_B \cdot C_L \cdot C_K \cdot C_S \cdot C_{By} \cdot C_{BO} \quad [5]$$

The head loss coefficients and factors in Eq. [5] are defined hereafter (Figure 3):

 ©2017, IAHR. Used with permission / ISSN 1562-6865 (Online) - ISSN 1063-7710 (Print)

- The basic (subscript B) head loss coefficient ξ_B is a function of the rack angle α, the bar angle β and the non-dimensional axial bar distance σ:

$$\xi_B = 245\left[0.0275 + (\sigma - 0.0815)\left(\frac{\alpha}{90°}\right)\right]\left(\frac{\beta}{90°}\right)^{5\sigma^{0.44}} \quad [6]$$

- The bar depth factor C_L is a function of α, σ and relative bar depth ε:

$$C_L = \varepsilon\left[1 + 9.4\sigma(1-\varepsilon) - 3.8(1-\varepsilon)\left(\frac{\alpha}{90°}\right)\right] \quad [7]$$

- The relative bar submergence factor C_κ is a function of σ and κ:

$$C_\kappa = \kappa^{6.6\sqrt{\sigma}} \quad [8]$$

- The bar shape factor C_s, is a function of α and σ:

$$C_S = 0.75 + \left(\frac{62° - \alpha}{90°}\right)4.5\sigma \quad [9]$$

- The bypass factor C_{By} is a function of θ and β:

$$C_{By} = 1 - \theta^{1.15\sin(\beta)} \quad [10]$$

- The bottom overlay factor C_{BO} is function of β. If no BO is installed, C_{BO} is equal to 1.

$$C_{BO} = 0.82(\sin(\beta))^{-0.8} \quad [11]$$

Equations [5]-[11] apply to rectangular and rounded bars without and with BO (here with a relative height of $0.11h_o$) and for the following parameter range: $15° \le \alpha \le 45°$; $45° \le \beta \le 90°$; $0.042 \le \sigma \le 0.167$; $0.75 \le \varepsilon \le 1.25$; $0.325 \le \kappa \le 1.0$ and $0 \le \theta \le 0.156$. The latter parameter covers the general relative discharge θ for bypass operation ranging from about 1% to 10% of Q according to worldwide experience, i.e. $0.01 \le \theta \le 0.1$. For angled racks with horizontal bars Ebel (2013) recommends θ = 0.02 to 0.05 and θ = 0.05 to 0.10 for oblique and frontal approach flow in plan view, respectively. Note that the parameters C_L, C_κ and C_S were determined for selected louver configurations, i.e. for β = 90°, and hence their application to classical and modified angled bar racks is only recommended for rough estimates.

In Figure 4, the measured (subscript M) head loss coefficients $\xi_{R,M}$ are plotted versus their corresponding predicted (subscript P) values $\xi_{R,P}$, using Eqs. [5]-[11] for the selected rack configurations: eight (S) from Kriewitz-Byun (2015) and six (L) from Moretti (2015) (Table 1). The predicted $\xi_{R,P}$ values match well with the measured $\xi_{R,M}$ values. From Figure 4, $\xi_{R,P}$ deviates from $\xi_{R,M}$ by 4% on average with a standard deviation of 6% and a maximum deviation of 15%. With the proposed new Eq. [5], head losses can be estimated for FGS with/without BO and for varying relative bypass discharges.

Figure 4 also highlights the effects of bar and rack parameters on the head loss coefficient ξ_R. The following relations are derived:

- Increasing the axial bar spacing B, i.e. decreasing σ, decreases ξ_R.
- Increasing α results in increasing ξ_R for both louver and MBR.
- Increasing β increases ξ_R; louvers cause significantly higher head losses compared to MBR, i.e. up to 5 times.
- Head loss values ξ_R are slightly lower for the 1:1 Froude-scaled model than for the 1:2 Froude-scaled model due to the effect of bypass.
- A BO particularly reduces ξ_R for louvers due to improved upstream and downstream flow field (Moretti, 2015) whereas it slightly increases ξ_R for MBR.

In summary, the newly modified angled bar rack configurations MBR are advantageous to highly reduce ξ_R compared to classical bar racks and louvers.

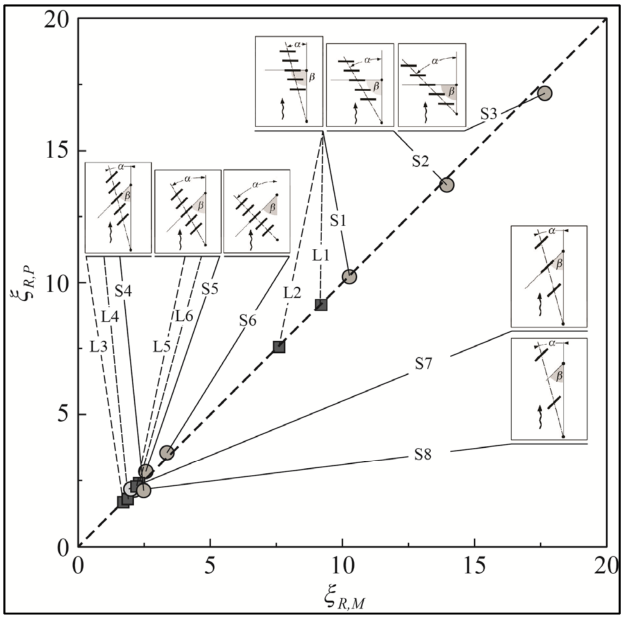

Figure 4. Comparison of the measured head loss coefficient $\xi_{R,M}$ with the calculated head losses coefficients $\xi_{R,P}$ for eight rack configurations from Kriewitz-Byun (2015) and six with bypass from Moretti (2015) (adapted from Boes et al., 2016).

3.2 Fish guidance efficiency

The FGE is defined as the percentage of fish successfully bypassed. The FGE of four MBR configurations were determined from the live-fish tests with five fish species (barbel, spirlin, grayling, eel and brown trout) (Table 2, Figure 5a) and the results are shown in Figure 5b. The FGE of L3 with a mild rack angle α = 15° is distinctly higher than that of L5 with α = 30°, which is in agreement with EPRI and DML (2001). However, this large difference is attributed to the highly differentiated behavior of grayling, which were tested only for the MBR with α = 30° (L5). For L5 without a BO, 65% of the graylings avoided to enter the bypass due to sudden flow velocity decrease at the bypass entrance. This condition was improved with the implementation of the BO, i.e. L6 (Figure 5b), resulting in a greatly increased FGE of 96% for grayling. Therefore, it is hypothesized that by optimizing the bypass flow conditions, which were unchanged for all rack configurations, the acceptance of graylings to enter the bypass can be increased even without the use of a BO (Kriewitz-Byun, 2015).

Overall, a BO significantly increases the FGE (L4 and L6) compared to non-BO configurations (L3 and L5). The mean cross-species averaged FGE of both L4 and L6 was ≥90% with a negligible difference between them, while the minimum FGE of L4 and L6 was 75% and 78%, respectively (Figure 5b).

In summary, the newly modified angled bar rack configurations MBR feature higher FGE compared to louvers which were also tested as to fish behavior in the research study of Kriewitz-Byun (2015) but not detailed herein.

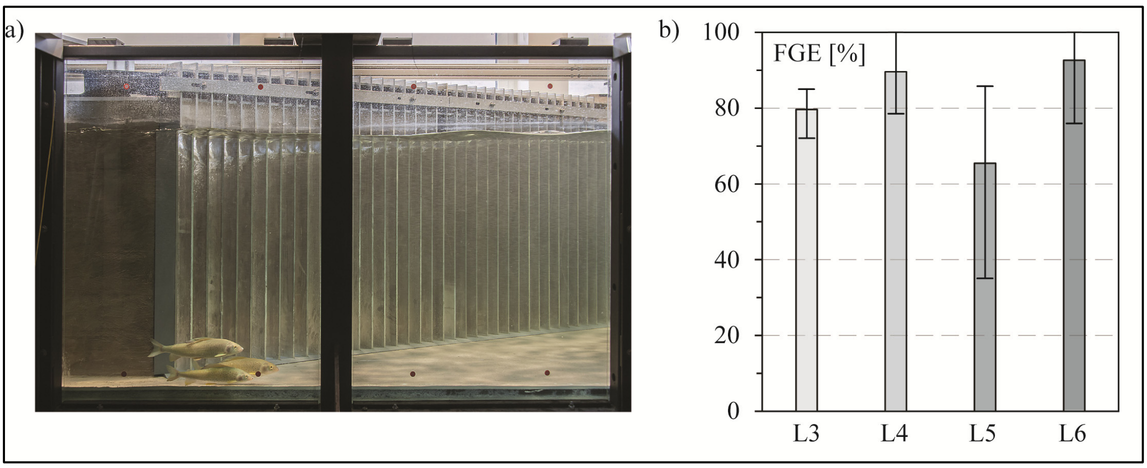

Figure 5. (a) Live-fish test (etho-hydraulic model test) with modified angled bar rack (MBR), bypass system (on the left) and fish species of grayling (photo: Flügel) and (b) mean, minimum and maximum cross-species averaged FGE for the rack configurations L3-L6 (Kriewitz-Byun, 2015; Boes et al., 2016).

©2017, IAHR. Used with permission / ISSN 1562-6865 (Online) - ISSN 1063-7710 (Print)

4 CONCLUSIONS

Hydraulic head losses were systematically investigated for a wide range of rack configurations at 1:1 and 1:2 Froude-scaled models at VAW of ETH Zurich. The results of this investigation enable the prediction of head losses at angled FGS with vertical bars including a new, modified version of angled bar racks, so called MBR, where the main angle α and the bar angle β were modified independently to further improve the applicability of FGS at HPP. Given the highly reduced head loss combined with a better FGE compared to louvers, this study recommends the use of MBR at pilot HPP to test their applicability under large-scale operating conditions.

ACKNOWLEDGEMENTS

The authors are greatly thankful for the support of Verband Aare-Rheinwerke (VAR), swisselectric research, the Swiss Federal Office of Energy (SFOE, BFE) and the Swiss Federal Office for the Environment (FOEN, BAFU). The study has been conducted in the framework of the Swiss Competence Center for Energy Research – Supply of Electricity (SCCER-SoE). The works of C.R. Kriewitz-Byun and G. Moretti are highly appreciated.

REFERENCES

Albayrak, I., Kriewitz, C.R., Hager, W.H. & Boes, R.M. (2017). An Experimental Investigation on Louvers and Angled Bar Racks. *Journal of Hydraulic Research,* 3, 1-17.

Amaral, S.V. (2003). *The use of Angled Bar Racks and Louvers for Guiding Fish at FERC-Licensed Projects.* FERC Fish Passage Workshop, Holden, USA.

Amaral, S.V., Winchell, F. C., McMahon, B.J. & Dixon, D. (2003). Evaluation of Angled Bar Racks and Louvers for Guiding Silver Phase American Eels. *Proceedings of Biology, Management and Protection of Catadromous Eels*, 367-376.

Bates, D.W. & Vinsonhaler, R. (1957). Use of Louvers for Guiding Fish. *Transactions of the American Fisheries Society*, 86(1), 38-57.

Boes, R., Albayrak, I., Kriewitz, C.R. & Peter A. (2016). Fischschutz und Fischabstieg mittels vertikaler Leitrechen-Bypass-Systeme: Rechenverluste und Leiteffizienz ('Fish protection and downstream fish migration by means of guidance systems with vertical bars: head loss and bypass efficiency'). *WasserWirtschaft*, 7(8), 29-35. (in German)

Ebel, G. (2013). Fischschutz und Fischabstieg an Wasserkraftanlagen - Handbuch Rechen- und Bypasssysteme ('Fish Protection and Fish Downstream Migration at Hydropower Plants – Handbook for Rack- And Bypass Systems'). *Mitteilungen aus dem Büro für Gewässerökologie und Fischereibiologie*, 4. (in German)

EPRI (Electric Power Research Institute). (1998). *Review of Downstream Fish Passage and Protection Technology Evaluations and Effectiveness* (EPRI Report No. TR-111517), Palo Alto, CA: EPRI.

EPRI (Electric Power Research Institute) & DML (Dominion Millstone Laboratories) (2001). *Evaluation of Angled Bar Racks and Louvers for Guiding Fish at Water Intakes* (Report No. 1005193), Palo Alto, CA and Waterford, CT: EPRI.

Flügel, D., Peter A. & Bös T. (2015). Untersuchungen zum Fischabstieg entlang eines vertikalen, schräg ausgerichteten Fischleitrechens an grösseren mitteleuropäischen Flusskraftwerken - Ethohydraulische Untersuchungen in einem Versuchsgerinne ('Investigation on Downstream Fish Migration along Vertical, Angled Fish Guidance Screens - Ethohydraulic Investigations in a Laboratory Flume').*Eawag, Kastanienbaum*, Switzerland (in German).

Kriewitz-Byun, C.R. (2015). Leitrechen an Fischabstiegsanlagen - Hydraulik und fischbiologische Effizienz, *Doctoral Dissertation*. ETH Zurich, Switzerland. (in German)

Larinier, M. & Travade, F. (2002). Downstream Migration: Problems and Facilities. *Bull. Fr. Peche Piscic*, *364*, 181-207.

Moretti, G. (2015). Strömungsstrukturen um fischleitende Strukturen ('Flow Field around Fish Guidance Structures'). *Master Thesis*, Laboratory of Hydraulics, Hydrology and Glaciology (VAW), ETH Zurich, Switzerland. (in German)

OTA (Office of Technology Assessment). (1995). *Fish Passage Technologies: Protection at Hydropower Facilities*, OTA-ENV-641, Washington, DC: U.S. Govt. Printing Office.

Raynal, S., Chatellier, L., Courret, D., Larinier, M. & Laurent, D. (2013). An Experimental Study on Fish-Friendly Trashracks - Part 2. Angled Trashracks. *Journal of Hydraulic Research*, 51(1), 67-75.

Taft, E. P., Hofmann, P., Eisle, P.J. & Horst, T. (1976). An Experimental Approach to the Design of Systems for Alleviating Fish Impingement at Existing and Proposed Power Plant Intake Structures. *Proceeding of the Third National Workshop on Entrainment and Impingement*, New York, 343-365.

Proceedings of the 37th IAHR World Congress
August 13 – 18, 2017, Kuala Lumpur, Malaysia

FLOW RESISTANCE OF SUBMERGED RIGID VEGETATION: FOCUS AND VALIDATION ON TWO LAYER APPROACH

VITTORIO PASQUINO[(1)] & PAOLA GUALTIERI[(2)\]

[(1,2)] Department of Civil, Construction and Environmental Engineering, University of Naples "Federico II", Napoli, Italy,
vittorio.pasquino@unina.it; paola.gualtieri@unina.it

ABSTRACT

Vegetation behavior in riparian environment represents an important research topic in hydraulics and ecohydraulics. Therefore, one of the most important research challenges is to deepen interactions between flow and vegetation, in order to better understand its effects on flow resistance and turbulent characteristics of the flow. In vegetated flow models, the flow regime is often separated in two layers: vegetated layer and surface layer. Flow resistance models, based on two-layer approach, are often tested with experimental data relative to vegetation density and submergence ratio (i.e., the ratio between h=flow depth and h_v=vegetation height, h/h_v) varying in wide ranges. The aim of the paper is to deepen how variability of submergence ratio and the non-dimensional vegetation density can affect the reliability of the flow resistance models. In particular, in this paper, the results of the statistical test applied to the most cited and used literature models for evaluating the flow resistance of rigid vegetation, are shown. The tests have been carried out with experimental data from literature, by the mean of different statistical parameters, considering the different ranges of vegetation density and submergence ratio. The results show that vegetation density and submergence ratio can affect the reliability of the model.

Keywords: Rigid vegetation; two-layer approach; flow resistance; density; submergence.

1 INTRODUCTION

The academic community is highly involved in contrasting floods and rainfall critical events due to the climate change by using natural and ecological alternatives and focusing on the importance of river rehabilitation. If in the past, the vegetation was considered as an unwanted source of flow resistance, it is nowadays usual to remove obstacles in river beds and leave vegetation growing in river beds, banks and edges, considering that vegetation has been proved to enhance soil stabilization, clean water and generally improving all the ecosystem balance.

The degree of influence in a vegetative channel depends on vegetation characteristics such as (a) flexibility, (b) distribution (i.e. density of the vegetation) and (c) degree of submergence. Physical and numerical models need to represent vegetation in a schematic, easily-quantifiable way, despite the variety of sizes, shapes and flexibility of real plants. In literature, most common approaches in laboratory tests and numerical simulations is to represent plants as rigid cylinders. Recently, the ability of these schematizations to reproduce the effects of vegetation on flow resistance and morphodynamic processes has been systematically tested (Vargas-Luna et al., 2015). In literature, for vegetated flows, rigid cylinders analogy is adopted in numerical and experimental works in different hydraulic conditions (Wu and Marsooli, 2012; Jahra et al., 2011; Bai et al., 2016; Chakraborty and Sarkar, 2016). As it is well known, open channel flow with submerged cylindrical roughness can be envisioned as two interacting flow layers: the vegetation layer, containing the cylindrical elements, and the surface layer, above them, up to the flow depth.Many flow resistance laws based on the two-layer model were developed (Stone and Shen, 2002; Huthoff et al., 2007; Baptist et al. 2007; Yang and Choi, 2010; Cheng, 2011; Li et al., 2015), where, in the vegetation layer, velocity is generally considered constant with the flow-depth, while, in the surface layer, different expressions of the flow velocity, with different theoretical background, are proposed. The two distributions are matched at the separation surface and, from the resulting distribution, the mean cross-sectional velocity is obtained, and the flow resistance is evaluated. For the velocity distribution in the surface layer, the most applied approaches are the logarithmic theory, in Stone and Shen (2002) and Yang and Choi (2010), the Kolmogorov theory of turbulence and its new approach developed by Gioia and Bombardelli (2002), in Huthoff et al. (2007; 2013), the genetic programming, developed by Baptist et al. (2007) the representative roughness height, proposed by Cheng (2011) and a new expression of the representative roughness height, proposed by Li et al. (2015). As mentioned before in all these works, the flow resistance is largely affected by two key parameters, that is the submergence (i.e., the ratio between h=flow depth and h_v=vegetation height, h/h_v) and the non-dimensional vegetation density $\lambda=mDh_v$, (m=numbers of cylinders per unit area, D=cylinder's diameter) that represents the frontal area of the cylinders impacting flow. Focusing on these two parameters, Huthoff et al. (2007), Augustijn

 ©2017, IAHR. Used with permission / ISSN 1562-6865 (Online) - ISSN 1063-7710 (Print)

et al. (2008), Nepf (2012b), Pasquino et al. (2016), pointed out that as the submergence ratio increases the shear layer resembles a boundary layer, in particular for h/h_v>5.

Again, Belcher et al. (2003) and successively Nepf (2012a; 2012b) describe three different regimes in vegetated beds, depending on vegetation density: sparse (λ <<0.1), transitional (λ ≈0.1), and dense (λ >0.23). For sparse vegetation, the shear layer resemble again a boundary layer, while for transitional and dense vegetation, the discontinuity at the top of the canopy generates a shear resembling a free shear layer, with an inflection point near the top of the canopy, in the velocity profile.

Effectively, in literature approaches, flow resistance models are generally tested merging all experimental data, without considering the performance of the model varying submergence and vegetation density. Considering the different behavior of the shear layer for different hydraulic conditions, and the different theoretical background of hydraulic models for vegetated beds, the performance of the most used two-layer model has been tested collecting 323 data from literature, for different combination of these two parameters.

2 STATE OF ART: THEORETICAL BACKGROUND AND FLOW RESISTANCE MODELS

As previously described, the two-layer approach divides the flow depth in two different layers. The first one, from the bottom of the channel to the top of the vegetation, called vegetation layer, and the second one, from vegetation's edge up to flow depth called surface layer (Figure.1). This approach is due to the different turbulent phenomena developing in vegetated flows. In fact, differently from boundary layer, vegetation causes a free shear layer with mixing layer characteristics (Raupach et al., 1996), due to the interaction between two parallel flows with different velocities. In particular, referring to mixing layer turbulence aspects, Nepf (2012b) observed that in the vegetation layer the stem-scale turbulence penetrates into the stems up to e δ= $[0.23 \pm 0.06](C_D a)^{-1}$ with a=non-dimensional vegetation density, expressed as the total roughness frontal area per unit ground area:

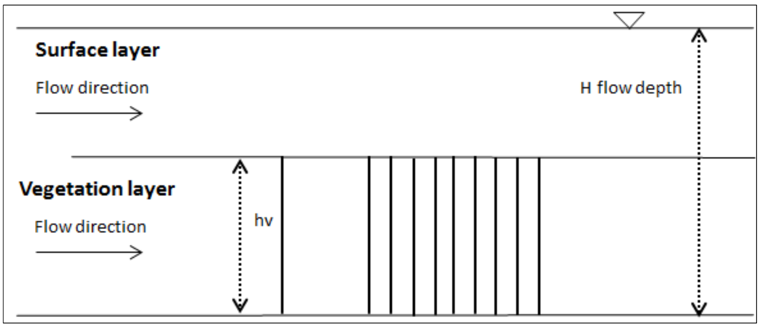

Figure 1. Typical scheme of the two layer approach in vegetated beds.

When for the vegetated flow the two layers approach is chosen, generally velocity distribution is considered constant in the vegetated layer and in the surface layer is expressed with a logarithmic law (Baptist et al., 2007; Yang and Choi, 2010) or with a power law (Huthoff et al., 2007). In particular, in the vegetation layer the most used approach considers the cylinder drag force expressed as follows (Douglas et al., 2005):

$$F_D = \frac{1}{2}\rho C_D A_p U^2 \qquad [1]$$

where C_D is the dimensionless drag coefficient, A_p is the frontal projected area of the vegetation elements, ρ is water density and U is the averaged velocity in the vegetation layer. In the surface layer the velocity distribution is expressed with a logarithmic law (Yang and Choi, 2010) or power law (Huthoff et al., 2007; 2013). It is noteworthy that nowadays there is a new trend in literature that reconsider the effective reliability of the Manning's formula (i.e. a power law) for all flow conditions (i.e. steady and unsteady) rather than Keleugan equation (i.e., a logarithmic law): (Ferguson 2010; Mrokowska et al. 2015). In Cheng (2011), a two-layer model, defining a representative roughness height for the vegetation and a new drag coefficient C_D, both related to vegetation density and to a new expression for hydraulic radius, was proposed. Successively Li et al. (2015), considered the representative roughness height in a new two-layer model, defined as dynamic two-layer model, obtained a flow resistance law. In order to better understand the different models proposed for the flow resistance, their theoretical backgrounds are synthetically described in the following paragraphs.

2.1 Stone and Shen (2002)

The authors developed a model expressing, initially, the bed shear stress with the Chèzy formula and successively defining an apparent velocity of the channel, U, derived from the area concentration of the stems. Expressing l^* as the ratio between the height of the vegetation and the flow depth (i.e., the inverse of the submergence), the authors described a relation between the mean velocity inside the vegetation layer U_V and l* as:

$$U_v = gSh(1 - \lambda l^*) \qquad [2]$$

where S is channel slope, h is flow depth, g is the gravity force and using the relation between U_v and U

$$U = \frac{U_v}{l*} \qquad [3]$$

They finally obtained:

$$U = \sqrt{\frac{2g}{C_D mD}}\sqrt{S}\left[(1 - D\sqrt{m})\sqrt{\left(\frac{h}{h_v} - \frac{1}{4}\pi m D^2\right)\frac{h}{h_v}}\right] \qquad [4]$$

where g, the gravity force, C_D the drag coefficient. The authors set the drag coefficient to a fixed value, C_D=1.05.

2.2 Huthoff et al. (2007)

The authors proposed an analytical solution of the depth-averaged flow velocity in case of rigid submerged vegetation, following the approach of Gioia and Bombardelli (2002), that derived theoretically Manning equation from Kolmogorov theory of turbulence (Frisch, 1995) and the concept of incomplete similarity (Barenblatt, 1986; 2003), so definitely obtaining:

$$U = \sqrt{\frac{2g}{C_D mD}}\sqrt{S}\left[\sqrt{\frac{h_v}{h}} + \frac{h-h_v}{k}\left(\frac{h-h_v}{(\frac{1}{\sqrt{m}}) - D}\right)^{\frac{2}{3}}\right] \qquad [5]$$

setting C_D =0.99.

2.3 Yang and Choi (2010)

The authors showed a two-layer depth averaged model applying a momentum balance to each layer and assuming a uniform velocity in the vegetation layer and the logarithmic law in the surface layer. In particular:

$$U = \left\{\sqrt{\frac{2g}{C_D mDh_v}} + \left[Cu\frac{\sqrt{g}}{\kappa}\left(\ln\left(\frac{h}{h_v}\right) - \frac{h-h_v}{h}\right)\right]\right\}\sqrt{hS} \qquad [6]$$

where κ is the vòn Kàrmàn constant and Cu is a parameter whose value is equal to 1 or 2, depending on the value of the product mD, less or more than 5, respectively, and fixing C_D =1.13

2.4 Baptist et al. (2007)

The authors developed a genetic programming using a set of 990 model simulation results of flow model with a huge variation of cylinders and hydraulic conditions. Definitely, C_D =1 they obtained setting:

$$U = \left(\sqrt{\frac{2g}{C_D mDh_v}} + \frac{\sqrt{g}}{\kappa}\ln\left(\frac{h}{h_v}\right)\right)\sqrt{hS} \qquad [7]$$

2.4 Cheng (2011)

The author, expressing the vegetation concentration as $\lambda c = \pi m D^2/4$ (i.e. the fraction of the bed area occupied by the stems), obtained:

$$U = \left[\sqrt{\frac{\pi(1-\lambda_C)^3 D}{2C_D \lambda_C k}}\left(\frac{h_v}{h}\right)^{3/2} + 4.54\left(\frac{h-h_v}{D}\frac{1-\lambda_C}{\lambda_C}\right)^{1/16}\left(\frac{h-h_v}{h}\right)^{3/2}\right]\sqrt{ghS} \qquad [8]$$

 ©2017, IAHR. Used with permission / ISSN 1562-6865 (Online) - ISSN 1063-7710 (Print)

The drag coefficient strictly depends on the value of a new expression of the hydraulic radius defined as r^* as $r^*=r(gS/v^2)^{1/3}$, where r= $(\pi/4)[(1-\lambda)/\lambda]\mathrm{D}$. The author proposed a new formulation for the drag coefficient C_D defined as:

$$C_D = \frac{130}{r^{*0.85}} + 0.8\left[1-\exp\left(-\frac{r^*}{400}\right)\right] \qquad [9]$$

2.5 Li et al.(2015)

The authors proposed the concept of the auxiliary bed, obtaining a dynamic two-layer model. Starting from the canopy penetration depth δ and considering the drag coefficient of Cheng (2011), the authors proposed a parameter named effective relative roughness height to estimate the friction factor of the suspension layer, obtaining:

$$U = \sqrt{gHS} + \left[\frac{1.96\left(h_s+\delta\right)^{\frac{5}{3}}}{\left(\lambda\delta\right)^{\frac{1}{6}} H^{\frac{3}{2}}} + (1-\lambda c)\frac{(h_v-\delta)\mathrm{h}^{*\frac{1}{2}}}{H^{\frac{3}{2}}}\right] \qquad [10]$$

where $h^*=2(1\text{-}\lambda c)/C_D a$ and $a=mD$. As mentioned before in the Introduction, Nepf (2012a; 2012b) pointed out the importance of vegetation density ah and submergence ratio. For ah<<0.1 vegetation can be considered as "sparse" and resemble a boundary layer when, for ah~0.1 the vegetation density is defined transitional and for ah>>0.1 (i.e. dense canopy) the mixing layer analogy can be considered as completely developed.

Furthermore, in Augustijn et al. (2008) it is well explained that for h/k>5 vegetation roughness can be approximated by a constant Manning coefficient n so, also in that hydraulic condition, the flow can be modelled by a boundary layer on a rough wall.Therefore, the different performance of various literature models can be probably also due to variability of the vegetation density and submergence in experimental test, that can affect the flow resistance formula. According to this consideration, in this paper flow resistance models proposed by Stone and Shen (2004), Huthoff et al. (2007), Baptist et al. (2007), Yang and Choi (2010), Cheng (2011) and Li et al. (2015), have been tested for different share of submergence and vegetation density.

3 MATERIALS AND METHODS

From literature, 323 experimental data have been collected (Shimizu et al., 1991; Dunn et al., 1996; Meijer and Van Velzen 1999; Lopez and Garcia, 2001; Stone and Shen, 2002; Poggi et al., 2004; Ghisalberti and Nepf, 2004; Murphy et al., 2007; Liu et al., 2008; Nezu and Sanjou, 2008; Yan, 2008; Yang, 2008; Cheng, 2011). First, experimental data were used to test each literature model, comparing calculated and measured velocity and plottng the results. In order to estimate the accuracy of the each models for the different condition of vegetation density and submergence, experimental data were divided in different ranges of vegetation density (i.e. sparse, transitional and dense) and submergence (i.e., low or high). In literature, by the knowledge of the Authors, there is not a unique statistical parameter to investigate hydraulic model performance for vegetated flows. For instance, Cheng (2011) and Li et al. (2015) used the relative prediction error ER; Huthoff et al. (2007), considered the coefficient of determination R^2 and the confidence interval for different geometric quantities in the model; Vargas-Luna et al. (2015) and Baptist et.al. (2007) used the coefficient of determination R^2 and the root mean square RMSE. In order to deepen the validity of every single formula for different hydrodynamic conditions, we decided to use six different statistical parameters, i.e. the root mean square RMSE, the mean absolute error MAE, the relative prediction error ER, the model efficiency EF, the coefficient of residual mass CRM and the mean bia deviation BIAS, hereafter described:

$$RMSE = \sqrt{\frac{\sum_{i=1}^{n}\left(x_{i-pred}-x_{i-meas}\right)^2}{n}};MAE = \frac{\sum_{i=1}^{n}\left|x_{i-pred}-x_{i-meas}\right|}{n};EF = \frac{\sum_{i=1}^{n}\left(x_{i-meas}-\bar{x}_{meas}\right)-\sum_{i=1}^{n}\left(x_{i-pred}-\bar{x}_{meas}\right)}{\sum_{i=1}^{n}\left(x_{i-pred}-\bar{x}_{meas}\right)^2} \qquad [11]$$

$$CRM = \frac{\sum_{i=1}^{n}\left(x_{i-pred}\right)-\sum_{i=1}^{n}\left(x_{i-val}\right)}{\sum_{i=1}^{n}\left(x_{i-meas}\right)};BIAS = \frac{\sum_{i=1}^{n}\left(x_{i-pred}-x_{i-meas}\right)}{n};ER = \frac{\sum_{i=1}^{n}\frac{\left|x_{i-pred}-x_{i-meas}\right|}{x_{i-meas}}}{n}$$

We decide to improve the statistical parameters including the MAE, EF and CRM considering a new research question based on the possibility of using a combination of metrics to assess model performance (Chai and Draxler, 2014). If the MAE is less sensitive to extreme values or outliers rather than RMSE, this last perform better for a normal distribution of the errors. According to this, we decided to use both in our study. Respectively, RMSE=0 (m/s), MAE=0 (m/s), EF=1 (-), CRM=0 (-), BIAS=0 (m/s) and finally ER=0 (-), indicate the model efficiency.

4 RESULTS AND DISCUSSION

In Figure 2 the test of each flow resistance model for increasing velocity is shown.

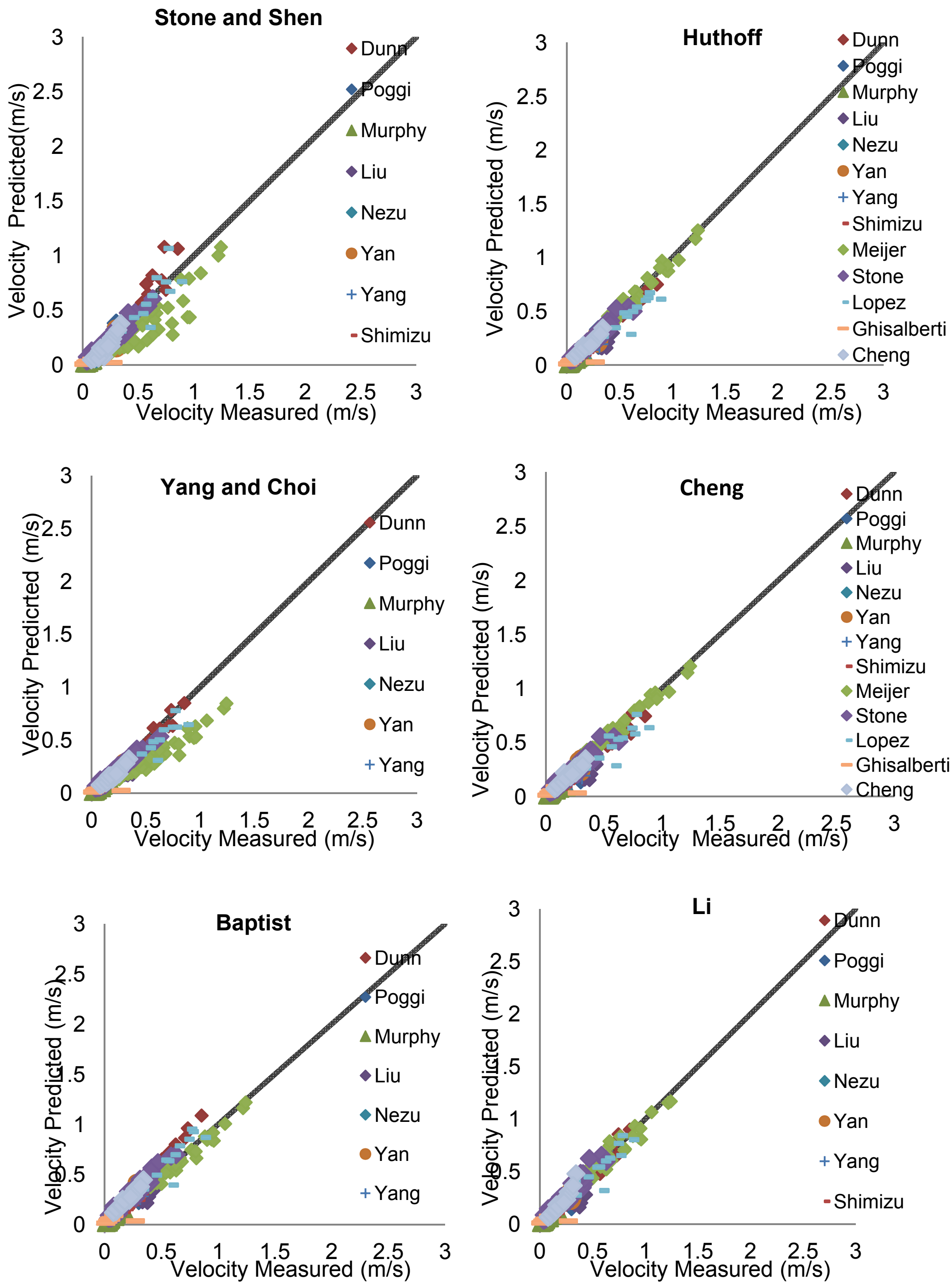

Figure 2 Comparison of predicted and measured velocity for all models using all 323 data.

 ©2017, IAHR. Used with permission / ISSN 1562-6865 (Online) - ISSN 1063-7710 (Print)

Several spreads can be observed, in particular Stone and Shen, and Yang and Choi models seem to slightly underestimate the velocities, while Baptist model seems to overestimate them. Moreover, Huthoff, Cheng and Li models seem to show the best fit with experimental data.
In Tabs.1, 2, 3, 4, statistical parameters evaluated for different condition of vegetation density and submergence are reported. In particular in Tab.2 results for sparse vegetation, (λ <0.1), are shown; in Tab. 3 for transitional density (λ ≈0.1), and, finally, in Tab. 4 for dense vegetation (λ >0.23); for each range of density, two submergences have been considered (i.e *h/hv*<5 or *h/hv* ≥5), in order to deepen in detail the performance of each model.

In Table 1, following the approach of literature we indicate different values of statistical parameters for all 323 data; considering literature reviews, thresholds for each parameters have been fixed, and in particular: MAE≤0.05 m/s;-0.005≤BIAS≤0.005 m/s; RMSE≤0.1 m/s; 0.85≤EF≤1.15; -0.15≤BIAS≤0.15;ER<0.18. Hereafter we highlight in yellow when a single parameter falls in the range.

Table 1. statistical parameters evaluated for different condition of vegetation density and submergence.

All Data (323 Data)	Stone-Shen	Huthoff	Yang-Choi	Cheng	Baptist	Li
MAE(m/s)	0.06	0.03	0.06	0.03	0.05	0.04
BIAS (m/s)	-0.05	-0.02	-0.05	-0.02	0.03	0.00
RMSE(m/s)	0.11	0.05	0.10	0.05	0.07	0.06
EF(-)	0.76	0.94	0.77	0.94	0.91	0.93
CRM(-)	0.18	0.09	0.20	0.06	-0.11	0.01
ER(-)	0.22	0.15	0.20	0.15	0.25	0.15

For all experimental data, it is noteworthy that Huthoff, Cheng and Li models show the best performance: all six parameters fall in the ranges with highest performance. Yang and Choi, and Stone and Shen models do not show good values, while Baptist model has five parameters in the ranges.
Considering Table 2

Table 2. Sparse vegetation.

λ <0.1--h/hv<5— (10 data)	STONE-SHEN	HUTHOFF	YANG-CHOI	CHENG	BAPTIST	LI
MAE (m/s)	0.19	0.11	0.07	0.12	0.15	0.08
BIAS (m/s)	0.12	-0.11	-0.03	-0.12	0.1	-0.07
RMSE (m/s)	0.21	0.11	0.08	0.12	0.16	0.09
EF (-)	-0.09	0.69	0.83	0.6	0.31	0.76
CRM (-)	-0.19	0.18	0.06	0.21	-0.16	0.11
ER (-)	0.29	0.22	0.15	0.24	0.23	0.17
λ <0.1--h/hv>5— (2 data)	**STONE-SHEN**	**HUTHOFF**	**YANG-CHOI**	**CHENG**	**BAPTIST**	**LI**
MAE (m/s)	0.13	0.19	0.2	0.24	0.09	0.23
BIAS (m/s)	0.13	-0.19	-0.2	-0.24	-0.09	-0.23
RMSE (m/s)	0.09	0.14	0.14	0.17	0.07	0.16
EF (-)	0.92	0.83	0.82	0.74	0.95	0.77
CRM (-)	0.33	0.33	0.34	0.41	0.16	0.39
ER (-)	0.22	0.33	0.34	0.41	0.16	0.39

In Table 2 we show statistical parameters relative to sparse vegetation. For low submergence, Yang and Choi model shows the highest performance rather than the other ones. Only Li model has three values in the ranges, while other models do not show good values for that condition. In case of high submergence, it is noteworthy that only two experimental data are available so it is necessary to underline that the lack of experimental data strongly affect the evaluation of the statistical parameters. Baptist model seems to show the best performance with three values; Stone and Shen model shows only two good values while other models do not show good values for that condition.

Table 3. Transitional density.

0.1< λ <0.23-- h/hv<5-(57 data)	STONE-SHEN	HUTHOFF	YANG-CHOI	CHENG	BAPTIST	LI
MAE (m/s)	0.02	0.04	0.04	0.04	0.06	0.03
BIAS (m/s)	-0.0001	-0.04	-0.04	-0.04	0.04	0.0004
RMSE (m/s)	0.05	0.07	0.06	0.07	0.07	0.05
EF (-)	0.93	0.85	0.87	0.87	0.86	0.90
CRM (-)	0.0003	0.16	0.14	0.14	-0.14	-0.001
ER (-)	0.1	0.16	0.14	0.16	0.21	0.13
0.1<λ <0.23 -- h/hv>5 (2 data)	STONE-SHEN	HUTHOFF	YANG-CHOI	CHENG	BAPTIST	LI
MAE (m/s)	0.02	0.14	0.16	0.11	0.04	0.14
BIAS (m/s)	-0.01	-0.14	-0.16	-0.11	0.001	-0.14
RMSE (m/s)	0.02	0.10	0.11	0.08	0.03	0.1
EF (-)	0.53	-14.12	-18.44	-8.00	-0.67	-13.28
CRM (-)	0.02	0.24	0.27	0.19	-56.00	-49.14
ER (-)	0.04	0.24	0.27	0.19	0.08	0.24

In Table 3 we analyze trends for transitional density; in case of low submergence Stone and Shen, Cheng, Yang and Choi and Li models show excellent performance for all six parameters. Huthoff and Baptist models also show good results. Even, in case of high submergence, only Stone and Shen and Baptist models show very good results, in spite of, again in this case, the lack of experimental data (only two data available).

Table 4. Dense vegetation.

λ>0.23-- h/hv<5 (244 data)	STONE-SHEN	HUTHOFF	YANG-CHOI	CHENG	BAPTIST	LI
MAE (m/s)	0.06	0.03	0.06	0.03	0.04	0.03
BIAS (m/s)	-0.06	-0.01	-0.05	-0.004	0.03	-0.003
RMSE (m/s)	0.11	0.04	0.10	0.04	0.06	0.05
EF (-)	0.73	0.95	0.72	0.94	0.91	0.95
CRM (-)	0.26	0.05	0.22	0.02	-0.11	0.01
ER (-)	0.25	0.13	0.20	0.14	0.26	0.14
λ >0.23-- h/hv>5 (8 data)	STONE-SHEN	HUTHOFF	YANG-CHOI	CHENG	BAPTIST	LI
MAE (m/s)	0.21	-0.05	-0.24	0.02	0.06	0.07
BIAS (m/s)	-0.21	0.02	0.21	-0.0002	-0.01	-0.07
RMSE (m/s)	0.27	0.05	-0.21	0.03	0.07	0.08
EF (-)	0.77	0.99	0.76	0.99	0.98	0.97
CRM (-)	0.29	0.02	0.29	0.0003	0.01	0.10
ER (-)	0.28	0.09	0.28	0.05	0.10	0.11

In Table 4 trends for dense regime are shown; in case of low submergence Huthoff, Cheng, Baptist and Li models show excellent performance. In case of high submergence, the trend of these models is confirmed and also Yang and Choi model shows two parameters in the good range. However, for dense regime, we can assume Huthoff, Cheng, Baptist and Li models as strong predictor of the flow velocity.

5 CONCLUSIONS

Although largely available in literature, the vegetation-flow interactions research topic is far from being completely clear. The rigid cylinder analogy is considered as reliable to model vegetated beds (Vargas-Luna et al., 2015), but in spite of this, some aspects about flow resistance and roughness height models needs to be deepened.

 ©2017, IAHR. Used with permission / ISSN 1562-6865 (Online) - ISSN 1063-7710 (Print)

In literature, vegetated beds can be arranged according to three level of density (sparse, transitional and dense) and two hydraulic conditions (low and high submergence), but, usually, flow resistance models are tested merging experimental data relative to different conditions. In the paper this problem is pointed out by the results of the statistical analysis carried out with reference to the most used and cited flow resistance models for the different condition of vegetation density and submergence. In fact, according to this considerations, we can assess that the future goals of the research are the following ones. To improve experimental evaluation of vegetated beds covering more values of the two meaningful parameters (i.e. submergence and vegetation density) and to validate again literature models trying to finally understand which theoretical background presents the best performance for vegetated beds and, eventually, define a "definitive" model for all hydraulic conditions.

REFERENCES

Augustijn, D.C.M., Huthoff, F. & Van Velzen, E.H. (2008). Comparison of Vegetation Roughness Descriptions, *Proceedings of International Conferences on Fluvial Hydraulics (River Flow)*, Cezme, Izmir, Turkey, 343-350.

Bai F., Yang Z., Huai W. & Zheng C. (2016). A Depth-Averaged Two Dimensional Shallow Water Model to Simulate Flow-Rigid Vegetation Interactions. *Procedia Engineering*, 154, 482 – 489.

Baptist, M.J., Babovic, V., Rodriguez Uthurburu, J., Keuzer, M., Uittenbogaard, R.E. & Mynett, A., Verwey,. (2007). On Inducing Equations for Vegetation Resistance. *Journal of Hydraulic Research*, 45(4), 435-450.

Barenblatt, G.I. (2003). *Scaling, Self-similarity and Intermediate Asymptotic*, Cambridge University Press, Cambridge, United Kingdom.

Belcher, S., Jerram, N. & Hunt, J. (2003). Adjustment of a Turbulent Boundary Layer to a Canopy of Roughness Elements. *Journal of Fluid Mechanics,* 488, 369–398.

Chai T. & Draxler R.R. (2014). Root Mean Square Error (RMSE) or Mean Absolute Error (MAE). Arguments Against Avoiding RMSE in The Literature. *Geoscientific Model Development*, 7, 1247-1250.

Chakraborty P. & Sarkar A. (2016). *Flow Characteristics through Submerged Rigid Vegetation over a Sinusoidal Perturbed Bed*. International Journal of River Basin Management, 14(3), 255-266.

Cheng, N. S. (2011).*Representative Roughness Height of Submerged Vegetation*, *Water Resources Research,* 47, 1-18.

Cheng, N. S., Nguyen, H. T., Tan, S. K. & Shao, S. D. (2012). Scaling of Velocity Profiles for Depth-Limited Open Channel Flows over Simulated Rigid Vegetation. Journal of Hydraulics Engineering, 138(8), 673–683.

Cheng, N. S. (2013). Calculation of Drag Coefficient for Arrays of Emergent Circular Cylinders with Pseudo-Fluid Model. *Journal of Hydraulic Engineering*, 139(6), 602–611.

Cheng, N. (2015). Single-Layer Model for Average Flow Velocity with Submerged Rigid Cylinders. *Journal of Hydraulic Engineering*, 141(10), 1-6.

Douglas, J., Gasiorek, J., Swaffield, J. & Jack, L. (2005). *Fluid mechanics*. Ed. 5. Pearson, Harlow.

Dunn, C., Lopez F. & Garcia M. (1996). *Mean Flow and Turbulence in a Laboratory Channel with Simulated Vegetation*, Hydro-systems Lab. Hydraulic Eng. Ser. 51, UIUL-ENG-96-2009,148 pp., Univ. of Illinois at Urbana-Champaign, Urbana, Illinois, IL, and USA.

Ferguson R. (2010). Time to abandon the Manning equation. *Earth Surface Processes and Landforms,* 35, 1873–1876.

Frisch, U. (1995). *Turbulence*. Cambridge University Press, Cambridge, United Kingdom.

Galema, A. (2009).Vegetation Resistance: Evaluation of Vegetation Resistance Descriptors for Flood Management, *Master Thesis.* University of Twente.

Huthoff, F., Augustijn, D.C.M. & Hulscher, S.J.M.H. (2007). Analytical Solution of the Depth-Averaged Flow Velocity in Case of Submerged Rigid Cylindrical Vegetation. *Water Resources Research*, 43, 1-10.

Huthoff, F.,Straatsma M.W., Augustijn, D.C.M. & Hulscher, S.J.M.H. (2013). Evaluation of a Simple Hydraulic Resistance Model Using Flow Measurements Collected in Vegetated Waterways. *Open Journal of Modern Hydrology*, 3, 28-37.

Jahra F., Kawahara Y., Fumiaki H. & Yamamoto H. (2011). Flow-Vegetation Interaction in a Compound Open Channel with Emergent Vegetation. *International Journal of River Basin Management*, 9,247-256.

Konings, A. G., Katul G. G. & Thompson S. E. (2012). A Phenomenological Model for the Flow Resistance Over Submerged Vegetation. *Water Resources Research*, 48(W02522), 1-9.

Li, S., Shi, H., Xiong, Z., Huai, W. & Cheng, N. (2015). New Formulation for the Effective Relative Roughness Height of Open Channel Flows with Submerged Vegetation. *Advances in Water Resources*, 86, 46-57.

Liu, D., Diplas, P., Fairbanks, J. D. & Hodges, C. C. (2008). *An Experimental Study of Flow through Rigid Vegetation*, *Journal of Geophysical Research, Earth Surface*, 113, 1-16.

Meijer, D. G. & Van Velzen, E. H. (1999). Prototype-Scale Flume Experiments on Hydraulic Roughness of Submerged Vegetation, *Proceedings of 28th IAHR Congress*, Graz, Austria.

Mrokowska, M. M., Rowinski, P. M. & Kalinowska, M. B.(2015). Evaluation of Friction Velocity in Unsteady Flow Experiments, *Journal of Hydraulic Research*, 53(5), 659-669.

Murphy, E., Ghisalberti, M. & Nepf, H. (2007). Model and Laboratory Study of Dispersion in Flows with Submerged Vegetation. *Water Resource Research*, 43(5), 1-12.

Nepf, H. M. & Vivoni, E. R. (2000). Flow Structure in Depth-Limited, Vegetated Flow. *Journal of Geophysical Research, C: Oceans*, 105(C12), 28547–28557.

Nepf, H. Ghisalberti, M. White, B. & Murphy E. (2007). Retention time and dispersion associated with submerged aquatic canopies, *Water Resource Research*, 43(W04422), 1-10.

Nepf, H. M. (2012a). Flow and Transport in Region with Aquatic Vegetation. *Annual Review of Fluid Mechanics*, 44, 123-142.

Nepf, H. M. (2012b). Hydrodynamics of Vegetated Channels. *Journal of Hydraulic Research*, 50(3), 262–279.

Nezu, I. & Sanjou, M. (2008). Turburence Structure and Coherent Motion in Vegetated Canopy Open-Channel Flows, *Journal of Hydro-environment Research*, 2(2), 62–90.

Pasquino, V., Gualtieri, P. & Pulci D.G., (2016). On Evaluating Flow Resistance of Rigid Vegetation Using Classic Hydraulic Roughness at High Submergence Levels: An Experimental Work, *Geo Planet. Earth and Planetary Sciences*, 269-277.

Raupach, M., Finnigan, J. & Brunet, Y. (1996). Coherent Eddies and Turbulence in Vegetation Canopies: The Mixing-Layer Analogy. *Boundary Layer Meteorology*, 60, 351–395.

Shimizu, Y., Tsujimoto, T., Nakagawa, H. & Kitamura, T. (1991). Experimental Study on Flow Over Rigid Vegetation Simulated By Cylindrical with Equi-Spacing, *Japan Society of Civil Engineers*, 31–40 (in Japanese).

Stone, B.M. & Shen, T.H., (2002). Hydraulic Resistance of Flow in Channels with Cylindrical Roughness. *Journal of Hydraulic Engineering*, 128(5), 500-506.

Stephan, U. & Gutknecht, D. (2002). Hydraulic Resistance of Submerged Flexible Vegetation. Journal of Hydrology, 269(1), 27–43.

Vargas-Luna A., Crosato A., Calvani G. & Uijttewaal W. (2015). Representing Plants as Rigid Cylinders in Experiments and Models. *Advances in Water Resources*, 93, 205-222.

Wu, W. & Marsooli, R. (2012), *A depth-averaged 2D shallow water model for breaking and* Non-Breaking Long Waves Affected By Rigid Vegetation. *Journal of Hydraulic Research*, 50(6), 558-575.

Yan, J. (2008). Experimental study of flow resistance and turbulence characteristics of open channel flow with vegetation, *Ph.D. Thesis*. Hohai University, China.

Yang, W. (2008). Experimental study of turbulent open-channel flows with submerged vegetation, *Ph.D. Thesis*. Yonsei University, Korea.

Yang, W. & Choi, S. (2010). A Two Layer Approach for Depth-Limited Open-Channel Flows with Submerged Vegetation, *Journal of Hydraulic Res*earch, 48(4) 466–475.

Yen, B. C. (2002). Open Channel Flow Resistance, Journal of Hydraulic Engineering, 128(1), 20-39.

 ©2017, IAHR. Used with permission / ISSN 1562-6865 (Online) - ISSN 1063-7710 (Print)

Proceedings of the 37th IAHR World Congress
August 13 – 18, 2017, Kuala Lumpur, Malaysia

INFLUENCE OF LONGITUDINARY DISCONTINUOUS VEGETATION ARRANGEMENT PATTERN ON TURBULENT STRUCTURE IN OPEN CHANNEL

TAKAYUKI TANAKA(1) & TERUNORI OHMOTO(2)

(1) Departments of Civil Engineering, National Institute of Technology, Toyota College, Toyota, Japan,
tanaka-c@toyota-ct.ac.jp
(2) Graduate School of Science and Technology, Kumamoto University, Kumamoto, Japan,
ohmoto@kumamoto-u.ac.jp

ABSTRACT

River vegetation fosters a rich ecological environment and creates a friendly riverside environment. Importance is attached, therefore, to the question of what vegetation should be like when designing and improving river channels. In view of concerns and problems such as the diversity of rivers, continuity of ecosystems and the deterioration of water quality that have been caused by stagnant water in vegetation communities, it is desirable that regions where the exchange of flows with the main flow region are promoted be provided. In this paper, the influence that arrangement patterns of longitudinal discontinuous vegetation zones gave to the flow resistance and turbulent structure in an open-channel is examined experimentally. Results showed that the relationship between flow depth and discharge significantly depends on the arrangement patterns and the reason could be explained by the difference of turbulent structure and spatial gradient of the dynamic pressure.

Keywords: Vegetation; cavity flow; flow resistance; turbulent flow structure; dynamic pressure.

1 INTRODUCTION

Vegetation in a river channel greatly affects the flow resistance characteristics of the channel. In-channel vegetation management, therefore, requires appropriate evaluation of flood safety. River channels are often found to have a series of plant communities lined up in the streamwise direction. In view of various factors such as diversity of rivers, ecosystem continuity and concern about water quality degradation due to stagnant flow in vegetation zones, it is desirable to create regions that promote water flow between vegetation zones and the main flow zone.

For the Gose River and the Shin Gose River running across Inuyama City, Aichi Prefecture, projects are underway for nature-oriented river works designed to create diverse flow fields by arranging environment-friendly groins in parallel and staggered patterns in the river channels. The effects of these river works, however, on flow resistance and flow structures have not been fully discussed.

Many vigorous studies have been made on flow resistance characteristics of an open channel with plant communities. Recent studies include those of Nepf (2000), Musleh (2006) and Noarayanan et al. (2012) involving experiments using vegetation models with different degrees of stiffness. In their study on an open channel with a discontinuous streamwise series of plant communities interrupted by non-vegetation regions, Yokojima (2015) looked at the case where trees are placed in the channel to form a continuous streamwise zone of trees and the case where trees are placed to form a discontinuous zone of trees interrupted by non-vegetation regions and conducted experiments and LES analyses to shed light on the behavior of large-scale horizontal vortices occurring around the trees. They also estimated drag coefficient distributions in the tree zone model by analytically simulating the two-dimensional flows around individual tree elements and the fluid force acting on each element by the immersed boundary method, and then performed a three-dimensional LES analysis. They showed that by so doing, the accuracy of estimation of the behavior of large-scale vortices passing around the trees placed in patches can be improved. The authors (2015) elucidated resistance characteristics of flow in an open channel with plant communities forming permeable side cavities and flow in an open channel with solid walls forming impermeable side cavities and analyzed turbulent flow characteristics and momentum transport characteristics to explain the flow resistance.

In view of the arrangement patterns of the environment-friendly groins constructed in the Gose River and the Shin Gose River, the authors (2016) also examined experimentally the resistance characteristics of flow in an open channel with plant communities arranged in parallel, in a staggered pattern or along one bank and explained the flow resistance from a number of viewpoints such as momentum transport characteristics at the boundaries of the main flow zone with vegetation zones and side cavities. Flow structures in the entire channel under these conditions, however, have not yet been discussed.

Focusing on flow in an open channel with a discontinuous streamwise series of plant communities. Therefore, this study examines the effects of different configurations of plant communities such as staggered or parallel on turbulence characteristics and flow structures including the spatial gradient of dynamic pressure.

2 EXPERIMENTAL APPARATUS AND METHOD

The experiments were conducted by using a circulating variable slope flume measuring 10m in length, 40m in width (B) and 25cm in height. A vegetation zone model was made by bonding 6.10 nylon bristles (0.242mm in diameter, flexural stiffness EI=1.45×104g·cm^2) cut to a uniform length H_v of 6.0 cm, which are flexible enough to be bent by the force of flowing water, to a plastic plate at 0.5cm intervals. Figure 1 shows the arrangement patterns of vegetation zones in the open channel. Each vegetation zone unit was 10cm wide, and its length L_v in the direction of flow was 30 cm. In arrangement P1, vegetation zones were placed in a parallel pattern along the right and left banks. In P2, vegetation zones were placed in a staggered pattern. In P3, vegetation zones were placed in pairs, and each pair was placed along one bank. In all arrangement cases, channel elements were arranged so that side cavities each having a length (L_c) of 30cm were formed. In the experiments, with the aim of creating a state of equilibrium of flow from the macroscopic point of view, vegetation zones and obstacles and cavities were placed alternately in the section at distances from the upstream end of the flume of 100cm to 940cm.

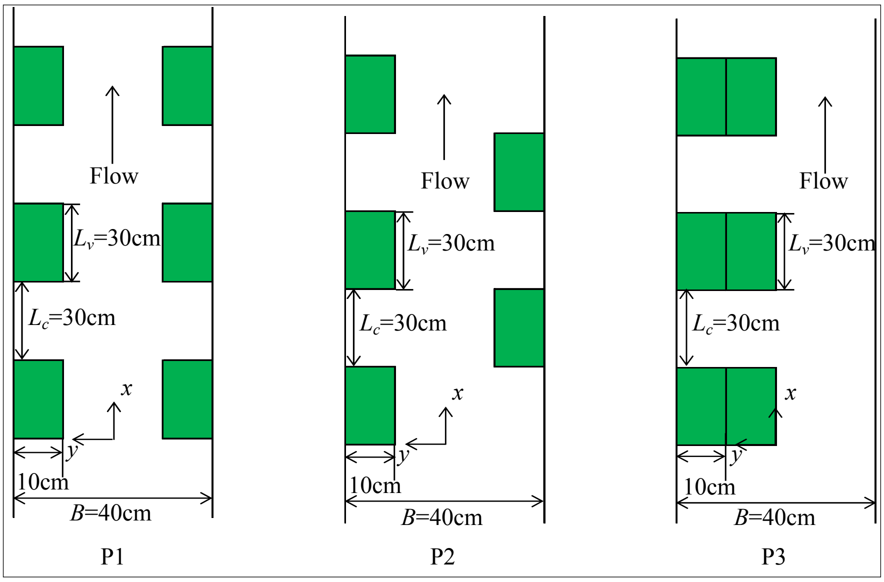

Figure 1. The arrangement patterns of vegetation zones in the open channel.

Table 1. Experiment conditions associated with flow resistance characteristics.

pattern	Flow discharge Q(l/s)	Bed slope I	Vegetation height H_v(cm)	Vegetation length L_v(cm)	Vegetation diameter d(mm)	Cavity length L_c(cm)
P1 P2 P3	2 ~ 12	1/1000	6.0	30	0.242	30

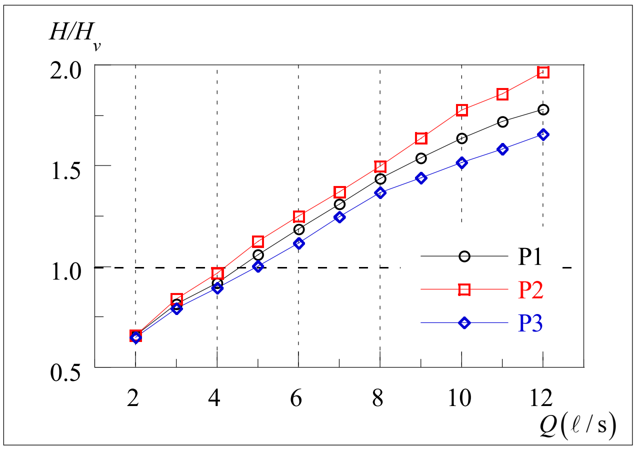

Figure 2. The relationship between the flow rate and water depth for each vegetation arrangement pattern.

©2017, IAHR. Used with permission / ISSN 1562-6865 (Online) - ISSN 1063-7710 (Print)

Table 2. Experiment conditions associated with flow mechanisms.

pattern	Flow discharge Q(l/s)	Bed slope I	Flow depth H(cm)	Mean flow velocity U_m(cm/s)	Froude number Fr	Friction velocity U_*(cm/s)
P1	4	1/1,000	5.06	19.8	0.28	2.23
P2			5.33	18.8	0.26	2.28
P3			4.91	20.4	0.29	2.19

Experiment conditions associated with flow resistance characteristics were set as shown in Table 1. Figure 2 shows the relationship between the flow rate and water depth for each vegetation arrangement pattern determined in the authors' study. The water depth is made dimensionless on the basis of vegetation height. Regardless of whether there is overflow or not, at all flow rates, P2 (staggered arrangement) showed the largest values of water depth, followed by P1 (parallel arrangement) and then P3 (one-bank arrangement). In this study, first in order to determine the relationship between resistance characteristics and flow structures in the non-overflow condition, attention is turned to the flow rate Q = 4l/s to examine the flow mechanism. Table 2 shows the experiment conditions. Friction velocity is calculated from $U_* = \sqrt{gHI}$.

The coordinate system is defined so as to cover mainly the region where a pseudo-uniform flow field is formed. The origin of the coordinate system is located at the mid-channel point at the bottom of the flume at a distance of 420 cm from the upstream end. In the right-hand coordinate system thus defined, the x-axis is oriented in the streamwise direction, the y-axis in the transverse direction and the z-axis in the vertical direction. Let u, v and w represent their respective flow velocity components; U, V and W, their averages; and u', v' and w', their fluctuation components.

For the purpose of investigating the flow mechanism, point measurement of flow velocity was conducted by using I-shaped electromagnetic flow meters. Flow velocity was measured at different points in the streamwise direction within the range of the pseudo-uniform flow field at x=15cm to 75cm (x/L_c= 0.5 to 2.5). Output signals at 100 Hz from the electromagnetic flow meters were converted from analog to digital, and a total of 4096 data sets per measurement point were processed statistically. Two-dimensionality is higher in the non-overflow condition than in the overflow condition, half-depth measurement results were used in this study. In view of the fact that vegetation zones were irregularly arranged in the streamwise direction, the method of measuring flow velocity by partially removing vegetation zones was not used. Instead, flow velocity was measured only in the non-vegetation zones.

3 HORIZONTAL DISTRIBUTION OF TIME-AVERAGED VELOCITY

Figure 3 shows the horizontal distributions of time-averaged velocity vectors and main flow velocity contours in each arrangement case. Flow velocity was measured at half depth (z/H=0.5), and the velocity vector V and the main flow velocity U were made dimensionless on the basis of the cross sectionally averaged flow velocity U_m.

As shown, in all cases, flow velocity is higher in the main flow zone than in the side cavity. It can be seen that in arrangement case P2 (staggered arrangement), the entire flow field meanders unlike in the other arrangement cases. Its influence is thought to be one of the factors that have caused flow resistance in P2 to become greater than in the other arrangement cases.

Examination of the flow in the cavity reveals that in all arrangement cases, flow opposite in direction to the main flow occurs although there are permeable vegetation zones immediately upstream and downstream of the cavity. This indicates that the flow is greatly affected by the resistance of the vegetation zones. This phenomenon is thought to have occurred because the vegetation zones used were relatively large for the size of the flume in comparison with other studies. It can be seen that in P1 and P2, circulating flows as can be seen in the case of flow in side cavities formed by impermeable obstacles are taking place. In P3, although such circulating flow cannot be seen, flow in the opposite direction can be observed in many regions in the side cavity because vegetation zone width is larger than in the other arrangement cases. Since there is flow toward the left bank occurring in the region near the left bank in the side cavity, there is a need for further study on flow velocity distribution in vegetation zones and three-dimensional flow structures.

These results have shown that under the experiment conditions used in this study, even in the case of flow in a side cavity formed by permeable obstacles, flow in the opposite direction occurs extensively near the inner walls of the cavity. These phenomena are likely to have significant influence on turbulence and momentum transport characteristics. The following sections of this study, therefore, focus on turbulence characteristics and the spatial gradient of dynamic pressure.

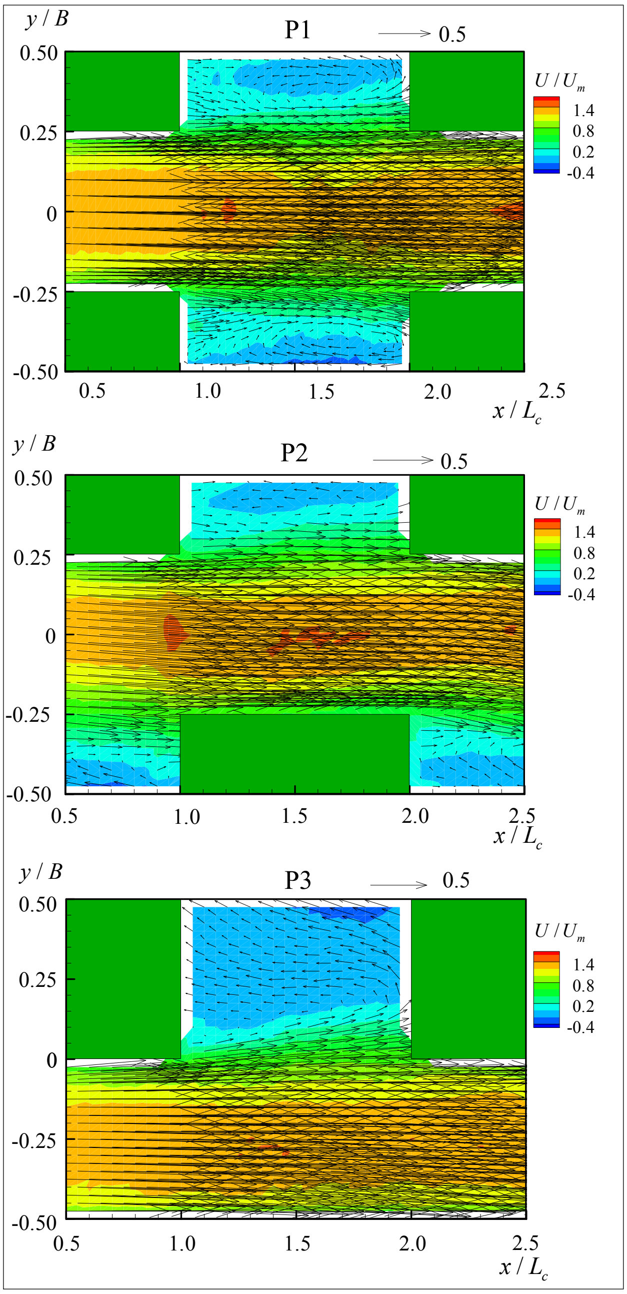

Figure 3. The horizontal distributions of time-averaged velocity vectors and main flow velocity contours in each arrangement case.

4 HORIZONTAL DISTRIBUTION OF REYNOLDS STRESS

Figure 4 shows horizontal contours of Reynolds stress $-\overline{u'v'}/U_m^2$. The Reynolds stress has been made dimensionless by using the cross sectional averaged flow velocity U_m.

In all arrangement cases, Reynolds stress shows negative values near the main flow zone–cavity boundary on the left bank side, while in P1 and P2 positive values are shown on the right bank side. This indicates that the momentum due to turbulence is transported from the main flow zone to the cavity.

Turning attention to P1, we notice that stress distribution is symmetrical with respect to the centerline of the channel because the vegetation zones are arranged in parallel. As shown, Reynolds stress shows large values in the region in the upstream half of the side cavity where velocity differences are noticeably large. In P2, where the vegetation zones are arranged in a staggered pattern, the Reynolds stress distribution also shows a pattern close to symmetry with respect to a point. Comparison with P1 reveals that in P2, under the influence of a higher degree of flow meandering, Reynolds stress shows larger values in the cavity, too.

Extreme values of Reynolds stress, too, tend to be larger in P2 than in P1 partly because of the occurrence of a water impact zone on the downstream side of the vegetation zone caused by the meandering of flow. This is thought to be why flow resistance becomes greater. It can be seen that in P3, stronger turbulence occurs extensively along the boundary between the main flow zone and the cavity than in the other arrangement cases.

 ©2017, IAHR. Used with permission / ISSN 1562-6865 (Online) - ISSN 1063-7710 (Print)

The reason for this is thought to be that because vegetation zone width is greater than in the other arrangement cases, main flow velocity did not increase significantly as in the other arrangement cases so that the main flow velocity differences between the main flow zone and the vegetation zones and the cavity became greater. It is thought likely, however, that since the vegetation zones in P3 were placed only along one bank, flow resistance became smaller than in P1 and P2, which had two each of main flow zone–cavity and main flow zone–vegetation zone boundaries in the cross-stream direction.

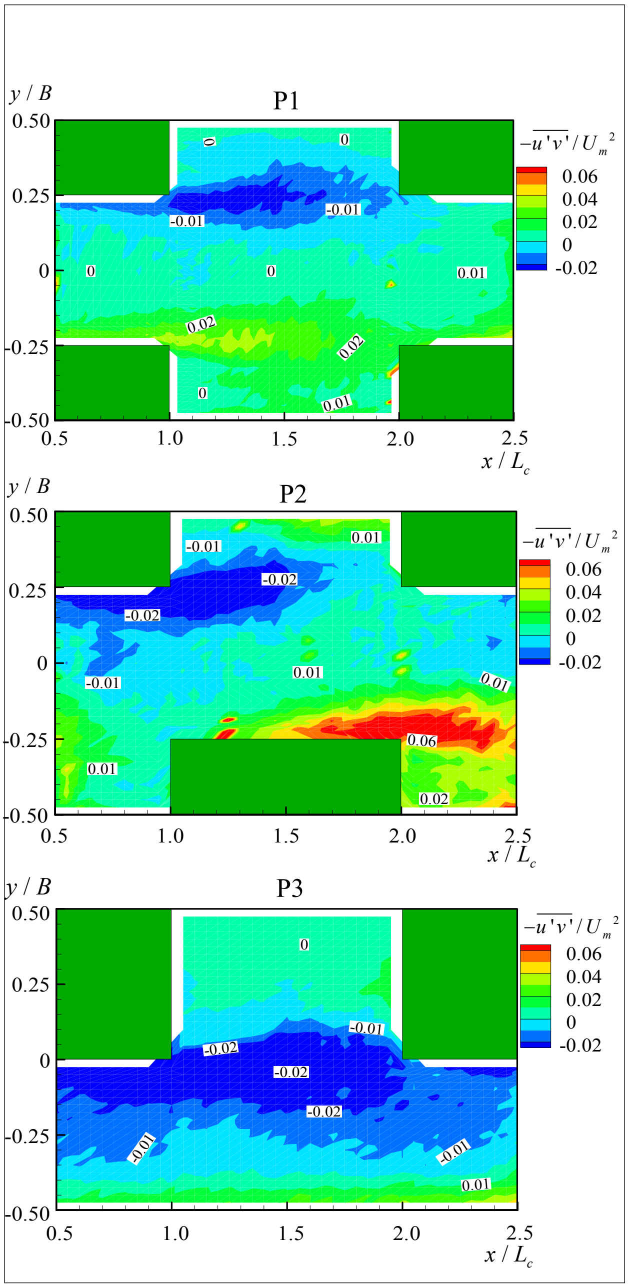

Figure 4. The horizontal distributions of shows horizontal contours of Reynolds stress $-\overline{u'v'}/U_m^2$ in each arrangement case.

5 HORIZONTAL SPATIAL GRADIENT OF DYNAMIC PRESSURE

Horizontal time-averaged velocity distributions have shown that in all vegetation arrangement cases, flow in the opposite direction occurred in the side cavity although the cavity walls were permeable. It is thought likely, therefore, that the pressure distribution around the cavity is altered because of such phenomena as impacting of the flow separating from the main flow zone or the vegetation zone upstream of the cavity on the vegetation zone downstream of the cavity. This study, therefore, looks at the spatial gradient of dynamic pressure in each arrangement case as in the authors' study (2015) on two-dimensional dynamic pressure gradients.

When the Reynolds number is sufficiently large, the Reynolds momentum equation can be written, if a vertically uniform flow field is assumed and if the viscosity term can be neglected, as

$$\frac{1}{\rho}\frac{\partial P}{\partial x}=-\frac{\partial\left(U^2+\overline{u'^2}\right)}{\partial x}+U\frac{\partial U}{\partial x}-\frac{\partial\left(UV+\overline{u'v'}\right)}{\partial y}+U\frac{\partial V}{\partial y}+F_x=\frac{1}{\rho}\frac{\partial P_d}{\partial x}+F_x \qquad [1]$$

where P is total pressure and P_d is dynamic pressure, and the external force F_x can be expressed, taking gravity into account, as $F_x = g\sin\theta$. Similarly, the equation for the transverse direction can be written as

$$\frac{1}{\rho}\frac{\partial P}{\partial y}=-\frac{\partial\left(UV+\overline{u'v'}\right)}{\partial x}+V\frac{\partial U}{\partial x}-\frac{\partial\left(V^2+\overline{v'^2}\right)}{\partial y}+V\frac{\partial V}{\partial y}+F_y=\frac{1}{\rho}\frac{\partial P_d}{\partial y}+F_y \qquad [2]$$

where F_y = 0 if gravity is taken into account. Since hydrostatic pressure takes the same value in a horizontal plane, pressure distribution is estimated by examining the spatial gradient distribution of dynamic pressure.

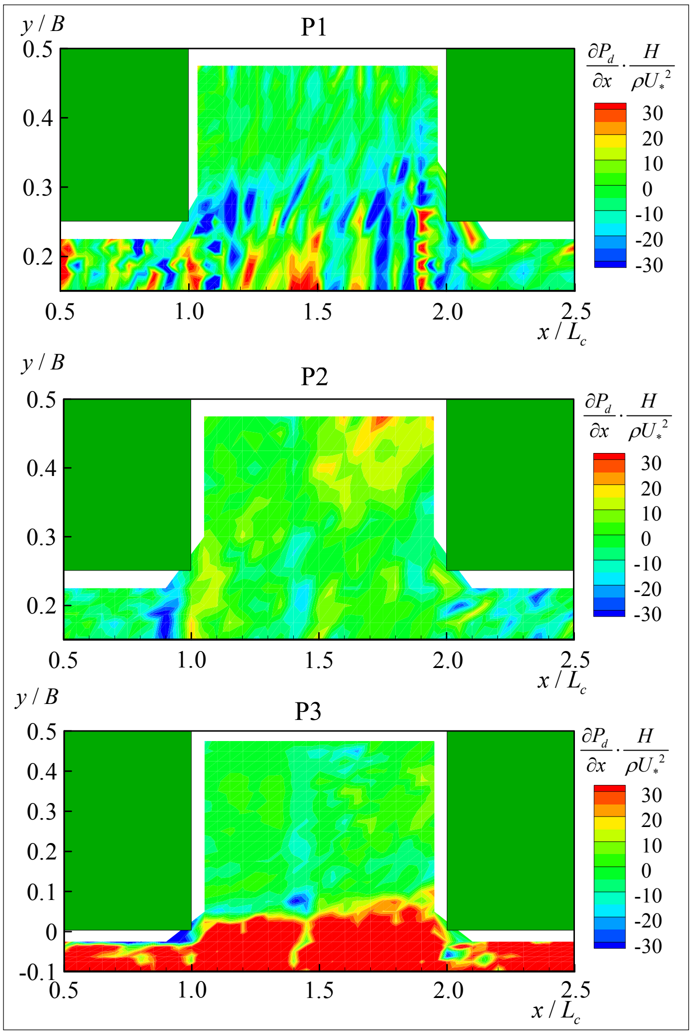

Figure 5. The spatial gradient of dynamic pressure in the streamwise direction in each arrangement case.

Figure 5 shows the spatial gradient of dynamic pressure in the streamwise direction in each arrangement case. Figure 6 shows the spatial gradient contours in the cross-stream direction. The dynamic pressure is made dimensionless on the basis of U_*^2/H. Mainly for the purpose of examining the phenomena occurring in and near the cavity and how vegetation zones act as flow obstacles, attention is turned mainly to the region in and near the left-bank side cavity.

As can be seen from the streamwise spatial gradient of dynamic pressure in P1, the fact that $\partial P_d / \partial x$ tends to show negative values at or near the boundary of the main flow zone and the cavity (y/B_e=0.25 to 0.30) indicates that the resulting favorable pressure gradient promotes the flow in the streamwise direction. The fact that $\partial P_d / \partial x$ tends to show positive values at or near the boundary of the main flow zone and the vegetation zone downstream of the cavity indicates that the vegetation zone is reducing flow velocity in the

 ©2017, IAHR. Used with permission / ISSN 1562-6865 (Online) - ISSN 1063-7710 (Print)

main flow direction. In the downstream half of the cavity zone, $\partial P_d / \partial x$ shows small negative values, indicating that the influence of the vegetation zone as a flow obstacle on dynamic pressure is small.
As can be seen from the transverse spatial gradient of dynamic pressure, $\partial P_d / \partial x$ shows negative values in and near the main flow zone–cavity boundary in the upstream half of the cavity, indicating that the flow toward the cavity is being promoted. Then, as if under the influence of the flow separating from the upstream vegetation zone, the flow advancing from the center of the cavity through the downstream half of the cavity toward the left bank is being promoted. This cross-sectional distribution of the spatial gradient of dynamic pressure is thought to be a factor contributing to the formation of circulating flow in the cavity.

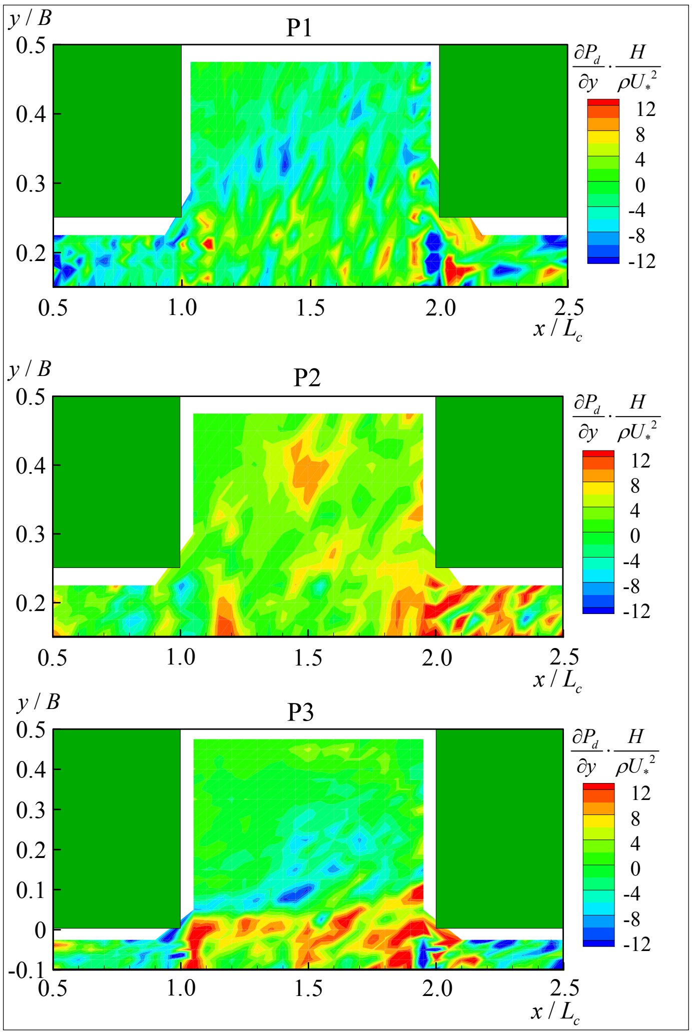

Figure 6. The spatial gradient of dynamic pressure in the cross-stream direction in each arrangement case.

Turning attention to the spatial gradient in the streamwise direction reveals that $\partial P_d / \partial y$ shows larger values than in the surrounding regions at around x/L_e=0.9 at or near the main flow zone–cavity boundary in the upstream half of the cavity, while in the other regions the spatial gradient of dynamic pressure in the streamwise direction shows smaller values than in P1. This is thought to be because the higher degree of flow meandering in P2 than in P1 makes the changes in the flow in the transverse direction greater than the changes in the flow in the main flow direction. In the cavity, $\partial P_d / \partial x$ shows positive values in the region near the left bank in the downstream half of the cavity, indicating that the occurrence of flow in the opposite direction is being promoted. Examination of the spatial gradient in the transverse direction in P2 reveals that $\partial P_d / \partial y$ shows negative values at and near the boundary of the upstream half of the cavity and the main flow zone, indicating that the flow into the cavity is being promoted. The fact that positive values are shown in the downstream half of the cavity indicates that the flow advancing toward the main flow zone is being promoted. In the cavity, unlike in P1, $\partial P_d / \partial y$ shows positive values in the region from the center of the cavity to the region immediately downstream of the cavity, indicating that the flow from the cavity toward the main flow zone is being promoted. The reason for this, too, is thought to be that because the staggered pattern of vegetation arrangement causes the flow to meander so as to generate flow into the cavity on the upstream side of the cavity, while on the downstream side of the cavity the left bank and the vegetation on the left bank side obstruct water flow so as to promote the flow advancing from the cavity toward the main flow zone.

Next, turning attention to the spatial gradient of dynamic pressure in the streamwise direction in P3 reveals that although $\partial P_d / \partial x$ shows negative values at and near the main flow zone–cavity boundary in the upstream half of the cavity as in the other arrangement cases, positive values are shown in most of the other regions. From this, it can be inferred that because vegetation zone width and cavity width are large in P3, an adverse pressure gradient occurs near the boundary so that the resistance to the flow in the main flow direction becomes large. The fact that $\partial P_d / \partial x$ shows small values in the cavity suggests that the vegetation is hardly functioning as a flow obstacle. The distribution tendency of the spatial gradient in the transverse direction is similar to the tendency shown in P1 at and near the main flow zone–cavity boundary and the main flow zone–vegetation zone boundary and in the cavity. The positive values of $\partial P_d / \partial y$, however, at and near the boundary with the main flow zone are larger than in P1, and positive values can be seen here and there in the downstream half of the cavity. The resultant distribution, therefore, is conducive to the occurrence of stronger flow in the opposite direction.

From these results, it can be concluded that in the staggered arrangement case, which showed a distribution tendency differing from the tendencies seen in the other arrangement cases, flow meandering was promoted so as to make flow resistance greater than in the other arrangement cases. Thus, it has been shown that because of the spatial gradient of dynamic pressure, the influence of vegetation zones acting as flow obstacles is not significantly large. It has also been suggested that the spatial gradient distribution of dynamic pressure differs depending on vegetation arrangement patterns, and such differences affect flow resistance and turbulence characteristics. As a next step, the authors will conduct a detailed study on each term of the Reynolds momentum equation and investigate the three-dimensional behavior of flow.

6 CONCLUSIONS

Focusing on flow in an open channel with a streamwise discontinuous series of plant communities, this study examined the effects of different patterns of plant communities such as staggered and parallel on flow turbulence characteristics and flow mechanisms including the spatial gradient of dynamic pressure. The findings of this study are listed below.

1) Examination of the horizontal distribution of time-averaged flow velocity revealed that in the case where vegetation zones were arranged in a staggered pattern, flow showed a higher degree of meandering than in the case where vegetation zones were arranged in parallel or along one bank only. This effect is thought to be a factor contributing to larger flow resistance in the staggered arrangement case than in the other arrangement cases. Under the experiment conditions used in this study, flow in the opposite direction was seen to occur extensively near the inner walls of the side cavities although the experiments dealt with flow in an open channel with side cavities formed by permeable obstacles (i.e. vegetation zones);
2) Examination of the horizontal distribution of Reynolds stress reveals that in all arrangement cases, Reynolds stress showed large values at and near the main flow zone–cavity boundary and the main flow zone–vegetation zone boundary in the cavity, and that turbulence-induced momentum was being transported from the main flow zone into the cavity. In the staggered arrangement case, flow resistance was higher than in the other arrangement cases probably because in the staggered arrangement case, extreme values of Reynolds stress were larger than in the two-bank arrangement case and, unlike in the one-bank arrangement case, there were main flow zone–cavity boundaries and main flow zone–vegetation zone boundaries along both banks;
3) With respect to the spatial gradient of dynamic pressure, the staggered arrangement case showed a distribution tendency differing from the tendencies observed in the other arrangement cases, and it was indicated that as flow meandering was promoted, flow resistance became higher than in the other arrangement cases. It was shown that the influence of the vegetation zones as flow obstacles was not significantly great. It was also shown that the spatial gradient of dynamic pressure differed depending on the arrangement patterns of vegetation zones, and such differences were affecting flow resistance and turbulence characteristics.

REFERENCES

Musleh, F.A. & Cruise, J.F. (2006). Functional Relationships of Resistance in Wide Flood Plains with Rigid Unsubmerged Vegetation. *Journal of the Hydraulic Engineering*, 132(2), 163-171.

Järvelä, J. (2005). Effect of Submerged Flexible Vegetation on Flow Structure and Resistance. *Journal of Hydrology*, 307(1), 233-241.

Nepf, H.M. & Vivoni, E.R. (2000). Flow Structure in Depth-limited, Vegetated Flow. *Jourmal of Geophysical Resources.: Oceans*, 105(C12), 28547-28557.

 ©2017, IAHR. Used with permission / ISSN 1562-6865 (Online) - ISSN 1063-7710 (Print)

Noarayanan, L., Murali, K. & Sundar, V. (2012). Manning's 'n' Coefficient for Flexible Emergent Vegetation in Tandem Configuration. *Journal of Hydro-Environment Research*, 6(1), 51-62.

Satoshi, Y., Yoshihisa. K. & Takuya, Y. (2015). Impacts of Vegetation Configuration on Flow Structure and Resistance in a Rectangular Open Channel. *Journal of Hydro-environment Research*, 9(2), 295–303.

Takayuki, T. & Terunori, O. (2015). Turbulent Structure in Open Channel with Permeable and Impermeable Side Cavities. *Journal of Applied Water Engineering and Research*, 4(1), 44-53.

Takayuki, T. & Terunori, O. (2016). Effects of Vegetation Arrangement Patten with Side Cavity on Flow Resistance and Turbulent Structure in Open Channel, *In 20th IAHR APD Congress*, Colombo, Sri Lanka.

Proceedings of the 37th IAHR World Congress
August 13 – 18, 2017, Kuala Lumpur, Malaysia

RELATIONSHIP INVESTIGATION BETWEEN THE DISSIPATION PROCESS OF SUPERSATURATED TOTAL DISSOLVED GAS AND WIND EFFECT IN FLOWING WATER

JUPING HUANG(1), WEI WANG(2), LELE WANG(3), RAN LI(4) & JINGJIE FENG(5)

(1,4,5)State Key Laboratory of Hydraulics and Mountain River Engineering, Sichuan University, Chengdu 610065, China
196088843@qq.com; liran@scu.edu.cn
(2)Sichuan Water Conservancy Vocational College, Chengdu 611833, China
(3)Fujian Provincial Investigation Design & Research Institute of Water Conservancy & Hydropower, Fuzhou 350000, China

ABSTRACT

Spillway discharges of hydroelectric projects may entrain a large amount of air into the plunge pool, which lead to supersaturation of total dissolved gas (TDG) and can cause lethal diseases for fish. Wind velocity is an important factor in the acceleration of the dissipation process of TDG. The quantitative relationship between the TDG dissipation process and wind velocity in flowing water has not been previously described. This paper performs a series of laboratory experiments in flowing water to investigate the effect of wind on the dissipation of supersaturated TDG. Moreover, this study numerically simulates TDG transport and dissipation to calibrate dissipation coefficients of supersaturated TDG using a two-dimensional $k \sim \varepsilon$ turbulence model. Based on the theoretical analysis, experimental data and simulated results, a quantitative relationship of the wind velocity and supersaturated TDG dissipation is established. The proposed correlation is a step forward in the research of dissipation process and can be used for prediction of TDG supersaturation downstream of high dams.

Keywords: Total dissolved gas; super saturation; wind; dissipation coefficient.

1 INTRODUCTION

Hydropower is one of the most important clean, reliable, efficient and renewable energy sources on earth. However, there are negative environmental effects from hydroelectric projects that impact downstream fish species. In particular, spillway discharges from hydroelectric projects may entrain a large amount of air into the plunge pool, which will lead to supersaturation of total dissolved gas (TDG) and can cause gas bubble trauma and even death on affected fish (Weitkamp and Katz, 1980; Weitkamp et al., 2003). Environmental assessment of TDG supersaturation is critical for the construction of ecologically friendly hydropower projects. Understanding and modeling of the dissipation process is of paramount importance to accurately predict TDG.

We define percent saturation of TDG as follows,

$$C = \frac{C_t}{C_S} \times 100 \quad [1]$$

where

C (%) represents the percent saturation of TDG, C_t (mg/L) represents the solubility of gas in water, C_S (mg/L) represents the saturated solubility of gas in water.

Roesner and Norton (1971) first proposed a physically-based model of TDG transport in a stilling basin. They found that the variation in TDG level was controlled by a mass transfer coefficient and the residence time of the bubbles in the stilling basin. In recent years, Orlins and Gulliver (2000), Politano and Carrica (2003), Politano et al. (2007, 2009, 2012), and Fu et al. (2010) simulated the TDG transport process with numerical models.

Considering the river velocity, the water depth and the molecular diffusion, the U.S Army Corps of Engineers (USACE, 2005) proposed a predictive formula for the dissipation coefficient by combining field observations from the Columbia River with first-order kinetics. In this regard, Feng et al. (2014) proposed a formula, involving the effects of water depth, friction velocity, hydraulic radius and Froude number, for estimating the dissipation coefficient of supersaturated TDG. In addition to these studies, many previous studies have focused on how the TDG dissipation process from supersaturation to saturation is associated with various conditions, such as water depth, turbulence characteristics, Reynolds number, sediment concentration and water temperature(Jiang et al., 2008; Qu, 2011;Feng, 2013; Shen et al., 2014).

However, little research has been reported on the quantitative effects of wind velocity related to the supersaturated TDG dissipation process. In a wind-driven system, such as in lakes and reservoirs, gas-liquid

 ©2017, IAHR. Used with permission / ISSN 1562-6865 (Online) - ISSN 1063-7710 (Print)

mass transfer is dominated by wind. Thus, the effect of wind on TDG dissipation should be taken into account. There are several formulations used to calculate the gas-liquid transfer rate. The most common ones are the two film theory (Whitman, 1923) and the surface renewal theory (Higbie, 1935; Danckwerts, 1953). O'Connor (1983) proposed a function for the relationship between the mass transfer coefficient and the wind velocity based on the theory of the liquid film and surface renewal considering the Schmidt number (Sc), the Reynolds number (Re), and the Weber number (We). Wanninkhof (1992) proposed a general formulation for an oxygen mass transfer coefficient as a function of mass transfer due to physical absorption and mass transfer enhancement due to the wind speed. Chu and Jirka (2003) determined the relationship of the transfer velocity, the reaeration coefficient and the wind shear velocity through experiments.

Most of these studies have focused on unsaturated dissolved oxygen transfer effect rather than on supersaturated TDG. Li et al. (2013) demonstrated that the dissipation process is different in dissolved oxygen compared to TDG. Therefore, it is necessary to conduct research on the quantitative relationship between the dissipation process of supersaturated TDG and wind velocity. Huang (2016) quantified the dissipation coefficients of supersaturated TDG in static water under different wind velocities. In our follow-up research, this paper investigates the effect of wind on the dissipation of supersaturated TDG in flowing water.

2 INTRODUCTION OF THE EXPERIMENT

Dissipation experiments on supersaturated TDG were conducted at the State Key Laboratory of Hydraulics and Mountain River Engineering (SKLH). The experiments were carried out in a Plexiglas channel with a size of 10 m*0.3 m*0.4 m and a slope of 0.2%, as shown in Figure 1. There was a cap on the top of the channel in order to avoid the influence of air to wind. The water depth was maintained at 0.13 m with two flaps which were placed in the inlet and outlet. To increase residence time of supersaturated TDG in the water and improve the effect of the dissipation of the supersaturated TDG, several cuboids with heights of 11.5 cm were placed in the channel at intervals of approximately 0.5 m.

The wind velocities were monitored by a hot-wire anemometer (TES-1341, Tes Electrical Electronic Corp., Taiwan). The measuring range for wind velocity is 0-30 m/s, with an accuracy of 1%. The TDG saturation level was measured using a total dissolved gas pressure (TGP) detector by a PT4 Tracker sensor (Point Four Systems, Inc., Canada). The measuring range for the TDG is 0-200% of saturation, with an accuracy of 1%. The temperature was monitored by a temperature sensor (L93-22, Hangzhou Loggertech Co. Ltd, China). The measuring range for temperature is -40 to 100℃, with an accuracy of 0.2℃.

At the beginning of the experiments, supersaturated water was generated by a TDG generation device (Li et al., 2012) and was added to the channel, the flow rate was 0.595 L/s, with a water depth of 0.13 m. Wind with different velocities was generated by an air blower. The water temperature inside the experimental water tank was maintained at 20℃ using a water bath.

Monitoring of the experimental data was started when the flow was steady. Six measurement points of wind velocity were placed at intervals of 2 m in the water channel, and the probes were 5 cm from the water surface. The measurement points for the saturation of TDG and temperature were placed in the inlet and the outlet.

Experimental cases were designed with different wind velocities. Experimental results are listed in Table 1.

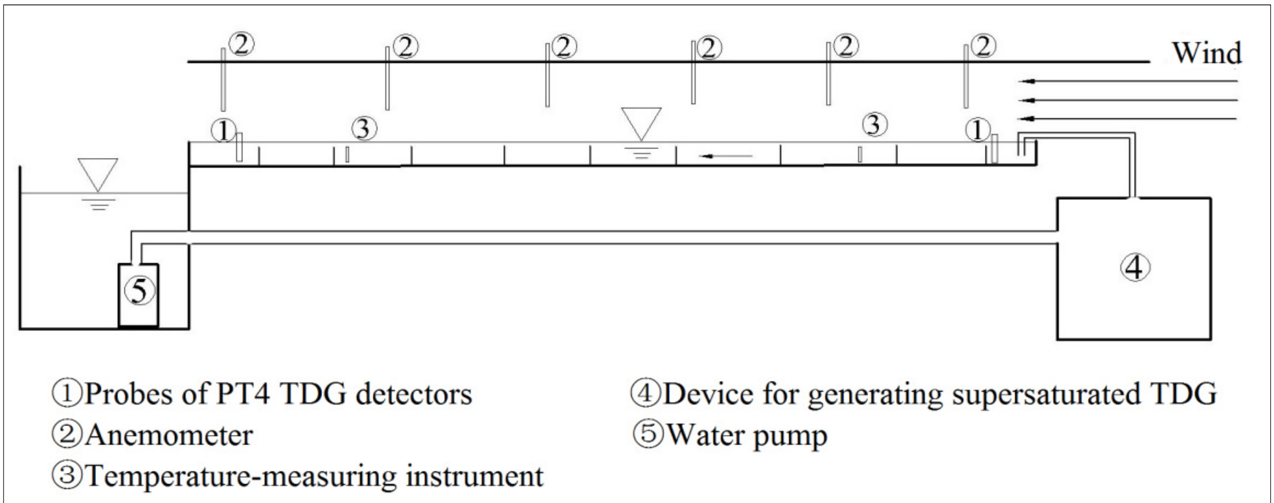

Figure 1. Sketch of experimental facility for supersaturated TDG dissipation in a closed channel.

2 CALIBRATION OF THE DISSIPATION COEFFICIENT OF SUPERSATURATED TDG

A horizontal two-dimensional $k \sim \varepsilon$ turbulence model for TDG transportation and dissipation was used to calibrate the dissipation coefficients of supersaturated TDG.

2.1 Model equations

(1)Continuity equation:

$$\frac{\partial u}{\partial x} + \frac{\partial v}{\partial y} = 0 \qquad [2]$$

where u , v (m/s) represent the flow velocities in the x , y directions, respectively.

(2)Momentum equation:

$$u\frac{\partial u}{\partial x} + v\frac{\partial u}{\partial y} = -\frac{1}{\rho}\frac{\partial p}{\partial x} + \frac{\partial}{\partial x}[(\upsilon+\upsilon_t)\frac{\partial u}{\partial x}] + \frac{\partial}{\partial y}[(\upsilon+\upsilon_t)\frac{\partial u}{\partial y}] \qquad [3]$$

$$u\frac{\partial v}{\partial x} + v\frac{\partial v}{\partial y} = -\frac{1}{\rho}\frac{\partial p}{\partial y} + \frac{\partial}{\partial x}[(\upsilon+\upsilon_t)\frac{\partial v}{\partial x}] + \frac{\partial}{\partial y}[(\upsilon+\upsilon_t)\frac{\partial v}{\partial y}] \qquad [4]$$

$$\upsilon_t = C_\mu \frac{k^2}{\varepsilon} \qquad [5]$$

where ρ (kg/m ^{3}) represents the density of water; p (N/m^2) represents the pressure; υ (m^2/s) represents the molecular viscosity coefficient, υ_t (m^2/s) represents the turbulent viscosity; k (m^2 /s^2) represents the turbulent energy, ε (m^2/s^3) represents the rate of energy dissipation, and C_μ is a constant (here, C_μ = 0.09).

(3)Equations of $k \sim \varepsilon$ turbulence model:

$$u\frac{\partial k}{\partial x} + v\frac{\partial k}{\partial y} = \frac{\partial}{\partial x}\left[(\upsilon+\frac{\upsilon_t}{\sigma_k})\frac{\partial k}{\partial x}\right] + \frac{\partial}{\partial y}\left[(\upsilon+\frac{\upsilon_t}{\sigma_k})\frac{\partial k}{\partial y}\right] + 2(\upsilon+\frac{\upsilon_t}{\sigma_k})(\frac{\partial u}{\partial y}+\frac{\partial v}{\partial x})\frac{\partial u}{\partial y} - \varepsilon \qquad [6]$$

$$u\frac{\partial \varepsilon}{\partial x} + v\frac{\partial \varepsilon}{\partial y} = \frac{\partial}{\partial x}\left[(\upsilon+\frac{\upsilon_t}{\sigma_k})\frac{\partial \varepsilon}{\partial x}\right] + \frac{\partial}{\partial y}\left[(\upsilon+\frac{\upsilon_t}{\sigma_\varepsilon})\frac{\partial \varepsilon}{\partial y}\right] + 2(\upsilon+\frac{\upsilon_t}{\sigma_\varepsilon})C_{\varepsilon 1}\frac{\varepsilon}{k}(\frac{\partial u}{\partial y}+\frac{\partial v}{\partial x})\frac{\partial u}{\partial y} - C_{\varepsilon 2}\frac{\varepsilon^2}{k} \qquad [7]$$

where σ_k represents the Prandtl number of the turbulent energy (here, σ_k=1.0), σ_ε represents the Prandtl number of the rate of the energy dissipation (here, σ_ε=1.3), and $C_{\varepsilon 1}$ and $C_{\varepsilon 2}$ are empirical constants (here, $C_{\varepsilon 1}$= 1.44 and $C_{\varepsilon 1}$ = 1.92).

(4) Equation of TDG transport and dissipation:

$$u\frac{\partial C}{\partial x} + v\frac{\partial C}{\partial y} = \frac{\partial}{\partial x}[(\upsilon+\frac{\upsilon_t}{\sigma_t})\frac{\partial C}{\partial x}] + \frac{\partial}{\partial y}[(\upsilon+\frac{\upsilon_t}{\sigma_t})\frac{\partial C}{\partial y}] + S \qquad [8]$$

where C (%) represents the percent saturation of TDG; σ_t represents the Prandtl number (here, σ_t =1.0); and S denotes the dissipation term of supersaturated TDG.

If we assume that the cross-section TDG saturation is relatively uniform, and that the supersaturated TDG dissipation process follows the first-order kinetics theory, the source team of TDG saturation follows the equation:

$$S = -K_w C \qquad [9]$$

where K_w (h^{-1}) represents the mass transfer coefficient.

 ©2017, IAHR. Used with permission / ISSN 1562-6865 (Online) - ISSN 1063-7710 (Print)

2.2 Mesh and boundary conditions

The dimensions of the mesh of the computational domain was average Δx=Δy=0.02 m. The grids topology of the simulation area is shown in Figure 2. The boundary conditions were the same as the experiments.

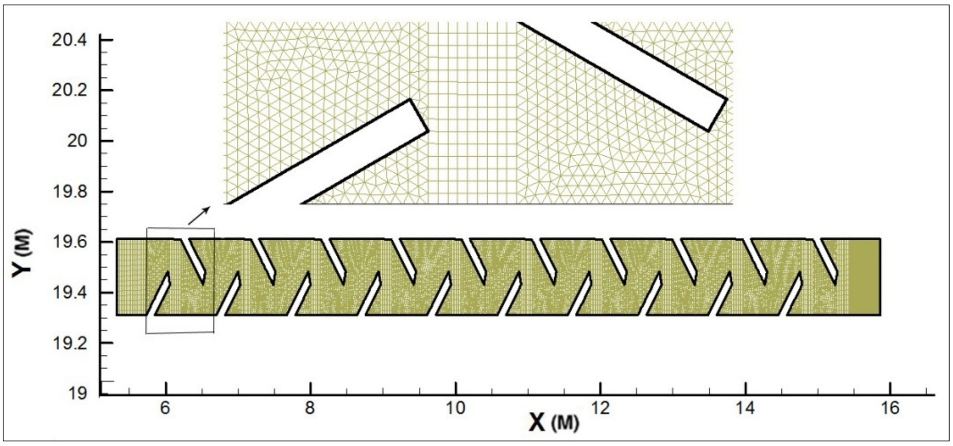

Figure 2. Sketch of the grids of the simulation area.

2.3 Simulation results

The distribution of the water velocity when the wind velocity was 11.3 m/s (case 11) is shown in Figure 3.

Based on a comparison of supersaturated TDG between the numerical simulations and experiments, the calibrated dissipation coefficients of supersaturate TDG are listed in Table 1. The distribution of the supersaturated TDG when wind velocity was 11.3 m/s (case 11) is shown in Figure 4.

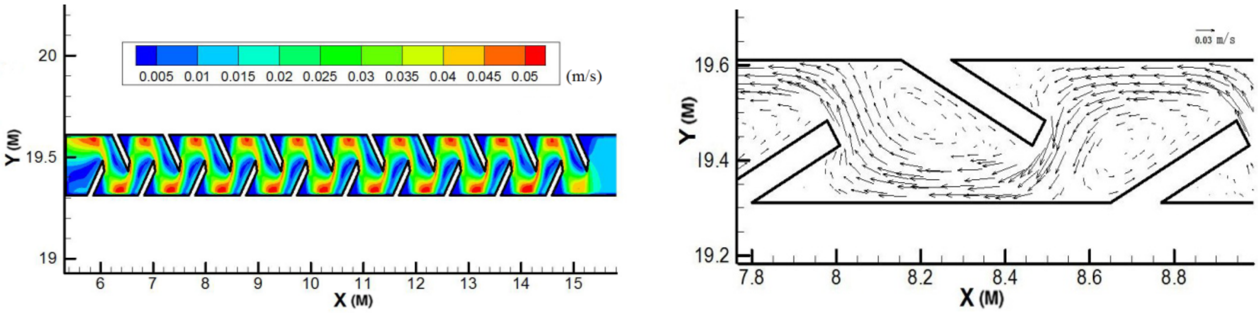

Figure 3. Distribution of the water velocity (wind velocity was 11.3m/s).

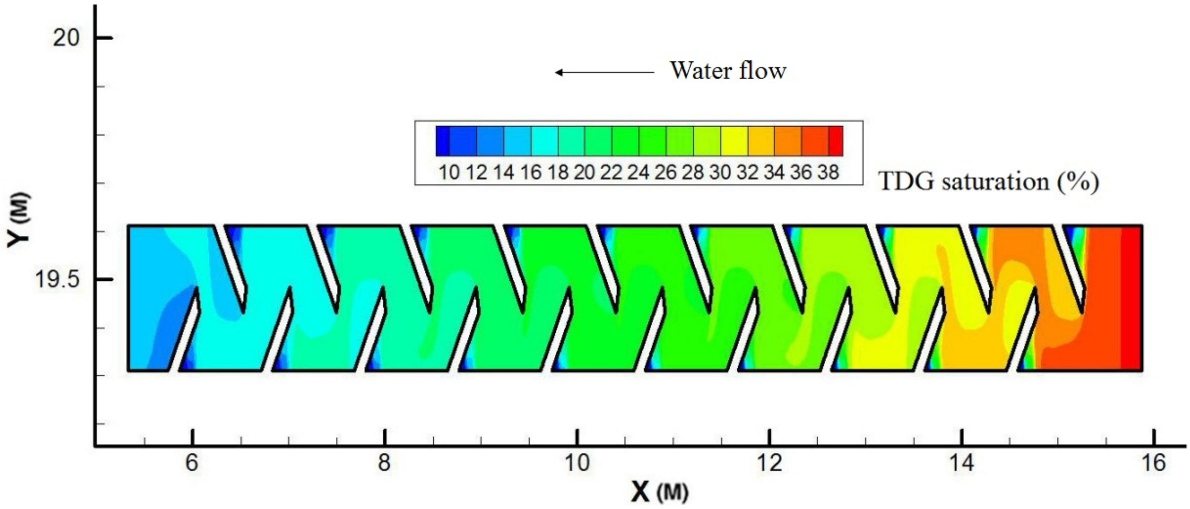

Figure 4. Distribution of TDG with the calibrated dissipation coefficient (wind velocity was 11.3m/s)

Table 1. Dissipation coefficients of supersaturated TDG in flowing water.

Case number	Wind velocity (ms^{-1})	Different TDG value between inlet and outlet (%)	Dissipation coefficient (h^{-1})	Dimensionless ratio number r	
				Actual value	Calculated value
1	0.0	1.2	0.17	1.00	1.00
2	5.8	4.7	0.87	5.12	7.22
3	5.9	7.1	1.29	7.59	7.57
4	6.5	11.1	2.15	12.65	9.17
5	6.9	12.2	2.50	14.71	10.73
6	7.5	12.8	2.71	15.94	12.81
7	7.8	16.4	3.25	19.12	14.25
8	9.0	15.4	3.27	19.24	21.33
9	9.3	16.2	3.77	22.18	23.96
10	10.6	20.6	5.02	29.53	37.88
11	11.3	24.3	6.35	37.35	48.29

3 RELATIONSHIP BETWEEN THE DISSIPATION COEFFICIENT AND WIND VELOCITY

The dimensionless ratio number r, as an indicator for the wind effect on the dissipation coefficient, was calculated using the following equation:

$$r=K_{\mathrm{w}} / K_0 \quad [10]$$

where K_{w} (h^{-1}) represents the dissipation coefficient with wind velocity W, for which the measured location of the wind velocity is 5 cm above the water surface in the experiment. K_0 (h^{-1}) is the dissipation coefficient in the windless condition.

By fitting the dimensionless ratio number r with the wind velocity, the relationship followed an exponential function (See Figure 5.):

$$r = K_w / K_0 = 1.407^w \quad [11]$$

The actual value and the calculated value of r are shown in Table 1. It can be noted that the calculated values of Eq. (11) are close to the experiment values. Comparing these results with reaeration in combined wind/stream driven flows (Mattingly, 1977; Chu and Jirka, 2003), we find that the transfer coefficient K_w increased significantly when wind appeared on the water surface. A magnitude of the coefficients in Eq. (11) is similar in undersaturated and supersaturated states.

Eq. (11) identifies the quantitative acceleration effect of wind velocity on the TDG dissipation process. It demonstrates that within a range of the experimental velocity, the higher the wind velocity is, the faster is the dissipation process. One important application of the formula is in numerical simulations of accurate assessment of the TDG dissipation process considering wind effect.

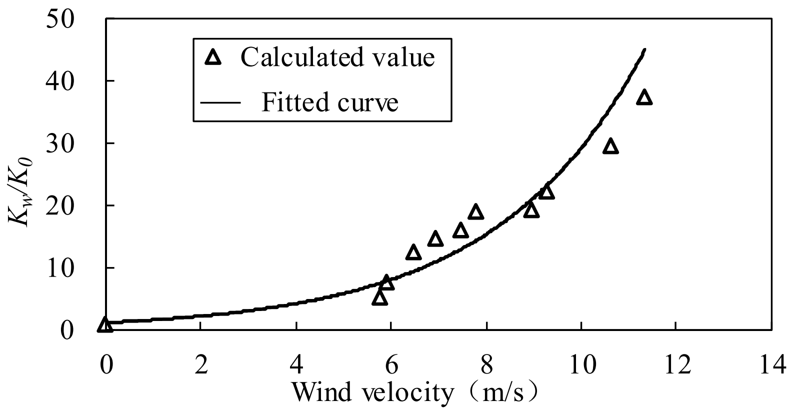

Figure 5. TDG dissipation coefficient (K_w/K_0) versus wind velocity under flowing conditions.

 ©2017, IAHR. Used with permission / ISSN 1562-6865 (Online) - ISSN 1063-7710 (Print)

4 DISCUSSION AND CONCLUSION

Experimental results indicate that wind can increase the dissipation coefficient of supersaturated TDG. A quantitative relationship $r = K_w / K_0 = 1.407^w$ between the supersaturated TDG dissipation coefficient and the wind velocity is determined using the experiments and numerical simulation. The process indicates that as the wind velocity increases, the difference between the supersaturated TDG in the inlet and outlet increases, and the dissipation coefficient increases.

Turbulent kinetic energy is the main influencing factor on the mass transfer process of the gas-liquid interface. The increase in the velocity gradient of the gas-liquid interface and the increase in the turbulent energy and the turbulent dissipation rate are caused by an increase in wind velocity. The turbulent energy and the turbulent dissipation rate increase, resulting in an increased mass transfer and dissipation process of supersaturated TDG.

Future studies are needed for the application of the proposed correlation to natural water bodies. A quantitative relationship is obtained when the experimental wind velocity is between 0 and 11.3 m/s. Further work should be conducted to verify whether the results are applicable when the wind velocity exceeds 11.3 m/s. Eq. (11) is obtained based on a single water area size. The eddy scale and water surface slope will change when the surface water area is different, and the effect of wind on water turbulence depends on many geometrical aspects, such as the length and width of the channel, water depth and so on. Further application is necessary to verify the results in this paper. Further work involves more comprehensive studies including addition of hydraulic parameters and physical effects.

ACKNOWLEDGEMENT

This work is supported by National Key R&D Program of China (Grant No. 2016YFC0401710), the Open Fund of State Key Laboratory of Hydraulics and Mountain River Engineering (SKHL1503).

REFERENCES

Chu, C. & Jirka, G.V. (2003). Wind and Stream Flow Induced Reaeration. *Journal of Environmental Engineering*, 129, 1129–1136.

Danckwerts, P.V. (1953). Continuous Flow Systems: Distribution of Residence Times. *Chemical Engineering Science,* 2(1), 1–13.

Feng, J.J., Li, R., Ma, Q. & Wang, L.L. (2014). Experimental and Field Study on Dissipation Coefficient of Supersaturated Total Dissolved Gas. *Journal of Central South University*, 21, 1995–2003.

Feng, J.J. (2013). The Dissipation Mechanism for Total Dissolved Gas Downstream of High Dams and Its Application, *phD Thesis.* Sichuan University, Chengdu, Sichuan, China. (In Chinese)

Fu, X.L., Li, D.W. & Zhang, X.F. (2010). Simulations of the Three-Dimensional Total Dissolved Gas Saturation Downstream of Spillways under Unsteady Conditions. *Journal of Hydrodynamics*, 22(4), 598–604.

Higbie, R. (1935). The Rate of Adsorption of a Pure Gas into a still Liquid during Short Periods of Exposure. *Transactions of American Institutional Chemical Engineering*, 31, 365–389.

Huang, J.P., Li, R., Feng, J.J., Xu, W.L. & Wang, L.L. (2016). Relationship Investigation between the Dissipation Process of Supersaturated Total Dissolved Gas and Wind Effect. *Ecological Engineering*, 95(2016), 430-437.

Jiang, L., Li, J., Li, R. & Li, K.F. (2008). A Study of Dissolved Gas Supersaturation Downstream of Zipingpu Dam. *Advance Water Science*, 19(3), 367–371.

Li, R., Qu, L., Li, J., Li, K.F., Deng, Y., Yi, W.M. et al., (2012). The Generation Experiment Device of Total Dissolved Gas Supersaturation by the Formation of Water Jetwith High Speed Air Flow: China, 201010124171.7 Authorized announcement, 2012-10-31.

Li, R., Hodges, B.R., Feng, J.J. & Yong, X.D. (2013). Comparison of Supersaturated Total Dissolved Gas Dissipation with Dissolved Oxygen Dissipation and Reaeration. *Environmental Engineering*, 139(3), 385–390.

Mattingly, G. E. (1977). Experimental Study of Wind Effects on Reaeration. *Journal of Hydraulic Division, American Society Civil Engineering*, 103(3), 311-323.

O'Connor, D.J. (1983). Wind Effects on Gas-Liquid Transfer Coefficients. *Journal of Environmental Engineering*, 109(3), 731–752.

Orlins, J.J. & Gulliver, J.S. (2000). Dissolved Gas Supersaturation Downstream of Spillway II: Computational Model. *Journal of Hydraulic Research*, 38(2), 151–159.

Politano, M.S. & Carrica, P.M. (2003). A Model for Turbulent Polydisperse Two-Phase Flow in Vertical Channels. *International Journal of Multiphase Flow*, 29(7), 1153–1182.

Politano, M.S., Carrica, P.M., Tuan, C. & Weber, L. (2007). A Multidimensional Two-Phase Flow Model for the Total Dissolved Gas Downstream a Spillway. *Journal of Hydraulic Research*, 45(2), 165–177.

Politano, M.S., Carrica, P.M. & Weber, L. (2009). A Multiphase Model for the Hydrodynamics and Total Dissolved Gas in Tailraces. *International Journal of Multiphase Flow,* 35(1), 1036–1050.

©2017, IAHR. Used with permission / ISSN 1562-6865 (Online) - ISSN 1063-7710 (Print)

Politano, M.S., Amado, A.A. & Bickford, S. (2012). Evaluation of Operational Strategies to Minimize Gas Supersaturation Downstream of a Dam. *Computers and Fluids*, 68(2), 168–185.

Qu, L. (2011). Relation of Total Dissolved Gas Supersaturation and Suspended Sediment Concentration of High-Dams. *Advance Water Science*, 22(6), 839–843.

Roesner, L.A. & Norton, W.R. (1971). *A Nitrogen Gas Model for the Lower Columbia River.* Water Resources Engineers, Inc., Walnut Creek, Calif, 1–350.

Shen, X., Liu, S.Y., Li, R. & Ou, Y.M. (2014). Experimental Study on the Impact of Temperature on the Dissipation Process of Supersaturated Total Dissolved Gas. *Journal of Environmental Science*, 26, 1874–1878.

US Army Corps of Engineers, (2005). *Technical Analysis of TDG Processes,* US Army Corps of Engineers-Northwest Division, Environmental Resources and Fish Planning Offices.

Wanninkhof, R. (1992). Relationship between Wind Speed and Gas Exchange over the Ocean. *Geophysical Research*, 97, 7373–7381.

Weitkamp, D.E. & Katz, M. (1980). A Review of Dissolved Gas Supersaturation Literature. *Transactions of American Fisheries Society*, 109(6), 659–702.

Weitkamp, D.E., Sullivan, R.D., Swant, T. & DosSantos, J. (2003). Gas Bubble Disease in Resident Fish of the Lower Clark Fork River. *Transactions of American Fisheries Society*, 132(5), 865–876.

Whitman, W.G. (1923). The Two-Film Theory of Gas Absorption. *Chemical Metall Engineering*, 29(4), 146–148.

 ©2017, IAHR. Used with permission / ISSN 1562-6865 (Online) - ISSN 1063-7710 (Print)

EFFECT OF UPSTREAM DISCHARGE REGULATION ON FISH HABITAT IN THE ANE RIVER, JAPAN

SHU ISHIZAKI(1), SHIGEYA MAEDA(2), AKIKO MINAGAWA(3), KOJI NODA(4), HISASHI KOBAYASHI(5), KOSHI YOSHIDA(6) & HISAO KURODA(7)

(1,2,5,6,7)Ibaraki University, Ibaraki, Japan
shigeya.maeda.15@vc.ibaraki.ac.jp
(3)The University of Shiga Prefecture, Shiga, Japan
(4)Tokyo Keizai University, Tokyo, Japan

ABSTRACT

Influence of river discharge variation on fish habitat is evaluated using two-dimensional hydrodynamic simulation, HSI (Habitat Suitability Index), and WUA (Weighted Usable Area). The river reach of interest is situated in the midstream of Ane River, Japan, which is affected by upstream flow regulation at the dam and water withdrawal for hydropower generation. An unsteady two-dimensional hydrodynamic model is calibrated and validated with observed data in 2015 and 2016. Quality of the reach as habitat of two adult fish species, *Rhinogobius flumineus* and *Nipponocypris temminckii*, is assessed by combining computed hydraulic variables and suitability indices on the fish. Analysis of spatial HSI distribution and WUA variation over discharge ranging from 0.5 – 50 m^3/s reveals that the flow environment in the reach is more preferable for *Rhinogobius flumineus* than *Nipponocypris temminckii.* The discharge where habitat begins to decrease sharply in the WUA/flow curve is derived, which could be used as a recommended minimum discharge in view of ecological conservation.

Keywords: Ecohydraulics; habitat suitability; hydrodynamic simulation; reservoir; river.

1 INTRODUCTION

Evaluation of fish habitat in rivers has received much attention in recent years for establishing sustainable water use. Generally, in Japan, river water is utilized in various ways such as agriculture, industry, daily life, hydropower generation, fishery, etc. These kinds of water use as well as flood control in a river cause temporal variation of stream water discharge, which often affects fish detrimentally. Although conservation of fish habitat in a river should be well planned for harmonized water use, effective methods to achieve this aim remain unclear.

Upstream discharge regulation based on the instream flow incremental methodology (IFIM) is one of the popular ways to determine the minimum flow suitable for target fish species in a river. Habitat suitability index (HSI) is often employed to evaluate the quality of fish habitat in a river section. Recent studies combining a hydrodynamic simulation model with HSI have procured most preferable stream discharge for a target fish. Using these approaches, for example, Yi et al. (2014) have examined the effect of constructing Manwan Reservoir on extinction risk of endemic fish species in the Lancang-Mekong River, and Chaina. Li et al. (2013) showed the Xiaowan dam had an immediate and profound impact on the fish fauna in a region of the Lancang-Mekong River. Boavida et al. (2015) have investigated the effects of hydropeaking in the habitat of the Iberian barbel in the Ocreza River, Portugal. Jowett and Biggs (2006) reviewed six New Zealand cases and showed that the modified flow regime by IFIM approach mostly succeeded in achieving the desired ecological outcomes. However, few researches have addressed the applicability of these methods to a small-scale and steep river section influenced by upstream flow regulation. In addition, it seems that this kind of simulation-based quantitative study has rarely been conducted for planning water allocation to multiple water use in a river in Japan.

In this study, the suitability of a midstream reach of the Ane River, Japan, as the habitat of adult of *Rhinogobius flumineus* and *Nipponocypris temminckii* (dark chub) is evaluated using two-dimensional hydrodynamic and HSI models. Flow analysis conducted under various values of assumed upstream current discharge results in estimation of HSI distribution and weighted usable area (WUA) in the reach. The results indicate preferable discharge levels for target fish species.

2 METHOD

2.1 Study area

The Ane River originates in the Ibuki mountain of Japan and flows into Lake Biwa. The length of the river is 39km and its watershed area is 686 km^2. The Anegawa dam reservoir, which was built in 2002, is located

©2017, IAHR. Used with permission / ISSN 1562-6865 (Online) - ISSN 1063-7710 (Print)

about 30 km upstream from the river mouth with capacity of 7.6 million cubic meters. A river reach having the length of 380 m and the width of around 23 – 50 m was chosen for evaluation of fish habitat in this study (Figure 1). The reach is located around 8 km downstream of the dam. The stream discharge fluctuates mainly because the dam regulates its outflow to undertake flood control, water supply, and maintaining an appropriate river flow for environmental conservation. Annual precipitation in the Nagahama meteorological observation station, which is located near the reach, ranged from 1,320 to 2,056 mm during 2002 – 2013. The outflow discharge from the dam was normally about $1.5 m^3/s$ and varied over the flow range of 0.5 - 50 m^3/s in the same period. Water intake from the river at the downstream side of the dam for hydropower generation decreases the stream discharge in the reach of interest because the water withdrawn for the power plant returns to the downstream side of the reach.

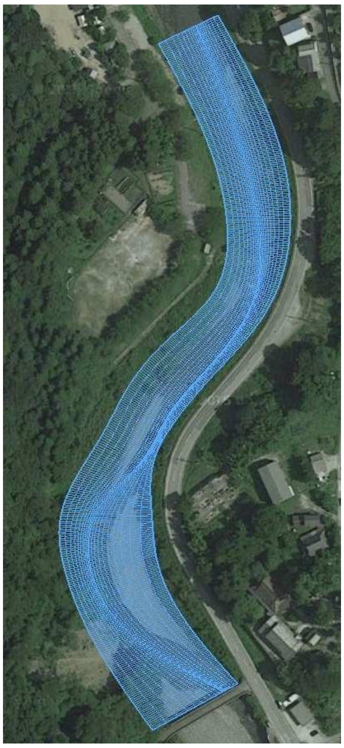

Figure 1. Computational mesh in the reach of interest.

The watercourse of the reach has a shape like a single-wave sinusoid, including two clear pool-riffle-run sequences as shown in Figure 1. A topographical survey of the river bed was undertaken at five transverse cross-sections of the reach on 27 July 2015. The river bed slope was measured as 1/118. Substrate composition was dominated by sand and gravel.

2.2 Fish

The target species of fish, *Rhinogobius flumineus* (called Fish 1 hereafter) and *Nipponocypris temminckii* (named Fish 2), were determined because of both the existence in the reach and availability of the suitability index (SI) curves, or preference curves, for the fish. Fish 1 is a family of gobies, omnivorous, and about 4 – 6 cm in total length. The fish prefers areas of low current velocity and stays around plant roots and gravels on a river bed (Kawanabe and Mizuno, 2001). Fish 1 was one of the predominant species in the upstream region of the Ane River, which was found by our fish capturing survey conducted on 21 October 2015. Fish 2 is a family of cyprinid, omnivorous, and about 15 cm in total length. The fish lives in low current pool (Kawanabe and Mizuno, 2001).

2.3 Hydrodynamic simulation

Nays2DH (iRIC Project) was adopted to solve unsteady two-dimensional Reynolds averaged Navier Stokes equation and continuity equation for estimating spatial distribution of hydraulic variables, i.e., water depth and current velocity, in the reach. Using the cross-sectional topography data on nine cross-sections, prepared with the survey and aerial photographs taken on 1 August 2015 (Google Earth), the river section was discretized into 7,700 quadrilateral cells with 8,106 nodes (Figure 1). The 2D hydraulic model was first calibrated at 1.12 m^3/s with data on water depth and current velocity measured on 18 October 2015. Downstream boundary condition was water depth of 0.32m. The time step was 0.01 sec. Total computational time was 1,200 sec., because the flow reached steady state at around 1,000 sec. In the model calibration, values of Manning's roughness coefficients in the pool, riffle, and run were adjusted so that the computed

 ©2017, IAHR. Used with permission / ISSN 1562-6865 (Online) - ISSN 1063-7710 (Print)

hydraulic variables match observed ones. Second, the model was validated at 1.48 m^3/s measured on 15 October 2016. Finally, the validated hydrodynamic model was run to estimate distributions of current velocity and water depth, which were employed as inputs to the HSI model under low (0.5 m^3/s) to high (50 m^3/s) discharge. The range of discharge was determined based on historical data. The uniform water depth was used as the downstream boundary condition in the computations.

2.4 Habitat suitability index

The SI curves representing preference on water depth and current velocity for the staying adult fish were obtained from literatures (Tsujimoto et al., 2000; Kawamoto et al., 1999). The preference curves for Fish 1 were created by the literature-based method, and those for Fish 2 were estimated by field survey in the Kiba River, Japan, by Kawamoto et al. (1999). The SI curves are illustrated in Figure 2. The habitat suitability ranges from unsuitable (0) to optimal (1) in the curves. Using both the SI curves and the computed hydraulic variables (i.e, nodal water depth h_i and velocity v_i), the SI values at the i-th of each node for the f-th fish, $\mathrm{SI}_h^f(h_i)$ and $\mathrm{SI}_v^f(v_i)$were computed. Then the i-th nodal HSI value was computed as the geometric mean of the SIs as follows

$$\mathrm{HSI}_i^f = \sqrt{\mathrm{SI}_h^f\left(h_i\right)\cdot \mathrm{SI}_v^f\left(v_i\right)}, \quad \forall i, f \qquad [1]$$

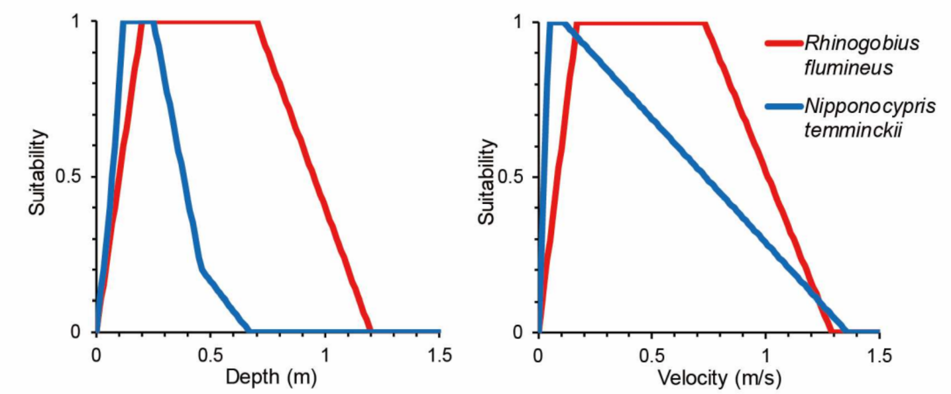

Figure 2. Suitability index curves for Fish 1 (*Rhinogobius flumineus*) and 2 (*Nipponocypris temminckii*).

2.5 Weighted usable area

The area of water surface in the reach will change depending on the upstream discharge. Therefore, the WUA was introduced to evaluate the quality and quantity of the fish habitat comprehensively. The value of WUA at the j-th element for the f-th fish was calculated with the elemental HSI which is estimated with four nodal HSI values in each cell, and the area of element a_j working as a weight

$$\mathrm{WUA}^f = \sum_{j=1}^{N_E} a_j \mathrm{HSI}_j^f \qquad [2]$$

Where HSI_j^f = elemental HSI at the j-th element for the f-th fish; and NE = total number of elements in the reach. It is noted that the WUA is a function of discharge, which represents overall effectiveness of the reach as the habitat of the target fish.

3 RESULTS AND DISCUSSION

3.1 Calibration and validation

Many previous studies on fish habitat evaluation in a river have employed hydrodynamic simulation with assumed various discharge levels due to importance of hydraulic conditions. This study also adopted the same approach to the reach in the Ane River. At the beginning, the Nays2DH hydrodynamic model was calibrated with the data obtained at seven observation points in 2015. By and large, the estimated depth and velocity matched the observed ones, although the computed current velocity tended to be overestimated. Figure 3 shows the computational result of water depth and velocity in the calibration of the hydrodynamic model. As can be seen in Figure 3, the estimated locations of pools and riffles were reproduced fairly accurately. Then, the model was successfully validated with seven sets of measured water depth and velocity in 2016.

3.2 HSI and WUA

Using the validated hydrodynamic model, spatial distributions of hydraulic variables were produced under given upstream discharge ranging from 0.5 – 50 m^3/s. Habitat suitability for Fish 1 and 2 at each node in the reach was evaluated with the nodal estimated water depth and velocity and fish preference by Eq.[1]. Next, the nodal HSI value was converted into elemental one by calculating arithmetical mean of four nodal HSIs in an element. Finally, WUAs for the fish with the elemental HSI were computed by Eq.[2]. Estimated distributions of nodal HSI at discharge of 0.5, 5, 10, and 50 m^3/s for fish 1 and 2 were demonstrated in Figures 4 and 5, respectively. These figures also show the expansion of predicted water surface areas depicted in gray color in the background.

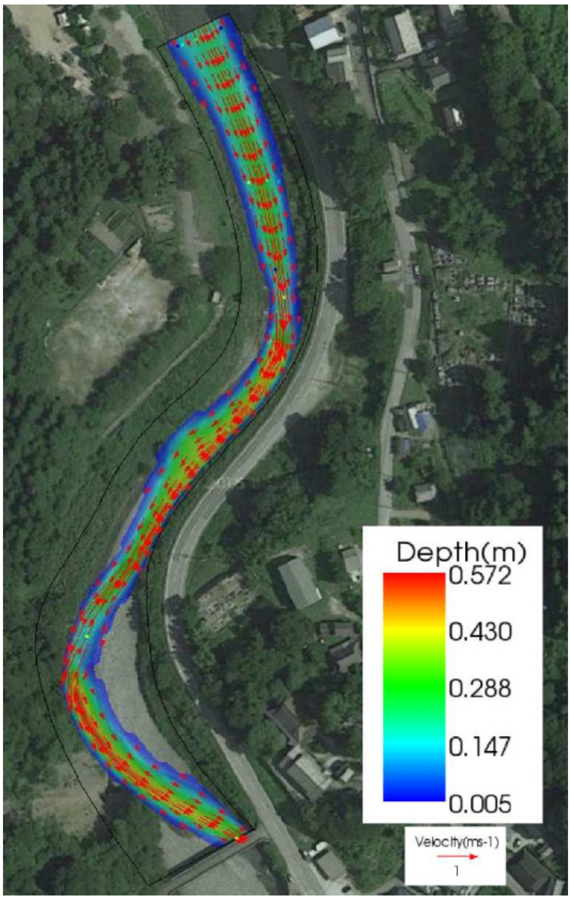

Figure 3. Distributions of computed water depth and current velocity in model calibration.

Comparison of Figures 4 and 5 clarifies the difference of influence of upstream discharge variation on the preferable area distribution for the fish. Regarding Fish 1, the area of high habitat suitability concentrated on the river pool under lower discharge (e.g., 0.5 and 5 m^3/s). Locations of high HSI area shift from the higher depth region to the riverbanks as the discharge increases, which is attributed to the preference in water depth and velocity defined in Figure 2. For fish 2, the whole tendency of HSI distribution change with discharge variation was similar to that of Fish 1. However, it was noted that the locational shift of high HSI region began with the smaller discharge level. Thus, Fish 2 is found weaker in the higher flow conditions than Fish 1.

The graphs of WUA as a function of discharge were drawn as the solid curves in Figure 6. For both fish, the WUA increased with increasing discharge at low rates, and then reached a maximum at a certain discharge. After that, the WUA began to decline with rising discharge. Figure 6 presents that the maximum WUAs of 6,810 and 4,140 m^2 occurred at 8 and 2 m^3/s for Fish 1 and 2, respectively. Fish 1 gained higher maximum value of WUA.

The region between the solid red and broken green lines in Figure 6 corresponds to the area of higher (i.e., 0.7 – 1) HSI, or highly preferable area. The medium and low HSI regions can be similarly defined. As can be seen, Fish 1 had the larger area of 'higher HSI' than Fish 2. Therefore, it can be confirmed that the flow environment is more suitable for Fish 1 than Fish 2 under assumed flow variation. This estimation is realistic, given that the number of caught Fish 1 was much larger than that of Fish 2 in our fish survey in 2015.

The minimum discharges at the point where WUAs began to decline sharply with decreasing flow (Jowett and Biggs, 2006) were derived as 2.3 and 1.2 m^3/s for Fish 1 and 2, respectively. Since the normal outflow discharge from the Ane River dam was around 1.5 m^3/s, requiring the minimum discharge of 2.3 m^3/s in the river would be more effective for conserving Fish 1.

 ©2017, IAHR. Used with permission / ISSN 1562-6865 (Online) - ISSN 1063-7710 (Print)

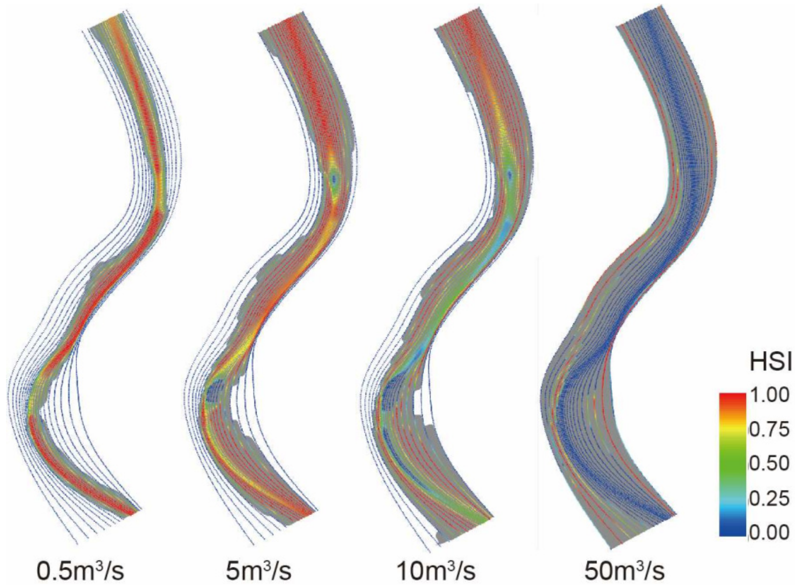

Figure 4. Distributions of estimated HSI at discharge of 0.5, 5, 10, and 50 m^3/s for Fish 1.

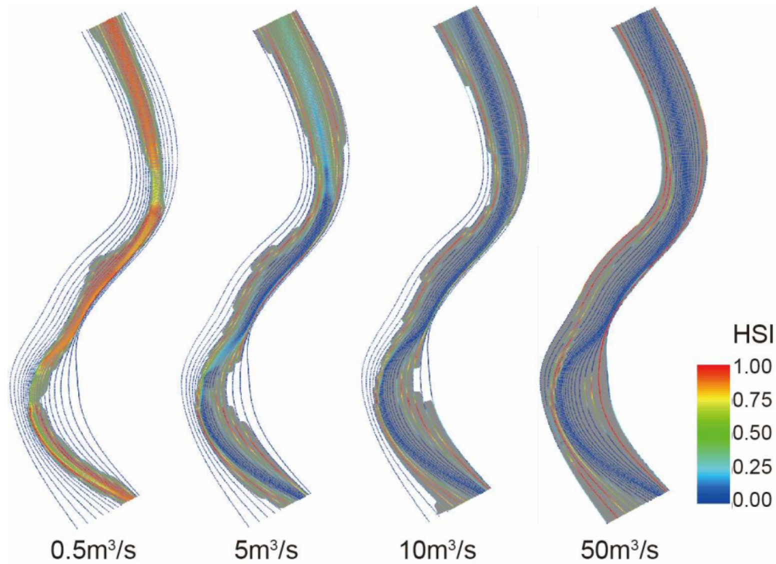

Figure 5. Distributions of estimated HSI at discharge of 0.5, 5, 10, and 50 m^3/s for Fish 2.

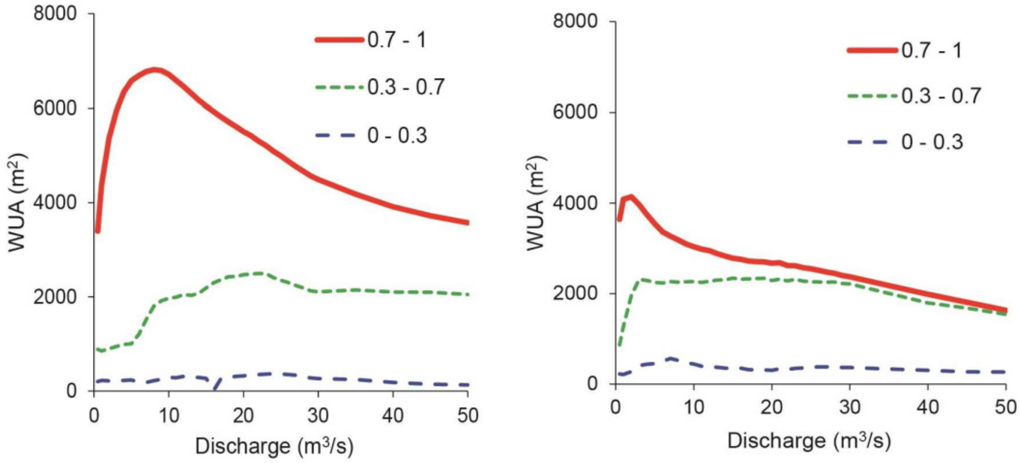

Figure 6. WUA/flow curves (solid lines) and high, medium, and low HSI regions for Fish 1 and 2.

4 CONCLUSIONS

Habitat suitability for staying adult of *Rhinogobius flumineus* and *Nipponocypris temminckii* in the reach of the Ane River is evaluated using hydrodynamic simulation, HSI and WUA. Flow regulation in the upstream side of the reach is found to significantly influence the HSI and the WUA in the downstream reach. The feature of this study is that it is conducted in quantitative and spatially-detailed way in the river with narrow width and steep slope in Japan. Although the river reach can provide larger preferable area for *Rhinogobius flumineus*, the current normal discharge causes to reduce the suitable area for the fish. The minimum required discharge for the fish is estimated from the WUA/flow curve, which could be used to plan water regulation more rationally by harmonizing conflicting goals about multiple water use and fish habitat conservation. In the future, evaluation of habitat suitability should be improved by considering other important factors such as substrate and vegetation. Since morphological change of river bed due to sediment transport alters hydraulic and ecological environments, it should also be taken into account in fish habitat evaluation from a long-term perspective.

ACKNOWLEDGEMENT

The authors would like to thank Dr. Kazuhiro Sugahara and Professor Takuya Ohkubo for helping in fish survey. The topography survey is supported by the Kitai Sekkei Company. Some morphological, hydraulic, and ecological information in the Ane River watershed are provided by Nagahama Civil Engineering Office, Anegawa Coastal Land Improvement District, Upstream Anegawa Fisheries Cooperative, and Maibara city. We are grateful to iRIC Project for supplying Nays2DH hydrodynamic simulation model. This study has been supported in part by JSPS KAKENHI Grant Number 26310301.

REFERENCES

Boavida, I., Santos, J.M., Ferreira, T. & Pinheiro, A. (2015). Barbel Habitat Alterations due to Hydropeaking. *Journal of Hydro-Environment Research*, 9, 237-247.

Jowett, I. & Biggs, B.J.F. (2006). Flow Regime Requirements and the Biological Effectiveness of Habitat-based Minimum Flow Assessments for Six Rivers. *International Journal of River Basin Management*, 4(3), 179-189.

Kawamoto, Y., Sekine, M., Jidong, Y., Kobayashi H. & Ukita, M. (1999). A Consideration on Compatibility of Fish Suitability-of-Use Curves among Rivers in IFIM. *Environmental Engineering Research*, 36, 271-276. (In Japanese)

Kawanabe, H. & Mizuno, N. (2001). *Freshwater Fish in Japan*. Yama-kei, 701. (In Japanese)

Li J., Dong, S., Peng, M., Yang, Z., Liu, S., Li, X. & Zhao, C. (2013). Effects of Damming on the Biological Integrity of Fish Assemblages in the Middle Lancang-Mekong River Basin. *Ecological Indicators*, 34, 94-102.

Tsujimoto, T., Tashiro, T. & Itoh, T. (2000). Fish Habitat Evaluation from View Point of Accessibility to Various Spaces in Life Cycle and Role of Microscopic Morphology in Rivers on Fish Habitat. *Advances in River Engineering*, 6, 167-172. (In Japanese)

Yi, Y., Tang, C., Yang, Z. & Chen, X. (2014). Influence of Manwan Reservoir on Fish Habitat in the Middle reach of the Lancang River. *Ecological Engineering*, 69, 106-117.

 ©2017, IAHR. Used with permission / ISSN 1562-6865 (Online) - ISSN 1063-7710 (Print)

DISCHARGE PREDICTION MODEL FOR SIMPLE CONICAL FLUMES IN TRAPEZOIDAL CANALS

ANIRUDDHA D. GHARE[1], AVINASH D. VASUDEO[2] & AVINASH M. BADAR[3]

[1,2]Department of Civil Engineering, Visvesvaraya National Institute of Technology, Nagpur 440010, India adghare@yahoo.co.in
[3] Department of Civil Engineering, KDK College of Engineering, Nagpur 440009, India

ABSTRACT

For better water management for agriculture, canal water flow measurement at desired location at desired time is essential. The flow measurement in canal can be carried out by using different flumes or electromagnetic devices, which are generally expensive. Most of the arrangements are of non portable type and require that those be permanently installed in canals for measurement of flow-rates. India is an agricultural country where large number of networks of canals are found, whose cross-sections are mostly trapezoidal. The scarcity of water over the globe necessitates the need for measurement of even small flows through the field canals for better conservation and management of water. The portable flumes with their discharge prediction models shall be of great help in small canal flow measurements leading to achievement of goal of water conservation. Literature shows a few demonstrated studies on the use of regular shaped obstructions viz. cylinders, prisms and cones for creation of constriction to the canal flow and the resulting stage-discharge relationships. However, literature shows limited number of experimental studies on conical obstructions in a trapezoidal channel. This study elaborates a flume where constriction is obtained by inserting a cone at the center of a trapezoidal canal. This arrangement is referred as a simple conical flume. An experimental investigation of two different portable conical flumes placed in a trapezoidal canal with side slopes of 1 H: 1V to produce critical flow conditions, has been carried out. The observations from the laboratory experiments on the flume have been analyzed and two different discharge prediction models have been developed for determination of discharge. The results from the developed mathematical models have been compared with the measured flow rates obtained from the additional experimental data that is collected for its validation. Thus, the presented calibrated flume can be an interesting alternative as compared to other stationary flumes for flow rate predictions, particularly in case of small trapezoidal open canals. However, more exhaustive experiments shall have to be conducted to propose a general discharge prediction model that would account for different constriction ratios as well as canal side slopes.

Keywords: Conical flume; canals; agriculture; discharge prediction; critical flow.

1 INTRODUCTION

Water conservation and increased irrigation water use efficiency are the needs of the hour. For efficient water management, water in agricultural canals must be measured, however small the size of channel may be. Many options are available for improving the efficiency of water use in farming such as efficient irrigation technologies, improved irrigation scheduling, regulated deficit irrigation and mainly, the measurement of water used for irrigation. As such, accurate flow measurement is necessary for the proper distribution and regulation of the irrigation water. As agriculture uses most of the world's fresh water, measuring water in open canal is an important step towards water conservation. There are different flow measuring devices used for canal flow measurements. However, there are only a few mobile devices which can register the flow rate at given location, at given point of time.

In India, Parshall flume (Parshall, 1926; Genovez et al., 1993) and cutthroat flumes are commonly in use for the measurement of discharge in canals. However, these flumes have lack of precision and high head-loss requirement. Further, these flumes are of fixed type. The investigated flume in this research is a simple conical flume which is a mobile type of flume. Discharge measurement is usually carried out by flow constriction due to canal side convergence. Construction or removal of fixed flumes in canals requires engineering knowledge.

In the present investigation for flow measurement in small open canal, a flume is introduced that consisted of a cone installed in perpendicular position in trapezoidal canal with a 1 H: 1V side slope (Fig. 1). This arrangement is referred as simple conical flume. Literature also shows the calibrated cylindrical flumes having been used for the same purpose (Badar and Ghare, 2012), however the stability of a cone is better as compared to a cylinder. The present experimental investigations are primarily based on the research carried out by Hager (1985, 1986, 1988). Circular cone was used to measure the discharge of a rectangular prismatic channel in the research by Hager (1985). Investigated flume belongs to a group in which the throat section is obtained with an object (the cone) immersed in the canal and not by canal-side convergence. The cone, which has the same characteristics as standard measuring flumes, is removable and can be replaced at any desired section along the canal network for the measurement of discharge in free flow condition. A mathematical calibration model is developed for two different simple conical flumes based on the experiments conducted in the laboratory for a trapezoidal channel having side slope as 1 H : 1V for free flow conditions.

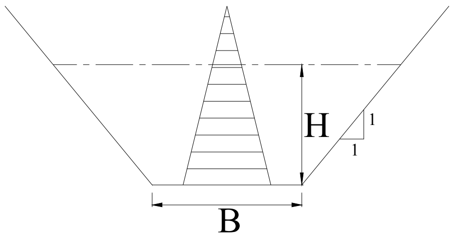

Figure 1. Cross-Sectional view of the Simple Conical Flume.

The present device (Figure 2) is very simple to install and problems of incorrect settlement, for example, of a Parshall flume (Genovez et al. 1993), are removed.

Figure 2. Photograph of one of the Cones (D=0.151 m) used in the experimentation.

The cone is developed and constructed by the authors. The cone is placed in a trapezoidal channel which is available in Hydraulics Laboratory of the K.D.K. College of Engineering, Nagpur, India. For free flow conditions, experiments on two different cones are carried out and their geometrical characteristics are provided in Table 1.

Table 1. Geometric Characteristics of Experimental flumes.

Parameter	Cone	
	1 (m)	2 (m)
Diameter at base, (D)	0.151	0.200
Height	0.200	0.640

2 EXPERIMENTAL FACILITIES

The experimental setup was made at the Hydraulics Laboratory of K.D.K College of engineering, Nagpur, India. Experimental setup consisted of a trapezoidal channel of length 4.9 m, base width (B) of 0.2 m and had side slope 1H : 1V. The side walls of channel were made up of mild steel and acrylic sheet. The smooth surfaced cone with 0.151 m and 0.160 m diameters at base, with corresponding heights as 0.20 m and 0.64 m, were used for creating obstruction to form critical flow.

Continuous flow of water was pressed by means of 10 H.P. pump into the channel with water re-circulation arrangement. The discharge was controlled by a flow regulating valve, which was measured with the help of a collecting tank of capacity 332.5 litre. The flow was stabilized by baffle walls provided on the upstream collecting tank of the channel. Cones were placed at a distance of 1.4 m from the downstream end of the channel for various discharges and the observations for ‘H’ were recorded. The depth of water on the upstream side of the cone at the stagnation point (H) was measured by a pointer gauge, mounted on a cart assembly rolling on sides of a trapezoidal channel. Fig. 3 shows photograph of one of the experimental runs of the simple conical flume.

 ©2017, IAHR. Used with permission / ISSN 1562-6865 (Online) - ISSN 1063-7710 (Print)

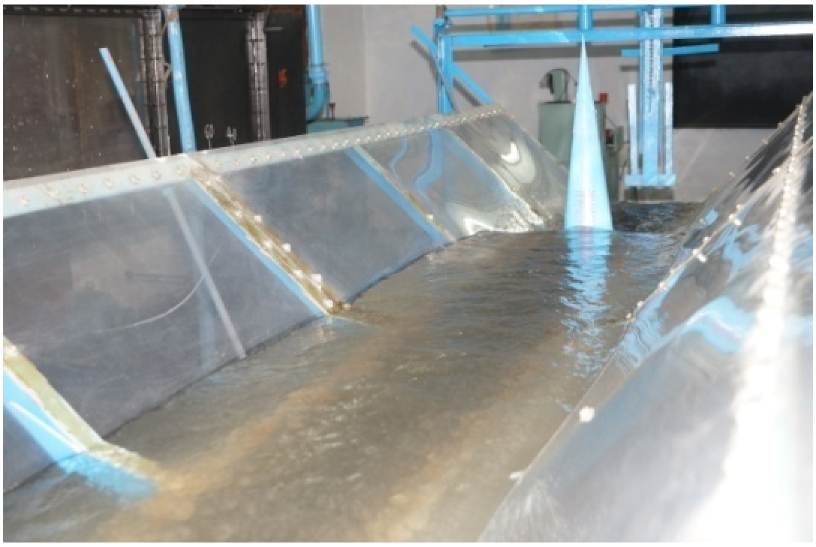

Figure 3. Photograph of Simple Conical Flume operating under Free Flow Conditions.

3 DISCHARGE RELATIONSHIP FOR SIMPLE CONICAL FLUME

It was observed that a good correlation existed between dimensionless parameters $\frac{Q_m}{\left(B^{\frac{5}{2}}g^{\frac{1}{2}}\right)}$ and $\frac{H}{D}$, and regression analysis was carried for all the available experimental data (Table 2). Q_m denotes the measured discharge whereas Q_c denotes the computed discharge.

Table 2. Computations for development of model -1.

B	D	H	Q_m	$\frac{H}{D}$	$\frac{Q_m}{\left(B^{\frac{5}{2}}g^{\frac{1}{2}}\right)}$	Q_c	% Error of Predicted Discharge, Q_c by proposed Model- 1
(m)	(m)	(m)	(m^3/sec)			(m^3/sec)	
0.2	0.151	0.1300	0.0146	0.8609	0.2606	0.0141	-3.6
0.2	0.151	0.1255	0.0129	0.8311	0.2302	0.0130	0.6
0.2	0.151	0.1195	0.0116	0.7914	0.2070	0.0116	-0.2
0.2	0.151	0.1150	0.0107	0.7616	0.1910	0.0106	-1.0
0.2	0.151	0.1115	0.0098	0.7384	0.1749	0.0099	0.6
0.2	0.151	0.1075	0.0090	0.7119	0.1606	0.0091	0.6
0.2	0.151	0.1030	0.0081	0.6821	0.1446	0.0082	1.2
0.2	0.151	0.0970	0.0069	0.6424	0.1232	0.0071	3.4
0.2	0.151	0.0915	0.0062	0.6060	0.1107	0.0062	0.5
0.2	0.151	0.0815	0.0047	0.5397	0.0839	0.0048	1.3
0.2	0.151	0.0730	0.0037	0.4834	0.0660	0.0037	-0.4
0.2	0.151	0.0665	0.0031	0.4404	0.0553	0.0030	-4.2
0.2	0.151	0.0610	0.0024	0.4040	0.0428	0.0024	1.2

The experimental data points of the first cone (D=0.151 m) for which the regression analysis was carried out, gave the relationship as

$$\frac{Q_m}{\left(B^{\frac{5}{2}}g^{\frac{1}{2}}\right)} = 0.3558\left(\frac{H}{D}\right)^{2.322} \qquad [1]$$

with coefficient of determination, R^2 = 0.998, which was very good.

The variation of dimensionless discharge and dimensionless head is plotted in Figure 4. Equation (1) is the mathematical model developed for prediction of discharge for simple conical flume for trapezoidal canal having side slope 1 H : 1V for free flow condition.

©2017, IAHR. Used with permission / ISSN 1562-6865 (Online) - ISSN 1063-7710 (Print)

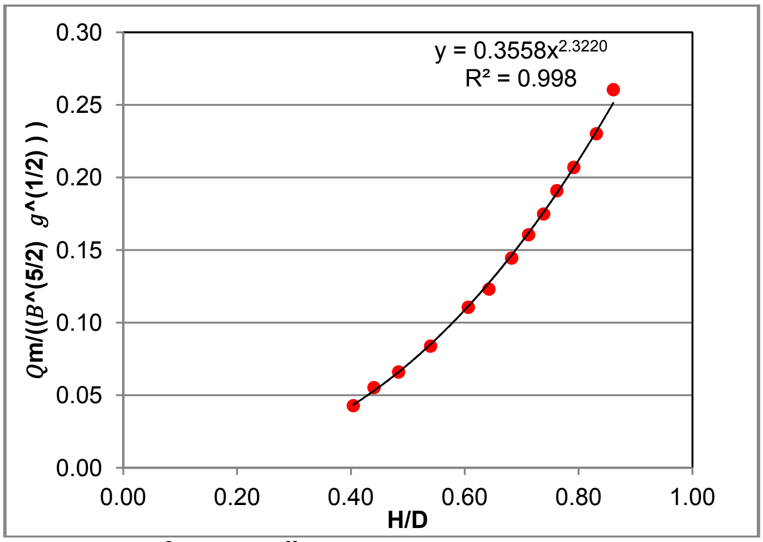

Figure 4. Relationship between $\frac{Qm}{\left(B^{\frac{5}{2}}g^{\frac{1}{2}}\right)}$ and $\frac{H}{D}$ obtained by regression analysis based on the experimental data for cone (D = 0.151 m).

Similarly, experiment was conducted for the second cone (D = 0.161 m) and regression analysis was carried out for all the available experimental data (Table 3). Equation (2) with a coefficient of determination, R^2 = 0.998 is another mathematical model developed for prediction of discharge for simple conical flume for trapezoidal canal having side slope 1 H : 1V. This {Eq. (2)} is very similar to the first model. The analysis is shown in Figure 5.

$$\frac{Q_m}{\left(B^{\frac{5}{2}}g^{\frac{1}{2}}\right)} = 0.3551\left(\frac{H}{D}\right)^{2.334} \qquad [2]$$

Table 3. Computation for Development of Model -2.

B	D	H	Q_m	$\frac{H}{D}$	$\frac{Q_m}{\left(B^{\frac{5}{2}}g^{\frac{1}{2}}\right)}$	Q_c	% Error of Predicted Discharge Q_c by proposed Model- 1
(m)	(m)	(m)	(m^3/sec)			(m^3/sec)	
0.2	0.16	0.1350	0.0133	0.8438	0.2381	0.0134	0.29
0.2	0.16	0.1310	0.0122	0.8188	0.2180	0.0125	2.10
0.2	0.16	0.1235	0.0106	0.7719	0.1893	0.0109	2.45
0.2	0.16	0.1145	0.0094	0.7156	0.1672	0.0091	-2.78
0.2	0.16	0.1025	0.0071	0.6406	0.1274	0.0070	-1.45
0.2	0.16	0.0925	0.0056	0.5781	0.0996	0.0055	-0.81
0.2	0.16	0.0900	0.0054	0.5625	0.0955	0.0052	-2.93
0.2	0.16	0.0880	0.0050	0.5500	0.0888	0.0049	-0.95
0.2	0.16	0.0810	0.0040	0.5063	0.0714	0.0041	1.55
0.2	0.16	0.0750	0.0033	0.4688	0.0593	0.0034	2.21
0.2	0.16	0.0675	0.0027	0.4219	0.0482	0.0027	-1.65
0.2	0.16	0.0630	0.0022	0.3938	0.0394	0.0023	2.26
0.2	0.16	0.0550	0.0017	0.3438	0.0300	0.0016	-2.07
0.2	0.16	0.0520	0.0014	0.3250	0.0253	0.0014	1.72

 ©2017, IAHR. Used with permission / ISSN 1562-6865 (Online) - ISSN 1063-7710 (Print)

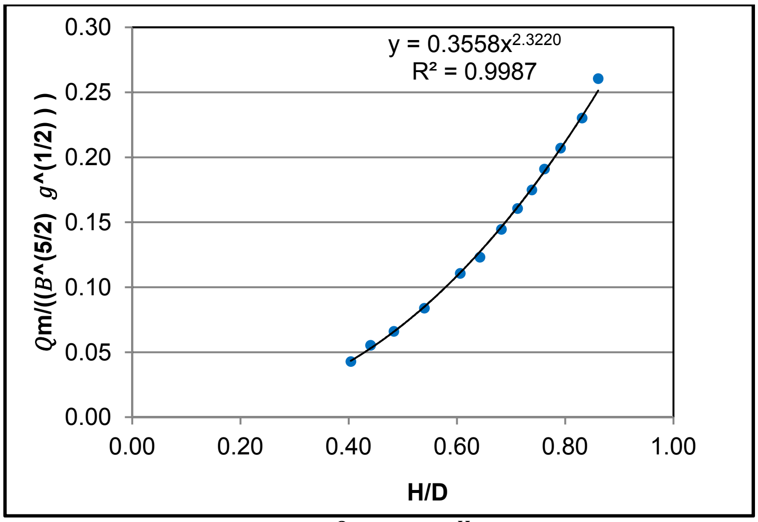

Figure 5. Relationship between $\frac{Q_m}{\left(B^{\frac{5}{2}} g^{\frac{1}{2}}\right)}$ and $\frac{H}{D}$ obtained by regression analysis based on the experimental data for cone (D =0.16 m)

Measured flow rates were compared with predicted discharges obtained by both the mathematical models. The results of comparison are shown in respective tables, which showed that the developed model predicted the discharge with less than ± 5% errors.

4 MODEL VALIDATION

Additional experimental observations on the upstream side of the cone were recorded for both the cones for different discharges. By using the developed mathematical models, the discharge was predicted for recorded observations and it was found that both the models predicted discharge with percentage error less than ± 5 %. Thus, the models were validated. The details of the validations are shown in Table 3.

Table 4. Validation of Mathematical Models.

Simple Conical Flume (D = 0.151 m) -1				Simple Conical Flume (D =0.16 m) -2			
H	Q_m	Q_c	% Error	H	Q_m	Q_c	% Error
m	m^3/s	m^3/s		m	m^3/s	m^3/s	
0.1740	0.0251	0.0242	-3.5	0.1275	0.0133	0.0135	0.8
0.1325	0.0128	0.0128	0.4	0.1230	0.0125	0.0124	-1.4
0.1265	0.0117	0.0115	-1.4	0.1175	0.0111	0.0111	-0.1
0.1180	0.0099	0.0098	-1.7	0.1125	0.0101	0.0101	-1.1
0.1085	0.0080	0.0080	0.9	0.1055	0.0087	0.0087	-0.6
0.0975	0.0064	0.0063	-2.5	0.1000	0.0077	0.0077	-1.3
0.0855	0.0047	0.0046	-1.1	0.0940	0.0067	0.0066	-2.0
0.0775	0.0038	0.0037	-3.7	0.0865	0.0055	0.0055	-1.3
0.0685	0.0028	0.0027	-2.7	0.0765	0.0042	0.0041	-3.7
0.0650	0.0024	0.0024	-0.5	0.0680	0.0032	0.0031	-2.5
0.0570	0.0019	0.0018	-8.2	0.0635	0.0028	0.0027	-4.9

5 CONCLUSIONS

Simple conical flume can be used as a mobile discharge measurement device for small sized trapezoidal canals on irrigation fields. The conical shape of flume, as compared to a cylindrical flume, offers better stability when placed in the water current in the channel. Proposed mathematical models can be used for predicting the discharges of small sized trapezoidal canals having side slope as 1H : 1V for free flow conditions. These models are validated by recording the different set of observations on these flumes and both the models predict the discharge with percentage error less than ± 5 %, hence stands validated. Simple conical flume also offers the advantage of a standard measuring flume with the particular characteristic of mobility. It may be used as a simple and quick-use measuring device in small trapezoidal-section irrigation canals, sewers or drains. The accuracy in discharge measurement of simple conical flume is comparable with the standard measuring flumes under free flow conditions. Such flow measurements can contribute to better water management in irrigation. However, the models can only work for the small range of constriction ratios considered in the experiments, for canals with 1 V: 1 H side slope. As the preliminary results are promising, laboratory experiments covering wider range of constriction ratios and a broader range of side slopes, can lead to a more versatile discharge prediction model for use of simple conical flumes.

REFERENCES

Badar, A.M. & Ghare, A.D. (2012). Development of Discharge Prediction Model for Trapezoidal Canals using Simple Portable Flume. *International Journal of Hydraulic Engineering,* 1(2), 37-42.

Genovez, A., Abt, S., Florentin, B. & Garton, A. (1993). Correction for Settlement of Parshall Flume. *Irrigation and Drainage Engineering, ASCE,* 119(6), 1081-1091.

Hager, W.H. (1985). Modified Venturi Channels. *Irrigation and Drainage Engineering, ASCE,* 111(1), 19-35.

Hager,W.H. (1986). Modified Trapezoidal Venturi Channels. *Irrigation and Drainage Engineering, ASCE,* 112(3), 225-241.

Hager, W.H. (1988). Venturi Flume of Minimum Space Requirements. *Irrigation and Drainage Engineering, ASCE,* 114(2), 226-243.

Parshall, R.L. (1926). The Improved Venturi Flumes. Trans, ASCE, 89, 841-880.

 ©2017, IAHR. Used with permission / ISSN 1562-6865 (Online) - ISSN 1063-7710 (Print)

Proceedings of the 37th IAHR World Congress
August 13 – 18, 2017, Kuala Lumpur, Malaysia

TURBULENT KINETIC ENERGY BUDGET IN OPEN CHANNEL FLOWS WITH FRACTAL BED ROUGHNESS

RICHARD MCSHERRY[(1)], THORSTEN STOESSER[(2)] & ROGER FALCONER[(3)]

[(1,2,3)] Hydro Environmental Research Centre, School of Engineering, Cardiff University, Cardiff, U.K,
mcsherryr@cardiff.ac.uk; stoesser@cardiff.ac.uk; falconerra@cardiff.ac.uk

ABSTRACT

Results from a large eddy simulation of open channel flow over a rough bed with self-affine fractal properties are presented. The surface is considered to be broadly representative of rough bed forms that occur naturally in streams and rivers. The double averaging methodology is applied to enable analysis of the vertical distribution of turbulent and form-induced stresses throughout the depth. It is observed that the form-induced stress is a significant contributor to the streamwise momentum balance in the roughness sub-layer, reaching a peak value equal to approximately 16% of the peak shear stress. Particular attention is given to the distribution of the TKE budget. Important similarities with results from studies of flows over gravel beds, both numerical and experimental, are observed. A relatively large contribution due to wake production (approximately 15% of the peak production due to mean shear) is observed, which is in contrast to gravel bed studies.

Keywords: Open channel flow; double averaging; turbulent kinetic energy; large eddy simulation.

1 INTRODUCTION

Almost all flows of practical interest within the field of environmental hydraulics occur over rough beds, where the bed roughness may take a number of forms including sand grains, gravel and dunes. Such roughness is known to have an important influence on the hydrodynamic drag and the turbulence statistics, as summarized by Raupach et al. (1991) and Jimenez (2004). The influence of the roughness is especially pronounced in the roughness sub-layer, which is defined as the region in which the roughness elements induce spatial heterogeneity of the time-averaged turbulence statistics. The Reynolds-averaged Navier Stokes (RANS) equations are not well suited to analysis of such flows, and the double-averaging (DA) methodology (Nikora et al., 2007) has therefore emerged as an effective conceptual approach to increase understanding of the way in which the bed-generated turbulence interacts with the mean flow in the presence of spatially heterogeneous bed roughness. Although DA analysis by Raupach et al. (1991) and Finigan (2000) showed that in flow over canopies the wake produced by the canopies gives rise to a significant new source term in the overall turbulence kinetic energy (TKE) budget–the "wake production" term. Subsequent studies on flow over gravel beds (Mignot et al., 2009, Dey and Das, 2012) have suggested that this term is negligible in such flows when compared to the TKE production in the mean shear layer. Recently Yuan and Piomelli (2014) found that, for flow over gravel beds, the influence of spatial heterogeneity on the redistribution of TKE and production of Reynolds stress in the roughness sub-layer may provide the link between the roughness geometry and the near-bed flow dynamics, and may therefore hold the key to understanding the relationship between spatial heterogeneity and drag generation.

The present study aims at shedding more light on the relationship between roughness geometry and near-bed flow dynamics by considering the TKE budget in open channel flows over a fractal surface. Presented in the paper are results from a large eddy simulation (LES) of turbulent open channel flow over a surface whose fractal properties may be considered to be broadly representative of gravel bed-type roughness. The following section introduces the numerical method that has been employed, followed by a discussion of the fractal bed properties and the double-averaging approach. Some key features of the computational set-up are then introduced. A few salient results are then discussed and finally conclusions are drawn.

2 NUMERICAL FRAMEWORK

The governing equations for an unsteady, incompressible, viscous flow of a Newtonian fluid are solved using a finite difference Navier Stokes solver that employs LES to resolve the largest, energy carrying turbulent eddies on a staggered Cartesian grid (Rodi et al., 2013). The effects of the smaller, dissipative scales of turbulent motion are modeled mathematically using the WALE sub-grid scale model (Nicoud and Ducros, 1999). The Cartesian velocity components are stored in staggered fashion on Cartesian grids; fourth-order central differences are employed for the convective and diffusive fluxes in the momentum equation, and the solution is advanced in time using the fractional step method along with a three-step Runge-Kutta

©2017, IAHR. Used with permission / ISSN 1562-6865 (Online) - ISSN 1063-7710 (Print)

prediction, followed by a correction step in which the Poisson equation is solved. The Immersed Boundary Method (Peskin, 1972), which maps Eulerian velocities onto Lagrangian point-based representations of non-fluid bodies in the flow, is used to define the geometries of the roughness elements. Our implementation of the Immersed Boundary Method follows Uhlmann's approach, which is itself a refinement of Fadlun et al.'s direct forcing approach (Uhlmann, 2005; Fadlun, et al., 2000; Kara, et al., 2015). For examples of previous studies in which earlier versions of the code have been applied to rough-bed flows, including extensive validation against experimental data, the interested reader is referred to Stoesser and Nikora (2008), Stoesser (2010), Bomminayuni and Stoesser (2011), Stoesser et al. (2008) and Cevheri et al. (2016).

3 COMPUTATIONAL SET-UP

The simulation was performed on a Cartesian grid of dimensions 6.144H x 3.072H x H, where H is the maximum flow depth, i.e. the height of the top of the domain above the bottom of the domain. The domain was discretized by approximately 63 million computational points and local mesh refinement was employed to concentrate grid resolution in the near-bed region. In the bottom 0.2H of the depth the grid comprised by 1024 x 512 x 80 (~42 million) points, whereas in the upper 0.8H of the depth the grid comprised 512 x 256 x 159 (~21 million) points. In the near-bed region the cell sizes in wall units were $\Delta x^+ = \Delta y^+ = 15.0$, $\Delta z^+ = 6.3$ and double those values in the upper 0.8H.

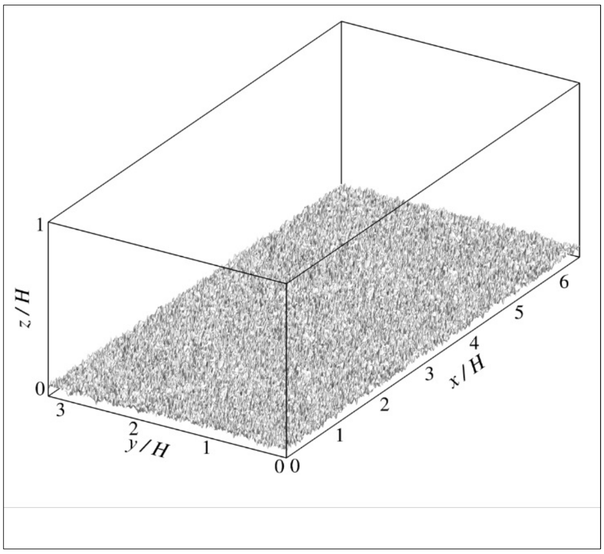

Figure 1. Computational domain including roughness topography.

Figure 1 presents the extent of computational domain along with the rough bed topography. The spatially heterogeneous fractal bed geometry was represented on the grid in a Lagrangian manner using the immersed boundary method. The bottom of the computational domain coincides with the lowest point on the bed, and a total of approximately 10.7 million immersed boundary points were used to define the bed. The roughness itself was designed by colleagues in the School of Engineering at the University of Aberdeen using a spectral synthesis method. The surface is self-affine in nature, a trait commonly exhibited by many rough natural surfaces including gravel beds and sand dunes. The roughness adopted for the present study has a spectral slope of -1, which is at the rougher end of the spectrum of naturally occurring rough surfaces.

Periodic boundary conditions were applied in the streamwise and spanwise directions, thereby mimicking an infintely long, infinitely wide channel. Free-slip and no-slip conditions were stipulated on the top and bottom walls respectively, while the immersed boundary points, by definition, achieve a no-slip condition at their individual locations. The mean flow was driven by a streamwise pressure gradient, dp/dx, that was corrected at each time step in order to maintain a constant mass flux through the domain and unambiguously provided the global bed shear velocity, u^* (=$\sqrt{(dp/dx.H)/\rho}$, where ρ is the fluid density). The bulk Reynolds number of the flow, Re, based on bulk flow velocity, U_b, and H, was 29000 and the relative submergence, defined as the ratio of channel depth to the maximum individual roughness crest height, k_c, was 9.8. The roughness Reynolds number, Re_k, based on the global friction velocity, u^*, and k_c, was approximately 255.

4 RESULTS

The double averaging methodology (Mignot et al., 2009; Nikora et al., 2007) is employed to decompose a given instantaneous flow quantity, theta, into a temporally and spatially averaged part, $\langle\bar{\theta}\rangle$, a turbulent fluctuation, θ', and a spatially-varying part, $\tilde{\theta}$, where angular brackets denote spatial averaging, an overbar denotes temporal averaging, a prime denotes a temporal fluctuation due to turbulence and a tilde denotes a spatial variation from the double averaged value.

 ©2017, IAHR. Used with permission / ISSN 1562-6865 (Online) - ISSN 1063-7710 (Print)

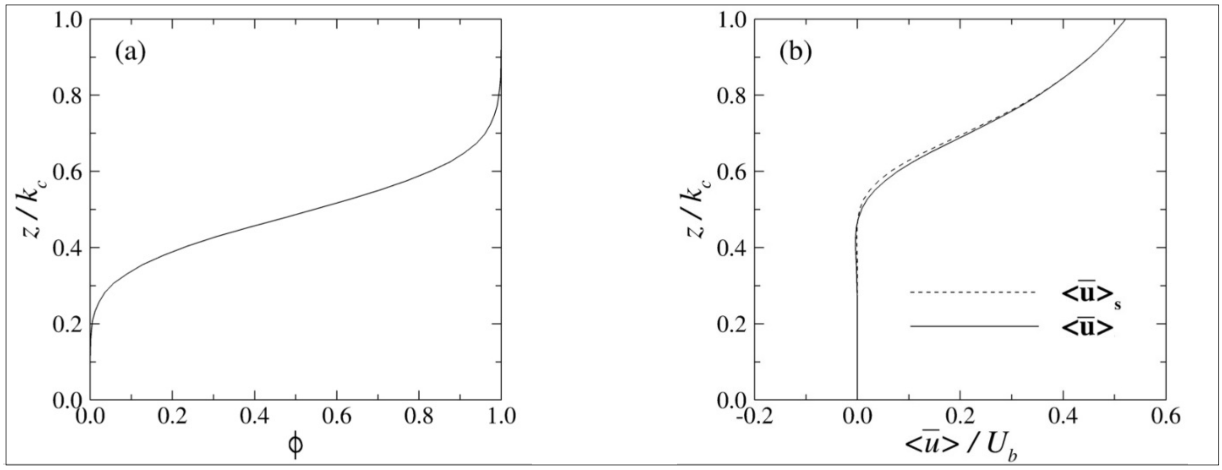

Figure 2. (a) roughness geometry function, (b) intrinsic and superficial averages of streamwise velocity.

If spatial averaging of the flow quantities is carried out in a plane parallel to the channel bed, the spatially-varying part will only be non-zero if the bed comprises some degree of spatial heterogeneity, as is of course the case in the vast majority of naturally occurring bed forms. Two approaches are possible for the spatial averaging operation: the intrinsic spatial average in a 2D plane parallel to the bed, $<\theta>$ takes into account only points within the fluid domain, while the superficial spatial average, $<\theta>_s$, takes into account all points in the plane, be they fluid or solid. The two quantities are related by $<\theta> = \Phi<\theta>_s$, where Φ is the roughness geometry function, i.e. the ratio of area occupied by fluid to total area of the averaging plane (Nikora, 2001). Figure 2(a) plots the roughness geometry function in the region below the roughness crests, while Figure 2(b) presents profiles of the double-averaged streamwise velocity, obtained from intrinsic and superficial averaging. As would be expected, the superficial average is lower than the intrinsic average, but the difference is marginal. Above the roughness crests the two profiles are of course coincident. It is interesting to note that in the interfacial sub-layer ($d \leq z \leq k_c$, where d ($\approx k_c/2$) is the mean bed elevation) the velocity varies almost linearly, which is in agreement with the definition of model (3) proposed by Nikora et al. (2004) for flow profiles in the interfacial sub-layer, and also agrees with the gravel bed DNS of Yuan and Piomelli (2014).

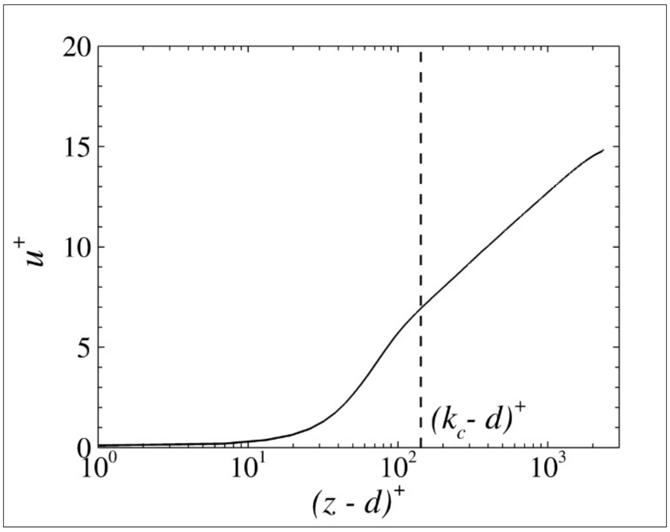

Figure 3. Double-averaged streamwise velocity profile.

Figure 3 presents the double-averaged streamwise velocity profile in the form of the Clauser plot. The presence of a well-established log layer is clearly visible, and it appears to extend from the water surface all the way down to $(k_c - d)^+$. This suggests that for this flow the form-induced sublayer (Nikora et al., 2001) is located entirely below the maximum roughness crest height.

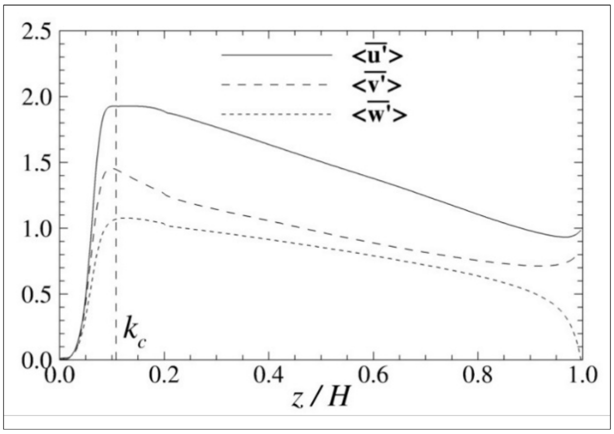

Figure 4. Turbulence intensity profiles.

Figure 4 presents profiles of the double averaged turbulence intensities. Peak intensities in all three directions are encountered close to the roughness crests, as would be expected. The shape of the $\langle\overline{u'}\rangle$ profile is noteworthy, as is it characterized by a relatively flat peak in comparison to profiles that have been reported in other studies of channel flows over rough and smooth beds. It is possible that this feature is related somehow to the bed geometry, and it will be interesting in future to investigate how this section of the profile changes when beds with different fractal properties are simulated.

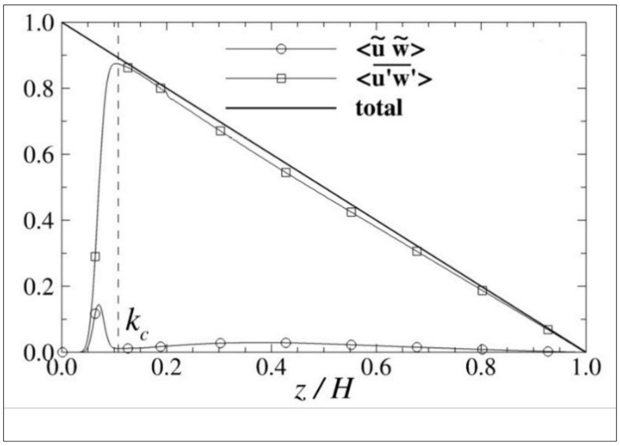

Figure 5. Profiles of shear and form-induced stresses.

Figure 5 presents profiles of the double-averaged shear, $\langle\overline{u'w'}\rangle$, and form-induced, $\langle\tilde{u}\tilde{w}\rangle$, stresses. As would be expected, the peak shear stress is observed to occur close to the roughness crests, while the form-induced stress reaches a peak within the interfacial sub-layer, at z/k_c ~ 0.7. The magnitude of the peak form-induced stress is approximately 16% of the peak shear stress, confirming that it plays a significant role in the momentum balance in the interfacial sub-layer.

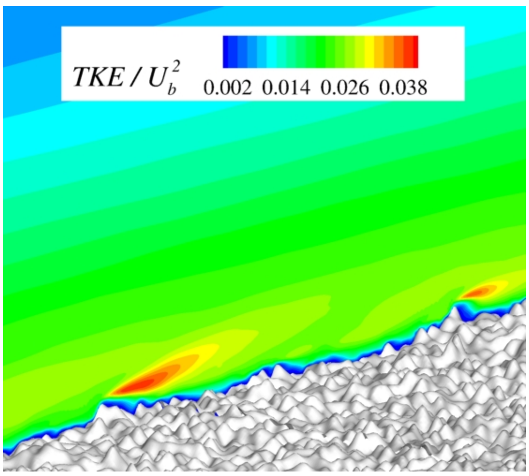

Figure 6. Contours of TKE in the x-z plane on the centreline of the domain.

 ©2017, IAHR. Used with permission / ISSN 1562-6865 (Online) - ISSN 1063-7710 (Print)

Figure 6 presents contours of the turbulent kinetic energy in an *x-z* plane on the centreline of the domain, in the near bed region. Very localized maxima are observed in the region immediately above the interfacial sublayer, in the wake of individual elevated points on the bed. The contours become relatively uniform at a height of approximately $z/H \approx 0.2$, suggesting that the influence of spatial heterogeneity in the bed topography on the TKE distribution is confined to the bottom 0.2*H* of the depth.

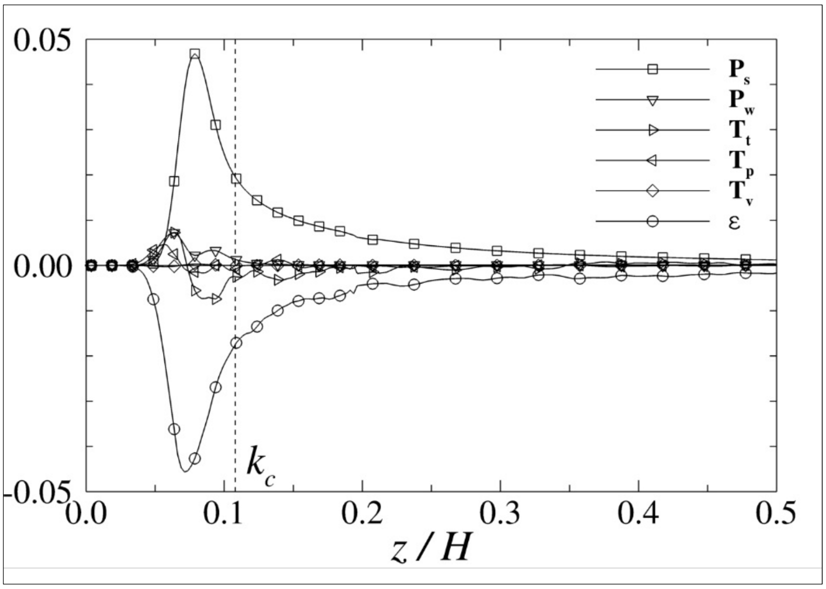

Figure 7. Vertical distribution of TKE budget terms.

Mignot et al. (2009) derived TKE budgets for open channel flow over rough beds, following the derivation of Raupach and Shaw (1982) for flow over vegetation canopies. The formulation is obtained by applying double-averaging to the TKE transport equation and reads:

$$-2\langle\overline{u_i'w'}\rangle\frac{\partial\langle\overline{u}_i\rangle_s}{\partial z}-\langle\widetilde{u_i'u_j'}\frac{\partial\widetilde{u}_i}{\partial x_j}\rangle_s-\frac{\frac{\partial}{dz}\langle\widetilde{u_i'u_i'}\widetilde{w}\rangle_s}{2}-\frac{\frac{\partial}{dz}\langle\overline{u_i'u_i'w'}\rangle_s}{2}-\frac{\partial}{\partial z}\langle\overline{p'w'}\rangle_s+\nu\frac{\partial^2}{\partial z^2}\langle\frac{\overline{u_i'u_i'}}{2}\rangle_s-\varepsilon=0 \qquad [1]$$

where the *i, j* notation is used interchangeably with *u*, *v* and *w* to denote velocity components in the *x*, *y* and *z* directions. The various terms have particular significance pertaining either to production, transport or dissipation of TKE. The first term, P_s, is the shear production term, i.e. the work of the bulk velocity against the mean shear. The second term, P_w, is the wake production term that results from the work done by wake-induced fluctuations in velocity against the local shear induced by the bed. The third, fourth, fifth and sixth terms, T_w, T_t, T_p and T_v, denote wake, turbulent, pressure and viscous transport respectively. Finally ε is the viscous dissipation.

Figure 7 presents the vertical distribution of TKE budget in the lower half of the flow depth. The mean shear and viscous dissipation are clearly the dominant terms, and it is interesting to note that the peak production due to mean shear occurs below the top of the roughness crests, an observation also made by Yuan and Piomelli (2014) and Mignot et al. (2009). In fact, in the present study the peak occurs at $z = 0.72k_c$, which agrees very well with the rougher of the two cases studied by Yuan and Piomelli ($z = 0.73k_c$). Also in accordance with the results of Yuan and Piomelli, the transport terms are observed to be negligible above the roughness sub-layer, with pressure transport being the most important source term in the lower third of the sub-layer, to be surpassed by the wake production and turbulent transport as *z* increases towards k_c. The peak wake production occurs at $z = 0.59k_c$ and has a magnitude of approximately 15% that of the peak shear production. This is notably higher than was observed in the studies of Yuan and Piomelli (2014) and Mignot et al. (2009) who state that peak P_w is generally less than 5% of P_s.

5 CONCLUSIONS

A large eddy simulation of open channel flow over a rough bed with self-affine fractal properties has been performed. The surface was designed by colleagues at the University of Aberdeen and is considered to be broadly representative of rough bed forms that occur naturally in streams and rivers. The double averaging methodology was applied to enable analysis of the vertical distribution of turbulent and form-induced stresses throughout the depth. It was observed that the form-induced stress is a significant contributor to the streamwise momentum balance in the roughness sub-layer, reaching a peak value equal to approximately 16% of the peak shear stress.

Particular attention was given to the distribution of the TKE budget. Important similarities with the gravel bed studies of Yuan and Piomelli (2014) and Mignot et al. (2009) were observed, particularly in relation to the location of the peak in TKE production due to mean shear and the contribution of pressure transport in the lower part of the interfacial sub-layer. A relatively large contribution due to wake production was observed (approximately 15% of the peak production due to mean shear).

ACKNOWLEDGEMENTS

This work is funded by the UK *Engineering and Physical Sciences Research Council* (EPSRC), who are funding this research. High Performance Computing (HPC) resources were provided by *Advanced Research Computing @ Cardiff* (ARCCA).

REFERENCES

Bomminayuni, S. & Stoesser, T. (2011). Turbulence Statistics in an Open-Channel Flow over a Rough Bed. *Journal of Hydraulic Engineering*, 137(11), 1347-1358.

Cevheri, M., McSherry, R. & Stoesser, T. (2016). A Local Mesh Refinement Approach for Large-Eddy Simulations of Turbulent Flows. *International Journal of Numerical Methods in Fluids*, 82(5), 261-285.

Dey, S. & Das, R. (2012). Gravel-Bed Hydrodynamics: Double-Averaging Approach. *Journal of Hydraulic Engineering*, 138(8), 707–725.

Fadlun, E.A., Verzicco, R., Orlandi, P. & Mohd-Yusof, J. (2000). Combined Immersed Boundary Finite Difference Methods for Three-Dimenaional Complex Flow Simulations. *Journal of Computational Physics*, 161(1), 35-60.

Finnigan, J. (2000). Turbulence in Plant Canopies. *Annual Review of Fluid Mechanics*, 32(1), 519–571.

Jiminez, J. (2004). Turbulent Flows Over Rough Walls. *Annual Review of Fluid Mechanics*, 36, 173–196.

Kara, S., Stoesser, T., Sturm, T.W. & Mulahasan, S. (2012). Turbulence Statistics in Compound Channels with Deep and Shallow Overbank Flows. *Journal of Hydraulic Research*, 50(5), 482-493.

Kara, M, Stoesser, T. & McSherry, R. (2015). Calculation of Fluid-Structure Interaction: Methods, Refinements, Applications. *Proceedings of the Institution of Civil Engineers-Engineering and Computational Mechanics*, 168(2), 59-78.

Mignot, E., Bartheleemy, E. & Hurther, D. (2009). Double-Averaging Analysis and Local Flow Characterization of Near-Bed Turbulence in Gravel-Bed Channel Flows. *Journal of Fluid Mechanics*, 618, 279–303.

Nicoud, F. & Ducros, F. (1999). Subgrid-Scale Stress Modelling Based on the Square of the Velocity Gradient Tensor. *Flow Turbulence and Combustion*, 62(3), 183-200.

Nikora, V., Goring, D., McEwan, I. & Griffiths, G. (2001). Spatially Averaged Open-Channel Flow Over Rough Bed. *Journal Hydraulic Engineering*, 127(2), 123–133.

Nikora, V., McEwan, I., McLean, S., Coleman, S., Pokrajac, D. & Walters, R. (2007). Double-Averaging Concept for Rough-Bed Open Channel and Overland Flows: Theoretical Background. *Journal of Hydraulic Engineering*, 133(8), 873–883.

Peskin, C.S. (1972). Flow Patterns Around Heart Valves: A Digital Computer Method for Solving the Equations of Motion. *PhD Thesis*, Albert Einstein College of Medicine, USA.

Raupach, M.R. & Shaw, R.H. (1982). Averaging Procedures for Flow Within Vegetation Canopies. *Boundary-Layer Meteorology*, 22(1), 79–90.

Raupach, M.R., Antonia, R.A. & Rajagopalan, S. (1991). Rough-wall Turbulent Boundary Layers. *Applied Mechanics Review*, 44(1), 1–25.

Rodi, W, Constantinescu, G. & Stoesser, T. (2013). *Large-Eddy Simulation in Hydraulics*. CRC Press, London, UK.

Stoesser, T. & Nikora, V. (2008). Flow Structure Over Square Bars at Intermediate Submergence: Large Eddy Simulation (LES) Study of Bar Spacing Effect. *Acta Geophysica*, 56(3), 876-893.

Stoesser, T., Braun, C., Garcia-Villalba, M. & Rodi, W. (2008). Turbulence Structures in Flow Over Two Dimensional Dunes. *Journal of Hydraulic Engineering*, 134(1), 42-55.

Stoesser, T. (2010). Physically Realistic Closure Scheme to Simulate Turbulent Channel Flow Over Rough Beds Within the Framework of LES. *Journal of Hydraulic Engineering*, 136(10), 812-819.

Uhlmann. M. (2005). An Immersed Boundary Method with Direct Forcing for the Simulation of Particulate Flows. *Journal Computational Physics*, 209(2), 448-476.

Yuan, J. & Piomelli, U. (2014). Roughness Effects on the Reynolds Stress Budgets in Near-Wall Turbulence. *Journal of Fluid Mechanics*, 760, R1, 1-12.

 ©2017, IAHR. Used with permission / ISSN 1562-6865 (Online) - ISSN 1063-7710 (Print)

Proceedings of the 37th IAHR World Congress
August 13 – 18, 2017, Kuala Lumpur, Malaysia

A PARAMETER SENSITIVITY ANALYSIS OF MICROCYSTIS VERTICAL DISTRIBUTIONS

QIAN YU(1), YONGCAN CHEN(2), ZHAOWEI LIU(3) & NA LI(4)

(1,4)State Key Laboratory of Simulation and Regulation of Water Cycle in River Basin, China Institute of Water Resources and Hydropower Research, Beijing, People's Republic of China; Research Center on Flood & Drought Disaster Reduction of the Ministry of Water Resources, China Institute of Water Resources and Hydropower Research, Beijing, People's Republic of China
yqcherie@126.com
(2) School of Environment and Resources, Southwest University of Science and Technology, Mianyang, Sichuan, People's Republic of China
chenyc@tsinghua.edu.cn
(3) State Key Laboratory of Hydroscience and Engineering, Tsinghua University, Beijing, People's Republic of China
liuzhw@mail.tsinghua.edu.cn

ABSTRACT

Microcystis blooms, which not only harm aquatic ecosystems but also threaten human and animal health, are worldwide problems. Modeling of Microcystis vertical distributions is very important to understand blue-green bloom formations and its competition for resources with other algae. In this paper, a new coupled model of simulating vertical population dynamics of Microcystis by coupling advection-diffusion equation and buoyancy regulation is developed. This coupled model includes a total of 10 parameters. A sensitivity analysis is conducted on these parameters to identify the key factors that impact on Microcystis vertical dynamics. According to numerical simulations, it is found that the vertical distributions of Microcystis and the corresponding mechanisms are different under different flow regimes with different turbulent diffusion coefficients (D). Hence, we conduct a sensitivity analysis in relatively calm water (D=0.17cm^2/s) and in turbulent water (D=400cm^2/s), respectively. The results of the sensitivity analysis show that the diameter of Microcystis colonies (d) and the form resistance of colony (Φ) play different roles in calm water and in turbulent water, respectively. Both d and Φ have much bigger influences in calm water than in turbulent water, which is due to different mechanisms of Microcystis vertical distributions. In calm water, self-migration of Microcystis determines the vertical distributions that most of Microcystisfloat upwards and gather on the surface of water. d and Φ are the main factors that impact on the vertical velocities of Microcystis. Hence, they have significant influences on population distributions in calm water. On the contrary, it is flow turbulence that determines the population dynamics in turbulent water. That is, Microcystis would distribute relatively uniform in the vertical. Therefore, the algae with faster net growth rate would take the advantage. Hence, the maximum growth rate and loss rate have more important impacts in turbulent water.

Keywords: Hydrodynamic turbulence; microcystis; sensitivity analysis; vertical distribution; modeling.

1 INTRODUCTION

Colony-forming and toxic Cyanobacterial blooms, such as Microcystis blooms, distribute widely all over the world (Huisman et al., 2004; Yu et al., 2015a). 108 countries at least have reported Cyanobacterial blooms (Harke et al., 2016). In high bloom seasons, usually in summer and early autumn with high temperature, the smelly blue-green scums will cover water surface of lakes and relatively calm waters, and even stretch to rivers downstream (Paerl and Huisman, 2008; Yu et al., 2015b). It is widely accepted that the buoyancy regulation controlled by the cell ballast helps Microcystis win the competition against other sinking algae in calm water (Visser et al., 1997). Microcystis blooms are a kind of harmful algal blooms (HABs), which would bring many serious problems to aquatic ecosystems and human life (Visser et al., 2016; Medina et al., 2016). First of all, the released microcystin from Microcystis would damage human liver and neuron-system (Visser et al, 2016). Secondly, Microcystis can release ugly smells which would lower down the entertainment functionality of water. Furthermore, as colony-forming Microcystis, the large gathering of Microcystis colonies will block the filtering system of water treatment plants, which will result in water crises. The last but not the least, the die-off of Microcystis consumes a large amount of oxygen, which can indirectly cause the death of fishes and other aquatic animals (Medina et al., 2016).

Vertical population distributions of coexisting algae can reflect the final dominant algae when nutrient is enough and temperature is suitable (Yu et al., 2015c). If most of Microcystis cells gather on the upper layer of water, Microcystis will take the advantage of light and then dominate. However, if Microcystis distribute uniformly, other algae with faster net growth rate may dominate (Yu et al., 2015c). A lot of variables (turbulent diffusion coefficient, light attenuation coefficient, form resistance of colony, length of the photoperiod, etc) have impacts on vertical distributions of Microcystis. The model designed by Yu et al. (Yu et al. 2015b) involves many parameters to describe the vertical population distribution of Microcystis. However, the parameters used in different models are distinct and various. This means it is difficult to directly compare the simulation results from different models. Besides, due to the large amount of parameters involved, it is hard to deduce which factor results in the variation in the vertical distribution of Microcystis without knowing the exact effects of each parameter. In summary, it is important to conduct the sensitivity analysis for the model input parameters, and analyze the exact impacts of those parameters on the vertical population distributions. This is necessary for the comprehensive understanding of the factors that determine the vertical population distribution (Guven and Howard, 2011).

In this work, we develop a coupled model driven by hydrodynamic turbulence and incident light, simulating vertical population distributions of buoyant Microcystis. There are ten parameters in total. In order to separately analyze the influence of each parameter on vertical distribution of Microcystis, we conduct a sensitivity analysis of all relative parameters.

2 NUMERICAL MODEL

The coupled model consists of three components (Yu et al., 2015b): (1) the advection-diffusion equations (Huisman et al., 2004), (2) the cell density model of Microcystis (Visser et al., 1997), and (3) the vertical migration velocity of Microcystis colonies (Aparicio Mediano et al., 2013). We assumed that nutrients are rich and water temperature is suitable. Hence, the net growth rates of Microcystis are limited by the incident light alone. In addition, we assumed that the buoyancy regulation of Microcystis is caused by temporal variations of carbohydrate in cells (Visser et al., 1997; Aparicio Mediano et al., 2013). The vertical population dynamic of Microcystis colonies can be described by the following equations:

$$\frac{\partial C}{\partial t}+(V+w)\frac{\partial C}{\partial z}=D\frac{\partial^2 C}{\partial z^2}+S \qquad [1]$$

$$S=p(I)\cdot C-l\cdot C \qquad [2]$$

$$p(I)=\frac{p_{\max}\cdot I}{H+I} \qquad [3]$$

where C is the abundance of Microcystis, V is the vertical migration velocity of Microcystis (V>0, sinking; V<0, rising), w is the vertical velocity of water, D is the vertical turbulent diffusion, p(I) is the growth rate of Microcystis under the condition of I(z), l is the loss rate of Microcystis, p_{max} is the maximal growth rate of Microcystis, and H is the light half-saturation constant.

If the intensity of the incident light is higher than the compensation irradiance, Microcystis cell accumulates carbohydrate and then the cell density increases. On the contrary, if the intensity of the incident light is lower than the compensation irradiance, Microcystis cell releases the carbohydrate and then the cell density decreases. The change in cell density can be described as equation [4]:

$$\begin{cases} I(z)>I_c, & \left(\dfrac{d\rho_{cell}}{dt}\right)_V=c1\cdot I(z)e^{-\frac{I(z)}{I_0}}+c2 \\ I(z)<I_c, & \left(\dfrac{d\rho_{cell}}{dt}\right)_V=c3\cdot\rho_1+c4 \end{cases} \qquad [4]$$

where I(z) is the incident light at the depth z, which can be calculated as equation [5], I_0 is the optimal irradiance, I_c is the compensation irradiance, ρ_{cell} is the density of Microcystis cell, ρ_1 is the initial density of Microcystis cell.

$$I(z)=\max\left\{I_m\cdot\sin\left(\frac{\pi\cdot\mathrm{mod}(t,86400)}{D_L}\right)\cdot\exp\left\{-K_{bg}\cdot z-\int_0^z k_m\cdot C(\sigma,t)d\sigma\right\},0\right\} \qquad [5]$$

where K_{bg} is the background turbidity of the water except self-shading of Microcystis, k_m is the light attenuation coefficient of Microcystis, I_m is the maximal diurnal light intensity on the surface of water, D_L is the length of the photoperiod.

According to the actual shape, Microcystis colonies can be treated as spheroids. This model also considered the Microcystis colonies with different diameters. The vertical movement of Microcystis colonies is calculated by Stokes' equation which is widely used in this field:

$$V=\frac{dz}{dt}=\frac{gd^2(\rho_{col}-\rho_w)}{18\nu\Phi} \qquad [6]$$

 ©2017, IAHR. Used with permission / ISSN 1562-6865 (Online) - ISSN 1063-7710 (Print)

$$\rho_{col} = \rho_{cell} n_{cell} \left(1 - n_{gas}\right) + \rho_{muc} \left(1 - n_{cell}\right) \quad [7]$$

where, g is the acceleration due to gravity, 9.8m/s^2, d is the diameter of colony, ρ_w is the density of water, ρ_{col} is the density of colony, v is the dynamic viscosity of water, 0.001kg/m·s, Φ is the form resistance of Microcystis colony, ρ_{muc} is the density of mucilage, n_{cell} is the volume percentage of cell in Microcystis colony, n_{gas} is the volume percentage of gas vesicle in cell.

The equations listed above were discretized with an implicit difference scheme. We assumed that there is no flux exchange at the surface and the bottom of the water where the following boundary condition function is specified:

$$(V + w) \cdot C + D \frac{\partial C}{\partial z} = 0 \quad [8]$$

3 MODEL VERIFICATION

The simulation results using the model developed in Section 2 had been verified with the real data observed in situ by Ibelings et al. (1991).The coupled model can precisely simulate the sinking of *Microcystis* colonies in the daytime and the floating in the night. In addition, the model can accurately simulate the vertical population distributions of *Microcystis* colonies. The results of verification have been published in Yu et al. (2015b).

4 PARAMETER SENSITIVITY ANALYSIS

As can be seen in equation [1] to equation [7], many variables have impacts on the vertical population distributions of Microcystis. We assumed that the initial population of Microcystis distributed uniformly in the vertical direction and the initial value of population was C_0=10^{7}cells/L. The standard values of all input parameters are listed in Table 1. A total of 10 parameters were included. According to the previous study (Yu et al., 2015b), there exists a location where most of Microcystis population gather (see Figure 1). At this location, the density of Microcystis is the same as water density. If water is less turbulent (D=0.01cm^2/s), a large number of Microcystis population will gather at that location, while very low populations distribute at other positions in the vertical. If water is a little more turbulent (D=0.5cm^2/s), less populations will gather at this position even though it still aggregates the largest population (see Figure 1). Hence, as hydrodynamic turbulence increases, the population at that location will decrease and the vertical distribution will tend to be more uniform. According to previous study (Yu et al., 2015c), uniform vertical distribution disadvantages the domination of Microcystis, while other algae with faster growth rate take the advantage. Therefore, the largest population can reflect the vertical distribution. If the largest population decreases when values of parameters change, the vertical distribution tends to be uniform in the vertical. In this work, we chose the largest population as the main object of study in order to reflect the vertical distribution.

The process of parameter sensitivity analysis consists of three steps:(1) Calculate the standard largest population of Microcystis with given standard parameters (see Table 1); (2) Vary the value of studied parameter by multiplying -90%, -60%，-30%，+30%，+60% and +90%, while keeping other parameters unchanged; (3) Simulate vertical population distributions of Microcystis and get the largest population, then calculate the difference between it and standard largest population. It is worth noting that Microcystis blooms usually break out in summer and early autumn. Hence, D_L is usually longer than 12 hour. In this work, we only considered D_L larger than 12h.

Table 1. Parameters and corresponding standard values.

Parameter		Value	Unit	Reference
Environmental Variables	I_m	1000	μmol photons/(m^2·s)	Huisman et al., 2004
	D_L	43200	s	
	K_{bg}	0.6	1/m	
	depth	3	m	
	D	1	cm^2/s	
Characteristics of Microcystis	k_m	0.034	cm^2/10^6 cells	Huisman et al., 2004
	d	100	μm	
	Φ	1		Reynolds et al., 2006
	p_{max}	0.008	1/h	Huisman et al., 2004
	l	0.004	1/h	Huisman et al., 2004

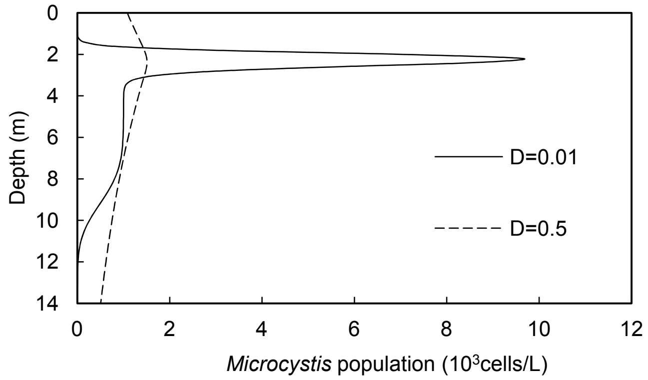

Figure 1. Vertical population profiles for colonies of 20μm in diameter under different turbulent diffusion coefficients (unit of *D* is cm^2/s).

Figure 2 shows the sensitive analysis of hydraulic turbulence (*D*) on the largest population of *Microcystis*. We assumed that the standard value of *D* is 1cm^2/s (see Table 1). *D* has a significant impact on the largest population. When *D* is 0.1cm^2/s, most of the populations gather in the largest population position. Hence, the amplitude of variation is very large (584%). However, when *D* is as large as 1.9 cm^2/s, the vertical distribution tends to be uniform and the range of variation tends to be smaller (within 100%). In view of distinct vertical distributions, we conducted sensitivity analysis under two different aquatic scenarios: less turbulent water (*D*=0.17cm^2/s) and turbulent water (*D*=400cm^2/s). We chose *D*=0.17cm^2/s as the representative of less turbulent water because Huisman et al. (2004) took this value as the representative of weak mixing water. In addition, we chose *D*=400cm^2/s as the representative of turbulent water due to the calculation using empirical formula. The velocity used in the formula was measured in situ by Yu et al. (2015c) in the Tanglang River, which is located downstream Lake Dianchi.

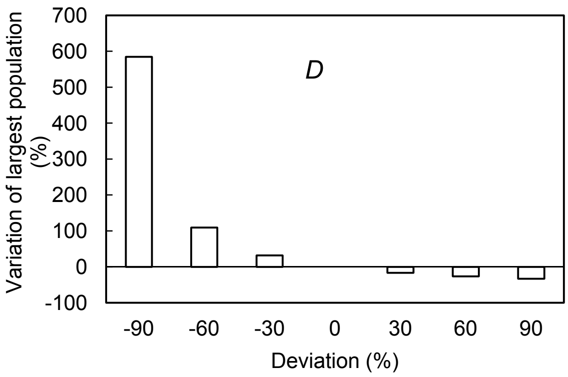

Figure 2. Sensitive analysis of hydraulic turbulence.

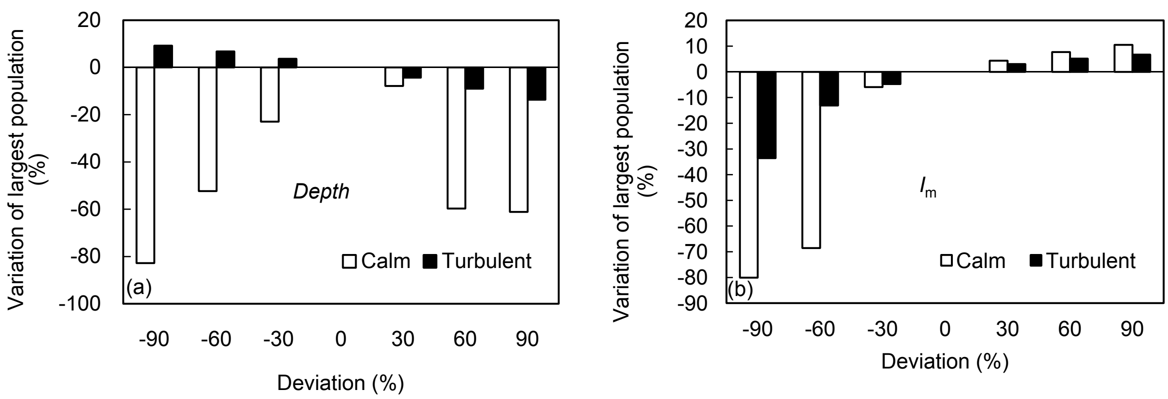

 ©2017, IAHR. Used with permission / ISSN 1562-6865 (Online) - ISSN 1063-7710 (Print)

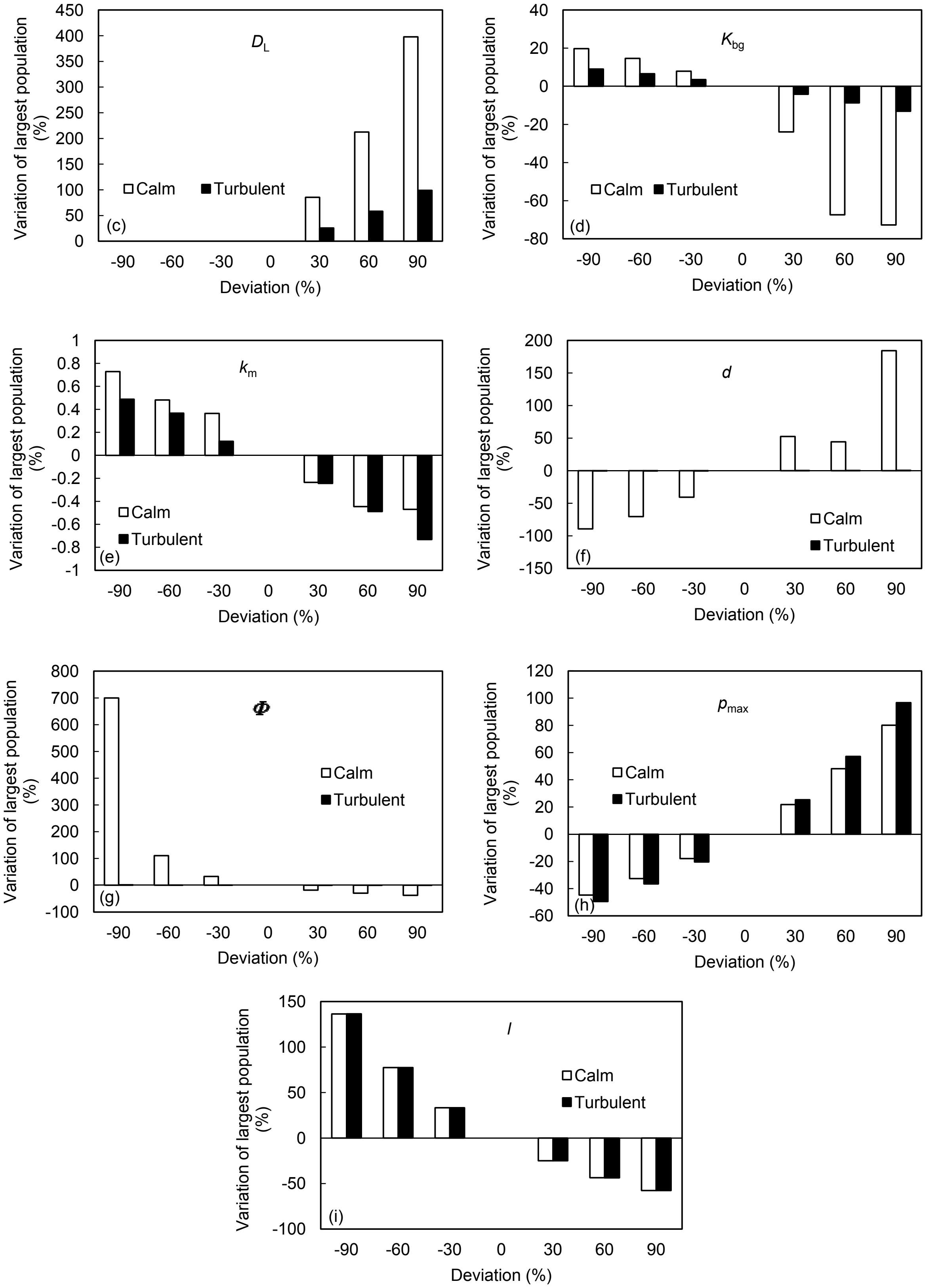

Figure 3. Sensitivity analysis of all parameters (a) Depth (b) I_m (c) D_L (d) K_{bg} (e) k_m(f) d (g) Φ (h) p_{max}(i) I.

Figure 3 shows the variation of largest population of Microcystis with the variation of different parameters. As shown in Figure 3, most of the parameters had big impacts on the largest population of Microcystis except the light attenuation coefficient of Microcystis(k_m). The weak impact of k_m is owing to the low initial population of Microcystis and low standard value of k_m.

©2017, IAHR. Used with permission / ISSN 1562-6865 (Online) - ISSN 1063-7710 (Print)

The diameter of Microcystis colony (d) and form resistance (Φ) showed the most remarkable differences in calm water and in turbulent water, respectively. Both d and Φ had much bigger impacts on the largest population in calm water than that in turbulent water. This is due to the fact of different mechanisms influencing vertical population distributions. For Microcystis, both the buoyant self-migration (see equation [6]) and the turbulence of water have an impact on its vertical population distribution. In less turbulent and even calm water, self-migration of Microcystis primarily determines the vertical population distribution. Hence, most of buoyant Microcystis will float upwards into the upper layer of water to have full photosynthesis. On the contrary, it is hydrodynamic turbulence overcoming self-migration that determines the vertical distribution (Yu et al., 2015c). d and Φ are two factors that directly influence self-migration velocity of Microcystis (see equation [6]). Hence, they have significant impact on the largest population in less turbulent water. However, in turbulent water, turbulence eddy will carry colonies and take them to positions with lower populations. Then, the population of Microcystis will distribute uniformly in the vertical. All algae, whether sinking or buoyant, distribute uniformly. Therefore, they have little impact on vertical distributions and the largest population, accordingly.

Loss rate (l) and maximum growth rate (p_{max}) have significant impacts on largest population in turbulent water (ranking No.1 and No.2, see Table 2). Nevertheless, their influences are smaller in less turbulent water. As aforementioned, turbulent water leads to relatively uniform vertical distribution of Microcystis. In this situation, l and p_{max} directly influence the net growth of Microcystis. The higher net growth the algae are, the more population would increase. Then more algae would gather in the largest population position. Hence, if green algae and diatoms with faster growth rate coexist with Microcystis in turbulent water, they may take the advantage and dominate. This explains why green algae and diatoms usually dominate in the middle and lower reaches of rivers where water is turbulent (Bahnwart et al., 1998).

I_m, D_L, K_{bg} and k_m will indirectly influence the net growth and then influence the largest population. Both the increase of I_m and D_L will increase the largest population of Microcystis. The impacts of D_L are much bigger than that of I_m. Both I_m and D_L directly influence the light intensity that algae can acquire. The population amount will be larger when they acquire more light. On the contrary, with the increase of K_{bg} and k_m, the largest population of Microcystis will decrease. This is due to the fact that both K_{bg} and k_m will decrease the incident light underwater. The higher the values of K_{bg} and k_m are, the lower the incident light is. The net growth of Microcystis will decline and then the largest population decrease accordingly.

Table 2. Sensitivity analysis ranking of all parameters.

	Calm water	**Turbulent water**
1	Φ	l
2	D_L	p_{max}
3	d	D_L
4	p_{max}	I_m
5	*Depth*	*Depth*
6	l	K_{bg}
7	I_m	Φ
8	K_{bg}	k_m
9	k_m	d

5 CONCLUSIONS

In this work, we conduct a sensitivity analysis on ten parameters to study their impacts on vertical population distribution of Microcystis. There are ten related parameters, including five environmental variables and five characteristics factors of Microcystis. Most of parameters show similar influence trends in less turbulent water and in turbulent water. Both d and Φ, directly influencing the vertical movement of Microcystis, play different roles in calm water and in turbulent water, respectively. They both have much more significant impacts in calm water than that in turbulent water. In turbulent water, l and p_{max}, which directly influence the net growth of Microcystis, mainly influence the largest population. The sensitivity analysis proves the different mechanisms influencing vertical distributions of Microcystis again. That is, in less turbulent water, self-migration of Microcystis mainly determines the vertical population distribution. However, in turbulent water, hydrodynamic turbulence primarily determines vertical distribution.

ACKNOWLEDGMENTS

This work is supported by National Science and Technology Support Project of China (No.2015BAB07B09 and No.2016YFC0502204), the National Natural Science Foundation of China (No.51579130), and Tsinghua University Initiative Scientific Research Program (No.2014z09112).

 ©2017, IAHR. Used with permission / ISSN 1562-6865 (Online) - ISSN 1063-7710 (Print)

REFERENCES

Aparicio, M., E., Uittenbogaard, R.E., Pires, L.D., Van de Wiel, B.J.H. & Clercx, H.J.H. (2013). Coupling Hydrodynamics and Buoyancy Regulation in Microcystis aeruginosa for its Vertical Distribution in Lakes. *Ecological Modellin*g, 248, 41-56.

Bahnwart, M., Hübener, T. & Schubert, H. (1998). Downstream Changes in Phytoplankton Composition and Biomass in a Lowland River–Lake System (Warnow River, Germany). *Hydrobiologia*, 391(1-3), 99-111.

Chen, Y.C., Yu Q., Zhu D.J. & Liu Z.W. (2014). Possible Influencing Factors on Phytoplankton Growth and Decay in Rivers: Review and Perspective. *Journal of Hydroelectric Engineering*, 33(4), 186-195. (In Chinese)

Guven, B. & Howard, A. (2011). Sensitivity Analysis of a Cyanobacterial Growth and Movement Model under Two Different Flow Regimes. *Environmental Modeling & Assessment*, 16(6):577-589.

Huisman, J., Sharples, J., Stroom, J.M., Visser, P.M., Kardinaal, W.E.A., Verspagen, J.M. & Sommeijer, B. (2004). Changes in Turbulent Mixing Shift Competition for Light between Phytoplankton Species. *Ecology*, 85(11), 2960-2970.

Ibelings, B.W., Mur, L.R. & Walsby, A.E. (1991). Diurnal Changes in Buoyancy and Vertical Distribution in Populations of Microcystis in Two Shallow Lakes. *Journal of Plankton Research*, 13(2), 419-436.

Medina, V.F., Griggs, C.S. & Thomas, C. (2016). Evaluation of the Destruction of the Harmful Cyanobacteria, Microcystis Aeruginosa, with a Cavitation and Superoxide Generating Water Treatment Reactor. *Bulletin of Environmental Contamination and toxicology*, 96(6), 791-796.

Paerl, H.W. & Huisman, J. (2008). Blooms like it Hot. *Science*, 320(5872), 57.

Reynolds, C.S. (2006).*The Ecology of Phytoplankton.* Cambridge: Cambridge University Press.

Visser, P.M., Passarge, J. & Mur, L.R. (1997). Modelling Vertical Migration of the Cyanobacterium Microcystis. *Hydrobiologia*, 349(1), 99-109.

Visser, P.M., Ibelings, B.W., Bormans, M. & Huisman, J. (2016). Artificial Mixing to Control Cyanobacterial Blooms: A Review. *Aquatic Ecology*, 50(3), 423-441.

Yu, Q., Chen, Y.C., Liu, Z.W., van de Giesen, N. & Zhu, D. (2015a). The Influence of a Eutrophic Lake to the River Downstream: Spatiotemporal Algal Composition Changes and the Driving Factors. *Water*, 7(5), 2184-2201.

Yu, Q., Liu, Z.W., Chen, Y.C. & Zhu, D. (2015b). Modelling Daily Variation in the Vertical Distribution of Microcystis. *China Environmental Science*, 35(6), 1840-1846. (In Chinese)

Yu, Q. (2015c). Source Apportionment of Pollutants and Variation Analysis in Phytoplankton Compositions in the Pudu River. Ph.D. Dissertation, Tsinghua University, Beijing, China.

Proceedings of the 37th IAHR World Congress
August 13 – 18, 2017, Kuala Lumpur, Malaysia

A SELF-ADAPTING FISHWAY ENTRANCE FOR THE LARGE VARIATION OF DOWNSTREAM WATER LEVEL

GUANGNING LI [(1)] & SHUANGKE SUN [(2)]

[(1,2)] China Institute of Water Resources and Hydropower Research, Beijing, China,
lgnchina@163.com; sunshuangke@163.com

ABSTRACT

The large variation of downstream water level is a big challenge for the design of fishway entrances. The normal fishway entrance is only suitable for a limited range of water level variation (0.5~1.0m). When the variation is larger, more entrances should be set up at different elevations along the downstream river, and separated in an expanse range. It is conflicted with the aggregation habit of the migratory fishes. The fishes are usually aggregated in a relatively small area in the tailrace channel and near to the dam. In addition, the flow fields of the entrances location away from the tailrace channel are always not suitable for the fish aggregation. Therefore, the entrances will be inefficient. The frequent switching the gates of the entrances are fussy operations and the project site conditions for arranging multi entrances have been confronted with many difficulties. In this paper, a compact self-adapting fishway entrance without gate for the large variation of downstream water level is proposed. The entrance is designed based on the law of the water depths change in the Vertical Slot Fishway (VSF). The entrance contains several parallel connected returning sections of VSF, and each returning section has its own opening to the river. Each opening has a specific bottom elevation, and the bottom of the opening is higher than the inner pool. When the water level in the adjacent pool is lower than the bottom of the opening, the water will move to the next inner pool normally. When the water depth in the pool is higher than the bottom of the opening, the water can flow out into the river, and forms a flow with proper velocity to attract fishes. The flow split ratios, flow patterns and velocity profiles of the openings under different scenarios were studied by hydraulic model tests. All the test results have proved that the opening will act as the main fish entrance when the downstream water level is higher than the bottom elevation within a certain range. The fishway entrance is compact, self-adapting and suitable for the large downstream water level variation when the openings bottom elevations are designed properly.

Keywords: Water level; variation; Vertical Slot Fishway; fishway entrance; hydraulic model test.

1 INTRODUCTION

The fishway entrance is crucial for the migrators to enter the fishways (Katopodis et al., 2011). A good fishway entrance has flow that maintains sufficient velocity (Baumann et al., 2012; Cheong et al., 2006), and enough sphere of influence affecting range in the river. That is to say, the discharge through the fish passage facility must be sufficient to compete with the flow in the river during the migration period (Larinier, 2011). Particular care must be taken when designing the entrance on major rivers. It must be verified that the velocity of the flow at the entrance is sufficiently high for all of the various water levels that may occur downstream of the facility during the migration period, particularly those during high water levels. When the downstream water level rises as a result of increased discharge in the river, the cross-section at the fishway entrance increases, and, as a consequence, the velocity at the entrance decreases and with it the attractively of the fishway. The normal fishway entrance is only suitable for a limited range of water level variation (0.5~1.0m) (FAO, 2002). When the variation is larger, more entrances are needed to be set up at different elevations along the downstream river, and separated in an expanse range. But in reality, the project site conditions for arranging multi entrances always confronted with many difficulties.

In order to deal with the large variation of downstream water level, some methods were developed to help the entrance to maintain a sufficiently high velocity (FAO, 2002). The most common solution is to install a movable flat gate at the entrance, which is adjusted to maintain a constant and predetermined difference in water levels between the fishway and the tailwater. The water level difference can maintain a stable velocity of the outflow (Williams et al., 2012). But it has to install two depth gauges, one upstream from the gate in the fishway and the other downstream close to the entrance of the pass to monitoring the water levels. What's more, the float gate blocked the lower part of the fishway entrance, that is not suitable for bottom-living fish. And the float gate consumes time and money to maintain it in a good condition. The frequent switching the gates of the entrances are fussy operations, particularly when there is more than one gate. Another method is to vary the discharge through the facility in relation to the downstream level, but it is not so economical. The auxiliary flow (Viviane et al., 2005) is needed, when a large flow of water is needed to attract fish into a fishway only a fraction may be allowed through the fishway itself in order to limit the size and the cost of the

 ©2017, IAHR. Used with permission / ISSN 1562-6865 (Online) - ISSN 1063-7710 (Print)

facilities. It is common to supply the auxiliary flow from the forebay through the special turbines. It is generally fed by gravity after dissipation of the energy in a pool or a well, and special design is needed. The collection gallery (Clay, 1961) with several entrances is suitable to collect the fish across the full width of the powerhouse in a large power plant. The gallery usually located over the turbine outlets stretches over the whole width of the obstacle. The gallery has various outlets, one next to each other, through which the attracting current is discharged. The collection gallery also need large amount of adding flow to maintain the velocity of the attraction current and the adding water devices need specified design and operation.

All the above solutions are complicated due to the added facilities, such as gates and special designed adding water facilities. And a large amount of auxiliary flow is unaccepted in some project. So, a new solution for the large variation of downstream water level is needed.

In this paper, a compact self-adapting fishway entrance without any gate suitable for the large variation of downstream water level was proposed. It was designed based on the law of the water depths changes in the Vertical Slot Fishway (VSF). (Rajaratnam et al., 1986; Marriner et al., 2016), and the flow split ratios, flow patterns and velocity profiles of the openings under different scenarios were studied by hydraulic model tests.

2 MATERIALS AND METHODS

2.1 The structure of the self-adapting fishway entrance

The self-adapting fishway entrance contains 42 VSF pools, including 4 turning pools (NO.10, NO.18, NO.26 and NO.34). The VSF sections are composed of regular pools connected in sequence forming linear ladders, and the turning pools all have a flat bottom (Rajaratnam ,1997; Marriner et al., 2014). In cases where the difference between upstream and downstream water levels is greater than the maximum allowable design slope, more segment of regular pools are required, leading to the use of more turning pools. The details of the regular pool are: L=2.7m, B=2.4m, p=0.8m, B=0.3m, θ=45° (Xu et al., 2009; Zhang et al., 2012). The NO.10 and NO.26 turning pools both have an opening to the river and specific bottom elevation. The bottom of the opening is 2 m higher than that of the inner pool. The bottom of 1# water outlet is 2 m higher than the bottom of NO.10 turning pool, and the bottom of 2# water outlet is 2 m higher than the NO.26 turning pool. When the water level in the turning pool is lower than the bottom of the opening, the water will flow to the pool downstream normally. When the water depth in the pool is higher than the bottom of the opening, the water will flow out into the river, and forms a current with proper velocity to attract fishes. The sketch of the water level adaptive fishway entrance is shown in Figure 1.

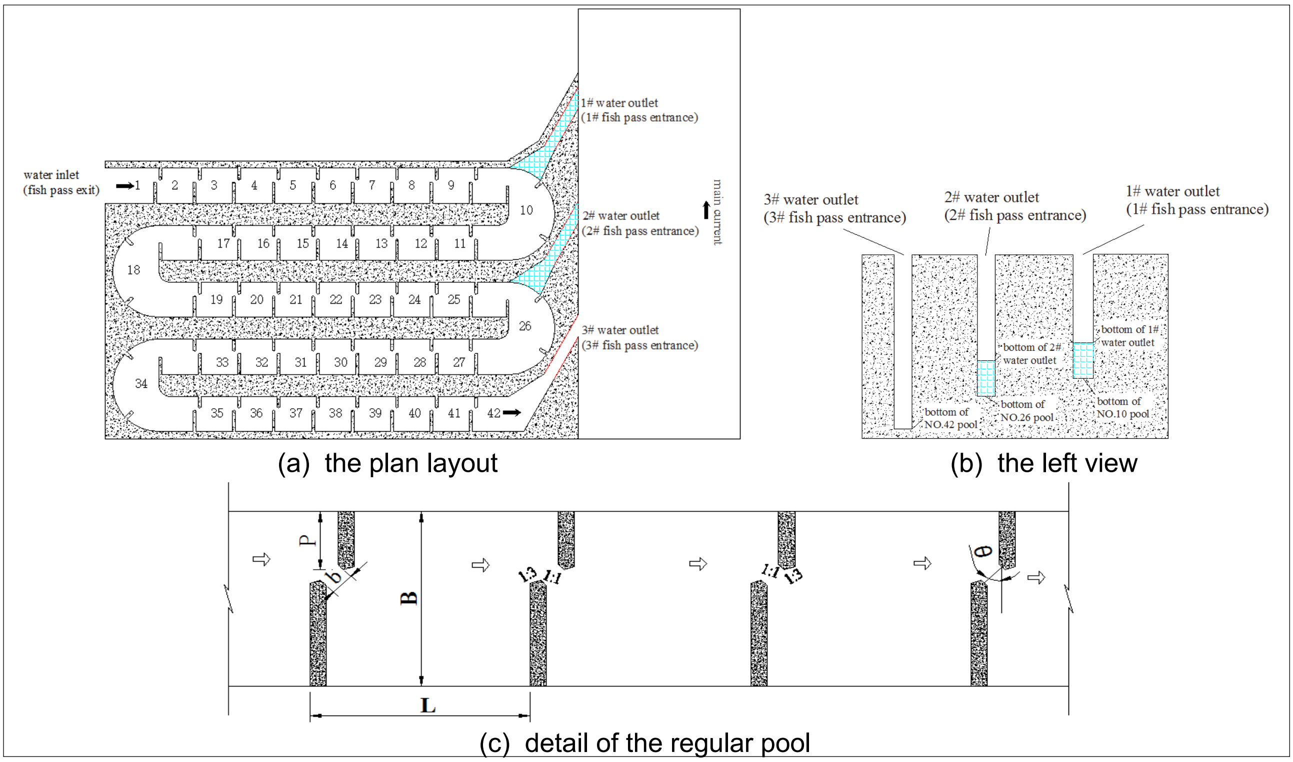

(a) the plan layout (b) the left view

(c) detail of the regular pool

Figure 1. Sketch of the water level adaptive fishway entrance.

2.2 Experimental Arrangement and Experiments

A hydraulic model of self-adapting fishway entrance was designed based on the law of gravity at a scale of 1:5. The hydraulic model included all the 42 VSF pools. An upstream tank and a downstream tank were built to control the water depth at the water inlet and the water level at the water outlet respectively. The water was cyclized between the two tanks by a pump, and the flow rate was measured by electromagnetic flowmeter. The water depth at central section of each pool was measured by a graduated scale, and the successive measures were made to obtain a stable mean value. The velocity was measured by an electromagnetic flow meter (P-EMS). The hydraulic model is shown in Figure 2.

Two set of experiments were designed, according different upstream water depth. The first set have a upstream water depth of 2.5m with varied downstream water levels (varied water depth at the water outlet), the second set have a upstream water depth of 1.75m with varied downstream water levels (varied water depth at the water outlet). All scenarios are listed in Table 1.

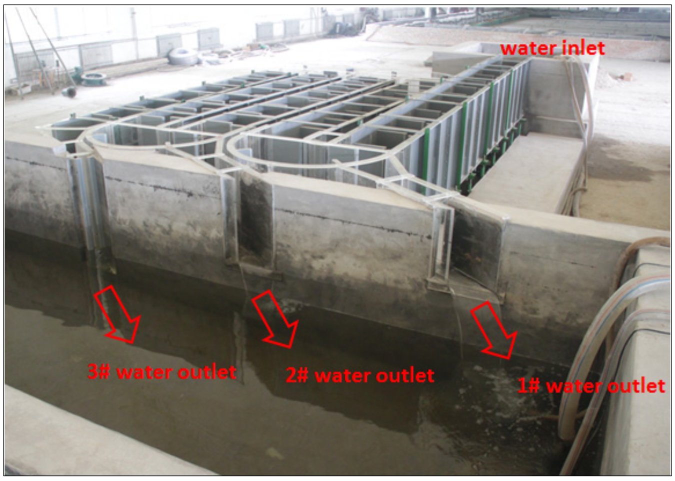

Figure 2. Overview of the hydraulic model.

Table 1. Typical test scenarios of varied upstream and downstream water levels.

Scenarios	Upstream water depth (m)	Downstream water depth (m)	Downstream water level (m)	Scenarios	Upstream water level (m)	Downstream water depth (m)	Downstream water level (m)
1	2.50	1.47	2.25	8	1.75	1.51	2.29
2		1.94	2.72	9		1.96	2.74
3		2.37	3.15	10		2.32	3.10
4		2.74	3.52	11		2.77	3.55
5		3.23	4.01	12		3.40	4.18
6		4.03	4.81	13		3.70	4.48
7		4.34	5.12				

3 RESULTS

3.1 The water profiles

The measured water surface profiles plotted against the pool bottom are shown in Figure 3 (the upstream water depth is 2.5m) and Figure 4 (the upstream water depth is 1.75m). Due to the great influence of tailwater river levels, the water surface profiles in a vertical slot fishway can be uniform, where the depth, h, of water in each pool is approximately the same; or non-uniform, with a backwater profile (M1 curve) or a drawdown profile (M2 curve) (Chow, 1959; Rajaratnam et al., 1986). In both data sets, the water surface profiles were found to be non-uniform with M1 or M2 type backwater curves, and the uniform conditions are rarely happened.

When the upstream water depth is 2.5m, the downstream water elevation is higher than 3.28m (the bottom elevation is 0.78 m), an M1 type backwater curve is expected; otherwise an M2 type backwater curve is expected. The floor elevation of the opening in Pool 10 is submerging in these scenarios, and an outflow into the river is expected. When an M1 type back water profile was occurred, the floor elevation of the opening in Pool 26 is submerged too, and the flow out from the opening, as shown in in Figure 3.

When the upstream water depth is 1.75m, the downstream water elevation is higher than 2.53m (the bottom elevation is 0.78m), an M1 type backwater curve is expected; otherwise an M2 type backwater curve is expected. The floor elevation of opening in Pool 10 is not submerging in these scenarios and thus no outflow into the river. When an M1 type back water profile was occurred, the floor elevation of opening in Pool 26 is submerged, and an outflow into the river is expected, as shown in in Figure 4.

 ©2017, IAHR. Used with permission / ISSN 1562-6865 (Online) - ISSN 1063-7710 (Print)

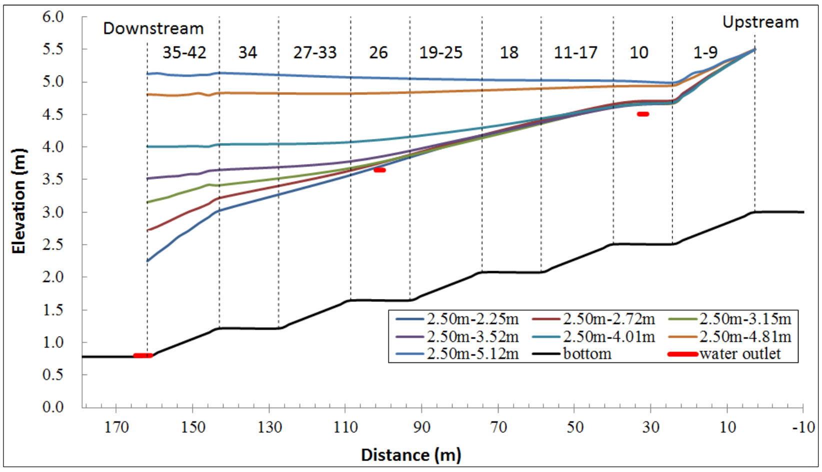

Figure3. Water surface profiles for Pools 1–42 of the self-adapting fishway entrance when the upstream water depth is 2.5m.

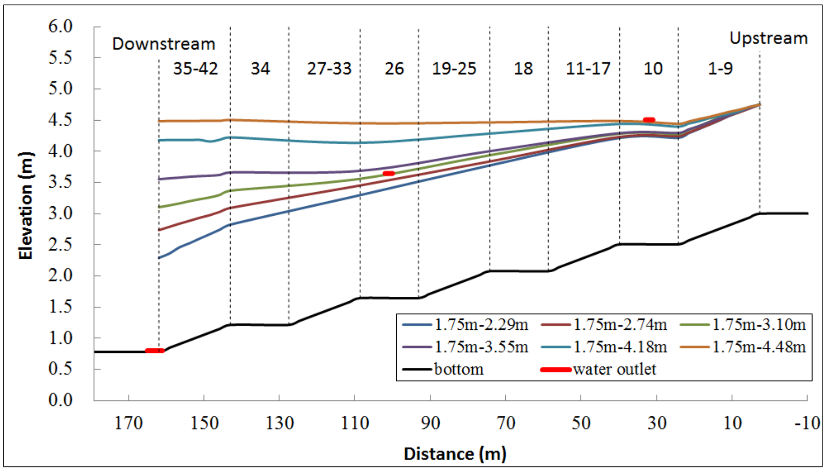

Figure 4. Water surface profiles for Pools 1–42 of the self-adapting fishway entrance when the upstream water depth is 1.75m.

3.2 The flow split ratio

The water outlets will act as the main fishway entrance when it worked as the main water outlet. Fishways are designed to run at uniform flow condition as this will require the minimum fishway length by having an equal water level drop in each pool. When the tailwater level rises above the uniform condition, the water level drop between pools, Δh, close to the downstream end of the fishway decreases. The backwater condition may diminish fish attraction to the fishway entrance due to lower flow velocities from decreased Δh values. In the self-adapting fishway entrance, when the tailwater level raised, the lower water outlet and the connecting VSF section all have a greater water depth, and the resistance was increased, the velocity was decreased, and the split ratio was decreased too. At the same time, the raised tail water level was higher than the bottom elevation of the opening of the turning pool, the water will flow out, and it will act as a fishway entrance.

When the upstream water depth is 2.5m and the downstream water elevation is 2.25m, the water depth at the 1#, 2# and 3# water outlets are 0.14m, 0m, 1.47m, the velocities are 1.02m/s, 0m/s, 0.44m/s, and the discharges are 18%, 0%, 82 of the total flow, respectively. In this scenario, the 3# water outlet acts as the main fishway entrance. When the downstream water elevation rise to 4.01m, the water depth at the 1#,2# and 3# water outlets are 0.11m,0 .43m,3.23m, the velocities are 1.3m/s,0.83m/s, 0.03m/s, and the discharges are 24%, 58% and 18% of the total flow, respectively. In this scenario, the 2# water outlet acts as the main fishway entrance. When the downstream water elevation rise to 5.12 m, the water depth at the 1#, 2# and 3# water outlets are 0.51m, 1.43m, 4.34m, the velocities are 1.05m/s,0.11m/s, 0.02m/s, and the discharges are 70%, 21% and 9% of the total flow, respectively. In this scenario, the 1# water outlet acts as the main fishway entrance. The flow split ratio are shown in Figure 5 and listed in Table 2.

When the upstream water depth is 1.75m, the downstream water elevation is 2.29m, there are no the water flow out through the 1# and 2# water outlets, the 3# water outlets discharge 100% of the total flow, with a velocity 0.27m/s and a water depth 1.5m, and it acts as the main fishway entrance. When the downstream water elevation rises to 4.18m, there are no water flows out through the 1# water outlet. The water depth at the 2# and 3# water outlets are 0.49m and 3.4m, the velocities are 0.55m/s and 0.03m/s, the discharges are 71% and 29% of the total flow, respectively. In this scenario, the 2# water outlet acts as the main fishway entrance. The flow split ratio are shown in Figure 6 and listed in Table 3.

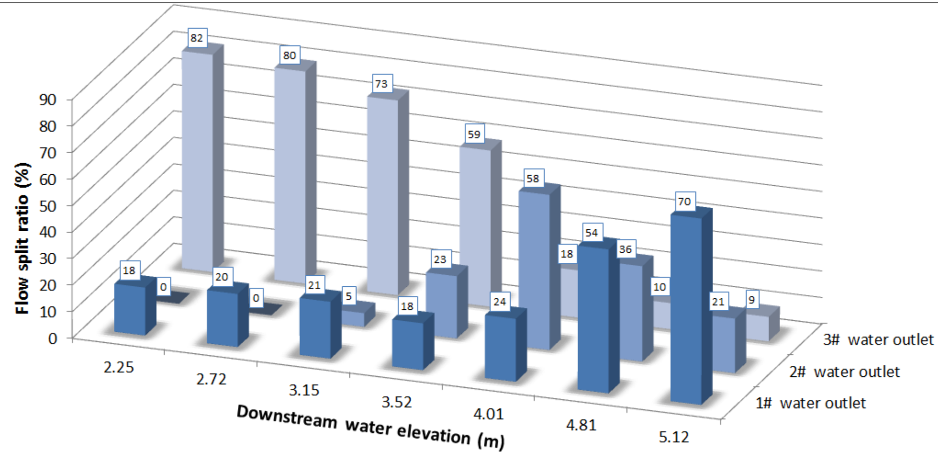

Figure 5. The flow split ratio of the self-adapting fishway entrance when the upstream water depth is 2.5m.

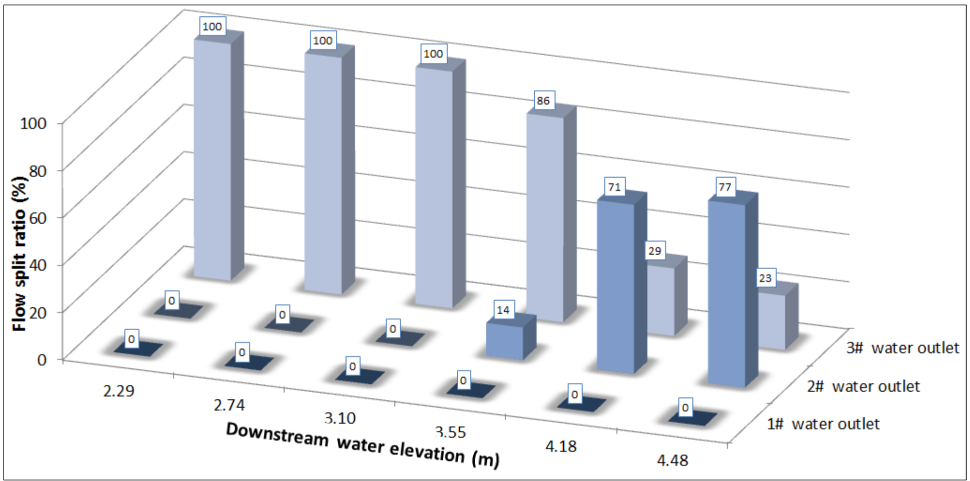

Figure 6. The flow split ratio of the self-adapting fishway entrance when the upstream water depth is 1.75m.

Table 2. The data of the water outlets when the upstream water depth is 2.5m

DWL (m)	1# water outlet				2# water outlet				3# water outlet			
	H (m)	U (m/s)	Q (l/s)	SR (%)	H (m)	U (m/s)	Q (l/s)	SR (%)	H (m)	U (m/s)	Q (l/s)	SR (%)
2.25	0.14	1.02	21.59	18	0.00	0.00	0.00	0	1.47	0.44	96.97	82
2.72	0.15	0.96	22.02	20	0.00	0.00	0.00	0	1.94	0.29	83.91	80
3.15	0.11	1.16	18.98	21	0.03	0.94	4.57	5	2.37	0.17	58.79	73
3.52	0.10	1.21	17.79	18	0.14	1.17	23.62	23	2.74	0.13	54.14	59
4.01	0.11	1.30	21.78	24	0.43	0.83	53.71	58	3.23	0.03	15.25	18
4.81	0.43	1.24	79.22	54	1.18	0.30	52.49	36	4.03	0.02	14.44	10
5.12	0.51	1.05	80.12	70	1.43	0.11	23.44	21	4.34	0.02	10.21	9

DWL: Downstream water level; H: water depth in the water outlet; U: velocity; Q: water quantity; SR: flow split ratios.

 ©2017, IAHR. Used with permission / ISSN 1562-6865 (Online) - ISSN 1063-7710 (Print)

Table 3. The data of the water outlets when the upstream water depth is 1.75m

DWL (m)	1# water outlet				2# water outlet				3# water outlet			
	H (m)	U (m/s)	Q (l/s)	SR (%)	H (m)	U (m/s)	Q (l/s)	SR (%)	H (m)	U (m/s)	Q (l/s)	SR (%)
2.29	0.00	0.00	0.00	0.00	0.00	0.00	0.00	0	1.51	0.27	61.90	100
2.74	0.00	0.00	0.00	0.00	0.00	0.00	0.00	0	1.96	0.23	68.49	100
3.10	0.00	0.00	0.00	0.00	0.00	0.00	0.00	0	2.32	0.19	64.61	100
3.55	0.00	0.00	0.00	0.00	0.04	0.98	6.28	14	2.77	0.09	36.25	86
4.18	0.00	0.00	0.00	0.00	0.49	0.55	40.49	71	3.40	0.03	15.61	29
4.48	0.00	0.00	0.00	0.00	0.81	0.24	29.14	77	3.70	0.01	8.01	23

DWL: Downstream water level; H: water depth in the water outlet; U: velocity; Q: water quantity; SR: flow split ratios.

4 DISCUSSIONS

A fishway entrance design needs to take into consideration the water surface profile, water depth, velocity and some other hydraulic factors (Oldani et al., 2002; Stuart et al., 2007; Croze et al., 2008). But the most important is to take biological criteria into account (Hai, 1980; Lucas et al., 2001; Rodríguez et al., 2006). As the fishway entrance design evolves to encompass fish communities, there are more variables to be accounted for in the design of a fishway. For example, having a uniform water surface profile may be targeted in the migration period. But in reality, the uniform flow conditions are rarely happened. In this way a fishway entrance must accommodate a wide range of natural variables. The perception of the current by aquatic organisms plays a decisive role in their oritation in rivers. Thus, it is necessary for the fishway entrance to maintain a sufficiently high velocity outflow, luring and guiding the fishes from the river into the fishway (Baek et al., 2014; 2015). When the downstream water level increased, the water depth was increased correspondingly, and the velocity was decreased. There need some solutions to deal with the situation, such as installing movable flat gate, varying the discharge and adding auxiliary flow, they are all aimed to maintain a proper velocity of the entrance outflow. But installing movable flat gate need some other facilities, such as water depth gauges and gate lifting devices, and the operation of the gate is fussy issues; especially when there is more than one gate. Varying the discharges of the fishway is not so economical. Adding auxiliary flow also need large amount water and the adding water devices need specified design and operation.

Based on the law of the water depths changes in the VSF (Rajaratnam et al., 1986; Wu et al., 1999; Marriner et al., 2014; Marriner et al., 2016), a water level adaptive fishway import was designed, and its water depth under deferent scenarios was studied by experiments. The water level adaptive fishway import does not have any gate, and it can change the main fishway inlet corresponding to the downstream water level. This is mainly because, when the downstream water was raised higher than the bottom elevation of the opening in the 2# water outlet, it is much easier to get out from the opening to the river for the water from the upstream, comparing to conquer the block force come from the big amount water body and the baffle plane, alone the way to the 3# water outlet. The split ratios of the typical scenarios have proved the effectiveness of the self-adapting fishway entrance. Thus, the fishway entrance is changed corresponding to the downstream water levels. The higher the downstream water level, the higher outlet will act as the main fishway entrance. It applies to other conditions too.

There is another advantage for the self-adapting fishway entrance. When the main fishway entrance changed, the relatively lower water outlets are still connected to the river, and they still are feasible paths for the fishes get into the outlet. It is important, especially for the bottom-living fishes, the lowest outlet always connected to the river, acting as an available path without any blocks (Goodwin et al., 2014).

There appears to be some deficiencies as well. When the lowest water outlet (3# water outlet) act as the main fish entrance, the velocities (0.19m/s~0.44m/s) are not sufficient enough. It needs some optimization to increase the velocities, such as narrow the width of the 3# water outlet. Additionally, in some scenarios it is unnecessary to let the water flow out from the higher water outlet. For example, senario1~senario 3, when the upstream water depth is 2.5m, the downstream water elevations are 2.25~3.15 m, the water depth at the 1# water outlets are 0.11~0.15m, the discharges are 18%~21%. In all these scenarios, the main fish entrance is the 3# water outlet, but part of the water can discharge from the 1# water outlet and form a water fall which no fishes can jump through. The split flow at the 1# water outlet reduces the flow rate and the current velocity in the main entrance.

5 CONCLUSIONS

In this paper, a self-adapting fishway entrance without any gate suitable for the large variation of downstream water level was proposed. The entrance contains several parallel connected returning sections of VSF, and some returning sections have opening to the river. Each opening has a specific bottom elevation, and the bottom of the opening is higher than the inner pool. When the water level in the adjacent pool is lower than the bottom of the opening, the water will move to the next inner pool normally. When the water depth in

©2017, IAHR. Used with permission / ISSN 1562-6865 (Online) - ISSN 1063-7710 (Print)

the pool is higher than the bottom of the opening, the water will flow out into the river, and form a current with proper velocity to attract fishes. The flow split ratios, flow patterns and velocity profiles of the openings under different scenarios were studied by hydraulic model tests. All the test results have proved that it can change the main fishway inlet corresponding to the downstream water level, and the opening will act as the main fish entrance when the downstream water level is higher than the bottom elevation within a certain range. It always maintains a sufficiently velocity in the water outlet, and keep the luring to the fishes. When the main fishway entrance changed, the relatively lower water outlets are still connected to the river, they still are feasible paths for the fishes getting into the outlet. It is important for the bottom-living fishes that the lowest outlet always connected to the river, acting as an available path. The fishway entrance is compact, self-adapting and suitable for the large downstream water level variation when the openings bottom elevations are designed properly.

ACKNOWLEDGEMENTS

This research was supported by the National Natural Science Foundation of China (No.51679261).

REFERENCES

Baumann, P. & Stevanella, G. (2012). Fish Passage Principles to be Considered for Medium and Large Dams: The Case Study of a Fish Passage Concept for a Hydroelectric Power Project on the Mekong Mainstream in Laos. *Ecological Engineering*, 48(7), 79-85.

Baek, K.O., Ku, Y.H. & Kim, Y.D. (2015). Attraction Efficiency in Natural-Like Fishways according to Weir Operation and Bed Change in Nakdong River. *Ecological Engineering*, 84, 569-578.

Baek, K.O. & Kim, Y.D. (2014). A Case Study for Optimal Position of Fishway at Low-Head Obstructions in Tributaries of Han River in Korea. *Ecological Engineering*, 64, 222-230.

Cheong, T.S., Kavvas, M.L. & Anderson, E.K. (2006). Evaluation of Adult White Sturgeon Swimming Capabilities and Applications to Fishway Design. *Environmental Biology of Fishes*, 77(2), 197-208.

Chow, V.T. (1959). *Open-Channel Hydraulics.* McGraw-Hill Book Co., New York, Chapter C9.

Clay, C.H. (1961). *Design of Fishways and Other Fish Facilities*. Department of Fisheries and Oceans, Ottawa, Canada.

Croze, O., Bau, F. & Delmouley, L. (2008). Efficiency of a Fish Lift for Returning Atlantic Salmon at a Large-Scale Hydroelectric Complex in France. *Fisheries Management and Ecology*,15(5-6), 467- 476.

FAO/DVWK. (2002). *Fish Passes-Design, Dimensions and Monitoring*. FAO, Rome.

Goodwin, R.A., Politano, M., Garvin, J.W., Nestler, J.M., Hay, D., Anderson, J.J., Weber, L.J., Dimperio, E., Smith, D.L. & Timko, M. (2014). Fish Navigation of Large Dams Emerges from Their Modulation of Flow Field Experience. *Proceedings of the National Academy of Sciences of the United States of America,* 111 (14), 5277–5282.

Zhao, X., Han, Z. & Hai, H. (1980). Experiments on the Current Overcoming Ability of Some Freshwater Fishes. *Journal of Fisheries of China*, 4(1), 31-37.

Katopodis, C. & Williams, J.G. (2001).The Development of Fish Passage Research in a Historical Context. *Ecological Engineering*, 48, 8-18.

Larinier, M. (2001). *Environmental Issues, Dams and Fish Migration*, FAO Fisheries Technical Paper, 419, 45-89.

Lucas, M.C. & Baras, E. (2001). *Migration of Freshwater Fishes*. Blackwell Science, Oxford, England.

Marriner, B.A.,Baki, A.B.M., Zhu D.Z., Jason D.T., Cooke, S.J. & Katopodis, C. (2014). Field and Numerical Assessment of Turning Pool Hydraulics in a Vertical Slot Fishway. *Ecological Engineerin*g, 63, 88-101.

Marriner, B.A., Baki, A.B.M., Zhu, D.Z., Cooke, S.J. & Katopodis, C. (2016). The Hydraulics of a Vertical Slot Fishway: A Case Study on the Multi-Species Vianney-Legendre Fishway in Quebec, Canada. *Ecological Engineering,* 90,190-202.

Oldani, N.O. & Baigun, R.M. (2002). Performance of a Fishway System in a Major South American Dam on the Parana River (Argentina-Paraguay). *River Research and* Applications,18(2), 171-183.

Rajaratnam, N., Katopodis, C., Wu, S. & Saburm, M.A. (1997). Hydraulics of Resting Pools for Denil Fishways. *Journal of Hydraulic Engineering*, 123(7), 632-638.

Rajaratnam, N., Vinne, G.V.D. & Katopodis, C. (1986). Hydraulics of Vertical Slot Fishways. *Journal of Hydraulic Engineering,*112 (10), 909-927.

Rodríguez, T.T., Agudo, J.P., Mosquera, L.P. & González, E.P. (2006). Evaluating Vertical-Slot Fishway Designs in Terms of Fish Swimming Capabilities. *Ecological Engineerin*g, 27(1), 37-48.

Stuart, I.G., Berghuis, A.P. & Long, P.E. (2007). Do Fish Locks Have Potential in Tropical Rivers? *River Research and Application*, 23(3), 269-286.

Viviane, P.F.M. & Carlos, B.M. (2005). Study of Power Capacity through the Auxiliary Water Flow of the Igarapava Dam Fishway. *Proceedings of the COBEM 2005: 18th International Congress of Mechanical Engineering*, Ouro Preto, MG.

 ©2017, IAHR. Used with permission / ISSN 1562-6865 (Online) - ISSN 1063-7710 (Print)

Williams, J.G., Armstrong, G., Katopodis, C., Larinier, M. & Travade, F. (2012). Thinking Like a Fish: A Key Ingredient for Development of Effective Fish Passage Facilities at River Obstructions. *River Research and Applications,* 28(4), 407-417.

Wu, S., Rajaratnam, N. & Katopodis, C. (2014). Structure of Flow in Vertical Slot Fishway. *Journal of Hydraulic Engineering,* 125(4), 351-360.

Xu, T. & Sun, S. (2009). Numerical Simulation of the Flow Structure in Vertical Slot Fishway. *Journal of Hydraulic Engineering,* 40(11), 1386-1391.

Zhang, G. & Sun, S. (2012). Effect of Slot Width on the Flow Structure of Vertical Slot Fishway. *Journal of Hydroelectric Engineerin*g, 43(1), 151-156.

Proceedings of the 37th IAHR World Congress
August 13 – 18, 2017, Kuala Lumpur, Malaysia

EFFECT OF BUOYANT JETS MERGING ON MEAN KINETIC ENERGY FLUX

PANAYOTIS C. YANNOPOULOS(1)

(1) Environmental Engineering Laboratory, Department of Civil Engineering,
University of Patras, University Campus at Rion, Patras, Greece
yannopp@upatras.gr

ABSTRACT

The mean flow and mixing properties of single and interacting round vertical turbulent buoyant jets issued in calm and uniform ambient environment have been determined by employing an advanced integral model (AIM), which uses composite profile functions for the transverse distributions of mean axial velocities and mean concentrations. The groups of N = 2, 5, 11 and 25 buoyant jets issued from equally spaced nozzles of equal diameter, located in horizontal series, and the groups of N = 3, 6, 12 and 24 buoyant jets issued from rosette-type formations have been solved. Two values of initial densimetric Froude number have been taken: 2.5 (plume-like) and 25 (jet-like).The half spacing between adjacent nozzles has been taken equal to the nozzle diameter. Then, the centreline and transverse distributions of velocities have been used to calculate the mean kinetic energy flux. The variations of maximum axial velocities and concentrations in buoyant jet cross-sections are plotted in diagrams versus the longitudinal distance, along with their asymptotes. In the same diagrams the semi-empirical expressions valid for plane/round plumes/jets are given for comparison. The effect of interacting buoyant jets on the mean kinetic energy flux is investigated in the whole buoyancy region and special care is paid on the asymptotic behaviour in the plume-like and jet-like cases. It was found that the variation of the kinetic energy flux is actually identical (all curves coincide practically to each other) for interacting plumes independent from their number and group formation. This behaviour implies self-similarity occurrence in plumes, while the constant divergence of the mean kinetic energy flux along the main flow direction indicates the application of the superposition method. For jets, it is observed that the kinetic energy flux variation differs significantly among the groups and especially from the variation of the plane jet.

Keywords: Buoyant jet interaction; turbulent jets/plumes; mean flow properties; superposition method; linear/rosette-type outfall.

1 INTRODUCTION

There is a plethora of natural and man-originated phenomena that occur on surface of water bodies and in the atmosphere where buoyant forces play a significant role in their evolution forming buoyant jets. There are also many cases where adjacent buoyant jets interact with each other forming more complicated flow and mixing fields. Some of the most common natural phenomena are the upward or downward density currents in lakes, sea and atmosphere, due to temperature and/or density differences, natural gas escapes from earth faults, volcano eruptions etc. Man-originated phenomena usually occur in engineering applications, i.e. when wastewater, thermal effluent or brine is discharged by multiport diffusers and rosette-type risers in water bodies, or when air pollutants, heat and moisture are emitted into the atmosphere by groups of heat exchangers, cooling towers, chimneys and vehicle exhausts. All aforementioned phenomena, as mainly governed by buoyancy, are evolving gradually to plumes and might be considered as composed by an infinite number of infinitesimal point or line plumes. Alternatively, an approximated simulation for practical applications could be a suitable group of a finite number of round or plane plumes issued from shortly spaced sources.

The present work is focused on the single round or plane vertical turbulent buoyant jet (Yannopoulos, 2006) and on the groups of N = 2, 3, 5, 11 and 25 interacting round vertical turbulent buoyant jets issued vertically upwards into calm and uniform ambient environment from equally spaced nozzles of the same size located shortly in a horizontal line or in rosette-type formations (Yannopoulos and Noutsopoulos, 2006a; Yannopoulos and Noutsopoulos, 2006b; Bloutsos and Yannopoulos, 2009; Yannopoulos, 2010). Since for these cases the longitudinal distribution of the mean axial velocity is obtained by solving the momentum and buoyancy flux equations, the longitudinal distribution of the kinetic energy flux for the mean flow can be calculated and compared to the corresponding distribution for the single vertical round turbulent buoyant jet and the limiting case of a group of infinite number of buoyant jets, as well as to the plane buoyant jet. Finally, important implications will be extracted regarding the application of superposition method in groups of adjacent plumes of any number and formation.

2 DEFINITIONS AND CONSIDERATIONS

The single or multiple turbulent buoyant jets considered are issued upwards from vertical round or slot nozzles of size D (diameter or slot width) into a quiescent ambient environment of uniform density, ρ_a. The

 ©2017, IAHR. Used with permission / ISSN 1562-6865 (Online) - ISSN 1063-7710 (Print)

initial jet density is $\rho_0 \leq \rho_a$. A Cartesian coordinate system O(x,y,z) and a cylindrical coordinate system O(φ,r,z) are considered with z-axis vertical and origin O at the centre of the jet exit. In the case of a line series of nozzles, x-axis connects the centres of nozzles at jet exit cross-sections. The main features of the buoyant jets, single or multiple, are shown in Figure 1 along with the coordinate systems. The over bar means a time averaging quantity. Since the present work examines only mean flow properties, this symbolization is thereafter omitted in the sake of simplicity. Mathematically, the flow and mixing fields can be predicted by the set of partial deferential equations (PDE) of continuity, momentum and conservation of buoyancy, which are written for the mean flow, using the Reynolds substitution for each variable X=x+x', where X is any instantaneous value with mean value x and fluctuation x' at time t; then PDE are time averaged. For turbulent buoyant jets, the viscosity term in the momentum equations is negligible compared to the corresponding turbulent term and omitted. The dynamic pressure term is also considered negligible, while for small density differences between jet and environment (ρ_a/ρ_0<0.1), Boussinesq's approximation is applicable. Under the aforementioned approximations and considering no swirl, the governing equations are written as:

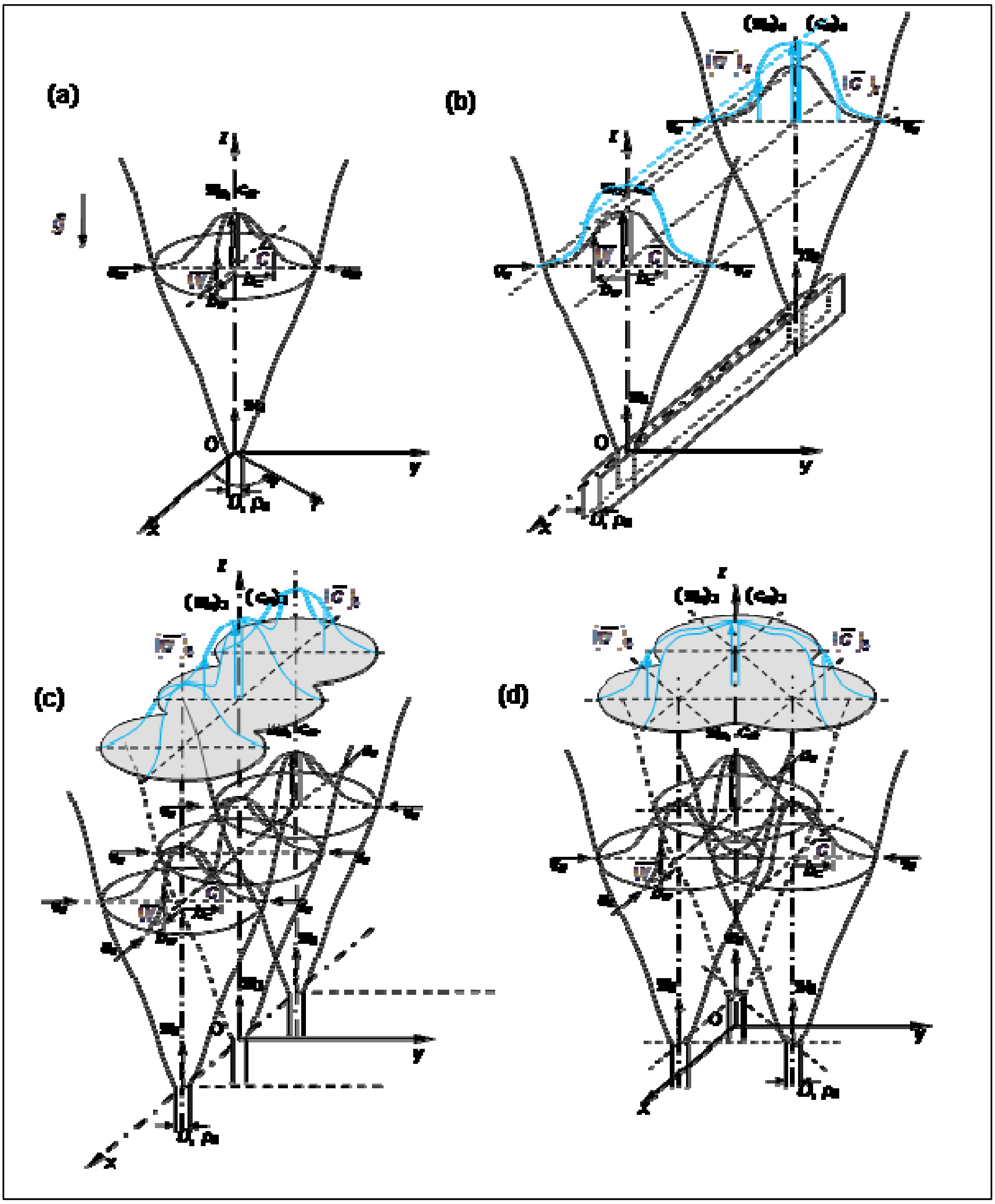

Figure 1. Vertical turbulent buoyant jets: (a) Round buoyant jet; (b) Slot (plane) buoyant jet; (c) Round buoyant jets in series; (d) Round buoyant jets on the apexes of a equilateral triangle.

Continuity $$\frac{\partial(r^i w)}{\partial z}+\frac{\partial(r^i v_i)}{\partial y_i}+\frac{\partial u_i}{\partial x_i}=0 \quad [1]$$

Momentum z $$\frac{\partial\left[r^i\left(w^2+w'^2\right)\right]}{\partial z}+\frac{\partial(r^i w v_i)}{\partial y_i}+\frac{\partial(w u_i)}{\partial x_i}=g_0' r^i c+\frac{\partial(r^i\tau_{zyi})}{\rho_0\partial y_i}+\frac{\partial\tau_{zxi}}{\rho_0\partial x_i} \quad [2]$$

Tracer $$\frac{\partial\left[r^i\left(wc+w'c'\right)\right]}{\partial z}+\frac{\partial(r^i v_i c)}{\partial y_i}+\frac{\partial(u_i c)}{\partial x_i}=-\frac{\partial(r^i v_i' c')}{\partial y_i}-\frac{\partial(u_i' c')}{\partial x_i} \quad [3]$$

Mean kinetic energy $$\frac{\partial(r^i w\omega_i)}{\partial z}+\frac{\partial(r^i v_i\omega_i)}{\partial y_i}+\frac{\partial(u_i\omega_i)}{\partial x_i}=g_0' r^i c\omega_i-r^i f \quad [4]$$

where, w = mean velocity in the z direction, $v_i \equiv v$ = mean velocity in y direction if i=0 (plane buoyant jet) or $v_i \equiv u_r$ in r direction if i=1 (round buoyant jet), $u_i \equiv u$ = mean velocity in x direction if i=0 or $u_i \equiv u_\varphi$ in φ direction if i=1; w', v_i', u_i', c' = corresponding fluctuations; $c=(\rho_a-\rho)/(\rho_a-\rho_0)$ = mean concentration at (x_i,y_i,z), $x_0 \equiv x$, $x_1 \equiv \varphi$, $y_0 \equiv y$, $y_1 \equiv r$, ρ = mean density, τ_{zyi}, τ_{zxi} = mean turbulent shear stresses acting on plane z and parallel to axis y_i or x_i, correspondingly; $g_0'= g_0(\rho_a-\rho_0)/\rho_0$ = apparent gravity acceleration; $\omega_i = (w^2+u_i^2+v_i^2)/2$ = kinetic energy for mean velocities; and f = remaining terms of mean kinetic energy.

The phenomena, where the present work is focused on, have been solved by employing the advanced integral model (AIM) proposed by the author (Yannopoulos, 2010), which is based on the concept of the entrainment restriction approach (ERA), but using composite functions in the transverse directions for the mean axial velocities and mean concentrations, instead of using typical Gaussian profiles. ERA is a particular integral method applied when the flow field has symmetry planes (Yannopoulos and Noutsopoulos, 2006a; Bloutsos and Yannopoulos, 2009). The composite profiles have been formed using the superposition method (SM). SM is based on the conservation of momentum for jet-like flows and conservation of the divergence of mean kinetic energy flux with respect to z in the main flow direction. AIM has managed to obtain 2nd order accuracy (errors less than10%). To get the centreline axial velocity and concentration distributions, the integral forms of Eqs. (1), (2) and (3) have been solved by applying the following boundary conditions:

- For the centreline of a linear or rosette-type diffuser

$$w=w_{mN},\, v_i=u_i=0,\, c=c_{mN},\, \tau_{zyi}=\tau_{zxi}=0,\, v_i'c'=u_i'c'=0 \quad [5]$$

- On the symmetry planes of a linear or rosette-type diffuser

$$v=u_\varphi=0,\;\; \tau_{zyi}=\tau_{zxi}=0,\, v_i'c'=u_i'c'=0 \quad [6]$$

- For y_i or $x_i \to\infty$ of a linear or rosette-type diffuser

$$w=0,\, v_i=v_{ie},\, u_i=u_{ie},\;\; c=0,\, \tau_{zyi}=\tau_{zxi}=0,\, v_i'c'=u_i'c'=0 \quad [7]$$

where, v_{ie} and u_{ie} = entrainment velocities in y and x direction, correspondingly, if i=0 or r direction if i=1. Finally, the system of equations is closed by assuming that the nominal widths of buoyant jets are considered to be approximated by the quasi-linear functions b_w=$K_w z$ and b_c=$K_c z$ for the mean velocity and concentration, where the spreading rate coefficients K_w and K_c are given by Yannopoulos (2006) as: K_w=0.11 for a round buoyant jet, K_w=0.132 for a plane buoyant jet and K_c=λK_w. The parameter λ have been calculated by the empirical formula given by Wang and Law (2002):

$$\lambda=\lambda_j-\left(\lambda_j-\lambda_p\right)\left(\frac{\mathrm{R}_N}{\mathrm{R}_p}\right)^{3/4} \quad [8]$$

where, λ_j=1.50 and 1.23 for plane and round jets, and λ_p=1.21 and 1.04 for plane and round plumes, correspondingly. R_N = the local Richardson number for the group of N interacting buoyant jets, which is found by Yannopoulos (2006) to be:

 ©2017, IAHR. Used with permission / ISSN 1562-6865 (Online) - ISSN 1063-7710 (Print)

$$\mathrm{R}_N = p\frac{\beta_N z}{\varepsilon_N} \qquad [9]$$

where, p=0.144, $\beta_N = 4g_0'\lambda_B t^2\int_0^{\infty}\mathrm{d}\frac{y}{t}\int_0^{\infty} w_N c_N\,\mathrm{d}\frac{x}{t}$ and $\varepsilon_N = 4t^2\int_0^{\infty}\mathrm{d}\frac{y}{t}\int_0^{\infty} w_N^3\,\mathrm{d}\frac{x}{t}$ for a linear diffuser and $\beta_N = 2g_0'\lambda_B Nt^2\int_0^{a_N/2}\mathrm{d}\frac{y}{t}\int_0^{\infty} w_N c_N\,\mathrm{d}\frac{x}{t}$ and $\varepsilon_N = 2Nt^2\int_0^{a_N/2}\mathrm{d}\frac{y}{t}\int_0^{\infty} w_N^3\,\mathrm{d}\frac{x}{t}$ for a rosette-type diffuser are the fluxes of buoyancy and mean kinetic energy for the composite field of N interacting buoyant jets; t = half spacing of the centres of successive nozzles of buoyant jets; a_N=2π/N angle between consecutive symmetry planes. Details on the computation of fluxes are provided by Yannopoulos (2010). For plane plumes $\mathrm{R}_N \rightarrow \mathrm{R}_p$=0.2907 and for round plumes $\mathrm{R}_N \rightarrow \mathrm{R}_p$=0.3521. Coefficient λ_B, which introduces the turbulence contribution in the mean buoyancy flux, have been calculated by the empirical formula given by Wang and Law (2002):

$$\lambda_B = \lambda_{Bj} - \left(\lambda_{Bj} - \lambda_{Bp}\right)\frac{\mathrm{R}_N}{\mathrm{R}_p} \qquad [10]$$

where λ_{Bj}=1.04 and 1.076 for plane and round jets, and λ_{Bp}=1.18 and 1.15 for plane and round plumes, correspondingly.

3 RESULTS AND DISCUSSION

The linear groups of N=2, 5, 11 and 25 and the rosette-type groups of 3, 6, 12 and 24 buoyant jets have been solved, which are issued vertically upwards in a stagnant ambient environment from equally spaced round nozzles of equal diameter. The cases of plume-like behaviour (F_0 = 2.5) and of jet-like behaviour (F_0 = 25), with half spacing t/D=1, have been examined and the longitudinal distributions of the maximum values of axial velocity and concentration at a cross-section, as well as the kinetic energy flux have been calculated, normalized and plotted in Figure 2 (a, b, c, d, e, f), regarding the linear group, and in Figure 3 (a, b, c, d, e, f), regarding the rosette-type group. These results are also compared to the cases of a single buoyant jet (N=1), an infinite row of buoyant jets (N=infinite) and the semi-empirical solutions for a single plane and round plume for the plume-like cases and for a single plane and round jet for the jet-like cases. The normalized distance Z is defined as $Z=(z/D)\mathrm{F}_0^{-4/(3+i)}$ and the normalized velocity and concentration as $W_N^*=(w_N/w_0)\mathrm{F}_0^{2(1+i)/(3+i)}$ and $C_N^*=(c_N/c_0)\mathrm{F}_0^{2(1+i)/(3+i)}$, correspondingly, where $\mathrm{F}_0=w_0/(g_0'D)^{1/2}$; w_N and c_N are the corresponding maximum values of axial velocities and concentrations at a cross-section of a group of N buoyant jets, and w_0 and c_0 their corresponding values at the source exit. The normalized kinetic energy is defined as $E_N^*=(\varepsilon_N/\varepsilon_0)\mathrm{F}_0^{2(1+i)/(3+i)}$, where ε_N is the kinetic energy flux of a group of N buoyant jets at a cross-section z, ε_0 is the value of the kinetic energy flux at the source exit; i=0 for plane buoyant jets and i=1 for round buoyant jets, according to the definitions given by Yannopoulos (2010).

Paying attention on Figures 2 (a, b) and 3 (a, b) regarding the plume-like cases, it is evident that the asymptotic behaviour of a group of $N\rightarrow\infty$ interacting plumes approaches fairly well the two-dimensional (plane plume) behaviour, both for velocities and concentrations, for either the linear group or the rosette-type formations. This fact is not evident for the corresponding jet-like cases shown in Figures 2 (d, e) and 3 (d, e), where the two-dimensional (plane jet) behaviour differs drastically from the infinite-jet asymptotes.

A very important implication is drawn, paying attention on Figures 2 (c) and 3 (c) regarding the plume-like cases, where the curves representing the variation of the mean kinetic energy flux in the main flow direction, for all the group formations examined, coincide to each other forming practically one curve. This curve has the same asymptotic behaviour with the limiting cases of the groups of infinite plumes, as well as with the two-dimensional (plane plume). This finding implies, on one hand, that self-similarity is actually obtained in plumes and, on the other, that the divergences of the kinetic energy flux with respect to main flow distance (i.e. for Z≥5) is conserved. The latter result inspired the application of the superposition method in plume groups by adding the individual local kinetic energy fluxes (i.e. w_j^3) for each plume of the group, which predicts linearity of the PDE of the mean kinetic energy in terms of w^3. Therefore,

$$\left(w^3\right)_N = \sum_{j=1}^{N} w_j^3 \qquad [11]$$

where, $(w^3)_N$ is the cubic power of the axial velocity at a predefined location of the composite flow field of the group of N plumes and w_j^3 is, at the same location (x,y,z), the cubic power of the axial velocity of the j-th plume considered as single. The concept expressed by Eq. [11] has been successfully applied for linear and rosette-type plume formations issued in quiescent surroundings, as well as for a row of plumes in a current

©2017, IAHR. Used with permission / ISSN 1562-6865 (Online) - ISSN 1063-7710 (Print)

(Yannopoulos, 1984; 1996; 2010; Bloutsos and Yannopoulos, 2005; Yannopoulos and Noutsopoulos, 2006b; Bloutsos and Yannopoulos, 2009; Lai and Lee, 2012).

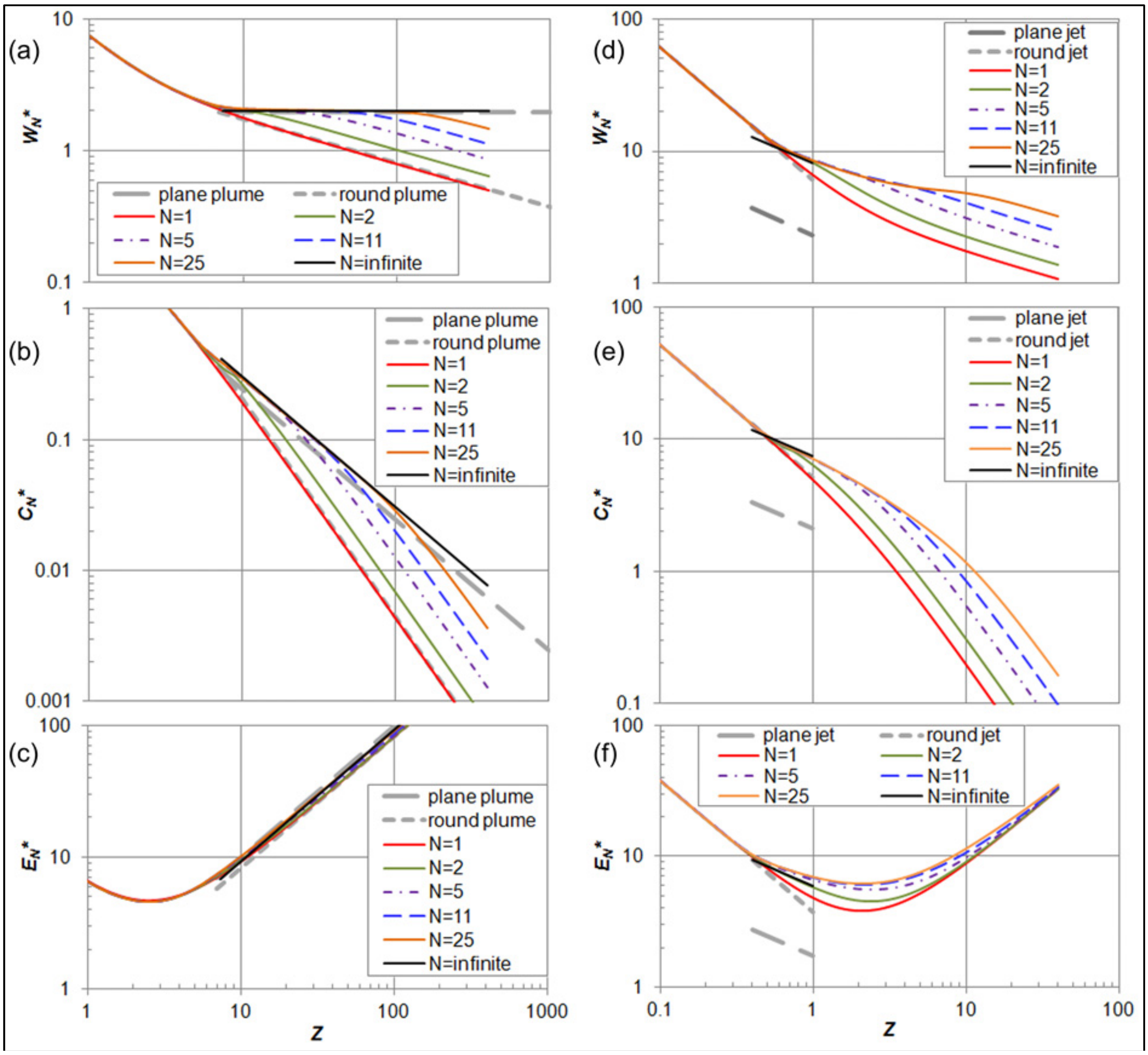

Figure 2. Normalized distributions along the main flow direction for linear groups; left column is the plume-like case (F_0=2.5); right column is the jet-like case (F_0=25): (a) and (d) mean axial velocity; (b) and (e) mean concentration; (c) and (f) mean kinetic energy flux.

The variation of the kinetic energy flux of the jet-like cases shown in Figures 2 (f) and 3 (f) differs appreciably between groups depending mainly on the number of buoyant jets. The asymptotic behaviour of a group of infinite jets is also very different than the two-dimensional (plane jet) behaviour, which means that the kinetic energy flux is inappropriate to be used for superposition solutions of buoyant jets in the jet-like buoyancy region. It is noticed that the jet-like case is a limiting behaviour of a buoyant jet, with a high Froude number, but not infinite, in contrary to the case of a pure jet, where Froude number is infinite and superposition method can be applied via local momentum fluxes due to the conservation of momentum. In this case, the momentum PDE becomes also linear with respect of w^2 (Yannopoulos and Noutsopoulos, 2006b; Yannopoulos, 2010).

4 CONCLUSIONS

From the results of the present work, it can be concluded that self-similarity holds in the plume groups, independent from the number of plumes and the type of group formation. The divergence of the mean kinetic energy flux with respect to the distance along the plume is conserved and has practically the same value for all the groups from 1 to infinite number of plumes, as well as for a two-dimensional (plane) plume. This finding inspired the application of the superposition method in obtaining the axial velocities of a group of plumes at predefined positions by adding the local kinetic energy fluxes of individual plumes. Linearity of kinetic energy PDE is revealed for plumes. The superposition method using the fluxes of kinetic energy is inappropriate to be used in groups of buoyant jets in the jet-like region of buoyancy.

 ©2017, IAHR. Used with permission / ISSN 1562-6865 (Online) - ISSN 1063-7710 (Print)

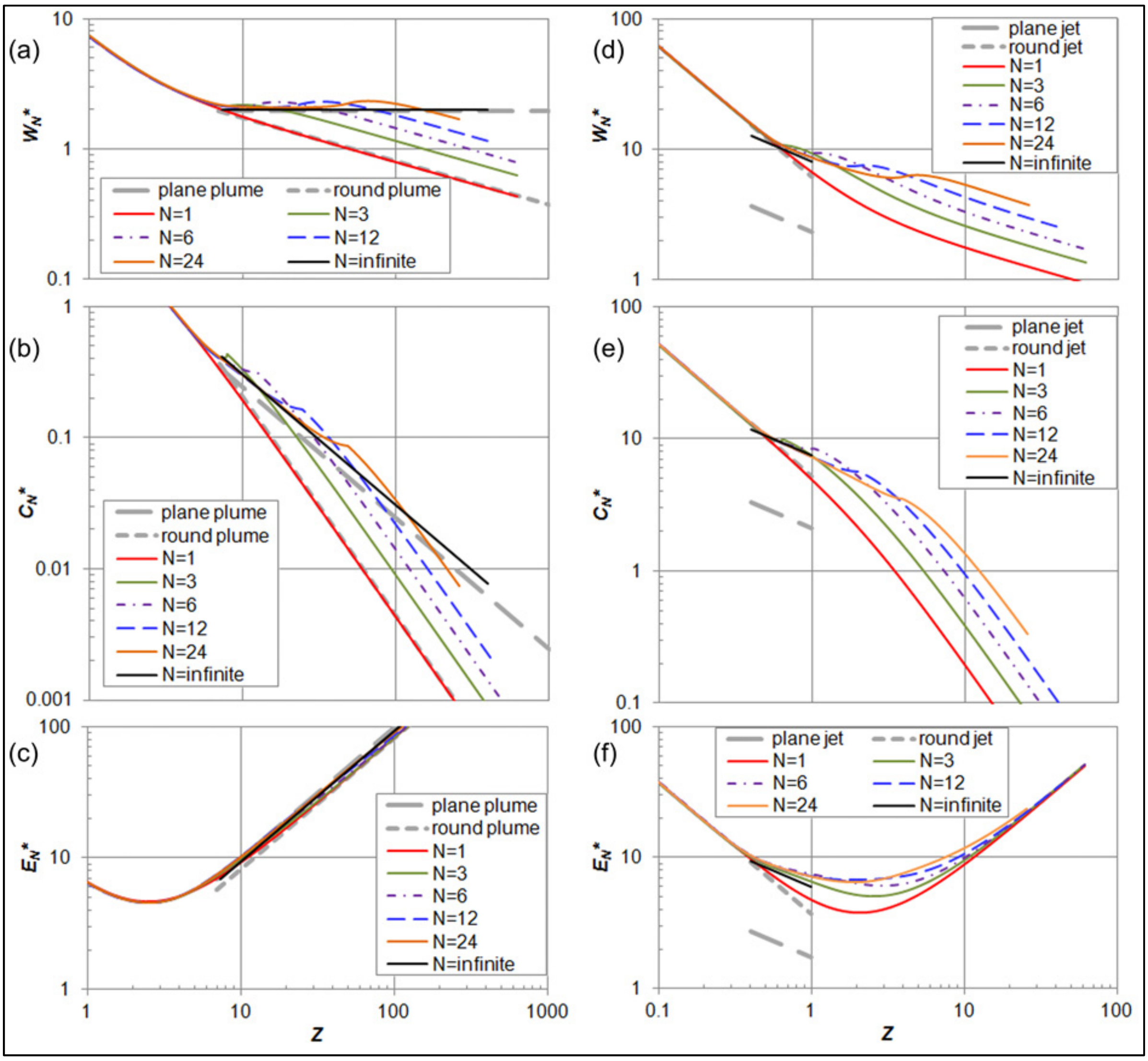

Figure 3. Normalized distributions along the main flow direction for linear groups; left column is the plume-like case (F_0=2.5); right column is the jet-like case (F_0=25): (a) and (d) mean axial velocity; (b) and (e) mean concentration; (c) and (f) mean kinetic energy flux.

REFERENCES

Bloutsos, A.A. & Yannopoulos, P.C. (2005). Three Round Turbulent Buoyant Jets Discharged Vertically from a Rosette. *IASME Transactions,* 2(3), 413-421.

Bloutsos, A.A. & Yannopoulos, P.C. (2009). Round Turbulent Buoyant Jets Discharged Vertically Upwards Forming a Regular Polygon. *Journal of Hydraulic Research,* 47(2), 263-274.

Lai, A.C.H. & Lee, J.H.W. (2012). Dynamic Interaction of Multiple Buoyant Jets. *Journal of Fluid Mechanics*, 708, 539–575.

Wang, H. & Law, A.W-K. (2002). Second-Order Integral Model for a Round Turbulent Buoyant Jet. *Journal of Fluid Mechanics,* 459, 397-428.

Yannopoulos, P.C. (1984). Interaction of Vertical Round Turbulent Buoyant Jets, *Ph.D. Dissertation*. Department of Civil Engineering, National Technical University of Athens, Athens, Greece. (in Greek)

Yannopoulos, P.C. (1996). Superposition Model for Multiple Plumes and Jets Predicting End Effects. *Journal of Geophysical Research,* 101, 15153-15176.

Yannopoulos, P.C. (2006). An Improved Integral Model for Plane and Round Turbulent Buoyant Jets. *Journal of Fluid Mechanics,* 547, 267-296.

Yannopoulos, P.C. & Noutsopoulos, G.C. (2006a). Interaction of Vertical Round Turbulent Buoyant Jets – Part I: Entrainment Restriction Approach. *Journal of Hydraulic Research,* 44(2), 218-232.

Yannopoulos, P.C. & Noutsopoulos, G.C. (2006b). Interaction of Vertical Round Turbulent Buoyant Jets – Part II: Superposition Method. *Journal of Hydraulic Research,* 44(2), 233-248.

Yannopoulos, P.C. (2010). Advanced Integral Model for Groups of Interacting Round Turbulent Buoyant Jets. *Environmental Fluid Mechanics*, 10(4), 415-450.

PREDICTION OF VERTICAL PROFILE OF STREAMWISE VELOCITY USING DOUBLE-AVERAGING METHOD

RAHMA YANDA[1], MORIHIRO HARADA[2] & ICHIRO TAMAGAWA[3]

[1] Dept. of Environmental and Renewable Energy System, Graduate School of Eng., Gifu University, Gifu, Japan,
u3815005@edu.gifu-u.jp
[2,3] River Basin Research Center, Gifu University, Gifu, Japan,
m-harada@green.gifu-u.ac.jp; tama@green.gifu-u.ac.jp

ABSTRACT

The vertical profile of streamwise velocity distribution is necessary information for sediment transport computation and aquatic habitat evaluation. However, predicting velocity distribution for hydraulically rough and low relative submergence is still challenging. In this study, we demonstrate a procedure as an approach for predicting the double-averaging (DA) vertical profile of streamwise velocity distribution for intermediate and low relative submergence condition based on a limited set of known parameters, such as flow discharge Q, bed slope or energy slope S, representative grain size diameter D_{84}, and channel width B. The procedure consists of two steps. First, the flow resistance prediction with variable-power equation (VPE) is used to calculate the depth-averaged parameters (mean flow depth h, depth-averaged velocity U and shear velocity u_*). Then, these parameters are used in the velocity distribution equation. The results of the measured parameters and predicted velocity profiles are compared using data measured from field and experimental flumes over cobble and gravel beds. On this basis, the mean flow depth, shear velocity, and depth averaged velocity are not found to be significantly different from those of the measurement data. In the bed elevation approach, it is not possible to obtain a good fit between the predicted and measured velocity profiles due to difficulties in representing the roughness height and standard deviation. However, the challenges of DA parameterization can be seen clearly on the relation with flow resistance. In addition, this approach may be a potential approach to describe the flow characteristics over rough beds instead of using turbulence or high cost numerical simulations.

Keywords: Double-averaging method (DAM); vertical distribution of streamwise velocity; low relative submergence.

1 INTRODUCTION

In river engineering, it is essential to understand the vertical profile of the streamwise velocity. The streamwise velocity determines the overall resistance to flow, which is necessary information for sediment transport computation and aquatic habitat evaluation. Shear velocity $\boldsymbol{u}_*$, which is one of parameters in flow resistance equations, is usually obtained through measured velocity distribution profile. In addition, the velocity measurements are made in the region for which the logarithmic distribution applies. However, when the bed condition is hydraulically rough and the relative submergence, i.e., the ratio of flow depth and roughness height, is low, the flow near the bed is spatially heterogeneous and three-dimensional. This condition may influence the flow over the whole depth and the vertical profile of the streamwise velocity may not always be logarithmic, especially the region near the bed (within the roughness layer) directly affected by bed roughness.

Double-averaging (DA) method is based on temporal and spatial averaging of the Navier-Stokes equation and recently applied in order to analyze the spatial heterogeneity of the time-averaged flow near the bed. Many research studies have been conducted in order to predict the DA velocity profile for intermediate and low relative submergence. They found that the logarithmic distribution still adequately describes vertical velocity distribution in the area above the roughness layer in gravel-bed flows (Dittrich and Koll, 1997; Franca et al., 2008). In studies investigating spherical-segment bed flows (Nikora et al., 2001), gravel-bed flows (McLean and Nikora, 2006) and glass-bead-bed flows (Shimizu et al., 1990), researchers also found that the double-averaging vertical profile of streamwise velocity over a two-dimensional (2D) bed forms a consistently linear distribution in the region near the bed and logarithmic region above it. Another researcher found that the exponential behavior strengthens with an increase in relative submergence within the roughness layer (Nikora et al., 2004a). Furthermore, Ferreira (2008) experimented with changes in the bed topography by adding sand to coarse-gravel beds and found that there were two linear (or double-linear) distributions of DA vertical profile of the streamwise velocity with different slopes within the interfacial and form-induced sublayers. These imply that the relative submergence and roughness geometry can influence the velocity profile forms near the bed.

Although the shape of DA vertical profile of the streamwise velocity for intermediate and low relative submergence flow have been suggested, however, there are still some unresolved issues in the

 ©2017, IAHR. Used with permission / ISSN 1562-6865 (Online) - ISSN 1063-7710 (Print)

parameterization of DA velocity profile for rough and low relative submergence. For example, Franca et al. (2008) found that even the logarithmic flow may well describe the velocity profile in the central depth region, the von Karman constant, which is universal and equal to 0.4, does not exist. Aberle et al. (2008) investigated that the upper limit of roughness layer (in other words, the lower limit of logarithmic layer) could not be identified due to a gradual increase of form induced stress toward the top of the roughness. In addition to the difficulties in determining the lower limit of the logarithmic layer, it was also challenging to determine the reference bed and the thickness of the roughness.

The present study intends (1) to clarify several issues related to the parameterization of double-averaging (DA) vertical velocity profiles, and (2) to demonstrate an approach for DA vertical profile of the streamwise velocity prediction through flow resistance equation for intermediate and low relative submergence conditions over rough bed (such as gravel- or cobble-bed). In the following sections, we first present the details of several past studies about the flow parameters for the roughness and logarithmic layers from the point of view of the DA framework, and also about the flow resistance equation. Second, we propose a procedure to predict the DA vertical profile of streamwise velocity distribution from generally known parameters obtained by the flow resistance equation. Then, these parameters performance are tested for the velocity distribution equations in DA framework. Finally, we outline the difficulties encountered in the parameterization of the procedure.

2 PAST RESEARCHES

2.1 Roughness layer

2.1.1 Interfacial sublayer

The roughness layer consists of interfacial sublayer and form-induced sublayer. The interfacial sublayer extends from the roughness trough $z_t$to the crest or top z_c (Figure 1) and is directly influenced by individual roughness elements. To parameterize the velocity distribution in the interfacial sublayer, Nikora et al. (2001) assumed that the flow dynamics below the roughness tops was primarily caused by the wake turbulence, which could be parameterized by the bed shear stress and constant eddy viscosity. These assumptions lead to the following linear velocity distribution,

$$\frac{\langle\bar{u}\rangle}{u_*} = C\frac{Z}{\delta} \text{ for } 0 \leq Z \leq \delta \qquad [1]$$

where $\langle\bar{u}\rangle$ is DA velocity, C is constant, where $C = \langle\bar{u}\rangle(\delta)/u_*$, and it should depend on the roughness geometry, $\delta \approx z_c - d_p$ is lower bound of the logarithmic layer in the displaced coordinate system (or the thickness of boundary layer), u_* is shear velocity, $Z = \mathrm{z} - z_t$ and d_p is the displacement height. Furthermore, Nikora et al. (2004) proposed linear distribution model (Eq. (2)) and an exponential distribution model (Eq. (3)) for interfacial sublayer region. They found that linear DA velocity shows exponential behavior as the relative submergence H_m/Δ increases, where H_m is the maximum flow depth, and Δ is the roughness height (Figure 2).

$$\frac{\langle\bar{u}\rangle(z) - \langle\bar{u}\rangle(z_c)}{u_*} = \frac{(z - z_c)}{l_c} \qquad [2]$$

$$\langle\bar{u}\rangle(z) = \langle\bar{u}\rangle(z_c) exp\beta(z - z_c) \qquad [3]$$

where $\langle\bar{u}\rangle(z_c)$ is DA velocity at the roughness crest, $l_c = \langle\bar{u}\rangle(z_c)/(d\langle\bar{u}\rangle/dz)_{z_c}$ is scale characterizing flow dynamics below the roughness crest and β is parameter.

The spatial heterogeneity of bed roughness makes it difficult to determine the roughness crest. Many researchers have suggested the use of z_{99}, which is 99% of observed bed elevations are smaller, as representative of bed crest (Aberle et al., 2008; Nikora et al., 2007b) for rough and irregular beds. This parameter has been chosen to minimize the influence of topography measurement errors and local effects due to the random nature of the beds. The roughness crest z_c is an important parameter when predicting the DA vertical profile of streamwise velocity distribution because the linearity of DA velocity disappears in the region above the roughness crest (Mclean and Nikora, 2006). In addition, the displacement height d_p is another important parameter to predict velocity profile within this layer.

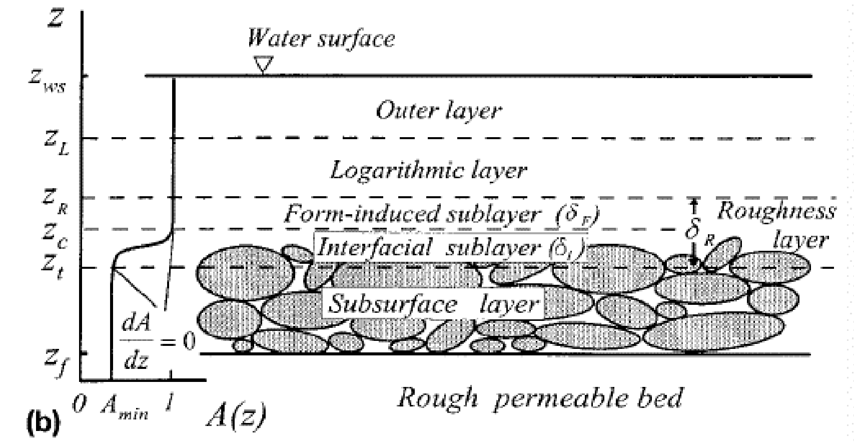

Figure 1. Flow subdivision for rough permeable bed.

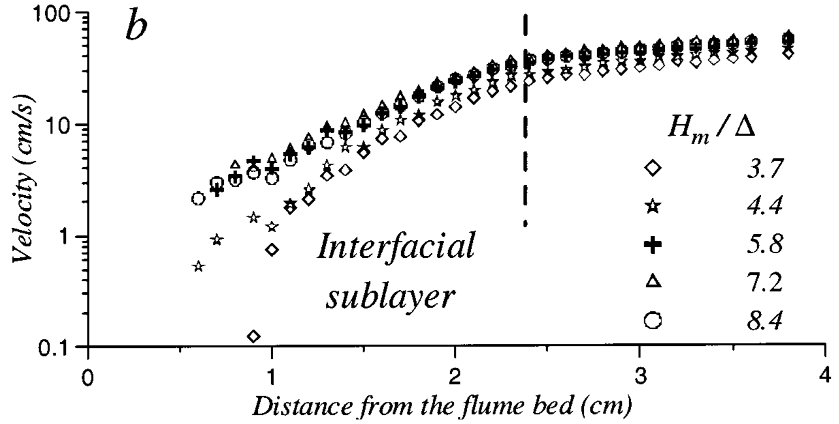

Figure 2. The influence of flow submergence on the velocity profile.

2.1.2 Form-induced sublayer

The flow in the form-induced sublayer is influenced by the individual roughness elements that affect the region just above the roughness crest (Nikora et al., 2001). According to Raupach et al. (1991), the roughness elements may influence the local flow structure within $0 < z - z_c < (1 - 4)\,\delta$, i.e., the thickness of form induced sublayer, $\delta_F = z_R - z_c$ (Figure 1) may be up to (1- 4) δ, where z_R is the lower limit of logarithmic layer. The upper limit of the form-induced layer is difficult to determine. Many studies assume that the potential transition effects in the form-induced sublayer can be neglected when making an approximation of the DA vertical velocity profile, and this assumption is supported by McLean and Nikora (2006) who found that the logarithmic region disappears when the water level approaches the roughness crest and the entire vertical profile of the streamwise velocity distribution becomes linear. Aberle et al. (2008) analyzed the spatial flow heterogeneity in terms of the form-induced stress over rough gravel beds for shallow flows. They stated that the upper limit for the roughness layer (or the upper limit of form-induced sublayer) could not be identified due to the gradual increase of form-induced stresses towards the roughness crests.

2.2 Logarithmic layer

McLean and Nikora (2006) concluded that the DA vertical profile of the streamwise velocity for flow over 2D bed forms consists of linear near-bed region and logarithmic region above. The equation used to represent the logarithmic distribution of the DA vertical velocity is similar to that of the log-law equation for smooth beds, except that some parameters are redefined. Nikora et al. (2002b) considered the following logarithmic parameterization of the logarithmic profile,

$$\frac{\langle\bar{u}\rangle(z)}{u_*} = \frac{1}{\kappa} ln\left(\frac{z - d_p}{z_R - d_p}\right) + \frac{\langle\overline{u_R}\rangle}{u_*} \qquad [4]$$

where $\langle\overline{u_R}\rangle$ is the double-averaging velocity at the integration level $z = z_R$. The plane defined by $z = d_p$ is situated somewhere between the top of the roughness layer and the roughness troughs. The zero-plane displacement d_p as the origin of the logarithmic profile is redefined as the position where large scale eddies "feel" the river bed (Nikora et al., 2002b).

 ©2017, IAHR. Used with permission / ISSN 1562-6865 (Online) - ISSN 1063-7710 (Print)

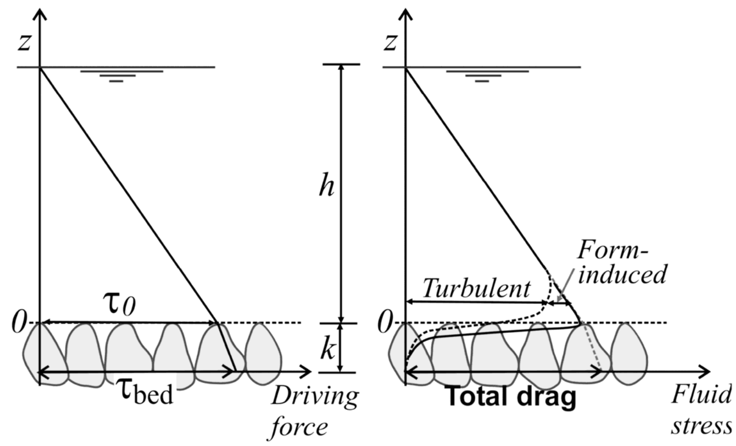

Figure 3. Momentum balance in 2D rough bed flow

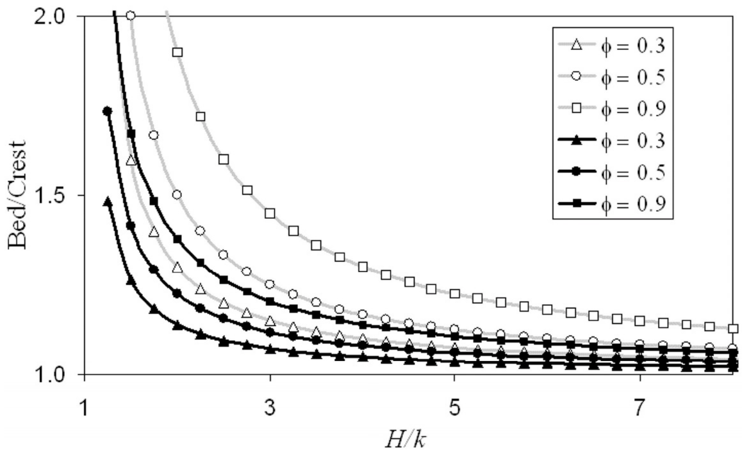

Figure 4. Ratio between the bed shear stress and the shear stress at roughness crest (white symbols) and between the corresponding shear velocities (black symbols), for a range of relative submergences H/k and 3 different porosities ϕ

In classical approach, the assumption that u_* is an equivalent way of expressing the bed shear stress is widely used in the open channel flows. Pockrajac et al. (2006) evaluated the shear velocity that is suitable for use as the universal velocity scale for flows over rough beds, and found that the shear velocity calculated by using the total fluid shear stress τ_0 (Eq. (5)) at the roughness crest (at $z = 0$ in Figure 3) can be significantly different from that calculated using the bed shear stress τ_{bed} (Eq. (6)), as can be seen from Figure 4, where ρ is the water density, g is the accelerated gravity, h is the mean flow depth, S is the bed or energy slope, ϕ is porosity of the rough bed, and k is the characteristic roughness height.

$$\tau_0 = \rho g h S \qquad [5]$$

$$\tau_{bed} = \rho g h\,(S + \phi k) \qquad [6]$$

Furthermore, they also showed that the shear velocity evaluated using the bed shear stress is over-estimated by the factor shown in Figure 4, so the κ is also over-estimated by the same factor. The zero-displacement for rough bed is also one of the parameters that is still difficult to define. Nikora et al. (2002b) found that d_p is typically located between roughness crest and trough, and tends to move towards the troughs for more energetic and sparse roughness elements. It is usually determined from a given data set of velocity gradients.

2.3 Flow resistance for gravel-bed rivers

For rough and low relative submergence flow conditions, the flow that is strongly affected by relatively large bed elements. Moreover, research into methods for generalizing DA velocity distributions are ongoing and modeling the flow resistance remains challenging because simple flow resistance equations often do not provide precise and reliable predictions of the mean velocity. In addition, mean flow depth measurements can be complicated and it may be difficult to determine the mean flow depth due to irregular bed topographies and water surfaces in rough stream conditions.

The flow discharge measurement is usually much more accurate than the flow depth measurement method. The use of non-dimensional hydraulic geometry equations has been suggested to link the mean

©2017, IAHR. Used with permission / ISSN 1562-6865 (Online) - ISSN 1063-7710 (Print)

velocity to the flow discharge (Rickenmann, 1990; Aberle and Smart, 2003; Ferguson, 2007). Rickenmann and Recking (2011) suggested the use of U^{**} and q^{**}, the non-dimensional hydraulic geometry equations (Eq. (7)), to link the mean velocity to the flow discharge, as has been proposed in many studies. These dimensionless variables were found to be useful when considering the limitations related to the development of a q-based approach at very low relative depths if the true average bed level for zero flow depth is not precisely known in the presence of large grains.

$$q^{**} = \frac{q}{\sqrt{gI_e D_{84}^3}}, U^{**} = \frac{U}{\sqrt{gI_e D_{84}}} \quad [7]$$

To determine the flow resistance equation that is suitable for both shallow and deep flows over rough river beds, Rickerman and Recking (2011) tested a large data set covering a wide range of bed slopes, grain diameters, flow discharges, and river widths. Their purpose was to evaluate the performance of several resistance equations (i.e., Manning-Strickler, Keulegan, Hey, Bathurst, Smart and Jaeggi, and Ferguson flow resistance equations). They found that flow resistance predicted by variable-power equation (VPE) (Eqs. (8) and (9)) by Ferguson (2007) exhibits the best performance for intermediate- and low-relative submergence, where D_{84} is representative grain size diameter, a_1 = 6.5 and a_2 = 2.5 are the calibrated parameter values suggested by Ferguson (2007), S is the bed or energy slope, q is the flow discharge per unit width of the channel, and U is the mean flow velocity. The VPE is an equation that considers the logarithmic velocity profile and deviations within the roughness layer. This equation is asymptotic to the Manning-Strickler (MS) and Roughness layer (RL) and provides a single resistance equation that is applicable to both the shallow and deep flows over coarse river beds.

$$a_1^2 {U^{**}}^5 + a_2^2 {U^{**}}^{10/3} {q^{**}}^{5/3} = a_1^2 a_2^2 {q^{**}}^3 \quad [8]$$

$$\sqrt{\frac{8}{f}} = \frac{U}{u*} = \frac{a_1 a_2 \left(\frac{h}{D_{84}}\right)}{\sqrt{a_1^2 + a_2^2 (h/D_{84})^{5/3}}} \quad [9]$$

In this section, some general assumptions related to the parameterization of DA vertical profile of the streamwise velocity and its distribution equations for intermediate or low relative submergence, especially for rough streams conditions, are presented. Furthermore, equations that can potentially be used to predict flow resistance in intermediate or low relative submergence have been explained. In the next section, an approach to predict the vertical profile of streamwise velocity distribution based on the flow resistance equation is presented.

3. APPROACH TO PREDICT DA VERTICAL PROFILE OF STREAMWISE VELOCITY

3.1 Outline of the procedure

The procedure for predicting the DA vertical profile of streamwise velocity distribution is as follows. First, the depth-averaged parameters, such as the flow depth h, shear velocity u_*, and depth-averaged velocity U are calculated from several known parameters (i.e., Q, D_{84}, B, and S) using the dimensionless equations (Eq. (7)) and Ferguson's flow resistance equation (Eqs. (8) and (9)). Second, the calculated parameters are used in velocity distribution equations. Then, the predicted velocity profile is compared to the field and experimental measurement data.

3.2 Data

To test the performance of the proposed approach, field measurement data from Venoge and Chamberonne River gathered by Franca et al. (2008) and the measurement data in experimental flumes gathered by Yanda et al. (2016) and Olsen and Koll (2010) were used. These data sets were obtained from gravel-armored layer and cobble beds. The detail measurement can be seen in Table.1. These data sets are within the intermediate relative submergence ($1.2 < h/D_{84} < 4$) and are also categorized as flow type III, which consist of a subsurface layer (if applicable), a roughness layer, and an upper flow region (Nikora et al. 2004).

In the table and the remainder of this paper, the data obtained from the Venoge, Chamberonne, Case A (Yanda et al., 2016) and gravel bed of Olsen and Koll experiment are referred to as Case I, II, III, and IV, respectively.

 ©2017, IAHR. Used with permission / ISSN 1562-6865 (Online) - ISSN 1063-7710 (Print)

Table 1. Data sources (measured parameters)

case	S	Q (m^3/s)	h (m)	B (m)	U (m/s)	u_*(m/s)	D_{84} (m)	z_m (m)
I	0.0033	0.800	0.21	6.30	0.605	0.078	0.074	0.024
II	0.0026	0.550	0.29	5.75	0.330	0.085	0.080	0.069
III	0.0103	0.065	0.19	0.50	0.674	0.098	0.118	0.080
IV	0.0270	0.091	0.17	0.90	0.582	0.214	0.044	0.040

3.3 Procedure for the flow resistance calculation

In the field, parameters such as Q, S, B and D_{84} are usually considered to be generally known. However, in rough stream conditions, the flow depth is difficult to determine due to the irregularity of bed topography and water surface. Consequently, the flow depth is considered to be an unknown parameter in this procedure. The non-dimensional hydraulic geometry in Eqs. (7) and (8) is used to iteratively calculate depth-averaged velocity U. Then, the mean flow depth h can be obtained from the continuity equation $Q = UBh$. The shear velocity can be calculated using the Ferguson flow resistance (Eq. (9)). The results of these calculations are shown in Table 2. A *T*-test is used to compare measured and calculated results.

3.4 Procedure for predicting the DA vertical profile of the streamwise velocity

Within the interfacial sublayer and logarithmic layer, the velocity distributions can be expressed as follows:

$$\frac{\langle\bar{u}\rangle}{u_*} = \frac{1}{\kappa}\ln\left[\frac{Z}{\delta}\right] + C \quad \text{for} \quad (z_L - z_t) \geq Z \geq \delta \qquad [10]$$

$$\frac{\langle\bar{u}\rangle}{u_*} = \mathrm{C}\frac{Z}{\delta} \quad \text{for} \quad 0 \leq \mathrm{Z} \leq \delta \qquad [11]$$

where z_L is the upper boundary of the logarithmic layer. Here, the z_t is assumed as the origin of logarithmic profile d_p type 3 (Nikora et al., 2002b). The calculated depth-averaged parameters are used in velocity distribution equations to predict velocity profiles. To accomplish that, information about the bed height (i.e., z_c and z_t) is required as a limit for employing Eqs. (10) and (11). However, the detailed bed elevation data is assumed to be unavailable in the procedure. Hence, the relationship between the representative grain size D_x and the standard deviation of the bed elevation σ_z is used, as was suggested by Coleman et al. (2011), where $D_{84} = 4.46\sigma_z$. It is then referred to as calculated bed elevation σ_z cal. The σ_z meas was obtained from measurement of bed elevation and is used for comparison with σ_z cal. Both σ_z cal and σ_z meas are used to determine z_c and z_t, where $z_c = z_m + \sigma_z$ and $z_t = z_m - \sigma_z$.

The constant parameter $C \approx 5.3$ (Dittrich and Koll, 1997) and $\kappa = 0.4$ were used in this procedure. In addition, the von-Karman constant value obtained from each measured velocity data κ_{meas} using Eq. (12) (Franca et al., 2008) were also used for comparison.

$$\kappa\frac{\langle\bar{u}\rangle(z) - \langle\overline{u_R}\rangle}{u_*} = ln\left(\frac{z - z_t}{z_R - z_t}\right) \qquad [12]$$

For DA velocity distribution profile prediction, Nikora et al. (2001) approximation is followed, where the roughness effect in the form induced sublayer is neglected. It leads to the assumption that the thickness of roughness layer equals to the thickness of induced sublayer $\delta_{Roughness\ layer} \approx \delta_{Induced\ sublayer} = \delta$, where $\delta = z_c - z_t$.

4. RESULTS AND DISCUSSIONS

4.1 Flow resistance

In the previous section, we presented an approach to predict the DA vertical profile of the streamwise velocity with limited set of known parameters (i.e., Q, S, B and D_{84}). The prediction was started by obtaining the parameters for velocity distribution equations from Eqs (7), (8) and (9). The flow resistance prediction with variable-power equation (VPE) was considered because it is a function asymptotic to the Manning-Strickler equation and represents the linear resistance relationship within the roughness layer. Furthermore, flow resistance can be calculated based on limited information about the streams topography with this equation. From Table. 2, there were some variations between the calculated parameters h_{cal}, u_{*cal}, U_{cal} and the measurement data. It arises because of the use of D_{84}, as known that it cannot describe the bed features especially in close packed bed arrangement (Coleman et al., 2011; Yanda et al., 2016). Moreover, the mean flow depth is usually obtained based on mean bed height information, not based on D_{84}. Even so, the variation of calculated parameters were statistically (for significant level 0.05) not significantly different from the measured values. It confirms the statement that q-based equation (Eq. (7)) for predicting the velocity is more robust and causes fewer errors in the input variables compared to those for the h-based equation (Ferguson, 2007; Comiti et al., 2009; Zimmerman, 2010).

Table 2. Calculated parameters

case	q (m^2/s)	q^{**}	U^{**}	U_{cal} (m/s)	h_{cal} (m/s)	u_{*cal} (m/s)
I	0.127	35.08	10.51	0.51	0.25	0.089
II	0.096	16.93	7.15	0.37	0.26	0.081
III	0.131	10.16	5.402	0.59	0.22	0.150
IV	0.101	21.20	8.07	0.87	0.12	0.175

4.2 Parameterization of the DA vertical velocity profile

For the proposed procedure, the parameters (i.e., h_{cal} , u_{*cal} , U_{cal}) were applied into the velocity distribution equations (Eqs. (10) and (11)). The linear and logarithmic distributions equations were limited by roughness height δ calculated using σ_z. The difference between σ_z *cal* and σ_z *meas* (Table. 3) was found to not significantly different (for significance level 0.05).

Table 3. Bed height

case	κ_{meas}	z_c	σ_z from measured data				σ_z calculated (Coleman et al, 2011)			
			σ_z meas (m)	z_c (m)	z_t(m)	δ (m)	σ_z cal (m)	z_c (m)	z_t (m)	δ (m)
I	0.19	0.08	0.020	0.044	0.004	0.040	0.017	0.041	0.007	0.033
II	0.33	0.14	0.033	0.102	0.036	0.066	0.018	0.087	0.051	0.036
III	0.29	0.14	0.028	0.109	0.053	0.056	0.026	0.107	0.054	0.053
IV	0.55	0.08	0.008	0.048	0.032	0.016	0.01	0.050	0.030	0.020

In Figure 5, the predicted and measured DA vertical profile of the streamwise velocity are presented. The predicted velocity profiles were obtained by trying several different parameters such as σ_z *cal,* σ_z *meas,* universal κ value, and κ from measurement data. We found the predicted velocity profiles that showed a good match with measured profiles if the κ from measurement data was used for Case I, but not for Cases II, III, and IV. Moreover, for Case II, III, and IV, the linear and logarithmic velocity profiles could not connect. These discrepancies can be caused by several reasons. First, the approach of using the standard deviation of the bed elevation σ_z to represents the height δ for the surface roughness. In Cases II, II, and IV, the real roughness height of each might be larger than the value obtained by our calculation. For Case I, the roughness height represented by σ_z showed its similarity with the roughness height obtained from measured velocity profile, where $\delta = z_R - d_p$ (details in Franca et al., 2008). Furthermore, in this procedure, we assumed that the roughness layer is in the same height of the roughness crest. As can be seen form Figure 5, the roughness crest z_c from σ_z calculation was found fairly far from the value obtained by measurement of bed elevation (showed by the horizontal black line) for all cases. In the real case, the bed roughness can still affect the flow above the roughness crest (Nikora et al., 2001), for example in Cases II and III.

Another reason is the value of von-Karman constant κ. Findings about the κ value equals to 0.41 is difficult to be found for intermediate and low relative submergence have been known (Franca et al., 2008; Pokrajac et al., 2006), the predicted velocity profile by using κ from measurement data could not help in this procedure. It was possibly caused by the difficulty to detect the constant κ value region. In addition, related to κ, the choice of universal shear velocity definition can affect κ value especially for shallow streams (Pokrajac et al., 2006).

The shear velocity u_* from measured data and flow resistance equation, according to Pokrajac et al. (2006), is based on the shear stress at the level of roughness crest (see Figure 3). In this procedure, because it will be used as one of key parameters to predict the velocity profile started from the roughness crest to the water surface, uncertainty of the shear velocity definitions can be significant.

 ©2017, IAHR. Used with permission / ISSN 1562-6865 (Online) - ISSN 1063-7710 (Print)

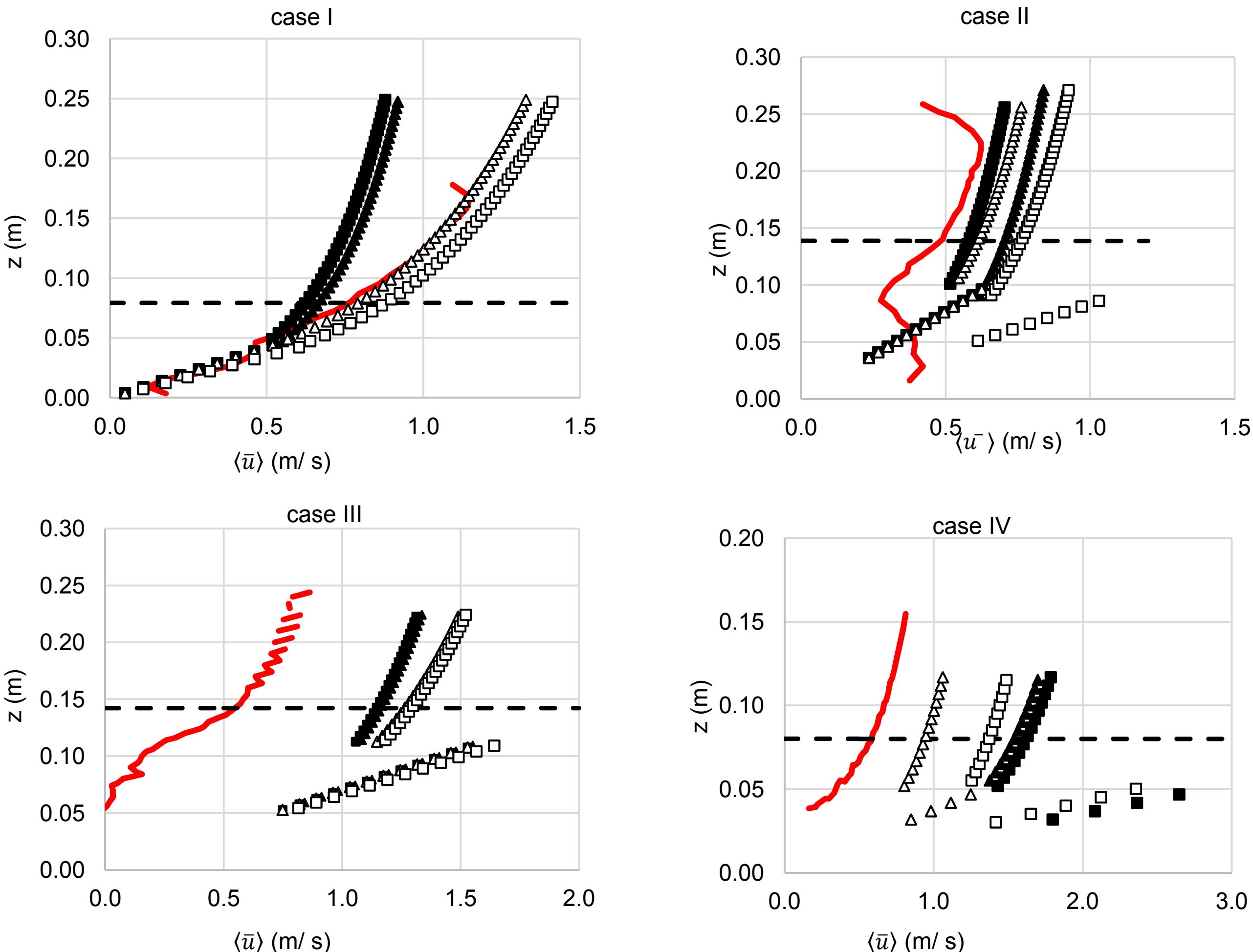

Figure 5. The measured and predicted DA vertical profile of streamwise velocity distribution. The red line is the measured velocity, the black horizontal line is the bed roughness crest z_c. The lines with black squares represent κ=0.4, C=5.3, $\sigma_z meas$; the lines with black triangles represent κ =0.4, C=5.3, $\sigma_z calc$; the lines with white squares represent κ from measured velocity, C=5.3, $\sigma_z calc$; and the lines with white triangles represent κ from measured velocity, C=5.3, $\sigma_z meas$.

From the procedure, we also found that another constant value C has possibility for the cause of discrepancies. The C value can be ranged from 5.3 - 6.0, which is probably due to differences in the roughness geometry (Nikora et al., 2001). Based on Figure 5, there is possibility that the value of C should be smaller than 5.3 as we used in this procedure. Mohajeri et al. (2015) also found that the C value can be smaller than 5.3 and depend on the relative submergence.

5 CONCLUSIONS

This paper proposes an approach for predicting the DA vertical profile of the streamwise velocity for intermediate or low relative submergence conditions based on a limited set of known parameters, such as Q, S, D_{84}, and B. The procedure consists of two steps. First, the flow resistance prediction with variable-power equation (VPE) is used to calculate the depth-averaged parameters h, U, and u_*. Then, these values are used in the velocity distribution equation. The calculated parameters and predicted profiles were then compared with measurement data. From the results show that the parameters $h_{cal}, u_{*cal}, U_{cal}$ calculated by using VPE are not statistically different from the measured values. However, the predicted velocity profiles were not a perfect match for the measured profiles. This is due to the difficulty in representing the roughness height, even though we attempted the approach of using the standard deviation of the bed elevation σ_z. Furthermore, the use of κ = 0.4 and C = 5.3 were found to be unsuitable and had varying values.

Although the results of this procedure were not a good fit for the measured velocity profiles, the challenges in DA parameterization can be clearly seen through this procedure. An area of further study identified in this research is to investigate the suitable definition of shear velocity used for flow resistance equation, so it can be reliable to be applied for DA velocity profile prediction for intermediate and low relative submergence. Moreover, study about the effect of relative submergence and bed geometries to the changes of roughness height and the constants (κ and C) is needed. This approach is expected to be useful for describing the flow characteristics over rough beds, especially with spatially heterogeneous and three-dimensional flows near the bed, as an alternative to using turbulence or high cost numerical simulations.

ACKNOWLEDGEMENTS

The research reported herein is partly supported by JSPS KAKENHI grand Number 16K2107403.

REFERENCES

Aberle, J. & G. M. Smart (2003). The Influence of Roughness Structure on Flow Resistance on Steep Slopes. *Journal of Hydraulic Research*, 41(3), 259–269.

Aberle, J., Koll, K. & Dittrich, A. (2008). Form induced stresses over rough gravel-beds. *Acta Geophysica*, 56(3), 584-600.

Bayazit, M. (1976). Free Surface Flow in a Channel of Large Relative Roughness. *Journal of Hydraulic Research*, 14, 115–126.

Coleman, S. E., Nikora, V. I. & Aberle, J. (2011). Interpretation of Alluvial Beds through Bed-Elevation Distribution Moments. *Water Resources Research*, 47(11), 1-14.

Comiti, F., D. Cadol. & E. Wohl. (2009). Flow Regimes, Bed Morphology and Flow Resistance in Self-Formed Step-Pool Channels. *Water Resource Research,* 45(4*)*, 1-18.

Dittrich, A. & Koll, K. (1997). Velocity Field and Resistance of Flow over Rough Surface with Large and Small Relative Submergence. *International Journal of Sediment Research*, 12(3), 21-33.

Ferguson, R. (2007). Flow Resistance Equations for Gravel and Boulder Bed Streams. *Water Resource Research*, 43, W05427, 1–12.

Ferreira, L. (2008). Impact of Sediment Overfeeding in Gravel-Bedded River's Salmonid Habitats, *MSc Thesis*. Instituto Superior Tecnico. Universidade Tecnica de Lisboa. Lisbon.

Franca, M. J., R. M. Ferreira. & U. Lemmin. (2008). Parameterization of the Logarithmic Layer of Double-Averaged Streamwise Velocity Profiles in Gravel-Bed River Flows. *Advances in Water Resources*, 31(6), 915 -925.

Katul, G., Wiberg, P., Albertson, J. & Hornberger, G. (2002). A Mixing Layer Theory for Flow Resistance in Shallow Streams. *Water Resource Research*, 38(11), 1250.

McLean, S. & V.I. Nikora. (2006). Characteristics of Turbulent Unidirectional Flow over Rough Beds: Double-Averaging Perspective with Particular Focus on Sand Dunes and Gravel Beds. *Water Resource Research,* 42(5), 1-11.

Mohajeri, S. H., S. Grizzi, M. Righetti, G.P. Romano. & V. Nikora. (2015). The Structure of Gravel-Bed Flow with Intermediate Submergence: A Laboratory Study. *Water Resource Research*, 51, 1-24.

Nikora, V., Goring, D., McEwan, I. & Griffiths, G. (2001). Spatially Averaged Open Channel Flow over Rough Bed. *Journal of Hydraulic Engineering*, 127(2), 123–133.

Nikora, V., Koll, K., McLean, S., Dittrich, A. & Aberle, J. (2002b). Zero-Plane Displacement for Rough-Bed Open-Channel Flows*. Proceeding of International Conference on Fluvial Hydraulics*, Vol. 1, 83–92.

Nikora, V., Koll, K., McEwan, I., McLean, S. & Dittrich, A. (2004a). Velocity Distribution in the Roughness Layer of Rough-Bed Flows. *Journal of Hydraulic. Engineering,* 130(10), 1036–1042.

Nikora, V., McLean, S., Coleman, S., Pokrajac, D., McEwan, I., Campbell, L., Aberle, J., Clunie, D. & Koll, K. (2007b). Double-Averaging Concept for Rough-Bed Open Channel and Overland Flows: Applications, *Journal of. Hydraulic Engineering*. ASCE, 133(8), 884-895.

Olsen, N. R. B., Aberle, J. & Koll, Ka. (2010). Resolving Large Bed Roughness Elements with an Unstructured Hexahedral Grid. *River Flow 2010* (ed. Dittrich, Koll, & Geisenhainer), 377-383.

Pokrajac, D., Finnigan, J. J., Manes, C., McEwan, I. & Nikora, V. (2006). *On the Definition of Shear Velocity in Rough Bed Open Channel Flows*. River Flow 2006 (ed. R. Ferreiara, E. Alves, J. Leal & A. Cardoso). 132.

Raupach, M. R., Antonia, R. A. & Rajagopalan, S. (1991). Rough- Wall Turbulent Boundary Layers. *Applied Mechanics Reviews*, 44(1), 1–25.

Rickenmann, D. (1990). Bedload Transport Capacity of Slurry Flows at Steep Slopes, *PhD Thesis*, Zurich, Switzerland. Volume 103, 249.

Rickenmann, D. & Recking, A. (2011). Evaluation of Flow Resistance in Gravel-Bed Rivers through a Large Data Set. *Water Resource Research*, 47, 1-22.

Shimizu Y., Tsujimoto T. & Nakagawa H. (1990). Experiment and Macroscopic Modelling of Flow in Highly Permeable Porous Medium under Free-Surface Flow. *Hydroscience and Hydraulic. Engineering*, 8, 69–78.

Yanda, R., Harada, M. & Tamagawa, I. (2016). The Effects of Sediment Supply on Hydraulic Characteristics of Flow over the Imbricated Cobbles. *Journal of Japan Society of Civil Engineers*, Ser. B1 (Hydraulic engineering), 72(4), 613-618.

Zimmermann, A. (2010). Flow Resistance in Steep Streams: An Experimental Study, *Water Resource Research*, 46(9), 1-18.

 ©2017, IAHR. Used with permission / ISSN 1562-6865 (Online) - ISSN 1063-7710 (Print)

EXPERIMENTAL STUDY ON IMPACTS OF HYDRODYNAMIC CONDITION ON GROWTH OF MICROCYSTIS AERUGINOSA

YANG SONG[1], LINGLEI ZHANG[2], JIA LI[3], MIN CHEN[4] & YAOWEN ZHANG[5]

[1,2,3,4,5] State Key Laboratory of Hydraulics and Mountain River Engineering, College of Water Resource & Hydropower, Sichuan University, Chengdu 610065, PR China,

sy.somnous.vip@qq.com; zhanglinglei@hotmail.com

ABSTRACT

The eutrophication and algal bloom in reservoir are sensitive to hydrodynamic condition. However, the relationship between hydrodynamic force and algae growth is not fully studied as an investigation mechanism. Focused on Microcystis aeruginosa which is frequently reported, widely spreading, strongly toxic and dominant species of algae-bloom in reservoirs, this study carries out a series of laboratory experiments to explore the responses of the algae to different hydrodynamic conditions created by the self-dependent hydraulic rotating device. During 90 days experimental period, the results indicates that: (1) M. aeruginosa treated with different representative flow velocities (0-0.5 m/s) shows significant differences in growth changes: the control (0m/s) group growth is slower than the dynamic groups with an exception of the one with the velocity of 0.5m/s and scanning electron microscopic (SEM) of the algae under 0.5 m/s proves that strong fluid shearing action could damage cell surface and disrupt their internal metabolism. Thus the hydrodynamic threshold system (covering flow velocity, turbulent dissipation, sheer stress) are established. (2) The changing of TN and TP demonstrated that a certain rage of hydrodynamic conditions could promote nutrient absorption in algal cells, the pH of the water tended to be weakly alkaline accompanied by algae growing and DO concentration under control fluctuated obviously (3) The results of enzyme activity (SOD, CAT, POD, AKP, ATP) detection showed that appropriate hydrodynamic conditions could enhance photosynthesis, reduce the oxidation degree relative to control (0m/s). The outcome would help further reveal the basic rule and action mechanism of algal bloom development, and also provide a useful reference for the prediction and hydraulic control of M. aeruginosa bloom.

Keywords: Hydrodynamic condition; algal bloom; Microcystis Aeruginosa; growth; laboratory experiment.

1 INTRODUCTION

With the development of industry and agriculture, wastewater containing nutrients were continuously imported into water bodies and then caused eutrophication. As the main characteristic and consequence of eutrophication, harmful algal blooms (HABs) breaks the normal ecological balance of aquatic organisms and seriously pollutes water quality, which threatening the water security and economic development (Anderson et al., 2002). Particularly, HABs induced by eutrophication is more likely to happen when a natural river transformed into the river-type reservoir because risk of eutrophication increased. Moreover, when the hydropower station was completed, flow condition of reservoir changed significantly, for example lower flow velocity and water self-purification ability which tremendously aggravating algal bloom. Over the past decade, HABs have been reported frequently around the world such as Three Gorges Reservoir in China (Ji et al., 2016), Sau Reservoir in Spain (Vidal et al., 2012), Daechung Reservoir in Korea (Oh et al., 2007) and Lake Erie in North America (Watson et al., 2016). Hence, the trend of algal bloom shows frequency increasing, field extending and harm aggravating. Due to its serious ecological and societal consequences, algal bloom in reservoir should be better prevented and controlled immediately.

Many eutrophic reservoirs experienced cyanobacterial blooms, in which Microcystis aeruginosa was the most common and typical species (Visser et al., 2016). As a main toxin-producing algae, M. aeruginosa owned characteristics of widely distributing, rapidly reproducing and long blooming time (Catherine et al., 2013). More specifically, it can form a green and stinky floating membrane on the surface of water during the period of bloom. Furthermore, this floating membrane continuously produces stubborn algal toxins, which causes an extremely adverse effect on water resources, aquatic environment and industrial and agricultural development (Jacoby et al., 2011; Falconer et al., 1994). Thus, M. aeruginosa as a main toxin-producing alga is investigated by many researchers. Generally, hydrodynamic force, photo-thermal effect, nutrient are three controlling environmental conditions in the process of particular algal bloom (Heisler et al., 2008; Onderka et al., 2007). In previous studies, observations of toxic algal blooms are fragmented, descriptive and mainly focused on nutrients, light and climate like that algae density was high-positive correlation with the amount of nutrients, long-term changes in nutrient composition could be the reason of shifting in the

©2017, IAHR. Used with permission / ISSN 1562-6865 (Online) - ISSN 1063-7710 (Print)

phytoplankton community structure and creating a light-shading condition could significantly reduce algal population in water column (Shukla et al., 2008; Li et al., 2014; Chen et al., 2009). However, these methods or conclusions could hardly be used to prevent HABs in practice. Even for some rivers or reservoirs with nutrient concentrations usually at a high level for example Jialing River (Long et al., 2011) where hydrodynamic conditions could be the main limiting factor of the algae growth under appropriate climate conditions. As an independent controllable factor especially in reservoir, hydrodynamic influence on algal bloom is one of most emerging topic that is remained to be solved in the field of freshwater environmental research.

Currently, many researches have been aiming to understand the effects of hydrodynamic conditions of water bodies on algal growth and summarized out some useful results. Michele et al. (2007) concluded that reservoir characteristics including water depth and water volume are greatly affected by the type of algal bloom by studying algal blooms in seven subtropical reservoirs. King et al. (2014) reported hydrodynamic conditions could strongly control filamentous macroalgae and low flow velocities likely contribute to algal proliferation in Florida spring-fed rivers. Huang et al. (2015) found moderate hydrodynamic disturbance was beneficial for algal growth in Lake Tai because phosphorus from bed sediment was released more quickly while strong hydrodynamic disturbance could inhibit algal growth. Li et al. (2015) found the algal removal rate under hydrodynamic cavitation reached 88%, which was more effective than ultrasonic cavitation. Ji et al. (2016) thought algal bloom in Xiangxi Bay could be prevented by raising the water level of Three Gorges Reservoir. Among these investigations, discussion about combination of external characterization and internal responds of algae cells is still rare. Especially, hydrodynamic threshold for algal growth remains unclear. The long-period observation of hydrodynamics effect on algae growth also needs to be evaluated.

In this study, we systematically analyzed the algal growth by hydrodynamic treatment, examined the changing of water parameters in the outside medium, and explored the mechanism of antioxidant system and energy metabolism in algal cells. The goals were: (1) explore the influence of hydrodynamic condition on algal growth (2) established a hydrodynamic threshold system for M. aeruginosa (3) discuss the combination of external water quality parameters and underlying internal-mechanisms responsible for hydrodynamic effect in M. aeruginosa.

2 Materials and method

2.1 Algae growth and treatment conditions

M. aeruginosa were purchased from Freshwater Algae Culture Collection at the Institute of Hydrobiology in Wuhan, China. Before hydrodynamic treatment, the algae cells were cultivated at 26±2°C in axenic BG-11 medium with light intensity of 2000 Lux and a light photoperiod of 12 h for 1 week. After environment-adaptive growing, a suspension of algae (0.96L) was homogeneously divided and transferred into self-dependent hydraulic rotating apparatuses (0, 5, 8, 11, 14, 17 rad/s) with diluting to 10L . Algae grown at static environment (0 rad/s) served as controls. The real apparatus consisted of a rotating cylinder attached four blades mounted inside an outer organic glass cylinder with a diameter of 28 cm and a height of 35 cm (Fig. 1). As 680 nm is the maximal absorbance peak of M. aeruginosa (Liang et al., 2005), the algal density was estimated by spectrophotometer (TU-1901, Beijing Purkinje General Instrument Co., Ltd., China) at this wavelength. The initial concentration of algae controlled in this experiment was about 2.5 $\times 10^8$ cells/L, corresponding to OD_{680} = 0.075.

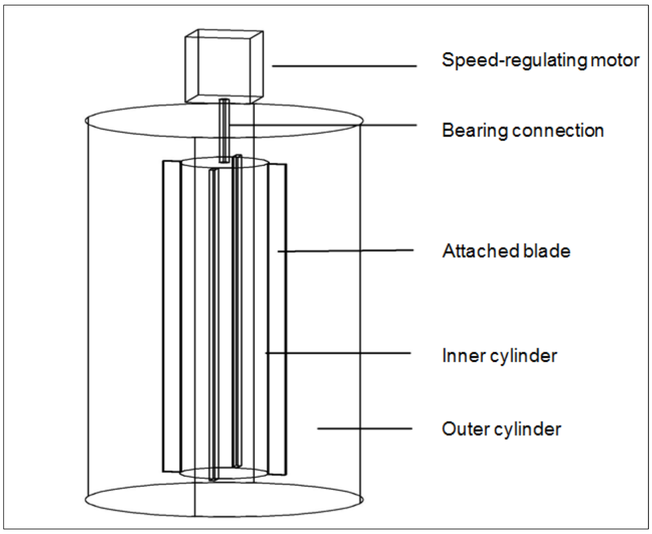

Figure 1. Schematic illustration of the experimental apparatus.

 ©2017, IAHR. Used with permission / ISSN 1562-6865 (Online) - ISSN 1063-7710 (Print)

2.2 Experimental design

The experiment was conducted for 90 days and algal sample of 100 ml was taken every six days after initiating hydrodynamic agitation. At each particular duration, the sample was immediately used for subsequent measurement and analysis. The concentration of chlorophyll (Chla), total nitrogen (TN) and total phosphorus (TP) were measured by a double beam UV-visible light spectrophotometer (TU-1901, 190–900 nm, China) following the method of China's national standard (Wei et al., 2002). Besides, dissolved oxygen (DO), turbidity (TU), pH were determined by three different types of portable devices (WTW-3310, HACH-2100Q, PHB-4).

Approximately 40ml algal sample was centrifuged at 5000 × g and 15°C for 10 min to obtain algal sediments. Then added 5 ml of 20 mM sodium phosphate buffer (pH 7.0) into algal sediments to wash and re-suspend. The fresh re-suspension was homogenized in a tissue-grinding apparatus (Tissuelyser-24, Shanghai Jingxin Experimental Technology, China) at 60 Hz for 180 s to extract intracellular enzymes under chilled circulation. After that, using 0.1ml of the extracted homogenate for estimation of the malondialdehyde (MDA) content according to Heath and Packer (1968) and expressed as nmol per 108 cells. Then most of the extracted homogenate was centrifuged at 10,000 × g and 4°C for 10 min again to obtain supernate fluid for further enzyme activity assays.

Superoxide dismutase (SOD, EC 1.15.1.1) activity was analyzed by the inhibition of nitroblue tetrazolium (NBT) according to Beauchamp and Fridovich (1971). Catalase (CAT, EC 1.11.1.6) activity was analyzed by decomposing H2O according to Aebi (1974). Peroxidase (POD, EC 1.11.1.7) activity was analyzed using the method of Sakharov and Ardila (1999). Each enzyme activity above is expressed as U per 108 cells. Alkaline phosphatase (AKP) activity and adenosine triphosphate (ATP) activity were determined by using commercial kits (NanJing JianChen Bioengineering institute, China). One unit of AKP activity was defined as enzyme reacts with base materials to produce 1mg phenols per 108 cells during 15min at 37°C. Similarly, one unit of ATP activity was defined as enzyme decomposes ATP to produce 1umol inorganic phosphorus per 108 cells during 1hour.

2.3 Flow analysis

All experimental apparatuses were run with the four blades attached to inside of a cylinder and operated at different rotational speed (0, 5, 8, 11, 14, 17 rad/s) to create different dynamic water environment. Meanwhile, angular velocity was regarded as the only control variable for each hydrodynamic group because it could be both calibrated and simulated in this study. However, angular velocity is not enough to describe hydrodynamic effects on M. aeruginosa cell growth and morphometry. In order to characterize hydrodynamic effects more intrinsically and practically, the parameters chosen here must reflect natural characteristics of flow independently and explain the potential reasons properly.

According to three-dimensional numerical simulation results (Fig. 2), flow velocity distribution in each apparatus is relative smooth and uniform when ignoring the boundary layer effect. Besides, simulated flow velocities at middle points of flow area (water depth = 5, 10, 15 cm) were basically consistent with the result from experimental measurement (Table 1). Through velocity validation, simulated flow characteristics could be considered to describe the real flow reasonably. Moreover, the hydrodynamic results of simulation could be reprocessing to explore average velocity, average shear rate and average turbulent dissipation using method of calculus as shown in Table 1. Based on these, we introduced representative flow velocities namely average flow velocities (0, 0.1, 0.2, 0.3, 0.4, 0.5 m/s) for experimental apparatuses to represent a range of typical situations.

For algal growth, nutrients absorption was considered extremely important. Batchelor microscale describes the smallest length scales dominated by turbulent fluctuations rather than molecular diffusion in scalar concentration, defined as

$$\eta = \left(\frac{D^2 \cdot \nu}{\varepsilon} \right)^{\frac{1}{4}} \qquad [1]$$

Where, D is the mass diffusivity ($m^2\ s^{-1}$), ν is the kinematic viscosity of fluid ($m^2\ s^{-1}$), ε is the mean rate of dissipation of turbulent kinetic energy ($m^2\ s^{-3}$).

Shear stress exposed to the microalgae is computed as:

$$\tau = \mu \cdot \gamma \qquad [2]$$

Where, τ is the shear stress (Pa), γ is the shear rate (s^{-1}), and μ is the dynamic viscosity (Pa s).

©2017, IAHR. Used with permission / ISSN 1562-6865 (Online) - ISSN 1063-7710 (Print)

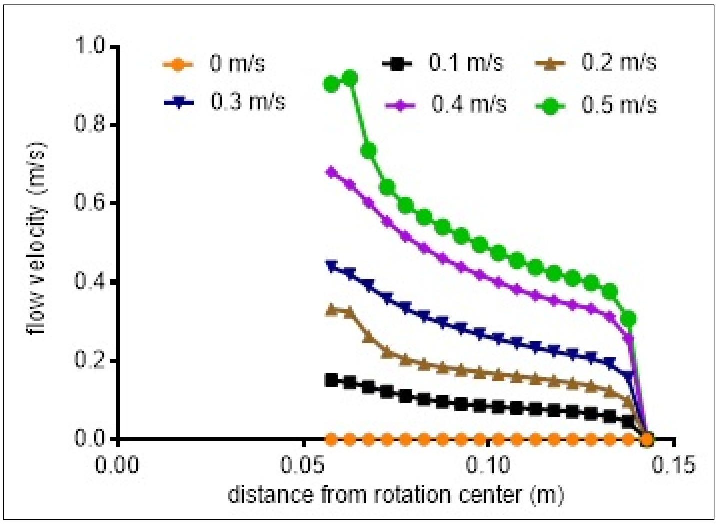

Figure 2. The radial distribution of depth-averaged velocity.

Table 1. Hydrodynamic indicators from mathematical simulation and laboratory experiment.

Angular velocity w (rad/s)	Average flow velocity v (m/s)	Average turbulent dissipation ε (m^2/s^3)	Average sheer rate $\gamma(s^{-1})$	Average sheer stress τ (Pa)	Average Batchelor microscale η (μm)	Simulated-flow velocity at middle of flow area (water depth = 5, 10,15 cm) V_1 (m/s)	Measured-flow velocity at middle of flow area (water depth =5, 10, 15 cm) V_2 (m/s)
0	0	0	0	0	∞	0	0
5	0.11	0.013	3.09	0.0031	2.97	0.13	0.12
8	0.20	0.049	4.52	0.0045	2.13	0.23	0.22
11	0.31	0.216	6.86	0.0069	1.47	0.33	0.32
14	0.40	0.410	8.62	0.0086	1.25	0.42	0.43
17	0.49	0.730	10.40	0.0104	1.08	0.51	0.51

2.4 Statistical analysis

All experiments were performed three times to ensure that deviations for different batches were controlled below 15%. All tested values are expressed as mean value ± standard deviation (SD). The average values, along with the maximum and minimum deviations, were described versus experiment day in Graphpad prism 6 to visually show whether and how the results were different.

3 Results and Discussion

3.1 Algae growth and hydrodynamic threshold system

Fig. 3 shows the changes of algal density and chl-a content in 90 days following different hydrodynamic treatments. For 36 days after experiment beginning, algal density of all experimental groups (0-0.5 m/s) gradually increased with rising of the concentrations of chlorophyll as shown in Fig. 3. However, the viability of algae under 0.5 m/s was not increased any further when experiment time exceeded 36 days. Initially, 0.1-0.4 m/s promoted algal growth slightly relative to control with algal density a little higher than control for approximately 10 days. Particularly, this growth promoting effects became more and more significant along with time and presented the maximum algal density 1.06×10^{10} cells/L and the maximum Chl-a concentration 5.55 g/m^3 under 0.3 m/s on day 84. Algal density under 0-0.2 m/s showed obviously decreasing at the middle time of experiment (approximately 48th day), but algal density under 0.3-0.4 m/s kept increasing up to approximately 84 days. During the whole experiment period, chlorophyll content showed the similar trend with algal density and the order of algal density was 0.3 > 0.4 > 0.2 > 0.1 > 0 >0.5 m/s.

Fig. 4 shows microcosmic distribution of algae cells after treatment for 38 days, when cells under 0.5 m/s became much sparser than other groups. Besides, cells under 0.3 m/s were dark green and largest number in all groups, which was consistent with the maximum algal density as shown in Fig. 3.

 ©2017, IAHR. Used with permission / ISSN 1562-6865 (Online) - ISSN 1063-7710 (Print)

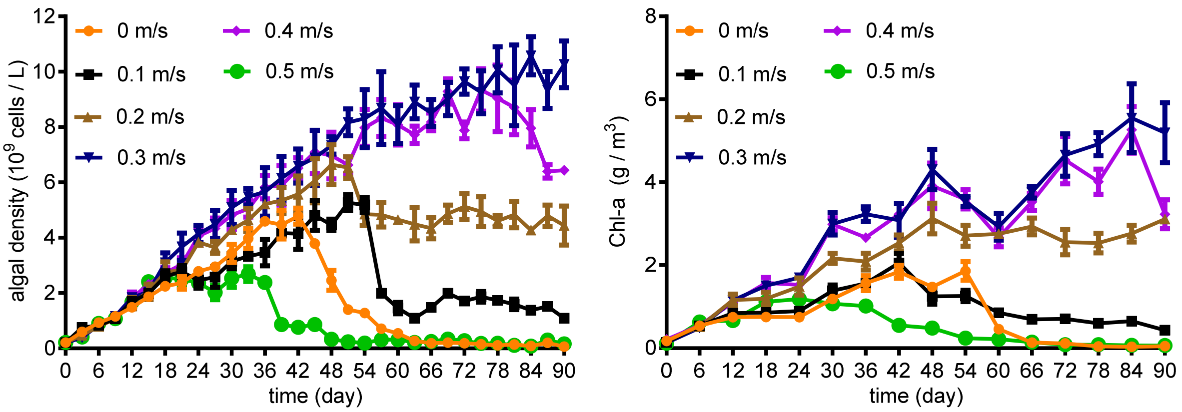

Figure 3. Changes in growth parameters of Microcystis aeruginosa. All values are mean of triplicates ± SD (n=3).

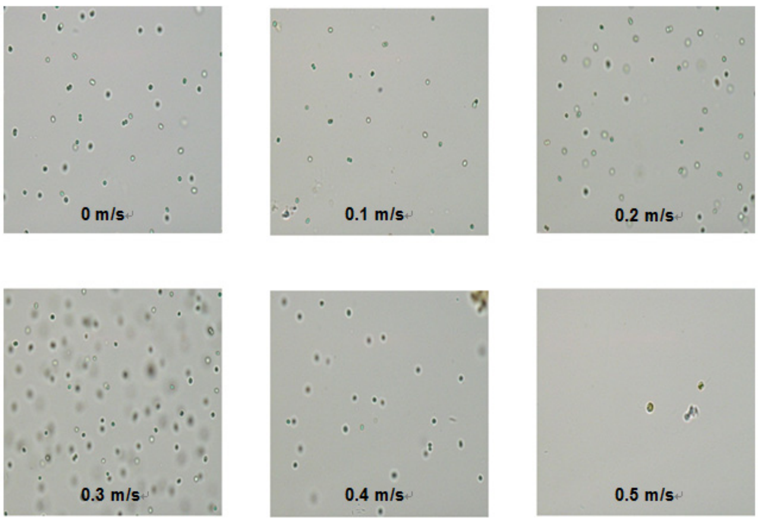

Figure 4. Microscope images of M. aeruginosa in all hydrodynamic groups (0-0.5 m/s) on day 38.

Simultaneously, a scanning electron microscope (SEM) was conducted to observe changes in the morphology of the algae. Thus dramatic changes in algal cell shape were clearly demonstrated in Fig. 5. Obviously, cell aberration was found under 0.5m/s, where bumps and depression could be clearly seen in the cell surface. After 38 days treatment, morphology of the algae in dynamic groups (0.1-0.5 m/s) had more or less stretching deformation while this phenomenon never occurred in the control group.

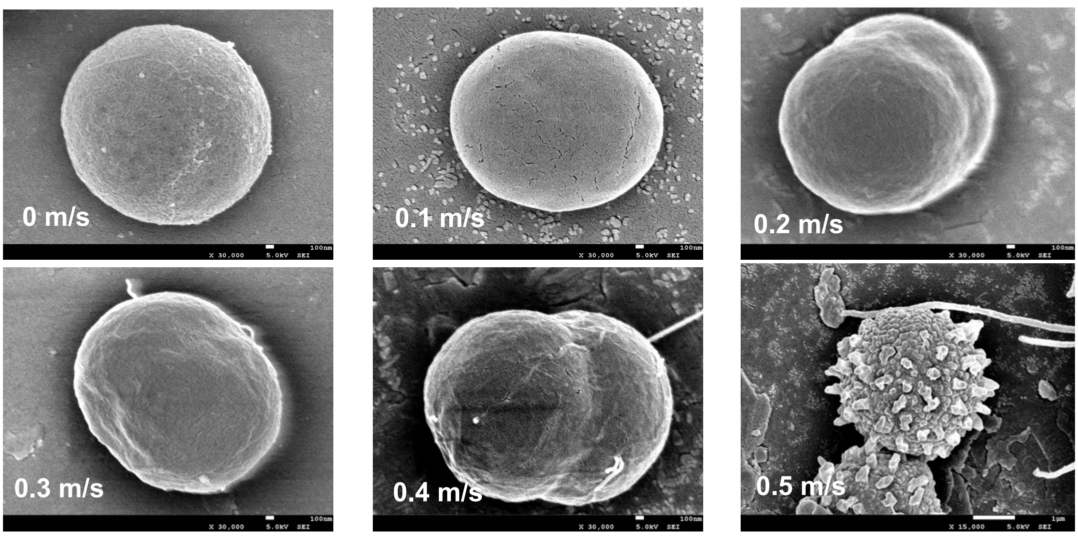

Figure 5. Scanning electron micrographs of M. aeruginosa in all hydrodynamic groups (0-0.5 m/s) on day 38.

Despite hydraulic actions vary a lot, the main effects of hydrodynamic condition on the algal growth can depend on flow velocity, sheer stress and water turbulence. The final and possible effects should be mixture and either positive or negative on algal growth. This experiment-simulation-integrated study has concentrated on the effects and mechanism of the algae growth under hydrodynamic treatment. During the 90 days experiment, hydrodynamic condition induced by speed –regulating motor was a single control factor which caused the significant growth difference among 0-0.5 m/s groups. 0.1-0.4 m/s were confirmed to have a positive effect on algal growth, especially at rapid proliferation period. Conversely, 0.5 m/s was harmful for algal growth and caused significant decrease of algal density from day 26 relative to control. Our results show that appropriate flow velocity benefits for the M. aeruginosa growth while high flow velocity are harmful. This is consistent with the findings of Huang et al. (2015; 2016). Besides, through the long-period observation, we found that 0.2, 0.3, 0.4 m/s could delay algal decline obviously for about 42 days relative to control, which activate algal productivity and prolong algal lifetime.

To characterize the effects of hydrodynamic condition on M. aeruginosa growth, the ratio of the growth rate under representative flow velocities to the growth rate under control, ug/us was introduced for analyzing. The relative growth indicator ug/us varies as a quadratic function of flow velocity, sheer stress, turbulent dissipation respectively (Fig. 6). Based on regression analysis, the dominant flow velocity for M. aeruginosa is determined at 0.24 m/s, which meaning that positive effect on algal growth reaches the peak and is consistent with experiment results. Besides, 0.5 m/s made algae grow poor and caused severe decline, indicating that growth-inhibition flow velocity is 0.5 m/s.

Normally, turbulent flow has both positive and negative effect on algal growth, which can also be verified by our experiment results. From SEM results (Fig. 5), high sheer stress is contributed to deformation of algal morphology and can be considered as a negative effect. Thus we define static-equivalent sheer stress to characterize the situation of positive and the negative effect caused by water turbulence reaching a balance namely equal to control (0 m/s). Static-equivalent sheer stress is determined at 0.0101 Pa (corresponding to the condition that u_g/u_s =1), beyond which severe sheer stress can be harmful for algal growth relative to control (Fig. 6). According to algal cell aberration under 0.5 m/s (Fig. 5), growth-inhibition sheer stress can be determined at 0.0104 Pa (corresponding to the condition that flow velocity =0.5 m/s). Previous studies thought turbulent flow could greatly enhance the circulation of nutrients within the algae cells and make material-exchange more convenient, which benefiting for algae cells to absorb nutrients from the medium for metabolization (Hadiyanto et al., 2013; Huang et al., 2016). In our study, we introduced Batchelor microscale to describe the positive effect of water turbulence on nutrients absorbing in algal cells. For M. aeruginosa, the mean cell diameter was about 5-8 μm, which could be comparable with Batchelor microscale (Table 1). Therefore, we chose turbulent dissipation functioned by Batchelor microscale as a hydrodynamic indicator to explore the positive effect of flow turbulent on nutrients absorbing for growth. Thus by regression analysis (Fig. 6), the dominant turbulent dissipation is determined at 0.334 m^2/s^3. All above, the hydrodynamic threshold system including flow velocity, sheer stress, and turbulent dissipation was expressed in Table 2. This conclusion is also supported by water quality and internal mechanism of algal cell below and can be a good reference for hydrodynamic-effect researches and control of M. aeruginosa bloom.

Table 2. Hydrodynamic threshold system for M. Aeruginosa.

Hydrodynamic indicator	Dominant	Static-equivalent	Growth-inhibition
Flow velocity (m/s)	0.25	/	0.5
Sheer stress (Pa)	/	0.0101	0.0104
Turbulent dissipation (m^2/s^3)	0.334	/	/

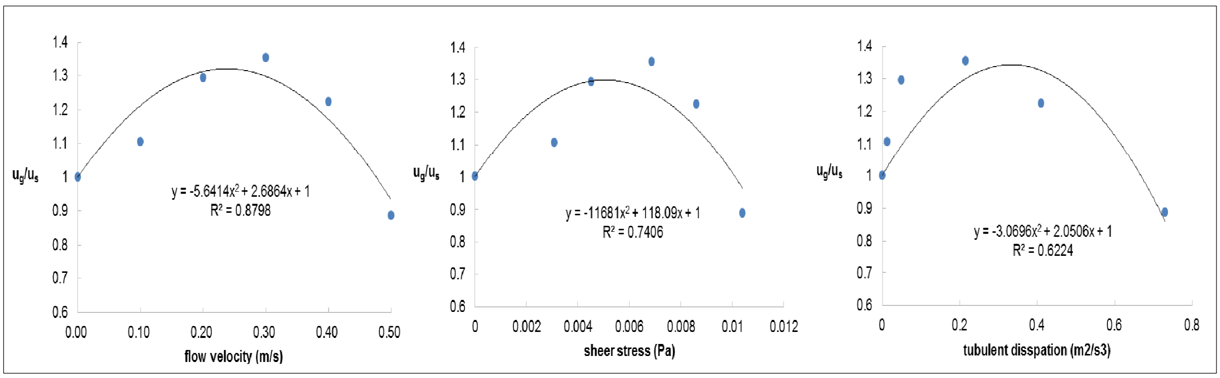

Figure 6. Non-dimensional growth indicator u_g/u_s versus hydrodynamic indicators: flow velocity, sheer stress, turbulent dissipation.

 ©2017, IAHR. Used with permission / ISSN 1562-6865 (Online) - ISSN 1063-7710 (Print)

3.2 Changes of water quality parameters under different flow velocities

The change in water quality outside the algae after hydrodynamic treatment is illustrated in Fig. 7. Obviously, the changing trend of TN and TP were almost synchronously and showed approximate opposite trend to algal growth. TN and TP in water under 0.5 m/s decreased in a short time and then increased to keep stable. Similar trend was found under 0 m/s where TN and TP decreased for 68 days and then increased to the levels which were lower than under 0.5 m/s. Moreover, both the trend of TN and TP in water under 0.1, 0.2, 0.3 and 0.4 m/s showed similar decreases with time. As for pH, all experimental water showed no significant differences and maintained at approximately pH 8.5 which interpreting that M. aeruginosa preferred to grow in weak alkaline environment. DO in water under 0 m/s increased to 12 mg/L for about 24 days and then followed a sharp decrease for another 24 days, subsequently fluctuated around 4mg/L. DO in all experimental water except control (0 m/s) were found fluctuating between 6 mg/L and 8 mg/L, which showing no significant differences.

The results show that consumption of nutrients (TN, TP) in water synchronically reflected demand of algal growth. The decrease of TN and TP in water under 0.1-0.4 m/s indicated that algae could grow well and continuously absorb the nutrients from water. Algae under 0.3 m/s grow best with the maximum consumption of TN (79.4%) and TP (75.7%), indicating that appropriate hydrodynamic condition promoted algal nutrient absorption. Whitford et al. (1961) earlier found 0.18 m/s made TP absorption rate increase at least 150% for freshwater alga. Hadiyanto et al. (2013) also reported hydrodynamic mixing could homogenize the nutrient distribution better for algal growth. However, the increasing of TN and TP under 0.5 m/s and control (0 m/s) found in mid-experiment could be results of nutrients releasing caused by algal death (Nedzarek et al., 2004). Besides, the phenomenon of nutrients increasing was found earlier (approximately 42 days) under 0.5 m/s rather than under control, which suggesting that 0.5 m/s significantly inhibited algal growth. Water pH could be regulated to weak alkaline in the process of algal growth, which is consistent with Xin et al. (2010) reported freshwater microalga, Scenedesmus sp grow well with initial pH= 8-10. The initial increment of DO in water under control (0 m/s) come mainly from algae photosynthesis. Moreover, diffusion of dissolved oxygen under control is weak and not enough intense to release oxygen molecule soon because of static water-air interface. On approximately day 30 after rapid growth period, most of algae under control come decline growth phase. Algae decomposition consumed much oxygen in water, leading a sharp decrease of dissolved oxygen. Unlike static water, DO under 0.1-0.5 m/s basically kept stable because turbulent water strengthened transfer and diffusion of oxygen molecule. Even algae decomposition massively occurred under 0.5 m/s, dissolved oxygen could be supplied by intense reaeration (Manson et al., 2015).

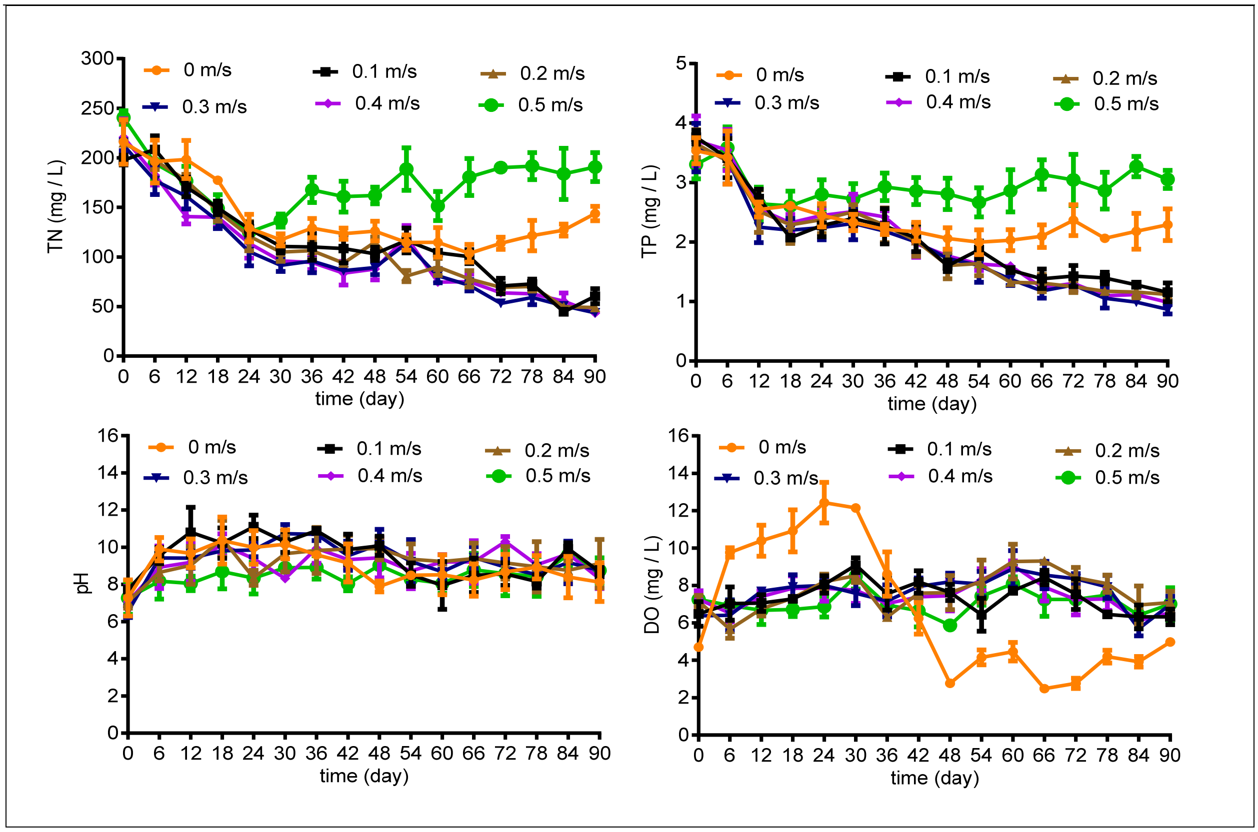

Figure 7. Changes in water quality parameters under different flow velocities. All values are mean of triplicates ± SD (n=3).

3.3 Responses of antioxidant system and energy metabolism in algal cells

Fig. 8 shows responses of lipid peroxidation and antioxidant enzymes in algal cells under different flow velocities. As main and typical indicators of oxidative stress, MDA content and antioxidant enzymes (SOD, POD, CAT) activities were assessed in algal cells (Fig. 8). For algal cells under 0.5 m/s, all the four parameters were significantly higher than other experimental groups especially in mid-experiment. MDA content in algal cells under 0.5 m/s increased significantly for about 60 days and the maximum increase was 162.6% higher than control. Besides, SOD, POD, CAT activities under 0.5 m/s showed similar trends of increasing gradually for about 66 days with the respective maximum increase of 141.5%, 409.7%, and 284.5% relative to control. However, MDA content in algal cells under 0-0.4 m/s similarly fluctuated at a relative low level when SOD, POD, CAT activities gradually decreasing and there were no significant difference among 0-0.4 m/s.

Generally, production and elimination of cellular free radicals were in a state of dynamic balance. Once the algal cell survived in adversity, free radicals generation could be accelerated and seriously damage cellular structure and function including membrane lipids (Ahn et al., 2003). As an important product of lipid peroxidation, MDA content indirectly indicates the level of free radicals generation and thereby to reflect the degree of membrane disruption (Chaudière et al., 1999). SOD, POD, CAT act as the main defense antioxidant enzymes to eliminate ROS and repair oxidative damage simultaneously (Walz et al., 2002). As the first line of antioxidant defense in cells, SOD decomposes ROS, $O^{2\bullet-}$, into H_2O_2 and O_2. Then toxic H_2O_2 is decomposed into H_2O and O_2 by CAT and POD. For algae under 0.5 m/s, MDA content and SOD, POD, CAT activities increased significantly and synchronously relative to control, which suggesting 0.5 m/s damaged algal cells by inducing free radicals generation. Li et al. (2015) reported similar increasing process of MDA content in M. aeruginosa cells by hydrodynamic cavitation and therewas positive correlation between MDA content and free radical levels. Wang et al. (2007) found that UV-B radiation promoted both MDA production and antioxidant enzymes activities including SOD, POD, CAT in Cyanobacterium and confirmed antioxidant system play a key role of defensing stress effectively. Thus these results reinforce the point additional free radicals generation is closely related to exogenous stress, 0.5 m/s in this study. Conversely, MDA content under 0.1-0.4 m/s were lower than control and SOD, POD, CAT activities presented a gradual decline, probably meaning that algae were not suffered from the velocities. Based on this, appropriate flow turbulence can be considered benefiting for cellular material exchange and free radicals elimination.

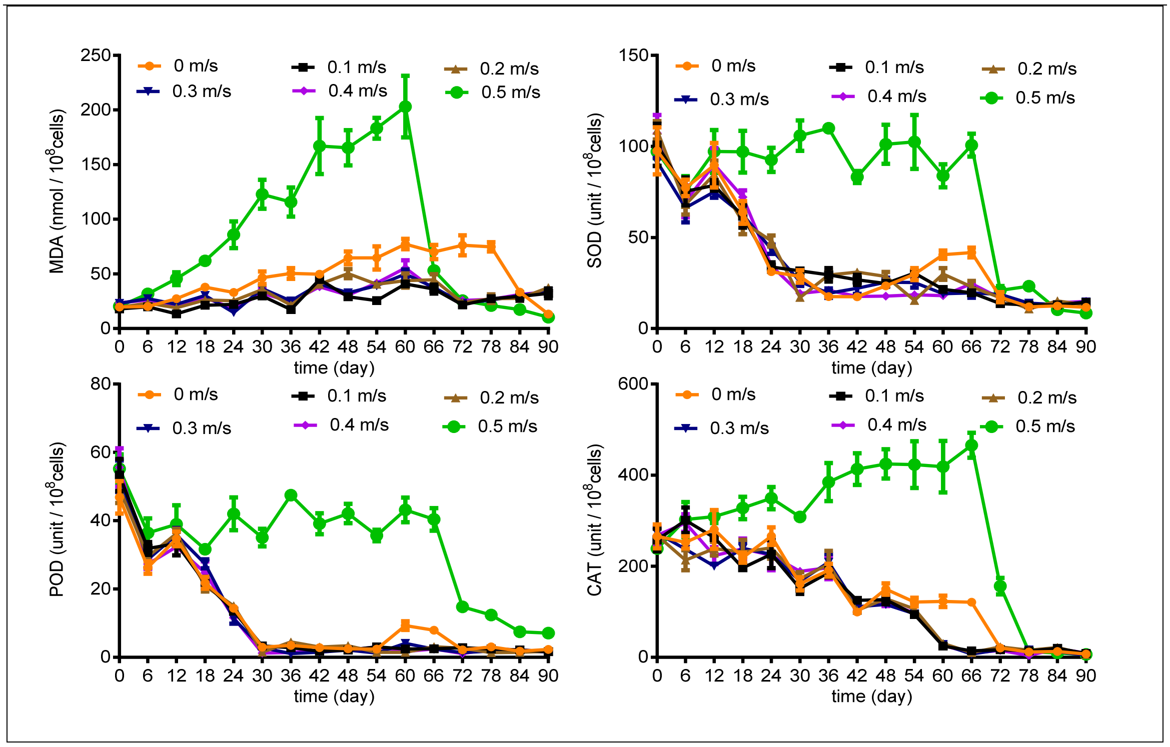

Figure 8. Effect of flow velocity on MDA concentration, antioxidant enzymes in algal cells. All values are mean of triplicates ± SD (n=3).

As another promising way to explore the potential internal-mechanism, response of energy metabolism in algal cells were investigated as shown in Fig. 8. It is clear that 0.1-0.4 m/s enhanced AKP activity in algal cells while 0.5 m/s inhibited AKP activity relative to control. The decreasing of AKP eactivity under control from day 48, which corresponding to the slightly increasing of TP, was caused by algae decline. Moreover, when algae was calculated in a new water turbulence environment (0.1-0.5 m/s), ATP enzyme activity was

 ©2017, IAHR. Used with permission / ISSN 1562-6865 (Online) - ISSN 1063-7710 (Print)

enhanced to synthesize more ATP stored for adaption. Along with the rapid algal growth under 0-0.4 m/s, ATP enzyme activity decreasing gradually because a large number of ATP was consumed. Although 0.5 m/s made algal cells synthesize amounts of ATP to accommodate high flow velocity but soon (approximately day 12) failed with algae decline and ATP enzyme activity sharply decreasing. Particularly, 0.1-0.4 m/s made ATP enzyme activity stablize eventually rather than decrease rapidly in control.

Phosphorus (P) is one of the essential nutrients for the growth of phytoplankton. Even though dissolved inorganic phosphorus (DIP) is bio-available and a preferred form for algal growth, algae can use dissolved organic phosphorus (DOP) when DIP is deficiency (Huang et al., 2007; Li et al., 2015). AKP is an inducible enzyme, which playing an important role in the degradation and mineralization of DOP into DIP and sometimes regarded as a useful indicator of P deficiency (Pu et al., 2014; Annis et al., 2002). In our experiment, increasing of AKP activity in algal cells under 0.1-0.4 m/s indicated that excessive consumption of DIP for algal rapid growth, which could be confirmed by the decreasing trend of TP in water (Fig. 7) and suggest that moderate flow velocity promotes algal growth. Particularly, decreasing of AKP activity in algal cells under control after 48 days which corresponded to the slightly increasing of TP might demonstrate algal decline without much need of DIP. The lowest AKP activity under 0.5 m/s indicated that high flow velocity caused growth inhibition and DIP/TP in the surrounding medium is enough. This is consistent with the results of Awasthi, 2012 who found that AKP activity in green algae (Scenedesmus quadricauda and Chlorella vulgaris) and cyanobacteria Anacystis nidulans could be inhibited by heavy metal (Ni, Zn, Cd) stress. ATP content is an important physiological indicator of energy metabolism (Jing et al., 2014) and could be reflected by ATP enzyme activity, which catalyzed ATP into ADP and phosphate radical with energy releasing. Focused on the process of energy releasing and P supplement for cell metabolism, 0.1-0.4m/s made algae grow rapid and consume amounts of ATP, leading ATP enzyme activity inhibited. Then when algal growth rate slowed down, ATP enzyme activity kept stable instead of decreasing. As for algae cells under 0.5 m/s, ATP enzyme activity was significantly inhibited probably because high flow velocity was harmful for algal growth as well as energy metabolism.

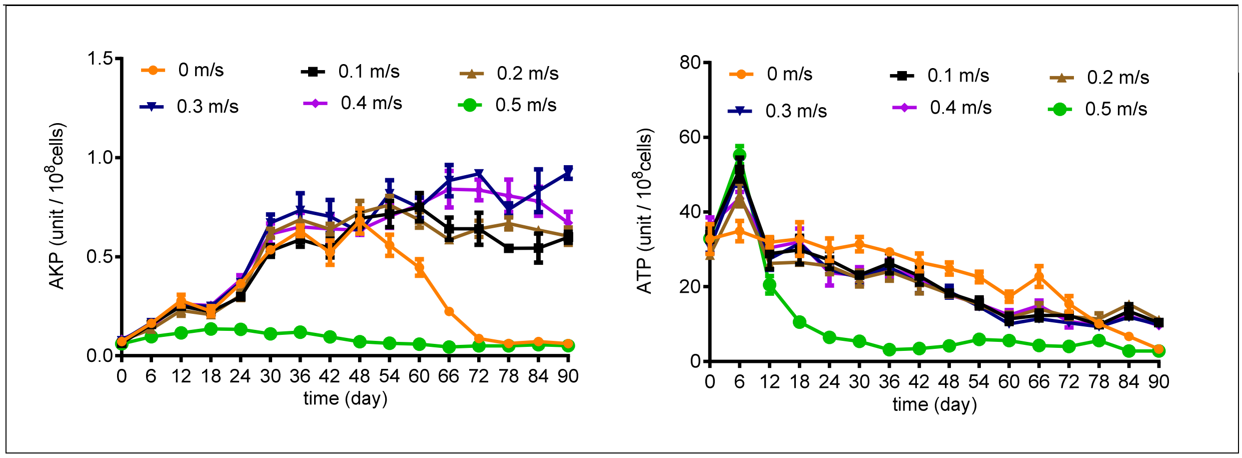

Figure 9. Effect of energy-related enzymes activity in algal cells. All values are mean of triplicates ± SD (n=3).

4 CONCLUSIONS

This experiment studied algal growth, water quality parameters and enzymes activities of antioxidant system and energy metabolism influenced by hydrodynamic condition. First, experimental results revealed hydrodynamic condition significantly affected algal growth following three aspects: (1) a low to moderate flow velocity promotes algal growth and prolong algal lifetime while too high flow velocity presented inhibition ; (2) high sheer stress causes cell aberration and inhibit algal growth; (3) water turbulence promote algal cells access to nutrients. Thus, based on these characterizes, hydrodynamic threshold system for M. aeruginosa were obtained. Second, responses of water quality parameters, antioxidant system and energy metabolism showed that appropriate hydrodynamic condition benefited for absorbing nutrient, reducing the oxidation degree and photosynthesis in algal cells. Finally, the hydrodynamic threshold system together with internal mechanism responses might be a useful reference for future study and control of M. aeruginosa bloom.

ACKNOWLEDGEMENTS

Grants from the National Natural Science Foundation of China (Nos. 51679156 and 51309170) and National Key R&D Program of China (No 2016YFC0502200) supported this work.

REFERENCES

Ahn, C.Y., Park, M.H., Joung, S.H., Kim, H.S., Jang, K.Y. & Oh, H.M. (2003). Growth Inhibition of Cyanobacteria by Ultrasonic Radiation: Laboratory and Enclosure Studies. *Environmental Science & Technology*, 37(13), 3031-3037.

Anderson, D.M., Glibert, P.M. & Burkholder, J.A.M. (2002). Harmful Algal Blooms and Eutrophication: Nutrient Sources, Composition and Consequences. *Estuaries and Coasts*, 25(4), 704-726.

Annis, E.R. & Cook, C.B. (2002). Alkaline Phosphatase Activity in Symbiotic Dinoflagellates (Zooxanthellae) as a Biological Indicator of Environmental Phosphate Exposure. *Marine Ecology Progress,* 245(4),11-20.

Awasthi, M. (2012). Relevance of Alkaline Phosphatase Activity of Immobilized Green Algae and Cyanobacteria for Heavy Metal Toxicity Monitoring. *Journal of Materials & Environmental Science*, 3(3), 446-451.

Catherine, Q., Susanna, W., Isidora, E.S., Mark, H., Aurélie, V. & Jeanfrançois, H. (2013). A Review of Current Knowledge on Toxic Benthic Freshwater Cyanobacteria--Ecology, Toxin Production and Risk Management. *Water Research,* 47(15), 5464-5479.

Chaudière, J. & Ferrari-Iliou, R. (1999). Intracellular Antioxidants: from Chemical to Biochemical Mechanisms. *Food & Chemical Toxicology an International Journal Published for the British Industrial Biological Research Association,* 37(9-10), 949-962.

Chen, X.C., He, S.B., Huang, Y.Y., Kong, H.N., Yan, L. & Li, C.J. (2009). Laboratory Investigation of Reducing Two Algae From Eutrophic Water Treated with Light-Shading Plus Aeration. *Chemosphere,* 76(9), 1303-1307.

Falconer, I.R., Burch, M.D., Steffensen, D.A., Choice, M. & Coverdale, O.R. (1994). Toxicity of the Blue-Green Alga (Cyanobacterium) Microcystis Aeruginosa in Drinking Water to Growing Pigs, as an Animal Model For Human Injury and Risk Assessment. *Environmental Toxicology & Water Quality,* 9(2), 131-139.

Hadiyanto, H., Steven, E., Tom, V.G. & Andrzej, S. (2013). Hydrodynamic Evaluations in High Rate Algae Pond (Hrap) Design. *Chemical Engineering Journal,* 217(217), 231-239.

Heisler, J., Glibert, P.M., Burkholder, J.M., Anderson, D.M., Cochlan, W. & Dennison, W.C. (2008). Eutrophication and Harmful Algal Blooms: A Scientific Consensus. *Harmful Algae,* 8(1), 3-13.

Huang, B., Ou, L., Wang, X., Huo, W., Li, R. & Hong, H. (2007). Alkaline Phosphatase Activity of Phytoplankton in East China Sea Coastal Waters with Frequent Harmful Algal Bloom Occurrences. *Aquatic Microbial Ecology*, 49(2), 195-206.

Huang J., Xi B. & Xu Q. (2016). Experiment Study of the Effects of Hydrodynamic Disturbance on the Interaction between the Cyanobacterial Growth and the Nutrients. *Journal of Hydrodynamics, Series B*, 411-422.

Huang, J., Xu, Q., Xi, B., Wang, X., Li, W. & Gao, G. (2015). Impacts of Hydrodynamic Disturbance on Sediment Resuspension, Phosphorus and Phosphatase Release, and Cyanobacterial Growth in Lake Tai. *Environmental Earth Sciences,* 74(5), 3945-3954.

Jacoby, J.M., Collier, D.C., Welch, E.B., Hardy, F.J. & Crayton, M. (2011). Environmental Factors Associated with a Toxic Bloom of Microcystis Aeruginosa. *Canadian Journal of Fisheries & Aquatic Sciences,* 57(1), 231-240.

Ji, D., Wells, S.A., Yang, Z., Liu, D., Huang, Y. & Ma, J. (2017). Impacts of Water Level Rise on Algal Bloom Prevention in the Tributary of Three Gorges Reservoir, China. *Ecological Engineering,* 98, 70-81.

Jing, H., Jing, W. & Hong, X. (2014). The Circadian Rhythms of Photosynthesis, Atp Content and Cell Division In Microcystis, Aeruginosa, Pcc7820. *Acta Physiologiae Plantarum,* 36(12), 3315-3323.

King, S.A. (2014). Hydrodynamic Control of Filamentous Macroalgae in a Sub-Tropical Spring-Fed River in Florida, USA. *Hydrobiologia,* 734(1), 27-37.

Li, H.M., Tang, H.J., Shi, X.Y., Zhang, C.S. & Wang, X.L. (2014). Increased Nutrient Loads from the Changjiang (Yangtze) River Have Led to Increased Harmful Algal Blooms. Harmful Algae*,* 39(39), 92–101.

Li, M., Li, L., Shi, X., Lin, L. & Lin, S. (2015). Effects of Phosphorus Deficiency and Adenosine 5 -Triphosphate (Atp) on Growth and Cell Cycle of the Dinoflagellate Prorocentrum Donghaiense. *Harmful Algae,* 47, 35-41.

Li, P., Song, Y., Yu, S. & Park, H.D. (2015). The Effect of Hydrodynamic Cavitation on Microcystis Aeruginosa: Physical and Chemical Factors. *Chemosphere,* 136, 245-251.

Wenyan, L., Jiuhui, Q., Libin, C., Huijuan, L. & Lei P. (2005). Inactivation of Microcystis Aeruginosa by Continuous Electrochemical Cycling Process in Tube Using Ti/RuO_2 Electrodes. *Environmental Science & Technology,* 39(12), 4633.

Long, T.Y., Wu, L., Meng, G.H. & Guo, W.H. (2011). Numerical Simulation for Impacts of Hydrodynamic Conditions on Algae Growth in Chongqing Section of Jialing River, China. *Ecological Modelling,* 222(1), 112-119.

Manson, J.R. & Wallis, S.G. (2015). *Hydraulic Influences on Dispersion and Reaeration in Rivers*. Rivers – Physical, Fluvial and Environmental Processes, GeoPlanet: Earth and Planetary Sciences, Spinger International Publishing, 543-556.

 ©2017, IAHR. Used with permission / ISSN 1562-6865 (Online) - ISSN 1063-7710 (Print)

Nedzarek, A. & Rakusa-Suszczewski, S. (2004). Decomposition of Macroalgae and the Release of Nutrient in Admiralty Bay, King George Island, Antarctica. *Suszczewski,* 17, 26-35.

Oh, H.M., Ahn, C.Y., Lee, J.W., Chon, T.S., Choi, K.H., & Park, Y.S. (2007). Community Patterning and Identification of Predominant Factors in Algal Bloom in Daechung Reservoir (Korea) Using Artificial Neural Networks. *Ecological Modelling,* 203(1), 109-118.

Onderka, M. (2007). Correlations between Several Environmental Factors Affecting the Bloom Events of Cyanobacteria in Liptovska Mara Reservoir (Slovakia), a Simple Regression Model. *Ecological Modelling,* 209(2), 412-416.

Pu, P., Zhang, Z. & Wang, M. (2014). Seasonal Variation and Significance of Alkaline Phosphatase Activity on Algal Blooming in Chongqing Urban Section of Jialing River. *Asian Journal of Chemistry,* 26(18), 6067-6072.

Shukla, J.B., Misra, A.K. & Chandra, P. (2008). Modeling and Analysis of the Algal Bloom in a Lake Caused By Discharge of Nutrients. *Applied Mathematics & Computation,* 196(2), 782-790.

Vidal, J., Marcé, R., Serra, T., Colomer, J., Rueda, F. & Casamitjana, X. (2012). Localized Algal Blooms Induced By River Inflows in a Canyon Type Reservoir. *Aquatic Sciences,* 74(2), 315-327.

Visser, P.M., Ibelings, B.W., Bormans, M. & Huisman, J. (2015). Artificial Mixing to Control Cyanobacterial Blooms: A Review. *Aquatic Ecology,* 50(3), 423-441.

Walz, C., Juenger, M., Schad, M. & Kehr, J. (2002). Evidence for the Presence and Activity of a Complete Antioxidant Defence System in Mature Sieve Tubes. *Plant Journal,* 31(2), 189-197.

Wang, G., Hu, C., Li, D., Zhang, D., Li, X. & Chen, K. (2007). The Response of Antioxidant Systems in Nostoc Sphaeroides, Against Uv-B Radiation and the Protective Effects of Exogenous Antioxidants. *Advances in Space Research,* 39(6), 1034-1042.

Watson, S.B., Miller, C., Arhonditsis, G., Boyer, G.L., Carmichael, W. & Charlton, M.N. (2016). The Re-Eutrophication of Lake Erie: Harmful Algal Blooms and Hypoxia. *Harmful Algae,* 56, 44-66.

Wei, F.S., Qi, W.Q., Sun, Z.G., Huang, Y.R. & Shen, Y.W. (2002). *Water and Wastewater Monitoring and Analysis Method*. China Environmental Science Press, Beijing.

Whitford, L.A. & Schumacher, G.J. (1961). Effect of Current on Mineral up Take and Respiration by a Fresh - Water Alga. *Limnology and Oceanography*, 6, 423-425.

Xin, L., Hu, H.Y., Ke, G. & Jia, Y. (2010). Growth and Nutrient Removal Properties of a Freshwater Microalga Scenedesmus, Sp. Lx1 under Different Kinds of Nitrogen Sources. *Ecological Engineering,* 36(4), 379-381.

Proceedings of the 37th IAHR World Congress
August 13 – 18, 2017, Kuala Lumpur, Malaysia

BAFFLE SYSTEMS TO FACILITATE UPSTREAM FISH PASSAGE IN STANDARD BOX CULVERTS: HOW ABOUT FISH-TURBULENCE INTERPLAY?

HANG WANG[1] & HUBERT CHANSON[2]

[1,2]The University of Queensland, School of Civil Engineering, Brisbane QLD 4072, Australia
hang.wang@uqconnect.edu; h.chanson@uq.edu.au

ABSTRACT

Waterway culverts are very common hydraulic structures along streams and water systems, in rural and urban drainage networks. Current expertise in environmental hydraulics of culverts is limited, sometimes leading to inadequate fish passage with adverse impact on the catchment eco-system. Recent recognition of the ecological impact of culverts on natural streams led to changes in culvert design guidelines. It is believed that fish-turbulence interplay may facilitate upstream migration, albeit an optimum design must be based upon a proper characterisation of both hydrodynamics and fish kinematics. Basic dimensional considerations highlight a number of key parameters relevant to upstream fish passage, including the ratio of fish speed fluctuations to fluid velocity fluctuations, the ratio of fish response time to turbulent time scales, the ratios of fish dimension to turbulent length scale, and the fish species. Combining the equation of conservation of momentum applied to an individual fish, the instantaneous thrust and power expended during fish swimming may be derived from fish kinematic data, including the associated energy consumption. Within basic assumptions, the present findings suggest that the culvert invert slope may affect significantly the energy spent by the fish to provide thrust during upstream culvert passage.

Keywords: Standard box culverts; fish passage; fsh-turbulence interactions; dimensional considerations; energy consumption.

1 INTRODUCTION

Culverts are covered channels designed to pass floodwaters beneath an embankment, typically a roadway or railroad. Figure 1 presents a few examples of standard box culverts in Australia. The three-cell structures seen in Figure 1 (Top) would be typical of a large majority of road culvert structures. Culverts may cost about 15% of total road construction costs (Hee, 1969). Their designs are very diverse, using various shapes and construction materials determined by stream width, peak flows, stream gradient, and minimum cost (Henderson, 1966; Hee, 1969). While the key design parameters of a culvert are its design discharge and the maximum acceptable afflux (Chanson, 2004), the variability in culvert dimensions is closely linked to the various constraints of each site (Figure 1), resulting in a wide diversity in flow patterns (Hee, 1969; USBR, 1987; Australian Standard, 2010).

In recent decades, recognition of the ecological impact of culverts on natural streams and rivers led to changes in culvert design guidelines (Behlke et al., 1991; Chorda et al., 1995). The culvert discharge capacity is basically based upon the hydrological and hydraulic engineering considerations, which may result in large flow velocities creating some fish passage barrier. In this paper, the interactions between the turbulence and fish are reviewed in the context of upstream fish passage in standard box culverts. Basic dimensional analysis is presented, before fish kinematics and energetic considerations are developed and results are discussed.

2 FISH-TURBULENCE INTERPLAY: A REVIEW

One of the primary ecological concerns regarding culvert crossings is the potential velocity barrier to upstream fish passage resulting from the constriction of the channel as illustrated in Figures 1 and 2A. Several jurisdictions developed culvert design guidelines to ensure that the designs will allow for the upstream passage of fish. In Canada, guidelines are based upon a number of criteria including the average flow velocity and minimum embedment depth (Hunt et al., 2012). For culvert rehabilitation applications, baffles may be installed along the invert to provide some fish-friendly alternative (Olsen and Tullis, 2013; Duguay and Lacey, 2014; Chanson and Uys, 2016). At low flows, baffles decrease the flow velocity and increase the water depth to facilitate fish passage. For larger discharges, baffles would induce locally lower velocities and generate recirculation regions. Unfortunately, baffles can reduce drastically the culvert discharge capacity for a given afflux (Larinier, 2002).

 ©2017, IAHR. Used with permission / ISSN 1562-6865 (Online) - ISSN 1063-7710 (Print)

(A) (B)

(C)

Figure 1. Standard box culverts in Australia.(A) Culvert outlet beneath Haydon Drive, Canberra ACT on 15 December 2011.(B) Culvert outlet on Marom Creek beneath Bruxner highway B6, Wollongbar NSW on 28 October 2016.(C) Culvert inlet along Gin House Creek, Carrara, Gold Coast QLD on 5 December 2007.

The critical parameters of a culvert in terms of fish passage are the dimensions of the barrel, including its length and cross-sectional characteristics and the invert slope. Generally, the box culverts are considered the most effective for fish passage, although the culvert length may be a key factor for some fish species, with long culverts limiting upstream fish passage (Brigg and Galarowicz, 2013). The behavioural response by fish species to culvert length, light conditions and flow turbulence could play a role in their swimming ability and culvert passage rate. The broad range of culvert designs results in a wide diversity in turbulent flow patterns observed in prototype culverts (Figure 2A). When the fish swimming power is greater than the maximum volumetric power (Bates, 2000), the fish may be able to pass the successive baffles and rest in each pool. There is no simple technical means for measuring the turbulence characteristics in fish passage with baffles, although it is understood that the flow turbulence plays a key role in fish behaviour (Liu et al., 2006; Yasuda, 2011; Breton et al., 2013). Several studies argued that the most important parameters to assist fish passage include the turbulence intensity, Reynolds stress tensor, turbulent kinetic energy, vorticity, and dissipation (Pavlov et al., 2000; Hotchkiss, 2002; Nikora et al., 2003). Recent observations showed that fish may take advantage of the unsteady character of turbulent flows (Liao, 2007; Wang et al., 2010) and it was shown that fish can save energy by swimming as a school (Plew et al., 2015; Chen et al., 2016). Importantly, the interactions between fish and turbulence are very complicated, and naive *"turbulence metrics cannot explain all the swimming path lines or behaviors*" (Goettel et al., 2015).

First mentioned by Leonardo Da Vinci (Keele, 1983), the interactions between swimming fish and vortical structures involve a broad range of relevant length scales (Lupandin, 2005; Webb and Cotel, 2011). The turbulent flow patterns are one key element determining the capacity of the system to pass successfully targeted fish species. A seminal discussion argued for the role of secondary flow motion and "*the importance of performing three-dimensional turbulent flow measurements to precisely identify the effects of secondary flows on fish motion*" (Papanicolaou and Talebbeydokhti, 2002). The discussion was extended by recent contributions, suggesting that "*a proper study of turbulence effects on fish behaviour should involve, in addition to turbulence energetics, consideration of fish dimensions in relation to the spectrum of turbulence scales*" (Nikora et al., 2003), and that large-scale "*turbulent structures associated with wakes can be beneficial if fish are able to exploit them*" (Plew et al., 2007).

While the literature on culvert fish passage focused mostly on fast-swimming fish species, recent studies acknowledged the needs for better guidelines for small-bodied fish including juveniles (Behlke et al., 1991; Fairfull and Witheridge, 2003; Rodgers et al., 2014; Forty et al., 2016; Wang et al., 2016a).

©2017, IAHR. Used with permission / ISSN 1562-6865 (Online) - ISSN 1063-7710 (Print)

3 DIMENSIONAL ANALYSIS AND SIMILITUDES

3.1 Basic considerations

In experimental fluid dynamics, the model study of a prototype is to provide reliable predictions of the flow properties of the associated prototype (Liggett, 1994; Foss et al., 2007; Novak et al., 2010). This type of study is based upon the basic concept and principles of similitude to ensure a reliable extrapolation of the results from the hydraulic model study to the prototype. That is, physical measurements from the model (*e.g.,* pressure, velocity, drag) are used to predict the extrapolated values for the same quantities to be present in the prototype flow (Henderson, 1966; Novak and Cabelka, 1994). The processing, analysis and interpretation of experimental data constitutes an essential activity in physical modelling (Darrozes and Monavon, 2014). Two basic principles are: (1) the simplest relationships have the fewest number of relevant variables and (2) they are dimensionless (Foss et al., 2007). The presentation of numerical results must have the most extensive validity, and dimensional analysis is the basic procedure to deliver dimensionless parameters.

For any dimensional analysis, the relevant parameters include the fluid properties and physical constants, the channel geometry and initial flow conditions. Considering the simple case of a steady turbulent flow in a rectangular open channel, a dimensional analysis yields a series of relationship between the flow properties at a location (x,y,z) and the upstream flow conditions, channel geometry and fluid properties:

$$d, \vec{V}, v', p, L_t, T_t, ... = F_1\left(x, y, z, B, k_s, \theta, d_1, V_1, v_1', \rho_w, \mu_w, \sigma, g, ...\right) \quad [1]$$

where d is the flow depth, V is the velocity, v' is a velocity fluctuation, p is the pressure, L_t and T_t are integral turbulent length and time scales, x, y and z are the longitudinal transverse and vertical coordinates, respectively, B is the channel width, k_s is the equivalent sand roughness height of the channel boundary, θ is the angle between the invert and horizontal, d_1, V_1 and v_1' are the inflow depth, velocity and velocity fluctuation, respectively, ρ_w and μ_w are the water density and dynamic viscosity, respectively, σ is the surface tension, and g is the gravity acceleration. In Equation [1], right handside term, the 4th, 5th and 6th variables characterise the boundary conditions, whereas the 7th, 8th and 9th terms are the inflow (initial) conditions, and the following terms are fluid and physical properties.

The Π-Buckingham theorem states that a dimensional equation such as Equation [1] with N dimensional variables may be simplified in an equation with N-3 dimensionless variables, when the Mass, Length and Time units are used among the N dimensional variables (Liggett, 1994). Thus Equation [1] may be rewritten as:

$$\frac{d}{d_c}, \frac{V_x}{V_c}, \frac{v_x'}{V_c}, \frac{p}{\rho_w \times g \times d_c}, \frac{L_t}{d_c}, T_t \times \sqrt{\frac{g}{d_c}} ... = \quad [2]$$
$$F_2\left(\frac{x}{d_c}, \frac{y}{d_c}, \frac{z}{d_c}, \frac{B}{d_c}, \theta, \frac{k_s}{d_c}, \frac{d_1}{d_c}, \frac{V_1}{\sqrt{g \times d_1}}, \frac{v_1'}{V_1}, \rho_w \times \frac{V \times D_H}{\mu_w}, \frac{g \times \mu_w^4}{\rho_w \times \sigma^3}, ...\right)$$

where d_c is the critical flow depth ($d_c = (Q^2/(g×B^2))^{1/3}$), V_c is the critical flow velocity, Q is the water discharge and D_H is the equivalent pipe diameter, or hydraulic diameter. In Equation [2], right handside term, the 7th term is the inflow Froude number (Fr_1), the 8th and 9th terms are the Reynolds number (Re) and Morton number (Mo). The Π-Buckingham theorem states that any dimensionless number can be replaced by a combination of itself and other dimensionless numbers. In Equation [2], the Morton number is introduced because it is a constant in most hydraulic model studies when both laboratory experiment and prototype flows use the same fluids, namely air and water.

Traditionally hydraulic model studies are performed using geometrically similar models. In the geometrically similar physical model, the flow conditions are said to be similar to those in the prototype if the model displays similarity of form (geometric similarity), similarity of motion (kinematic similarity) and similarity of forces (dynamic similarity) (Liggett, 1994; Chanson, 1999). If any similarity (geometric, kinematic or dynamic similarity) is not fulfilled, scale effects may take place. Scale effects yield discrepancy between the model data extrapolation and the prototype performances. In a physical model, true similarity can be achieved if and only if each dimensionless parameter (or Π-terms) has the same value in both model and prototype:

$$\begin{aligned} Fr_m &= Fr_p \\ Re_m &= Re_p \\ Mo_m &= Mo_p \end{aligned} \quad [3]$$

where the subscripts m and p refer to the model and prototype conditions, respectively. Scale effects may take place when one or more dimensionless terms have different values between the laboratory and

 ©2017, IAHR. Used with permission / ISSN 1562-6865 (Online) - ISSN 1063-7710 (Print)

prototype. Let us consider a prototype culvert flow (Figure 2A) and fish passage experimental flumes in Figures 2B and 2C, how can we extrapolate the laboratory results to full-scale real-world culverts with minimum scale effects?

(A)

(B)

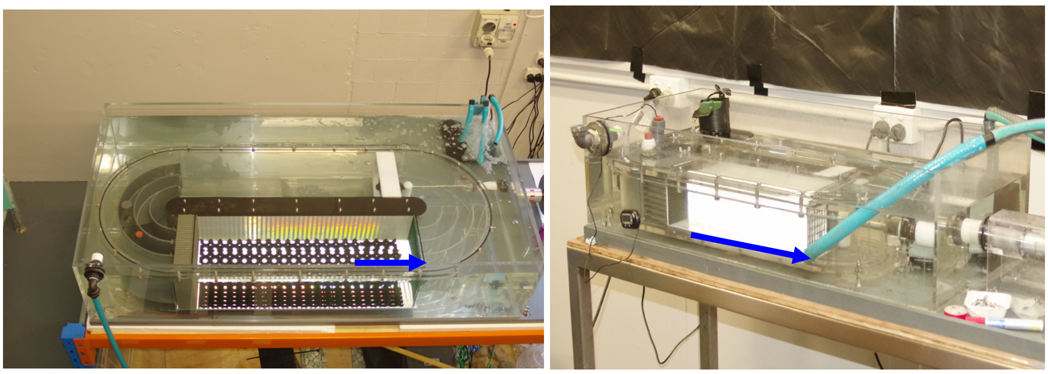

(C)

Figure 2. Physical modelling of culvert hydraulics: Comparison between a prototype culvert operation and laboratory studies of upstream fish passage in culverts - Blue arrow shows flow direction. (A) Multi-cell box culvert inlet along Norman Creek, Brisbane QLD during a small flood on 20 May 2009. (B) 12 m long 0.5 m wide tilting flume in the UQ Bio-hydrodynamics laboratory, looking upstream for Q = 0.261 m^3/s and θ = 0. (C) Medium-size and small-size recirculating water tunnels.

Open channel flows including culvert flows are typically studied based upon a Froude similarity because gravity effects are important (Henderson, 1966; Liggett, 1994; Chanson, 1999). The turbulent flow motion is dominated by viscous and dissipative effects. Thus, a true similarity of culvert flow requires achieving identical Froude, Reynolds and Morton numbers in both the prototype culvert and its laboratory model (Equation [3]). This is impossible to achieve using geometrically similar models unless working at the full-scale. Practically, the Froude and Morton dynamic similarities are simultaneously employed with the same fluids, air and water, used in prototype and model. In turn, the Reynolds number is grossly underestimated in laboratory flow conditions. This may lead to viscous-scale effects in small-size hydraulic models seen in Figure 2C.

Similarly, a dimensional analysis may be conducted for the fish motion in a turbulent flow (Alexander, 1982; Blake, 1983). Considering the simplified motion of a fish travelling upstream in a prismatic open channel with a steady turbulent flow, the dimensional considerations yield a series of relationship between the fish motion characteristics at a location (x,y,z), the fish characteristics, the channel boundary conditions, the turbulent flow properties and the fluid properties. It becomes:

$$\vec{U}, u', O_2, \tau_f, ... = F_3\begin{pmatrix} x, y, z, \\ L_f, l_f, h_f, \rho_f, \text{specie}, \\ B, k_s, \theta, \\ d, V, v', L_t, T_t, \\ \rho_w, \mu_w, \sigma, g, ... \end{pmatrix} \qquad [4]$$

where U is the Eulerian fish speed for a fixed observer, positive upstream since this study is concerned with the upstream fish passage, u' is a fish speed fluctuation, O_2 is the oxygen consumption, τ_f is the fish response time, L_f, l_f and h_f are the fish length, thickness and height, respectively, and ρ_f is the fish density. While Equation [4] is simplistic, for example, ignoring the effects of fish fatigue, the Π-Buckingham theorem implies that Equation [4] may be rewritten in dimensionless form as:

$$\frac{U}{V_c}, \frac{u'}{v'}, O_2, \frac{\tau_f}{T_t}, ... = F_4\begin{pmatrix} \frac{x}{d_c}, \frac{y}{d_c}, \frac{z}{d_c}, \\ \frac{L_f}{L_t}, \frac{l_f}{L_t}, \frac{h_f}{L_t}, \frac{\rho_f}{\rho_w}, \text{specie}, \\ \frac{B}{d_c}, \frac{k_s}{d_c}, \theta, \\ Fr, Re, Mo, \frac{L_t}{d_c}, T_t \times \sqrt{\frac{g}{d_c}}, ... \end{pmatrix} \qquad [5]$$

3.2 Discussion

The present result (Equation [5]) emphasises a number of key parameters and variables relevant to the upstream fish passage in turbulent open channel flows, including the ratio u'/v' of fish speed fluctuations to fluid velocity fluctuations, the ratio τ_f/T_t of fish response time to turbulent time scales, the ratios of fish dimension to turbulent length scale and the fish species. To date, few studies provided quantitative and detailed characteristics of both fish motion and fluid flow (Nikora et al., 2003; Plew et al., 2007). Even fewer studies reported fish speed fluctuations and fluid velocity fluctuations, as well as fish response time and integral time scales (Wang et al., 2016a). The fish swimming accelerations have also important implications in terms of energy expenditure required to swim against the current over a period of time.

The effect of intrusive probe sensor on laboratory hydrodynamics is rarely considered, despite non-trivial flow disturbances and blockage and Equation [2] did not account for such effects. A recent investigation tested systematically the impact of an acoustic Doppler velocimeter (ADV) in a 0.5 m wide channel (Simon and Chanson, 2013). Even though the sampling volume was 50 mm away from the probe head, the submerged ADV system induced some blockage effect which affected adversely the flow motion including increasing locally the water depth and generating some turbulence in the stem wake. Blockage effects were also documented in a 0.25 m wide channel with a 'vane wheel' propeller meter (Wang et al., 2016b). The propeller casing induced some blockage effect, generating a local fluid acceleration around the propeller, with its readings overestimating the longitudinal velocity by 5% to 30% depending upon the propeller elevation. The usage of intrusive instruments in small flumes and tunnels, as seen in Figure 2C, could lead to biased data.

4 FISH KINEMATICS AND ASSOCIATED ENERGY CONSUMPTION

4.1 Basic considerations

When a fish swims upstream in a culvert barrel, its motion provides critical information on locomotion dynamics that can be used to calculate energy expenditure, with significant implications for the understanding of energetics and biomechanics of aquatic propulsion (Lauder, 2015). Assuming carangiform propulsion, the main forces acting on each fish individual include the thrust force, the gravity force, the buoyancy force, the

 ©2017, IAHR. Used with permission / ISSN 1562-6865 (Online) - ISSN 1063-7710 (Print)

shear/drag force, the lift force, the virtual mass force (or inertial force). Newton's law of motion applied to a fish yields:

$$m_f \times \frac{d\vec{U}}{dt} = \vec{F}_{thrust} - \vec{F}_{drag} - \vec{F}_{inertial} - m_f \times \vec{g} + \vec{F}_{lift} + \vec{F}_{buoyancy} \qquad [6]$$

where m_f is the fish mass. The virtual mass force might be neglected when the fish density is about the water density. The buoyancy and lift forces act along the normal direction: *i.e.,* perpendicular to the flow streamlines. The drag force acts along the flow direction, and includes a skin friction component and a form drag component. The former is associated with a boundary layer development along the fish surfaces, while the latter is linked to the vortex and wake development downstream of the fish. For a fish swimming upstream along a streamtube and neglecting the virtual mass force, Newton's law of motion applied to the fish in the longitudinal x-direction yields in first approximation:

$$m_f \times \frac{\partial U_x}{\partial t} = F_{thrust} - F_{drag} - m_f \times g \times \sin\theta \qquad [7]$$

where the forces acting on the fish are the thrust (F_{thrust}), drag force (F_{drag}), and the last term is the gravity force component in the flow direction. For a fish in motion, the drag force may be expressed as (Lighthill, 1969):

$$F_{drag} = C_d \times \rho_w \times (\overline{U_x} + V_x)^2 \times A_f \qquad [8]$$

where C_d is the drag coefficient, U_x is the fish speed positive upstream, V_x is the fluid velocity at the fish location, positive downstream, A_f is the projected area of the fish. $\overline{U_x} + V_x$ is the mean relative fish speed over a control volume selected such that the lateral surfaces are parallel to the streamlines and that it extends up to the wake region's downstream end (Figure 3A) (Alexander, 1982). In Equation [8], the total drag force (F_{drag}) includes a combination of the skin friction on the fish skin surfaces and the form drag and turbulence dissipation in the wake of the fish (Schultz and Webb, 2002).

An estimate of the drag coefficient (C_d) might be derived from trajectory data when the fish drifts (Figure 3B). During drifting in a horizontal channel, the fish deceleration is driven by the drag force. In first approximation, Newton's law of motion becomes:

$$m_f \times \frac{\partial U}{\partial t} \approx -C_d \times \rho_w \times (\overline{U_x} + V_x)^2 \times A_f \qquad [9]$$

Namely the drag force and drag coefficient may be derived from the rate of deceleration, assuming implicitly that the form drag is identical during glide and during thrust, and unaffected by body motion. Figure 3A presents a typical time-variation of fish speed and acceleration during a drift event, for a fish individual swimming next to the corner between a rough sidewall and rough invert (Wang et al., 2016a). For that individual event and fish, Equation [9] gives: $C_d \times A_f = 1.8 \times 10^{-4}$ m^2.

Despite its underlying assumptions, Equation [7] implies that the fish thrust may be derived from the fish acceleration, fish speed and fluid velocity time-series. In turn, the rate of working of the fish and associated energy consumption may be estimated with a fine temporal scale.

The power that the fish expends during swimming is the product of the thrust and the relative fish speed. Neglecting efforts spent during lateral and upward motion, the mean rate of work by the fish is expressed by Equation [10a] (Lighthill, 1960; Behlke et al., 1991). Combining with Equations [7] and [8], it yields Equation [10b]:

$$P = F_{thrust} \times (U_f + V_x) \qquad [10a]$$

$$P = \left(m_f \times \frac{\partial U}{\partial t} + C_d \times \rho_w \times (\overline{U_x} + V_x)^2 \times A_f + m_f \times g \times \sin\theta \right) \times (U_f + V_x) \qquad [10b]$$

with P the instantaneous power spent by the fish to provide thrust and (U_x+V_x) is the local relative fish speed, at the fish location. Equation [10] expresses the rate of working by the fish, to counterbalance the effects of inertia, drag and gravity.

©2017, IAHR. Used with permission / ISSN 1562-6865 (Online) - ISSN 1063-7710 (Print)

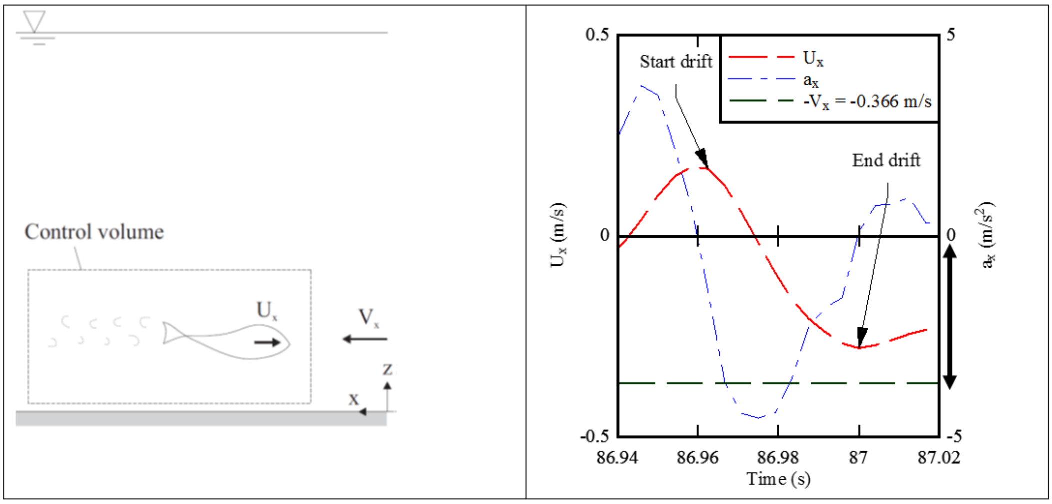

Figure 3. Drag force on a swimming fish (A, Left) Definition sketch of drag force acting on swimming fish. (B, Right) Time-variation of fish speed and acceleration during a drift event - Data from Wang et al. (2016a), Duboulay's rainbowfish No. 22 (m_f = 3.6 g, L_f = 72 mm) swimming along a rough sidewall, fluid flow conditions: V_x = +0.366 m/s, v_x' = 0.315 m/s, θ = 0 - The double-edged arrow shows the relative fish speed $U_x + V_x$.

The energy spent by the moving fish during a time (T) is:

$$E = \int_{t=0}^{T} P \times dt \qquad [11a]$$

$$E = \int_{t=0}^{T} \left(m_f \times \frac{\partial U}{\partial t} + C_d \times \rho_w \times (U_x + V_x)^2 \times A_f + m_f \times g \times \sin\theta \right) \times (U_f + V_x) \times dt \qquad [11b]$$

where t is the time. If T is the time of transit in a culvert structure, Equation [11] provides some estimates of the energy spent by the fish to navigate the culvert, albeit it does not take into account the heat transfer nor any fish metabolism.

4.2 Energetic considerations

The present results provide a deterministic means to quantify the power and energy expended by the moving fish, to counterbalance the drag, inertia and gravity forces (Equations [10] & [11]). Recently, fish kinematic data were recorded with fine spatial and temporal resolution in a 12 m long and 0.5 m wide open channel (Wang et al., 2016a). Figure 4A shows a typical fish trajectory data, with the fish mass and length, and flow conditions listed in the figure caption. The fish swam against the current (*i.e.,* upstream), next to the corner of the channel, exhibiting some carangiform locomotion. For the entire 100 s time series, the fish progressed upstream by 99 mm. Visual recordings, fish trajectory data and fish speed time series showed that the time-series could be sub-divided into some quasi-stationary motion where fish speed fluctuations were small and short upstream burst facilitated by a few strong tail-beats. The instantaneous power and energy spent by the moving fish were calculated using Equations [10] and [11] (Figure 4B). For the same fish and trajectory data shown in Figure 4A, results are presented in Figure 4B. On average, the mean rate of work by the fish was 9.0 mW, with a standard deviation of 2.9 mW, while the first, second and third quartiles were 7.3 mW, 8.7 mW and 10.3 mW, respectively, and the maximum power spent by the fish reached 161 mW. The power distribution was skewed with a preponderance of small power values relative to the mean. Forthe entire trajectory, the energy spent by the moving fish was 0.89 J.

The results may be extrapolated to a 10 m long box culvert barrel, a structure similar to the standard culvert seen in Figure 1A. During the upstream fish migration, assuming that the fish swimming behaviour was identical to the trajectory data shown in Figure 4A, the energy spent by the moving fish would be 89.9 J for a 10 m long horizontal culvert barrel. Assuming that the fish swimming capability and flow conditions are un-affected by the channel slope, Equations [10] and [11] may be applied to test the effects of bed slope (θ) on the same fish individual. For a same 10 m long culvert, the energy spent by the moving fish would be 202 J and 1210 J for a bed slope of θ = 0.05° and θ = 0.5°, respectively. The former slope would be typical of a mild slope flood plain, while the latter would correspond to a steep flood plain. Within the present assumptions, the

 ©2017, IAHR. Used with permission / ISSN 1562-6865 (Online) - ISSN 1063-7710 (Print)

findings suggest that the channel slope may affect significantly the instantaneous power and energy spent by the fish to provide thrust during upstream culvert passage.

More generally, the bed slope has a drastic impact on the optimum design of fish-friendly culverts. With very flat bed slopes, the energy spent by the moving fish to migrate along the culvert is drastically smaller, hence facilitating upstream fish migration, but the head loss available is very small. The latter implies that any baffle system may drastically reduce the discharge capacity for a given afflux, this increasing substantially the cost of the culvert structure. On another hand, a steep bed slope may provide a greater head loss available, allowing for a wider range of baffle systems without adverse reduction in discharge capacity, albeit with a greater power spent by the moving fish. The latter might be particularly detrimental to weak-swimming fish species.

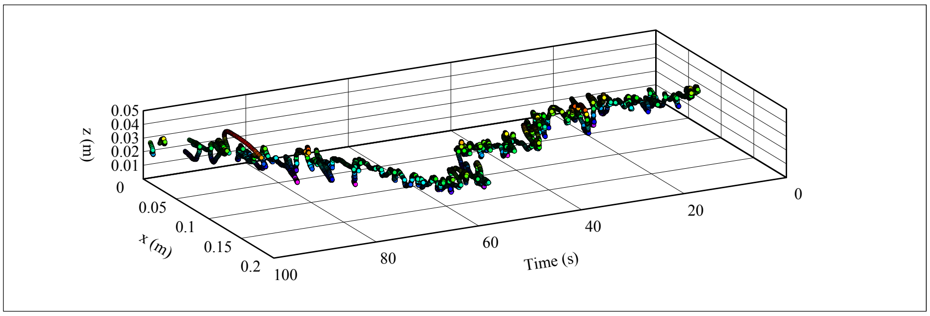

(A)

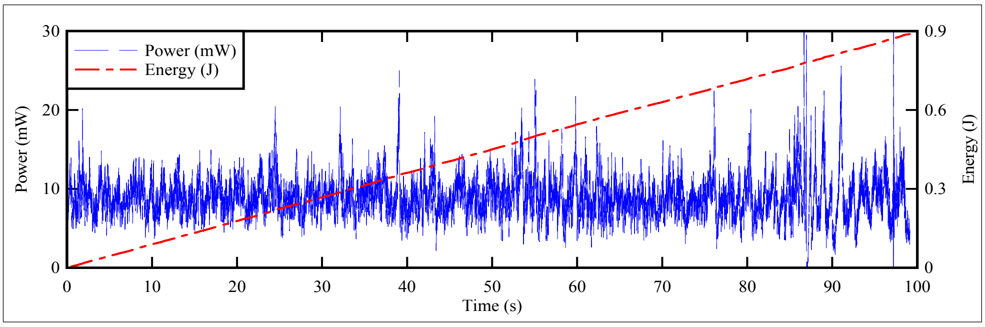

(B)

Figure 4. Time-variations of power expended during fish swimming and energy spent by the moving fish - Data from Wang et al. (2016a), Duboulay's rainbowfish No. 22 (m_f = 3.6 g, L_f = 72 mm) swimming along a rough sidewall in an 0.5 m wide open channel, fluid flow conditions: V_x = +0.366 m/s, v_x' = 0.315 m/s, θ = 0.(A) Fish trajectory next to the left rough sidewall (B) Instantaneous power P and energy E spent by the moving fish during the trajectory shown in Figure 4A.

5 CONCLUSIONS

Standard box culverts may constitute barriers to the upstream passage of weal swimming fish, with adverse impact on the upstream and downstream catchment bio-diversity. It is believed that fish-turbulence interplay may facilitate upstream migration, albeit an optimum design must be based upon a careful characterisation of both hydrodynamics and fish kinematics. Basic dimensional considerations highlight a number of key parameters relevant to the upstream fish passage, including the ratio of fish speed fluctuations to fluid velocity fluctuations, the ratio of fish response time to turbulent time scales, the ratios of fish dimension to turbulent length scale, and the fish species. The latter may be possibly a most important variable, since design guidelines developed for one species might be inadequate for another species.

The application of the equation of conservation of momentum provides a deterministic method to quantify the fish thrust and instantaneous power expended during fish swimming. Using kinematic data recorded with fine spatial and temporal resolution, the associated energy consumption may be estimated and the effects of bed slope be tested. Within basic assumptions, the present findings suggest that the bed slope may have a drastic impact on the optimum design of fish-friendly culverts, since the invert slope affects both the energy spent by the fish to provide thrust during upstream culvert passage and the total head loss available.

The present study paves the way for an improved knowledge of fish-turbulence interplay relevant to upstream fish passage in culverts. This is significant given the recent efforts to design cost-effective standard box culverts with enhanced fish passage capability.

ACKNOWLEDGEMENTS

The authors thank their students Ramith Fernando, Rui Shi, Amelia Tatham, Joseph Dowling, Urvisha Kiri, Caitlyn Johnson and Laura Beckingham (UQ). They further thank Professor Craig Franklin, Dr Matthew Gordos and Dr Pippa Kern for helpful discussions and inputs. The financial support through the Australian Research Council (Grant LP140100225) is acknowledged.

REFERENCES

Alexander, R.M. (1982). *Locomotion of Animals*. Tertiary Level Biology. Chapman and Hall, USA.

Australian Standard (2010). *Precast Reinforced Concrete Box Culverts. Part 1: Small Culverts (Not Exceeding 1200 Mm Span and 1200 Mm Height)*, Standards Australia AS 1597.1-2010, 2nd edition, 245 pages.

Bates, K. (2000). *Fishway Guidelines for Washington State*. Washington Department of Fish and Wildlife, 57.

Behlke, C.E., Kane, D.L., McLeen, R.F. &Travis, M.T. (1991). *Fundamentals of Culvert Design for Passage of Weak-Swimming Fish*, Report FHW A-AK-RD-90-10, Department of Transportation and Public Facilities, State of Alaska, Fairbanks, USA, 178 pages.

Blake, R.W. (1983). *Fish Locomotion*. Cambridge University Press, UK.

Breton, F., Baki, A.B.M., Link, O. Zhu, D.Z. & Rajaratnam, N. (2013). Flow in Nature-Like Fishway and its Relation To Fish Behaviour. *Canadian Journal of Civil Engineering*, 40(6), 567–573.

Brigg, A.S. & Galarowicz, T.L. (2013). Fish Passage through Culverts in Central Michigan Warmwater Streams. *North American Journal of Fisheries Management*, 33(3), 652-664.

Chanson, H. (1999). *Physical Modelling of Hydraulics. In the Hydraulics of Open Channel Flow: An Introduction*. Butterworth-Heinemann, 1st edition, London, UK, Chapter 14, 261-283.

Chanson, H. (2004). *The Hydraulics of Open Channel Flow: An Introduction*. Butterworth-Heinemann, 2nd edition, Oxford, UK, 630 pages.

Chanson, H. & Uys, W. (2016). Baffle Designs to Facilitate Fish Passage in Box Culverts: A Preliminary Study. *Proceedings of 6th IAHR International Symposium on Hydraulic Structures*, *Hydraulic Structures and Water System Management*, Portland OR, USA, 295-304, 312-321.

Chen, S.Y., Fei, Y.H.J., Chen, Y.C., Chi, K.J. & Yang, J.T. (2016). The Swimming Patterns and Energy-Saving Mechanism Revealed from Three Fish in a School. *Ocean Engineering*, 122, 22-31.

Chorda, J., Larinier, M. & Font, S. (1995). *Le Franchissement par les Poissons Migrateurs des Buses et Autres Ouvrages de Rétablissement des Ecoulements Naturels lors des Aménagements Routiers et Autoroutes. Etude Expérimentale*, Rapport HYDRE n°159 - GHAAPPE n°95-03, Groupe d'Hydraulique Appliquée aux Aménagements Piscicoles et à la Protection de l'Environnement, Service d'Etudes Techniques des Routes et Autoroutes, Toulouse, France, 116 pages (In French).

Darrozes, S.S. & Monavon, A. (2014). *Analyse Phénoménologique des Ecoulements. Comment traiter un Problème de Mécanique des Fluides avant de résoudre les Equations*. Presses Polytechniques et Universitaires Romandes, Lausanne, Switzerland, 480 pages (In French).

Duguay, J. & Lacey, R.W.J. (2014). Effect of Fish Baffles on the Hydraulic Roughness of Slip-Lined Culverts. *Journal of Hydraulic Engineering*, ASCE, 141(1), 1-10

Fairfull, S. & Witheridge, G. (2003*). Why do Fish Need to Cross the Road? Fish passage requirements for waterway crossings*, NSW Fisheries, Cronulla NSW, Australia, 1-14.

Forty, M., Spees, J. & Lucas, M.C. (2016). Not Just for Adults! Evaluating the Performance of Multiple Fish Passage Designs at Low-Head Barriers for the Upstream Movement of Juvenile and Adult Trout Salmo Trutta. *Ecological Engineering*, 94, 214-224.

Foss, J.F., Panton, R. & Yarin, A. (2007). *Nondimensional Representation of the Boundary-Value Problem. in Springer Handbook of Experimental Fluid Mechanics*, Springer, Editors C. TROPEA, A.L. YARIN and J.F. Foss, Part A, Chapter 2, 33-82.

Goettel, M.T., Atkinson, J.F. & Bennett, S.J. (2015). Behavior of Western Blacknose Dace in a Turbulence Modified Flow Field. *Ecological Engineering*, 74, 230-240.

Hee, M. (1969). Hydraulics of Culvert Design Including Constant Energy Concept. *Proceeding 20th Conference of Local Authority Engineers*, Dept. of Local Government, Queensland, Australia, 9, 1-27.

Henderson, F.M. (1966). *Open Channel Flow*. MacMillan Company, New York, USA.

Hotchkiss, R. (2002). *Turbulence Investigation and Reproduction for Assisting Downstream Migrating Juvenile Salmonids*, Part I. *BPA* Report DOE/BP-00004633-I, Bonneville Power administration, Portland OR, 138.

Hunt, M., Clark, S. & Tkach, R. (2012). Velocity Distributions near the Inlet of Corrugated Steep Pipe Culverts. *Canadian Journal of Civil Engineering*, 39(12), 1243-1251.

Keele, K.D. (1983). *Leonardo Da Vinci's Elements of the Science of Man*. Academic Press, USA, 1-400.

Larinier, M. (2002). Fish Passage through Culverts, Rock Weirs and Estuarine Obstructions. *Bulletin Français de Pêche et Pisciculture*, 364 (18), 119-134.

Lauder, G.V. (2015). Fish Locomotion: Recent Advances and New Directions. *Annual Review of Marine Science*, 7, 521-545.

Liao, J.C. (2007). A review of Fish Swimming Mechanics and Behaviour in Altered Flows. *Philosophical Transactions of the Royal Society B*, 362(1487), 1973-1993.

 ©2017, IAHR. Used with permission / ISSN 1562-6865 (Online) - ISSN 1063-7710 (Print)

Liggett, J.A. (1994). *Fluid Mechanics*. McGraw-Hill, New York, USA.
Lighthill, M.J. (1960). Note on the Swimming of Slender Fish. *Journal of Fluid Mechanics*, 9(2), 305-317.
Lighthill, M.J. (1969). Hydromechanics of Aquatic Animal Propulsion. *Annual Review of Fluid Mechanics*, 1(1), 413-446.
Liu, M.M., Rajaratnam, N. & Zhu, D.Z. (2006). Mean Flow and Turbulence Structure in Vertical Slot Fishways. *Journal of Hydraulic Engineering*, ASCE, 139(4), 424-432.
Lupandin, A.I. (2005). Effect of Flow Turbulence on Swimming Speed of Fish. *Biology Bulletin*, 32(5), 461-466.
Nikora, V.I., Aberle, J., Biggs, B.J.F., Jowett, I.G. & Sykes, J.R.E. (2003). Effects of Fish Size, Time-to-Fatigue and Turbulence on Swimming Performance: a Case Study of Galaxias Maculatus. *Journal of Fish Biology*, 63(6), 1365-1382.
Novak, P. & Cabelka, J. (1981). *Models in Hydraulic Engineering. Physical Principles and Design Applications*. Pitman Publication, London, UK, 459 pages.
Novak, P., Guinot, V., Jeffrey, A. &Reeve, D.E. (2010). *Hydraulic Modelling - an Introduction*. CRC Press, Taylor & Francis, London, UK, 599 pages.
Olsen, A. & Tullis, B. (2013). Laboratory Study of Fish Passage and Discharge Capacity in Slip-Lined, Baffled Culverts. *Journal of Hydraulic Engineering*, ASCE, 139(4), 424-432.
Papanicolaou, A.N. & Talebbeydokhti, N. (2002). Discussion of Turbulent Open-Channel Flow in Circular Corrugated Culverts. *Journal of Hydraulic Engineering*, ASCE, 128(5), 548–549.
Pavlov, D.S., Lupandin, I.A. & Skorobogatov, M.A. (2000). The Effects of Flow Turbulence on the Behavior and Distribution of Fish. *Journal of Ichthyol*, 40, S232-S261.
Plew, D.R., Nikora, V.I., Larne, S.T., Sykes, J.R.E. & Cooper, G.G. (2007). Fish Swimming Speed Variability at Constant Flow: *Galaxias maculatus*. *New Zealand Journal of Marine and Freshwater Research*, 41(2), 185-195
Plew, D.R., Klebert, P., Rosten, T.W., Aspaas, S. & Birkevold, J. (2015). Changes to Flow and Turbulence Caused by Different Concentrations of Fish in a Circular Tank. *Journal of Hydraulic Research*, IAHR, 53 (3), 364-383.
Rodgers, E.M., Cramp, R.L., Gordos, M., Weier, A., Fairfall, S., Riches, M. & Franklin, C.E. (2014). Facilitating Upstream Passage of Small-Bodied Fishes: Linking the Thermal Dependence of Swimming Ability to Culvert Design. *Marine and Freshwater Research*, 65(8), 710-719.
Schultz, W.W. & Webb, P.W. (2002). Power Requirements of Swimming: Do New Methods Resolve Old Questions? *Integrative and Comparative Biology*, 42(5), 1018-1025.
Simon, B. & Chanson, H. (2013). *Turbulence Measurements in Tidal Bore-like Positive Surges over a Rough Bed,* Hydraulic Model Report No. CH90/12, School of Civil Engineering, The University of Queensland, Brisbane, Australia, 176 pp.
USBR (1987). *Design of Small Dams*. Bureau of Reclamation, US Department of the Interior, Denver CO, USA, 3rd edition.
Wang, H., Chanson, H., Kern, P. & Franklin, C. (2016a). Culvert Hydrodynamics to enhance Upstream Fish Passage: Fish Response to Turbulence. *Proceedings of 20th Australasian Fluid Mechanics Conference*, Australasian Fluid Mechanics Society, G. Ivey, T. Zhou, N. Jones, S. Draper Editors, Perth WA, Australia, Paper 682, 4 pages.
Wang, H., Beckingham, L.K., Johnson, C.Z., Kiri, U.R. & Chanson, H. (2016b). *Interactions between Large Boundary Roughness and High Inflow Turbulence in Open channel: a Physical Study into Turbulence Properties to Enhance Upstream Fish Migration*, Hydraulic Model Report No. CH103/16, School of Civil Engineering, The University of Queensland, Brisbane, Australia, 74 pp.
Wang, R.W., David, L. & Larinier, M. (2010). Contribution of Experimental Fluid Mechanics to the Design of Vertical Slot Fish Passes. *Knowledge and Managementof Aquatic Ecosystems*, 396(02), 21.
Webb, P.W. & Cotel, A.J. (2011). *Stability and Turbulence*. in Encyclopedia of Fish Physiology: from Genome to Environment, Academic Press, Dan Diego, USA, 1-3, 581-586.
Yasuda, Y. (2011). *Guideline of Fishway for Engineers*, Corona Publishing, NPO Society for Fishway in Hokkaido, Japan, 154 pages (In Japanese).

SWIMMING FISH HABITAT EVALUATION CONCEPT FOCUSING ON FLOW CHARACTERISTICS AROUND THE ROUGHNESS LAYER IN STREAMS

MORIHIRO HARADA[(1)], RAHMA YANDA[(2)] , YUKIO ONODA[(3)] & YUICHI KAYABA[(4)]

[(1)]River Basin Research Center, Gifu University, Gifu, Japan
m-harada@green.gifu-u.ac.jp
[(2)] Dept. of Environmental and Renewable Energy System, Graduate School of Eng., Gifu University, Gifu, Japan
u3815005@edu.gifu-u.jp
[(3)] Aqua Restoration Research Center, Public Works Research Institute, Kakamigahara, Japan
onoda77@pwri.go.jp
[(4)] River Restoration Team, Water Environment Research Group, Public Works Research Institute, Tsukuba, Japan
y-kayaba@pwri.go.jp

ABSTRACT

In this paper, a method of habitat evaluation for water-column fish is proposed that focuses on the velocity profile, which is spatially heterogeneous in the roughness layer. Experimental testing is conducted using three different methods to evaluate the habitat volume of swimming fish within the velocity profiles of four different bed conditions. In order to investigate the flow characteristics of the boulder-bed, the first set of experiments was performed within a large flume. After the velocity conditions are confirmed, the activity of living, swimming fish is observed under those conditions for the second set of experiments. *Opsariichthys platypus* (*Zacco platypus*), which is a dominant fish species among Japanese freshwater fish, is used for the living fish experiment. Based on the results of the two experiments, the accuracy of the three methods is analyzed. The first method uses a depth-averaged velocity, the second method uses a velocity profile averaged in the same depth of each of the vertical transects and porosity profile of the bed, and the third method uses the velocity profiles from each of the vertical transects. The second method is found to be the most effective in providing a quantitative estimation for fish habitats with changes in river bed conditions if the averaged velocity profiles are known or predicted by another model, such as the double-averaging method (DAM).

Keywords: Habitat evaluation procedure (HEP), water-column fish, flume experiment, velocity profile, roughness layer.

1 INTRODUCTION

In the upper and middle reaches of rivers, the heterogeneity of a river bed environment is a function of the river bed morphology and sediment sorting. Sediment size and diameter play a considerable role in the latter aspect. From a hydraulics point of view, the flow of water in a boulder- and cobble-bed river with low to intermediate relative submergence is analogous to flow over a surface with large relative roughness. The roughness layer, is located near the river bed; as such, it is a flow region that is strongly affected by bed topography. It provides a heterogeneous hydraulic condition that ensures a wide, three-dimensional flow velocity in the roughness layer (Nikora et al., 2004). In a boulder-cobble bed stream, the thickness of the roughness layer is large compared to the body size of an aquatic species, because of the large roughness elements (boulders). Yanda et al. (2016) investigated the hydraulic characteristic changes within the roughness layer due to bed topography changes and observed the decrease of the roughness layer thickness as the bed roughness was reduced. Therefore, to properly address the habitat quantity and quality of fish in the upper and middle reaches, flow characteristics in the range of low to intermediate relative submergence must be considered. However, current habitat evaluation procedures (HEP) do not consider these flow characteristics. Most habitat suitability index (HSI) models (Waddle, 2001) use depth-averaged velocity for the index velocity. Flow characteristics that vary with changes in the bed condition should also be appropriately considered in a habitat evaluation procedure, because the region of the roughness layer in rivers is used by a variety of fish species in fresh water including benthic, ground fish, and water-column fish.

In this paper, a method is proposed for the habitat evaluation of water-column fish that focuses on the velocity profile, which is spatially heterogeneous in the roughness layer. Experimental testing is conducted using three different methods for evaluating the habitat volume of swimming fishes within the velocity profiles of four different bed conditions. In order to investigate flow characteristics of the boulder-bed, the first set of experiments is performed within a large flume located in the Aqua Restoration Training Center in Gifu, Japan. After the velocity conditions are confirmed, the activity of living, swimming fish is observed under those conditions for the second set of experiments. *Opsariichthys platypus* (*Zacco platypus*), which is a dominant fish species among Japanese freshwater fish, is used in the living fish experiment. Based on the results of the two experiments, the accuracy of these three methods is discussed.

 ©2017, IAHR. Used with permission / ISSN 1562-6865 (Online) - ISSN 1063-7710 (Print)

2 METHODS

2.1 Experimental flume setup and measurements

Figure 1 shows the schematic presentation of the experimental flume. The experimental flume was 1.5 m wide and 25 m long. The artificial boulder-bed longitudinal slope was set to 0.003 (1/300). This setup enabled the simulation of an armor coated boulder-bed, which is typically found downstream of old, large dams (Harada et al., 2014). The four different river-bed conditions were as follow: 1) boulder-only to imitate an armor-coated boulder bed, 2) boulder and gravel set to the first ratio 3) boulder and gravel set to the second ratio and 4) mostly gravel covering over the boulder. In each condition, the stream bed topography was measured using a depth sensor of Kinect for Windows (Microsoft) before and after water passed. The flow discharge was set to 28.0 m^3/min in all cases. Table 1 shows the flow conditions for each case. The average bed height was estimated using the bed topography measurement. The shear velocity was calculated from the average water depth and energy slope by the water level profile. The cross-section average velocity was from 65.9 cm/s to 85.2 cm/s. In case 4, the averaged water depth d_m was larger than case 3 in spite of the bed condition being smoother.
The cause of this can be explained as follows: the water level reached the top cover of the cage at the downstream end, because the average bed height was sufficiently high. This caused a water level rise in the upstream section of case 4.

The velocity measurement was conducted in the vertical transects along the line (as shown in Figure 2) with the use of an acoustic Doppler velocimeter (MicroADV 16MHz down-looking type, Sontek). The number of vertical transects was 10 for cases 1, 2, and 3 for cases 3, 4, respectively. The longitudinal spacing of transects was 10 cm. Vertical measurements were conducted with a spacing of 1.0 cm starting from the bed height to half of the water depth, and then followed by a spacing of 2.0 cm until close to the water surface. The sampling rate of ADV was set to 50 Hz and the measurement period of velocity was greater than 40 seconds for each point.

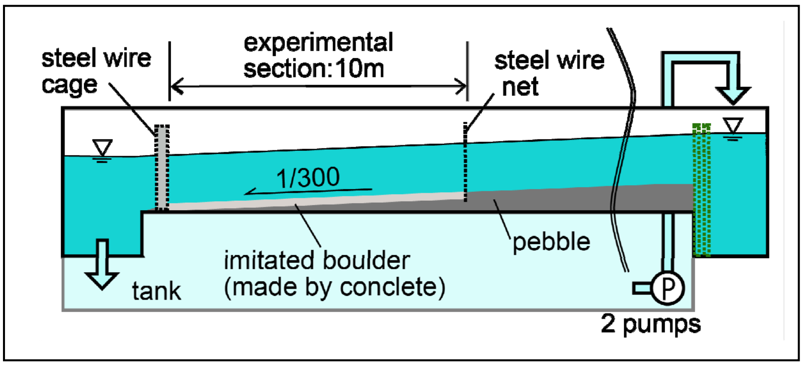

Figure 1. Schematic image of experimental flume

Table 1. Flow condition

Case	Discharge Q [m^3/min]	Average bed height from datum Z_m [cm]	Average water depth d_m [cm]	Shear velocity U* [cm/s]	Cross-sectionaverage velocity V_m [cm/s]
1	28.0	-4.2	47.2	6.4	65.9
2	28.0	-1.7	43.7	7.4	71.1
3	28.0	0.5	36.5	7.4	85.2
4*	28.0	8.1	38.9	9.0	80.0

*Not entirely accurate because the water level reached the top cover of the cage at the downstream end

©2017, IAHR. Used with permission / ISSN 1562-6865 (Online) - ISSN 1063-7710 (Print)

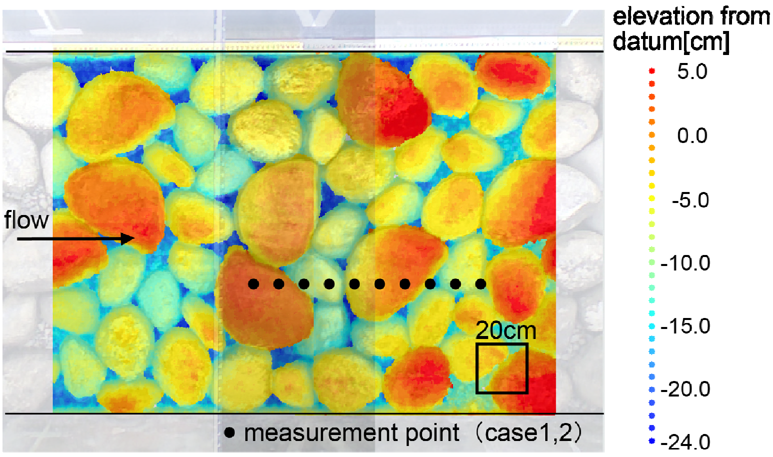

Figure 2. Bed topography (case1) and arrangement of velocity measurement transect

2.2 Living fish experiment

For the living fish experiment, the experimental section of the flume was confined to 10 m in length using a steel wire net to prevent the fish from escaping. In each river-bed condition scenario, 30 *Opsariichthys platypus*fish (average total length (TL) =11.7 cm and average body length (BL) =9.7 cm, N=120) were placed in the experimental section. After the fish became acclimated to the water conditions and environment, fish activity was observed through an acryl side wall from an underground darkroom beside the flume (Figure 3).

To evaluate the suitability as a swimming habitat, the positions of individual swimming fish were observed and recorded several times (N=3 to 9). The position of each fish was categorized into three parts, (a) experimental section, (b) downstream end, and (c) upstream end. The population that was not observed was classified as (d) lost or hidden. It was observed that individual fish could not continue swimming in the experimental section and tended to gather around the (b) downstream end or (c) upstream end. This was because the steel wire net made the flow velocity slower around the upstream end of the experimental section. Moreover, the region near the steel wire cage in the downstream end was not the preferable location for fish.

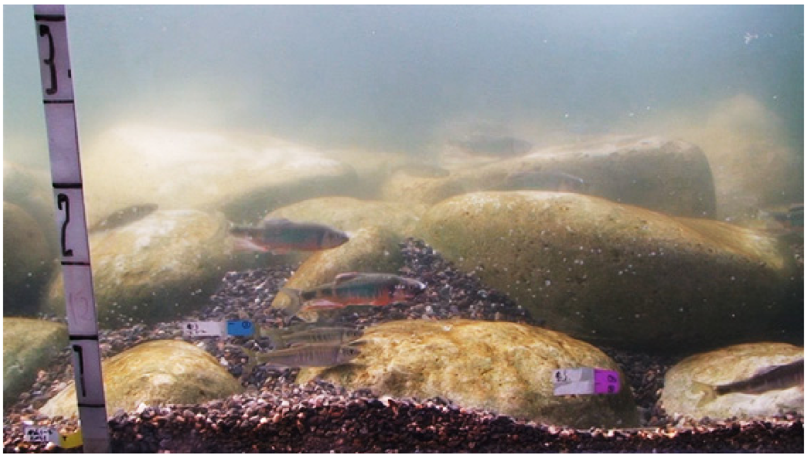

Figure 3. Observation of fish activity through the acryl side wall

2.3 Habitat evaluation

Three habitat evaluation methods were applied to the measurement results. The cruising speed of the swimming fish was used as the index velocity for the swimming fish habitat. According to past studies on fish physiology (Brett, 1964; Videler et al., 1991), the cruising speed is different for each species, and also varies with water temperature. The cruising speed of swimming fish is often expressed by multiplying the body length (standard length) by from two to four around. For this study, the index velocity was set as three times the body length (3BL), 30cm/s, with an average body length (BL) of 9.7 cm. Figure 4 shows the relationship between measurement, analysis and evaluation methods. Each method involved the evaluation of the specific volume where the flow velocity was below the index velocity. The first method used a depth-averaged velocity, the second method used a velocity profile that was averaged in the same depth of each vertical transect (double-averaged streamwise velocity profile) and porosity profile of the bed surface, and the third method used the velocity profiles from each of the vertical transects directly.

 ©2017, IAHR. Used with permission / ISSN 1562-6865 (Online) - ISSN 1063-7710 (Print)

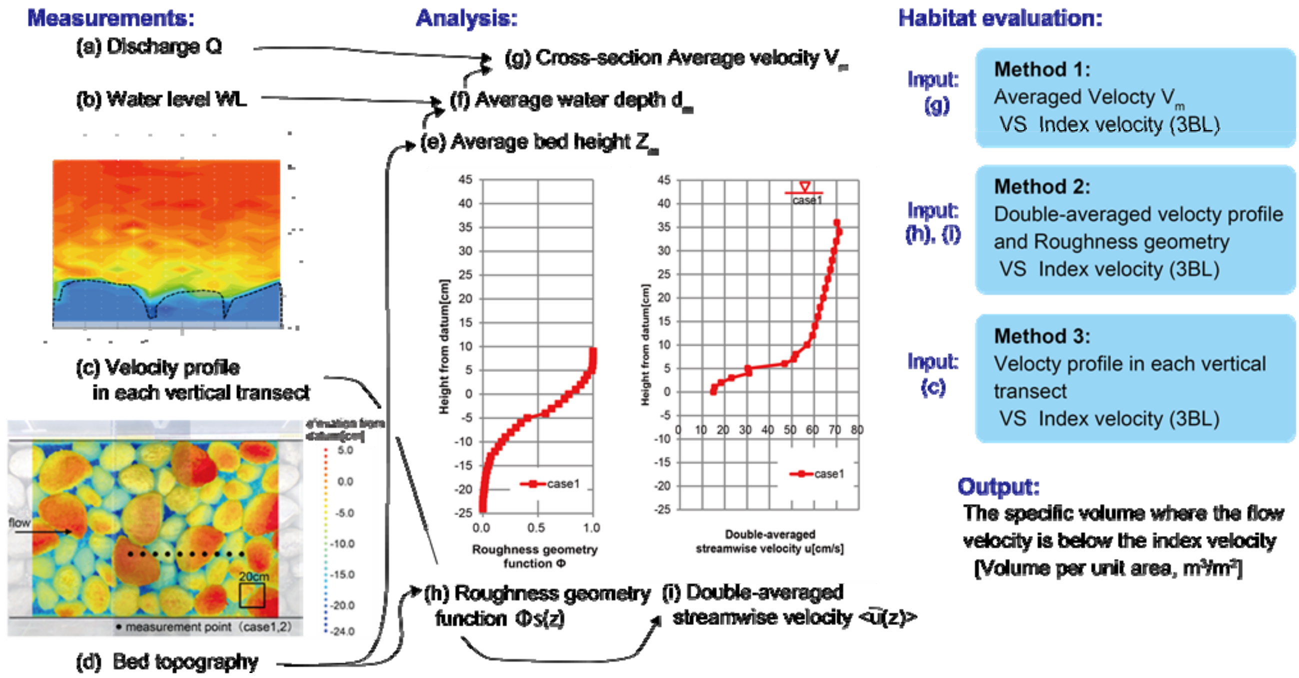

Figure 4. Swimming fish habitat evaluation methods

3 RESULTS AND DISCUSSION

3.1 Velocity distribution and bed topography

Figure 5(a) shows the porosity profiles that were calculated from the bed topography measured by the Sensor Kinect. Adding gravels (cases 2 to 4) resulted in the increase of the average bed height and reduction in the thickness from the lowest point to the highest point. In other words, the thickness of the interfacial sublayer (Nikora and McLean, 2007) decreased. This porosity profile was defined as the roughness geometry function ($\Phi s = V_f / V_0$, where V_f is the volume of fluid and V_0 is the total volume). The double-averaged (time-space averaged) velocity profiles are shown in Figure 5(b). In response to the change in the bed condition, the velocity near the bottom largely increased.

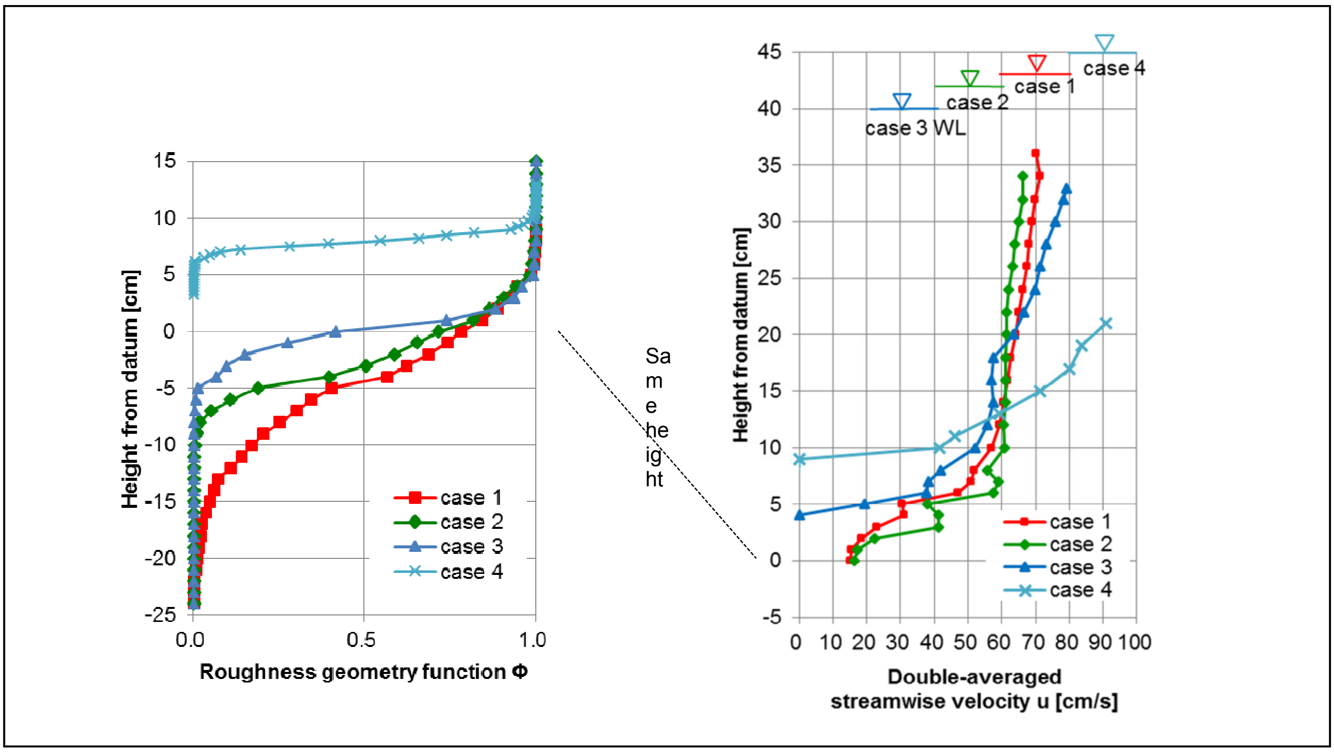

Figure 5(a). Porosity profiles **Figure 5(b)**. Double-averaged velocity profile
(Roughness geometry function Φs)

©2017, IAHR. Used with permission / ISSN 1562-6865 (Online) - ISSN 1063-7710 (Print)

3.2 Swimming fish activity

In case1, 60% of the fish continued swimming and remained within the experimental section; others tried to escape or were lost (not found) in the section. As bed conditions began to vary from cases 2-4, the number of fish that continued staying in the experimental section declined until eventually reaching 20% of the original number. However, in case 4, the fish population that continued swimming in the experimental section was larger than in case 3. As shown in Table 1, the average velocity in case 4 was smaller than in case 3, because of the water level rising near the downstream end. This was regarded as the primary cause of the tendency that case 3 and case 4 reversed.

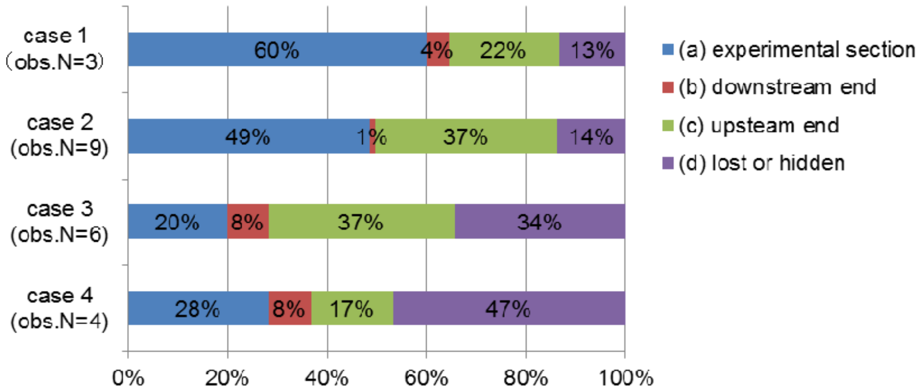

Figure 6. Observed position of individual fish

3.3 Habitat evaluation

The specific volume at which the flow velocity was below the index velocity is shown in Figure 7. The first method indicated that there was no habitat because the depth average velocity exceeded the index velocity (3BL, 30cm/s). The second and third methods indicated that there were some volumes around the bottom (0.02-0.08 m^3/m^2). The space volume in which the fish could continue swimming in the roughness layer was counted. The third method tended to have smaller evaluation values than the second method. The order of the evaluation value of the second method and the third method was 1,2,4,3 and 1,3,4,2, respectively.

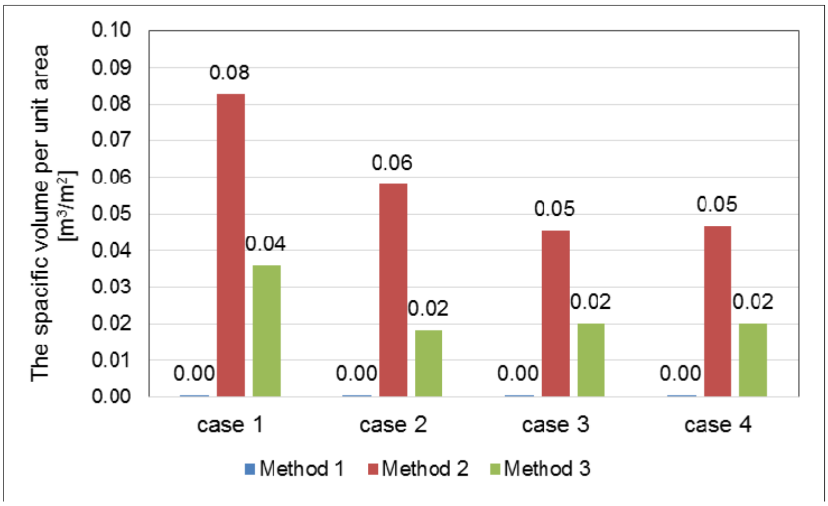

Figure 7. Evaluation result: the specific volume where the flow velocity is below the index velocity (3BL)

3.4 Discussion

From the living fish experiment, it was observed that the fish could continue swimming even if the average velocity exceeded their cruising speed (see Figures 3 and 6). From the double-averaged velocity profiles shown in Figure 5(b), the space where the flow velocity was below the index velocity was observed near the bottom. This domain was located below the highest point of the channel bed. The domain in which the fish could continue swimming is presumed to be in the roughness layer, particularly in the interfacial sublayer in this experiment. The habitat evaluation method that uses depth-averaged velocity is not able to successfully evaluate this situation. Hence, the second and third methods are considered superior to the first method. To analyze the accuracy of the second and third methods, Figure 7 was compared with Figure 6. Figure 6 portrays the percentage of (a) expressed suitability for the swimming fish habitat. The difference in the results of the two methods was not substantial. The second method clearly expressed the order of (a),

 ©2017, IAHR. Used with permission / ISSN 1562-6865 (Online) - ISSN 1063-7710 (Print)

and the third method was more complicated. In summary, the second method is better for providing a quantitative estimation of a fish habitat in consideration of changes in river bed conditions. In addition, the second method is more practical to employ. Habitat evaluation in consideration of the existence of the roughness layer is enabled by combining this method with the double-averaging concept for rough-bed open channel.

4 CONCLUSIONS

In this study, experimental testing is conducted using three different methods for evaluating the habitat volume of swimming fishes within the velocity profiles of four different bed conditions. In order to investigate flow characteristics of the boulder-bed, the first set of experiments is performed within a large flume. After confirmation of correct velocity conditions, the activity of living, swimming fish is observed in those conditions for the second set of experiments. Based on these results, the accuracy of the three methods is discussed. In conclusion, the second method, which uses the double-averaged velocity profile and the roughness geometry, is found to provide the best quantitative estimation for fish habitat with changes in river bed conditions.

ACKNOWLEDGEMENTS

The research reported herein is partly supported by JSPS KAKENHI Grand Number 16K2107403.

REFERENCES

Brett, J. R. (1964). The respiratory metabolism and swimming performance of young sockeye salmon. *Journal of the Fisheries Board of Canada*, 21(5), 1183-1226.

Harada, M., Yukio, O. & Yuichi, K. (2014). A study on effects of sediment supply on fish habitat of boulder-bed rivers, *Journal of Japan Society of Civil Engineers*, Ser. B1 (Hydraulic Engineering), 70(4),1339-1344. (In Japanese).

Nikora, V., Koll, K., McEwan, I., McLean, S. & Dittrich, A. (2004). Velocity distribution in the roughness layer of rough-bed flows. *Journal of Hydraulic Engineering*, 130(10), 1036-1042.

Nikora, V. & McLean, S. (2007). Double-averaging concept for rough-bed open-channel and overland flows: Applications. *Journal of hydraulic Engineering*, 133(8), 884–895.

Videler, J. J. & Wardle, C. S. (1991). Fish swimming stride by stride: speed limits and endurance. *Reviews in Fish Biology and Fisheries*, 1(1), 23-40.

Waddle, T. (2001). *PHABSIM for Windows user's manual and exercises.*PHABSIM (No. 2001-340, pp. 0-288).

Yanda, R.Harada,M. & Tamagawa,I. (2016). The Effects of Sediment Supply on Hydraulic Characteristics of Flow over the Imbricated Cobbles, *Journal of Japan Society of Civil Engineers*, Ser. B1 (Hydraulic Engineering), 72(4):613-618.

Proceedings of the 37th IAHR World Congress
August 13 – 18, 2017, Kuala Lumpur, Malaysia

TRANSVERSE MIXING COEFFICIENT IN RANDOM CYLINDER ARRAYS – A CFD VALIDATION STUDY

MAHSHID GOLZAR(1), FRED SONNENWALD(2), IAN GUYMER(3) & VIRGINIA STOVIN(4)

(1,2,4) Department of Civil and Structural Engineering, University of Sheffield, Sheffield, UK
(1) mgolzar1@sheffield.ac.uk
(3) School of Engineering, University of Warwick, Coventry, UK
(3) I.Guymer@warwick.ac.uk

ABSTRACT

Understanding the flow and mixing processes in vegetated flows is essential for hydraulic engineers to be able to improve the performance of water bodies such as treatment wetlands and ponds. Cylinder arrays have been used in several laboratory studies, but such studies are time-consuming. The aim of this paper is to find an efficient, alternative, validated, way for conducting such studies. Traditional Computational Fluid Dynamics (CFD) models can be considered as an alternative. A previous laboratory study on transverse dispersion coefficients within random cylinder arrays, Tanino and Nepf (2008) is modelled in ANSYS Fluent 16.1. The Reynolds Stress turbulence closure model is used to solve the steady sate flow field. A transient scalar model has been used to model tracer dispersion within the arrays. The resulting CFD generated transverse dispersion coefficients are then compared with the previously reported laboratory ones. The comparison shows acceptable agreement between the CFD and laboratory data, which leads to the validation of the method used in this study. The results of this study demonstrate the potential of CFD models to be used as an efficient way for studying flow and mixing within artificially vegetated flows.

Keywords: CFD; random cylinder array; transverse dispersion coefficient; scalar transport; validation.

1 INTRODUCTION

Vegetated flows play a significant role in environmental processes. Considering their protecting effect on natural water bodies ponds and wetlands are clear examples of such roles. For hydraulic engineers to be able to improve the performance of such treatment bodies, it is essential to understand the characteristics of flow and mixing taking place within them. Several studies were performed to fulfill this purpose, and all suffer from a common disadvantage that is being extremely time-consuming even to model the simplest models of vegetated flow in laboratory. This problem has resulted in limited data on mixing in simple representations of vegetated flows, i.e. cylinder arrays. Thus finding a more efficient way of representing and investigating the flow and mixing within such flows is required.

Certain aquatic vegetation types are approximately cylindrical (Tanino and Nepf, 2009); therefore cylinder arrays as a simple yet representative laboratory set of the vegetated flows have been used in several laboratory studies e.g. White and Nepf (2003); Hamidifar et al. (2015); Sonnenwald et al. (2016).

The aim of this study is to validate the CFD modelling methodology as an efficient alternative method for investigating the mixing characteristics of cylinder arrays. After a brief introduction on the laboratory data used for validation, the methodology is explained in detail. The post processing and results are discussed afterwards and finally the CFD results are compared with the laboratory data.

2 LABORATORY DATA USED FOR VALIDATION

A laboratory investigation of transverse dispersion coefficient, D_y, within randomly distributed emergent cylinders with diameter, d=0.0064 m, was undertaken by Tanino (2008). The arrays were built based on solid volume fractions of ϕ=0.010-0.350. A range of mean pore velocities, U_p, were tested and the transverse dispersion coefficient was measured for each case, over variable longitudinal distances from injection point, x. It was suggested, and experimentally shown, that the net transverse dispersion can be expressed as the linear superposition of turbulent diffusion and mechanical dispersion, caused by the heterogeneous velocity field within the array. A more detailed explanation can be found in Tanino and Nepf (2008) and Tanino (2008). The reported results and characteristics of the laboratory setup are presented in Table 1, in which $\langle Sn \rangle_A$ is the average surface-to-surface distance between a cylinder in the array and its nearest neighbour, Re_d and $Re_{\langle Sn \rangle_A}$ are the stem diameter and pore Reynolds numbers respectively, and n is the number of cases for which $Re_{\langle Sn \rangle_A} > 74$ (ϕ=0.010-0.270) and $Re_{\langle Sn \rangle_A} > 53$ (ϕ=0.350).

 ©2017, IAHR. Used with permission / ISSN 1562-6865 (Online) - ISSN 1063-7710 (Print)

Table 1. Experimental condition of laboratory data used for validation (Table 3.3 from Tanino, 2008, all values are presented here with the original precision)

ϕ	$d/\langle S_n \rangle_A$	$K_{yy}/(U_p d)$	n	U_p [m/s]	Re_d	$Re_{\langle Sn \rangle A}$	x/d
0.010	0.28	0.21±0.02	51	0.014-0.031	83-190	290-660	55-168
0.031	0.58	0.24±0.01	56	0.010-0.027	67-180	120-310	7-174
0.060	0.93	0.20±0.01	44	0.015-0.026	97-170	100-180	23-124
0.091	1.3	0.18±0.01	61	0.032-0.066	230-480	180-370	22-134
0.15	2.0	0.17±0.01	35	0.031-0.058	190-370	94-180	43-223
0.20	2.7	0.13±0.01	48	0.038-0.065	210-340	78-130	80-225
0.27	4.0	0.17±0.02	36	0.045-0.070	300-480	74-120	27-152
0.35	5.9	0.24±0.02	16	0.046-0.056	320-390	53-66	36-145

3 METHODS

The experiments were modelled using ANSYS Fluent 16.1 (ANSYS® Academic Research, Release 16.1). The model built to regenerate each data point is explained in detail in §3.1. Limitations of the mesh building tool in ANSYS 16.1, mean that the maximum ϕ that may be represented decreases as the physical size of the channel model increases. It was therefore necessary to decide on the minimum channel length and width that would be representative for the mixing characteristics of the array. The scalar transport steps are explained in §3.2. The results are presented in §4.2, and the modelled outputs are compared with the laboratory reported data in §4.3.

3.1 Flow Setup

The process of finding the minimum representative channel length and width is explained in this section. The rest of the models were built based on the same method but with a different geometry, i.e. with the minimum representative channel length and width but differing solid volume fractions.

3.1.1 Geometry

The initial set-up was based on the ϕ=0.010 scenario, i.e. the first row in Table 1. A two dimensional 0.40 m wide, 1.40 m long channel, with 175 cylinders of 0.0064 m diameter resulting in a solid volume fraction of ϕ=0.010 and frontal facing area per unit volume of a=2.00 m^{-1} was set as the geometry. The cylinders were randomly distributed along the channel using the rand function of MATLAB allowing a distance of 0.002 m from the channel edges and so that stems did not overlap. The laboratory cylinder array was built using a similar approach (Tanino 2008). This arrangement of cylinders resulted in an average edge to edge spacing of $\langle Sn \rangle_A$= 0.021 m.

The channel was modelled in 2D. The array used in the laboratory study was vertically uniform and the vertical profiles of longitudinal velocity (Figure 3-7 in Tanino, 2008) showed that the vertical variations in velocity were negligible comparing to transverse ones. Therefore one can justify that a two dimensional model can be representative of the laboratory channel and the CFD results can be comparable to the laboratory ones.

3.1.2 Mesh

The channel was meshed with global 0.001 m mesh cells. The model was proved to be mesh-independent at this size. Then the region surrounding each of the cylinders was meshed with a 3 level finer mesh, in a way that each edge was meshed with 80 cells of 0.00025 m, which in total summed up to 689,778 nodes and 1,362,316 elements for the whole channel. All the mesh cells were triangular, built based on the proximity and curvature Advanced Size Function. This function is designed by ANSYS to automatically refine the mesh based on local proximity and local curvature of the geometry. Both the inlet and outlet of the channel were match controlled making it possible to set a periodic boundary condition, as will be explained in the next section. A sample of meshing around the cylinders is shown in Figure 1.

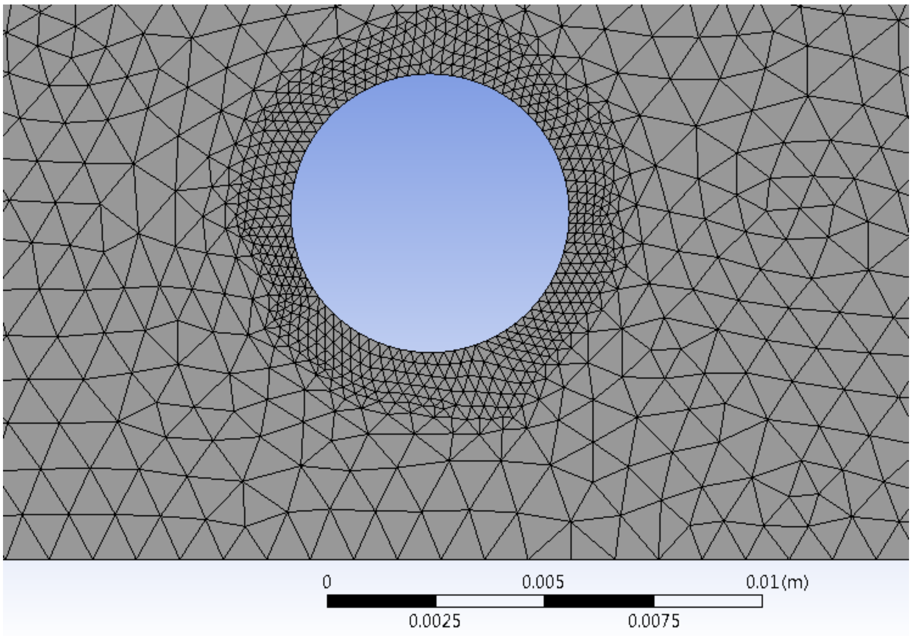

Figure 1. A sample of meshing around the cylinders. Cylinders were 0.0064 m in diameter.

3.1.3 Boundary conditions and flow set-up

The inlet and outlet boundaries were set as periodic boundaries which was chosen to provide a developed flow field independent of the length of the channel. The inlet mass flow was set equal to 8.983 kg/s which is equivalent to inlet velocity of 0.023 m/s. This inlet velocity is the mean value of the reported U_p range used in the laboratory for this solid volume fraction, ϕ=0.010, i.e. U_p = 0.014-0.031 m/s in Table 1. The Reynolds Stress Model (RSM with 5 equations) turbulence closure model was set along with the enhanced wall treatment as the near-wall treatment method. This model is the most complete 2D turbulence model available in ANSYS Fluent as it allows for anisotropic Reynolds stresses develop. The RSM model constants were left at default values. All the cylinder edges and the left and right sides of the channel were set as wall boundaries with no slip condition. The method for spatial discretization of all the variables was set to second order upwind using the coupled scheme solver.

3.2 Scalar Transport Setup

After solving the flow and turbulence equations in steady state, the model was switched to transient and set for scalar transport modelling. A user defined scalar was defined with the same density and molecular diffusivity as water and the Schmidt number of 1.0. The spatial discretization of the scalar and the transient formulation were set to second order upwind and second order implicit, respectively. The flow and turbulence equations were deactivated and the scalar was released at the injection point, as shown in Figure 2, for 100 time steps of Δt=0.01 s i.e. a 1.00 second pulse injection. The model is time-step insensitive at this time-step.

Once the pulse injection was stopped, simulation was continued at Δt=0.01, allowing the scalar to be advected and dispersed along the channel. Two lines were defined at x=0.05 m and x=1.35 m to remove the scalar from the channel before and after each in order to stop the plume recirculating through the periodic boundary, (the lines are shown in Figure 2). The scalar concentration was recorded at each time step at every 0.05 m over 25 cross-sectional recording lines also shown in Figure 2. This concentration data was then used to calculate the longitudinal and transverse dispersion coefficients. Note that the longitudinal dispersion coefficients are not discussed further within this paper.

Considering the available two dimensional mixing data for this model, both two and one dimensional optimizations were possible to estimate the dispersion coefficients. A comparison between two and one dimensional optimizations on the advection-dispersion coefficient was performed by Sonnenwald et al. (2017) for a similar problem and it was shown that the difference is negligible. So in this study one dimensional optimizations were done separately for each dimension, to estimate the longitudinal and transverse mixing coefficients.

The longitudinal dispersion coefficient was calculated based on a one dimensional optimization of the routing solution to the longitudinal advection-dispersion equation:

$$\frac{\partial C}{\partial t} + u\frac{\partial C}{\partial x} = D_x\frac{\partial^2 C}{\partial x^2} \qquad [1]$$

©2017, IAHR. Used with permission / ISSN 1562-6865 (Online) - ISSN 1063-7710 (Print)

where C is the tracer concentration; t is time; u is the longitudinal velocity and D_x is the longitudinal dispersion coefficient, (Rutherford 1994).

It should be mentioned that the longitudinal optimization was done first and the resulting optimized longitudinal velocity was used for estimating travel time in the optimization of D_y. The optimized longitudinal velocity values were also used for non- dimensionalizing the transverse dispersion coefficient.

Concentration values were temporally averaged over each recording line, resulting in concentration versus transverse distance profiles for each cross section. Between each pair of cross sections, the downstream concentration was predicted and the transverse dispersion coefficient was estimated based on a one dimensional optimization of the routing solution to the transverse advection-dispersion equation:

$$\frac{\partial C}{\partial t} + v\frac{\partial C}{\partial y} = D_y\frac{\partial^2 C}{\partial y^2} \qquad [2]$$

where v is the transverse velocityy is the transverse distance; and D_y is the transverse dispersion coefficient (Rutherford, 1994).

4 RESULTS

The resulting flow field and mixing characteristics for the sample model are presented in §4.1 and § 4.2 respectively. Justification for the minimum representative channel size is provided in §4.3 and all the CFD results are compared with the laboratory data in §4.4.

4.1 Flow Results

The resulting u-velocity field after solving the flow and turbulence equations, for the sample geometry is shown in Figure 2.

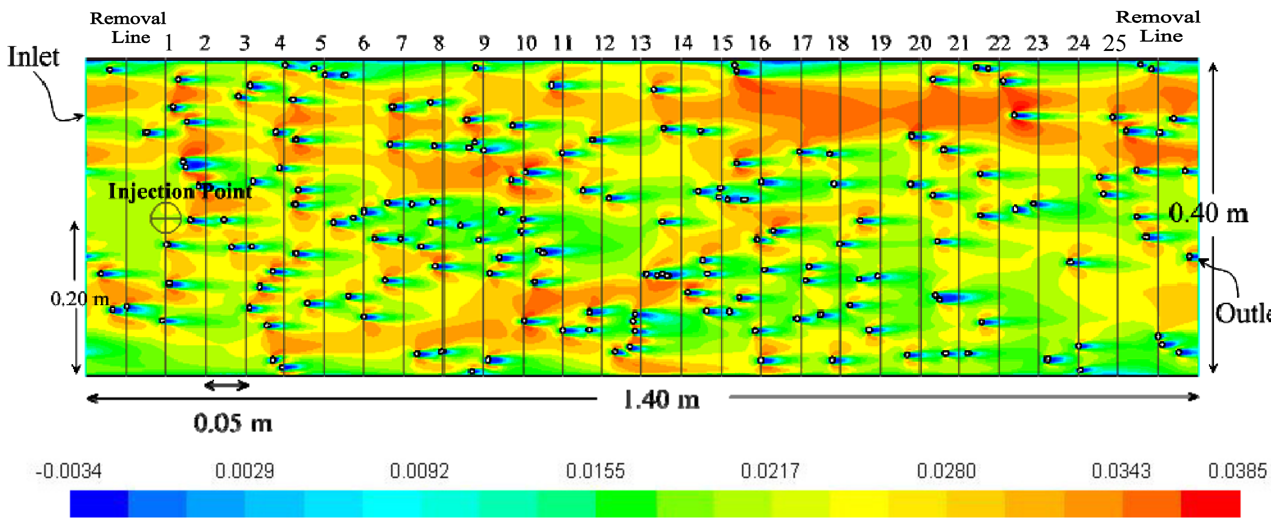

Figure 2. u-velocity contours, ϕ=0.010, inlet velocity=0.023 m/s

4.2 Scalar Transport Results

A sample of the downstream and upstream transverse concentration profiles along with the predicted downstream concentration profile is presented in Figure 3. The longitudinal concentration profiles are also shown in Figure 3.

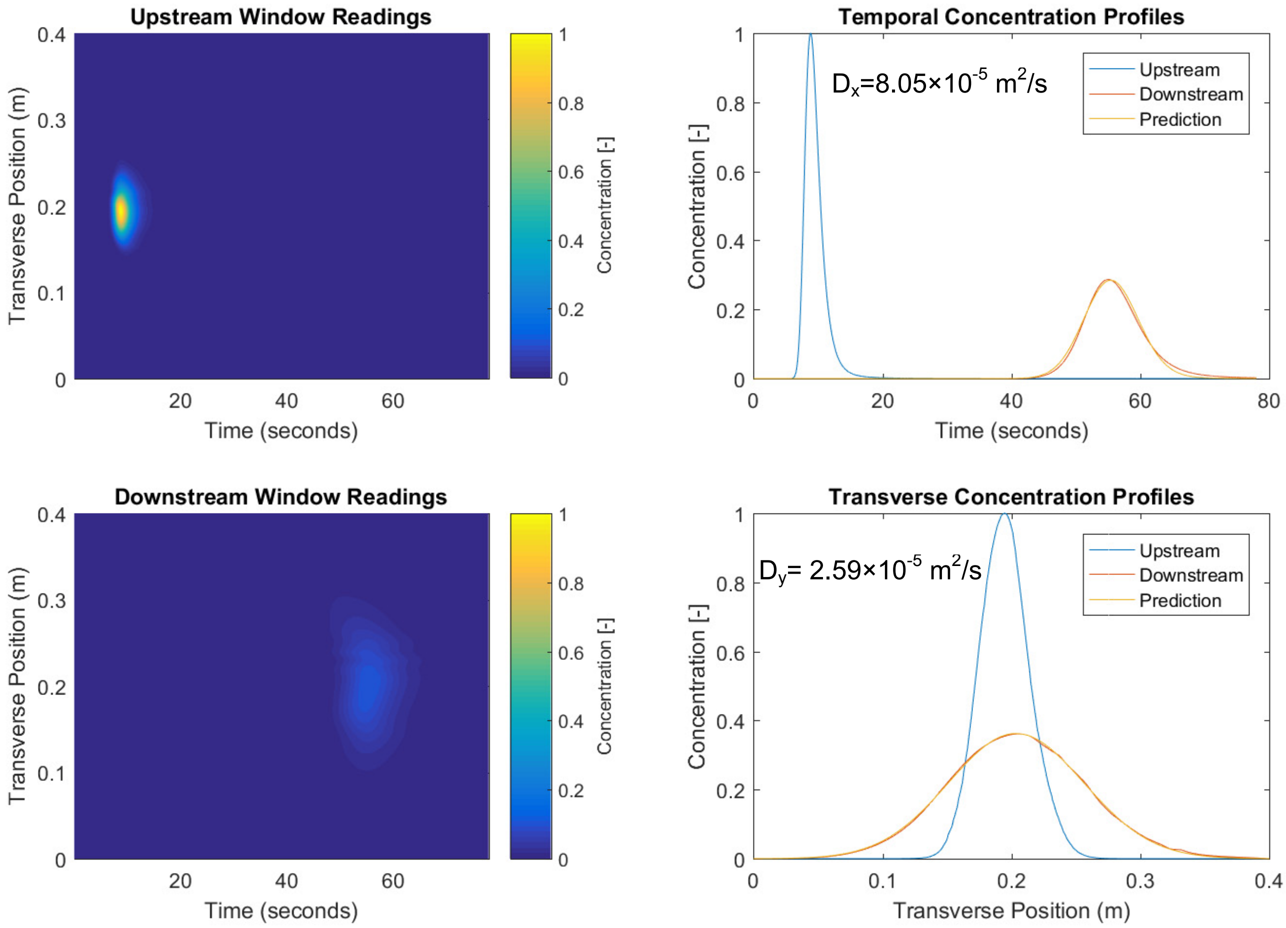

Figure 3. A sample plot of upstream and downstream concentration along with the predicted downstream concentration (upstream=cross section No. 5 and downstream=cross section No. 25 on Figure 2.)

4.3 Finding the minimum representative channel size

The transverse dispersion coefficients were estimated between each possible pair of cross sections and then were grouped based on the distance between the upstream and downstream cross sections. The injection point cross section was not considered to avoid possible numerical dispersion. So from cross section number 2 to cross section number 25 there are 299 different possible scenarios grouped in 24 groups of 0.05 m to 1.15 m small longitudinal channel units, with 0.05 m intervals. The mean standard deviation of trnsverse disperision coefficent of each group was calculated and is shown in Figure 4.

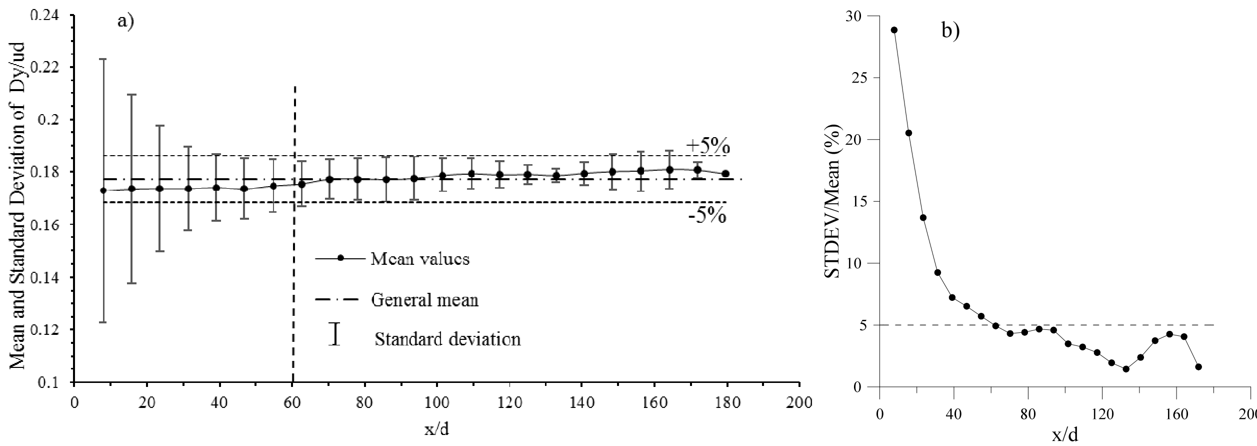

Figure 4. a) Mean and standard deviation and b) Non-dimensional standard deviation of non-dimensional transverse dispersion coefficient for ϕ=0.010

 ©2017, IAHR. Used with permission / ISSN 1562-6865 (Online) - ISSN 1063-7710 (Print)

Taking a standard deviation of less than 5% of the mean value as a criterion for an acceptable value, then one can say that, for ϕ=0.010, the minimum length required to fulfil this criterion is 0.384 m.

If the above conclusion is generalized, and also assuming that with increasing the solid volume fraction the required representative array length decreases, then the minimum required length would be 0.38 m or less. The spread of the plume over the width of the channel over the longitudinal distance of 0.35 m, i.e. from cross section No. 2 to cross section No. 9 in Figure 2, is less than 0.20 m, Figure 5.

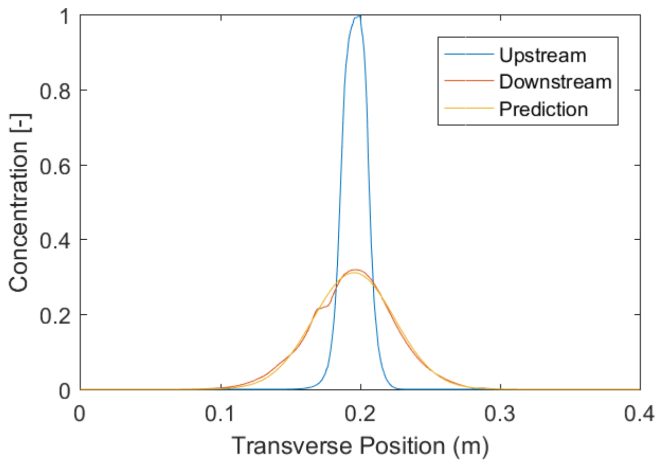

Figure 5. The spread of tracer plume over the channel width (upstream=cross section No. 2 and downstream=cross section No. 9 on Figure 2.)

Thus, the rest of the cases were built as 0.20 m (wide) × 0.60 m (long) channels. Considering the upstream and downstream tracer removal lines at x=0.05 m and x=0.55 m respectively, and the injection point at x=0.10 m, this leaves 0.35 m for the tracer to be advected and dispersed over the channel length and width. The rest of cases with different solid volume fractions presented in Table 1 were modelled based on the same method as was explained above. The resulting transverse dispersion coefficients are compared with the laboratory data in § 4.4.

4.4 Validation

Eight geometries, representing the different values of solid volume fractions presented in Table 1, were modelled following all the procedures explained above. Three different inlet velocities, i.e. the minimum, mean and maximum of the reported range of velocities in Table 1, were set as input velocity for each geometry. An example of channel geometry with u-velocity contours for ϕ=0.091 and inlet velocity of u_{inlet}=0.049 m/s is shown in Figure 6. The scalar was injected at x=0.10 m from the inlet and its concentration was recorded at every 0.05 m. The transverse dispersion coefficient was then estimated based on the concentration on cross section number 2 (at x=0.15 m) and cross section number 9 (at x=0.50 m).

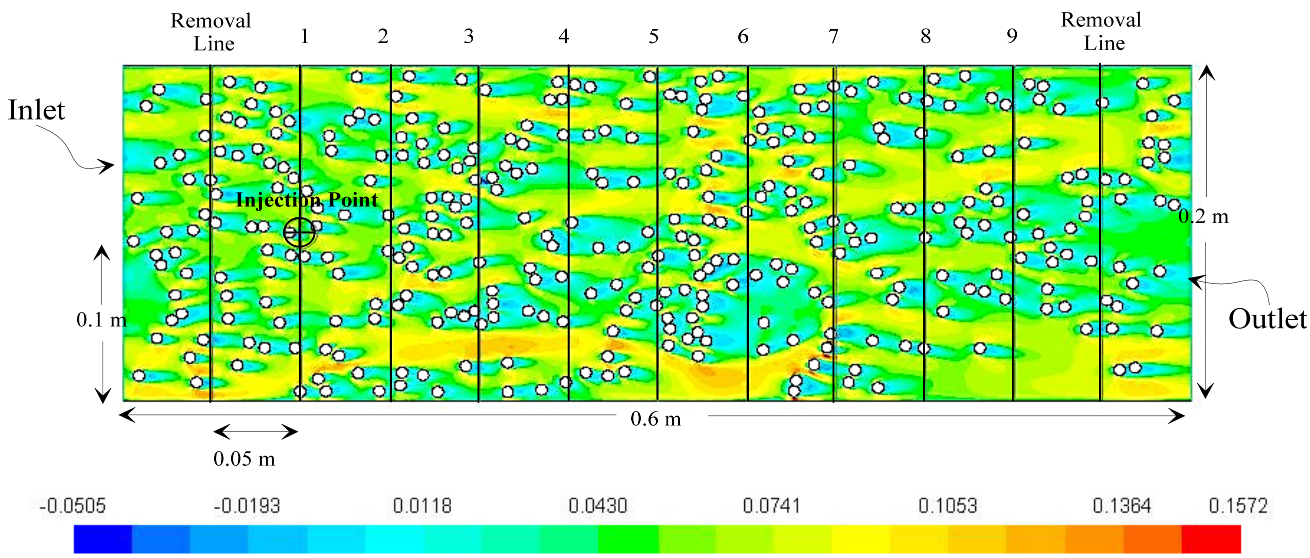

Figure 6. u-velocity contours, ϕ=0.091, the inlet velocity=0.049 m/s

A sample of upstream and downstream concentration profiles along with the predicted downstream concentration for ϕ=0.091 is shown in Figure 7.

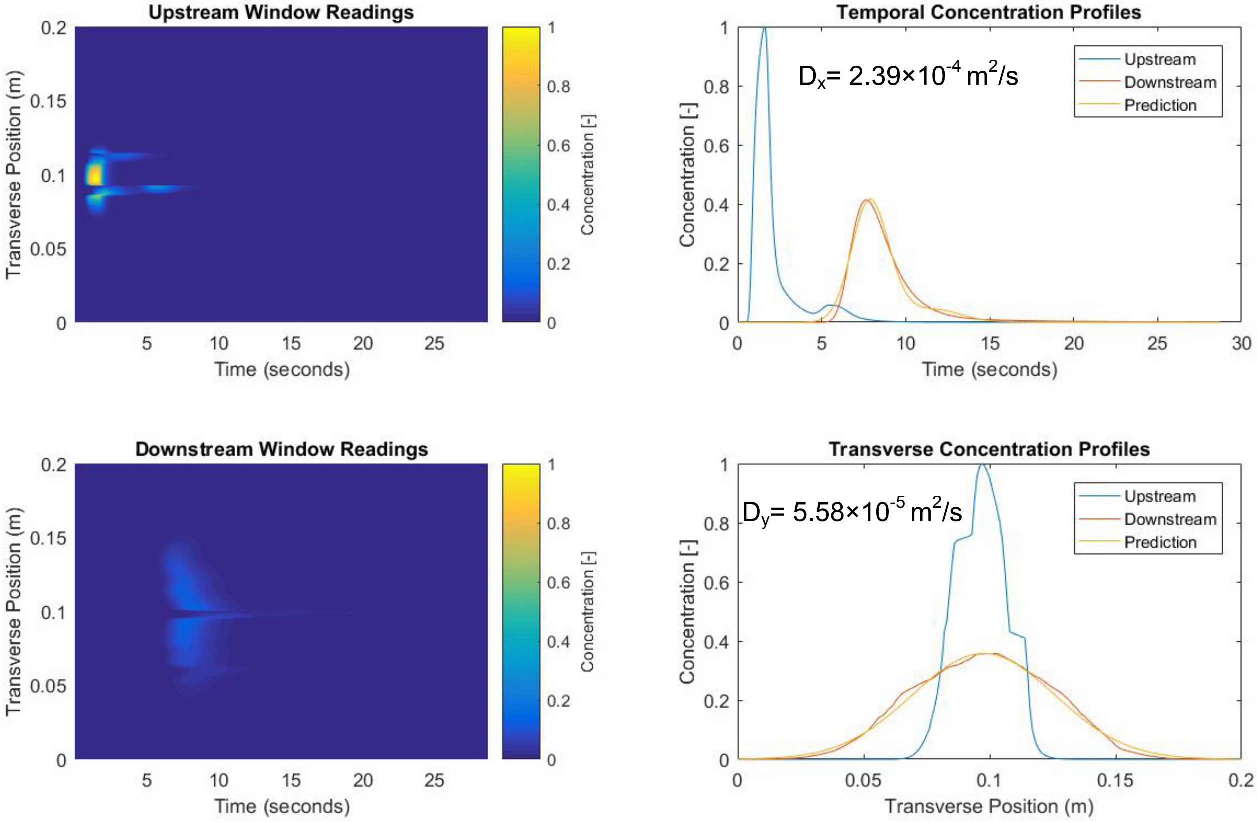

Figure 7. Upstream and downstream concentration along with the predicted downstream concentration for ϕ=0.091 (upstream=line No. 2, downstream=line No. 8 on Figure 2.)

The resulting transverse dispersion coefficients were non-dimensionalized by the cylinder diameter i.e. 0.0064 m and the optimized longitudinal velocity for each case. The normalized transverse dispersion coefficients resulting from CFD models are compared to laboratory data from Tanino and Nepf (2008), in Figure 8.

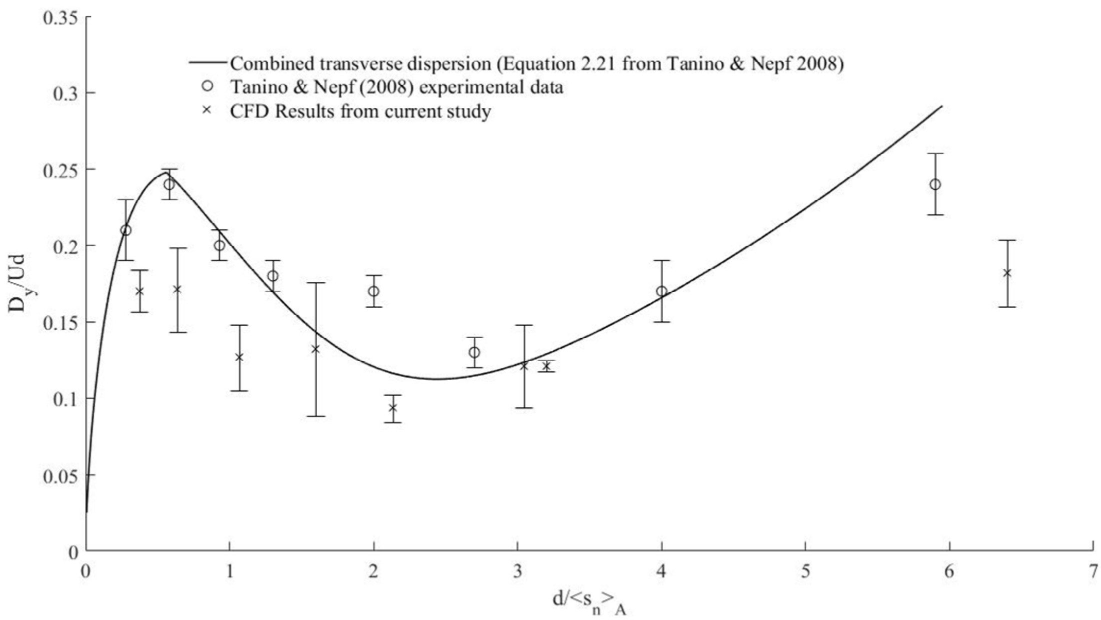

Figure 8.. Comparison between CFD results and laboratory data

 ©2017, IAHR. Used with permission / ISSN 1562-6865 (Online) - ISSN 1063-7710 (Print)

5 DISCUSSIONS

It can be observed from Figure 8, that the trend of laboratory data is regenerated by the CFD results to an acceptable level which lead to the validation of the CFD method used in this study and also supporting the theoretical relations suggested by Tanino and Nepf (2008), i.e. that the net transverse dispersion can be expressed as the linear superposition of turbulent diffusion and mechanical dispersion.

The difference between CFD results and laboratory data can be investigated from different aspects. The CFD models used in this study were 2D models which means neglecting the effect of bed role in the mixing processes. Not all of the laboratory condition can be modelled and regenerated in CFD models, e.g. the wooden dowels used in laboratory have a certain wall friction which was not modelled in CFD, and the same is true for the channel boundaries. On the other hand the laboratory errors and uncertainties also should be considered as a source of difference between CFD and laboratory data.

The turbulence model used in this study, i.e. RSM, was shown to be able to model the heterogeneous flow field generated by the presence of random cylinder arrays. It shows that traditional RANS models, all of which have the disadvantage of the eddy-viscosity assumption and isotropic turbulent kinetic energy, can still provide useful insights into small-scale hydrodynamic processes in this type of engineering application.

In general it can be concluded that the described CFD modelling tool and procedure provides an acceptable way of representing and quantifying mixing within cylinder arrays. The use of this tool can be justified to investigate other conditions such as different solid volume fractions, different spacing patterns of cylinders, and differnet cylinder diameter distributions in future studies.

6 CONCLUSIONS

- A CFD modelling method based on applying a 2D Reynolds Stress turbulence Model (RSM) to model the heterogeneous flow field and mixing within random cylinder arrays was evaluated by comparing the CFD results with a previously published laboratory study.
- The CFD transverse dispersion coefficients generated in this study showed a good agreement with laboratory data.
- The method used in this study was validated and is suggested to be used for the future studies.

REFERENCES

ANSYS Fluent. (2015). ANSYS.

Hamidifar, H., Omid, M.H. & Keshavarzi, A. (2015). Longitudinal Dispersion in Waterways with Vegetated Floodplain. *Ecological Engineering*, 84, 398-407.

Rutherford, J.C. (1994). *River Mixing*. John Wiley & Son Ltd.

Sonnenwald, F., Guymer, I., Marchant, A., Wilson, N, Golzar, M. & Stovin, V. (2016) Estimating Stem-Scale Mixing Coefficients in Low Velocity Flows. *Sustainable Hydraulics in the Era of Global Change: Advances in Water Engineering and Research*, 733-740.

Sonnenwald, F., J. R. Hart, P. West, V. R. Stovin. & I. Guymer (2017), Transverse and Longitudinal Mixing in Real Emergent Vegetation at Low Velocities, *Water Resources Research*, 53(1), 961–978.

Tanino, Y. & Nepf, H.M. (2008). Laboratory Investigation of Mean Drag in a Random Array of Rigid, Emergent Cylinders. *Journal of Hydraulic Engineering*, 134(1), 34-41.

Tanino, Y. & Nepf, H.M. (2009). Laboratory Investigation of Lateral Dispersion Within Dense Arrays Of Randomly Distributed Cylinders at Transitional Reynolds Number. Physics of Fluids, 21(4), 1-10.

Tanino, Y. (2008). Flow and Solute Transport in Random Cylinder Arrays: A Model for Emergent Aquatic Plant Canopies, *Phd Thesis*, Massachusetts Institute of Technology.

White, B.L. & Nepf, H.M. (2003). Scalar Transport in Random Cylinder Arrays at Moderate Reynolds Number. *Journal of Fluid Mechanics*, 487, 43-79.

Proceedings of the 37th IAHR World Congress
August 13 – 18, 2017, Kuala Lumpur, Malaysia

CHARACTERIZATION OF THE FLOW IN A VERTICAL SLOT FISHWAY WITH MACRO-ROUGHNESSES USING UNSTEADY (URANS AND LES) SIMULATIONS

AURELIEN BALLU[1], GERARD PINEAU[2], DAMIEN CALLUAUD[3] & LAURENT DAVID[4]

[1,2,3,4] Institut Pprime ; CNRS – Université de Poitiers –isae ensma, Chasseneuil du Poitou, France
aurelien.ballu@univ-poitiers.fr; gerard.pineau@univ-poitiers.fr; damien.calluaud@univ-poitiers.fr; laurent.david@univ-poitiers.fr

ABSTRACT

The European Water Framework Directive aims to restore the ecological continuity of European rivers and streams and more specifically the free circulation of aquatic species. To fulfill those requirements, vertical slot fishways (VSF) are built to provide the possibility for fish to cross dams or weirs. Initially, such devices have veen constructed to allow the migration of fish species with an important swimming capacity like salmonids. Currently, more and more VSFs are equipped with macro-roughnesses fixed on their bed to help small or benthic species to cross obstructions. Macro-roughnesses are most often stones or concrete cylinders. To study the effects of such macro-roughnesses on the pool flows, unsteady 3D flow simulations are carried out. This paper presents the results of 3D URANS and LES studies of a VSF with and without equally spaced cylinder-shape macro-roughnesses. The volume of fluid method is used to simulate the free surface and the interaction between the two phases (water and air). Results show that both URANS and LES models are in good agreement with experimental velocity profiles. However, the turbulent kinetic energy is quite under-estimated when using the URANS model. Finally, the LES method is used to characterize the effect of macro-roughnesses on the flow. It is shown that the zone in the vicinity of the macro-roughnesses gives potentially more favorable flow condition for benthic species. The present study demonstrates that LES calculation can give a useful modelling of the flow existing inside a VSF with macro-roughnesses. It can provide valuable information of the flow characteristics, especially in areas where the experimental measurements are complicated to implement.

Keywords: Vertical slot fishway; numerical simulation; URANS; LES; macro-roughnesses.

1 INTRODUCTION

Most fish species is doing migration to reach suitable spawning areas, to find areas of growth or to fleeing poor habitat conditions. The many obstacles (weirs, dams) along rivers constitute real obstacles to these migrations, which can lead to the partial or total suppression of access to spawning grounds and to the reduction and sometimes complete disappearance of species. To allow these species to move freely in rivers, crossing devices such as vertical slot fishways (VSF) are built on rivers. Flow in vertical slot fishways has been extensively studied both experimentally (Wu et al., 1999; Puertas et al., 2004; Liu et al., 2006; Tarrade et al., 2008; Wang et al., 2010) and numerically (Khan, 2006; Cea et al., 2007; Heimerl et al., 2008; Chorda et al., 2010; An et al., 2016; Klein & Oertel, 2016) and is now relatively well characterized. However, the presence of macro-roughnesses in such fishways has been little studied (Bourtal, 2012; Branco et al., 2015). The macro-roughnesses are mostly rock blocks or concrete cylindrical studs placed on the floor of the VSFs. Macro-roughnesses are used to create more favorable flow conditions for bottom species (benthic species) and to provide them hydraulic shelters. Unsteady 3D numerical simulations of flow in a vertical slot fishway with and without macro-roughnesses were performed using Star-CCM+. A comparison of the URANS and LES models with experimental velocity profiles carried out in a reduced model is proposed to define the most realistic method to model the flow inside VSFs.

2 EXPERIMENTAL SETUP

The Pprime Institute of the University of Poitiers-CNRS has a reduced model of vertical slot fishway. This model was designed on the basis of the mean dimensions of the VSFs constructed in France with a geometrical scale of 1/4 relating to Froude similitude. The model is shown schematically on Figure 1. The system operates in a closed loop. A centrifugal pump (1) is used to transfer the water from the retention tanks (2 and 3) located downstream of the VSF (4) to the feed tank upstream (5). The water flows then by gravity through the five pools VSF and return to the retention tank. The length of the pools is L=0.75 m and the width of the vertical slots is b=0.075 m, giving the ratio L/b equal to 10. The width of the pools is B=0.675 m, i.e. B/b=9. The geometry of the pools is similar to the design 1 studied by Rajaratnam et al. (1986).

 ©2017, IAHR. Used with permission / ISSN 1562-6865 (Online) - ISSN 1063-7710 (Print)

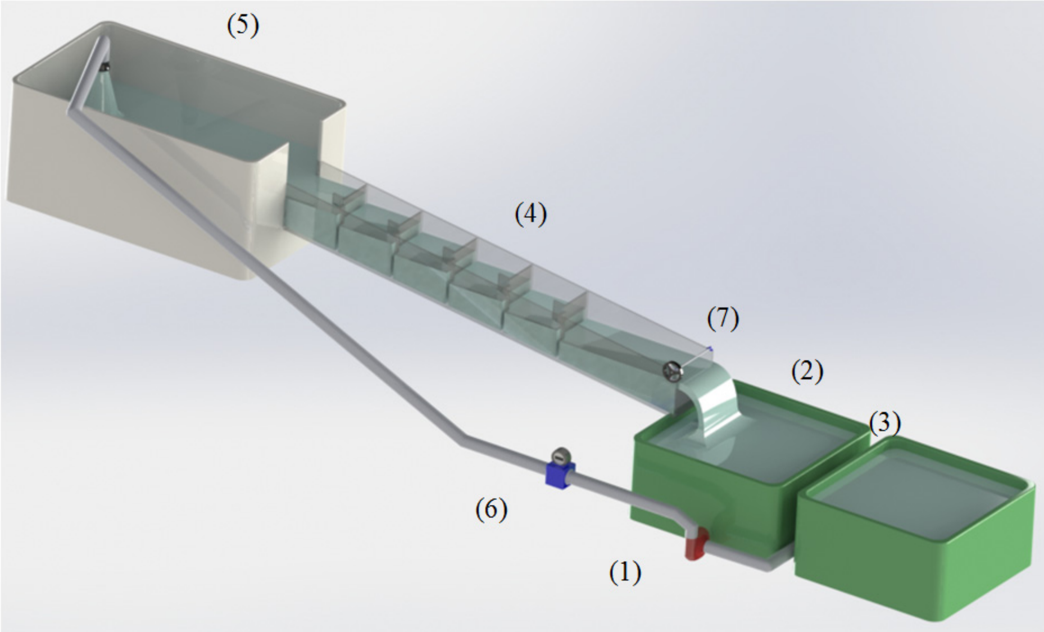

Figure 1. Experimental setup.

For the experiments presented here, the slope of the VSF was set to s=7.5% and the discharge to Q=0,023 m^3/s. The macro-roughnesses arranged on the bottom of the VSF model are c, equally spaced cylindrical studs with a diameter of 0.035 m and a height of 0.05 m.

The density d_r is defined as the ratio of the elementary surface covered by three elements of macro-roughnesses (S_r) to the total surface of the patch of cylinders (S_t) (figure 2). In the studied configuration, a density is set to d_r=15%.

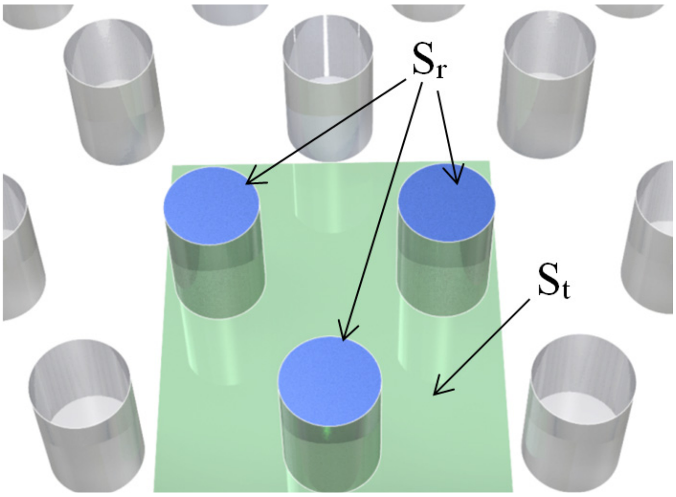

Figure 2. Density of macro-roughnesses

Flow velocity measurements were performed in the third pool of the fishway, in smooth floor configuration (classical configuration) and also with the presence of macro-roughnesses, using an Acoustic Doppler Velocimeter (ADV) to obtain average velocity and turbulent kinetic energy profiles. The sampling rate of the ADV is 50Hz over a 300 seconds acquisition time. A phase/space filter has been used considering that is one of the more objective filter for turbulent free surface flow (Goring et al., 2002). The origin of the coordinate system linked to the fishway (X, Y, Z) is located at the bottom of the VSF, at the intersection of the plane formed by the upstream wall and the side wall (small deflector side) (Figure 3). The X-axis is in the direction of the flow and parallel to the floor, the Y-axis points towards the inside of the pool, the Z-axis is therefore directed upwards. Another axis, Z' is defined as the absolute vertical axis. A transverse profile (B) is defined in a plane parallel to the floor at a distance Z/b = 2 and X/b=4,67. For this profile, the first and the last points are located at 50 mm from the walls. A vertical profile (D) has also been measured along the Z'-axis at Y/b=2,95 from X/b=4,5 at the first point, located 10 mm above the macro-roughnesses to X/b=4,8 at the free surface. The sampling interval for all profiles is 15 mm. The position of the profiles is given in the figure 3.

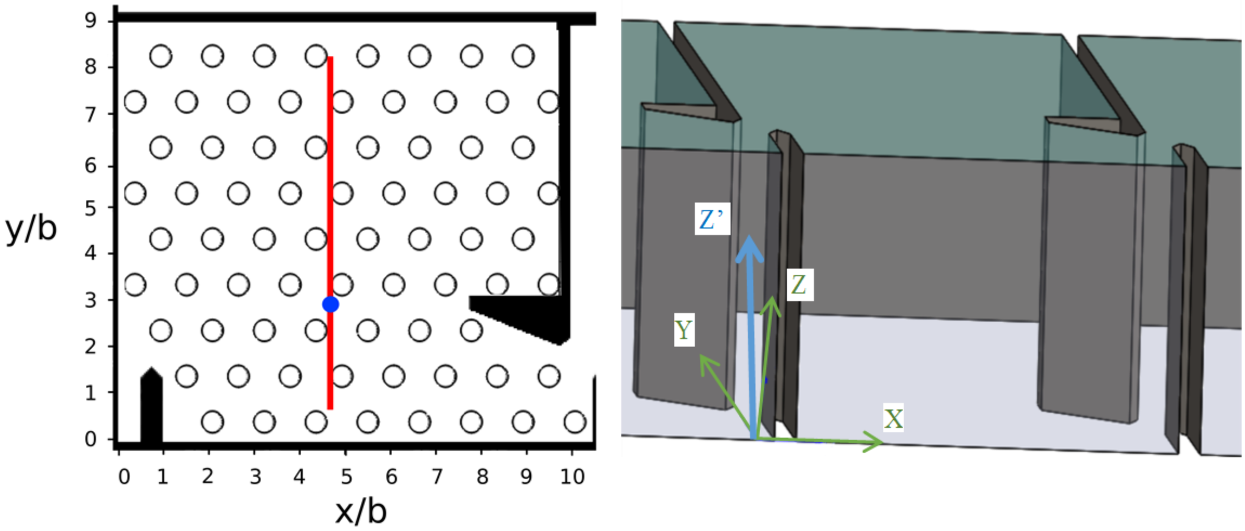

Figure 3. Left: position of the velocity profiles (profile B in red and D in blue). Right: position and orientation of the coordinate system linked to the fishway (X, Y, Z). The Z'-axis defines the vertical direction of the absolute coordinate system.

3 NUMERICAL MODELS

3.1 Model description

Numerical simulations give access to quantities that are difficult to measure experimentally and thus complement physical analysis. In this paper, simulations of the flow were conducted in Unsteady Reynolds-Averaged Navier-Stokes (URANS) and Large Eddy Simulation (LES) with Star-CCM+ software, for the same configuration used for the experimental measurements (5 pools, B/b=9, Q=0,023 m^3/s and s=7.5%), with a smooth floor configuration and with macro-roughnesses. The URANS method uses the Reynolds decomposition principle. It is based on the decomposition of the instantaneous variables (pressure, velocities) of the flow in an average part and a fluctuating part. The use of the mean operator on the Navier-Stokes equations leads to a loss of information making the system of equations to be solved open. The use of turbulence models is thus necessary to close the system of equations. In the present case a k-ε low Reynolds turbulence model was used. Contrary to the URANS method that models all the turbulence spectrum, the Large Eddy Simulation method (LES) consists of solving large flow structures that are highly dependent on geometry and models only small ones, that are supposed to be more universal, thanks to a sub grid-scale model. The Wall Adapting Local Eddy-viscosity (WALE) model developed by Nicoud and Ducros (1999) was used for simulations. By construction, this model makes the turbulent viscosity tend towards a zero value without damping function. It is particularly suitable for complex geometries and has therefore been used in this study. To simulate free surface flow, the Volume of Fluid (VOF) method was used. This method is based on a function which makes it possible to define the volume fraction of one of the two fluids present in a control volume.

An implicit temporal discretization scheme is used for both methods. This scheme consists of two nested loops: a loop in physical time which allows to describe the unsteady evolution and a loop in dual time which seeks to reach a quasi-stationary state. For spatial discretization, a second order upwind scheme and a third order scheme (MUSCL) was used for URANS and LES respectively.

3.2 Boundary conditions

Hydrostatic pressure conditions and volume fraction of each phase (water and air) are set at the input and output of the calculation domain. Water levels are derived from experimental measurements of water heights on the VSF of the laboratory. No-slip wall boundary conditions have been specified on all the solid walls. The area of calculation has been enlarged above the fishway, thus enabling the boundary to be moved away from the area of the free surface of the flow. A symmetry condition has been imposed on the boundaries of this enlargement. Boundary conditions are recalled on the figure 4.

 ©2017, IAHR. Used with permission / ISSN 1562-6865 (Online) - ISSN 1063-7710 (Print)

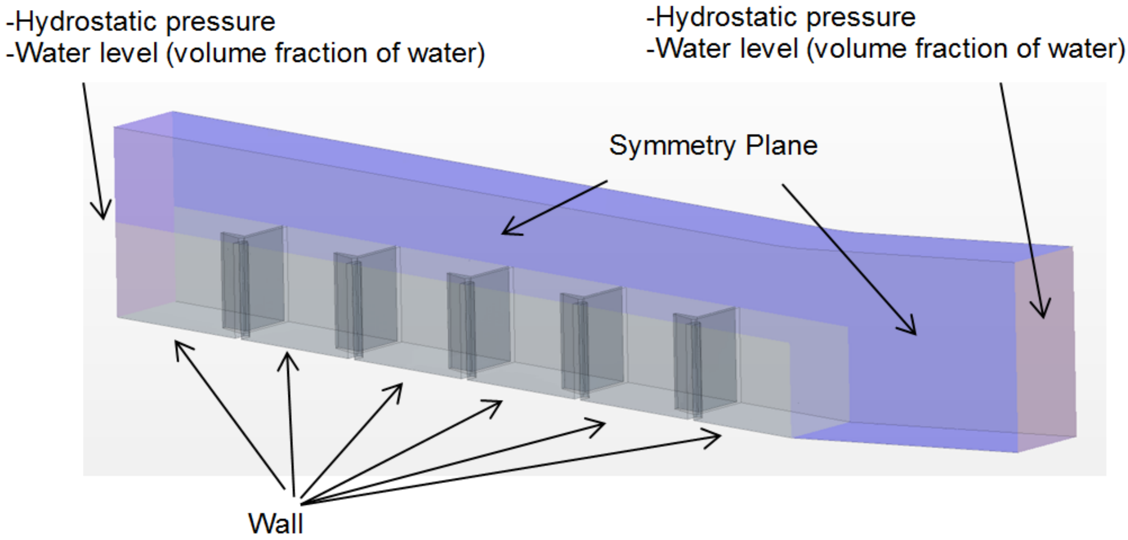

Figure 4. Boundary conditions used for LES and URANS simulations.

3.3 Mesh

The size T* of the cells of the different parts of the mesh of the simulation domain has been defined with respect to the width of the slot (T*/b). In URANS modeling, this ratio has been set to 1/4 (figure 5), which makes it possible on the one hand to obtain a good definition of the geometry but also to have reduced spatial discretization errors. Since the water level is determined experimentally, the mean position of the free surface in each pool can be estimated. The mesh has been refined to T*/b=1/8 in an area around this position (+/- 20%). The part of the domain which contains only air (above the free surface) has been meshed with a mesh size T*/b=1. For the simulation of the flow in the VSF in the vicinity of macro roughnesses, a refinement (T*/b=1/8) was carried out in an area delimited by the height of the cylinders.

In LES simulation, the mesh size used for the URANS simulations was retained to mesh all the pools except the third, corresponding to the reference pool. In this pool, the cell size of the core mesh is T*/b=1/8 (figure 5).

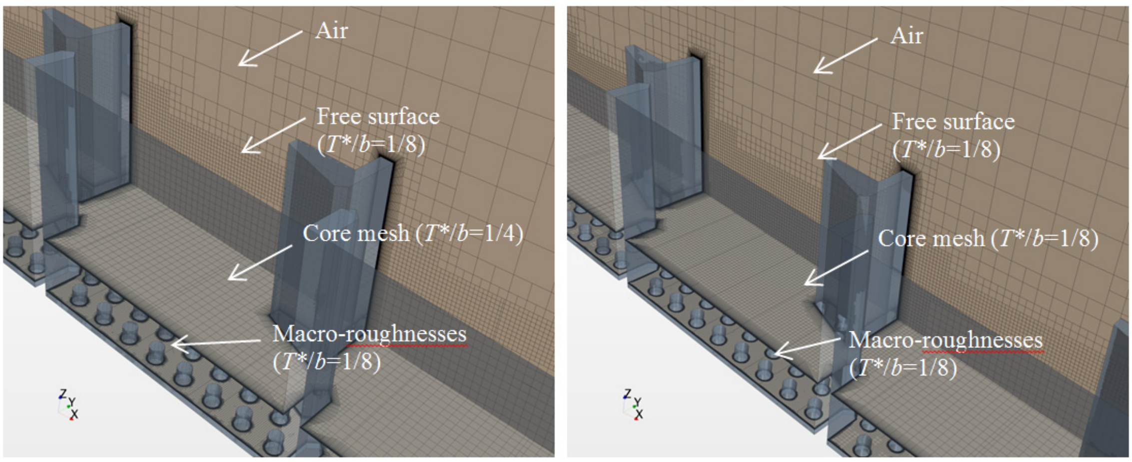

Figure 5. Mesh generated for simulation of the flow in a VSF with macro-roughnesses. Left: mesh generated for URANS simulation, right: mesh generated for LES simulation.

The k-ε turbulence model used for URANS simulations is integrable down to the wall (low-Reynolds turbulence model). Thus, the first inner node of the boundary layer mesh should be located in the viscous sub-layer, which at $y^+=1$, where y^+ is the non-dimensional wall distance, defined as:

$$y^+ = \frac{y_w . u_\tau}{\nu} \qquad [1]$$

where y_w the normal distance from the wall (m), u_τ the wall friction velocity (m/s) and ν the kinematic viscosity (m^2/s).

In URANS simulation, u_τ is deduced from an estimation of the friction coefficient gives by Schultz-Grunow expression:

©2017, IAHR. Used with permission / ISSN 1562-6865 (Online) - ISSN 1063-7710 (Print)

$$C_f = \frac{0,37}{\log\left(U_\infty x / \nu\right)^{2,584}} \qquad [2]$$

where C_f is the friction coefficient (-), U_∞ is the velocity of the flow (m/s), x the direction of the flow (m) and ν the kinematic viscosity (m^2/s).
The same condition must be observed in LES for the near-wall region to be correctly solved. However, the wall friction velocity was estimated from the URANS results.
The thickness $\delta(x)$ of the boundary layer mesh was estimated to be equal to 0.03 m from the equation which gives the evolution of the turbulent boundary layer thickness on a flat plate (Chassaing, 2000):

$$\frac{\delta(x)}{x} \cong \frac{0,37}{R_e(x)^{1/5}} \qquad [3]$$

Where $R_e(x)$ is the Reynolds number (-).
Unlike URANS simulations, in LES the anisotropy of the near-wall mesh must be very limited. To resolve inner-layer eddies, the streamwise and spanwise grid sizes in wall unit respectively $\Delta x^+ \cong 100$ and $\Delta z^+ \cong 20$ have been used (Piomelli and Balaras, 2002).

3.4 Initial conditions and computational parameters

In URANS, a starting water level is imposed at the output of the simulation domain (Figure 6). The result is a residual water level in the VSF. This initial state corresponds to a configuration in which the entrance of the fishway would be closed and the exit is left free. In LES, the initial conditions are derived from the URANS calculations such as pressure, velocity and volume fraction of fluid (Figure 6).

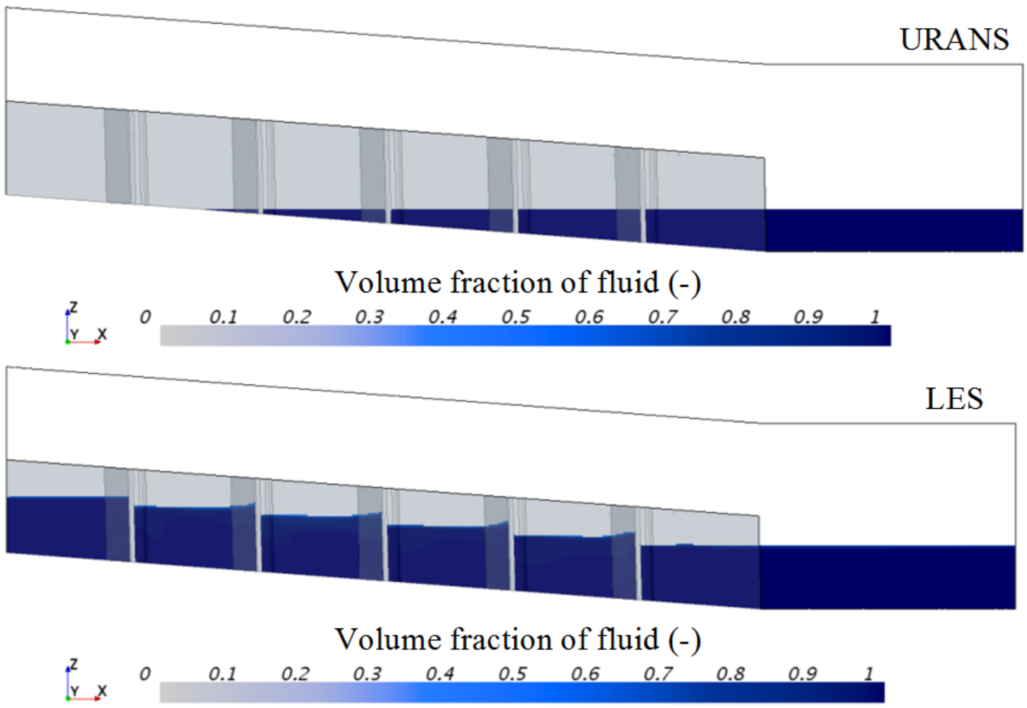

Figure 6. Initial conditions of the volume fraction of water (in blue) for URANS and LES methods.

Concerning the computational time step, for calculation precision requirements, its value has been set to Δt =10 ms in relation to the cell size of the computational domain and the kinematics of the flow.
In the case of the URANS simulation, the equilibrium of the water levels in each of the pools is reached after 20 seconds of simulation. The calculation of the statistical turbulent quantities of the flow is calculated only from this equilibrium state. The overall time of simulation was set to 300s corresponding to the acquisition time of the experimental measurements. Since the flow is already fully developed at the beginning of the LES simulations, the overall simulation time is based on the convergence of mean and fluctuating component of velocity in the center of each pool.

 ©2017, IAHR. Used with permission / ISSN 1562-6865 (Online) - ISSN 1063-7710 (Print)

4 COMPARISON OF RESULTS

A comparative study of the flow characteristics is carried out to determine which of URANS or LES simulation is the most appropriate method to model the flow inside a VSF with and without macro-roughnesses. The magnitude of the velocity $\|V\|_{3D}$ and the turbulent kinetic energy k_{3D} were normalized by the maximum velocity given by:

$$V_d = \sqrt{2.g.s.L} \quad [4]$$

where g is the acceleration due to gravity (m/s^2), s the slope of the VSF and L the length of the pools (m).

The 3D non-dimensional magnitude of the flow velocity $\frac{\|V\|_{3D}}{V_d}$ and turbulent kinetic energy $\frac{k_{3D}}{V_d^2}$ profiles obtained from experimental measurements and from both URANS and LES simulations (URANS and LES) are plotted in figures 7 and 8, respectively for the smooth floor and the macro-roughnesses configurations.

The estimated errors due to spatial discretization for URANS simulations are calculated from the Grid Convergence Index (GCI) method (Celik et al., 2008). Concerning experimental measurements, the uncertainties are estimated from the ADV constructor specification. Uncertainties are shown in the figures 7 and 8 in the form of error bar.

To give an objective character to the comparisons, the correlation coefficient r² and the relative standard deviation σ_m between the experimental and numerical curves have been calculated. The correlation coefficient was used here to evaluate the degree of resemblance between the numerical curves and the experimental curves.

In both the smooth floor and macro-roughnesses configuration (figure 7 and 8), the mean velocity curves $\frac{\|V\|_{3D}}{V_d}$ of the profiles B obtained by URANS and LES simulations are similar to those obtained experimentally. The passage of the jet induces a strong increase in the velocity and the turbulent kinetic energy of the flow at Y/b=3 (figure 7 a,b and figure 8 a,b). On both sides of the jet, two zones of lower intensity with local minimum velocity, reflect the existence of two recirculation zones indicating the existence of the first flow pattern (Wu et al., 1999). The URANS and LES simulations clearly reproduce this flow topology.

This visual observation is confirmed by high correlation coefficients, whether for the URANS simulation or for the LES simulation (Table 1). With and without macro-roughnesses, the errors on the mean velocity are quasi-equivalent in URANS and LES and relatively reasonable for the transversal profile B and for the vertical profile D (σ_m= 18,7% for the LES and σ_m= 19,3% for the URANS). The turbulent kinetic energy $\frac{k_{3D}}{V_d^2}$ is underestimated by the two methods for the two configurations and for profiles B and D. However, the turbulent kinetic energy is better modeled in LES than in URANS, and this, whatever the profile studied with σ_m= 27% against σ_m= 58,5% for the URANS. It should be noted that the correlation coefficients calculated between the LES simulation and the experimental profiles are high for profiles B and D compared to those obtained with URANS method. This characteristic indicates that the numerical simulation LES give a correct distribution of the turbulent kinetic energy in the flow inside the VSF. The relative standard deviations mean σ_m and the coefficients of correlations r² are given in Table 1.

Table 1. σ_m and r^2 calculated between the velocity profiles and the turbulent kinetic energy derived from the numerical simulations and those resulting from the experimental measurements.

		Without macro-roughnesses				With macro-roughnesses			
		Profile B		Profile D		Profile B		Profile D	
		σ_m (%)	r^2 (-)	σ_m (%)	r^2 (-)	σ_m (%)	r^2 (-)	σ_m (%)	r^2 (-)
$\frac{\|V\|_{3D}}{V_d}$	URANS	24,1	0,92	8,7	-0,87	28,8	0,87	15,7	0,56
	LES	23,6	0,93	8,3	0,93	28,5	0,89	14,2	0,91
$\frac{k_{3D}}{V_d^2}$	URANS	59,2	0,85	53,5	-0,76	66,0	0,95	55,4	0,55
	LES	32,7	0,98	19,3	0,80	28,8	0,98	27,0	0,74

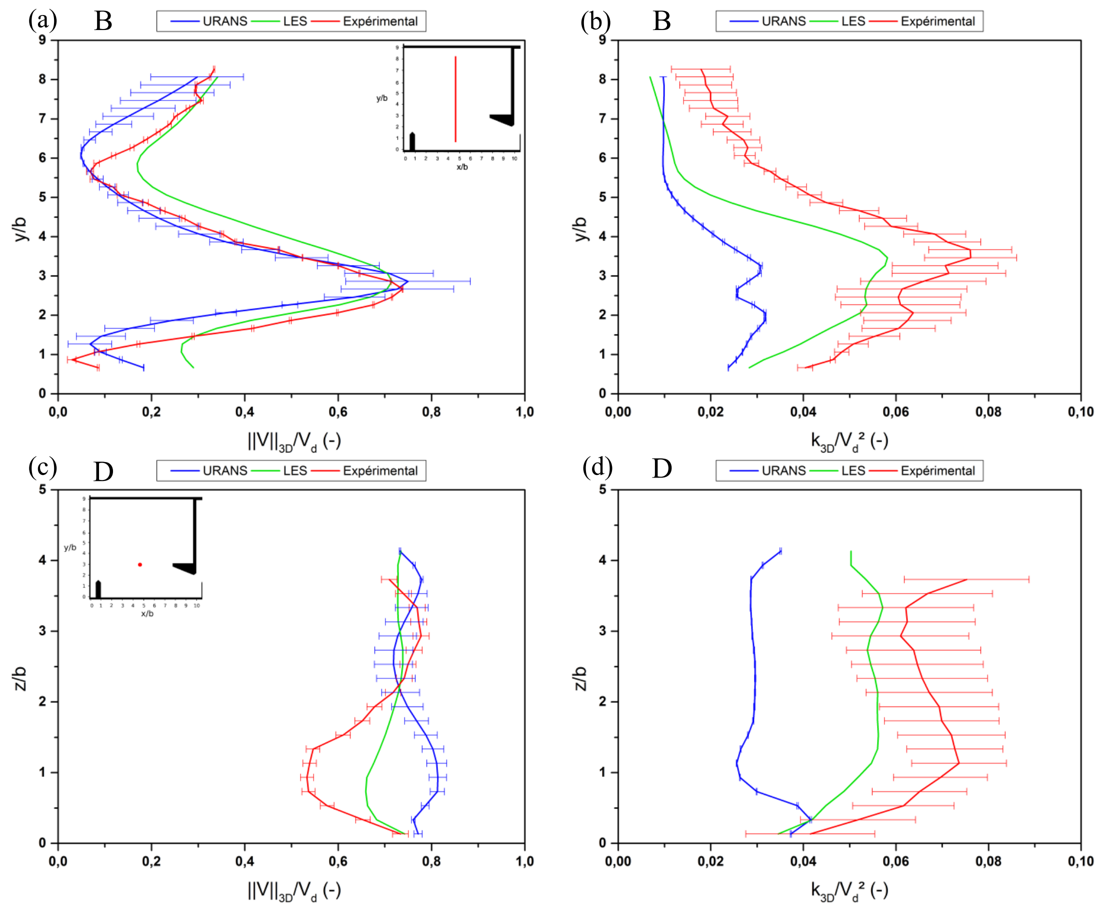

Figure 7. Velocity and turbulent kinetic energy profiles obtained with URANS, LES and experimental measurements without macro-roughnesses. a) and b) : profile B; c) and d) profile D.

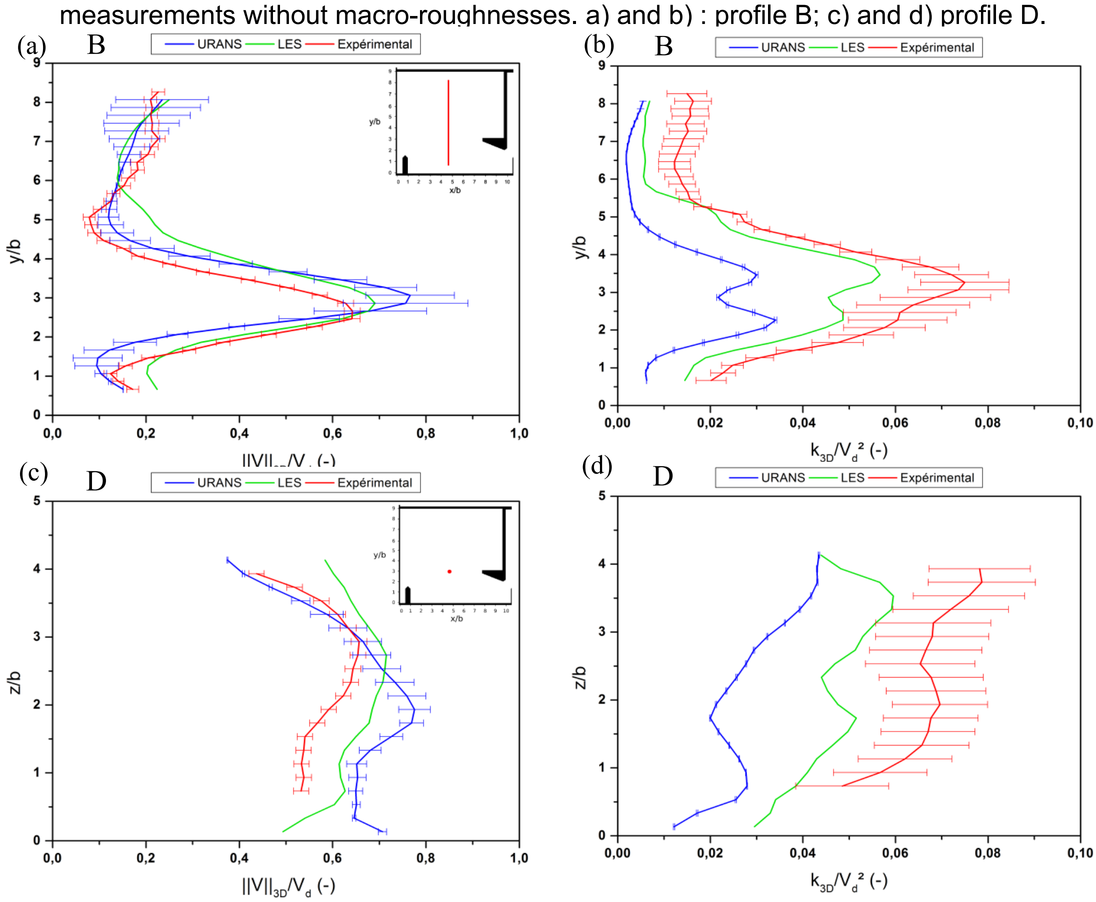

Figure 8. Velocity and turbulent kinetic energy profiles obtained with URANS, LES and experimental measurements with macro-roughnesses. a) and b) profile B; c) and d) profile D.

 ©2017, IAHR. Used with permission / ISSN 1562-6865 (Online) - ISSN 1063-7710 (Print)

5 CONCLUSIONS

The aim of this work was the validation of unsteady 3D simulations inside a vertical slot fishway with or without roughnesses placed on the bottom of the pool. LES and URANS simulations have been calculated with the presence of a free surface and compared with ADV measurements inside exactly the same geometry. The results obtained in LES are generally closer to the experimental results than those resulting from the URANS simulation. The study of the flow with and without the presence of macro-roughnesses should then be done on the basis of the results obtained in LES. It should be noted that the average velocity are slightly overestimated and that the kinetic energy is on average underestimated by about 30%. However, the overall topology and the distribution of the kinematic quantities are very close to those obtained experimentally.

ACKNOWLEDGEMENTS

This work was supported by the “Office National de l'Eau et des Milieux Aquatiques” (ONEMA), “Voies Navigables de France” (VNF) and the CPER-FEDER.

REFERENCES

An, R., Li, J., Liang, R. & Tuo, Y. (2016). Three-Dimensional Simulation and Experimental Study for Optimising a Vertical Slot Fishway. *Journal of Hydro-environment Research*, 12, 119-129.

Bourtal, B. (2012). Modification De L’écoulement Turbulent au Sein de Passes A Poissons A Fentes Verticales Par L’insertion D’obstacles. *PhD Dissertation*, Université de Poitiers.

Branco, P., Santos, J.M, Katopodis, C., Viseu, T., Ferreira, M.T. & Pinheiro, A.N. (2015). *The Influence of Bottom Rugosity on the Performance of Upstream Fish Movements through a Pool-Type Fishway Under Different Discharges*. The Hague, Netherland.

Cea, L., Pena, L., Puertas, J., Van der Vinne, G.V.C. & Pena, E. (2007). Application of Several Depth-Averaged Turbulence Models to Simulate Flow in Vertical Slot Fishways. *Journal of Hydraulic Engineering*, 133(2), 160-172.

Celik, I. B., Ghia, U., Roache, P.J. & Freitas, C.J. (2008). Procedure for Estimation and Reporting of Uncertainty Due to Discretization in CFD Applications. *Journal of fluids Engineering-Transactions of the ASME*, 130(7).

Chassaing, P. (2000). Turbulence En Mécanique des Fluides: Analyse Du Phénomène En Vue De Sa Modélisation À L’usage De L’ingénieur, Édité Par CÉPADUÉS. *Coll. POLYTECH de l’INP de Toulouse*, 255.

Chorda, J., Maubourguet, M.M., Roux, H., Larinier, M., Tarrade, L. & David, L. (2010). Two-Dimensional Free Surface Flow Numerical Model for Vertical Slot Fishways. *Journal of Hydraulic Research*, 48(2), 141-151.

Goring, D. & Nikora, V. (2002). Despiking Acoustic Doppler Velocimeter Data. *Journal of Hydraulic Engineering*, 128(1), 117-126.

Heimerl, S., Hagmeyer, M. & Echteler, C. (2008). Numerical Flow Simulation of Pool-Type Fishways: New Ways with Well-Known Tools. *Hydrobiologia,* 609(1), 189-196.

Khan, L.A. (2006). A Three-Dimensional Computational Fluid Dynamics (CFD) Model Analysis of Free Surface Hydrodynamics and Fish Passage Energetics in a Vertical-Slot Fishway. *North American Journal of Fisheries Management*, 26(2), 255-267.

Klein, J. & Oertel, M. (2016). Vertical Slot Fishway: Evaluation of Numerical Model Quality. *International Junior Researcher and Engineer Workshop on Hydraulic Structures*, Germany.

Liu, M., Rajaratnam, N. & Zhu, D.Z. (2006). Mean Flow and Turbulence Structure in Vertical Slot Fishways. *Journal of Hydraulic Engineering*, 132(8), 765-777.

Nicoud, F. & Ducros, F. (1999). Sub grid-Scale Stress Modelling Based on the Square of the Velocity Gradient Tensor. *Flow, Turbulence and Combustion*, 62(3), 183-200.

Piomelli, U. & Balaras, E. (2002). Wall-Layer Models for Large-Eddy Simulations. *Annual Review of Fluid Mechanics*, 34(1), 349-374.

Puertas, J., Pena, L. & Teijeiro, T. (2004). Experimental Approach to the Hydraulics of Vertical Slot Fishways. *Journal of Hydraulic Engineering*, 130(1), 10-23.

Rajaratnam, N., der Vinne, G.V. & Katopodis, C. (1986). Hydraulics of Vertical Slot Fishways. *Journal of Hydraulic Engineering*, 112(10), 909-927.

Tarrade, L., Texier, A., David, L. & Larinier, M. (2008). Topologies and Measurements of Turbulent Flow in Vertical Slot Fishways. *Hydrobiologia*, (609), 177-188.

Wang, R., David, L. & Larinier, M. (2010). Contribution of Experimental Fluid Mechanics to The Design of Vertical Slot Fish Passes. *Knowledge and Management of Aquatic Ecosystems,* (396), 02.

Wu, S., Rajaratnam, N. & Katopodis, C. (1999). Structure of Flow in Vertical Slot Fishway. *Journal of Hydraulic Engineering*, 125(4), 351-360.

FLOW IN THE COMPOUND OPEN CHANNEL WITH GROUP OF COLUMN AND CHARACTERISTICS OF FISH BEHAVIOR

MUNEYUKI AOKI(1)

(1) Department of Civil and Environmental Engineering, Toyo University, Kawagoe-shi, Saitama, Japan
aoki037@toyo.jp

ABSTRACT

In this study, the aim is to make clear the characteristics of fish behavior flowing in compound open channel. Additionally, it also pays attention to whether a group of pile dike or trees is used in the evacuation place of fish. Therefore, the model experiments are carried out by using a compound cross-section open channel where the group of column (for example; group of pile dike, trees and all) has been set up, to measure the flow and to observe the movement of real fish. The real fish used for the experiment is Tribolodon hakonensis. 10 Tribolodon hakonensis are used for one experiment. The average body lengths (BL) are 0.05(m). These fish are common and popular in Japan. When the experiments are carried out, water temperature is 23~26 degree Celsius. In case of Run1, the fish are always swimming and moving on the wall side of left bank. Because flow velocity is rapid and columns are not set up, fish are not able to use the characteristic behavior of swimming against the flow and to evacuate. In case of Run2, fish move into the group of column where low flow-channel occurs because flow velocity decreases in the group of column. In case of Run3, the fish do not go into the group of column. Because secondary flow has developed, fish is swept away to the flood channel. Moreover, Reynold's stress increases when there is a group of column on the flood channel. Therefore, it is thought that the fish get stranded in the flood channel in this situation.

Keywords: Compound open channel; Reynold's stress; columns; fish behavior.

1 INTRODUCTION

In 1992, the Biodiversity Treaty was adopted. The purposes of this treaty were (1) biodiversity conservation, (2) the sustainable use of component of the biological diversity and (3) the distribution that is having an even balance with fairness of the profit that the use of the genetic resource causes, and Japan concluded a treaty in 1993 (Biodiversity Center of Japan HP). As a result of the distribution of rivers and wetlands on the animals, plants and vegetation, investigation of natural environment into damp ground or monitoring investigation of the creature reproduction ground have been carried out. In addition, as for rivers, the River Act is revised in 1997, and "river environment" starts to receive attention. According to the above statement, it is worth pointing out that the number of articles of study on environment and ecology in rivers increases. Moreover, on the webpage of the Ministry of Land, Infrastructure, Transport and Tourism River Bureau in Japan, there were various manual guidelines on river environment maintenance published, and "a basic policy made with a many nature river" was issued in 2006 (Ministry of Land, Infrastructure, Transport and Tourism, Water and Disaster Management Bureau HP). These two are subsequently combined, and the study examples for "fish" inhabiting a river increase.

In later years, under the influence of climate change caused by global warming, precipitation increases by torrential rain, and flood has become a frequent occurrence. Most of the rivers in Japan are consisted of compound cross-section open channels where a rise of the river water is first established and the water is subsequently released during a low channel and flood safely is thus ensured. The flow in compound cross-section open channels shows the aspect of three-dimensional complicated flows such as horizontal whirlpools or flows to be formed in a low channel and the rise of a river border part that it is related with its floor (Ikeda et al., 1995, 2000). Nevertheless, efforts to elucidate the flow structure have been increasing (Tominaga et al., 1990). However, there is still a lack of study on the action of fish in the compound cross-section open channels. In particular, during flooding, it is important to understand the action or behavior of fish when water quantity (velocity) increases or decreases rapidly. Further, it is also crucial to comprehend more on the fish habitat. Therefore, it may be said that it is indispensable for a future river plan in consideration of biological diversity to clarify action properties of the fish at the time of a water quantity (velocity) increase and decrease rapidly.

The fish swimming speed depends on the fish species, but usually understands that swimming speed in time is related to the body length (BL). For example, the Tribolodon hakonensis usually swims at 0.4BL (m/s) (Aoki et al., 2009). It is said that the fish have the ability to respond even to the slightest change of flow. At the time of a flood, the fish is washed away and cannot move upstream.

 ©2017, IAHR. Used with permission / ISSN 1562-6865 (Online) - ISSN 1063-7710 (Print)

In this study, the main purpose is to make clear the characteristics of fish behavior flowing in compound open channels. Additionally, it also pays attention to whether a group of column is used in the evacuation place of fish. Therefore, the model experiments are carried out by using a compound cross-section open channel where the group of column (for example; figure 1 shows groups of pile dike, trees and all) has been set up, to measure the flow and to observe the movement of real fish. To accomplish them, experiments in small compound cross-section open channels are conducted.

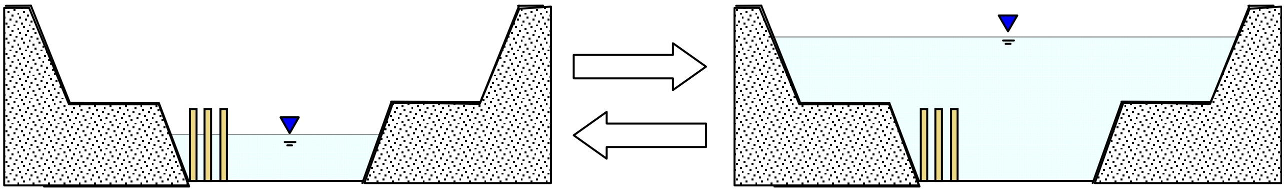

Figure 1. a) Pile dikes at the low-flow channel.

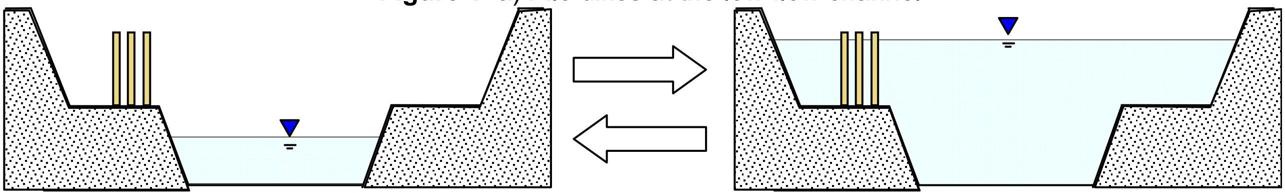

Figure 1. b) Pile dikes at the flood channel.

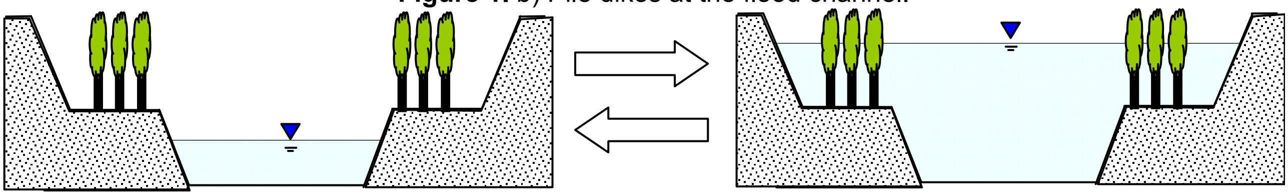

Figure 1. c) Trees at the flood channel.

2 EXPERIMENTAL METHOD

The experiments were carried out by using small compound cross-section open channels in the laboratory, to measure the flow and to observe the movement of real fish. Figure 2 shows the compound cross-section open channel used for the experiments. The column was made of wood whose diameter was 0.5 centimeters, and was set up in the right side of the open channel. The alignment of group of column was zigzags for high effect of the flow velocity to decrease. The group of column area was *b* (=0.085(m) x *L* (=1.925(m) and the total number of columns for each case was 122. Figure 3 shows the distribution of group of column in the compound cross-section open channel.

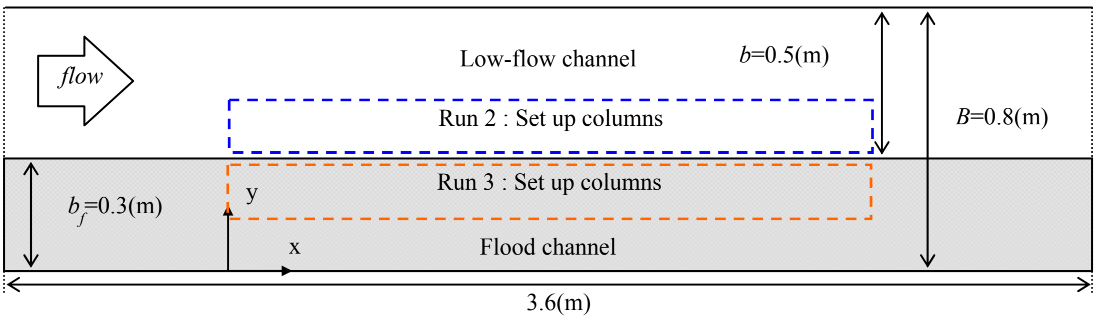

Figure 2. a) Plain view of the channel.

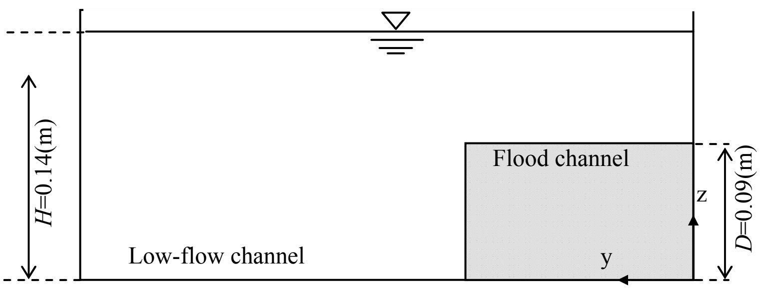

Figure 2. b) Sectional view of the channel.

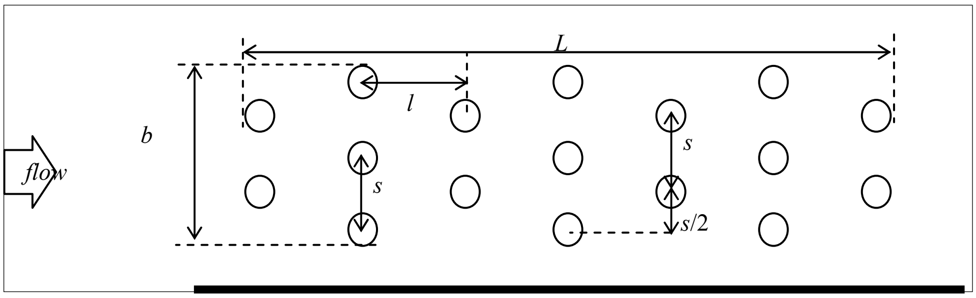

Figure 3. Distribution of group of column.

Table 1 shows the cases considered in the experiments. Water quantity was not changed and it was experimented in all 3 cases. S (=0.04(m) is the interval in transverse direction and l (=0.04(m) is the interval in the downstream direction.

Table 1. Cases considered in the experiments.

Case	Flow quantity (m^3/s)	Set up columns
Run1	0.028	None
Run2	0.028	Low-flow channel
Run3	0.028	Flood channel

Figure 4 shows the measurement points for hydraulics quantity. Points of x direction were -0.02(m), 0.00(m), 0.02(m)~1.92(m); each 0.1(m) and 1.94(m). Points of y direction were 0.05(m), 0.15(m), 0.19(m), 0.25(m), 0.31(m), 0.35(m), 0.39(m), 0.45(m), 0.55(m) and 0.75(m). The flow velocity and water depth were measured at each point.

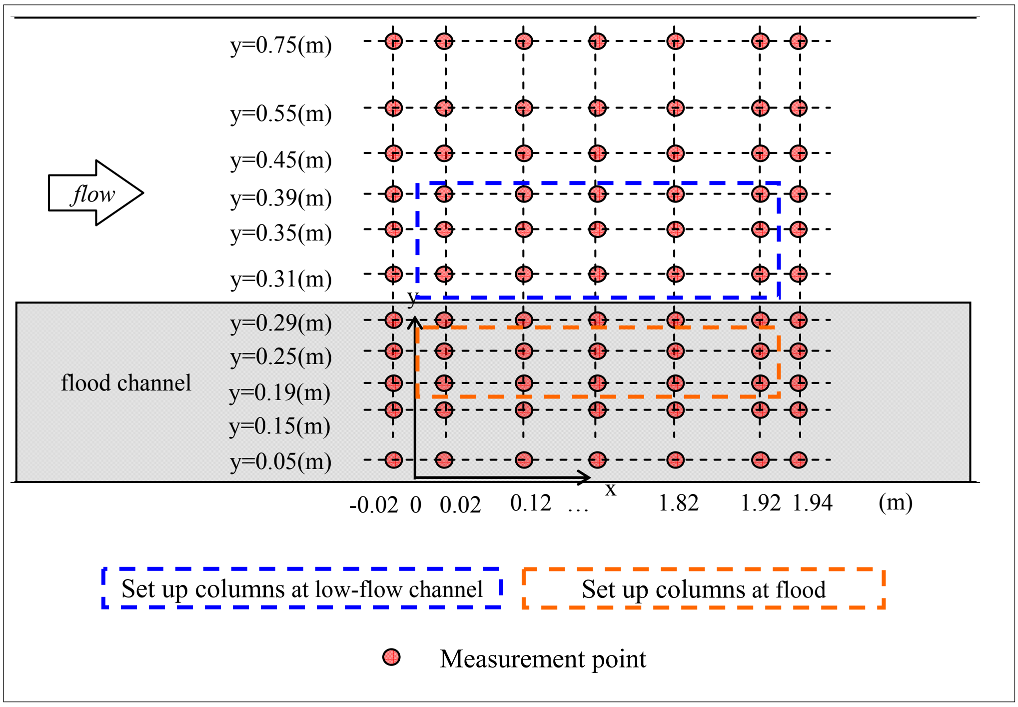

Figure 4. Measurement points for hydraulics quantity.

The real fish used in the experiment was Tribolodon hakonensis; as shown in figure 5. 10 Tribolodon hakonensis were used for one experiment (30 (min)). The average body lengths (BL) were 0.05(m). These fish are common and popular in Japan. When the experiments were carried out, water temperature was set at 23~26 degree Celsius.

 ©2017, IAHR. Used with permission / ISSN 1562-6865 (Online) - ISSN 1063-7710 (Print)

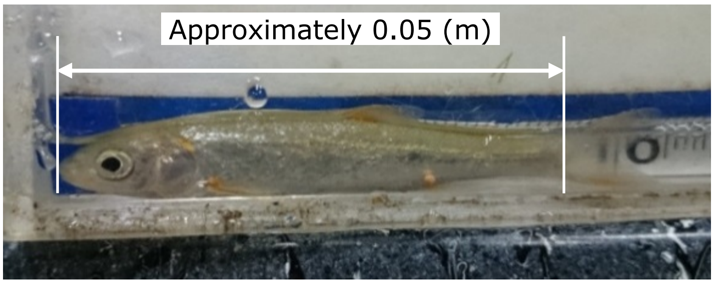

Figure 5. Tribolodon hakonensis.

3 RESULTS OF EXPERIMENTS

3.1 Hydraulic experiments

Figure 6 shows the flow velocity u in x direction. The flow velocity u decreased by the group of column in Run2 and Run3. Figure 7 shows the flow velocity u reduction rate of the group of column and the ratio was 50~80(%).

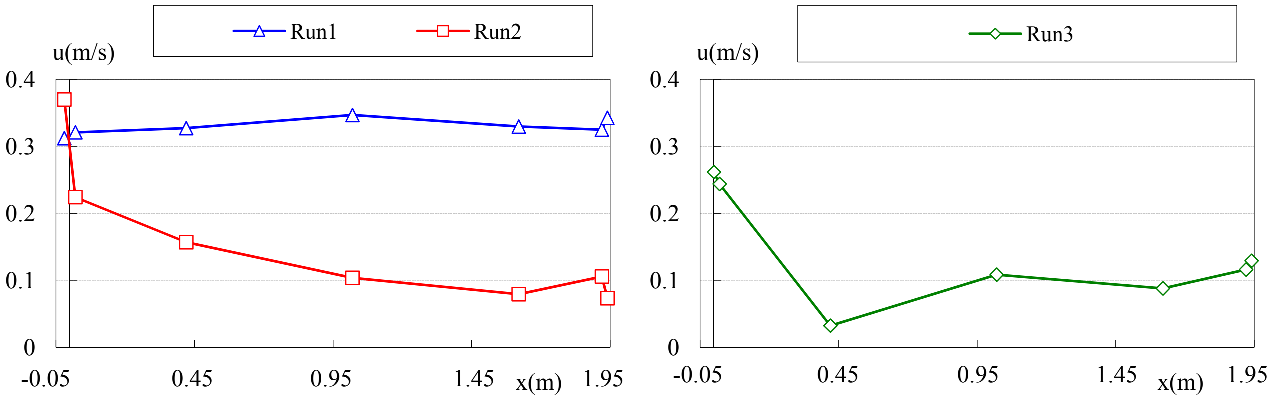

(Left; Run1, Run2 (y=0.39(m), z=0.02(m)) (Right; Run3 (y=0.25(m), z=0.11(m))
Figure 6. Flow velocity u in x direction.

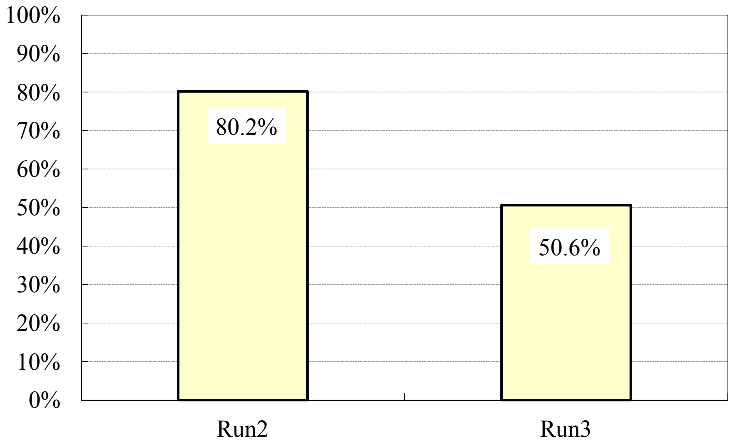

Figure 7. Decrease rate of flow velocity u by group of column.

Figure 8 shows the vw vector diagram and Reynolds stress diagram in each case. A vortex was formed in Run1 (figure 8 a) where the group of column was not installed at the flood channel. On the other hand, in Run2 where the group of column was installed in the low-flow channel right bank, the secondly flow was more significantly formed (figure 8b). In addition, in Run3 where the group of column was installed in the flood channel, the secondly flow more significant than Run2 was formed.

In Run1, Reynolds stress developed at the flood channel. On the other hand, it was revealed that Reynolds stress developed around the group of column in Run2 and Run3. In Run3, the Reynolds stress was approximately 2 times than Run2. H/D of these experiments was 1.56, and the characteristic of the compound cross-section open channel flow was shown in this experiment channel (Nezu et al., 1990).

©2017, IAHR. Used with permission / ISSN 1562-6865 (Online) - ISSN 1063-7710 (Print)

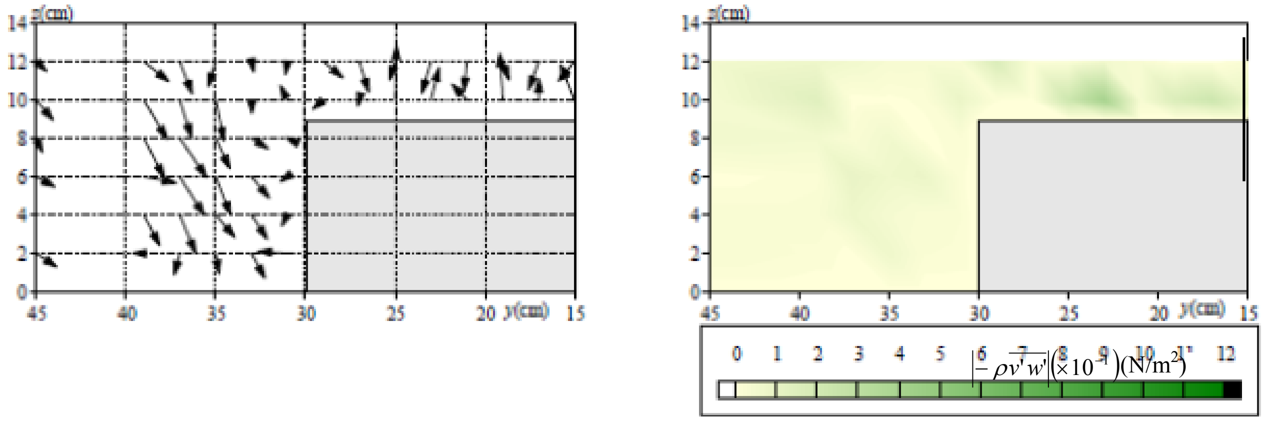

(Left; vw vector) (Right; Reynolds stress)

Figure 8. a) Vw vector and Reynolds stress in Run1.

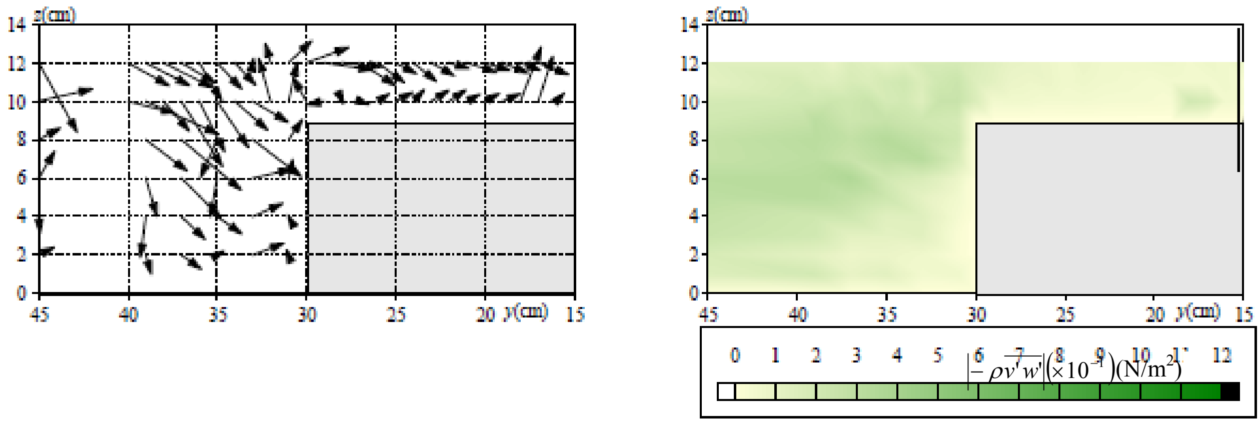

(Left; vw vector) (Right; Reynolds stress)

Figure 8. b) Vw vector and Reynolds stress in Run2.

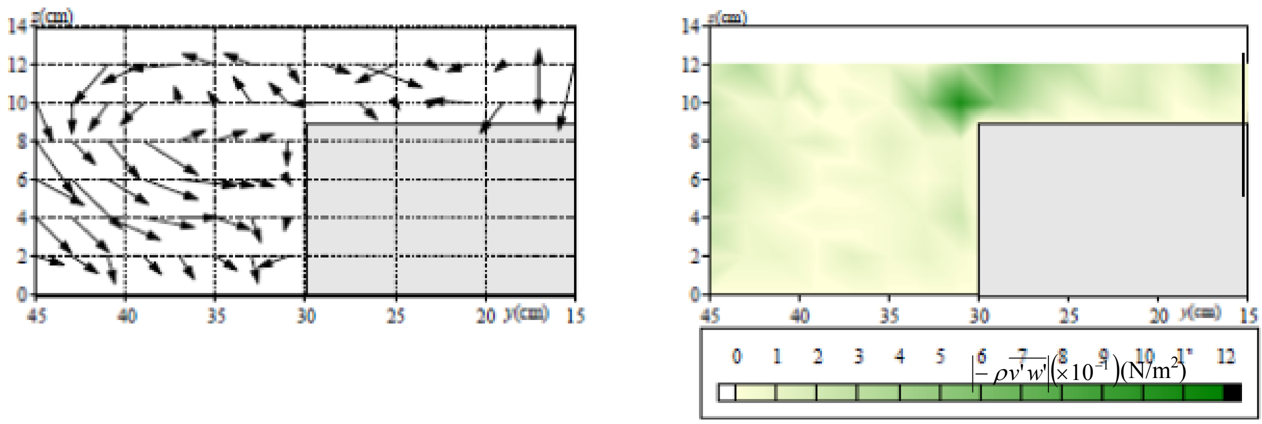

(Left; vw vector) (Right; Reynolds stress)

Figure 8. c) Vw vector and Reynolds stress in Run3.

3.2 Observation of real fish movement

Figure 9 shows the presented ratio of fish in each case. The presented ratio is defined in [1].

$$\text{The presented ratio} = \frac{\text{The total number of present fish in a mesh}}{(\text{The count of 1 minute}\times 30\text{ minutes})\times 10\ \textit{Toribolodon hakonensis}} \quad [1]$$

In Run1, the fish existed on the wall side of downstream and did not move to the upstream. In Run2, the existence of the fish in the group of column was expected. On the other hand, the existence of the fish in group of column in Run3 was not anticipated. In Run2, flow velocity in the group of column was less than 4BL (m/s), while flow velocity at other places was 8BL (m/s). Therefore, it was thought that there was fish which

 ©2017, IAHR. Used with permission / ISSN 1562-6865 (Online) - ISSN 1063-7710 (Print)

evacuated into the group of column. Moreover, flow velocity in the group of column was also less than 4BL (m/s) in Run3. However, the fish did not exist in the group of column.

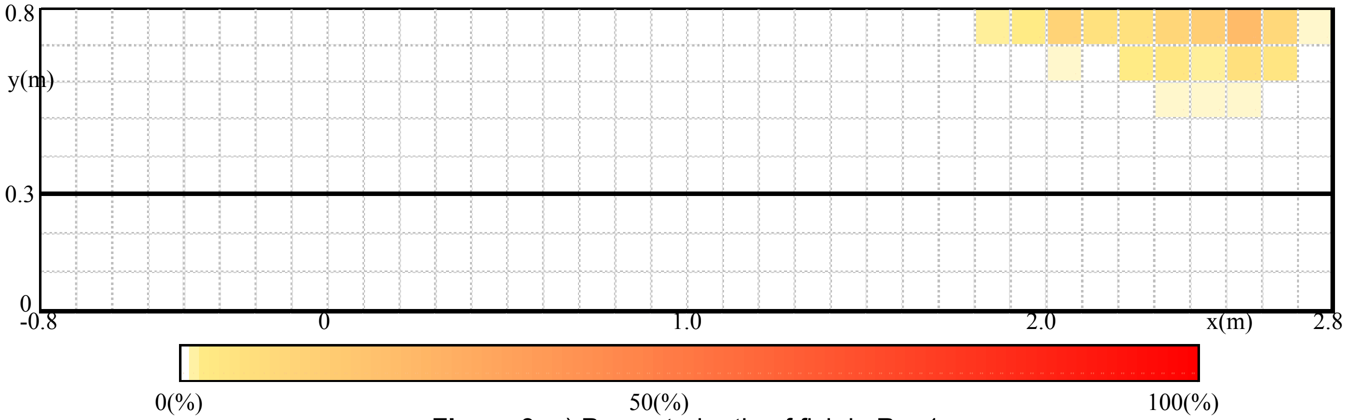

Figure 9. a) Presented ratio of fish in Run1.

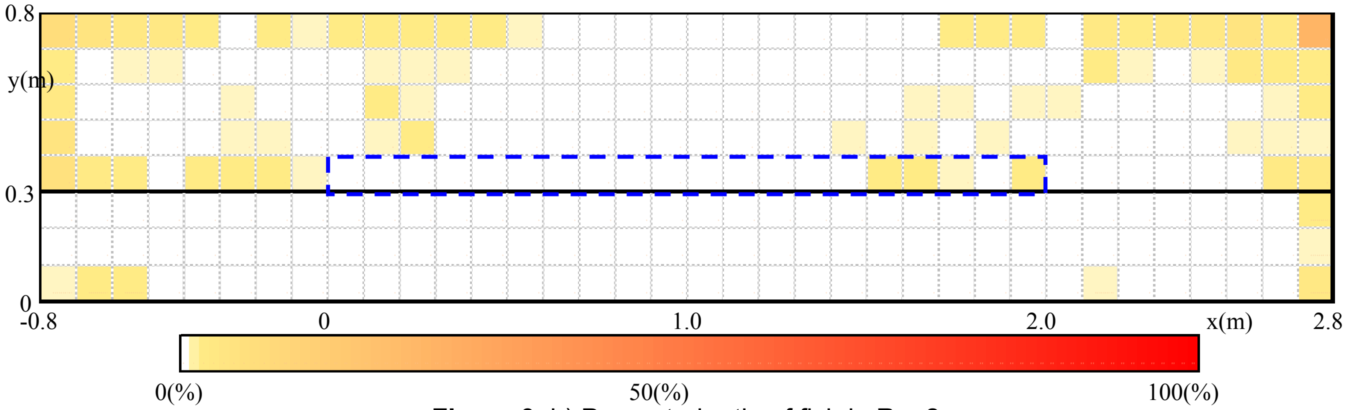

Figure 9. b) Presented ratio of fish in Run2.

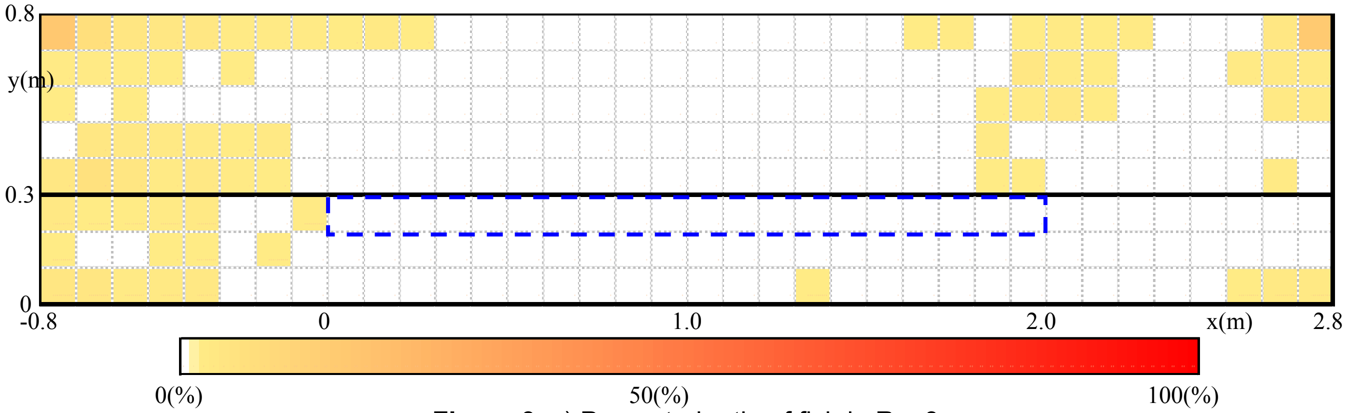

Figure 9. c) Presented ratio of fish in Run3.

4 CONCLUSIONS

When a low-flow channel or flood channel is installed with a group of column, the scale of the secondly flow increases caused by mizuhane influence. In addition, it might contribute to river erosion and scour due to the scale of the secondly flow than the case that sets up a group of column in the low-flow channel. The flow grows bigger in a compound cross-section open channel where a group of column is installed.

As for compound cross-section open channel flow, the flow is rather complicated. On the other hand, a choice enthusiast enacted domain is expanded for the fish in a crossing direction and the depth of the water direction. In addition, the domain allows the fish to choose because there is a group of column being expanded. Therefore, it becomes a factor that greatly changes the swimming point or behavior of the fish.

REFERENCES

Aoki, M., Somei, K., Kohara, M., Yoshino, T. & Fukui, Y. (2009). On the Hydraulic Function of Pile Dike using Thinned Wood and its Effectiveness as Fish Habitat. *Environmental Systems Research*, *JSCE*, 37, 19-28. (Japanese)

Biodiversity Center of Japan HP. Available: http://www.biodic.go.jp/ [Accessed 01/02/2017]

Ikeda, S., Murayama, Y. & Kuga, T. (1995). Stability of Horizontal Vortices in Compound Open Channel Flow and their 3-D Structure. *Journal of Society of Civil Engineers*, *JSCE*, 509(II-30,) 131-142. (Japanese)

Ikeda, S., Sano, T., Fukumoto, M. & Kawamura, K. (2000). Organized Horizontal Vortices and Lateral Sediment Transport in Compound Open Channel Flows. *Journal of Society of Civil Engineers*, *JSCE*, 656 (II-52), 135-144. (Japanese)

Ministry of Land, Infrastructure, Transport and Tourism, Water and Disaster Management Bureau HP. Available: http://www.mlit.go.jp/en/mizukokudo/index.html [Accessed 01/02/2017]

Nezu, I., Onitsuka, K., Sagara, Y. & Iketani, K. (2000). Effects of Relative Depth between Main-Channel and Flood-Plain on Turbulent Structure in Compound Open-Channel. *Journal of Society of Civil Engineers*, *JSCE*, 649(II-51), 1-15. (Japanese)

Tominaga, A., Eaki, K. & Kobatake, S. (1990). Three-Dimensional Turbulent Structure in Compound Open Channel Flows. *Journal of Society of Civil Engineers*, *JSCE*, 417(II-13), 129-138. (Japanese)

 ©2017, IAHR. Used with permission / ISSN 1562-6865 (Online) - ISSN 1063-7710 (Print)

EFFECTS OF THE POOL-AND-WEIR-FISHWAY WITH GRAVEL DEPOSIT ON MOVEMENT OF TORIBOLODON HAKONENSIS

MUNEYUKI AOKI[(1)] & KEITA SAITO[(2)]

[(1)] Department of Civil and Environmental Engineering, Toyo University, Kawagoe-shi, Saitama, Japan
[(1)]aoki037@toyo.jp
[(2)] Graduate Student of Master Course, Course of Civil and Environmental Engineering, Toyo University, Kawagoe-shi, Saitama, Japan

ABSTRACT

The purposes of this study are to examine the hydraulics characteristics in the pools with gravel deposit and characteristics of fish behavior on it. To complete them, the experiments in the small pool-and-weir-fishway are done. The experiments have been carried out by using the small pool-and-weir-fishway in the laboratory, to measure the flow velocity, water depth and to observe the movement of real fish. The real fish used is *Tribolodon hakonensis* for the experiments. For one experiment, 10 *Toribolodon hakonensis* are used. Those average body lengths is 0.085(m). In these experiments, the attention is focused on flow in the pool with gravel deposit and fish behavior. Especially, fish behavior mainly depends on hydraulic quantity; flow velocity and water depth. The explanation of the experiments cases are as follow. Flow quantity of Run1 is 0.008(m^3/s) and Run2 is 0.016(m^3/s). Condition of Pools bed of Run1-1 and Run2-1 are without gravel. On another front, in the pools of Run1-2 and Run2-2 gravel is depositing. Real fish run up approximately 0.02(m) of on the bed or gravel. In case of Run2-1, real fish employ the unique movement of fish against the flow in the pool. However, in case of Run2-2, real fish stayed often on the gravel. In cases of Run1-2 and Run2-2 run-up ratio has decreased more than Run1-1 and Run2-1 because flow in pools decreased the plunging flow area by the gravel. Moreover, run-up ratio of Run1-2 is the worst. Additionally, vorticity of flow increased in the pool, especially on the gravel. If gravel is deposited in the pool-and-weir-fishway, fish cannot easily run-up in the pools. Because, plunging flow area is decreased and vorticity of flow is increased.

Keywords: Pool-and-Weir-Fishway; Gravel Deposit; Flow; Vorticity; Fish Behavior.

1 INTRODUCTION

There are river mouth weirs and intake weirs, headworks, many river crossing structures including the dam in the rivers in wide ranges from the river mouth to the headstream. A continuity of the vertical section-like movement will be intercepted for the fish. Therefore, a fish-way is arranged to a river crossing structure, and fish and Crustacea can move upstream of a river. Until now, a fish-way has been established for a *Plecoglossus altivelis altivelis* and a *Oncorhynchus keta* which had high fisheries value in the country and overseas.

In addition, the fish-way is greatly distributed between three types (pool, stream and operation), and the pool-and-weir-fishway of the pool type is the most popular. In fact, the study about the pool-and-weir-fishway for *Plecoglossus altivelis altivelis* and *Oncorhynchus* department fish was conducted flourishingly in the country and overseas (e.g., Izumi et al., 2006; Bruce et al., 1989; Katopodis, 2005; Onitsuka et al. 2008; Takashima et al., 1984 and etc.). In the last few years of river environment and ecosystemic maintenance, consciousness to growth has increased by revisions of the River law in Japan. In this way, the fish-way studies for a *Toribolodon hakonensis* or a *Opsariichthys platypus* increase, too and come in response to the biodiversity (e.g., Hayashida et al., 2000; Kosaka et al., 2013; Onitsuka et al, 2007).

On the other hand, flow velocity and water depth in a pool-and-weir-fishway remarkably fluctuate for a change of the water quantity. In addition, there are various problems including the outbreak of the side wave and air bubbles (Nakamura and Wada, 1995), and deposit of sand and gravel in a pool of fish-way (Homma et al., 1993). As the results, the run-up ratio and the approach ratio to the fish-way decreased and showed that gravel deposit led to fish-way functional decline (Aoki et al., 2015). However, the factors of the functional decline do not become clear.

This study paid its attention to flow condition and the fish action in the pool at the time of the stone sedimentation in the stairs-type fishway in particular. Moreover, purposes of this study are to make the factors of the fish-way functional decline clear. Therefore, the model experiments carried out by using an open channel where the pool-and-weir-fishway had been set up, to measure the flow and to observe the movement of real fish. To complete them, the experiments in small pool-and-weir-fishway were done.

©2017, IAHR. Used with permission / ISSN 1562-6865 (Online) - ISSN 1063-7710 (Print)

2 EXPERIMENTAL METHODS

The experiments were carried out by using the small pool-and-weir-fishway in the laboratory, to measure the flow and to observe the movement of real fish. Figure 1 shows the pool-and-weir-fishway used for the experiments. Table 1 shows the cases considered in the experiments. As for the authors, overflow velocity of fish-way confirmed that a fish was easy to penetrate to the fish-way at the time of velocity of approximately 7BL (m/s) at the time of mean length BL (m) of the fish. Therefore, flow quantity Q set it in Run2-1 without gravel so that the overflow velocity of the fish-way the partition became approximately 7BL (m/s). In addition, flow velocity of the approximately 7BL (m/s) is the flow velocity that fish are easy to show the unique movement of fish against the flow in side wall of an open channel (Aoki et al., 2009). The deposit of the gravel in the pool spread the gravel of representative particle size d_{60}=15(mm) all uniformly as thickness 0.2 (m) with floor in each pool.

The real fish that used is *Tribolodon hakonensis* for the experiment. 10 *Tribolodon hakonensis* were used for one experiment. Those average body lengths (BL) were 0.08(m). These fish are common and popular in Japan. When the experiments were carried out, water temperature was 18~22 degree.

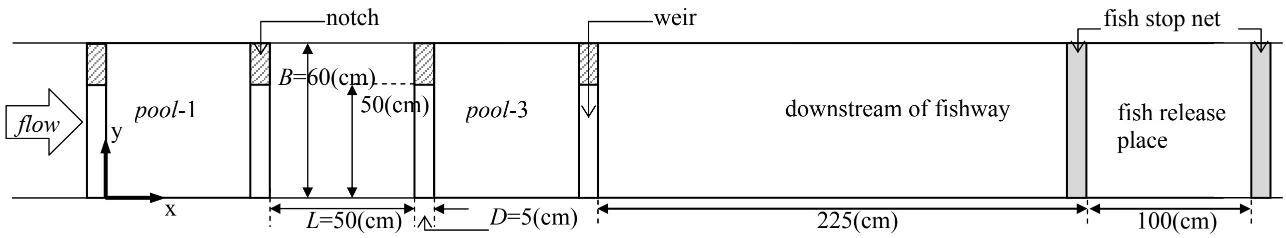

(a)

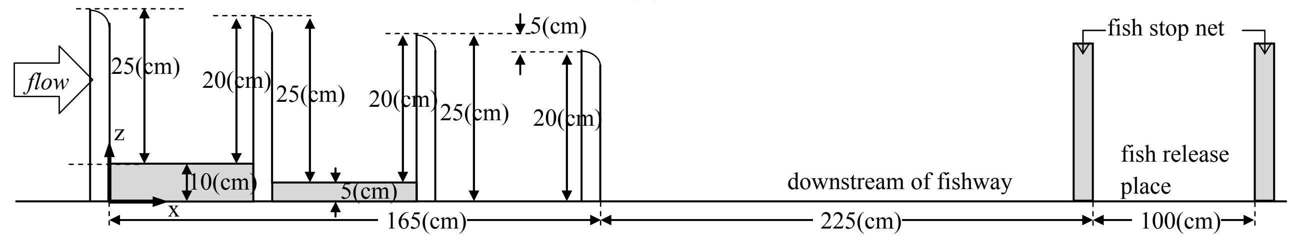

(b)

Figure 1. a) Plain view of the pool-and-weir-fishway b) Side view of the pool-and-weir-fishway.

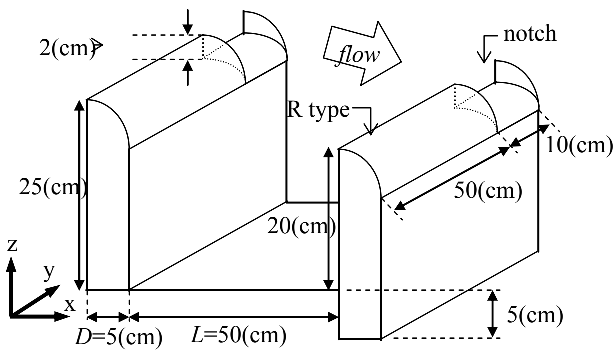

Figure 2. Enlarged view of the pool.

Table 1. Cases considered in the experiments.

	Water quantity, Q(m^3/s)	Gravel
Run1-1	0.008	None
Run1-2	0.008	Deposit
Run2-1	0.016	None
Run2-2	0.016	Deposit

 ©2017, IAHR. Used with permission / ISSN 1562-6865 (Online) - ISSN 1063-7710 (Print)

3 RESULTS OF EXPERIMENTS

3.1 Observe the movement of real fish

Figure 3 shows approach ratio F_{Er} and run-up ratio R_r in each case.

$$F_{Er} = \frac{F_E}{F_T} \times 100(\%) \quad [1]$$

$$R_r = \frac{F_c}{F_T} \times 100(\%) \quad [2]$$

where, F_c: number of fish of completed run up, F_e: number of fish of approached into fish-way, F_T: number of total fish

Figure 3 shows approach ratio F_{Er} and run-up ratio R_r in each case. R_r decreased 18(%) and 10 (%) each in Run1-2, Run2-2 with the stone in comparison with Run1-1, Run2-1 without the gravel. Moreover, FEr decreased 2(%) and 12 (%) each in Run1-2, Run2-2 with the stone in comparison with Run1-1, Run2-1 without the gravel. This was a tendency like the study of the past. In addition, this study paid its attention to flow condition and the fish action in the pool in Run2 which R_r and F_{Er} were higher in than Run1, because it makes a factor of the fish-way functional decline at the time of the sedimentation clear.

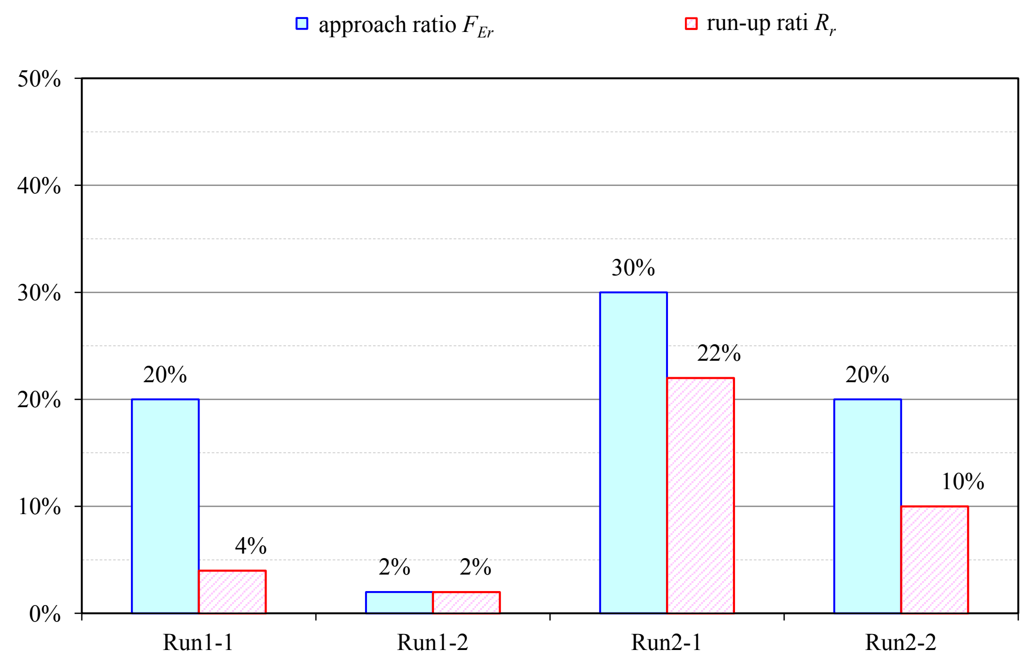

Figure 3. Approach ratio and run-up ratio in each case.

Figure 4 shows fish-way passage Transit time of fish in Run2. In Run2-1 and Run2-2, the maximum time when a fish passed a fish-way did not have the difference. However, it was 907.3 (s) in average transit time of Run2-2 and was 3.4 times of Run2-1. In the fish-way passage central value of the transit time of fish, it was 1,264 (s) in Run2-2. On the other hand, it was greatly different from 19(s) in Run2-1. It was p=0.01, and a different thing was significantly shown as a result that a fish performed t-test of the average time passed the fish-way. Therefore the gravel deposit disturbed the smooth run up of the fish and let a fish stay. Additionally, the swimming point of the fish was a point of the high approximately 2(cm) from a bed of the sidewall (y=2.5(cm) and y=57.5(cm): notch region) neighborhood.

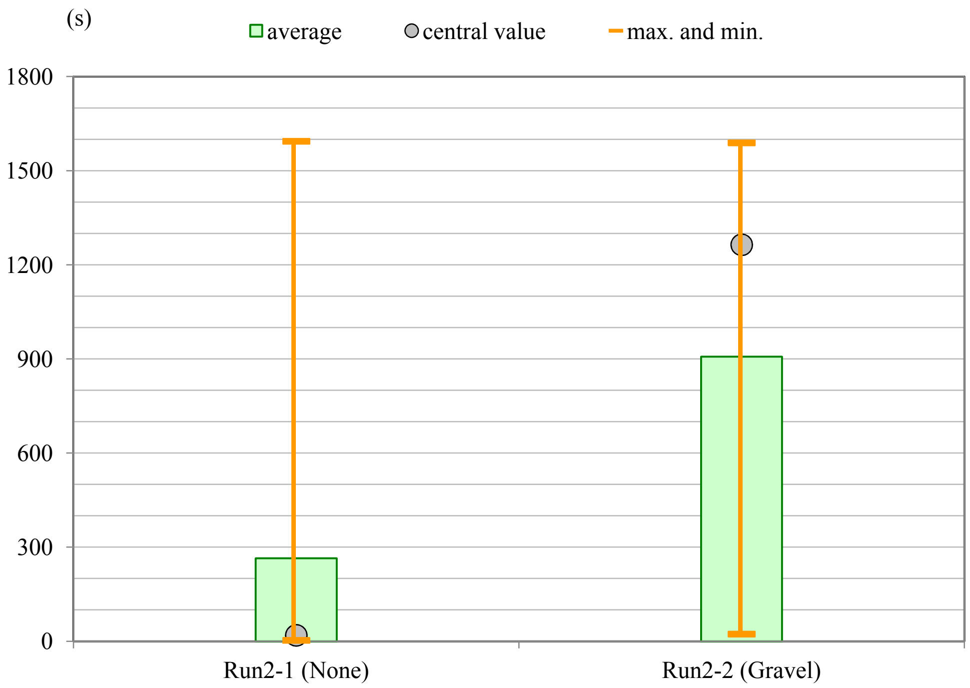

average time	264.4(s)	907.3(s)
central value	19(s)	1,264(s)
Minimum time	3(s)	23(s)
Maximum time	1,594(s)	1,589(s)

Figure 4. Fish-way passage the transit time of fish in Run2.

3.2 Hydraulic experiments

Figure 5 shows uw vector, water level in x direction, gravel deposition thickness and vorticity ω_y in Run2. As for the flow of Run2-1 and Run2-2, a plunging flow is formed of the whole pool. It is said that a fish is easy to run up as for plunging flow. On the other hand, the domain of the plunging flow is reduced in Run2-2 by the gravel deposit. Then, the attention point is vorticity ω_y in the pool. In Run2-1 and Run2-2, the upper downstream side partition was a counterclockwise rotation from the lower upstream side partition in the pool. Additionally, the flow in the fish-way that paid its attention to vorticity ω_y showed a plunging flow generally.

4 CONCLUSIONS

1) In what a gravel deposited in a pool, the fish-way average transit time of the fish increased in comparison with a state without the gravel. These results were significantly different and showed that the gravel deposit let obstruction, a fish of the smooth going up of the fish stay.

2) With or without the gravel deposit in the pool, a plunging flow was formed. Vorticity ω_y is to pay the attention and can grasp the flow in the pool.

 ©2017, IAHR. Used with permission / ISSN 1562-6865 (Online) - ISSN 1063-7710 (Print)

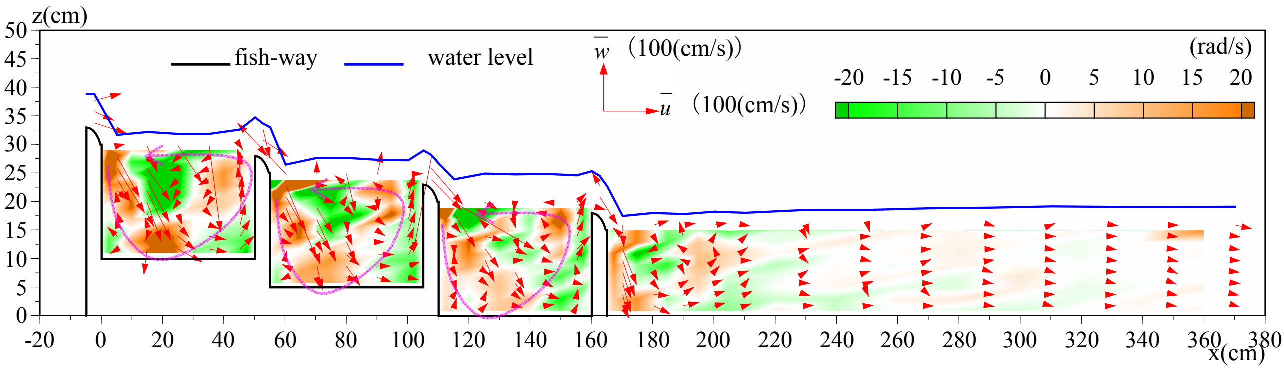

(a)

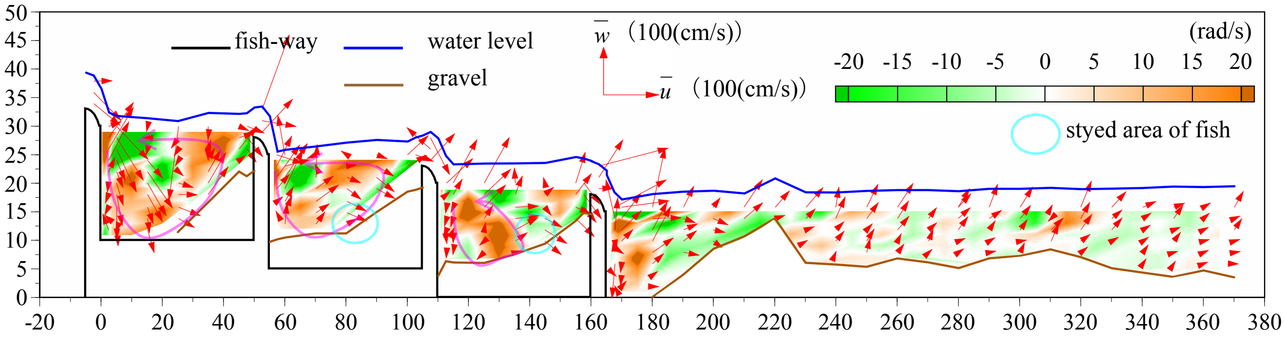

(b)

Figure 5. a) uw vector, water level in x direction, gravel deposition thickness and vorticity ω_y in Run2-1 b) uw vector, water level in x direction, gravel deposition thickness and vorticity ω_y in Run2-2

REFERENCES

Aoki, M., Somei, K., Kohara, M., Yoshino, T. & Fukui, Y. (2009). On the hydraulic function of pile dike using thinned wood and its effectiveness as fish habitat. *Environmental Systems Research*, *JSCE*, 37, 19-28 (Japanese)

Aoki, M., Yoshino, T. & Fukui, Y. (2009). Flow in the downstream of a fish-way with a priming water and fish behavior to it. *Journal of Japan Society of Fluid Mechanics*, JSFM, 28(6), 485-494 (Japanese)

Aoki, M., Mukai, T., Kikuchi, Y. & Matsuki, K. (2015) On the effect of the fish behavior on gravel deposit in a pool-and-weir-fishway. *Journal of Society of Civil Engineers B1*, *JSCE*, 71(4), I_1099-I_1104 (Japanese)

Bruce, M., Dick, W., Clark, T. & Frank, O. (1989). Effects of Flow and Weir Design on the Passage Behavior of American Shad and Salmonids in an Experimental Fish Ladder. *North American Journal of Fisheries Management*, 9(1), 60-67

Hayashida, K., Honda, T., Kayaba, Y. & Shimatani, Y. (2000). The characteristic of the plunging flow and the streaming flow in the pool-weir-fishway and the swimming behavior of *leuciscus hakonensis*. *Environmental Systems Research*, *JSCE*, 28, 333-338 (Japanese)

Homma, H., Abe, H. & Mizuyama, T. (1993). Flow at slit fishways and whole-width fishways. *Journal of the Japan Society of Erosion Control Engineering*, *JSECE*, 45(6), 25-31

Izumi, M., Ito, R., Yataya, K. & Azuma, N. (2006). Ascending fishes hydraulic characteristics of the full-cross-sectional overflow stepped-pool type fishway in the Iwaki River Diversion weir of the Iwaki River. *Journal of Society of Irrigation, Drainage and Rural Engineering*, 245, 55-64 (Japanese)

Katopodis, C. (2005). Developing a toolkit for fish passage, ecological flow management and fish habitat works. Journal of Hydraulic Research, 43(5), 451-467

Kosaka, Y., Aoki, M. & Fukui, Y. (2013). A study on the behavior of straying fish in a pool-and-weir-fishway. *Journal of Society of Civil Engineers B1*, *JSCE*, 69(4), I_1315-I_1320 (Japanese)

Nakamura, S. & Wada, K. (1995). Field observation of water surface oscillation in a pool-weir fishway. *Journal of Society of Civil Engineers*, *JSCE*, 521 / II-32, 207-215 (Japanese)

Onitsuka, K., Akiyama, J., Kiuchi, D., Takahashi, Y. & Iiguni, Y. (2007). Effect of location of notch on migration rate in pool-and-weir-fishway. *Annual Journal of Hydraulic Engineering*, *JSCE*, 51, 1279-1284 (Japanese)

Onitsuka, K., Akiyama, J., Kiuchi, Iiguni, Y. & Mori, Y. (2008). Effect of notch in pool-and-weir-fishway on migration rate. *Annual Journal of Hydraulic Engineering*, *JSCE*, 52, 1201-1206 (Japanese)

Takashima, N. & Nakamura, S. (1984). Experimental study on the behavior of Ayu in fishladder. *Annual Journal of Hydraulic Engineering*, *JSCE*, 28, 353-358 (Japanese).

©2017, IAHR. Used with permission / ISSN 1562-6865 (Online) - ISSN 1063-7710 (Print)

Proceedings of the 37th IAHR World Congress
August 13 – 18, 2017, Kuala Lumpur, Malaysia

INFLUENCE OF WATER DIVERSION ON THE MICRO-ECOSYSTEM OF SHALLOW EUTROPHIC LAKE TAIHU, CHINA

JIANGYU DAI(1), SHIQIANG WU(2), XIUFENG WU(3), DAN CHEN(4), WANYUN XUE(5), QIANQIAN YANG(6) & FANGFANG WANG(7)

(1,2,3,5,6,7) State Key Laboratory of Hydrology-Water Resources and Hydraulic Engineering, Nanjing Hydraulic Research Institute, Nanjing, 210029, P. R. China
jydai@nhri.cn; sqwu@nhri.cn; xfwu@nhri.cn; wyxue@nhri.cn; yangqianqian@nhri.cn; 717044621@qq.com
(4) Nanjing Institute of Environmental Sciences, MEP, Nanjing, 210042, P. R. China
chendan_nies@163.com

ABSTRACT

The Water Diversion from Yangtze River to Taihu Lake is a typical eco-hydraulic engineering towards the ecological problems in the large shallow eutrophic Lake Taihu, China. To explore the quantitative relationships among different flow discharges and environmental parameters from the Wangyu River and Lake Taihu, we construct the micro-ecosystems modeling Lake Taihu in the laboratory, with five groups of flow discharges according to the practical discharges of the Wangyu River. Each micro-ecosystem has a volume of 15 L and is studied for a period of 30 days (25 days for the water diversion period and 5 days for the stop period). The results shows that the flow discharges has different extents of impact on the physicochemical and biological characteristics of the micro-ecosystems. The contents of total nitrogen, nitrate, active silicon and bacterial cell abundance in the experimental groups with the flow discharges corresponding to those higher than the 100 m^3/s are all decreased comparing to the control group, with the lowest values in the period of 10 to 15 day. After the stop period, the contents of sensitive biotic and abiotic parameters are all recovered with different extents and not to be the initial state of this experiment, which revealed that the effects of the short-term water diversion on lake ecosystems are resilient and durable. There were quantitative relationships among the flow discharge, content interpolation and variation of water nutrients, with different relationships in different periods of water diversion. The influence of water diversion on lake ecosystems is not only related with the direct impacts of external inputs, but also with the indirect effects of variation in internal lake habitats affected by water diversion.

Keywords: Water diversion; micro-ecosystem; inflow discharge; quantitative relationship; Lake Taihu.

1 INTRODUCTION

Lake eutrophication is the widespread environmental problem all over the world (Schindler, 1974; Qin, 2009). Nutrient enrichment in eutrophic lakes can promote the algae proliferation, and thus might produce cyanobacterial blooms (Paerl et al., 2011). Serious cyanobacterial bloom is a great threat to water quality and ecological function of lakes. As an important engineering measure, coping with cyanobacterial blooms and their impacts on lake ecosystems, water diversion engineering can transfer the foreign water into lakes to enlarge the environmental capacity and shorten the lake residence period, and has been applied in many eutrophic lakes worldwide (Hosper, 1998; Hu et al., 2008; Li et al., 2011; White et al., 2009; Zhai et al., 2010).

Lake Taihu is the third largest eutrophic freshwater lake in China and is also troubled in frequent cyanobacterial blooms in most of the year (Qin et al., 2007). The Water Diversion from Yangtze River to Taihu Lake (WDYT) is a typical eco-hydraulic engineering giving consideration to both environmental improvement and water supply of Lake Taihu Basin (Wang and Wang, 2008; Dai et al., 2016). Previous studies revealed that the water level (Hu et al., 2008; Hao et al., 2012), water age (Li et al., 2011) and lake currents (Hu et al., 2008; Li et al., 2013) of Lake Taihu had been significantly influenced by WDYT under the condition of the limited inflow discharge. However, as an important operation parameter of the water diversion engineering, the inflow discharge represents not only the water flow, but also the inputs of quantities of nutrients and organisms. Higher inflow discharge can improve the hydrodynamic conditions of lakes, and will also potentially import more nutrients and alien biological species. The suitable inflow discharge and time length for water diversion are critical to increase economic and ecological benefits of this kind of engineering.

Previous researches about the optimization of water diversion scheduling are mainly based on the hydrodynamic impacts on lakes (Hao et al., 2012; Li et al., 2011; Li et al., 2013; Xie et al., 2008; Zhao et al., 2012). Few studies take the physicochemical and biological effects into consideration. Generally, field monitoring is a popular way to investigate the ecological effects of water diversion. However, because of uncertain environmental factors like wind wave, the responsive relationships between the different inflow discharges and ecological effects cannot be revealed clearly. The reconstruction of lake aquatic micro-ecosystem provides an alternative approach to resolve this problem. The model aquatic micro-ecosystem

 ©2017, IAHR. Used with permission / ISSN 1562-6865 (Online) - ISSN 1063-7710 (Print)

methodology, mainly comprised of microbes, abiotic substances and environmental conditions, has been widely used in the studies of lake eutrophication (Psenner et al., 2008). Moreover, as the most diverse and active microbe in lakes, bacteria are sensitive to variations of limnetic environments and are always taken as one of indexes representing the evolution of lake ecosystems (Paerl et al., 2003; Shade et al., 2011).

Therefore, to reveal the relationship between inflow discharge and ecological elements in Lake Taihu, we constructed the model aquatic micro-ecosystem of Lake Taihu to uncover the ecological influences of WDYT on Lake Taihu. The contents of water physicochemical parameters and bacterial abundance were measured simultaneously. Quantitative relationships between different inflow discharges and measured parameters were also recovered. Finally, this study proposed the suitable inflow discharges for WDYT based on its impacts on the model aquatic micro-ecosystem of Lake Taihu.

2 MATERIALS AND METHODS

2.1 Model aquatic micro-ecosystem construction

Gonghu Bay is the typical eutrophic water region of Lake Taihu and is always influenced by frequent cyanobacterial blooms during most of the year (Jiao et al., 2013). Wangyu River is the largest water diversion channel importing water from Yangtze River to Lake Taihu (Ma et al., 2014). Gonghu Bay is the first water-receiving area of the imported water from Wangyu River (Figure 1). We collected the water and surface sediment from the sampling site in Gonghu Bay to construct the model aquatic micro-ecosystem of the Lake Taihu. The water of Wangyu River was collected during the period of water diversion to be as the imported water in the micro-ecosystem experiment.

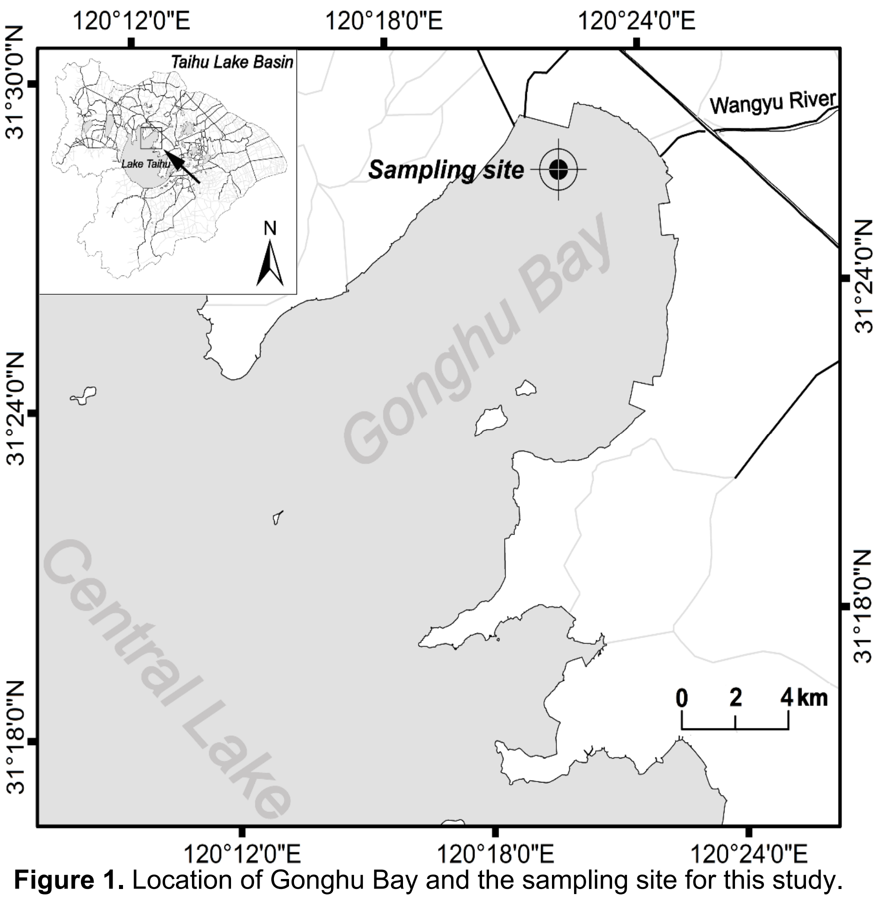

Figure 1. Location of Gonghu Bay and the sampling site for this study.

In the laboratory, the collected lake sediment was mixed homogeneously and allotted into 18 equal amounts. Each amount was putted into a 30cm high transparent cylindrical organic glass container of which the diameter is 35 cm. The thickness of the sediment layer is about 5 cm in each container. After this, the 15 L of collected lake water was slowly poured into each container and was stood for 5 days to shape a steady water-sediment interface. This steady ecosystem was the model aquatic micro-ecosystem of the eutrophic Gonghu Bay. During the modelling experiment, the river water was imported into the micro-ecosystem by regulating the threaded valve to control the inflow discharge. Each drop of water is calculated by 0.05 mL. The schematic diagram of the model aquatic micro-ecosystem is as Figure 2.

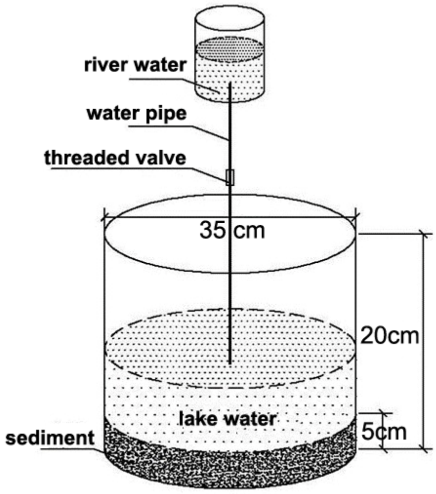

Figure 2. The schematic diagram of the model aquatic micro-ecosystem

2.2 Experiment setting up and sampling

This experiment had one control group and 5 treatment groups. Each group had 3 replicates. The control group was the non-diversion group, whereas the 5 treatment groups had different inflow discharge treatments. The inflow discharges were determined based on the average inflow discharge in 2013, according to the ratio of the average water volume of Gonghu Bay to the 15 L of the model aquatic micro-ecosystem. Corresponding to the practical inflow discharges of 25, 50, 100, 150 and 200 m^3/s in the Wangyu River, we set the five modelling inflow discharges of 216 mL/d (T1), 432 mL/d (T2), 864 mL/d (T3), 1296 mL/d (T4) and 1728 mL/d (T5), respectively.

The initial day of this experiment was at the Dec 9th, 2013. The whole period of this experiment lasted for 30 days, from which the first 20 days were the period of water diversion and the last 10 days were the stop period of water diversion. The water samples of the micro-ecosystems were collected at 9:00 of the 1, 3, 5, 7, 10, 15, 20, 25, 30 days. The last two collections were used to determine the recovery of the micro-ecosystems after stopping water diversion. During the whole period of this experiment, the air temperature of the laboratory was controlled to be about 25℃. The water-sediment interface must be protected to avoid the nutrient releasing during the sampling process.

2.3 Measurement of abiotic and biotic parameters

Before each sampling, the water temperature, pH, dissolved oxygen (DO) and turbidity were detected using the AP-2000 multi-parameter analyzer (HACH, China). After this, a 500 mL water sample was collected from each container for measuring the contents of water total nitrogen (TN), total phosphorus (TP), ammonia (NH_3-N), nitrate (NO_3-N), soluble reactive phosphorus (SRP), dissolved organic carbon (TOC) and active silicate (SiO_3-Si). Moreover, a 50 mL additional water sample was collected from each container for bacterial cell abundance counting.

The contents of TN, TP, NH_3-N, NO_3-N and SRP were measured according to the methods in the literature (Jin and Tu, 1990). DOC and active silicate contents were analyzed using the multi N/C 3100 TN/TOC analyzer (Analytik Jena, Germany) and the method in the literature (Wang et al., 2002), respectively. Water bacterial cell abundance counting was according to the 4',6-diamidino-2-phenylindole (DAPI) labelling method used in the Lake Taihu (Gao et al., 2007).

2.4 Statistical analysis

The dynamics of water parameters in each group were compared using the repeated measures ANOVA in the SPSS 16.0 software (SPSS, China). Differences in bacterial cell abundance among each group were compared using the one-way ANOVA. The variation rates of the sensitive aquatic parameters were the percentages of the difference between the values in the 25th and initial days to the values in the 25th day. The recovery rates were the percentages of the difference between the values in the 25th and 30th days to the values in the 25th day. The Pearson correlation method was used to detect the linear correlation among bacterial cell abundances and water parameters. The statistical figures were plotted using the software Sigmaplot v13.0 (Systat Software Inc., USA).

 ©2017, IAHR. Used with permission / ISSN 1562-6865 (Online) - ISSN 1063-7710 (Print)

3 RESULTS AND DISCUSSIONS

3.1 Dynamics of aquatic biotic and abiotic variables in different groups

The values of the physicochemical parameters of the collected water from Wangyu River is shown in Table 1. From these river parameters, the values of pH, TN, NO_3-N, SO_3-Si were significantly lower than these in the lake water, whereas the contents of DO, turbidity and TP in the river water were higher (One-way ANOVA, $P<0.05$). The water temperature of the six groups were controlled to be 24~26℃ and were not significantly different among different groups (Repeated measures ANOVA, $P<0.05$).

Table 1. The mean values and standard deviations of the river physicochemical parameters.

Physicochemical parameters	Mean values	Standard deviations
pH	7.67	0.19
DO (mg L^{-1})	9.27	0.57
Turbidity (NTU)	27.0	3.3
TN (mg L^{-1})	1.09	0.09
TP (mg L^{-1})	0.068	0.015
SRP (mg L^{-1})	0.005	0.002
NO_3-N (mg L^{-1})	0.92	0.10
NH_3-N (mg L^{-1})	0.12	0.08
DOC (mg L^{-1})	2.85	0.63
SiO_3-Si (mg L^{-1})	3.07	0.86

The dynamics of the water physicochemical parameters in each group were revealed in Figure 3. The pH values of each group were at the range of 8.35~8.78 during the experiment. Although the pH value was significantly lower than the lake water in the micro-ecosystem, the pH values of the lake water were not profoundly influenced. Moreover, the differences in pH values were also not evidently among different treatment groups (Repeated measures ANOVA, P>0.05, Figure 3a). The little impact of pH was because the transient discharge of the river water was much less than the water in the micro-ecosystem.

The DO contents in each group increased along with the process of water diversion and tended to be stable at the 15th day. The repeated measures analysis among different groups showed that the DO contents in group T5 were higher than other groups and no significant difference was found among other groups (Figure 3b). Previous studies (Han and Wen, 2004) demonstrated that the DO contents might be influenced by many factors such as water temperature, illumination, water depth and so on. The higher DO contents in the group T5 might be related to the higher inflow discharge and DO content of the river water. Additionally, the water turbidities in each group were all significantly decreased during the experiment (Figure 3c). In the hydrostatic condition of this experiment, the inflow discharge had no significant impact on the turbidities of the aquatic micro-ecosystems. The imported particles and suspended substances were all precipitated on the surface of sediments.

The repeated measures ANOVA of water TN and NO3-N showed that the control group was different from each treatment group except the group T1 and T2 (Repeated measures, P<0.05). The higher inflow discharge was, the lower water TN and NO3-N contents were. The TN and NO3-N contents in each group showed the same increasing trend until the 15th day (Figure 3d&e). The increase of TN contents in the control group might be related to the nutrient release from the sediments (Peng, 2011). The dynamics of NH3-N contents were different from the TN and NO3-N contents, but the contents in the control group were also higher than in the groups T3, T4 and T5 (Repeated measures, P<0.05, Figure 3f).

The TP and SRP contents in each group were all decreased during the first 5 days and were increased to be stable after 10 days, which was attributed to the precipitation of particulate phosphorus and the release of sedimentary phosphorus. During the whole experiment, there was no difference in the TP and SRP contents among the 6 groups (Repeated measures, P>0.05, Figure 3g&h).

Dissolved organic carbon is the important carbon source for aquatic heterotrophic microbes. The DO content is related to the abundance, community and activity of microbes (Bai et al., 2004; Feng et al., 2006; Zhou et al., 2007). The same as the trends of TP and SRP, the DOC contents were increased and tended to be stable at the 10th day. There was no significant difference among the 6 groups, which was attributed to the same level of DOC contents in the river and lake water (Figure 3i).

As an indispensable nutrient for the phytoplankton, the active silicate plays an important role on the aquatic primary production (Ragueneau et al., 2002). During this experiment, the SiO3-Si contents in each group showed a decreasing trend, which was connected with the lower contents in the river water (Figure 3j). The repeated measures ANOVA among different groups revealed that contents of the control group were significantly different from those of the groups T3, T4 and T5 (Repeated measures ANOVA, P<0.05). This result indicated that the inflow discharges higher than 100m3/s could profoundly influence the active silicate contents in the eutrophic lake regions. After stopping the water diversion, the active silicate contents in each group was always higher than the content of 6.0 mg L-1. This content is suitable for the growth of diatom and increases the competitiveness of diatom against other algae species (Sun et al., 2007).

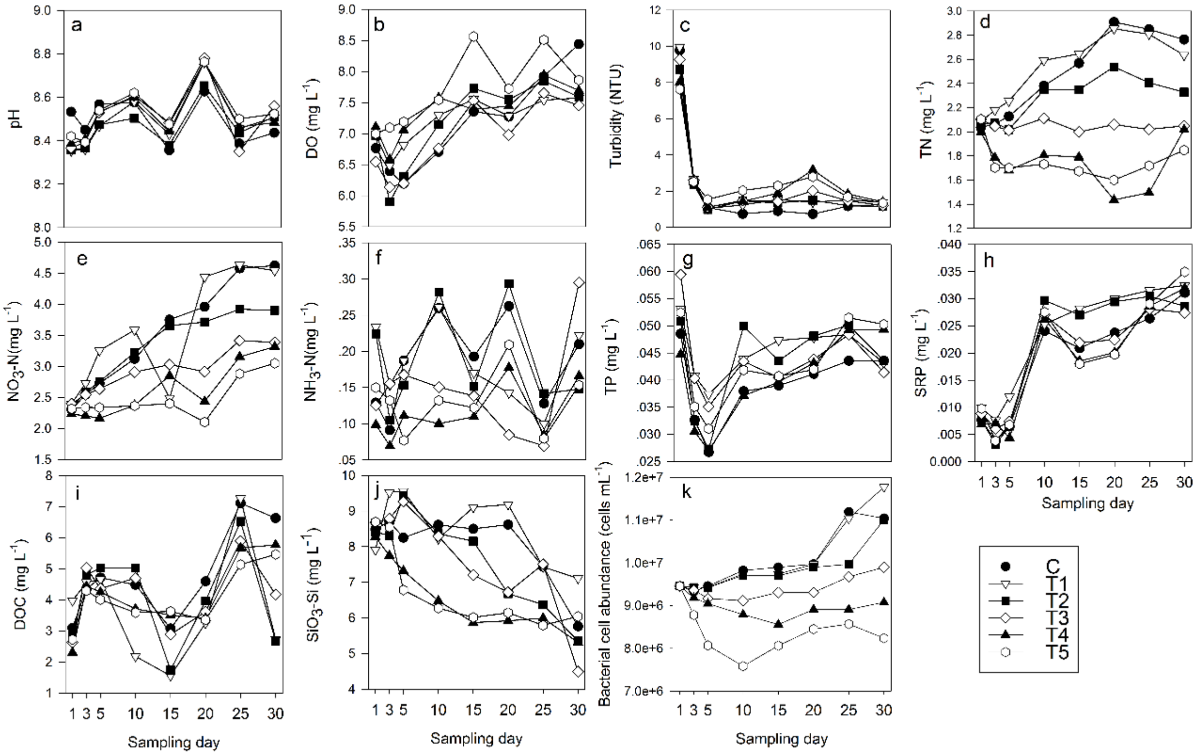

Figure 3. Variations of aquatic biotic and abiotic variables in lake micro-ecosystems during this experiment.

Because the initial bacterial cell abundance of the river water was 3.11×106 cells mL-1 and was significantly lower than the initial one of 9.46×106 cells mL-1 in the lake water, bacterial cell abundances in the groups of T3, T4 and T5 were decreasing during the period of water diversion. The one-way ANOVA comparison among different groups showed that bacterial cell abundances in groups of T3~T5 were significantly lower than the control groups (P<0.05). The dynamics of T1 and T2 groups were similar to the control group (Figure 3k). After 15 days of water diversion, the bacterial cell abundances tended to be increasing in the high inflow discharge groups of T4 and T5. The main reason for this phenomenon is due to the release of endogenous nutrition from lake suspended substances and sediments. Bacteria are sensitive to environmental changes and their growth periodicity is short, thus bacterial cell abundances in the experimental groups can response to aquatic habitat variations quickly (Paerl et al., 2003). Additionally, the average values of bacterial cell abundances in the five treatment groups were negative correlated with the inflow discharges, which indicated there might be some quantitative relationships between inflow discharges and bacterial cell abundances.

3.2 Reversibility of the micro-ecosystems influenced by water diversion

According to the repeated measures results, DO, TN, NO_3-N and SiO_3-Si were the sensitive aquatic parameters. During the period of water diversion at the 25^{th} day, only the variation rate of the DO content in group T5 (21.6%) was higher than that (17.0%) in the control group, while the DO contents in other groups were lower. However, the recovery rates of all treatment groups were negative, which indicated the DO contents decreased after water diversion (Figure 4a).

The variation rate of TN contents in the control group was 21.7%, while those in groups T3~T5 were -9.1%, -9.5% and -19.3%, respectively. After stopping water diversion, the recovery rates of the treatment groups were at the range of 30.3%~37.2% (Figure 4b). The increase of TN content was attributed to the release of sedimentary nitrogen. Similarly, the NO3-N content in the control group was also increased in compared to the initial day. There was no significant recovery rates in each group (Figure 4c).

Because the active silicate content in the river water was lower than in the lake, the variation rates in each treatment group was negative and had positive correlation with the inflow discharges. After water diversion, the active silicate content in each group decreased in contrast to the contents at the 25th day (Figure 4d), which was related to the absorption of the sediments.

The variation rates of bacterial cell abundances were negative correlated with the inflow discharges at the 25th day. In the groups T4 and T5, the variation rates were negative. After stopping water diversion for 5 days, the recovery rates of bacterial cell abundances in groups T1~T4 were all positive, whereas negative in

 ©2017, IAHR. Used with permission / ISSN 1562-6865 (Online) - ISSN 1063-7710 (Print)

group T5 (Figure 4e). Although bacterial cell abundances might be recovered for a longer time, the impacts of water diversion with the high inflow discharge could not be recovered in a short-term period.

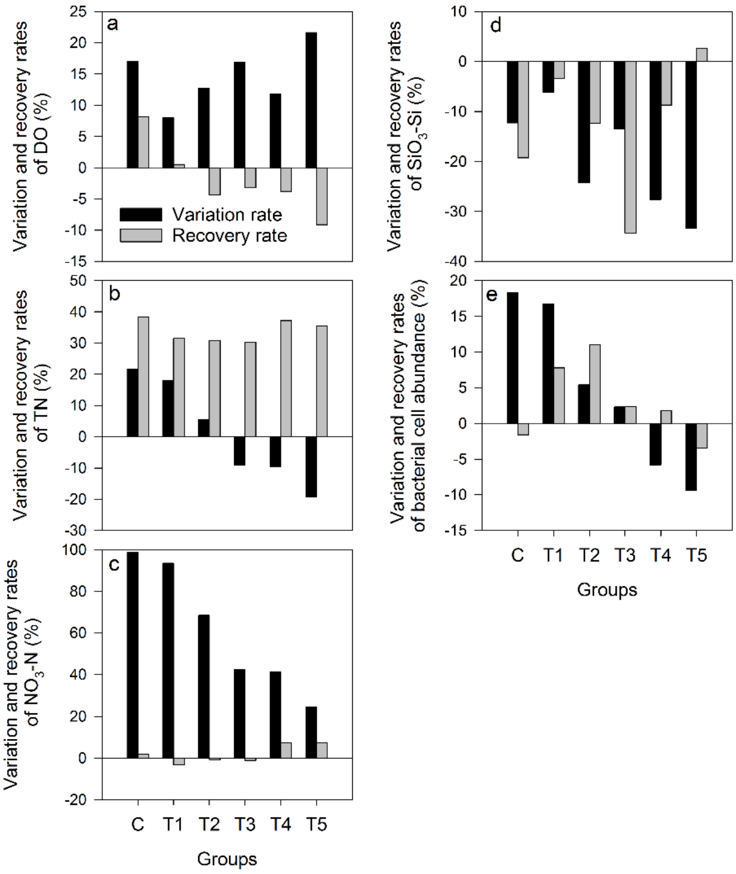

Figure 4. The variation and recovery rates of sensitive aquatic variables during the experiment.

The recovery of the sensitive aquatic parameters indicated that the influences of water diversion on lake ecosystems were reversible and durable. As for the eutrophic lake regions in Lake Taihu, the WDYT engineering has the positive contribution to environmental improvement and should be running for a long-term.

3.3 Relationships between inflow discharges and aquatic variables

Because the ecological effects induced by water diversion are time sensitive, the responses of aquatic ecosystem at different periods of water diversion are different. In this study, the quantitative linear relationships between the variation values of sensitive aquatic parameters and the inflow discharges were recovered at the 5th, 15th and 25th days, respectively. The variations of TN, NO_3-N, SiO_3-Si and bacterial cell abundance parameters were most correlated with the inflow discharges. The fitting linear curves between the variations of TN contents and inflow discharges were in Figure 5a. The quantitative relationships were positive at the 5th and 15th day, respectively, while it is negative at the 25th day. The negative quantitative relationship at the 25th day was related with the release of sedimentary nitrogen when the TN content was decreased by the water diversion. The quantitative relationship between NO_3-N contents and the inflow discharges were similar (Figure 5b).

The fitted linear curves of the active silicate contents were not well as the nitrogen contents (Figure 5c). At the initial term of water diversion, increasing the inflow discharge could quickly decrease the content of active silicate in the micro-ecosystem. At the mid-term and last term of water diversion, the quantitative relationships were negative and the effects of increasing inflow discharges were not evident. The bacterial cell abundances were well positive correlated with the inflow discharges at different periods of water diversion (Figure 5d).

In this study, we attempted to recover the quantitative relationships between inflow discharges and the variations of sensitive aquatic parameters, which demonstrated the ecological forecast of water diversion was available. Because of the unmanageable field conditions, it is difficult to conclude the quantitative relationships between inflow discharges and the aquatic conditions. The construction of aquatic micro-ecosystem provides a feasible way. However, the structures of lake ecosystems are always complicated and are influenced by many influencing factors, constructing the more similar lake ecosystem can demonstrate the actual quantitative relationship more accurate.

To reveal the quantitative relationships between bacterial cell abundances and environmental changes induced by water diversion, the Pearson correlation analysis was conducted to select the significant correlated physicochemical parameters. The contents of TN and NO3-N were significant correlated with bacterial cell abundances (Figure 6a&b). The aquatic nitrogen was the necessary nutrient for bacterial growth and proliferation. In freshwater lakes, the contents of nitrogen are always positive correlated with bacterial cell abundances (Feng et al., 2006). In this research, the improvement of different inflow discharges on contents of nitrogen are different. The model inflow discharge equivalent to the actual discharge of 100m3/s had made an obvious improvement to the water quality of the model aquatic micro-ecosystem. Increasing the inflow discharge might improve the ecological conditions in the northern part of Lake Taihu more quickly.

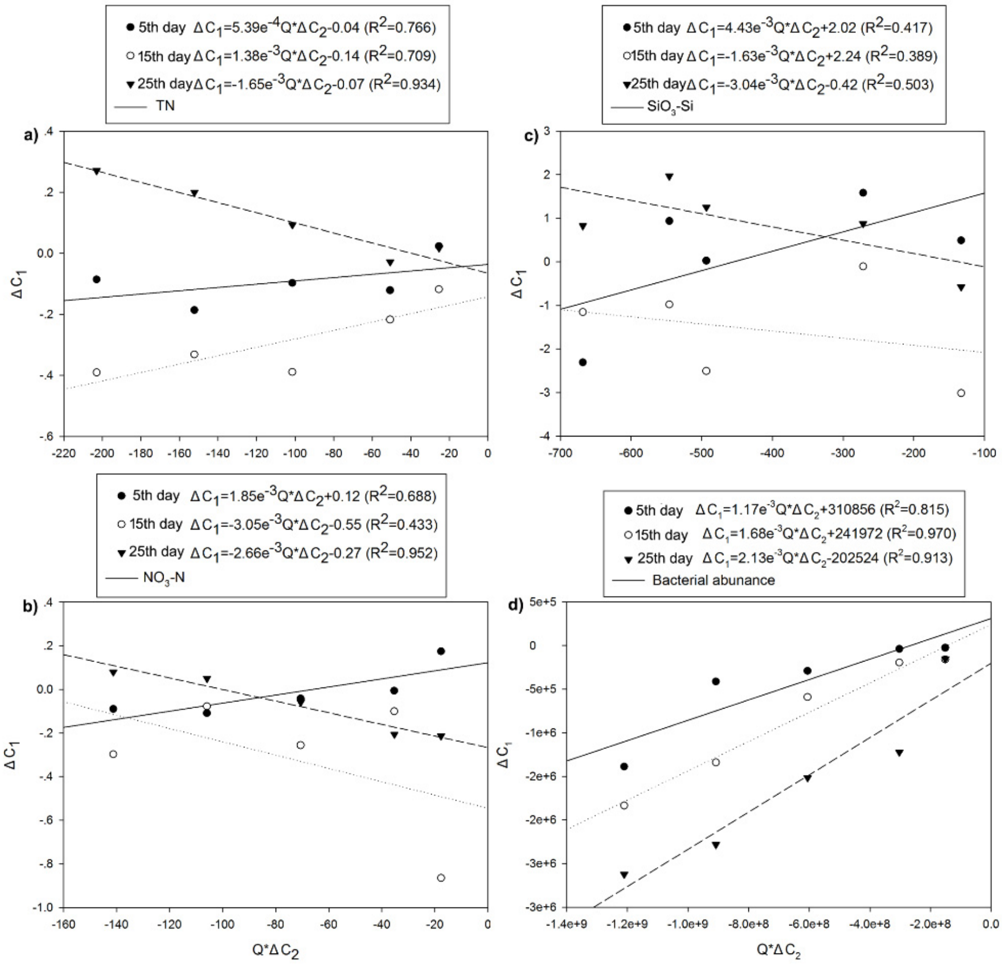

Figure 5. The quantitative relationships between the variations of lake parameters (ΔC_1) and the quantities of inflow substances higher than lake water ($Q^*\Delta C_2$) at different days.

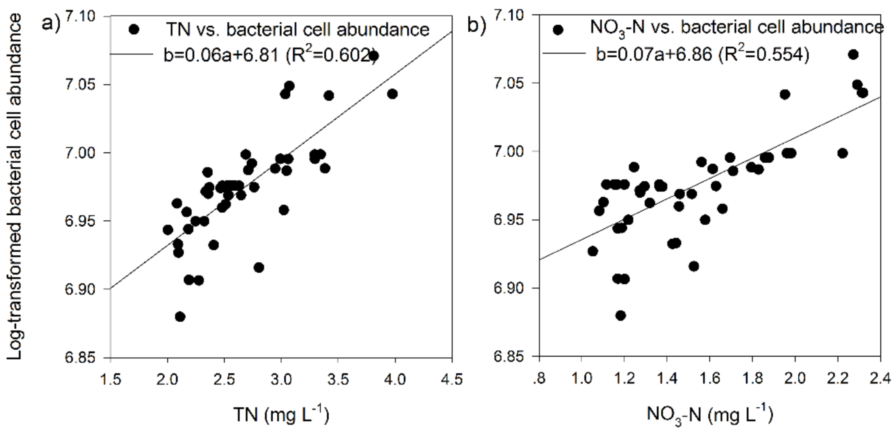

Figure 6. The quantitative correlations between bacterial cell abundances and the contents of nitrogen in the micro-ecosystems.

 ©2017, IAHR. Used with permission / ISSN 1562-6865 (Online) - ISSN 1063-7710 (Print)

4 CONCLUSIONS

In this study, we constructed the model aquatic micro-ecosystems to uncover the environmental effects of water diversion from Yangtze River to Lake Taihu on Gonghu Bay. The results revealed that the improvement of water diversion was positive correlated with the inflow discharges. The inflow discharges equal or greater than 100m^3/s significantly decreased the lake nitrogen contents and increased water oxygen contents. The influences of water diversion on the micro-ecosystems were reversible and durable. The variations of nitrogen and silicate contents induced by water diversion were quantitative correlated with the inflow discharges. At the initial, mid-term and last periods of water diversion, the quantitative relationships were different, which depends on the sensitivity of different parameters. As a kind of sensitive microbes, the decrease of bacterial cell abundance in lake water was quantitatively correlated with inflow discharges and the variations of physicochemical parameters. This indicated that the environmental changes induced by water diversion had significant biological impacts in the short time. The different quantitative correlations between bacterial cell abundances and inflow discharges at different periods of water diversion demonstrated the time sensitive of the ecological impacts of water diversion.

ACKNOWLEDGEMENTS

This work was jointly funded by the Projects of National Natural Science Foundation of China (Grant No. 51479120; 51479121; 51679146), the Program of International S&T Cooperation of China (2015DFA01000), the Special Research Funds for Public Welfare of the State Ministry of Water Resources (201501015-01), the Natural Science Foundation of Jiangsu Province (Grant No. BK20141075), and the Special Research Fund of Nanjing Hydraulic Research Institute (Y116006). Finally, we are grateful to the anonymous reviewers for their constructive comments and helpful suggestions.

REFERENCES

Bai, J., Zhang, H., Li, K. & Sun, J. (2004). Limiting Factors of Biomass and Production of Marine Heterotrophic Bacterioplankton. *Journal of Ocean University of Qingdao*, 34, 594-602.

Dai, J.Y., Wu, S.Q., Lv, X.Y., Yang, Q.Q., Wu, X.F., Zhou, J. & Wang, F.F. (2016). Effect of Water Diversion on Spatial-Temporal Dynamics of Organic Pollutants in Gonghu Bay, Lake Taihu. *Journal of Hydroecology*, 37(1), 39-46.

Feng, S., Gao, G., Qin, B. & Chen, M. (2006). Variability of Bacterioplankton in the North Zone of Lake Taihu. *Journal of Lake Sciences*, 6, 012.

Gao, G., Qin, B., Sommaruga, R. & Psenner, R. (2007). The Bacterioplankton of Lake Taihu, China: Abundance, Biomass, and Production. *Hydrobiologia*, 581(1), 177-188.

Han, S. & Wen, T. (2004). Phosphorus Release and Affecting Factors in the Sediments of Eutrophic Water. *Chinese Journal of Ecology*, 23(2), 98-101.

Hao, W.B., Tang, C.Y., Hua, L. & Kumud, A. (2012). Effects of Water Diversion from Yangtze River to Taihu Lake on Hydrodynamic Regulation of Taihu Lake. *Journal of Hohai University*, 40(2), 129-133.

Hosper, S.H. (1998). Stable States, Buffers and Switches: An Ecosystem Approach to the Restoration and Management of Shallow Lakes in the Netherlands. *Water Science & Technology*, 37(3), 151-164.

Hu, W., Zhai, S., Zhu, Z. & Han, H. (2008). Impacts of the Yangtze River Water Transfer on the Restoration of Lake Taihu. *Ecological Engineering*, 34(1), 30-49.

Jiao, Y., Chen, Q., Chen, X., Wang, X., Liao, X. & Jiang, L. (2013). Occurrence and Transfer of a Cyanobacterial Neurotoxin Β-Methylamino-L-Alanine within The Aquatic Food Webs of Gonghu Bay (Lake Taihu, China) to Evaluate the Potential Human Health Risk. *Science of the Total Environment*, 468-469C, 457-463.

Jin, X. & Tu, Q. (1990). The Standard Methods for Observation and Analysis of Lake Eutrophication. *China Environmental Science Press, Beijing*, 240.

Li, Y., Acharya, K. & Yu, Z. (2011). Modeling Impacts of Yangtze River Water Transfer on Water Ages in Lake Taihu, China. *Ecological Engineering*, 37(2), 325-334.

Li, Y., Tang, C., Wang, C., Anim, D.O., Yu, Z. & Acharya, K. (2013). Improved Yangtze River Diversions: Are They Helping to Solve Algal Bloom Problems in Lake Taihu, China? *Ecological Engineering*, 51(1), 104-116.

Ma, Q., Tian, W. & Wu, Z. (2014). Total Phosphorus and Total Nitrogen Concentrations of The Water Diverted from Yangtze River to Lake Taihu Through Wangyu River. *Journal of Lake Sciences*, 26(2), 207-212.

Paerl, H.W., Dyble, J., Moisander, P.H., Noble, R.T., Piehler, M.F., Pinckney, J.L., Steppe, T.F., Twomey, L. & Valdes, L.M. (2003). Microbial Indicators of Aquatic Ecosystem Change: Current Applications to Eutrophication Studies. *FEMS Microbiology Ecology*, *46*(3), 233-246.

Paerl, H.W., Xu, H., McCarthy, M.J., Zhu, G., Qin, B., Li, Y. & Gardner, W.S. (2011). Controlling Harmful Cyanobacterial Blooms in a Hyper-Eutrophic Lake (Lake Taihu, China): The Need for a Dual Nutrient (N & P) Management Strategy. *Water Research*, *45*(5), 1973-1983.

Peng, H. (2011). Effects of Resuspension on the Transfer and Transformation of Nitrogen and Phosphorus Species at Sediments-Water Interface in Simulative Lake System. *Research Journal of Chemistry & Environment*, 15(4), 14-17.

Psenner, R., Alfreider, A. & Schwarz, A. (2008). Aquatic Microbial Ecology: Water Desert, Microcosm, Ecosystem. What is Next? *International Review of Hydrobiology*, 93(4-5), 606–623.

Qin, B., Xu, P., Wu, Q., Luo, L. & Zhang, Y. (2007). Environmental Issues of Lake Taihu, China. *Hydrobiologia*, 581(1), 3-14.

Qin, B. (2009). Lake Eutrophication: Control Countermeasures and Recycling Exploitation. *Ecological Engineering*, 35(11), 1569-1573.

Ragueneau, O., Chauvaud, L., Leynaert, A., Thouzeau, G., Paulet, Y.M., Bonnet, S., Lorrain, A., Grall, J., Corvaisier, R., Le Hir, M. & Jean, F. (2002). Direct Evidence of a Biologically Active Coastal Silicate Pump: Ecological Implications. *Limnology and Oceanography*, *47*(6), 1849-1854.

Schindler, D.W. (1974). Eutrophication and Recovery in Experimental Lakes: Implications for Lake Management. Science, 184(4139), 897.

Shade, A., Read, J.S., Welkie, D.G., Kratz, T.K., Wu, C.H. & Mcmahon, K. D. (2011). Resistance, Resilience and Recovery: Aquatic Bacterial Dynamics after Water Column Disturbance. *Environmental Microbiology*, 13(10), 2752-2767.

Sun, L., Jin, X.C., Yang, W., Xu, M., Zhong, Y., Zhu, L. & Zhuang, Y.Y. (2007). Effects of Silicate on the Community Structure of Phytoplankton in Enclosures. Environmental Science, 28(10), 2174-2179.

Wang, P. & Wang, C. (2013). Water Quality in Taihu Lake and the Effects of the Water Transfer from the Yangtze River to Taihu Lake Project. *Comprehensive Water Quality & Purification*, 136-161.

Wang, X.F., Wei, F.S. & Qi, W.Q. (2002). The Analytic Methods for Natural Water and Wastewater Monitor. *China Environmental Science Press, Beijing*.

White, J.R., Fulweiler, R.W., Li, C.Y., Bargu, S., Walker, N.D., Twilley, R.R. & Green, S.E. (2009). Mississippi River Flood of 2008: Observations of a Large Freshwater Diversion on Physical, Chemical, and Biological Characteristics of a Shallow Estuarine Lake. *Environmental Science & Technology*, 43(15), 5599-5604.

Xie, X.Y., Qian, X., Qian, Y., Zhang, Y.C. & Tian, F. (2008). Numerical Simulation of Hydrodynamics and Water Quality for Water Transfer from Yangtze River to Chaohu Lake. *China Environmental Science*, 12, 1133-1137.

Zhai, S.J., Hu, W.P. & Zhu, Z.C. (2010). Ecological Impacts of Water Transfers on Lake Taihu from the Yangtze River, China. *Ecological Engineering*, 36(4), 406-420.

Zhao, Y.X., Zhang, W.S., Jing, W.U. & Wang, Y. (2012). Numerical Simulation of Water Diversion to Improve the Water Quality of the Donghu Lake in Wuhan City. *Resources & Environment in the Yangtze Basin*, 21(2), 168-173.

Zhou, D. (2007). Influences of Do and Organic Carbon on Simultaneous Nitrification and Denitrification. *Chinese Journal of Environmental Engineering*, 1(4), 25-28.

 ©2017, IAHR. Used with permission / ISSN 1562-6865 (Online) - ISSN 1063-7710 (Print)

THE DIFFERENCE IN RIPARIAN VEGETATION PATTERN BASED ON THE CHANNEL CHARACTERISTICS AND THE MECHANISM OF ITS FORMATION

TAKASHI ASAEDA [(1)] & KELUM SANJAYA[(2)]

[(1,2)] Department of Environmental Science and Technology
Saitama University, Saitama 338-8570, Japan
asaeda@mail.saitama-u.ac.jp
[(1)]Research Institute of Chuo University, Tokyo 112-8551, Japan
[(2)] Department of Limnology and water technology, Faculty of Fisheries and Marine Sciences & Technology, University of Ruhuna, Matara, Sri Lanka, 81000

ABSTRACT

Steep slope segments of rivers that originally covered with gravels, transport gravelly sediments and fill up the river channel. But, a significant vegetation encroachment can be seen on these riparian areas in modern days and the reason is not yet clear. Therefore, we hypothesized that a reduction in movable gravelly sediments may have caused the difference. With that, the objective of the study is to assess the effect of soil erosion and deposition processes on riparian vegetation colonization. The recovery process of vegetation after sediment deposition or erosion is investigated in six rivers by aerial photographs. Field investigations have been carried out at depositional and erosional locations. In addition, the vegetation colonization is modeled with the Dynamic Riparian Vegetation Model (DRIPVEM) for further understanding the intact processes. The survey conducted with aerial photos elucidated that the vegetation colonization is significantly delayed at sites where gravel is deposited in comparison to sediment eroded sites. The sandy rivers has a faster recovery of vegetation compared to gravelly rivers. Moreover, the tree recovery begin slowly by recruitment from seeds at deposited sites of gravelly sediments, whereas the new shoots sprouted in the next spring from the collapsed live trees, achieving a rapid recovery in the succeeding years at eroded sites. The sediment nutrient and moisture are significantly higher at the eroded sites in comparison to gravel deposited sites. The simulated results are also in agreement with the observations in the present study. The results suggest that the gravelly sediment deposition creates a resistance for the colonization of riparian vegetation. Because, the gravel sediments are deposited after washing during floods and free from fine sediments, thus gravels lack moisture and nutrients. The reduction of gravel sediment seems to be the major reason for the rapid increase of riparian vegetation Japanese rivers.

Keywords: Gravel sediment; steep rivers; vegetation recovery; riparian vegetation; nutrient; moisture.

1 INTRODUCTION

The riparian vegetation often depends on the hydrological regime and plays a key role in the hydrological cycle. Therefore, ecological and hydrological functions of rivers need to be understood to maintain and support healthy ecosystems. However, very often, development activities do not pay much attention to the sensitivity of riparian ecosystems (Richter et al., 2003). But the biggest challenge is to realize the physical and ecological processes within these ecosystems, the interactions and feedbacks of those processes. However, this is essential for the restoration of ecosystems to their typical form.

The fine sediment inflow to river channels has increased due to the gradual de-forestation in catchments over a long period in many parts of the world (Soutar, 1989). In fact, rivers in large flat terrains transport fine sediments which are deposited and accumulate in rivers by changing the channel morphology (Prosser et al., 2001). The riparian vegetation can colonize easily since this fine sediment contains enough nutrient and moisture.

However, the Japanese rivers are short and steep thus the riparian area was filled with gravels in contrast to continental rivers. But the major issue is that these gravelly habitats have recently been covered with thick vegetation cover in comparison to the 1950s, creating several issues on biodiversity and peak discharge in rivers (Asaeda et al., 2013). In the meantime, there are clear evidences about extensive river gravel mining in the recent past, intensive river regulation activities and afforestation in river basins, which limit sediment production (Asaeda and Sanjaya, 2015). Nevertheless, the exact reason is not yet clear. Therefore, we hypothesized that the reduction of gravelly sediments in river channels may have significantly contributed to the difference of the vegetation cover in Japanese rivers. An investigation was carried out to understand the course sediment and its interaction with riparian vegetation colonization since this could be a better example for filling the information gap between gravelly sediment and vegetation colonization resistance.

©2017, IAHR. Used with permission / ISSN 1562-6865 (Online) - ISSN 1063-7710 (Print)

2 METHODOLOGY

2.1 Site selection

The availability of contiguous aerial images at suitable scale (less than 1:20000) and resolution (less than 1 m) for 5 to 10 years after a major flood event, the availability of flood level data for the period of the aerial images obtained, and the bed sediment type of the rivers were the factors considered when the sites were selected (figure 1).

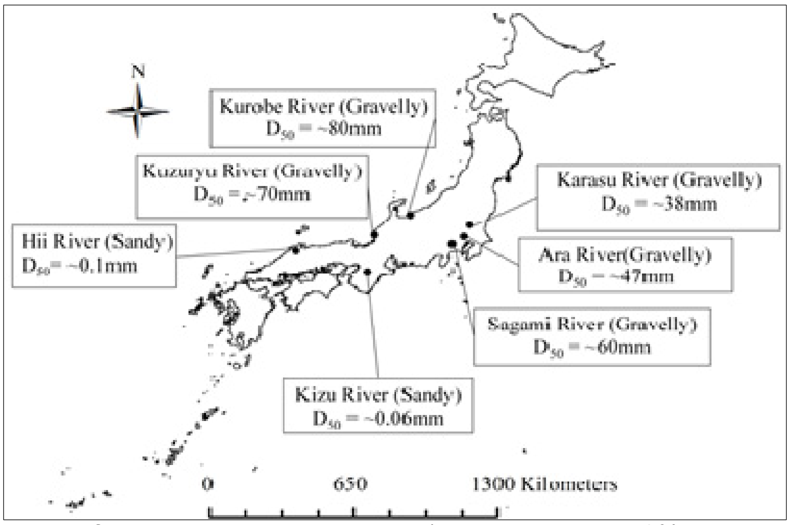

Figure 1. The locations of the studied rivers in Japan (D_{50} denotes the 50% particle size in each river).

2.2 Aerial photo survey

Contiguous aerial photos obtained from the Geo Spatial Information Authority of Japan (http://mapps.gsi.go.jp/maplibSearch.do#1) and the flood level data for the relevant rivers gathered from the Water Information System MLIT, Japan (http://www1.river.go.jp/) were used in the study. Georeferencing and processing the aerial photos were conducted by ArcGIS 9.3 (ESRI Inc., USA). The aerial photos obtained for the analysis were from 1976-1987 in Ara River, 1993-2007 in Kurobe River, 1972-2000 in Sagami River, 1982-1994 in Kuzuryu River, 1976-2004 in Hii River and from 2004-2012 in Kizu River.

The deposition or erosion was identified by the characteristics of the channel and the vegetation before and after the flood and the river cross sectional data obtained in every five year intervals supported for confirmation. The vegetation transition was observed starting from the year the deposition or erosion was identified. The number of years that was taken for trees and herbs to invade about 10% of the total area were counted as the delay time (Müllerová et al., 2005). Collectively, 34 independent depositional locations and 35 erosional locations were studied by aerial photos.

2.3 Field survey

The field investigations were carried out at Kumagaya Sandbar in Ara River and a sandbar in Karasu River. A survey was conducted on the Kumagaya Sandbar to count all trees, to obtain their GPS location, and to obtain the height and diameter at breast height in January 2007. There was a flood with a flood stage of 5.12m from 7th to 9th of September 2007, and the entire sandbar was submerged. All individual trees were surveyed from November 2007 to January 2008 after the flood. The recruitments by seeds and the vegetative recruitments from fallen live trees were also counted and their locations were recorded. The topographical survey of the sandbar from the mean water level was carried out in 2007 and 2008. Herbs were sampled in 2010 and 2014 at 16 points across the bar with 50 cm × 50 cm quadrats from July to October, when the herbs gain their highest biomass. The herb samples were carefully cleansed by tap water and separated into species before subdividing into above and belowground biomass. The dry weight was measured for above and belowground biomass after drying at 85°C for 48h. Soil samples were collected at the herb sampling points and they were separated for stones and fine sediments (approximately less than 1 mm in diameter). Sizes of all stone samples were measured and the fine components were sieved, according to (ASTM, 2002), to obtain the mean particle size distribution. The moisture content and the C, H, N content of particles less than 0.2 mm in diameter was measured by CHN coder (Yanaco, MTA 330 C).

The next site which is one of the major tributaries of the Tone River, the Karasu River was located near its confluence with the Tone River (36°16'1.12"N, 139°10'39.10"E). Ten 50 cm x 50 cm quadrats, Q1 to Q10, were sampled along a cross-section from the levee to the shoreline, having 20 m spacing among quadrats to cover the eroded, deposited and undisturbed sandy soil. The sampling was conducted on August 4, October 5 and November 16, 2012. During this period, three floods occurred, on September 1, September 5 and

 ©2017, IAHR. Used with permission / ISSN 1562-6865 (Online) - ISSN 1063-7710 (Print)

September 21, in which 8 of the 10 quadrats were inundated, and Q1 and Q2 were not disturbed since they were located in the elevated area. The flood recurrence is approximately once in 10 years in this area. Q2, Q3 and Q4 were on the river terrace, covered with herbs while Q1 to Q4 were composed of sandy soil. From Q5 to Q8 were on deposited gravel, which were transported by the floods. Q9 and Q10 were at the shoreline and eroded by the flood. Particle size, total nitrogen, total carbon and moisture content were analyzed for selected quadrats, including the erosional and depositional sites.

2.4. Model simulation

The simulation was conducted to test the influence of gravelly sediment on riparian vegetation colonization. The DRIPVEM (Sanjaya and Asaeda, 2016) was used to simulate the vegetation coverage in the different types of river channels with typical river morphology. The particle size of the bed materials was changed from fine to coarse, although assumed as uniform particle size. The assumption of the initial nitrogen content in eroded sites was 100mg/kg since the subsurface nitrogen is exposed, while the nitrogen content in cleansed deposited gravelly sediment was considered as zero. Annual nitrogen fallout was assumed to be 1mgN/m^2/yr as projected by previous studies (Ohrui and Mitchell, 1997) and different every year flood peaks were used in the simulation. The particle size of the deposited sediment was given as either 0.1mm or 50.0mm to simulate the case of fine or coarse sediment channels. Then the fraction of the deposited area was changed from 0.0 - 1.0. Simulation was conducted for 50 years until dynamically steady condition is achieved. Then the vegetation coverage was obtained as the average values of the last 10 years in the simulated period.

2.5 Statistical analysis

The data were analyzed by SPSS for Windows (release 13, SPSS INC., Chicago, IL) software. The homogeneity of variances and the normality of data were tested by Levene's test prior the analyses. One-way ANOVA, together the Tukey's post-hoc test were used to compare means and all p-values were considered significant at <0.05.

3 RESULTS AND DISCUSSION

With the aerial photo survey, it was observed that the sediment deposition suppressed the vegetation colonization in gravelly rivers in comparison to sandy rivers. For instance, a major flood with a maximum discharge of 2943.2m^3/s occurred on 19th September 1991 in Sagami River. The sediment deposition in Figure 2a was observed after the flood. The next major flood occurred on 16th September 1998 with a discharge of 2646.3m^3/s. After the sediment deposition at the end of year 1991, the tree colonization was observed by 1997 June. Similarly, a large flood with a discharge of 2100.30 m^3/s occurred on 29th September 2004 in Kizu River and there was not a major flood until the flood occurred on 8th October 2009 with a discharge of 3376 m^3/s. Figure 2b shows the deposition of a sandbar at the 2004 flood in Kizu River. However, the vegetation colonization was observed by 31st October 2005. Fast vegetation colonization was observed in sandy Kizu River in comparison to gravelly Sagami River.

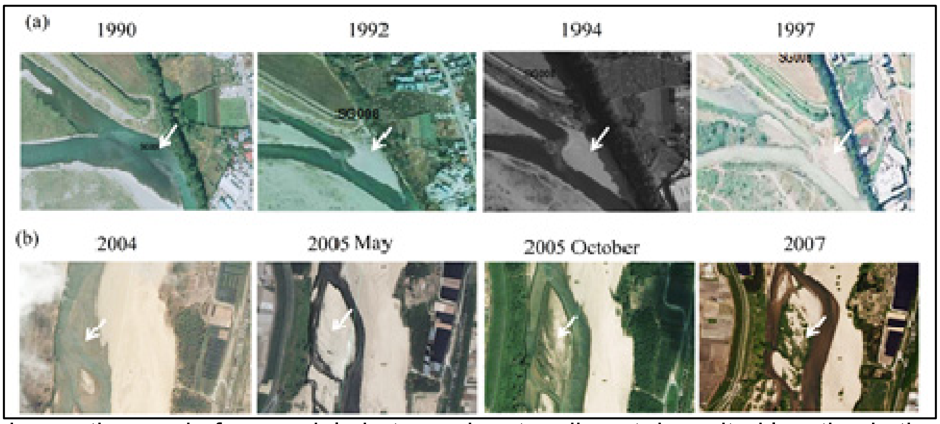

Figure 2. An observation made from aerial photographs at sediment deposited location in the Sagami River (a) and Kizu River (b) (the arrows indicate the sediment deposited location).

When considering all the deposited and eroded sites observed by aerial photos, herbs grew at the erosional sites even in the first year after the flood, whereas it took approximately 2.9 ± 0.7 years at the depositional sites in gravelly rivers and 1.2 ± 0.4 years in sandy rivers (Figure 3a). The herb colonization delay was significantly higher at depositional locations ($F = 119.05$, $p < 0.0001$). The observed delay in tree colonization was approximately 6.5 ± 1.5 years at the depositional sites in gravelly rivers. The shortest herb colonization delay was observed in the Kizu River for both depositional and erosional sites. Similarly, the shortest tree colonization delay was observed in the sandy Kizu River (Figure 3b). Tree colonization was significantly delayed at depositional locations in comparison with erosional locations in gravelly rivers (F = 29.05, p < 0.0001).

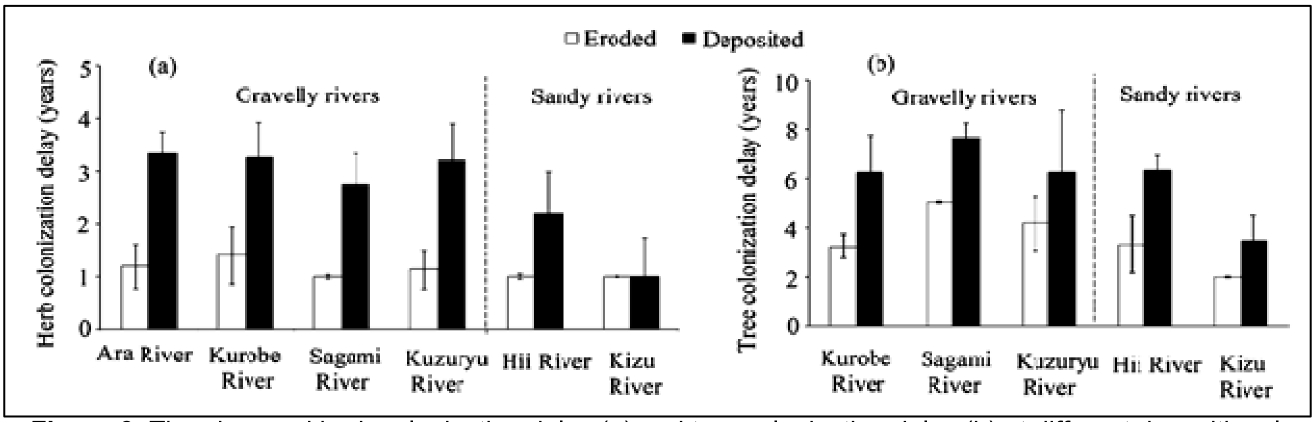

Figure 3. The observed herb colonization delay (a) and tree colonization delay (b) at different depositional and erosional sites in the studied rivers (Error bars indicate standard deviation).

In the field studies carried out in Kumagaya Sandbar in Ara River, little recruitment from seeds was observed and the larger fraction was sprouted from fallen trees (Figure 4). Therefore, the vegetative growth was the dominant type in both the depositional and erosional sites. The collapsed trees were buried and died in the depositional sites, whereas in the erosional site, the trees were alive, although collapsed and new shoots emerged in the following spring. Therefore, there is a resistant for recruitment of trees in the depositional site. In addition, the recruitments from seeds were significantly suppressed in depositional site in comparison to erosional site.

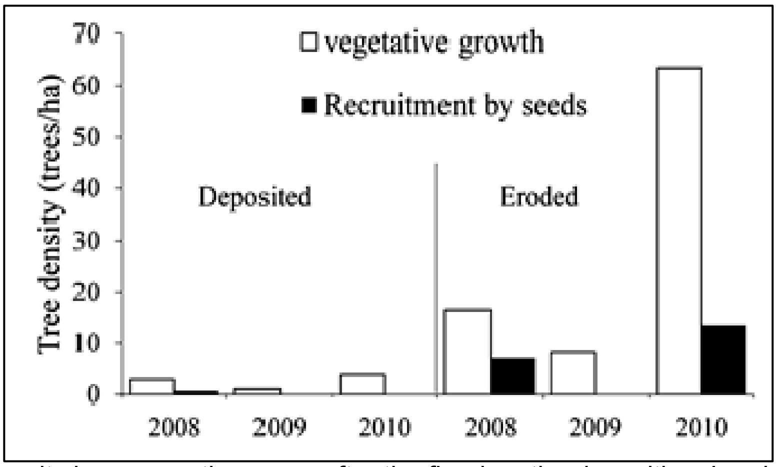

Figure 4. Tree density in consecutive years after the flood on the depositional and erosional sites at Kumagaya Sandbar in Ara River.

In the sediment samples collected from the Kumagaya sandbar in Ara River, fine sediment was the greatest fraction at the erosional site with D_{50} (50% sediment particle sizes) values of 4.7 ± 1.1 cm and 1.7 ± 0.7 cm at the depositional and erosional sites respectively, whereas at the Karasu River, D_{50} was 3.32 ± 2.44 cm at the depositional sites and 0.047 ± 0.013 cm at the erosional sites.

A higher moisture content was encountered in the sandy and erosional sites (figure 5a), whereas moisture was significantly lower at the depositional sites (F = 24.38, p < 0.0001) in the Ara River; similarly, moisture was significantly lower in the depositional areas in the Karasu River (F = 123.1, p = 0.0001). The TC (Total Carbon) and TN (Total Nitrogen) contents were significantly higher in the sandy and erosional sites (figure 5b and 5c) in comparison with the depositional sites (F = 4.80, p = 0.042; and F = 5.76, p = 0.026, respectively, for the Ara River; and F = 13.785, p = 0.006; and F = 16.792, p = 0.003, respectively, for the Karasu River). Further, the herb biomass was significantly lower at depositional site than in erosional or sandy site even seven years after the flood (Figure 5d).

 ©2017, IAHR. Used with permission / ISSN 1562-6865 (Online) - ISSN 1063-7710 (Print)

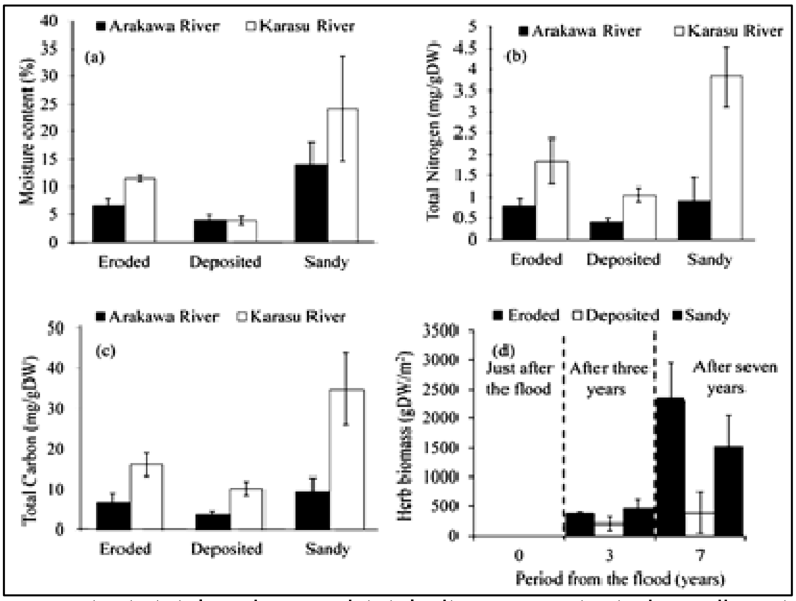

Figure 5. The moisture content, total carbon and total nitrogen contents in sediment samples collected in 2010 on the Kumagaya Sandbar in Ara River, on the sand bar at the conjunction of the Karasu and Tone rivers in 2012 and the herb biomass on the Kumagaya Sandbar, three and seven years after the flood (Error bars indicate standard deviation).

As a significant influence on riparian vegetation colonization by the availability of gravelly sediments was observed, the relationship must be clearly understood. Usually the nutrients and moisture are considered as the primary requirements for plant growth and development are the crucial factors if a sufficient seed bank exists for vegetation colonization (Goodson et al., 2002). Accordingly, our results suggested that the moisture and nutrient contents were significantly low on the depositional gravelly sediments, in comparison with the erosional and non-erosional sandy soil. Generally, the high permeability and the low absorption of moisture in the riparian gravelly substrates account for the low moisture and the low inorganic nutrient availability for vegetation (Toda et al., 2005). But, the suspended fine sediment and organic matters settle in shallow inundation areas or in areas with declining water levels at the later stage of floods, which gradually increases the fraction of fine sediments that contain moisture and nutrients in those areas.

Except the anthropogenic nitrogen supply, the atmospheric fallout and nitrogen fixation are the primary nitrogen sources in the riparian zone (Asaeda et al., 2015c). However, fine sediments and nutrients cannot sufficiently accumulate on a gravelly substrate before being disturbed by flood inundation. Therefore, understanding the relationship of the nutrients, moisture and seed availability with depositional and erosional processes is important.

In our study, riparian vegetation colonized quickly on erosional sites in gravelly rivers, whereas no significant difference was observed between the erosional and depositional sites in sandy rivers. The reason could be that, the underlying sediments could be exposed after the removal of the gravelly sediment on the surface at erosional sites. This exposed substrate by erosion has the original seed bank of woody and herbaceous plants, the original levels of organic matter, moisture and nutrients, and fine sediments in the matrix of gravelly sediment, although partially removed by interstitial currents through the surface stone layer (Hill, 2011). Therefore, herbaceous vegetation can colonize soon after the flood, even though it requires relatively high amounts of nutrients compared with trees.

Moreover, the rivers are short and steep in mountainous islands and peninsulas such as Japan, and have only a short flat area before flowing into the sea (Yoshimura et al., 2005, Kantoush and Sumi, 2010). Therefore, they are often subjected to short but high floods with respect to their catchment size particularly in the monsoonal zones. During these floods, a large gravelly sediment load is distributed over and within the midstream channel and the riparian zone (Kale and Hire, 2004). When sediment is transported, organic matter and fine sediment adsorbed to this gravelly sediment is washed off. On the contrary, the gravelly sediment is transported along the bed surface, whereas litter and seeds float and fine sediment is carried as suspended matters (Kondolf et al., 2014). In addition, the influence of the soil particle size and nutrient retention in riparian soil is well documented (Bechtold and Naiman, 2006; Toda et al., 2005). Toda et al. (2005) demonstrate a reducing trend of soil total nitrogen content when the soil particle size increases. The gravelly sediment lacks fine sediments and organic matter, which otherwise retain moisture and nutrients for a long period after a flood. Thus, the accumulation of fine sediment is required to increase the moisture and available inorganic nutrients before the development of a herbaceous vegetation colony. However, accumulation of fine sediment and organic matter is a slow process in the absence of inundation (Asaeda and Rashid, 2012).

©2017, IAHR. Used with permission / ISSN 1562-6865 (Online) - ISSN 1063-7710 (Print)

Therefore, this could be a reason for significantly delaying the vegetation colonization in the depositional areas in the gravelly rivers compared to Hii and Kizu Rivers.

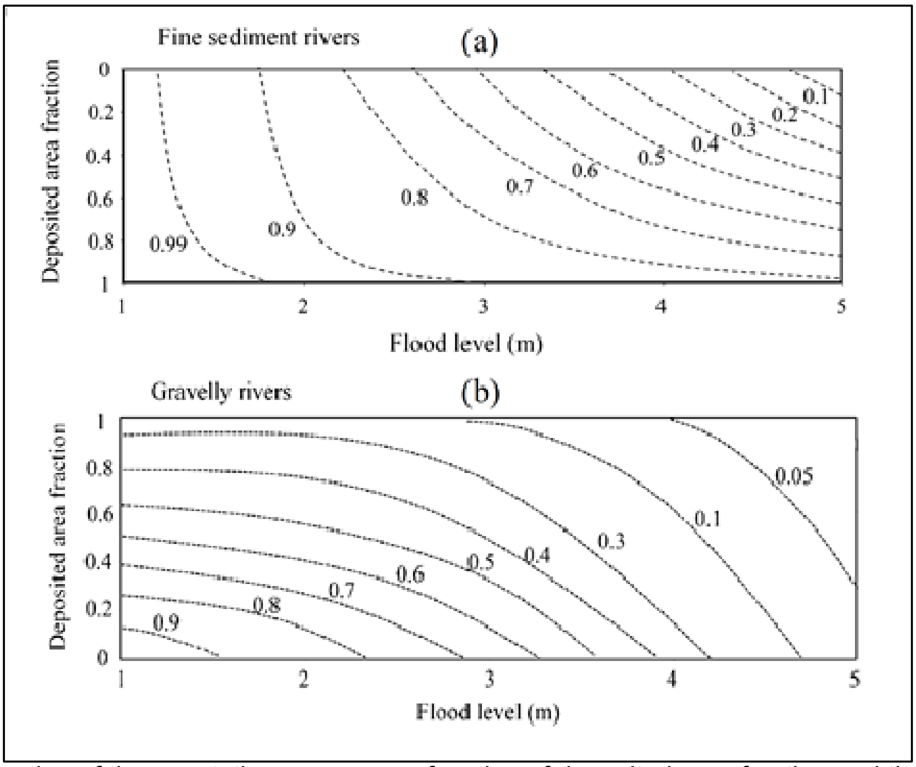

Figure 6. Fraction of the vegetation covers as a function of deposited area fraction and the flood level.

The model simulation was conducted to test the effect of the gravelly sediment and floods on vegetation colonization. In addition to the influence of the flood peaks, the gravel deposition had a greater influence on the fraction of vegetation cover (figure 6b). When increase the gravel sediment fraction in the deposited area, vegetated area fraction was decreased while the fine sediment deposition failed to decline the vegetated area fraction (figure 6a).

Considering above facts, the major driving force of extensive afforestation in Japanese river systems can be related to the major outcome of our study. At the same time, the reasons given by previous studies are also equally important. In Japanese rivers, flood control projects curtail the peak discharge that reduces the flushing effect of riparian vegetation (Azami et al., 2004). However, the reduction in flood levels is not large in many rivers and is compensated by the intensification of flood peaks due to climate change (Knox, 1993; Milly et al., 2002; Ikeda et al., 2005; Luo et al., 2015). Therefore, clear relationship was not established between peak flood volume and vegetation coverage in the river channel (Asaeda et al., 2013). Although, dam construction stabilizes the downstream channel and increases the vegetation coverage, the effect is limited to about 20 to 30 km downstream from the dam (Uddin et al., 2014). Eutrophication of river water may also accelerate the growth of vegetation, but the nutrient concentrations in river water are much less than those in soil pore-water, except in highly eutrophic rivers. Thus, no correlation exists between nutrient conditions and pollution levels of water and vegetation coverage (Asaeda et al., 2013). Therefore, other fundamental mechanisms must be considered to understand excessive vegetation colonization along modern Japanese rivers.

For centuries, the upstream catchments of Japanese rivers were deforested to meet the demand for wood as energy source and construction material (Conrad, 1998). Hence, a large quantity of sediment was discharged into the river channel. Therefore, just after the World War II, when the old aerial photos were taken, river channels in all parts of Japan were filled with gravelly sediments, mainly because of the large sediment inflows from mountainous catchments with low forest coverage and a limited number of dams. But the sediment production in the upstream area has decreased in modern days due to the afforestation of mountainous catchments, like in other parts in the world (Piégay et al., 2004). Erosion control projects have also been conducted in the upstream areas of steep rivers to eliminate the sediment flow. The development of the mountain slopes for housing and agricultural lands also reduced the former sediment production even in the tributaries in suburbs of large cities. In addition, large quantities of aggregates were mined from rivers during the post war reconstruction in the 1960s and 1970s. Although sediment mining was prohibited in the 1970s in many rivers, previously constructed dams and weirs continue to cut off gravelly sediment inflows from upstream mountainous reaches. Therefore, the gravelly sediment supply, which can delay vegetation

 ©2017, IAHR. Used with permission / ISSN 1562-6865 (Online) - ISSN 1063-7710 (Print)

colonization until the next flood renews the habitat, may have reduced. With these facts, we suggest that the reduction of gravelly sediment inputs may be a major reason for the significant increase of vegetation cover in Japanese rivers.

4 CONCLUSION

Unexpectedly, a significant afforestation can currently be seen in the riparian zones of all Japanese rivers. Therefore, identifying the cause and effect of this afforestation is crucial for suggesting a solution to manage these systems and for future restorations. Our study presents a new hypothesis and the results were fairly supported the hypothesis. Importantly, gravel deposition was the determining factor in the delay of vegetation colonization, and with erosional processes and sand or fine sediments; the vegetation colonization process was faster. Therefore, the lack of gravel sediment deposition may play a major role in generating thick vegetation in modern Japanese rivers.

ACKNOWLEDGEMENTS

This study was supported by the river fund from River Foundation, Japan; a Grant-in-Aid of Scientific Research (B) (No.24360198), from the Japan Society for the Promotion of Science; a Development Grant for River Management Technology from the Ministry of Land, Infrastructure, Transportation and Tourism, Japan; a Grant by the Sumitomo Foundation, Japan; and a Grant by the Tokyu Foundation, Japan.

REFERENCES

Asaeda, T., Rashid, M., Dong, M. & Uddin, F. (2013). The Most Effective Factors Responsible for Increase in the Vegetation Coverage of River Channels. *E-proceedings of the 2013 IAHR World Congress,* 2013 Chengdu,China.

Asaeda, T. & Rashid, M.H. (2012). The Impacts of Sediment Released from Dams on Downstream Sediment Bar Vegetation. *Journal of Hydrology,* 430**,** 25-38.

Asaeda, T., Rashid, M.H. & Ohta, K. (2015c). Nitrogen Fixation by Pueraria Lobata as a Nitrogen Source in the Midstream Sediment Bar of a River. *Ecohydrology,* 9(6),995–1005.

Asaeda, T. & Sanjaya, H.L.K. (2015). Does Sediment Shortage Cause River Forestation? A Numerical Approach. *E-proceedings of the 36th IAHR World Congress.*

ASTM (2002). *Standard Test Methods for Sieve Analysis and Water Content of Refractory Materials*, Standard C92–95. West Conshohocken: ASTM International.

Azami, K., Suzuki, H. & Toki, S. (2004). Changes in Riparian Vegetation Communities Below a Large Dam in a Monsoonal Region: Futase Dam, Japan. *River Research and Applications,* 20**,** 549-563.

Bechtold, J.S. & NaimaN, R.J. (2006). Soil Texture and Nitrogen Mineralization Potential Across a Riparian Toposequence in a Semi-Arid Savanna. *Soil Biology and Biochemistry,* 38**,** 1325-1333.

Conrad, T. (1998). *The Green Archipelago.* USA, Ohio University Press.

Goodson, J., Gurnell, A., Angold, P. & Morrissey, I. (2002). Riparian Seed Banks along the Lower River Dove, UK: Their Structure and Ecological Implications. *Geomorphology,* 47**,** 45-60.

Hill, A.R. (2011). Buried Organic-Rich Horizons: Their Role as Nitrogen Sources in Stream Riparian Zones. *Biogeochemistry,* 104**,** 347-363.

Ikeda, T., Yoshitani, J. & Terakawa, A. (2005). Flood Management under Climatic Variability and its Future Perspective in Japan. *Water Science and Technology,* 51**,** 133-140.

Kale, V.S. & Hire, P.S. (2004). Effectiveness of Monsoon Floods on the Tapi River, India: Role of Channel Geometry and Hydrologic Regime. *Geomorphology,* 57**,** 275-291.

Kantoush, S.A. & Sumi, T. (2010). River Morphology and Sediment Management Strategies for Sustainable Reservoir in Japan and European Alps. *Annuals of Disas. Prev. Res. Inst., Kyoto Univ***,** (53), 821-839.

Knox, J.C. (1993). Large Increases in Flood Magnitude in Response to Modest Changes in Climate. *Nature,* 361**,** 430-432.

Kondolf, G.M., Gao, Y., Annandale, G.W., Morris, G.L., Jiang, E., Zhang, J., Cao, Y., Carling, P., Fu, K. & Guo, Q. (2014). Sustainable Sediment Management in Reservoirs and Regulated Rivers: Experiences from Five Continents. *Earth's Future,* 2**,** 256-280.

Luo, P., He, B., Takara, K., Xiong, Y.E., Nover, D., Duan, W. & Fukushi, K. (2015). Historical Assessment of Chinese and Japanese Flood Management Policies and Implications for Managing Future Floods. *Environmental Science & Policy,* 48**,** 265-277.

Milly, P.C.D., Wetherald, R.T., Dunne, K. & Delworth, T.L. (2002). Increasing Risk of Great Floods in a Changing Climate. *Nature,* 415**,** 514-517.

Müllerová, J., Pyšek, P., Jarošík, V. & Pergl, J. (2005). Aerial Photographs as a Tool for Assessing the Regional Dynamics of the Invasive Plant Species Heracleum Mantegazzianum. *Journal of Applied Ecology,* 42**,** 1042-1053.

Ohrui, K. & Mitchell, M.J. (1997). Nitrogen Saturation in Japanese Forested Watersheds. *Ecological Applications,* 7**,** 391-401.

©2017, IAHR. Used with permission / ISSN 1562-6865 (Online) - ISSN 1063-7710 (Print)

Piégay, H., Walling, D.E., Landon, N., He, Q., Liébault, F. & Petiot, R. (2004). Contemporary Changes in Sediment Yield in an Alpine Mountain Basin Due to Afforestation (the Upper Drôme in France). *Catena,* 55(2)**,** 183-212.

Prosser, I.P., Rutherfurd, I.D., Olley, J.M., Young, W.J., Wallbrink, P.J. & Moran, C.J. (2001). Large-Scale Patterns of Erosion and Sediment Transport in River Networks, with Examples From Australia. *Marine and Freshwater Research,* 52**,** 81-99.

Richter, B.D., Mathews, R., Harrison, D.L. & Wigington, R. (2003). Ecologically Sustainable Water Management: Managing River Flows for Ecological Integrity. *Ecological Applications,* 13**,** 206-224.

Sanjaya, K. & Asaeda, T. (2016). Assessing the Performance of a Riparian Vegetation Model in a River with a Low Slope and Fine Sediment. *Environmental technology***,** 38(5), 1-12.

Soutar, R. (1989). Afforestation and Sediment Yields in British Fresh Waters. *Soil Use and Management,* 5, 82-86.

Toda, Y., Ikeda, S., Kumagai, K. & Asano, T. (2005). Effects of Flood Flow on Flood Plain Soil and Riparian Vegetation in A Gravel River. *Journal of Hydraulic engineering,* 131**,** 950-960.

Uddin, F.J., Asaeda, T. & Rashid, M.H. (2014). Factors Affecting the Changes of Downstream Forestation in the South American River Channels. *Environment and Pollution,* 3**,** 24-40.

Yoshimura, C., Omura, T., Furumai, H. & Tockner, K. (2005). Present State of Rivers and Streams in Japan. *River Research and Applications,* 21**,** 93-112.

 ©2017, IAHR. Used with permission / ISSN 1562-6865 (Online) - ISSN 1063-7710 (Print)

SOME OBSERVATIONS ON THE MIXING OF TWO RIVERS WITH A DIFFERENCE IN DENSITY: THE CASE OF THE NEGRO/SOLIMÕES CONFLUENCE, BRAZIL

CARLO GUALTIERI [(1)], MARCO IANNIRUBERTO[(2)], JIM BEST[(3)]

[(1)] Department of Civil, Architectural and Environmental Engineering, University of Napoli Federico II, Napoli, Italy
[(1)]carlo.gualtieri@unina.it
[(2)] Instituto de Geociências - Universidade de Brasília, Campus Universitário Darcy Ribeiro - ICC Centro, Brasília / DF, Brazil
[(3)] Departments of Geology, Geography & GIS, Mechanical Science & Engineering and Vent Te Chow Hydrosystems Laboratory, University of Illinois at Urbana-Champaign, Champaign, IL, USA

ABSTRACT

Confluences are common components of all riverine systems, and characterized by converging flow streamlines and potential mixing of separate flows. The fluid dynamics of confluences possess a highly complex structure with several common types of flow features. The confluence of the Negro and Solimões Rivers, Brazil, ranks among the largest river junctions on Earth and its study may provide some general insights into large confluence dynamics and processes. An investigation has been recently conducted at this confluence at both low and high flow conditions. During this field research, a detailed series of acoustic Doppler velocity profiling (ADCP) transects, water quality samples and high-resolution seismic data are collected to investigate the key hydrodynamic and sediment transport features within this confluence. This paper firstly presents findings concerning the hydrodynamics and morphodynamics from these field studies. Second, the paper identifies and discusses the main processes controlling turbulent mixing at the Negro/Solimões confluence, and more generally at confluences with large differences in velocity and water chemistry / sediment concentration between the merging rivers. These processes are: (1) a difference in velocity, i.e. shear, between the rivers, (2) a difference in density, i.e. lateral (and vertical) stratification, between the rivers, (3) bed friction, and (4) form roughness. Our analysis suggests that the dynamics of the mixing interface in this type of river confluence can be explained as a combination from these processes.

Keywords: Environmental hydraulics; river confluences; turbulent mixing; lateral stratification; upwelling/downwelling.

1 INTRODUCTION

Confluences are ubiquitous components of all riverine systems, and are characterized by converging flow streamlines, mixing of flows and a highly complex three-dimensional flow structure. The region where the local hydrodynamics are influenced by the convergence and realignment of the combining flows at the confluence is known as the Confluence Hydrodynamic Zone (CHZ). The CHZ generally includes a zone of flow stagnation near upstream junction corner; an area of flow deflection as tributary flows enter confluence; shear layer and/or mixing interface between the two converging flows; a possible zone of separated flow below the downstream junction corner(s); flow acceleration within the downstream channel; and flow recovery at the downstream end of the CHZ as illustrated in Figure 1 (Best, 1987; Trevethan et al., 2015a). It is widely acknowledged that the hydrodynamics and morphodynamics within the CHZ are influenced by (1) the planform of the confluence; junction angle of the confluence, (2) momentum flux ratio of the merging streams (M_R) and (3) the level of concordance between channel beds at the confluence entrance (Mosley, 1976; Best, 1987; 1988). Furthermore, any differences in the water characteristics (temperature, conductivity, suspended sediment concentration) between the incoming tributary flows and subsequent possible stratification may also impact the local processes within the confluence (Biron and Lane, 2008).

The shear layer in a confluence is generated by differences in the velocities, or momentum flux, of the converging flows, and is characterized by high levels of turbulence and the occurrence of large-scale coherent flow structures. Furthermore, confluences may develop a mixing interface due to differences in water characteristics (temperature, pH, conductivity) and suspended sediment concentrations. Within the CHZ, the shear layer and mixing interface are typically coincident, but in some cases the downstream mixing interface may extend further than the shear layer. Depending on the angles between the two incoming rivers and the downstream channel, and the momentum flux ratio between the confluent flows, the mixing interface may display Kelvin–Helmholtz, or wake-mode type, flow characteristics (Best, 1987; Rhoads and Sukhodolov, 2008). Helical flow cells are also often observed within confluences, although the presence, characteristics and origin of these cells remains controversial within the scientific community.

Most studies of confluences have focused either on laboratory confluences or on small natural confluences, with only a limited number of studies conducted about large river confluences (channel width

©2017, IAHR. Used with permission / ISSN 1562-6865 (Online) - ISSN 1063-7710 (Print)

>100 m). The confluence of the Negro and Solimões Rivers near Manaus ranks among the largest on Earth and its study may provide some general insights into large confluence dynamics and processes.

This paper presents some findings concerning the hydrodynamics and morphodynamics from two field studies carried out in 2014 and 2015 at the Negro/Solimões confluence. In addition, the paper also identifies, compares and discusses the main processes controlling turbulent mixing at the Negro/Solimões confluence, and more generally at confluences with large differences in velocity and water chemistry between the merging flows.

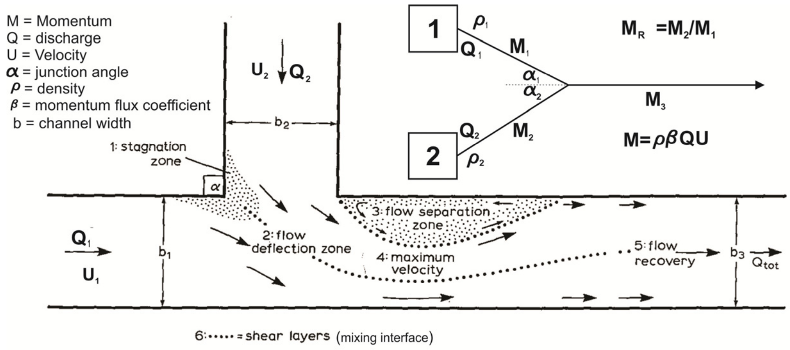

Figure 1. Descriptive model of flow dynamics and key hydrodynamic features at a confluence, slightly modified from Best (1987) (Trevethan et al., 2015a)

2 FIELD SITE AND INSTRUMENTATION

The confluence of the Negro and Solimões Rivers is located near Manaus in Northern Brazil, where these rivers merge to form the Amazon River approximately 1600 km upstream from its mouth at the Atlantic Ocean. This confluence is famous for the meeting of the black and white waters of the two rivers, with contrasting physico-chemical characteristics and sediment load related to the different geology within these two catchments in the Amazon Basin.

As part of the CLIM-Amazon Project, a joint European and Brazilian Research Project funded by the EU that investigated climate and sedimentary processes of the Amazon River Basin, two field studies were conducted at this confluence in both low (October 2014, FS−CNS1 campaign) and relatively high flow conditions (April/May 2015, FS−CNS2 campaign) (Trevethan et al., 2015a; 2015b; 2016). In these field trips, acoustic Doppler velocity profiling (ADCP) and high-resolution seismic methods, such as echo-sounding and sub-bottom profiling, were used, as well as water sampling for the measurement of several water physico-chemical parameters (temperature, conductivity, pH, turbidity, dissolved oxygen, oxygen isotopes) and suspended sediment concentrations.

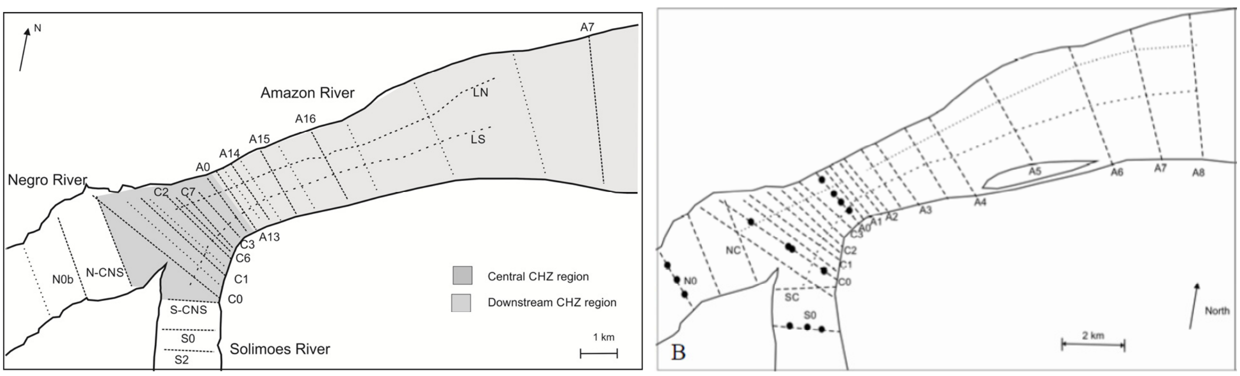

Figure 2. Map of confluence of Negro and Solimões rivers, with sampling positions during Field Study FS−CNS1 (left) and FS−CNS2 (right) are highlighted. Dots show the locations where vertical profiles were collected in FS−CNS2 (Trevethan et al., 2015a; 2016)

During both FS−CNS1 and FS−CNS2, a Teledyne RDI 600 kHz Rio Grande acoustic Doppler current profiler (ADCP) was used to collect cross-sectional measurements at key locations within the confluence, as indicated by lines in Figure 2. In total, 99 cross-sectional transects were collected, namely 51 in FS−CNS1 at 28 different locations and 48 in field study FS−CNS2 at 26 different locations. In addition to the cross-sectional measurements, two and three longitudinal profiles along both sides of the Amazon River were collected during field study FS−CNS1 and FS−CNS2, respectively. So the total number of ADCP profiles was 53 and 51 in FS−CNS1 and FS−CNS2, respectively. The ADCP was used to measure three-dimensional water velocities over the water depth along the transect, as well as water temperature near the surface and backscatter

 ©2017, IAHR. Used with permission / ISSN 1562-6865 (Online) - ISSN 1063-7710 (Print)

intensity, which after a proper calibration could be related to suspended sediment concentration (Szupiany et al., 2009).

During FS−CNS1, water samples at the surface, 10 m, and 20 m depths at twelve locations within confluence were collected. These water samples were used to understand the characteristics of the two tributary rivers (temperature, pH, conductivity) and measure local suspended sediment concentration (SST) and oxygen isotope values. In FS−CNS2, vertical physico-chemical profiles were collected with a YSI EVO2 multi-parameter probe. The locations are indicated by black points in Figure 2B). For each vertical profile, this probe measured the variation in temperature, pH, conductivity, turbidity, chlorophyll and dissolved oxygen concentrations with depth. Further water samples were collected at Sites S0 and N0 to measure the local SST concentration on the Solimões and Negro rivers respectively.

3 KEY OBSERVATIONS ON HYDRODYNAMICS AND MORPHODYNAMICS

Table 1 lists the measured principal median flow properties of the Negro and Solimões rivers at the ADCP transects just upstream of the confluence (N-CNS and S-CNS, three for each river and each field study) during both the field trips. Table 1 shows that large differences in discharge and flow velocities were observed in the Solimões River between field studies FS−CNS1 and FS−CNS2, whereas on the Negro River these differences were smaller.

From FS−CNS1 to FS−CNS2, the maximum depth-averaged velocity remained almost constant in the Negro River, but the Solimões River increased from 2.2 to 2.6 m/s. Furthermore, from low to high flow conditions, the Negro channel increased in depth, from 24 to 31 m, but not in width, whereas in the Solimões River the width increased from 1.6 to 1.9 km and the depth from 27 to 28 m. Thus, from FS−CNS1 to FS−CNS2, the channel aspect ratio decreased in the Negro River but was almost constant in the Solimões River. Finally, from FS−CNS1 to FS−CNS2, the median flow direction in the Negro River remained unchanged, whereas in the Solimões River a significant change in direction occurred.

Table 1. Main flow properties of Negro and Solimões Rivers during FS−CNS1/FS−CNS2

	Field trip	Q (m^3s)	A (m^2)	W (m)	h_{med} (m)	W/h_{rect} (-)	V_{avg} (m/s)	$V_{depth\text{-}avg}$ (m/s)	Dir (°)	V_{max} (m/s)
Negro	FS−CNS1	24510	65839	2830	24.4	115	0.37	0.41	59	0.69
	FS−CNS2	33501	90533	2875	31.3	91	0.37	0.44	58	0.67
Solimões	FS−CNS1	63380	45560	1589	27.2	56	1.42	1.35	289	2.20
	FS−CNS2	105205	63937	1925	28.6	58	1.65	1.56	255	2.59

Legend: Q = discharge; A = cross-sectional area; W = width; h_{med} = median depth; W/h_{rect} = median of the aspect ratio; V_{avg} = median of the cross-section velocity (Q/A); $V_{depth\text{-}avg}$ = median of the depth-averaged velocity; Dir = median of flow direction degrees from North; V_{max} = maximum depth-averaged velocity

Table 2 lists the measured median water characteristics of the Negro and Solimões rivers at the ADCP transects just upstream of the confluence (N-CNS and S-CNS) during both field trips. It can be seen that distinct differences in the water characteristics of the two rivers were present, with these measured differences in water characteristics being similar to those observed in previous studies at the confluence (Laraque et al., 2009). In particular, water density was higher in the Solimões River with a slightly larger difference in FS−CNS2. This created a lateral stratification in the confluence with an associated mixing interface. Again, the water conductivity, pH and turbidity were larger in the Solimões River. Finally, the range of the suspended sediment concentration/total suspended solids (SST) observed for both the field studies was 0.1 > SST > 0.2 g/L and SST < 0.02 g/L in the Solimões and Negro waters respectively.

Table 2. Main water characteristics of Negro and Solimões Rivers during FS−CNS1/FS−CNS2

	Field trip	Basin area (km^2)	Q (m^3s)	T °C	ρ_w (Kg/m^3)	Cond. (μS/cm)	pH	SST (mg/L)	M (MN)
Negro	FS−CNS1	687000	24510	30.3	995.49	7	5.6	8.3	9.1
	FS−CNS2		33501	29.0	995.90	13	5.0	4.1	11.6
Solimões	FS−CNS1	2150000	63380	29.6	995.70	79	6.9	185.3	89.3
	FS−CNS2		105205	28.0	996.19	80	6.7	108.6	172.4

Legend: Q = discharge; T = water temperature; ρ_w = water density (based on water temperature); Cond. = water conductivity; SST = total suspended sediments; M = momentum flux

Previous confluence studies have largely acknowledged that the momentum flux ($M_R=\rho_N Q_N V_{avg\text{-}N}/\rho_S Q_S V_{avg\text{-}S}$), discharge ($Q_R=Q_N/Q_S$) and velocity ($V_R=V_{avg\text{-}N}/V_{avg\text{-}S}$) ratios can be related to the observed hydrodynamic and morphodynamic features within the confluence, where the subscripts S and N represent the Solimões and Negro rivers, respectively. These ratios for field studies FS−CNS1 and FS−CNS2 are listed in Table 3.

Table 3. Discharge, velocity and momentum flux ratios during FS−CNS1/FS−CNS2

Field trip	Q_R	V_R	M_R
FS−CNS1	0.39	0.26	0.10
FS−CNS2	0.32	0.22	0.07

The relatively high values of these ratios are indicative of the large difference in the flow properties of the two tributary rivers. It is worth noting that there is a large junction angle of approximately 80° between the Negro and Solimões rivers (Figure 2). This large junction angle means that the Solimões River effectively enters the confluence almost perpendicular to the main flow direction of the Negro River, therefore the waters of the Solimões must undergo a large change in flow direction (60-70°) as it becomes the Amazon River, while the Negro waters do not.

At the beginning of the central confluence region, the channel width was approximately 5.0 and 5.5 km in FS−CNS1 and FS−CNS2, respectively. The channel narrows downstream to approximately 2.0 km about the transects CNS3 and A0 near the beginning of the Amazon River main channel, with the channel width gradually expanding to over 5 km about 16 km downstream. In the last 2 km leading up to the confluence, the Solimões River had a channel width of approximately 1.6 and 2.0 km in field studies FS−CNS1 and FS−CNS2, respectively, while the channel width of the Negro River expanded from approximately 2.5 to 2.9 km with no significant changes between FS−CNS1 and FS−CNS2.

Figure 3 shows the depth-averaged velocity data (magnitude and direction) collected at each location within the confluence of the Negro and Solimões Rivers on 30-31/10/2014 (FS−CNS1) and 29-30/04/2015 (FS−CNS2) (Trevethan et al., 2016). Figures were plotted using the Velocity Mapping Tool software (Parsons et al., 2013). Figure 4 presents the difference in velocity magnitude (left) and flow direction (right) between the Negro and Solimões rivers on 3010/2014, 31/10/14 and on 30/04/2015.

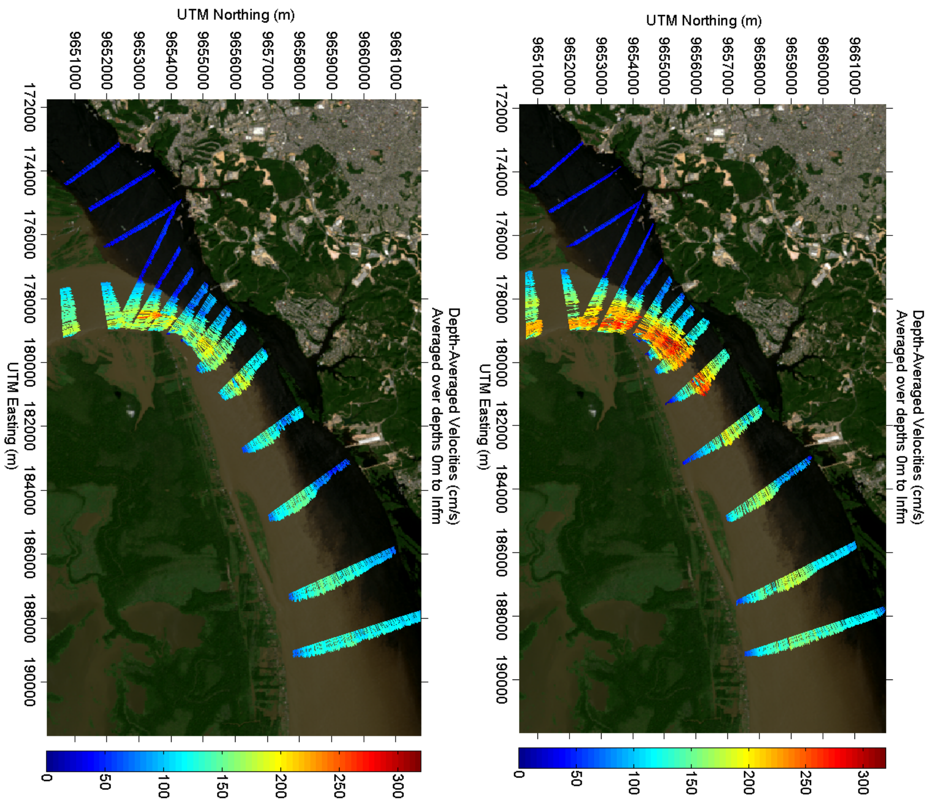

Figure 3. Depth-averaged velocities obtained from ADCP transects collected within the confluence of the Negro and Solimões rivers on 30-31/10/14 (left) and 29-30/04/2015 (right) during FS−CNS1 and FS−CNS2, respectively (Trevethan et al., 2016)

Figure 3(left) shows that on the Negro River at both transects N0 and N-CNS the flow velocity is relatively uniform over the channel width, with a median value of 0.4 m/s. Conversely in the Solimões River, the depth-averaged velocity distribution varies over the channel width, from approximately 2 m/s in the main channel near the right bank and decreases almost linearly towards the left bank, with a depth-averaged velocity of approximately 1 m/s observed at the left side of the three Solimões transects (S2, S0 and S-CNS).
As these two rivers enter the confluence, the channel width is almost 5 km, with the two waters merging about a strong and easily visible mixing interface. For the low flow conditions observed during FS−CNS1, this mixing

 ©2017, IAHR. Used with permission / ISSN 1562-6865 (Online) - ISSN 1063-7710 (Print)

interface begun approximately 100 m upstream on the Solimões side of the central spit between the two rivers, with evidence of a stagnation zone between the two waters either side of the spit. Further, the upstream extent of the stagnation zone appears to end before the location of transect CNS0, with the two waters being deflected and locally aligned about the mixing interface downstream of this transect (Trevethan et al., 2015a). Through the central confluence region, as the waters of the Negro and Solimões merged and realigned with the downstream channel of the Amazon River, the flow in all portions of the confluence accelerated as the confluence width narrows, as the flow is confined between the Alter do Chão Formation rocky bank of the left margin and the Careiro Island on the right. Within this central confluence region, a maximum depth-averaged velocity magnitude of almost 2.5 m/s was observed near the right bank at transect CNS1 (Figure 3(left)). After transect CNS1, which was located about 0.5 km downstream the confluence apex, the flow direction of the Solimões waters largely changed as it realigned with the flow direction of the Amazon River around transects A0 and A13 (Figure 4(right)).

Approximately at downstream transect CNS3, a flow separation zone with recirculation was observed just downstream of the junction corner of the Solimões and Amazon Rivers. The recirculation cell within the separation zone was located from transect CNS3 to A13 and had a width of about 300 m and a length of approximately 1.0 km (Trevethan et al., 2015a). As part of this recirculation cell, an upstream velocity magnitude of approximately 0.3 to 0.6 m/s was observed near the right bank at Sites A0 and A13 (Trevethan et al., 2015a). The separation region ended at upstream transect A16, and indicates that this zone had a length of approximately 2.5 km. Furthermore, in this region there was a significant lateral deflection of the Solimões flow as the flows realigned with the Amazon channel, which may be related to the observed flow separation zone.

Under the flow conditions observed on 31/10/2014, complete realignment of the Negro and Solimões waters with the Amazon River channel occurred by transect A13, which was located about 2.7 km downstream of the junction apex (Figure 4(right)).

In CNS0, the difference in the depth-averaged velocity magnitude in the Negro and Solimões rivers, i.e. $\Delta V_{depth\text{-}avg}$, was more than *c.* 0.88 m/s. From transect A14 (approx. 3.3 km downstream the junction), the median depth-averaged velocities of the Solimões portion decreased, while that of the Negro portion increased, so $\Delta V_{depth\text{-}avg}$ decreased (Figure 4(left)). This would seem to indicate the transfer of momentum from the Solimões to the Negro side of the Amazon channel due to velocity shear. At transect A16, $\Delta V_{depth\text{-}avg}$ between the Solimões and Negro portions was approximately 0.05 m/s (Figure 4(left)). Notably, on 30/10/2014 $\Delta V_{depth\text{-}avg}$ was negligible at transect A6 that was located 6.6 km downstream the junction apex (Figure 4(left)).

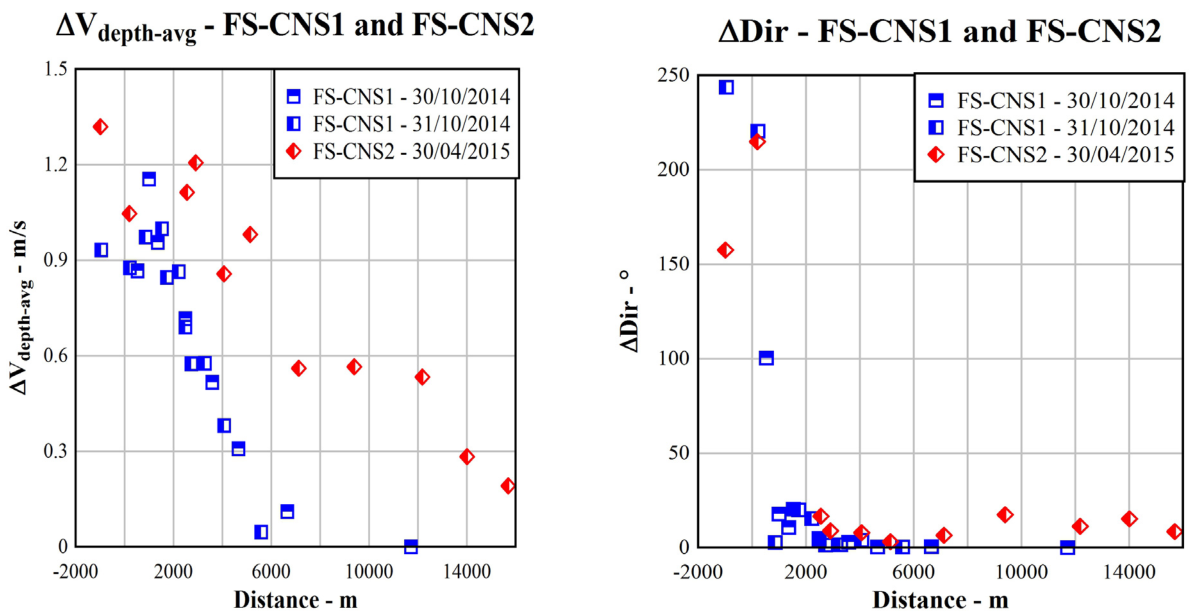

Figure 4. Difference in depth-averaged velocity magnitude (left) and in flow direction (right) between the Negro and Solimões river portions on 30/10/2014, 31/10/2014 and 30/04/2015

For the relatively high flow conditions observed during Field Study FS−CNS2, the depth-averaged velocities observed on the Solimões side of the confluence were up to 3.0 m/s and were significantly larger than those observed on the Negro side of the confluence, which ranged between 0.35 and 1.1 m/s at the start and finish of the CHZ respectively (Figure 3(right)). It can be generally seen in the Amazon channel that on the Solimões side velocities decreased, whilst on the Negro side flow velocities increased with distance downstream of the confluence until the depth-averaged velocities became relatively uniform around transect

©2017, IAHR. Used with permission / ISSN 1562-6865 (Online) - ISSN 1063-7710 (Print)

A8, indicating the approximate end to the CHZ about Site A8. Even on 30/04/2015, the flow direction of the Solimões changed mostly to realign with the flow direction of the Amazon River around transect A0 (Figure 4(right)).

On 30/04/2015, the difference in the depth-averaged velocity magnitude in the Negro and Solimões rivers, i.e. $\Delta V_{depth\text{-}avg}$, was more than 1 m/s. From A0, which was located 2.9 km downstream the junction, $\Delta V_{depth\text{-}avg}$ started to decrease. At the end of the considered reach, at transect A8 that was located 15.7 km downstream of the junction apex, the difference was about 0.19 m/s (Figure 4(left)). Comparing low flow and high flow conditions, it can be seen that $\Delta V_{depth\text{-}avg}$ was larger in the latter flow conditions, both immediately upstream and downstream of the junction apex (Figure 4(left)). Furthermore, on 30/04/2015 the separation zone region with recirculation at downstream transect CNS3 had a larger size, as it ended approximately at transect A4, which would indicate that this zone had a length of more than 4.0 km. In both flow conditions, $\Delta V_{depth\text{-}avg}$ tended to decrease moving downstream, but the data indicated that the transfer of momentum from the Solimões to the Negro side of the Amazon channel was comparatively weaker at high flow conditions than at low flow conditions (Figure 4(left)), while the rate of realignment was similar (Figure 4(right)).

From the analysis of the seismic profiles, Trevethan et al. (2015b) identified that the Negro side of confluence was characterized by a rocky bed with fine sand cover, a mid-channel peak/bar of apparent sedimentary origin occupied the mixing interface, whilst on the Solimões side of the confluence a bed consisting predominantly of coarser materials was present. A scour hole (up to approx. 65 and 70 m deep at low and relatively high flow conditions, respectively) is characterised by eroded Cretaceous bedrock, with deposited sediment present on the Solimões side of the CHZ around the region of maximum velocity at the entrance to the Amazon River downstream, whereas no avalanche faces were easily discernible at either tributary mouth bar during the field studies. Several bedrock terraces were observed in the CHZ on the Solimões side. Finally, downstream on the Solimões side of Amazon River, only large bed-forms indicating bed-load transport and possible accretion further downstream towards end of CHZ were discovered (Trevethan et al., 2015b).

4 KEY OBSERVATIONS ON MIXING

4.1 Some remarks on turbulent mixing in rivers

Turbulent mixing is the process by which a solute/suspended matter is transported under the action of random turbulent fluctuations in the flow. Given the complex nature of these fluctuations, it is accounted for using a turbulent diffusion coefficient, D_t , and its dimension is [L²/T]. From dimensional reasoning, it can be related to turbulent length and velocity scales, L_T and U_T, respectively, as:

$$D_t = L_T\, U_T \qquad [1a]$$

In a plane shear flow, turbulence is generated by vertical velocity shear which arises as a result of bed friction (Rutherford, 1994). Since shear velocity u* is a measure of bed friction, it could be selected as the velocity length scale in Eq. (1a). This is also consistent with literature for vertical diffusivity and longitudinal dispersion coefficient. However, there is controversy about the proper length scale to be used in Eq. (1a). It is very common to assume flow depth h as a length scale for transverse diffusivity, that is $h=L_T$, since this parameter controls the largest vertical eddies. Hence, we obtain:

$$D_t = \beta\, h\, u^* \qquad [1b]$$

Where β is a numerical coefficient depending on the direction of mixing, i.e. vertical or lateral.

Although transverse mixing is a significant process in river hydraulics, no theoretical basis exists for the prediction of its rate, which is based upon the results of experimental work conducted in laboratory channels or in streams and rivers. It is believed that transverse, or lateral, mixing in a river is due to following causes (Rutherford, 1994; Gualtieri, 2010; Bouchez et al., 2010):

- Turbulence generated by the channel boundaries, which involves many eddies of various sizes and intensities, all embedded in one another (Pope, 2000). These eddies are responsible for both momentum and mass transfer, according to the Reynolds analogy, resulting in solute/contaminants mixing far exceeding that occurring at the molecular scale. In addition, it could also be expected that in a turbulent flow the largest eddies regulate the rate of turbulent diffusion. In a river, lateral mixing may be due to transverse eddies that rotate horizontally, about a vertical axis;
- Vertical variations in the transverse velocity (velocity shear), which are significant in the vicinity of channel banks and further contribute to transverse spreading of any solutes/contaminants;
- Secondary currents, which cause solute/contaminants to move in opposite directions at different depths, thereby increasing the rate of mixing (Henderson, 1966; Rutherford, 1994; Chanson, 2004).

 ©2017, IAHR. Used with permission / ISSN 1562-6865 (Online) - ISSN 1063-7710 (Print)

- The analysis of an extensive literature data set collected in straight rectangular laboratory channels yielded (Gualtieri and Mucherino, 2007):

$$D_{t\text{-}y} = 0.166\, h\, u^* \qquad [2]$$

Whereas in river reaches with meanders and bends, the β coefficient is usually even larger, in the range from 0.2 to 1.1 and from 0.2 to 3.3, respectively (Rutherford, 1994). Within river confluences, there is a lack of knowledge about the value of the turbulent mixing coefficient because the confluence hydrodynamics is very complex. Bouchez et al. (2010) using ADCP data obtained a value of β of 1.5 for the Purus/Solimões confluence.

4.2 Turbulent mixing at the Negro/Solimões confluence

The above findings concerning the hydrodynamic and morphodynamic features at the Negro/Solimões confluence have already demonstrated the complexity of the flow. Furthermore, visual observations during the field studies highlighted complex features affecting mixing, such as Kelvin-Helmholtz and asymmetric instability waves along the stratified mixing interface, lateral rolling over of these instability waves, forming large vortices of Solimões waters with diameters of up to 40 m, lateral bursting of these large vortices at relatively large distances (i.e. 100's m) into the Negro side of the mixing interface. In the central CHZ regions, large turbulent surface boils (> 50 m) on the Solimões side of the mixing interface, with no boils observed on Negro side or in mixing interface, indicate the impact of the stratified mixing interface on local hydrodynamics. Further downstream, large turbulent boils were observed on the Negro side, and within the mixing interface, as well as on Solimões side of channel (Trevethan et al., 2015a).
These observations suggest that the processes potentially involved in the mixing of the two rivers are:

- Differences in velocity, i.e. shear, between the merging rivers;
- Lateral stratification, possibly increased by lateral forces;
- Effect of bed friction and form drag due to bed topographies and change in channel width.

Figure 5 shows the distribution of depth-averaged velocity and backscatter intensity at the CNS0 transect, which was located approximately 220 m downstream of the confluence, on 31/10/2014 and 02/05/2015. It can be observed that the large difference in both depth-averaged velocity and backscatter exist from the Negro and the Solimões side in the initial part of the confluence, with a sharp drop across the shear layer/mixing interface. In low flow conditions, the sharp drop was in the order of 10's metres, while in relatively high flow conditions, the sharp drop was narrower in width, i.e. of the order of few metres.

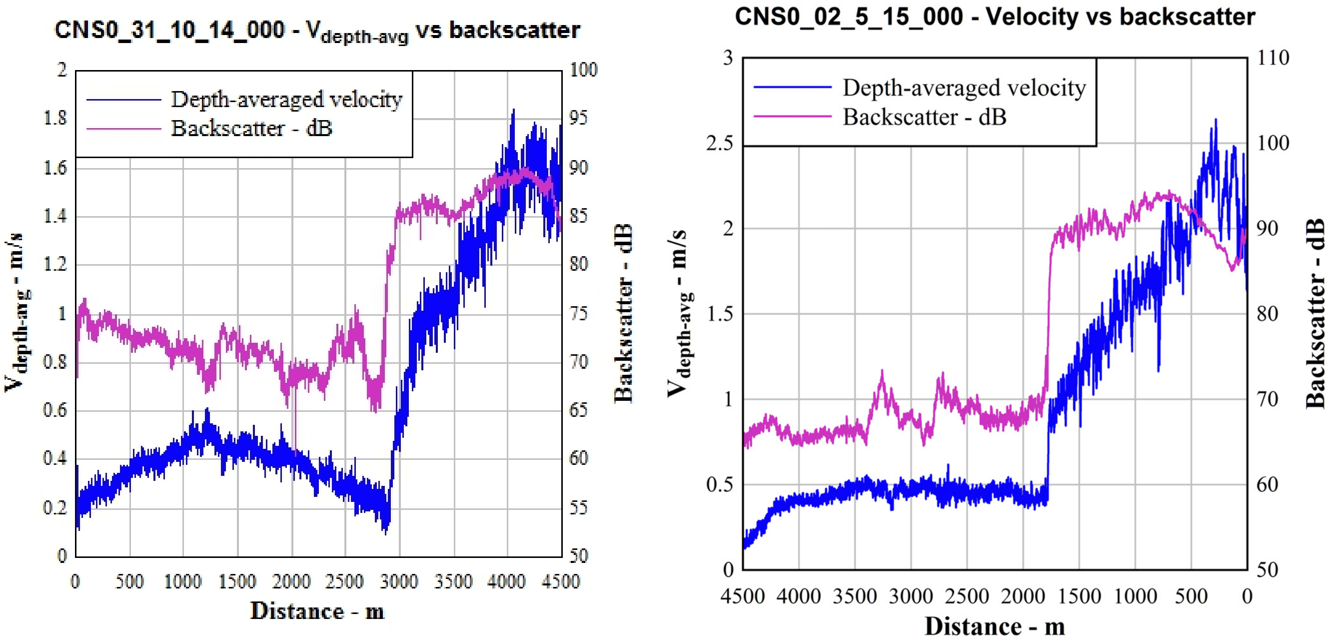

Figure 5. Depth-averaged velocity magnitude and backscatter on 31/10/2014 (left) and on 30/04/2015 (right) at the entrance of the CHZ

Analysis of backscatter intensity data revealed a quite complex pattern of mixing. Figure 6 shows the distribution in the cross-section of backscatter intensity on 31/10/2014 at sites CNS0, CNS1 and A13, which are located approximately 220, 850 and 2700 m downstream of the confluence. It can be seen that the denser waters from the Solimões were entering at the Negro side and moving close to the bed. This pattern was observed even at relatively high flow conditions and confirmed by past observations done at the Negro/Solimões confluence (Laraque et al., 2009).

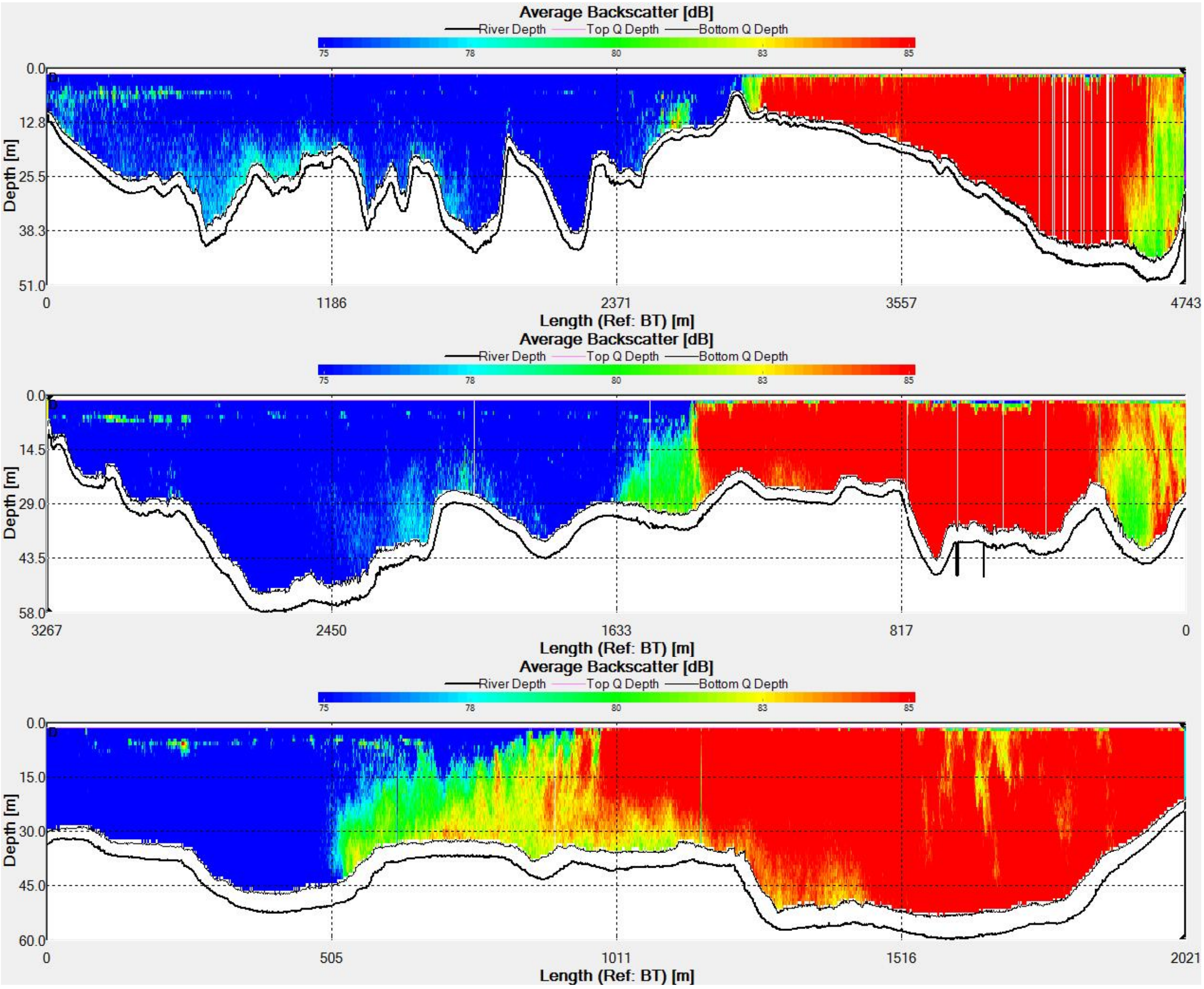

Figure 6. Distribution of backscatter intensity on 31/10/2014 at transects CNS0 (up), CNS1 (medium) and A13 (bottom)

The analysis of the water chemistry data collected during the two field studies also revealed some interesting patterns in the values of conductivity that confirm the above findings from the backscatter intensity. Figure 7 presents the distribution of conductivity collected near the surface, and at 10 and 20 m depths at transect A0 and plotted with the ADCP backscatter intensity. The transect A0 was located approximately 2500 m downstream of the confluence junction, and shows the initial mixing of waters close to the bed as the Solimões plume is entering the Negro pool.

Lastly, the interaction between the flow at the confluence and the bed topography observed during the field studies was investigated. Figure 8 shows the distribution of the backscatter intensity and vertical velocity on 29/05/2015 at transect A14, that was located approximately 3700 m downstream of the confluence junction. Large negative vertical velocities (downwelling) were observed as the Solimões waters were moving close to the bed below the Negro pool. The ADCP surveys revealed the nature of this topographic interaction and suggest that the routing of sediment-laden fluid within the junction, and the patterns of downwelling/upwelling, were significantly influenced by these flow-bedrock interactions.

Further analysis is needed to better clarify the effect of bed friction and change in channel width on mixing at the Negro/Solimões confluence.

 ©2017, IAHR. Used with permission / ISSN 1562-6865 (Online) - ISSN 1063-7710 (Print)

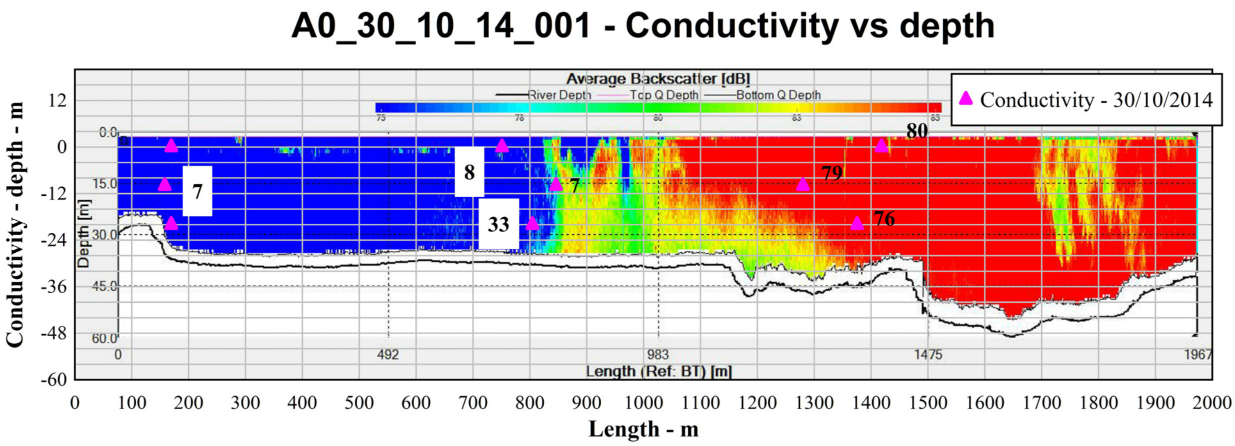

Figure 7. Distribution of water conductivity at transect CNS0 on 30/10/2014 on contour plot of ADCP backscatter intensity

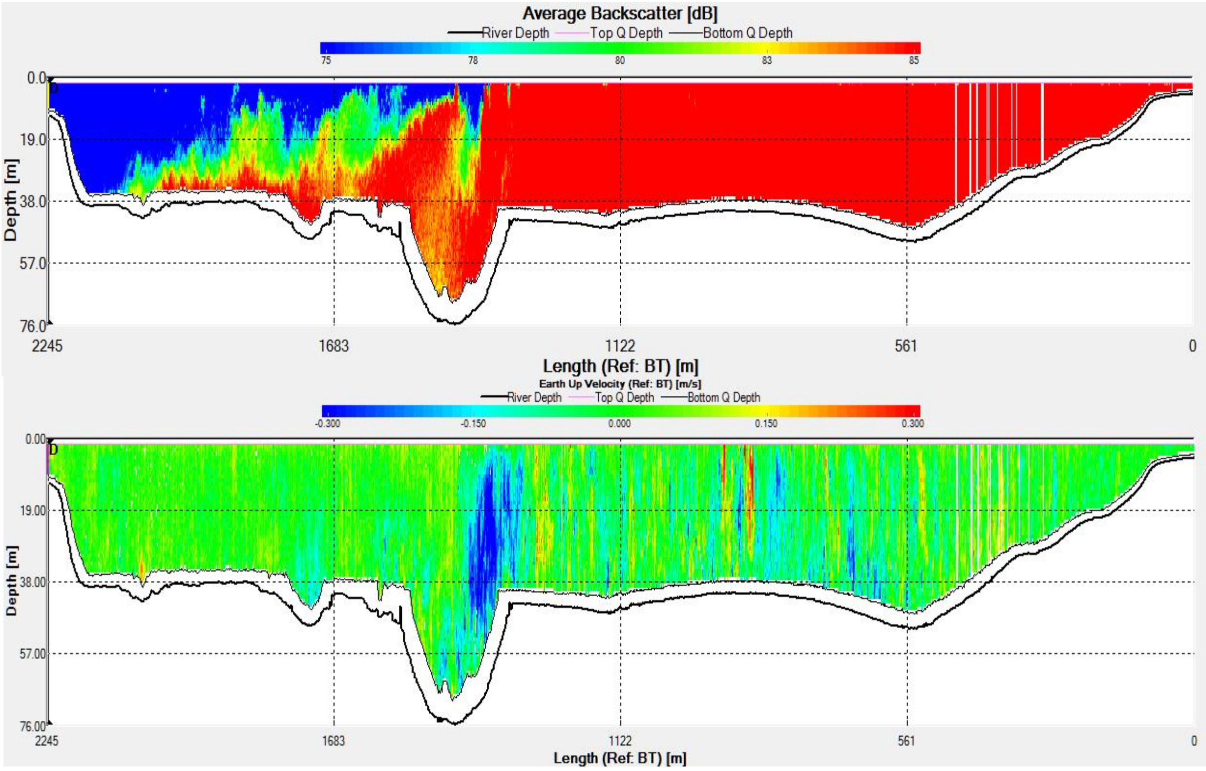

Figure 8. Distribution of the backscatter (up) and vertical velocity (bottom) at transect A14 on 29/05/2015

5 CONCLUSIONS

In the last four decades, a wide body of theoretical, experimental, and field research has emerged concerning the dynamics of river confluences. Yet, despite recent advances in the understanding of confluences, to date most studies have focused on laboratory or small natural confluences.

The paper presents some key observations concerning the hydrodynamics and morphodynamics at the Negro/Solimões confluence in the Amazon Basin, which ranks among the largest on Earth. These observations come from two large field studies conducted at this confluence at both low and relatively high flow conditions using ADCP, seismic measurements and water chemistry sampling. The paper identified and discussed the main processes controlling turbulent mixing at confluences with large differences in velocity and water chemistry between the merging rivers. This analysis highlights the role of differences in velocity and density between the rivers on mixing, as well bed topography in creating patterns of flow downwelling/upwelling. Future analysis will investigate the effect of bed friction and change in channel width on mixing.

ACKNOWLEDGEMENTS

The authors acknowledge this research was carried out within the Clim-Amazon European Laboratory in Brazil funded by grant agreement FP7 INCO-LAB n° 295091 from the European Commission and the partial support from the MIUR PRIN 2010-2011 Research Project HYDROCAR. The authors acknowledge Dr. Mark Trevethan for his role in the Clim-Amazon, the CPRM (Geological Survey of Brasil) and Prof. Roberto Ventura Santos for supplying the research vessel, instrumentation, technical assistance with sampling; Bosco Alfenas, Andrè Martinelli Santos, Daniel Moreira, Arthur Pinheiro, Paulo Melo, Nilda Pantoja, Andre Zumak and João Andrade for their assistance with sampling during the field campaigns.

References

Best, J. L. (1987). Flow Dynamics at River Channel Confluences: Implications for Sediment Transport and Bed Morphology*. Society of Economic Paleontologists and Mineralogists*, 27-35.

Best, J.L. (1988). Sediment Transport and Bed Morphology at River Channel Confluences. *Sedimentology*, 35, 481-498.

Best, J.L. & Rhoads, B.L. (2008). Sediment Transport, Bed Morphology and The Sedimentology of River Channel Confluences. *River confluences, tributaries and the fluvial network*, 45-72.

Biron, P. & Lane, S. (2008). Modelling Hydraulics and Sediment Transport at River Confluences. *River confluences,tributaries and the fluvial network*, 17-43.

Bouchez, J., Lajeunesse, E., Gaillardet, J., France-Lanord, C.,Dutra-Maia, P. & Maurice, L. (2010). Turbulent Mixing in The Amazon River: The isotopic Memory of Confluences*. Earth and Planetary Science Letters*, 290, 37−43.

Chanson H. (2004), *Environmental Hydraulics of Open Channel Flows*, Elsevier Butterworth-Heinemann, Burlington, MA, USA, Book, 430.

Gualtieri, C. (2010). RANS-Based Simulation of Transverse Turbulent Mixing in a 2D Geometry. *Environmental Fluid Mechanics*, 10(1), 137−156.

Gualtieri, C. & Mucherino, M. (2007). Transverse turbulent diffusion in straight rectangular channels. *5th International Symposium On Environmental Hydraulics (ISEH 2007),* Tempe, USA.

Gualtieri, C., M.Trevethan, M.Ianniruberto, N.Filizola, M.De Oliveira & A.Santos (2015). Hydrodynamics and Mixing at the Confluence of Rio Negro and Rio Solimões. *6th Observation Service HYBAM Scientific Meeting,* Cusco, Perù.

Gualtieri, C., Filizola, N., De Oliveira, M., Trevethan, M., Martinelli Santos, A., Ianniruberto & M. Field observations of hydrodynamics and sediment transport at the confluence of Rio Negro and Rio Solimões. *Comptes Rendus Geoscience.* (submitted)

Henderson F.M. (1966), Open channel flow, *Macmillan Series in Civil Engineering, New York, NY, USA*, 522.

Laraque, A., Guyot, J. & Filizola, N. (2009). Mixing processes in the Amazon River at The Confluences of The Negro and Solimões Rivers, Encontro Das Aguas, Brazil. *Hydrological Processes*, 23, 3131-3140

Mosley, P. (1976). An Experimental study of channel confluences. *Journal of Geology*, 84, 535-562

Parsons, D., Jackson, P., Czuba, J., Engel, F., Rhoads, B., Oberg, K., Best, J., Mueller, D., Johnson, K. & Riley, J. (2013). Velocity Mapping Tool (VMT): a Processing and Visualization Suite for Moving-vessel ADCP Measurements. *Earth Surface Processes and landforms*, 38, 1244-1260.

Pope S.B. (2000). Turbulent Flows. *Cambridge University Press,* Cambridge, U.K.

Rhoads, B. & Sukhodolov, A. (2008). Lateral Momentum Flux and The Spatial Evolution Of Flow within a Confluence Mixing Interface. *Water Resources Research*, 44(8).

Rutherford, J.C. (1994). *River Mixing*, John Wiley & Sons, Chichester, U.K., 348

Szupiany, R., Amsler, M., Parsons, D. & Best, J. (2009). Morphology, Flow Structure and Suspended Bed Sediment Transport at Large Braid-Bar Confluences. *Water Resources Research*, 45(5).

Trevethan, M., Martinelli, A., Oliveira, M. Ianniruberto, M. & Gualtieri, C., (2015a). Fluid dynamics, Sediment Transport and Mixing about the Confluence of Negro and Solimões Rivers, Manaus, Brazil. *In 36th IAHR World Congress*, The Hague, The Netherlands, June 28-July 3, 2015.

Trevethan, M., Ianniruberto, M., Santos, A., De Oliveira, M., Filizola, N. & Gualtieri, C. (2015b). Morphodynamics and Hydrodynamics Features Observed about The Confluence of Negro and Solimões Rivers, Brazil. *9th Symposium on River, Coastal and Estuarine Morphodynamics (RCEM 2015)*, Iquitos, Perù, August 30-September 3, 2015.

Trevethan, M., Ventura Santos, R., Ianniruberto, M., Santos, A., De Oliveira, M. & Gualtieri, C. (2016). Influence of tributary water chemistry on hydrodynamics and fish biogeography about the confluence of Negro and Solimões rivers, Brazil. *11th International Symposium on EcoHydraulics (ISE 2016)*, Melbourne, Australia, February 2-7, 2016.

 ©2017, IAHR. Used with permission / ISSN 1562-6865 (Online) - ISSN 1063-7710 (Print)

LARGE EDDY SIMULATION OF A ROUND THERMAL BUOYANT JET IN A CROSS FLOW

YIZHOU XIAO [1], WENXIN HUAI [2], ZHONGHUA YANG [3] & MENG GAO [4]

[1, 2, 3, 4]State Key Laboratory of Water Resources and Hydropower Engineering Science, Wuhan University, Wuhan, China,
[1]vivianshaw1117@163.com; [2]wxhuai@whu.edu.cn; [3]yzh@whu.edu.cn; [4]gm60024@whu.edu.cn

ABSTRACT

Round thermal buoyant jets in cross flow occur in many natural and engineering applications. Examples of this flow configuration include oceanic outfalls, wastewater or pollutant discharges, which depend on environmental conditions, change in the ambient fluid, and impact on the environment. The large eddy simulation (LES) of round vertical thermal buoyant jets in cross flow has been conducted using the subgrid-scale model to capture turbulent performances. First, the simulations at previous experimental flow conditions for different temperature and velocity configurations in a cross-flow are conducted, and results obtained from simulations are in good agreement with Zeng's experimental data, thus validating the numerical reliability. The jet scalar and vector characteristics have been acquired, including jet trajectories, velocity, and temperature field. Additionally, instantaneous vortex structures and counter-rotating vortex pairs are analyzed and have been evaluated based on all numerical simulations. Results indicated that LES has a strong and authentic simulation of the detailed turbulent structure than that through experiments or other calculation models.

Keywords: Buoyant jet; large eddy simulation; velocity; temperature; vorticity.

1 INTRODUCTION

Jet in a cross flow has received much attention in many practical applications. Examples of this flow configuration include oceanic outfalls, wastewater or pollutant discharges, which depend on environmental conditions, change in the ambient fluid, and impact on the environment. These configurations require a good understanding of the jet in a cross flow, which is often related to different properties, such as temperature and density.

In recent years, jet in a cross flow has been investigated experimentally and numerically. Wright (1977) studied experimentally on a round, turbulent buoyant jet in an ambient cross flow, which emphasized the developments of jet trajectories, characteristic dilutions, and height of rising. Large eddy simulation (LES) was conducted by Michele (1996), who investigated the turbulent flow with heat transfer in different geometrical configurations. The application of the three subgrid-scale (SGS) models in LES for investigating the turbulent flow field and wall heat transfer was considered by Wu (2002). Huai (2009; 2011; 2015) has conducted the LES of turbulent flow with vegetation, which studied the interaction of flow and vegetation. The horizontal buoyant wall jet was studied by Huai (2010), who applied the realizable $k-\varepsilon$ model to simulate the buoyant wall jet and gave the results of cling length, centerline trajectory and temperature dilutions at certain sections. Li (2011) has studied the interaction between a plane wall jet and a parallel offset jet through the LES, which obtained the mean stream-wise velocity, the turbulent intensity and dilute characteristics. The LES of turbulent mixing in a non-isothermal jet in cross flow configuration was studied with a hybrid Eulerian–Lagrangian computational methodology by Mostafa (2015). A detailed numerical investigation of submerged dense jets with 45° inclination was also performed using LES by Zhang (2015), who captured jet trajectory, geometrical features, and cross-sectional profiles. The LES of a round jet penetrating into a cross flow was conducted by Petri (2016), who concluded that an intense backflow near the flat wall existed, and the unsteady boundary condition slightly increased the spreading of the jet.

Increasing attention was paid to the LES, which is currently a trend in computational fluid dynamics. Moreover, numerical studies on the jet in a cross flow, in which temperature is considered as a factor, are limited. Therefore, in this study, 3D LES was adopted in the calculation of a round thermal buoyant jet in a cross flow at a rectangular open flume. A comparison of the simulated results and experimental data reported in the literature by Zeng (2005) was performed for the validation of the LES predictions. The effects of the temperature on flow field were analyzed, especially the influence on the flow at the water surface. The detailed information of instantaneous velocity field was evaluated, which showed the time–spatial distribution of velocity. Furthermore, instantaneous vortex structures were captured, especially the counter-rotating vortex pairs shown at the spanwise cross sections, and the variation of the vortex pairs in the direction of the flow was obtained and analyzed.

©2017, IAHR. Used with permission / ISSN 1562-6865 (Online) - ISSN 1063-7710 (Print)

2 Mathematical approaches

2.1 Governing equations

In the LES, the filtered continuity, momentum, and energy equations for incompressible flows are as follows (Gao 2017):

$$\frac{\partial \rho}{\partial t}+\frac{\partial}{\partial x_i}\left(\rho \overline{u_i}\right)=0 \quad , \qquad [1]$$

$$\frac{\partial}{\partial t}\left(\rho \overline{u_i}\right)+\frac{\partial}{\partial x_j}\left(\rho \overline{u_i}\,\overline{u_j}\right)=-\frac{\partial \overline{p}}{\partial x_i}+\frac{\partial}{\partial x_j}\left(\mu \frac{\partial \overline{u_i}}{\partial x_j}\right)-\frac{\partial \tau_{ij}}{\partial x_j} \quad , \qquad [2]$$

and

$$\frac{\partial\left(\rho T\right)}{\partial t}+\mathrm{div}\left(\rho \boldsymbol{u} T\right)=\mathrm{div}\left(\frac{k}{c_p}\mathrm{grad}T\right)+S_T \quad , \qquad [3]$$

where ρ is the fluid density, *t* is the time, $\overline{u_i}$, $\overline{u_j}$ are the velocity components, $\overline{p}$ is the pressure, *T* is the temperature, c_p is the specific heat capacity, *k* is the heat transfer coefficient of fluid, S_T is the viscous dissipation term, τ_{ij} is the SGS stress, and $\tau_{ij}=\rho\overline{u_i u_i}-\rho\overline{u_i}\,\overline{u_j}$. In this study, the SGS model is adopted to solve the SGS stress.

The SGS model is important in the LES. According to Smagorinsky's basic SGS model, the form of SGS stress is assumed as follows (Huai 2015):

$$\tau_{ij}-\frac{1}{3}\tau_{kk}\delta_{ij}=-2\mu_t\overline{S_{ij}} \quad , \qquad [4]$$

where μ_t is the turbulent viscosity of the SGS. The equation of μ_t is as follows:

$$\mu_t=\left(C_s\Delta\right)^2\left|\overline{S}\right| \quad . \qquad [5]$$

$$\left|\overline{S}\right|=\sqrt{2\overline{S_{ij}}\,\overline{S_{ij}}} \quad , \qquad [6]$$

$$\overline{S_{ij}}=\frac{1}{2}\left(\frac{\partial \overline{u_i}}{\partial x_j}+\frac{\partial \overline{u_j}}{\partial x_i}\right) \quad , \qquad [7]$$

and

$$\Delta=\left(\Delta_x\Delta_y\Delta_z\right)^{1/3} \quad , \qquad [8]$$

where Δ_i represents the mesh size along the *i*-axis direction, C_s is the Smagorinsky's constant. According to Van Driest model, C_s is calculated by the equation below.

$$C_s=C_{s0}(1-e^{y^+/A^+}) \quad , \qquad [9]$$

 ©2017, IAHR. Used with permission / ISSN 1562-6865 (Online) - ISSN 1063-7710 (Print)

where y^+ is the closest distant to the wall, A^+ is the semi-empirical constant, A^+=25.0, and C_{s0} is the Van Driest constant, C_{s0}=0.1.

2.2 Flow configuration and boundary condition

The flow configuration was based on those used in the experiments conducted by Zeng (2005) as illustrated in Figure 1 and described in Table 1. The origin of the Cartesian coordinates was set at the center of the jet nozzle, which had a diameter of *D*. The jet nozzle was located in the middle of the flume baseboard, and the jet direction was perpendicular to the flume baseboard. The simulated domain of the rectangular flume had a length (*L*), width (*W*), and height (*H*) of more than 860, 120, and 60 *D*, respectively. The water depth was 20 cm and the ambient velocity was 10 cm/s.

The velocity inlet boundary condition, with configurations shown in Table 1, was adopted at the inlet of the cross flow and the jet nozzle. The wall condition was set at the baseboard and the side walls of the flume. Furthermore, the air inlet at the top of the flume was set as a symmetry boundary condition, which was the default that no fluid flows through the boundary.

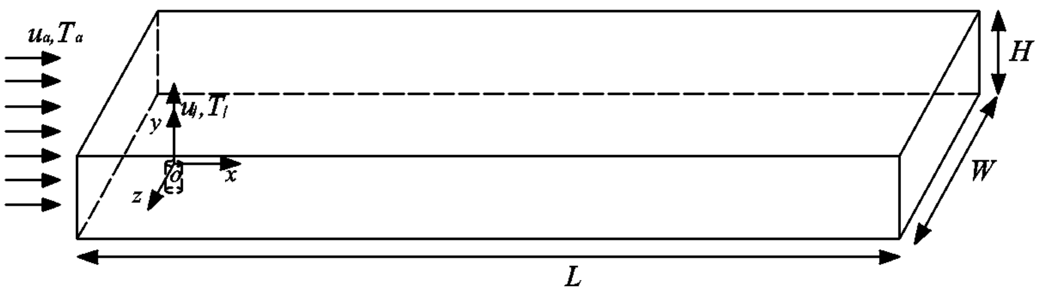

Figure 1. Schematic of the domain in the jet in a cross-flow.

2.3 Computational method

LES was applied in the simulations. The TruVOF method of FLOW-3D, which only computed the unit of the fluid, not the unit of the air, was adopted to reduce the time of convergence. Meshes were generated by the FAVOR (Fractional Area Volume Obstacle Representation) method, which used the finite difference method to simulate complicated models. Additionally, the FAVOR method used fewer hexahedron grid units to smoothen and eliminate the rough regions, which build a mesh model without any distortion. The simulations were considered convergent when the residual was less than 1×10^{-5} for the governing equations.

Table 1. Calculated conditions.

Case	Jet velocity u_j (cm/s)	Ambient velocity u_a (cm/s)	Velocity ratio R	Jet temperature T_j (□)	Ambient Temperature T_a (□)	H/D
1	60	10	6	34	13	24.7
2	80	10	8	34	14.5	24.7
3	100	10	10	34	13	24.7

3 RESULTS OF COMPUTATION

3.1 Comparison with experiments

The LES predictions were compared to the experimental results obtained from the present study by Zeng (Zeng et al., 2005). Figures 2 and 3 show the comparison of the computed temperature and velocity, respectively, with the measurement data along the flume centerline. The approximate agreement between the computational results and experimental data was good. In both the experimental data and computational results, the temperature decayed rapidly near the jet nozzle, and temperature stratification existed when the jet diffused to flume downstream, which appeared as a high-temperature region at the water surface and a low-temperature region at the bottom of the flow. In Figure 3, the jet was bent to the downstream by ambient flow, and the jet and ambient flow were mixed together. Additionally, the velocity at the water surface was higher than that of the bottom of the flow.

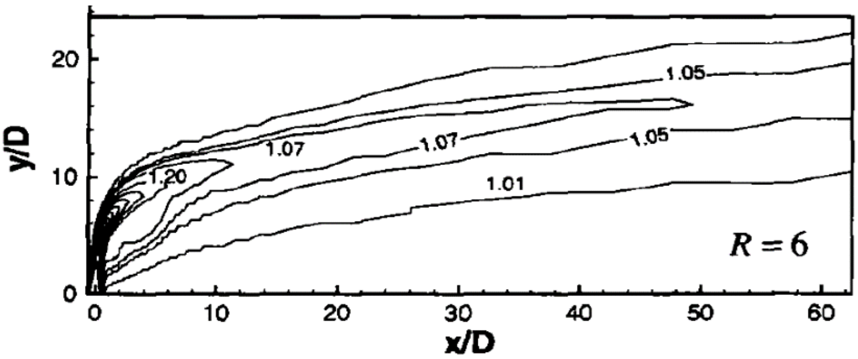

(a) Experimental results by Zeng (2005)

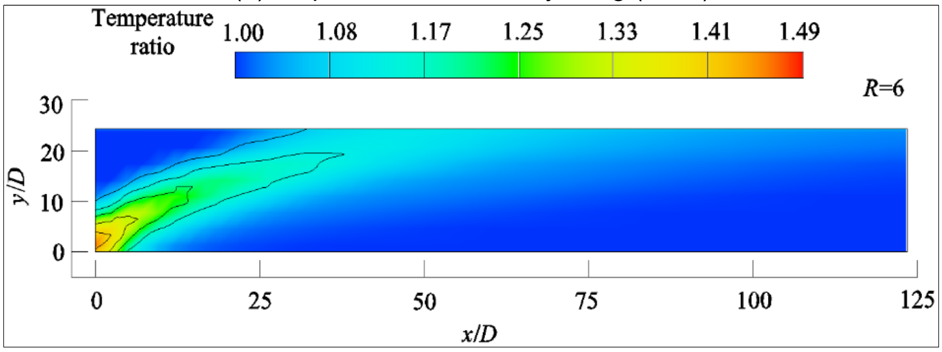

(b) Computational results

Figure 2. Comparison of the temperature between the experimental and the calculated results (*Z*=0).

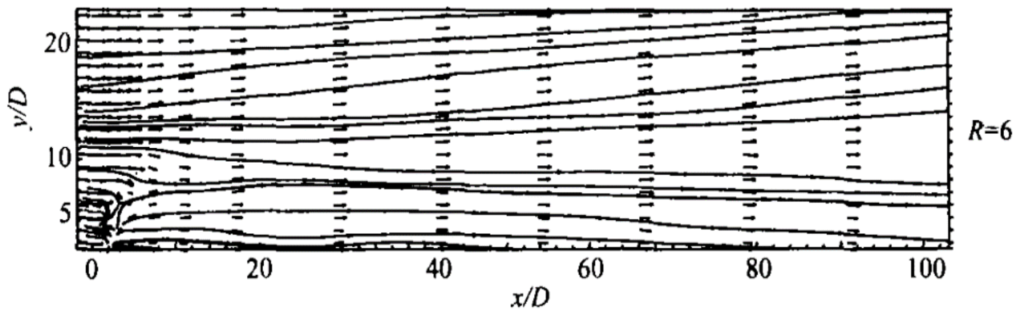

(a) Experimental results by Zeng (2005)

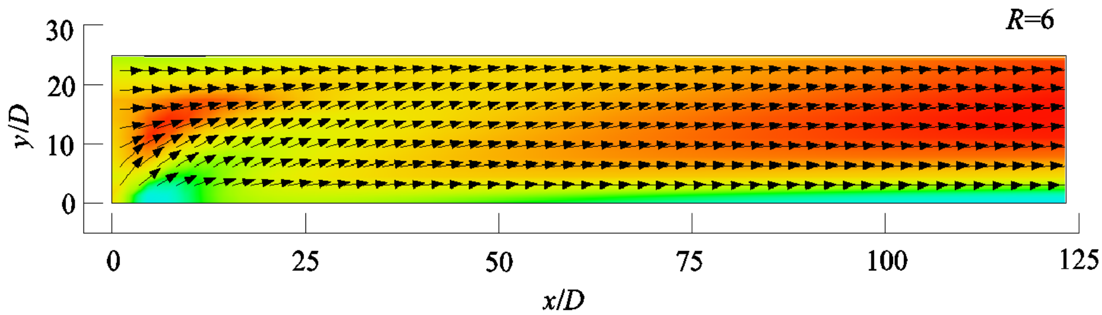

(b) Computational results

Figure 3. Comparison of the velocity vector between the experimental and the calculated results (*Z*=0).

3.2 Temperature field

Bifurcation phenomenon in the thermal buoyant jet was captured in these LES simulations as illustrated in Figures 4 and 5. In Figure 4, two high-temperature regions at a spanwise cross-section appeared as the jet flowed to the downstream; this phenomenon means that bifurcation occurred.

 ©2017, IAHR. Used with permission / ISSN 1562-6865 (Online) - ISSN 1063-7710 (Print)

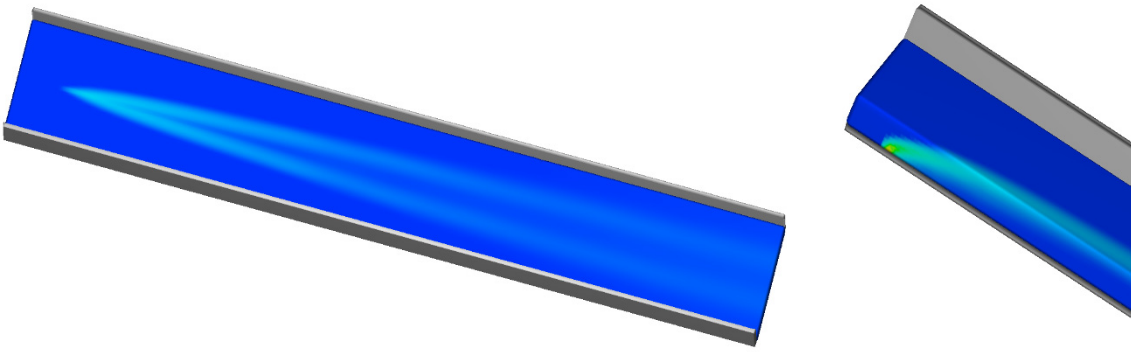

(a)Temperature field from a plan view (b) Longitudinal profile of Figure 4(a)

Figure 4. Temperature field (*R*=6).

Figure 5 displays the variation of temperature at the water surface. Moreover, the bifurcation angles of the high-temperature regions in the different velocity ratios were measured and calculated as 8°, 8°, and 9°. Zeng (2005) mentioned that the angle of the two high-temperature regions in the experiments of a thermal buoyant jet in a cross flow was 8°–10°. These values presented a satisfactory agreement between the experimental and the simulated results.

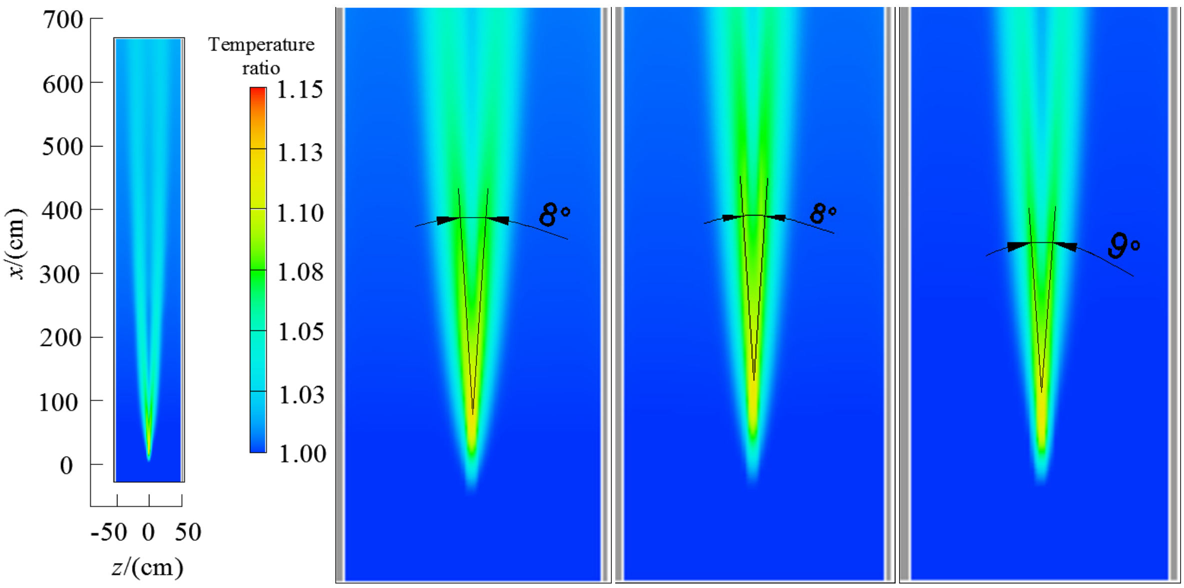

(a) *R*=10 (b) *R*=6 (c) *R*=8 (d) *R*=10

Figure 5. Temperature field of horizontal cross sections (*Y*=20).

3.3 Velocity field

Figure 6 shows instantaneous velocity field at the water surface. From an overall perspective, the flow field was approximately steady as time went by and water continuously flowed in the system. When time was at 105 s, the whole flow field had displayed its prototype. At 210 s, the whole flow field was approximately stable. Velocity downstream was higher than that around the jet nozzle. In addition, turbulence appeared obviously at the downstream flume, and the location of the intensive turbulence wandered along the downstream flume. This time–spatial distribution mirrored fully the trend of the jet flow.

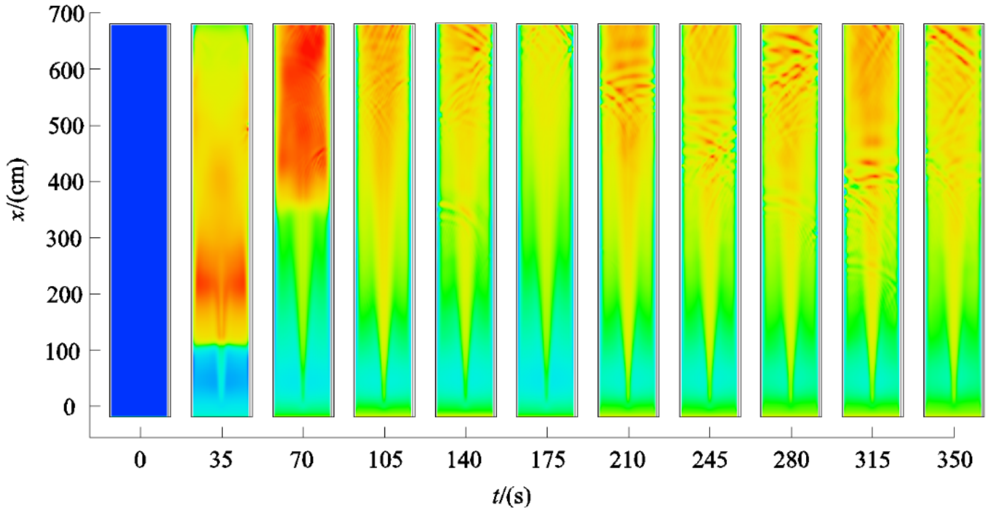

Figure 6. Instantaneous velocity field at the water surface (*R*=10, *Y*=20).

3.4 Vorticity

LES not only predicted the instantaneous velocity fields but also gave the vorticity of the flow field. Figure 7 illustrates the variation of the vorticity of the spanwise cross sections in the flow direction. The intensity of vorticity field has increased greatly because of the existence of thermal buoyant jet flow. In the same cross section, the vorticity intensity at the middle of the flume was apparently higher than that on both sides of the cross section. In Figure 7, the maximum intensity of vorticity appeared near the jet nozzle, and the positive and negative vorticities were generated at the same spanwise cross sections. The intensity of vorticity weakened in the flow direction. The shape of the positive and negative vorticities was kidney-like, which was called counter-rotating vortex pairs.

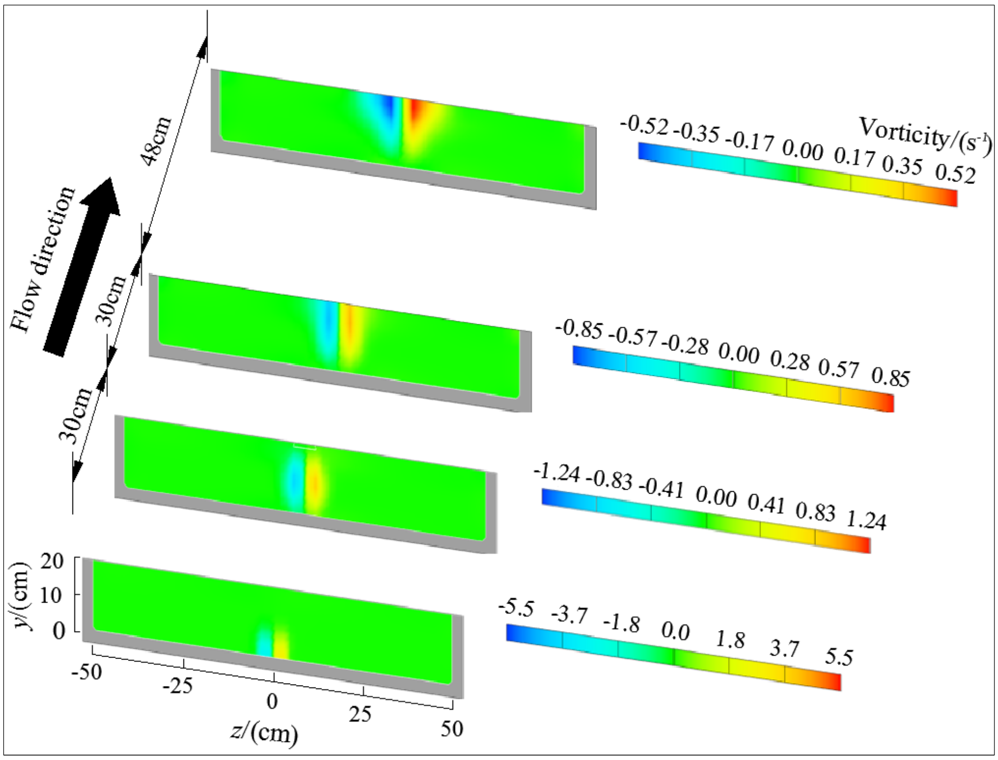

Figure 7. Variation of the vorticities of spanwise cross sections in the flow direction (*R*=8).

4 CONCLUSIONS

In this study, the round vertical thermal buoyant jet was simulated using LES with Smagorinsky's SGS model, and the computed results were compared with the previous experimental data. The results predicted by LES have agreed well with the experimental results, which covered the temperature ratios, velocity contours, and velocity vectors along the flume centerline. The computed results showed that two high-temperature regions existed at the water surface, namely, bifurcation phenomenon, and the angle of bifurcation of these regions was 8°–10°. The instantaneous velocity field at the water surface was captured

 ©2017, IAHR. Used with permission / ISSN 1562-6865 (Online) - ISSN 1063-7710 (Print)

through simulations, and turbulence appeared obviously at the downstream flume. In addition, a variation of the vorticities of spanwise cross sections along the flume was obtained, which illustrated that the vortex pair existed at the spanwise cross sections. This research provided a good understanding of a round vertical thermal buoyant jet in a cross flow through the LES, and the improvement of the vortex structure requires being explored in a further study.

ACKNOWLEDGEMENTS

This work was supported by grants from the National Natural Science Foundation of China (Nos.11672213, 51439007 and 11372232).

REFERENCES

Gao, M., Huai, W.X., Li, Y.T. & Wang, W.J. (2017). Numerical Study of the Flow and Dilution Behaviors of Round Buoyant Jet in Counterflow. *Journal of Hydrodynamics*, 29(1), 172-175.

Huai, W.X., Gao, M., Zeng, Y.H. & Li, D. (2009). Two-Dimensional Analytical Solution for Compound Channel Flows with Vegetated Floodplains. *Applied Mathematics and Mechanics*, 30(9), 1121-1130.

Huai, W.X., Li, Z.W., Qian, Z.D., Zeng, Y.H. & Han J. (2010). Numerical Simulation of Horizontal Buoyant Wall Jet. *Journal of Hydrodynamics*, 22(1), 58-65.

Huai, W.X., Wu, Z.L., Qian, Z.D. & Geng, C. (2011). Large Eddy Simulation of Open Channel Flows with Non-Submerged Vegetation. *Journal of Hydrodynamics*, 23(2), 258-264.

Huai, W.X., Xue, W.Y. & Qian, Z.D. (2015). Large-Eddy Simulation of Turbulent Rectangular Open-Channel Flow with an Emergent Rigid Vegetation Patch. *Advances in Water Resources*, 80, 30-42.

Li, Z.W., Huai, W.X. & Han, J. (2011). Large Eddy Simulation of the Interaction between Wall Jet and Offset Jet. *Journal of Hydrodynamics*, 23(5), 544-553.

Mostafa, E., Asghar, A. & Farhad, A.J. (2015). Turbulent Mixing In Non-Isothermal Jet In Crossflow. *International Journal of Heat and Mass Transfer*, 89, 1239-1257.

Michele, C. (1996). Large-Eddy Simulations Of Turbulent Flow With Heat Transfer In Simple And Complex Geometries Using Harwell-FLOW3D. *Applied Mathematical Modeling*, 20, 262-271.

Petri, M. & Timo, S. (2016). Large-Eddy Simulation of a Round Jet in a Cross-Flow. *International Journal of Heat and Fluid Flow*, 27, 402-415.

Wright, S.J. (1977). *Effects of Ambient Crossflows and Density Stratification on the Characteristic Behavior of Round Turbulent Buoyant Jets*. California Institute of Technology, Book, Chapter 3.

Wu, H.W. & Perng, S.W. (2002). LES Analysis of Turbulent Flow and Heat Transfer in Motored Engines with Various SGS Models. *International Journal of Heat and Mass Transfer*, 45, 2315-2328.

Zeng, Y.H. & Huai, W.X. (2005). Experiments on a Round Turbulent Buoyant Jet in a Cross-Flow. *Journal of Experiments in Fluid Mechanics*, 19(3), 39-46. (In Chinese)

Zeng, Y.H. (2005). Stability and Mixing Character for Buoyant Jets in Quiescent Shallow Water. Wuhan University. (In Chinese)

Zhang, S., Jiang, B.X., Law, A.W.K. & Zhao, B. (2016). Large Eddy Simulations of 45° Inclined Dense Jet. *Environmental Fluid Mechanics*, 16(1), 101-121.

©2017, IAHR. Used with permission / ISSN 1562-6865 (Online) - ISSN 1063-7710 (Print)

FREE SURFACE TURBULENT FLOW AROUND SINGLE BOTTOM MOUNTED CUBE AT LOW RELATIVE SUBMERGENCE

KEN VUI CHUA[1], RICHARD MCSHERRY[2] & THORSTEN STOESSER[3]

[1,2,3] School of Engineering, Cardiff University, Cardiff, United Kingdom
ChuaKV@cardiff.ac.uk, McSherryR@cardiff.ac.uk, Stoesser@cardiff.ac.uk

ABSTRACT

This paper describes the use of large eddy simulation to study turbulent low submergence flow over a single bottom mounted cube. Two simulations have been carried out. The first case is a plane channel simulation that replicates a laboratory experiment for validation purposes while the second case concerns open channel flow past a bottom mounted cube, with free surface deformation captured using the level set method. Streamlines, mean streamwise velocity, shear stress and turbulent kinetic energy profiles at the symmetry plane of the cube are presented in the validation section and reasonably good agreement against the experiment is achieved. The free surface open channel simulation reveals significant deformation of the water surface downstream of the cube, including a large dip followed by a standing wave that is characterised by a pronounced bow shape. Q-criterion iso-surfaces are plotted to highlight the turbulent structures shed by the cube and the extent to which large energy-carrying vortices interact with the free-surface.

Keywords: Large eddy simulation; free surface; turbulent flow; level-set method.

1 INTRODUCTION

Flow over bluff body represents a very interesting engineering situation that involves complex phenomena like flow separation and reattachment, high turbulence, large-scale turbulent structures, as well as unsteady vortex shedding. Researchers, over the past decades, are using simple geometries like bottom mounted cube or square cylinder in open channel as idealised test cases to predict and investigate the fundamental properties and behaviour of a turbulent flow. Numerical models like the Reynolds-averaged Navier-stokes (RANS) turbulence models are popular among researchers but still fall short in accuracy especially in relatively high turbulent cases. With the advancement in supercomputing technology together with increasing cost efficiency of high performance supercomputers, large eddy simulation (LES) is slowly gaining its fame in being the more suited and greater potential numerical method for calculating complex flows (Rodi, 1997).

In the field of hydraulics, the vast majority of simulations of flows involving water surfaces to date have employed the so-called rigid lid approximation, in which a fixed (generally flat) surface or lid is used to represent the water surface. By definition, the shear stress at the lid is zero, as is the component of the fluid velocity in the direction normal to it, but the pressure is free to vary as it would along a wall, which in turn produces zero shear stress there. This rigid lid assumption has never been perfect and is continuously being challenged and investigated. To assess the validity this assumption, Komori et al. (1993) carried out a direct numerical simulation (DNS) which included the surface variations in their computation by including the kinematic boundary condition and compared the results with those from the rigid simulations of Lam & Banerjee (1992). They found that the free-surface deformations and near-surface normal velocities are negligible and concluded that the rigid lid assumption is valid. However, Koken and Constantinescu (2009) and Paik and Sotiropoulos (2005) both used detached eddy simulation (DES) to simulate a long rectangular structure attached to the side wall and had shown that the rigid lid assumption is only strictly applicable to low Froude number (i.e. $Fr \leq 0.5$) flows. Kara et al. (2015a) performed two LES simulations for flow through the same bridge contraction geometry, one with a rigid lid boundary and one with a free-surface capturing algorithm, the level-set method (LSM). The bulk Reynolds number was 27,200 and although the bulk Froude number was relatively low at $Fr = 0.37$, locally values of $Fr = 0.78$ were reached as a result of the significant constriction imposed on the flow by the abutment (the ratio of channel width to abutment width was 3). Kara et al.'s results showed that although the first order statistics and bed shear stresses were very similar for the two simulations, the instantaneous turbulence structure and second order statistics showed significant disparity. Their study highlighted the limitation of the rigid lid approximation and the requirement for more sophisticated approaches for the simulation of turbulent flows with complex water-surface deformations.

The aforementioned free-surface capturing algorithm, LSM has recently become a popular method in tackling the multi-phase free surface flows. The level-set method was originally proposed by Osher and Sethian (1988) and was developed for the computation and analysis of the motion of an interface between two fluid phases in two or three dimensions. In the LSM the interface is represented by the zero set of a smooth

 ©2017, IAHR. Used with permission / ISSN 1562-6865 (Online) - ISSN 1063-7710 (Print)

distance function, ϕ, that is defined for the entire physical domain. The conservation equations are solved for both liquid and gas phase and the interface is advected according to the local velocity vector. It was observed in the LES simulation carried by Yue et al. (2006) that the LSM was able to accurately and realistically calculate the unsteady free-surface motion and also provided evidence of boils, upwelling and downdraft at the water surface. Kara et al. (2015b)performed LES of flow through a submerged bridge with overtopping, using LSM to capture the free-surface dynamics. The simulation revealed very complex flow phenomena, including a plunging nappe and standing wave at the surface downstream of the bridge, a horizontal recirculation in the wake of the lateral abutment and vertical recirculation created by the plunging flow. The simulation results agreed very well with complementary experimental measurements in terms of the water surface deformation.

Two large eddy simulations are presented in this paper. The first case was carried out with a bottom-mounted cube in a plane channel and served as a validation case, while the second case was carried out in an open channel with the same bottom-mounted cube. The cases are henceforth referred to as case PC and case OC respectively. The open channel flow case was characterised by low relative submergence, and the interaction between the vortex shedding from the cube and the freely undulating surface is the main interest of this paper. The numerical method used to perform the simulations is presented in the next section. The computational set-ups for the two cases are then introduced. Results from the validation study are then presented and discussed in a subsequent section, as are results of the open channel free surface case. Some conclusions pertaining to key results are then drawn in the final section.

2 NUMERICAL FRAMEWORK

This section presents details of a numerical solver that is used by the authors and co-workers for LES of open channel flows with complex free-surface interactions. The governing equations for an unsteady, incompressible, viscous flow of a Newtonian fluid are solved using the in-house code HYDRO3D (Stoesser and Nikora, 2008; Bomminayuni and Stoesser, 2011; Stoesser, 2010; Kara et al., 2015c; Stoesser et al., 2015). An LES approach is employed to simulate directly the large, energy carrying eddies while scales smaller than the grid size are accounted for using the WALE subgrid scale model (Nicoud and Ducros, 1999). The code is a refined and improved version of the open-channel LES code that was validated for flow over dunes (Stoesser et al., 2008), flow in compound channel (Kara et al., 2012), and flow in contact tanks (Kim et al., 2010; 2013). HYDRO3D is based on finite differences with staggered storage of the Cartesian velocity components on uniform Cartesian grids. Second-order central differences are employed for the diffusive terms while convective fluxes in the momentum and level-set are approximated using a fifth-order weighted essentially non-oscillatory (WENO) scheme. The WENO scheme offers the necessary compromise between numerical accuracy and algorithm stability. A fractional-step method is used with a Runge-Kutta predictor and the solution of a pressure-correction equation in the final step as a corrector. A multi-grid method is employed to solve the Poisson equation. The free-surface is captured using the level set method (LSM) developed by (Osher and Sethian, 1988). As explained in Section 1, the LSM employs a level set signed distance function, ϕ, which has zero value at the phase interface and is negative in air and positive in water. The code is parallelized via domain decomposition, and the standard Message Passing Interface (MPI) accomplishes communication between sub-domains.

3 COMPUTATIONAL SETUP

For case PC, which replicates numerically the experiments of Martinuzzi (1992) and Martinuzzi and Tropea (1993), a cube is mounted on the lower wall of a plane channel and occupies half of the domain height, i.e. H/k = 2, where H is the domain height and k is the cube height. The top and bottom boundaries of the domain are set to no-slip condition. Fully developed turbulent flow was applied at the inflow boundary which was achieved by performing a precursor simulation of turbulent open channel flow with periodic streamwise boundary conditions. When the flow in this precursor simulation was judged to be fully developed it was continued for a further 10,000 time steps and the 2D instantaneous flow field from the outflow plane was saved at every time step. This produced 10,000 2D planes of instantaneous turbulent flow which were applied at successive time steps at the inflow boundary of the cube simulation in a cyclical manner, thereby ensuring a continuous fully-developed turbulent inflow for the duration of the simulation. Convective and periodic conditions were stipulated at the outflow and lateral boundaries respectively. The Reynolds number of the flow based on bulk velocity and cube height was Re = 40,000 and the flow was deemed to be fully developed in the section in which the cube was placed.

For case OC, the upper fixed wall (of case PC) was replaced by a free water surface initially placed at a height $H = 2k$, such that the relative submergence was H/k = 2, and the Reynolds number based on water depth and bulk velocity was kept at Re = 40,000. The global Froude number was 0.6. Figure 1 presents the computational domain that was employed: it extended $3k$ upstream, $4k$ laterally and $7k$ downstream of the cube centre. In the vertical direction the domain extended $3.5k$ above the bed, with the top $1.5k$ occupied by

©2017, IAHR. Used with permission / ISSN 1562-6865 (Online) - ISSN 1063-7710 (Print)

the air phase. The domain was discretised by a uniform grid with 600 x 384 x 300 (= 69 million) grid points. The cube was represented by immersed boundaries.

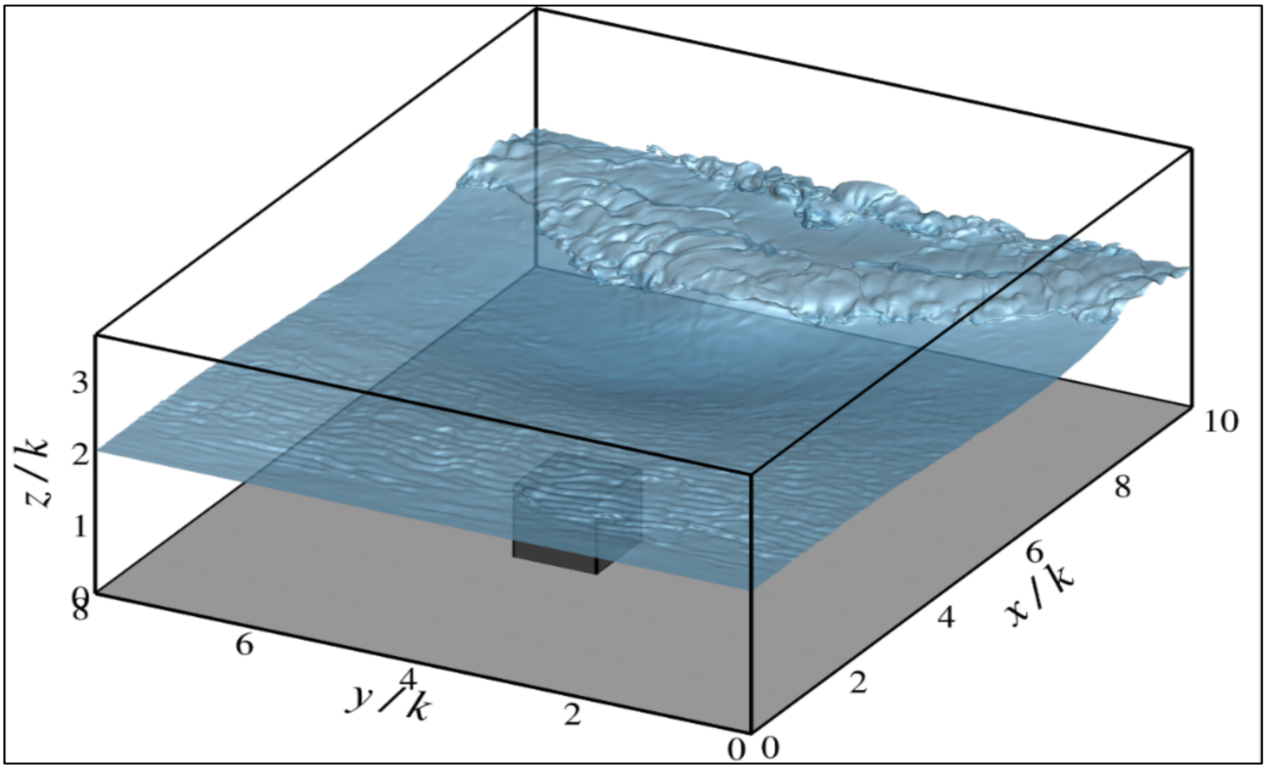

Figure 1. Full domain of case OC with free surface.

4 VALIDATION

Figures 2 and 3 show the streamlines in the symmetry plane at the centre of the domain and near the channel floor for both experimental and LES (case PC) results. As observed in figure 2, the locations and sizes of the recirculation zones are very accurately represented in the LES case. The reattachment of flow happens at approximately the same location (x/k ≈ 2.6, where x/k=0.0 is the leading edge of the cube) in the streamwise direction. The streamlines on the channel bed shows very good agreement too when compared to the experiment (figure 3). A pair of counter-rotating vortices behind the cube are clearly seen in both experiment and LES. Figure 4 are vertical profiles of flow quantities extracted from the symmetry plane of the cube. Figure 4 (top row) presents the mean streamwise velocity profiles at three x-locations, x/k=0.5, 2.5 and 4.0. The LES results show a generally good agreement against the experimental results both on the top of the cube and also in the separation and development regions. Figure 4 (mid row) compares the profiles of shear stress u'w' at the same x-locations as the mean velocity profiles. On the top of the cube, the LES does not seem to have completely resolved the negative peak of the shear stress. Also, this high shear stress region appears to be thinner and sharper for the experimental results. Increasing the grid resolution close to the top of the cube might help to resolve this imperfection. The LES profiles at x/k=2.5 and 4.0 are not smooth which indicates an inefficient in averaging time. A more developed result will be presented later in the conference. In the turbulent kinetic energy profiles (figure 4, bottom row), first two profiles are located on the roof of the cube at x=0.5 and x=1.0 (trailing edge of the cube). The TKE profile at x=0.5 matches the peak TKE quite well. In contrast, the TKE profile at x=1.0 suffer to reach the experimental peak value.

 ©2017, IAHR. Used with permission / ISSN 1562-6865 (Online) - ISSN 1063-7710 (Print)

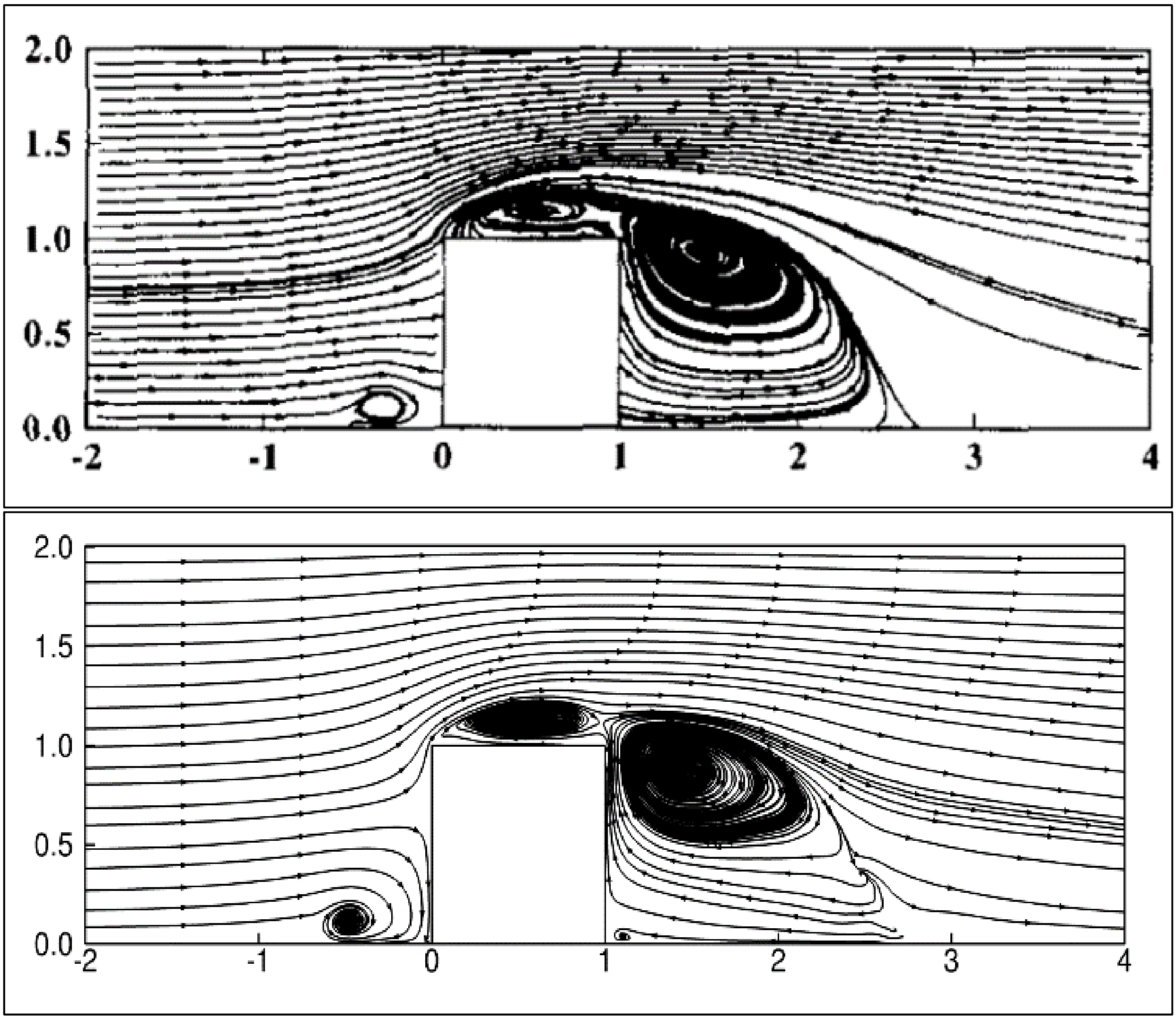

Figure 2. Streamlines in symmetry plane (XZ plane) for experiment (left) and LES (right).

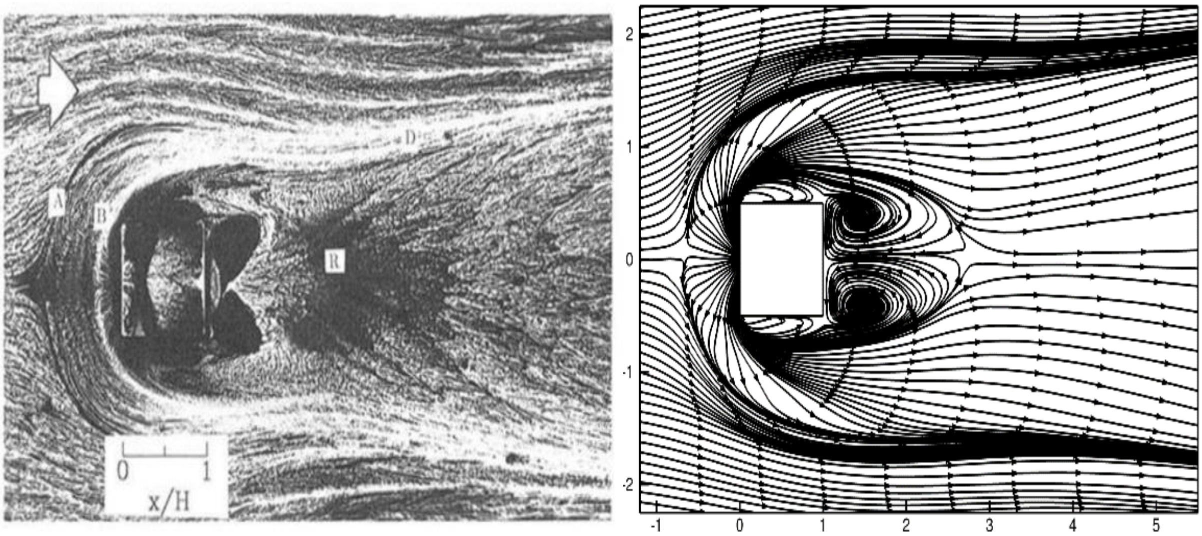

Figure 3. Streamlines near the channel floor (XY plane) for experiment (left) and LES (right).

©2017, IAHR. Used with permission / ISSN 1562-6865 (Online) - ISSN 1063-7710 (Print)

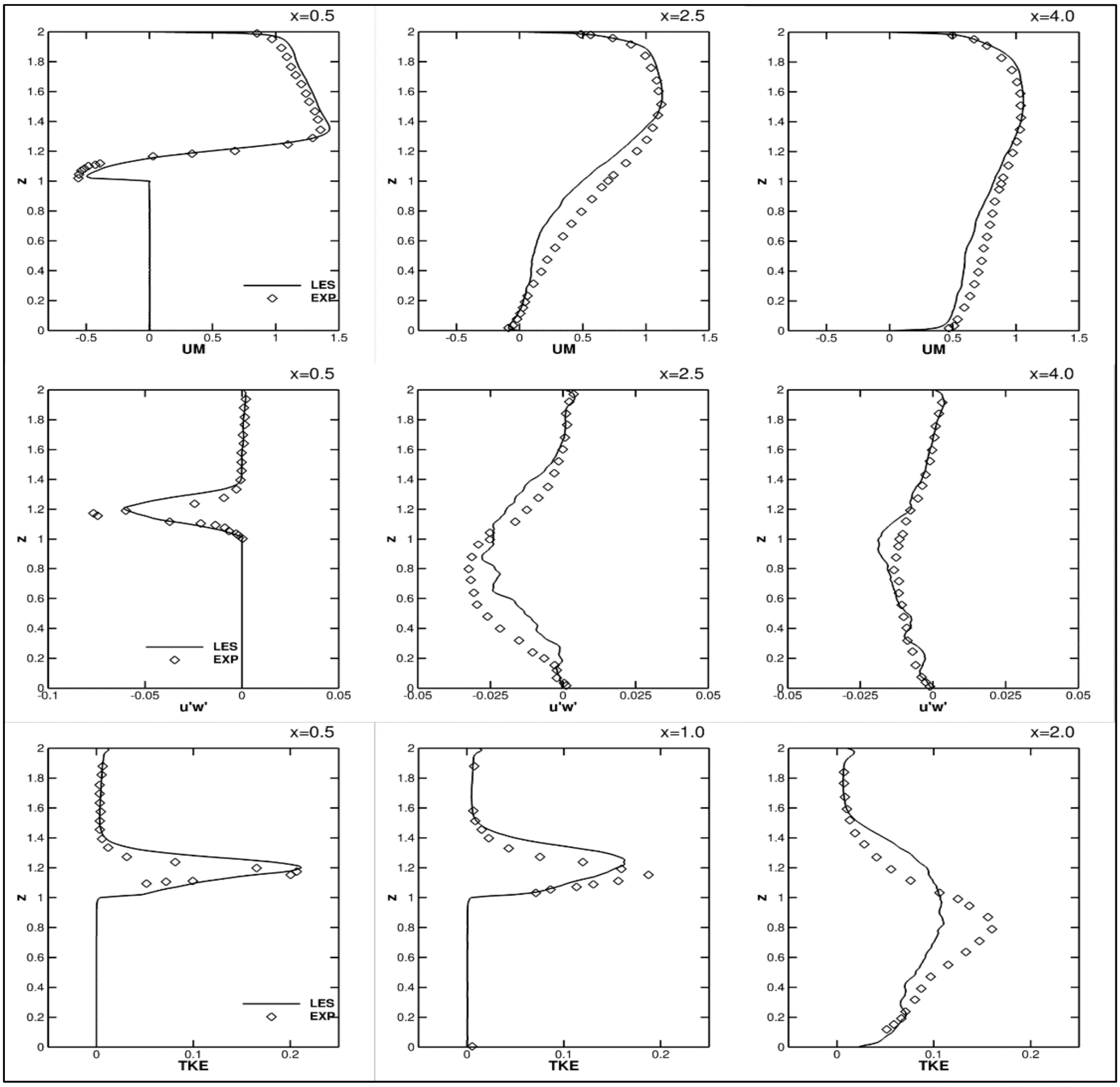

Figure 4. Comparison of profiles of (top row) mean streamwise velocity, (mid row) shear stress, and (bot row) turbulent kinetic energy.

5 RESULTS AND DISCUSSION

Figure 5 presents contours of instantaneous normalised streamwise velocity at an arbitrary moment in time, on the mid plane of the domain for case OC. The position of the water surface is included as the black line as a reference. At the front corner of the cube, a small eddy is seen. The water surface experiences a notable dip immediately downstream of the cube, and this is due to the significant local acceleration in the upper part of the water column and a strong recirculating region in the cube wake. The flow decelerates markedly downstream of the recirculation zone and causes a standing wave, above the reattachment zone.

Figures 6(a)-(c) present views of Q criterion iso-surfaces at the same moment in time, from different perspectives, as well as an iso-surface of the instantaneous water surface. The standing wave that manifests downstream of the cube displays a pronounced bow shape, owing to the three-dimensionality of the submerged obstacle. The wave appears breaks further downstream away from the centreline and the minimum water level is found in the centreline of the channel and approximately 1.5*k* downstream of the cube. In terms of turbulent flow structures, there is a well-defined horseshoe vortex upstream of the cube as well as an arch vortex that is generated at the leading edge of the cube, breaks into vertical vortices sideways of the cube and a horizontal roller-type vortex on the top of the cube. All three vortices are being convected by the flow into the downstream area of the cube. Figure 6(b) shows that the roller vortex deforms and appear as hairpin-type vortices in the cube wake. Figure 6(c) highlights the dip in the water surface downstream of the cube, and suggests that the turbulent structures generated by the cube eventually travel upwards towards the surface, downstream of the standing wave. This observation suggests that using a rigid lid assumption for the water surface in this case would likely result in the loss of some unique and important details of the flow.

 ©2017, IAHR. Used with permission / ISSN 1562-6865 (Online) - ISSN 1063-7710 (Print)

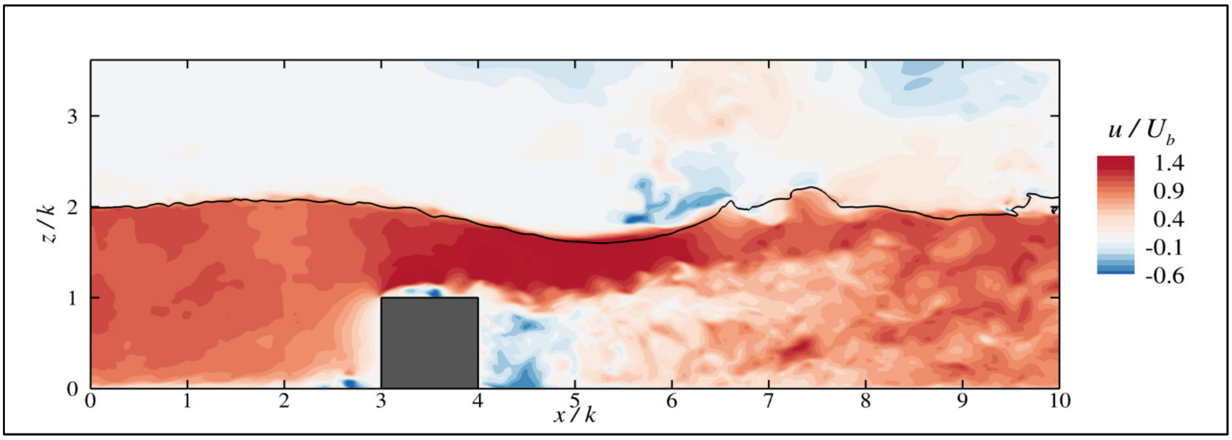

Figure 5. Instantaneous streamwise velocity contour at symmetry plane with free surface (black line).

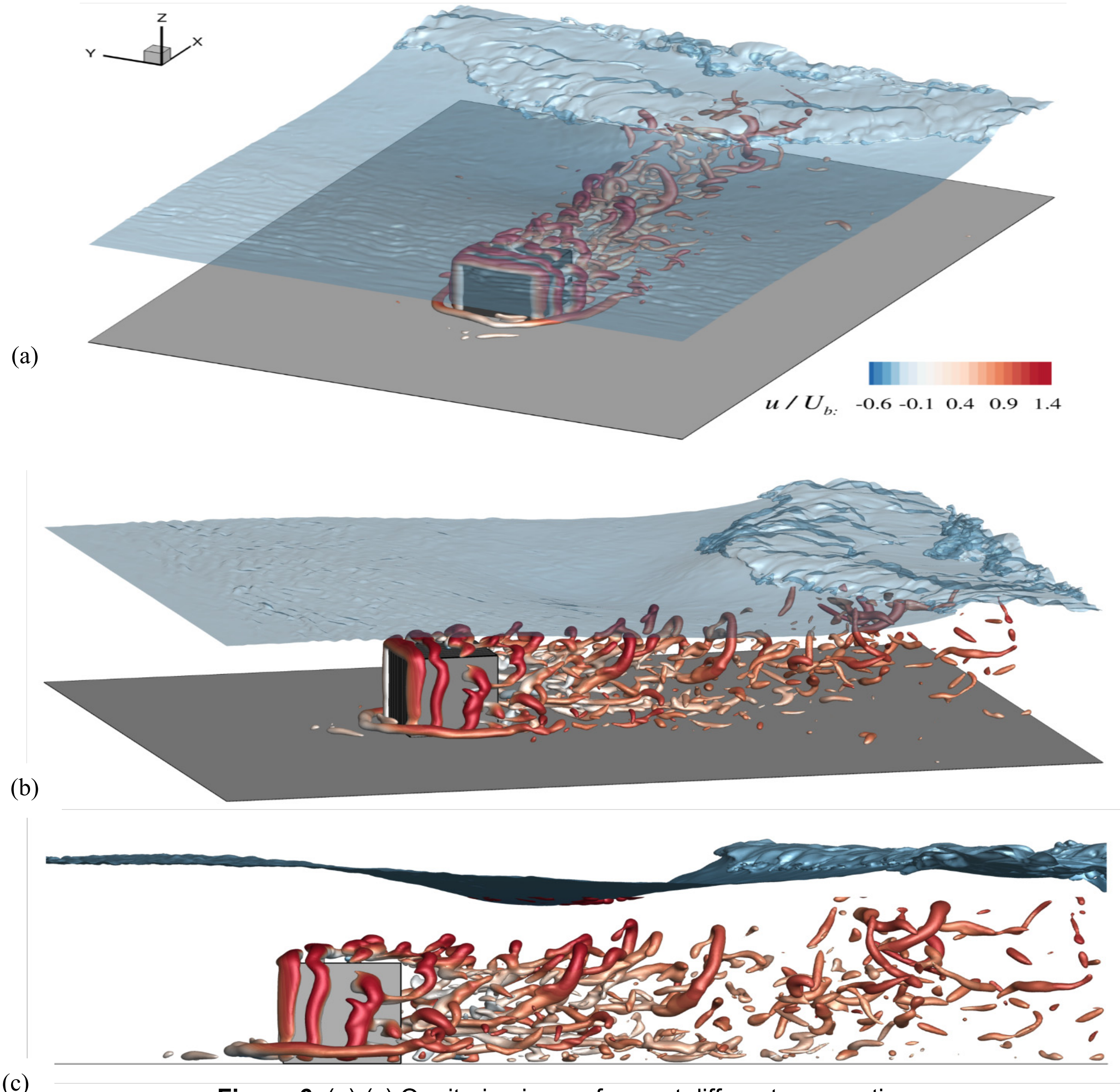

Figure 6. (a)-(c) Q-criterion iso-surfaces at different perspectives.

6 CONCLUSION

Large eddy simulations of flow over a single bottom-mounted cube are simulated. The first simulation replicated laboratory experiments that were carried out in a plane channel, and served as a validation case. The overall agreement between LES and experimental data is reasonably good, demonstrating the ability of the LES code to predict such complex three-dimensional flow. The second simulation showcased the use of the level-set method in representing the free surface in a low submergence turbulent open channel flow over a bottom-mounted bluff body. A very notable dip followed by a standing wave in the water surface downstream of the cube are clearly observed. Further, the Q-criterion iso-surfaces highlighted the turbulent flow structures in the form of roller-type vortex and hair-pin vortex, which propagate downstream and seemingly travel upwards towards the water surface. The results give a good indication that the method is capable of predicting very complex flows that are characterised by strong interactions between the bulk flow and the free-surface, and permits the identification of turbulent structures and events that would be very difficult to achieve experimentally.

ACKNOWLEDGEMENTS

This work was supported by the UK Engineering and Physical Sciences Research Council (EPSRC). The computations presented in the paper were carried out on Cardiff University's supercomputer Raven, hosted by Advanced Research Computing @ Cardiff (ARCCA), and High Performance Computing Wales' Cardiff Hub.

REFERENCES

Bomminayuni, S. & Stoesser, T. (2011). *Turbulence Statistics in an Open-Channel Flow over a Rough Bed*. Journal of Hydraulic Engineering, 137(11),1347–1358.

Kara, M.C., Stoesser, T. & McSherry, R. (2015c). Calculation of Fluid–Structure Interaction: Methods, Refinements, Applications. In *Proceedings of the Institution of Civil Engineers - Engineering and Computational Mechanics*. 59–78.

Kara, S., Kara, M.C., Stoesser, T. & Sturm, T.W. (2015a). *Free-Surface versus Rigid-Lid LES Computations for Bridge-Abutment Flow*. *Journal of Hydraulic Engineering*, 141(9), 1-9.

Kara, S., Stoesser, T. & Sturm, T.W. (2012). Turbulence Statistics in Compound Channels with Deep and Shallow Overbank Flows. *Journal of Hydraulic Research*, 50(5), 482–493.

Kara, S., Stoesser, T., Sturm, T.W. & Mulahasan, S. (2015b). Flow Dynamics through a Submerged Bridge Opening with Overtopping. *Journal of Hydraulic Research*, 53(2), 186–195.

Kim, D., Kim, D.-I., Kim, J.-H. & Stoesser, T. (2010). Large Eddy Simulation of Flow and Tracer Transport in Multichamber Ozone Contactors. *Journal of Environmental Engineering*, 136(1), 22–31.

Kim, D., Stoesser, T. & Kim, J. (2013). The Effect of Baffle Spacing on Hydrodynamics and Solute Transport in Serpentine Contact Tanks. *Journal of Hydraulic Research*, 51(5), 558–568.

Koken, M. & Constantinescu, G. (2009). An Investigation of the Dynamics of Coherent Structures in a Turbulent Channel Flow with a Vertical Sidewall Obstruction. *Physics of Fluids*, 21(8), 1-16.

Komori, S., Nagaosa, R., Murakami, Y., Chiba, S., Ishii, K. & Kuwahara, K. (1993). *Direct Numerical Simulation of Three‐Dimensional Open‐Channel Flow with Zero‐Shear Gas–Liquid Interface*. Physics of Fluids A: Fluid Dynamics, 5(1), 115–125.

Lam, K. & Banerjee, S. (1992). *On the Condition of Streak Formation in a Bounded Turbulent Flow*. Physics of Fluids A: Fluid Dynamics, 4(2), 306–320.

Martinuzzi, R. (1992). *Experimentelle Untersuchung der Umströmung wandgebundener, rechteckiger, prismatischer Hindernisse - Google Scholar*. University of Erlangen.

Martinuzzi, R. & Tropea, C. (1993). The Flow around Surface-Mounted, Prismatic Obstacles Placed in a Fully Developed Channel Flow (Data Bank Contribution). *Journal of Fluids Engineering,* 115(1), 85.

Nicoud, F. & Ducros, F. (1999). Subgrid-Scale Stress Modelling based on the Square of the Velocity Gradient Tensor. *Flow, turbulence and Combustion*, 62(3), 183–200.

Osher, S. & Sethian, J.A. (1988). Fronts Propagating with Curvature-Dependent Speed: Algorithms based on Hamilton-Jacobi Formulations. *Journal of Computational Physics,* 79(1), 12–49.

Paik, J. & Sotiropoulos, F. (2005). Coherent Structure Dynamics Upstream of a Long Rectangular Block at the Side of a Large Aspect Ratio Channel. *Physics of Fluids*, 17(11), 115104.

Rodi, W. (1997). *Comparison of LES and RANS Calculations of the Flow Around Bluff Bodies*. *Journal of Wind Engineering and Industrial Aerodynamics,* 69–71, 55–75.

Stoesser, T. (2010). Physically Realistic Roughness Closure Scheme to Simulate Turbulent Channel Flow over Rough Beds *within the Framework of LES*. *Journal of Hydraulic Engineering,* 136(10), 812–819.

Stoesser, T., Braun, C., García-Villalba, M. & Rodi, W. (2008). Turbulence Structures in Flow over Two-Dimensional Dunes. *Journal of Hydraulic Engineering*, 134(1), 42–55.

Stoesser, T., McSherry, R. & Fraga, B. (2015). Secondary Currents and Turbulence over a Non-Uniformly Roughened Open-Channel Bed. *Water*, 7(9), 4896–4913.

Stoesser, T. & Nikora, V. (2008). Flow Structure over Square Bars at Intermediate Submergence: Large Eddy Simulation Study of Bar Spacing Effect. Acta Geophysica, 56(3), 876–893.

Yue, W., Lin, C.-L. & Patel, V.C. (2006). Large-Eddy Simulation of Turbulent Flow over a Fixed Two-Dimensional Dune. *Journal of Hydraulic Engineering,* 132(7), 643–651.

 ©2017, IAHR. Used with permission / ISSN 1562-6865 (Online) - ISSN 1063-7710 (Print)

OBSERVATIONS OF FLOATING SEED DISPERSAL IN VEGETATED OPEN CHANNEL FLOW

XIAOGUANG LIU(1), YUHONG ZENG(2) & XI ZHU(3)

(1,2,3) State Key Laboratory of Water Resources and Hydropower Engineering Science, Wuhan University, Wuhan, Hubei 430072, China.
Email: yhzeng@whu.edu.cn

ABSTRACT

In this study we conduct some specific experiments to investigate the effects of stem density and flow velocity on the interaction processes between two types of particle and emergent vegetation in an open channel flow. We propose a new definition of the probability that a particle interacts with a stem which seems more plausible, and preliminarily explore the particle-stem interaction processes (interaction and capture). We also determine a length scale to assess the model performance (for vegetation characteristics and arrangement in this study) and propose a dimensionless parameter to evaluate the adsorption capacity for the floating particle attached to the stem. Some experiment phenomena have been observed in this experiments were presented for further analysis and research.

Keywords: Hydrochory; floating seeds; longitudinal dispersion; emergent vegetation.

1 INTRODUCTION

Hydrochory, i.e. seed and propagule dispersal in fluvial systems, which enables long-distance dispersal along river corridors and consequently enhances longitudinal connectivity and gene flow between distant parts of a catchment (Merritt and Wohl, 2006). It is an important process both for the distribution and abundance of single species (Nilsson et al., 2010). Most aquatic plant seeds have the ability to float, and long floating time can enhance seeds dispersal distance by afloat for longer advection times (eg., Nilsson and Danvind, 1997; Nilsson et al., 2010). The behavior of floating particles differs substantially from that of suspended sediments as the particles are affected by hydrodynamic characteristics that developed at the free surface (eg., wind and surface tension effects) (Defina and Peruzzo,2010). Many empirical and semi-empirical models were proposed mainly aimed at assessing the seed dispersal distance, or the probability distribution of distances reached by seeds or plant fragments (Defina and Peruzzo, 2010; Groves et al., 2009). For example, Defina and Peruzzo (2010) have proposed a stochastic model to simulate the transport and diffusion of floating particles in open channel with staggered and random distributed vegetation under low flow velocity. Their model is one-dimensional and describes particle-vegetation interactions along the curvilinear axis corresponding to the generic particle trajectory. A stochastic model was proposed to simulate the transport and diffusion of floating particles and the trapping mechanisms (Defina and Peruzzo, 2010): Defining P_i as the probability that a particle interacts with a stem while travelling the distance along its path, therefore, on a stem over a path whose length is $\Delta s_1 = \frac{s_1}{P_i}$, and P_c is the probability that a particle permanently captured when it interacts with a stem. As a particle passes through an array of stems, the mean centre-to-centre spacing between adjacent cylinders in any direction is $s_1 = \frac{1}{\sqrt{n_s}}$, n_s being the number of stems per unit area; the mean spacing along any straight transect, e.g., on a line parallel to the downstream direction is $s_2 = \frac{1}{n_s d_s}$, as presented in the work of White and Nepf (2003). The distance X traveled by particles before permanent captured can be measured and the distribution is given as

$$P(X > L) = \mathrm{e}^{-L/\lambda} \quad [1]$$

in which

$$\lambda = \frac{-\Delta s_1}{\ln(1 - P_i P_c)} \quad [2]$$

©2017, IAHR. Used with permission / ISSN 1562-6865 (Online) - ISSN 1063-7710 (Print)

is the particle mean path length before permanent captured and can be determined fitting experimental data. Peruzzo et al. (2012) has considered the low flow velocity condition and developed a physically based model to predict the impact of surface tension on the fate of floating particles within a region of emergent vegetation. In this study, floating seeds dispersal in aquatic systems with low and moderate flow velocities and the medium density vegetation array is considered, i.e., the influence of surface tension can't be ignored and the stem spacing is assumed to be far greater than the seed size. The purposes of this investigation is to gain further insight into the impact of flow velocity and stem density on floating particle dispersal, and advance the model proposed by Peruzzo et al. (2012) that describe the impact of surface tension on a particle passing through the array of stems.

2 MODEL AND EXPERIMENTS METHOD

2.1 Particle interaction with a stem with a diameter *d*

Floating particles are attracted toward stems by the rising meniscus when passing through the array of stems at low-flow velocity, and capillary forces were believed to play an important role in the interaction between colloidal particle attached to the stem, for which the attraction response is caused by surface tension, i.e., the Cheerios effect. The Weber number, We, the ratio between the fluid's inertia to its surface tension, is used to evaluate the effect of the Cheerios effect. Shimeta and Jumsrs (1991) and Palmer (2004) suggested that the probability of interaction Pi should be determined by the ratio between a length b which is the distance between the outmost trajectory lead to collision and stem diameter. But when $b>d$, the P_i can be greater than 1, which is contradictory. Actually, floating particles under the influence of surface tension can be attracted to the cylinder once We is far less than the unit. The characteristic length scale of the meniscus can be defined as the capillary length,

$$1/q=\sqrt{\frac{\sigma}{\rho_0 g}} \qquad [3]$$

ρ_0 is the density difference between liquid and air, g is the acceleration of gravity, σ is the liquid surface tension. Based on preliminary comparison between the model and experimental observation, the length scale s_1 is considered to perform better than s_2 when the stems are evenly distributed and have no branch, which differs from the simulated vegetation used in Defina and peruzzo's experiments. To reasonably estimate P_i, a calculation unit within random stems region is used to define the probability that a particle interacts with a stem (see Figure 1), Z_0 is the distance between the outermost trajectories that lead to collision with stem, thus, we proposed a new equation to describe P_i .

$$P_i=\frac{Z_0}{\beta_0 s_1} \qquad [4]$$

where β_0 is a correction factor, and can be given as $\beta_0=\frac{sin\theta}{\theta}$, $\theta=\frac{2\pi}{3(\pi n s_1^2-1)}$ is the mean angle between the two line segments of two adjacent stems on the unit circle, considering $s_1=\frac{1}{\sqrt{n_s}}$, we find that θ is independent of vegetation density (see Figure 1, the dashed circle).

2.2 Particle capture by a stem with a diameter *d*

The mean gap between stems is much larger compared to the particle size in this experiments, therefore, the net trapping, i.e., stems overlap enough to form a netlike structure that intercepts the floating particle (Defina and peruzzo,2010), is neglected. In this experiments, the stem Reynolds number R_d is in the range $80<R_d<400$, within the range, eddies are shed continuously from each side of the circle boundary, forming rows of vortices in its wake (see Figure 2). Influenced by the periodic vortex shedding, the particle in the wake will periodically vibrate, thus, a trapped particle has possibility to shake off due to periodically Vortex shedding. The vortex shedding frequency (*f*) can be given as

$$f=\frac{S_r u}{d_s} \qquad [5]$$

Where S_r is the Strouhal number, in this experiments, the stem Reynolds number R_d is in the range $80<R_d<400$, in this range, S_r can be estimated by the empirical formula presented by Fey et al., (1998).

$$S_r=0.2684-\frac{1.0356}{\sqrt{R_d}} \qquad [6]$$

 ©2017, IAHR. Used with permission / ISSN 1562-6865 (Online) - ISSN 1063-7710 (Print)

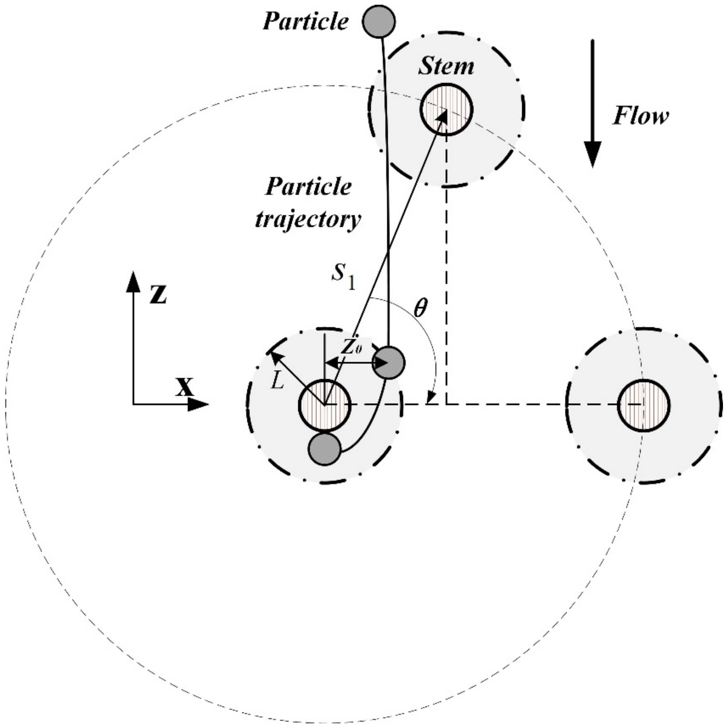

Figure 1. Definition of the probability of particle collision with a stem in a calculation unit, the dotted bold line surrounding the stems denotes the capillary-affected area.

The amplitude (A) of the particle periodically vibrating in this experiments and approximately A=0.5d_s, therefore, the maximum transverse velocity of the particle periodically vibrating behind the stem can be described as

$$u_{xm} = 2\pi Af \quad [7]$$

The attracted particle 3pinning round the stem can produce centrifugal force (F_e), which may push the particle out of the wake by overcoming the Cheerios effect,

$$F_e = \frac{8m_p\pi^2u^2S_r^2A^2}{d_s^3 + d_s^2d_p} \quad [8]$$

For the particle floating on the water, the drag force (F_d) due to the flow is considered to be proportioned to the square of the bulk velocity, and can be given as

$$F_d = \beta_1 C_d \rho A_p u^2 \quad [9]$$

Where β_1 is a scale factor, A_p is the projected area of the submerged part of the particle, C_d is the particle drag coefficient, and assumed to C_d =1.0. To consider the mechanism of particle escaping from the stem, the ratio (e) between the adsorption capacity, i.e., capillary force and the escape capability, i.e., the drag force and centrifugal force is used to describe the capture probability P_c,

$$e = \frac{F_d + F_e}{F_c} = \frac{\left(\frac{8m_p\pi^2Sr^2A^2}{d_s^3 + d_s^2d_p} + \beta_1\rho A_p\right)u^2}{\frac{\pi}{2}d_pd_sq\sigma sin(\alpha_p + \varphi_p)sin(\alpha_s + \varphi_s)sin(\varphi_s)sin(\varphi_p)K_1(q\frac{d_p + d_s}{2})} \quad [10]$$

If e<1.0, the adsorption capacity can't overcome the escape capability, the particle will remain attached to the stem, whereas the adsorption capacity can overcome the escape capabilities and particles may escape from the stems.

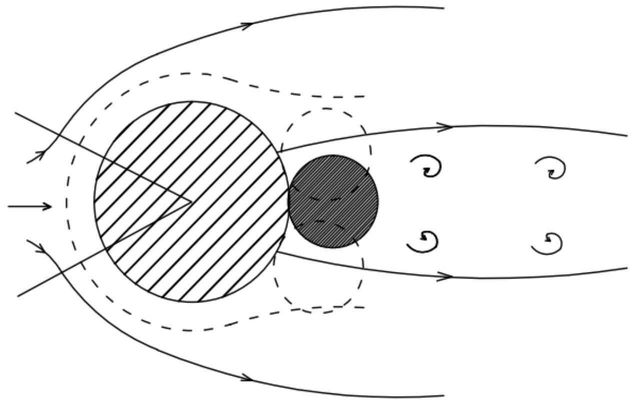

Figure 2. Flow round a stem which is normal to flow path at 80<R_d <400, a particle is drawn into the vortex shedding region behind a stem and possibly out of the region into the free stream.

Based on the analysis of the particle capture mechanism (Eq.8), a dimensionless parameter $\eta = \frac{(\rho_0 + 1)d_p^2}{(\rho_0 - 1)(d_s + d_p)^2}$ can be used to evaluate the adsorption capacity for the floating particle attached to the stem, i.e., the escape velocity u_e, which increases with the increasing η.

3 Experiments

The laboratory experiment was carried out in a rectangular flume 18 m long, 1.0 m wide, and 0.5 m deep, with glass sidewalls and bottom. The recirculated flow discharge *Q* was measured by an Electromagnetic Flowmeter, and a tail gate located at the exit of the flume can be adjusted to maintain a steady flow. A random array of rigid round wooden cylinders with a diameter ds of 0.6 cm was constructed on two PVC boards to create a test section with a length of 4 m, width of 0.6 m. The cylinders were symmetrically placed along the central axis of the flume to eliminate the sidewall effect. Four different random arrays were constructed and five discharges were tested for each array (see table 1). Two types of particle are used in the experiments to mimic buoyant seeds: Particle A is a regular wooden ball with a diameter of 0.6 cm and a relative density of 0.71; Particle B is Calamus seed that can be described approximately disc-shaped having a diameter of 0.8 cm and thickness (h_p) of 0.2 cm, and a relative density of 0.68, we painted evenly all particles with white dye to get a better observation and track effect. Approximately 200 particles are individually released 50 cm upstream of the test section, all of experiment runs are recorded by a digital camera mounted over the flume.

All the experimental observations are performed from the Lagrangian point of view. Video analysis contributes in understanding the mechanisms for floating particles trapping and escaping from stems and recognize the relevant aspects of the interaction between floating particles and stems. Recorded frames are extracted and analyzed to determine particle velocity approaching the stems and measure the duration of temporary and permanent (particle retention time is greater than 300s) trapping events, and the distance traveled by each particle before being permanently captured is also measured.

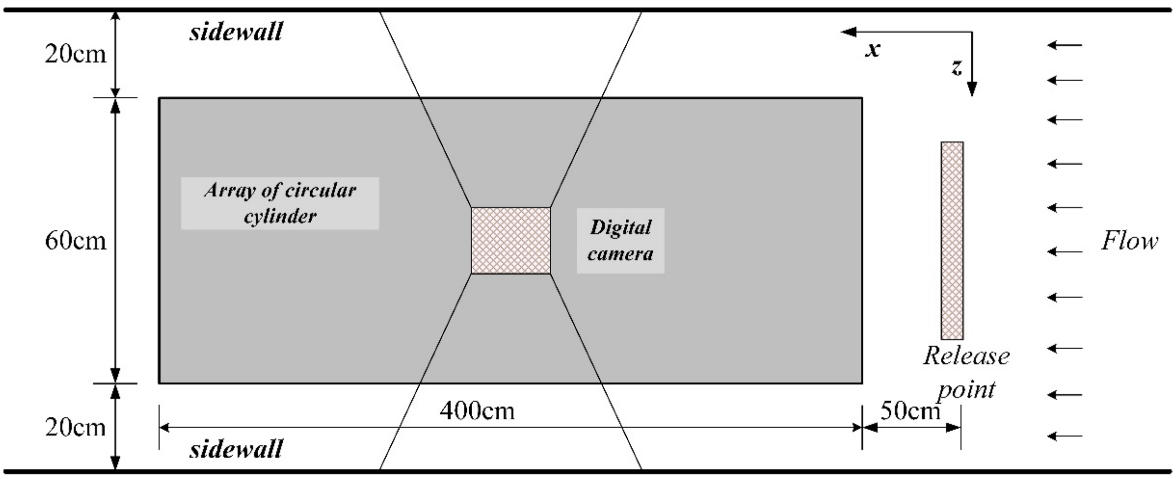

Figure 3. Top view of the experimental flume channel

 ©2017, IAHR. Used with permission / ISSN 1562-6865 (Online) - ISSN 1063-7710 (Print)

Table 1. Summary of experimental conditions

$u(ms^{-1})$	R_d	$We(10^{-2})$	$n_s(m^{-2})$	$d_s(m)$
0.0190	114	2.97	1164	0.006
0.0282	169.2	6.54	1164	0.006
0.0426	255.6	14.92	1164	0.006
0.0529	317.4	23.00	1164	0.006
0.0636	381.6	33.25	1164	0.006
0.0167	100.2	2.29	932	0.006
0.0297	178.2	7.25	932	0.006
0.0388	232.8	12.37	932	0.006
0.0430	258	15.20	932	0.006
0.0539	323.4	23.88	932	0.006
0.0166	99.6	2.26	720	0.006
0.0250	150	5.14	720	0.006
0.0375	225	11.56	720	0.006
0.0474	284.4	18.47	720	0.006
0.0585	351	28.13	720	0.006
0.0148	88.8	1.80	554	0.006
0.0243	145.8	4.85	554	0.006
0.0388	232.8	12.37	554	0.006
0.0469	281.4	18.08	554	0.006
0.0538	322.8	23.79	554	0.006

Most of seeds in nature are hydrophilic (including the particle A and B used here), and once the meniscus between the particle and the stem is below the undisturbed level, capillary forces were believed to play an important role in the interaction between colloidal particles attached to the stem. For buoyant particles floating on the water, h_1 is the particle height above the saturation line, h_2 is the meniscus height, α_p is the particle-water contact angle, ψ_p is the meniscus slope angle at the particle and cylinder contact line, i.e., the undisturbed level and ψ_s is the meniscus slope angle at the stem contact line. The meniscus slope angles of particle and stem have no significant change when particle gradually approaches the stem, and it can be assumed that the meniscus angle remains constant during the transport process. The following formula is derived by geometry analysis.

$$\cos(\varphi_p + \alpha_p) = (\frac{d_p}{2} - h_1) \Big/ \frac{d_p}{2} \quad [11]$$

The weight ($m_p g$) of a floating particle in equilibrium is balanced by a capillary force (F_c) and the net pressure force (F_p),

$$F_c + F_p = m_p g \quad [12]$$

For floating spherical wood particle, capillary force F_{cwood} is given by

$$F_{cwood} = -\pi\sigma d_p \sin\varphi_p \sin(\varphi_p + \alpha_p) \quad [13]$$

For floating Calamus seed, capillary force F_{ccala} is given by

$$F_{ccala} = -\pi\sigma d_p \sin\varphi_p \quad [14]$$

h_2 is moderately small for spherical wood particle and Calamus seed in experimental observations, then, the net pressure forces are represented respectively by

$$F_{pwood} = \pi\rho g(d_p - h_1 - h_2)^2(\frac{d_p}{2} - \frac{d_p - h_1 - h_2}{3}) \quad [15]$$

$$F_{pcala} = \frac{1}{4}\pi\rho g d_p^2(h_p - h_1 - h_2) \quad [16]$$

Using Eqs.(10-14) with the measuring results of h_1 and h_2, α_p and ψ_p for Particle A and Particle B can be obtained. The results of calculating and measuring angles are presented at Table 2.

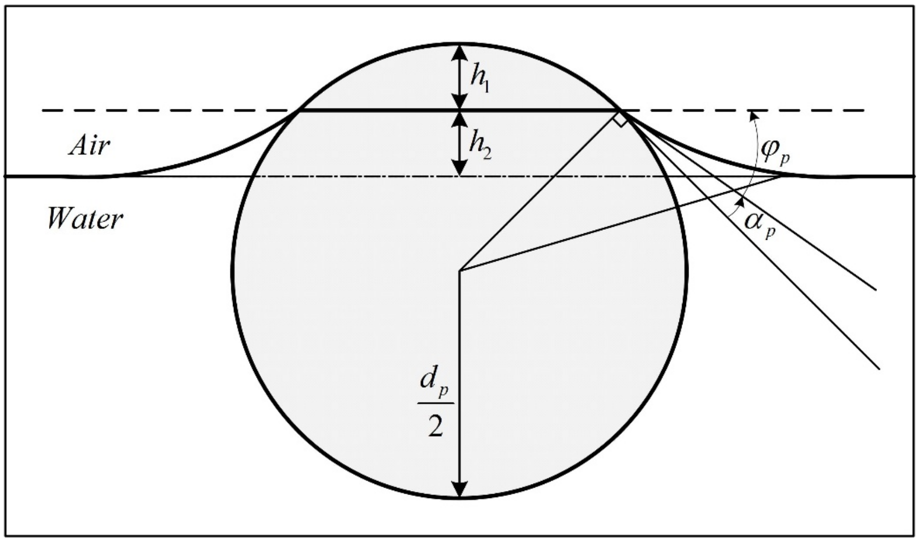

(a) Particle A

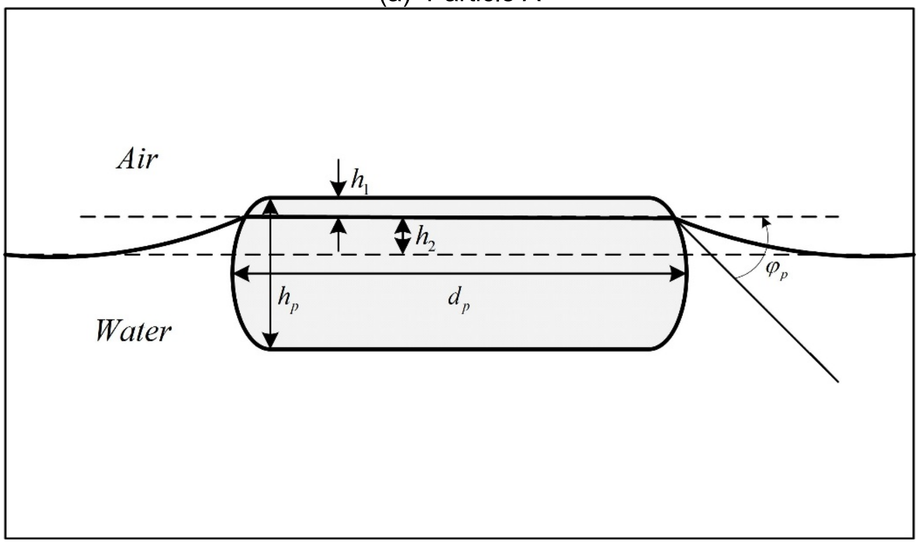

(b) Particle B

Figure 4. Sketch of hydrophilic particles in equilibrium on the water. (a) particle A; (b) Particle B.

Table 2. Summary of particles characteristics and model parameters

Particle type	**Average Diameter (*mm*)**	**Particle Mass (g)**	**Particle Density (gcm^{-3})**	$\alpha_p(Deg)$	$\varphi_p(Deg)$	$\varphi_s(Deg)$	$\alpha_s(Deg)$
Particle A	6.0	0.080	0.7044	21.29	26.90	25.00	75.00
Particle B[1]	8.0	0.068	0.6785	82.95	7.05	25.00	75.00

1The average thickness of Particle B is approximately 2.0 mm.

4 RESULTS AND DISCUSSION

4.1 Experimental data Processing and analysis

In this experiments, within the Lagrangian framework, the distance traveled by each particle before being permanently captured is measured, the particle mean path length (λ) before permanent capture can be determined by fitting which with Eq.(1) and identified as a function of bulk flow velocity (see Figure 6). As an illustration, the probability a particle has of travelling a distance *X* greater than *L* for particle A and B with two different bulk velocities under n_s=720 m^{-2} are shown as Figure 5.

 ©2017, IAHR. Used with permission / ISSN 1562-6865 (Online) - ISSN 1063-7710 (Print)

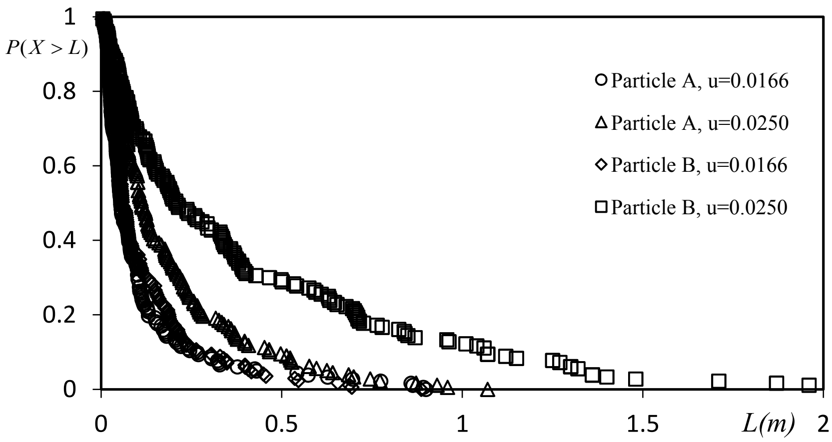

Figure 5. Experimental probability distribution *P(X>L)* is plotted versus *L*.

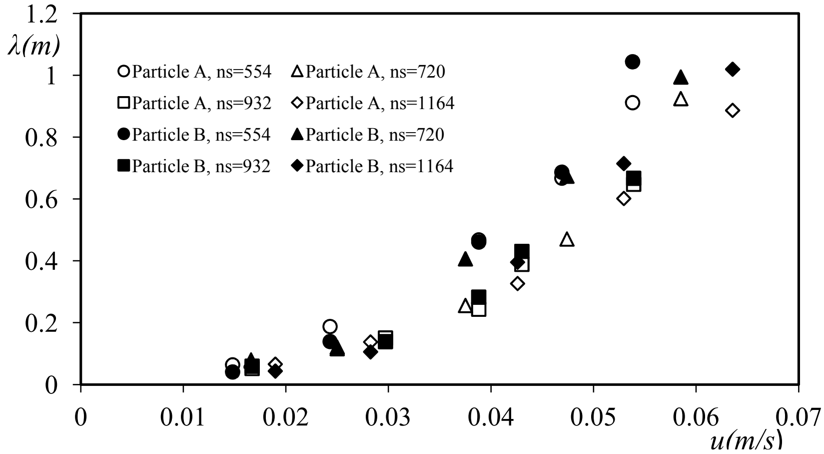

Figure 6. The particle mean path length (λ) is plotted as a function of bulk flow velocity.

To observe how the mean path length varies with the bulk flow velocity, λ exponentially increases with the bulk flow velocity. This illustrates, with the flow velocity increasing, the Cheerios effect is not sufficient to capture the particles gradually; for another, the increasing velocity also reduce the probability that particles interact with stems, the particles are more likely to travel farther. For the same particle type, λ increases more dramatically with the increasing velocity under low stem density, i.e., the particle mean path length is most sensitive to the velocity variation. Analyzing the experimental data of video material, the number of permanent captures, N_i, and the number of measured temporary interaction events, N_c, can be respectively determined for each experimental run. As a particle passes through the array of stems, the total number of interaction points N_t, using the measured path length X and s_1, can be described as

$$N_t = 1 + X/s_1 \quad [17]$$

the probability P_i can be estimated to be,

$$P_i = \frac{N_i + N_c}{N_t} \quad [18]$$

.

when the probability P_c is moderately small, the mean path length can be approximated as (Defina and Peruzzo, 2010)

$$\lambda = \frac{-\Delta s_1}{\ln(1 - P_i P_c)} \approx \frac{-\Delta s_1}{P_i \ln(1 - P_c)} \quad [19]$$

,

the probability P_c then can be estimated by

$$P_c = 1 - \exp\left(\frac{-\Delta s_1}{\lambda P_i}\right) \quad [20]$$

.

©2017, IAHR. Used with permission / ISSN 1562-6865 (Online) - ISSN 1063-7710 (Print)

Following the work of Peruzzo et al., (2012), we define u_e as the escape velocity, the velocity below which particles will remain attached to the stem, i.e., $P_c|u<u_e = 1.0$; increasing of the ratio u/u_e reduces the probability P_c; they suggest that the probability of capture P_c decays exponentially with u/u_e, specifically

$$P_c = \begin{cases} 1 & u/u_e \le 1 \\ e^{1-u/u_e} & u/u_e > 1 \end{cases} \qquad [21]$$

By analyzing the recorded frames and computing Eqs.(15,16), the probability P_i can be estimated and shown in Table 3, varying with the bulk flow velocity; the particle floating on the water, the deformation of liquid-liquid interface due to two adjacent particles, gives rise to capillary forces on the particles which cause them to cluster, a small amount of particles clustering will enlarge the probability P_i due to the Cheerios effect. with the mean path length, the probability Pc can be computed by Eq.(18), and the probability P_c can be considered to be as a function of the bulk velocity (see Figure 8).

Table 3. Summary of the results of the probability Pi by analyzing the recorded frames.

n_s (m^{-2})											
554			720			932			1164		
***u* (ms^{-1})**	***Pi* (A)**	***Pi* (B)**	***u* (ms^{-1})**	***Pi* (A)**	***Pi* (B)**	***u* (ms^{-1})**	***Pi* (A)**	***Pi* (B)**	***u* (ms^{-1})**	***Pi* (A)**	***Pi* (B)**
0.0148	0.399	0.508	0.0166	0.319	0.329	0.0167	0.386	0.353	0.0190	0.388	0.400
0.0243	0.239	0.278	0.0250	0.268	0.282	0.0297	0.231	0.234	0.0282	0.280	0.281
0.0388	0.150	0.148	0.0375	0.178	0.151	0.0388	0.178	0.166	0.0426	0.189	0.152
0.0469	0.121	0.118	0.0474	0.147	0.115	0.0430	0.156	0.141	0.0529	0.139	0.120
0.0538	0.102	0.091	0.0585	0.116	0.084	0.0539	0.134	0.117	0.0636	0.112	0.098

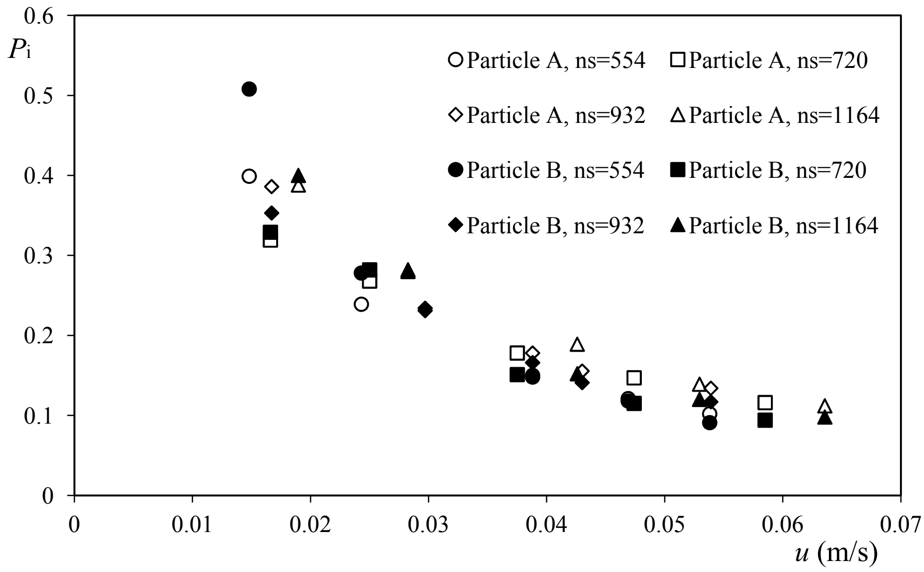

Figure 7. The probability Pi is plotted as a function of bulk flow velocity.

Figure 7 indicates the probability Pi exponentially decreases with increasing flow velocity, it can be assumed that the adsorption capacity of the Cheerios effect decreases with the increasing flow velocity, the particle has lower probability to collide with the stem. Under the same stem density, the dispersal ability of Particle A is greater than Particle B at very low velocity (u<0.04 m/s), however, with the flow velocity increasing, the dispersal ability of Particle A becomes less than Particle B.

Figure 8 indicates the probability P_c decreases with increasing flow velocity, it can be assumed that, at very low flow velocity, the adsorption capacity can overcome the escape capability, i.e., the Cheerios effect is effective for particle capturing; When the velocity is small to a certain extent, the probability P_c is expected to approach unity. It can be observed that, colliding with another particle can push a trapped particle out of the wake into the free stream. Therefore, the probability P_c is less than the probability that a particle is permanently captured due to the Cheerios effect. The escape velocity (u_e) can be estimated by fitting equation (19), and plotted as a function of the flow velocity in Figure 9. Figure 9 indicates the escape velocity (u_e)

 ©2017, IAHR. Used with permission / ISSN 1562-6865 (Online) - ISSN 1063-7710 (Print)

increases linearly with increasing flow velocity, with data fitting, which can be described as the following empirical formula,

$$u_e = 10^{-5} n_s + 0.0158 \quad [22]$$

The formula is deduced based on limited data, and need more researches to validate and amend. It can be argued that, the higher stem density means harder to overcome the adsorption capacity. For example, the scale factor of the drag force decreases with increasing stem density. As can be noticed, there is no significant difference in the change trend of escape velocity between particle A and B which have the similar density and different shapes, it suggests that different particle shapes have no effect on the escape velocity. Considering the critical state of the particle capturing with the escape velocity, an approximate formula is given below to estimate β_1,

$$e(u = u_e) = 1 \quad [23]$$

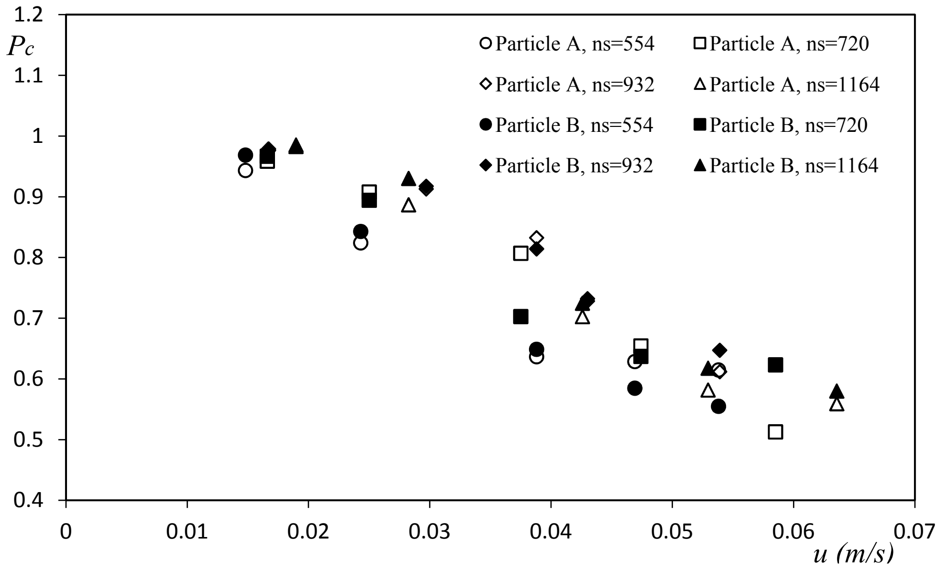

Figure 8. The probability P_c is plotted as a function of bulk flow velocity.

Table 4. Summary of the calculating the scale factor β_1 for Particle A and B

	n_s (m^{-2})			
	554	**720**	**932**	**1164**
β_1 (Particle A)	1.22	1.15	1.08	0.98
β_1 (Particle B)	0.72	0.67	0.60	0.55

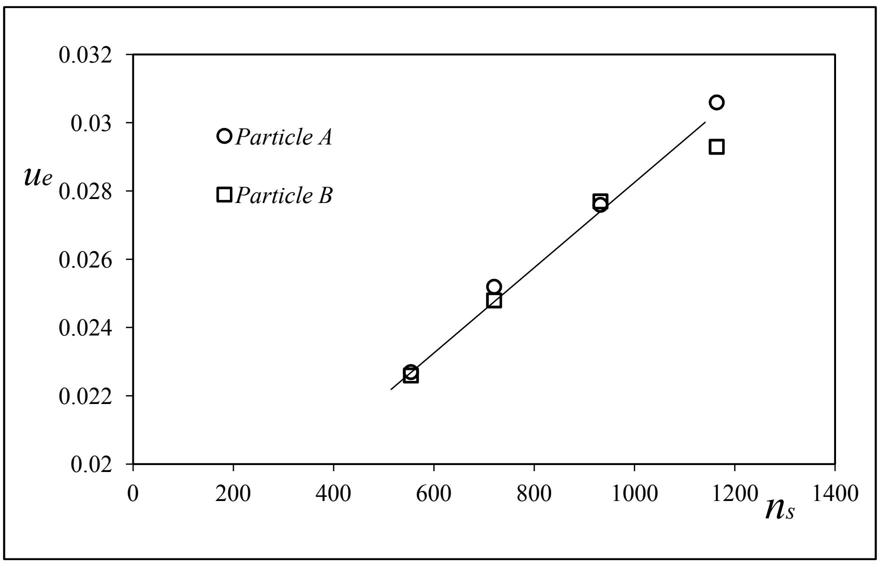

Figure 9. The probability Pc is plotted as a function of the stem density.

©2017, IAHR. Used with permission / ISSN 1562-6865 (Online) - ISSN 1063-7710 (Print)

4. CONCLUSION

In this study we proposed a new definition of the probability Pi, and which seems more plausible to those with Shimeta and Jumsrs (1991) and Palmer (2004). We explored the effects of stem density and flow velocity on the interaction processes between two types of particle and emergent vegetation in an open channel flow through laboratory (with low and moderate flow velocities and the medium density vegetation array), the role of the surface tension in capturing floating particles within emergent vegetation was also noticed. We found that the particle mean path length exponentially increases with the bulk flow velocity; with the flow velocity increasing, the dispersal ability of Particle A becomes less than Particle B; the particle escape velocity increases linearly with increasing flow velocity (Eq. 20), and we preliminarily proposed a dimensionless parameter to evaluate the adsorption capacity for the floating particle attached to the stem. Some experiment phenomena observed in this experiments (e.g., there is no significant difference in the change trend of escape velocity between particle A and B) deserved deeper study.

REFERENCES

Danvind, M. & Nilsson, C. (1997). Seed Floating Ability and Distribution of Alpine Plants along a Northern Swedish River. *Journal of Vegetation Science*, 8(2), 271-276.

Defina, A. & Peruzzo, P. (2010). Floating Particle Trapping and Diffusion in Vegetated Open Channel Flow. *Water Resources Research*, 46(11).

Fey U, König M, Eckelmann H. (1998). A New Strouhal-Reynolds-Number Relationship for the Circular Cylinder in the Range 47< Re< 2× 105 .*Journal Of Physics Fluids*, 10(7), 1547-1549.

Groves, J.H., Williams, D.G., Caley, P., Norris, R.H. & Caitcheon, G. (2009). Modelling Of Floating Seed Dispersal in a Fluvial Environment. *River Research and Applications*, 25(5), 582-592.

Merritt, D.M. & Wohl, E.E. (2006). Plant Dispersal along Rivers Fragmented By Dams. *River Research and Applications*, 22(1), 1-26.

Nilsson, C., Brown, R.L., Jansson, R. & Merritt, D.M. (2010). The Role of Hydrochory In Structuring Riparian And Wetland Vegetation. *Biological Reviews*, 85(4), 837-858.

Palmer, M.R., Nepf, H.M. & Ackerman, J.D. (2003). Observations of Particle Capture on a Cylindrical Collector: Implications for Particle Accumulation and Removal in Aquatic Systems. *Limnology & Oceanography*, 49(1), 76-85.

Peruzzo, P., Defina, A. & Nepf, H. (2012). Capillary Trapping of Buoyant Particles within Regions of Emergent Vegetation. *Water Resources Research*, 48(7), 1-9

Shimeta, J.E.F.F. & Jumars, P.A. (1991). Physical Mechanisms and Rates of Particle Capture by Suspension-Feeders. *Oceanography Marine Biology Annual Rev*iew, 29(19), 191-257.

White, B.L. & Nepf, H.M. (2003). Scalar Transport in Random Cylinder Arrays at Moderate Reynolds Number. *Journal of Fluid Mechanics*, 487, 43-79.

 ©2017, IAHR. Used with permission / ISSN 1562-6865 (Online) - ISSN 1063-7710 (Print)

EXPERIMENTAL STUDY OF TURBULENCE ON KILLING LIMNOPERNA FORTUNEI LARVAE IN PIPELINES

CHENDI ZHANG [1], MENGZHEN XU [2] & ZHAOYIN WANG [3]

[1, 2, 3] State Key Laboratory of Hydroscience and Engineering, Tsinghua University, China
chendinorthwest@163.com, mzxu@tsinghua.edu.cn, zywang@tsinghua.edu.cn

ABSTRACT

Golden mussel (*Limnoperna fortunei*) is an invading macro-invertebrate species in water transfer pipelines, easily leading to heavy biofouling and pipe clogging. The species invades the pipelines during its planktonic larva stage, which is suitable to be killed by high frequency turbulence. To explore the hydraulic characteristics and killing mechanism of turbulence in pipelines, plates with hole diameters of 3 mm (PP3) and 6 mm (PP6), and wires with mesh spacing of 3 mm (WM3) and 2 mm (WM2) have been selected as turbulence-generating materials (TGMs) and are installed in a 12.6 m-long experimental pipe (average flow velocity≈1 m/s) with a space of 50 cm. The downstream flow field of the TGMs is measured by an Acoustic Doppler Velocimeter (ADV). The experimental results illustrates that the TGMs triggers a disturbance of flow velocity both transversely and longitudinally downstream. The distribution of the downstream turbulence intensity of the TGMs presents mostly a uniform transverse pattern. The TGMs increases the frequency of the dissipation range in the energy spectra for turbulence and results in the decrease of the length scale of the dissipative eddies, i.e. the Kolmogorov length scale. The larvae-killing tests indicates that the veliger community would be heavily damaged when the dissipation range was in a similar or smaller length scale than the veliger body length.

Keywords: Limnoperna fortunei larvae; turbulence-generating materials; high frequency turbulence; mortality.

1 INTRODUCTION

Golden mussel (Limnoperna fortunei, Dunker, 1856), is a freshwater invasive species of Mytilidae. The species, with extremely high environmental adaptability, is capable to survive in a very wide range of aquatic habitats with temperature range of 0 to 35°C, flow velocity range of 0.1 to 2 m/s, water depth range of 0.1 to 40 m and dissolved oxygen range of 0.2 to 11.3 mg/L (Darrigran et al., 2011, 2012). Golden mussels enter water transfer facilities during their planktonic veliger stages (Darrigran et al., 2007). The adults have golden yellow or dark brown shells and are able to aggregate in high density with their byssal threads attaching to the substrate (Xu, 2012; Montalto and Rojas Molina, 2014). The invasion and mass aggregation of golden mussels usually cause serious biofouling to water transfer projects and hydraulic structures (Ricciardi, 1998; Darrigran, 2002; Perez et al., 2003).

Intensive invasion by golden mussels has been found to take place mainly during the stage of planktonic veligers (Darrigran et al., 2007; Xu et al., 2015b). Therefore, attention has been drawn to the destruction of planktonic veligers. Rehmann et al. (2003), employed an aerating pump to generate high-frequency turbulence in the water, trying to prevent zebra mussel invasions. It was found that the mortality of zebra mussel veligers would increase if the Kolmogorov scale of turbulent eddies approached their body lengths. Since zebra mussels belong to the same family as golden mussels, the two species share many biological and ecological characteristics (Morton, 1979; Ricciardi, 1998; Karatayev et al., 2007). Xu et al. (2012) tested introducing airflows into the water using an aerating pump and found that the mortality of golden mussel veligers also increased significantly. Considering economic efficiency for engineering application, Xu (2012) designed a high-frequency turbulence generating system by installing pore plates at different cross sections in a pipeline, which was proven to be effective in enhancing the mortality of golden mussel veligers.

Xu (2012) tested the killing effect of the turbulence generated by pore plates with hole diameters of 10 mm and plate-to-plate spacing of 50 cm. However, other types of turbulence generating materials (TGMs) were not studied in Xu's trial and the hydraulic characteristics of the generated turbulence were not explored. The mechanism of veliger mortality resulting from turbulence in pipelines remained poorly understood. The purpose of the present study was to reveal the hydraulic characteristics of the turbulence field downstream of the TGM, and to understand the killing mechanism. Four types of TGMs were installed inside the experimental pipeline. The characteristics of the downstream flow fields of the TGMs were measured, and the turbulence intensity and spectrum were analyzed. The mortality tests for golden mussel veligers were conducted afterwards to examine the enhancement of the veliger death rate after the water flowed through the pipeline with TGMs.

©2017, IAHR. Used with permission / ISSN 1562-6865 (Online) - ISSN 1063-7710 (Print)

2 METHODS

2.1 Experimental system

The pipeline turbulence experiment was conducted on the bank of the downstream reservoir of the Langyashan pumped storage power station (PSP), which is located in the southern suburb of Chuzhou city, Anhui Province, in the lower Yangtze River basin.

The experimental system consists of a forebay, an experimental flume, and a tailrace conduit. Two submersible pumps (the lift and discharge were 7 m and 60 m^3/h for one of the pumps, and 15 m and 25 m^3/h for the other) were installed in the downstream reservoir and kept pumping water to the forebay. A gate was set up at the inlet weir of the flume (0.8 m wide and 0.68 m high) to control the inflow discharge (Section 1-1 in Fig. 1). An overflow weir at the outlet was to keep the maximum water depth at 0.385 m (Section 2-2 in Fig. 1).

A 12.6 m-long experimental pipeline of UPVC (Unplasticized Polyvinyl Chloride) material with an internal diameter of 0.154 m was placed at the bottom of the experimental flume, and was connected to a pulse pump (lift of 15 m and discharge of 25 m^3/h) at the inlet. The water from the forebay at a discharge of 0.018 m^3/s flowed through the pipeline only once in the killing tests. During the hydraulic measurements and killing tests, a 0.4 m-long extension pipe was connected to the outlet of the pipeline to keep the flow regime at the outlet as pipe flow instead of jet flow.

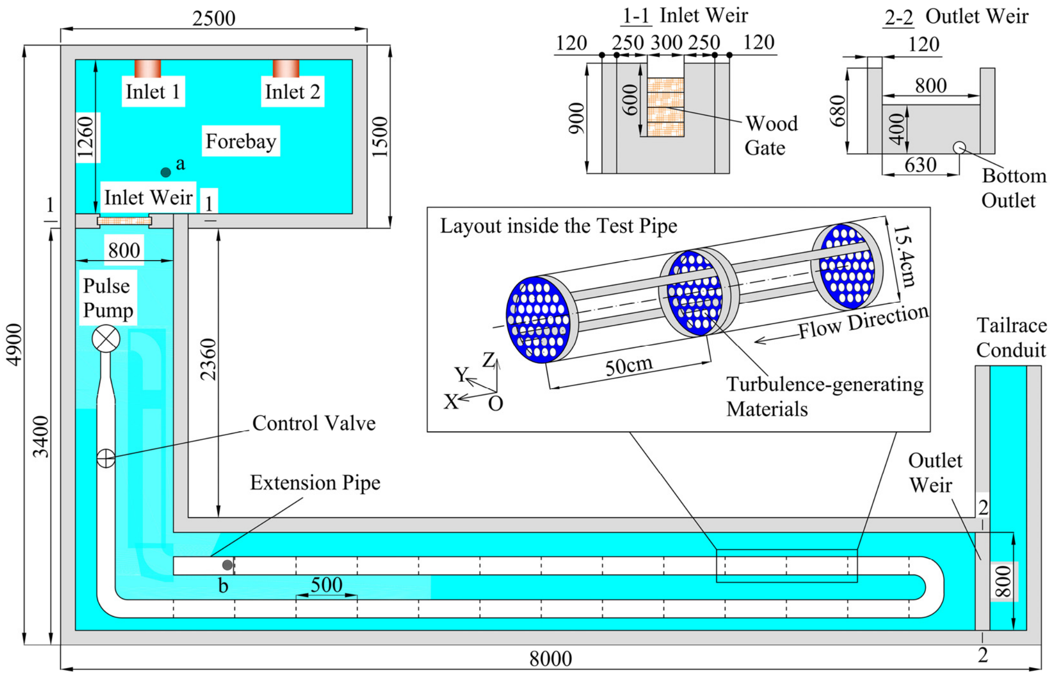

Figure 1. Plan view schematic of experimental system set-up and interior layout (units: mm). Points a and b refer to sampling locations for golden mussel veligers.

Based on the previous tests of Xu (2012), pore plates (PPs) are applicable for generating high-frequency turbulence if installed perpendicular to the flow direction in the pipeline because alternate jets and wakes are produced downstream (Yan et al., 2005). Two models of PPs and two models of wire mesh (WM) materials were tested in this study (Table 1).

Table 1. Turbulence-generating material (TGM) parameters.

Code	Type	Hole shape	Aperture /mm	Distance between neighboring holes /mm	Porosity/ %
PP3	Pore Plate	Round	3	1.96	0.36
PP6	Pore Plate	Round	6	2.34	0.52
WM2	Wire Mesh	Rectangular	2	0.42	0.68
WM3	Wire Mesh	Rectangular	3	0.91	0.64

Porosity=Pore area/total area

Flow velocity and turbulence characteristics were measured with a Vectrino Acoustic Doppler Velocimeter (ADV) manufactured by Nortek, Norway. The ADV was installed in a bracket fixed on a slider with a 1.1 m-long rail (Fig. 2a). Given that the probe was 5 cm away from the sampling location to minimize its disturbance to water (Garcia et al., 2005) and that the probe itself occupied a certain space, the measuring points were assigned on only one half side of the measuring section on two measuring lines, H and V (Figs.

 ©2017, IAHR. Used with permission / ISSN 1562-6865 (Online) - ISSN 1063-7710 (Print)

2b and 2c). The sampling time at each measuring point was 60 s at 200 Hz to guarantee the volume of each measurement is larger than the threshold of 5000 as suggested by Chanson et al. (2007) for the analysis of the first and second statistical moment.

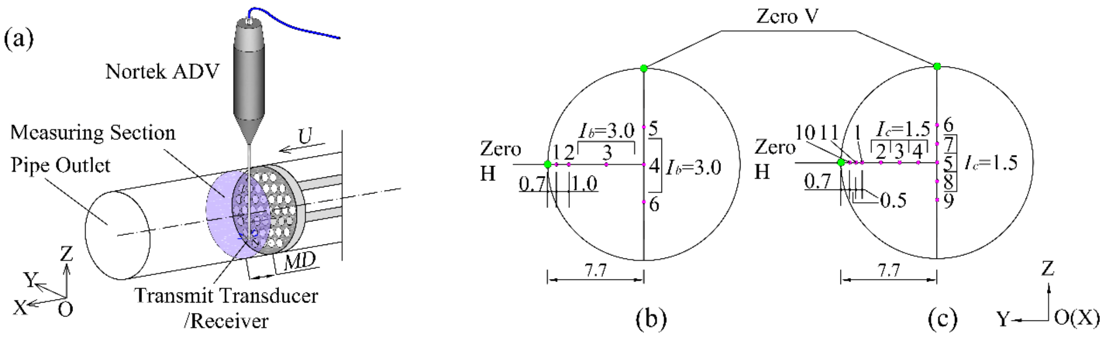

Figure 2. (a) Schematic diagram of the ADV installation. *MD*: measuring distance, which refers to the distance between the last TGM and the measuring section; (b) Layout of 6 measurement points. I_b refers to the interval from point 2 to point 6 and I_b = 3.0 cm. (c) Layout of 11 measuring points. I_c refers to the interval from point 2 to point 9 and I_c = 1.5 cm. Most of the tests were done with the layout in (c). Zero points of all the measuring lines are marked in green points in (b) and (c). Units are in cm.

2.2 Experimental procedure

Based on the experimental results of Xu (2012), 50 cm was selected as the TGM spacing. When measuring the downstream flow fields of the TGMs, the measuring sections of hydraulic characteristics were set at a Measuring Distance (MD) of 2.5, 5.0, 10.0, 17.0, 25.0 and 50.0 cm.

The killing tests were conducted after the golden mussel veliger density in the reservoir were stably over 500 /m^3. Water samples were taken both before at point “a” (Fig. 1) and after turbulence treatment at point “b” (Fig. 1) by the TGMs at almost the same time. For each water sample, 120 L of water was taken by a siphon and filtered through a plankton net with meshes of 50 μm (Xu et al., 2015b). After about an hour of settling, the concentrated samples were extracted and observed in a microscope-camera system (SmartV Camera & MIVNT Image Analysis Software, Yongheng Shanghai).

2.3 Data processing

Raw data from the ADV cannot be used directly for spectrum analysis because of its noise and spikes (Chanson et al., 2007). The velocity records with signal-to-noise ratio less than 15 dB were abandoned in the denoising process (Russello et al., 2006) and acceleration Thresholding Method was utilized in the despiking process (Goring and Nikora, 2002).

The energy spectrum was calculated using the Welch (1967) method based on Fourier Transformation (Pope, 2000):

$$E = \frac{1}{2\pi}\int_{-\infty}^{\infty} R_{uu}(t)e^{-i\omega t}dt \qquad [1]$$

where $\omega = 2\pi f$ is the angular frequency; f is the frequency; and $R_{uu}(t)$ is the temporal autocorrelation function of the fluctuating velocity.

3 RESULTS AND DISCUSSION

3.1 Flow velocity distribution

U, V, and W are time-average velocities corresponding to the directions X, Y, and Z respectively. The measurements along line V were considered when analyzing the velocity and turbulence intensity distribution. Since the magnitude of U was much larger than V and W, the following discussions are focused on the characteristics of U.

©2017, IAHR. Used with permission / ISSN 1562-6865 (Online) - ISSN 1063-7710 (Print)

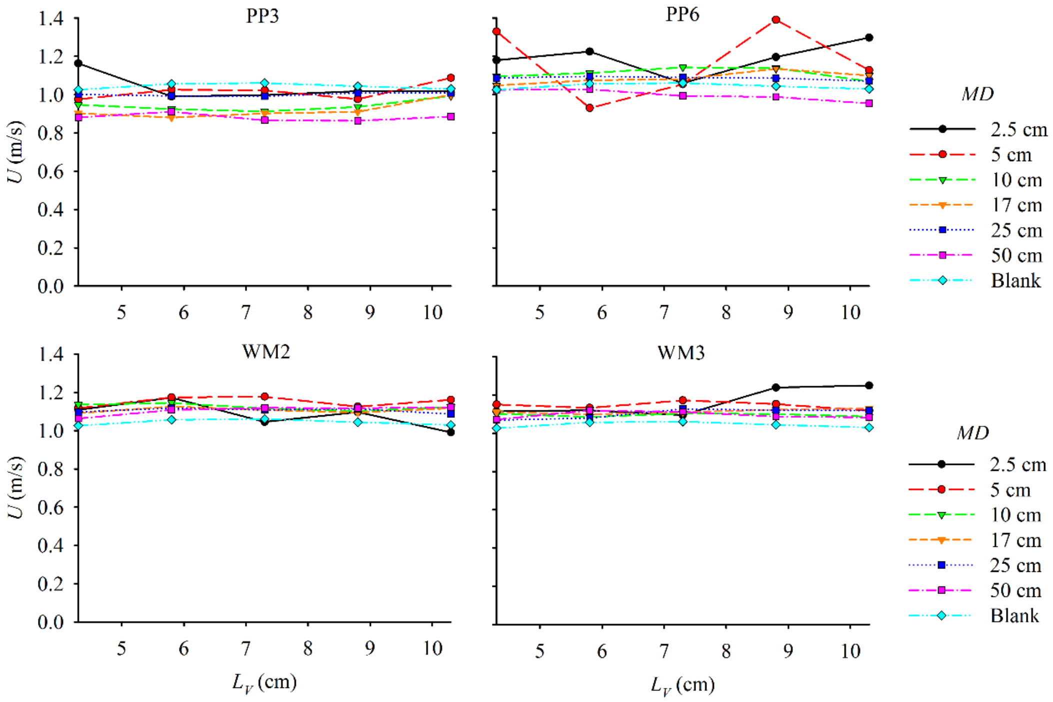

Figure 3. Distribution of U for TGMs. L_V refers to the distance from a measuring point to the zero point.

In general, the transverse distribution of U was symmetrical as expected except that a fluctuation of U existed transversely within the MD of 5 cm (Fig. 3), especially for PP6. Fig. 3 illustrates that the PP3 installation resulted in a decrease of flow velocity compared with the pipe without TGMs (Table 1), but this TGM had a uniform transverse distribution of flow velocity. In contrast, when PP6s were installed, the flow velocity fluctuated significantly within 5 cm downstream, which might be attributed to the intensive jets and wakes downstream because of its large aperture and distance between neighboring holes (Table 1). As for WM2 and WM3, both resulted in a relatively even distribution of flow velocity and similar velocity magnitude as that in the pipeline without TGMs, indicating that the WMs of different apertures hardly had any influence on the flow capacity of the pipe.

The arithmetic mean of velocity along line V (U_{mean}) at each measuring section was calculated as a reference for the longitudinal distribution of flow velocity downstream from the TGM. It was found that U_{mean} was larger in the downstream area close to the TGM (Fig. 4a). This is related to the reduction of the effective area for the water passage at the TGM, leading to an increase of upstream pressure energy and the resulting transformation of this energy into kinetic energy in the area downstream of the TGM. The U_{mean} for WMs kept decreasing after water flowed through a WM but reached an almost constant level beyond MD = 10 cm, which was different from PPs because of the WMs' lower resistance. In accordance with the findings shown in Fig. 3, the transverse fluctuation, which only lasted for less than 10 cm, was relatively large after the water just passed through the TGM (Fig. 4b).

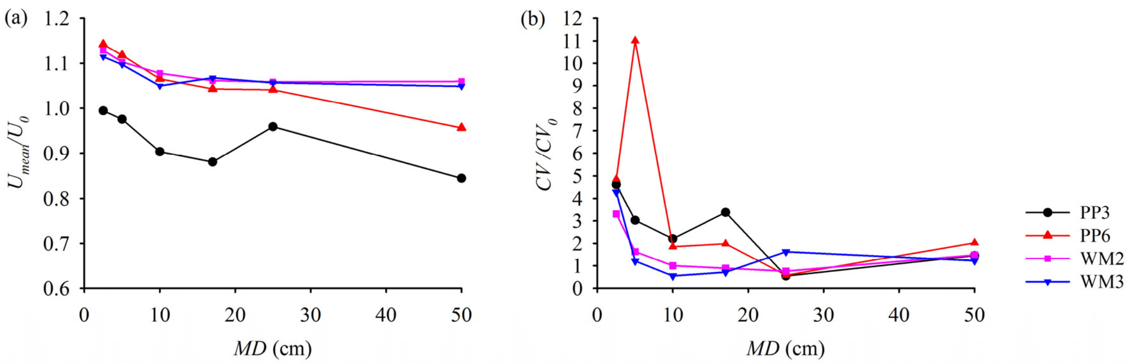

Figure 4. (a) Longitudinal distribution of U_{mean}/U_0; (b) Longitudinal distribution of CV/CV_0. U_{mean} and U_0 are the arithmetic mean of the velocities measured in line V with TGMs and without TGMs, respectively. CV and CV_0 refer to the coefficient of variation of the velocities in line V when TGMs are installed and when they are not installed, respectively.

 ©2017, IAHR. Used with permission / ISSN 1562-6865 (Online) - ISSN 1063-7710 (Print)

3.2 Distribution of turbulence intensity

Because the turbulence intensity in the Z direction was the largest in magnitude and most intensively influenced by the TGMs in all three directions and would experience the least noise (Hussein et al., 1994; Voulgaris and Trowbridge, 1998), the data for the Z direction were utilized in the turbulence analysis.

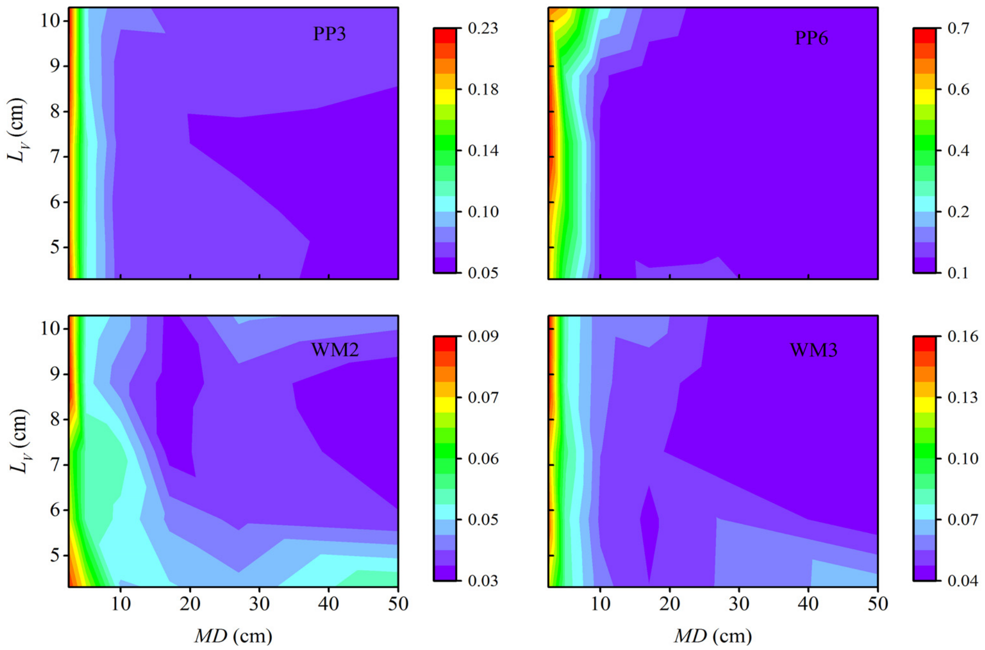

Figure 5. Distribution of σ_w where σ_w refer to the turbulence intensity in the Z direction with TGMs.

The downstream distribution of the turbulence intensity with the PP installation shows a banded feature with intensity decreasing along the pipeline in a transversely uniform way. For WMs, the turbulence intensity also decreased along the pipeline but did not show a distinct banded distribution because the turbulence intensity around the boundary layer exceeded that in the central area (Fig. 5), particularly for WM2. The turbulence intensity in the majority of the downstream area of WM2 was smaller than that of the pipe without TGMs except for the area close to the TGM (within 3 cm) (Fig. 6). Consequently, the turbulence induced by the pipe wall and TGM bracket was not negligible or even stronger than that in the main flow area and the transverse distribution was not uniform. The downstream turbulence intensity of the PPs exceeded that of the WMs to a large extent (Fig. 6), e.g., the maximum of the downstream turbulence intensity of PP6 was over 12 times stronger than that of WM2.

It appeared in the longitudinal profile of the turbulence intensity that the area affected by the TGMs was spatially limited. The largest value occurred within the 5 cm-long area downstream of the TGMs and the intensity decreased as the water flowed farther downstream, reaching a constant value close to that for the pipeline without TGMs after 10 cm away from the TGMs (Fig. 6).

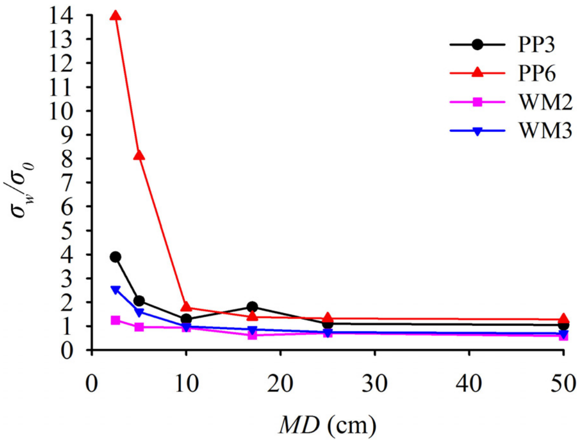

Figure 6. Longitudinal distribution of σ_w/σ_0 where σ_w and σ_0 refer to the turbulence intensity in the Z direction at the measuring section center with the TGMs and without the TGMs, respectively.

3.3 Energy spectrum

The energy spectrum of *W* at the center of each measuring section was calculated and compared with its counterpart in the pipeline without TGMs. For the PPs, the spectra had a relatively small slope (even close to 0 for PP6) when the water immediately past the PP (Fig. 7), and, thus, the starting point of the inertial subrange substantially increased, even approaching the extremity of the measurement range for PP6. The inertial subrange started from the lower frequency conditions when the water flowed farther than 5 cm away from the PPs. The frequency of the inertial subrange was higher with the WM installation than that for the pipe without TGMs but lower than that for the PPs (Fig. 7).

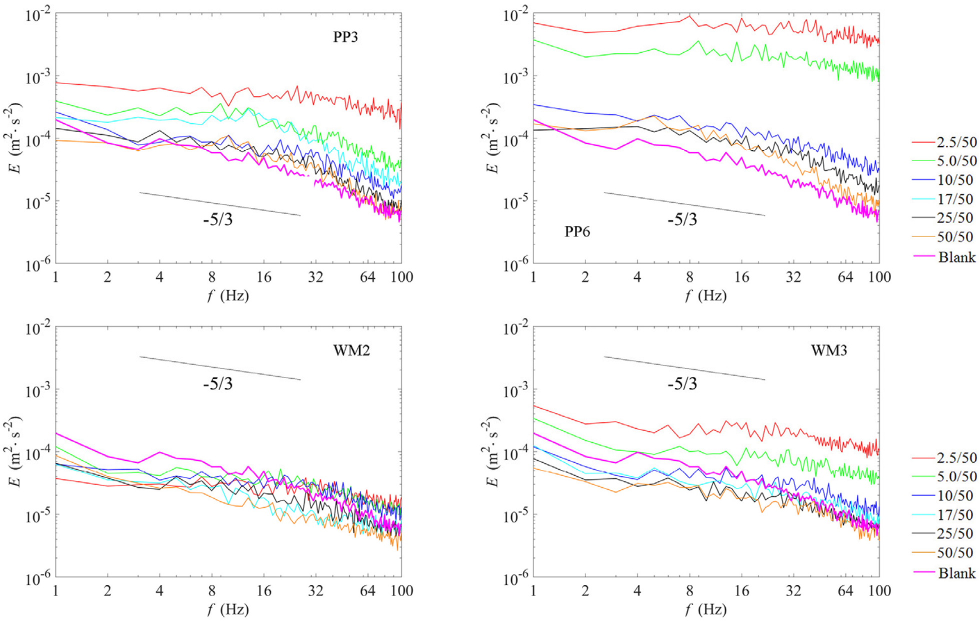

Figure 7. Energy spectra of the center in the measuring sections at different *MD*s.

The turbulent energy of the high-frequency range (>50 Hz) for the PPs was enhanced to a large extent in comparison to the pipeline without TGMs: the increase was over 10^3 times for PP6 and 10^2 times for PP3 (within the measurement range) than the corresponding values for the pipe without TGMs (Fig. 7). The turbulent energy for the WMs also increased when the water just passed the TGM, but to a much smaller degree compared with that for the PPs. The largest increase for WM3 was 10 times higher than that for the pipe without TGMs. In contrast, there was a decrease in the turbulent energy of the low-frequency range (<20 Hz) for WMs (Fig. 7).

3.4 Killing tests

Three death modes of veligers were found after treatment by the TGMs: (a) tissues of the veligers were broken and released out from the shells (Fig. 8a); (b) empty shells because all the tissues were released (Fig. 8b); and (c) the shells were damaged (Fig. 8c). The death modes were the same as those observed in the killing experiments with high-frequency turbulence generated by aerating pumps (Xu et al., 2015a). Therefore, it was reasonable to assume that the two experimental conditions might share the same mechanism for killing golden mussel veligers, i.e. the shear stress produced by eddies with similar scales as the veligers could kill the veligers.

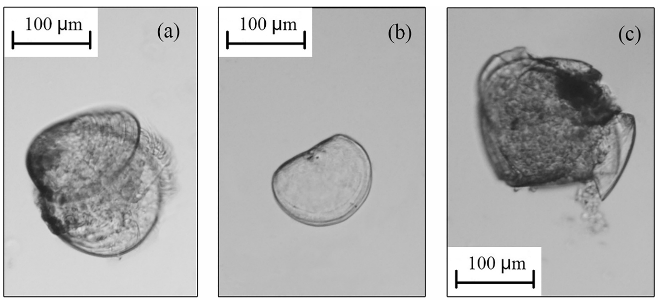

Figure 8. Status of veligers after treatment with high frequency turbulence.

 ©2017, IAHR. Used with permission / ISSN 1562-6865 (Online) - ISSN 1063-7710 (Print)

The death rate of golden mussel veligers at sampling point “a” in the forebay was used as the control and the increase of the death rate from “a” to “b” was defined as the killing rate of the veligers. As listed in Table 2, the killing rate of PP6 was the highest in both layouts. The killing rate of PP3 was smaller than PP6. The WMs had larger flow capacities but even lower killing rates than PP6, illustrating that the turbulence intensity was another key factor in the evaluation of the killing efficiency of the TGMs. In summary, TGMs with higher flow capacities and the ability to generate stronger turbulence should be chosen as the preferred materials.

Table 2. Death rates of golden mussel veligers in killing tests.

TGM	U_{mean1} /U_0	σ_{w1} /σ_0	Test	WT /℃	DR_0 /%	DR_1 /%	ΔDR /%
PP3	0.994	3.893	T1	23.8	19.39	46.31	26.92
			T2	23.8	66.67	91.56	24.89
PP6	1.142	13.94	T1	24.0	33.33	63.30	29.97
			T2	24.0	25.64	64.15	38.51
WM2	1.129	1.252	T1	24.0	30.00	46.15	16.15
			T2	24.0	46.91	52.31	5.40
WM3	1.115	2.554	T1	24.0	25.21	36.22	11.01
			T2	24.0	20.81	38.25	17.44

U_{mean1} and σ_{w1} refer to the arithmetic mean of the velocities measured in line V and the turbulence intensity of Z direction at the measuring section center at MD = 2.5 cm with the TGMs, respectively. WT is water temperature. Ti refers to the i-th test for the same TGM number. DR_0 is the death rate of golden mussel veligers at the sampling location “a”, while DR_1 is the death rate at the sampling location “b”. ΔDR equals to DR_1- DR_0, indicating the killing rate.

According to the Taylor’s hypothesis of frozen turbulence (Taylor, 1938), the length scale of the turbulence decreases as the frequency increases under a constant convection velocity. The energy spectra illustrated that both the PP and WM installations resulted in an increase of the starting frequency of the inertial subrange, which led to the extension of the spectrum to a higher frequency and the insufficiency of the measurement range to demonstrate the entire inertial subrange. Since the inertial subrange is expected to follow a f -5/3 slope according to the Kolmogorov law (Pope, 2000), the start at a higher frequency will result in the end at a higher frequency, which is also the starting point for the dissipation range. Therefore, the dissipation range will exhibit a higher frequency and a smaller length scale, even close to the Kolmogorov scale. Rehmann et al. (2003) made the hypothesis for the mortality of zebra mussel veligers that the shear forces generated by turbulence of the same length scale with Kolmogorov length could threaten the veligers, which was proven by the increase of veliger mortality when the Kolmogorov length became comparable or even shorter than the body lengths of the veligers. Because zebra mussels and golden mussels have many common or close biological characteristics (Morton, 1979; Ricciardi, 1998; Karatayev et al., 2007), it is reasonable to explain the mechanism of the killing of golden mussel veligers using turbulence by the length scale of turbulence.

4 CONCLUSIONS

A spatially short fluctuation in the longitudinal distribution of flow velocity emerged immediately after the water passed a TGM for all the four TGMs. The fluctuation lasted only a short distance longitudinally and then the water returned to a similar state as the pipe without TGMs. The transverse distribution of flow velocity for PPs also presented fluctuation in the close downstream area of the last TGM while exhibited uniform feature for the WMs, indicating the different flow capacities of PPs and WMs.

The highest turbulence intensity was distributed in a 3 cm-long longitudinal zone downstream of the TGMs and then decreased rapidly to a stable value. The distribution of turbulence intensity showed a distinct banded feature for most tested TGMs. Both the PPs and WMs were capable of improving the starting frequency of the inertial subrange in the energy spectrum, and, thus, reducing the length scale of the dissipation range.

Results of the killing tests demonstrated similar death modes of golden mussel veligers as for zebra mussels in previous experiments (Rehmann et al. (2003)) in which high-frequency turbulence was generated by aerating pumps. Therefore, similar killing mechanisms were assumed, i.e. when the dissipation ranges of turbulent eddies had length scales similar to the body lengths of the mussel veligers, shear stress generated by the eddies would damage the veligers.

ACKNOWLEDGEMENTS

This study was supported by the Natural Science Foundation of China (51409146), China Association for Science and Technology "Young talents lifting project", Tsinghua University Project (20151080440), and the State Key Laboratory of Hydroscience and Engineering project (2016-KY-04).

REFERENCES

Chanson, H., Trevethan, M. & Koch, C. (2007). Discussion of Turbulence Measurements with Acoustic Doppler Velocimeters. *Journal of Hydraulics Engineering,* 133(11), 1283-1286.

Darrigran, G., Damborenea, C. & Greco, N. (2007). Freshwater Invasive Bivalves in Man-Made Environments: A Case Study of Larvae Biology of *Limnoperna Fortunei* in a Hydroelectric Power Plant in South America. *AMBIO*, 36(7), 575-579.

Darrigran, G., Damborenea, C., Drago, E., Ezcurra de Drago, I. & Paira, A. (2011). Environmental Factors Restrict the Invasion Process of Limnoperna Fortunei (Mytilidae) in the Neotropical Region: A Case Study from the Andean Tributaries. *Annales de Limnologie-International Journal of Limnology,* 47(3), 221 - 229.

Darrigran, G., Damborenea, C., Drago, E., Ezcurra de Drago, I., Paira, A. & Archuby, F. (2012). Invasion Process of *Limnoperna Fortunei* (Bivalvia, Mytilidae): The Case of Uruguay River and Emissaries of the Iberá Wetland, *Argentina. Zoologia*, 29(6), 531-539.

Dunker, W. (1856). Mytilacea nova collectionis Cumingiana. *Proceeding of Zoological Society of London,* 24, 358-366.

Garcia, C.M., Mariano, I.C., Nino, Y. & Garcia, M.H. (2005). Turbulence Measurements with Acoustic Doppler Velocimeters. *Journal of Hyd*raulics Engineering, 131(12), 1062 – 1073.

Goring, D.G. & Nikora, V.I. (2002). Despiking Acoustic Doppler Velocimeter Data. *Journal of Hydraulics Engineering*, 128(1), 117–126.

Hussein, H.J., Capp, S.P. & George, W.K. (1994). Velocity Measurements in a High-Reynolds-Number, Momentum-Conserving, Axisymmetrical, Turbulent Jet. *Journal of Fluid Mechanics,* 258, 31 – 75.

Karatayev, A., Boltovskoy, D., Padilla, D. & Burlakova, L. (2007). The Invasive Bivalves Dreissena Polymorpha and *Limnoperna Fortunei*: Parallels, Contrasts, Potential Spread and Invasion Impacts. *Journal of Shellfish Research*, 26(1), 205-213.

Montalto, L., & Rojas M.F. (2014). Byssal Hairs in the Invasive Asian Freshwater Bivalve *Limnoperna Fortunei* (Mytilidae) in the Paraná River System with Comments on this Species in South America. *Molluscan Research,* 34, 127–138.

Morton, B. (1979). Freshwater Fouling Bivalves. *Proceedings of the First International Corbicula Symposium.* Texas Christian University, Fort Worth, Texas.

Perez, M., Garcia, M., Traversa, L. & Stupak, M. (2003). Concrete Deterioration by Golden Mussels. *Conference on Microbial Impact on Building Materials,* 8-9 September 2003, Lisbon, Portugal.

Pope, S.B. (2000). *Turbulent Flows.* Cambridge University Press.

Rehmann, C.R., Stoeckel, J.A. & Schneider, D.W. (2003). Effect of Turbulence on the Mortality of Zebra Mussel Veligers. *Canadian Journal of Zoology*, 81, 1063-1069.

Ricciardi, A. (1998). Global Range Expansion of the Asian Mussel *Limnoperna Fortunei* (Mytilidae): Another Fouling Threat to Freshwater Systems. *Biofouling*, 13(2), 97-106.

Russello, P.J., Lohrmann, A., Siegel, E. & Maddux, T. (2006). Improvements in Acoustic Doppler Velocimetery. *The Seventh International Conference on Hydroscience and Engineering,* September 10-13, 2006, Philadelphia, Pennsylvania.

Taylor, G.I. (1938). The Spectrum of Turbulence. *Proceedings of the Royal Society,* A164, 476-490.

Voulgaris, G. & Trowbridge, J.H. (1998). Evaluation of the Acoustic Doppler Velocimeter (ADV) for Turbulence Measurements. *Journal of Atmospheric and Oceanic Technology,* 15(1), 272 – 289.

Welch, P.D. (1967). The Use of Fast Fourier Transform for the Estimation of Power Spectra: A Method based on Time Averaging over Short, Modified Periodograms. *IEEE Transactions on Audio Electroacoustics,* AU-15, 70–73.

Xu, M.Z. (2012). Experimental Study of Macroinvertebrate *Limnoperna fortunei* Invasion and Prevention in Water Transfer Tunnels, *PhD Thesis.* Tsinghua University, Beijing. (In Chinese with English abstract)

Xu, M.Z., Cao, X.W., Wang, Z.Y. & Wang, X.Z. (2012). Attachment Characteristics of Golden Mussels (*Limnoperna Fortunei*) in Water Transport Projects. *Journal of Tsinghua University (Science & Technology)*, 52(2), 170-176.

Xu, M.Z., Darrigran, G., Wang, Z.Y., Zhao, N., Lin, C.C. & Pan, B.Z. (2015a). Experimental Study on Control of *Limnoperna Fortunei* Biofouling in Water Transfer Tunnels. *Journal of Hydro-Environmental Research*, 9(2), 248-258.

Xu, M.Z., Wang, Z.Y., Zhao, N. & Pan, B.Z. (2015b). Growth, Reproduction and Attachment of the Golden Mussel (*Limnoperna Fortunei*) in Water Diversion Projects. *Acta Ecologica Sinica*, 35, 70-75.

Yan, J., Tang, H.W., Cheng, N.S., Zhou, Y.L., (2005). Review on study of vibrating grid turbulence and its application. *Shuili Xuebao*, 36(12): 1503-1509 (in Chinese with English abstract).

 ©2017, IAHR. Used with permission / ISSN 1562-6865 (Online) - ISSN 1063-7710 (Print)

COMPARATIVE STUDY ON WATER WAVES GENERATED BY SUBMERGED LANDSLIDE

HAI-XIAO JING[1], WEN WANG[2], ZHEN-DONG YANG[3] & GUO-DONG LI[4]

[1,2,3,4] State Key Laboratory Base of Eco-hydraulic Engineering in Arid Area, Xi'an University of Technology, Xi'an, China,
jinghx@xaut.edu.cn

ABSTRACT

Prediction of water waves generated by submerged landslide is of great importance in hydraulic engineering. This paper presents a comparative investigation of this problem. Two numerical models, one based on nonlinear shallow water equations and another based on extended Boussinesq equations, are firstly introduced. Then the two models are used to investigate the generation and propagation of water waves by submerged landslide. Two cases are investigated in this paper, one is water waves generated by instantaneous movement of seabed, the other is water waves generated by moving landslide over a flat bottom. The accuracy of the two models are validated by comparing against the experimental data available. The effects of dispersion on the generated water waves at both near field and far field are investigated by comparing the numerical results by these two models. Besides, the effects of slide length, height and velocity on the generated waves are also investigated for the second case.

Keywords: Landslide generated water waves; boussinesq equations; shallow water equations; dispersion.

1 INTRODUCTION

Water waves generated by submerged landslide can cause huge disaster and have been studied extensively in the past decades. Due to the complexity of this phenomenon, many empirical formulas have been proposed by mainly experimental investigations and theoretical analysis to predict effectively the wave height and speed (Di Risio et al., 2011). However, in practical engineering, the results by different empirical formulas differ greatly (Liu et al., 2015). The range of application for each empirical formula is limited. For this purpose, numerical models is a better choice for this problem. In recent years, there are several numerical models which have been developed to investigate this phenomenon, such as numerical models based on shallow water equations, Boussinesq equations, Reynolds averaged Navier-Stokes equations (RANS) and smoothed particle hydrodynamics (SPH) model (Heidarzadeh et al., 2014). Numerical model based on shallow water equations has been a popular choice for this problem due to its less computational efforts. However, recent studies have shown that dispersion may play important role when the slide is in accelerated or decelerated motion (LØvholt et al., 2015; Glimsdal et al., 2013). Hence, it is necessary to clarify the effects of dispersion on landslide generated water waves and to make it clear the validity of both dispersive and non-dispersive water wave models for this problem.

In this paper, Boussinesq equations including dispersion and shallow water equations for landslide generated waves are introduced firstly. The Boussinesq equations by Beji and Nadaoka (1996) are the extended by including the terms representing bottom movement. Then, the one dimensional (1D) form of the equations are solved numerically by fourth order predictor-corrector finite difference method. Finally, the numerical model developed is used to study the characteristics of water waves generated by submerged landslide. Several cases with different slide thicknesses, lengths and velocities are carried out. The numerical results are compared against the ones by shallow water equations. Dispersion effects for each cases are then discussed. Finally, some conclusions are drawn.

2 NUMERICAL MODEL

2.1 Governing equations

The extended Boussinesq equations with dimensionless variables are given by

$$\frac{\partial \eta}{\partial t} + \nabla \cdot \left[\left(h_0 + \delta h_0 + \varepsilon \eta \right) \bar{\boldsymbol{u}} \right] + \frac{\delta}{\varepsilon} \frac{\partial h_1}{\partial t} = 0 \quad [1]$$

$$\frac{\partial \bar{\boldsymbol{u}}}{\partial t} + \varepsilon \bar{\boldsymbol{u}} \nabla \cdot \bar{\boldsymbol{u}} + \nabla \eta + \mu^2 \Gamma_{20} = 0 \quad [2]$$

©2017, IAHR. Used with permission / ISSN 1562-6865 (Online) - ISSN 1063-7710 (Print)

Where, $\eta(x,y,t)$ is free surface elevation, $h_0(x,y)$ is the still water depth without slide and is independent of time, $h_1(x,y,t)$ is the height of slide, is function of both space and time, this means that the slide can be deformable. $\bar{\boldsymbol{u}}(x,y,t)$ is depth averaged velocities in x, y directions. $\nabla = (\partial/\partial x, \partial/\partial y)$ is horizontal gradient operator. μ , ε and δ are dimensionless parameters representing dispersion, nonlinearity and relative slide height, respectively.

$$\begin{aligned}\Gamma_{20} &= (1+\beta)\frac{h_0^2}{6}\frac{\partial}{\partial t}\nabla\nabla\cdot\bar{\boldsymbol{u}} - \frac{h_0}{2}\frac{\partial^2}{\partial t^2}\nabla h_1 - (1+\beta)\frac{h_0}{2}\frac{\partial}{\partial t}\nabla\nabla\cdot(h_0\bar{\boldsymbol{u}}) \\ &\quad + \beta\frac{h_0^2}{6}\nabla(\nabla^2\eta) - \beta\frac{h_0}{2}\nabla\nabla\cdot(h_0\nabla\eta)\end{aligned} \qquad [3]$$

β is a free parameter which can be used to optimize the linear dispersion of the equations. $\beta = 0.593$ will be used in the following numerical cases. This equations can be reduced to the Boussinesq equations by Beji and Nadaoka(1996) if we set $h_1 = 0$, this means no slide.

The shallow water equations can be obtained by neglecting the dispersive terms (i.e. term Γ_{20}) in Eq. [1] and [2]. It is noted that only the mass equation [1] is modified due to the inclusion of slide in shallow water equations, the momentum equation keeps unchanged.

2.2 Numerical method

In this section, fourth order finite difference method is used to solve the one dimensional (1-D) form of the extended Boussinesq equations. This method has been widely used to solve Boussinesq-type equations and the accuracy and stability of this method have been validated (Wei and Kirby, 1995). For the shallow water equations, we just neglect the dispersive terms in the extended Boussinesq equations and the numerical method keeps unchanged and will not repeat.

To facilitate the implementation of the numerical method, the 1-D extended Boussinesq equations with dimensional variables are rewritten as follows.

$$\frac{\partial\eta}{\partial t} = E(\eta,u) - \frac{\partial h_1}{\partial t} \qquad [4]$$

$$\frac{\partial U}{\partial t} = F(\eta,u) + \frac{h_0}{2}\frac{\partial^3 h_1}{\partial x\partial t^2} \qquad [5]$$

Where,

$$U = u + (1+\beta)\frac{h_0^2}{6}\frac{\partial^2 u}{\partial x^2} - (1+\beta)\frac{h_0}{2}\frac{\partial^2(h_0 u)}{\partial x^2} \qquad [6]$$

$$E(\eta,u) = -\frac{\partial}{\partial x}\left[(h_0 + h_1 + \eta)u\right] \qquad [7]$$

$$F(\eta,u) = -u\frac{\partial u}{\partial x} - g\frac{\partial\eta}{\partial x} - \beta\frac{gh_0^2}{6}\frac{\partial^3\eta}{\partial x^3} + \beta\frac{gh_0}{2}\frac{\partial^2}{\partial x^2}\left(h_0\frac{\partial u}{\partial x}\right) \qquad [8]$$

Where, all the variables are dimensional but also use the same notations for simplicity.

Due to the exist of dispersive terms, the lower order derivative terms (e. g. the first order derivative with respect to time or space) have to be discretized using higher order schemes to avoid the truncation error to be the same order as the dispersive terms. Hence, Fourth order predictor-corrector scheme is used for time marching.

For the predictor step, third order explicit Adams-Bashforth scheme, given by

 ©2017, IAHR. Used with permission / ISSN 1562-6865 (Online) - ISSN 1063-7710 (Print)

$$\eta_i^{*n+1} = \eta_i^n + \frac{\Delta t}{12}\left[23E_i^n - 16E_i^{n-1} + 5E_i^{n-2}\right] - \left(h_{1i}^{n+1} - h_{1i}^n\right) \quad [9]$$

$$U_i^{*n+1} = U_i^n + \frac{\Delta t}{12}\left[23F_i^n - 16F_i^{n-1} + 5F_i^{n-2}\right] + \frac{h_{0i}}{2\Delta t}\left[\left(\frac{\partial h_1}{\partial x}\right)_i^{n+1} - 2\left(\frac{\partial h_1}{\partial x}\right)_i^n + \left(\frac{\partial h_1}{\partial x}\right)_i^{n-1}\right] \quad [10]$$

Where, i and n denote spatial and temporal node indices. With the predicted values of U_i^{*n+1}, the predicted values of velocity u_i^{*n+1} can be obtained by solving Eq. [6], where a tridiagonal system needs to be solved.

For the corrector step, we use the fourth order Adams-Moulton method, given by

$$\eta_i^{n+1} = \eta_i^n + \frac{\Delta t}{24}\left[9E_i^{*n+1} + 19E_i^n - 5E_i^{n-1} + E_i^{n-2}\right] - \left(h_{1i}^{n+1} - h_{1i}^n\right) \quad [11]$$

$$U_i^{n+1} = U_i^n + \frac{\Delta t}{24}\left[9F_i^{*n+1} + 19F_i^n - 5F_i^{n-1} + F_i^{n-2}\right] + \frac{h_{0i}}{2\Delta t}\left[\left(\frac{\partial h_1}{\partial x}\right)_i^{n+1} - 2\left(\frac{\partial h_1}{\partial x}\right)_i^n + \left(\frac{\partial h_1}{\partial x}\right)_i^{n-1}\right] \quad [12]$$

Where, E_i^{*n+1} and F_i^{*n+1} will be evaluated by using the predicted values of η_i^{*n+1} and u_i^{*n+1}. The corrected values of velocity u_i^{n+1} can be obtained by solving Eq. [6].

For the spatial derivative terms, fourth order accurate four-point central difference scheme is used to discretize the first order spatial derivative terms, three-point central difference scheme is employed for the second order spatial derivative terms, and four-point central difference scheme for the third order spatial derivatives. Reflecting and absorbing boundary conditions following exactly the ones in Lin and Man (2007) are used.

3 CASES AND ANALYSIS

3.1 Water waves generated by instantaneous movement of seabed

To validate the two numerical models, the experiment by Hammack (1973) is employed in this section. In the experiment, the generation and propagation of water waves by sudden movement of seabed are studied. In a flat flume with water depth $h = 0.05\text{m}$, the bottom with length $b = 12.2h = 0.61\text{m}$ is pushed upward for one case and downward for another instantaneously. A fully reflecting wall is set at the left boundary. The amplitude of the bottom movement is $A = 0.1h = 0.005\text{m}$. The duration time of bottom movement is $T_s = 0.13\text{s}$. Grid size $\Delta x = 0.005\text{m}$ and time step $\Delta t = 0.002\text{s}$ are used for the computation. The free surface elevations at various locations are measured. The results are given in figures 1 and 2 for the upward and downward movement, respectively.

For the upward movement of seabed, it can be found from figure 1 that both numerical results agree well with the experimental data at the section near the source (that is $\left(x-b\right)/h = 0$). Shallow water equations fail to reproduce the small oscillations after the main wave. While the extended Boussinesq equations can predict the small oscillations but with larger amplitude of oscillations. For the main wave, the amplitudes of both numerical results are slightly greater than the experimental one. At the stations far away from the source(that are $\left(x-b\right)/h = 20$ and $\left(x-b\right)/h = 180$), the oscillations increase due to the effects of dispersion, and it can be found that the numerical results by extended Boussinesq equations agree better with the experimental data than the ones by shallow water equations. Numerical model based on shallow water equations fails to predict the evolution of this transient wave. However, it can be seen that the model based on extended Boussinesq equations predicts greater amplitudes of the oscillations. This is probably due to the weak dispersion property of the Boussinesq equations. Higher order Boussinesq-type equations can be expected to give better results.

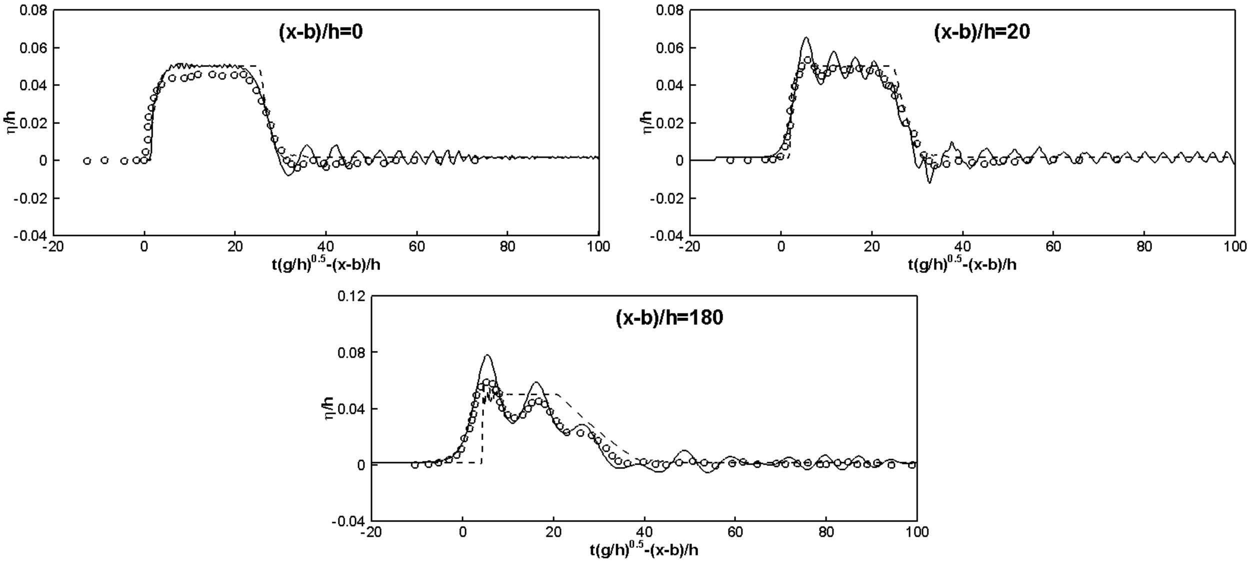

Figure 1. Comparisons of free surface elevations at different locations for upward movement of seabed (solid line: results by extended Boussinesq equations; dashed line: results by shallow water equations; circles: experimental results by Hammack).

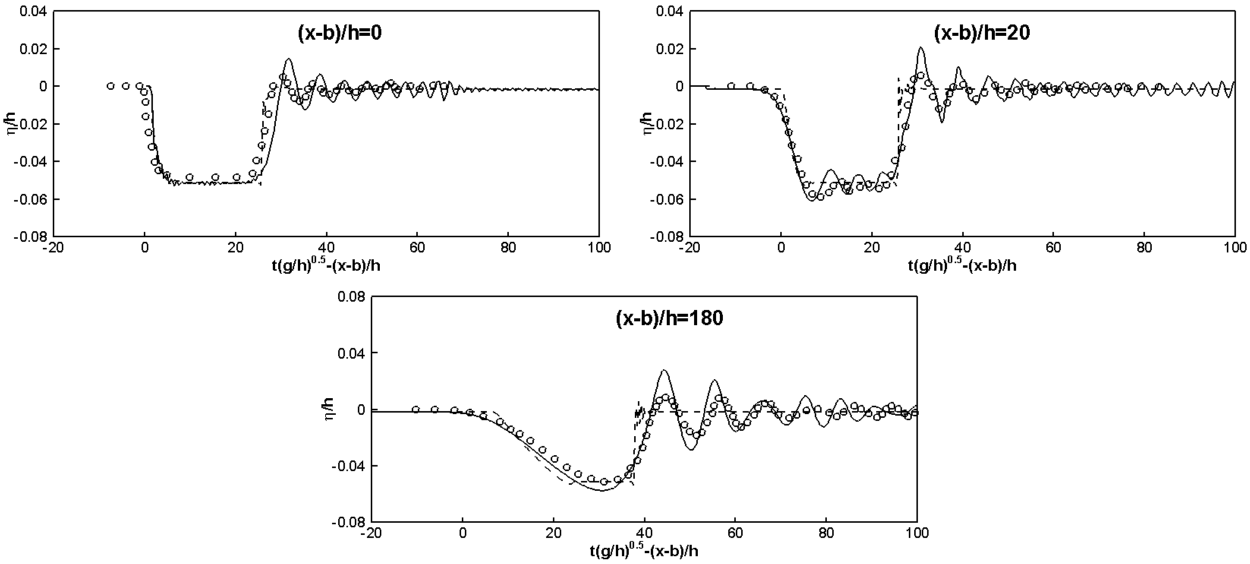

Figure 2. Comparisons of free surface elevations at different locations for downward movement of seabed (solid line: results by extended Boussinesq equations; dashed line: results by shallow water equations; circles: experimental results by Hammack).

For the downward movement of seabed (figure 2), similar results can be obtained. At the near field, dispersive effect is limited and both numerical results agree well with the experimental data. However, with the propagation of the waves, dispersion becomes more and more important. Hence, numerical results by extended Boussinesq equations predict better results.

From previous studies, the length of the generated waves is comparative to the length of moving seabed. For this case, we get $\mu = h/L = 0.05\text{m}/0.61\text{m} = 0.082$, which is small and means that the shallow water assumption is met. This is may be the reason why both numerical models predict well the main waves for the two cases.

3.2 Water waves generated by a moving submerged landslide over a flat seabed

A submerged landslide moves with constant speed at a flat seabed. The shape of slide is given in Eq. [13]. A is the maximum height of slide. Computation domain is $L = 20000\text{m}$, water depth $h = 100\text{m}$. At the beginning, the center of the slide is located at $x = 10000\text{m}$. The slide is assumed to start and stop suddenly. For all the cases below, the distance of slide motion is the same, that is $L_m = 1600\text{m}$. The computational domain is

 ©2017, IAHR. Used with permission / ISSN 1562-6865 (Online) - ISSN 1063-7710 (Print)

divided into equal grids with size $\Delta x = 4.0m$. The time step $\Delta t = 0.1s$. The total computational time is $T = 300s$.

$$h_1(\mathrm{x,t}) = \frac{A}{2}\left[1-\cos\left(\frac{2\pi}{L_s}\left(x-x_s-u_s t\right)\right)\right] \quad [13]$$

Seven cases are studied for this problem, the setup of the cases are given in table 1. Three dimensionless parameters are introduced for the analysis. These are slide Froude number $F_r = v_s/\sqrt{gh}$, $\mu = h/L_s$ representing the dispersion property and $\delta = A/h$ denoting the nonlinearity of the water waves.

Table 1. Cases setup.

case	L_s (m)	A (m)	v_s (m/s)	F_r	μ	δ
1	1000	1	20	0.64	0.1	0.01
2	1000	1	31.3	1	0.1	0.01
3	1000	1	40	1.28	0.1	0.01
4	666.7	1	20	0.64	0.15	0.01
5	500	1	20	0.64	0.2	0.01
6	1000	2	20	0.64	0.1	0.02
7	1000	5	20	0.64	0.1	0.05

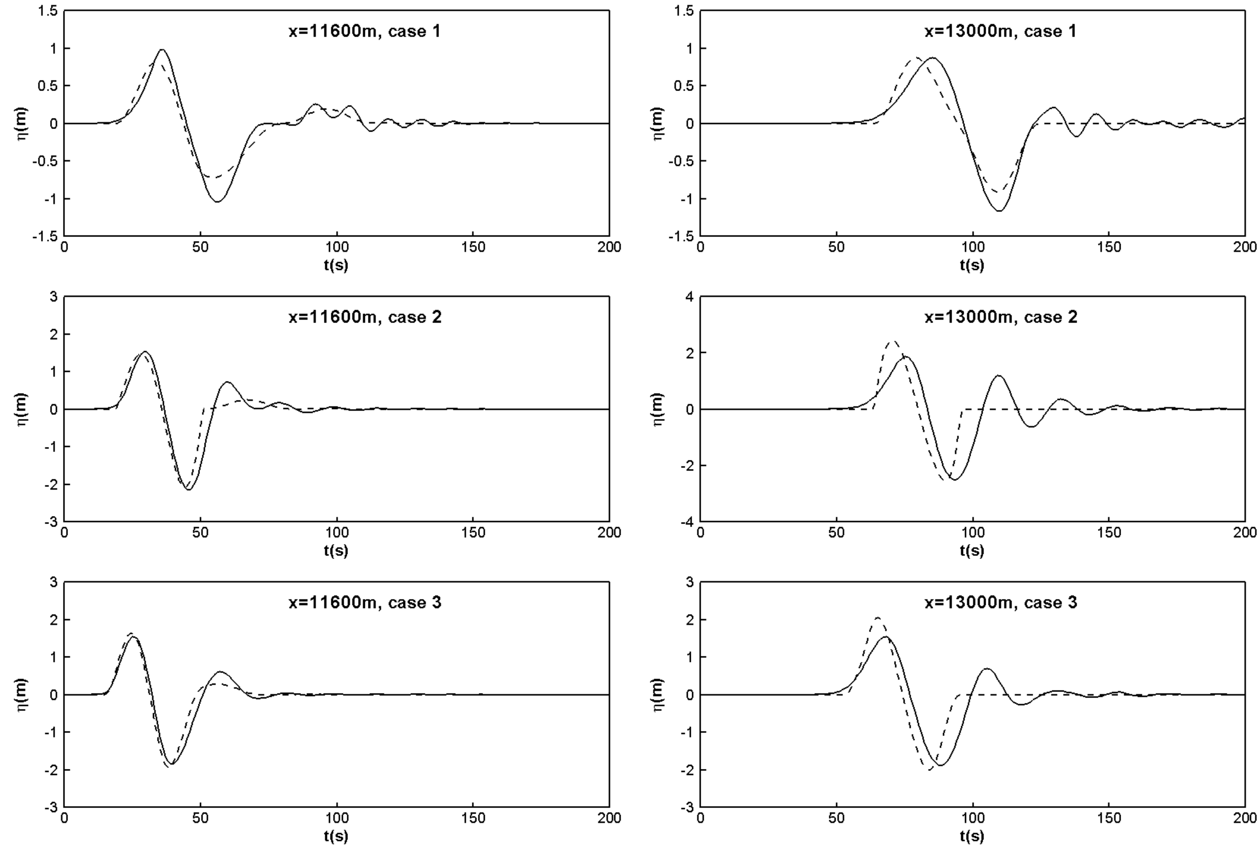

Figure 3. Comparisons of time history of free surface elevations by two numerical models for various slide velocities (solid line: results by extended Boussinesq equations; dashed line: results by shallow water equations).

Figure 3 shows the comparisons of free surface elevations at two locations for different slide velocities (or F_r). Where, $x = 11600\mathrm{m}$ is the location of center of slide when it stops moving, and $x = 13000\mathrm{m}$ is the location far away from the slide (the distance is $14h$). It can be found from the figure that at the location near the slide ($x = 11600\mathrm{m}$) the results by two models agree well for different slide velocities except for case 1 where extended Boussinesq equations predict higher wave amplitude. At the location far away from the slide (that is $x = 13000\mathrm{m}$), the results by two models differ obviously. Shape of the leading wave changes and more oscillating tails appear for the results by extended Boussinesq equations. With the increase of slide velocity, the difference between two numerical models becomes smaller. This means that the dispersive effects become weaker.

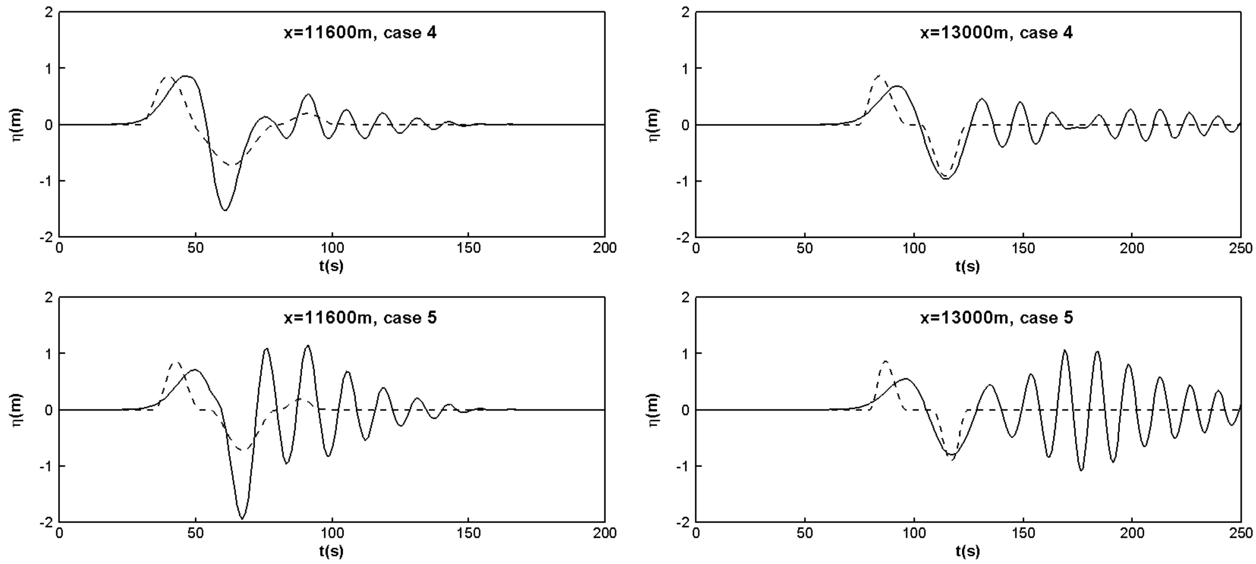

Figure 4. Comparisons of time history of free surface elevations by two numerical models for various slide lengths (solid line: results by extended Boussinesq equations; dashed line: results by shallow water equations).

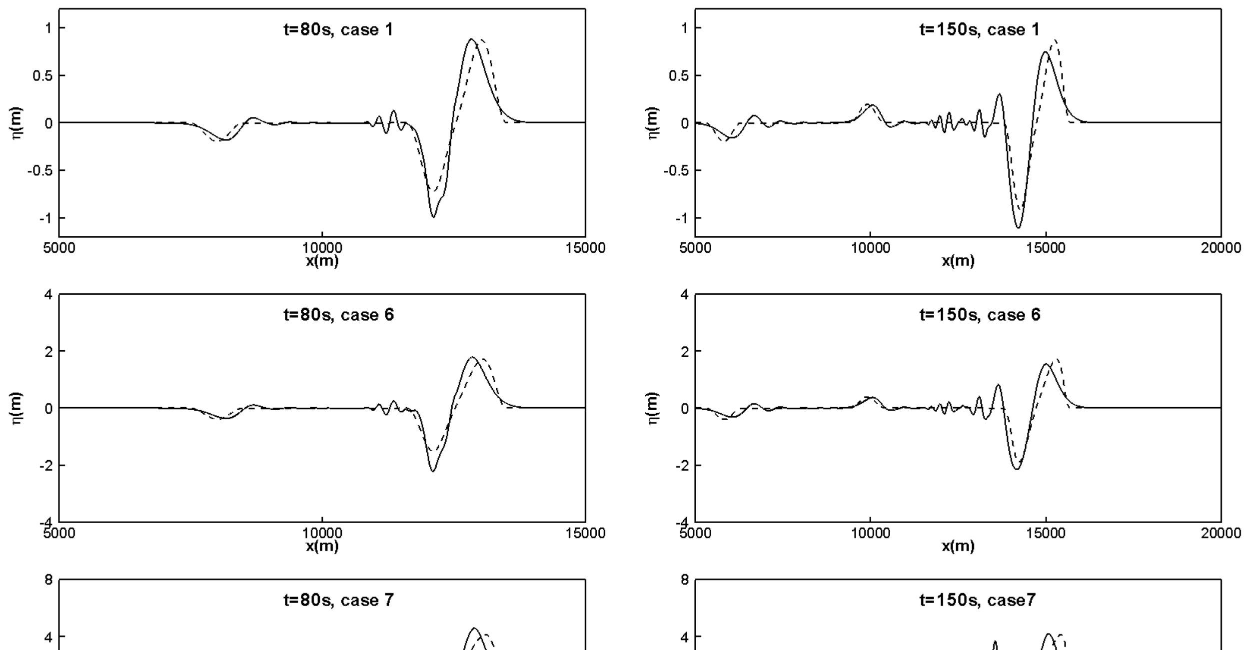

Figure 5. Comparisons of snapshots of free surface elevations by two numerical models for various slide heights (solid line: results by extended Boussinesq equations; dashed line: results by shallow water equations).

Figure 4 shows the comparisons of free surface elevations by two numerical models for various slide lengths. It can be seen that with the decrease of slide length (or increase of μ), the numerical results by two

 ©2017, IAHR. Used with permission / ISSN 1562-6865 (Online) - ISSN 1063-7710 (Print)

models deviate greatly even at the station near the slide ($x = 11600\mathrm{m}$). Dispersion plays more important role with the slide length decreases.

The comparisons of snapshots of free surface elevations for various slide heights are given in figure 5. Where, at $t = 80\mathrm{s}$ the slide just stops moving. It can be obtained that with the increase of slide height (or *δ*) the amplitude of the leading wave increases. For the leading wave, two numerical models predict almost the same amplitude and phase. Dispersion becomes important with time increasing, as is found for other cases.

4 CONCLUSIONS

This paper presents a comparative investigation of the generation and propagation of water waves by landslide. Numerical models based on shallow water equations and extended Boussinesq equations are used. Two cases are studied, one is water waves generated by instantaneous movement of seabed and the other is water waves generated by moving slide over a flat bed. We conclude that at near field both numerical models can be used for the water waves generated by instantaneous movement of seabed. While at far fields dispersion becomes important and numerical model based on extended Boussinesq equations is a better choice. For the water waves generated by moving submerged slide, dispersion becomes more important. And it is obtained that the effect of dispersion become becomes more important with the decrease of slide Froude number F_r and increase of μ, which representing the relative length of slide. Hence, it must be very careful for the choice of numerical models for the second case.

ACKNOWLEDGMENTS

The research reported herein is funded by Natural Science Foundation of Education Department of Shaanxi Province, China (No. 16KJ1543).

REFERENCES

Beji, S. & Nadaoka, K. (1996). A Formal Derivation and Numerical Modelling of the Improved Boussinesq Equations for Varying Depth. *Ocean Engineering*, 23, 691-704.

Di Risio, M., De Girolamo, P. & Beltrami, G.M. (2011). Forecasting Landslide Generated Tsunamis. *Environmental Sciences "The Tsunami Threat-Research and Technology"*, InTech, 6, 978-953.

Glimsdal, S., Pedersen, G.K., Harbitz, C.B. & LØvholt, F. (2013). Dispersion of Tsunamis: Does it Really Matter?. *Natural Hazards and Earth System Sciences*, 13, 1507-1526.

Hammack, J.L. (1973). A Note on Tsunamis: Their Generation and Propagation in an Ocean of Uniform Depth. *Journal of Fluid Mechanics*, 60, 769-799.

Herdarzadeh, M., Kastel, S. & Yalciner, A.C. (2014). The State-of-the-Art Numerical Tools for Modeling Landslide Tsunamis: A Short Review. *Submarine Mass Movements and Their Consequences*. 37, 483-495.

LØvholt, F., Pedersen, G., Harbitz, C.B., Glimsdal, S. & KIM, J. (2015). On the Characteristics of Landslide Tsunamis. *Philosophical Transactions of the Royal Society of London A: Mathematical, Physical and Engineering Sciences*, 373.

Lin, P. & Man, C. (2007). A Staggered-Grid Numerical Algorithm for the Extended Boussinesq Equations. *Applied Mathematical Modelling*, 31, 349-368.

Liu, Y., Wu J. & Li H. (2015). Surge Prediction Study of Reservoir Bank Landslide near a Hydropower Dam. *Advances in Geosciences*, 5, 114-129. (In Chinese)

Wei, G. & Kirby, J. (1995). Time Dependent Numerical Code for Extended Boussinesq Equations. *Journal of Waterway, Port, Coastal, and Ocean Engineering*, 121, 251-261.

Proceedings of the 37th IAHR World Congress
August 13 – 18, 2017, Kuala Lumpur, Malaysia

ELECTRIFIED FLEXIBLE FISH FENCES

MARKUS AUFLEGER(1), HEIDI BÖTTCHER(2), BARBARA BRINKMEIER(3), GÜNTER UNFER(4) & BERNHARD ZEIRINGER(5)

(1,2,3)Unit of Hydraulic Engineering, University of Innsbruck, Innsbruck, Austria
markus.aufleger@uibk.ac.at; heidi.boettcher@uibk.ac.at; barbara.brinkmeier@uibk.ac.at
(4,5) Institute of Hydrobiology and Aquatic Ecosystem Management, University of Natural Resources and Life Sciences, Vienna, Austria
guenther.unfer@boku.ac.at; bernhard.zeiringer@boku.ac.at

ABSTRACT

The flexible fish fence consists of horizontally clamped steel ropes. It is placed in front of the intakes to the turbines of hydropower plants and arranged in a way that it directs the fish towards a downstream fish passage facility. The electrified flexible fish fence is a significant advancement to the original prototype, as the steel ropes are used as electrodes to create an electrical field. The electrified version of the flexible fish fence is functioning as a guiding system to prevent fish from entering turbines and to guide downstream migrating fish towards a downstream passage facility. Therefore, it combines both, a mechanical as well as a behavioral barrier and guiding system.

Keywords: Ecohydraulics; hydropower; fish protection; Ethohydraulic experiments; fish migration.

1 INTRODUCTION

The climate targets that have been formulated by the European Union support future investments in hydropower. This might compromise the environmental objectives of the EU Water Framework Directive (WFD). The WFD postulates the safe migration of fish. This implies that up- and downstream migrating fish must be able to bypass hydropower plants in both directions. In regards to downstream migration, so far only structural barriers (e.g. intake screens) have been utilized to achieve a satisfactory rate of fish protection. Intake screens protect the turbine blades from damages caused by floating debris and, at the same time, can act as a mechanical barrier to prevent the fish from swimming into the turbine intakes during their downstream migration (Aufleger et al., 2015; Böttcher et al., 2015). Depending on turbine type and fish size, many organisms are injured or killed if they enter the turbine. The smaller the gaps between the bars of the screens, the better the fish are held back.

Only the usage of very fine racks prevents small fish from passing through the turbines. The required small spacing between screen bars, however, leads to substantial energy losses and high costs in construction and operation. Hence, they are often only an option for small hydro power plants. Typically, the bars of the screens are arranged in an upright position at the turbine intakes, i.e. in front view the bars extend vertically. Considering the typical body shape of fish, screens with horizontally extending bars are expected to better halt fish from entering the turbines. These are increasingly being used in new hydroelectric power plants but give rise to by no means negligible investment and maintenance costs.

2 FLEXIBLE FISH FENCES (NON–ELECTRIFIED)

2.1 Concept

The flexible fish fence differs from the fish protection screen in its fundamental construction and mode of operation (Brinkmeier et al., 2013; Böttcher et al., 2014). The mechanical fish protection barrier is constructed through multiple steel cables or steel ropes which are mounted parallel to each other. Typically, the cables are braced horizontally below the water surface between two or more abutments. In this way, large span widths can be achieved inexpensively. Each individual cable can be braced at one or more abutments, and also cast off from them, independently of the other cables. Therefore, a steering/tension device for each cable is attached to at least one of the abutments for repeatedly stretching tights and relaxing the corresponding cable. The device can be made by multiple winches or hydraulic cylinders.

The flexible fish fence can easily be completely opened by relaxing individual cables. This can be particularly important during high flows or floods to avoid log jams and harmful interactions with the bed material. Further, the flexible fish fence is cleaned by partially or completely relaxing some or all cables and stretching them tight afterwards. Flexible fish fences are no turbine protection systems. This task must be undertaken by different measures. Within the scope of an ecological upgrade of a hydro power plant, the turbine protection and the debris removal can be further ensured through the existing much coarser intake trash rack and the corresponding automatic cleaning systems.

 ©2017, IAHR. Used with permission / ISSN 1562-6865 (Online) - ISSN 1063-7710 (Print)

2.2 Preliminary results of ethohydraulic experiments

Within the scope of a research project, financially supported by the Austrian Research Promotion Agency (FFG), a comprehensive series of ethohydraulic experiments was carried out in a 2.0 m wide test flume in an outdoor research area of the University of Natural Resources and Life Sciences (BOKU, Vienna) in Lunz am See (Lower Austria). The tests were performed with three fish species (grayling, chub and brown trout) which were caught in adjacent rivers. Each fish was marked by pit tagging. The layout of the testing facility is presented in Figure 1. Each experiment was conducted with about 25 fish and lasted for 60 minutes. Before the start, fish were acclimatized for 45 minutes in the upstream section of the flume. Flow velocity was 0.5 m/s. At the start of the experiment, the corresponding barrier was removed. Fish were free to remain upstream of the flexible fish fence (blue color in Fig. 1 and Fig. 2) or to use the bypass intended to provide safe downstream migration (green color). The number of fish swimming through the flexible fish fence in direction of the virtual intake of the hydro power plant (red color) is considered as an important indicator for the efficiency of the specific layout of the fence.

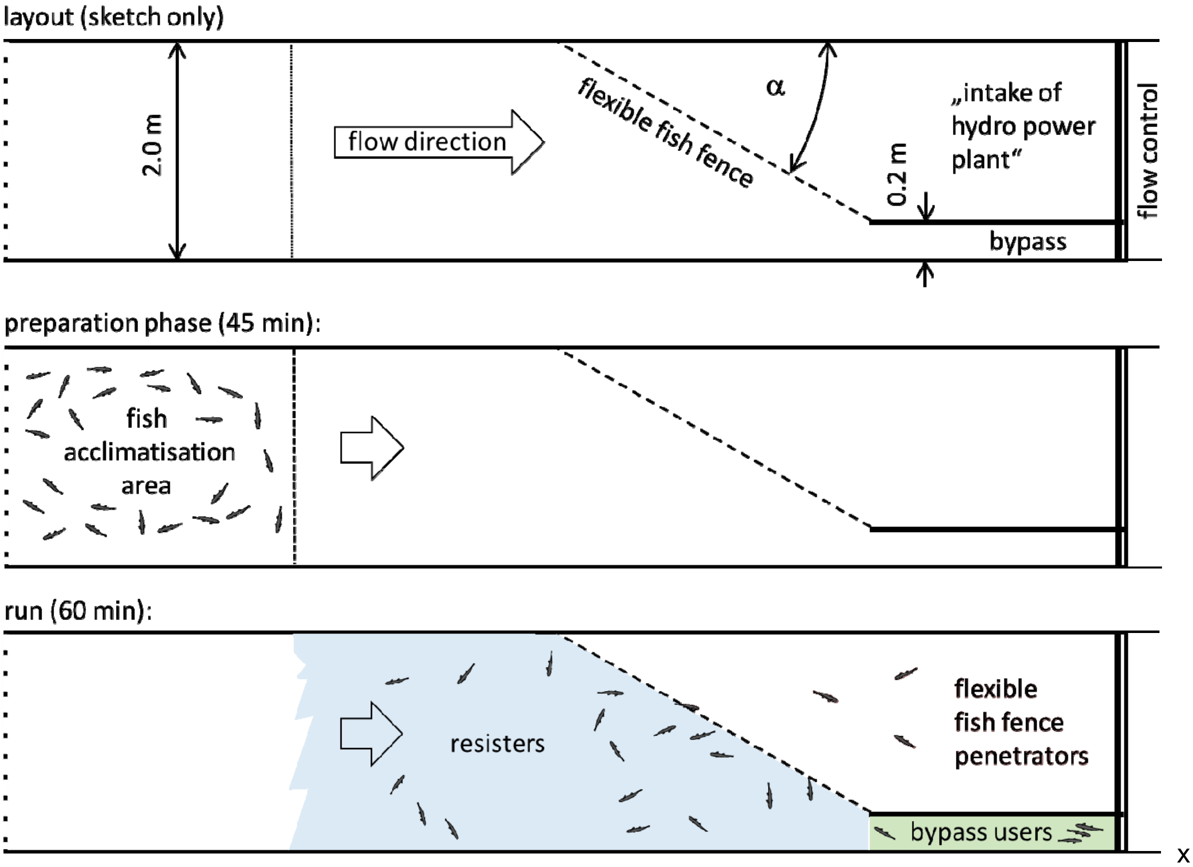

Figure 1. Ethohydraulic experiments – layout and testing method (test phases, colors refer to the illustration of the results in Figure 2).

Within several months of research, numerous experimental runs were performed. Multiple experimental setups were conducted where parameters like flow velocity, downstream slope of the fence, and the open vertical widths between the cables were varied.

Figure 2 illustrates an important result: The efficiency of a fish protection system based on a flexible fish fence depends on the vertical width between the steel ropes. At a spacing of 20 mm, a higher number of fish swam through the fence compared to a vertical width of 10 mm. The smaller vertical width setup prevented all movements through the fence. The preliminary results indicate that the influence of the horizontally braced flexible fish fence on downstream fish migration has to be considered as a mechanical barrier only. The 20 mm vertical width of the ropes did not restrict chub and trout movements as much as it did for grayling.

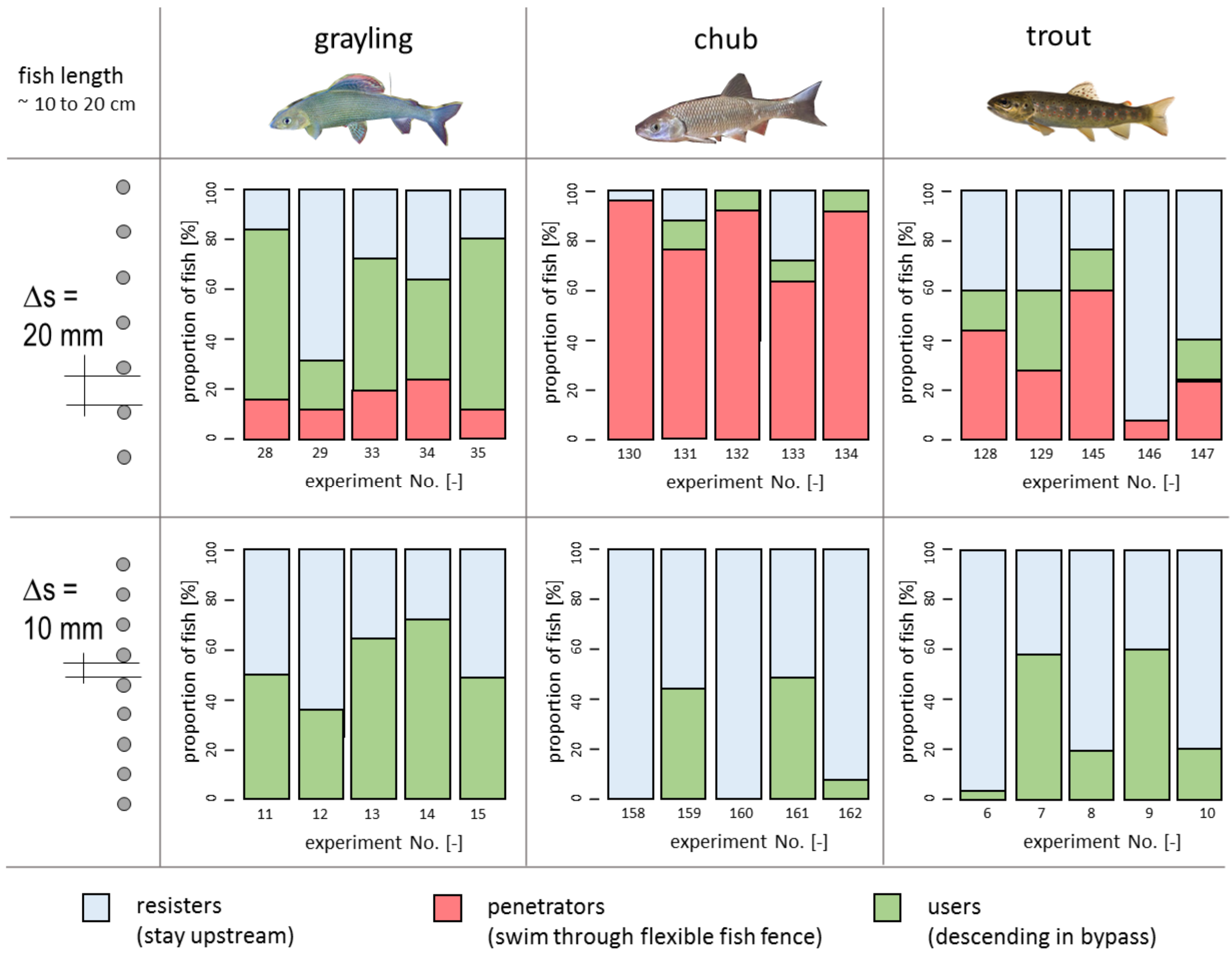

Figure 2. Ethohydraulic experiments – results for flexible fish fences (non–electrified) with vertical open widths between the steel ropes of 20 mm and 10 mm (flow velocity: 0.5 m/s).

These results underline that a cost-effective fish screen of horizontally braced steel ropes fulfills the requirements of a fish protection system at least within the meaning of a mechanical barrier (with 10 mm spacing). Due to the lower investment costs and their important system advantages (e.g. their robustness, relatively low hydraulic losses, and the possibility of lowering the cables to the riverbed in the case of high flows), flexible fish fences can be considered as an attractive alternative to large horizontal steel racks which require a lot of efforts concerning the related traditional bearing structure typically consisting of rigid concrete and steel elements.

There remains a clear dependency between the required vertical width between the steel cables and the efforts which must be made for transferring the resulting horizontal loads to the ground and for keeping the fence free from debris for trouble-free operation of the hydro power plant. The bigger the required spacing between the horizontally braced ropes is, the greater the advantages of the flexible fish fences compared to other systems will be.

3 ELECTRIFIED FLEXIBLE FISH FENCES

3.1 Basic idea of the electrified flexible fish fence

Since the very beginning of the research related to the flexible fish fences, additional external stimulations like vibrations, light or electrical currents were considered as additional effects, which might enhance the efficiency of the fish protection system. As steel cables themselves are electrical conductors, it was suggested that they could serve as elements of an electrified version of the flexible fish fence.

3.2 Fish protection using electrical fields

Electric guidance and barrier systems are used to change fish behavior. While guidance systems are supposed to attract fish to specific locations (e.g. bypass), the objective of an electric barrier is to block fish movement completely. These systems create an electric field by placing a conductive anode and cathode in the water and passing a current between the conductors (Little, 2015), which causes a physiological reaction in the aquatic species. The cathode usually has an avoiding effect, while the anode has an attractive effect on

 ©2017, IAHR. Used with permission / ISSN 1562-6865 (Online) - ISSN 1063-7710 (Print)

fish. Very close to the anode and cathode galvanic anesthesia may occur, an effect which is used in electrofishing, but should be avoided in the case of electric guidance or barrier systems. The effect of such electric systems depends not only on the conductivity of the water but also on the fish size and fish species. Recent applications of fish barriers use direct current (DC) or pulsed DC (Svoboda and Hutcherson, 2014). To avoid habituation effects in fish behavior, the pulse rates can be randomly controlled (Schmalz, 2010). Furthermore, peak voltage, peak current, pulse width and frequency have to be considered to trigger the desired fish response (Svoboda and Hutcherson, 2014). Since electric fields show a radial propagation, a straight fish guiding to a bypass is often difficult. In addition, diadromous species often react moderately to behavioral barriers, especially when the bypass is not easy to find. Best practice examples for hydroelectric power plants are largely missing. Only Pugh et al. (1971) were able to achieve a rejection rate of 69-84% of salmon smolts.

3.3 Preliminary ethohydraulic tests with electrical flexible fish fences

Within the scope of the ethohydraulic experiments for the flexible fish fences, an alternative approach of the system was investigated, where the horizontally braced steel ropes were electrified. An electrical switch (provided from expert companies in Germany and Poland) was used as energy source. This switch was developed to deliver targeted power surges which are adjustable in terms of the maximal voltage, to scare fish away from turbine intakes. The flexible fish fence presented in Chapter 2 was adopted in a way that allowed to change the order of the positive (+) and negative (-) charges of the steel cables. 30 preliminary experiments were carried out. Numerous parameters were changed. Besides using different fish species and increasing the maximal voltage, a systematic variation of the settings of positively (+) and negatively (-) charged cables was performed (Figure 3). A vertical open width between the horizontally braced cables of 30 mm was chosen for all preliminary experiments.

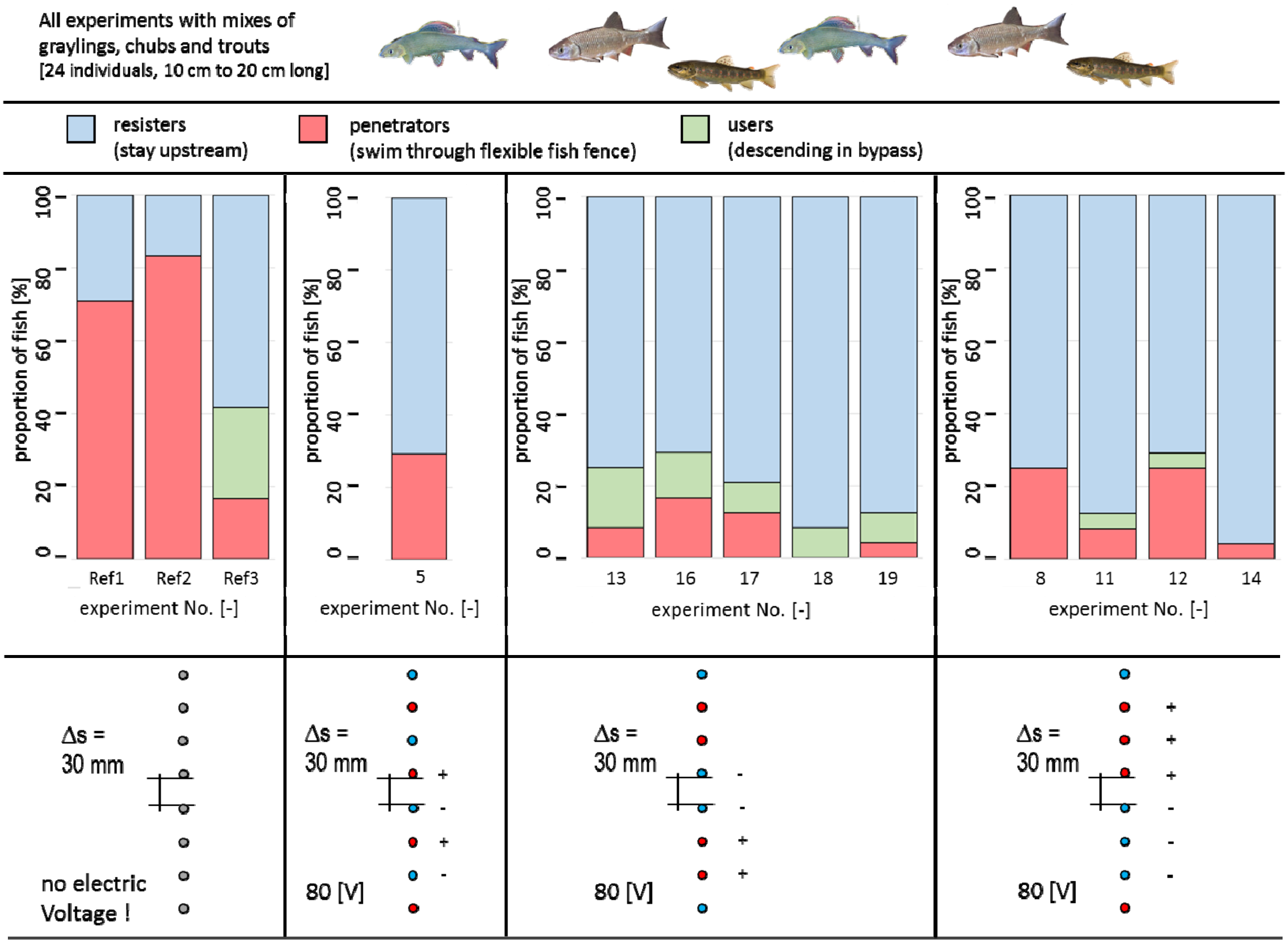

Figure 3. Ethohydraulic experiments – first results for electrified flexible fish fences with vertical open widths of 30 mm, flow velocity of 0.5 m/s, and different electrical settings (left column: reference tests without electrical voltage).

The results in Figure 3 indicated that the electrical field influenced fish behavior. The percentage of fish swimming through the flexible fish fence decreased significantly if an electrical current was present. Even though the type of impact of the electrical field on the fish was still not known in detail, the preliminary results

©2017, IAHR. Used with permission / ISSN 1562-6865 (Online) - ISSN 1063-7710 (Print)

indicated that the electric field had a repellent effect on fish. Video sequences of the experiments showed that most of the fish did not approach the ropes as soon as electricity was applied to the system.

4 CONCLUSIONS

Currently, the development of an electrified version of the flexible fish fence is in progress. First results of ethohydraulic experiments prove the fundamental efficiency of the system to prevent fishes from swimming through a plane in space created by a combination of a mechanical barrier and an electrical field. Electrified flexible fish fences have the potential to efficiently and directly create an electrical field in the water column with unprecedented spatial coverage, to reach a so far not possible homogeneity and coverage in its scaring effect, to allow larger vertical distances between individual rack elements (ropes) compared to a non-electrified version of the flexible fish fences (which reduces construction cost and operational cost) and to serve as the basis for the establishment of a cost-effective and potent fish protection and fish-guiding system that is suitable for small, medium and large run-of-river plants. Further ethohydraulic experiments are planned to investigate and improve the effects of the electrified flexible fish fence.

ACKNOWLEDGEMENTS

We appreciate the financial support of the Austrian Research Promotion Agency (FFG) and the excellent cooperation within the research team (University of Innsbruck, University of Natural Resources and Life Sciences (Vienna), Albatros Engineering GmbH, (Herzogendorf, Austria)).

REFERENCES

Aufleger, M. & Brinkmeier, B. (2015). Wasserkraftanlagen mit niedrigen Fallhöhen – Verschiedene Konzepte im kritischen Vergleich. *Österreichische Wasser- und Abfallwirtschaft,* 67(7-8), 281-291.

Böttcher, H., Unfer, G., Zeiringer, B., Schmutz, S. & Aufleger, M. (2015). Fischschutz und Fischabstieg – Kenntnisstand und aktuelle Projekte in Österreich. *Österreichische Wasser- und Abfallwirtschaft*, 67(7-8), 299-306.

Böttcher, H., Brinkmeier, B. & Aufleger, M. (2014). Flexible Fish Fences. *Proceedings of the 10th ISE 2014*, Trondheim.

Brinkmeier, B., Böttcher, H. & Aufleger, M. (2013). Flexible Fish Fences. *Proceedings of 2013 IAHR World Congress*, Chengdu.

Little, D. (2015). *Effect of Electric Fish Barriers on Corrosion and Cathodic Protection,* Scoping Study, Bureau of Reclamation, Denver, CO.

Pugh J.R., Monan G.L. & Smith J.R. (1971). Effect of Water Velocity on the Fish Guiding Efficiency of an Electrical Guiding System. *Fishery Bulletin,* 68, 307–324.

Schmalz W. (2010). Untersuchungen zum Fischabstieg und Kontrolle möglicher Fischschäden durch die Wasserkraftschnecke an der Wasserkraftanlage Walkmühle an der Werra in Meiningen - Abschlussbericht. Im Auftrag der Thüringer Landesanstalt für Umwelt und Geologie, Breitenbach.

Svoboda, C.D. & Hutcherson, J. (2014). *Literature Review of Electric Barriers for Returning Adult Salmonids,* Bureau of Reclamation, Denver, CO.

 ©2017, IAHR. Used with permission / ISSN 1562-6865 (Online) - ISSN 1063-7710 (Print)

CAN DAM MANAGEMENT OFFSET IMPACTS OF CLIMATIC VARIBILITY ON AQUATIC HABITAT?

ROHAN BENJANKAR[1], DANIELE TONINA[2], MOHAMMAD M. SOHRABI[3], JAMES A. MCKEAN[4], QUIWEN CHEN[5] & DMITRI VIDERGAR[6]

[1,2,3]Center for Ecohydraulics Research, University of Idaho, Boise, USA
rohanb@uidaho.edu
[4]Rocky Mountain Research Station, US Forest Service, Boise, USA
[5]Center for Eco Environmental Research, Nanjing Hydraulic Research Institute, China
[6]Bureau of Reclamation, Boise, Idaho, USA
[1]Department of Civil Engineering, Southern Illinois University Edwardsville, Edwardsville, USA

ABSTRACT

Dams have been important structures for food and energy production but affect hydrological processes, sediment transport, water temperature, and potentially play a role on habitat loss. In this study, we focus on the impacts of dam operation on fish habitat and analyze if flow regulation can offset impacts of climatic variability on aquatic habitat based on 2D hydrodynamic flow and fish habitat model. We use the South Fork Boise River (SFBR), Idaho, as a study site, which is impacted by Anderson Ranch Dam operation. Our results show that regulated flows increase habitat and maintain good habitat year around compared to the unregulated flows. Summer months are a critical period for fish habitat for unregulated cases in all climatic conditions. Summer temperatures are comparatively higher than those preferred by Bull trout. This study suggests that dam management has the potential to offset negative impacts on fish habitat from future climate change effects.

Keywords: Aquatic habitat; regulated flows; unregulated flows; hydrodynamic modeling; climatic variability.

1 INTRODUCTION

Dam management affects hydrological and fluvial processes, and water temperature, and potentially habitat loss and aquatic biodiversity reduction (Poff et al., 1997; Ward et al., 2001). High stream temperatures can cause an increase in predation rates, effect growth rates and reproduction, and survival of salmonids (Marine et al., 2004; Poole et al., 2001). Typically, regulated flow reduces magnitude of peak flows and increase minimum base flows and impacts stream thermal regimes spatially and temporally (Angilletta et al., 2008). Furthermore, changing climate will impact the thermal regime of river systems as well as shift the availability of certain aquatic habitats selected by different species (Perry et al., 2005). The interaction among flow and timing of reservoir releases on stream ecosystem and thermal regime is often overlooked in river flow management (Olden et al., 2010). Studies have shown that reservoir management could manipulate water temperatures via flow release, to accommodate aquatic species requirements (Null et al., 2013; Sinokrot et al., 2010; Yates et al., 2008).

We use South Fork Boise River (SFBR), Idaho, USA as a study site, which is impacted by Anderson Ranch Dam operation and contains critical rearing habitat for the threatened Bull Trout. We discuss application of a process-based integrated model, which couples catchment hydrology, hydraulics, water temperature and fish habitat models to quantify impacts of dam operation on aquatic habitats for dry, average and wet climatic conditions. Furthermore, we analyze if flow regulation can offset impacts of climatic variability on aquatic habitat.

2 Methods

2.1 Study area

The South Fork Boise River (SFBR) watershed hydrology (drainage area of 3,382 km^2) is snowmelt dominated. Our study was focused on a 23 km long upper open canyon reach with pools, riffles and runs with several braided sections and side channels (Figure 1). We selected three functional climatic conditions to represent typical wet, average and dry climatic years based on measured flows at USGS gage from 1946 to 2012.

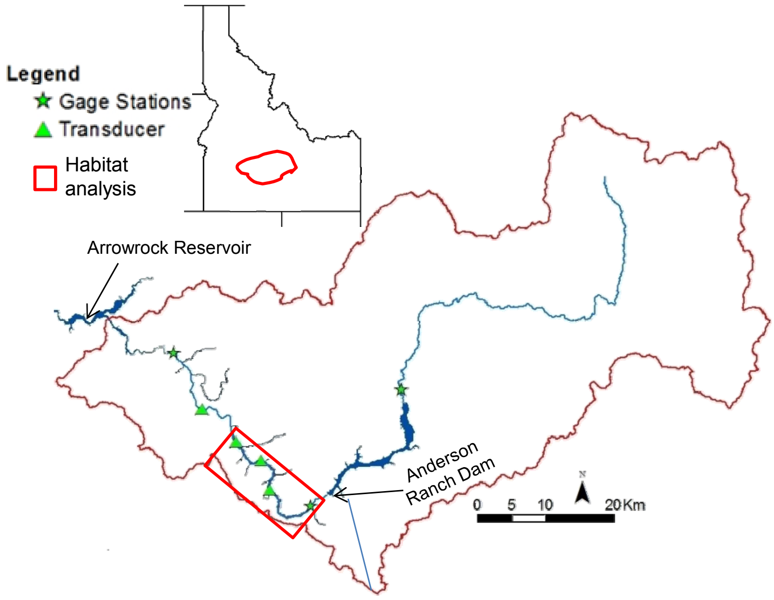

Figure 1. South Fork Boise River Basin and study area.

2.2 Integrated model

We developed an integrated modeling framework that couples catchment hydrology, hydraulics, water temperature and biological (fish habitat) models to analyze impacts of dam operation on aquatic habitats. Digital elevation model (DEM) of terrestrial and submerged topography, surveyed with the aquatic-terrestrial Experimental Advanced Airborne Research LiDAR (EAARL) were used for river bathymetry (McKean et al., 2009). We developed a fish habitat model in ArcGIS using 2D simulated hydraulic variables water depth and velocity, water temperature and univariate rearing habitat preference criteria for Bull Trout (Figure 2, left). We assigned temperature suitability between 1 (<16^{o}C) and 0 (>22°C) based on daily maximum temperature (DMT). For 16-22°C, suitability was linearly interpolated.

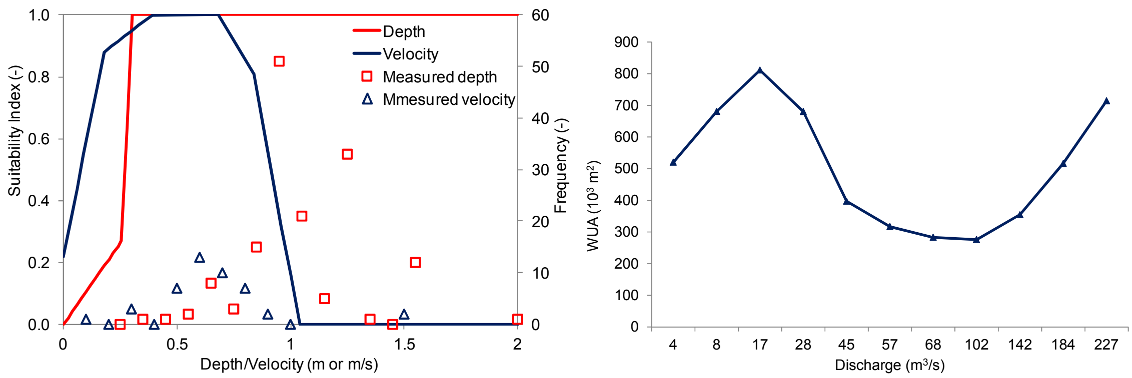

Figure 2. Habitat preference curves for Bull Trout (left) and WUA as a function of discharges (right).

2.3 Data analyses

Discharge-WUA (Q-WUA) curves were developed from a range of discharges 4, 8, 17, 28, 45, 57, 68, 85, 102, 142, 184 and 227 m^3/s by applying the integrated model. Then, we developed habitat time series for different climatic conditions for dry (2007), average (2010) and wet (2006) under dam regulated, un-regulated and modified scenarios based on Q-WUA curve and mean daily discharges. We quantified the impacts of dam operation on aquatic habitat by comparing WUA between regulated and unregulated scenarios and analyzed if dam management can offset those impacts. Furthermore, we analyzed the potential impact of low flow release through dam (4 m^3/s) lower than current minimum flow of 8 m^3/s as an option for future water management to compensate for drought conditions.

 ©2017, IAHR. Used with permission / ISSN 1562-6865 (Online) - ISSN 1063-7710 (Print)

3 RESULTS AND DISCUSSIONS

3.1 Dam impact

Our analyses showed Bull Trout rearing habitats were consistent in late-fall (October and November), winter (December, January and February) and early-spring months (March) as a result of regulated higher low-flows and colder stream temperature less than 16°C (Figure 3). However, habitat decreased in summer and early-fall months as a result of higher flow release.

Habitat decreased considerably in summer months for the unregulated scenario than for the regulated scenario due to lower base flows and higher stream water temperature (Figure 3) (e.g., Muhlfeld et al., 2012). Water temperature in the unregulated scenario was much higher (>22°C) than the current regulated water temperature for the South Fork Boise River(USBR, 2013). Therefore, we speculate that regulated case maintains favorable Bull Trout habitat during summer months (Figure 3).

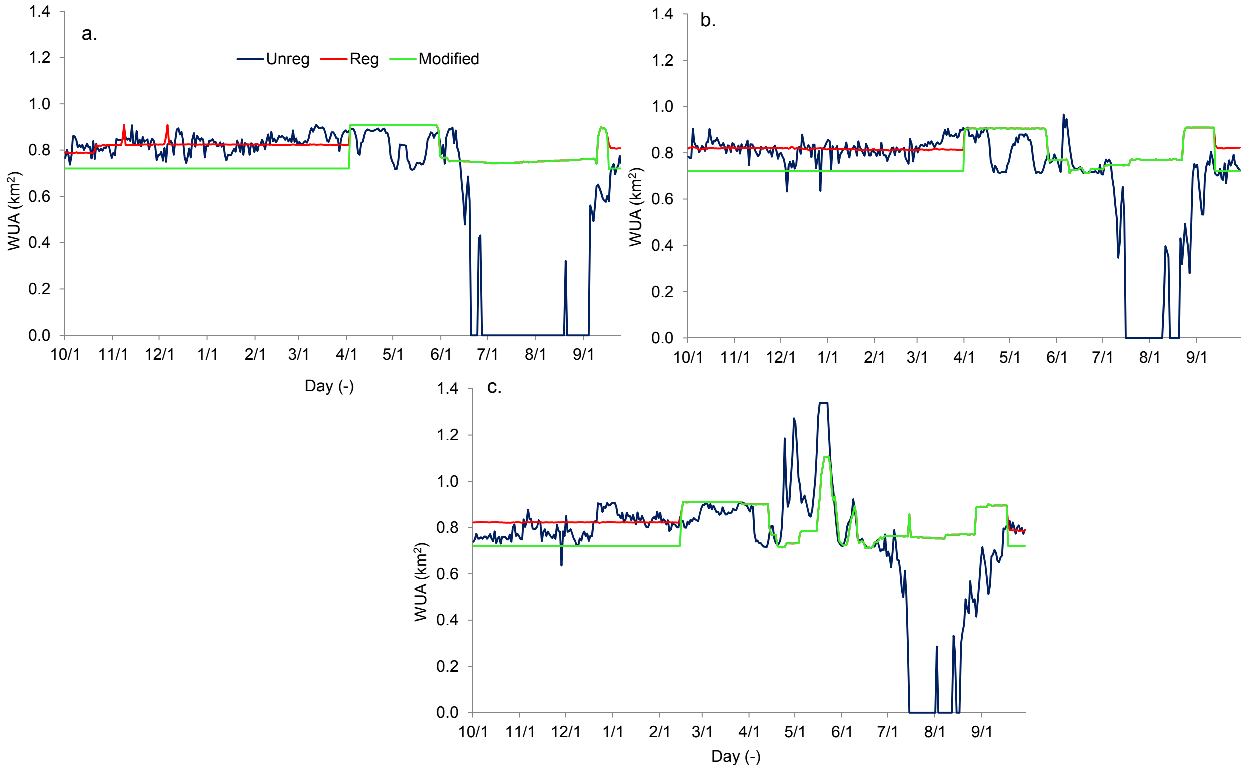

Figure 3. WUA for regulated, modified and unregulated flows for a. dry (2007), b. average (2010), and c. wet (2006) climatic years.

Habitat qualities for modified low flow were noticeably lower than those for the regulated scenario (Figure 3). The results were consistent with other studies where degradation of habitat occurred due to low flow in channel as a result of dam management (e.g., Muhlfeld et al., 2012; Yarnell et al., 2010). Therefore, we suggest that modification (lowering) of dam release flows less than the current minimum flow of 8 m^3/s would degrade Bull trout rearing habitat in the SFBR system.

3.2 Can dam management offset degraded habitat?

Stream temperatures were higher than 16°C for the majority of summer days in the unregulated scenario but the regulated stream temperatures were within the range suitable for Bull Trout rearing habitat. Our result suggested that dam management can offset impacts of low flows and high water temperature on aquatic habitat by increasing historic low flows and decreasing water temperature specifically during dry climatic cases. Therefore, dam management could mitigate some climate change impacts on the stream water temperature, consequently for aquatic ecosystem as other previous studies suggested (Null et al., 2013; Yates et al., 2008).

4 CONCLUSIONS

Our results show that regulated flows maintain good habitat throughout the year for adult Bull Trout in the SFBR system. Summer months are a critical period for fish habitat in the SFBR system for unregulated cases in all climatic conditions. Regulated flows maintain uniform habitat throughout the summer period for all three climatic conditions because Anderson Ranch Dam releases water temperatures within the range that Bull

Trout prefers. This suggests that dam management has the potential to offset negative impacts on fish habitat quality from future climate change effects especially during dry climatic years.

ACKNOWLEDGEMENT

The study is funded by the United States Bureau of Reclamation (USBR). We thank Danish Hydraulic Institute (DHI) for proving license for MIKE software packages.

REFERENCES

Angilletta, M.J., Steel, E.A., Bartz, K.K., Kingsolver, J.G., Scheuerell, M.D., Beckman, B.R. & Crozier, L.G. (2008). Big Dams and Salmon Evolution: Changes in Thermal Regimes and their Potential Evolutionary Consequences. *Evolutionary Applications,* 1, 286–299.

Marine, K.R. & Cech, J.J. (2004). Effects of High Water Temperature on Growth, Smoltification, and Predator Avoidance in Juvenile Sacramento River Chinook Salmon. *North American Journal of Fisheries Management,* 24, 198-210.

McKean, J.A., Nagel, D., Tonina, D., Bailey, P., Wright, C.W., Bohn, C. & Nayegandhi, A. (2009). Remote Sensing of Channels and Riparian Zones with a Narrow-Beam Aquatic-Terrestrial LIDAR. *Remote Sensing,* 1, 1065-1096.

Muhlfeld, C.C., Jones, L., Kotter, D., Miller, W.J., Geise, D., Tohtz, J. & Marotz, B. (2012). Assessing the Impacts of River Regulation on Native bull Trout (Salvelinus confluentus) and West slope Cutthroat Trout (Oncorhynchus clarkii lewisi) Habitats in the Upper Flathead River, Montana, USA. *River Research and Applications,* 28, 940-959.

Null, S.E., Ligare, S.T. & Viers, J.H. (2013). A Method to Consider Whether Dams Mitigate Climate Change Effects on Stream Temperatures. *Journal of the American Water Resources Association,* 49(6), 1456-1472.

Olden, J.D. & Naiman, R.J. (2010). Incorporating Thermal Regimes into Environmental Flows Assessments: Modifying Dam Operations to restore Freshwater Ecosystem Integrity. *Freshwater Biology,* 55, 86-107.

Perry, A.L., Low, P.J., Ellis, J.R. & Reynolds, J.D. (2005). Climate Change and Distribution Shifts in Marine Fishes. *Science,* 308, 1912-1915.

Poff, N.L., Allan, J.D., Bain, M.B., Karr, J.R., Prestegaard, K.L., Ricther, B.D., Sparks, R.E., & Stromberg, J.C. (1997). The Natural Flow Regime. *Bioscience,* 47(11), 769-784.

Poole, G., Dunham, J., Hicks, M., Keenan, D., Lockwood, J., Materna, E., McCullough, D., Mebane, C., Risley, J., Sauter, S., Spalding, S. & Sturdevant, D. (2001). *Scientific Issues Relating to Temperature Criteria for Salmon, Trout and Char Native to the Pacific Northwest*, United States Environmental Protection Agency.

Sinokrot, B.A. & Gulliver, J.S. (2010). In-Stream Flow Impact on River Water Temperatures. *Journal of Hydraulic Research* 38(5), 339-349.

U. S. Bureau of Reclamation, (USBR). (2013). *Biological Assessment for Bull Trout Critical Habitat in the Upper Snake River Basin,* Boise, Idaho: U.S. Department of the Interior Bureau of Reclamation.

Ward, J.V. & Tockner, K. (2001). Biodiversity: Towards a Unifying Theme for River Ecology. *Freshwater Biology,* 46, 807-819.

Yarnell, S.M., Viers, J.H. & Mount, J.F. (2010). Ecology and Management of the Spring Snowmelt Recession. *Bio Science,* 60, 114-127.

Yates, D., Galbraith, H., Purkey, D., Huber-Lee, A., Sieber, J., West, J., Herrod-Julius, S. & Joyce, B. (2008). Climate Warming, Water Storage and Chinook salmon in California's Sacramento Valley. *Climatic Change,* 91, 335-350.

 ©2017, IAHR. Used with permission / ISSN 1562-6865 (Online) - ISSN 1063-7710 (Print)

CHARACTERISTICS OF CONCRETE FILTER FOR DRINKING WATER

RIZALDI MAADJI(1), RADIANTA TRIATMADJA(2), FATCHAN NURROCHMAD(3) & SUNJOTO(4)

(1,2,3,4)Doctoral Student of Civil and Environmental Engineering Department, Faculty of Engineering, Universitas Gadjah Mada, Yogyakarta, Indonesia
rizaldi_maadji@yahoo.com; tsipil.ft@ugm.ac.id

ABSTRACT

Capacity and capability of filter in reducing microbiology contaminant found in water is determined by physical characteristic of concrete filter. Kamulyan (2014) research is about structure of constituent particle on concrete filter, filter particle diameter, and concrete filter porosity as the main factors affecting physical characteristics of concrete filter to diminish suspended particle. Clean water supplies for drinking water should meet the requirements of by international regulations, such as World Health Organization (WHO) and American Public Health Association (APHA). Microbiology parameter is used as the standard or guidance for drinking water supply in several countries. Total coliforms and Escherichia coli (E. coli) can be applied as indicators that show the drinking water quality (Tallon et al., 2005). Ratio of sand and cement affects filtration discharge capacity, and effectiveness in filtering unwanted substance and microbe. Concrete filter thickness was very effective for removing microbiology (E. Coli and coliform) in drinking water.

Keywords: Characteristics of concrete filter; microbiology of drinking water.

1 INTRODUCTION

Concrete filter is a filter made from a mixture of sand and cement with a certain ratio. Concrete filter molded in a 4-inch diameter of PVC pipe, with a particular filter thickness. Triatmadja (2008), conducted a preliminary assessment of the concrete filter which could reduce turbidity up to 95%. Kamulyan (2014), examined the ability of concrete in reducing turbidity with three filter models using three different diameters of concrete. The smaller the diameter of the sand, the higher the turbidity reduction ability can be.

Concrete filter can also reduce the content of microbes in the water. Maadji, et al., (2016), performed filtration in two stages. The first stage of filtration was using coarse concrete filter (CCF), and then the results of the first stage filtration was filtered again using fine concrete filter (FCF). The test results showed the reduction of microbial content in water with rejection rate of 0.9871, log removal value (LRV) of 1.85, and reduce turbidity to below 5 Nephelometric Turbidity Units (NTU).

Reduction of E. coli bacteria though concrete filter has also been done by Maadji, et al. (2016). Filter with 12 cm of thickness could reduce the total content of the E. coli bacteria (Most Probable Number = 0).

Based on those previous researches, the physical characteristics of the concrete filter that greatly affect the ability of filtration to reduce turbidity and microbiology in water are filter thickness and the ratio of sand - cement (m). Regulation of the Minister of Health of the Republic of Indonesia Number 492 year 2010 on Drinking Water Quality Requirements, oblige terms on microbiological parameters for drinking water must be free of E. coli and coliform content. This study examines the concrete filter characteristics, in particular the most effective thickness and m of the concrete as a filter for drinking water.

Drinking water should satisfy the requirements of physical, microbiological, chemical and radioactive. Terms of drinking water quality with microbiological parameters using total of coliforms and E. coli as an indicator bacterium in accordance with the international regulations of the World Health Organization (WHO) and the American Public Health Association (APHA).

2 FILTRATION THEORY

Filtration of water is to flow the water through filter bed. Suspensions and colloidal particles larger than the pores of the bed are retained and remain on bed filter. Purchas and Sutherland (2002), distinguished four basic mechanisms of filtration namely surface straining, depth straining, depth filtration and cake filtration.

Each filtration process will involve a combination of two or more mechanisms of filtration (Crittenden, et al., 2012). The screening process will quickly clog the media, such as pores getting blocked, thus requiring some kind of cleansing process. The mechanism of filtration that occurs in concrete filter is depth filtration and cake filtration. In the depth filtration, the particles trapped in the filter. Such behavior involves a complex mix of physical mechanisms. Particles were firstly brought into contact with the pore walls (or very close) with inertia force or hydraulic or with Brownian motion (molecular). Then the particles become attached to the pore walls or other particles by means of van der Waals and other surface styles. The magnitude of this force can be

©2017, IAHR. Used with permission / ISSN 1562-6865 (Online) - ISSN 1063-7710 (Print)

influenced by changes in factors such as the concentration and type of ions in aqueous solution. This mechanism affects the efficiency of the filter thickness.

Influent suspension material can be deposited on top of the bed filter cake in the form of particles or thick layer accumulated at the surface of the medium, and then act as a filter media for the next filter. If the particle (or particles) are larger than the pores, the filtration cake can follow an initial period of surface straining. Cake filtration can occur even when all the particles are smaller than the pores (down even about one-eighth of the pore diameter), especially if the solid concentration is relatively high (e.g., more than 2% by weight in liquid). This happens with bridging particles on the entrance to the pores, to form the basis on which the cake will grow (Purchas and Sutherland, 2002).

In depth filtration, the particles are released continuously throughout the filter through the transportation process and sticking in grain filter. Disappearance of particles in the filter depends on the concentration of particles, similar to the first-order rate equation, Eq. [1] by Iwasaki, 1937 (Crittenden, et al., 2012).

$$\frac{\partial C}{\partial z} = -\lambda\, C \qquad [1]$$

where:

λ = filtration coefficient, m^{-1}
C = concentration of mass or number of particles, mg/L atau L^{-1}
z = filter depth, m

If the filtration coefficient is known, it would be possible to calculate the concentration of particles effluent from the filter. However, filtration is a complex process where filtration coefficient can vary in time and filter depth and depending on the nature of the bed filter (grain shape and size distribution, porosity, thickness), the suspension influent (turbidity, particle concentration, particle size distribution, particle and water density, viscosity of water, temperature, pretreatment levels), as well as operating conditions (filtration rate). The complexity of the filtration mechanism and variations in the nature of water resources led to the absence of models that can predict the performance of specific filter (Crittenden, et al., 2012).

3 MATERIALS AND METHODS

3.1 Preparation of Concrete Filter

In this study concrete filter was designed with uniform gradations in grain size range of 0.1 – 0.2 mm. Permeability of concrete filter = 0 at m = 2 (Maadji et al., 2016). The ratio of sand - cement varied from m = 3, m = 4, m = 5 and m = 6. Requirements for concrete durability maximum ratio of 1:6 in weight (Murdock, 1999). Optimum water cement ratio (WCR) used was 0.4 (Kardiyono, 2007) and the filter thickness varied from the thickness of 5 cm, 10 cm and 15 cm, so that the concrete filter consists of 12 models and each model was made into 5 pieces of filter.

Good concrete made from a mixture of sand aggregate in a state of Saturated Surface Dry (SSD), and the absorption of free water to water-cement ratio can be achieved in accordance with mix design (Shetty, 2005). Density of sand is planned with a specific gravity SSD = 2.7337 gr/cm^3.

Variations of thickness and m of the filter characteristics into twelve models of filters. Each model filter printed as many as 5 samples. Filtration test carried out in parallel to 5 samples that have the same characteristics of thickness and m.

3.2 Concrete Filter Installation

Flow of Raw Water Tank (RWT) is pumped into a constant head tank to the filter. The total head approximately 206 cm. Constant head tank also divide flow into five flow distributions to the filter column so that the flow is distributed before entering into the concrete filter.

Flow test is carried out in parallel on 5 concrete filters which have similar characteristics (filter thickness and m). Discharge parameters were measured at the same time and rate of filtrate turbidity performed on the filter outlet valve (VF_O), see Figure 1.

Turbidity levels were measured by taking samples of water with 200 mL bottles. Water samples were taken from RWT. Filtrated water sample is taken from each of VF_O. Discharge measurements and sampling turbidity conducted approximately 1 hour after the filtration process (one period filtration), after 60 minutes the measurement conducted to the second and third period.

 ©2017, IAHR. Used with permission / ISSN 1562-6865 (Online) - ISSN 1063-7710 (Print)

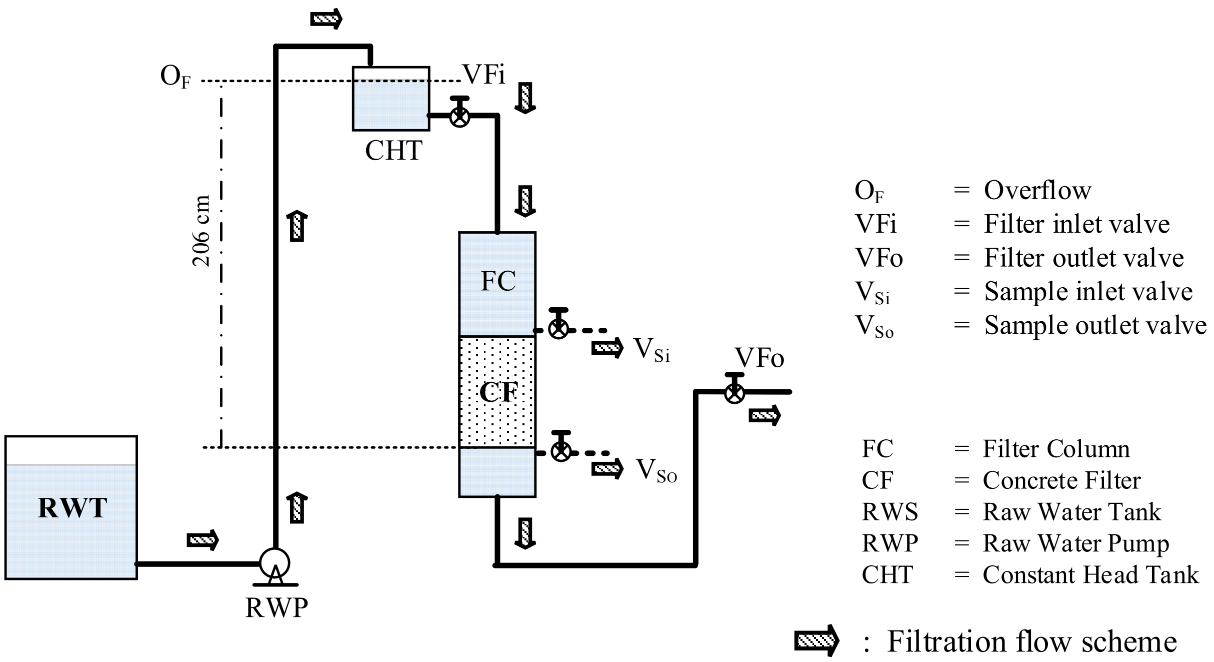

Figure 1. Scheme of Flow Filtration

3.3 Raw Water

Raw water is collected from the Code River that passes through residential areas in Yogyakarta. The content of water microbiology (E. coli and coliforms) were tested using the Microbiology Test Kit (Figure 2 & 3). The number of bacteria in the sample is determined by the number of colonies on plates or kit. The unit is used to express the number of bacterial colonies or is cfu/mL (cfu = colony forming units).

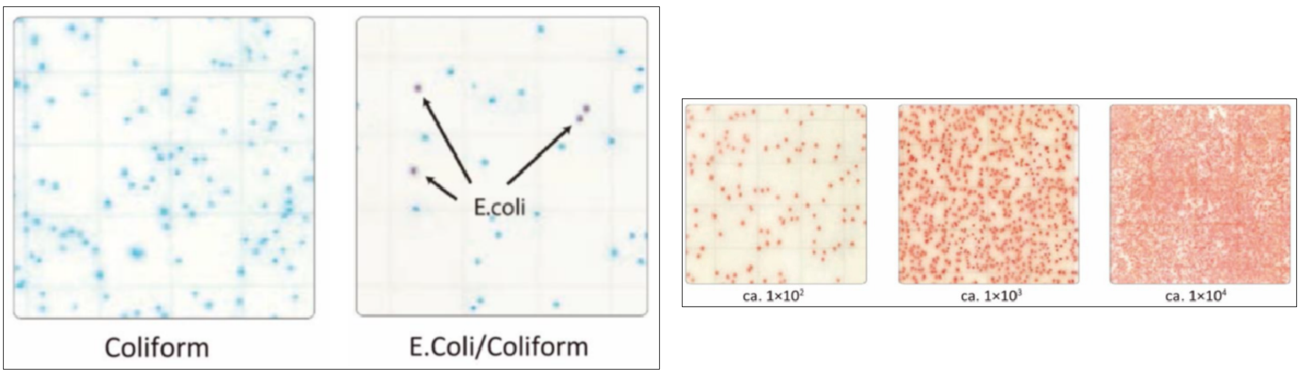

Figure 2. Aerobic Count Microbiology Test Kit

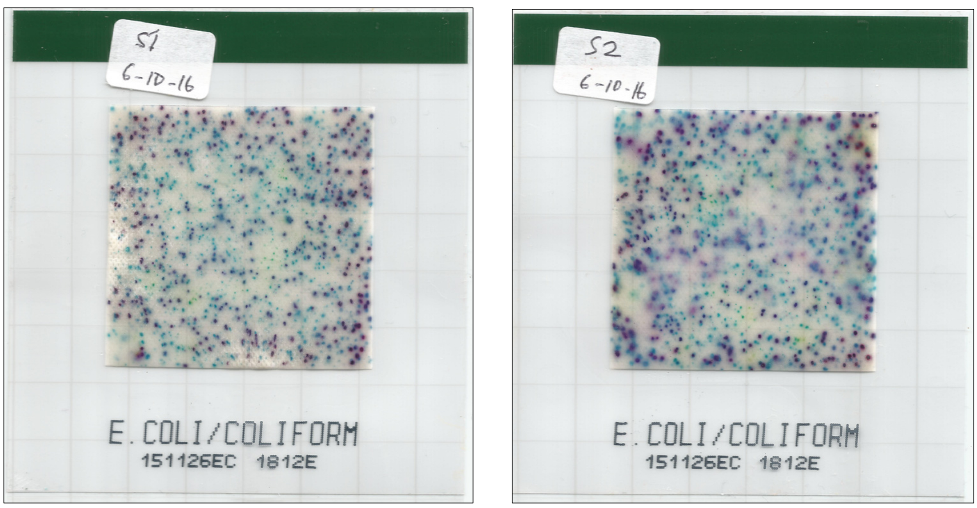

Figure 3. Count Microbiology Test Kit Code River (E. coli ±300 cfu and coliform ±600 cfu)

3.4 Method of Microbiology Sampling

A common characteristic of bacteria such as prokaryotic species are microscopic size, multiply by binary fission and has a short generation time. Bacteria can multiply rapidly in a favorable environment where a single cell divides into two cells, which are then split into 4, 8, 16, and so on. Most bacteria under optimal conditions, split every 1-3 hours. Some species, such as E. Coli, generation time is just 20 minutes, so at this stage the number of single eukaryotic cells can give rise to colonies heavier than the mass of the Earth in just two days, but in reality, this does not happen because (Reece, et al., 2014):

i. The cells eventually deplete their own nutrient supply
ii. Poisoning with metabolic wastes, faced competition from other microorganisms, or
iii. Consumed by other organisms.

Considering the characteristics of the bacteria, then the sampling was done directly from special faucets (V_{si} and V_{so}) before and after the concrete filtration (see Figure 4).

Figure 4. Water (1 mL) Sampling for Microbiology Test through Taps Before and After Concrete Filter.

Water microbiological samples were taken using sterile disposable pipette as much as 1 mL, then dripped into microbiology test kits. Microbiological test sample was incubated in 35□C temperature for 24 hours. For every one filtration process is executed, microbiological sampling before and after the filter was made during the second period of filtration.

4 RESULTS AND DISCUSSION

4.1 Hydraulic Characteristics of Concrete Filter

The porosity influence on permeability mechanism that became the main property of a concrete filter is important to understand. Permeability is a parameter of the structure of hydrated cement paste is associated with porosity as a major factor that can be determined by the amount of discharge filtration capacity. Great influence on the permeability of capillary segmentation illustrates the fact that the permeability is not a simple function of porosity. Therefore, it is necessary to study the influence of the thickness of the filter. The amount of discharge filtration based on variation of m and thickness of the filter is shown in Figure 5 and 6.

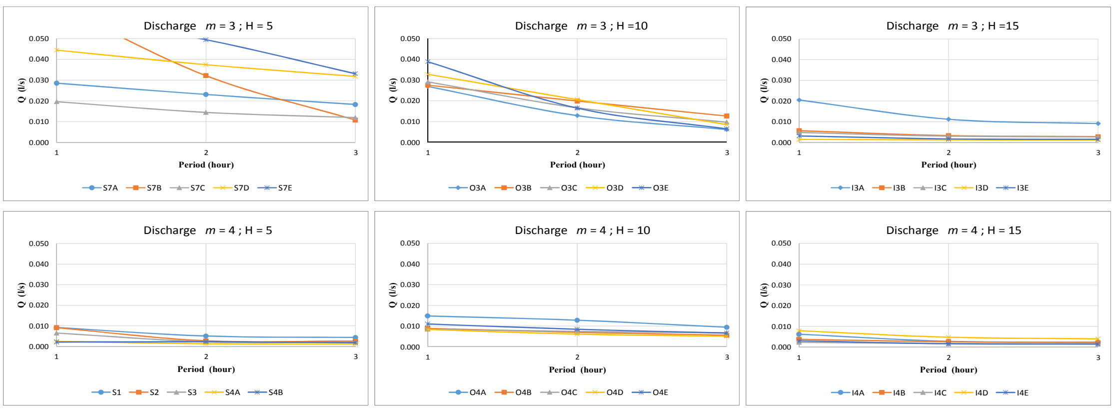

Figure 5. Filter Discharge (m = 3 and m = 4, with H = 5 cm, 10 cm, and 15 cm)

©2017, IAHR. Used with permission / ISSN 1562-6865 (Online) - ISSN 1063-7710 (Print)

The filtration process starts consecutively on a filter with the characteristic *m* = 3 with a thickness (H) = 5 cm and then H = 10 cm, followed by H = 15 cm, then with *m* = 4, with H = 5 cm; 10 cm and 15 cm

Discharge filtration capacity on a filter with *m* = 3 and H = 5 cm in the first period (Hour) is 0.020-0.066 l/s; in the second period discharge decreased by 0.014-0.050 l/s; and in the third period amounted to 0.011-0.033 l/s. More are given in Table 1.

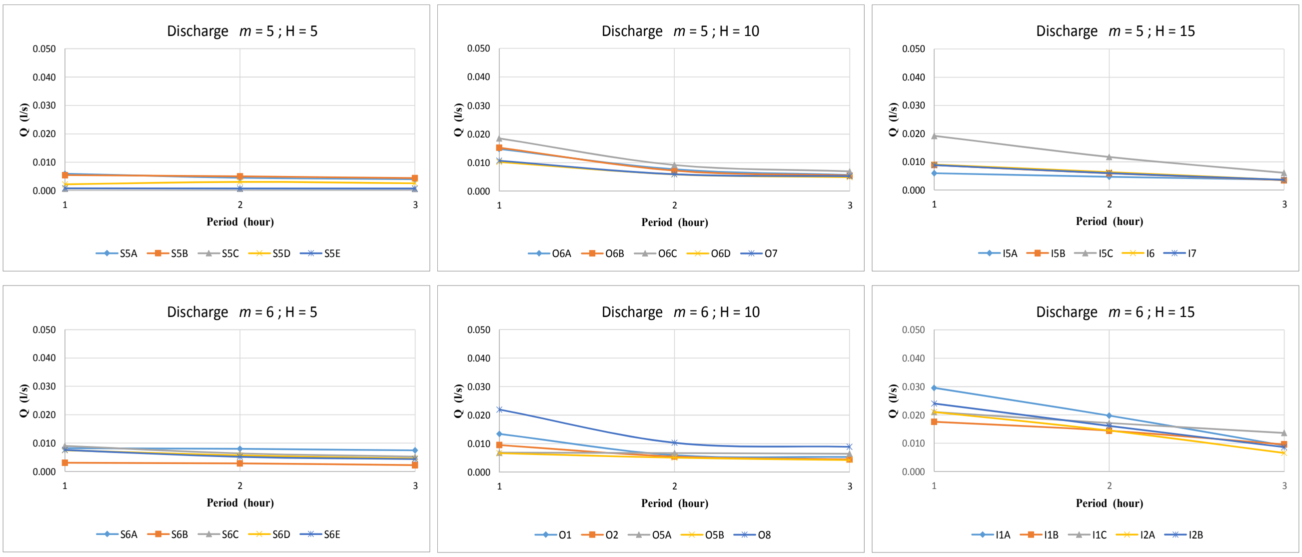

Figure 6. Filter Discharge (*m* = 5 and *m* = 6, with H = 5 cm, 10 cm, and 15 cm)

Table 1. Filter characteristics of the filtration discharge.

No.	Filter Characteristics	Period I average (l/s)	Period II average (l/s)	Period III average (l/s)
1	*m* = 3 ; H = 5 cm	0.043	0.032	0.022
2	*m* = 3 ; H = 10 cm	0.033	0.017	0.009
3	*m* = 3 ; H = 15 cm	0.011	0.006	0.005
4	*m* = 4 ; H = 5 cm	0.006	0.003	0.003
5	*m* = 4 ; H = 10 cm	0.012	0.009	0.007
6	*m* = 4 ; H = 15 cm	0.005	0.003	0.003
7	*m* = 5 ; H = 5 cm	0.003	0.003	0.002
8	*m* = 5 ; H = 10 cm	0.014	0.008	0.006
9	*m* = 5 ; H = 15 cm	0.013	0.008	0.005
10	*m* = 6 ; H = 5 cm	0.006	0.005	0.005
11	*m* = 6 ; H = 10 cm	0.014	0.008	0.007
12	*m* = 6 ; H = 15 cm	0.024	0.017	0.010

In general, the filtration discharge decreased in the second and third period. In the filter with *m* = 3, filter thickness effect on a decrease in discharge. The thicker the filter, the smaller the discharge. For filter with *m* = 4, *m* = 5, and *m* = 6, the thickness did not affect the decline of discharge.

The filter with *m* = 4, *m* = 5, and *m* = 6, with H = 10 cm and H = 15 cm, the effect of m to the discharge capacity of filtration is significant. The greater the value of m, the more porous filter, so that the discharge increases.

Discharge capacity remains small at H = 5 cm with a great value of *m* (m = 5 and *m* = 6). In addition to the influence of physical characteristics of filter, the discharge capacity of filtration is also strongly influenced by the quality of raw water sources, such as turbidity (Figure 7 and 8). Filter characteristics H = 5 cm, H = 10 cm, *m* = 5, and *m* = 6 could not filter turbidity (> 1 NTU).

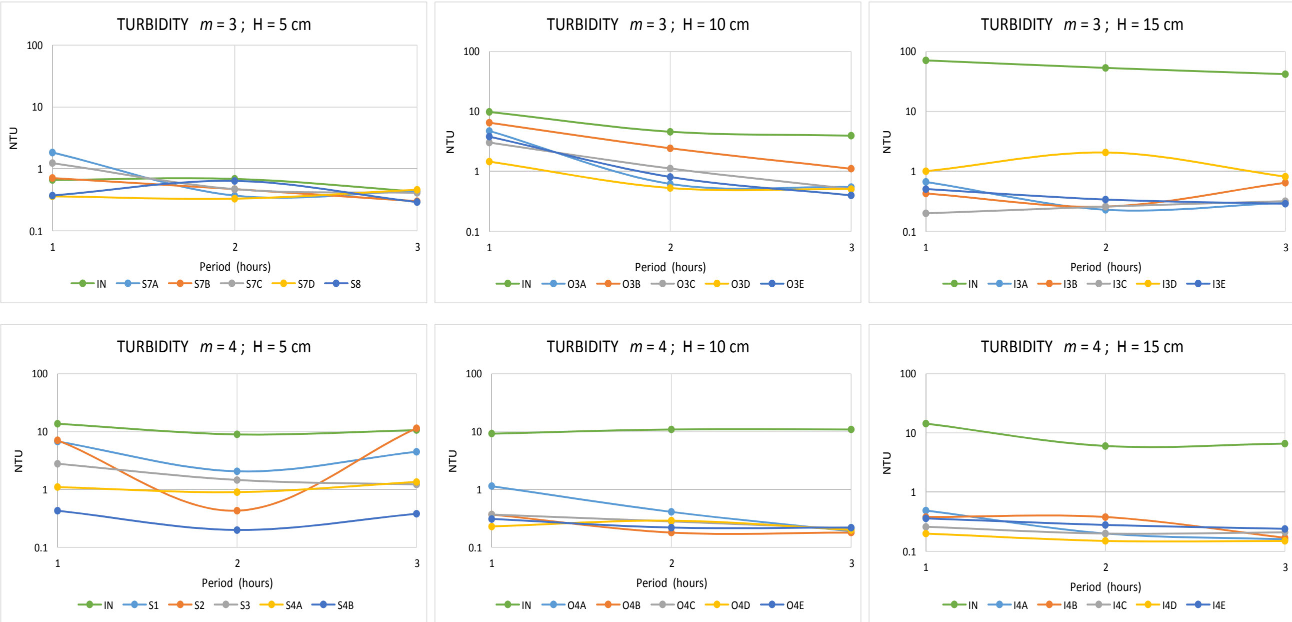

Figure 7. Turbidity Filter (*m* = 3 and *m* = 4, with H = 5 cm, 10 cm, and 15 cm)

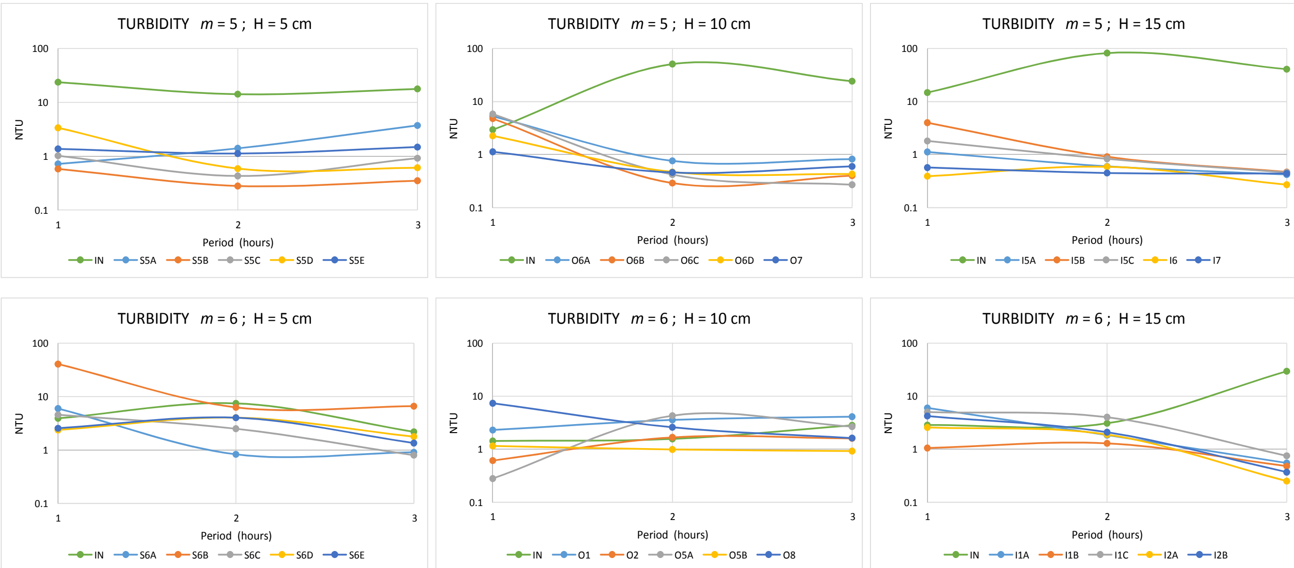

Figure 8. Turbidity Filter (*m* = 5 and *m* = 6, with H = 5 cm, 10 cm, and 15 cm)

4.2 Concrete Filter Performance

The study was conducted to determine the ability of the concrete filter in reducing turbidity (Table 2) and eliminate microbiological content in the water.

Table 2. Concrete Filter ability to Reduce Turbidity

No	**Filtrate Filter**	**Average Turbidity**			**No**	**Filtrate Filter**	**Average Turbidity**		
		Period I (NTU)	Period II (NTU)	Period III (NTU)			Period I (NTU)	Period II (NTU)	Period III (NTU)
1.	*m* = 3 ; H = 5 cm	0.90	0.46	0.38	7.	*m* = 5 ; H = 5 cm	1.41	0.76	1.42
2.	*m* = 3 ; H = 10 cm	3.91	1.10	0.62	8.	*m* = 5 ; H = 10 cm	3.85	0.48	0.50
3.	*m* = 3 ; H = 15 cm	0.56	0.63	0.48	9.	*m* = 5 ; H = 15 cm	1.58	0.68	0.41
4.	*m* = 4 ; H = 5 cm	3.63	1.01	3.79	10.	*m* = 6 ; H = 5 cm	11.23	3.54	2.29
5.	*m* = 4 ; H = 10 cm	0.48	0.28	0.20	11.	*m* = 6 ; H = 10 cm	2.34	2.62	2.18
6.	*m* = 4 ; H = 15 cm	0.34	0.24	0.19	12.	*m* = 6 ; H = 15 cm	3.78	2.22	0.48

 ©2017, IAHR. Used with permission / ISSN 1562-6865 (Online) - ISSN 1063-7710 (Print)

Concrete filters that reduce the turbidity to below 1 NTU is the filter characteristics: *m* = 3, with H = 15 cm and *m* = 4, with H = 15 cm.

The ability of the concrete filter in lowering the levels of microbiological water (Coliforms and E. Coli) is shown by Figure 9 and 10.

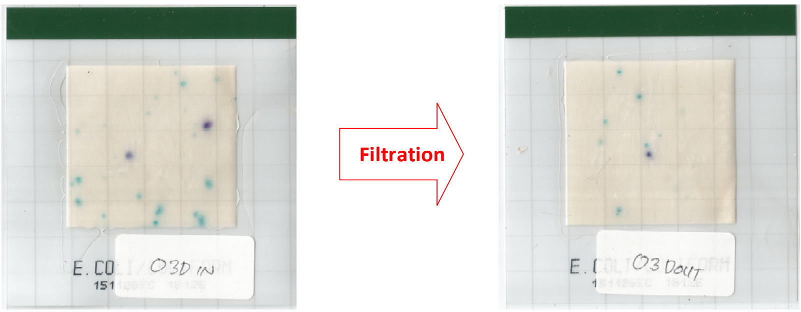

Input sample (IN)
The number of colonies (E. Coli) = 2 CFU
The number of colonies (Coliforms) = 17 CFU

Output sample (OUT)
The number of colonies (E. Coli) = 1 CFU
The number of colonies (Coliforms) = 7 CFU

Figure 9. Sample Results of Microbiology Test Kit Before (IN) and After Filtratition (OUT)

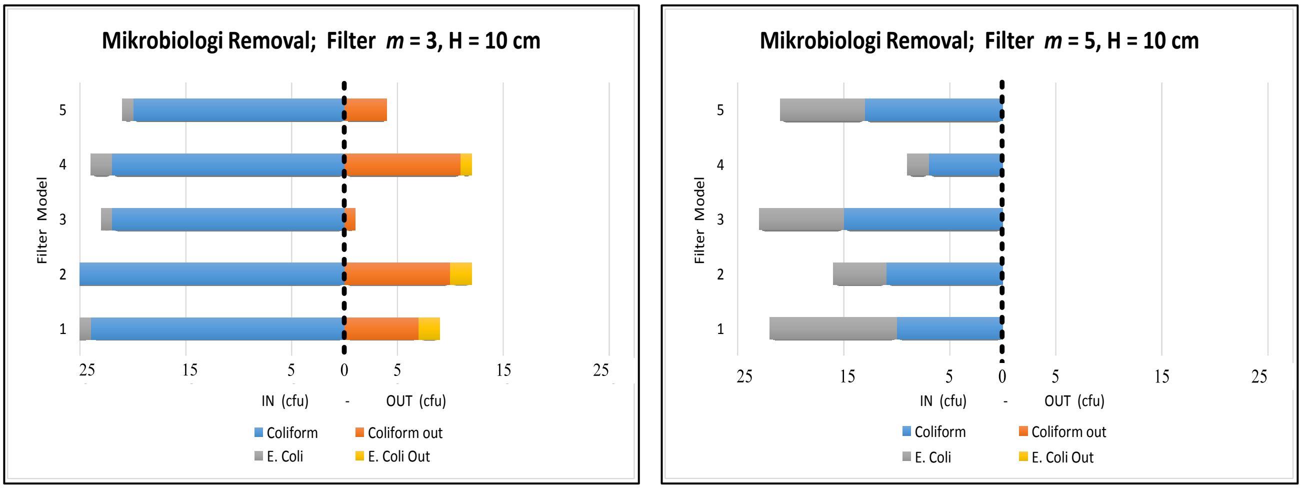

Figure 10. Mikrobiologi Removal (*m* = 3, and *m* = 5, with H = 10 cm)

Characteristics of filter that can filter out bacteria E. Coli and Coliform are:

i. *m* = 3 , H = 15 cm
ii. *m* = 4 , H = 10 cm
iii. *m* = 4 , H = 15 cm
iv. *m* = 5 , H = 5 cm
v. *m* = 5 , H = 10 cm
vi. *m* = 5 , H = 15 cm

Characteristics of concrete filters with thickness (H) = 5 cm generally cannot eliminate the bacterial content, while the filter *m* = 5 with H = 5 cm, 10 cm and 15 cm can eliminate the content of microbiological water possibly because of the sedimentation of particles (cake) and a layer of transparent film that formed on the surface of the filter, as shown in Figure 11.

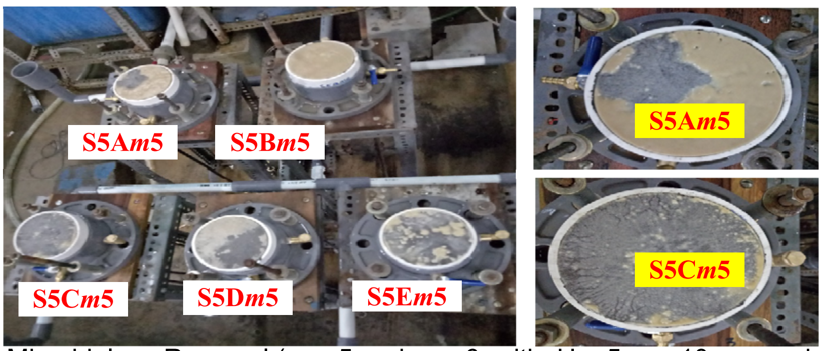

Figure 11. Microbiology Removal (*m* = 5 and *m* = 6, with H = 5 cm, 10 cm, and 15 cm)

Cake layer on the surface of filter *m* = 5 with H = 5 cm is composed of two different types of layers, especially on the filter S5Am5 and S5Cm5. Discharge filtration in the first period of S5Am5 = 0.006 l/s, while the S5Cm5 & S5Em5 = 0.001 l/s. The type of layer on the filter S5Am5 and S5Bm5 are dominant with a layer of thick brown (brown viscous) as the result of filtration filter *m* = 5 with H = 10 cm. Discharge mean filtration on filter (*m* = 5 with H = 10 cm) > 0:01 l/s. This means lining Brown Viscous increase filtration capacity. On the contrary, the transparent film layer clogs the bed filter (Figure 12).

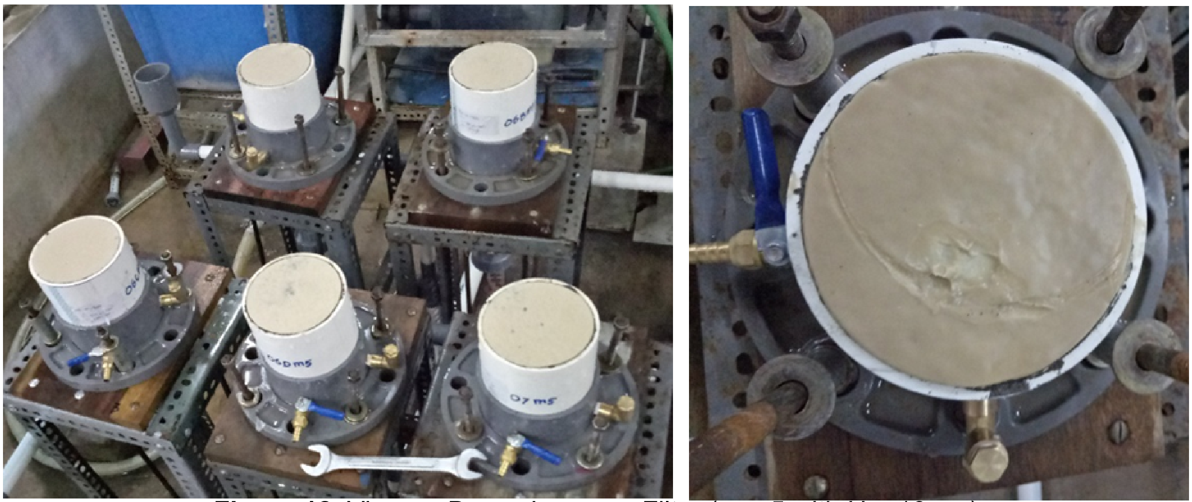

Figure 12. Viscous Brown Layer on Filter (*m* = 5 with H = 10 cm)

Surface biological mat or schmutzdecke, consist of algae, bacteria, and other microorganisms, including protozoa and rotifers. The main mass of schmutzdecke located on the surface of the filter, with a smaller amount of biomass that continue to be active in bed filter. Bacterial removal by the filter is also a function of population and the growth of living organisms in the schmutzdecke. Type of algae present in schmutzdecke has proved critical to the performance of the filter. If filamentous algae were dominant in the filter, then the biological mat with high tensile strength will be formed. The result is a decrease in biological mat buoyancy, increased filtration rate, and decreased resistance to flow. Filamentous algae (moss) has the ability to stick to the surface of the filter and translocate nutrients (McNair, et al., 1987).

The phenomenon of the coating on the surface of Filter Concrete as happened in filtration Slow Sand Filter, known as Schmutzdecke. Moss also greatly increase the specific surface area of the filter by extending the capabilities of sorptive and interceptive of bed filter above the water-filter interface upward to the top of the moss. The specific increase on the bed surface improve particle removal efficiency. Conversely, if a small unicellular algae were dominant at schmutzdecke, however, the resistance of the filter schmutzdecke increased, resulting in rapid clogging of the bed filters and rapid rate decline of filtration. Therefore, the type of algae (filamentous or unicellular) which is in schmutzdecke affect filter performance and long filtration cycles. Before filtration rate decreased significantly, the surface of the filter should be cleaned or scraped.

5 CONCLUSIONS

Concrete filter with *m* = 4 and H = 15 cm typically satisfy the requirement for producing drinking water that has turbidity of level of less than 1 NTU, with CFU of zero.

ACKNOWLEDGEMENTS

The research was fully funded by Lembaga Pengelolaan Dana Pendidikan (LPDP) Kementerian Keuangan Republik Indonesia via Scholarship of Indonesia Education (BPI Afirmasi). We would like to express our sincere gratitude for The Hydraulic Laboratory of Civil and Environmental Engineering Department, Faculty of Engineering, Universitas Gadjah Mada is acknowledged for its support throughout the research.

REFERENCES

Crittenden J.C., Trussell R.R., Hand D.W., Howe K.J. & Tchobanoglous G. (2012). *MWH's Water Treatment : Principles and Design*. Third Edition, MWH, John Wiley & Sons, Inc. Book, Chapter 11.

Kamulyan, B. (2014). Karakteristik Hidraulik Filtrasi dan Cucibalik Filter Beton, *Dissertation*. Universitas Gadjah Mada, Yogyakarta.

Kardiyono, T. (2007), *Teknologi Beton*, Biro Penerbit Teknik Sipil dan Lingkungan Universitas Gadjah Mada, Yogyakarta.

 ©2017, IAHR. Used with permission / ISSN 1562-6865 (Online) - ISSN 1063-7710 (Print)

Maadji, R., R.Triatmadja, F.Nurrochmad & Sunjoto (2016). The Development of Concrete Filter for Drinking Water Filtration, *Proceeding of the International Seminar on Water Resilience in a Changing World*, Bali, Indonesia, July 29th – 31st, 2016, Indonesian Association of Hydraulic Engineers, 648 – 658 pp.

Maadji, R., R.Triatmadja, F.Nurrochmad & Sunjoto (2016). Reduksi Bakteri *E. Coli* dalam Filtrasi Filter Beton untuk Air Minum, Presented in *Pertemuan Ilmiah Tahunan PIT XXXIII & Kongres XII HATHI*, Indonesian Association of Hydraulic Engineers, Nov 25th – 27th, 2016, Semarang, Indonesia.

McNair, D.R., Ronald, C., Sims, D.L., Sorensen & Matthew, H. (1987). Schmutzdecke Characterization of Clinoptilolite-Amended Slow Sand Filtration. *Journal (American Water Works Association) with JSTOR*, 79(12), 74-81.

Murdock, L.J. & Brook, K.M. (1999). *Concrete Materials and Practice* (Indonesian version). Penerbit Erlangga, Jakarta, Indonesia, Book, Chapter 4.

Purchas, B.D. & Sutherland K., (2002), *Handbook of Filter Media.* Elsevier Science & Technology Books, Book, Chapter 1.

Reece, J.B., Lisa, A., Michael, L.C., Steven, A.W., Peter, V.M. & Robert, B.J. (2014). *Campbell Biology*, tenth edition, Pearson, Book, Chapter 27.

Shetty, M. S. (2005). *Concrete Technology: Theory and Practice*. Multicolour Illustrative Edition, S. Chand & Company Ltd., New Delhi.

Tallon, P., Magajna, B., Lofranco, C. & Leung T.K. (2005). Microbial Indicators of Faecal Contamination in Water: A Current Perspective. *Water, Air, and Soil Pollution*, 166,139-166.

Triatmadja, R. (2008). Kajian Awal Prospek Filter Beton Pasir sebagai Teknologi Tepat Filtrasi Air Bersih, *Prosiding Seminar Nasional Teknologi Tepat Guna Penanganan Sarana Prasarana.*Indonesia.

World Health Organization (WHO) (2004). *Guidelines for Drinking-water Quality*, Third Edition, Volume 1 Recommendations, Geneva.

INCEPTION POINT FOR DIFFERENT CONFIGURATION ON MODELING OF STEPPED SPILLWAYS

DENIK SRI KRISNAYANTI[(1)], VERY DERMAWAN[(2)], MOH. SHOLICHIN[(3)] & DIAN SISINGGIH[(4)]

[(1)] Department of Civil Engineering, Nusa Cendana University, Kupang, East Nusa Tenggara, Indonesia,
denik.krisnayanti@gmail.com
[(2,3,4)] Department of Water Resources, Brawijaya University, Malang, East Java, Indonesia,
veryderma@yahoo.com; sholichin67@gmail.com; suikoken@gmail.com

ABSTRACT

An investigation has been made to predict the location of the inception point of the air entrainment over the stepped spillways by assuming the different configurations steps on the spillways as a kind of roughness. The physical model is constructed with a broad-crested weir, step heights of 25, 50, 100 mm, and Froude numbers ranging from 0.795 to 8.694. The configurations of steps are flat steps and pooled steps. A new relationship for predicting the location of the inception point is developed, applicable for slope of 30˚ stepped spillways. This relationship is similar to Chanson's, but it is optimized for flat stepped and pooled stepped with a broad-crested weir.

Keywords: Inception point; flat steps; pooled steps.

1 INTRODUCTION

The main purpose of the stepped spillway is energy dissipation by air inception and internal friction of the flow. In comparison with smooth spillways, the flow velocity is reduced and the high aeration of the flow changes the characteristics of the flow. Stepped spillways have gained popularity over the last two decades with the evolution of the roller-compacted concrete (RCC) dam-construction technique.

Advantages of stepped spillways include ease of construction, reduction of cavitation risk potential, and reduction of the stilling-basin dimensions at the downstream toe due to significant energy dissipation along the chute. The flow leaves the stepped chute at the lower velocity and a smaller energy dissipate are required (Chinnarasri et al., 2004).

Flow over a stepped spillway can be divided into three separate flow regimes, namely nappe, transition, and skimming flows. Nappe flow occurs for small discharges. There are three types of nappe flows which are nappe flow with fully developed hydraulic jump, nappe flow with partially developed hydraulic jump, and nappe flow without hydraulic jump. Transition flows occurs for intermediate discharges. Skimming flow occurs if the depth of flow is sufficiently large when compared to the step height on a relatively steep stepped spillway. Modern stepped spillways are designed to operate with skimming flow regime. Schematic representations of three regimes are shown in Figure 1.

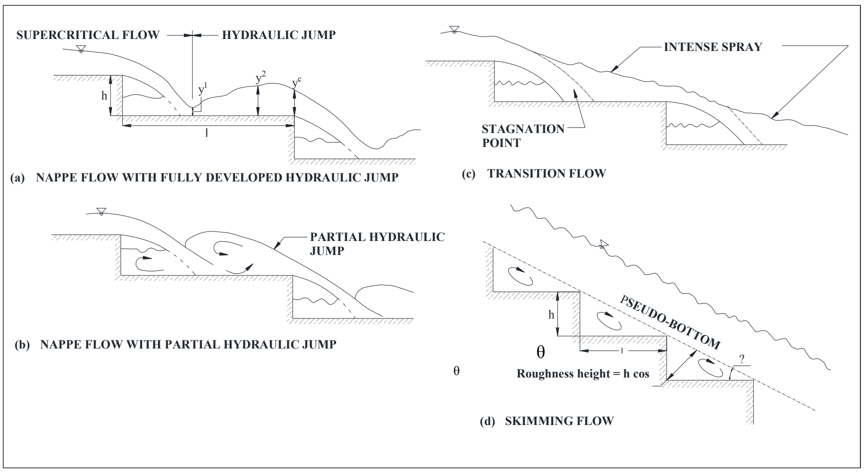

Figure 1. Flow regime on stepped spillway

Energy dissipation in skimming flow condition can be observed from the inception point of aeration where the turbulent boundary layer reaches the free surface. The inception point of air entrainment characterized by changes the water upstream without aeration (non-aerated flow region), then towards the aerated flow region.

 ©2017, IAHR. Used with permission / ISSN 1562-6865 (Online) - ISSN 1063-7710 (Print)

It can be observed from appearance of white bubbles on the surface of the flow. The inception point of air entrainment is important for determining design parameters for training walls and stilling basins (Hunt et.al., 2009).

The scope of this research is to 1) examine the observed inception point location on the differences configurations of stepped spillway, 2) evaluate the effect step height against the inception point of the air entrainment, 3) evaluate the effect of additional sill on the edge of steps against the inception point of the air entrainment, and 4) determine the inception point empirical relationships developed from Chanson's formula.

1.1 Air Entrainment on Stepped Chutes

Air entrainment occurs on stepped spillways for skimming flow regime, when the turbulent boundary layer appears at the free surface. This process is similar to that on the smooth spillways, with flow regimes characterized by non-aerated, gradually varied, and uniform flow. Air entrainment increases the bulk flow depth, and this is used as a design parameter for the training walls. Also, the presence of air within the boundary layer reduces the shear stress between the flow layers and hence the shear force. The resulting drag reduction reduces the energy dissipation above the spillway and hence its efficiency (Chanson, 1993). The changes in flow region on stepped spillway for skimming flow conditions can be seen in Figure 2.

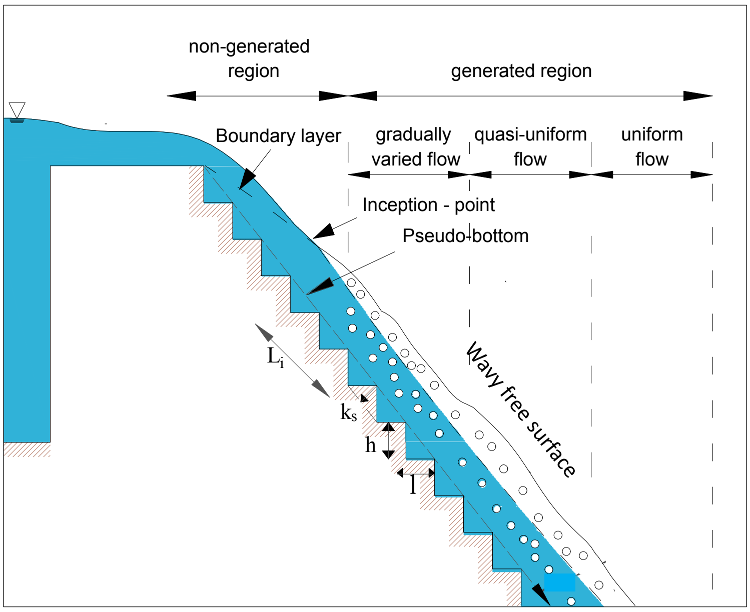

Figure 2. The inception point in skimming flow over stepped spillway

In calculations of air entrainment on stepped chutes, the pseudo-bottom formed by the external edges of steps is taken as the chute invert profile and the parameter (h cos θ) is the surface roughness, instead of the usual sand grain roughness ks as in the case of smooth spillways (Khatsuria, 2005).

1.2 Location of the Inception Point

Based on the theory of boundary layer, it showed that the flow properties at the inception point in smooth spillways can be calculated using the formula (Wood et al., 1983):

$$L_i = 13.6(\sin\theta)^{0.0796}(F_h)^{0.713}k_s \qquad [1]$$

Where L_i = distance from the downstream edge of the broad-crested weir to the inception point, θ = channel slope, F_h = Froude number defined in terms of the roughness height: $F_h = q \,/\, \sqrt{g(\sin\theta)k_s^3}$ with q = unit discharge, g = acceleration due to gravity, k_s = the surface roughness.

This relationship covered a range of chute slopes, roughness, and discharges. The relationship was later enhanced by Chanson (1994b; 2002) for application in stepped spillways gave:

$$L_i = 9.719(\sin\theta)^{0.0796}(F_h)^{0.713}k_s\,. \qquad [2]$$

The difference between the relationship developed by Wood et al. (1983) and Chanson (2002) is that Chanson's relationship takes into account step height within the step roughness term (ks = h cos θ and h = step height). Equation [2] is applicable for stepped spillways having ogee crested weirs, with $1 \le F_h \le 100$, and channel slope of θ ≥ 27˚. Chanson (1994b) further improved his relationship by conducting a sensitivity analysis such that the coefficient 13.6 in Wood et al. (1983) relationship changed to 9.719. Different interpretations of the inception point location may be the reason for scatter diagram observed in data presented by Chanson (1994b; 2002).

Chamani (2000) found that his observation agreed well with Equation [2] and modified as:

$$L_i = 8.29(F_i)^{0.85} k_s . \quad [3]$$

Where F_i = inception Froude number: $F_i = q / \sqrt{g(h/l)k_s^3}$. Like Equation [2], Chamani's relationship (2000) is based on steep stepped chutes model with channel slope of 51.3˚ ≤ θ ≤ 59˚.

Boes and Hager (2003b) used some of the same data as Chanson (1994b; 2002) and modified for stepped spillways with channel slope of 26˚ < θ < 75˚:

$$L_i = 5.90(\cos\theta)^{0.20}(\sin\theta)^{-1} F_h^{\,0.80} k_s . \quad [4]$$

The major difference between Equation [4] and Equation [2] is the definition of inception point. Chanson (1994b) defined the inception point as the location where the turbulent boundary layer reaches the free surface whereas Boes et al. (2003b) defined the inception point as the location where the air concentration on the pseudo bottom of the chute is approximately 1%.

Hunt and Kadavy (2011) supported the theory Boes et al. (2003b) that the turbulence appears on the free surface where air concentration reaches 1% at the pseudo bottom of the chute for stepped spillways with channel slope of 14˚. The results of modification relationship Hunt et al. (2011) as:

$$L_i = 6.10(\sin\theta)^{0.08}(\sin\theta)^{-1} F_h^{\,0.86} k_s . \quad [5]$$

The difference between Equation [5] and Equation [2] is the result of θ, h, and/or type of crest. Whereas Hunt et al. (2011) uses stepped spillway having a broad crested weir and Chanson (1994b) uses ogee weir.
The relationships developed by Chanson (1994b), Chamani (2000), Boes et al. (2003b) were developed for steep chute slope (θ ≥ 27˚), the relationships by Hunt et al. (2011) were developed for flatter stepped spillway.

2 EXPERIMENTAL SETUP

The model tests were carried out in a recirculating flume located at the hydraulic laboratory of Water Resources Engineering Department, Brawijaya University, Indonesia. Figure 3 illustrates the schematic of 2D model used during testing. Water was pumped from reservoir to upstream tank and flow to the Rehbock measurement and water entered the stepped channel through stilling tank. The stepped spillways are made of acrylic having thickness of 0.01 m and side walls with height of 0.6 m. The flume is 0.5 m wide and 7.0 m length spillway model.

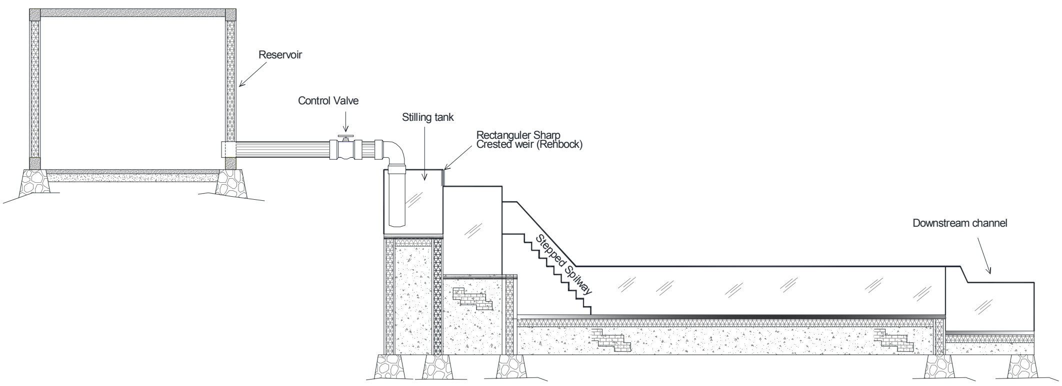

Figure 3. Experimental setup for stepped spillway model

The depth across of channel is measured by a point gauge. The velocity is measured by two methods, first by a pitot tube and second by calculating discharge flow on the Rehbock measurement. The inception point was recorded by photographically, by definition that the inception point distance (L_i) is calculated from the downstream edge of the spillway crest to the point where white water appears on the free surface as illustrated in Figure 4.

 ©2017, IAHR. Used with permission / ISSN 1562-6865 (Online) - ISSN 1063-7710 (Print)

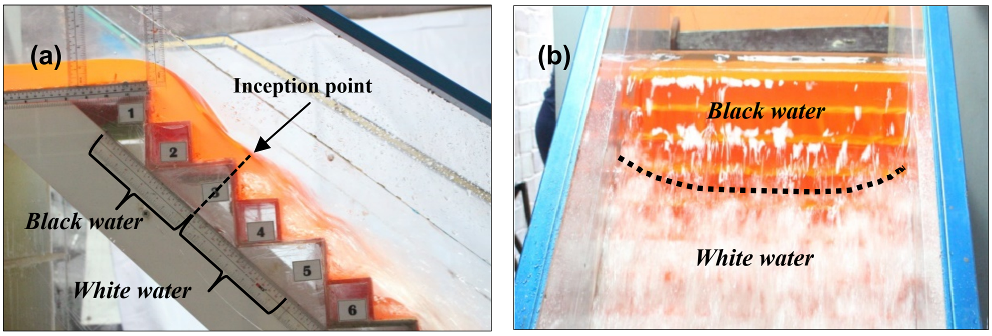

Figure 4. The visual observation of inception point for stepped spillway (a) side view and (b) front view (θ = 45˚, h= 50 mm, Q = 12.510 l/s)

In Figure 4(b), flow over on crest spillway having a smooth flow and glossy appearance. The boundary layer grows from the spillway chute in the non-aerated region close to the spillway crest. The water surface becomes undulating pattern from the inception of air entrainment transporting air between the irregular waves in the undulating surface. At the inception point, where the boundary layer reaches the free surface, air entrainment by the multitude of vortices in the turbulent commences (Frizell, 2006).

The slope of the stepped spillway (θ) is 30˚ with number of steps 10, 20, and 40, respectively. The discharge varied from 3.457 – 30.669 l/s, the Froude number range (0.980< Fr < 8.694) and was measured by the Rehbock weir tank. Two types of step were tested in the study, that is, flat and pooled steps. The dimensions of the step can be defined as h/l, where h = step height and l = horizontal length. For the case of pooled steps, the characteristic height (m) of end sill were 15 mm for number step (N) = 10, 7.5 mm for N = 20 and 3.75 mm for N = 40. Further details on the experimental configurations are illustrated in Figure 5. To investigate the effect of macro-roughness on stepped spillway to value of the inception point are shown in Fig. 6.

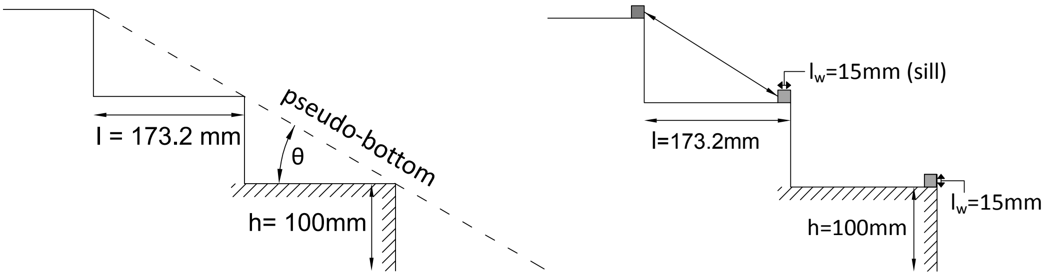

Figure 5. Sketch of the tested stepped macro-roughness: conventional steps and steps with end sills

No	y_c (cm)	h (cm)	q (cm^2/s)	k_s (cm)	v (m/s)	F_h
1	2	3	4	5	6	7
θ = 30˚ ; N = 40 steps						
1	1.750	2.500	69.135	2.165	0.395	0.980
2	1.850	2.500	75.144	2.165	0.406	1.065
3	2.000	2.500	84.466	2.165	0.422	1.197
4	2.125	2.500	92.507	2.165	0.435	1.311
5	2.187	2.500	96.585	2.165	0.442	1.369
6	3.500	2.500	195.542	2.165	0.559	2.771
7	4.000	2.500	238.907	2.165	0.597	3.386
8	4.250	2.500	261.650	2.165	0.616	3.708
9	7.000	2.500	553.077	2.165	0.790	7.839
10	7.500	2.500	613.381	2.165	0.818	8.694

No	y_c (cm)	h (cm)	q (cm^2/s)	k_s (cm)	v (m/s)	F_h
1	2	3	4	5	6	7
θ = 30˚ ; N = 20 steps						
1	3.500	5.000	195.542	4.330	0.559	0.980
2	3.750	5.000	216.863	4.330	0.578	1.087
3	4.000	5.000	238.907	4.330	0.597	1.197
4	4.125	5.000	250.192	4.330	0.607	1.254
5	4.250	5.000	261.650	4.330	0.616	1.311
6	4.375	5.000	273.278	4.330	0.625	1.369
7	7.000	5.000	553.077	4.330	0.790	2.771
8	7.500	5.000	613.381	4.330	0.818	3.074
θ = 30˚ ; N = 10 steps						
1	7.000	10.000	553.077	8.660	0.790	0.980
2	7.500	10.000	613.381	8.660	0.818	1.087
3	8.000	10.000	675.730	8.660	0.845	1.197
4	8.250	10.000	707.651	8.660	0.858	1.254

Figure 6. Data of critical depth (y_c), step height (h), unit discharge (q), surface roughness (k_s), velocity (v), and Froude number (F_h)

©2017, IAHR. Used with permission / ISSN 1562-6865 (Online) - ISSN 1063-7710 (Print)

3 RESULTS AND DISCUSSION

The distance of inception point is done by measurement and theory analyzing from previous researcher as shown in Figure 7. Empirical equations of stepped spillway model from previous researchers are compared with Wood's equation on smooth spillway θ = 50˚.

No	q (cm^2/s)	k_s (cm)		F_h		L_i (cm)											
						Observed		The calculation of theoritical formula									
						Krisnayanti (2016)		Chanson (1994b)		Chamani (2000)		Matos (2000)		Boes et al. (2000b)		Boes et al.(2003b)	
		Flat	Pooled	Flat	Pooled	Flat	Pooled	Flat	Pooled	Flat	Pooled	Flat	Pooled	Flat	Pooled	Flat	Pooled
1	2	3	4	5	6	7	8	9	10	11	12	13	14	15	16	17	18
N = 40																	
1	69.135	2.165	2.490	0.980	0.795	13.775	14.167	19.626	13.800	12.997	12.507	8.878	10.210	20.680	19.858	25.372	25.372
2	75.144	2.165	2.490	1.065	0.864	14.333	18.400	20.828	14.645	13.951	13.425	9.438	10.854	22.216	21.334	27.121	27.121
3	84.466	2.165	2.490	1.197	0.971	18.700	23.700	22.639	15.918	15.409	14.828	10.284	11.827	24.567	23.591	29.781	29.781
4	92.507	2.165	2.490	1.311	1.063	23.450	23.700	24.155	16.985	16.648	16.020	10.994	12.643	26.565	25.510	32.029	32.029
5	96.585	2.165	2.490	1.369	1.110	24.233	28.600	24.910	17.515	17.269	16.618	11.348	13.050	27.569	26.474	33.153	33.153
6	195.542	2.165	2.490	2.771	2.247	33.500	34.100	41.189	28.962	31.452	30.267	19.044	21.900	50.568	48.559	58.289	58.289
7	238.907	2.165	2.490	3.386	2.746	44.300	44.000	47.513	33.408	37.290	35.884	22.060	25.369	60.073	57.687	68.419	68.419
8	261.650	2.165	2.490	3.708	3.007	44.400	44.233	50.695	35.646	40.287	38.768	23.582	27.120	64.960	62.380	73.582	73.582
9	553.077	2.165	2.490	7.839	6.356	94.500	106.000	86.445	60.782	76.115	73.245	40.849	46.976	123.652	118.740	133.913	133.913
10	613.381	2.165	2.490	8.694	7.049	108.250	106.500	93.064	65.437	83.113	79.980	44.073	50.684	135.161	129.793	145.472	145.472
N = 20																	
1	195.542	4.330	4.980	0.980	0.795	17.725	29.075	39.252	27.600	19.361	18.631	17.756	20.419	41.359	39.716	50.744	50.744
2	216.863	4.330	4.980	1.087	0.881	18.300	37.750	42.258	29.713	21.142	20.344	19.157	22.031	45.209	43.413	55.124	55.124
3	238.907	4.330	4.980	1.197	0.971	28.780	38.750	45.278	31.836	22.955	22.089	20.568	23.653	49.134	47.182	59.562	59.562
4	250.192	4.330	4.980	1.254	1.017	29.350	38.750	46.793	32.902	23.873	22.973	21.277	24.468	51.124	49.093	61.803	61.803
5	261.650	4.330	4.980	1.311	1.063	37.500	47.625	48.311	33.969	24.799	23.864	21.988	25.286	53.131	51.020	64.057	64.057
6	273.278	4.330	4.980	1.369	1.110	38.750	37.500	49.832	35.039	25.733	24.763	22.701	26.106	55.155	52.964	66.324	66.324
7	553.077	4.330	4.980	2.771	2.247	52.750	77.000	82.379	57.923	46.854	45.087	38.087	43.800	101.135	97.118	116.578	116.578
8	613.381	4.330	4.980	3.074	2.492	68.750	87.000	88.687	62.359	51.162	49.233	41.093	47.257	110.549	106.158	126.641	126.641
N = 10																	
1	553.077	8.660	9.959	0.980	0.795	43.750	55.520	78.504	55.199	28.842	27.755	35.512	40.839	82.719	79.433	101.487	101.487
2	613.381	8.660	9.959	1.087	0.881	53.750	56.980	84.516	59.426	31.494	30.307	38.315	44.062	90.418	86.827	110.247	110.247
3	675.730	8.660	9.959	1.197	0.971	56.250	58.700	90.556	63.673	34.195	32.906	41.136	47.307	98.268	94.365	119.125	119.125
4	707.651	8.660	9.959	1.254	1.017	56.750	70.700	93.586	65.803	35.563	34.223	42.554	48.937	102.247	98.186	123.606	123.606

Figure 7. Summary of unit discharge (q), surface roughness (k_s), Froude number (F_h), inception point (L_i)

Based on Figure 7, Li increases as q increases for the same tested flows. This implies that the location of inception point moves toward downstream with increasing discharge. Figure 7 is illustrated in the graph shown in Figure 6. It was found that the ratio (L_i/k_s) on a smooth spillway greater than (L_i/k_s) on stepped spillway. This suggests that stepped spillway provides the shortest distance to the inception point compared to a smooth spillway. So that dissipation energy of stepped spillway is greater than smooth spillway.

Figure 8 also shows the difference of the empirical formula for flat stepped based on visual observations of some previous researchers, particularly for the large discharge. For q = 261.650 cm^2/s on the number step 40 is obtained relative difference of calculated value between Chamani and Matos amounted to 41.46%. Hence, there are no objective criteria for determining the inception point. It can also be observed that steps of chute spillway causing the inception point moved closer on spillway crest.

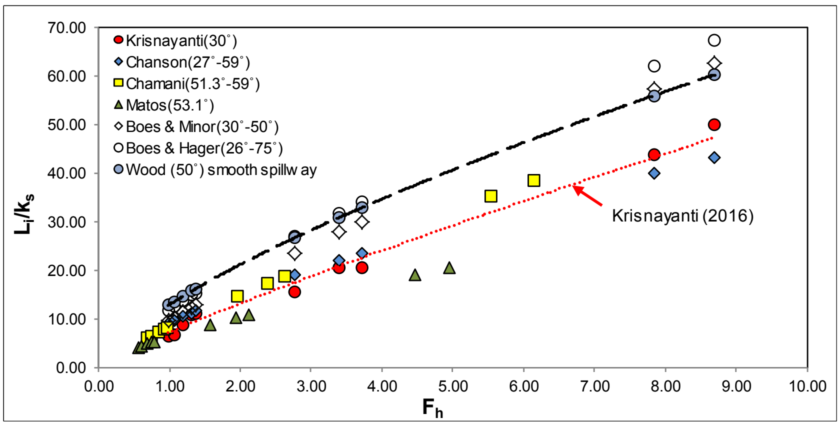

Figure 8. The comparison location of inception point on flat stepped with previous researchers

©2017, IAHR. Used with permission / ISSN 1562-6865 (Online) - ISSN 1063-7710 (Print)

The result of data analysis for pooled steps with N = 40 illustrated in Figure 9. The empirical formula of Alghazali (2014) has a large deviation with the measurement model is approximately 61.76%. While the smallest deviation of the formula Boes et al. (2000b) is 20.41%.

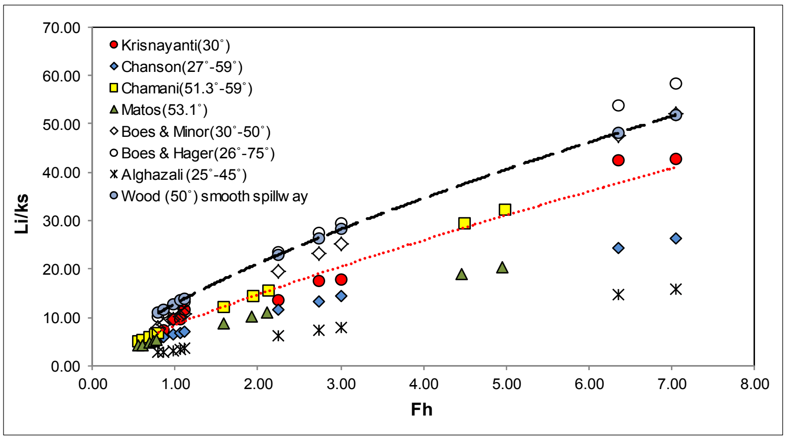

Figure 9. The comparison of the ratio (L_i/k_s) as a function of the Froude number (F_h) on pooled stepped

Deviations between this physical model and empirical formula of Alghazali (2014) could be due to slope angle (θ) of stepped spillway, the discharge per unit width (q) and the difference of number step (N). The difference of number step influence on height of step (h) and it would affect surface roughness (k_s) of stepped spillway.

The comparison of inception point between flat steps and pooled steps are illustrated in Figure 10.

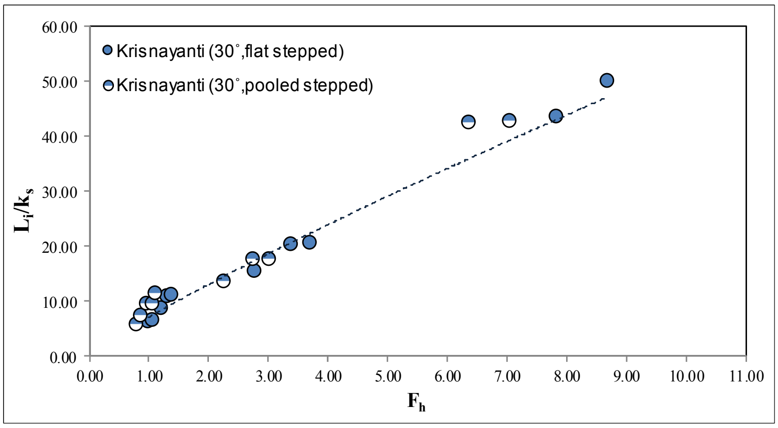

Figure 10. The comparison location of inception point between flat steps and pooled steps

Figure 10 shows the pooled stepped have a ratio (L_i/k_s) almost coincide with data of the flat stepped spillway. Although, the designs with configurations pooled steps did not provide any advantageous performances in terms of inception point. The instability of flow on pooled steps were in-stationary/ three dimensional pattern and associated with some strong splashing have influence on measurement of distance inception point.

The data in Figure 7 were further examined to determine if a new relationship could be developed to more accurately predict L_i when θ = 30˚ and 0.980≤F_h≤8.694 on flat steps, 0.795≤F_h≤7.049 on pooled steps. The modification empirical equations for the location of air inception point for flat steps and pooled steps for the slope angles 30° in Figure 11.

Equation [2] was modified such that: (1) the exponent to sin (θ) was held constant at 0.0796; (2) the exponent 0.713 of F_h was replaced by 0.98 on flat steps and 0.88 on pooled steps; (3) the value of constant 9.719 changed for consistency with Equation [2] be 6.144 on flat steps and 8.056 on pooled steps. The differences between Equation [2] and [6] could be a result of slope of channel (θ), step height (h), number step (N), and the type of crest.

If the result of the Equation [6] is compared to [5], there is a very small deviation, which is only about 0.01 at a constant value and 0.16 on the value of the Froude number (F_h). This is because of the similarity of crest type (broad-crested). The differences between Hunt et al. (2011) and this research are slope of channel (θ), step height (h) and number step (N). The new relationship for flat stepped have closest value with Hunt's formula (2011), so it could be used to further analysis on the same boundary of stepped spillway.

Angle of Channel	Type of Stepped	The formulation of measurement results		Suggested Formula	
1	2	3	4	5	6
Number Step		L_i/k_s	R^2	Converted from Chanson's Formula	R^2
N = 40					
30˚	flat steps	$\frac{L_i}{k_s} = 7.1565(F_h)^{0.872}$	0.975	$\frac{L_i}{k_s} = 7.5577(\sin\theta)^{0.0796}(F_h)^{0.872}$	1.000
30˚	pooled steps	$\frac{L_i}{k_s} = 8.4156(F_h)^{0.8133}$	0.954	$\frac{L_i}{k_s} = 8.8873(\sin\theta)^{0.0796}(F_h)^{0.8133}$	1.000
N = 20					
30˚	flat steps	$\frac{L_i}{k_s} = 5.122(F_h)^{1.0277}$	0.825	$\frac{L_i}{k_s} = 5.4125(\sin\theta)^{0.0796}(F_h)^{0.9723}$	1.000
30˚	pooled steps	$\frac{L_i}{k_s} = 7.8179(F_h)^{0.8677}$	0.947	$\frac{L_i}{k_s} = 8.2614(\sin\theta)^{0.0796}(F_h)^{0.8677}$	1.000
N = 10					
30˚	flat steps	$\frac{L_i}{k_s} = 5.3544(F_h)^{1.0336}$	0.860	$\frac{L_i}{k_s} = 5.6581(\sin\theta)^{0.0796}(F_h)^{1.0336}$	1.000
30˚	pooled steps	$\frac{L_i}{k_s} = 6.5117(F_h)^{0.8603}$	0.647	$\frac{L_i}{k_s} = 6.8811(\sin\theta)^{0.0796}(F_h)^{0.8063}$	1.000

Figure 11. Suggested empirical equations (L_i/k_s) for angle of slope θ = 30˚

The modification result for all of number step on stepped spillway is given:

$$L_i = 6.114(\sin\theta)^{0.0796}(F_h)^{0.98}k_s\text{, for flat steps } \theta = 30^\circ \qquad [6]$$

and,

$$L_i = 8.056(\sin\theta)^{0.0796}(F_h)^{0.88}k_s\text{, for pooled steps } \theta = 30^\circ [7]$$

Equation [7] has a constant value is higher than the Equations [6]. This shows that the value of length inception point (L_i) on pooled steps has a tendency smaller than the flat stepped type. It means the location of inception point (L_i/k_s) getting closer to crest of stepped spillway. But, the use of step with sill or pooled steps needs to be further evaluated to apply in the practically.

4 CONCLUSIONS

It can be concluded that for the same model test, the location of air inception point moves downstream as the discharge (q) increases. For the same discharge, the location of air inception point is closer to the crest for larger step heights (h). The location of air inception point is closer to the crest in pooled stepped compared with flat stepped. Research showed that Chanson's relationship, Equation [2] effectively forecast L_i for θ = 30˚, F_h < 10, and different configuration of stepped spillway. This model study was constructed with a broad-crested weir, step heights of 25, 50, 100 mm, and Froude numbers ranging from 0.795 to 8.694. Equation [6] and [7], for predicting the location of air inception point on stepped spillway with have the boundary models like as this research. The air inception point in the limits of this study especially on flat stepped showed that Hunt's relationship results (2011) were the closest to the experimental results. For pooled stepped shown the value of length inception point (Li) has a tendency smaller than the flat stepped type. It means the location of inception point (L_i/k_s) getting closer to crest of stepped spillway. But, the use of step with sill or pooled steps needs to be further evaluated to apply in the practically.

ACKNOWLEDGEMENTS

The authors thank to Suhardjono (Brawijaya University) and Djoko Legono (Gadjah Mada University) for their support and advice in this research. The first writer acknowledges with thanks to The Ministry of Technology Research and Higher Education for scholarship of domestic graduate program (BPPDN) in the financial support of this research.

 ©2017, IAHR. Used with permission / ISSN 1562-6865 (Online) - ISSN 1063-7710 (Print)

REFERENCES

Alghazali, N.O., & Jasim, S. M. (2014). Location of Air Inception Point for Different Configurations of Stepped Spillways. *International Journal of Civil Engineering and Technology*, 5(4), 82-90.

Boes, R. M. &Hager, W. H. (2003b). Hydraulic Design of Stepped Spillways. *Journal of Hydraulic Engineering*, 129(9), 671 - 679.

Boes, R. & Minor, H. (2000b). Guidelines for The Hydraulic Design of Stepped Spillways. *Proc. Int. Workshop on Hydraulics of Stepped Spillways* (pp. 163 - 170). Balkema, Rotterdam: VAW, ETH Zurich, Minor, H.E., and Hager, W.H. (eds).

Chamani, M. (2000). *Air Inception in Skimming Flow Regime Over Stepped Spillways*, International Workshop on Hydr of Stepped Spillways. Balkema, Rotterdam: © Swets & Zeitlinger.

Chanson, H. (1993). Stepped Spillway Flows and Air Entrainment. *Canada Journal of Civil Engineering*, 422-435.

Chanson, H. (1994b). Hydraulics of Skimming Flows Over Stepped Channels and Spillways. *Journal of Hydraulic Researh*, 32(3), 445 - 460.

Chanson, H. (2002). *The Hydraulics of Stepped Chutes and Spillways*.

Chinnarasri, C. & Wongwises, S. (2004). Flow Regimes and Energy Loss on Chutes with Upward Inclined Steps. *Canada Journal of Civil Engineering*, 31, 870 - 879.

Frizell, K.H. (2006). *Research State-of-the-Art and Needs for Hydraulic Design as Stepped Spillways*, Denver, Colorado: U.S. Department of the Interior Bureau Reclamation, Technical Service Center, Water Resources Researh Laboratory.

Guenther, P., Felder, S. & Chanson, H. (2013). Flow Aeration, Cavity Processes and Energy Dissipation on Fat and Pooled Stepped Spillways for Embankments. *Environmental Fluid Mechanics*, 13(5), 503-525.

Hunt, S. L. & Kadavy, K. C. (2011). Inception Point Relationship for Flat-Sloped Stepped Spillways. *Journal of Hydraulic Engineering*, 137(2), 262-266.

Krisnayanti, D.S. (2016). Modeling of Geometry Stepped Spillway for the Inception Point on Skimming Flow Condition, *Disertation*. Brawijaya University, Malang, Indonesia.

Khatsuria, R. (2005). *Hydraulics of Spillways and Energy Dissipators*. New York: Marcel Dekker.

Matos, J., Sanchez, M., Quintela, A. & Dolz, J. (2000). *Air Entrainment and Safety against Cavitation Damage in Spillways over RCC Dams - Hydraulics of Stepped Spillways*. Netherlands: Balkema Publisher; © Swets & Zeitlinger.

Matos, J. (2000b). Hydraulic Design of Stepped Spillways Over RCC Dams. *Proceedings of the International Workshop on Hydraulics of Stepped Spillways*. Zurich, Switzerland, 187-194

Wood, I. & Ackers, P. L. (1983). General Method for Critical Point on Spillways. *Journal of Hydraulic Engineering*, 109(2), 308 - 312.

Proceedings of the 37th IAHR World Congress
August 13 – 18, 2017, Kuala Lumpur, Malaysia

DETERMINATION OF ENVIRONMENTAL FLOW IN ARID AND SEMI-ARID REGIONS

ELNAZ ZEHTABIAN(1), ARDALAN IZADI(2) & FARHAD YAZDANDOOST(3)

(1,2,3)Department of Civil Engineering, K.N. Toosi University of Technology, Tehran, Iran
elnaz.zehtabian@alumni.ut.ac.ir; a.izadi@mail.kntu.ac.ir; yazdandoost@kntu.ac.ir

ABSTRACT

Biodiversity of rivers are often exposed to multiple threats, making river systems vulnerable ecosystems, while rapid increase of population, agricultural and industrial developments exert severe pressure on policy makers to overlook the environmental requirements of river systems. To address this challenge, it is imperative to include the Environmental Flow Assessment (EFA) as an integral part of river basin management. Unfortunately, less attention has been paid to EFA in arid and semi-arid regions where river environmental problems tend to exacerbate as a result of prevailing water shortages. Zayandeh Rood River located in the arid and semi-arid region of central Iran has been selected as the case study here. Hydrological (Tennant and Flow Duration Curve-FDC) and Hydraulic rating method (Wetted perimeter method) have been employed here. The results show that while the Tennant method and the FDC method report the same values at 13.9 M^3/s as the need of environmental flow, the results based on the plotted curve in the wetted perimeter method reveal the amount of EF around 22. Given the important impact of the environmental flow allocations on the IWRM model of the river basin, it is imperative to estimate EF as accurately as possible for inaccuracies and uncertainties may impose huge risks both to the environmental conditions and the water resources allocation decisions.

Keywords: Integrated water resources management (IWRM); environmental flow assessment (EFA); Zayandeh Rood River; hydrological method; hydraulic rating method.

1 INTRODUCTION

Rivers and their biodiversity are always more subjected to many risks than the other ecosystems. Some water resources development plans, such as dam construction, which may result in many unfavorable consequences like changing the natural rivers regime, reducing water availability and producing polluted water downstream make the river ecosystem problems more severe (Tharme, 2003). Therefore, recognizing hydrological changes of rivers and respecting to their environmental needs has led to the development of a research branch termed as "Environmental Flow Assessment" (Arthington and Zulacki 1998). In simple terms, this assessment can reveal how much water must flow in the river, in order to maintain the characteristics of the river basin ecosystems. Water resource development projects, population growth, and development in agriculture and industry sectors, can cause changes in the normal pattern of river flow regime, and reduce water availability in the downstream, increased water pollution and ecosystem degradation (Arthington, et al 2004). It can be said that, maintenance and durability of the river ecosystems and its biodiversity, are the main goals of allocating water to the environment.

There is a basic difference between the terms "environmental flow assessment" and "environmental flow requirements". Identifying hydrological changes of rivers and their impacts on the environment has caused the establishment of environmental flow assessment, in which the quality and quantity of water needed for sustainable water resources of ecosystems are estimated. The hydrological flow regime, which is appropriate in all ecological terms, can be considered as "environmental flow assessment" (EFA). "Environmental flow requirement" (EFR) is related to the future condition and policy related to the ecosystem. Furthermore, the average of total annual environmental flow volume is expressed as EFR. Considering environmental flow for rivers as the intrinsic element, can lead to providing more water flow for streams and floodplains. This higher share of water allocation can help the health of rivers. Furthermore, maintaining plants health, prevention of river bank erosion, making human life healthier, improvement of water quality, reduction of erosion costs, attracting tourism and natural refinement of rivers are the other advantages of considering environmental flow for rivers.

Many methods have been developed for determination of environmental flow in rivers. These methods have their specific capabilities according to data required and complexity of use. About 207 methods in 44 countries of the world have been developed for EFA. All these methods are classified in the form of four distinct methods namely; hydrologic, hydraulic rating, habitat simulation and holistic methods (Tharme, 2003). Hydrological methods are based on hydrological characteristics. They are one of the simplest and most widely used methods in the world. These methods are known as lookup for desktop table methods that rely on recorded data of previous years. In these methods, environmental flow is considered as a percentage of

 ©2017, IAHR. Used with permission / ISSN 1562-6865 (Online) - ISSN 1063-7710 (Print)

average annual discharge of river or a flow likely to exceed the specified flow duration curve in time scale of monthly, annually or seasonally (Richter, 1996). The most well-known approaches of hydrological methods are: Tennant method, Texas method, flow duration curve method, RVA method and desktop reserve method.

Hydraulic rating method was first introduced in the USA and has been strengthened along with habitat simulation methods or/and with holistic methods. Hydraulic methods estimate the environmental flow through considering morphological characteristics of rivers. These methods can be classified into hydrological and habitat simulation methods in terms of accuracy and difficulty, use of time series of data and information of critical cross-sections. In this method, EFA is derived through charts of hydraulic parameters-discharge. Generally, by finding the point in which the slope of the curve changes abruptly gives an indication of the EFR. This reduction occurs when the flow rate is reduced. Therefore, a threshold for flows can be identified based on hydraulic parameters (Arthington, et al 2004). The most popular method of this category is the wetted perimeter method (Jowett, 1997).

Habitat simulation methods, are one of the most popular and complex methods for EFA. In these methods, besides the hydrological and hydraulic parameters, biological parameters according to the critical species are influencing. Habitat simulation methods set environmental targets by establishing a connection between discharge and habitat characteristics such as water depth, velocity and even complex hydraulic parameters such as shear stress (Tharme, 2003). In these methods, habitat conditions are directly related to the needs of dominant species lives. In these methods, the curve representing the habitat sustainability index is used in order to, evaluate required environmental flow. This curve shows the probability that a particular flow is equaled to or exceeded from.

In this paper, Zayandeh Rood River located in central part of Iran with an arid and semi-arid climate is selected as the case study. Lack of integrated water resources management in this area has led to negligence of environmental flow requirements. Progressive droughts in Zayandeh Rood River basin and consequent water shortages in all types of demands have created many problems for the stakeholders. To face this challenge, this research aims to estimate EF of Zayandeh Rood River and incorporate this vital demand within the integrated supply-demand model of the basin to facilitate scenario generation and decision-making.

2 METHODOLOGY

2.1 Tennant method

In this study, the environmental flow was estimated by determining a certain percentage of the average annual natural flow in the river. Tennant concluded from 58 cross sections of 11 rivers in the western regions of the United States of America (Tennant, 1976) that at least 10% of the average annual flow (AAF) for surviving fish habitat in short time, 30% of AAF for maintaining fair condition of survival and 60% of AAF for excellent conditions of fish habitat are needed. These values have been widely used, without considering the physical or environmental features of rivers. Simplicity and using the average annual hydrograph are the main factors of making Tennant method popular. Table 1 shows different suggested percentages of AAF for the river conditions.

Table1. Suggested percent of AAF in rivers based on Tennant method (Tennant, 1976).

Suggested percent of AAF in rivers		River
Spring- Summer	**Autumn-Winter**	**Conditions**
60	40	Very excellent
50	30	Excellent
40	20	Good
30	10	Adequate
10	10	Weak
0-10	0-10	Severe damage

Table 1 was suggested based on very detailed data gathered from certain sections of habitats such as water width, depth, velocity, temperature, bed and side channels grain size, estuaries, islands, vegetation, birds, invertebrates, fish, etc. Tennant has compiled these relatively complex data and then he converted them to a simple method that requires less data. In using the Tennant method, there are three main assumptions:

i. This method is a basic method. Therefore, it cannot address flow changes especially seasonal fluctuations.
ii. It is suitable for large water areas where seasonal fluctuations are less.
iii. Channel geometry is not included in the calculations.

2.2 Flow duration curve method (FDC)

In this method, the average daily flow curves sorted from maximum to minimum, are used as a function of probability that a particular flow (Q (i) time series, where i=1 represents the largest average daily flow during a year) is equaled to or exceeded from. In FDC analysis, data are analyzed in normal conditions.

2.3 Wetted perimeter method

In this method, while the flow changes are considered within simulation hydraulic sections, habitat features are not included explicitly in the process of environmental flow calculation. The basic concept in this method is based on the fact that the more wetted perimeter is available, more fish habitats will be provided. Therefore, the relationship between discharge and wetted perimeter is required to determine the environmental flow. To do this, cross sections having less depth and more velocity (referred to as riffles in geomorphology), are the critical ones. Steps of EF calculation for wetted perimeter method are listed as follow:

i. Determining the relationship between wetted perimeter and discharge of flow.
ii. Detecting failure point (slight change in discharge, will reduce wetted perimeter more severely).
iii. In some cases, the obtained curve may become irregular resulting in multi-point curvatures. In this situation, the critical discharge is considered equivalent to the lowest point of failure.
iv. By determining the failure point, the minimum required environmental flow for sections can be deducted.

In this method, there are reasonable uncertainties. The most important one is the location of failure point of the curve. The appropriate procedure for selection is dependent on the relationship between the wetted perimeter and the flow rate. This relationship is a function of geometry of cross sections and how depth can fluctuate versus variation of flow rate. Geometric shape of cross sections, are usually fluctuating from triangles to rectangles. Manning equation (Eq. [1]) can describe the relationship between wetted perimeter and discharge in triangular (Eq. [2]) and rectangular (Eq.[3]) cross sections (Gippel, 1998) as follows:

$$Q = \frac{1}{n} A R^{\frac{2}{3}} S^{\frac{1}{2}} \quad [1]$$

$$p = cq^{b} \quad [2]$$

$$p = alnq + 1 \quad [3]$$

In these equations, $q=Q/Q_{max}$, A is cross sectional area in m^2, R is the hydraulic radius (m), S is the slope, $p=P/P_{max}$, a and b are coefficients of regression line in the associated curve.

3 CASE STUDY

The Zayandeh Rood River in Gavkhooni catchment in central part of Iran was selected as the case study here. The length of the Zayandeh Rood River is 405 km. There are 15 hydrological stations along the length of the river. The first one is on the regulatory dam and the last one is Varzaneh station which is the nearest one to the Gavkhooni wetland. The average slope of Zayandeh Rood River bed is 0.2 %. Western and southern parts of Gavkhooni catchment are covered by mountainous areas and western parts are also located in eastern slopes of central Zagros Mountain. The northern and eastern parts of the catchment are located in hills and plains of central plateau of Iran. Figure 1 shows the layout of the Gavkhooni catchment. The annual average rainfall in Gavkhooni varies between 1400 mm in western part of the catchment to 100 mm in the Gavkhooni wetland. The basin's evaporation fluctuates between 1700 mm to 3100 mm per year.

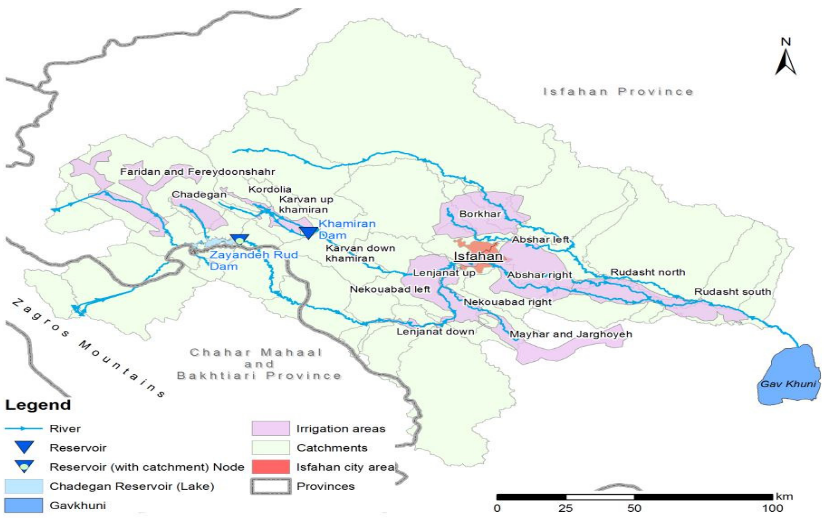

Figure 1. General layout of Gavkhooni catchment

 ©2017, IAHR. Used with permission / ISSN 1562-6865 (Online) - ISSN 1063-7710 (Print)

For hydrological calculation of Zayandeh Rood River, the data of Zayandeh Rood regulatory dam station was used. The monthly average flow of this station during 1969-2006 was used. In this station, the annual average flow for these 48 years is around 46/4 M^3/s. Figure 2 shows the monthly and cumulative discharge of regulatory dam station. According to figure 2, in January, February and March, the average flow is less than 10% of the total flow of the river. In such cases, any over withdrawal of water from river may cause various problems. Therefore, considering the Q_{90} as the judgment criteria is problematic. In figure 3, longitudinal profile of Zayandeh Rood River is shown.

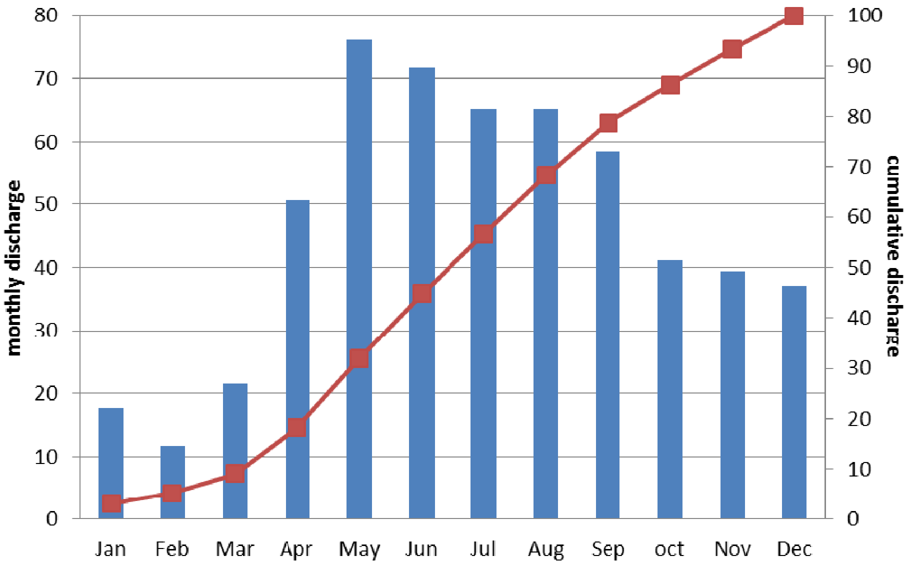

Figure 2. Monthly and cumulative discharge of regulatory dam station.

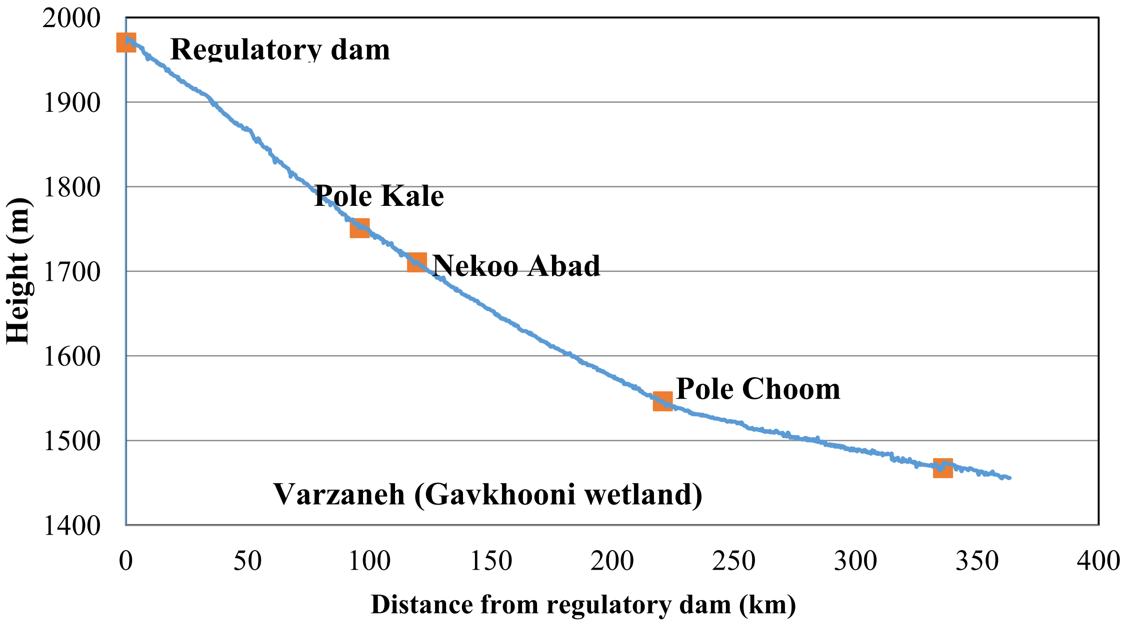

Figure 3. Longitudinal profile of Zayandeh Rood River and some stations.

4 RESULTS

4.1 Hydrologic method

The results of the Tennant method for hydrologic data of the Zayandeh Rood River during 1969-2006 are shown in Table 2. According to this table, the average annual flow of spring-summer and autumn-winter were calculated around 2.81 and 6.64 M^3/s respectively. Table 3 presents the comparison of Tennant results with observed discharges in Varzaneh station, which is the last station of Zayandeh Rood River, and the nearest station to the Gavkhooni wetland. According to this table, in the months of June, July, August and September, the river faced severe conditions. These results indicated that the environmental flow was not provided along the river. Generally, 30% and 60% of the annual average flow (AAF) were considered as the fair and the ideal

©2017, IAHR. Used with permission / ISSN 1562-6865 (Online) - ISSN 1063-7710 (Print)

conditions for survival of aquatic organisms. These amounts were equivalent to 13.9 M^3/s and 27.8 M^3/s, respectively.

Table 2. Results of Tennant method.

Discharge calculated based on Tennant method		Suggested percent of AAF in rivers		Management class
Spring- Summer	Autumn-Winter	Spring- Summer	Autumn-Winter	
38.76	11.24	60	40	Very excellent
32.3	8.43	50	30	Excellent
25.84	5.62	40	20	Good
19.38	2.81	30	10	Adequate
6.46	2.81	10	10	Weak
6.46-0	2.81-0	0-10	0-10	Severe damage

Table3. Classification of observed discharge in Varzaneh station based on Tennant method.

Month	Observed discharge	River condition
January	7.18	Good
February	5.31	Adequate
March	6.33	Good
April	10.89	Weak
May	13.28	Weak
June	4.54	Severe damage
July	2.28	Severe damage
August	1.71	Severe damage
September	1.99	Severe damage
October	3.1	Adequate
November	5.58	Good
December	7.18	Good
Mean	5.84	-

In the FDC method, the hydrologic data of 1969-2006 was also used. The daily discharge sorted from maximum to minimum and probability of flow that has been exceeded from specified amount of flow, were assessed. Table 4 summaries these results. As the typical-average ecological condition was chosen as the class of river management, Q_{90} had been considered as the minimum acceptable environmental flow of the river (according to Table 4). Q_{90} is the amount of flow that the discharge of the river in 90% of the times is higher than this flow.

According to the FDC plotted in Figure 4, Q_{90} was about 13.67 M^3/s as the environmental flow of Zayandeh Rood River. The results of EF for the other management classes are condensed in Table 4.

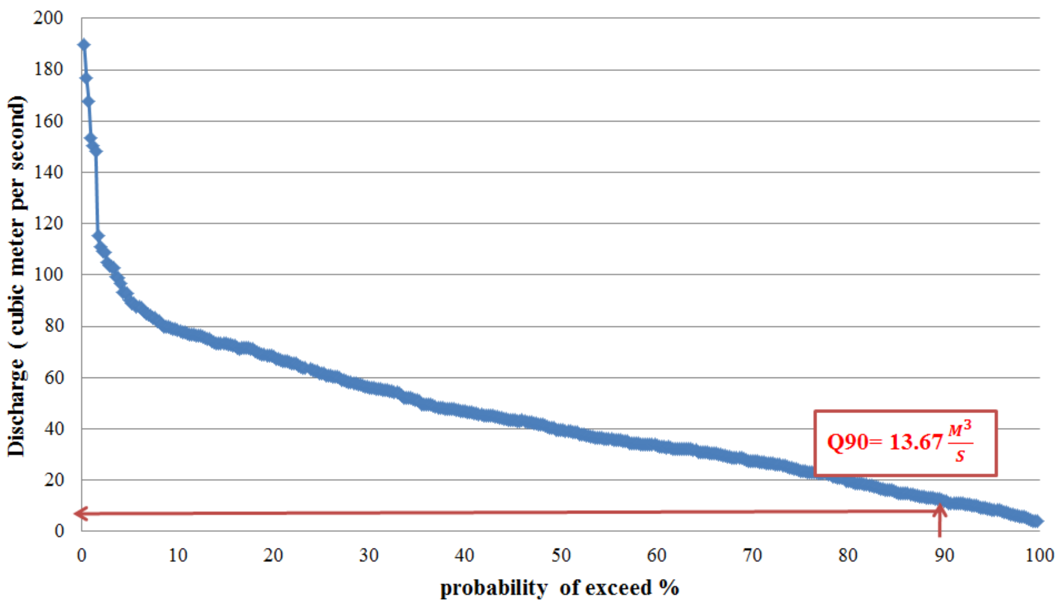

Figure 4. Flow duration curve of Zayandeh Rood River.

 ©2017, IAHR. Used with permission / ISSN 1562-6865 (Online) - ISSN 1063-7710 (Print)

Table 4. Class of management according to ecological conditions.

Calculated discharge from flow duration curve (M^3/s)	Index	Ecological Conditions	Management Class
35.85	Q_{50}	Natural condition and slight changes in river's habitat	Normal
19.62	Q_{75}	Changes are minor and conditions are largely undisturbed	Favorable
13.67	Q_{90}	Some sensitive species are damaged, alien species have been partially damaged	Typical- Average
-	N/A	The only resistant strains remain and alien species have been imposed into ecosystem	Critical

4.2 Hydraulic method

In this research, the index of measuring environmental flow was used as the wetted perimeter method. The failure point of curve is the point that a little change in wetted perimeter causes sudden drop in discharge. The sudden drop of discharge can cause significant degradation in quality of habitat for fish and other organisms. To analyze the hydraulic parameters of Zayandeh Rood River in different sections, the HEC-RAS 1-D modeling software was used. Varzaneh station was chosen as the representative cross section at the downstream of Zayandeh Rood River. Figure 5 shows the cross section of Zayandeh Rood River in Varzaneh station. Figure 6 shows the wetted perimeter-discharge curve of Varzaneh station. Table 5 represents the results of HEC-RAS along with variation of different ratio of wetted perimeter to the discharges in Varzaneh station.

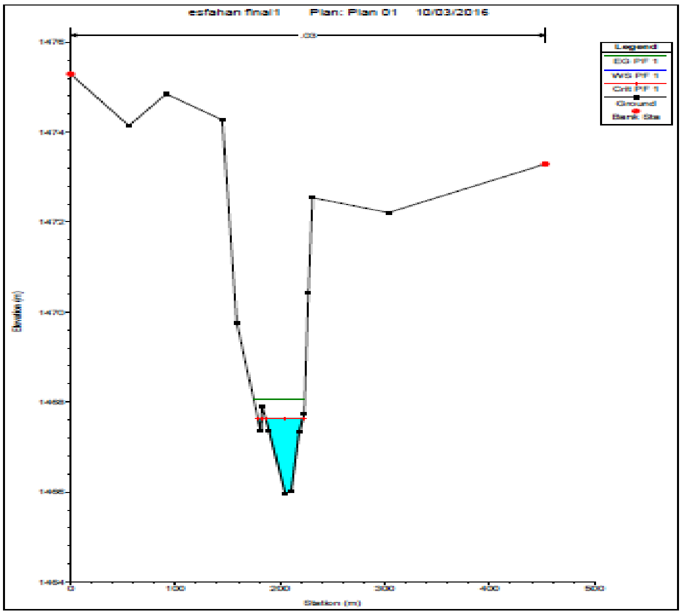

Figure 5. Cross section of Zayandeh Rood River in Varzaneh station.

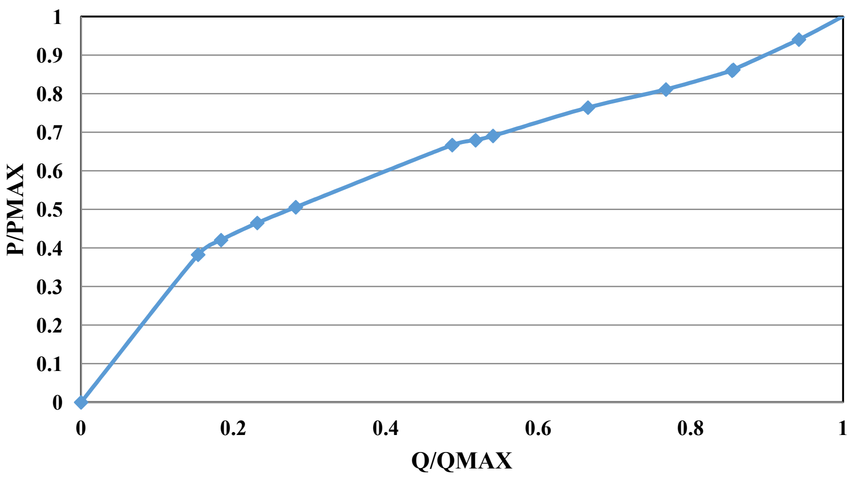

Figure 6. Wetted perimeter-discharge curve of Varzaneh station.

Table5. Results of HEC-RAS and variation of wetted perimeter versus discharge.

Q/Q_{MAX}	P/P_{MAX}	P	H	A	Q
0.15	0.38	1.75	0.6	5.94	11.7
0.23	0.47	2.13	0.74	8.21	17.62
0.28	0.51	2.32	0.81	9.56	21.47
0.49	0.67	3.05	1.06	14.83	37.12
0.52	0.68	3.11	1.09	15.5	39.46
0.54	0.69	3.16	1.11	16.01	41.2
0.67	0.76	3.5	1.22	18.88	50.7
0.77	0.81	3.72	1.31	21.07	58.5
0.85	0.86	3.94	1.37	23	65.12
0.86	0.87	3.95	1.38	23.05	65.24
0.94	0.94	4.31	1.45	25.28	71.8
1.0	1	4.58	1.5	26.86	76.22

Failure point of the curve was calculated based on the maximum curvature of the curve and the slope method. 14 M^3/s and 22 M^3/s were respectively the results of these two methods as the indicator of Zayandeh Rood River environmental flow. As seen, the rate of environmental flow in slope method was twice the amount of the maximum curvature method. These results were completely different with those of Gippel et al (1998) which claimed that the maximum curvature method usually provides higher amount of environmental flow than slope method. On the contrary, the result of maximum curvature method was very close to the results of environmental flow obtained from hydrologic methods. Therefore, a figure of 14 M^3/s may be regarded as the appropriate estimation for the environmental flow of Zayandeh Rood River.

5 CONCLUSIONS

Many rivers in arid and semi-arid areas of Iran are rapidly running dry. Consequently, ecosystems of these water resources are faced with serious environmental risks. Lack of flow in Zayandeh Rood River as the most important river of central plateau of Iran is a major cause of concern. This research is carried out to assess the Environmental Flow (EF) of Zayandeh Rood River realistically and practically for inclusion in integrated assessments. The Tennant method and the Flow Duration Curve (FDC) method are used here for analyzing EF as the hydrological methods, while slope method and maximum curvature method are used to calculate EF based on hydraulic methods. The results show various figures for the minimum EF. It is concluded that the hydrological methods are more consistent with the result of maximum curvature method in Varzaneh station than those obtained from the slope curve. The slope curve method may not be useful for arid and semi-arid regions suggesting the greatest EF values.

REFERENCES

Arthington, A.H., Tharme, R., Brizga, S.O., Pusey, B.J. & Kennard, M.J. (2004). Environmental Flow Assessment with Emphasis on Holistic Methodologies. *Proceedings of the Second International Symposium on the Management of Large Rivers for Fisheries,* 2, 37-65.

Arthington A.H. & Zalucki J.M. (1998). *Comparative Evaluation of Environmental Flow Assessment Techniques: Review of Methods,* Occasional Paper No. 27/98. Land and Water Resources Research and Development Corporation: Canberra, Australia.

Gippel, C.J. & Stewardson, M.J. (1998). Use of Wetted Perimeter in Defining Minimum Environmental Flows. *Regulated Rivers: Research and Management*, 14(1), 53-67.

Jowett, I.G. (1997). Instream Flow Methods: A Comparison of Approaches. *Regulated Rivers: Research and Management*, 13(2), 115-127.

Richter, B.D., Baumgartner, J.V., Powell, J. & Braun, D.P. (1996). A Method for Assessing Hydrologic Alteration within Ecosystems. *Conservation Biology*, 10(4), 1163-1174.

Tennant, D.L. (1976). Instream Flow Regimens for Fish, Wildlife, Recreation and Related Environmental Resources. *Fisheries*, 1(4), 6-10.

Tharme, R.E. (2003). A Global Perspective on Environmental Flow Assessment: Emerging Trends in the Development and Application of Environmental Flow Methodologies for Rivers. *River Research and Applications*, 19(5-6), 397-441.

 ©2017, IAHR. Used with permission / ISSN 1562-6865 (Online) - ISSN 1063-7710 (Print)

MODELLING THE IMPACT OF MICROBIAL SOURCES ON WATER QUALITY: A STUDY ON THE DESIGNATED SAMPLING POINT IN SWANSEA BAY, UK

JONATHAN KING[(1)], REZA AHMADIAN[(2)], AMYRHUL ABU BAKAR[(3)], & ROGER A. FALCONER[(4)]

[(1,2,3,4)]Hydro-Environmental Research Centre (HRC), Cardiff School of Engineering, Cardiff University, Cardiff CF24 3AA, UK.
AhmadianR@cf.ac.uk

ABSTRACT

This study employs a computational fluid dynamics approach to investigate the impact of microbial sources on water quality in Swansea Bay, UK. Two models have been set up using TELEMAC-2D and TELEMAC-3D, covering the period from October – November 2012. The results indicate the importance of using a high horizontal grid resolution in proximity to submerged outfalls to accurately capture the shape of the effluent plume. The 3D model was able to accurately capture variations in *Escherichia coli* concentration throughout the day whereas the 2D model was incapable.

Keywords: Faecal indicator organisms (FIOs); numerical modelling; designated sampling point (DSP); water quality, TELEMAC.

1 INTRODUCTION

The revised Bathing Water Directive (rBWD) (2006/7/EC) requires the monitoring of two Faecal Indicator Organisms (FIOs); intestinal enterococci (IE) and *Escherichia coli* (*E.coli*), to determine compliance of a bathing water with the specified standard. These organisms are present in the gut of warm blooded animals and are a flag for faecal contamination, which can be attributed to bathers contracting gastroenteritis (Kay et. al., 1994; Cabelli et. al., 1982). In the event of reduced or unsatisfactory water quality, source apportionment is necessary to identify key inputs with significant detrimental impact. Identification allows local authorities to focus resources on the reduction of source loading at specific locations enabling cost-effective improvements in water quality.

Swansea Bay is a popular tourist location and bathing site in the Severn Estuary, South Wales, UK, (see Figure 1). Sources of faecal matter include combined sewer overflow spills, long sea outfalls, excrement from the local seabird population and diffuse pollution from agricultural sources upstream of the main estuaries.

In order to monitor compliance with the European Directive, water quality samples are taken intermittently throughout the bathing season. To ensure comparability between samples, readings are taken at a single location, the designated sampling point (DSP), which is assumed representative of the whole bay. However, to account for the large tidal range experienced in the Severn Estuary, sampling is in fact carried out along a 1.5km transect perpendicular from the DSP on the beach front, see Figure 2(a); samples are taken in knee deep water, the distance from the beach front dependent on the phase of the tide.

Not only do samples taken at a high or low tide show different levels of FIOs but samples taken during the flood or ebb tide also show notable variation. This is partly due to the dilution effect caused by the release of effluent during high water. Previous sampling studies have also shown a diurnal pattern in IE concentration, with elevated concentrations during the morning and evening (Smart Coasts, 2013). Given the similar decay characteristics of IE and *E.coli*, the latter can also be considered to demonstrate a similar temporal variation.

The flow within the bay is predominantly driven by a large recirculation eddy caused by a headland to the west of the region, Mumbles Head. As a result of this complex flow regime, the large tidal range and varied sampling location, it is difficult to determine which faecal sources have the most significant impact on the bay throughout the day.

It is clear that a single DSP with a location dependent on the time of sampling, as is currently practiced, may not provide readings representative of the whole bathing water. This argument is strengthened when considering the degree to which the DSP is subject to local effects, whereby small inputs have a detrimental effect on water quality in the vicinity of the DSP while having little to no impact elsewhere in the bay.

This paper forms part of an ongoing body of research to study the suitability of the DSP as a representative location. For simplicity, this paper focuses on the impact of *E.coli* though findings are transferrable to studies focusing on IE. TELEMAC-2D and TELEMAC-3D, developed by Électricité de France (Hervouet, 2007), are widely used in water quality studies (Bedri et. al., 2011; Kopmann and Markofsky, 2000) and have been used here to carry out depth-averaged and three dimensional hydrodynamic simulations respectively.

©2017, IAHR. Used with permission / ISSN 1562-6865 (Online) - ISSN 1063-7710 (Print)

2 METHODOLOGY

2.1 Computational setup

This study uses both TELEMAC-2D and TELEMAC-3D to solve the shallow water equations. The principal advantage of the TELEMAC suite for this study is its use of an unstructured mesh. This has the ability to adapt to irregular boundaries and allows a variable grid resolution throughout the domain. The 2D grid is shown in Figure 1; cell size varies from 1000m throughout the domain to 25m in Swansea Bay. An open boundary with a tidal forcing is imposed along the westward edge of the domain where the Severn Estuary / Bristol Channel meets the Celtic Sea. Following the analysis of the results from this model, two further 2D grids were developed with a resolution of 50m and 5m in Swansea Bay, see Section 3.2.

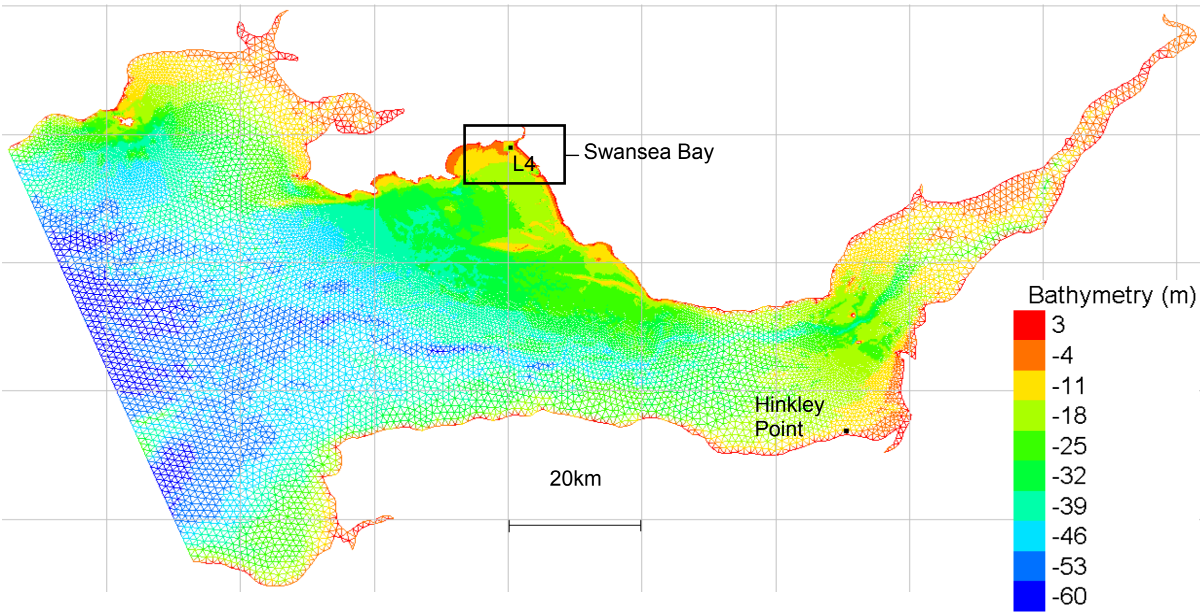

Figure 1. Unstructured computational mesh of the Severn Estuary with interpolated bathymetry (m above / below Mean Sea Level (MSL)) and position of Swansea Bay within the Severn Estuary. Black dots indicate the location of Hinkley Point tide gauge and ADCP survey point L4 used for hydrodynamic validation, see Section 3.1.

The 3D model uses 5 sigma layers in the vertical axis, with a lower grid resolution of 50m within the bay to reduce the total computational load; 13331 nodes and 264237 elements in each horizontal layer, 66655 nodes and 1321185 elements in total. While the 2D grid includes the main estuary flowing into the bay, this was excluded from the 3D model to reduce unnecessary vertical refinement within the river reach (see Figure 2).

2.2 FIO modelling

In total, the bay is subject to 85 inputs; 42 sources of surface water, 42 sources of sewage effluent and 1 industrial effluent discharge. Collected as part of the Smart Coasts Sustainable Communities project (Smart Coasts, 2013), data is available from 21/10/2012 to 19/11/2012 detailing *E.coli* inputs into the bay in 15 minute intervals. This covers the primary surface water and sewage discharges into the bay; data was unavailable for combined sewer overflows (CSOs) discharges. Sources discharging into the three main estuaries of the bay; Tawe, Neath and Afan, were lumped at their most downstream location for simplification, reducing the number of inputs to 15; see Figure 2(b).

 ©2017, IAHR. Used with permission / ISSN 1562-6865 (Online) - ISSN 1063-7710 (Print)

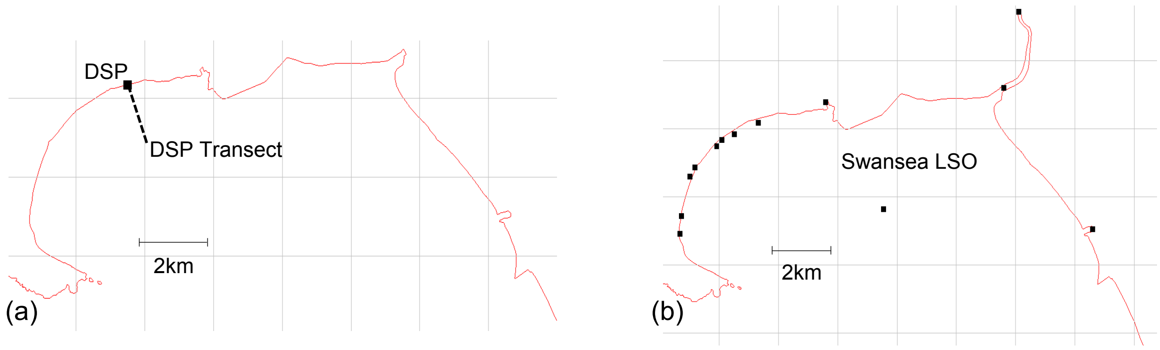

Figure 2 (a) Location of the DSP and DSP transect within Swansea Bay (b) Lumped *E.coli* inputs implemented within the 2D model, including Swansea Long Sea Outfall (LSO). The red lines indicate the 3D and 2D domain boundaries, respectively

Bacterial decay is known to be a function of temperature, light intensity, salinity, sediment interactions and predation and is not constant throughout the day (Bedri et. al., 2016; Perkins et. al., 2016; de Brauwere et. al., 2014; Schnauder et. al., 2007; Kay et. al., 2005). This study uses a simplified approach whereby the decay rate is considered a first order reaction, considering the time taken for a 90% reduction in concentration; T90 (Guillaud et. al., 1997). A constant decay rate with a T90 value of 30h was used in both 2D and 3D cases. This was selected as a conservative value to aid initial set up and calibration and does not necessarily reflect the decay processes observed within Swansea Bay. This will be the focus of future research stemming from this study.

3 RESULTS

3.1 Hydrodynamic validation

Figures 3 and 5 show good agreement between simulated and observed water levels at Hinkley Point (see Figure 1) for both 2D and 3D simulations. Figures 3 and 4 show good agreement between simulated velocities and water levels and those recorded during an ADCP survey of Swansea Bay in July – August 2012. Validation was also carried out at additional locations in the Severn Estuary and Swansea Bay but has been excluded from this paper for brevity.

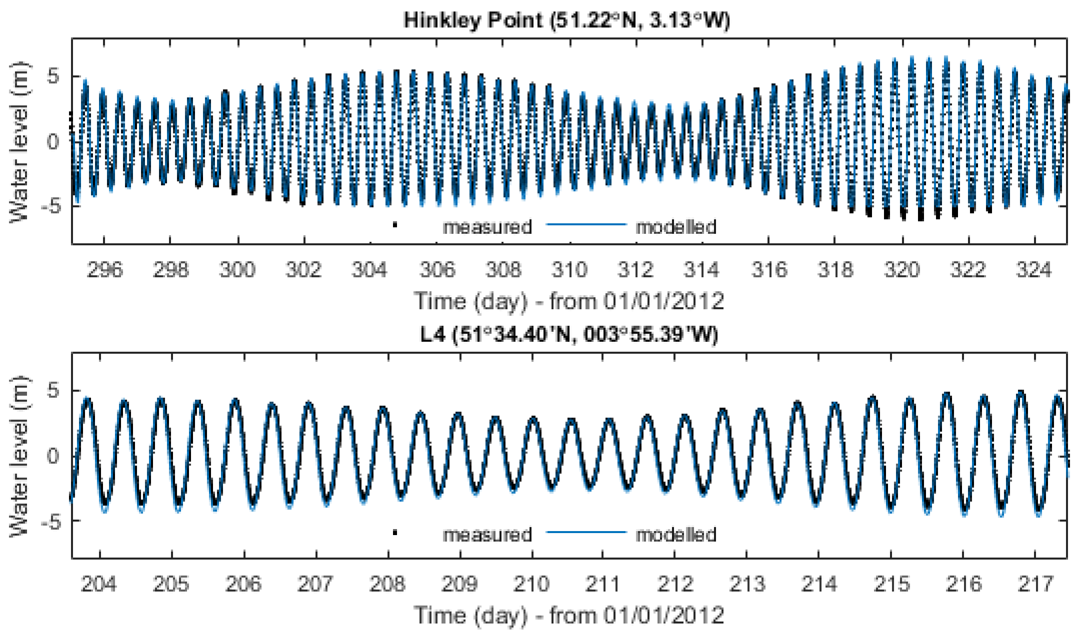

Figure 3. Time series of water levels predicted by TELEMAC-2D and measured data at British Oceanographic Data Centre (BODC) Hinkley Point tide gauge (top) and ADCP survey site L4 (bottom), (see Figure 1).

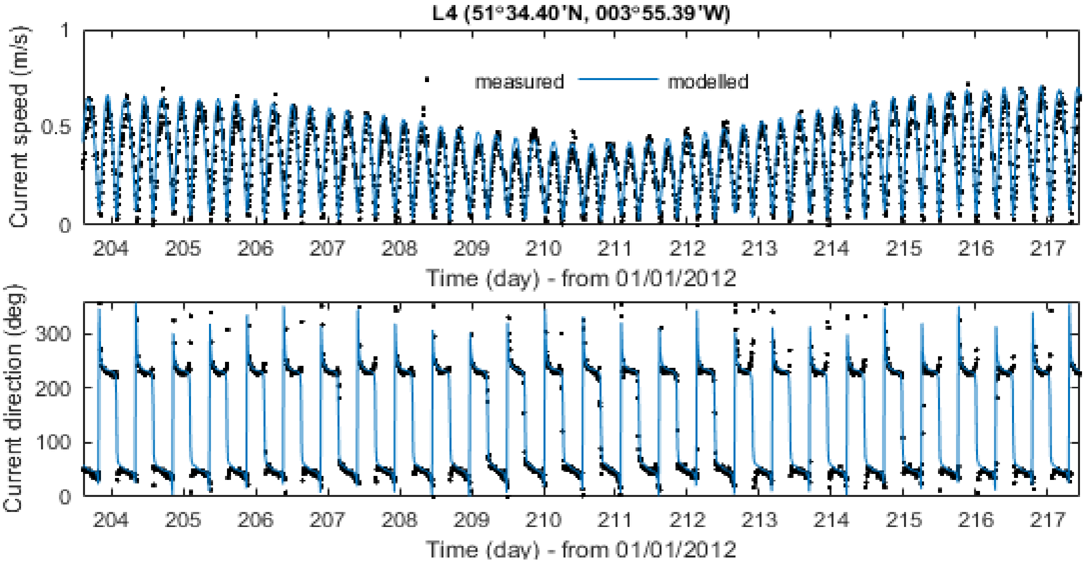

Figure 4. Time series of velocity components predicted by TELEMAC-2D and measured ADCP data at survey site L4 (see Figure 1).

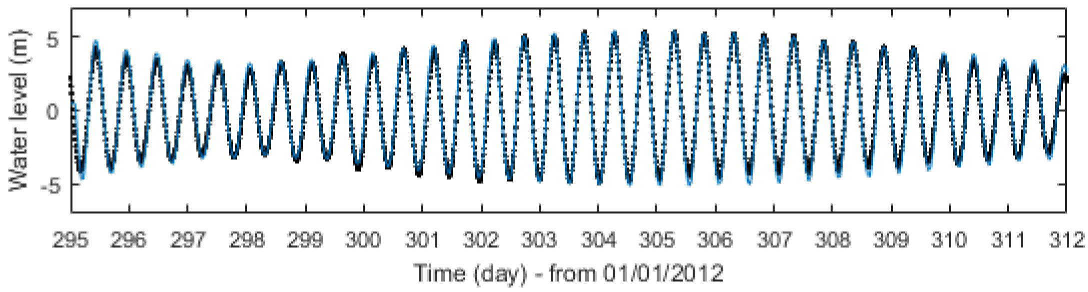

Figure 5. Time series of water levels predicted by TELEMAC-3D and measured data at British Oceanographic Data Centre (BODC) Hinkley Point tide gauge (see Figure 1).

3.2 FIO analysis

Data of *E.coli* concentrations throughout the day is available from a measurement survey carried out on 15/11/2012 for the Smart Coasts (2013) project. Figures 6 and 7 show the 2D simulated and measured concentration of *E.coli* at Site 1, located within 400m of Swansea Sewage Treatment Works Long Sea Outfall (LSO), see Figures 2(b) and 9.

Due to computational limitations, the 2D model was not run for an extended duration to coincide with the measurement survey and the two time series are not directly comparable. However, two observations can be made. Firstly, the model does not predict *E.coli* concentrations comparable with those observed by an order of magnitude. Secondly, while the model appears capable of capturing the peak in *E.coli* concentration, this is a diurnal occurrence suggesting a tidal influence whereas a singular event is captured in the measured data. Both could be attributed to the temporal difference in the data sets, however, further investigation is required to determine the extent to which this is the case.

Comparison between simulated and measured *E.coli* concentrations at the DSP are not shown due to differences of three orders of magnitude between the two data sets, indicating that the 2D model is incapable predicting water quality at this location. Further investigation into this is to be made in future research.

 ©2017, IAHR. Used with permission / ISSN 1562-6865 (Online) - ISSN 1063-7710 (Print)

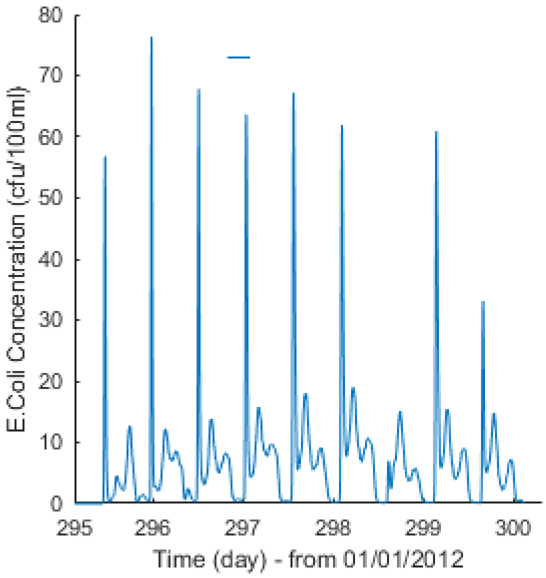

Figure 6 *E.coli* concentration at Site 1 predicted by the 2D model, from 21/10/2012 (day 295)

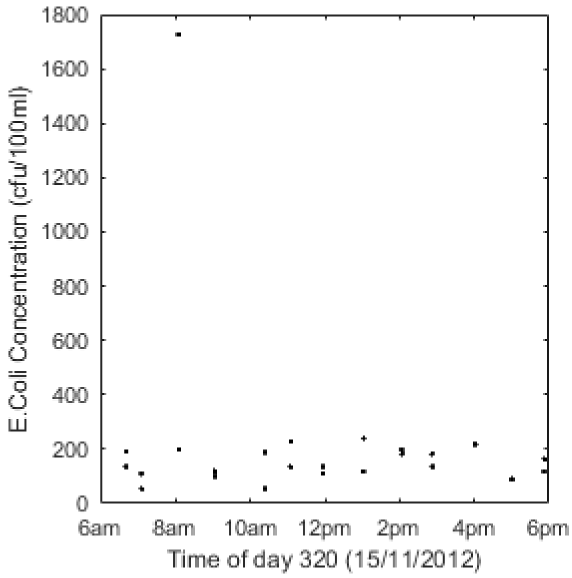

Figure 7 Measured *E.coli* concentration at Site 1

3.2.1High Resolution 2D Modelling of Swansea Long Sea Outfall

To better understand the advection of E.coli plumes within the bay and the potentially inaccurate results previously discussed, two new 2D domains were set up. In each case, the grid was refined to 50m and 5m, respectively in the region surrounding Site 1 and Swansea LSO. Focusing on deep water ignores any localised nearshore effects that may occur at the DSP due to repeated wetting / drying and the proximity to multiple beach outlets. The two grids (50m and 5m) contain 86407 nodes and 170917 elements, 331407 nodes and 660927 elements, respectively. Results from each simulation are shown in Figure 8. River discharges are not considered to have an impact on water quality at Site 1 and have been excluded in order to isolate the impact of grid resolution on advection of the plume from Swansea LSO.

A significant variation in the simulated *E.coli* concentration can be seen in response to changes in the grid resolution. While the results obtained from (a) give an indication of the temporal variation, they do not predict all peaks, of which the relative magnitude is more pronounced in (b) and (c) compared to the lower concentration observed throughout the majority of each day (see Figure 8). This can be attributed to numerical diffusion whereby a fixed concentration of *E.coli* released into a computational cell will be instantaneously reduced based on the volume of the cell, dampening the response. Parallels can be drawn between this concept and that which occurs when using finite element methods as in TELEMAC-2D.

In addition, during the differencing step carried out to calculate the dispersion of *E.coli* between adjacent cells, a lower grid resolution results in the distribution of *E.coli* over a larger area. This can be seen in Figure 9 in the shape of the plume released from Swansea LSO in each case. At the time step shown the simulated *E.coli* concentrations at Site 1 for the 50m, 25m and 5m resolution grids are 15 cfu/100ml, 26 cfu/100ml and 46 cfu/100ml, respectively. The effluent plume is more defined when using a higher grid resolution, predicting a higher *E.coli* concentration at a given time as the plume passes a fixed observation point.

Focusing on the results from (c) at Site 1, there is a strong correlation between the time of high tide and the peaks in *E.coli* concentration (above 50 cfu/100ml), see Figure 10. The absence of such a correlation at midday on 24th October (day 298) can be attributed to a reduced discharge from Swansea LSO; 0.03 m^3/s, compared to an average of 0.4 m^3/s over the entire time series, resulting in a significant reduction in concentration.

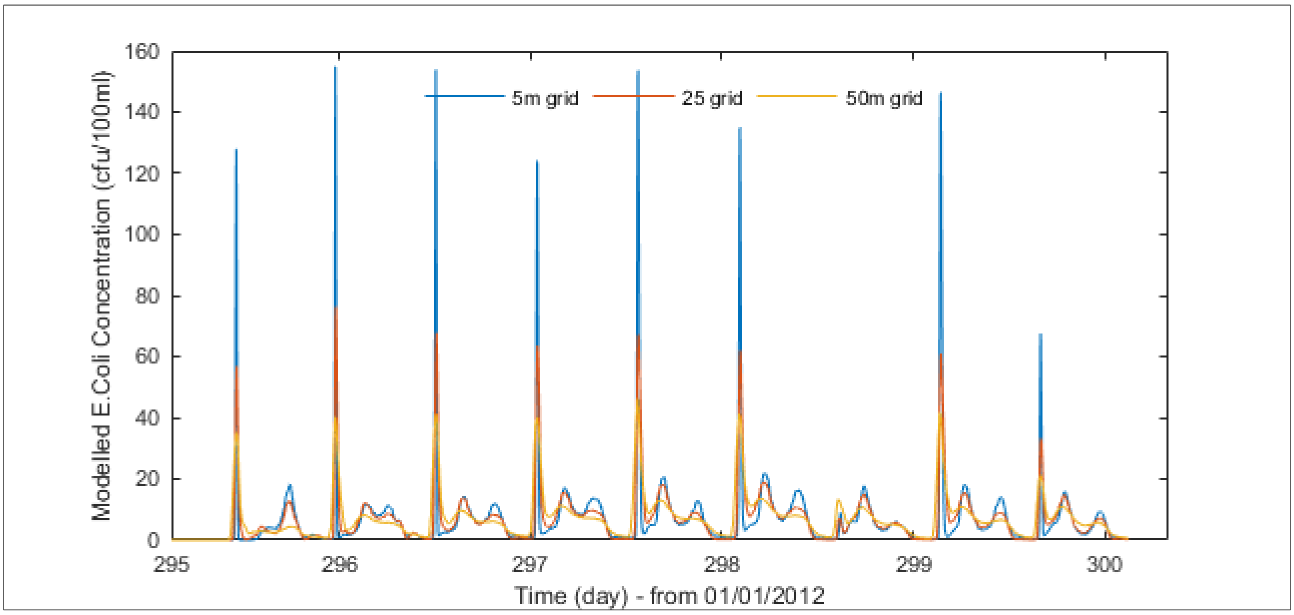

Figure 8. Plot of modelled *E.coli* concentration at Site 1 for 2D grids of; (a) 50m, (b) 25m and (c) 5m resolution around Site 1 and Swansea LSO.

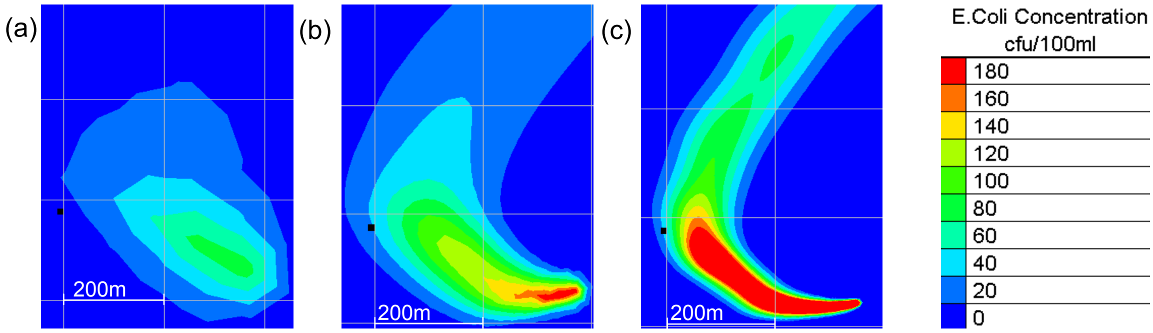

Figure 9. Effluent plume released from Swansea LSO observed at high tide +1 hour, for 2D grids of; (a) 50m (b) 25m (c) 5m resolution. Black dot = Site 1.

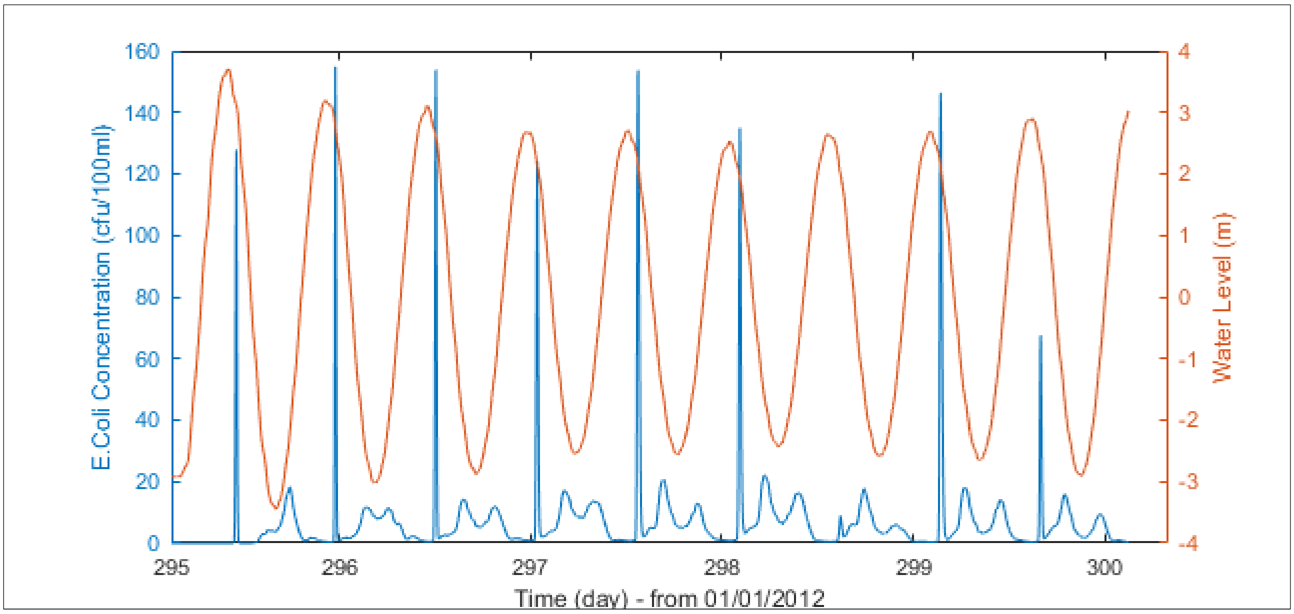

Figure 10. Tidal phase and modelled *E.coli* concentration at Site 1 using model (c).

 ©2017, IAHR. Used with permission / ISSN 1562-6865 (Online) - ISSN 1063-7710 (Print)

3.2.2 3D Modelling

Vertically averaged *E.coli* concentrations predicted by TELEMAC-3D are shown in Figures 11 and 12. Considering Figure 11, although the model does not predict the spike in *E.coli* concentration measured on 15/11/2012, it predicts concentrations of a similar magnitude to those recorded throughout the remainder of the day. This suggests an important source or transport process is missing from the model. For example, a tidally dominated effluent plume as seen in Figures 8, 9 and 10.

Inspection of the model input series shows that from 28/10/2012 (day 302) onwards the magnitude of flow and *E.coli* load inputs to the bay increase to persistently higher levels in both sewage releases and surface water discharges, the outcome of which is reflected in Figure 11. Given the time of year, this is typical of storm events in the UK which are known to increase bacterial levels in receiving water bodies (Bedri et. al., 2016; deBrauwere et. al., 2014; Schnauder et. al. 2007).

While this highlights the importance of running the 2D model for a longer duration as a progression of this research, it is of note that there are remarkable differences in the modelled response prior to this point, specifically in relation to model (b), Figure 6. In contrast to the defined peaks predicted by the 2D model, those predicted by the 3D model are more frequent and less defined. As the simulation progresses, it is those which coincide with the ebb tide that become more pronounced suggesting influence from another source than Swansea LSO and potential flow stratification which is not captured by the 2D model.

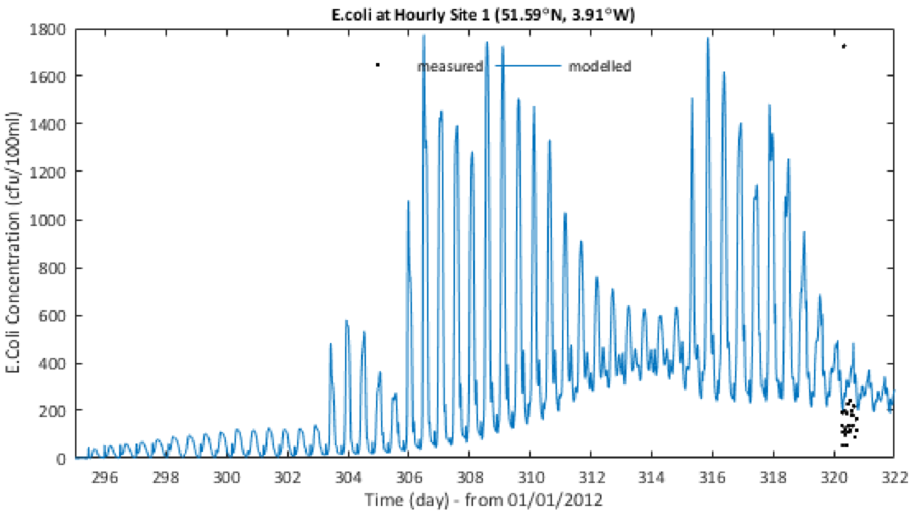

Figure 11. Vertically averaged *E.coli* concentration predicted by TELEMAC-3D at Site 1.

Figure 12 shows the vertically averaged *E.coli* concentration along the DSP transect; the observation location at the shoreline moving with the tidal cycle. Simulated levels of *E.coli* are of an order of magnitude with and show good correlation to the measured data indicating the 3D model is capable of accurately predicting the *E.coli* concentration at the DSP.

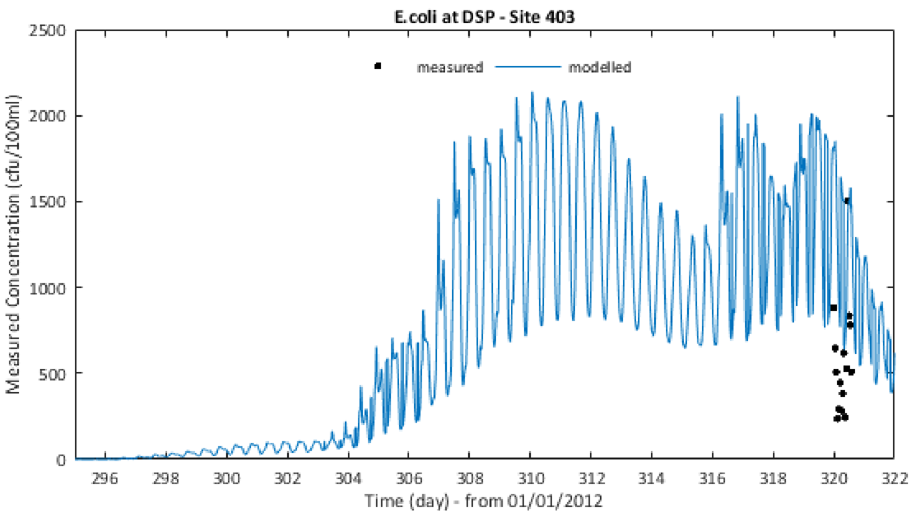

Figure 12. 2D Averaged results from the 3D model of E.coli concentration along the DSP transect.

©2017, IAHR. Used with permission / ISSN 1562-6865 (Online) - ISSN 1063-7710 (Print)

4 CONCLUSIONS

Two hydrodynamic models were set up to investigate the impact of bacterial sources on water quality within Swansea Bay, UK. Simulations were carried out using TELEMAC-2D and TELEMAC-3D respectively to predict the concentration of *E.coli* within the bay, treating the decay rate as constant. Further simulations are necessary to confirm the extent to which the 2D model is capable of predicting water quality within the bay, however, results indicate that it cannot capture the influence of all sources. Results from the 3D model are encouraging and indicate the ability of the model to accurately predict *E.coli* concentrations at the nearshore DSP. Offshore results indicate that further refinement of the model is required.

In addition, the 2D model was refined in the region surrounding Swansea Sewage Treatment Works Long Sea Outfall to study the impact of grid resolution on the advection and diffusion of the effluent plume. It has been shown that simulated *E.coli* concentrations are strongly correlated with grid resolution. Higher resolution models are able to capture the transport of the plume throughout the tidal cycle better, resulting in higher peak concentrations when the plume passes an observation point.

ACKNOWLEDGEMENTS

This research was funded by WISE EPSRC grand EP/L016214/1 as part of the Water Informatics Science & Engineering Centre for Doctoral Training.

REFERENCES

Bedri, Z., Bruen, M., Dowley, A. & Masterson, B. (2011). A Three-Dimensional Hydro-Environmental Model of Dublin Bay. *Environmental Modeling and Assessment,* 16(4), 369–384.

Bedri, Z., Corkery, A., O'Sullivan, J.J., Deering, L.A., Demeter, K., Meijer, W.G., Masterson, B. (2016). Evaluating a Microbial Water Quality Prediction Model for Beach Management under the Revised EU Bathing Water Directive. *Journal of Environmental Management,* 167(FEBRUARY), 49–58.

Cabelli, V.J., Dufour, A.P., McCabe, L.J. & Levin, M.A. (1982). Swimming-Associated Gastroenteritis and Water Quality. *American Journal of Epidemiology,* 115(4), 606–616.

de Brauwere, A., Ouattara, N.K. & Servais, P. (2014). Modeling Fecal Indicator Bacteria Concentrations in Natural Surface Waters: A Review. *Critical Reviews in Environmental Science and Technology*, 44(21), 2380–2453.

European Parliament, C. of the E.U. (2006). Directive 2006/7/EC of the European Parliament and of the Council of 15 February 2006 concerning the Management of Bathing Water Quality and Repealing Directive 76/160/EEC. *Official Journal of the European Union*, L 064(1882), 37–51.

Guillaud, J.F., Derrien, A., Gourmelon, M. & Pommepuy, M. (1997). T90 as a Tool for Engineers: Interest and Limits. *Water Sciences and Technology*, 35(11–12), 277–281.

Kay, D., Fleisher, J., Salmon, R.L., Jones, F., Wyer, M.D., Godfree, A.F., Zelenauch-Jacquotte, Z. & Shore, R. (1994). Predicting likelihood of Gastroenteritis from Sea Bathing: Results from Randomised Exposure. *The Lancet,* 344(8927), 905–909.

Kay, D., Stapleton, C.M., Wyer, M.D., McDonald, A.T., Crowther, J., Paul, N. & Gardner, S. (2005). Decay of Intestinal Enterococci Concentrations in High-Energy Estuarine and Coastal Waters: Towards Real-Time T90 Values for Modelling Faecal Indicators in Recreational Waters. *Water Research*, 39(4), 655–667.

Hervouet, J.-M. (2007). *Hydrodynamics of Free Surface Flows: Modelling with the Finite Element Method*. Chichester: John Wiley & Sons, 360.

Perkins, T.L., Perrow, K., Rajko-Nenow, P., Jago, C.F., Jones, D.L., Malham, S.K., & McDonald, J.E. (2016). Decay rates of Faecal Indicator Bacteria from Sewage and Ovine Faeces in Brackish and *Freshwater Microcosms with Contrasting Suspended Particulate Matter Concentrations. Science of the Total Environment, 572, 1645-1652.*

Kopmann, R. & Markofsky, M. (2000). Three-Dimensional Water Quality Modelling with TELEMAC-3D. *Hydrological Processes,* 14(13), 2279–2292.

Schnauder, I., Lin, B. & Bockelmann-Evans, B. (2007). Modelling Faecal Bacteria Pathways in Receiving Waters. *Proceedings of the ICE - Maritime Engineering*, 160(4), 143–153.

Smart Coasts = Sustainable Communities (2013). Smart coasts. Available at: http://www.smartcoasts.eu/index.aspx [Accessed 23 January 2017].

 ©2017, IAHR. Used with permission / ISSN 1562-6865 (Online) - ISSN 1063-7710 (Print)

LONGITUDINAL DISPERSION IN COMPOUND CHANNELS: THE ROLES OF FLOODPLAIN VEGETATION AND FLOW DEPTH

HOSSEIN HAMIDIFAR[1] & MARYAM ASKARI[2]

[1, 2] Water Engineering Department, Shiraz University, Shiraz, 7144, Iran.
hamidifar@shirazu.ac.ir

ABSTRACT

Due to the complexity in cross section, flow in a compound channel is completely different from that in a simple channel. The presence of vegetation over floodplains increases the level of complexity. In this paper, the effects of the floodplain vegetation density as well as relative flow depth on the longitudinal dispersion coefficient in an asymmetric compound channel are studied. A 10% solution of Potassium Permanganate is used as a tracer. Using image processing technique, variations of the tracer concentration at the three sections downstream of the release point are measured. The standard moment method has been used for calculation of the longitudinal dispersion coefficient in each section. The results showed that the dimensionless form of the longitudinal dispersion coefficient increases and decreases with relative flow depth as well as vegetation density, in the main channel and over the floodplain, respectively

Keywords: River; pollution transport; water quality; vegetation; flow relative depth.

1 INTRODUCTION

Rivers are among the natural resources affect the life in adjacent areas. When a contaminant is released into the river, it will be vertically and laterally well-mixed. Then, longitudinal dispersion becomes the principal mechanism responsible for spreading the contaminant cloud and for reducing high concentrations. Longitudinal dispersion is an important process in pollution transport in natural or manmade waterways. In its most general form, the one-dimensional transport of solutes can be described using the advection–dispersion equation (ADE) as:

$$\frac{\partial C}{\partial t}+U\frac{\partial C}{\partial x}=K\frac{\partial^2 C}{\partial x^2} \qquad [1]$$

where C is the contaminant concentration is the mean flow velocity, K is the longitudinal dispersion coefficient and x and t represent space and time respectively.

An accurate prediction of the longitudinal dispersion coefficient (K) is necessary to control the levels of pollution in sections of rivers kilometers long. Hence, it is of great interest to ecologists, river managers, and environmental engineers. Many factors such as the flow conditions, channel geometry and obstructions, and effluent discharge affect the value of K. The longitudinal dispersion is principally associated to the velocity-shear generated by vertical or horizontal velocity gradients in the flow. These shear flows are influenced by turbulent mixing as well as molecular motion. Several researchers have studied the dispersion process. Currently, it is possible to estimate the longitudinal dispersion coefficient with available empirical formulas, analytical formulations or conducting costly field tracer tests. However, some studies have shown that the empirical formulas can predict the longitudinal dispersion coefficient within an order of magnitude.

Natural rivers mostly have a compound cross section consisting of a narrow main channel bordered by one or two floodplains. The difference in flow velocity between the main channel and the floodplain produces strong lateral shear layers (Shiono and Knight, 1991). Hence, the flow structure in compound channels is much more complicated compared to simple channels. So, precise measurements of velocity components and contaminant transport in compound channels in field conditions are very challenging. Therefore, many studies are still placed on the well-focused laboratory measurements. A schematic view of an asymmetric compound channel (i.e. a compound channel with one floodplain placed adjacent the main channel) is shown in Figure 1.

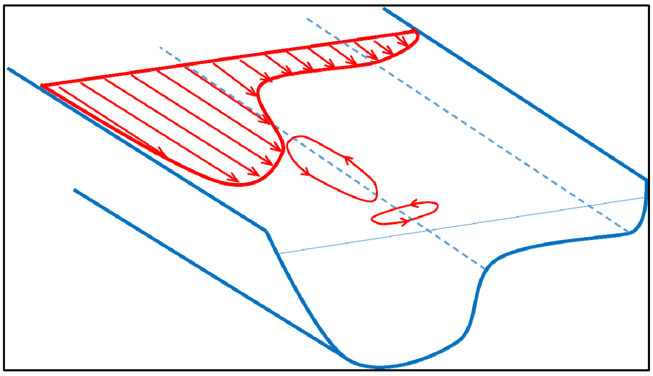

Figure 1. Schematic view of an asymmetric compound channel showing transverse velocity distribution and transitional vortices at the interface between main channel and floodplain.

The strong interaction at the interface between the high velocity main channel flow and the slower floodplain flow, transfer momentum from the main channel to the floodplains (Shiono and Knight, 1991). The interaction has a considerable effect on the flow structure, channel conveyance and pollutant transport. However, few of the previous studies have considered the effect of complexity of the cross section on the longitudinal dispersion coefficient. Some researchers have developed numerical and analytical models to predict the contaminant transport in compound channels (for example: Prinos, 1992; Djordjevic, 1993; Shiono et al., 2003; Shiono and Feng, 2003). However, due to the complex flow structure and strong secondary currents, the investigations needs to be improved by more studies.

Floodplains are usually covered with various types of vegetation. In recent years, river engineers prefer to implement innovative scenarios to combine methods to prevent the surroundings from inundating and stimulating ecological roles simultaneously. These goals can be achieved by preserving natural riverbank and floodplain vegetation (Järvelä, 2002), which are called bioengineering techniques. Floodplain vegetation have an effective contribution on the flow hydraulics and pollutant transport (Hamidifar et al., 2013; 2015). Usually, vegetation reduces the mean flow velocity and bed shear stress (Nepf, 1999; Bennett et al., 2002; Hopkinson and Nepf, 1999). Some studies have showed that the presence of vegetation on the floodplain increases the turbulence level at the interface of the main channel and the vegetated floodplain (McBridge et al., 2007; Yang et al., 2007).

Also, vegetation affects flow structure depending its type, density, flexibility, submergence, frontal area, etc. (Stone and Shen, 2002; Järvelä, 2002; Wilson et al., 2006). Vegetation density have a major impact on flow velocity by increasing or decreasing the frontal area (Petryk and Bosmajian, 1975). As velocity distribution is the key parameter in longitudinal dispersion of pollutants in waterways, the effects of presence of vegetation on pollutant transport must be well understood. In this paper, the effects of flow depth and vegetation density on the longitudinal dispersion coefficient are investigated experimentally.

2 MATERIALS AND METHODS

The experimental setup is completely described in Hamidifar et al. (2015) with the main characteristics of the experimental setup are briefly recalled here. The present experiments have been carried out using a rectangular flume 18 m long, 0.9 m wide and 0.6 m high. The flume cross section composed of a main channel 0.45 m wide, 0.14 m high and a flat floodplain o.45 m wide forming an asymmetric compound channel. A calibrated rectangular sharp crested weir was used to measure the discharge.

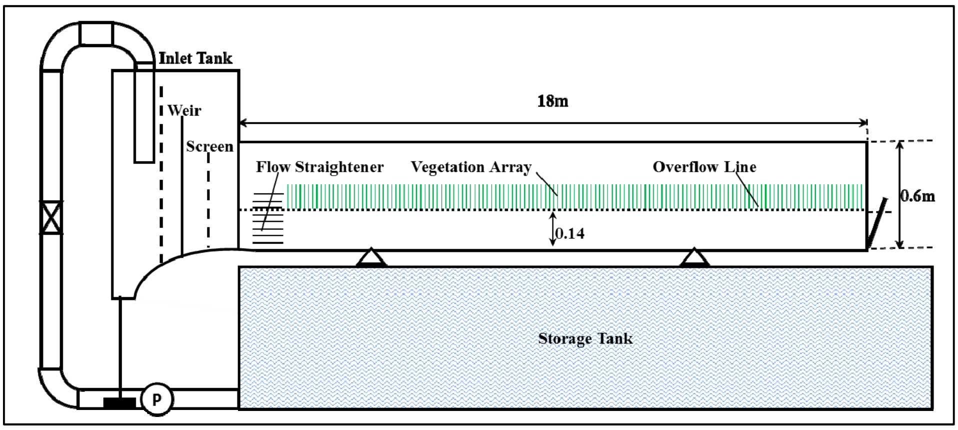

Figure 2. Schematic view of the experimental setup.

 ©2017, IAHR. Used with permission / ISSN 1562-6865 (Online) - ISSN 1063-7710 (Print)

A sideways-looking Nortek Vectrino+ Acoustic Doppler Velocimeter (ADV) with a sample frequency rate of 200 Hz and sampling duration of 120 s was used to measure three-dimensional instantaneous velocities. A schematic sketch of the experimental setup is shown in Figure 2. A 10 g/L solution of Potassium permanganate was used as a tracer. The tracer was injected suddenly using a half-tube filled with the dye solution and released uniformly across the flume width. The injection section was taken sufficiently far downstream of the start of the flume such that the flow was fully developed which is determined by the measured velocity profiles. The spreading of the tracer cloud was recorded at three locations 4.00, 6.44 and 8.88 m downstream of the injection point using three digital video capturing cameras. Then, the captured videos were used to extract image sequences.

Image processing as a modern technique is used by many researchers in pollutant transport studies (Sullivan, 1996; Nepf et al., 1997; Nepf, 1999). In this technique, the Beer–Lambert Law is used to relate the pixel intensity to the dye concentration. The Beer–Lambert Law can be written as:

$$\log(I_0/I)=\epsilon bC \qquad [2]$$

where I_0 and I are the initial and final pixel intensity, respectively, ε is the, b the path length over which the light is attenuated and C the contaminant concentration. The standard moment method has been used for calculation of the longitudinal dispersion coefficient in three sections. A total of 12 experiments were conducted with three different flow relative depths (Dr), defined as the ratio of flow depth over the floodplain to that in the main channel and three vegetation (φ), defined as the percentage of the bed are covered with vegetation in plan view.

3 RESULTS AND DISCUSSION

Using the Buckingham theory, the longitudinal dispersion coefficient (K) is nondimensionalized with (U_*H), where U_* and H are the bed shear velocity and flow depth respectively. Variations of the K/U_*H in the main channel are shown in Figure 3 for different relative flow depths and vegetation density. It is seen in Figure 3 that for a given flow relative depth, the dimensionless longitudinal dispersion coefficient increases with vegetation density (φ). Also, the dimensionless longitudinal dispersion coefficient increases generally with flow relative depth.

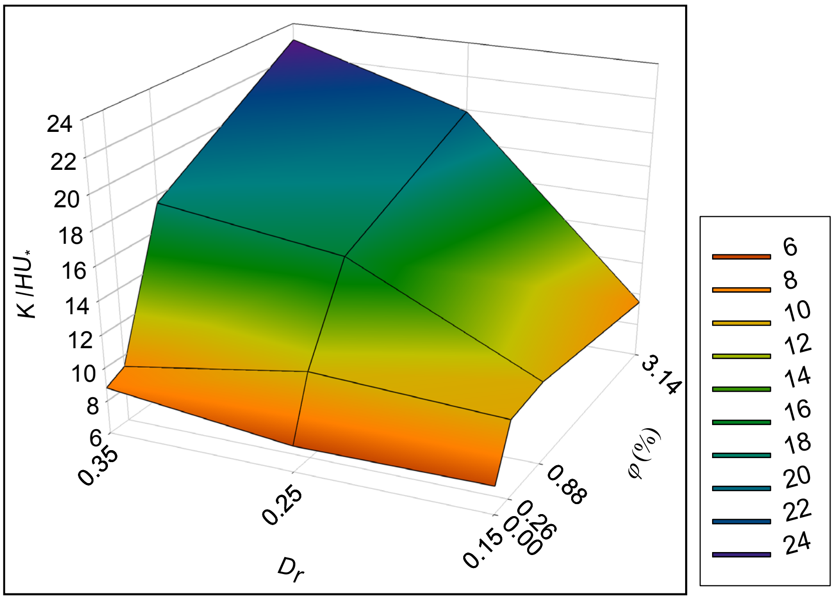

Figure 3. Variations of K/U_*H in the main channel against Dr and φ.

Figure 4 shows the variations of the K/U_*H over the floodplain. Unlike the trend of variations of K/U_*H in the main channel, the nondimensional longitudinal dispersion coefficient over the floodplain decreases with both flow relative depth and vegetation density. The decreasing trend of K/U_*H can be attributed to the fact that as the vegetation density increases, the flow is more diverted from the floodplain toward the main channel. This leads to an increase in the flow velocity in the main channel while the flow velocity over the floodplain decreases. Also, the velocity distribution over the floodplain becomes more uniform across the floodplain width. Consequently, the shear flow as an important factor for enhancement of the longitudinal dispersion decreases. It can be seen in Figure 4 that the maximum value of the vegetation density in the present study (φ=3.14%) gives the minimum value of the K/U_*H.

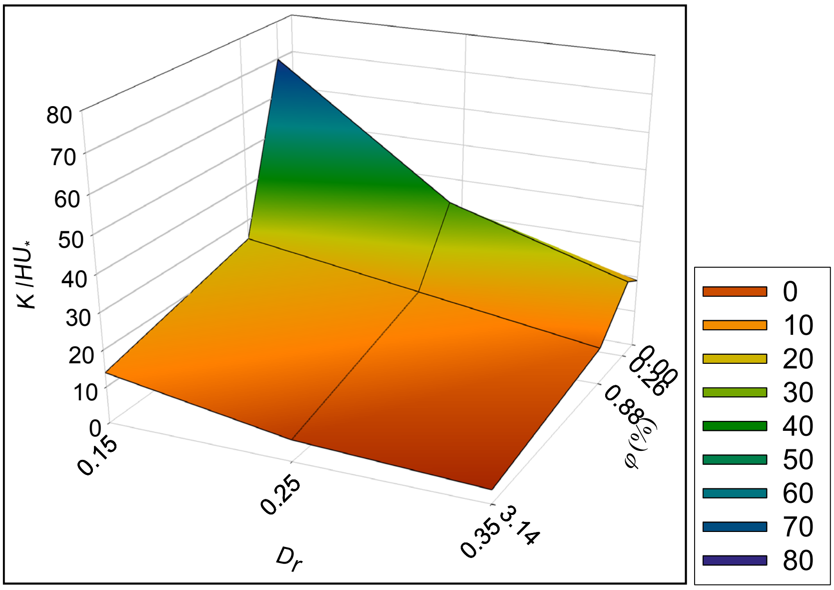

Figure 4. Variations of K /U*H over the floodplain against Dr and φ.

The decreasing trend of K/U*H with flow relative depth may seem inconsistent with the previous studies. Generally, it is reported in the literature that the longitudinal dispersion coefficient increases with flow depth (Fischer et al., 1979,). It should be noted that the trend of variations of K may be completely different to that of K/U*H. Considering the nondimensional longitudinal dispersion coefficient, it can be seen that the as the flow depth increases, K/U*H decreases. However, due to the greater values of K in the main channel, the contribution of flow depth in the variations of K/U*H is not very considerable compared to the K value. Hence, as observed in Figure 3, the nondimensional longitudinal dispersion coefficient increases with flow relative depth in the main channel while it decreases over the floodplain.

4 CONCLUSIONS

Estimating the longitudinal dispersion coefficient is of great interest to environmental river engineers involved in river water pollution control. Water quality is severely influenced by the presence of vegetation. Vegetation density have a great influence on the fate and transport of contaminants in rivers. In this paper, the effects of flow relative depth as well as vegetation density on the longitudinal dispersion coefficient in an asymmetric compound channel were investigated experimentally. The results showed that the nondimensional longitudinal dispersion coefficient in the main channel increases with both the flow relative depth and vegetation density. On the other hand, due to the presence of vegetation over the floodplain, the flow alters toward the main channel and hence a fairly tranquil flow with a relatively uniform velocity distribution develops on the floodplain. The uniform velocity distribution results in a reduction of nondimensional longitudinal dispersion coefficient with vegetation density.

REFERENCES

Bennett, S.J., Pirim, T. & Barkdoll, B.D. (2002). Using Simulated Emergent Vegetation to Alter Stream Flow Direction Within a Straight Experimental Channel. *Geomorphology*, 44(1–2), 115–126.

Djordjevic, S. (1993). Mathematical Model of Unsteady Transport and its Experimental Validation in Compound Open Channel Flow, *Journal of Hydraulic Research*, 31(2), 229–248.

Fischer, H.B, List, E.J., Koh, R.C.Y., Imberger. J. & Brooks, N.H. (1979). *Mixing in inland and coastal waters.* Academic Press, New York, pp 483.

Hamidifar, H., Omid, M.H. & Keshavarzi, A. (2015). Longitudinal Dispersion in Waterways with Vegetated Floodplain. *Ecological Engineering*, 84, 398–407.

Hamidifar, H. & Omid, M.H. (2013). Floodplain Vegetation Contribution to Velocity Distribution in Compound Channels. *Journal of Civil Engineering and Urbanism*, 3(6), 357–361.

Hopkinson, L. & Wynn, T. (2009). Vegetation Impacts on near Bank Flow. *Ecohydrology*, 2(4) 404-418.

Jarvela, J. (2002). Flow Resistance of Flexible and Stiff Vegetation: A Flume Study with Natural Plants. *Journal of Hydrology*, 269(1-2), 44-54.

McBride, M., Hession, W.C., Rizzo, D.M. & Thompson, D.M. (2007). The Influence of Riparian Vegetation on near-Bank Turbulence: A Flume Experiment. *Earth Surface Process and Landform,* 32(13), 2019-2037.

Nepf, H. (1999). Drag, Turbulence, and Diffusion in Flow through Emergent Vegetation, *Water Resources Research*, 35(2), 479–489.

Nepf, H.M., Sullivan, J.A. & Zavistoski, R.A. (1997). A Model for Diffusion within Emergent Vegetation. *Limnology and Oceanography*, 42(8), 1735-1745.

 ©2017, IAHR. Used with permission / ISSN 1562-6865 (Online) - ISSN 1063-7710 (Print)

Petryk, S. & Bosmajian, G. (1975). Analysis of Flow through Vegetation. *Journal of Hydraulic Engineering*, 101(HY7), 871-884.
Prinos, P. (1992). *Dispersion in Compound Open Channel Flow, in: Hydraulic and Environmental Modelling: Estuarine and River Waters*. Ashgate Publishing Ltd. 359-372.
Shiono, K. & Feng, T. (2003). Turbulence Measurements of Dye Concentration and Effects of Secondary Flow on Distribution in Open Channel Flows. *Journal of Hydraulic Engineering*, 129(5), 373–384.
Shiono, K. & Knight, D.W. (1991). Turbulent Open Channel Flows with Variable Depth across the Channel. *Journal of Fluid Mechanics*, 222, 617–46.
Shiono, K., Scott, C.F. & Kearney, D. (2003). Predictions of Solute Transport in a Compound Channel Using Turbulence Models, *Journal of Hydraulic Research*, 41(3), 247–258.
Stone, B.M. & Shen, H.T. (2002). Hydraulic Resistance of Flow in Channels with Cylindrical Roughness. *Journal of Hydraulic Engineering*, 128(5), 500–506.
Sullivan, J.A. (1996). Effects of Marsh Grass on Diffusivity, *Masters Thesis*. Massachusetts Institute of Technology, Cambridge, MA.
Wilson, C.A.M.E., Yagci, O., Rauch, H. & Olsen, N.R.B. (2006). 3D Numerical Modelling of a Willow Vegetated River/Floodplain System. *Journal of Hydrology*, 327, 13-21.
Yang, K., Cao, S. & Knight, D.W. (2007). Flow Patterns in Compound Channels with Vegetated Floodplains. *Journal of Hydraulic Engineering*, 133(2), 148-159.

Proceedings of the 37th IAHR World Congress
August 13 – 18, 2017, Kuala Lumpur, Malaysia

IMPACT OF BOUNDARY CONDITIONS ON A NUMERICAL MODEL OF FLOW OVER A POROUS BED AS AN APPROACH OF A RIVER'S HYPORHEIC ZONE

EDWIN SAAVEDRA-CIFUENTES[(1)], ANTONIO PREZIOSI-RIBERO[(2)], JORGE ALBERTO ESCOBAR-VARGAS[(3)] & LEONARDO DAVID DONADO[(4)]

[(1,2,4)] Water Resources Engineering Research Group (GIREH)
Universidad Nacional de Colombia, Bogotá, Colombia
eysaavedrac@unal.edu.co[(1)]; apreziosir@unal.edu.co[(2)], lddonadog@unal.edu.co[(4)]
[(3)] Pontificia Universidad Javeriana, Bogotá, Colombia
jorge-escobar@javeriana.edu.co

ABSTRACT

Several recent advances have been made on the development of numerical simulations for the flow dynamics on the hyporheic zone of rivers, generally for the interaction of a channel flow over a permeable bed, where the mixing of surface and subsurface water is evident. This work has taken into account a quick revision of the different conceptual and numerical applications of these advances, identifying their different assumptions and simplifications, such as unidimensional models of velocity fluctuation and coupled models of turbulent and laminar flow regimes. Special interest is shown in how the interface between the turbulent surface flow and the laminar flow in the porous media is managed, and the impacts of the imposed boundary conditions on the velocity and pressure fields. Consequently, a two-dimensional numerical model has been proposed and implemented in the CFD package OpenFOAM® adopting the existence of pressure and velocity fluctuations coming from the turbulent surface flow of an idealized river, assuming a whole uninterrupted computational domain containing both surface and porous flows, and characterizing the porous river bed using an apparent viscosity as a continuous space that represents the tortuosity of the flow inside the porous matrix. The case of study is a flow over a trapezoidal obstacle in order to visualize and quantify the dissipation of the velocity when entering into the porous bed, as well as to characterize the flow path within the hyporheic zone. Finally, a discussion is made on the evident impact of the different initial and boundary conditions evaluated, and on the nature of the transitional damping zone of the velocity and pressure fluctuations between the surface and porous spaces.

Keywords: Hyporheic zone; numerical simulation; apparent viscosity; surface water – groundwater interaction.

1 INTRODUCTION

Hyporheic flows are important for the environmental stability of fluvial aquatic ecosystems and an essential factor for the equilibrium in a river corridor. The mixing of surface water and groundwater in this zone provides the exchanges of nutrients and gases, basic inputs for the life development (Boano et al., 2014; Cardenas, 2015). This approach can be understood as a solute transport problem, but in order to characterize these solutes exchanges between the surface and the ground flows, from a numerical simulation point of view, the hydrodynamics must be first defined.

These exchanges due to the hyporheic flows are present at a very wide scale and defining an exact limit to their importance might be quite complex (Bencala, 2000). However, the present model is focused at the small scales for hyporheic exchanges, where hydrodynamic drivers are the main causes of flow between the surface and permeable beds, particularly turbulence of the free surface flow (Boano et al., 2014). At this scale of interest, turbulence is the main driver for the exchange between the surface flow and the permeable bed.

For the hyporheic zone hydrodynamic problem, a conciliation between two different flow regimes has to be made: the free surface flow whose velocity fields is clearly distorted by the turbulence effects, and a porous region usually assumed as a region of laminar flow. However, turbulence near a permeable wall is dominated by vortical structures, which are the culprits for the momentum exchanges between the channel and the permeable bed (Breugem et al., 2006).

Some approaches to simulate this hydrodynamic behavior have been developed, in this work they have been subdivided in two main categories:

1.1 Unidimensional Models of Velocity Attenuation:

Higashino and Stefan (2008) proposed a model for the damping of a theorized vertical velocity pulse trough a porous medium, as it is schematized in the Figure 1. For their model, it was assumed that the pressure distribution in the domain corresponded to a hydrostatic condition, thus the model would require the solution of the Burgers equation instead of the Navier-Stokes momentum conservation equation. Evidently, in a unidimensional model the solution for the mass conservation term becomes trivial, so in all the approaches of this category, incompressibility of the flow and mass conservation are left aside. Higashino solved the

 ©2017, IAHR. Used with permission / ISSN 1562-6865 (Online) - ISSN 1063-7710 (Print)

Burgers equation by adding to the diffusion term, the concept of apparent viscosity, whose deduction and analysis is delved into later.

The top limit of the domain in the models of this category correspond to the immediate free surface – porous bed interface. The boundary condition at this limit is a theorized velocity pulse, represented by a sinusoidal pulse (Higashino and Stefan, 2008; Penaloza-Giraldo,et al., 2015) or by field gathered data like an ADV vertical velocity signal (Preziosi-Ribero et al., 2016). Peñaloza-Giraldo (2015) solved a similar problem for the dissipation of a velocity pulse through a viscous interface, solving the Burgers equation by introducing a high-order SMPM numeral scheme.

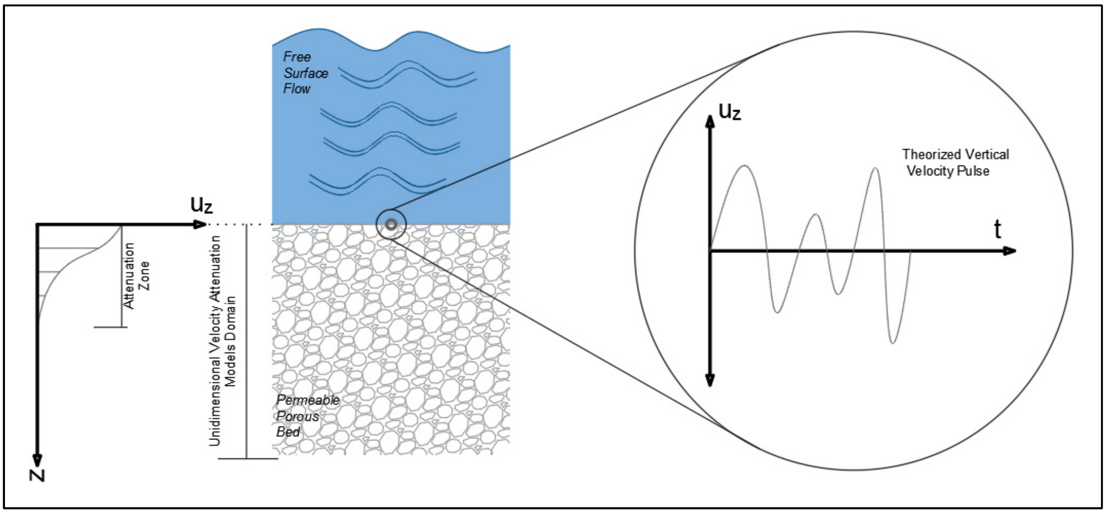

Figure 1. Study domain for the Unidimensional Velocity Attenuation Models

1.2 Coupled Multidomain Models

This category gathers the approaches to the problem where both surface and sub-superficial regimes are taken into account. A bidimensional approach of the problem was presented by Cardenas and Wilson (2007), in which the porous bed was assumed as a completely laminar regime. A no-slip condition was imposed on the interface between the surface water and the bed, hence, only the pressure field calculated on the surface would determine the flow under that limit. It is to be noticed that in this approach, the information can only travel from the surface domain to the porous domain, but not in the other direction, so an important assumption in this model is the independence of the surface flow regarding the flows underneath.

Discacciati et al. (2002) presented an analysis made for the coupling of the Navier-Stokes equations used in solving a surface flow hydrodynamics and the Darcy's law which describes the laminar flow expected inside a porous region. The no-slip condition between the two subdomains was rejected because both the velocity and pressure fields at the surface and inside the permeable bed interact simultaneously with each other. Hence, both the velocity and pressure fields at the bottom of the surface subdomain must be equal to the velocity and pressure fields at the top of the porous domain. But the existence of an attenuation zone was neglected because at the very top of the porous domain, it was assumed the validity of the Darcy's law, meaning that a laminar flow is assumed for the whole porous medium.

Lara et al. (2010) presented a three dimensional model to calculate the interaction of waves and porous coastal interaction. Even though it was not the same described problem of a channel flow over a porous bed, it solved the same set of Navier Stokes equations that describe surface flow. In this model, the authors solved the hydrodynamics inside the porous subdomain by a Volume Averaged Reynolds Averaged Navier Stokes equations (VARANS), which characterize the porous media by its porosity and a Forchheimer coefficients. This model was corroborated with experimental measurements, showing that their numerical approach was a good approximation for homogeneous porosity problems.

Breugem et al. (2006) have studied the influence of the permeability of the bed beneath a surface flow by simulating a flume via DNS in order to capture the dynamics of turbulence. The flow through the permeable bed was resolved using a Volume Average Navier Stokes (VANS) set of equations where the porosity and the particle size defined the porous subdomain. It was found that the velocity profile inside the permeable bed would decrease exponentially due to the diffusion of momentum and a removal of it. Another DNS simulation of turbulence was developed by Rosti et al. (2015) using the same approach of VANS for the porous media and a pseudo-spectral numeric scheme.

Finally, Silva et al. (2016) presented an approach similar to the model proposed in this paper, in which they solved the RANS equations for both the surface and permeable-bed domains, penalizing the flow in the porous bed by adding a momentum source term defined by means of the Forchheimer equation that takes into account the porosity and the particle size simulated.

2 MODEL OF COUPLED SURFACE AND POROUS SPACES

In general terms, the proposed model by the authors is the solution of the Reynolds Averaged Navier Stokes equations in an uninterrupted domain that contains both superficial and porous regions. The continuity of the solution of the velocity and pressure fields is guaranteed at the interface between the two regions, but the flow development on the porous region is restricted by a higher diffusivity term, similar to the Higashino's approach. Figure 2 shows these assumptions for the proposed model: u is the velocity and P is the pressure, the subindexs s, l and p represent the superficial region, the interface and the porous domain respectively. ν_m is the viscosity of the water and ν_p is an apparent viscosity with which the porous medium will be represented.

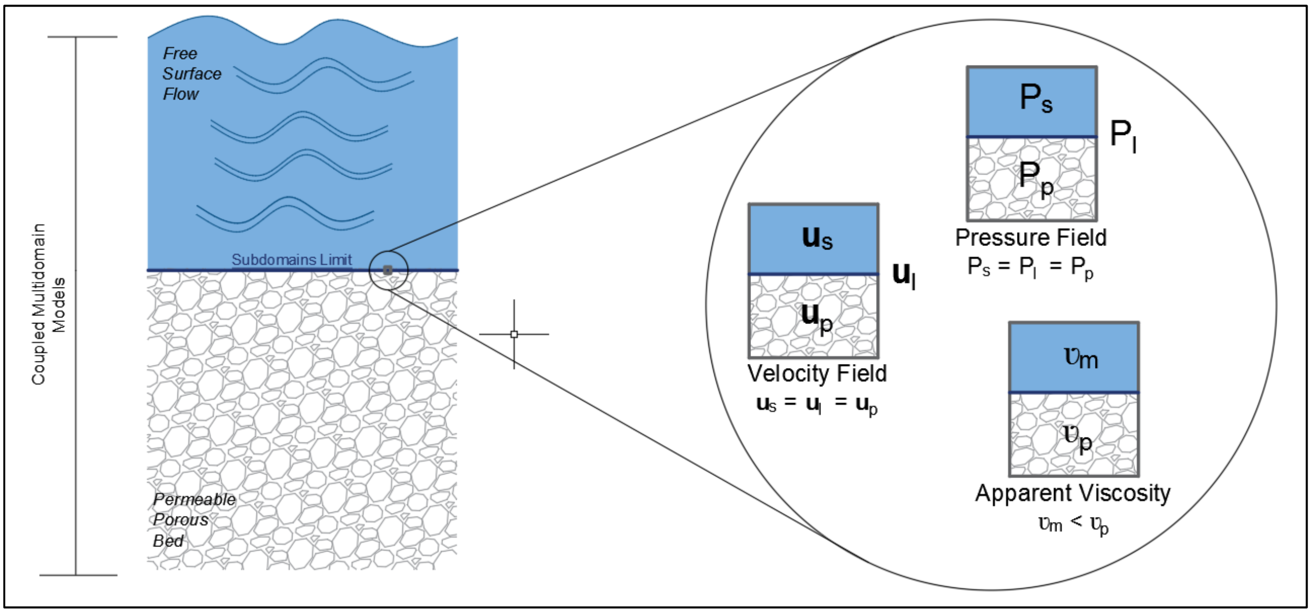

Figure 2. Study domain and main assumptions for the Proposed Model

2.1 Governing Equations

The starting point for this development is the Navier-Stokes equations for momentum and mass conservation for an incompressible flow. In Equations 1 and 2, $\boldsymbol{u}$ correspond to the velocity vector, ρ to the fluid's density, P to pressure and g to the gravitational acceleration.

$$\frac{\partial \boldsymbol{u}}{\partial t} + (\boldsymbol{u} \cdot \nabla)\boldsymbol{u} - \nu \nabla^2 \boldsymbol{u} = -\frac{1}{\rho}\nabla P + g \qquad [1]$$

$$\nabla \cdot \boldsymbol{u} = 0 \qquad [2]$$

For a surface flow, the diffusion term, ν corresponds to the kinematic viscosity of the fluid, in this case it is assumed constant with $\nu = \nu_m = 10^{-6}\, m^2/s$ as value. But for the region in the domain where the porous region can be founded, this diffusion takes a greater value, simulating the tortuosity of the flow, hence restricting the velocity field. Therefore, at the porous subdomain ν will be equal to the apparent viscosity ν_{ap}.

2.2 Apparent Viscosity

ν_{ap} is a diffusive term that emulates the effects of the tortuosity of the porous medium, representing the difficulty for the water to flow through an obstructed medium as a porous matrix. The relationship between this fictitious parameter and the characteristics of the porous medium is given by considering as true two different laminar flow models. One is to assume the porous media as a capillary tube model and the other is the approach of the hydraulic radius models, from which the Kozeny-Carman equation is deduced (Bear, 1970). Combining this two approaches, the expression used at the unidimensional approaches for calculating the apparent viscosity is found, as seen in Equation 3. It is important to note that this expression can lead to values of apparent viscosity lower than the molecular viscosity of the water, which is the lowest limit for this diffusion term.

$$\nu_{ap} = 5.625\, \nu_m \left[\frac{d}{d_s e}\right]^2 \qquad [3]$$

 ©2017, IAHR. Used with permission / ISSN 1562-6865 (Online) - ISSN 1063-7710 (Print)

In Equation 3, e represents the voids ratio, d the pore length and d_s the solid particle size. This equation is written in furtherance to show that the apparent viscosity can be calculated from two ratios measured from a porous medium: the voids ratio, known as the relation between the volume of pores (voids) and the volume of solids, and the pore size-particle size ratio. For the volumetric ratio, a smaller porosity will result in a higher apparent viscosity, but to a bigger pore size, the flow will be slower in the porous media. Although counterintuitive, this is consistent regarding the capillary tube model taken into account. Notwithstanding the aforementioned relation, this equation shows a parabolic relation $Pore\ Lenght^2 \propto 1/\nu_{ap}$, exhibited in the Figure 3.

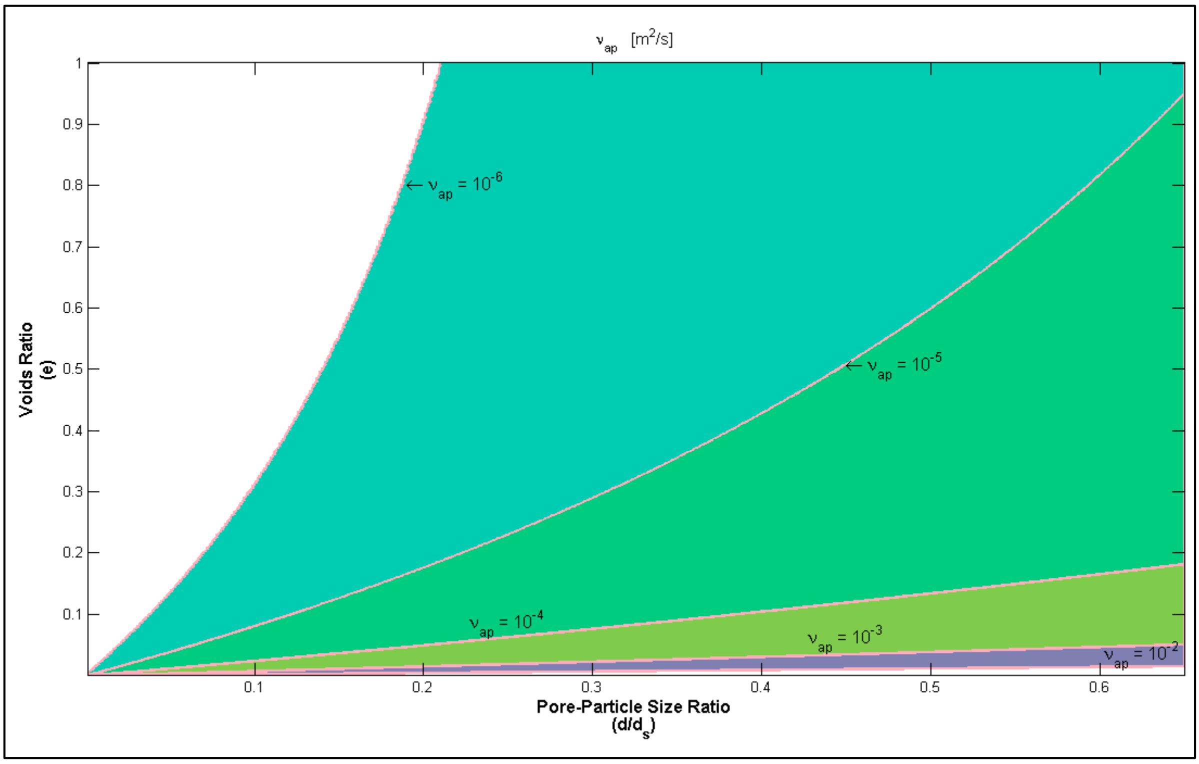

Figure 3. Relationship between the voids-ratio, pore-particle size ratio and the apparent viscosity

For a sand and gravel mixture, the porosity can vary between 20 – 30% (0.25 – 0.43 void ratio) (Fetter, 2001). For a polydisperse sand, this value tends to fall between 30 – 35%, although this value might increase for larger size particles with untouching faces (Nimmo, 2004) as the case for a high-mountain river. Particularly for a sediment bed on a river, this sediment porosity can be calculated from semi empirical formulations as a function of the mean diameter of the sediment mixture (Wu and Wang, 2006).

3 STUDY CASE

3.1 Geometry

The simulation executed was the case of a bidimensional $6.10m$ length tilted channel with a trapezoidal obstacle at $X = 1.10m$ of the same material of the permeable bed. A depth of $0.80m$ of porous media were adopted and the computational domain was extended vertically over $0.55m$ for the free surface flow. A steady main flow was set by giving a $0.1\ m/s$ horizontal velocity at the inlet of the domain. A constant 0.01% slope was set for the flume. Figure 4 shows the two computational domains set for the problem, blue representing the free surface flow and gray the permeable region. A more refined meshing was set near the trapezoidal obstacle. The grids in Figures 4(a) and 4(b) differ in the position of the boundary conditions given to the porous media, in order to evidence their influence in the resultant flow path inside the bed.

3.2 Boundary and Initial Conditions

In terms of the velocity, it was set to a permanent horizontal velocity of 0.1m/s at the inlet and a zero gradient condition was set at the free surface flow outlet. No-slip conditions were set for the lower limit of the computational domain and the side limits of the porous region. For the computational domain shown in Figure 4(a), it has also been analyzed, the effect of a Newmann type boundary condition (BC) set at the right side of the porous domain, identified as BC_3, allowing the outlet to be the entire right face of the domain. Finally, a hydrostatic condition was set for the initial pressure field. For closure, the RANS equations were used to describe the effects of the turbulence in the entire computational domain, having a k-epsilon turbulence model proposed for this purpose. Table 1 shows the three different boundary conditions sets analyzed in this work.

©2017, IAHR. Used with permission / ISSN 1562-6865 (Online) - ISSN 1063-7710 (Print)

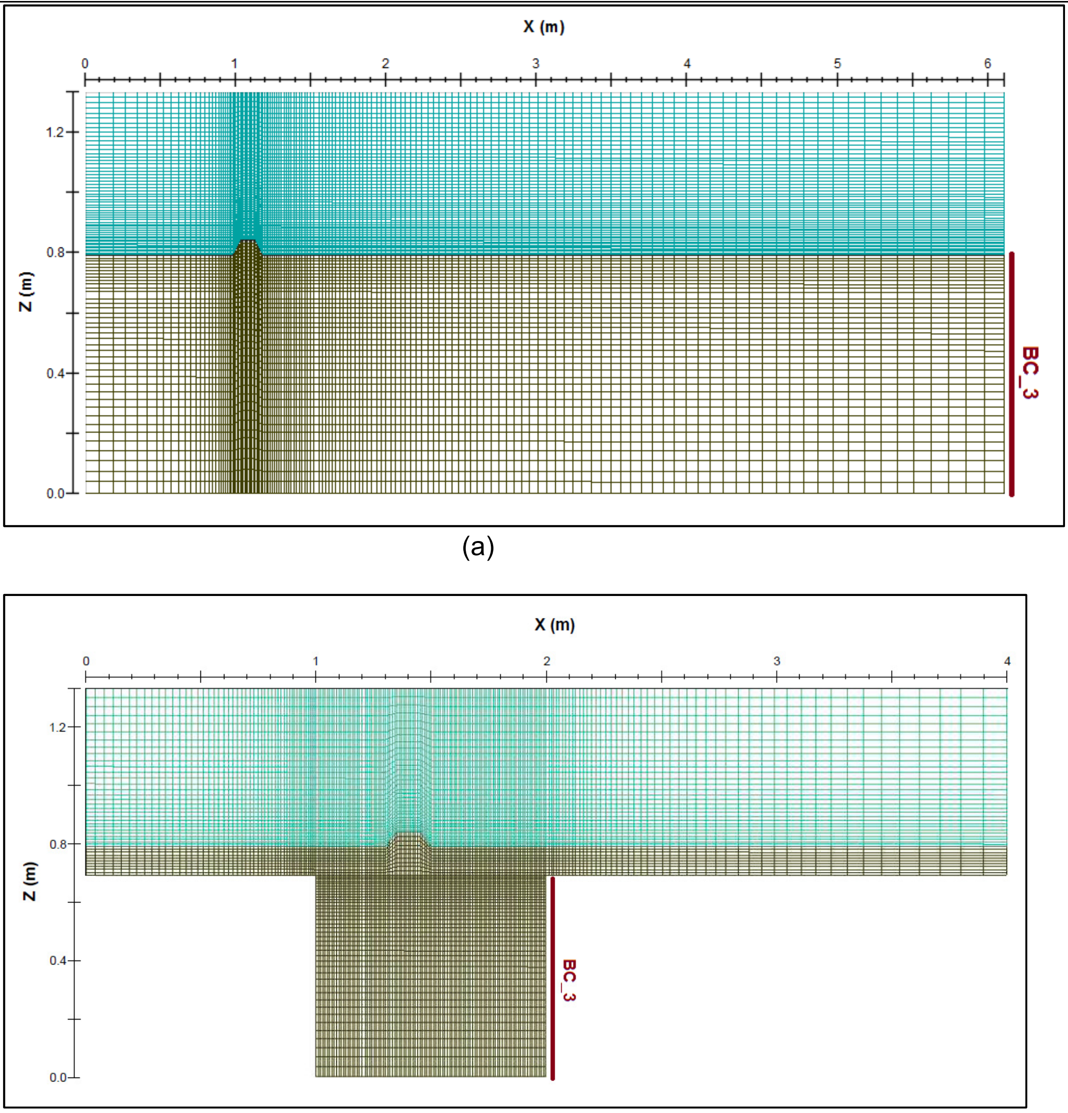

(a)

(b)

Figure 4. Computational Domains

Table 1. Boundary Condition Cases

BC CASE	COMPUTATIONAL DOMAIN	BOUNDARY CONDITION AT BC_3
A	Figure 4(a)	$\boldsymbol{u} = 0$
B	Figure 4(a)	$\nabla \boldsymbol{u} = 0$
C	Figure 4(b)	$\boldsymbol{u} = 0$

4 RESULTS

Figure 5 shows the streamlines and flow directions evidenced for the different cases of boundary conditions and for two values of apparent viscosities. Figures 5(a), 5(c) and 5(e) are the result of the simulation for an apparent viscosity of $10^{-2}\ m^2/s$ and Figures 5(b), 5(d) and 5(f) for an apparent viscosity of $10^{-5}\ m^2/s$. As predicted, for higher values of apparent viscosity, the flow through the porous media was more restricted than for values close to the molecular viscosity of the water. Formation of large vortexes could be evidenced when the apparent viscosity was low. Consistently with the apparent viscosity definition, higher values of ν_{ap} could be interpreted as lower values for porosity or void-ratio, however, accordingly with the definition aforementioned, the order of magnitude of apparent viscosity for which an non-turbulent flow can be developed were given for unrealistic values of porosity and pore-particle size ratios.

 ©2017, IAHR. Used with permission / ISSN 1562-6865 (Online) - ISSN 1063-7710 (Print)

Figures 5(a) and 5(b) show the BC case A where the porous region is bounded by a no-slip condition in all of its limits, except for interface with the surface flow. This restriction affected the paths of the subsurface flow, obligating them to eventually come out as surface flow, independently of the configuration of the trapezoidal obstacle. For Figures 5(c) and 5(d), the BC case B was set where the no-slip condition is removed for the right frontier, allowing an outlet for the subsurface regions as well as the free surface flow region. As represented, the flow paths evidenced before are now given by the channel tilt, so by this restriction no fluid can be found returning to the superficial domain, which might be the case for high mountain rivers in areas with great longitudinal slopes. Finally, Figures 5(e) and 5(f) represent the BC case C where a no-slip condition is set but closer to the trapezoidal obstacle. This exercise shows that the flow paths generated underneath the obstacle have a very different behavior than those shown in the figures before, so it is the evident of the influence that an imposed Dirichlet boundary condition could have in the simulation of the flow.

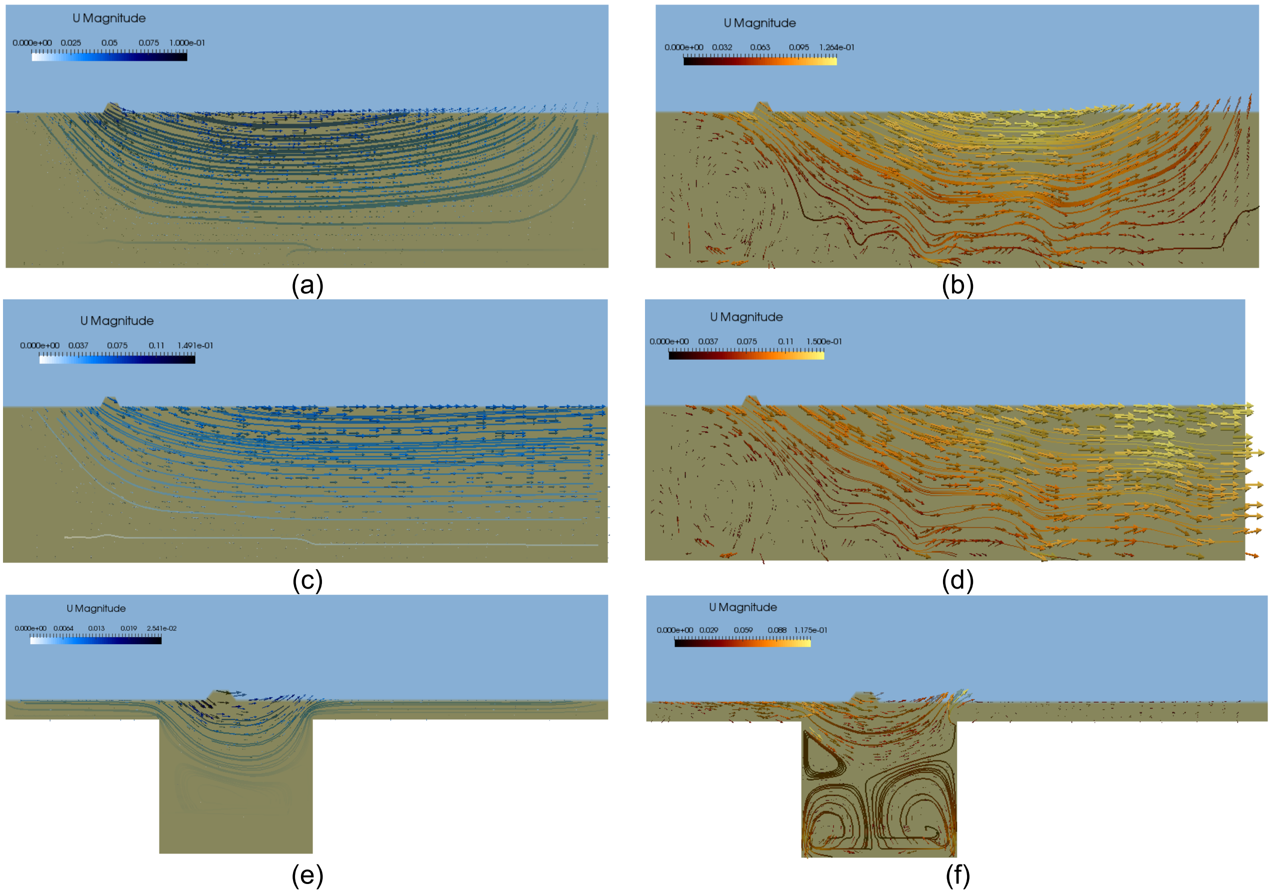

Figure 5. Streamlines for the velocity fields in the porous region for different boundary conditions

The simulation of the flume over an impervious bed has been developed for the same geometry in order to show the main differences with the velocity profile that is formed in the free surface region. Figure 6 shows the horizontal velocity profiles on four different locations for different values of apparent viscosity and on the three cases evaluated.

For the three BC cases, the velocity profile at the point before reaching the trapezoidal obstacle decelerates due to its presence, with this effect being stronger for the impermeable bed case because the no-slip condition must be satisfied on the obstacle's surface. However, when the apparent viscosity of the obstacle is smaller than $10^{-4}\ m^2/s$, the deceleration of the main flow is not evident anymore. On the contrary, at the interface between regions, a peak velocity can be evidenced as the addition of the surface flow going through the porous trapezoid and the preceding inertia of the flow that has already developed under the interface.

In every value of apparent viscosity and every case studied, the velocity reaches a maximum when the bed is impermeable, which is an effect of the continuum principle because the flow is being restricted to a tighter geometry, consequently it acquires a higher velocity.

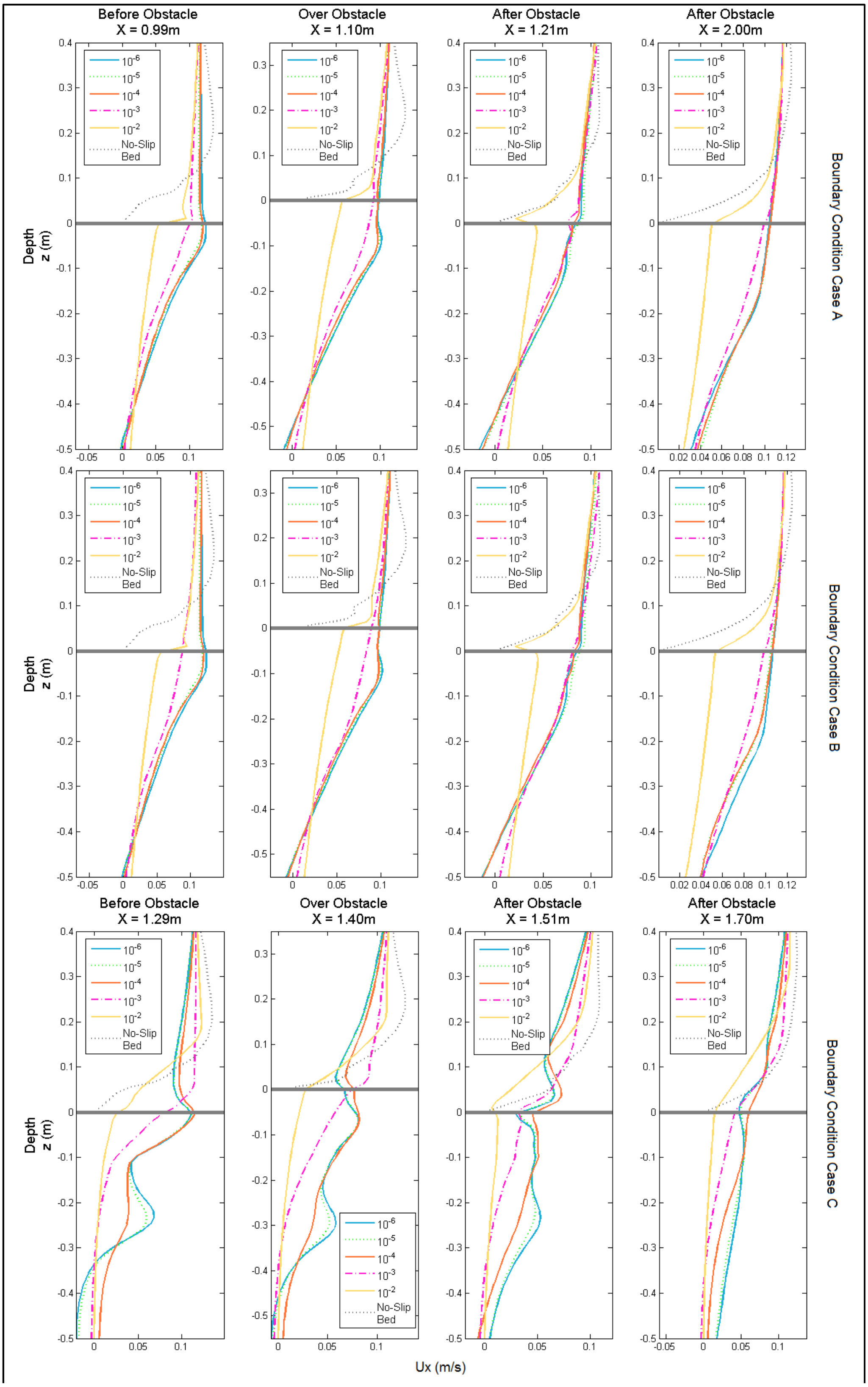

Figure 6. Velocity profiles for the BC cases set and different ν_{ap} values on four locations of the stream

For the BC cases A and B in Figure 6, the behavior of the velocity after the obstacle is similar for the impermeable bed and a high value of apparent viscosity. However, for values greater than $10^{-3}\ m^2/s$, the flow behaves almost as a unique flow where the impact of the porous bed presence is no longer evident. This gives an idea for the order of magnitude of the apparent viscosity in order to correctly simulate the existence of a permeable porous bed. This behavior contradicts the values obtained from Equation (3) when common values of voids ratio and pore size particle size ratio are used, which vary only from orders of magnitude between $10^{-5}\ m^2/s$ and $10^{-4}\ m^2/s$.

 ©2017, IAHR. Used with permission / ISSN 1562-6865 (Online) - ISSN 1063-7710 (Print)

For the BC case C in Figure 6, the velocity profiles for the surface region differ from the ones developed for the aforementioned computational domain. It can be observed of a higher influence of the obstacle for a larger range of values of apparent viscosity, however, as it was shown for the other state of boundary conditions, this deflections of the velocity field are not the result of the presence of a permeable bed but are a consequence of the restrictions imposed beneath the obstacle. Likewise, the subsurface velocity profiles are deflected because of the formation of the vortical structures resultant from the narrowed boundaries in this region, and not an effect of the presence of the permeable interface.

5 CONCLUSIONS

Numerical simulations of a complete domain containing both free surface flow and porous permeable regions have been performed by coupling these two spaces via the diffusive term in the Navier-Stokes equations for momentum conservation, adopting an apparent viscosity as a higher diffusion coefficient for the momentum transfer inside a porous region and setting different boundary conditions for those cases. A k-epsilon turbulence model was adopted as closure for the Navier-Stokes equations, allowing the development of secondary flows inside the porous region in order to evaluate the appropriateness of the proposed diffusive term.

It has been shown of a brief state of the art of numerical simulations made for the problem of a free flow over a permeable bed and its applications for the particular small scales hyporheic flow of a river where the flow exchanges between surface water and groundwater are mainly driven by the turbulence of the flow above. In that order, a numerical model has been proposed to recollect the approaches of unidimensional velocity attenuation and coupled multidomain models into the bidimensional model described above, considering the effects of both pressure and velocity simultaneously in the free surface region and the permeable bed.

It is clear that the presence of a permeable boundary has a direct effect on the development of the flow above because the no-slip condition that would exist for an impermeable bed is no longer restrictive for the development of a continuous velocity field. However, a restriction to the flow must exist on the bed surface and inside the porous region in order to emulate the tortuosity of the flow. For this model, a diffusive type term similar to the viscosity was implemented and it was found that it has to have an order of magnitude of $10^{-2}\ m^2/s$ in order to clearly emulate the effects of a flow inside a porous media.

Nevertheless, this order of magnitude is contradictory with the deduction of apparent viscosity given by Higashino and Stefan (2008), but it has to be taken into account that these definitions were derived from two different laminar models for porous media and the proposed model simulates the turbulent flow developed in that same media. Further work will be focused to correctly define a diffusive term from the characteristics of a permeable bed and evaluate if this only term is enough to correctly describe the flow inside the porous media.

Regarding the influence of the boundary conditions. It has been found that a special care has to be taken with these restrictions if a numerical simulation is expected to serve as a phenomenological model, because it would lead the simulation of the flow only descriptive as just a particular case. For this study case, it was shown that the location of the boundaries affected the flow paths inside the porous regions notably, especially for the case where a narrowed porous region was imposed. A deeper evaluation of a correct way to impose boundary conditions for this kind of numerical simulations is expected to be made in the near future, aside from calibrations with physical models.

REFERENCES

Bear, J. (1970). *Dynamics of Fluids in Porous Media*. New York. American Elsevier.

Bencala, K. E. (2000). Hyporheic Zone Hydrological Processes. *Hydrological Processes*, 14(15), 2797-2798.

Boano, F., Harvey, J. W. W., Marion, A., Packman, A.I.I., Revelli, R., Ridolfi, L. & Wörman, A. (2014). Hyporheic Flow and Transport Processes: Mechanisms, Models, and Biogeochemical Implications. *Reviews of Geophysics*, 52(4), 603-679.

Breugem, W. P., Boersma, B. J. & Uittenbogaard, R. E. (2006). The Influence of Wall Permeability on Turbulent Channel Flow. *Journal of Fluid Mechanics,* 562, 35-72.

Cardenas, M. B. (2015). Hyporheic Zone Hydrologic Science: A Historical Account of its Emergence and a Prospectus. *Water Resources Research*, 51(5), 3601-3616.

Cardenas, M. B. & Wilson, J. L. (2007). Hydrodynamics of Coupled Flow Above and Below a Sediment-Water Interface with Triangular Bedforms. *Advances in Water Resources*, 30(3), 301-313.

Discacciati, M., Miglio, E. & Quarteroni, A. (2002). Navier-Stokes/Darcy Coupling: Modeling, Analysis, and Numerical Approximation. *Revista Matemática Computlense.* 22(2), 315-426.

Fetter, C.W. (2001). *Applied Hydrogeology*. Prentice-Hall Inc.

Higashino, M. & Stefan, H. (2008). Velocity Pulse Model for Turbulent Diffusion from Flowing Water into a Sediment Bed. *Journal of Environmental Engineering*, 134(7), 550-561.

Nimmo, J. R. (2004). Porosity and Pore Size Distribution. *Encyclopedia of Soils in the Environment*, 3, 295–303.

Penaloza-Giraldo, J. A., Escobar-Vargas, J. A. & Donado, L. D. (2015). A Spectral Multidomain Penalty Method Solver for the Simulation of the Velocity Attenuation in Hyporheic Flows. *Procedia Environmental Sciences*, 25, 206–213.

Preziosi-Ribero, A., Escobar-Vargas, J. A., Penaloza-Giraldo, J. A. & Donado, L. D. (2016). A High Order Element Based Method for the Simulation of Velocity Damping in the Hyporheic Zone of a High Mountain River. *EGU Goephysical Research Abstracts*, 18, 10673.

Rosti, M. E., Cortelezzi, L. & Quadrio, M. (2015). Direct Numerical Simulation of Turbulent Channel Flow over Porous Walls. *Journal of Fluid Mechanics*, 784, 396-442.

Silva, A. M. F., Mumford, K. G., Mirzaei, S. H. S., Fruetel, C. & Rey, A. (2016). Physical and Numerical Modeling of Hyporheic Flow through a Gravel Bar. *River Flow 2016 - Constantinescu, Garcia & Hanes (Eds).* 1364-1369.

Wu, W. & Wang, S. S. Y. (2006). Formulas for Sediment Porosity and Settling Velocity. *Journal of Hydraulic Engineering*, 132(8), 852–862.

 ©2017, IAHR. Used with permission / ISSN 1562-6865 (Online) - ISSN 1063-7710 (Print)

A HIGH ORDER ELEMENT BASED METHOD TO ESTIMATE HYPORHEIC FLOW IN RIVERS USING THE BURGERS' EQUATION

ANTONIO PREZIOSI-RIBERO[1], EDWIN SAAVEDRA-CIFUENTES[2], JORGE A. ESCOBAR-VARGAS[3] & LEONARDO DAVID DONADO [4]

[1,2,3,4] Universidad Nacional de Colombia, Sede Bogotá, Facultad de Ingeniería, Grupo de Investigación de Ingeniería de Recursos Hídricos GIREH, Bogotá, Colombia,
e-mail apreziosir@unal.edu.co; eysaavedrac@unal.edu.co; lddonadog@unal.edu.

[4] Pontificia Universidad Javeriana, Facultad de Ingeniería. Bogotá, Colombia,
e-mail jorge-escobar@javeriana.edu.co

ABSTRACT

This paper proposes the use of the Burgers' Equation to represent flow in porous channels beds to obtain mean velocity profiles to model Hyporheic Flow (HF). The solution was achieved by using a Spectral Multi Domain Penalty Method (SMPM), with a fractional step scheme including nonlinear advective and diffusive terms, solved using an explicit and an implicit scheme respectively. The model proposed to consider the stream bed as the computational domain with homogeneous and isotropic conditions set in the viscous term of the equation. The results of this research can be compared with Large Eddy Simulations (LES) and different experimental results to evaluate the viability of the use of a continuum model that represents the HF accurately. Moreover, the size of the Hyporheic Zone (HZ) can be estimated according to the flow profile obtained from the modeling process. The results obtained show that the velocity profile at the top of the domain decreases with depth and depends on the viscosity term and the velocity signal used as the model's input, as demonstrated in previous studies.

Keywords: Hyporheic flow; hyporheic zone; burgers' equation; spectral methods; turbulence modeling.

1. INTRODUCTION

The Hyporheic Zone (HZ) is a key element in the river systems (Boano et al., 2014). In fact, this is the place where the Groundwater Surface Water Interactions (GWSWI) take place. In the region where HZ contaminants are deposited, nitrogen is removed and biota grows thanks to the various microorganisms and processes that are present. Because of these reasons, the HZ has been a subject of study in different sciences like Ecology, Hydrology, and Hydrogeology for the last 50 years. Nevertheless, the study of this topic poses a challenge to the scientists due to the complexities of heterogeneous media, turbulent processes, and the difficulties of obtaining experimental data to validate different models (Buss et al., 2009).

The main models used to represent Hyporheic Flow (HF) consist of the coupling of two separate domains with Boundary Conditions (BC) that transfer velocity and pressure between them (Discacciati et al., 2002). Generally, in the top part of these models, the Navier-Stokes (NS) equations with some simplification are solved, and for the porous media, Darcy's Law (DL) is used to estimate the flow (Huang et al., 2008) (Cardenas & Wilson, 2007). The velocity range managed in the porous media flow near the free surface flow produces a Reynolds number high enough to make DL inaccurate, theoretically speaking (Bear, 1975). Furthermore, the presence of momentum transport between media due to turbulent processes is neglected by the models proposed. The latter results in underestimation of flow and transport by several orders of magnitude due to the changes in flow properties like viscosities and diffusion coefficients (Tennekes & Lumley, 1972). Therefore, there is a need for a model that can include the phenomena left behind by previous models to characterize and quantify the HF.

Some recent models have included the effects of turbulence and velocity fluctuations, like the ones developed by Higashino & Stefan (2009) and Peñaloza-Giraldo et al, (2015). In these cases, different velocity signals were used as input and their damping along a porous domain was represented. Their results were coherent among studies, in the sense that the highest damping of the velocity signal takes part in the top of the porous domain, closer to the position where the free surface flow is located. In addition, the dependency of the velocity reduction on the viscous term shows that the smaller the resistance to flow, the deeper the penetration of a turbulent velocity signal into the media studied (Higashino & Stefan, 2008).

Our research's basic aim is to study the expansion of the results presented by Higashino & Stefan (2009) and Peñaloza-Giraldo et al, (2015) by expanding the one dimensional theoretical model, first to a one-dimensional model fed by a continuous velocity signal gathered in a high mountain stream, and then using the velocity field from a large eddy simulation in a two-dimensional case. For this purpose, we propose the use of a Spectral Multi-Domain Penalty Method (SMPM) to solve the Burgers' equation in one and two dimensions.

This document presents an analysis of the results obtained for the one-dimensional simulation for various cases examined and the proposal of the two-dimensional model fed by a Large Eddy Simulation (LES) being currently developed at Northwestern University.

This document is set to the following structure: firstly, the governing expression for the physical phenomenon is presented. Then, the one-dimensional model is presented with the numerical approach used for the solution. After that, the results of different simulations are shown and compared, and finally the two-dimensional model is proposed with the conditions and the expected results based on the one-dimensional results obtained previously.

2. GOVERNING EXPRESSION AND PHYSICAL MODEL

2.1 From Navier-Stokes equations to Burgers' equation

The incompressible NS equations [1] are used as the starting point for the numerical model. In these equations, $\boldsymbol{u_i}$ represents the velocity field, $\boldsymbol{P}$ the pressure, $\boldsymbol{x_i}$the spatial domain and $\boldsymbol{t}$ the time. The term $\boldsymbol{\nu}$ used in the equation is the kinematic viscosity coefficient, which is a property of the fluid. When the condition of hydrostatic pressure is assumed [2], the pressure term of [1] will be equivalent to the external forces applied in the momentum equation and generating Burgers' equation [3]. The pressure in the streamwise and transverse direction, for the multidimensional case, are neglected recalling that hydrostatic pressure over a horizontal plane is equal in all directions.

$$\frac{\partial u_i}{\partial t} + u_j \frac{\partial u_j}{\partial x_i} = \frac{-1}{\rho} \frac{\partial P}{\partial x_i} + \nu \frac{\partial^2 u_i}{\partial u_i \partial u_j} + g_z \qquad [1]$$

$$\frac{dP}{dz} = -\rho g_z \qquad [2]$$

$$\frac{\partial u_i}{\partial t} + u_j \frac{\partial u_j}{\partial x_i} = \nu \frac{\partial^2 u_i}{\partial u_i \partial u_j} \qquad [3]$$

2.2 Apparent viscosity coefficient

The only resistance to flow in the Burgers' equation is the kinematic viscosity of the fluid. In our case, and as used by Higashino et al. (2008) and Peñaloza-Giraldo et al. (2015), water kinematic viscosity is replaced by an apparent viscosity that is dependent of physical properties of the river bed that is being analyzed in equation [4]. The apparent viscosity $\boldsymbol{\nu}$ is a function of the kinematic viscosity of the fluid $\boldsymbol{\nu_0}$, the porosity of the riverbed $\boldsymbol{\phi}$, the mean diameter of the sediment $\boldsymbol{d}$ and the mean separation between particles in the riverbed $\boldsymbol{d_s}$ (Bear, 1975).

$$\nu = \left(\frac{\nu_0}{32}\right)\left(\frac{1}{5.6 \times 10^{-3}}\right)\left(\frac{1-\phi}{\phi^2}\right)\left(\frac{d}{d_s}\right)^2 \qquad [4]$$

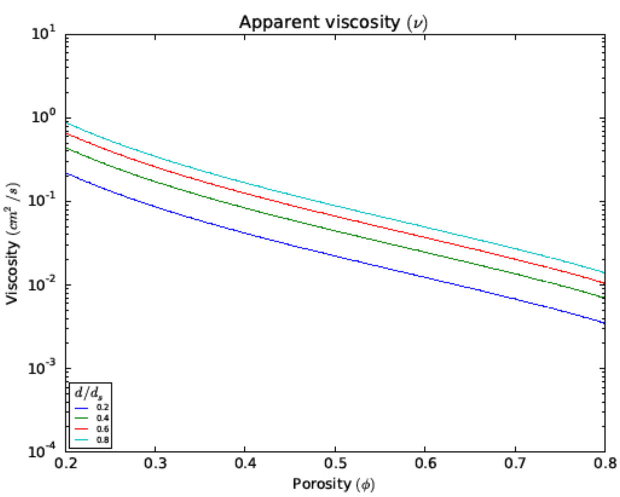

Figure 1. Apparent viscosity as a function of porosity

©2017, IAHR. Used with permission / ISSN 1562-6865 (Online) - ISSN 1063-7710 (Print)

Figure 1 shows the relationship between porosity and viscosity for different values of the relationship between the mean grain size and the mean separation between grains in the riverbed analyzed. For the sake of our model, the values of apparent viscosity are modified between different runs of the model to test its sensibility to the change of this parameter. Three values of viscosity were used, i.e. one hundred, one thousand and ten thousand times of water kinematic viscosity ($\mathbf{1.5} \times \mathbf{10^{-2}} \boldsymbol{cm^2/s}$).

As it is shown in Figure 1, the apparent viscosity value, in a range of porosity varying 0.4 to 0.8, has an order of magnitude that varies between *O(10^{-3})* to *O(10^{-1})* cm^2/s. This value exceeds by nearly three orders of magnitude the kinematic viscosity of water, thus the opposition to the flow is higher with the apparent viscosity than with the typical kinematic viscosity of water.

Regarding the grain size $\boldsymbol{d}$ and the separation between them, $\boldsymbol{d_s}$, it is intuitive that the separation is smaller than the mean diameter of the particle, hence the term $\boldsymbol{d/d_s}$ is greater than one and tends to considerable values in compact riverbeds. As this term grows, the viscosity will increase proportional to its square, pointing the importance of the cohesion of the material studied.

As regards to the behavior of the apparent viscosity in function of the porosity, it is clear that with low values of $\boldsymbol{\phi}$ the viscosity will grow asymptotically to the apparent viscosity axis, and when getting close to 1.0, the viscous effect caused by the riverbed will cancel this apparent viscosity.

2.3 Velocity signals

The velocity signals were captured in the Gualí River, in the municipality of Honda, in Colombia. Time series of circa 3 minutes were gathered using an Acoustic Doppler Velocimeter (ADV) near the river bed with a sampling frequency of 200 Hz. Figure 2 shows a typical velocity signal gathered in the river. As expected by the log law of flow in channels, the magnitude of the velocity in the streamwise direction near the river bed approaches to zero.

Nevertheless, not all the signals gathered in the field were used for the modeling since some measurements were interrupted by large sediments carried by the river that exposed the equipment to physical damage. As a matter of fact, for this document only three signals were analyzed and used as input for the one-dimensional model.

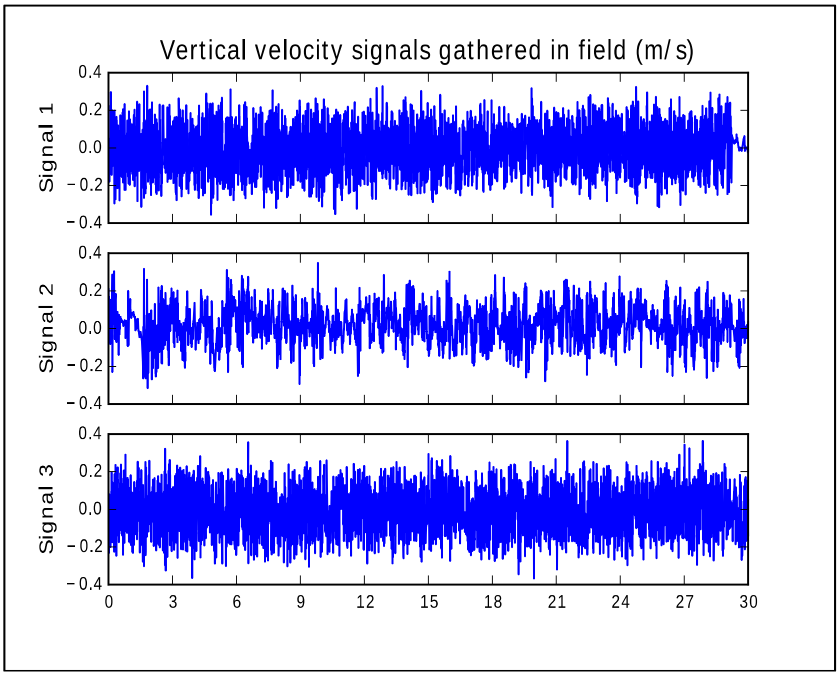

Figure 2. Sample of three velocity signals

3. NUMERICAL MODEL

General explanation and mention of the numerical schemes used: The numerical scheme used for the modeling of HF is a Spectral Multi Domain Penalty Method (SMPM), which consists of mainly three parts. Firstly, the time discretization via a high order Adams-Bashforth scheme, then a linearization and explicit solving of the advective term and finally a fully implicit scheme to solve the diffusive part of the code.

This is an element based method that has proven to be ideal to solve nonlinear problems due to the management of information between nodes, as a result of the discretization of the domain in smaller subdomains that control the transfer of information via filters in their ends. Moreover, the method has faster convergence than typical schemes like finite differences or finite volume method.

3.1 Numerical scheme

The numerical scheme implemented for solving the Burgers' equation uses the skew-symmetric form for the nonlinear term, as shown in equation [5].

$$\frac{\partial u}{\partial t} + \underbrace{\frac{1}{2}\left[u \cdot \frac{\partial u}{\partial z} + \frac{\partial}{\partial z}(u \cdot u)\right]}_{N(u)} = \underbrace{\nu \frac{\partial^2 u}{\partial z^2}}_{L(u)} \qquad [5]$$

The term $\boldsymbol{N(u)}$ is solved using a high order Adams-Bashfort explicit scheme, and the viscous term of the equation $\boldsymbol{L(u)}$ is solved using an implicit scheme with a GMRES solver due to the non-symmetric characteristics of the matrix. Equations [6] and [7] show the schemes solved by the numerical method.

$$\frac{\hat{u} - \sum_{q=0}^{J_i-1} \alpha_q u^{n-q}}{\Delta t} = \sum_{q=0}^{J_e-1} \beta_q N(u^{n-q}) \qquad [6]$$

$$\frac{\gamma_0 u^{n+1} - \hat{u}}{\Delta t} = \nu \left.\frac{\partial^2 u}{\partial z^2}\right|^{n+1} \qquad [7]$$

The values for the coefficients $\boldsymbol{\alpha_q}$, $\boldsymbol{\beta_q}$ and $\boldsymbol{\gamma_0}$ are used in third order rigidly stable schemes (SS3), and the values used were reported in Karniadakis (1991) and Peyret (2002). For further reference, the reader can consult the papers by Hesthaven (1997; 1998; 1996) and Peñaloza-Giraldo et al. (2015).

3.2 Computational domain

For both cases (one and two dimensional), the mesh used was unstructured, since it is assumed that the velocity signal decreases exponentially in the top part of the domain. Taking this into account, it is not necessary to have a fine mesh refinement at the bottom of the boundary, where the differences in velocity are expected to be minimal with respect to the difference in the top of the domain. Figures 3 and 4 show the computational domain used for the one and two dimensional cases respectively.

For the one dimensional case, the subdomains had a size that followed an exponential pattern similar to the Zeno paradox, i.e.: 0.5, 0.25, 0.125 and so on until the level of 0.03125 times the total vertical domain. This discretization allowed the capturing of most the results in the top part of the mesh, where, as it was said before, is where velocity damps exponentially. The bottom part of the domain is not as refined, but it has 12 points between 0.25 and the full domain (quantities are given relative to a total domain of length 1.0). Figure 3 shows the discretization of the domain used as an exercise for a presentation by Preziosi-Ribero (2016).

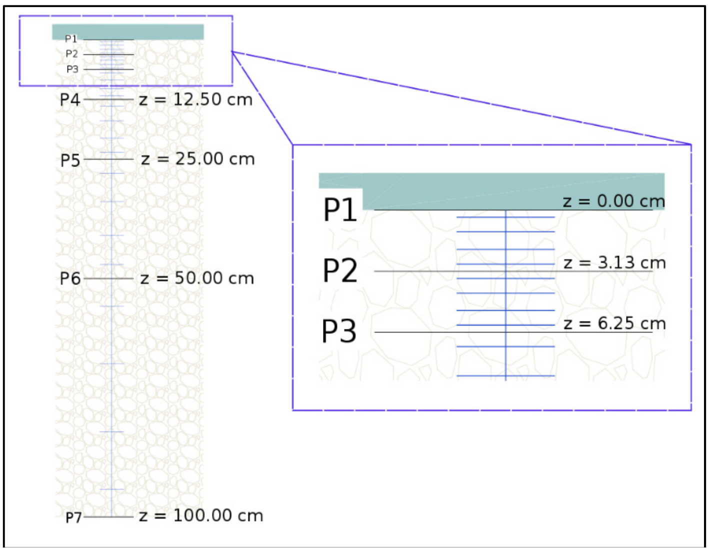

Figure 3. One-dimensional domain schematic

 ©2017, IAHR. Used with permission / ISSN 1562-6865 (Online) - ISSN 1063-7710 (Print)

3.3 Boundary conditions

Since the domains proposed do not only take account of the porous media in the riverbed without considering the free surface flow, the boundary conditions for the top of the proposed models are the velocity signals shown in section 2.3. For the one-dimensional case, only the vertical velocity is considered, and is imposed as a Drichlet boundary condition. For the bottom boundary condition, the one-dimensional model imposes a Neumann boundary condition that sets a zero change of velocity in space. This means that the water can flow freely following the natural conditions of groundwater flow. In the results section, the velocities in the subsurface are small and can be related with Darcy's flow.

4 RESULTS AND DISCUSSION

4.1 Instantaneous velocity evolution over depth

Figure 4 presents the evolution of the velocity signal over the depth of the domain for two different apparent viscosities (100 times water mean kinematic viscosity, i.e. $\mathbf{1.5 \times 10^{-4} m^2/s}$ on the left, and 10 000 times water kinematic viscosity, i.e. $\mathbf{1.5 \times 10^{-2}\ m^2/s}$ on the right column). The aim of this figure is to track

how the peaks in the input signal are reduced while the velocity pulse travel in depth. As it is expected, the deeper the signal is reconstructed, the flatter it is and getting closer to the mean value. There are no qualitative differences between the results plotted.

For the rest of the document, the values of apparent viscosities used in the numerical simulations will be shown in multiples of the mean water kinematic viscosity ($\boldsymbol{\nu_0}$), i.e. $\mathbf{1,5 \times 10^{-6}\ m^2/s}$. Hence, a value of 1000 times water kinematic viscosity will be equivalent to $\mathbf{1.5 \times 10^{-3}\ m^2/s}$, and will be expressed as $\mathbf{1000\nu_0}$.

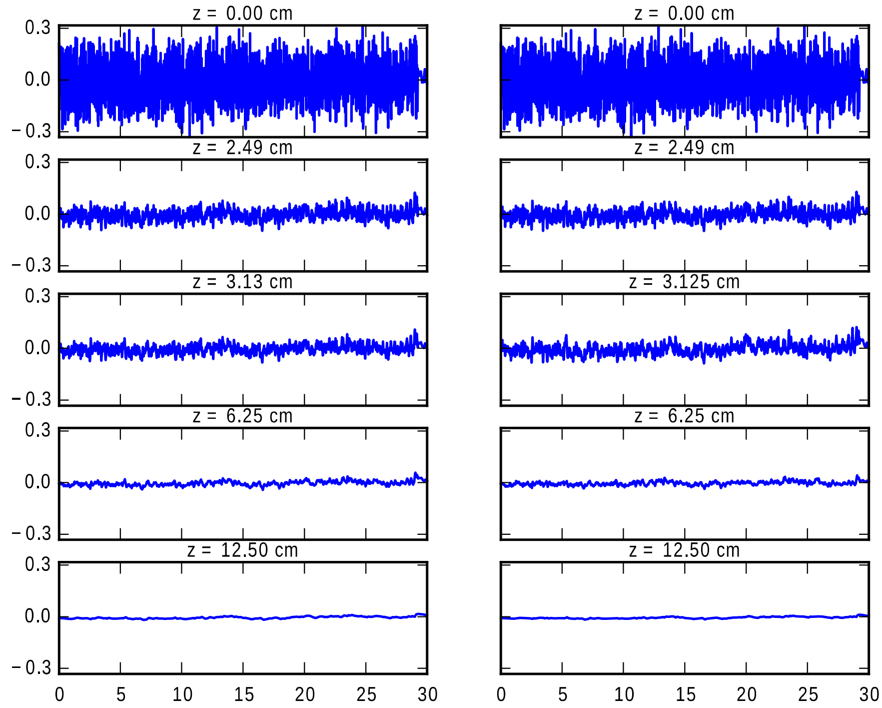

Figure *4.* Instant velocity reduction over depth for two apparent viscosities ($1.5 \times 10^{-4}\ m^2/s$ (left) and $1.5 \times 10^{-2}\ m^2/s$ (right)) *(100 times and 10 000 times water kinematic viscosity)*

4.2 Mean velocity signal damping

The one-dimensional model results for the mean velocity profiles with different apparent viscosities are shown in Figure 5. The x axis shows nondimensional velocity, normalized with the maximum velocity of the boundary condition and y axis shows the depth normalized to the maximum depth to collapse the curves. There is a velocity reduction after the second subdomain, however, in some profiles, a shape is formed in the top part, suggesting that there is a local velocity minimum in the top part of the domain, then an increase of the velocity to a local maximum and finally a decrease that goes until the bottom of the domain.

As Figure 4 shows, the two orders of magnitude (100 times) difference in the apparent viscosity coefficients is not visible by inspecting the results of the velocity signal. Indeed, both columns in this figure are similar and there are no concluding facts about their differences. Nonetheless, both viscosities achieve the objective of reducing the peaks of the velocity signal until a quasi-steady velocity is reached at the bottom of the domain. Hence, the fluctuations of the velocity are suppressed as the depth of the domain increases.

It is also interesting to observe that the proposed model assumes that the top boundary condition affects the whole domain as it is imposed, i.e. there is no lag between the response in the bottom of the domain and the fixing of a velocity value on top of it. Thus, our results show that the instant velocity diffuses inside the domain rather than traveling inside of it and affecting the bottom parts with some lag.

The behavior of the mean velocity profiles is not collapsed in Figure 5. However, the shape of the mean velocity profiles suggests that there is a reduction of the velocity to a minimum in the top part of the domain, followed by an increase and a monotonic decrease. These results can be compared with the results obtained from physical experiments by Pokrajac (2013), Manes et al. (2012) and several other researchers in the field of turbulence near porous or rough walls.

Figure 5 shows also that the depth at which the minimum mean velocity is reached depends on the apparent viscosity selected for the modeling. Hence, a lower value of viscosity will allow the velocity minimum to be found deeper in the domain than with higher values. This result is especially visible in the profiles of case 3 that is shown in purple and yellow lines in Figure 5.

Although it was expected that the velocities in the deep part of the domain were lower for all the cases modeled with high viscosity, our results do not show a clear tendency for explaining the value of the velocity in the lower part of the domain. Indeed, we expected lower values of velocities for the cases with higher viscosities (green, cyan, and yellow curves), i.e. 10 000$\boldsymbol{\nu_0}$ and the cases with lower values of viscosity (blue and purple curves), i.e. 100$\boldsymbol{\nu_0}$ do not follow the pattern expected.

The profile of the mean velocity for case 3 and viscosity of 100$\boldsymbol{\nu_0}$ in Figure 5 (purple line) shows a minimum value near 0.3$\boldsymbol{z}$ and then an increase over the depth of the domain. This result can be catalogued as close to the experimental cases (the $\boldsymbol{x}$ axis scale is logarithmic), but way more pronounced than the other curves. The most plausible explanation for this curve is the presence of noise inside the turbulent signal. There is an effective damping of the velocity in the turbulent signal, but there is also damping of uncorrected noise that alters the results all over the domain, as suggested by Brand et al. (2016).

Furthermore, the velocity profiles obtained for case 1 (blue and green curves) are very close even when the values of the apparent viscosity are two orders of magnitude apart one from the other.

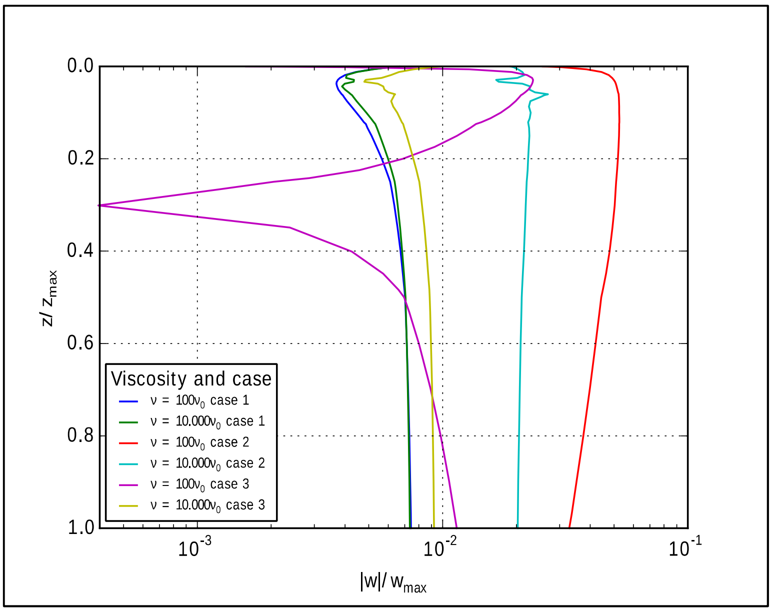

Figure 5. Mean velocity profiles over depth

 ©2017, IAHR. Used with permission / ISSN 1562-6865 (Online) - ISSN 1063-7710 (Print)

4.3 Velocity RMS

The Root Mean Square (RMS) of the velocity signal tracks the amount of turbulence that a velocity signal carries. According to turbulence studies (Pope, 2011, Davidson et al., 2013) the velocity can be decomposed in a mean component and a fluctuation. For the one-dimensional case, the RMS of the vertical velocity is calculated for each one of the subdomain depths. Figure 6 shows the evolution of this quantity over depth. The horizontal axis shows the value of the velocity RMS and the vertical axis shows the nondimensional depth of the domain. Again, it is expected that it diminishes with depth since the turbulence of the signal is being diffused by the apparent viscosity coefficient.

The velocity RMS is used to show how well auto-correlated are the values of a series. For the case analyzed, it is expected that on the top of the domain these values have a high RMS and as the depth increases, the RMS does too. Consequently, the shape of the curves for the three cases analyzed follow the expected pattern. However, the only force opposing to the flow in the model is the viscosity coefficient, therefore it is expected that with higher viscosity the RMS of a case with higher viscosity decreases faster than a case with lower viscosity.

Despite suggesting that this behavior is explained fully for the cases of $100\boldsymbol{v_0}$ and 10 $000\boldsymbol{v_0}$, it is not possible to argue the same with the case of $1000\boldsymbol{v_0}$. Indeed, in these cases it appears as the RMS decreases faster than with a higher viscosity. Nevertheless, in all the analyzed cases the value of the velocity RMS at the bottom of the domain is close to zero, showing that the velocity signals in those depths tend to a stable mean value with no noticeable fluctuations, as shown in Figure 4.

From Figure 6 it is also noticeable that the fluctuations of velocity reaches values between $\mathbf{10^{-4}}$ and $\mathbf{10^{-6}}\ \boldsymbol{m/s}$ for all the cases with all the viscosities used. The latter shows that the fluctuations are damped in the first fifth of the domain to negligible values that in the bottom are close to $\mathbf{10^{-6}}\ \boldsymbol{m/s}$. In this paper the concept of turbulent kinetic energy is not applicable since the turbulence phenomena is three-dimensional and relies on the transfer of momentum between the $\boldsymbol{x}, \boldsymbol{y}$ ans $\boldsymbol{z}$ axis. Therefore, multiplying and obtaining the turbulent kinetic energy in one-dimensional case is not physically representative.

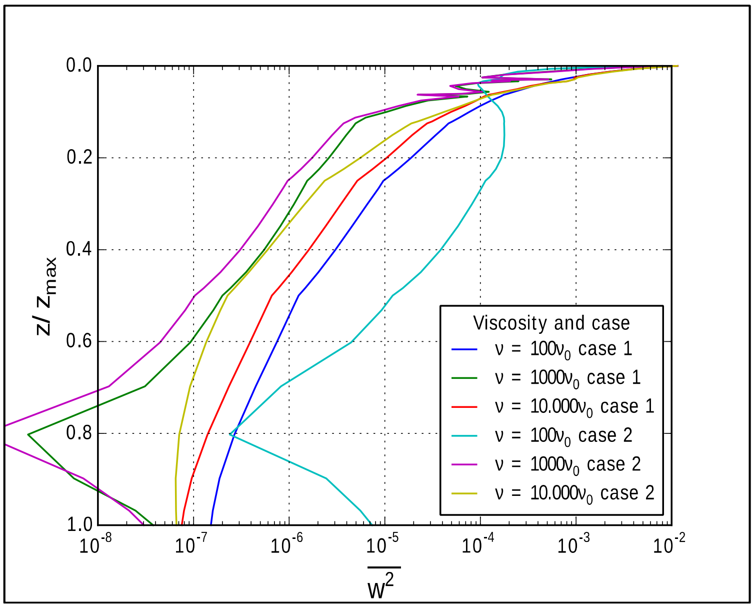

Figure 6. RMS of velocity results over depth

5 TWO-DIMENSIONAL MODEL PROPOSAL

5.1 Geometric discretization and characteristics

As regarding the two-dimensional domain, the same mesh discretization as the one used in the one-dimensional model was not used since it is not convenient to manage two dimensions using the Zeno paradox. Nonetheless, the mesh discretization followed the principle of having more points in the top of the domain than in the bottom. To achieve this purpose, the size of each one of the top three subdomains is half of the size of the bottom ones. A schematic of the mesh is shown in Figure 7.

5.2 Input signal and boundary conditions

Regarding the two-dimensional model proposed, the input is not gathered from physical measurements since the resolution of the velocity requires to set up several ADV near a river or flume bed. Hence, the result of a Large Eddie Simulation (LES) near a porous bed is used as the velocity input for the model proposed.

©2017, IAHR. Used with permission / ISSN 1562-6865 (Online) - ISSN 1063-7710 (Print)

The resolution of the velocity signal is limited to the resolution of the LES model, and for the case studied the temporal resolution is 0.2 s.

The main limitation of the proposed two-dimensional model is the temporal resolution of the velocity signal used as input. Firstly, a coarse velocity signal implies the use of a coarse mesh in the Burgers' equation model, since the stability conditions for the numerical solution must be met. Secondly, the timescale of the turbulence attempted to be modeled is coarser than the processes recorded for the one-dimensional case analyzed.

The streamwise and vertical velocities are taken as the input for the top boundary condition of the model. For the two-dimensional case, the bottom of the domain is set as a Dirichlet boundary condition, since the model from which the top velocities were acquired has a no slip condition in the bottom. In the case of the two-dimensional domain, the streamwise boundary conditions are periodic, which means that the flow going out in the right side of the domain is the same flow entering in the left boundary. This type of conditions prevent the influence and recirculation of flow in unwanted directions that are not expected for the flow. Moreover, it is expected that there is flow recirculating over the domain several times due to the time of the simulation that is close to 120 seconds.

5.3 Expected results and possible limitations

As with the one-dimensional model, our first expected result is the damping of the magnitude of the velocity with depth. Therefore, the fluctuations in the velocity signals used as input should be reduced in the same order or magnitude than the results shown for the one-dimensional case. It is also expected that the mean velocity profiles have a similar shape to the one suggested by our results in the one-dimensional case. Nevertheless, it is expected to find a difference in the magnitude of the results between x (streamwise) and z (vertical) directions. The two-dimensional model also has a limitation representing the turbulence phenomena. However, the concept of *"Burgulence"* or the simplification of turbulence in two dimensions can be used to assess and interpret the results obtained. Furthermore, the presence of two dimensions allow comparison between spatially averages quantities over the z axis with results in the one-dimensional model proposed in the previous sections.

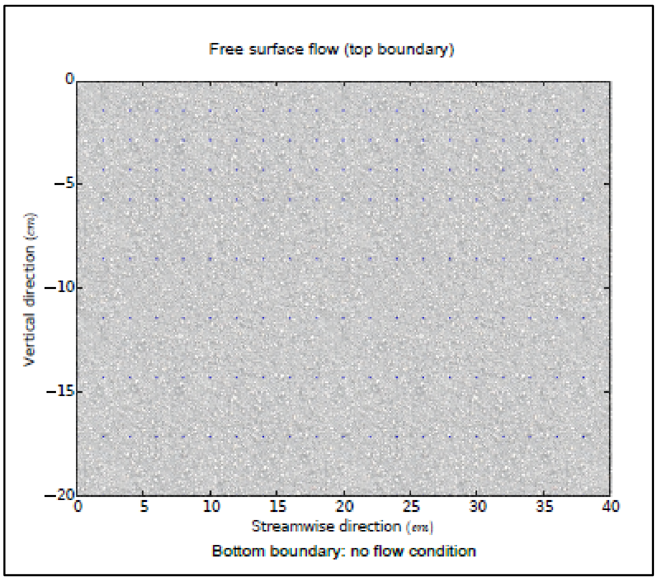

Figure 7. Two-dimensional domain schematic

6 CONCLUSIONS

The Burgers' equation represents the damping of a water velocity inside the porous media. Indeed, this results show that most of the velocity signal is diffused in the top part of the domain, and finally gets to a nearly constant value that is close to the porewater Darcy's velocity. Hence, the proposed model can represent a transition between the free surface water flow and the porous media laminar flow.

The method used to solve the Burger' equation shows stable results and proves to manage accurately the nonlinear advective term of the expression without showing aliasing or differences in spatial results. Moreover, this method is preferred over finite differences or finite volumes due to its precision. Furthermore, the use of a Neumann boundary condition proves that the velocity in the bottom of the domain has realistic values and there is no accumulation of it neither in space nor in time.

The mean velocity profiles suggest that the behavior of the velocity using the Burgers' equation can be compared with experimental results like the one proposed by Pokrajac (2013). Nonetheless, it is suggested to

 ©2017, IAHR. Used with permission / ISSN 1562-6865 (Online) - ISSN 1063-7710 (Print)

calibrate the parameters to understand their physical significance and relation with the physical properties of the stream or flume studied.

The vertical velocity RMS suggests that the analyzed signals approach a mean value in the top 20 % of the domain. Hence, the active layer where it is expected to have a small timescale is in the top centimeters of the domain, regardless of the total depth. Further analysis in the two-dimensional case will explain the relationship between the velocity signals and elucidate their differences at least n orders of magnitude.

The two-dimensional model proposed is a good alternative to explore ideal cases and test its functionality and reliability against direct numerical simulations and physical experiments in controlled environments. Besides, the apparent viscosity used can be calibrated when compared with experimental results to tackle HF problems with known coefficients.

REFERENCES

Bear, J. (1975). *Dynamics of Fluids in Porous Media*. Soil Science, 120(2), 162-163.

Boano, F., Harvey, J. W., Marion, A., Packman, A., Revelli, R., Ridolfi, L. & Worman, S. (2014). Hyporheic Flow and Transport Processes: Mechanisms, Models, and Biogeochemical Implications. *Reviews of Geophysics*, 52(4), 603-679.

Brand, A., Noss, C., Denkel, C. & Holzner, M. (2016). High-Resolution Measurements of Turbulent Flow Close to the Sediment – Water Interface Using a Bistatic Acoustic Profiler. *Journal of atmospheric and oceanic technology*, 33(4), 769-788.

Buss, S. R., Kai, Z., Cardenas, M. B., Fleckenstein, J., Hannah, D. M., Hepell, K. & Kaeser, D. H. (2009). *The hyporheic handbook.* Bristol: Environment Agency.

Cardenas, M. B. & Wilson, J. (2007). Hydrodynamics of Coupled Flow Above and Below a Sediment-water Interface with Triangular Bedforms. *Advances in Water Resources*, 30(3) 301-313.

Davidson , P. A., Kaneda, Y. & Sreenivasan, K. R. (2013). *Ten chapters in turbulence.* Cambridge.

Discacciati, M., Miglio, E. & Quarteroni, A. (2002). Mathematical and Numerical Models for Coupling Surface and Groundwater Flows. *Applied Numerical Mathematics*, 43(1-2), 57-74.

Hesthaven, J. S. (1997). A Stable Penalty Method for the Compressible Navier-Stokes Equations: II. One Dimentional Domain Decomposition Schemes. *Journal of scientific computing*, 18(3), 658-685.

Hesthaven , J. S. (1998). A Stable Penalty Method for the Compressible Navier-Stokes Equations: III. Multidimensional Decomposition Schemes. *Journal of scientific computing*, 20(1), 62-93.

Hesthaven, J. S. & Gottlieb, D. (1996). A Stable Penalty Method for the Compressible Navier-Stokes Equations: I. Open Boundary Conditions. *Journal of scientific computing*, 17(3), 579-612.

Higashino, M. & Stefan, H. (2008). Velocity Pulse Model for Turbulent Diffusion from Flowing Water into a Sediment Bed. *Journal of Environmental Engineering*, 134(7), 550-561.

Higashino, M. & Stefan, H. (2009). Pore Water Flow Due to Near-Bed Turbulence and Associated Solute Transfer in a Stream or Lake Sediment Bed. *Water Resources Research*, 45(12).

Huang, C., Shen, M. L. & Chang, H. H. (2008). Propagation of a Solitary Wave over Rigid Porous Beds. *Ocean Engineering*, 35(11), 1194-1202.

Karniadakis, G. E. (1991). High-Order Splitting Methods for the Incompressible Navier-Stokes Equations. *Journal of computational physics*, 97(2), 414-443.

Manes, C., Ridolfi , L. & Katul, G. (2012). A Phenomenological Model to Describe Turbulent Friction in Permeable-Wall Flows. *Geophysical Research Letters*, 39(14).

Peñaloza-Giraldo, J., Escobar-Vargas, J. & Donado-Garzon, L. (2015). A Spectral Multidomain Penalty Method Solver for the Simulation of the Velocity Attenuation in Hyporheic Flows. *Procedia Environmental Sciences*, 25, 206-213.

Peyret, R. (2002). *Spectral Methods for Incompressible Viscous Flow.* Springer-Verlag.

Pokrajac, D., Manes, C. & Mcewan, I. (2013). Peculiar Mean Velocity Profiles within a Porous Bed of an Open Channel. *Physics of fluids*, 19(9), 098109.

Pope, S. B. (2011). *Turbulent flows.* Cambridge University Press.

Preziosi-Ribero, A., Escobar-Vargas, J., Penaloza-Giraldo , J. & Donado-Garzon, L. (2016). A High Order Element Based Method for the Simulation of Velocity Damping in the Hyporheic Zone of a High Mountain River. *EGU General Goephysical Research Abstracts*, 18, 10673.

Tennekes, & Lumley. (1972). *A first course in turbulence.* Cambridge: MIT Press.

Proceedings of the 37th IAHR World Congress
August 13 – 18, 2017, Kuala Lumpur, Malaysia

3D HYDRODYNAMIC-HABITAT MODELLING FOR PREDICTION OF YELLOW PERCH HABITAT

PARNA PARSAPOUR-MOGHADDAM(1), COLIN D. RENNIE(2), CHRIS K. ELVIDGE(3) & STEVEN J. COOKE(4)

(1,2) Department of Civil Engineering, University of Ottawa, Ottawa, Canada
ppars036@uottawa.ca; colin.rennie@uottawa.ca
(3,4) Department of Biology, Carleton University, Ottawa, Canada
chris.k.elvidge@gmail.com; steven.cooke@carleton.ca
(4) Institute of Environmental Science, Carleton University, Ottawa, Canada

ABSTRACT

Hydro-morphodynamic changes can negatively impact riverine ecosystems, potentially leading to the decline and even extirpation of fish species. Hence, it is important to simulate the local fish habitat availability based on the river hydro-morphodynamic characteristics. Appropriate management strategies can then enhance the fish population and accordingly, condition of river ecosystems. Habitat Suitability Index (HSI) models are among the most widely used habitat models that define the quality of habitat for different fish species. The quality of habitat depends on hydraulic variables such as flow depth, velocity, and substrate. However, to obtain an overall estimate of the physical habitat, one should combine individual HSIs. Here we propose a novel method to estimate the composite habitat suitability index. To do so we use juvenile Yellow Perch, an important sportfish, in a meandering clay-bed creek in Ottawa, Canada as a model. Delft3D is employed to simulate 3D hydro-morphodynamic processes of the river. The results of this model are fed into the developed fish habitat model. A fish sampling survey via electrofishing was conducted in the study reach to provide the fish population density estimates. The developed fish habitat model was validated with the results of the fish sampling survey to evaluate the performance of the model. The proposed hydrodynamic-fish habitat model yields habitat availability predictions that matches the spatially distributed presence of juvenile Yellow Perch in the study reach. This suggests that, if appropriate fish habitat suitability indices are developed, a properly set-up and calibrated Delft3D composite numerical model can be employed to predict the availability of fish habitat in a reach.

Keywords: Hydro-morphodynamics; Fish habitat; composite habitat suitability index; Yellow Perch.

1 INTRODUCTION

River hydro-morphodynamic processes affect the quality of habitat for fish and other aquatic species. For effective river management and improved conditions of aquatic ecosystems, it is essential to know how the fish populations are linked to their habitats (Portt et al., 2006). However, detailed hydrodynamic assessment of fish habitats is challenging (Katopodis, 2003). Several fish habitat models were developed and suggested over the past few decades to provide insight for river management. Fish habitat models can be used to preserve a deteriorating species or habitat, inform restoration plans, and improve the health and condition of an ecosystem (Tash and Litvaitis, 2007). With advances of numerical models, it is now possible to elucidate some of the existing problems in habitat simulations.

There are different fish habitat models available in the literature (see de Kerckhove et al. 2008). One of the most widely used methods is habitat suitability index (HSI) modelling, which quantifies the quality of habitat to support particular species at different life stages (Bovee, 1986; Hardy, 1998; Fukuda, 2009; Conallin et al., 2010). The habitat suitability index varies from 0 (the most unsuitable condition) to 1 (optimal condition) for a given species in a study area. HSIs can be determined based on: 1- literature review or expert professional judgement, 2- Richness of the fish population collected in a specific study area, 3- Measured data from Category 2 in addition to the other habitat combinations in a study area (e.g. Jacobs, 1974; Edmondson & Winberg, 1971). Physical habitat normally depends on various parameters such as flow depth, velocity, substrate, etc (Leclerc et al., 1995). Results of HSI modelling lead to individual indices which need to be combined to obtain a composite suitability index (CSI) for the overall habitat quality. During the past few decades, several statistical methods were used and suggested to develop Habitat Suitability Index curves (e.g. Bovee,1986; Korman et al., 1994; Vismara et al., 2001; Beecher et al., 2002; Larocque et al., 2014). However, there are still some uncertainties in estimation of the CSI values (Noack et al., 2010). To alleviate the existing limitations, different methods of CSI calculation have been proposed over the past few years (Noack et al., 2012). Here we propose a novel method to estimate the CSI. We then compare the results

 ©2017, IAHR. Used with permission / ISSN 1562-6865 (Online) - ISSN 1063-7710 (Print)

of the proposed approach with one of the most widely used method for CSI estimation. To evaluate the performance of each model, we validate the models with results of the fish sampling survey.

2 Study Area

Watts Creek is a meandering clay-bed river which is located in Ottawa that flows into the Ottawa River at Shirley's Bay in the Kanata region. The creek flows north and east through National Capital Commission greenbelt forest land. Watts Creek provides important cool-water fish habitat. However, it is subject to erosion and degradation which can negatively affect the available fish habitat (Dillon, 1999). The rate of erosion and its influence on the fish community is still not clear. Thus, it is important to understand the hydro-morphodynamic processes in the Watts Creek watershed to optimize the potential fish habitat for the native fish community.

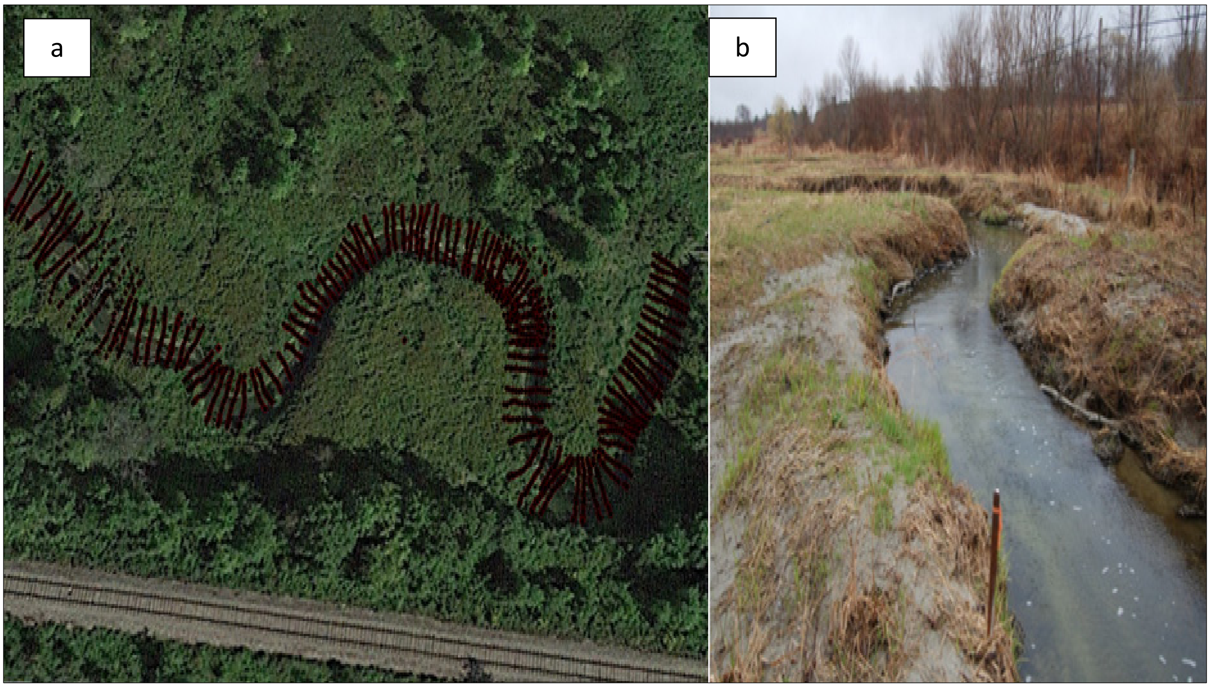

Figure 1. (a) Overview of the Watts Creek study reach M4, including surveying points. Flow from left to right (b) upstream end of M4 facing downstream. Rail line is immediately adjacent to the south of the river.

In this study, we focus on part of the reach which is adjacent to the City of Ottawa rail line (Figure 1a). The rail line confines the meander planform and has caused excessive erosion in the outer banks (Figure1b). Previous studies showed that this part of the reach has high fish richness (Maarschalk-Bliss, 2014).

3 METHODS

3.1 3D model setup

In the present study, a Delft3D numerical model was employed for 3D hydrodynamic modelling of the study area. To set up a 3D hydrodynamic model of the reach, a detailed orthogonal curvilinear 3D grid was first developed covering the areas of interest. Topography and bathymetric data for the creek were collected by Total Station survey. The collected bathymetric data were then interpolated over the generated grid. The time step was designated in a way to meet the stability condition with respect to the grid cell size. Initial and boundary conditions required for 3D hydrodynamic modelling were estimated based on data collected with an acoustic Doppler current profiler (aDcp).

3.2 Fish sampling survey

In order to relate fish populations with particular habitat features in Watts Creek, fish sampling was conducted in the study reach. A fish population survey was carried out during summer low flow conditions and covered all except for the very end of the numerical study reach. The spatial distribution of fishes was assessed using a backpack electrofisher (Figure 2). The fish caught within individual 5 m subreaches were recorded independently to allow for association with discrete habitat elements spatially distributed throughout the reach. All fish captured within each transect were held separately until they could be measured and identified. Figure 3 shows different types of fish captured during fish sampling.

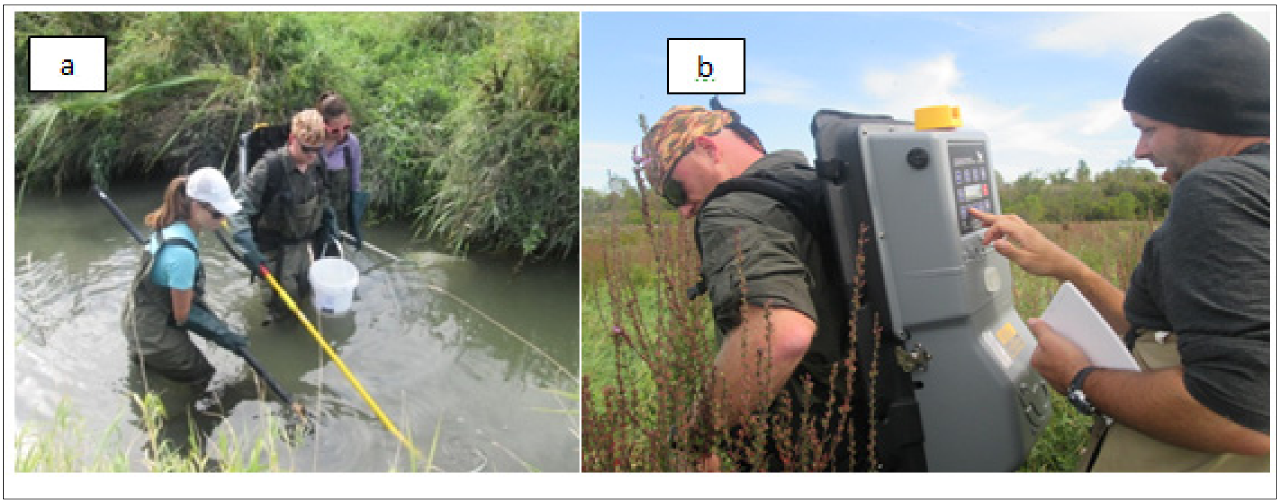

Figure 2. (a) Fish sampling using backpack electrofishing (L-R: J. Foster, C.K. Elvidge, K. Birnie-Gauvin) (b) Backpack electrofisher (L-R: C.K. Elvidge, S.J Cooke).

Figure 3. Different types of fish caught in the studied reach.

3.3 Fish habitat model

In this study, a fish habitat model was developed for Yellow Perch which is an important type of sportfish. As is shown in Figure 4, Yellow Perch habitat suitability curves used herein were based on Krieger et al. (1984). Table 1 shows the categories used for analysis of the substrate; spatially distributed substrate was incorporated in the habitat model based on field reconnaissance.

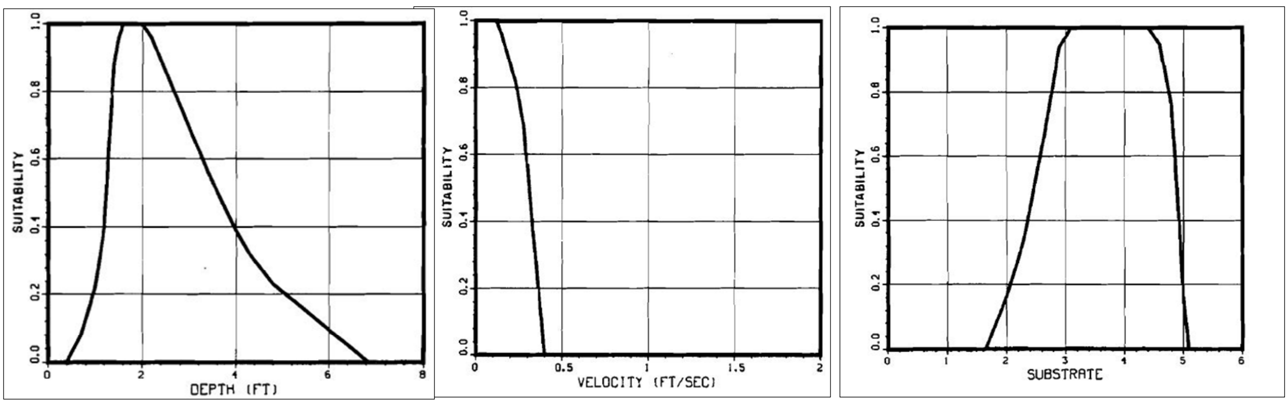

Figure 4. Habitat suitability curves for juvenile Yellow Perch based on (a) flow depth (b) velocity (c) substrate (from Krieger et al., 1984).

 ©2017, IAHR. Used with permission / ISSN 1562-6865 (Online) - ISSN 1063-7710 (Print)

Table 1. Substrate classification used in the substrate suitability curve (from Krieger et al., 1984).

1	Plant detritus/organic material
2	mud/soft clay
3	silt (particle size < 0.062 mm)
4	sand (particle size 0.062-2.000 mm)
5	gravel (particle size 2.0-64.0 mm)
6	cobble/rubble (particle size 64.0-250.0 mm)
7	boulder (particle size 250.0-4000.0 mm)
8	bedrock (solid rock)

Several mathematical operators could be used to calculate CSI that are normally based on independence and equal weighting of all variables (Ahmadi-Nedushan et al., 2006). Some of the most common ones are shown below (from Noack, 2012):

Product: $$\prod_{i=1}^{n} \mathrm{HSI_i} \quad [1]$$

Geometric mean: $$\left(\prod_{i=1}^{n} \mathrm{HSI_i}\right)^{\frac{1}{n}} \quad [2]$$

Arithmetic mean: $$\frac{\sum_{i=1}^{n} \mathrm{HSI_i}}{n} \quad [3]$$

Minimum: $$\min\,(HSI_i \dots HSI_n) \quad [4]$$

In this study, we used fuzzy-based overlay available in ArcGIS. Fuzzy overlay defines the possibility of being the member of multiple sets. There are different ways to combine the data based on fuzzy-overlay analysis (Hillier, 2007). In this study, we employed Fuzzy Gamma rule using Equation 5:

$$\left(1-\prod_{i=1}^{n}(1-HSI_i)\right)^{\gamma}\left(\prod_{i=1}^{n} HSI_i\right)^{(1-\gamma)} \quad [5]$$

If $\gamma = 0$, the Fuzzy Gamma method is equivalent to Product method, while if $\gamma = 1$ the Fuzzy Gamma method yields results equivalent to the Fuzzy Sum equation. If $1 > \gamma > 0$ then the Fuzzy Gamma equation yields results in between Fuzzy Sum and multiplication of HSIs. We optimized γ to yield the best habitat estimates. We then compared the resulting CSI from the Fuzzy Gamma method with those obtained from the Product approach, which is one of the most common techniques to estimate CSI (Ahmadi-Nedushan et al., 2006). To investigate which method yields a more accurate or realistic result, we validated the models with results of the fish sampling survey.

4 RESULTS

Table 2 and Figure 5 provide Yellow Perch abundances measured in each sampling area. Figure 6 shows the results of the predicted habitat suitability map based on the proposed Gamma approach, whereas Figure 7 depicts habitat suitability map based on the standard Product method. It should be noted that the optimized γ in the proposed Gamma approach was obtained as $\gamma = 0.7$.

By comparing Figures 6 and 7 with Figure 5, it can be seen that both methods reveal the primary locations of best Yellow Perch habitat. However, the Gamma method provides the opportunity for better identification of locations of moderate habitat. For instance, in sections S18 and S20, the Product method was not capable of predicting the presence of the habitat while this is well predicted by Gamma approach. Moreover, the Gamma approach was shown to provide a wider range of predicted habitat quality than the Product approach.

Due to the multiplication nature of the Product method, if one individual HSI is low or zero, even if all other variables have high HSI values, the Product method will yield low habitat quality. Thus, the productive composite HSI may not be a good representative of the total habitat quality. As can be seen, both methods could not predict the Yellow Perch availability near the upstream and downstream end of the reach which can be due to the effects of the boundaries.

There can still be some uncertainties due to the inaccuracies of the numerical simulations, the effect of the boundary conditions, specification of the type of the bed substrate, fish habitat model predictions, and the results of the fish sampling survey. Further study is needed to investigate how to alleviate the existing uncertainties on the available fish habitat models.

Table 2. Yellow Perch Abundance in Each Section Based on Fish Sampling Results.

Sections	Yellow Perch Abundance
S1	0
S2	5
S3	5
S4	9
S5	17
S6	5
S7	0
S8	2
S9	1
S10	11
S11	0
S12	0
S14	0
S15	0
S16	0
S17	0
S18	0
S19	1
S20	0
S21	2

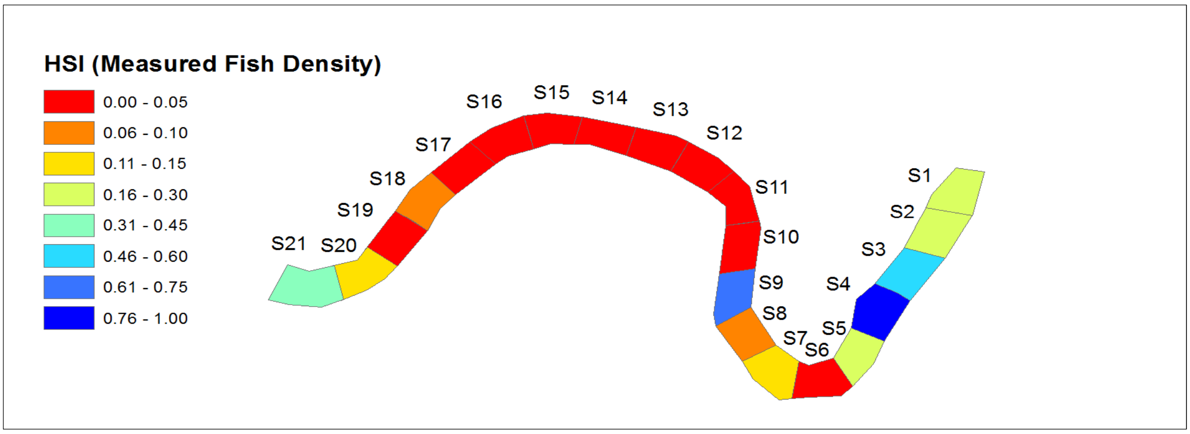

Figure 5. Relative abundances of Yellow Perch measured during the fish sampling survey.

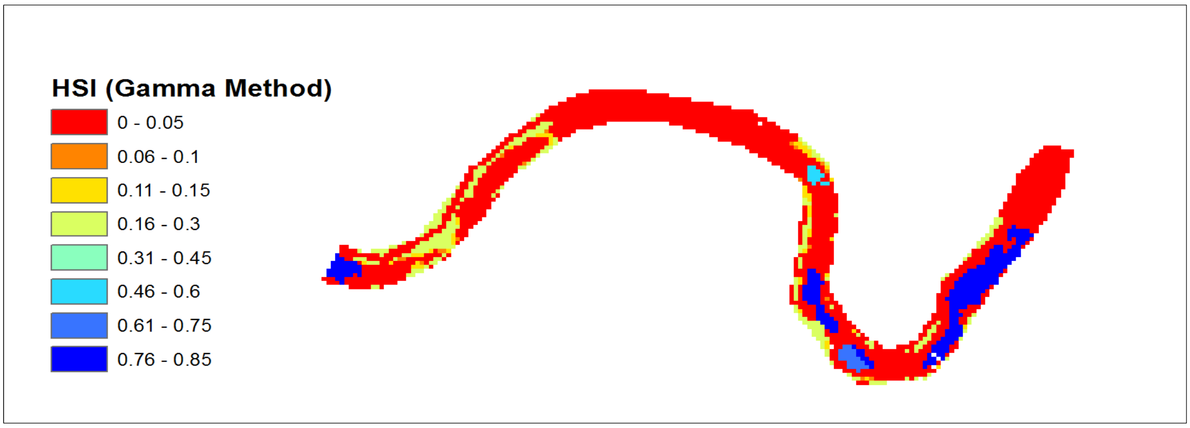

Figure 6. Composite habitat suitability map of the Yellow Perch based on the Fuzzy Gamma method.

 ©2017, IAHR. Used with permission / ISSN 1562-6865 (Online) - ISSN 1063-7710 (Print)

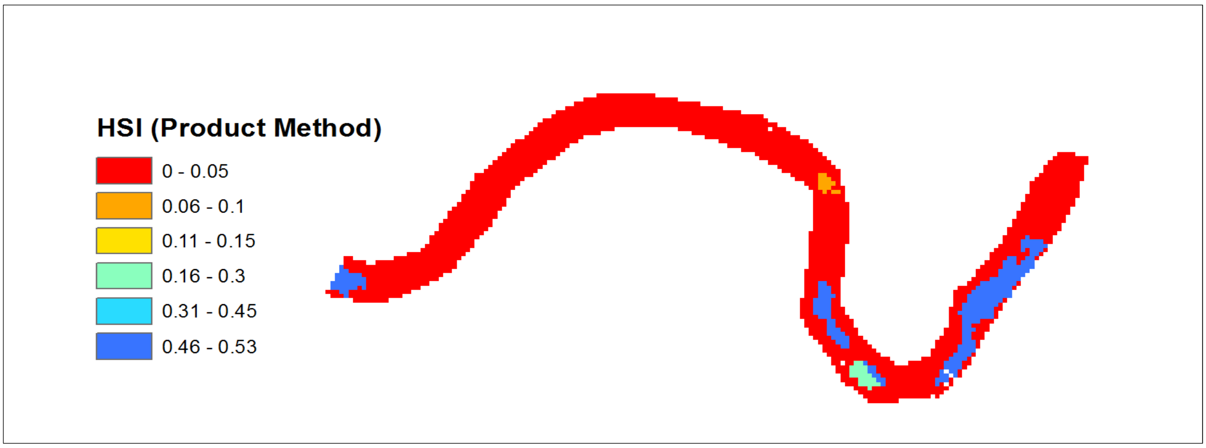

Figure 7. Composite habitat suitability map of the Yellow Perch based on the Product method.

5 CONCLUSIONS

Hydrodynamic-based fish habitat models are essential tools for decision makers in river management. This study presented a new method to link the channel hydro-morphodynamic processes to habitat utilization by the fish community in a clay bed urban stream. The main focus of this study was to investigate the habitat availability for juvenile Yellow Perch which is an important sportfish. 3D hydro-morphodynamic characteristics of the river were simulated using the Delft3D numerical model. The outputs of the hydro-morphodynamic model were fed in to the developed fish-habitat model. Fish sampling survey was carried out to provide the spatially distributed fish population density in the study reach which was then employed to validate the fish habitat model. The results confirmed that the developed fish habitat model could adequately predict the locations of fish presence in the study area. This suggests that, if appropriate fish habitat suitability indices are available, a properly set-up and calibrated Delft3D numerical model can be used to predict fish habitat availability in a reach. It was demonstrated that the Gamma method to obtain the composite HSI is a more nuanced approach than the conventional product method, and allows for better identification of moderate habitat. However, both 3D hydrodynamic and fish habitat models as well as the fish sampling measurements could exert some uncertainties on the results. Considering the existing uncertainties, further study should investigate how to improve the performance of this type of fish habitat model.

REFERENCES

Ahmadi-Nedushan, B., St-Hilaire, A., Bérubé, A., Rosbichaud, É., Thiémonge N. & Bobée B. (2006). A Review of Statistical Methods for the Evaluation of Aquatic Habitat Suitability for Instream Flow Assessment. *Rivers Research and Application,* 22(5), 503-523.

Beecher H.A., Caldwell B.A. & Demond S.B. (2002). Evaluation of Depth and Velocity Preferences of Juvenile Coho Salmon in Washington Streams. *North American Journal of Fisheries Management,* 22(3), 785-795.

Bovee, K.D. (1986). *Development and Evaluation of Habitat Suitability Criteria for Use in the Instream Flow Incremental Methodology* (No. FWS/OBS-86/7), USDI Fish and Wildlife Service.

Conallin, J., Boegh, E. & Jensen, J.K. (2010). Instream Physical Habitat Modelling Types: An Analysis as Stream Hydromorphological Modelling Tools for EU Water Resource Managers. *International Journal of River Basin Management*, 8(1), 93-107.

De Kerckhove, D.T., Smokorowski, K.E. & Randall, R.G. (2008). *For Fisheries and Aquatic Sciences. Great Lakes Lab. A Primer On Fish Habitat Models (No. 2817)*, Department of Fisheries and Oceans, Sault Ste. Marie,Ottawa, Canada.

Dillon Consulting Ltd. (1999). *Shirley's Brook and Watts Creek Subwatershed Study*, Environment AECOM, Project Number: 60264539, 105 Commerce Valley Drive West, Floor 7, Markham, Ottawa, Canada.

Edmondson, W.T. & Winberg, G.G. (1971). *A manual on methods for the assessment of secondary productivity in fresh waters.* Blackwell Scientific Publications, Oxford and Edinburgh.

Fukuda, S. (2009). Consideration of Fuzziness: Is it Necessary in Modelling Fish Habitat Preference of Japanese Medaka (Oryzias Latipes). *Ecological Modelling*, 220(21), 2877-2884.

Hardy, T.B. (1998). The Future of Habitat Modeling and Instream Flow Assessment Techniques. *Regulated Rivers – Research and Management*, 14(5), 405–420.

Hillier, A. (2007). *Arcgis 9.3 Manual*. Chicago.

Jacobs J. (1974). Quantitative Measurement of Food Selection. *Oecologia*, 14(4), 413-417.

Katopodis, C. (2003). Case Studies of Instream Flow Modelling For Fish Habitat in Canadian Prairie Rivers. *Canadian Water Resources Journal*, 28(2), 199-216.

Korman J., Perrin C.J. & Lekstrum T. (1994). *A Guide for the Selection of Standard Methods for Quantifying Sportfish Habitat Capability and Suitability in Streams and Lakes of British Columbia*, Report to B.C. Environment Fisheries Branch, Vancouver: British Columbia.

Krieger, D.A., Terrell, J.W. & Nelson, P.C. (1984). *Habitat Suitability Information: Yellow Perch. Western Energy and Land Use Team*, Division of Biological Services, *Research and Development, Fish and Wildlife Service*, US Department of the Interior.

Larocque, S.M., Hatry, C. & Enders, E.C. (2014). *Development of Habitat Suitability Indices and Bioenergetics Models for Arctic Grayling (Thymallus Arcticus)*, Oceans and Science, Central and Arctic Region, Fisheries and Oceans Canada, Freshwater Institute.

Leclerc, M., Boudreault, A., Bechara, T.A. & Corfa, G. (1995). Two-Dimensional Hydrodynamic Modeling: A Neglected Tool in the Instream Flow Incremental Methodology. *Transactions of the American Fisheries Society*, 124(5), 645-662.

Maarschalk-Bliss, S.M. (2014). Seasonal Variation in Assemblage Structure and Movement of Small Stream Fish in an Urban Environment, *Doctoral Dissertation*. Carleton University, Canada.

Noack, M. (2012). Modelling Approach for Interstitial Sediment Dynamics and Reproduction of Gravel-Spawning Fish, *Doctoral Dissertation*. University of Stuttgart, Germany.

Noack, M., Schneider, M. & Wieprecht, S. (2010). Aquatic Habitat Simulation Tools: Univariate Preference Functions versus Multivariate Fuzzy–Logic. *Proceeding of International Symposium on Ecohydraulics*, Seoul.

Portt, C.B., Coker, G.A., Ming, D.L. & Randall, R.G. (2006). *A Review of Fish Sampling Methods Commonly Used In Canadian Freshwater Habitats*, Canadian Technical Report Fisheries Aquatic Sciences, 2604.

Tash, J.P. & Litvaitis J.A. (2007). Characteristics of Occupied Habitats and Identification of Sites for Restoration and Translocation of New England Cottontail Populations. *Biological Conservation*, 137(4), 584-598.

Vismara R., Azzellino A., Bosi R., Crosa G. & Gentili G. (2001). Habitat Suitability Curves for Brown Trout (Salmo Trutta Fario L.) in The River Adda, Northern Italy: Comparing Univariate and Multivariate Approaches. *Regulated Rivers: Research & Management*, 17(1), 37-50.

 ©2017, IAHR. Used with permission / ISSN 1562-6865 (Online) - ISSN 1063-7710 (Print)

Proceedings of the 37th IAHR World Congress
August 13 – 18, 2017, Kuala Lumpur, Malaysia

DYNAMICS CHARACTERISTICS OF NITROGEN IN EXPERIMENTAL ENCLOSURES IN THE PANJIAKOU RESERVOIR, HEBEI PROVINCE, CHINA

SUILIANG HUANG [1], MIN WU [2], CHANGJUAN ZANG [3], SHENGLAN DU [4], WENWEN KONG [5], JOSEPH DOMAGALSKI[6], MAGDALENA GAJEWSKA[7], ADAM SZYMKIEWICZ[8] & ROMUALD SZYMKIEWICZ[9]

[1,2,3,4,5]Key Laboratory of Pollution Processes and Environmental Criteria of Ministry of Education, Tianjin Key Laboratory of Environmental Remediation and Pollution Control, College of Environmental Science and Engineering, Nankai University 1, Tianjin, China,
slhuang@nankai.edu.cn
[6]U.S. Geological Survey 2, Sacramento, United States,
joed@usgs.gov
[7,8,9]Faculty of Civil and Environmental Engineering, Gdańsk University of Technology (GUT) 3, Gdańsk, Poland,
adams@pg.gda.pl

ABSTRACT

Fish culturing in inland freshwater has a potential impact on water quality, especially for drinking water sources. In this paper, nitrogen dynamics were investigated under the condition of culturing bighead carp and common carp with added fish food (Phosphorus dynamics will be discussed elsewhere because its behavior is different from nitrogen). Nearly fifty days of observation indicated that the reservoir water was typically “nitrogen-rich” water, and nitrate -nitrogen (NO_3^--N) was the main nitrogenous form and accounted for 70 percent of measured total nitrogen (TN). TN, dissolved total nitrogen (DTN) and NO_3^--N concentrations in the enclosures with the addition of fish food were significantly lower than those in the control enclosure without fish food and the reservoir water. However, presence of fish food greatly increased ammonia-nitrogen (NH_4^+-N) and particulate total nitrogen (PTN) concentrations ($p<0.05$) when compared to the reservoir water. Culturing bighead carp and common carp showed insignificant contributions to TN, NH_4^+-N and NO_3^--N concentrations. Harvesting fish can remove 3.22%, 29.21% and 20.66% of nitrogen in enclosures with culturing bighead carp, common carp and mixed bighead carp and common carp, respectively. Though TN concentrations in the fish culturing enclosures were somewhat lower than those in the surrounding reservoir water, contributions from long-term nutrient release of uneaten food, senescent algae, fish feces and polluted sediment to the algae growth and nutrient dynamics should be taken into fully consideration, which may be helpful to the reservoir management and safety of the water supply.

Keywords: Fish food; bighead carp; common carp; nitrogen flux; enclosure experiment.

1 INTRODUCTION

With the dramatically increasing demands of fishery products, cage aquaculture has become one of the most important and commonly used intensive fishery strategies in the lakes, reservoirs, rivers and coastal zones since the 1990s in China (Guo et al., 2003). In recent years, more attention has been paid to marine cage aquaculture (Guo et al., 2009). For instance, concern has been elevated about the environment impacts of marine aquaculture (Buschmann et al., 2006; Lee et al., 2003; Karakassis et al., 2000). These impacts include the modification of benthic communities, increased nutrient loads in coastal waters and the associated problem of harmful algal blooms (Buschmann et al., 2006). However, recently little research has focused on the effect of cage aquaculture in inland water bodies. Due to their important functions and low current velocities of inland freshwater like lakes and reservoirs, it is necessary to understand the effect of aquaculture activities in these environments (Johnson et al., 2001).

Wastes, mainly uneaten food, and feces and urine, can be released directly into receiving water during fish cage culture process (Sugiura et al., 2006; Piedrahita, 2003), and may deteriorate the receiving water quality and hinder the water uses. Previous research demonstrated that nutrients released from fish culture sites had affected an area 3-9 times the size of the aquaculture zone (Anderson et al., 2002). If nutrient accumulation exceeds the culturing water self-purification capability, it may result in environmental problems such as water quality deterioration, algae bloom, and reduction in fish productivity (Guo et al., 2009; Hargreaves, 1998).

Fish culturing may influence the nitrogen flux in a reservoir at a detectable level. Much of the research on nitrogen cycling in shallow aquatic ecosystems has been conducted in estuarine or lacustrine environments (Felsing et al., 2006; Hawarth et al., 1988). Compared to terrestrial animals that mostly use carbohydrates and lipids, fish use proteins for energy production to a large extent (Hepher, 1988). It is concluded that fish protein requirement is about 2-3 times higher than that of mammals, and ammonium secretion is one of the end products of protein metabolism (Walsh et al., 1995). Results from different fishery culture systems demonstrated that only 25% of N added as feed or other nutrient input was utilized by the target organism

©2017, IAHR. Used with permission / ISSN 1562-6865 (Online) - ISSN 1063-7710 (Print)

(Hargreaves, 1998). In general, the accumulation of nitrogenous compounds (e.g., NH_4^+-N and NO_2^--N (nitrite-nitrogen)) may be toxic to fish (Wu et al., 2012; Kaggwa et al., 2010; Chen et al., 2006; Neori et al., 2004). In the previous paper (Huang et al., 2016), the function of Panjiakou Reservoir and its basic information has been introduced. It is the key hydraulic project that diverts water from the Luanhe River to Tianjin City and Tangshan City for supplying drinking water. Since the 1990s, stimulated by the economic profit, fish cage culturing has gradually developed to become the first industry and major economic income to the surrounding population. Published literature (Wang et al., 2008; Domagalski et al., 2007) reported that the culturing area has accounted for 1.7% of the total water surface. According to the water monitoring results, Wang and Liu (2008) found that the total nitrogen (TN) and chemical oxygen demand (COD) concentrations were 19.3% and 4.8% higher in the common carp culturing water than that in the control reservoir water (Wang et al., 2008). In addition, silver carp and common carp growth resulted in a 17.6% and 20.9% decline in the dissolved oxygen (DO) concentrations when compared to the reservoir water.

In order to manage the Panjiakou Reservoir at a level to guarantee the safety of the drinking water supply, the Haihe River Conservancy Commission, the river basin management agency for the reservoir funded the present research to determine the impact of fish cage culturing on nutrients especially nitrogen dynamics in the Panjiakou Reservoir. In this study, two kinds of fish (bighead carp and common carp) were cultured in the five different enclosures installed in the Panjiakou Reservoir. The objectives of the research were:

i. To test the variations in concentrations of the different culturing designs;
ii. To assess the relationships of various chemical and ecological factors during the culturing period;
iii. To determine the contribution of fish culturing to the nitrogen removal.

2 MATERIALS AND METHODS

2.1 Experimental sites

The Panjiakou Reservoir (118°15´E, 40°25´N) is located in Qianxi County, Tangshan City, northern Hebei Province, China with a useable water surface area of approximately 40 km^2 and water storage of 2.93× 10^9 m^3 and with three major tributaries, being the Luanhe River, Liuhe River and Baohe River (SPSS, 2003). The Panjiakou Reservoir's primary task and management objective is irrigation, flood control and fishery, and drinking water supply to the Tianjin City. In the past two decades, however, stimulated by the economic profit, fish cage-culturing has gradually developed and became the first industry and major income to the surrounding villages. It was reported (Cao et al., 2007; SPSS, 2003) that fish cage-culturing in the Panjiakou Reservoir began in the late 1980s and has spread all over the reservoir with nearly 17,000-25,000 cages (official number), of which 7,000-10,000 are bait-eating fish including common carp (*Cyprinus carpio*), crucian carp (*Carassius auratus*) and grass carp (*Ctenopharyngodon idellus*). The other 10,000-15,000 cages contain planktivorous silver carp (Hypophthalmichthys molitrix) and bighead carp (Aristichthis nobilis).

It was found by Wang and Liu (Cao et al., 2007) that the total nitrogen (TN), total phosphorus (TP) and chemical oxygen demand (COD) concentrations were 19.3%, 238% and 4.8% higher and dissolved oxygen (DO) was 20.9% lower in the common carp culturing water than that in the control reservoir water, and fish food addition greatly elevated the nutrients concentration and promoted algae growth. Detailed information can be found elsewhere (Huang et al., 2016).

2.2 Experimental set-up and operation

Five analogous waterproof and polythene enclosures A, B, C, D and E, as shown in Fig.1, were installed and the dimensions of the enclosures A, B and E were 2.9m in length, 2.9m in width and 1.5m in depth.

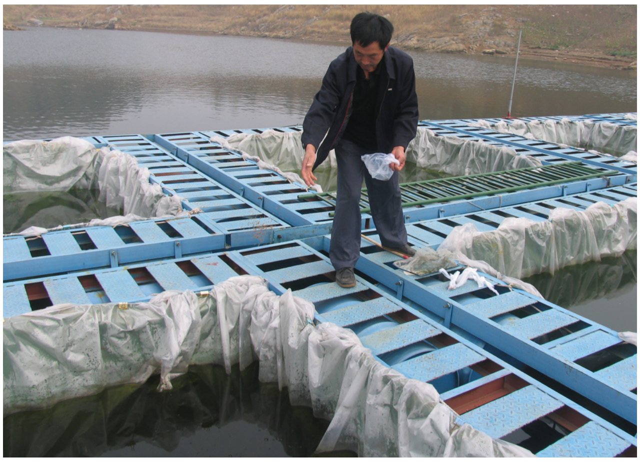

Figure1. Experimental enclosures in the representative intensive fish culturing water area.

 ©2017, IAHR. Used with permission / ISSN 1562-6865 (Online) - ISSN 1063-7710 (Print)

In the present study, enclosures A, B, C and D were designed to examine the contribution of: fish food, culturing bighead carp with fish food, culturing common carp with fish food, and mixed culturing both bighead carp and common carp with fish food to the algae growth dynamics, while enclosure E served as the experimental control without fish or fish food. This experimental setup did not consider replicates of enclosures (Harvey et al., 2011; Fraser et al., 2004; Zou et al., 2002; Smith, 1983) mainly due to paramount work of chemical analysis. All the experimental fishes were obtained from adjacent fishery farms with the similar weight of 250±20 g (mean ±S.D) for bighead carp and 63±9 g for common carp, respectively. Soybean meal bought from the local fish farm was used as the fish diet. The organic matter, total nitrogen and total phosphorus content of the soybean meal were 88.20%, 4.67% and 0.81%, respectively.

After two days of acclimation and water quality stabilization, bighead carp and common carp were stocked into the enclosures. Fish food was added three times a day with the dosages of 16.7 g to the enclosures A and B, and 20.0 g to the enclosures C and D, the selected dosages and feeding frequency were comparable to those used for the adjacent fishery farm. The fish food nutrient analysis indicated that OM, TN and TP accounted for 85±2%, 4.76±0.58% and 0.87±0.04% of the total mass, respectively. During the experimental running period, all the fish survived. Detailed information can be found elsewhere (Huang et al., 2016).

2.3 Water sampling and analysis

Water samples for both enclosures and reservoir were collected at an interval of 2 days from 18th August 2009 to 6th October, 2009. Compared to enclosures, reservoir water samples determine the background values for algae biomass and water quality variables. All samples were analyzed on the same day. They were analyzed for the following parameters: COD, ammonia-nitrogen (NH_4^+-N), nitrate-nitrogen (NO_3^--N), dissolved total nitrogen (DTN), particulate total nitrogen(PTN), total nitrogen (TN), electric conductivity (EC), total dissolved solids (TDS), chlorophyll-a (Chl-a), dissolved oxygen (DO), water temperature (T) and pH. Water quality parameters including COD, NH_4^+-N, NO_3^--N, TN, SRP, DTP and TP were determined according to standard methods (Huang et al., 2016) if not stated otherwise. PTN was the difference between TN and DTN. A YSI 6600 V2-2 Multi-Parameter Water Quality Sonde was used for DO, EC, TDS, Chl-a, T and pH analysis, respectively. Each variable test had parallel samples.

Water samples were also analyzed to investigate the variation in dominant algae fractions and species. A JKY/FluoroProbe-BBE and high power microscope (XSP-36) were used to measure the biomass of total algae, *Cyanophyta* (blue-green algae), *Chlorophyta* (green algae), *Bacillariophyta* (diatom) and *Cryptomonas* expressed in 104cells/L water.

At the end of the experiment, both bighead carp and common carp were netted and weighed. Experimental fish were rinsed and then wiped with gauze to remove mucus. Scale and fish skin were removed and the fish meat was dried to a constant weight at 50°C. Dried fish meat was subsequently powdered, wet digested, and analyzed for TN content according to a method provided by Cao et al (2007). This method transforms nitrogen in fish meat into $(NH_4)_2SO_4$ through digestion with H_2SO_4 followed by distillation of NH_3 in an alkaline medium. The ammonia was collected in sulphuric acid (0.05N) which is back titrated with standard sodium hydroxide solution. The results were expressed as mg of N per g of fish tissue (wet weight).

2.4 Statistical analysis

All statistical tests were performed using the Statistical Package for the Social Sciences (SPSS) software package (SPSS, 2003). Significances were defined as $p<0.05$, if not stated otherwise. A one-way analyses of variance (ANOVA) and the Tukey's significant difference multiple range tests were carried out to assess the differences between means of the algae densities (Fraser et al., 2004), nutrient concentrations and other water quality variables in different enclosures and the surrounding reservoir water. In addition, data obtained from enclosures A, B, C and D were fitted with two-way ANOVA to examine the influences of bighead carp and common carp and their interactions with each other on the nitrogen dynamics. For all ANOVA, the tested variables were normally distributed.

3 RESULTS

3.1 Water quality parameters analysis

From August 18th to October 6th in 2009, the water temperature of the reservoir and enclosure water declined (Huang et al., 2016). For the entire experimental period, nutrient concentrations of COD, NH_4^+-N, NO_3^--N, DTN, and TN for the tested enclosures and the surrounding reservoir water are summarized in Table 1. There were no significant differences in these nutrient mean concentrations between the enclosure E and the reservoir water. The COD and NH_4^+-N mean concentrations were significantly higher while NO_3^--N, DTN and TN mean concentrations were significantly lower in fish food presented enclosures A, B, C, and D than those in control enclosure E and the reservoir water (Table 1). As a whole, the COD and $NH4^+$-N mean concentrations in enclosure A, B, C and D were 2.5-4.0 times higher than enclosure E and reservoir water, while NO_3^--N, DTN and TN mean concentrations in enclosure E and reservoir water were 1.2-3.9 times higher

©2017, IAHR. Used with permission / ISSN 1562-6865 (Online) - ISSN 1063-7710 (Print)

than those in enclosures A, B, C and D. Among all the fish food present enclosures, the bighead carp feeding enclosure had the significantly lowest mean TN, NO_3^--N concentrations of 3.02mg/l and 0.77mg/l, respectively ($p<0.05$, Table 1).

Table 1. Mean concentrations ± SD for water quality parameters and biomass of algae in reservoir water and closures.

Variables	Reservoir water	Culturing water Enclosure A	Enclosure B	Enclosure C	Enclosure D	Enclosure E
COD (mg/l)	$3.49±0.33^a$	$14.09±7.73^b$	$11.80±5.38^b$	$12.67±7.55^b$	$11.50±5.15^b$	$3.72±0.32^a$
NH_4^+-N (mg/l)	$0.11±0.04^a$	$0.30±0.13^b$	$0.30±0.13^b$	$0.27±0.12^b$	$0.28±0.16^b$	$0.08±0.05^a$
NO_3^--N (mg/l)	$3.00±0.53^b$	$0.91±0.77^a$	$0.77±0.50^a$	$1.10±0.62^a$	$0.98±0.42^a$	$3.09±0.55^b$
DTN (mg/l)	$4.07±0.23^b$	$2.20±1.00^a$	$1.90±0.92^a$	$2.11±1.16^a$	$1.88±1.21^a$	$4.16±0.20^b$
PTN（mg/L）	$0.4±0.1^a$	$1.8±0.2^c$	$1.0±0.1^b$	$1.27±0.1^b$	$1.2±0.1^b$	$0.4±0.1^a$
TN (mg/l)	$4.47±0.28^d$	$4.05±0.53^c$	$3.02±0.99^a$	$3.51±0.90^b$	$3.21±1.10^{a,b}$	$4.57±0.20^d$
T (°C)	23.55±2.34	22.86±2.49	22.93±2.49	23.01±2.45	22.95±2.51	23.28±2.34
DO (mg/l)	$8.93±0.65^b$	$6.94±4.93^{a,b}$	$6.22±3.95^a$	$7.85±2.71^{a,b}$	$6.29±4.40^a$	$11.80±1.68^c$
TDS (mg/l)	$351.96±3.41^c$	$335.96±10.39^b$	$333.76±11.28^b$	$336.00±3.44^b$	$336.08±7.67^b$	$327.96±11.87^a$
EC (μs)	$542.04±5.14^c$	$516.80±16.06^b$	$513.40±17.45^b$	$516.92±5.31^b$	$517.08±11.68^b$	$504.56±18.29^a$
pH (-)	$8.42±0.15^b$	$8.27±0.48^{a,b}$	$8.18±0.46^a$	$8.22±0.33^{a,b}$	$8.15±0.46^a$	$8.79±0.20^c$
Chl-a (μg/l)	$5.36±1.69^a$	$27.78±13.65^b$	$52.96±25.32^c$	$89.99±81.21^d$	$58.76±35.69^c$	$3.27±1.45^a$
Algae	$2.60E+6^a$	$1.17E+8^c$	$2.40E+7^{a,b}$	$4.07E+7^b$	$4.37E+7^b$	$3.39E+6^a$

Values with a different superscript letters indicate significant difference at p ≤0.05 based on Turkey's HSD; experimental enclosures A (fish food without fish) and B (fish food with bighead carp) and C (fish food with common carp) and D (fish food with bighead carp and common carp) and E (without fish food and fish).

Except for the above mentioned nutrient variables, changes in values of the other measured parameters T, DO, EC, TDS, pH and Chl-a concentration are also given in Table 1. The mean water temperature recordings for the reservoir water were insignificantly higher than that in the tested enclosures. Regardless of culturing fish or not, the presence of fish food significantly reduced the pH and DO concentrations in enclosures A, B, C, and D when compared to enclosure E. EC and TDS values were significantly lower in enclosure E than those in the enclosures A, B, C, D. However, fish species had little effect on EC and TDS concentrations among the enclosures A, B, C and D. Total algae biomass and Chl-a were employed to evaluate the phytoplankton biomass. Chl-a concentrations and algae biomass were significantly lower in the reservoir water and enclosure E than those in other enclosures with fish food. Chl-a values in enclosures B, C and D were 2-3 times higher than those in the enclosure A, and the highest mean Chl-a concentrations appeared in enclosure C with the value of 89.99 μg/l (Table 1). Nevertheless, total algae biomass concentrations in enclosure A were 2-5 times higher than those in enclosures B, C and D (Du et al., 2014).

3.2 Nitronen dynamics

Fig.2 and Fig.3 show variations in NH_4^+-N, NO_3^--N, PTN (difference between TN and DTN), DTN and TN concentrations for the tested enclosures and the surrounding reservoir water. The different fractions of nitrogen for enclosure E and reservoir water showed a similar pattern during the entire testing period. In general, NH_4^+-N, PTN, DTN and TN concentrations in enclosure E and the reservoir water fluctuated with a slightly declining trend (Fig.2 and Fig.3). However, the NO_3^--N concentrations in enclosure E and the reservoir water are irregular and no clear tendency can be detected. For fish food present enclosures A, B, C and D, after the decline during the first sampling week, NH_4^+-N concentrations irregularly fluctuated for nearly one month, and then showed an increasing trend in general. Except for 24th August, NO_3^--N concentrations gradually decreased and were almost depleted at the end of the experiment. Compared to the initial conditions, TN concentrations in fish feeding enclosures B, C, and D generally declined with the extension of the experimental period (Fig.2). However, TN concentrations in enclosure A initially decreased to the lowest value of 3.3 mg/l on 5th September and then gradually increased to a stable value of nearly 4.8 mg/l at the end of the test. DTN and PTN concentrations varied in two different patterns in fish food present enclosures. DTN concentrations almost linearly decreased before 13th September and then remained at a relatively stable level, while PTN gradually increased during the whole experimental period in a fluctuating status.

 ©2017, IAHR. Used with permission / ISSN 1562-6865 (Online) - ISSN 1063-7710 (Print)

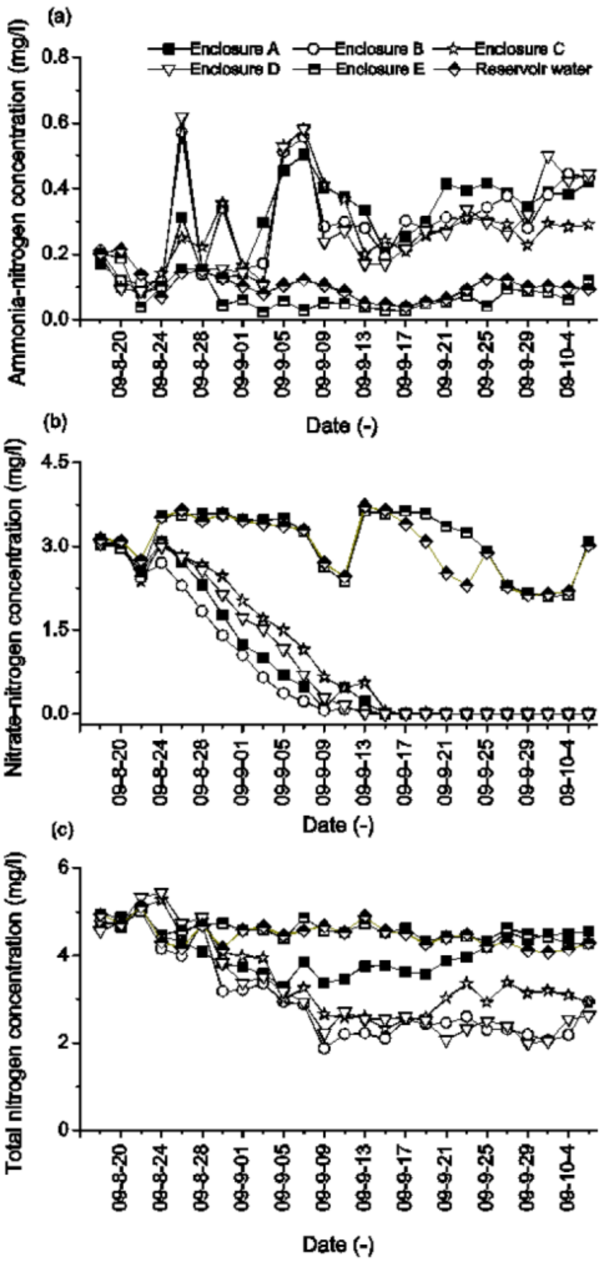

Figure 2. Variations in (a): Ammonia-nitrogen, (b): Nitrate-nitrogen, and (c): Total nitrogen concentrations during the experimental period for reservoir water and enclosures.

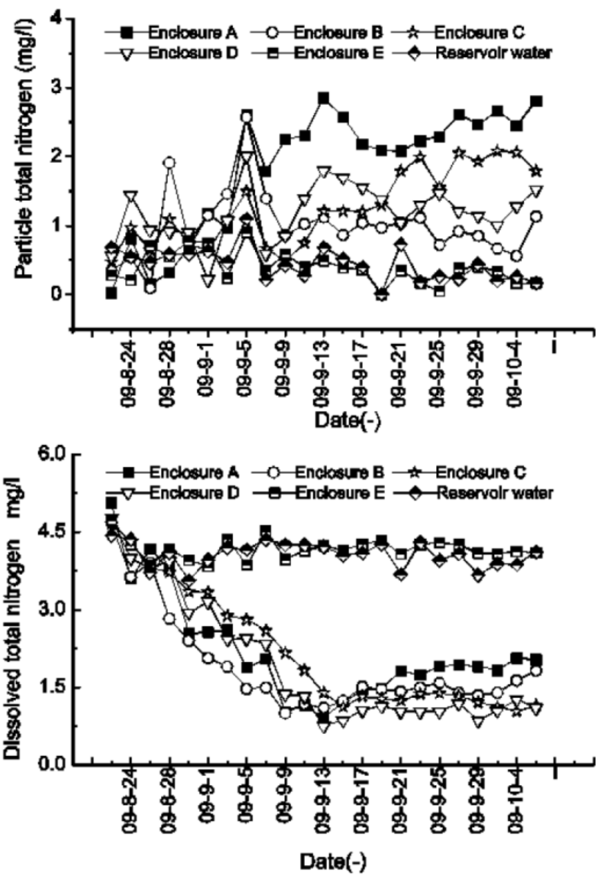

Figure 3. Variations in (a): Particulate total nitrogen, (b): Dissolved total nitrogen concentrations during the experimental period for reservoir water and enclosures.

Results from a further two-way ANOVA indicated that fish feeding had no significant effect on culturing water NH_4^+-N and NO_3^--N concentrations ($p>0.05$, Table 3). However, bighead carp led to significant statistical differences in TN concentrations at $p<0.001$, while the presence of common carp was not important (Table 3). Furthermore, the interaction between bighead carp and the common carp on TN concentrations was significant at $p=0.046$ (Table 3).

3.3 Fish biomass production and nitrogen removal

For enclosures B, C and D, fish were netted and weighed to trace the variations in biomass. After nearly fifty days of feeding, 109.96 g, 131.69 g and 131.69 g of TN were inputted from added fish food (percentage of nitrogen in fish food is 4.76±0.58%) in Enclosures B, C and D, respectively and 165 g and 83 g increases in bighead carp biomass were obtained for enclosures B and D, respectively (Table 4). For common carp, fish food addition led to 1632 g and 1079 g fish biomass increase for enclosures C and D, respectively. However, fish feeding did not result in a significant change in total nitrogen content in per gram fish meat for both bighead carp and common carp (Cao et al., 2007; Zou et al., 2002). As shown in Table 4, fish netting contributed 3.54g, 38.47g and 27.21g mean TN removal to enclosures B, C and D, respectively.

Table 2. Correlation matrix for COD, NH_4^+-N, NO_3^--N, DTN, TN, water temperature, DO, TDS, EC, pH and Chl-a for the representative enclosure D. The corresponding p values are shown in parentheses.

	COD	NH_4^+-N	NO_3^--N	DTN	PTN	TN	T	DO	TDS	EC	pH	Chl-a	Algae
COD	1.000	(0.029)	(<0.001)	(<0.001)	(0.126)	(<0.001)	(<0.001)	(0.052)	(0.001)	(0.001)	(0.053)	(<0.001)	(<0.001)
NH_4^+-N	0.436	1.000	(0.015)	(0.165)	(0.447)	(0.011)	(0.003)	(<0.001)	(0.003)	(0.003)	(<0.001)	(0.606)	(0.064)
NO_3^--N	-0.922	-0.480	1.000	(<0.001)	(0.037)	(<0.001)	(<0.001)	(0.008)	(<0.001)	(<0.001)	(0.014)	(<0.001)	(<0.001)
DTN	-0.845	-0.300	0.867	1.000	(0.011)	(<0.001)	(<0.001)	(0.144)	(0.018)	(0.018)	(0.183)	(0.001)	(<0.001)
PTN	0.328	0.167	-0.436	-0.519	1.000	(0.448)	(0.120)	(0.343)	(0.317)	(0.325)	(0.622)	(0.133)	(0.065)
TN	-0.849	-0.502	0.868	0.816	-0.167	1.000	(<0.001)	(0.028)	(0.007)	(0.007)	(0.034)	(0.003)	(<0.001)
T	-0.937	-0.574	0.948	0.812	-0.342	0.848	1.000	(0.004)	(<0.001)	(<0.001)	(0.005)	(0.002)	(<0.001)
DO	-0.401	-0.717	0.530	0.322	-0.212	0.447	0.568	1.000	(<0.001)	(<0.001)	(<0.001)	(0.507)	(0.351)
TDS	0.643	0.585	-0.685	-0.512	0.230	-0.544	-0.738	-0.738	1.000	(<0.001)	(<0.001)	(0.339)	(0.009)
EC	0.642	0.584	-0.678	-0.510	0.226	-0.545	-0.732	-0.732	0.999	1.000	(0.001)	(0.351)	(0.009)
pH	-0.399	-0.727	0.495	0.295	-0.111	0.434	0.556	0.978	-0.672	-0.665	1.000	(0.452)	(0.295)
Chl-a	0.686	0.111	-0.669	-0.679	0.330	-0.575	-0.609	0.142	0.209	0.204	0.161	1.000	(0.009)
Algae	0.908	0.376	-0.839	-0.759	0.391	-0.719	-0.863	-0.199	0.533	0.534	-0.233	0.803	1.000

Table 3. Results of two-way analyses of variance examining the role of bighead carp and common carp on the culturing water ammonia- nitrogen (NH_4^+-N), nitrite- nitrogen (NO_3^--N) and total nitrogen (TN) concentrations.

Variable	Factor	F-ratio	p
NH_4^+-N	Bighead carp	0.072	0.788
	Common carp	1.118	0.293
	Bighead carp and common carp	0.018	0.893
NO_3^--N	Bighead carp	0.301	0.585
	Common carp	0.762	0.385
	Bighead carp and common carp	0.001	0.970
TN	Bighead carp	13.707	<.001
	Common carp	0.951	0.332
	Bighead carp and common carp	4.095	0.046

Table 4. Mean ±SD for total nitrogen (TN) content and total nitrogen removal by fish harvesting in October 2009.

Enclosures	Input of Nitrogen from added fish food (g)	Fish species	Weight increment (g)	TN content (mg N/g meat)	TN removal (mg N)
B	107.1±13.1	Bighead carp	165	21.46±0.83	3.54±0.71
C	128.5±15.7	Common carp	1632	23.57±0.76	38.47±1.29
D	128.5±15.7	Bighead carp	83	21.46±0.83	1.78±0.23
		Common carp	1079	23.57±0.76	25.43±1.10

The weight increment and TN removal for each enclosure was the sum of the meat weight and nitrogen removal, respectively.

4 DISCUSSION

There are various sources of nitrogen for Panjiakou Reservoir (Domagalski et al., 2007). The highest total nitrogen concentration was approximately 4.70 mg/l. However, the phosphorus concentration in the water was very low and less than 0.10mg/l (Wang et al., 2008). Thus, the molar ratio of nitrogen and phosphorus in the Panjiakou Reservoir reached 91, and greatly exceeded the optimum nitrogen and phosphorus atom ratio 16 for algae growth, suggesting that phosphorus limits the growth of algae (Smith, 1983).

Availability of NO3--N and NH4+-N commonly limits autotrophic and heterotrophic productivity in many aquatic environments, including reservoir and lake (Harvey et al., 2011), and both of them are the important nitrogen sources for algae. In the present study, NO_3^--N is the main constituent of the DTN and TN (Table 1) and its concentration in water decreased with the increase of the total algae biomass. Success of non-N-fixing algae was correlated with the depletion in NO_3^--N (Jacoby et al., 2000). Furthermore, ability of some algae to dominate could even reduce the NO_3^--N concentrations to less than 0.02 mg/l (Blomqvist et al., 1994), which is close to our observations (Fig.2). Our study occurred during the seasonal transition from late summer to early autumn, and the water temperature was negatively correlated with the total algae biomass. This can be partly used to explain why blue-green algae are more prone to blooms in warm spring and hot summer rather than cold winter (Hargreaves et al., 1998; McQueen et al., 1987).

Fish food is the most important nutrient source, which caused COD increases in the enclosure A, B, C and D (Fig.3). Organic and inorganic nutrient manipulation is commonly employed to enhance fish yields which are dependent on the development of autotrophic food webs. This, as a result, resulted in increasing availability of nitrogen to the algae. However, nitrogen discharged from fish culturing may degrade the receiving water quality. Fish food inputs organic matter into culturing water, where bacteria consuming organic matter convert organic nitrogen into NH_4^+-N (Butturini et al., 2000). Increases in NH_4^+-N and decreases in NO_3^--N concentrations observed in our study can be found elsewhere, e.g., Ziemann et al. 1992 measured an

 ©2017, IAHR. Used with permission / ISSN 1562-6865 (Online) - ISSN 1063-7710 (Print)

increase of NH_4^+-N and a decrease of NO_3^--N in the effluent from marine fish and shrimp ponds compared to nearby receiving streams (Ziemann et al., 1992). In the fish culturing environments, increases in NH_4^+-N and decreases in NO_3^--N usually can be explained as the combined results of the nitrogen biogeochemical process such as ammonia mineralization, volatilization and adsorption, NH_4^+-N and NO_3^--N uptake by phytoplankton and nitrification – denitrification (Hargreaves, 1998).

Nevertheless, TN concentrations in all the fish food present enclosures were lower than those observed in the control enclosure E and the surrounding reservoir water (Fig.2 and Table 1). This phenomenon may be possibly caused by the following. The first one is that the fish food dosage cannot satisfy the nutrient requirement for the phytoplankton growth; therefore, nitrogen contained in the culturing water was partly consumed. The second is that the nitrogen added in the form of soybean meal can supply the benthic algal growth. The third one is that the nitrogen would settle down to water bottom as senescent algae or unused food. Research demonstrated that as much as 50% of the algae standing crop (about 10 g algae dry weight m-2d-1) may settle to the sediment surface each day (Piedecausa et al., 2009; Schroeder et al., 1991). Another simulation model predicted that 48% to 66% of added N would settle to the pond bottom in the form of phytoplankton in semi-intensive shrimp ponds (Lorenzen et al., 1997). Alternatively, oxygen consumed by mineralization of fish food and respiration of fish and other organisms created anoxic conditions in which denitrifying bacteria metabolizing organic carbon transform NH_4^+-N and NO_3^--N, NO_2^--N into N_2, considered another path for nitrogen loss in the water (Harvey et al., 2011; Baker et al., 1999). Moreover, there was part of nitrogen assimilated and utilized by fish.

TN: TP (total phosphorus) may be used as a useful tool to clarify these results. After analyzing 17 lakes or reservoirs located worldwide, Smith concluded that cyanobacteria tended to dominate in lakes or reservoirs where the TN: TP mass ratio was less than 29 (Zou et al., 2002). This conclusion has led to the so-called "TN: TP" rule which states that increasing the mass ratios above 29 will reduce the proportion of cyanobacteria as a fraction of the total algal biomass. In this study, TN: TP for fish presented enclosures and the surrounding reservoir water were 7.8 and 113.0, respectively. It is found that fish food addition greatly reduced the TN: TP ratio to the level of less than 29 and stimulated cyanobacteria outburst, which indirectly resulted in an abundance of nitrogen utilization and TN concentration decrease. Similar conclusions have also been published elsewhere, i.e. "N:P rule" is more applicable to systems when N or P loadings are very small and N, P inputs may be under the assimilative capacity of the phytoplankton (Paerl et al., 2001).

The continuous supply of nutrients including fish food and other inorganic compounds can effectively stimulate the algae growth (Figueredo et al., 2009; Tang et al., 2006), therefore algae biomass was significantly correlated with all the nitrogen fractions (Table 2). The positive correlation between COD and NH_4+-N suggests that organic matter generation and nitrogen release occurred together in the fish culturing practices. With the continuous supply of fish food and increase in algae biomass, decomposition of the organic matter contained in the fish food, and respiration of aquatic organisms consumed abundant oxygen and produced organic or inorganic acid (Zang et al., 2011; Hargreaves et al., 1998), thus facilitating the decline in pH and DO values. This can partly explain the negative correlations between NH_4^+-N and pH, DO values (Table 2). Moreover, the algae can utilize NO_3^--N to support their growth, and the lower NO_3^--N concentrations are usually accompanied with high algae biomass or Chl-a values (Suzuki et al., 1997). This contributed the most to the negative correlation between NO_3--N and Chl-a in the present study (Table 2).

Finally, nitrogen removal by fish netting was evaluated. Though TN content before culturing was not measured, values reported by Zou et al and Cao et al can be used for reference because of the similar fish biomass and stock environments (Cao et al., 2007; Zou et al., 2002) (natural Chinese ponds or reservoirs without fish food application). During the entire experimental period, calculated amounts of 109.96g, 131.69 g and 131.69 g TN were added to the enclosures B, C and D in the form of soybean meal. According to Table 4, fish netting resulted in 3.54 g, 38.47 g and 27.21 g TN removal in enclosures B, C and D, corresponding to 3.22%, 29.21% and 20.66% reduction of the added TN. These findings are comparable with others who reported only 11%-36% of nitrogen added as feed can recovered by the target organism (Hargreaves, 1998). Considering the nitrogen geochemical process, denitrification and ammonia volatilization are the two important approaches for nitrogen reduction. The rate of denitrification depends on temperatures, concentrations of nitrate, organic carbon, oxygen and denitrifying bacteria (Acosta et al., 1994). Due to low concentrations of nitrate, nitrogen removal by denitrification was ignored in these fish culturing enclosures (Kaggwa et al., 2010). Ammonia volatilization is strongly affected by pH, ammonia concentrations, temperatures, evaporation rate and wind speed. With pH rising, volatilization is enhanced, while it is not important at pH$<$7.5. It was reported that about 30% and 8% of the added N were lost by volatilization in an intensive shrimp pond and semi-intensive pond, respectively (Piedecausa et al., 2009). The mean pH in fish culturing enclosures here was about 8.2, thus the ammonia volatilization happened easily. Under the multiple influence of above nitrogen geochemical processes, TN concentrations in enclosures A, B, C and D were somewhat lower than those in the control enclosure and reservoir water.

5 CONCLUSIONS

Nitrogen dynamics were investigated under the condition of culturing bighead carp and common carp with added fish food. Panjiakou Reservoir water is a typical "nitrogen rich" water in nearly fifty days, and NO_3^--N is the major constituent of the TN. Our study found that the addition of fish food and culturing fish with fish food increased the NH_4^+-N and COD concentrations, while reducing NO_3^--N and TN concentrations during the short tested period. Panjiakou Reservoir has poor circulation and exchange times of months and years rather than days. Nitrogen control is of particular concern for the safety of the drinking water supply. Nitrogen mass balance calculation indicated that common carp can recover nearly 50% of the added TN in the form of soybean meal, about 4 times higher than that for bighead carp. It is implicated that bighead carp is more effective for the control of algae blooms, while common carp is more useful in the reduction of the total nutrient loadings. Finally, for the sustainable drinking water supply consideration, fish culturing style (e.g. fish species and stock density) and the contribution of cage culturing and environmental boundary conditions such as seasonal alternation, sedimentation, wind and disturbance to the water quality should be studied in detail.

ACKNOWLEDGEMENTS

This work was financed by NSFC (Grant No. 11672139) and NSF of Tianjin (Grant No. 15JCYBJC22500).

REFERENCES

Acosta-Nassar, M.V, Morell, J. M. & Corredor, J.E. (1994). The Nitrogen Budget of a Tropical Semi-Intensive Freshwater Fish Culture Pond. *Journal of World Aquaculture Society*, 25(2), 261-270.

Anderson, D.M., Glibert, P.M. & Burkholder, J.M. (2002). Harmful Algal Blooms and Eutrophication: Nutrients Sources, Composition and Consequences. *Estuaries*, 25(4b), 704-726.

Baker, M.A., Dahm, C.N. & Valett, H.M. (1999). Acetate Retention and Metabolism in the Hyporheic Zone of a Moutain Stream. *Limnology and Oceanography*, 44, 1530-1539

Blomqvist, E., Pettersson, A. & Hyenstrand, P. (1994). Ammonium- Nitrogen, a Key Regulatory Factor Causing Dominance of Non-Nitrogen-Fixing Cyanobacteria in Aquatic Systems. *Archiv für Hydrobiologie*, 13(2), 141-164.

Buschmann, A.H., Riquelme, V. A. & Hernández-González, M.C., Varela, D., Jiménez, J.E., Henríquez, L.A., Vergara, P.A., Guíñez, R. & Filún, L. (2006). A review of Impacts of Salmonid Farming on Marine Coastal Ecosystems in the Southeast Pacific. *Journal of Marine Science*, 63, 1338-1345.

Butturini, A, Battin, T.J. & Sabater, F. (2000). Nutrification in Stream Sediment Biofilms: The Role of Ammonium Concentration and DOC Quality. *Water Research*, 34, 349-639.

Cao, Y.X., Cui, H.P., Liu, Y.Q. & Ge, R.L. (2007). Analysis of Nutrient Composition between Cultured Fish in Pond and Reservoir. *Journal of Inner Mongolia University for Nationalities*, 22(5), 555-558. (In Chinese)

Chen, S., Ling, J. & Blancheton, J.P. (2006). Nitrification Kinetics of Biofilm as Affected by Water Quality Factors. *Aquaculture Engineering*, 34(3), 179-197.

Domagalski, J., Lin, C. & Luo, Y., Kang, J., Wang, S., Brown, L.R., Munn, M.D. (2007). Eutrophication Study at the Panjiakou-Daheiting Reservoir System, Northern Hebei Province, People's Republic of China: Chlorophyll-a Model and Sources of Phosphorus and Nitrogen. *Journal of Agricultural Water Management*, 94(1-3), 43-53.

Du, S.L., Huang, S.L., Pan, H.C., Zang, C.J., Wu, M., Lin, C., Guo, Y., Gao, F. & Miklas, S. (2014). Monitoring Algal Bloom through Relationships between Chlorophyll A and Phytoplankton. *Environmental Engineering and Management Journal*, 13(4), 805-815.

Felsing, M., Telfer, T. & Glencross, B. (2006). 15N-Enrichment of an Aquaculture Diet and Tracing of Cage Culture Waste in and Estuarine Environment. *Journal of Applied Ichthyology*, 22(5), 419-426.

Figueredo, C.C. & Giani, A. (2009). Phytoplankton Community in the Tropical Lake of Lagoa Santa (Brazil): Conditions Favoring a Persistent Bloom of Cylindrospermopsis Raciborskii. *Limnologica*, 39(4), 264-272.

Fraser, L.H., Carty, S.M. & Steer, D. (2004). A Test of Four Plant Species to Reduce Total Nitrogen and Total Phosphorus from Soil Leachate in Subsurface Wetland Microcosms. *Bioresource Technology*, 94(2), 185-192.

Guo, L.G. & Li, Z.J. (2003). Effects of Nitrogen and Phosphorus from Fish Cage-Culture on the Communities of Shallow Lake in Middle Yangtze River Basin of China. *Aquaculture*, 226(1-4), 201-212.

Guo, L.G., Li, Z.J. & Xie, P. Ni, L.Y. (2009). Assessment Effects of Cage Culture on Nitrogen and Phosphorus Dynamics in Relation to Fallowing in a Shallow Lake in China. *Aquaculture International*, 17, 229-241.

Harvey, B.N., Johnson, M.L., Kiernan, J.D. & Green, P.G. (2011). Net Dissolved Inorganic Nitrogen Production in Hyporheic Mesocosms with Constrasting Sediment Size Distribution. *Hydrobiologia*, 658, 343-352.

Hargreaves, J.A. (1998). Nitrogen Biogeochemistry of Aquaculture Ponds. *Aquaculture*, 166(3-4), 181-212.

Hawarth, R.W. & Marino, R. (1988). Nitrogen Fixation in Freshwater, Estuaries and Marine Ecosystems. 1. Rates and Importance. *Limnology Oceanography*, 33(4), 669-687.

Hawarth, R.W. & Marino, R. (1988). Nitrogen Fixation in Freshwater, Estuaries and Marine Ecosystems. 2. Biogeochemical Controls. *Limnology Oceanography*, 33(4), 688-701.

 ©2017, IAHR. Used with permission / ISSN 1562-6865 (Online) - ISSN 1063-7710 (Print)

Huang, S.L., Wu, M., Zing, C.J., Du, S.L., Domagalski, J., Gajewska, M., Gao, F., Lin, C., Guo, Y., Liu, B.Y., Wang, S.M., Luo, Y., Szymkiewicz, A. & Szymkiewicz, R. (2016) Dynamics of Algae Growth and Nutrients in Experimental Enclosures Culturing Big Head Carp and Common Carp: Phosphorus Dynamics. *International Journal of Sediment Research*, 31,173 - 180.

Jacoby, J.M., Collier, C.D. & Welch, E.B., Hardy, F.J. & Crayton, M. (2000). Environmental Factors Associated with a Toxic Bloom of Microcystis Aeruginosa. *Canadian Journal of Fisheries and Aquatic Sciences*, 57(1), 231-240.

Johnson, N., Revenga, C. & Echeverria, J. (2001). Managing Water for People and Nature. *Science*, 292, 1071-1072.

Kaggwa, R.C., Dam, A.A. & Kipkemboi, J. & Danny, P. (2010). Evaluation of Nitrogen Cycling and Fish Production in Seasonal Ponds (Fingerponds) in Lake Victoria Wetlands, East Africa using a Dynamic Simulation Model. *Aquaculture Research*, 42, 72-90.

Karakassis, I., Tsapakis, M., Hatziyanni, E., Papadopoulou, K.-N. & Plaiti, W. (2000). Impact of Cage Farming of Fish on the Seabed in Three Mediterranean Coastal Areas. *Journal of Marine Science*, 57, 1462-1471.

Lee, J.H.W., Choi, K.W. & Arega, F. (2003). Environmental Management of Marine Fish Culture in Hong Kong. *Marine Pollution Bulletin*, 47, 202-210.

Lorenzen, K., Struve, J. & Cowan, V.J. (1997). Impact of Farming Intensity and Water Management on Nitrogen Dynamics in Intensive Pond Culture: A Mathematical Model Applied to Thai Commercial Shrimp Farms. *Aquaculture Research*, 28, 493–507.

McQueen, D.J. & Lean, D.R.S. (1987). Influence of Water Temperature and Nitrogen to Phosphorus Ratios on the Dominance of Blue-Green Algae in Lake St. George, Ontario. *Canadian Journal of Fisheries and Aquatic Sciences*, 44(3), 598-604.

Neori, A., Chopin, T., Troell, M., Buschmann, A.H., Kraemer, G.P., Halling, C., Shpigel, M. & Yarish, C. (2004). Integrated Aquaculture: Rationale, Evolution and State of the Art Emphasizing Seaweed Biofiltration in Modern Mariculture. *Journal of Aquaculture*, 231(1-4), 361–391.

Paerl, H.W., Fulton, R.S., Moisander, P.H. & Dyble, J. (2001). Harmful Freshwater Algal Blooms, with an Emphasis on Cyanobacterial. *The Scientific World Journal*, 1(4), 76-113.

Piedecausa, M.A., Aguado-Gimenez, F., Garcia-Garcia, B., Ballester, G. & Telfer, T. (2009). Settling Velocity and Total Ammonia Nitrogen Leaching from Commerical Feed and Faecal Pellets of Gilthead Seabream (Sparus aurata L. 1758) and Seebass (Dicentrarchus labrax L.1758). *Aquaculture Research*, 40, 1703-1714.

Schroeder, G.L., Alkon, A. & Laher, M. (1991). *Nutrient Flow in Pond Aquaculture Systems. Aquaculture and Water Quality.* Baton Rouge, LA: World Aquaculture Society, 489–505.

Smith, V.H. (1983). Low Nitrogen to Phosphorus Ratios Favor Dominance by Blue-Green Algae in Lake Phytoplankton. *Science*, 221(4611), 669-671.

SPSS. (2003). *Analytical Software,* Statistical Package for the Social Sciences (SPSS) Headquarters, Chicago, Illonois, USA.

Sugiura, S.H., Marchant, D.D., Wigins, T., Kelsey, K. & Ferraris, R.P. (2006). Effluent Profile of Commercially used Low-Phosphorus Fish Feeds. *Environmental Pollution*, 140(1), 95-101.

Suzuki, K., Handa, N., Nishida, T. & Wong, C.S. (1997). Estimation of Phytoplankton Succession in a Fertilized Mesocosm during Summer using High-Performance Liquid Chromatographic Analysis of Pigments. *Journal of Experimental Marine Biology and Ecology*, 214(1-2), 1-17.

Tang, H., Xie, P., Xie, L. & Chen, F. (2006). Effect of Enclosure and Nutrient Enrichment on Microcystis Blooms in Donghu Lake. *Chinese Journal of Oceanology and Limnology*, 24(3), 278-284.

Walsh, P.J. & Wright, P.A. (1995). *Nitrogen Metabolism and Excretion.* Florida, USA: CRC Press, 352-353.

Wang, L.M. & Liu, D.W. (2008). Influence of Cage Culture on Water Quality in Panjiakou Reservoir. *Hebei Fisheries*, 6, 43-44. (In Chinese)

Wu, M., Huang, S.L., Zang, C.J., Du, S.L. & Scholz, M. (2012). The Release of Nutrient from Fish Food and Effect on Microcystis Aeruginosa Growth Characteristics. *Aquaculture Research*, 43, 1460-1470.

Zang, C.J., Huang, S.L., Wu, M., Du, S.L., Scholz, M., Gao, F., Lin, C., Guo, Y. & Dong, Y. (2011). Comparison of Relationships between pH, Dissolved Oxygen and Chlorophyll-a for Aquaculture and Non-Aquaculture Waters. *Water, Air and Soil Pollution,* 219(1-4), 157-174.

Ziemann, D.A., Walsh, W.A., Saphore, E.G. & Fulton-Bennett, K. (1992). A Survey of Water Quality Characteristics of Effluent from Hawaiian Aquaculture Facilities. *Journal of the World Aquaculture Society*, 23(3), 180-191.

Zou, Q., Wu, S.G., Gao, S.B. & Jian, D. (2002). Comparison and Analysis of Nitrogen and Phosphorus Content for Bighead Carp and Silver Carp during Different Growth Period. *Freshwater Fisheries*, 22(6), 33-34.

Proceedings of the 37th IAHR World Congress
August 13 – 18, 2017, Kuala Lumpur, Malaysia

FAECAL COLIFORM ATTACHMENT TO SETTLEABLE SUSPENDED SEDIMENT PARTICLES OF DIFFERENT SIZES

DEJUN ZHU(1), LEI JIANG(2), YONGCAN CHEN(3) & TAO WU(4)

(1,4) Department of Hydraulic Engineering, Tsinghua University, Beijing, China,
zhudejun@tsinghua.edu.cn, wut2012@qq.com
(2) Changjiang Institute of Survey,Planning, Design and Research, Wuhan, China
beiai-qq25@163.com
(3)School of Environment and Resource, Southwest University of Science and Technology, Mianyang, China
chenyc@tsinghua.edu.cn

ABSTRACT

Faecal bacteria exist in surface waters as either free cells or cells attached to suspended sediment particles, and the attachment has a great impact on the fate and transport of faecal bacteria. In modeling efforts, the attachment is commonly mathematically described by a linear partition model, *i.e.,* the concentration of attached bacteria per unit mass of suspended sediments linearly increased with the free floating bacteria concentration. However, the attachment in fact has not yet been well understood. The impact of many factors like the particle size among others is still not clear. In this study, controlled laboratory attachment experiments were conducted to investigate the impact of particle size on the attachment of Faecal coliforms (FC) to suspended sediments in surface waters. In the experiments, the suspended sediment samples (particle diameter ranging from 5 μm to 62 μm) were separated into four subsamples with different ranges of particle size, and the experimental results of the four subsamples were compared. It was found that the attachment can be well described by the linear model and the partition coefficients ranging from 0.1376 g/L to 0.9387 g/L had a greater value with finer particles. With some assumptions, the attached FC concentration per unit surface area of the suspended particles was calculated. And it was found that the attached FC concentration per unit surface area also linearly increased with the free floating FC concentration whilst did not vary with the particle size. This finding can help to refine water quality models to more accurately simulate and predict the fate and transport of faecal bacteria in surface waters.

Keywords: Faecal coliforms; attachment; settleable suspended sediments; particle size; surface water.

1 INTRODUCTION

The pathogen contamination has been a major public health concern all over the world and the presence of pathogen correlates well with the faecal contamination in surface waters (Leclerc et al., 2001). Faecal contamination is usually indicated by faecal indicator bacteria. Faecal coliforms (FC) used to be the most commonly used indicator bacteria worldwide, and they are still the principle indicator bacteria in many countries, *e.g.,* China.

Indicator bacteria in surface waters move freely with flow or interdependently with suspended sediments by attaching to them (Gannon et al., 1983), and the attachment will influence the bacterial transport and fate processes significantly. Settling of attached bacteria will accelerate the bacterial transfer into the bottom sediments and therefore purify the contaminated surface water due to their higher settling velocity (Jeng et al., 2007). Meanwhile, the settled bacteria in the bottom sediments may experience a favorable physical, chemical and biological environment and survive much longer than in the overlying water. Thus, the bottom sediments harbor a very high population of faecal bacteria and pose a potential risk for water quality of the overlying water (Jeng et al., 2007).

Water quality management and remediation usually depend on the accuracy of the numerical models to capture transport and fate processes of bacteria (Soupir et al., 2010). Therefore, quantitative representation of the partition between the free-floating and attached bacteria is extremely important for a better modeling performance. The attached fraction, defined as the ratio of attached indicator bacteria concentration to total concentration, was found to be highly variable (Jiang et al., 2015). More recently, the linear model as in Equation [1] was employed by some researchers to improve the predictive capabilities of microbial water quality modeling (Bai and Lung, 2005).

$$P = \frac{C_s}{S} = kC_w \qquad [1]$$

 ©2017, IAHR. Used with permission / ISSN 1562-6865 (Online) - ISSN 1063-7710 (Print)

where P = the mass specific concentration of the attached bacteria (cfu/g), S = the sediment concentration, (g/L), C_s = the sediment associated bacteria concentration (cfu/L), C_w = the free-floating bacteria concentration (cfu/L), and k = the partition coefficient (L/g). The linear model was originally proposed to describe the attachment of faecal bacteria to soil particles in groundwater (Gantzer et al., 2001) and was experimentally validated that it was also suitable for describing the attachment of indicator bacteria to suspended sediments in surface waters. According to Equation [1], the attached fraction increases with the sediment concentration.

Particle size was also reported by many researchers to be an important factor responsible for the highly variable attached fractions. Though the findings of different researchers were often contradictory, several researchers found that feacal bacteria prefer to associate with particles finer than 30 μm in diameter. Auer and Niehaus (1993) reported that the extremely fine particles in the size range 0.45 ~ 10 μm had the largest adsorption amount and the attached proportion of faecal coliforms to this faction reached to 90.5%. Jeng (2007) observed that about 70 ~ 80% of attached faecal bacteria were associated with suspend sediments ranging from 10 μm to 30 μm. However, some other researchers reported that higher attached fraction to larger particles or no correlations between that attached fraction and particle size. The investigations conducted by Schillinger and Gannon (1985) showed that most of the indicator organisms was associated with suspended particles larger than 30 μm and 52 μm. Meanwhile, Borst and Selvakumar (2003) observed no correlation between the faecal coliforms or faecal streptococcus concentrations and mean particle size.

In this study, controlled laboratory experiments were conducted to further understand the characteristics of the attachment of FC to suspended sediments in surface waters. The emphasis of this study is to examine the impact of particle size on the attachment.

2 MATERIALS AND METHODS

In the study, bacteria-sediment-water mixtures were prepared and then unattached/attached bacteria were separated and enumerated. The results were analyzed to illustrate the attachment of FC to sediments. Each experiment was conducted in triplicate. A brief introduction of the materials and methods is given in this section, and a more detailed description and validation of the methods can be found in Jiang et al. (2015).

2.1 Sediments of different particle size

The sediments were taken from a river in Beijing, China and soaked in distilled water for several days followed by air drying before experiments. The sediments that passed a 0.0625 mm sieve were used in the experiments. The organic matter, caution exchange capacity, Zeta Potential, specific gravity, BET specific surface area and average pore size of the cohesive sediments were 2.5%, 8.61×10^{-3} cmol/g, -44.27 mV, 2.650, 4700 dm^2/g, and 9.615 nm, respectively. The mineral composition of the suspended sediments determined by X-ray diffraction was quartz, feldspar, chlorite and illite. Four sediment fractions of different particle sizes of 62 ~ 31 μm, 31 ~ 16 μm, 16 ~ 8 μm and 8 ~ 5 μm were obtained by repeated sedimentation based on the Stoke's law.

2.2 Bacteria and bacteria-sediment-water mixture

The FC bacteria in the experiments were isolated from local waste water and preserved at 4 °C in a refrigerator for later use. Before the experiments, the bacteria were activated at 44.5 °C for 7 h. Then, 1 mL of the FC culture was transferred to two 1000 mL Erlenmeyer flasks, each containing 200 mL of beef extract peptone. The flasks were incubated at 44.5 °C and shaken at 150 rpm for 24 h. Then, the bacteria were harvested by centrifugation at 12000 r/min for 15 min and washed twice with sterile distilled water. The harvested bacteria were mixed with 500 mL sterile distilled water and the initial concentrations were examined. In the experiments, 0.15 g sediments with particle sizes of 62 ~ 31 μm, 31 ~ 16 μm, 16 ~ 8 μm or 8 ~ 5 μm were added to 100 mL FC suspension in another 300 mL Erlenmeyer flask to obtain bacteria-sediment-water mixture with different particle sizes, P1, P2, P3 or P4. Then, the flask was stirred at 300 rpm on a rotary shaker at 25 °C for 1 h. The initial FC concentration in the flask was controlled in the range of 10^1 ~ 10^6 cfu/L. This range corresponded to the common faecal bacteria concentration in surface waters.

2.3 Separation of unattached/attached bacteria

The filtration technique used by many researchers (Gannon et al., 1983; Schillinger and Gannon, 1985; Auer and Neuhaus, 1993) was employed to separate the free-floating and attached bacteria. Ideally, the selected filter membrane should allow free-floating FC to pass and retain almost all the sediment particles. As shown in Table 1, the mass percentage of particles < 5 μm was only about 0.75% and negligible. In fact, particles finer than 5 μm are unsettleable under natural water conditions and have a negligible impact on the bacteria exchange between sediments and water column (Schillinger and Gannon, 1985). So, a pore size of 5 μm was selected, and the FC pass the 5 μm pore were regarded as the free-floating group. In each experiment, 100 mL of the mixture was poured through a filter in a vacuum filtration apparatus. The filtrate was collected to analyze the free-floating FC bacteria number using the MF technique and the filter was removed from the filtration apparatus to further analyze the number of attached bacteria.

©2017, IAHR. Used with permission / ISSN 1562-6865 (Online) - ISSN 1063-7710 (Print)

2.4 Bacteria enumeration

In this study, we used the membrane filtration (MF) technique (SEPA, 2007) to enumerate the bacteria. The experiments were conducted at 25 ± 0.5°C and at pH of 7 ± 0.5. In some of the experiments, it was checked that the sum of the free-floating bacteria number and the attached bacteria number was equal to the initial bacteria number in the suspension before sediments being added (data not shown). These results indicated that the impacts of die-off/regrowth were negligible during the experiments.

3 RESULTS AND DISCUSSION

3.1 Attachment of FC to sediment particles

The measured concentration of attached bacteria (P) per unit mass for different sediment particle sizes (D) was plotted against the free-floating bacteria concentration (C_w) in Figure 1. It can be seen that for each particle size, P linearly increased with C_w. All the dots according to each sediment concentration and particle size were fitted using a straight line and the values of the coefficient of determination (R^2) were 0.9755, 0.9867, 0.9888 and 0.9926 for P1, P2, P3 and P4, respectively. The good fitness of the liner partition model illustrated the validity of the linear partition model in describing the attachment of FC to suspended sediments.

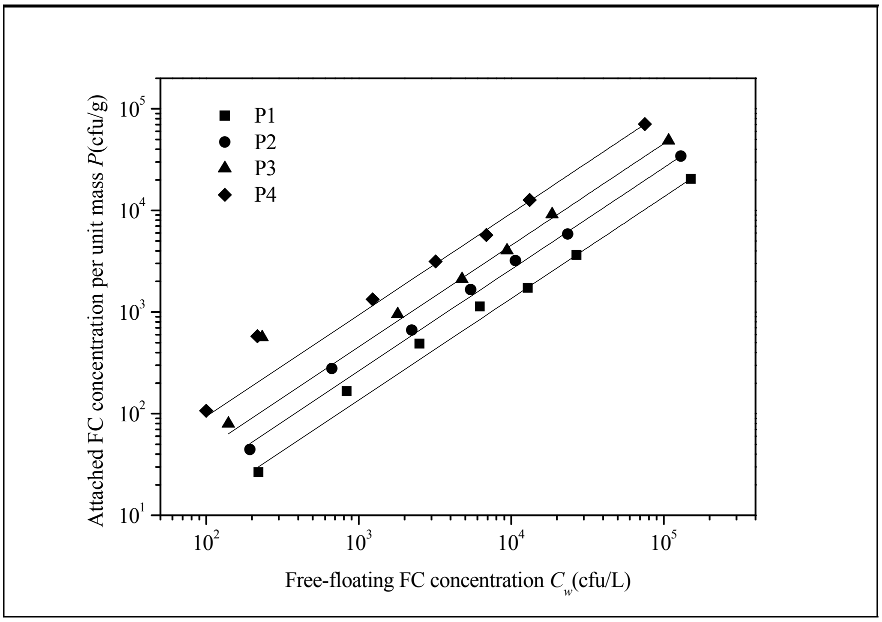

Figure 1. Relationship between attached FC concentration per unit mass and free-floating FC concentration for different particle size.

The partition coefficient (k) was calculated for each particle size and they significantly increased with the decrease of particle size (D) with values of 0.1376 L/g, 0.2611 L/g, 0.4797 L/g and 0.9387 L/g for P1, P2, P3 and P4, respectively. The k value for P4 was 5.58, 3.02 and 2.10 times larger than that for P1, P2 and P3, respectively, which indicated that the finer particles exhibited much larger adsorption capacity than the coarse ones.

3.2 Attached FC concentration per unit surface area

To further investigate the impact of particle size on attachment, we calculated the attached FC number per unit surface area, p.

$$p = \frac{n_s}{A_a} = \frac{C_s}{A_s \cdot S} \qquad [2]$$

where p = the attached FC number per unit surface area (cfu/dm^2), n_s = the number of attached FC (cfu), A_a = total surface area of sediments available for FC attachment (dm^2), and A_s = specific surface area of sediments (dm^2/g).

The pores on the sediment surface will increase the specific surface area by orders of magnitude and the BET specific surface area includes the surface area of the pores. The averaged pore size of the suspended sediments in the experiments was 9.615 nm, and it was much smaller than the cell size of faecal bacteria. This meant that faecal bacteria have little chance to enter the pores on the surface of the suspended sediments. Thus, instead of using the BET specific surface area, we determined the specific surface area

 ©2017, IAHR. Used with permission / ISSN 1562-6865 (Online) - ISSN 1063-7710 (Print)

available for FC attachment by classifying the particles into 14 fractions as in Table 1 and assuming all the particles were spherical and of the same density of 2.65 g/cm^3. The assumptions and detailed calculation procedures can be found in Oliver et al. (2005).

Table 1. Parameters for calculating specific surface area of sediments available for attachment.

Particle size D/μm	Median diameter D_m/μm	Mass percentage f_i/%
62~52	57	12.919
52~42	47	7.809
42~32	37	4.273
32~28	30	6.855
28~24	26	5.981
24~20	22	5.789
20~16	18	6.377
16~14	15	4.791
14~12	13	5.317
12~10	11	6.434
10~8	9	8.459
8~7	7.5	6.993
7~6	6.5	8.311
6~5	5.5	9.696

The concentration of attached bacteria per unit surface area (p) versus free-floating bacteria concentration (C_w) was plotted in Figure 2. In Figure 2, the experimental results of Jiang et al. (2015) were also included. The experiments were conducted under same conditions except that in Jiang et al. (2015), the sediments were not subdivided into four subsamples with different particle sizes, instead, they used four different sediment concentrations ranging from 0.5 g/L to 2.0 g/L. And, the results got from the four sediment concentrations were denoted by S1, S2, S3 and S4. The significant linear increasing relationship between p and C_w has been observed from this figure, and the ratio of p to C_w does not vary with particle size.

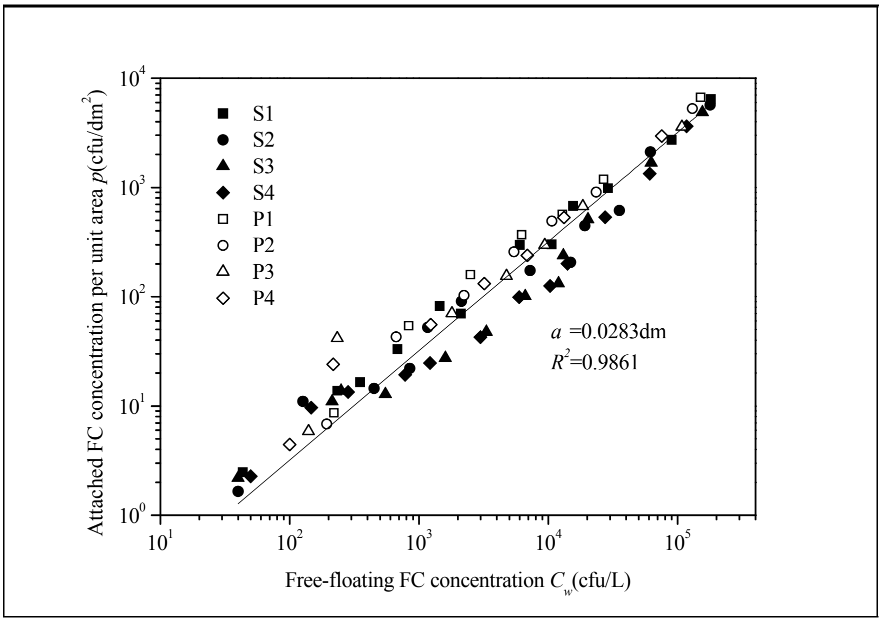

Figure 2. Relationship between attached FC concentration per unit surface area and free-floating FC concentration.

Manipulating Equations [1] and [2] gives that:

$$\frac{p}{C_w} = \frac{k}{A_s} \quad [3]$$

Since the LHS of Equation [3] does not change, the equation means that the partition coefficient increase linearly with the specific surface area.

4 CONCLUSIONS

Accurate representations of sediment-bacteria associations in surface waters are lacking in modeling performance. The experimental results indicated that the linear partition model can be used to characterize FC attachment to suspended sediments and the fitted partition coefficients significantly increased with the decrease of particle size. Further investigation showed that the attached FC concentration per unit surface area also linearly increased with the free floating FC concentration whilst did not vary with the particle size, this means that the partition coefficient in the linear model is proportional to the specific surface area of the sediment particles.

It is worth noting that the pores of the suspended sediments are usually smaller than the cell size of faecal bacteria. This meant that faecal bacteria have little chance to enter the pores on the surface of the suspended sediments. Thus, instead of the BET specific surface area being used, the specific surface area available for FC attachment was calculated based on the assumption of shape, size and density of the particles.

ACKNOWLEDGEMENTS

The financial support from the National Natural Science Foundation of China (No. 51509136) is gratefully acknowledged.

REFERENCES

Auer, M.T. & Niehaus, S.L. (1993). Modeling Fecal Coliform Bacteria-Ⅰ. Field and Laboratory Determination of Loss Kinetics. *Water Research*, 27, 693-701.

Bai, S. & Lung, W.S. (2005). Modeling Sediment Impact on the Transport of Fecal Bacteria. *Water Research*, 39, 5232-5240.

Borst, M. & Selvakumar, A. (2003). Particle-Associated Micro-Organisms in Stormwater Runoff. *Water Research,* 37, 215-223.

Gannon, J.J., Busse, M.K. & Schillinger, J.E. (1983). Fecal Coliform Disappearance in a River Impoundment. *Water Research*, 17, 1595-1601.

Jeng, H.C., England, A.J. & Bradford, H.B. (2007). Indicator Organisms Associated with Stormwater Suspended Particles and Estuarine Sediment. *Journal of Environmental Science and Health*, 40, 779-791.

Leclerc, H., Mossel, D.A., Edberg, S.C. & Struijk, C.B. (2001). Advances in the Bacteriology of the Coliform Group: their Suitability as Markers of Microbial Water Safety. *Annual Reviews in Microbiology*, 55, 201-234.

Schillinger, J.E. & Gannon, J.J. (1985). Bacterial Adsorption and Suspended Particles in Urban Stormwater. *Journal of the Water Pollution Control Federation,* 57, 384-389.

Soupir, M.L., Mostaghimi, S. & Dillaha, T. (2010). Attachment of Escherichia Coli and Enterococci to Particles in Runoff. *Journal of Environmental Quality*, 39, 1019-1027.

Jiang, L., Chen, Y.C., Zhu, D.J. & Z. W. Liu (2015). Faecal Coliform Attachment to Settleable Suspended Sediments in Fresh Surface Waters: Linear Partition Model Validation and Sediment Concentration Effects. *Water Science and Technology: water supply*, 15(4), 864-870

 ©2017, IAHR. Used with permission / ISSN 1562-6865 (Online) - ISSN 1063-7710 (Print)

MICROHABITAT MODELLING FOR AN ENDANGERED FRESHWATER FISH, LUFUA ECHIGONIA, IN A SPRING-FED URBAN STREAM

YUKI MATSUZAWA(1), MITSURU OHIRA(2) & SHINJI FUKUDA(3)

(1)School of Agriculture, Tokyo University of Agriculture and Technology, Saiwai-cho 3-5-8, Fuchu, Tokyo 183-8509, Japan
s169461t@st.go.tuat.ac.jp
(2, 3) Institute of Agriculture, Tokyo University of Agriculture and Technology, Saiwai-cho 3-5-8, Fuchu, Tokyo 183-8509, Japan
shinji-f@cc.tuat.ac.jp

ABSTRACT

This study assessed microhabitat conditions of an endangered freshwater fish, *Lefua echigonia*, using field observed ecohydraulic data and a machine learning-based habitat model. We made a series of monthly field surveys in a spring-fed, small urban stream in Japan: one for understanding longitudinal distributions of the fish and the other for understanding species interactions among fish fauna in the target river. Random forests (RF) was applied as a tool to analyze the relationship between physical habitat conditions and the presence/absence of *L. echigonia*. As a result, 12 freshwater fish species were observed in the river, of which longitudinal distributions of these species were relatively stable across the year. This may be partially due to its nature of spring water having stable temperature regime (around 18 °C) within a year except summer when water temperature rises up to 25 °C. RF-based habitat model showed high performance for modelling longitudinal distribution of *L. echigonia*, with two kinds of ecological information, namely variable importance and response curves. Variable importance suggested the importance of hydraulic parameters of flow velocity and water depth, and the presence/absence of aquatic vegetation. Response curves illustrated the important instream habitat conditions such as shallow water with low flow velocity, and larger proportion of vegetation and medium- to large-sized gravels. The habitat information can be used to identify potential habitats for *L. echigonia*. Future works should consider seasonal dynamics of habitat conditions and their suitability to various life-stages of *L. echigonia* such as spawning and interactions with other competitive aquatic species.

Keywords: Conservation; endangered freshwater fish; habitat model; microhabitat; urban stream.

1 INTRODUCTION

Small streams including urban rivers and agricultural canals can provide important instream habitats for freshwater ecosystems such as fish, invertebrates and aquatic vegetation. However, infrastructure development for cities and agriculture for better quality of life and higher productivity has degraded such habitats by highly modified and regulated control and management activities, which, in return, has impacts on human life through degraded ecosystem services. Environmental management based on a better understanding of the ecology of existing ecosystems and impact of human activities is needed for our sustainable living with nature. In order to achieve this, both qualitative and quantitative information can play a role in a decision-making process. In this study, the authors investigated microhabitats of an endangered freshwater fish, *Lefua echigonia*, based on monthly field surveys in Yagawa river and habitat modelling with a predictive machine learning method, namely Random Forests (RF; Breiman, 2001). We discuss the specificity of microhabitat conditions of the fish species in the target system in comparison with previous research in other areas.

2 METHODS

Our target fish, *L. echigonia* is a small freshwater fish dwelling in spring-fed streams and channels where human impacts of urbanization and agricultural intensification can be the major threat for their habitat degradation. We made two kinds of field surveys in Yagawa River (totaled 1.5 km long) in Tokyo, Japan for assessing microhabitat conditions of the fish. The first survey aims to understand longitudinal distribution of the fish along the stream, in which fish sampling with physical habitat measurement (i.e., water depth, flow velocity, substrates, percent vegetation coverage, etc.) was conducted to cover the entire river from the downstream end to the upstream end. The second survey was designed to investigate seasonal changes of fish fauna at 15 different survey stations (Figure 1), for which a 10-m-long reach was set and sampling effort was kept the same across the stations. The surveys were both conducted every month from June 2015 to May 2016. Body length and weight of sampled *L. echigonia* were recorded and released to where they were captured. Physical habitat conditions measured were water depth (cm), flow velocity (mm/s), substrate coverage (%; large-sized gravels, medium-sized gravels, small-sized gravels and sand/clay), percent vegetation coverage (%), and others. We used the package “randomForest” (Liaw and Wiener, 2002) as a RF

©2017, IAHR. Used with permission / ISSN 1562-6865 (Online) - ISSN 1063-7710 (Print)

tool of microhabitat modelling for its predictive performance and the ability to extract ecological information such as variable importance and response curves.

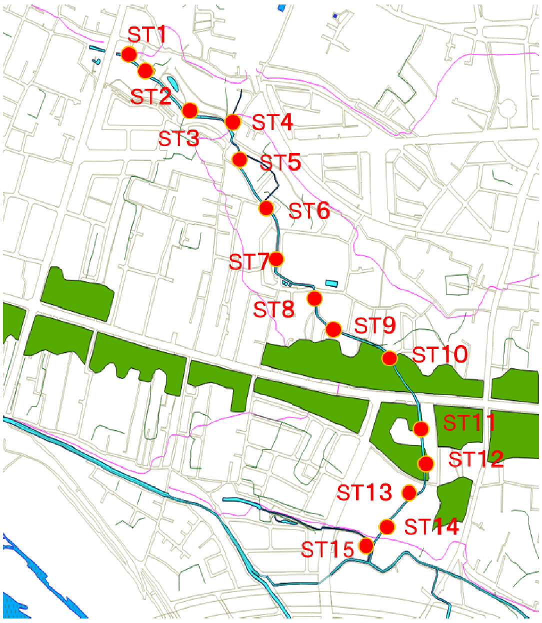

Figure 1. Locations of fish fauna survey.

3 RESULTS

As a result, the distribution of *L. echigonia* in the first survey changed with time because of its life stage from juvenile to adult. For instance, juvenile *L. echigonia* can be found throughout the river from April to June when spawning takes place. The distribution range shrank with time and becomes stable in around October and November partly because of habitat selection with growth. In the second survey, 12 fish species were observed of which four species of *L. echigonia*, *Nipponocypris temminckii*, *Rhynchocypris logowskii steindachneri*, and *Rhynchocypris oxycephalus jouyi*, in the order of dominance, were captured (Table 1). While *L. echigonia* and *R. o. jouyi* were found in similar stations such as ST1 and ST3, *N. temminckii* and *R. l. steindachneri* were mostly captured in ST6 and ST7 which can be characterized as relatively deep and open water in the target reach. Specifically, *N. temminckii* was not found between ST1 and ST4. It is seen from Figure 2 that the population density of *L. echigonia* was negatively correlated with *N. temminckii* and *R. l. steindachneri* while *N. temminckii* and *R. l. steindachneri* co-occurred in their main habitat in the river. These results indicate habitat differentiation within the small urban river.

Table 1. Dominant fish species in Yagawa River.

	Scientific name	Common name
a	Lefua echigonia	Japanese eight-barbel loach
b	Nipponocypris temminckii	Dark chub
c	Rhynchocypris logowskii steindachneri	Amur Minnow
d	Rhynchocypris oxycephalus jouyi	Chinese minnow
e	Misgurnus anguillicaudatus	Weather loach
f	Oryzias latipes	Japanese medaka
g	Gnathopogon elongatus	Field gudgeon

RF-based habitat models could successfully represent the presence/absence of the fish. The variable importance indicated that velocity was the most important for modelling longitudinal distributions of *L. echigonia*, followed by water depth and the presence/absence of vegetation (Figure 3). While the other habitat parameters except velocity, depth and P/A of vegetation showed limited importance, openness above sampling point, indicating canopy coverage above water, was found to have almost no importance in this habitat modelling. Response curves (Figure 4) show how *L. echigonia* responds to a given habitat condition. For instance, *L. echigonia* occurred in a relatively slow flowing and shallow water bodies (Figure 4A–4B), in which a slight increase in habitat potential in a fast flowing range can also be observed. The fish showed a tendency to stay in an area with relatively larger percent coverage of vegetation and large- and medium-sized gravels (Figure 4D–4F).

 ©2017, IAHR. Used with permission / ISSN 1562-6865 (Online) - ISSN 1063-7710 (Print)

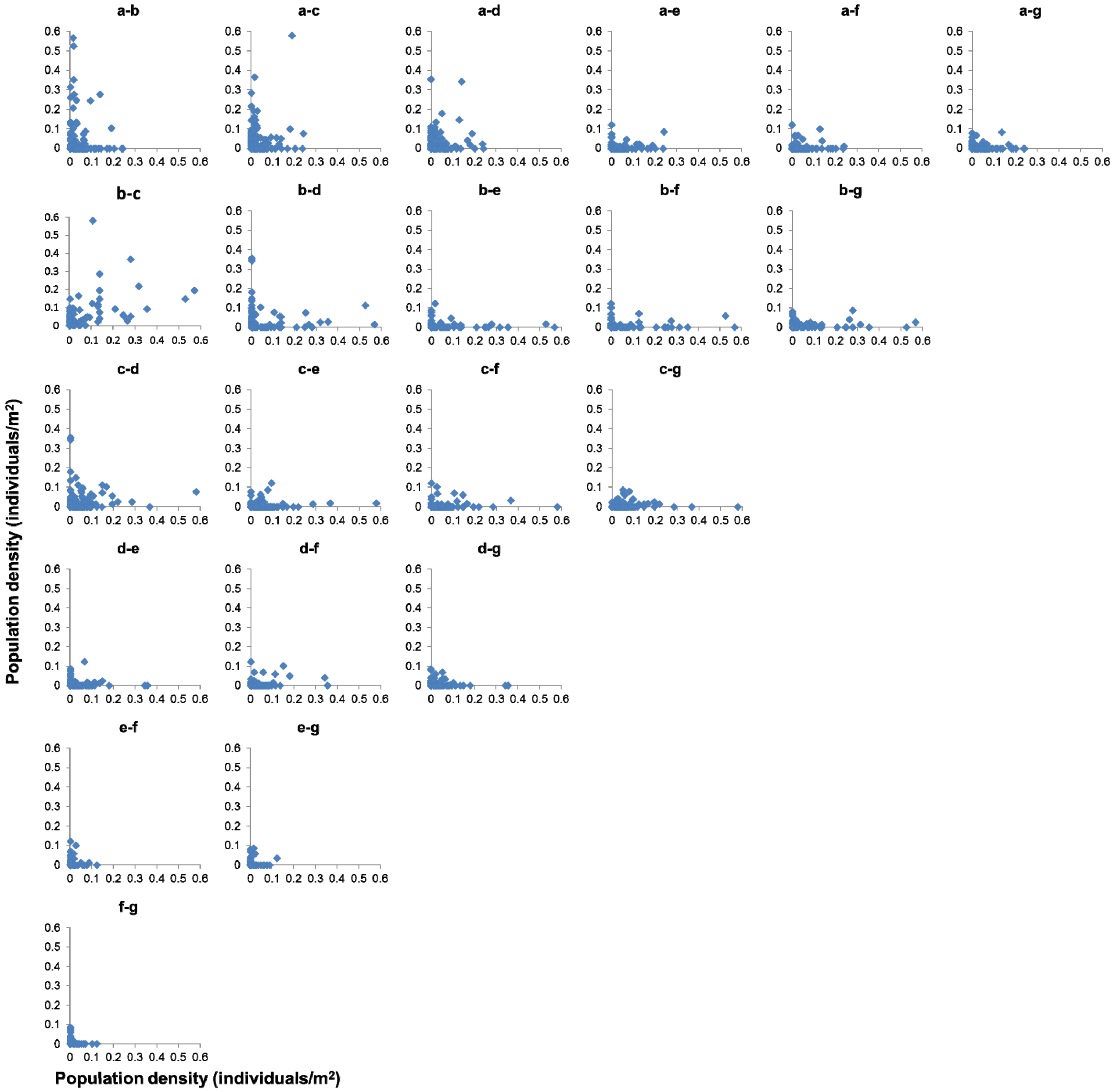

Figure 2. Scatter diagrams of fish population density of fish species captured in Yagawa river: **a**: Lefua echigonia, **b**: Nipponocypris temminckii, **c**: Rhynchocypris logowskii steindachneri, **d**: Rhynchocypris oxycephalus jouyi, **e**: Misgurnus anguillicaudatus, **f**: Oryzias latipes, **g**: Gnathopogon elongates.

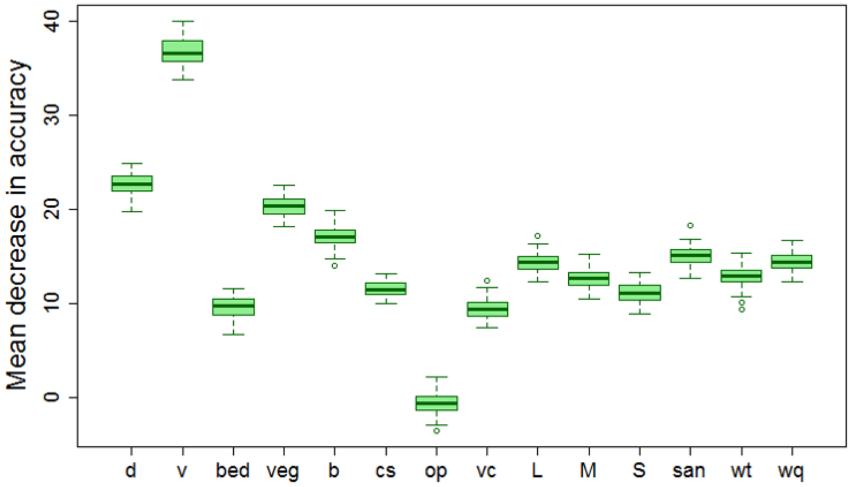

Figure 3. Variable importance computed by random forests: d: water depth, v: flow velocity, bed: dominant substrate, veg: presence/absence of vegetation, b: stream width, cs: channel structure, op: openness, vc: percent vegetation coverage, L: percentage of large-sized gravels, M: percentage of medium-sized gravels, S: percentage of small-sized gravels, san: percentage of sand/clay, wt: water temperature, wq: electrical conductivity.

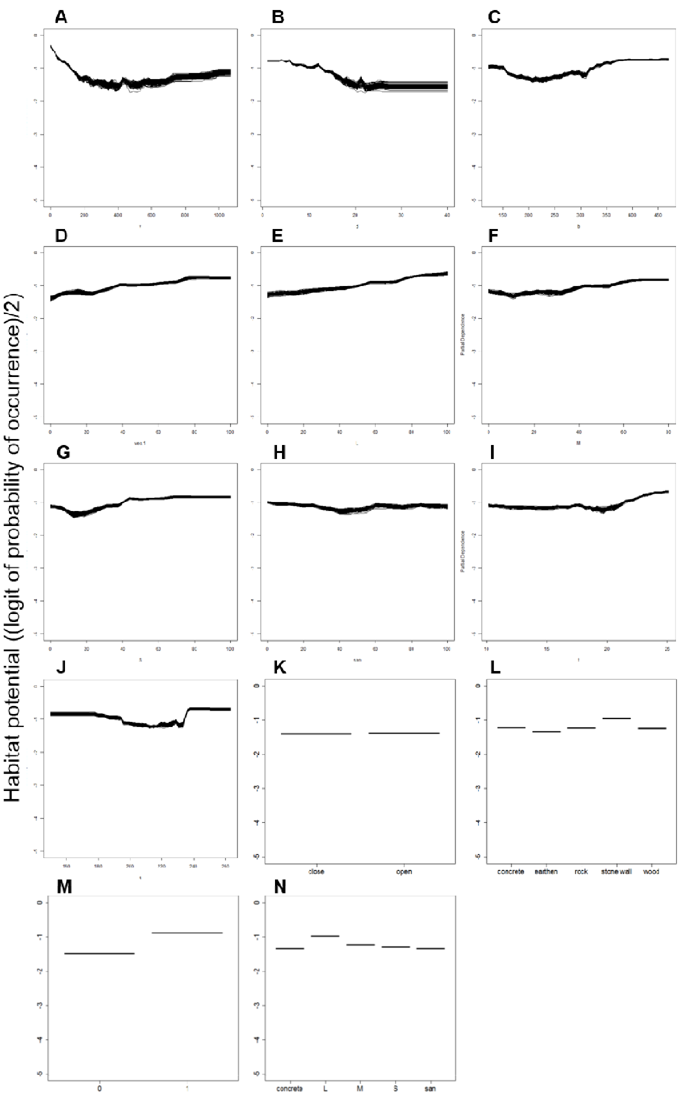

Figure 4. Response curves computed by random forests: A: flow velocity, B: water depth, C: stream width, D: percent vegetation coverage, E: percentage of large-sized gravels, F: percentage of medium-sized gravels, G: percentage of small-sized gravels, H: percentage of sand/clay, I: water temperature, J: electrical conductivity, K: openness, L: channel structure, M: presence/absence of vegetation, N: dominant substrate.

©2017, IAHR. Used with permission / ISSN 1562-6865 (Online) - ISSN 1063-7710 (Print)

4 DISCUSSION

Habitat models have been widely applied for habitat prediction and for better understanding of species' ecology (Fukuda et al., 2013; Fukuda and De Baets, 2016). Higher habitat potential in a slow flowing water can be explained by the sampling positions of *Lefua echigonia*, which were in many cases behind obstacles such as large rocks, wood debris, fallen leaves and instream structures. In these areas, flow velocity is low even though mean cross-sectional flow velocity is high. Conventional flow monitoring methods can fail to capture this kind of specific flow conditions and may lead to a wrong conclusion regarding habitat requirement for this species. For a better understanding of the ecology of this species, further studies in a laboratory flume may be needed to understand swimming ability that can be a good indicator for habitat suitability for velocity.

Higher habitat potential for shallow water and wider stream widths may also reflect features of the main *L. echigonia* habitats where the largest population can be found. This area is a protected area with abundant spring water which provides stable habitat conditions throughout the year. Shallower water may be preferred because other species can be present in a deeper area where species competitions for resources and space may be high. Vegetation coverage may be important to alleviate such a competition.

Monthly survey on fish fauna suggested potential inter-species competition between *L. echigonia* and *N. temminckii*. For instance, these species co-occurred in the same reach (e.g., ST7), in which *N. temminckii* may compete in resource uses or directly predate *L. echigonia*. The co-occurrence was possible because of habitat differentiation between deep and fast flowing water for *N. temminckii* and shallow and slow flowing water with aquatic vegetation for *L. echigonia*. As such, habitat heterogeneity in a reach may allow for coexistence of different species even under competition.

5 CONCLUSIONS

We investigated *L. echigonia* microhabitat based on a series of field survey and RF-based habitat modelling as a tool to identify key habitat information of the species. *L. echigonia* was captured mainly in ST1–ST3 where large-sized gravels and aquatic vegetation can be observed. The fish dominated in ST13 and ST14 where large-sized gravels and litters formed step-pool structures in the stream. Velocities in the slow flowing regions such as pool and behind obstacles must be measured in order to quantify habitat requirement for the *L. echigonia*. The habitat differentiation may be ascribed to differences in habitat requirement as well as the results of inter-species competition. Further studies are needed to investigate more specific habitat conditions in relation to swimming ability of *L. echigonia* and the ways of habitat restoration considering biophysical environment in the river.

ACKNOWLEDGEMENTS

This study was supported in part by the Grant-in-Aid for Challenging Exploratory Research (26660190) of the Ministry of Education, Culture, Sports, Science and Technology (MEXT), Japan. The authors thank Shiho Saito, Satoshi Onoue and Kosei Aoki for their contribution to the field surveys in Yagawa.

REFERENCES

Breiman, L. (2001). Random Forests. *Machine Learning,* 45, 5–32.

Fukuda, S. & De Baets, B. (2016). Data Prevalence Matters when assessing Species' Responses using Data-Driven Species Distribution Models. *Ecological Informatics,* 32, 69–78.

Fukuda, S., De Baets, B., Waegeman, W., Verwaeren, J. & Mouton, A.M. (2013). Habitat Prediction and Knowledge Extraction for Spawning European Grayling (*Thymallus* L.) using a Broad Range of Species Distribution Models. *Environmental Modelling & Software,* 47, 1–6.

Liaw, A. & Wiener, M. (2002) Classification and Regression by Random Forest. R News, 2(3), 18–22.

FIELD SURVEY OF MICROPLASTICS IN JAPANESE RIVERS

KOUKI KUDOU[(1)], TOMOYA KATAOKA[(2)], YASUO NIHEI[(3)] AND HIROFUMI HINATA[(4)]

[(1,2,3)] Dept. of Civil Eng., Faculty of Science and Technology, Tokyo University of Science,
7616609@ed.tus.ac.jp, tkata@rs.tus.ac.jp
[(4)] Dept. of Civil and Environmental Eng., Faculty of Engineering, Ehime University.

ABSTRACT

Microplastics (MPs) are a major concern in the ocean environment worldwide. Microplastics influence not only the water environment, but also the ecosystem because, due to their small size, microplastics can easily end up in the mouth of aquatic organisms. There has been many researches on, and many surveys of, MPs in the ocean, but there has been few researches on MPs in rivers around the world. As the first step in research on MPs in rivers, in the present study, we considered the fundamental methodology of an MPs survey. Then, we investigated the distribution of MPs in 21 locations on 18 Japanese rivers. We found that the particle count density of MPs in the rivers was one order of magnitude lower than that in the sea near Japan. The methodological problem of contamination of our survey results due to plastics in the materials is also discussed.

Keywords: Microplastics; riverine litter; marine debris; plastic pollution; particle count density.

1 INTRODUCTION

It has recently become clear that there are a lot of small pieces of plastic less than 5 mm in diameter, called microplastics (hereinafter called MPs), in the marine environment. Several of their influences on the marine environment and ecosystem are known (Thompson et al., 2004).

MPs can be divided into primary MPs and secondary MPs, depending on how the MPs are generated. Primary MPs are fine during production for example resin pellets, scrub and synthetic fibers detached by washing (Browne et al., 2011). Secondary MPs are produced by fragmentation of large plastic debris that has deteriorated with exposure to ultraviolet rays and changes in temperature (Andrady, 2011). It is quite difficult to collect MPs because MPs are very fine. MPs remain in the natural environment for a long time since they decompose with difficulty.

Consequently, several risks to coastal environment have been identified. For example, MPs adsorb and concentrate persistent organic pollutants at low concentrations in the ocean and may become a transportation medium for contaminants to non-contaminated marine areas (Mato et al., 2001). When aquatic organisms become contaminated with MPs, not only can this damage the inside of their bodies physically, but contaminants can also migrate from the MPs to their body tissues (Tanaka et al., 2013).

There has been a lot of research on the above topics for MPs in oceans and along coastlines. For oceans, it has been reported that MPs have accumulated in the convergence zone of each of the large subtropical gyres (Law et al., 2010, Eriksen et al., 2014, Cózar et al., 2014). The particle count density in the North Pacific Ocean is particularly high, at 105,000 pieces/km^2. Additionally, the average density in six ocean areas, including the North and South Pacific Ocean, the North and South Atlantic, the Indian Ocean and the Mediterranean, is 63,000 pieces/km^2 (Eriksen et al., 2014). Meanwhile, the particle count density in the East Asian Sea is 1,720,000 pieces/km^2 (Isobe et al., 2015). This value is 16 times greater than that for the North Pacific and 27 times greater than the average value for these six oceans. For that reason, it has been pointed out that the East Asian Sea around Japan is a hot spot for MPs.

In the oceans, the current status of MP pollution is becoming clear due to a lot of research. However, the current status in rivers is not clear and survey methods are not unified because there has been few researches and then survey methods are not established (Eerkes-Medrano et al., 2015). The rivers are known to be the main source of marine plastic debris (Jambeck et al., 2015), and many MPs have flowed into the sea through the rivers. Riverine litter has repeatedly been cast from river banks and has flowed out to sea from there (Funamoto et al., 2016), and plastic debris has deteriorated and been fragmented by ultraviolet rays and changes in temperature.

In this study, we present the fundamental methodology for surveying MPs in rivers and report the results of our survey of many Japanese rivers.

 ©2017, IAHR. Used with permission / ISSN 1562-6865 (Online) - ISSN 1063-7710 (Print)

2 FIELD SURVEY AND ANALYSIS METHOD

2.1 Procedure for the field survey in rivers

Since there are few surveys on MPs in rivers, at first we considered the alignment of the fundamental methodology of a MPs survey with that of general surveys of water quality in rivers. For oceans, a MPs survey is conducted on a ship, but for rivers, collection of MPs samples was done on a bridge above the river, as for surveys of water quality. The survey procedure for MPs from a bridge was as follows.

i. A plankton net is dropped to collect MPs from the bridge into the river near the streamline.
ii. The net is fixed near the water surface for a predetermined time.
iii. The net is pulled up from the river to the bridge.
iv. The net is immersed in a bucket filled with river water to wash inside of the net.
v. Samples collected at the net are moved to sampling bottles.

To collect MPs, we used a plankton net 30 cm in diameter, 75 cm in length, and with a mesh size of 0.1 mm. The flow meter was attached at the aperture of the net to measure the water volume passing through the net. In addition, we attached a rope to the plankton net to drop it down and pull it up. When the velocity of flow was less than 0.3 m/s, the accuracy of flow meter measurement dropped. So an electromagnetic current meter or a radio current meter was also used. At each survey location, the above measurement steps were carried out in three sets of 10 minutes and one set of 30 minutes, as shown in Table 1. The measuring times, use of flow meter and bucket type were different, depending on each survey day. This is the result of reviewing the survey method as shown later.

Table 1. Outline of field survey and tools.

Date	River	Location	Measuring time	Flow meter	Tool Bucket
	Edogawa	Noda			
Aug. 4, 2015	Nakagawa	Yoshikoshi			
	Ohori	Komagi			
Aug. 31, 2015	Mogami	Shonai Ohashi			
Sept. 1, 2015		Kurotaki		Not used	
Sept. 17, 2015	Asahi	Kohoku			
Oct. 13, 2015	Edogawa	Noda			
Oct. 22, 2015	Miyara	Kawahara			
	Edogawa	Noda			
	Nakagawa	Yoshikoshi	10 minutes × 3 times		
Nov. 18, 2015	Yoro	Kasumi			
	Obitsu	Nakagawa			
	Koito	Rokusan			Plastic
Nov. 19, 2015	Kurokawa	Kurumagaeri			
Dec. 4, 2015	Nakagawa	Yoshikoshi			
	Tama	Maruko			
Dec. 8, 2015	Tsurumi	Shin Yokohama Ohashi			
	Arakawa	Nishiarai		Used	
Dec. 22, 2015	Sumida	Shirahige			
May 13, 2016	Edogawa	Noda			
	Naka	Nakagawa Hodokyo			
Jul. 7, 2016	Kuji	Tomioka			
	Tone	Sakae	30 minutes × 1 time		
	Nakagawa	Shinkai			
Jul. 27, 2016	Arakawa	Jisui			Aluminum
	Sagami	Sagami Ohashi			

2.2 Survey sites

Table 1 shows the details of the field survey, including the field sites. The survey sites comprised rivers in 14 class A river systems and 4 class B river systems. These rivers have urban areas in their basin areas, except for the Kurokawa and Miyara Rivers. Due to outflowing MPs that have accumulated on the river bank, a large number of MPs may be transported during floods. However, the task of surveying during floods is quite difficult due to damage to the net by large debris (e.g., driftwood) and clogging of the net by large amounts of suspended sediments. Therefore, in this study, the field survey on MPs was carried out when water levels were low.

Table 2. Material and specific gravity of the main plastics.

Material	Specific gravity
Polyethylene (PE)	0.910–0.965
Polypropylene (PP)	0.900–0.910
Polystyrene (PS)	1.04–1.09
Polymethyl methacrylate (PMMA)	1.17–1.20
Nylon	1.01–1.14
Polyurethane (PU)	1.10–1.50
Polyethylene terephthalate (PET)	1.34–1.39
Polyvinyl chloride (PVC)	1.35–1.45

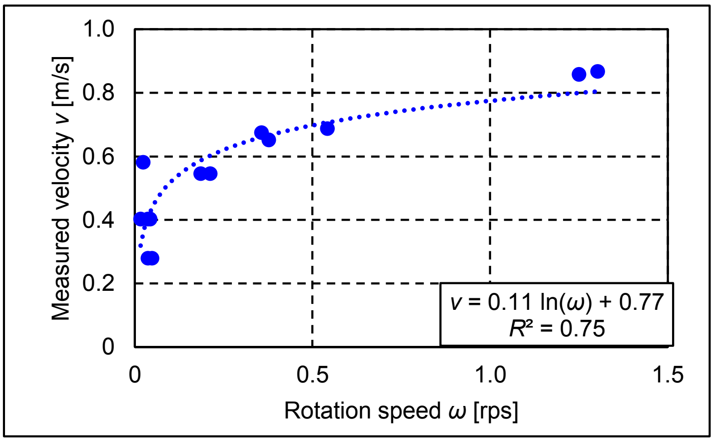

Figure 1. Relationship with rotation speed and flow velocity

2.3 Method of analysis for MPs

2.3.1 Extraction of MPs from collected samples

Samples collected at each survey station were washed the inside of the net with the river water. In light of the fact that most MPs have a low specific gravity, the following method was used to extract MPs from the sample. The sample was added to saturated saline solution (whose specific gravity is about 1.2), and then MPs floating on the surface were scooped out by a net and transferred to a petri dish. The materials that were extracted by using saturated saline were PE, PP, PS, PMMA and nylon, as shown in Table 2. Various additives are used to impart various functions to plastic, and then the specific gravity changes due to the additives. Therefore, although PET with a specific gravity larger than 1.2 usually sinks in saline solution, it was found in this study.

2.3.2 Measurement of size

In order to measure the size of the MPs, the square frames starting at 5 mm square and decreasing by 0.5 mm were marked on filter paper. Then, the size of the frame and the MP candidates were compared and sizes were measured. From 2016 onwards, photos were taken using a microscope and a digital camera for microscope work, and the size of the MPs candidates was measured from these photos.

2.3.3 Material identification

We obtained the infrared absorption spectrum of the collected MPs candidates using Fourier Transform Infrared Spectroscopy (hereinafter called FTIR) and determined the materials of the MPs candidates. Substances absorb infrared light in specific wave number bands depending on their chemical structure. It is possible to identify the material of the plastic by examining the wave number band in which the peak of the infrared absorption spectrum occurs. It is efficient to identify the plastic using FTIR before measuring the size of an MP. However, in this study, the size of all MP candidates was measured before identification of the MP because MPs are frequently crushed when FTIR is used for MP.

 ©2017, IAHR. Used with permission / ISSN 1562-6865 (Online) - ISSN 1063-7710 (Print)

2.3.4 Evaluation of MP particle count density

We examined the relationship between velocity of flow and rotation speed of the flow meter (that is, number of rotations/unit time) to convert number of rotations into the water volume passing through the net per unit time. Figure 1 shows the correlation between the velocity v m/s measured during the MPs survey and rotation speed ω rps. The data in Fig. 1 was taken from the measured values in the Edogawa, Yoro, Obitsu, Koito, Kurokawa, and Tsurumi Rivers. This correlation could be approximated by the following equation's 95% confidence intervals (R^2 = 0.75, n =13, p = 0.0001).

$$v = 0.11\ln(\omega) + 0.77 \qquad [1]$$

Using this equation, the rotation speed of the flow meter was converted into velocity of flow at the aperture of the net. Then, the water volume passing through the net was calculated by multiplying the velocity with the area of the aperture of the net. Before introduction of the flow meter, the water volume passing through the net was calculated using the velocity measured by an electromagnetic current meter or a radio current meter. Then, the number of MPs identified by using FTIR was divided by the water volume passing through the net. In this way, MPs particle count density was calculated. Note that the flow velocity was measured not just at the aperture of the net. It means that the above relationship should be changed with precise measurement of velocity at the aperture in near future.

3 MEASUREMENT PROBLEMS OF THE FIELD SURVEY METHOD

In the initial stage of the survey, we did not consider the material of the survey tools and surrounding environment at the survey sites. However, since the main target of the survey is plastic, contamination of the sample MPs by MPs added by the field survey methods were a concern. Therefore, we reviewed the survey method and tools and summarized the factors in contamination of the sample in Table 3.

Table 3. Factors in MP contamination due to survey tools and methods.

Class		Contaminating factor	Contaminating material	Influence on data	Improvement plan
Tools	Plastic bucket		PE, PP	Present	Use of aluminum bucket
	Washing bottle	Damage during survey Peeling of material	PE	Negligible influence[1]	Visual check of damage
	Sampling bottle			Negligible influence[1]	Use of stainless bottle
	Vinyl tape	Contact of rope with bridge Peeling of material	PVC	Absent	No target
	Rain boots	Peeling of material	PVC	Absent	No target
	Rubber gloves	Peeling of material during wash of the net	PU	Absent	Check of spectral characteristics
	Rope	Contact of rope with bridge	PET	Absent	Use of natural fiber rope
	Life jacket	Peeling of fiber	PET	Absent	Visual check of damage
	Plankton net	Damage during survey Peeling of material	Nylon	Negligible influence[1]	Check of spectral characteristics
Procedure	1. Drop of the net from bridge	Shavings of bridge girder, handrail and rope Falling of bridge accretion	Mainly PET (due to rope)	Absent[2]	No friction of rope on bridge girder and handrail, Use of natural fiber rope
	2. Fixation of the net near water surface	—	—	Absent	—
	3. Raising of the net from the river	Shavings of bridge girder, handrail and rope Falling of bridge accretion	Mainly PET (due to rope)	Absent[2]	No friction of rope on bridge girder and handrail, Use of natural fiber rope
	4. Net washing to collect the samples 5. Transfer of samples to bottles	Adhesion of debris collected on road Containing of MP in river water for washing the net	Mainly PET (due to rope)	Absent[3]	Not putting net directly on road, filtering river water, and wash of net

i. After checking visually that there was no damage, the water stirred in the wash bottle and the sampling bottle was analyzed; however, MPs were not detected.
ii. The fragments of paint peeled off the handrail have a specific gravity of 1.2 or more and sink when extracting MPs, so these are not covered in this paper.

©2017, IAHR. Used with permission / ISSN 1562-6865 (Online) - ISSN 1063-7710 (Print)

iii. As a result of the analysis of road sediment at six locations, one MP (PS) was detected only in one place, but that is the place where soil is collected, so there is no problem if investigation is carried out while avoiding such a place.

4 RESULTS OF SURVEY

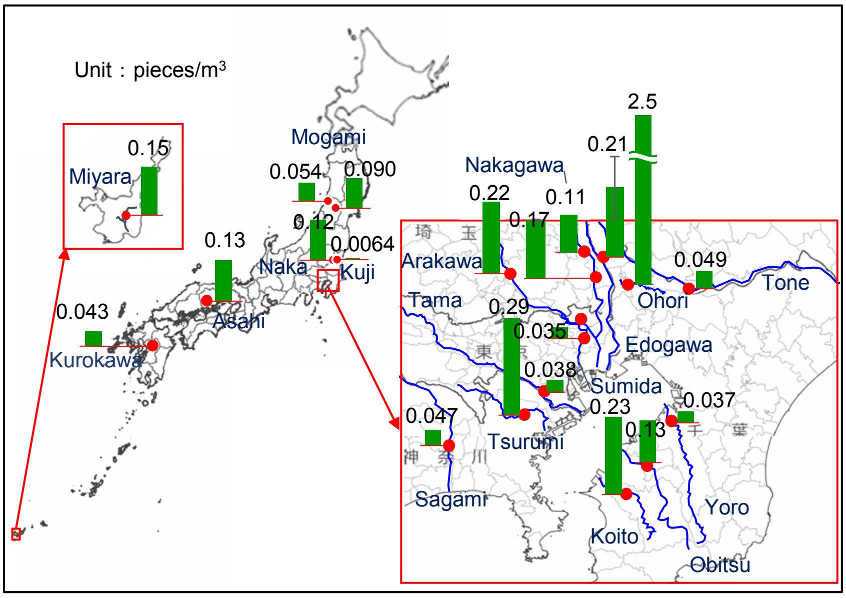

Figure 2. Map of MPs particle count density.
(A blank map is created by the Geospatial Information Authority of Japan.)

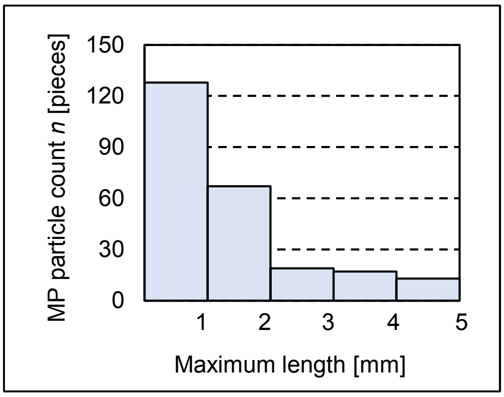

Figure 3. MPs size distribution.

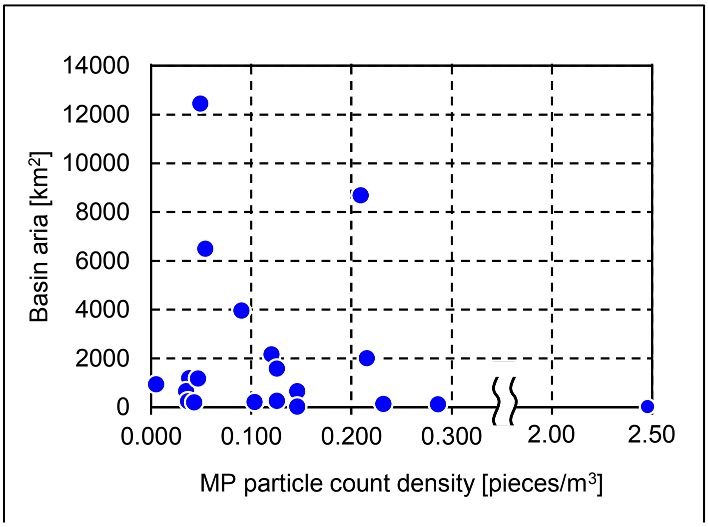

Figure 4. Relationship between basin area and MPs particle count density.

 ©2017, IAHR. Used with permission / ISSN 1562-6865 (Online) - ISSN 1063-7710 (Print)

4.1 Spatial distribution of MPs particle count density

Figure 2 shows the spatial distribution of the MPs particle count density obtained by the field survey. The result of 21 investigation points on 18 Japanese rivers is shown. The results indicated that in the rivers, the maximum MPs particle count density was 2.5 pieces/m^3, the minimum was 0.0064 pieces/m^3, the average was 0.22 pieces/m^3, and the median was 0.11 pieces/m^3. The particle count density of MPs in the rivers was one order of magnitude lower than that in the sea near Japan (0.03–491 pieces/m^3, the average was 3.74 pieces/m^3, Isobe et al., 2015). Since the ocean is accumulation zone of MPs, the MPs particle count density in the ocean may be higher than that of the rivers due to the flow of MPs from land into the ocean through the rivers over several decades.

The maximum particle count density was observed in the Ohori River. The catchment of the Ohori River has an urbanization rate of 80%, and it is a main river flowing into Lake Tega, where eutrophication is well-known in Japan. Therefore, the watershed characteristics, such as land use and the population in the river environment, and pollution by MPs may be related. In addition, MPs were found in all rivers investigated in this study. As mentioned above, the possibility of contamination of the measurement equipment cannot be completely denied. Therefore, we must be careful to deal with investigation points where the number of MPs is 5 or less.

Figure 3 shows the distribution of MPs sizes. Maximum lengths of less than 2 mm account for 70% of the total MPs. Maximum lengths of less than 1 mm, on their own, already account for more than 50% of MPs. Plastics seem to have repeated miniaturization since small MPs are the majority.

4.2 Relationship between watershed characteristics and MPs particle count density

In order to consider the relationship between watershed characteristics and MPs particle count density mentioned above, the graph of the correlation between basin characteristics for the nearest water level observation from each survey point and MPs particle count density is shown in Figure 4. From the result, there is no clear relationship between watershed characteristics and MPs particle count density. However, detailed studies which are based on not only watershed area but also on other watershed characteristics must be conducted in future.

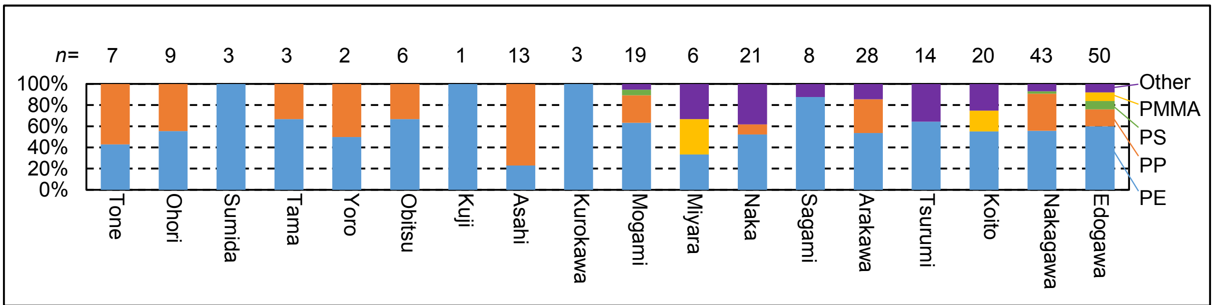

Figure 5. MPs materials in each river

4.3 MPs materials

Figure 5 shows a summary of MPs materials across all surveyed rivers. Since the MPs were separated by saline solution, plastics that have specific gravity of 1.2 or less are the main subjects of this study and these materials are PE, PP, PS, PMMA, nylon and so on. Among them, PE and PP have been identified and account for 70% of the total.

There is the possibility of overestimation of PE and PP due to plastic contamination caused by use of plastic buckets, but in the Sagami and Nakagawa Rivers, where an aluminum bucket was used, PE and PP account for 80% of the total of the materials in each river. Therefore, there is a high possibility that PE and PP have also been correctly identified in the other survey rivers. In addition, the composition of materials in each survey river is different. PE and PP were only in the Tone, Ohori, Sumida, Tama, Yore, Obitsu, Kuji, Asahi and Kurokawa Rivers. In contrast, PS, PMMA and others were in the Mogami, Miyara, Naka, Sagami, Arakawa, surumi, Koito, Edogawa and Nakagawa Rivers.

5 CONCLUSION

We organized a survey of MPs in 18 Japanese rivers and found that the particle count density of MPs in the rivers, 0.0064–2.5 pieces/m^3, was an order of magnitude lower than that in the sea near Japan, 0.03–491 pieces/m^3, the average was 3.74 pieces/m^3 (Isobe et al., 2015). Furthermore, the majority of the MPs found were less than 2 mm in size. In future, we will compare detailed watershed characteristics, such as land use, population, sewerage maintenance rate and the pollution status of MPs.

In our field survey, the contamination of our results due to the use of plastic tools and contact with plastic during the survey procedure was one of our concern. Substitutable plastic tools will be substituted and non-substitutable tools will be checked for damage before and after investigation and characteristic of infrared absorption spectrum acquired using FTIR. During the survey procedure, it is necessary not to have tools in contact with the bridge and/or the road.

REFERENCES

Andrady, A.L. (2011). Microplastics in the Marine Environment, *Marine Pollution Bulletin*, 62(8), 1596-1605.

Browne, M.A., Crump, P., Niven, S.J., Teuten, E., Tonkin, A., Galloway, T. & Thompson, R., (2011). Accumulation of Microplastic on Shorelines Woldwide: Sources and Sinks, *Environmental Science & Technology*, 45(21), 9175-9179.

Cózar, A., Echevarría, F., González-Gordillo, J.I., Irigoien, X., Úbeda, B., Hernández-León, S., Palma, Á.T., Navarro, S., García-de-Lomas, J., Ruiz, A., Fernández-de-Puelles, M.L. & Duarte, C.M. (2014). Plastic Debris in the Open Ocean, *Proceedings of the National Academy of Sciences*, 111(28), 10239-10244.

Eerkes-Medrano, D., Thompson, R.C. & Aldridge, D.C. (2015). Microplastics in Freshwater Systems: A Review of the Emerging Threats, Identification of Knowledge Gaps and Pri-Oritisation of Research Needs, *Water Research*, 75, 63-82.

Eriksen, M., Lebreton, L.C.M., Carson, H.S., Thiel, M., Moore, C.J., Borerro, J.C., Galgani, F., Ryan, P.G. & Reisser, J. (2014). Plastic Pollution in the World's Oceans: More than 5 Trillion Plastic Pieces Weighing over 250,000 Tons Afloat at Sea, *PloS One*, 9(12), e111913.

Funamoto, Y., Nihei, Y. & Minami, M. (2016). Study on Behavior of Floating Litters in Edo and Mogami Rivers using GPS Floats, *Journal of Japan Society of Civil Engineers, Ser. B1 (Hydraulic Engineering)*, 72(4), 979-984.

Isobe, A., Uchida, K., Tokai, T. & Iwasaki, S. (2015). East Asian seas: A Hot Spot of Pelagic Microplastics, *Marine Pollution Bulletin*, 101(2), 618-623.

Jambeck, J.R., Geyer, R., Wilcox, C., Siegler, T.R., Perryman, M., Andrady, A., Narayan, R. & Law, K.L. (2015). Plastic Waste Inputs from Land into the Ocean, *Science*, 347(6223), 768-771.

Law, K.L., Morét-Ferguson, S., Maximenko, N.A., Proskurowski, G., Peacock, E.E., Hafner, J. & Reddy, C.M. (2010). Plastic Accumulation in the North Atlantic Subtropical Gyre, *Science*, 329(5996), 1185-1188.

Mato, Y., Isobe, T., Takada, H., Kanehiro, H., Ohtake, C. & Kaminuma, T. (2001). Plastic Resin Pellets as a Transport Medium for Toxic Chemicals in the Marine Environment, *Environmental Science & Technology*, 35(2), 318-324.

Tanaka, K., Takada, H., Yamashita, R., Mizukawa, K., Fukuwaka, M. & Watanuki, Y. (2013). Accumulation of Plastic-Derived Chemicals in Tissues of Seabirds Ingesting Marine Plastics, *Marine Pollution Bulletin*, 69(1), 219-222.

Thompson, R.C., Olsen, Y., Mitchell, R.P., Davis, A., Rowland, S.J., John, A.W.G., McGonigle, D. & Russell, A.E. (2004). Lost at Sea: Where is all the Plastic?, *Science*, 304(5672), 838.

 ©2017, IAHR. Used with permission / ISSN 1562-6865 (Online) - ISSN 1063-7710 (Print)

DRAG AND REYNOLDS STRESS DISTRIBUTION WITHIN SUBMERGED VEGETATION CANOPIES

NINA NIKORA[1]

[1] School of Engineering, University of Aberdeen, Fraser Noble Building, King's College, Aberdeen, AB24 3UE, United Kingdom,
n.nikora@abdn.ac.uk

ABSTRACT

Vertical profile of the primary Reynolds stress within a submerged vegetation canopy reflects complex mechanics of flow-vegetation interactions. Over the last few decades, extensive studies focusing on both qualitative and quantitative descriptions of the Reynolds stress within aquatic canopies have been carried out. Although these studies have advanced our knowledge of mechanics of flow-vegetation interactions, further research in this area is still required. In particular, there is a need for development of new simple physically-based relationships describing the Reynolds stress profiles within submerged vegetation canopies. This paper addresses this issue and proposes a physically justified formulation for the Reynolds stress profile within the canopy region. According to this formulation, the vegetation layer is subdivided into the upper and lower canopy regions with distinctly different momentum transport and drag-forming mechanisms. The key parameters of the proposed relationship are the penetration depth (i.e., the distance from the bed to a point where the downward turbulent flux becomes negligible) and the ratio of drag forces acting in the upper and lower canopy regions. The relationship was tested using extensive laboratory experiments that show that the relationship parameters are affected by both bulk flow conditions and vegetation characteristics.

Keywords: Vegetated flow; reynolds stress; drag; open-channel flow.

1 INTRODUCTION

Many phenomena in open-channel flows such as flow resistance, transport of pollutants, deposition and erosion of sediments are directly influenced by the primary Reynolds stress. Although for flows over smooth and sedimentary rough beds, extensive data on Reynolds stress are already available, the information for vegetated flows remains limited, especially for the region within vegetation canopies. The available data suggest that the Reynolds stress in vegetated flows peaks around the top of the canopy and then it rapidly decays downward (Nepf and Vivoni, 2000; Poggi et al., 2004). The sharp decrease in the Reynolds stress within the canopy region is mainly caused by the drag due to vegetation elements. Researchers found that the vertical distribution of the Reynolds stress within the canopy is affected by vegetation parameters (e.g., plant morphology, density, and flexibility) and flow characteristics (e.g., relative submergence) (Nepf and Vivoni, 2000; Poggi et al., 2004b; Nezu and Sanjou, 2008). Researchers proposed two simple models, also known as the first-order closure models, Poggi et al. (2009) developed a model based on a mixing length concept) and complex models Lopez and Garcia (2001) employed $k-\varepsilon$ and $k-\omega$ models to analyze turbulence structure of open-channel flow with submerged vegetation) to predict vertical profiles of the Reynolds stress for flows with submerged vegetation.

Although past studies have provided some insights into the Reynolds stress distribution for aquatic flows, further research is still required. In particular, development of simple physically-based relationships describing the Reynolds stress profiles within the canopy region is needed. The goal of this paper, therefore, is to develop a physically justified relationship of the Reynolds stress distribution within a submerged vegetation canopy. In the following section, a relationship describing the vertical profile of the Reynolds stress within the canopy is first derived. This is followed by a description of experimental data and methods. Then, the proposed formulation was tested using extensive laboratory experiments and the effects of flow and vegetation characteristics on the driving parameters were identified.

2 RELASHIONSHIP FOR THE REYNOLDS STRESS DISTRIBUTION WITHIN THE VEGETATION CANOPY

In general, the vertical distribution of the Reynolds stress in open-channel flows with vegetated beds can be complex, especially in the near bed region where the time-averaged flow is spatially heterogeneous. Hence, the use of the time-(ensemble-) averaged hydrodynamic equations for this region is not practicable due to high spatial variability of flow velocities and turbulence characteristics. In order to resolve this issue, researchers use the double-averaged (in both time and space domains) Navier-Stokes (DANS) equations that explicitly contain important additional terms such as form-induced stresses and viscous and form drag terms for the flow region within the canopy (Nikora et al., 2007; Nepf, 2012). Considering steady, uniform, and two-

©2017, IAHR. Used with permission / ISSN 1562-6865 (Online) - ISSN 1063-7710 (Print)

dimensional (2D) open-channel flow within the vegetation canopy and neglecting effects of vegetation porosity, the DANS momentum equation for the longitudinal velocity component can be presented as:

$$0 = gS_e + \frac{1}{\rho}\frac{d\tau}{dz} - F_{Dx} \qquad [1]$$

where g and ρ are gravity acceleration and water density, respectively; S_e and S_b are the energy gradient and the bed slope, respectively; z is the vertical coordinate (with origin at a channel bed); $F_{Dx} = F_{Vx} + F_{Px}$, F_{Vx} and F_{Px} are the total drag, the viscous and form (pressure) drag forces per unit fluid mass, respectively; and τ is the total fluid stress (i.e., the total vertical momentum flux $\tau/\rho = -\langle \overline{u'w'} \rangle - \langle \tilde{u}\tilde{w} \rangle + \langle \nu \partial \overline{u} / \partial z \rangle$, where the first term on the right-hand side of τ/ρ is the spatially-averaged Reynolds stress, the second term is the form-induced (also known as dispersive) stress, and the third term is the double-averaged viscous stress).

Effects of vegetation porosity in [1] are neglected, as for most aquatic canopies the porosity only weakly depends on z (e.g., Righetti, 2008) and, furthermore, it is close to 1.0 (Nikora et al., 2008; Nepf, 2012). It is worth noting, that in high-Reynolds number open-channel flows with submerged high-density vegetation, the main contributor to the total vertical momentum flux τ/ρ is $-\langle \overline{u'w'} \rangle$ (Poggi et al., 2004a). Poggi et al. (2004a) found that for dense canopies contribution of $-\langle \tilde{u}\tilde{w} \rangle$ to τ/ρ be less than 5%. Furthermore, above the viscous sub-layer $\langle \nu \partial \overline{u} / \partial z \rangle$ is negligible compared to $-\langle \overline{u'w'} \rangle$.

The total drag force F_{Dx} in [1] is commonly parameterized using a relationship:

$$F_{Dx} = 0.5 C_D a \langle \overline{u} \rangle^2 \qquad [2]$$

where C_D is the drag coefficient; a is vegetation density, i.e., the total frontal vegetation area A_{fv} per unit fluid volume V_f, $a = A_{fv}/V_f$ (Nikora et al., 2004), and $\langle \overline{u} \rangle$ is the local double-averaged velocity.

Equation [2] shows that for homogeneous vegetation with height-independent density a (i.e., a = const), the drag force F_{Dx} may change with the vertical coordinate z only if C_D and/or $\langle \overline{u} \rangle$ change with z. Considering the findings of the experimental studies of vertical profiles of C_D and $\langle \overline{u} \rangle$ (Dunn et al., 1996; Nepf and Vivoni, 2000), we can subdivide the vegetation canopy into two regions: the lower canopy (LC) and the upper canopy (UC) (Figure 1).

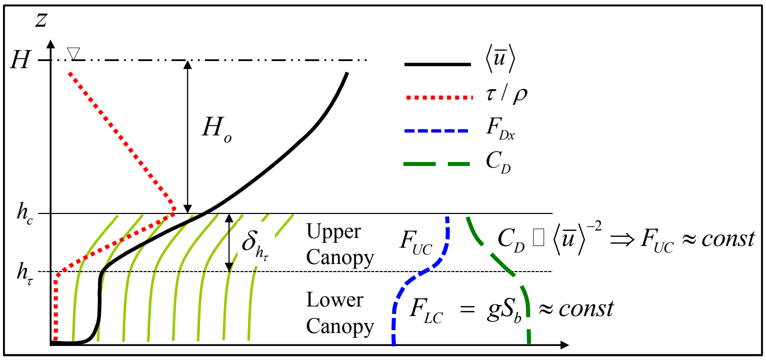

Figure 1. Conceptual representation of the vertical profiles of the Reynolds stress, drag coefficient, and total drag force within the vegetation canopy.

Within the LC region, the flow is mainly controlled by the balance of the gravity and total drag forces, while the total vertical momentum flux is negligible (Figure 1), i.e., $\tau/\rho \approx 0$. In this canopy region, the flow velocity and drag coefficient profiles are approximately constant. Thus, from Eq. [1] it follows that within the LC region the total drag force is approximately constant, i.e., $F_{Dx} = F_{LC} = gS_b$. In the upper part of the canopy, the total

 ©2017, IAHR. Used with permission / ISSN 1562-6865 (Online) - ISSN 1063-7710 (Print)

vertical momentum flux τ / ρ significantly contributes to the momentum balance, as schematically shown in Figure 1. Within this region, the mean velocity increases with increase in z, resulting in decreasing C_D following a relationship $C_D \sim \langle \overline{u} \rangle^{-\beta}$ where the submerged flexible vegetation $\beta \approx 2$ (Dunn et al., 1996; Nepf and Vivoni, 2000). Hence, within the UC region we have $C_D \langle \overline{u} \rangle^2 \approx$ const and, therefore, the total drag force $F_{Dx} = F_{UC}$ is also likely to be approximately constant, similar to the situation in the LC region. Thus, assuming that the drag force within the canopy is constant (i.e., $F_{Dx} =$const) after integration of Eq. [1] we obtain a linear relationship for the total fluid stress within the UC region:

$$\tau(z) / \rho = (F_{Dx} - gS_b)z + C \qquad [3]$$

where C is an integration constant.

At $z = h_\tau$, where the total vertical momentum flux $\tau(h_\tau) / \rho = 0$ (Figure 1), the integration constant is equal to $C = -(F_{Dx} - gS_b)h_\tau$. The elevation $z = h_\tau$ subdivides the vegetation canopy into the LC and UC regions with different momentum transport and drag-forming mechanisms. In the UC, the momentum transport is dominated by the total vertical momentum flux, while in the LC it is dominated by the gravity effect (Nepf and Vivoni, 2000). Parameters h_τ and $\delta_{h_\tau} = h_c - h_\tau$ are the thicknesses of the UC and LC regions, respectively; they may be considered as integral measures of the flow-vegetation interactions. Finally, substituting $C = -(F_{Dx} - gS_b)h_\tau$ into [3] the relationship for the distribution of the total fluid stress within a submerged vegetation canopy can be summarized as:

$$\tau(z) / \rho \begin{cases} \tau_{UC}(z) / \rho = (F_{Dx} - gS_b)(z - h_\tau) & \text{for } z \geq h_\tau \\ \tau_{LC}(z) / \rho = 0 & \text{for } z < h_\tau \end{cases} \qquad [4]$$

Considerations presented above allow us to obtain the ratio of the drag force F_{UC} in the UC to the drag force F_{LC} in the LC, i.e., F_{UC} / F_{LC}. Expressing each term of Eq. [1] individually for the LC and UC regions (Figure 1) and integrating it one obtains:

$$gS_b h_c + \tau_{h_c} / \rho - F_{UC}(h_c - h_\tau) - F_{LC} h_\tau = 0 \qquad [5]$$

where τ_{h_c} is the total fluid stress at the top of the canopy. Recalling that the drag force in the LC is $F_{LC} = gS_b$ (Figure 1) and rearranging [5], we obtain:

$$\frac{F_{UC}}{F_{LC}} = 1 + \frac{\tau_{h_c} / \rho}{gS_b (h_c - h_\tau)} \qquad [6]$$

The ratio of drag forces [6] is a measure of the relative contributions of the UC and LC regions to the total momentum sink (drag) within the entire vegetation canopy. This ratio is likely to be controlled by flow and vegetation characteristics. For steady and uniform 2D flow $\tau_{h_c} / \rho = gS_b H_o$ (H_o is the depth of the overflow above the vegetation canopy). Substituting it into Eq. [6] we derive:

$$\frac{F_{UC}}{F_{LC}} = \frac{H}{h_c - h_\tau} - \frac{h_\tau}{h_c - h_\tau} = \left(1 - \frac{h_\tau}{h_c}\right)^{-1} \frac{H}{h_c} - \left(\frac{h_c}{h_\tau} - 1\right)^{-1} \qquad [7]$$

Equation [7] shows that the dependence of the ratio of drag forces on relative submergence is in general non-linear. For emergent conditions, i.e., $H / h_c = 1$ and $h_\tau / h_c = 1$, the ratio $F_{UC} / F_{LC} = 0$, implying that there is no UC region. When $H / h_c \to \infty$, e.g., for terrestrial canopies, the LC region becomes negligible. Previous studies have shown that with the increase in H/h_c from 1 to some threshold value, the ratio h_τ/h_c rapidly decreases from 1 tending to a constant value (Nepf and Vivoni, 2000; Wilson et al., 2003; Nezu and Sanjou, 2008; Okamoto and Nezu, 2009). The threshold value of the relative submergence, when h_τ/h_c becomes approximately constant, depends on vegetation characteristics. For example, for flexible vegetation, h_τ/h_c reaches a constant value at $H/h_c \approx 2$ (Nepf and Vivoni, 2000) while for rigid vegetation, it becomes constant at $H/h_c \approx 4$ (Nezu and Sanjou, 2008). Thus, for a relatively high submergence (e.g., $H/h_c \geq 2-4$) the ratio h_τ/h_c is approximately constant and Eq. [7] becomes linear, i.e.:

$$\frac{F_{UC}}{F_{LC}} = b\frac{H}{h_c} + c \qquad [8]$$

where $b = \left(1-(h_\tau/h_c)_{const}\right)^{-1}$ and $c = -\left(1/(h_\tau/h_c)_{const} - 1\right)^{-1}$ are constants, as $(h_\tau/h_c)_{const} \approx$ const. Coefficients b and c in [8] are likely to be dependent on vegetation properties.

Thus, using the DANS momentum equation for steady and uniform 2D open-channel flow within the vegetation canopy, a simple relationship [4] for the total fluid stress and an expression for the drag force ratio [7] are deduced. An extensive programme of laboratory experiments was carried out to test the proposed relationships. The details on the experimental data and their analysis are presented in the following section.

3 EXPERIMENTS AND METHODS

3.1 Experimental set-up

Laboratory experiments were carried out in a 12.5 m long and 0.3 m wide rectangular glass-sided tilting flume (Figure 2). An adjustable weir located at the discharge tank was used to minimize backwater effects and extend the section of (quasi-)uniform flow. The water discharge was measured by an electromagnetic flow meter Sitrans MAG 5100 W. Ten piezometric intakes tapped along the centre line of the flume bed were used to measure water surface slope. The water depth H and deflected canopy height h_c were measured at ten evenly-spaced cross-sections along the flume using decimal rulers glued to the glass side wall of the flume.

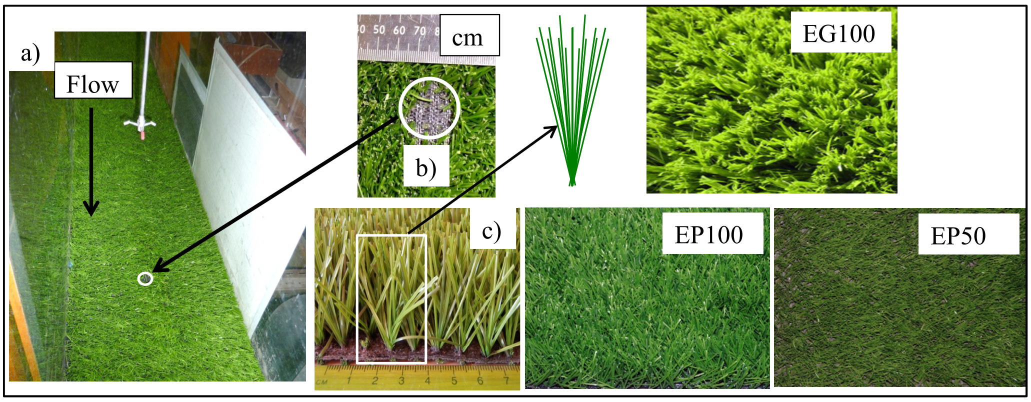

Figure 2. Experimental set-up: a) Armfield flume fully covered by artificial flexible grass EP100; b) a measurement hole within the vegetation canopy EP100; side view of EP100.

A three-component Nortek down-looking ADV was used to measure instantaneous velocities. The streamwise, lateral and vertical coordinates are denoted as x, y and z, respectively, with $z = 0$ at the flume bed. The corresponding local time-averaged velocity components and turbulent fluctuations in each direction are defined as $\bar{u}$, $\bar{v}$, $\bar{w}$ and u', v', w', respectively. Trial experiments showed that removal of 4 plants (Figure 2c) from a small area of approximately 2 by 2 cm² was required to enable measurements within the canopy and to avoid interception of plant stems by the ADV sampling volume (Figure 2a,b). Synchronized measurements with two ADVs separated along the channel were conducted. ADV #1 was fixed above the measurement hole, while ADV #2 was first located 20 cm upstream of the hole and then it was placed 20 cm downstream of the hole. The measurements showed that the removal of the plants had negligible impact on the measured velocity statistics above the canopy, consistent with Ikeda and Kanazawa (1996) and

 ©2017, IAHR. Used with permission / ISSN 1562-6865 (Online) - ISSN 1063-7710 (Print)

Ghisalberti and Nepf (2004). A sampling duration of 120 s, sampling frequency of 25 Hz, and standard ADV measurement volume of 0.25 cm³ were used.

Two types of artificial flexible garden grasses, i.e., EasyPlants (EP) and EverGreens (EG), have been selected (Figure 2 and Table 1) to conduct laboratory experiments. In all experiments, the artificial flexible garden grass covered the whole bed of the flume. Both types of grasses, i.e., EP and EG, are made of individual stems of thiolon LSR (lower sliding resistance) and polyethylene, respectively. The stems are arranged as groups of uniformly distributed plants weaved to a thin black plastic base (Figure 2c). Each plant consists of exactly 16 for EP100/EP50 and on average 20.8 (varied from 19 to 24) for EG100 individual stems. The key parameters for both grasses are shown in Table 1, including the total frontal vegetation area per unit fluid volume a ; porosity $\phi = V_f / V_t$, where V_t is the total canopy volume; and the stem flexural rigidity $J = EI$ defined as the product of the stem Young's modulus E and the second moment of area I . The stem flexural rigidity for both types of grasses is comparable to those for real grasses of approximately the same stem length ($J = 5.80\times10^{-6}$ Nm²; Kouwen and Li, 1980) and for natural aquatic vegetation ($J = 4.96\times10^{-6} - 5.55\times10^{-5}$ Nm² in Miller et al., 2012). In the present experiments, the canopies had porosity values ranging from 0.97 to 0.99, comparable to those of most aquatic plants (Nikora et al., 2008).

Experiments have been conducted for each grass (Table 1). The experiments involved measurements of the: (a) bulk hydraulic parameters (water depth, water surface level, flow rate, and channel bed slope); (b) vegetation characteristics (canopy height, density, geometrical and biomechanical characteristics, and porosity), and (c) instantaneous velocities measured at a single location in the middle of the flume (along and across the channel). For each vertical profile, the velocity time series were collected at multiple points from the channel bed up to the maximum vertical position possible with the ADV (i.e., approximately 7 cm below the water surface). Depending on the flow submergence and bed slope, the number of measuring points in the vertical varied from 10 to 54, with an average of 25. The spacing between measuring points was 0.5-3 mm in the near-bed region (from the bed up to approximately 1.5 h_c) and then 10-14 mm. The ranges of the main experimental parameters are shown in Table 1.

Table 1.Grass characteristics and ranges of experimental parameters.

Grass ID	a	ϕ	J	No. of exper.		S_b	$U_m = \frac{Q}{A}$	$\frac{H}{h_c}$	$\frac{B}{H}$	u_{*m}	$\mathsf{R} = U_m H / \nu$
	(1/m)	(-)	(Nm²)			(%)	(m/s)	(-)	(-)	(cm/s)	(-)
EG100	372	0.98	42.29 E-07	32	from	0.05	0.15	3.00	0.71	1.92	2.32E+04
					to	1.00	0.85	9.72	2.30	9.00	1.61E+05
EP100	268	0.97	7.73 E-07	31	from	0.05	0.17	3.49	0.75	1.84	3.40E+04
					to	0.40	0.57	11.81	2.52	5.97	1.17E+05
EP50	134	0.99	7.73 E-07	29	from	0.05	0.17	3.64	0.74	2.00	3.32E+04
					to	0.40	0.56	12.66	2.38	5.24	1.17E+05

3.2 Data analysis

In the proposed relationship [4], the total fluid stress is approximately equal to the Reynolds stress, i.e., $\tau(z)/\rho \approx -\left\langle \overline{u'w'} \right\rangle (z)$, since contributions from both form-induced (Poggi et al., 2004a) and viscous stresses are negligible. Therefore, [4] can serve as a relationship of the Reynolds stress distribution within the canopy. In the present study, the primary Reynolds stress is determined as:

$$RS_{ver} = \left(\overline{u'w'}^2 (z) + \overline{v'w'}^2 (z) \right)^{1/2} \qquad [9]$$

where the second term on the right-hand side of [9] is used to eliminate potential probe misalignment effects in the computation of the primary Reynolds stress. In order to scale various flow quantities, e.g., velocity statistical moments, the shear velocity was estimated from the turbulent stresses directly measured at the canopy top as follows:

$$u_{*m}^2 = \frac{1}{2} \sum_{i=1}^{N=2} \left(\overline{u'w'}^2 + \overline{v'w'}^2 \right)^{1/2} \qquad [10]$$

where the two highest values of the Reynolds stresses are averaged to reduce uncertainty. These maximum values typically occur around the canopy top.

The parameters of Eq. [4] for the UC region, i.e., the gradient $A = (F_{UC} - gS_b)$ and intercept $C = -(F_{UC} - gS_b)h_\tau = -Ah_\tau$, are found by best fitting the measured profiles [9] to Eq. [4] using the experimental data within the range $z / h_c = 0.55 - 0.9$. This range has been determined by visual assessment of the measured vertical profiles of the Reynolds stress. Then, using the obtained parameters A and C, the constant drag force F_{UC} for the UC and the level h_τ of the negligible vertical turbulent transport of momentum are determined as follows:

$$F_{UC} = A + gS_b \quad [11]$$

$$h_\tau = -\frac{C}{F_{UC} - gS_b} = -\frac{C}{A} \quad [12]$$

In order to compare estimates of h_τ from [12] with the penetration depth h_p proposed in Nepf and Vivoni (2000), their "10%-technique" was applied to the vertical profiles of Reynolds stress [9]. Specifically, the parameter h_p is estimated as the distance from the channel bed to an elevation where RS_{ver} decays to 10% of its maximum value.

4 TESTS

4.1 Vertical profiles of mean velocities and turbulent stresses

Representative vertical profiles of the normalised time-averaged velocity $\overline{u} / u_{*m}$ and the vertical Reynolds stress $RS_{*ver} = RS_{ver} / u_{*m}^2$ are shown in Figure 3. The normalised mean velocities collapse well on a single curve within the canopy and a thin region above it, up to $z / h_c \approx 1.5 - 2.0$. However, the measured velocities in the outer flow region demonstrate noticeable divergence, which most likely reflects combined effects of the wake region and the secondary currents (Figure 3a). The ratio $\overline{u} / u_{*m}$ at the canopy top, which is generally affected by both the vegetation density and flow submergence, is close to 6.1, on average, varying between 5 and 7.4. The vertical Reynolds stress RS_{*ver} peaks at the canopy top or slightly above it (Figure 3b). The vertical distributions RS_{*ver} are fairly close to linear in the upper canopy $(z / h_c \approx 0.5 - 0.9)$ as well as in the adjacent layer above the canopy $(z / h_c \approx 1.1 - 3)$. Deviations from non-linearity in the outer flow region, i.e., near the water surface, are most likely attributed to the effects of the secondary currents combined with the near-surface effects that are likely to increase with increasing relative submergence H / h_c and decreasing vegetation density. The values of RS_{*ver} within the lower part of the canopy, i.e., at $z / h_c < 0.5$, are fairly close to zero confirming that the vertical turbulent transport of momentum is negligible within this region.

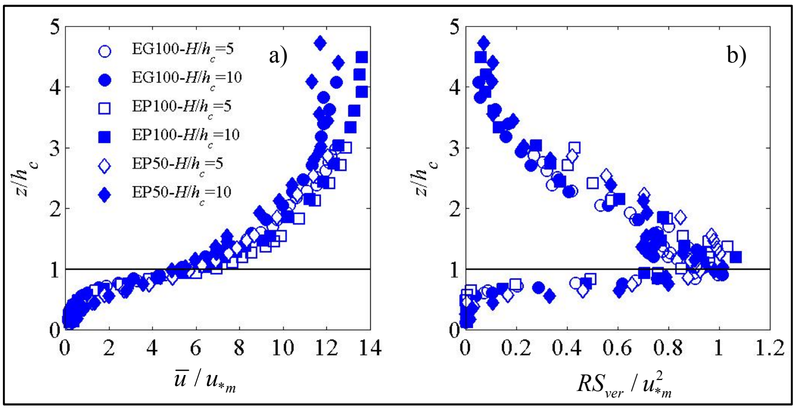

Figure 3. Representative normalized profiles of the: (a) mean velocity and (b) Reynolds shear stress. Horizontal solid lines denote the top of the canopy.

 ©2017, IAHR. Used with permission / ISSN 1562-6865 (Online) - ISSN 1063-7710 (Print)

4.2 Test of the Reynolds stress relationship

The Reynolds stress relationship [4] is tested using the experimental data for all three data sets described in section 3.1. Representative vertical profiles of the measured and calculated Reynolds stresses are shown in Figure 4. The data demonstrated that Eq. [4] approximates the Reynolds stress distribution within the upper canopy very well. This implies that the parameters A and C in [11] and [12] can be used to estimate the upper canopy drag force F_{UC} and the depth of negligible vertical turbulent transport of momentum h_τ. Note also that the vertical Reynolds stress RS_{ver} is fairly close to 0 within the LC region, i.e. below h_τ.

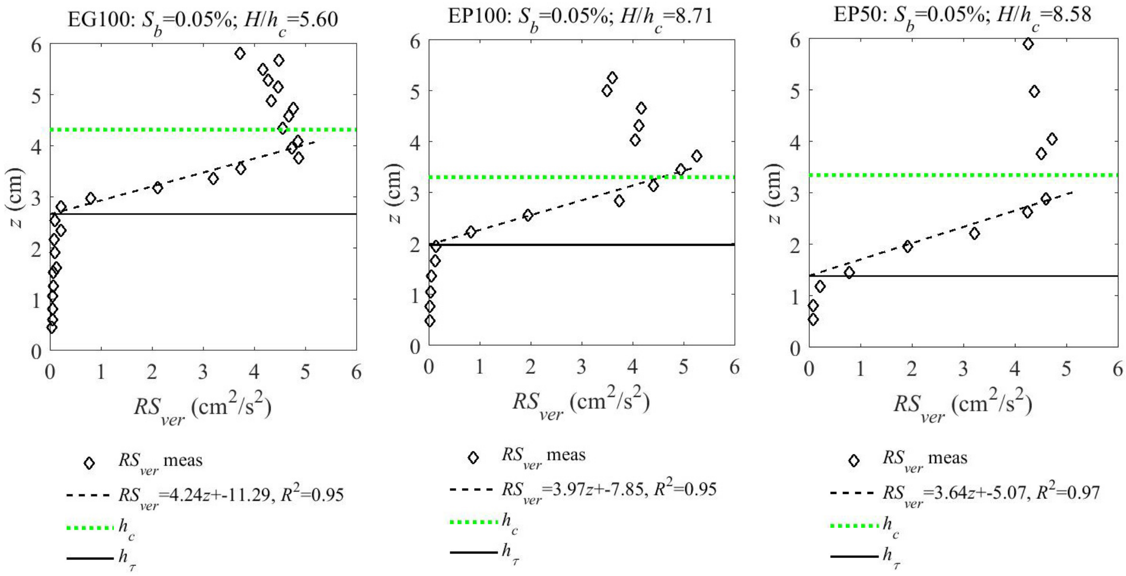

Figure 4. Tests of the Reynolds stress distribution model [4] within the submerged vegetation canopy.

The comparison between the depth of negligible vertical turbulent transport of momentum h_τ and the penetration depth h_p estimated using Nepf and Vivoni's (2000) 10%-technique is shown in Figure 5. The data show that h_τ / h_c values are approximately 10% smaller than h_p / h_c, i.e., $h_\tau / h_c \approx 0.9 h_p / h_c$, consistent with the proposed linear model [4]. Indeed, this difference is expected, as h_p / h_c corresponds to the position where the Reynolds stress is equal to 10% of its maximum value, while h_τ / h_c corresponds to the position where the Reynolds stress is equal to 0. Figure 5 shows that for a given vegetation type, e.g., EP, with decrease in vegetation density, both h_τ / h_c and h_p / h_c decreases, which are consistent with Nepf and Vivoni (2000). Furthermore, Figure 5 illustrates that for a given canopy density, e.g., EG100, increase in bed slope S_b leads to decrease in penetration depth.

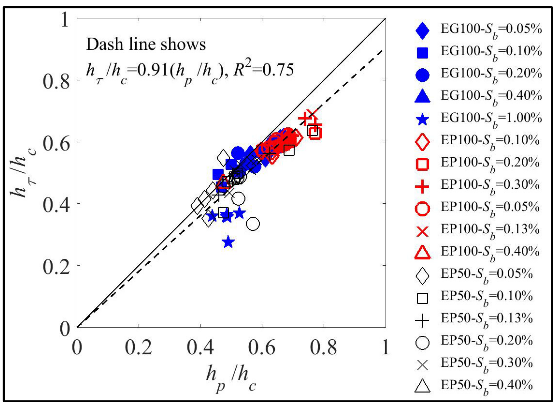

Figure 5. Correlation of h_τ / h_c with the penetration depth h_p / h_c estimated using Nepf and Vivoni's (2000) 10%-technique. Solid line denotes $y = x$ relationship.

Figure 6a demonstrates the dependence of F_{UC} / F_{LC} on relative flow submergence H / h_c. The data show that with the increase in H / h_c, the ratio of drag forces F_{UC} / F_{LC} increases. For an experimental range of H / h_c, covered in the present study, i.e., $H / h_c = 3 - 12.7$, the following ranges of F_{UC} / F_{LC} have been obtained: 3.1−13.6 for EG100, 3.1−12.2 for EP100 and 3.7−11.8 for EP50. Figure 6a shows that for a given value of relative submergence, the ratio of drag forces F_{UC} / F_{LC} increases with the increase in vegetation density. In general, the drag force ratio F_{UC} / F_{LC} may be comparable to the ratio of the turbulent stress gradient $\partial \left\langle -\overline{u'w'} \right\rangle / \partial z$ to the pressure gradient $g\partial H / \partial x$ (or to the gradient of the channel bed $\partial z_b / \partial x$ for uniform flow, where z_b is the bed elevation), proposed in Nepf and Vivoni (2000). Indeed, taking into account that $g\partial z_b / \partial x = gS_b = F_{LC}$ and considering the flow within the UC region, Eq. [1] can be re-written as:

$$\frac{F_{UC}}{F_{LC}} - 1 = \frac{1}{\rho} \frac{d\tau / dz}{F_{LC}} \qquad [13]$$

The right-hand term in [13] is equivalent to the ratio $\left(\partial \left\langle -\overline{u'w'} \right\rangle / \partial z \right) / \left(g\partial z_b / \partial x \right)$. In agreement with [13], the Nepf and Vivoni (2000) data in Figure 6a, which covers flexible low-density vegetation with $ah_c = 0.88$, are consistent with the drag force ratio F_{UC} / F_{LC} values.

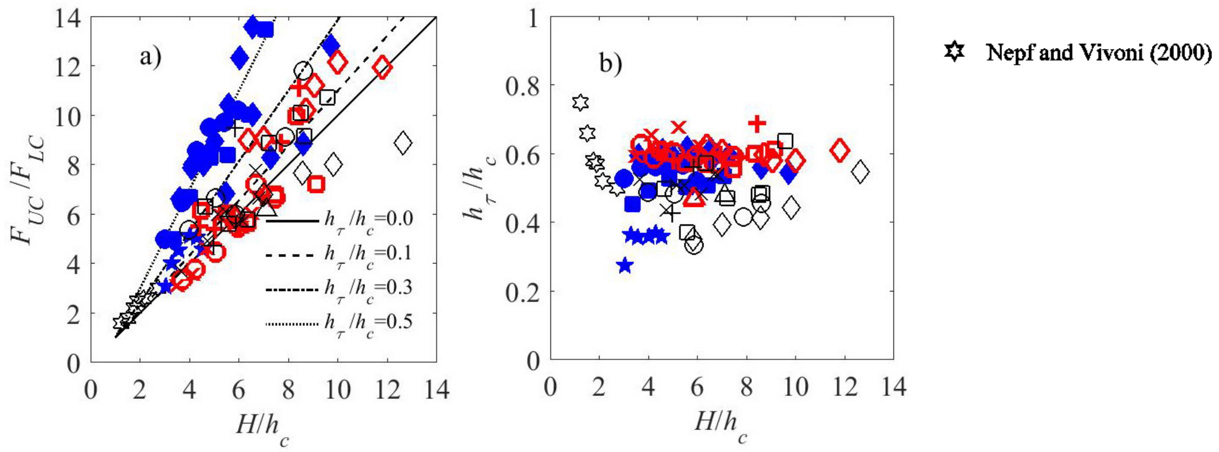

Figure 6. Dependence of F_{UC} / F_{LC} (a) and h_τ / h_c (b) on H / h_c. Black lines of different styles in plot (a) show tests of Eq. [8] for a range of h_τ / h_c values. Symbols are as shown in Figure 5.

Figure 6a also serves as a test for Eq. [7], covering a range of h_τ / h_c from 0 (the turbulent stress penetrates to the bed) to 0.5 (the total vertical momentum flux is fully absorbed within the upper half of the canopy). The experimental data demonstrated that Eq. [7] approximates the drag force ratio fairly well. For example, the EG100 data points closely collapse around a straight theoretical line for $h_\tau / h_c = 0.5$, consistent with Eq. [7] and the average value of the unconfined limit of h_τ / h_c = 0.53 (Figure 6b). A good agreement between the experimental data and Eq. [7] suggested that when the penetration depth reaches its unconfined limit, i.e., becomes independent of relative submergence and only depends on vegetation parameters, the dependence of F_{UC} / F_{LC} on H / h_c can be described by a simple linear relationship [8].

The dependence of h_τ / h_c on the relative submergence is illustrated in Figure 6b. The data show that for a range of H / h_c, investigated in the present study, the ratio h_τ / h_c remains approximately constant with increase in the relative submergence, consistent with the expectations. Figure 6b also shows that for a given H / h_c value, the ratio h_τ / h_c increases with the increase in the vegetation density. Furthermore, for given

 ©2017, IAHR. Used with permission / ISSN 1562-6865 (Online) - ISSN 1063-7710 (Print)

values on both of the vegetation density and relative submergence, increasing bed slope leads to decrease in h_τ / h_c, as seen in Figure 5.

Unfortunately, the present study does not cover $H / h_c < 3$. However, based on the results of Nepf and Vivoni (2000) who demonstrated that the relative penetration depth decreased from around 1 for emergent vegetation, i.e., $H / h_c = 1$, to an unconfined limit at $H / h_c \approx 2$ (their data are also shown in Figure 6b), it is reasonable to assume that h_τ / h_c should be decreasing within the range $H / h_c = 1 - 3$. This assumption may be further supported by the results of Nezu and Sanjou (2008) who also found that the relative penetration depth reaches its unconfined limit, but at much higher value of the flow submergence $H / h_c \approx 4$. The noted discrepancy between Nezu and Sanjou (2008) and Nepf and Vivoni (2000) data most likely relates to the significant differences in plant rigidities [flexible in Nepf and Vivoni (2000) versus rigid in Nezu and Sanjou (2008)], morphologies, and densities. Potential effects of secondary currents should not be dismissed as well.

5 CONCLUSIONS

A new physically-based relationship describing the Reynolds stress profiles within the submerged vegetation canopy is proposed. The relationship is deduced using the DANS momentum equation for steady and uniform 2D open-channel flow within the vegetation canopy. The key parameter of the proposed relationship h_τ subdivides the canopy into the upper and lower canopy regions with different momentum transport and drag-forming mechanisms. In the upper canopy, the momentum transport is dominated by the total vertical momentum flux, while in the lower canopy part, it is dominated by the gravity action. The ratio of the drag forces acting in the upper and lower canopy regions is approximated by a simple non-linear relationship that links this ratio to the relative penetration depth $h_\tau / /h_c$ and flow submergence H / h_c. When $h_\tau / /h_c$ approaches a constant value above some threshold flow submergence the relationship $F_{UC} / F_{LC} = f(H / h_c)$ becomes linear. The drag force ratio F_{UC} / F_{LC} may be interpreted as a measure of the relative contributions of the upper and lower canopy regions to the total momentum sink (drag) occurring within the entire vegetation layer. The experimental data supported the proposed relationship fairly well, confirming the assumption that the total drag within the submerged vegetation canopy is approximately constant within both the upper and lower canopy regions. The experimental data also showed that the relationship parameters were affected by the flow and vegetation characteristics.

REFERENCES

Dunn, C., Lopez, F. & Garcia, M. (1996). Mean Flow and Turbulence Structure Induced by Vegetation: Experiments. *Hydraulic Engineering Series (HES 51).*

Ghisalberti, M. & Nepf, H.M. (2004). The Limited Growth of Vegetated Shear Layers. *Water Resources Research*, 40(7).

Ikeda, S. & Kanazawa, M. (1996). Three-dimensional Organized Vortices above Flexible Water Plants. *Journal of Hydraulic Engineering*, 122(11), 634-640.

Kouwen, N. & Li, R.M. (1980). Biomechanics of Vegetative Channel Linings. *Journal of the Hydraulics Division*, 106 (ASCE 15464).

Lopez, F. & Garcia, M.H. (2001) Mean Flow and Turbulence Structure of Open-Channel Flow through Non-Emergent Vegetation. *Journal of Hydraulic Engineering*, 127(5), 392–402.

Miller, O., Albayrak, I., Nikora, V. & O'Hare, M. (2012). Biomechanical Properties of Aquatic Plants and their Effects on Plant-Flow Interactions in Streams and Rivers. *Aquatic Sciences*. 74(1), 31-44.

Nepf, H.M. (2012). Hydrodynamics of Vegetated Channels. *Journal of Hydraulic Research*, 50(3), 262-279.

Nepf, H.M. & Vivoni, E.R. (2000). Flow Structure in Depth-Limited, Vegetated Flow. *Journal of Geophysical Research*, 105(C12), 28,547-28,557.

Nezu, I. & Sanjou, M. (2008). Turbulence Structure and Coherent Motion in Vegetated Canopy Open-Channel Flows. *Journal of Hydro-environment Research*, 2(2), 62-90.

Nikora, V., Koll, K., McEwan, I., McLean, S. & Dittrich, A. (2004). Velocity Distribution in the Roughness Layer of Rough-Bed Flows. *Journal of Hydraulic Engineering*, 130 (10), 1036-1042.

Nikora, V., Larned, S., Nikora, N., Debnath, K., Cooper, G. & Reid, M. (2008). Hydraulic Resistance due to Aquatic Vegetation in Small Streams: A Field Study. *Journal of Hydraulic Engineering*, 134(9), 1326-1332.

Nikora, V., McEwan, I., McLean, S., Coleman, S., Pokrajac, D. & Walters, R. (2007). Double Averaging Concept for Rough-Bed Open-Channel and Overland Flows: Theoretical Background. *Journal of Hydraulic Engineering*, 133(8), 873-883.

Okamoto, T. & Nezu, I. (2009). Turbulence Structure and “Monami” Phenomena in Flexible Vegetated Open-Channel Flows. *Journal of Hydraulic Research*, 47(6), 798-810.

Poggi, D., Katul, G.G & Albertson, J. D. (2004a). A Note on the Contribution of Dispersive Fluxes to Momentum Transferwithin Canopies. *Boundary-Layer Meteorology*, 111(3), 615-621.

Poggi, D., Porporato, A., Ridolfi, L., Albertson, J. D. & Katul, G. G. (2004b). The Effect of Vegetation Density on Canopy Sub-Layer Turbulence. *Boundary-Layer Meteorology*, 111(3), 565-587.

Poggi, D., Krug, C. & Katul, G.G. (2009). Hydraulic Resistance of Submerged Rigid Vegetation Derived from First-Order Closure Models. *Water Resources Research*, 45(10).

Righetti, M. (2008). Flow Analysis in a Channel with Flexible Vegetation using Double-Averaging Method. *Acta Geophysica*, 56(3), 801–823.

Wilson, C.A.M.E., Stoesser, T., Bates, P.D. & Batemann Pinzen, A. (2003). Open Channel Flow through Different Forms of Submerged Flexible Vegetation. *Journal of Hydraulic Engineering*, 129(11), 847-853.

 ©2017, IAHR. Used with permission / ISSN 1562-6865 (Online) - ISSN 1063-7710 (Print)

A TIME CHANGE OF OXYGEN CONSUMPTION RATE AT URBAN RIVER MOUTH

KOUJI UNO[(1)], MISAKI KITAMURA[(2)] , GOZO TSUJIMOTO[(3)] & TETSUYA KAKINOKI[(4)]

[(1,4)] Kobe City College of Technology, Kobe, Japan
uno@kobe-kosen.ac.jp, Kakinoki@kobe-kosen.ac.jp
[(2)] Osaka Gas Cooperation Ltd., Osaka, Japan
[(3)] Kumamoto University, Kumamoto, Japan
tgozo@kumamoto-u.ac.jp

ABSTRACT

Formation of poor oxygenation at the bottom layer water and bottom sediment in the semi-closed water zone near urban area is a typical agenda and many findings have been reported. However, most of them targeted sea area and there are few reports on the urban river mouth. In this study, to clarify the characteristics of a time change of oxygen consumption rate at urban river mouth, laboratory experiments were conducted. Sampling spot was Ikuta River mouth in Kobe City, Japan. In this river mouth, a fluvial artificial lagoon is developed. In each of the laboratory experiment, time change of dissolved oxygen of bottom sediment, both of fluvial artificial lagoon and main stream was measured. From the series of laboratory experiments, the oxygen consumption rate at fluvial artificial lagoon is larger than main stream.

Keywords: Oxygen consumption rate; fluvial artificial lagoon; sediment on the surface layer; Ikuta river mouth; urban area.

1 INTRODUCTION

In the semi-closed water area at urban area in Japan, the water environment and bottom sediment condition have been attempted to improve and variable effects have been confirmed. However, especially in the closed-off section of the bay where the topography is complicated, poor oxygen water mass still remained on the sea bottom and there has been no living organism. On the other hand, the chance of the runoff by the concentric on short term rain has increase due to the climate change and it has great potential to improve not only water environment but also bottom sediment condition. However, such effects were not examined yet. In either case, regardless of such environmental impacts, it is expected that the oxygen consumption rate is changed at different times.

It is important to measure and evaluate quantitatively the oxygen consumption immediately above the bottom sediment to make the process of forming of poor oxygen water mass and the spatial scale of it clear. Therefore, numerous research studies have been conducted to date. Hosoi et al. (1992) measured the amount of oxygen consumption of bottom sediment at urban river in tidal section in Tokushima City, Shikoku Island, Japan and they found out that the constant number of oxygen consumption rate correlates well with ignition loss of bottom sediment and ferrous ion in pore water. Nakamura et al. (1996) investigated the oxygen consumption rate of bottom sediment and the characteristic of the elution of nutrient salt and they clarified that the elusion flux of phosphorus and the amount of oxygen consumption depend on the concentration of dissolved oxygen in water just above bottom sediment. Tokunaga et al. (2005) found out the negative relationship between turbidity and dissolved oxygen concentration in high turbidity layer by the round clock field observation in the closed-off section of Ariake bay. Li et al. (2010) investigated the spatial distribution of the oxygen consumption rate from the surface of bottom sediment in Isahaya Bay in summer season and they found out that the oxygen consumption rate tends to increase with water temperature in bottom layer.

In the vicinity of Kobe port, the target area in this study, some field studies were carried out. Irie et al. (2007) attempted to measure and formulate the oxygen consumption rate of bottom sediment core sampled in Omaehama beach, Nishinomiya City. On the other hand, Endo et al. (2009) studied the characteristics of seasonal change of oxygen consumption of bottom sediment in Sakai-Senboku Port.

However, the above described studies targeted sea area but the studies on oxygen consumption rate at the urban river mouth are still very few. Urban river is rare flesh water source at closed-off section of bay and the runoff from it by local severe rain is expected as a driving force for breaking closed nature of the bay. Therefore, it is necessary to study oxygen consumption at the urban river mouth and it is also important to consider about improvement of the water environment at estuary in urban area.

Per the above described social background, we carried out laboratory experiments to grasp the characteristic of oxygen consumption of the bottom sediments sampled in the different flow characteristic.

2 MATERIAL AND METHOD

2.1 Outline of study site

The study site is Ikuta River mouth in Chuo Ward, Kobe City, Hyogo Prefecture, Japan (Figure 1.). Ikuta River originates from Mt. Maya and Mt. Shakunage in Rokko cordilleran and it pours into Kobe Port via Nunobiki dam and urban area. The river is categorized as "second class River" which is managed by local government. Its length and basin area are 1.8 km and 11km^2, respectively. In upstream of this river, there is a historic fall and it was the sampling point of drinking water for sailors visited Kobe Port. It is a legend that "Kobe water" is very fresh and it keeps good in equator. Today, water quality of Ikuta River is kept in good condition. The actual measured value of T-N, T-P and BOD at Onoe Bridge are 0.64 mg/L, 0.011 mg/L, and 1.1 mg/L, respectively.

In this river mouth, there is a fluvial artificial lagoon with 1200 m^2. This lagoon connects to main stream of Ikuta River and the water level is changed in time with tide (Figure 2). In this study, to consider the difference of oxygen consumption rate by the difference of running water type, sampling points were set both in fluvial artificial lagoon and main stream of Ikuta River.

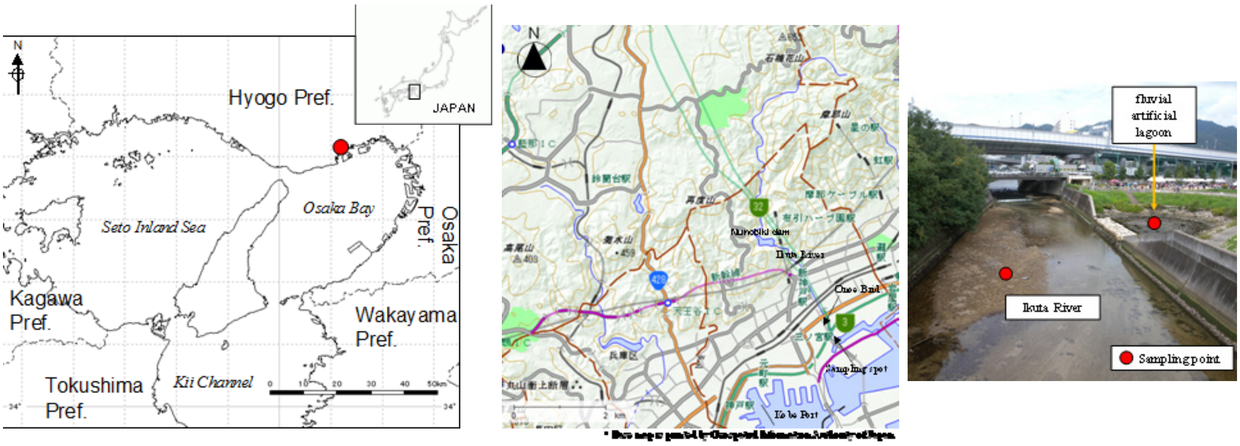

Figure 1. Study site (Ikuta River Mouth).

Figure 2. Fluvial artificial lagoon (Ikuta River mouth).

Table 1. Tide and weather condition on sampling date.

sampling date	sampling time	tide	water level from M.W.L (cm)	previous 1week precipitation (mm)	temperature (deg C)
2015/8/14	12:51	spring	-54	38.5	31.6
2015/9/27	12:20	spring	-52	27.0	26.2
2015/10/21	6:38	neap	-32	0	18.2
2015/11/18	6:18	neap	-53	37.5	17.0
2015/12/16	6:20	spring	-51	69.0	13.5
2016/1/13	6:35	half	-28	0	4.4

 ©2017, IAHR. Used with permission / ISSN 1562-6865 (Online) - ISSN 1063-7710 (Print)

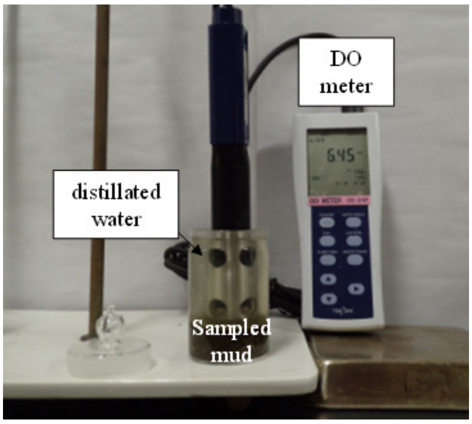

Figure 3. Measurement of dissolved oxygen.

Method of Laboratory experiment.

Table 1 shows tide and weather conditions on the sampling date. The laboratory experiment was conducted once a month from August, 2015 to January, 2016. At each experiment, the bottom sediment on surface layer both in main stream of Ikuta River and fluvial artificial lagoon was sampled at the timing of ebb tide and it was immediately brought back to the laboratory. The specimens for measuring dissolved oxygen were prepared by the following procedure. Firstly, the sampled bottom sediment was set up to one-third of the glass cylinder bottle (H: 8cm, D: 4.7cm). The total number of bottom was 11, in fluvial artificial lagoon and main stream of Ikuta River, respectively.

Secondly, the distillated water was poured into each bottle and dissolved oxygen (initial DO) just above the bottom sediment was measured immediately (Figure 3). Finally, these specimens were sealed hermetically and they were kept in constant temperature reservoir under dark conditions. Each specimen was opened in a certain sequence and dissolved oxygen (final DO) just above the bottom sediment was measured. The measurement interval was about 30 minutes for the first 3 hours and after that it was shifted to about 1 hour. In parallel with the measurement of dissolved oxygen, the ignition loss to grasp the amount of organic matter and median diameter of sediment bottom by image analysis was proposed by Uno et al. (2010).

2.2 Decreasing rate of dissolved oxygen and oxygen consumption rate

Generally, the process of oxygen consumption is described as shown in the following equation [1].

$$V\frac{d(DO)}{dt}+Sv[DO]=0 \quad [1]$$

where [DO] : the concentration of dissolved oxygen at time t (h), V (m^3) : amount of water in the bottle, S (m^2) : area of bottom sediment and v (m/h) : oxygen consumption rate from surface of bottom sediment. In this equation, the concentration of dissolved oxygen in the bottom sediment is not considered due to impossibility to measure it and compare with the result of Li et al. (2010). Equation [1] rewrites with water depth of bottle h=V/S=0.04 (m) as shown in the following equation [2].

$$\frac{d(DO)}{dt}+\frac{v}{h}[DO]=0 \quad [2]$$

Moreover, v/h, the second term of Eq. [2], is replaced with the decrease rate of dissolved oxygen from surface layer of bottom sediment c_s (1/h) and rewrites Equation [2] as shown in the following equation [3].

$$\frac{d(DO)}{dt}+c_s[DO]=0 \quad [3]$$

The solution for the above equation is

$$\frac{[DO]}{[DO]_0}=\exp(-C_s t) \quad [4]$$

where $[DO]_0$ is the initial dissolved oxygen measured just after preparing sample bottle. From equation [4], we can see that the concentration of dissolved oxygen decreases in an exponential fashion. In this study, we calculated the decrease rate of dissolved oxygen from surface layer of bottom sediment c_s and oxygen consumption rate from the measurement value of dissolved oxygen and discuss about the characteristics of oxygen consumption in bottom sediment at urban river mouth.

3 RESULTS AND DISCCUSIONS

3.1 Time series of the amount of dissolved oxygen and the decrease rate of dissolved oxygen from surface layer of bottom sediment

Figures 4 (a) and (b) show the time series of the amount of dissolved oxygen and the decrease rate of dissolved oxygen from surface layer of bottom sediment (August, 2015 – January, 2016).

Firstly, as for the time series of the amount of dissolved oxygen, the value in main stream of Ikuta River was higher than in fluvial artificial lagoon in any seasons and the difference between them increases in summer season. In the main stream of Ikuta River, there is fresh water supply from upstream, therefore, the flow ability is higher than in the fluvial artificial lagoon. Moreover, consumers such as micro benthos and microorganism are difficult to inhabit in such a flow environment and the amount of oxygen consumed by them is primarily few. Incidentally, it is expected that the reason of the temporal increase of the dissolved oxygen in these figures is the entrainment of oxygen at the timing of opening the stopple and measurement.

Secondly, as for seasonal change of the amount of dissolved oxygen, both in main stream of Ikuta River and fluvial artificial lagoon, it tends to be higher in summer than winter. Generally, the amount of dissolved oxygen increase in lower water temperature. However, obtained results indicated opposite tendency. In this study, after September 2015, bottom sediment was sampled in early morning, therefore, the amount of dissolved oxygen was already little from the start of the laboratory experiment.

On the other hand, as for the decrease rate of dissolved oxygen from surface layer of bottom sediment in fluvial artificial lagoon, expected for December 2015, it was drastically reduced just after the beginning of laboratory experiment. This shows that the living organisms in the sample bottle immediately consumed dissolved oxygen and their activity became low. Under the dark condition, photonic synthesis could not occur and supply of oxygen was not expected. Therefore, the decrease rate of dissolved oxygen generally continued to be flat. In December 2015, it is expected that the bottom sediment was completely replaced in both main stream of Ikuta River and fluvial artificial lagoon by runoff due to the torrential rain just before the sampling.

As for the decrease rate of dissolved oxygen from surface layer of bottom sediment in main stream of Ikuta River, it was lower than in fluvial artificial lagoon and continued to be flat from the start. The number of attached organism is few in main stream of Ikuta River, it is expected that the amount of oxygen consumption is smaller than in fluvial artificial lagoon.

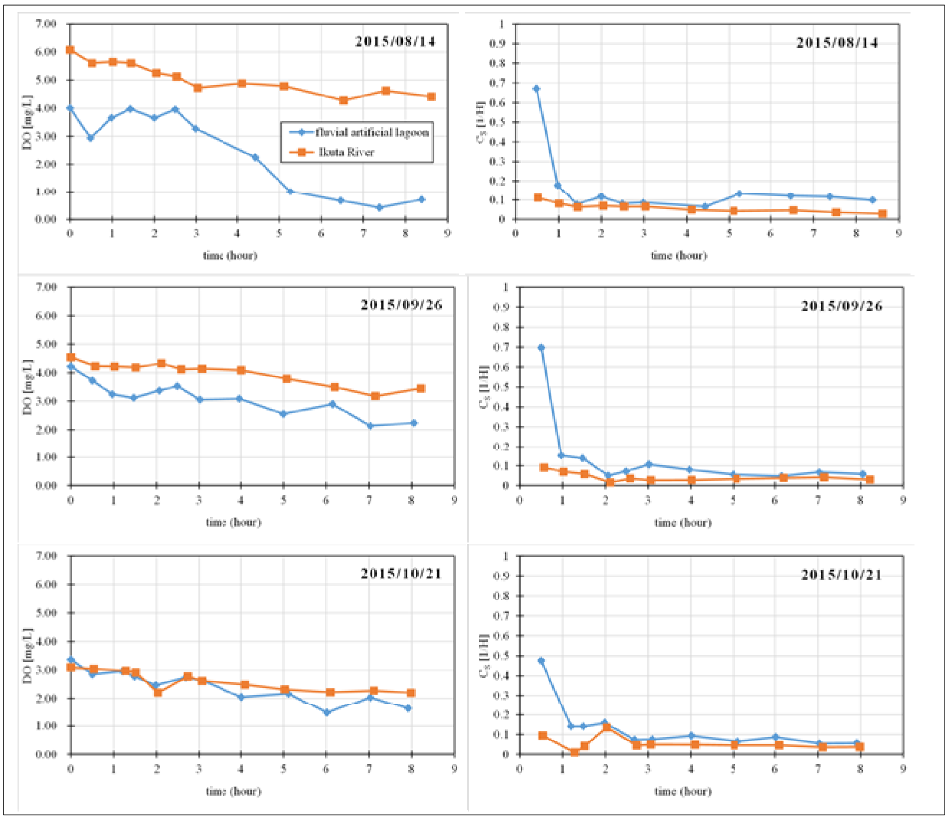

Figure 4 (a). Time series of the amount of dissolved oxygen and the decrease rate of dissolved oxygen from surface layer of bottom sediment.

 ©2017, IAHR. Used with permission / ISSN 1562-6865 (Online) - ISSN 1063-7710 (Print)

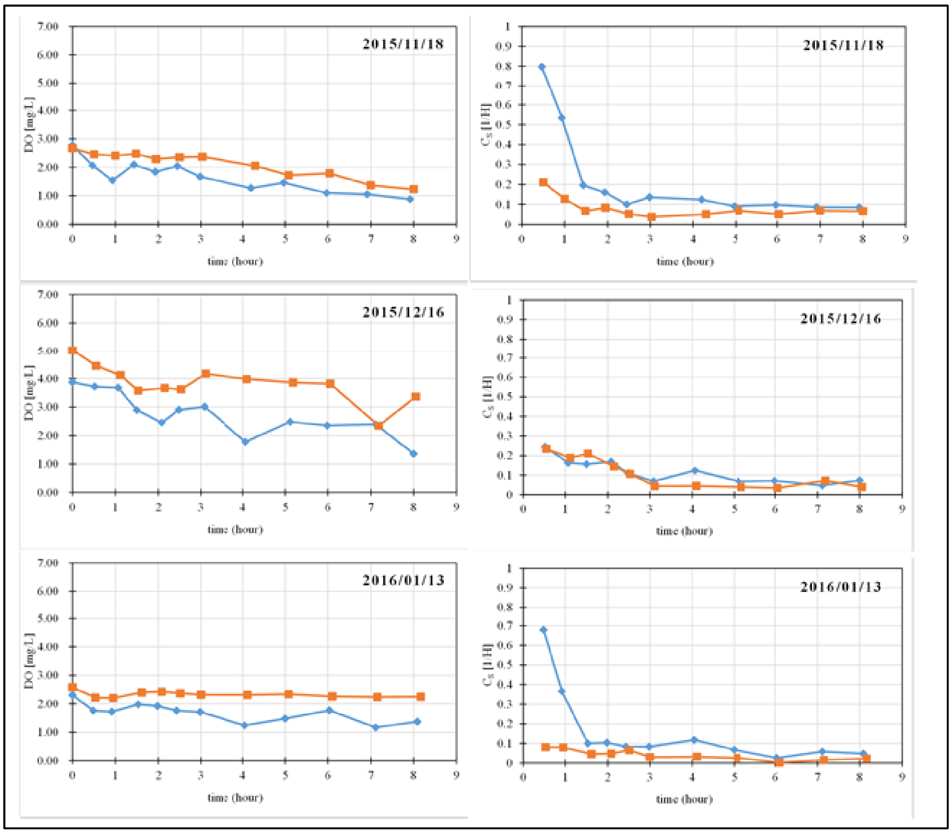

Figure 4 (b). Time series of the amount of dissolved oxygen and the decrease rate of dissolved oxygen from surface layer of bottom sediment.

3.2 Seasonal change of oxygen consumption rate, ignition loss, median diameter

Figure 5 shows seasonal change of the maximum, minimum and average value and standard deviation of oxygen consumption rate both in main stream of Ikuta River and fluvial artificial lagoon. The average value in fluvial artificial lagoon shifted from 0.01 to 0.02 m/h and it reduced from summer to winter as little as possible.

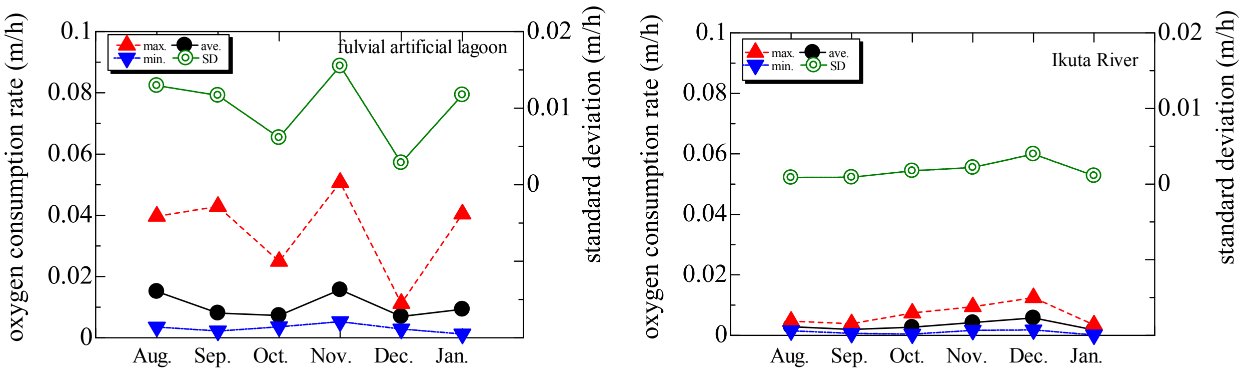

Figure 5. Seasonal change of oxygen consumption rate.

In December 2015, the measured value of ignition loss (Figure 6) and mean diameter (Figure 7) in fluvial artificial lagoon came close to that in main stream of Ikuta River due to the sediment supply from main stream by the runoff. In January 2016, the discharge was small and it was easy to accumulate organic matter, therefore, the ignition loss in fluvial artificial lagoon shifted to an increasing trend. On the other hand, as for the oxygen consumption rate, it was smaller and was not over 0.01 m/h. According to previous study in Isahaya Bay (Lee et al.), the oxygen consumption rate indicates from 3.18×10^{-3} to 1.68×10^{-2} (m/h) and its average value is 9.06×10^{-3} m/h. This average value is between fluvial artificial lagoon and main stream of Ikuta River. In other words, the bioactivity of fluvial artificial lagoon equals to more than that of Isahaya Bay.

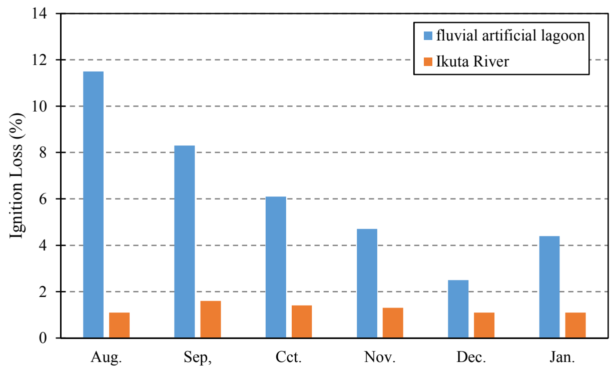

Figure 6. Seasonal change of ignition loss

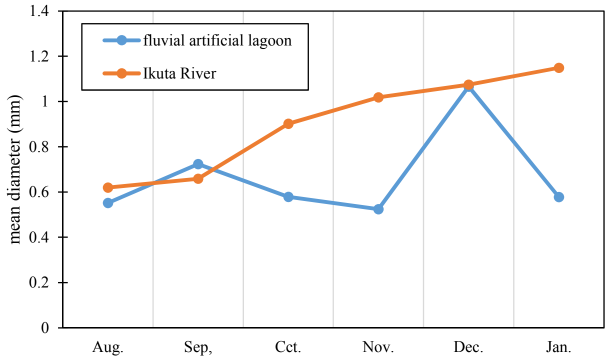

Figure 7. Seasonal change of mean diameter.

Figure 8 shows the relationship between ignition loss and oxygen consumption rate. We can see that the threshold of oxygen consumption rate is around 0.006 m/h. The determination coefficient R^2 is 0.576 and there is a strong positive correlation between them. Ignition loss indicates the amount of organic matter contained bottom sediment and it indirectly shows a potential of inhabitation possibility for living organisms. Actually, the activity of living organisms in the fluvial artificial lagoon is higher than in main stream of Ikuta River.

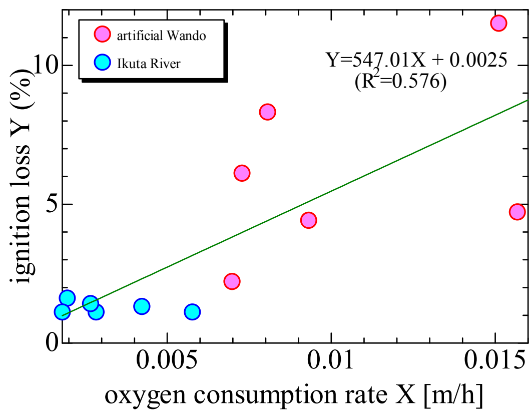

Figure 8. Relationship between ignition loss and oxygen consumption rate.

4 CONCLUSIONS

4.1 Outline of study site

In this study, the laboratory experiments were conducted to grasp the characteristic of oxygen consumption of bottom sediment sampled in the mouth of Ikuta River which is typical urban river at Kobe Port in Osaka Bay. In the fluvial artificial lagoon with strong stationary, the organic matter is easy to accumulate and bioactivity is high, therefore, the oxygen consumption rate increases. Moreover, it is also clarified in dark and sealed conditions, initial oxygen consumption is remarkable. On the other hand, in main stream of Ikuta River with high flow ability, the bottom sediment contains much oxygen in the gap, however, the living organisms are difficult to settle on the bed due to the irregular flow. Therefore, the oxygen consumption rate is smaller than that in the fluvial artificial lagoon and its time series are also not remarkable.

In this laboratory experiment, we did not preprocess sampling bottom sediment. Therefore, the obtained data may be influence by respiratory action of living organisms in it. Generally, the material using overlaying sand is inorganic matter, therefore, in our near future works, similar laboratory experiments for inorganic sediment bottom will be done.

REFERENCES

Endo, T. & Shigematsu, T. (2010). Seasonal Variations in Characteristics of Oxygen Consumption by the Bottom of Ports and Harbors. *Journal of Japan Society of Civil Engineers, Ser. B2 (Coastal Engineering)*, 65(2009), No.1, 1051-1055. (In Japanese)

Hosoi, Y., Murakami, H. & Kozuki, Y. (1992). Oxygen Consumption by Bottom Sediment. *Journal of Japan Society of Civil Engineer,* 456(II-21), 83-92. (In Japanese)

 ©2017, IAHR. Used with permission / ISSN 1562-6865 (Online) - ISSN 1063-7710 (Print)

Irie, M., Kubota. Y., Nakatsuji, K. & Nishida S. (2007). Estimation of Dissolved Oxygen Consumption in Sand Beach In homogeneously contaminated. *Proceedings of coastal Engineering*, JSCE, 54, 1026-1030. (In Japanese)

Li, H. & Matsunaga, N. (2010). Oxygen Consumption Rate of Sediment in Isahaya Bay. *Journal of Japan Society of Civil Engineer B*, 66(4), 8 335-343. (In Japanese)

Nakamura, Y., Inoue, N., Yamamuro, M., Kamiya, H. & Ishitobi, H. (1996). Experiment on Oxygen Consumption and Elution under Continuous Culture System by using Undisturbed Soil Core. *Annual Journal of Coastal Engineering*, 43, 1091-1095. (In Japanese)

Tokunaga, T., Matsunaga, N., Abe, A., Kodama, M. & Yasuda, H. (2005). Field Observations of a High Turbidity Layer in Western Area of Ariake Sea and Laboratory Experiments of Oxygen Consumption by Suspended Solids. *Proceedings of JSCE*, 782, 117-129. (In Japanese)

Uno, K., Hamamori, A., Tsujimoto, G. & Kakinoki, T. (2010). Environment Monitoring on Coastal Sediment by using Digital Camera Images in Narugashima at Awaji Island. *Journal of Japan Society of Civil Engineers, Ser. B2 (Coastal Engineering)*, 66(1), 676-680. (In Japanese)

©2017, IAHR. Used with permission / ISSN 1562-6865 (Online) - ISSN 1063-7710 (Print)

Proceedings of the 37th IAHR World Congress
August 13 – 18, 2017, Kuala Lumpur, Malaysia

EXPERIMENTAL STUDY ON THE MULTI-LEVEL INTAKE STRUCTURE OF HYDROPOWER STATION

CAIHUAN WANG(1), WENGANG DUAN(2) & DONGMEI HOU(3)

(1,2,3) Changjiang River Scientific Research Institute, WUHAN, CHINA
8900345@qq.com

ABSTRACT

With the development of high dam hydropower station construction, the harmful effect of cold water cannot be ignored. MLIS (Multi-Level Intake Structures) are usually set up in front of the station inlet to take surface water of the reservoir, thus reducing the negative effect of the cold water to downstream ecological environment, which is widely used as an effective method to reconcile the contradiction between the project construction and environment protection. However, MLIS will significantly change the hydraulic characteristic of inlet. Thus, in this study, a model test study about the MLIS, the study on the height of the MLIS in different reservoir levels, the characteristic swirl of the inlet structure, the fluctuating pressure upon the stoplog gate and the effect of the stoplog gate to the head loss of the inlet and the pressure distribution, and the study on the characteristics of the water hammer pressure when the generator was shutdown were conducted. Then, a comprehensive understanding on MLIS was obtained, which have significant value for similar projects.

Keywords: Multi-level intake structure; low temperature water discharge; Stoplog gate; hydropower station; experimental study.

1 INTRODUCTION

In the process of running the hydropower project, the phenomenon of water temperature stratification in the direction of depth might occur in front of a dam. As a result, in winter, water body in front of the dam is almost isothermal; in spring and in summer, the temperature of the water on the surface water is higher than that on the bottom. The water inlet positions of hydropower stations with high dam and large capacity unit are usually lower, for that, the submerged depth to avoid harmful whirl at the inlets of hydropower stations are proportional to the inlet flow and the pipe diameters of the units under the condition of hydropower station running at a high level and surplus water can seldom be released from the surface weep hole, the temperature of the water discharged through the station will be lower than the water of natural waterway before dam building, therefore the ecological system downstream will be impacted.

Temperature of water discharged through hydropower station is deeply studied based on requirements for environmental protection of downstream river and running mode of reservoir, and some high dam hydropower stations are provided with water body temperature control device. Multi-level intake stoplog gate is one type of temperature control structure in high dam hydropower station. In USA, inlets of the stations Hungry Horse Dam and Glen Canyou Dam were reconstructed with stoplog gate for multi-level taking upon study[1-2], indicates that downstream eco-environment was repaired to some extent. At present, stoplog gate is provided for multi-level taking in most high dam hydropower stations in China, including Jinping I Hydropower Station (Dam height: 305.0m), Nuozhadu Hydropower Station (Dam height: 261.5m), Guangzhao Hydropower Station (Dam height: 200.5m) and Tingzikou Hydropower Station (Dam height: 115.0m)[3-5]. These are many high dam hydropower stations in China, and all of them are under construction, except Guangzhao Hydropower Station that has been built up and put into operation. Although favorable in improving water temperature characteristics of downstream waterway, stoplog gate can complicate water flow structure in front of inlet and worsen hydraulic characteristic and head loss. Moreover, there is little mature experience in designing and operating stoplog gate in front of inlet, and hydraulic characteristics of stoplog gate need further study. In this study, hydraulic characteristics of stoplog gate were preliminarily explored and analyzed based on the stoplog gate model at the inlet of a large hydropower station.

2 CHARACTERISTICS OF ENGINEERING LAYOUT AND MODEL DESIGN

2.1 Characteristics of engineering layout

The pivot project (maximal dam height, 115.0m; normal storage level, 458.0m; capacity, 3.468 billion m^3) includes concrete gravity dam, power house at dam toe, flood release structure and navigation structure. The station was installed with 4 sets of 275MW water turbine generators (single generator capacity, 275MW; total installed capacity, 1100MW), and bottom of its inlet was 418.0m in elevation. The trash rack was laid out with the 4 generators connected. At the inlet of each generator, 2 side piers and 3 central piers were provided. Both side pier and central pier were 1.2m thick, and the pier length parallel to flow direction was 5.0m. On the

 ©2017, IAHR. Used with permission / ISSN 1562-6865 (Online) - ISSN 1063-7710 (Print)

upper structure of trash rack pier, there were 3 layers of beams connected to the dam. The trash rack was heightened to the top of the dam from the elevation of 415.0m. The Hole size (W×H) was 5.5m×50.0m, built with 2 trash rack slots. At inlet of diversion pipe (diameter, 8.7m), there is 1 bulkhead gate and 1 service gate. Given the ecological and environmental requirements of downstream waterway, in front of the inlet, stoplog gates were placed in the standby trash rack slot to take surface water upon different heights of stoplog gates. With a view to the running characteristics of the reservoir and temperature of discharged water required for environmental protection, maximum superposed height during running of the stoplog gate was preliminarily considered as 28.0m, and the stoplog gate was divided into 10 segments (height of segment: 2.8m). For layout of the inlet, see Fig. 1.

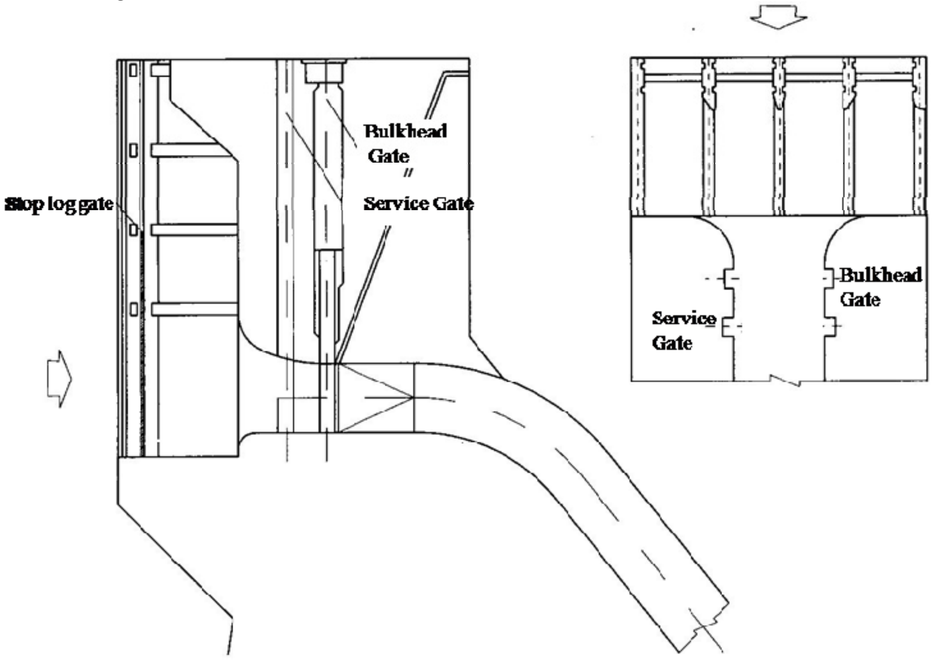

Figure 1. Layout of the hydropower station water inlet.

2.2 Model design

In inlet hydraulics model test, it is necessary to take swirl at water surface into consideration. Since swirl-inhibiting effects of viscous force and surface tension of flow in ordinary model are stronger than the actual effects, swirl in model can be dissimilar with the actual swirl. In the design method normally adopted to bring similar swirl of similar Froude number to reduce impacts of viscous effects and surface tension. Constraints are established for Reynolds number and Weber number of model. Namely, Reynolds number $R_e>3.0\times10^4$, and Weber number $W_e>120$.

The length scale (L_r) of the inlet hydraulics model adopted for this hydropower station was 50. Designed as Gravity force similarity criterion, the flow scale, λ_Q, flowing pressure scale, λ_P, flow speed scale, λ_V and the time scale, λ_t were 17677.67, 50, 7.07 and 7.07, respectively. R_e and W_e under different running conditions are shown in Table 1. As seen from the table, under each condition, R_e and W_e of the model met the constraints stated above.

Table 1. R_e and W_e of the model flow.

Reservoir level (m)	Flow (m^3/s)	Mean inlet flow (m/s)	Height of hole *d* (m)	Submerse depth of hole center *s* (m)	R_e	W_e
458	432	1.44	16.95	33.65	3.6×10^4	191
447	430	1.43	16.95	20.53	5.3×10^4	188

Note: water temperature, 20℃; Viscosity coefficient of flow, $\nu=1.01\times10^{-6}m^2/s$; surface tension coefficient of water, σ=0.0735N/m; water density, $\rho=999.1kg/m^3$

The model consisted of reservoir, trash rack pier structure in front of inlet, diversion pipe and volute section controlling flow of generator. The model trash rack pier structure and the 4 diversion pipes were made of polymethyl methacrylate. The reservoir was plastered with cement grout. The volute was installed with a valve which can be opened and closed like guide vane of water turbine, and its opening/closing time was controllable.

3 ISSUES SOLVED IN MODEL TEST

For different reservoir levels, proper stoplog gate height shall be selected by model test, to prevent unfavorable swirl in front of the inlet. This is the precondition for safe running of generator. Besides, the requirement of the station for taking surface water shall be met whenever possible. Since stoplog gate was set in front of the inlet to shield bottom flow, water in the connection section of the inlet, at the downstream of stoplog gate, flows from top to bottom. This is influential for forming conditions of swirl, hydraulic characteristics in flow pass at the inlet, fluctuation characteristic of flow in gate shaft as well as water head loss at the inlet which were studied and analyzed by model test. In addition, because of the stoplog gate in front of the inlet, a structure like shaft is formed in front of pressure diversion pipe. For normal conditions and load rejection of generator, flowing pressure (or additional flowing pressure) applied on stoplog gate and side walls at the sides of the connection section of the inlet is an important basis for structural design, and normally cannot be made clear without model test.

4 RESULT AND ANALYSIS

4.1 Height of stoplog gate under normal running condition of generator

Normal water level of the station is 458.0m, under which single generator diversion flow quantity is 432m^3/s. In the model test, changes for flow regime before and after placement of stoplog gate in front of the intake was observed. During the running of the 4 generators before placing stoplog gate, flow at the connection section of the inlet was gentle, and no swirl occurred on water surface; after 10 segments of stoplog gates were placed, traveling superficial swirl (maximal diameter, 1.5m; maximal depth of swirling water body, 0.5m) occurred intermittently on the end of the trash rack pier without depression in its center; after 9 segments were placed, traveling superficial swirl at the connection section of the inlet shrank (maximal diameter, 1.0m) occurred. Given that the designed maximum number of stoplog gate is 10 segments for the station, to verify the reliability that unfavorable swirl does not occur at the connection section of the inlet under normal water level and after placement of 10 segments of stoplog gates, during simultaneous running of the 4 generators, stoplog gate was increased to 11 segments to observe flow regime of swirl. As indicated in the result, although water depth on the top of stoplog gate fell from 15.0m to 12.2m and flow speed there rose about 20%, no significant change has occurred in flow regime at the connection section of the inlet. The occurrence of superficial swirl increased slightly, and maximum diameter of swirl increased to 1.8m. From this results, under normal water level with 10 or less segments of stoplog gates, there is no unfavorable swirl at the connection section in front of pressure pipe, thus the requirement for safe running of the station can be met.

During simultaneous running of the 4 generators under flood control level of 447.0m and single generator diversion flow of 430m^3/s, a few possible heights of stoplog gate were also tested. During simultaneous running of the 4 generators, after 8 segments of stoplog gates were placed, significant fluctuation (maximum fluctuation, 0.2m) occurred on water surface at the connection section in front of pressure inlet pipe, and vertical swirl without air (maximum diameter, 1.5m; maximum depth of swirling water body, 0.5m) occurred behind each side pier corresponding to generator without depression in its center. Such swirl occurred every 90s and lasted for 30s for once, appropriately. After 7 segments of stoplog gates were placed, a similar flow regime occurred, but fluctuation on water surface at the connection section, dimension of vertical swirl and occurrence of swirl were all lower. After 9 segments of stoplog gates were placed and the weir crest head at the top of stoplog gate was 6.8m relative to reservoir level, water flew through stoplog gate like drop, and water surface at the connection section of the inlet was much lower than reservoir level. These phenomena shall be prohibited during the running of generator. Given this, under this water level, at most 8 segments of stoplog gates can be placed.

4.2 Pressure distribution characteristics of stoplog gate

As observed from the test results above, during simultaneous running of the 4 generators, at the water level of 458.0m, at most 10 segments of stoplog gates can be placed; at the water level of 447.0m, at most 8 segments of stoplog gates can be placed. The test result of time average pressure applied at the front center and back center of stoplog gate under unfavorable stress on stoplog gate is shown on Fig. 2.

 ©2017, IAHR. Used with permission / ISSN 1562-6865 (Online) - ISSN 1063-7710 (Print)

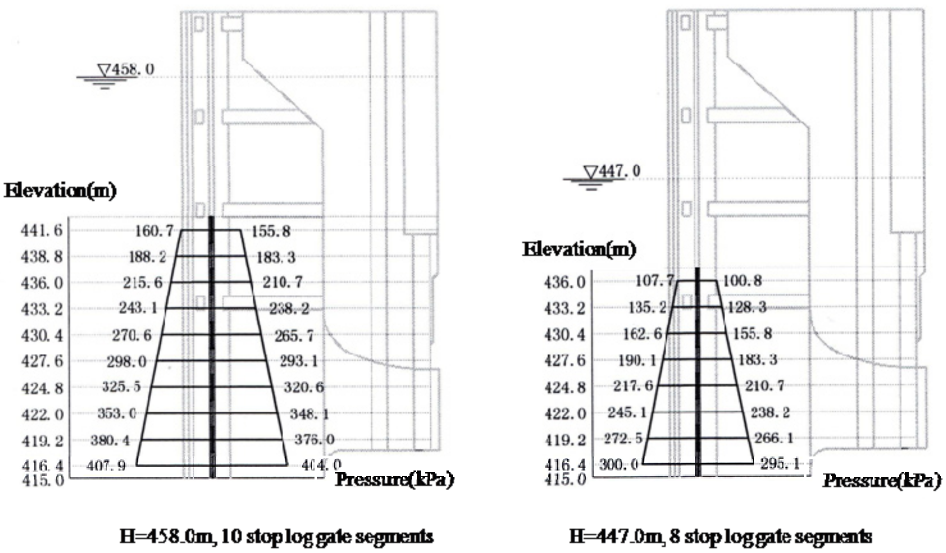

Figure 2. Pressure Distribution on the stoplog gate.

As indicated from the results, in the upstream of stoplog gate, time-average pressures at measurement points distributed basically like hydrostatic pressure, and head of each piezometer tube was close to reservoir level; in the downstream of stoplog gate, although flow structure at the connection section of the inlet was more complicated, time average pressures at measurement points were also distributed basically like hydrostatic pressure, and head of each piezometer tube was only 0.3~0.7m lower than reservoir level. At the same elevation of stoplog gate, pressure of the upstream face was higher than that of the downstream face.

Table 2 shows the fluctuating pressure on downstream face of stoplog gate. As observed from the test, root-mean-square value of fluctuating pressure applied on each stoplog gate panel falls in the range 0.37×9.81kPa~0.86×9.81kPa. Normally, maximum fluctuating pressure occurred on the stoplog gate is close to the top, and water depth above top of stoplog gate was inversely proportional to maximum fluctuating pressure.

Table 2. Head versus fluctuating pressure of the stoplog gate under Normal operation condition.

Test condition	**Head on top of stoplog gate H(m)**	**Root-mean-square value of fluctuating pressure** σ (9.81kPa)				
		Segment 2	Segment 4	Segment 6	Segment 8	Segment 10
H=458.0m, 9 segments of stoplog gates, simultaneous running of 4 generators	17.8	0.49	0.61	0.51	0.63	-
H=458.0m, 10 segments of stoplog gates, simultaneous running of 4 generators	15.0	0.51	0.63	0.55	0.52	0.71
H=447.0m, 7 segments of stoplog gates, simultaneous running of 4 generators	12.4	0.44	0.37	0.57	-	-
H=447.0m, 8 segments of stoplog gates, simultaneous running of 4 generators	9.6	0.47	0.39	0.49	0.86	-

4.3 Time-average pressure at inlet section of pressure pipe

During simultaneous running of the 4 generators under the reservoir level of 458.0m, time average pressures on the top, the center and the bottom of inlet section of pressure pipe were observed and analyzed. Fig. 3 shows the pressure distribution before and after the placement of stoplog gates. As seen from the figure, under each test condition, the time average pressure was higher than 25.6×9.81kPa throughout inlet section of pressure pipe; pressure at each measurement point fell with the increase of stoplog gate number, while frictional pressure changed gently with low amplitude. As seen in the result, after stoplog gate was placed in front of the inlet, all the time average pressures on the top, the center and the bottom of inlet section of pressure pipe changed to some extent. Compared to the results without placement of stoplog gate, the pressure drop at top measurement point was most significant, followed by that at central measurement point

©2017, IAHR. Used with permission / ISSN 1562-6865 (Online) - ISSN 1063-7710 (Print)

and that at bottom measurement point. At the position 2.3 times of pipe diameter behind the inlet of pressure pipe, pressure drops at top measurement point, central measurement point and bottom measurement point at same section were basically balanced.

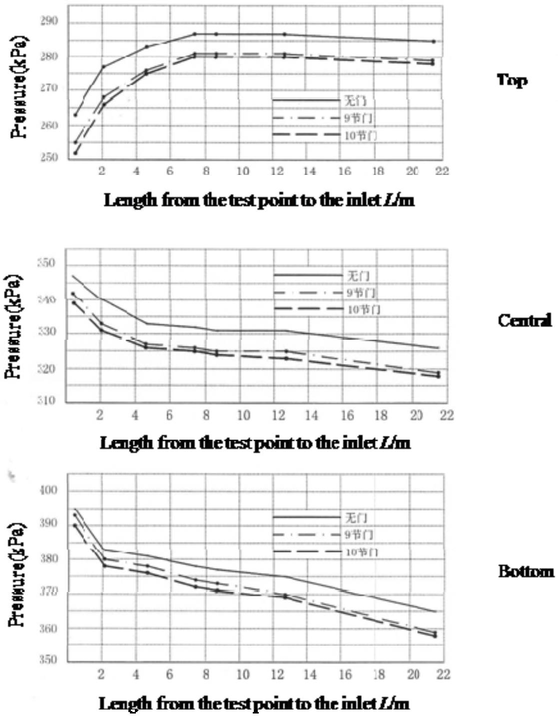

Figure 3. Distribution of the pressure on inlet flow pass section.

4.4 Head loss at inlet section with stoplog gate

By placing different segments of stoplog gates, the observed sections were in front of the reservoir and the start section of pressure pipe behind the rapid operating gate. Local head loss coefficient, ξ between the 2 sections was calculated by,

$$\xi = \frac{h_w}{V^2/2g} \qquad [1]$$

- h_w - difference of total energy head between the 2 sections (m) ;
- V- mean flow velocity at the start section of circular pipe (m/s);
- g - gravitational acceleration (m/s^2).

Table 3 lists the test and calculation results. As indicated in the model test, without placement of stoplog gate, head loss at the inlet section was less. Under the reservoir level of 458.0m, the head loss and head loss coefficient were 0.28m and 0.104, respectively; under the reservoir level of 447.0m condition, they were 0.25m and 0.094, respectively. The difference of head loss coefficient under the two levels was reflected by extent of impact on flow by the support beam at the section in front of the inlet. After stoplog gate was placed, both head loss and head loss coefficient at the inlet section increased a lot, incremental with decrease in water depth above top of top stoplog gate. It is indicated that, the local head loss produced by stoplog gate played a major role in total head loss at the inlet section after stoplog gate was placed. Under the reservoir level of 458.0m, head loss coefficient was 0.383 and 0.458 when 9 segments and 10 segments of stoplog gates were placed, increasing by 3.7 and 4.4 times, respectively; under the reservoir level of 447.0m, head loss coefficient was 0.557 and 0.613 when 7 segments and 8 segments of stoplog gates were placed, increasing by 5.9 and 6.5 times, respectively.

 ©2017, IAHR. Used with permission / ISSN 1562-6865 (Online) - ISSN 1063-7710 (Print)

Table 3. Head loss and head loss coefficient at the inlet.

Test condition	Head on top of stoplog gate (m)	Q (m^3/s)	V (m/s)	h_w (m)	C
H=458.0m, simultaneous running of 4 generators, 10 segments of stoplog gates	15.0	432×4	7.26	1.23	0.458
H=458.0m, simultaneous running of 4 generators, 9 segments of stoplog gates	17.8	432×4	7.26	1.03	0.383
H=458.0m, simultaneous running of 4 generators, before placement of stoplog gate	—	432×4	7.26	0.28	0.104
H=447.0m, simultaneous running of 4 generators, 8 segments of stoplog gates	9.6	430×4	7.22	1.63	0.613
H=447.0m, simultaneous running of 4 generators, 7 segments of stoplog gates	12.4	430×4	7.22	1.48	0.557
H=447.0m, simultaneous running of 4 generators, before placement of stoplog gate	—	430×4	7.22	0.25	0.094

4.5 Impact of load rejection on flowing pressure of stoplog gate panel

In the test, simultaneous load rejection on 2 generators and load rejection on 1 generator were considered. Fig. 4 shows the maximum additional pressure produced by load rejection on stoplog gate. As shown in the figures, during simultaneous running of the 4 generators, simultaneous load rejection on 2 generators produced higher additional pressure than load rejection on 1 generator. Under the same load rejection, additional pressure was induced by stoplog gate decreased from bottom to top.

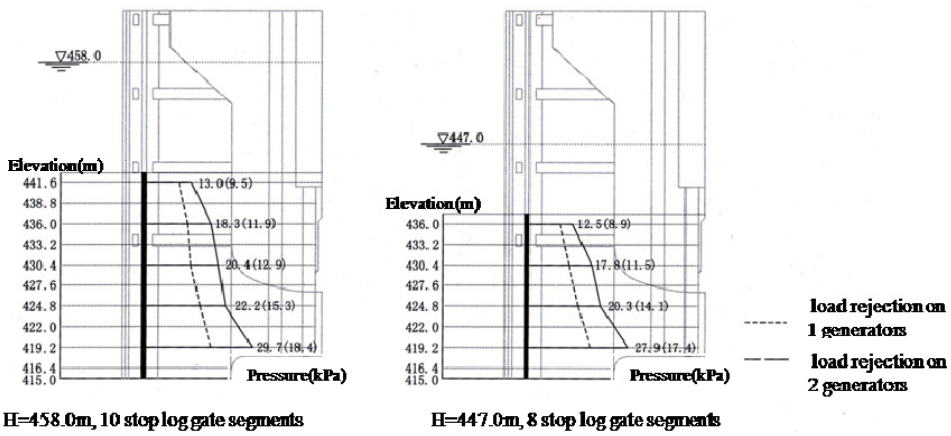

Figure 4. Water hammer pressure distribution nearby the stoplog gate.

During simultaneous running of the 4 generators under the reservoir level of 458.0m with 10 segments of stoplog gates, when load rejection occurred simultaneously on 2 generators and the guide vane was closed for 8s, maximum additional pressure caused by downstream panel of stoplog gate fell in the range 1.33×9.81kPa ~3.03×9.81kPa; when load rejection occurred on 1 generator and the guide vane was closed for 8s, maximum additional pressure caused by stoplog gate fell in the range 0.97×9.81kPa ~1.88×9.81kPa.

During simultaneous running of the 4 generators under the reservoir level of 447.0m with 8 segments of stoplog gates, when load rejection occurred simultaneously on 2 generators and the guide vane was closed for 8s, maximum additional pressure caused by downstream panel of stoplog gate fell in the range 1.27×9.81kPa ~2.84×9.81kPa; when load rejection occurred on 1 generator and the guide vane was closed for 8s, maximum additional pressure caused by stoplog gate fell in the range 0.91×9.81kPa ~1.77×9.81kPa.

5 CONCLUSION

(1) Under the condition for generator safe running, quantity of stoplog gate placed at the inlet was preliminarily established in the model test. During simultaneous running of the 4 generators under the reservoir level of 458.0m, at most 10 segments of stoplog gates can be placed in front of the inlet; during simultaneous running of the 4 generators under the reservoir level of 447.0m, at most 8 segments of stoplog gates can be placed in front of the inlet.

©2017, IAHR. Used with permission / ISSN 1562-6865 (Online) - ISSN 1063-7710 (Print)

(2) Under normal running condition of generator, time-average pressures induced by upstream and downstream panels of stoplog gate were distributed basically like hydrostatic pressure; under unfavorable condition that the most segments of stoplog gates were placed during simultaneous running of the 4 generators, at the same elevation of stoplog gate, pressure on upstream face was 0.3×9.81kPa~0.7×9.81kPa higher than that applied on downstream face; root-mean-square value of fluctuating pressure applied on downstream panel of stoplog gate was 0.37×9.81kPa~0.86×9.81kPa. Normally, maximum fluctuating pressure occurred on the top stoplog gate and was inversely proportional to head above top of stoplog gate.
(3) When stoplog gate was set in front of the inlet, time-average pressures on the top, the center and the bottom of inlet section of pressure pipe changed to some extent. Compared to that without stoplog gate, pressure in front of the inlet of pressure pipe dropped at top measurement point, central measurement point and bottom measurement point at the same section were decreased. 2.3 times of pipe diameter behind the inlet of pressure pipe, pressure drops at measurement points at the same section were basically balanced.
(4) The set of stoplog gate changes the flow path in front of the inlet of ordinary station. Since local flow resistance was impacted by stoplog gate and support beam of the trash rack, both head loss and head loss coefficient at the inlet section increased a lot, incremental with decrease in water depth above the stoplog gate. In the condition that ordinary water taking for ecological purpose was met, placing stoplog gate increases the head loss at the inlet section by 4~6 times, and impacted the benefit of power generation.
(5) From the model test results, simultaneous load rejection on 2 generators produced higher additional pressure than load rejection on 1 generator. Under the same load rejection, additional pressure induced by stoplog gate decreased from bottom to top. The maximum additional pressure was 3.03×9.81kPa. The difference between time-average pressures induced by upstream panel and downstream panel of stoplog gate was less than 1.0×9.81kPa. As a result, it should be noted that instant load produced on downstream panel of stoplog gate under load rejection can be higher than the upstream load.

ACKNOWLEDGEMENTS

The research reported herein was funded by National Natural Science Foundation of China (51379020，51279013) and The National Key Research and Development Program of China (2016YFC0401904).

REFERENCES

Du, X.H., Yu, W.Q. & Rui, J.L. (2008). Hydropower Ecology Practice Selective Withdrawal Structures. *Water Power*, 34(12), 28-32.

You, X., Tang, B.H., Zhang, J.X. & Qin, Y.T. (2010). Influences of Multi-Level Intake Structure of Stoplog Gate at Inlet of Jinping 1st Stage Hydropower Station on River Regime and Structural Safety. *Advances in Science and Technology of Water Resources*, 30(4), 46-50.

Zhang, J.X., Zhang, D., Wu, Y.H., Zhang, W.Y. & You, X. (2010). Experimental Study on Hydraulic Characteristics of the Stratified Intake for the First-Stage Jinping Hydropower Station. *Journal of Hydroelectric Engineering,* 29(2), 1-6.

 ©2017, IAHR. Used with permission / ISSN 1562-6865 (Online) - ISSN 1063-7710 (Print)

POTENTIAL SUITABLE HABITAT SIMULATION OF THE HOMONOIA RIPARIA LOUR IN YUNNAN, CHINA

YUJUN YI[1] & YANG ZHOU[2]

[1,2] Ministry of Education Key Laboratory of water and sediment Science, School of Environment, Beijing Normal University, Beijing 100875, China
yiyujun@bnu.edu.cn; zhouyang@qq.com

ABSTRACT

Climate change and dam construction give pressure on riparian plants. Here, a quantitative prediction of their influence on riparian species was executed. *Homonoia riparia (H. riparia) Lour*, a medicinal plant with high ecological and economic value, is a riparian plant and native to Yunnan Province, China. Its population has declined significantly and the species has become locally endangered in recent decades. In order to evaluate the habitat of *H. riparia Lour*, a habitat suitability model was established. Based on the habitat requirements of this species, the key eco-factors influencing species distribution were selected. One positional variable, three topographic variables and eight bioclimatic variables were employed to model its distribution and potential habitat. Owing to the advantages of using presence-only data, small sample sizes and gaps, and performing well with incomplete data, a MAXENT model was employed to simulate the habitat suitability distribution. The results show that seven variables, namely, annual mean temperature, altitude, precipitation seasonality, precipitation of coldest quarter, the distance to the nearest river, temperature seasonality, and precipitation during the driest month, are the significant factors to determine *H. riparia Lour*'s suitable habitat. Habitat suitability for three historical periods and two future climate warming scenarios were calculated. The habitat suitability of *H. riparia Lour* in Yunnan Province is predicted to improve with global warming. The number of dams, backwater area, and water level fluctuation range were the key factors influencing the habitat fragmentation.

Keywords: Climate change; habitat suitability simulation; maxent; Homonoia Riparia Lour; dam.

1 INTRODUCTION

A habitat is the combination of the organism-inhabited space and all eco-factors in that space, including abiotic environments and other organisms that are necessary for the existence of individuals or groups. Habitat's quantity and quality have a significant impact on the species "presence – absence" and species richness. Habitat loss leads to spatial pattern of residual habitat changing through impacting micro-environment and the arrangement of plants patch. Thus, habitat loss has negative effects on species richness, the negative effects have two characteristics: long duration and high-intensity (Kruess and Tscharntke, 1994; Kruess, 2003; Grez et al., 2004). Habitat loss is the main reason for species endangering, species extinction and the decline in biodiversity (Tilman et al., 2001; Fischer and Lindenmayer, 2007; Gardner et al., 2008). Several reasons, such as climate change, land use change *etc.*, make the area of the habitat of wild animals and plants decrease, their habitat's quality degrades and habitat loss (Liu et al., 2001; Grimm et al., 2008). *Ilex khasiana Purk.*, a critically endangered tree species of northeastern India, was influenced by habitat loss, only *ca.* 3000 individuals of *Ilex khasiana Purk* are surviving today (Adhikari et al., 2012). An ever-increasing human population, the most important being the increasing demand on land for agriculture, industries and the urbanization, has strong impacts on the habitat of Malabar nut (*Justicia adhatoda L.*), a medicinal plant. The population of Malabar nut (*Justicia adhatoda L.*) is shrinking in Dun Valley, India due to habitat loss (Yang et al., 2013). By 2010, about one fifth of the entire world's plants species are at risk of extinction (Brummitt and Bachman, 2010).

Homonoia riparia Lour is a rheophyte native species in Yunnan Province, China. It is a medical plant with high ecological and economic values. Its population number has decreased sharply in Yunnan, China in recent decades. The field investigation in 1984 (before the Manwan reservoir's construction) showed that there were at least four habitats of *Homonoia riparia Lour* in the Manwan reservoir area and the species abundance was significantly more than 400, while only one habitat among these four remained in 1997 (after the Manwan reservoir's construction). Two habitats in Manwan reservoir and one habitat below the Manwan dam disappeared. Only scattered *Homonoia riparia Lour* distributed in the floodplain between the upstream and the estuary of Luozha River, but their growths in 1997 were worse than in 1984 (Wang et al., 2000). However, few researches about the habitat quality of *Homonoia riparia Lour* have been taken. As a consequence, researching the habitat preference of *Homonoia riparia Lour*, developing a habitat suitability model to calculate this species's spatial distribution, and seeking suitable survival conditions for *Homonoia riparia Lour*, are crucial to *Homonoia riparia Lour*'s protection and rehabilitation.

The first task was to understand the relationship between the environment and the distribution of *Homonoia riparia Lour*. To do so, we built a species distribution model (SDM) as a function of the climate, topography and position variables. Species distribution models (SDMs) mainly use the distribution data of species (presence or absence) and the environment data to estimate species niche by specific algorithm, and then project the niche onto landscape, reflect the preference to habitat in the form of probability (Guisan and Thuiller, 2005; Elith and Leathwick, 2009). The results can be explained as the probability of species presence, species richness, habitat suitability, and so on. SDMs have been used to predict the distribution range of plant diseases and insects, model the distribution of species, community or ecosystem, assess the impact of climate, land use and other environmental changes on species distributions (Thomas et al., 2004; Thuiller, 2004), evaluate the risk of species invasion and proliferation (Beerling et al., 1995; Peterson, 2003), filter unsurveyed areas with high suitability for precious endangered species (Raxworthy et al., 2003; Engler et al., 2004), contribute to the site selection of natural conservation area (Ferrier, 2002), help to identify the areas for species reserves, and reintroduction (Adhikari et al., 2012). Typical SDMs include BIOCLIM (Busby, 1991), BIOMAPPER (Hirzel et al., 2002), BRT (Friedman et al., 2000), CLIMEX (Sutherst et al., 1995), DOMAIN (Carpenter et al., 1993), GAM (Yee & Mitchell, 1991), GARP (Stockwell & Peters, 1999), GLM (Lehmann et al., 2002), MAXENT (Phillips et al., 2004), *etc.*

SDMs are based on the species presence and absence data. Those data can be obtained from the field investigation, specimen records, and literatures. In practice, it is very hard to get the absence data. Even the absence data can be obtained, its reliability is very low. Sometimes, the presence data of rare and endangered species are also limited. Elith et al. (2006) used 16 methods to model the distributions of 226 species from six regions around the globe. The results indicated that the predictive ability of Maxent was always stable and reliable, and it outperformed several SDMs (such as GARP, DOMAIN, BIOCLIM, GAM, GLM et al.) for presence-only data (Elith et al., 2006). As a result, among SDMs, MAXENT was selected due to its advantages as follows: (1) the input species data can be presence-only data, (2) both continuous and categorical data can be used as input environmental variable in MAXENT, (3) its prediction accuracy is always stable and reliable, even with incomplete data, small sample sizes and gaps, (4) a spatially explicit habitat suitability map can be directly produced, and (5) the importance of individual environmental variables can be evaluated by a built-in jackknife test.

This study is based on the occurrence records of *Homonoia riparia Lour,* to model its habitat suitability distribution, so that protecting and rehabilitating the habitat of *Homonoia riparia Lour.* Therefore, the main aim of this study includes: (1) select key environmental variables, which highly correlated with *Homonoia riparia Lour*'s distribution, (2) based on maximum entropy principle, Maxent model was developed to quantify the relationship between *Homonoia riparia Lou*r's presence and environmental variables (including position variable, topographical variables and bioclimate variables), (3) the habitat suitability of *Homonoia riparia Lour* in three historical periods (1950 – 1959, 1975 – 1985 and 2000 – 2009) were simulated by established model, (4) the habitat suitability distribution of *Homonoia riparia Lour* under two climate warming scenarios (RCP2.6 and RCP8.5, given by IPCC) were predicted.

2 STUDY AREA AND SPECIES

2.1 Study area

Yunnan Province, is located in southwestern of China, (21°8′N ～ 29°15′N, 97°31′E ～ 106°11′E), with a total area of about 390,000 square kilometers, accounting for 4.11% of the national territory area. Landforms in Yunnan Province are complex and diverse, the north side is higher than the south, and significant difference was found between the north and south, thus special subtropical monsoon climate and tropical plateau monsoon climate formed. There are regional difference and vertical variability in climate of Yunnan. The annual temperature difference is small and the diurnal temperature difference is large. The rainfall is plentiful, wet and dry season are clear, but the precipitation distribution is not uniform. The annual precipitation in most parts of Yunnan province is about 1100 mm, the precipitation in the southern part may be up to 1600 mm. The seasonal distribution and regional distribution of precipitation are uneven, rainfall in winter is sparse and rainfall in summer is abundant. The special geographical location and complex natural environment of Yunnan Province have brought up very rich biological resources. Yunnan is the province with the richest wildlife species and ecosystem types in China. The composition of biological resources in Yunnan Province is complex, there are a lot of endemic genera, endemic species, rare and endangered species, the total number of species in taxa in Yunnan Province is close to or above half of the national number, rare species accounted for 67.5% of the total in the country, ranking first in China (Jia and Zhang, 2006). Due to the restrictions of natural and geographical conditions and other factors, the diversity of biological resources in Yunnan has the characteristics of vulnerability, Yunnan is one of the 17 key regions of biodiversity in China and one of the 34 global most species-rich hotspots, its biodiversity ranks the first in China and attracts attentions both in China and abroad (Yunnan biodiversity conservation strategy and action plan, 2013).

 ©2017, IAHR. Used with permission / ISSN 1562-6865 (Online) - ISSN 1063-7710 (Print)

2.2 Species

Homonoia riparia Lour, euphorbiaceae, evergreen shrub, is 1 ~ 3 m high. It is a kind of Rheophyte, common along the bank of drains and on rocky river beds, also grows in evergreens (Shukla, 1997; Rao and Kumari, 2008). And, also grows in regularly flooded places (Hanum and Maesen, 1997). *Homonoia riparia Lour* has many aliases in China, such as Shuima, Xiagongchashu, Shuizhuimu, Xiyangliu. In China, it mainly distributes in Yunnan Province, also distributes in Guangxi Province, Guangdong Province, *etc.* (China Plant Science Research Institute, 1972). *Homonoia riparia Lour* is a medical plant. Its root is a medicinal part, can be used to treat hepatitis, joint pain, stomachache, empyrosis *etc.*, and has detoxification and diuretic effect (Xishuangbanna family medicine research office, 1980; Che et al., 2009). *Homonoia riparia Lour* is a deep-rooted tree, it has good resistance to drowning and scouring, is beneficial for preventing erosion, fixing sands and then reinforcing dikes (Wei, 1992). Investigations in recent years have shown that the number of *Homonoia riparia Lour* in Yunnan Province has decreased as compared to 1950 – 1959.

3 METHODS

3.1 Data sources

Fifty one occurrence records of *Homonoia riparia Lour* in Yunnan Province were collected from the databases including field survey data in June and December 2010, Global Biodiversity Information Facility (http://www.gbif.org), National Specimen Information Infrastructure (http://www.nsii.org.cn/), the Chinese Virtual Herbarium (http://www.cvh.org.cn/), and literatures (Wang et al., 2000).

Bioclimatic variables are very biologically meaningful for defining the habitat suitability of a species in a certain environment condition. Data for 19 bioclimatic variables were from http://www.worldclim.org. Chinese geographical base map was from National Fundamental Geographic Information System (http://nfgis.nsdi.gov.cn). Variables including the distance to the nearest river, altitude, aspect and slope, were calculated according to the longitude and latitude coordinates and DEM by Arcgis 9.3. The DEM data were from http://www.gscloud.cn/. The spatial resolutions of all environmental data used in this model are all 30 arc-seconds (often referred to as 1 km spatial resolution).

The climate data of three historical periods (1950 – 1959, 1975 – 1985 and 2000 – 2009) were from the China meteorological data sharing service system (http://cdc.cma.gov.cn/home.do). In the fifth IPCC report, making the total Radiative Forcing (RF) in 2100 as an index, four Representative Concentration Pathways (RCPs) were set, there were the total RF in 2100 reaching 2.6 W/m^2, 4.5 W/m^2, 6.0 W/m^2 and 8.5 W/m^2 as compared to 1750, respectively (The fifth IPCC report). Here, two scenarios, RCP2.6 and RCP8.5 were selected. In four RCPs, RCP2.6 is the only scenario in which global warming in 2100 do not exceed 2℃ as compared to 1850 – 1900. *Homonoia riparia Lour* 's habitat suitability distribution in this two scenarios were modeled respectively. The climate data are the climate projections from global climate models (GCMs) for RCP2.6 and RCP8.5, and there are averages between 2061 and 2080. There are available on http://www.worldclim.org.

3.2 Variables selection

In order to select variables that can contribute more to the model, eliminate multicollinearity between variables, establish model that has better performance using less variables, the cross-correlations (Pearson correlation coefficient, r) and principal component analysis (PCA) among 19 bioclimate variables of 51 species occurrence records were tested. 19 bioclimate variables of 51 species occurrence records were extracted from the corresponding layers by Arcgis 9.3. Only one variable from a set of highly cross-correlated variables ($r > 0.8$) was reserved, which variable can be kept is based on both correlation analysis and PCA. For instance, bio3 and bio2 were correlated ($r = 0.804$), so were bio3 and bio4 ($r = -0.913$), considering the result of PCA, bio3 was dropped, bio2 and bio4 were reserved. According to the contributions of 19 bioclimate variables to every extracted principal component and the correlation analysis between 19 bioclimate variables, eight bioclimate variables (bio1, bio2, bio4, bio7, bio12, bio14, bio15, and bio19) were extracted.

3.3 Maximum Entropy (MaxEnt) model

In 1957, Jaynes proposed a maximum entropy theory (Maximum Entropy, MAXENT), the essence of the theory is: on the basis of partial knowledge, the most reasonable inference about the unknown probability distribution is the most uncertain or the most random inference that matches the known knowledge, this is the only unbiased choice we can make, any other choice would mean that we have introduced other constraints and assumptions, but these constraints and assumptions cannot be derived based on the information we have (Jaynes, 1957).

Set a random variable (ξ), it has n different results, X1, X2, ⋯ ,Xn, the occurrence probability of every result is p1, p2, ⋯ , pn, respectively, the uncertainty of ξ is entropy. The formula of entropy is:

$$H(\xi)=\sum_{i=1}^{n}p_i\log\frac{1}{p_i}=-\sum_{i=1}^{n}p_i\log p_i \quad [1]$$

The application of maximum entropy theory in species habitat suitability prediction can be expressed as: if we know nothing about the species' life habit and local ecological conditions, the most reasonable prediction is that the probabilities of the area that is suitable for the species and that is not suitable are both 0.5. In Maxent model, the presence information of species and local ecological conditions are information, it reduces uncertainty. The more information is the more uncertainty reduces. Maxent model is to establish a model with the maximum entropy, which is in accordance with the known knowledge (Phillips et al., 2006; Phillips and Dudík, 2008). Based on the maximum entropy theory, a java-based software, Maxent, which can be used for habitat suitability simulation, was developed by Phillips et al. (2006). The Maxent (version 3.3.3) used here is from http://www.cs.princeton.edu/ ~ schapire/MaxEnt/, which can be downloaded freely for scientific researches. The training data was 75% sample data selected randomly and the test data were the remaining 25% sample data. The habitat suitability curve of each variable was calculated and the contribution of each variable to the habitat model of *Homonoia riparia Lour* was calculated by Jackknife test.

There are four possible prediction results of the model: (1) the species exists actually, the prediction result is also presence, this is true positive (TP), (2) the species does not exist actually, but the prediction result is presence, this is false positive (FP), (3) the species exists actually, but the prediction result is absence, this is false negative (FN), and (4) the species does not exist actually, the prediction result is also absence, this is true negative (TN). Generally, two types of errors always occur in the prediction results of SDMs: FN and FP. These two types of errors both relate to the threshold, which is used to determine presence or absence. The frequently-used indexes evaluating SDMs performance are calculated based on true positive, false positive, true negative and false negative, including Kappa (Cohen, 1960), TSS (true skill statistic) (Allouche et al., 2006), AUC (area under ROC (receiver operating characteristic curve)) (Hanley and Mcneil, 1982) and so on.

A number of different thresholds are set to calculate a series of sensitivities (positive rate in the positive results, $\frac{TP}{TP+FP}$) and specificities (negative rate in the negative results, $\frac{TN}{TN+FN}$), sensitivity is set as ordinate, 1-specificity is set as abscissa, then ROC can be obtained. The larger AUC is, the better model performance is. AUC is not affected by threshold, so it is an excellent index to evaluate model performance (Vanagas, 2004). In Maxent model, AUC is employed to evaluate model performance. In general, AUC is between 0.5 and 1. AUC < 0.5 is not according to the actual situation, it occurs hardly in reality. It represents that the distribution is random that AUC is 0.5. Model performance is categorized as fail (0.5 – 0.6), poor (0.6 – 0.7), fair (0.7 – 0.8), good (0.8 – 0.9), excellent (0.9 – 1) (Swets, 1988). The closer the AUC to 1, the better the model performance is.

4 RESULTS AND DISCUSSION

4.1 Model performance and variables' contribution

The calculated ROC showed that the AUC values of training data set and test data sets were 0.899 and 0.840, respectively. According to Table 2, results of the model are satisfactory with the given set of training and test data. The results of the jackknife test of variables' contribution shows that Bio1 and altitude provided very high gains (> 1.0) when used independently, it indicated that Bio1 and altitude contained more useful information by themselves than other variables. Bio1 and altitude were the two most important predictors of *Homonoia riparia Lour*'s habitat suitability distribution. Bio15, Bio19, distance, Bio4, Bio14 had moderate gain when used independently, there were important predictors. Other remaining variables, Bio2, Bio7, Bio12, aspect and slope, had low gains when used in isolation, and they did not contain a lot of information by themselves. In a conclusion, Bio1, altitude, Bio15, Bio19, distance, Bio4, Bio14 are key factors among the all 12 variables for *Homonoia riparia Lour*'s habitat distribution.

4.2 Variables' response to suitability

Response curves show the relationship between environmental variables and the logistic probability of presence (also known as habitat suitability) quantitatively, and they deepen the understanding of the ecological habit of species. The responses of 12 variables to *Homonoia riparia Lour*'s suitability were illustrated in Figure 1. According to the response curves, the suitable elevation range is 0 m – 1200 m, which is consistent with the descriptions in Xishuangbanna Dai medicine Zhi (XNDRO, 1980). It records that *Homonoia riparia Lour* mainly grows at altitude of 50 ~ 1400 m, riverside with sand or gravel or scrub at hillside. Figure 2 shows the aspect distribution. No records were found in the aspect between 320° and 360°. According to the record, 1/3 of sample points are located at the aspect during 100° ~ 140° (southeast). That means the *Homonoia riparia Lour* can be generally adapted to aspect, but prefer southeast. Slope of all sample points are lower than 12 degree, 92.2% of sample points lower than 9 degree. The distance from 75%

 ©2017, IAHR. Used with permission / ISSN 1562-6865 (Online) - ISSN 1063-7710 (Print)

of sample points to river are less than 1800 m. It means that the *Homonoia riparia Lour* normally live on the flat flood plain. The distance from sample points to river are show in Figure 3. It shows that among 51 sample points, half of them are smaller than 800 m. Since the width of river, such as Lancang River, is about 800 m, points (< 800 m) can be considered on the immediately riverside. Furthermore, the calculated result shows that the suitability is higher as the distance to river is lower. This hangs together well with Homonoia is a kind of water plants, and the living environment for the river sand, stream matches the life habits of a rocky place (Tang et al., 1996).

The suitable Bio1 is higher than 20℃, this means that the Homonoia prefers warm place. The flora of China (1996) recorded that Homonoia live in the south of Yunnan, downstream of Yalong river and Jinsha river in Sichuan province, Nanpan river in Guizhou province, the south and west of Guangxi province, Hainan in China, and some countries in Southeast Asia (Tang et al.,1996). The *Homonoia riparia Lour* normally distributed in areas where Bio2 is higher than 6.2℃, Bio4 and Bio7 are lower than 4.3℃ and 25℃, respectively, Bio12, Bio14, and Bio19 are higher than 1100 mm, 12.5 mm, and 50 mm, respectively, and Bio15 is lower than 80. Lower variation of seasonal rainfall and higher precipitation in coldest season are conducive to Homonoia.

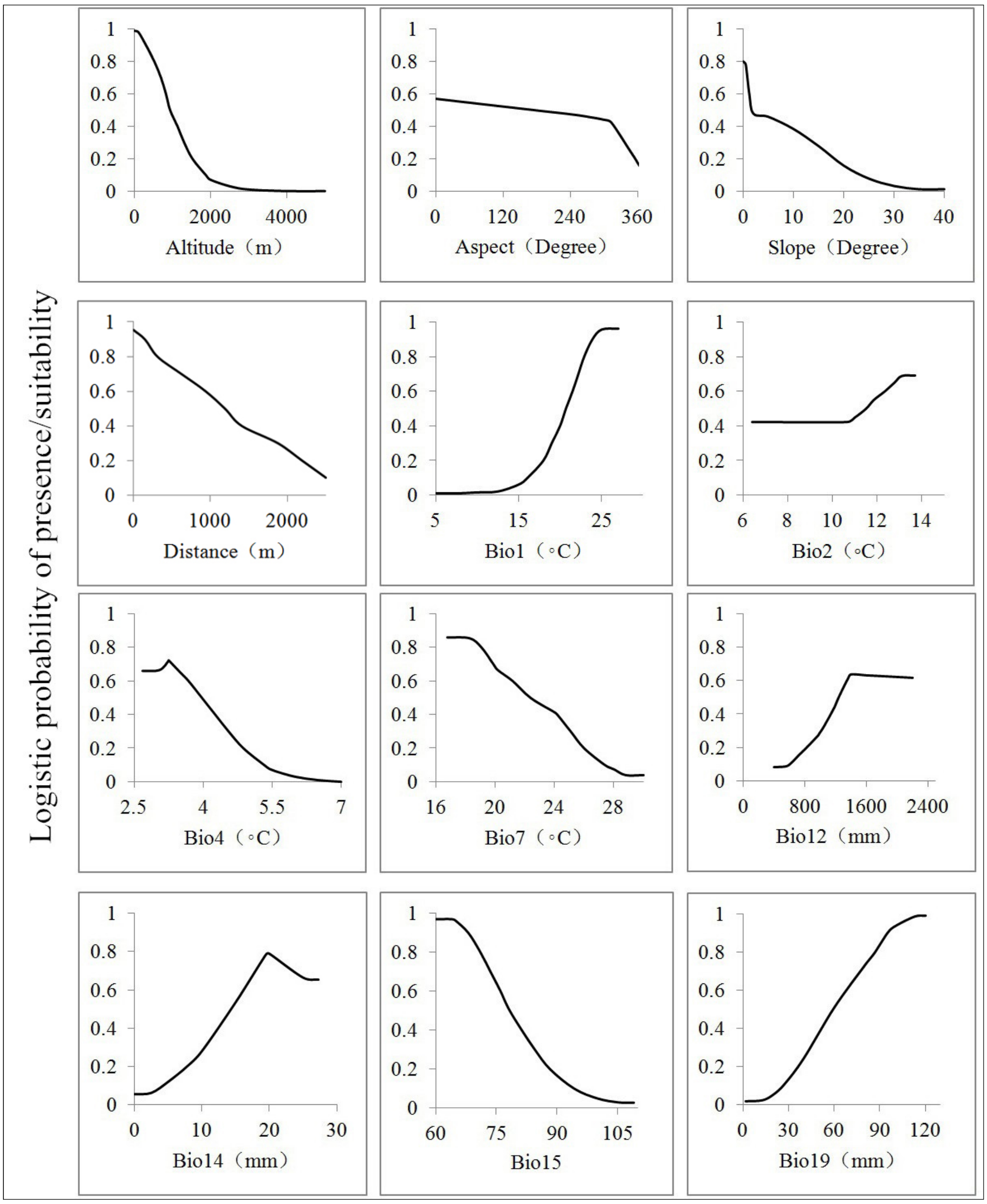

Figure 1. Response curves of 12 environmental variables in *Homonoia riparia Lour*'s habitat distribution model. Bio1: Annual Mean Temperature (℃); Bio2: Mean Diurnal Range (Mean of monthly (max temp-min temp)) (℃); Bio4：Temperature Seasonality (℃); Bio7: Temperature Annual Range (℃); Bio12: Annual Precipitation (mm); Bio14: Precipitation of Driest Month (mm); Bio15: Precipitation Seasonality; Bio19: Precipitation of Coldest Quarter (mm)).

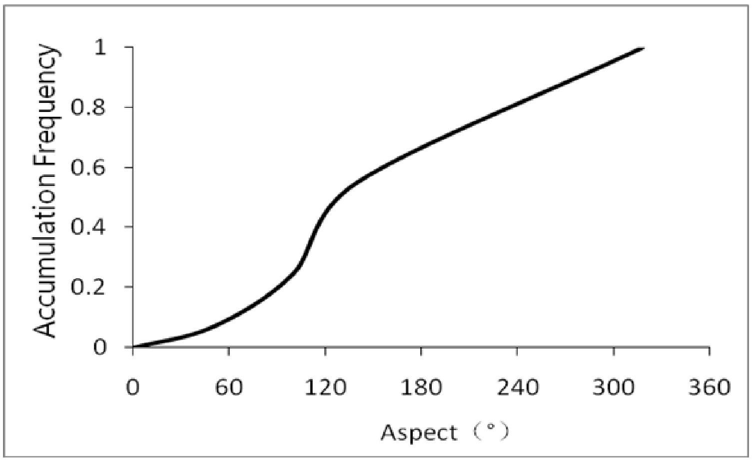

Figure 2. Accumulation frequency of aspect distribution of *Homonoia riparia Lour* sample points.

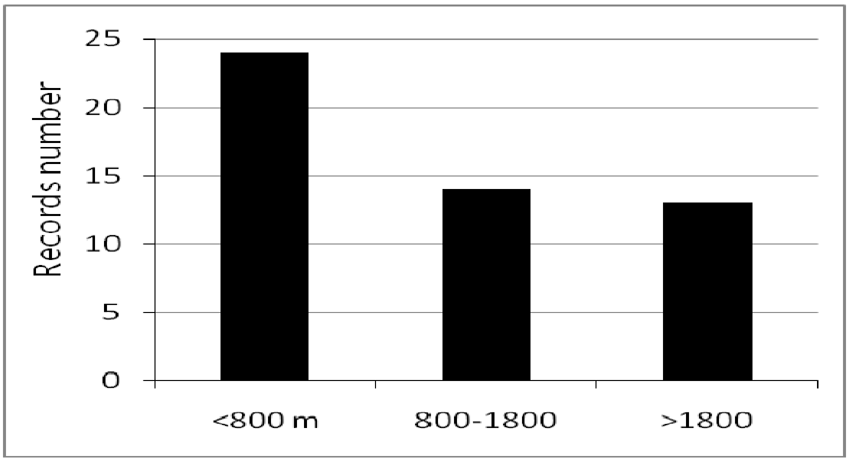

Figure 3. The distance frequency distribution of *Homonoia riparia Lour* sample points to river.

4.3 The *Homonoia riparia Lour* Distribution

The annual mean temperature is the most important variable for *Homonoia riparia Lour* distribution. As the annual average temperature increases, the suitable degree of habitat increases. Therefore, the suitability of southern region is higher than the northern region and 84.8% of habitat with suitability larger than 0.6 are distributed in southern Yunnan province.

The elevation and the distance to the nearest river are the next two important variables. The suitable habitats are distributed along the rivers and suitability increases as the distance to the river decreases. Areas with habitat suitability larger than 0.6 are along rivers, such as middle reach of Nu River, upper and lower reach of Lancang River, middle and lower reach of Lixianjiang, Yuanjiang, and some tributaries at lower Lancang river. Areas with habitat suitability of 0.3 – 0.6 are located at middle reach of Lancang River, lower reach of Nu River, and some other small tributaries. The habitat suitability of *Homonoia riparia Lour* in other areas are smaller than 0.3. This corresponds well with the record that *Homonoia riparia Lour* prefers running water plants (Tang et al., 1996).

4.4 Habitat suitability simulation of three historical periods

The habitat suitability distributions for three historical periods (1950 – 1959, 1975 – 1985, 2000 – 2009) are simulated. In view of space perspective, the suitability of south Yunnan was higher than north and the suitability was higher when the distance to the nearest river was shorter in three historical periods. In view of time perspective, from 1950 – 1959 to 2000 – 2009, *Homonoia riparia Lour*'s habitat suitability increased gradually, the area with high suitability (＞ 0.6) became larger gradually. The area with suitability larger than 0.6 was 3069 km^2 in 1950 – 1959, and was 3701 km^2 in 1975 – 1985. As compared to 1950 – 1959, *Homonoia riparia Lour*'s habitat suitability in 1975 – 1985 improved, the area with suitability larger than 0.6 increased by 632 km^2, the area with suitability larger than 0.6 at downstream of Lancang River and some tributaries at downstream of Lancang River improved significantly. This result was in accordance with the historical investigation result that *Homonoia riparia Lour*'s population number at Lancang River watershed in

 ©2017, IAHR. Used with permission / ISSN 1562-6865 (Online) - ISSN 1063-7710 (Print)

1975 – 1985 was more than 1950 – 1959 (Wang et al., 2000). In 2000 – 2009, *Homonoia riparia Lour*'s habitat suitability improved continually, the area with suitability larger than 0.6 was 7020 km^2, increased by 3319 km^2 as compared to 1975 – 1985 (a 0.9 time increase), increased by 3951 km^2 as compared to 1950 – 1959 (a 1.3 times increase). The area with the suitability larger than 0.6 in 2000 – 2009 was accounted for 1.80% of the Yunnan Province's total area. However, according to the survey data, *Homonoia riparia Lour*'s population number at Lancang River watershed in 2000 – 2009 decreased as compared to 1975 – 1985, a number of the original existed habitats disappeared (Wang et al., 2000; Zhao et al., 2014).

Table 1 shows the comparison of the investigation results of habitat condition and growth status of *Homonoia riparia Lour* in Manwan Reservoir area in 1984 and 2010. Before the construction of Manwan Reservoir (1984), there were at least four *Homonoia riparia Lour* habitats and the total area was larger than 2300 m^2, and species abundance in Manwan Reservoir was larger than 400. But, there was only one habitat with an area of 1200 m^2 left in 2010 and other three habitats already disappeared. Owing to the habitat degradation and loss, *Homonoia riparia Lour*'s abundance decreased by more than 96%, its averaged height decreased by 0.6 m. *Homonoia riparia Lour* has been in the high ecological risk (Zhao et al., 2014).

Table 1.HomonoiaripariaLour's habitat condition and growth status before and after the construction of Manwan Reservoir (Zhao et al., 2014).

Habitat number	1		2		3		4	
	before	after	before	after	before	after	before	after
Altitude (m)	922		920		930		985	
Aspect (°)	0		SE40		NW81		NE15	
Slope (°)	0		5		4		5	
Habitat area (m^2)	>1500	1200	>200	0	>200	0	>200	0
presence/absence[a]	+	+	+	-	+	-	+	-
Species height(m)	1.6	1.0	1.7	0	1.2	0	2	0
Species coverage (%)	25	2	30	0	30	0	60	0
species abundance	>200	14	>50	0	>50	0	>100	0

[a] +, presence; -, absence.

In 1986, Manwan Reservoir at the middle reach of main stream of Lancang River was started construction. Then Dachaoshan hydroelectric station (starting construction in 1996), Xiaowan hydroelectric station (starting construction in 2002) were started construction in succession at the main stream of Lancang River. The construction of dams impounded water, and the water level in front of dam raised. As a consequence, some lands were submerged including the original existed *Homonoia riparia Lour*'s habitats. At the same time, water level in reservoir varied seriously in order to meet the requirement of power generation. Huge daily and annual water level fluctuation in reservoir has been happened. Daily water level variation is about six m in reservoir during the field survey period. This would seriously influence the habitat of riverine plants. At the same time, the water detained in reservoir, so that the water in downstream reduced, river width narrowed, the distance of plants originally living near water to the river bank changed. *Homonoia riparia Lour*'s living environments changed, the original suitable survival condition was not obtained. *Homonoia riparia Lour*'s habitat area and distribution area decreased, the species abundance reduced. In a conclusion, dam construction induced the changes of ground water and underground water levels, *Homonoia riparia Lour*'s original habitats lost.

4.5 Suitable habitat distribution at globe warming situation

In the fifth IPCC report, making the total Radiative Forcing (RF) in 2100 as an index, four future climate warming scenarios were set, RCP2.6 and RCP8.5 were two of them. The computed results of *Homonoia riparia Lour*'s habitat suitability in RCP2.6 and RCP8.5 showed that the *Homonoia riparia Lour*'s habitat suitability increased as climate warming and the warmer the climate is, the higher the habitat suitability is. In RCP8.5, the area suitable for *Homonoia riparia Lour*'s survival and the suitability were both larger than RCP2.6 (Figure 4). In RCP2.6, the habitat suitability of the midstream of Nujiang River, the upstream and downstream of Lancang and some tributaries at downstream of Lancang River, Yuanjiang River and Lixianjiang River was greater than 0.6, the habitat suitability of a few regions at downstream of Nujiang River, most regions at midstream of Lancang River and some places far from tributaries at downstream of Lancang River, *etc.* were between 0.3 and 0.6, the habitat suitability of other places far from river system was less than 0.3. In RCP2.6, the area with habitat suitability less than 0.3 accounted for 87.23% of Yunnan Province's total area, was about 3.4 × 105 km^2, the area with habitat suitability between 0.3 and 0.6 accounted for 9.49%, was about 3.7 × 104 km2, the area with habitat suitability larger than 0.6 accounted for 3.28%, was about 1.3 × 104 km^2. As compared to the result in 2000 – 2009, in RCP2.6, the area with habitat suitability larger than 0.6 was nearly doubled. In RCP8.5, the habitat suitability of places near river system (including Nujiang River, Lancang River, Yuanjiang River, Lixianjiang River, *etc.*) was greater than 0.6, the habitat suitability of places far from river system was between 0.3 and 0.6, the habitat suitability of other places was less than 0.3. In RCP8.5, the area with habitat suitability less than 0.3 accounted for 79.66% of Yunnan Province's total area, was about 3.1 × 105 km^2, the area with habitat suitability between 0.3 and 0.6 accounted for 14.26%, was about 5.6 × 104 km^2, the area with habitat suitability larger than 0.6 accounted for 6.08%, was about 2.4 × 104 km^2. As compared to the result in 2000 – 2009, in RCP8.5, the area with habitat suitability larger than 0.6 approximately increased by 2.5 times and the area with habitat suitability between 0.3 and 0.6 approximately increased by 50%. As compared to RCP2.6, in RCP8.5, the area with habitat suitability larger than 0.6 was nearly doubled and the area with habitat suitability between 0.3 and 0.6 was approximately increased by 50%.

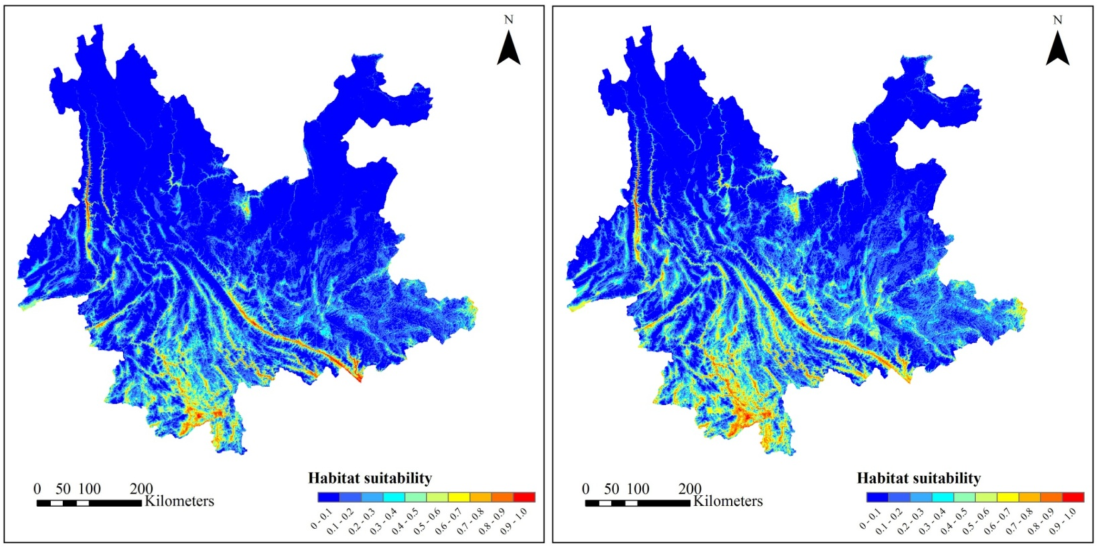

(a)RCP2.6 (b) RCP8.5

Figure 4. Suitable habitat distribution of HomonoiaripariaLour at two globe warming situations (a. RCP2.6; b. RCP8.5).

The result showed that the climate warming had positive effect on the habitat suitability and suitable area of *Homonoia riparia Lour*'s. However, the natural distribution of *Homonoia riparia Lour* was under threaten, and its population has decreased significantly. This might be due to the disturbance of riverine eco-system caused by the construction and operation of hydraulic projects.

5 CONCLUSIONS

In this study, we established a *Homonoia riparia Lour* habitat suitability model to evaluate and predict the existing and potential habitat quality of *Homonoia riparia Lour*.

Homonoia riparia Lour is a native endangered species in Yunnan Province, China. It is a medical plant with high ecological and economic value. It can protect river bank from erosion. In recent decades, its population in Yunnan Province has declined significantly.

Using the maximum entropy theory, based on the Yunnan Province Root of Riparian Homonoia historical distribution data and the data of environmental variables, *Homonoia riparia Lour*'s habitat suitability model was developed. Based on the correlation analysis and principal component analysis, twelve environmental variables (the distance to the nearest river, altitude, aspect, slope and 8 bioclimatic variables) were selected to establish *Homonoia riparia Lour* habitat distribution mode. AUC index was employed to evaluate model performance. AUC values of training dataset and test dataset were 0.899 and 0.840, respectively. This indicates that the model is satisfactory with the given set of training and test data.

Among twelve variables, *Homonoia riparia Lour*'s habitat suitability distribution was mainly influenced by seven variables: annual mean temperature, altitude, precipitation seasonality, precipitation of coldest quarter, the distance to the nearest river, temperature seasonality, and precipitation of driest month. *Homonoia riparia Lour*'s habitat suitability become excellent (> 0.8) when the altitude is lower than 100 m, the distance to river is less than 150 m, Bio1 is between 25℃ and 27℃, Bio4 is about 3.2℃, Bio14 is about 20 mm, Bio15 is between 60 and 65, and Bio19 is between 112 mm and 120 mm. Regions with habitat suitability greater than 0.6 almost distributed along rivers. The closer it is, the higher the suitability is. The habitat suitability of other places far from river system is low.

 ©2017, IAHR. Used with permission / ISSN 1562-6865 (Online) - ISSN 1063-7710 (Print)

On the overview of space, the suitability of south was higher than north. This is reasonable since *Homonoia riparia Lour* prefers warm place. From 1950 – 1959 to 2000 – 2009, both the habitat suitability and the area with high suitability (> 0.6) of *Homonoia riparia Lour* were promoted. The trend from 1950 – 1959 to 1975-1985 is in accordance well with the historical investigation (Wang et al., 2000). The habitat suitability of 2000 – 2009 is still increase as compared to 1975 – 1985. While, the field survey on 2010 showed that *Homonoia riparia Lour*'s habitat degraded and lost, the abundance decreased by more than 96%, and its averaged height decreased by 0.6 m, this species is in highecological risk (Zhao et al., 2014). The reason would be the construction of hydroelectric stations. The construction and operation of hydraulic projects induced the changes of ground water level, underground water level in reservoir area and below the dam. The environmental conditions of original habitats of *Homonoia riparia Lour* were changed greatly, and this species were impacted significantly.

The simulation results of *Homonoia riparia Lour*'s habitat suitability in RCP2.6 and RCP8.5 showed that the *Homonoia riparia Lour*'s habitat suitability increased as the climate warming and the warmer the climate is, the higher the habitat suitability is. In RCP8.5, both the suitability and suitable area of *Homonoia riparia Lour* were larger than RCP2.6. So, the climate warming is good at *Homonoia riparia Lour*. In order to protect *Homonoia riparia Lour*, only minimizing the disturbance of human activities is needed. If the *Homonoia riparia Lour* has stable and nature habitat, with more and more suitable climate situation, the abundance and population of this species will be recovered soon.

REFERENCES

Adhikari, D., Barik, S. K. & Upadhaya, K. (2012). Habitat Distribution Modelling for Reintroduction of Ilex Khasiana Purk., a Critically Endangered Tree Species of Northeastern India. *Ecological Engineering*, 40, 37-43.

Allouche, O., Tsoar, A. & Kadmon, R. (2006). Assessing the Accuracy of Species Distribution Models: Prevalence, Kappa and the True Skill Statistic (TSS). *Journal of applied ecology*, 43(6), 1223-1232.

Beerling, D. J., Huntley, B. & Bailey, J. P. (1995). Climate and the Distribution of Fallopia Japonica: use of an Introduced Species to Test the Predictive Capacity of Response Surfaces. *Journal of Vegetation Science*, 6(2), 269-282.

Brummitt, N. A. & Bachman, S. P. (2010). *Plants under Pressure—A Global Assessment: The First Report of the IUCN Sampled Red List Index for Plants. Kew, UK: Royal Botanic Gardens*.

Busby, J.R. (1991). *BIOCLIM-A Bioclimate Analysis and Prediction System.* Nature Conservation: Cost Effective Biological Surveys and Data Analysis, 64–68. CSIRO, Melbourne.

Carpenter, G., Gillison, A.N. & Winter, J. (1993). DOMAIN: A Flexible Modelling Procedure for Mapping Potential Distributions of Plants and Animals. *Biodiversity and conservation*, 2(6), 667-680.

Che, R.Y., Zhao, J. & Wang, S.Y. (2009). Determination of Content of Riparsaponin H. Riparia Lour Extract by High Performance Liquid Chromatography. Journal of Third Military Medical University, 31, 2275-2277.

Cohen, J. (1960). A Coefficient of Agreement for Nominal Scales. *Educational and psychological measurement*, 20(1), 37-46.

Elith, J. & Leathwick, J.R. (2009). Species Distribution Models: Ecological Explanation and Prediction across Space and Time. *Annual Review of Ecology, Evolution, and Systematics*, 40, 667-697.

Elith, J., Graham, C.H., Anderson, R.P. & Loiselle, B.A. (2006). Novel Methods Improve Prediction of Species' Distributions from Occurrence Data. *Ecography*, 29, 129–151.

Ferrier, S. (2002). Mapping Spatial Pattern in Biodiversity for Regional Conservation Planning: Where to from here?. *Systematic biology*, 51(2), 331-363.

Fischer, J. &Lindenmayer, D.B. (2007). Landscape Modification and Habitat Fragmentation: A Synthesis. *Global ecology and biogeography,* 16(3), 265-280.

Friedman, J., Hastie, T. & Tibshirani, R. (2000). Additive Logistic Regression: A Statistical View of Boosting. *The annals of statistics*, 28(2), 337-407.

Grimm, N.B., Faeth, S.H., Golubiewski, N.E., Redman, C.L., Wu, J., Bai, X. & Briggs, J.M. (2008). Global Change and the Ecology of Cities. *Science*, 319, 756-760.

Guisan, A. & Thuiller, W. (2005). Predicting Species Distribution: Offering More than Simple Habitat Models. *Ecology letters*, 8(9), 993-1009.

Hanley, J.A. & McNeil, B.J. (1982). The Meaning and use of the Area under a Receiver Operating Characteristic (ROC) Curve. *Radiology*, 143, 29–36.

Hirzel, A.H., Hausser, J., Chessel, D. & Perrin, N. (2002). Ecological-Niche Factor Analysis: How to Compute Habitat-Suitability Maps Without Absence Data. *Ecology*, 83, 2027–2036.

Institute of Botany, the Chinese Academy of Sciences (IBCAS) (1972). *Pictorial Handbook of Chinese Advanced Botany*, Science Press, Beijing. (In Chinese)

Jaynes, E. T. (1957). Information Theory and Statistical Mechanics. *Physical review*, 106(4), 620.

Jia, J. & Zhang, S.X. (2006). The Characteristics of the Current Situation and Protection of Biodiversity in Yunnan. *Green China*, 7, 50-54.

Kruess, A. & Tscharntke, T. (1994). Habitat Fragmentation, Species Loss, and Biological Control. *Science*, 264, 1581–1584.
Lehmann, A., Overton, J.M. & Leathwick, J.R. (2002). GRASP: Generalized Regression Analysis and Spatial Prediction. *Ecological modelling*, 157(2), 189-207.
Peterson, A.T. (2003). Predicting the Geography of Species' Invasions via Ecological Niche Modeling. *The quarterly review of biology*, 78(4), 419-433.
Phillips, S. J. & Dudík, M. (2008). Modeling of Species Distributions with Maxent: New Extensions and a Comprehensive Evaluation. *Ecography*, 31(2), 161-175.
Phillips, S.J., Anderson, R.P. & Schapire, R.E. (2006). Maximum Entropy Modeling of Species Geographic Distributions. *Ecological modelling*, 190(3), 231-259.
Phillips, S.J., Dudík, M. & Schapire, R.E. (2004). A Maximum Entropy Approach to Species Distribution Modeling. *Proceedings of 21st International Conference on Machine Learning*, 655–662. ACM Press, New York.
Raxworthy, C.J., Martinez-Meyer, E., Horning, N., Nussbaum, R.A., Schneider, G.E., Ortega-Huerta, M.A. & Peterson, A.T. (2003). Predicting Distributions of Known and Unknown Reptile Species in Madagascar. *Nature*, 426, 837–841.
Stockwell, D. (1999). The GARP Modelling System: Problems and Solutions to Automated Spatial Prediction. *International journal of geographical information science*, 13(2), 143-158.
Sutherst, R.W., Maywald, G.F. & Skarratt, D.B. (1995). *Predicting Insect Distributions in a Changed Climate.* Insects in Changing Environment, 59–91. Academic Press, London.
Swets, J.A. (1988). Measuring the Accuracy of Diagnostic Systems. *Science,* 240, 1285-1293.
Tang, C.L., Zhou, L.H. & Wu, Z.Y. (1996). *Flora of China*. Science Press, Beijing. (In Chinese)
Thomas, C. D., Cameron, A., Green, R. E., Bakkenes, M., Beaumont, L. J., Collingham, Y. C. & Hughes, L. (2004). Extinction Risk from Climate Change. *Nature*, 427(6970), 145-148.
Thuiller, W. (2004). Patterns and Uncertainties of Species' Range Shifts under Climate Change. *Global Change Biology*, 10(12), 2020-2027.
Tilman, D., Fargione, J., Wolff, B., D'Antonio, C., Dobson, A., Howarth, R., Schindler, D., Schlesinger, W.H., Simberloff, D. & Swackhamer, D. (2001). Forecasting Agriculturally Driven Global Environmental Change. *Science*, 292, 281–284.
Vanagas, G. (2004). Receiver Operating Characteristic Curves and Comparison of Cardiac Surgery Risk Stratification Systems. *Interactive Cardiovascular and Thoracic Surgery,* 3, 319–322.
Wang, Z.Z., Zhang X.M., Jin, Z.Z. Chuan, Y.M, Hu Z.Z., Zhang W.X. & Yang F.Q. (2000). *The Ecological Environment and Biological Resources of Manwang Hydropower Station Reservoir along Lancang River in Yunnan, China.* Yunnan Science and Technology Press, China. (In Chinese)
Wei, F.N. (1992). Guang Xi some Genus of the Euphorbiaceae of Brief Records on Classification. *Guangxi Plant,* 12, 193-208. (in Chinese)
Xishuangbanna National Drug Research Office (XNDRO). (1980). *Xishuangbanna Dai Medicine Zhi*. State Health Bereau Press, China. (In Chinese)
Yang, X.Q., Kushwaha, S.P.S., Saran, S., Xu, J. & Roy, P.S. (2013). Maxent Modeling for Predicting the Potential Distribution of Medicinal Plant, Justicia Adhatoda L. In Lesser Himalayan Foothills. *Ecological engineering*, 51, 83-87.
Yee, T.W. & Mitchell, N.D. (1991). Generalized Additive Models in Plant Ecology. *Journal of vegetation science*, 2(5), 587-602.
Yi, Y., Cheng, X., Wieprecht, S. & Tang, C. (2014). Comparison of Habitat Suitability Models using Different Habitat Suitability Evaluation Methods. *Ecological Engineering*, 71, 335-345.
Yunnan Environmental Protection Department (YEPD). (2013). *Joint Meeting of Biodiversity Conservation in Yunnan Province,* Yunnan Biodiversity Conservation Strategy and Action Plan. (In Chinese).
Zhao, Q.H., Liu, S.L., Deng, L., Dong, S.K. & Wang, C. (2014). Soil Degradation Associated with Water-Level Fluctuations in the Manwan Reservoir, Lancang River Basin. *Catena*, 113, 226–235.

 ©2017, IAHR. Used with permission / ISSN 1562-6865 (Online) - ISSN 1063-7710 (Print)

DETERMINING CRITICAL VEGETATION CONDITIONS IN THE MACQUAIRE MARSHES USING AN ECO-HYDRAULIC APPROACH

STEVEN G. SANDI[(1)], JOSE F. RODRIGUEZ[(2)], PATRICIA SACO[(3)], LI WEN[(4)] & NEIL SAINTILAN[(5)]

[(1,2,3)] School of Engineering, University of Newcastle, Newcastle, NSW, Australia
e-mail jose.rodriguez@newcastle.edu.au

[(4)] Science Division, NSW Office of Environment and Heritage, Sydney, Australia

[(5)] Department of Environmental Sciences, Macquarie University, Sydney, NSW, Australia

ABSTRACT

The Macquarie Marshes is a freshwater system located in the lowland floodplain of the Macquarie River, in NSW, Australia. As water flow enters the system, water is distributed to a number of swamps and lagoons via a network of anabranching channels. The marshes house unique plant communities that serve as a sanctuary for many species of migratory waterbirds, fisheries and other types fauna. In the past decades, a significant deterioration in plant communities has been observed due to a reduction of the input discharges to the marshes for industrial, agricultural and domestic usage. In recent years, there has been a slow recovery of some areas of the site which has been accomplished by delivering controlled environmental flows from an upstream dam. However, computational tools are required in order to provide a better assessment of watering strategies. In this publication we analyze the evolution of six vegetation patches by implementing a combination of green fractional cover and minimum inundation over a series of 23 years. We simulate floods by implementing a quasi-2D hydrodynamic model over a rectangular cell grid and combine the results. This approach allowed to determine critical watering conditions leading to a transition from understory wetland vegetation (Common Reed and Water Couch) to terrestrial species as well as minimum inundation required to trigger a recovery. Our approach also revealed that watering thresholds for understory species may be used as an indicator of critical conditions for River Red Gum.

Keywords: Macquarie Marshes; vegetation dynamics; critical plant conditions; fractional coverage.

1 INTRODUCTION

The Macquarie Marshes is an iconic freshwater wetland system and some areas are recognized as of International importance under the Ramsar convention. A collection of mosaic like features such as lagoons, swamps, reed beds and surrounding woodland is one of the key features of this system which promotes a high biodiversity for many species of fauna, particularly breeding sites for waterbirds. The marshes support one of three extensive River Red Gum forests (*Eucalyptus Camaldulensis*) in the Murray Darling Basin as well as one of two extensive reed beds of Water Couch (*Paspallum Distichum*) and Common Reed (*Phragmites Australis*) (OEH, 2012). In general, vegetation communities of the Macquarie Marshes suffered great deterioration during the past decades which reduced habitat availability (Rogers et al., 2010). It has been recognized that this deterioration was product of a general decrease of inflows because of water diversions and controlled water releases from the Burrendong dam (Kingsford, 2000). Vegetation mapping revealed a significant change from wetland to terrestrial vegetation in the period from 1991 to 2008 (Bowen and Simpson, 2010), but in the past few years the plant communities of the Macquarie Marshes have shown a positive response to environmental flow releases and water strategies implemented in the marshes by the regulatory authorities.

In this paper we define critical conditions for different vegetation patches in the northern region of the Macquarie Marshes (Figure 1a). This analysis is also an update in the development of an eco-hydraulic vegetation evolution model for the Macquarie Marshes. The model implements a set of deterministic rules in order to determine vegetation succession from wetland vegetation to terrestrial species. Previous work has been focused on obtaining vegetation transitions rules for different vegetation associations (Sandi et al., 2015; Sandi et al., 2016a; Sandi et al., 2016b), especially Common Reeds and Water Couch. Additionally, a full assessment of the previously developed transition rules was presented by Sandi et al. (2016b) concluding that further research was required in order to obtain more transition rules. This publication also addresses transition rules for River Red Gum association patches. The model by Sandi et al. (2016b) was based on the period from 1991 to 2008 due to the availability of vegetation maps for these two years. Here, we have extended the analysis for the period from 2008 to 2013.

©2017, IAHR. Used with permission / ISSN 1562-6865 (Online) - ISSN 1063-7710 (Print)

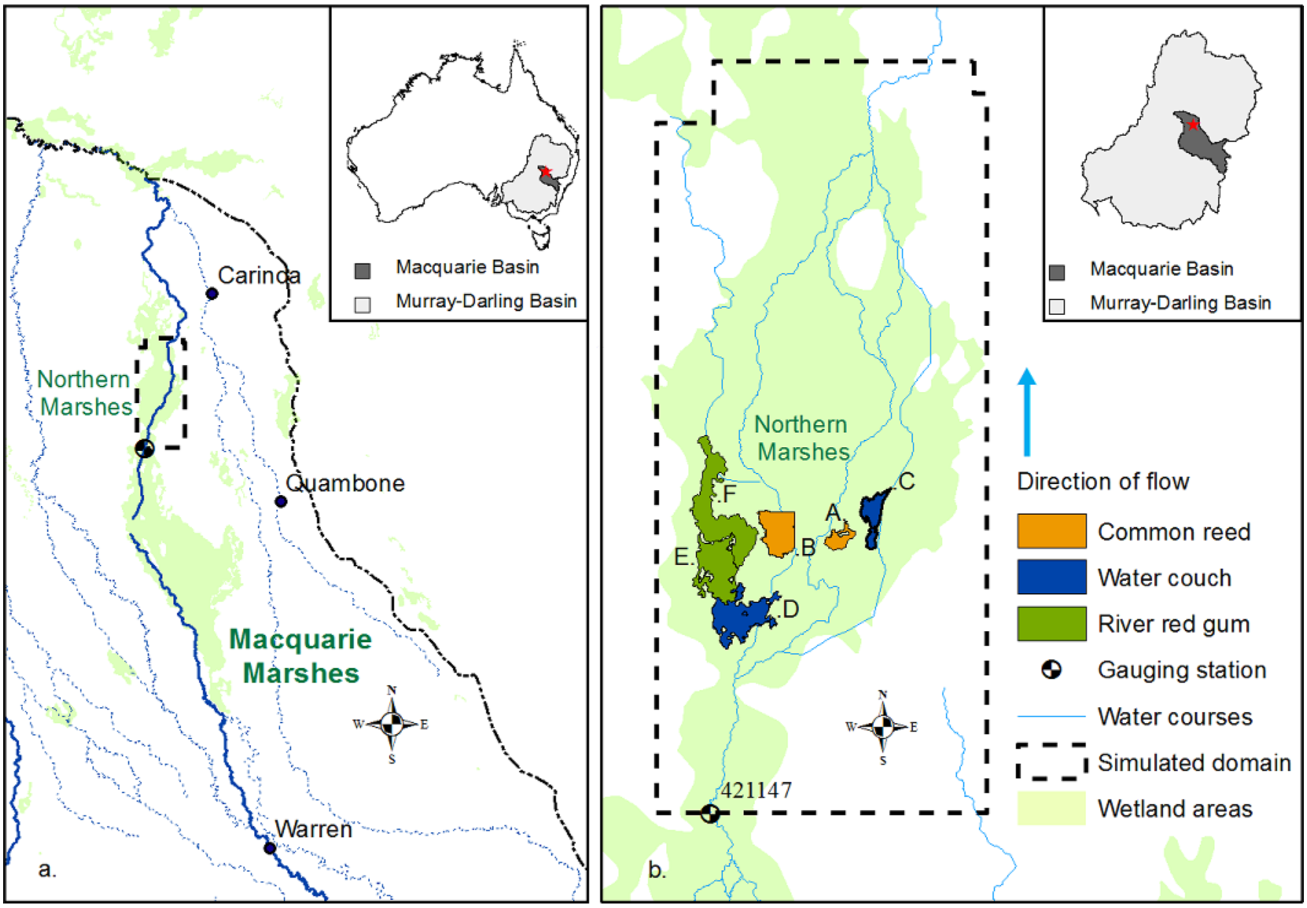

Figure 1. a) Location of the Macquarie Marshes b) Description of study area.

2 METHODS

2.1 Study site and hydrodynamic model set-up

The northernmost part of Macquarie Marshes is an inland wetland system that covers around 325 Km^2 of the lowland floodplain of the Macquarie River, before it joins the Barwon River. This area was selected for the development of the eco-hydraulic model because it holds most of the Macquarie Marshes Ramsar site, data availability and because it hosts most of the plant associations present in the Macquarie Marshes. The low gradient of the floodplain (0.00036 m/m) produces a meandering well defined channel that becomes almost imperceptible as it reaches the core marshes and branches into multiple directions so that there is no specific flow path. Water is delivered to vegetation communities during flood events, when the overbank flows are able to connect the multiple swamps, lagoons, reed beds and woodlands that conform the mosaic of the Macquarie Marshes.

A large scale approach is used in order to minimize computational cost so a quasi 2D-hydrodynamic model, the VHHMM 1.0 (Riccardi, 2000), was built on a 90 m squared digital elevation model (DEM). The implemented resolution describes the domain with a total of 40096 active elements which allows for feasible data processing and simulation of the site with no compromise to the overall results. The VHHHMM 1.0 implements a numerical solver for simplified Saint-Venant mass and momentum conservation equations. The momentum conservation equation describes discharge relations of the link between active elements and it can take different forms based on the type of element (channel-channel, channel-floodplain and floodplain-floodplain). There are also special relations for hydraulic structures such as culverts and bridges. Water depth in every element at every time-step is calculated from the mass conservation equation. Methods for model calibration are presented by Sandi-Rojas et al. (2014). Daily discharges were obtained from the Pillicawarrina gauging station (No. 421147) located in the Macquarie River. The simulations were carried for a sequence of 23 consecutive years covering the period from June 1990 to May 2013. Initial conditions were assumed as no flow, which agrees with very low flows generally observed in June and May. After 2002 and until 2008, the discharges entering the Macquarie Marshes had a considerable reduction (Figure 2). Our new analysis includes simulation of five additional hydrologic years, from 2009 to 2013.

 ©2017, IAHR. Used with permission / ISSN 1562-6865 (Online) - ISSN 1063-7710 (Print)

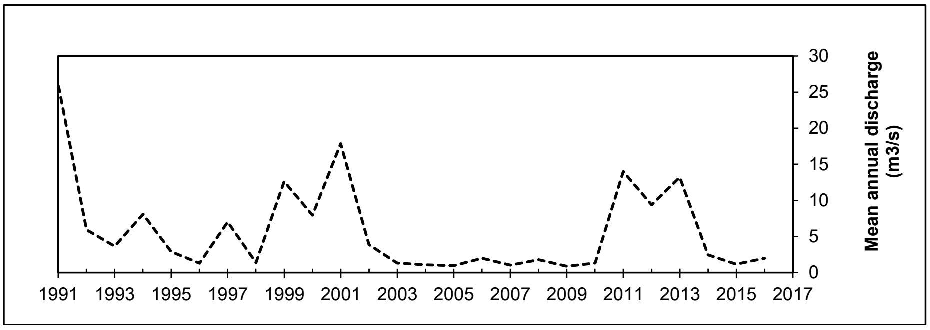

Figure 2. Mean discharges entering the Macquarie Marshes.

2.2 Selected vegetation patches

During the period from 1991 to 2008, most of the wetland area that transitioned to terrestrial species and dryland corresponds to understory species such as Water Couch and Common Reed (Bowen and Simpson, 2010). Some of these patches showed a transition back to wetland vegetation by the year 2013; however, many of them were still invaded by terrestrial vegetation. We have selected four vegetation patches of Common Reed and Water Couch (Figure 1b) in order to see the effects of water delivery to understory species. Vegetation conditions at the beginning of the period were assumed to be good. Non-transitional patches reported little change in 2008 and 2013. On the other hand transitional patches presented a complete shift to terrestrial species in 2008, mainly invaded by chenopod shrubland. In 2013, the transitional Common Reed patch reverted back to original conditions. Though the forest and woodland overstories had very little change in extent from 1991 to 2008 (Bowen and Simpson, 2010), the condition of some of the patches was heavily affected. We have selected two River Red Gum patches. Patch E was reported to have 80% dead trees and the understory was encroach by terrestrial species in 2008. A full list and description of the selected patches is presented in Table 1.

Table 1. Patch transition history.

Patch	Vegetation on 1991	Vegetation on 2008	Vegetation on 2013	Changes	Conditions
A	Common reed	Terrestrial	Common reed	Transitional	- Transition back to wetland understory by 2013
B	Common reed	Common reed	Common reed	Non transitional	- Good condition in 2008 and 2013
C	Water couch	Terrestrial	Terrestrial	Transitional	- Complete transition
D	Water couch	Water couch	Water couch	Non transitional	- Good condition in 2008 and 2013
E	River red gum	River red gum	River red gum	Non transitional	- <10 % dead trees - Chenopod shrubland invasion in 2008
F	River red gum	River red gum	River red gum	Non transitional	- 80% dead trees - Healthy mixed marsh understory during the whole period

2.3 Fractional coverage and minimum inundation

Use of seasonal fractional cover maps, developed by the Joint Remote Sensing Research Project (JRSRP) (OEH, 2014), in combination with a hydraulic description of the flow regime has proven to be a convenient approach for studying vegetation evolution in the Macquarie Marshes(Sandi et al., 2016a). Changes in green and baresoil coverage can suggest critical conditions or succession of plant associations to terrestrial species. However, frequency of inundation is the determining factor for a vegetation succession. Our model estimates vegetation response according to water requirements which are different for every plant association. These requirements are time aggregated characteristics such as the range of inundation depth and the percent exceedance time during a hydrologic year (Sandi et al., 2015). In this publication, we focus the analysis on the areas with minimal inundation. Water delivery strategies in the Macquarie Marshes estimate that an inundation period of three months is adequate for maintaining the health of most the plant communities. Therefore, we consider the minimum inundation when 5 cm of water are exceeded 25% of the time.

3 RESULTS AND DISCUSSION

Figure 3 presents the relation of minimum inundation against fractional green coverage for understory species during the period of 1991 to 2008. Results revealed that less than 15% of the patch area with minimal flood is a threshold for potential terrestrial and dryland vegetation invasion of Common Reed (Figure 3a). Fractional green data shows that in average 60 % of Patch B remains green even on the cases where minimum inundation approaches the area threshold. This relation as well as the inundation area threshold is better represented in Figure 4b, where Patch B had minimum inundation in only 15% of the area from 2003 to 2010 without a significant change on green coverage. In the transitional case, Patch A, fractional green coverage decreased form 50% in 1991 to practically no green coverage in 2005 (Figure 4a). Common Reed is a resilient species that can survive extended periods without water by slowing down growth, shedding leaves, and by having quick recovery to following inundations (Roberts and Marston, 2011). Patch A had a period of withering-recovery for most of the 1990's with a frequency of 0.5 adequate minimum inundation up until 2002. The following nine dry years lead to a complete transition to terrestrial species. According to our results, the recovery of Patch A was triggered after 2011 when minimum inundation requirements where met again. This recovery is more likely due to colonization from surrounding patches since it is unlikely for rhizomes to survive almost a decade without water and also because Common Reed does not generate long lived seed banks (Rogers, 2011). Additionally, 2011 to 2013 floods for Patch A were small in comparison to Patch B; but seedlings require low depths and short duration in order to establish, making recolonization possible. According to our results, critical frequency of minimum inundation can be defined as one in two years. However, in order to have a complete transition to terrestrial species a Common Reed patch should undergo four years without an adequate minimal flood (2002-2003). Given this analysis, in 2013, Patch A was still under critical conditions and it could transition back to terrestrial vegetation. Further simulation of hydrologic years 2014 to 2016, which are low flow years (Figure 2), will provide insight in the persistence of this vegetation patch, but it is likely that the patch have undergone stress and it might require adequate minimum flood during 2017 in order to survive.

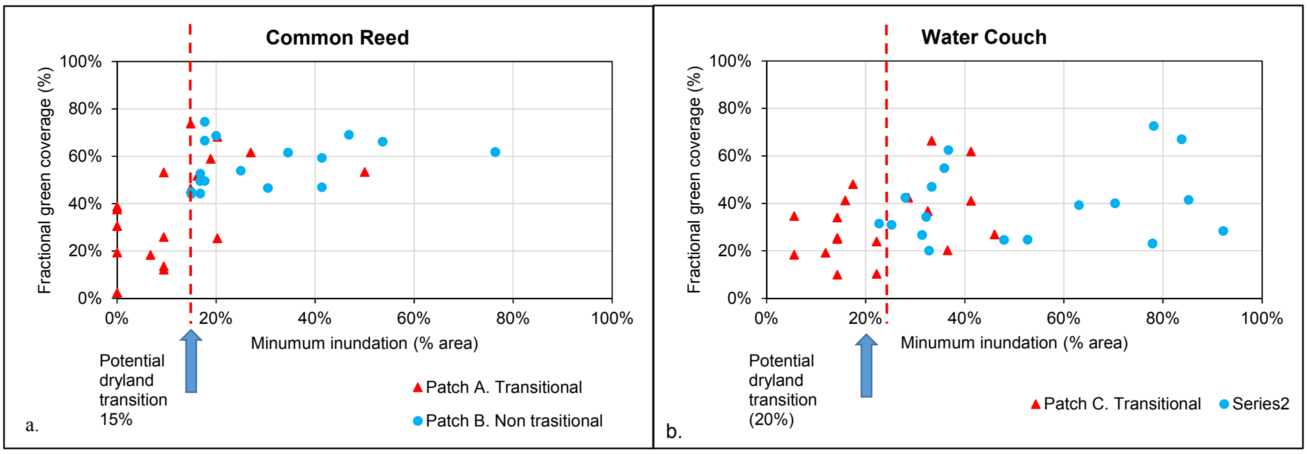

Figure 3. Thresholds for potential dryland and terrestrial species encroachment on a) Common Reed and b) Water Couch patches.

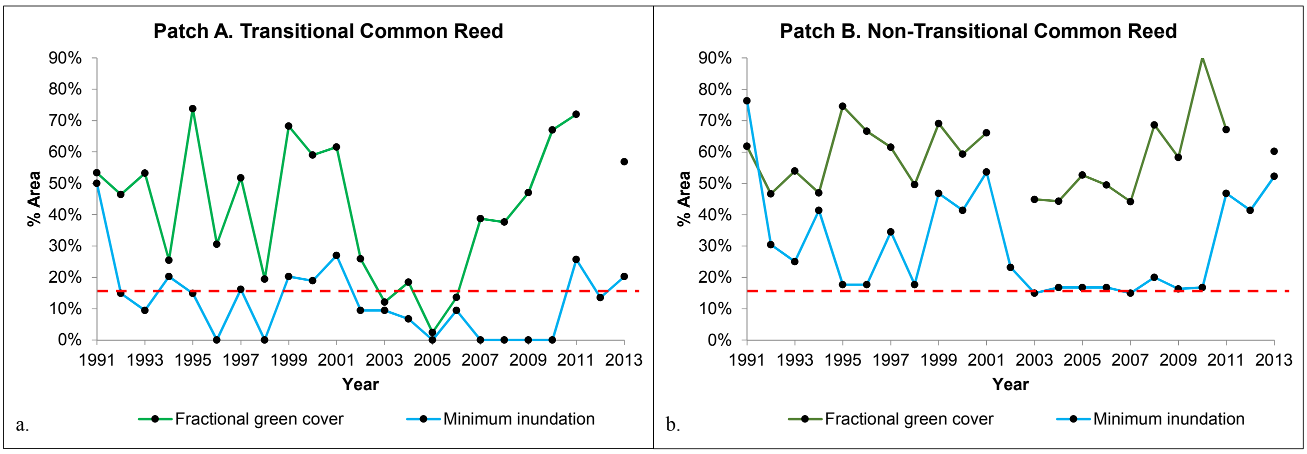

Figure 4. Fractional green cover and minimum inundation evolution for a) transitional and b) non- transitional Common Reed patches.

 ©2017, IAHR. Used with permission / ISSN 1562-6865 (Online) - ISSN 1063-7710 (Print)

A similar analysis of the Water Couch patches showed some important differences in relation to critical conditions. First, the area threshold for minimum inundation is of 20% (Figure 2b), and and transitional patch (Patch C) had frequency of adequate minimum inundation of 67% from 1991 to 2003 (Figure 5a). This shows that Water Cocuh is a less resilient species than Common Reed since it requires almost annual adequate minimum inundation in order to survive. Reproduction of this species is usually from rootstock so in cases of one year with little flood plant recovery is possible, but consecutive dry years may put a significant stress on the plant community specially because seedlings are sensible to dry conditions (Roberts and Marston, 2011). On the other hand, prolonged overwatering can also rot the plants leading to losses in green cover extent. Seasonal green fractional coverage maps are a good indicator of the conditions for Water Cocuh as they represent autumm season from March to May, which is after the season of growth in summer (December to February). Our analysis suggest that the transition to terrestrial species that occurred in Patch C is a combination of little growth in 1995 to 1998 and overwatering in the years 1999 to 2001. After 2006, fractional green coverage increased which represents the establishment of the terrestrial species and the dissication of Water Couch. Distance from the patch to main water courses is recognized as an important factor for determining persistance of vegetation (Bino et al., 2015). In our analysis, distance to channels is replaced by the use hydrodynamic simulations that predict the hydraulic conditions on site and by considering the proximity of other vegetation patches with the same vegetation. This is evidenced by the transitional Water Couch patch that was unable to reestablish after 2011 despite experiencing adequate minimum inundation because it was far from other patches that could potentially colonize (Figure 5b). Given this result, we can infer that Patch C reached critical conditions by the year 2003 and made complete transition to terrestrial species by 2005. Recent water delivery to the patch was unable to trigger a recovery possibly due to rootstock dying off.

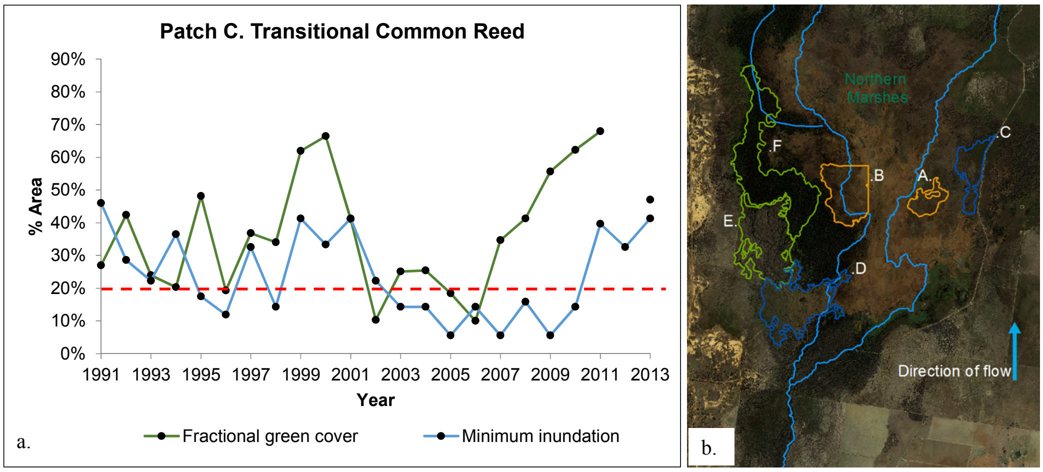

Figure 5. a) Fractional green cover and minimum inundation evolution for transitional Water Couch patch. b) Patch location in relation to water courses.

Determining critical conditions for overstory species such as River Red Gum is complicated because these trees can survive under a wide range of watering conditions. The understory of Patch E was reported as having invasion of terrestrial species by 2008 (Table 1) while understory present in patch F remained with healthy mixed marsh from 1991 to 2013. This is consistent with the position of Patch E, which is located further away from the water course than patch F and also higher in the floodplain. Patches of River Red Gum woodland that are closer to water courses receive more water than forests at the fringe of the marshes. Figure 6 presents green coverage and minimum inundation evolution in Patches E and F. Specific water requirements for plant associations have an overlap of range of water depth and exceedance time for River Red Gum and Water Couch (Sandi et al., 2015), so Water Couch minimal inundation area threshold is used as an indicator of dry conditions for understory species in River Red Gum patches. Watering conditions in Patch E were insufficient to support understory species from 2003 to 2005 which is evidence by a drop of green fractional coverage. Roberts and Marston (2011) reported that forest and woodlands higher in the floodplain require a minimum frequency of inundation of four in ten years and a maximum dry interval of seven consecutive years. The dry period from 2003 to 2010 evidently lead to the reported dying of 80% of the trees of Patch E and colonization of terrestrial evidenced by the increased green coverage after 2006. Inflows over the following years produce high inundation from 2011 to 2013; however, there was no recovery because dry trees probably were no longer capable of epidemic growth and new seedling and sapling may have drowned. The latter is evidenced by the loss of terrestrial vegetation species by the year 2013 more likely due to drowning. Further simulation of low flow years 2014 to 2016 are likely to reveal small inundation that are insufficient for maintaining understory or juvenile overstory vegetation on the patch.

In Patch F there was no decline of fractional green vegetation during the dry period (Figure 6b). Understory area threshold indicate little inundation in 2005 and 2007, but in 2008 an increase in the inundation produced good health of the understory as reported by Bowen and Simpson (2010). River Red Gums located lower in the floodplain can maintain optimal conditions up to a maximum of three consecutive dry years (Roberts and Marston, 2011). Our results show that Patch F was able to maintain optimal conditions during the whole period of analysis which is consistent with River Red Gum persistence of 90% estimated by Catelotti et al. (2015). Based on this results, we propose the use of understory area thresholds as indicators for River Red Gum; however, a differentiation is necessary for patches with healthy wetland understory. An interval of three dry years can transition a good condition patch to one with poor conditions and another consecutive seven dry years will completely transition the patch to terrestrial vegetation. For recovery and survival of the patch, adequate minimum inundation of understory species can be used as an indicator.

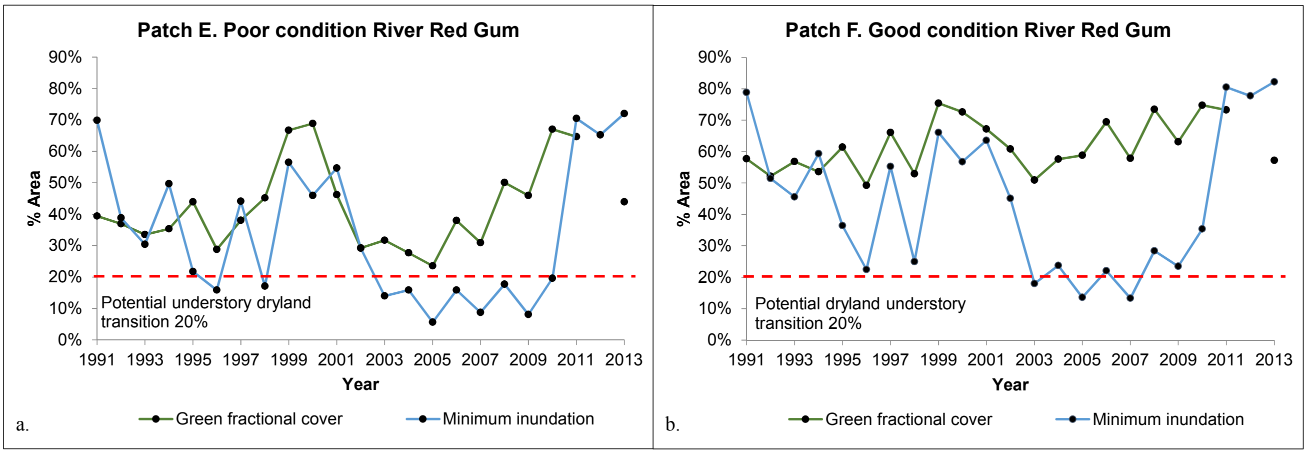

Figure 6. a) Fractional green cover and minimum inundation evolution for a) poor condition and b) good condition River Red Gum patches.

4 CONCLUSIONS

The use of fractional green coverage maps in combination with hydrodynamic modelling has proven an effective tool for analyzing vegetation transition rules in the Macquarie Marshes. Focus on minimum inundation lead to simple rules that can be used for vegetation shift predictions in future research. Additionally, including a period of five years of flow simulations provided insight on recovery of Common Reed and Water Couch patches which had not been possible in previous analysis. Finally, critical watering conditions of understory species may be used as a long term indicator of the conditions of River Red Gum, but differentiation on the understory condition must be carried out.

REFERENCES

Bino, G., Sisson, S.A., Kingsford, R.T., Thomas, R.F. & Bowen, S. (2015). Developing State and Transition Models of Floodplain Vegetation Dynamics as a Tool for Conservation Decision-Making: A Case Study of the Macquarie Marshes Ramsar Wetland. *Journal of Applied Ecology,* 52**,** 654-664.

Bowen, S. & Simpson, S. (2010). *Changes in Extent and Condition of the Vegetation Communities of the Macquarie Marshes Floodplain 1991-2008*, Final report to the NSW Wetland Recovery Program. Sydney: River and Wetlands Unit, Department of Environment, Climate Change and Water, NSW.

Catelotti, K., Kingsford, R. T., Bino, G. & Bacon, P. (2015). Inundation Requirements for Persistence and Recovery of River Red Gums (Eucalyptus camaldulensis) in Semi-Arid Australia. *Biological Conservation,* 184**,** 346-356.

Kingsford, R. T. (2000). Ecological Impacts of Dams, Water Diversions and River Management on Floodplain Wetlands in Australia. *Austral Ecology,* 25**,** 109-127.

OEH (2012). *Macquarie Marshes Ramsar Site: Ecological Character Description Macquarie Marshes Nature Reserve and U-Block Components*, Sydney: NSW Department of Premier and Cabine.

OEH (2014). *Seasonal Fractional Cover - Landsat, JRSRP Algorithm*, NSW coverage, Joint Remote Sensing Research Project.

Riccardi, G. (2000). A Cell Model for Hydrological-Hydraulic Modeling. *Journal of Environmental Hydrology,* 8(15), 1-13.

Roberts, J. & Marston, F. (2011). *Water Regime for Wetland and Floodplain Plants: A Source Book for the Murray-Darling Basin, Canberra.* National Water Commission.

Rogers, K. (2011). *Vegetation. Flodplain Wetland Biota in the Murray-Darling Basin: Water and Habitat Requirements*. Australia.

 ©2017, IAHR. Used with permission / ISSN 1562-6865 (Online) - ISSN 1063-7710 (Print)

Rogers, K., Ralph, T. & Imgraben, S. (2010). *Water Requirements of Biota, Geomorphology and Climate Change in the Macquarie Marshes*. Ecosystem Response Modelling in the Murray-Darling Basin. CSIRO Publishing, Melbourne.

Sandi-Rojas, S.G., Rodríguez, J.F., Saco, P., Riccardi, G., Wen, L., Saintilan, N., Stenta, H., Trivisonno, F. & Basile, P.A. (2014). *Macquarie River Floodplain Flow Modeling: Implications for Ecogeomorphology*. River Flow 2014. CRC Press.

Sandi, S.G., Rodriguez, J.F., Saco, P.M., Saintilan, N., Wen, L. & Kuczera, G. (2015). Development of a Vegetation Dynamics Model for Freshwater Wetland Assesment in the Macquarie Marshes. *36th Hydrology and Water Resources Symposium* 2015 Hobart, Tasmania.

Sandi, S.G., Rodriguez, J.F., Saco, P.M., Wen, L. & Saintilan, N. (2016a). Linking Hydraulic Regime Characteristics to Vegetation Status in the Macquarie Marshes. *11th International Symposium on Ecohydraulics 2016.* Melbourne, Australia.

Sandi, S.G., Rodriguez, J.F., Saco, P.M., Wen, L. & Saintilan, N. (2016b). *Simulation of The Vegetation State and Flow Regime Interaction in the Macquarie Marshes.* River Flow 2016. CRC Press.

Proceedings of the 37th IAHR World Congress
August 13 – 18, 2017, Kuala Lumpur, Malaysia

HYDRODYNAMIC INFLUENCE OF HEAD-HORN STRUCTURE OF CAVE FISH SINOCYCLOCHEILUS TILEIHORNES ON FLOW FIELD

FAKAI LEI[(1)], MENGZHEN XU[(2)], ZIQING JI[(3)], ZHAOYIN WANG[(4)] & MICHAEL ANDREW BISSET[(5)]

[(1,2,3,4,5)] State Key Laboratory of Hydroscience and Engineering, Tinghua University, Beijing, China,
lfj@mails.tsinghua.edu.cn
[(5)]Department of Physics, Tinghua University, Beijing, China,

ABSTRACT

Sinocyclocheilus Tilei.hornes (Tilei.) is one of the species of Chinese blind cave fishes, which has specific structures, e.g. head-horn. During thousands or millions of years living in caves, the species has developed a number of unusual adaptions, such as typical pigmentation and eyes degeneration into needle-like size or useless, developing a horn of two tile-like bulges. However, the function of the horn is not yet understood. The aim of this study is to reveal whether or how the horn function in helping the blind cavefish move and prey. Scientific hypothesis is proposed that the horn helps strengthen the interaction between the cave fish and the water flow, and make it easier to sense the signal from water flow. In this study, we attempt to understand the hydrodynamic image characteristics produced by the head horn of Tilei. by comparison of the pressure, flow field, resistance and lift force of Tilei. and *Sinocyclocheilus Angus.tiporus* (Angus., a species that has similar size and body shape as Tilei., but without horn) under the same hydrodynamic conditions. Numerical simulations were conducted using CFD (computational fluid dynamics) software. Simulation results show that there was a flow stagnation and high-pressure zone under the horn of Tilei., resulting in the pressure gradient of Tilei. as high as twice of that of Angus.. In addition, Tilei. received significantly higher drag force and lift force than Angus. under the same flow condition. Such phenomenon was more remarkable under higher simulated flow velocity, which suggests that Tilei. might be slow swimmers. Furthermore, it was indicated that the interaction between the cave fish and the water flow was much more intensive for Tilei. than for Angus., given the projection speed of the water flow as a standard. Therefore, we believe that the head-horn structure of cavefish may help strengthen their sense efficiency in water flow.

Keywords: Blind fish; lateral line; computational fluid dynamics (CFD); 3D scan; pressure gradient.

1 INTRODUCTION

Cavefishes, or hypogean fishes, in a broad sense, are fish-shaped animals living in caves or similar circumstances; in a narrow sense, are fishes living in some perennial water karst caves, underground rivers and lakes or other special ecological environments (Zhao et al., 2009). Some species of the cavefishes, termed as troglobites, can only live in cave or similar circumstance and often display specific features adapting themselves to subterranean life, such as the rudimentary eyes and scales and loss of pigmentations; while some of the cavefishes, termed as troglophile, appear in a cave or groundwater environment periodically; the third group, termed as trogloxene, live close to caves or at the very entrance of the caves, but cannot live exclusively inside the caves (Schiner et al., 1854).

There are 122 typical troglobite fish species known in the world, belonging to 10 orders, 19 families and 53 genera (Romero et al., 2001; Zhao et al., 2009). They mainly inhabit tropical and subtropical regions between the latitude of 40°and the Tropic of Capricorn (Zhao et al., 2006). To adapt the cave environment with constant darkness and little food, they have evolved some characteristics that save energy, e.g. loss of eyesight, to ensure that they survive more easily (Jaggard et al., 2017).

Much attention has been paid on the degraded visual system of cavefishes. Using research technique, it was found that the eye primordia of cavefish formed during the embryonic period did not grow as the embryonic developed according to the studies of anatomy, gene and protein. The embryonic eye gradually embedded into the blind fish's orbital (Zhao et al., 2009). Langecher (1995) and Romero (2009) confirmed that the visual organs degeneration of cavefish would affect some of their behaviors, such as territorial behavior, invasive behavior and others.

Besides the visual system, the lateral line system of cavefish has also been widely studied. Montgomery (2001) did a lot of work on the lateral line system of Mexican cavefish *Astyanaxs fasciatus* (Astyanax) by comparing the reaction of the fishes before and after treated with cobalt and gentamicin, which could destroy the lateral line system. His study verified that the lateral line system played an important role in sensing the surrounding environment. Similar studies were also carried out by Coombs (2014) and Kulpa (2015). The localization mechanism of the lateral line system was studied, applying PIV (Particle Image Velocity) techniques and CFD (Computational Fluid Dynamics) simulations. It was assumed that the lateral line of

 ©2017, IAHR. Used with permission / ISSN 1562-6865 (Online) - ISSN 1063-7710 (Print)

Mexican cavefish could figure out the surrounding hydrodynamic images through the sensing of the water pressure, flow velocity, pressure gradient, and other such signals carried by water flow (Windsor, 2008; 2010). Based on such assumption, the localization mechanism was understood and used in explaining how Mexican cavefish moved towards a wall but never collided with the wall (Windsor, 2008; 2010). Coombs (2014) implemented a pressure gradient sensing experiment and Engelmann (2002) studied how fishes sense a vibration source using the similar techniques as Windsor (2008; 2010).

These previous studies help us understand the function of the lateral line system of Mexican cavefish Astyanax. However, they did not yet explain how the lateral line system function in turbulent flow. In addition, most of these studies were carried out for Astyanax, which has a much simpler shape feature compared with the Chinese cavefishes Tilei. and Rhino. (Figure 1). Thus, it was suspected that whether the knowledge obtained from Mexican cavefish studies are also be applicable for Tilei. and Rhino.. In fact, Jeffery (2000) investigated the distribution of the superficial nuromast of Astyanax, and indicated that Astyanax has more surface neuromasts than the trogloxene species of the same family of Astyanax. On the contrary, Yang (2016) showed that the number of neuromasts in the adult Sinocyclocheilus species ranked as the following: *Sinocyclocheilus graham* (trogloxene) > *Sinocyclocheilus Rhino.cerous* (troglophile) > *Sinocyclocheilus anshuiensis* (troglobites). It means that the better the fish dwells to the cave, the weaker their lateral line system is, which is paradoxical to the Darwin's doctrine of evolution in somehow as the lateral line system was believed as the most important alternative organ for the degraded eyesight.

Attention were also paid on the special structure 'head horn' of Tilei. and Rhino., which might help the cavefishes sense the surroundings. Inspired by the Darwin's doctrine of evolution, Chen (1994) believed that the head horn in Rhino. was a synthetical sensory organ. Li et al. (1997) suggested that the head horn could be a protective organ rather than a sensory organ based on anatomy of the horn. However, none of them could demonstrate their hypotheses.

To our best knowledge, this study is the first to use digital simulation to research the head horn structure of chinese cave fish Tilei. and Rhino., which make use of the 3D scan technology and ANSYS FLUENT model to calculate the flow field and pressure distribution of the fish under the different water flow conditions. Comparing the flow fields and pressure distributions differences between Tilei. and Angus., we wish to figure out the function of the head horn on the darkness-underground environment adapting process of blind cave fishes. Something imperfect is that we only simulated the scene that a constant flow passed along the immobile fish models, which may not be able to reflect the fact that in the underground river or cave, the water flow is very slow and the relative velocity is produced mainly by the swimming of cave fish. What is more, so far, is that we only attempted FLUENT Laminar single - phase flow 3D model, which may not be suitable if the simulated velocity is higher than some threshold.

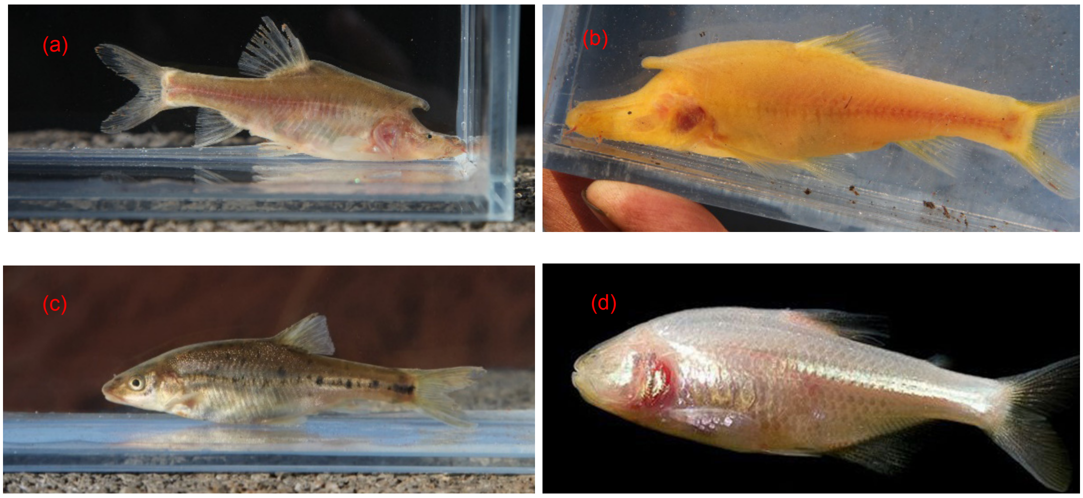

Figure 1. Studied cavefishes: (a) *Sinocyclocheilus Tilei.hornes* (Tilei.), (b) *Sinocyclocheilus Rhino.cerous* (Rhino.), (c) *Sinocyclocheilus Angus.tiporus* (Angus.), (d) *Astyanax fasciatus* (Astyanax).

2 MATERIALS AND METHODS

Tilei., Rhino., and Angus. are sympatric species of Cypriniformes, and their mature individuals share similar sizes (Table 1). The major difference is that Tilei. and Rhino. have head horn structures, while Angus. does not. Therefore, the influence of the head horn structure could be implied by comparing the flow field characteristics surrounding the species with and without horn. As Tilei. and Rhino. share similar biological features: the approximately similar size, duckbilled head and head horn, loss of eyesight, we could just study one species of them for the study of head horn. Tilei. was selected as the objective and the characteristics and function of the head horn were studied.

The 3D digital models of Tilei. and Angus. were obtained, applying a 3D scanning technology (Insight3 scanner produced by the Italian Open Technologies Company) on the specimens sampled from Luoping in Yunnan Province in the southwest of China. The scanner supports the axis alignment, feature alignment (i.e., no point splicing) and point alignment, and is able to control the resolution being less than or equal to 0.05 mm. The fish model can be ensured to bear a close resemblance to the real fish; in fact, we can even distinguish the fish texture. Figure 2 shows the scanning models of the specimens of Tilei. and Angus.. After repairing and sparsing the model mesh using the Geomagic Control, the digital models were loaded into ANSYS CFD module for simulation of the hydrodynamic characteristics and the force surrounding the fish models. The simulation was carried out under the condition that a constant flow passed along the immobile fish models. The differences in pressure distribution, resistance and lift force between the two fishes were therefore indicated to show the function mechanism of the head horn structure.

Table 1. Sizes of 3D models of Angus. and Tilei.

Species	Length(cm)	Width(mm)	Height(mm)	Area(cm^2)	Volume(cm^3)
Angus.	10.130	1.102	2.259	46.074	12.2103
Tilei.	8.957	1.064	2.181	37.316	4.4162

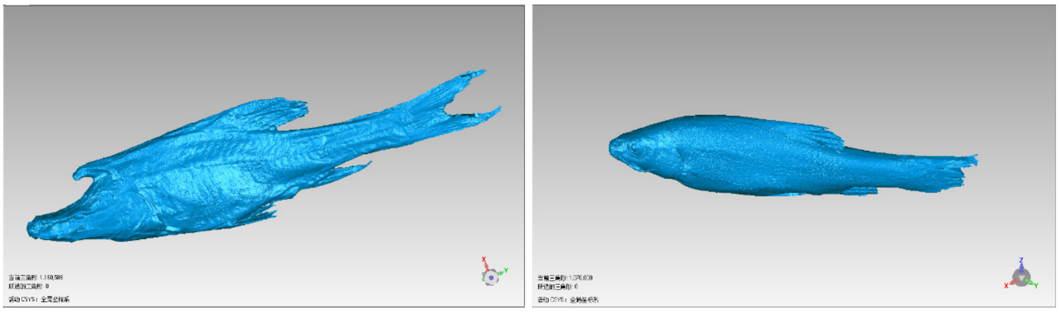

(a) (b)

Figure 2. The 3D digital fish model built by 3D scanning: (a) Tilei., (b) Angus.

ANSYS ICEM was applied to build calculation model. To avoid the influence of the fish tail to the flow field, the fish body was kept straight. Moreover, the fish head was kept facing towards the coming flow, and the flow velocity around the fish was simulated. The computational area was assigned to be ten times of the fish body size to ensure that the flow field was large enough and noisy information created by the interaction between the fish and water flow could be ignored. The mesh parameters were set in the ANSYS ICEM as follows:

(1) Mesh type: Tetra / Mixed,
(2).Mesh Method: Robust (Octree),
(3).Smooth Iterations: 5,
(4).Min quality: 0.4.

The simulation was performed using FLUENT Laminar single - phase flow 3D model and SIMPLIC iterative algorithm. The physical parameters of water flow were assigned as follows: the gravitational acceleration g = 9.73 m/s^2, the density of water, ρ = 991 kg/m^3, the kinematic viscosity coefficient, $\mu = 1.144 \times 10^{-3}$ kg/(m·s), considering that the cavefish specimens were sampled from high elevation (1900 m a.s.l.) and the water temperature was measured as 18.5 degrees centigrade.

3 RESULT AND DISCUSSION

3.1 The pressure distribution

All simulation scenarios showed that the pressure distribution could be divided into several parts for both Tilei. and Angus. (Figure 2). From the head to the widest part at the middle of the fish bodies, the pressure value decreased sharply, and from the widest part to the tail, the pressure value increased remarkably. The maximum pressure appeared at the region around the nose; while the minimum pressure appeared at the widest part. The pressure distribution pattern was similar to that reported for the Mexican cavefish (Windsor, 2010). The specific characteristic of the pressure distribution of Tilei. is that a flow stagnation and high-pressure zone was presented under its horn, causing the pressure gradient in the head lateral line region to be twice higher than Angus..

Figure 3 (a)-(f) show the pressure distributions along Tilei. at different flow velocities u=0.01, 0.05, 0.2, 0.4, 0.6, 1.0, and 1.5 m/s. Figure 3 (A)-(F) show the pressure distributions along Angus. for the corresponding velocities. It was indicated that the pressure value varied at different velocities, while the pressure gradient direction did not change. Therefore, the head horn was supposed to be helpful for Tilei. to sense gradient

 ©2017, IAHR. Used with permission / ISSN 1562-6865 (Online) - ISSN 1063-7710 (Print)

changes even it is very subtle. Windsor (2010) confirmed that, using their lateral line sensory system cavefishes were able to get detailed information by gliding alongside them and sensing pressure gradient changes in the flow field around their bodies.

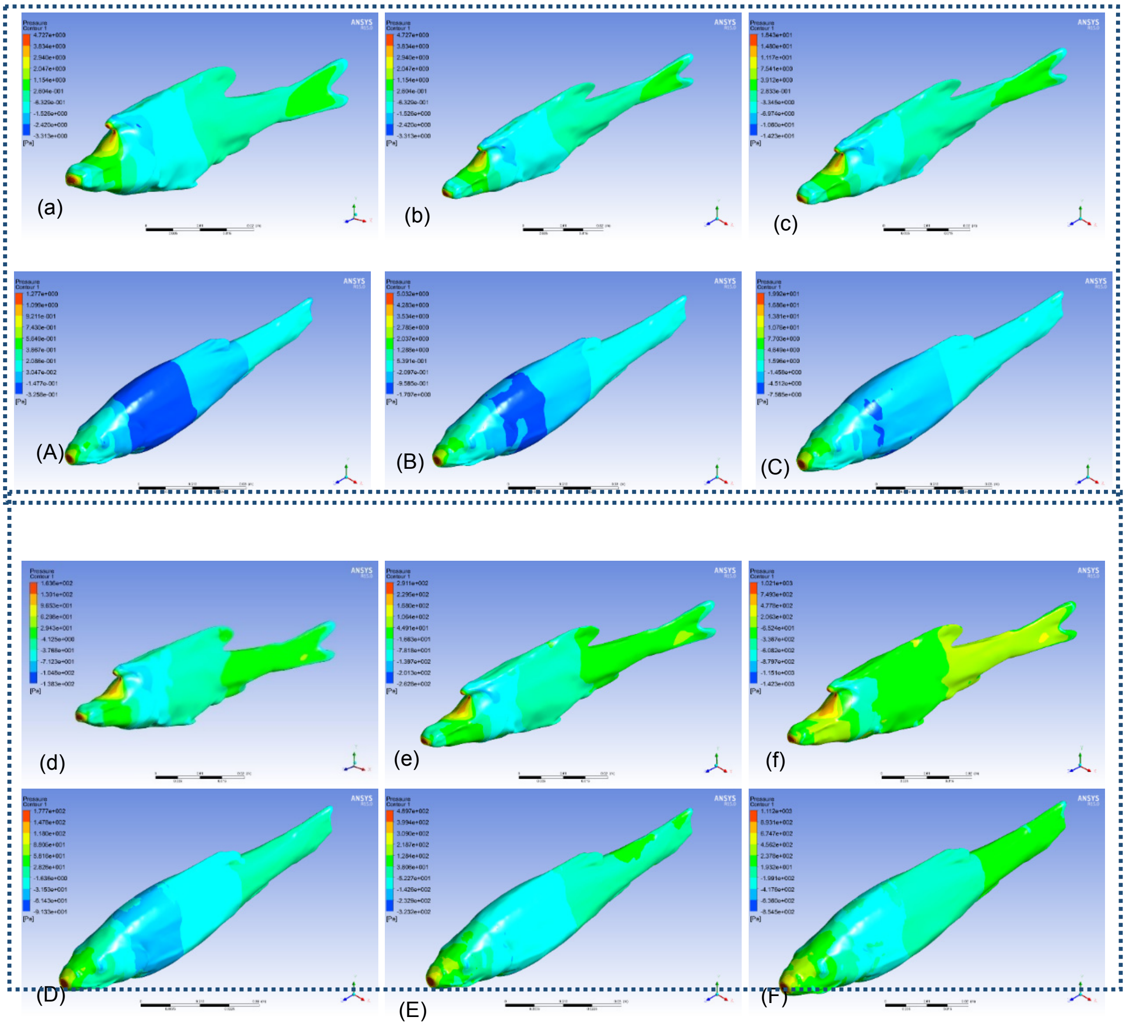

Figure 3. Pressure distributions along Tilei. (a-f) and Angus. (A-F) revealed by Computational Fluid Dynamics (CFD) simulations for the condition of one constant flow passed along the still fish: (a, A) v=0.05 m/s, (b, B) v=0.10 m/s, (c, C) v=0.20 m/s, (d, D) v=0.40 m/s, (e, E) v=0.60 m/s, (f, F) v=1.00 m/s, (g, G) v=1.50 m/s.

3.2 The drag force and lift force of cavefish

As the fish was still in the flow, it was forced by the drag force, F_D, which was parallel to the flow direction, and the lift force, F_L, which was vertical to the flow direction. The drag force was composed of a friction resistance, F_f and a pressure resistance, F_p:

$$F_D = F_f + F_p \qquad [1]$$

Where the frictional resistance, F_f was related to the viscosity of the water flow, and the pressure resistance, F_p was mainly dependent on the shape of fish. Both F_f and F_p can be expressed as the product of the kinetic energy (ρu ^ 2) / 2 of the unit volume water flow, the area of a certain fish surface and a resistance coefficient:

$$F_f = 0.5C_f \rho u^2 A_f \qquad [2]$$

$$F_p = 0.5C_p \rho u^2 A_p \qquad [3]$$

where C_f and C_p were the resistance coefficient of friction resistance and pressure resistance, respectively. A_f was the area of shear stress, A_p was the projection area of the fish in the perpendicular direction of the flow.

©2017, IAHR. Used with permission / ISSN 1562-6865 (Online) - ISSN 1063-7710 (Print)

Therefore, the drag force can be expressed as

$$F_D = 0.5 C_D \rho u^2 A_D \qquad [4]$$

where C_D was the resistance coefficient of drag force, and A_D was the projection area of the fish in the perpendicular direction of the flow. Therefore, A_D was equal to A_p, $A_D = A_p$

The lift force was expressed as

$$F_L = 0.5 C_L \rho u^2 A_L \qquad [5]$$

where C_L was the coefficient of lift force, and A_L was the max projection area of the fish.
Considering the difference of the fish size, the drag force and lift force were calculated per weight as

$$F_{Dp} = 0.5 C_D \rho u^2 A_D / G \qquad [6]$$

$$F_{Lp} = 0.5 C_L \rho u^2 A_L / G \qquad [7]$$

where G was the weight of the fish.

F_{Dp} and F_{Lp} were calculated for the inlet velocities u=0.01, 0.05, 0.2, 0.4, 0.6, 0.8, 1.0, and 1.5 m/s and are shown in Figures 4 and 5.

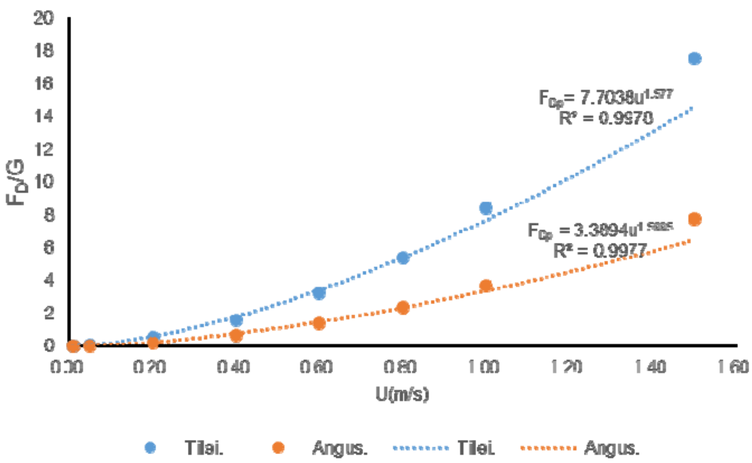

Figure 4. Relations between unit weight drag force and flow velocity for Tilei. and Angus.

The unit weight drag force was positively correlated to the flow velocity for both Tilei. and Angus.. The relationship between the drag force and the inlet flow velocity was indicated as $F_{Dp} = 7.7038u^{1.5770}$, $R^2 = 0.9978$ for Tilei., and $F_{Dp} = 3.3894u^{1.5995}$, $R^2 = 0.9977$ for Angus.. Tilei. received significantly higher drag force than Angus. under the same flow condition. This phenomenon was more remarkable as the inlet flow velocity increased. It is suggested that Tilei. might be a slower swimmer compared with Angus.. Our field investigation also indicated that the habitat of Tilei. was restricted in the low flow velocity zone.

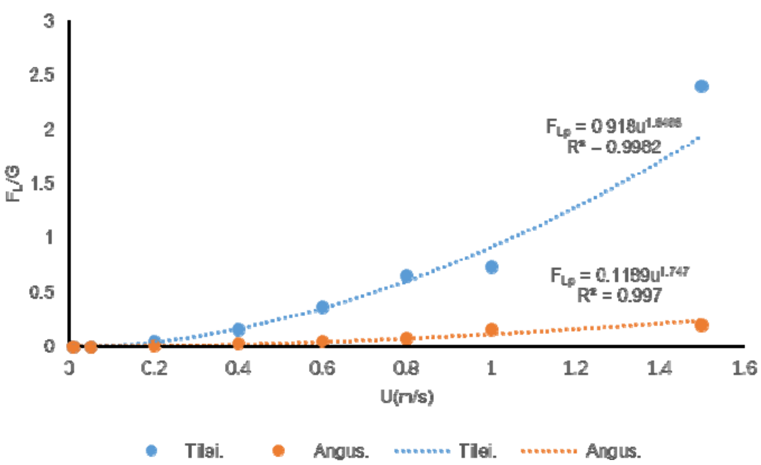

Figure 5. Relations between unit weight lift force and flow velocity for Tilei. and Angus.

©2017, IAHR. Used with permission / ISSN 1562-6865 (Online) - ISSN 1063-7710 (Print)

Lift force displayed the same variation pattern as the drag force: $F_{Lp} = 0.918u^{1.8468}$, $R^2 = 0.9982$ for Tilei., and $F_{Lp} = 0.1189u^{1.7470}$, $R^2 = 0.9970$ for Angus.. The lift force was mainly affected by the flow velocity and for the same flow condition, Tilei. received significantly higher lift force than Angus.. This finding explains the phenomenon that Tilei. prefers to swim at the water surface, where it consumed less energy for uplifting.

3.3 Flow field characteristics around the head

For the existence of the water viscosity and the collision between the fish and water flow, the water flow was unavoidable to encounter resistance from the fish. Therefore, the flow direction and velocity was forced to change. In general, the more intensive the interaction between the flow field and fish, the easier for the fish to sense the surroundings. In other words, the fish could easily sense the signal created by obstacle, food, and natural enemies in the flow if the interaction between the flow field and the fish was strong enough. In order to quantify the intensity of the interaction, we calculated the projection speed in the x, y plane for the middle section which was 0.15 times of the body length from the fish mouth. The projection speed was expressed as

$$v_p = \sqrt{(v_x^2 + v_y^2)} \qquad [8]$$

where v_p was the projection speed, v_x, v_y were the velocity in the direction of the X axis and Y axis, respectively. Figure 6 shows the projection speed, given the inlet velocity of 0.4 m/s.

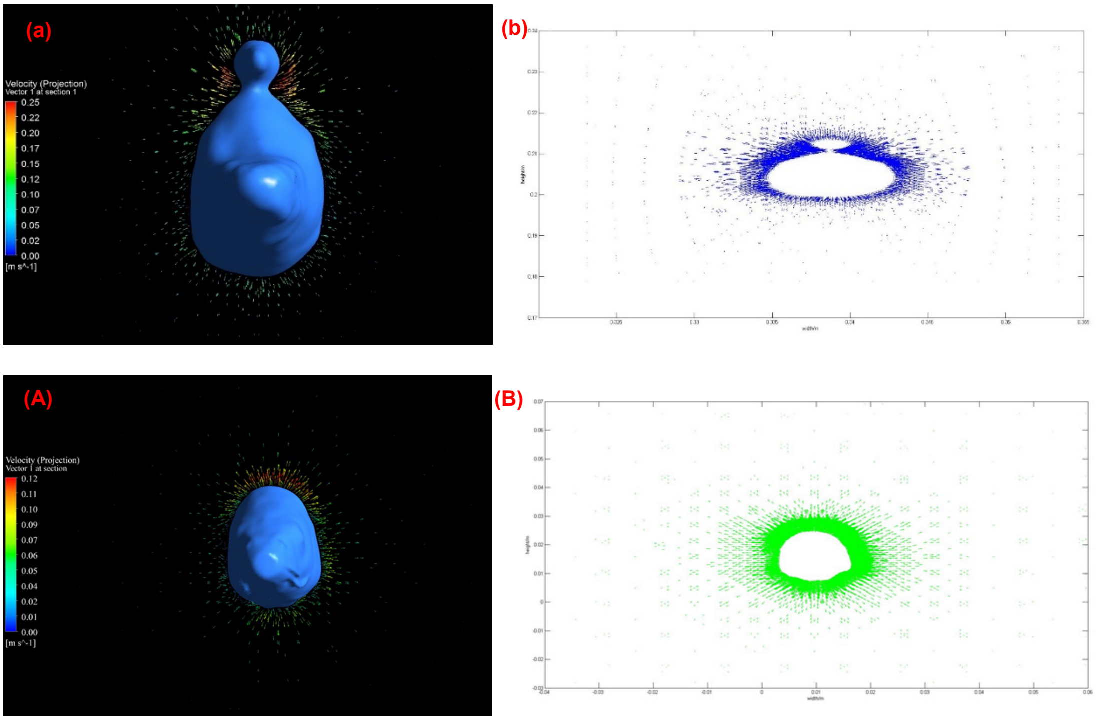

Figure 6. The projection speed distribution in the x, y plane for the middle section which was 0.15 times of the body length from the fish mouth: (a) and (A) show the projection speed variation, plotted in CFD-post; (b) and (B) show the effective zone that the fish interacted with the flow field, plotted in the Matlab software.

It was indicated that the fish could only influence the flow field remarkably around the fish body within a range of about three times their body size. Such influence could be ignored if the distance from the fish body was farther than three times of their body size. Given the condition of inlet velocity as V_{in}=0.4 m/s, the highest projection speed of Tilei. was 0.25 m/s, which was much higher than the projection speed for Angus. (0.12 m/s). The projection speed directions for these two fishes showed obvious difference. The projection speed direction for the Angus. was almost vertical to the fish surface and toward outside, while the direction for Tilei. showed more complicated distribution. Taking the head horn of Tilei. as the dividing line, the projection velocity above the head horn was toward to the upside, while the velocity below the head horn was toward to the downside. It means that the angel between Tilei. flow direction and water flow was always smaller than 90 degrees. This phenomenon suggested that the interaction between Tilei. and water flow was stronger than the interaction between Angus. and water flow. Therefore, the head horn of Tilei. could improve its ability to sense signal from water flow.

©2017, IAHR. Used with permission / ISSN 1562-6865 (Online) - ISSN 1063-7710 (Print)

4 CONCLUSIONS

Lateral line has been believed as the main sense organ for blind cavefishes. For Mexican blind cavefish, the lateral line system is more developed than troglophile and surface fish. However, for Chinese blind cavefish Tilei., which has a head horn on the head, the lateral line system is less developed than troglophile and trogloxene species. It seems that the evolution of sense organ of Tilei. is contrary to Darwin's doctrine of evolution. This study has been designed to explain such contradiction. The simulation results of the pressure distribution along the fish and force situation of Tilei. and Angus. indicated that given the same flow condition, Tilei. with the head horn encounter higher pressure gradient within the head lateral line region than Angus. without the head horn. The head horn structure, helped Tilei. to sense even very subtle changes in pressure. In addition, Tilei. received significantly higher drag force than Angus., which suggested that Tilei. might be a slower swimmer compared with Angus.. Moreover, Tilei. was also subjected to a significantly higher lift force than Angus.，which explained the laboratory observation that Tilei. preferred to swim at the water surface. The differences of drag force and lift force between Tilei. and Angus. was even more remarkable as the inlet flow velocity increased. These findings could explain why Tilei. and the other troglebites that have such head horn structures prefer habitats with low flow velocity underground environment. Nevertheless, the projection speed of Tilei. was found to be much higher than that of Angus., which indicated that Tilei. contacted with water flow more intensively than Angus., allowing the lateral line system of Tilei. to have more chances to sense signal from the water flow. In a word, this study suggests that the head horn may strengthen the sense efficiency of blind fishes.

ACKNOWLEDGEMENTS

This study was financially supported by the Tsinghua university (2015THZ02-1), State Key Laboratory of Hydroscience and Engineering (2016-KY-04) and International Science & Technology Cooperation Program of China (2014DFG72010). We would like to thank Vadim Zakirov from Russia for the ANSYS guidance.

REFERENCE

Baker, C.F. & Montgomery, J.C. (1999b). The Sensory Basis of Rheotaxis in the Blind Mexican Cave Fish, Astyanax fasciatus. *Journal of Comparative Physiology A: Neuroethology, Sensory, Neural, and Behavioral Physiology,* 184, 519-527.

Engelmann, J., Hanke, W. & Bleckmann, H., (2002). Lateral Line Reception in Still and Running Water. Journal of Comparative Physiology A: Neuroethology, Sensory, and Behavioral Physiology, 188(7), 513-526.

Jeffery, W.R., Strickler, A.G., Guiney, S., Heyser, D.G., & Tomarev, S.I. (2000). Prox 1 in Eye Degeneration and Sensory Organ Compensation during Development and Evolution of the Cavefish Astyanax. *Development Genes and Evolution,* 210, 223–230.

James, J., Beatriz, G.R., Bethany, A.S., Ian, O., Pavel, M., Masato, Y. & Alex, C.K. (2017). The Lateral Line Confers Evolutionarily Derived Sleep Loss in the Mexican Cavefish. *Journal of Experimental Biology,* 220, 284-293.

Langecher, T.G., Neumann, B. & Hausberg, C. (1995). Evolution of the Optical Releasers for Aggressive Behavior in Cave-Dwelling Astyanaxs fasciatus (Teleostei: Cyprinidae). *Revue Suisse de Zoologie,* 106(2), 347-359.

Romero, A. & Paulson, K.M. (2001). It's a Wonderful Hypogean Life: A Guide to the Troglomorphic Fishes of the World. *Environmental Biology of Fishes,* 62, 13–41.

Romero, A., Zhao, Y. & Chen, X. (2009). The Hypogean Fishes of China. *Environmental Biology of Fishes,* 86, 211-218.

Windsor, S.P., Tan, D. & Montgomery, J.C. (2008). Swimming Kinematics and Hydrodynamic Imaging in the Blind Mexican Cave Fish (Astyanax fasciatus). *Journal of Experimental Biology,* 211, 2950-2959.

Windsor, S.P., Norris, S.E., Cameron, S.M., Mallinson, G.D. & Montgomery, J.C. (2010). The Flow Fields involved in Hydrodynamic Imaging by Blind Mexican Cave Fish (Astyanax fasciatus). Part I: Open Water and Heading towards a Wall. *Journal of Experimental Biology,* 213, 3819-3831.

Windsor, S.P., Norris, S.E., Cameron, S.M., Mallinson, G.D. and Montgomery, J.C. (2010). The Flow Fields involved in Hydrodynamic Imaging by Blind Mexican Cave Fish (Astyanax fasciatus). Part II: Gliding Parallel to a Wall. *Journal of Experimental Biology,* 213, 3832-3842.

Schiner, J.R. (1854). Fanua der Adelsberger, Lueger und Magdalener-Grotte. In: Schmidl A. Die Grotten und Höhlen von Adelsberg, Lueg, Planina und loos. Wien, Braumüller.

Yang, J.X., Chen, X.L., Bai, J., Fang, D.M. & Qiu, Y. (2016). The Sinocycheilus Cavefish Genome Provides Insights into Cave Adaptation. *BMC Biology,* 14(1), 1-13.

Zhao, Y.H. & Zhang, C.G. (2006). Cavefishes: Concept, Diversity and Research Progress. *Biodiversity Science,* 14(5), 451-460.

Zhao, Y.H. & Zhang, C.G. (2009). *Endemic Fishes of Sinocyclocheilus (Cypriniformes Cyprinidae) in China-Species Diversity, Cave Adaptation, Systematics and Zoogeography.* Science Press.

 ©2017, IAHR. Used with permission / ISSN 1562-6865 (Online) - ISSN 1063-7710 (Print)

IS THERE ENOUGH EVIDENCE TO INFORM EFFECTIVE FISHWAY DESIGN IN THE TEMPERATE SOUTHERN HEMISPHERE?

MARTIN A WILKES [(1)], MORWENNA MCKENZIE[(2)] & J ANGUS WEBB[(3)]

[(1,2)] Coventry University, Centre for Agroecology, Water & Resilience, Coventry, United Kingdom
martin.wilkes@coventry.ac.uk
[(3)] University of Melbourne, Department for Infrastructure Engineering, Australia
angus.webb@unimelb.edu.au

ABSTRACT

The development of hydropower and other infrastructure that disrupts river connectivity poses a serious threat to highly endemic and genetically distinct freshwater fish species in temperate parts of the Southern Hemisphere. Such locations have been neglected in previous reviews on fish passage. Fishways have long been constructed to mitigate the impacts of riverine barriers on fish, yet they have failed for all but the largest, strongest swimming taxa. This is a particular problem in the temperate south, where the majority of species are small-bodied with low swimming performance. Using the Eco Evidence method for rapid evidence synthesis, we undertook an assessment of evidence for effective fishway design focusing on species representative of the temperate south. Systematic literature searches resulted in 630 publications. Through a rigorous screening process, these were reduced to 46 publications containing 76 evidence items across 19 hypotheses relating to design criteria for upstream and downstream passage. Each evidence item was weighted according to the robustness of its study design. These weightings contributed towards the support or rejection of each hypothesis using well-established thresholds. We found an overwhelming lack of evidence for effective fishway design in the temperate south. Particular deficiencies were found with regard to the design of effective facilities for downstream passage. The attraction and entrance of upstream migrating fish into fishways is also relatively under-researched. Given the urgent need for effective fishways in the temperate south, these results justify an approach to fishway design based on a combination of empirical data and expert knowledge. In the meantime, significant resources should be assigned to improve the evidence base through high quality research. The particular deficiencies identified here could guide that research agenda.

Keywords: Fish passage; fishway design; hydropower; non-sport fish; southern hemisphere.

1 INTRODUCTION

Given that the majority of freshwater fish species must undertake some form of migration (e.g. for feeding, refuge, reproduction) in order to complete their life-cycle and maintain gene flow, loss of connectivity caused by hydropower dams poses a serious problem. A range of smaller structures such as low-head hydropower plants, culverts, weirs and tidegates can also represent barriers to migrating fish (Kemp and O'Hanley, 2010), and their cumulative impacts can be severe (Larinier, 2008; McKay et al., 2013). Facilities designed to maintain passable conditions for fish have been constructed for centuries but often fail for all but the strongest swimming taxa, such as salmonids (Katopodis and Williams, 2012).

The negative environmental consequences of impoundments are such that many large economies in the Northern Hemisphere have begun to remove barriers for migration, including large dams in some cases (e.g. East et al., 2015). The Southern Hemisphere, however, presents a different problem because of intense pressure for rapid economic development and the relative lack of knowledge on the needs of native species (Roscoe & Hinch, 2010). Much attention has been drawn to the inadequate provision for passage of tropical fish, particularly in South America where hydropower development is especially rapid (Barletta et al., 2010; Zarfl et al., 2015). The conclusion consistently reached by commentators is that designs exported from the Northern Hemisphere are unsuitable for passing diverse neotropical communities (Quirós, 1989; Makrakis et al., 2011; Roscoe and Hinch, 2010; Duarte et al., 2012; Katopodis and Williams, 2012). The situation is just as serious in temperate regions of the Southern Hemisphere (the 'temperate south', including New Zealand and southern parts of Australia, Argentina, Australia and Chile), which have been neglected in important reviews by Quirós (1989), Pringle et al. (2000) and Barletta et al. (2010).

With relatively weak swimming abilities, the so-called 'non-sport' species (adult body length <150 mm) that characterise freshwaters in the temperate south are particularly vulnerable to habitat fragmentation – many river structures may constitute 'velocity barriers' to migration (Link and Habit, 2015). The majority of species native to Chile and 74% of New Zealand's species are threatened or at risk (Link and Habit, 2015; Goodman et al., 2014). Their ranges are also hotspots for hydropower development (Zarfl et al., 2015). Chile, for example, is one of the world's hydropower hotspots (Goodwin et al., 2006; Zarfl et al., 2015). The development of large hydropower schemes in Australia and New Zealand has now peaked but there is still considerable growth in small hydropower capacity (Bahadori et al., 2013).

The overall 'effectiveness' of a fishway (Kemp and O'Hanley, 2010) is indicated by a suite of metrics describing the ability of individuals of target species to locate and enter the facility and pass the barrier without significant consequences in terms of fitness. Effectiveness for upstream passage is a composite of three 'efficiency' metrics (Cooke and Hinch, 2013). *Attraction efficiency* describes the proportion of fish motivated to pass the barrier that can locate the entrance to the fishway. *Entrance efficiency* is the proportion of fish attracted to the entrance that subsequently enter. *Passage efficiency* is defined as the number of fish exiting the fishway as a proportion of those entering. For downstream passage, *guidance efficiency* is the proportion of fish passing through the route intended by the design of screens and bypasses, rather than through hydropower turbines. *Turbine entrainment* may result in injury and mortality due to excessive shear, turbulence and pressure fluctuations, in addition to mechanical injuries such as blade strike (Pracheil et al., 2016). Given the proliferation of hydropower dams and other barriers to fish migration in the temperate south, our aim was to assess the evidence for design criteria that would optimise the effectiveness of fishways for non-sport species. We evaluated a total of 19 hypotheses (Table 1, Table 2) using the Eco Evidence method and software for literature evidence synthesis (Norris et al., 2012; Webb et al., 2015).

Table 1. Causal hypotheses evaluated within the Eco Evidence analysis. (↑) indicates a hypothesised increase, (↓) a decrease and (**Δ**) a qualitative change. See Table 2 for detailed descriptions of causes.

Hypothesis	Cause	Effect
	Upstream passage	
A1	↑Proportion of flow in fishway	↑Attraction efficiency
A2	↓Distance of entrance from barrier	↑Attraction efficiency
E1	↓Mean water velocity at entrance	↑Entrance efficiency
E2	↓Velocity gradient	↑Entrance efficiency
E4	↓Turbulence intensity at entrance	↑Entrance efficiency
E5	↓□Drop height	↑Entrance efficiency
P1	**Δ**Fishway type	↑Passage efficiency
P2	↓Mean water velocity in fishway	↑Passage efficiency
P3	↓Fishway length	↑Passage efficiency
P4a	□Turbulence intensity in fishway	↑Passage efficiency
P4b	**Δ**Baffle presence and configuration	↑Passage efficiency
P4c	**Δ**Flow regime	↑Passage efficiency
P4d	↑Climbing substrate	↑Passage efficiency
	Downstream passage	
G1	**Δ**Screen design	↑Guidance efficiency
G2	**Δ**Bypass design	↑Guidance efficiency
T1	□Pressure fluctuation	↑Mortality (barotrauma)
T2	**Δ**Turbine design	↑Mortality (blade strike)
T3	□Turbine revolution speed	↑Mortality (blade strike)
T4	**Δ**Turbine type	↑Mortality (shear, turbulence)

2 METHODS

For the review we used the Eco Evidence method, described in full by Norris et al. (2012). Eco Evidence maximises transparency and repeatability, and provides readily interpretable results (Webb et al., 2013). The method centres on the synthesis of *evidence items*, which are the summarized findings from a study. There are eight stages to an Eco Evidence review (Norris et al., 2012). These stages can be consolidated into four broad categories: (i) problem formulation and context, (ii) hypothesis generation, (iii) literature search and evidence extraction, and (iv) evidence assessment and reporting. We describe each of these stages below within a framework that follows the PRISMA (preferred reporting items for systematic reviews and meta-analyses) statement (Liberati et al., 2009) as closely as possible for ecological studies (Nakagawa and Poulin, 2012).

2.1 Problem formulation and context

Our overall research question was: *is there sufficient evidence to inform effective fishway design for non-sport species?* Though our review focused on species native to the temperate south, the scarcity of empirical data relating specifically to these species necessitated a wider scope. We therefore considered evidence relating to any freshwater species with an adult body length of <250 mm TL, a broader category than previously proposed for non-sport fish (<150 mm TL; Link & Habit, 2015). Our rationale for this was that body length is a key determinant of swimming speed (Lauder, 2015) and mortality due to turbine entrainment

 ©2017, IAHR. Used with permission / ISSN 1562-6865 (Online) - ISSN 1063-7710 (Print)

(Coutant & Whitney, 2000). Because eel and lamprey are components of the freshwater fish fauna in the temperate south, we also considered evidence relating to angulliform species of any body length.

Table 2. Descriptions of causes used in hypotheses.

Cause	Description
Proportion of flow in fishway	The proportion of total streamflow discharged from the fishway, plus any auxiliary attraction flow
Distance of entrance from barrier	The physical distance of the fishway entrance from the barrier. Alternatively, the distance of the entrance from the maximum upstream limit of migration if this differs from the barrier location
Mean water velocity at entrance	The time-averaged water velocity at the entrance to the fishway
Velocity gradient	Linear flow acceleration or deceleration at the fishway entrance
Turbulence intensity at entrance	The magnitude of fluctuations in instantaneous velocities at the fishway entrance
Drop height	The vertical elevation of a physical drop between the downstream water surface elevation and the upstream bed level
Fishway type	The type of fishway (e.g. pool-and-weir, vertical slot, Denil, nature-like bypass, rock ramp)
Mean water velocity in fishway	The time-averaged water velocity in the fishway. Alternatively, as velocity is rarely reported, the longitudinal fishway slope or head difference as a surrogate
Fishway length	The total length of the fishway
Turbulence intensity in fishway	The magnitude of fluctuations in instantaneous velocities in the fishway
Baffle presence and configuration	The presence and/or size, shape, configuration of baffles in the fishway
Flow regime	The prevailing flow regime in the fishway (plunging or streaming)
Climbing substrate	The presence and type of roughness elements designed to aid climbing fish
Screen design	The type and design parameters of fish screening devices (e.g. physical, hydrodynamics, electrical, acoustic, light)
Bypass design	The type and design parameters of fish bypasses for downstream movement (e.g. surface or submerged bypass)
Pressure fluctuation	The ratio of maximum to minimum pressure or the rate of pressure change that a fish is exposed to when passing through turbines or other infrastructure
Turbine design	The design of turbines, including the number, configuration, shape and spacing of blades
Turbine revolution speed	The number of revolutions of the turbine per unit time
Turbine type	The type of turbine present (e.g. Francis, Kaplan, bulb, Pelton, crossflow, Archimedes)

2.2 Hypothesis generation

We focused on four effects consistent with the literature on fishway effectiveness metrics, namely attraction, entrance, passage and guidance efficiency (Kemp and O'Hanley, 2010), as well as fish mortality due to turbine entrainment (Table 1). Our initial set of causes was based on our understanding of fishway design criteria from the global literature (Larinier and Marmulla, 2004; Roscoe and Hinch, 2010; Bunt et al., 2012; Brown et al., 2014; Pracheil et al., 2016). During the literature search, we refined our set of hypotheses. Hence the names of our final hypotheses are not entirely consecutive.

2.3 Literature search and evidence extraction

The literature search focused on two databases: ISI *Web of Science* and the *University of Massachusetts Fish Passage Reference Database* (EWRI-ACS, 2009). We used a series of systematic search strings to query these databased. In addition to the results of the systematic literature search, a number of other sources relevant to the review were included that were sourced through colleagues, our own knowledge of the literature, and from the reference lists of obtained publications. See Greenhalgh and Peacock (2005) for a justification of this approach. Results of the literature search were filtered by reviewing abstracts or scanning the full source. A total of 630 unique articles were filtered down to 72 articles through this initial screening process. The remaining articles were assessed in full by at least one assessor but could still be excluded at this stage. After this final screening we were left with 46 articles containing 76 individual evidence items across the 19 hypotheses (Figure 1).

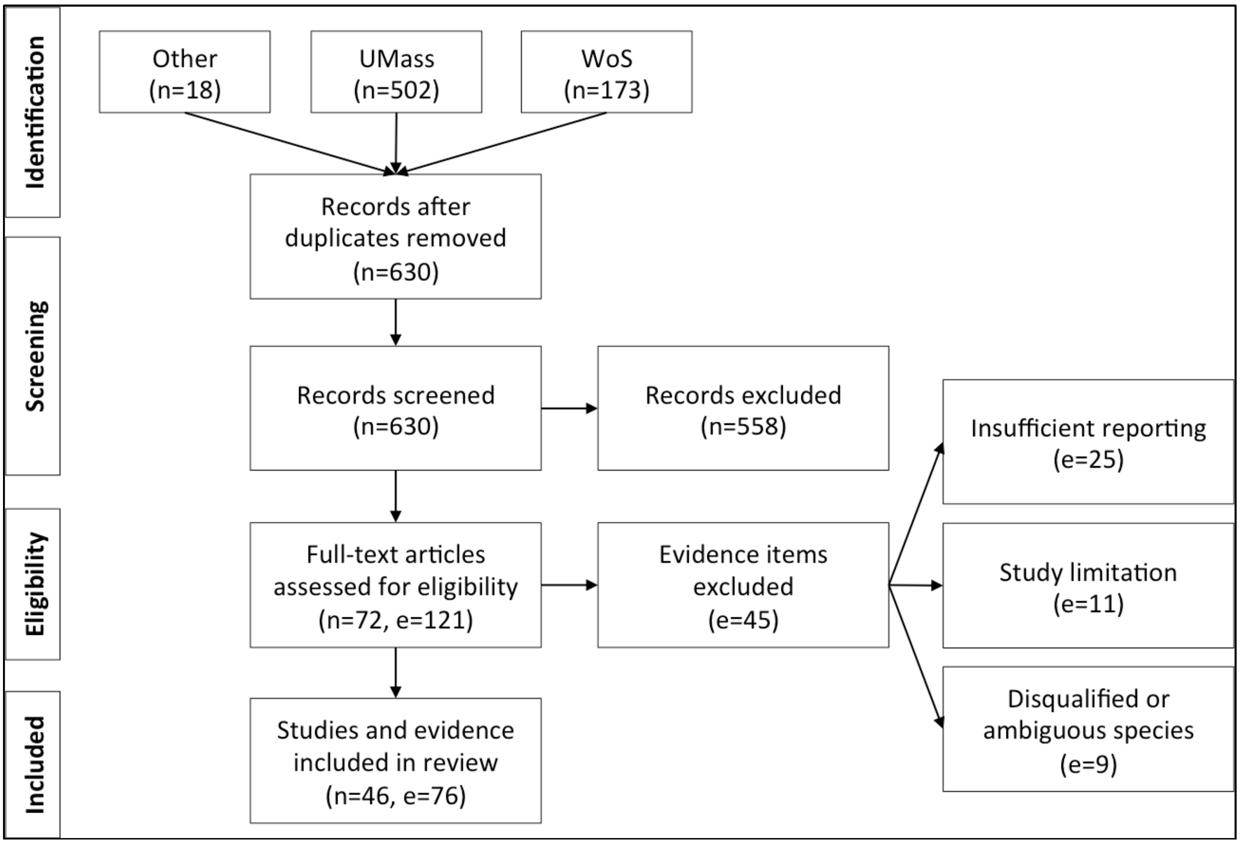

Figure 1. Inclusion and exclusion of studies in the systematic review, as suggested by the PRISMA statement (Liberati et al., 2009). n = number of studies, e = number of evidence items, WoS = Web of Science, UMass = University of Massachusetts Fish Passage Reference Database.

2.4 Evidence assessment

An individual article could contain screened evidence across one or more hypotheses. Each evidence item was given a weight based on its inferential strength using standard Eco Evidence weightings (Norris et al., 2012). For each hypothesis we summed evidence weights supporting the hypothesis and weights refuting the hypothesis. We used the standard Eco Evidence thresholds for assigning a nominal outcome for each hypothesis (Figure 2). For hypotheses with sufficient but somewhat inconsistent evidence (weight >20 for support and >0 for refute) we decomposed results into sub-hypotheses focusing on three taxonomic groups: (i) angulliform fish, (ii) Galaxiidae (including Retropinnidae), and (iii) other taxa. These groups were used to reduce potential differences (*e.g.* rheotactic behaviour) in the response of the taxa considered. If articles reported evidence for multiple taxonomic groups within the same hypothesis, a separate item of evidence was considered for each group.

3 RESULTS

Across the 19 hypotheses tested, plus six sub-hypotheses split by taxonomic group or qualitative cause, the most common outcome was 'insufficient evidence' (n=16, including one instance of 'no evidence'). Seven hypotheses were supported, one was rejected, and there was one instance of inconsistent evidence (Figure 3). We did not find sufficient evidence to support either hypothesis relating to attraction efficiency (Figure 3). The majority of evidence items initially screened for hypothesis A1 were excluded, largely because they failed to quantify attraction efficiency. Of the four hypotheses relating to entrance efficiency, an outcome of insufficient evidence was returned for two (Figure 3). Hypothesis E5 was strongly supported. We were unable to find any evidence for hypothesis E2.

We also returned a result of insufficient evidence for hypothesis P1. An outcome of inconsistent evidence was returned for hypothesis P2 but decomposition into taxonomic groups demonstrated sufficient evidence to support the hypothesis for anguilliform and galaxiid species, whilst the hypothesis was rejected by a small margin for other taxa. Evidence relating to hypothesis P2 constituted the largest proportion (27%) of items found across the whole review. Hypothesis P4b was supported across all taxa. However, a more detailed analysis showed that there was only sufficient evidence to support this hypothesis for galaxiids. We also found support for P4c but this related to only two species across three separate studies. Outcomes of insufficient evidence were returned for hypotheses P4a and P4d.

We found sufficient evidence to support hypothesis G1 by a narrow margin (Figure 3). An outcome of insufficient evidence was returned for hypothesis G2 with only four evidence items all relating to a single

 ©2017, IAHR. Used with permission / ISSN 1562-6865 (Online) - ISSN 1063-7710 (Print)

species, *Anguilla anguilla*. We found insufficient evidence to support any of the four hypotheses relating to mortality due to turbine entrainment (Figure 3), with just four studies contributing evidence.

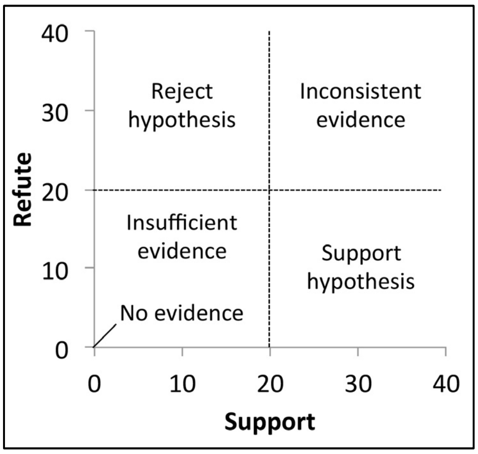

Figure 2. Eco Evidence outcome thresholds. Axis units are summed evidence points across evidence items supporting (x) and refuting (y) the hypothesis.

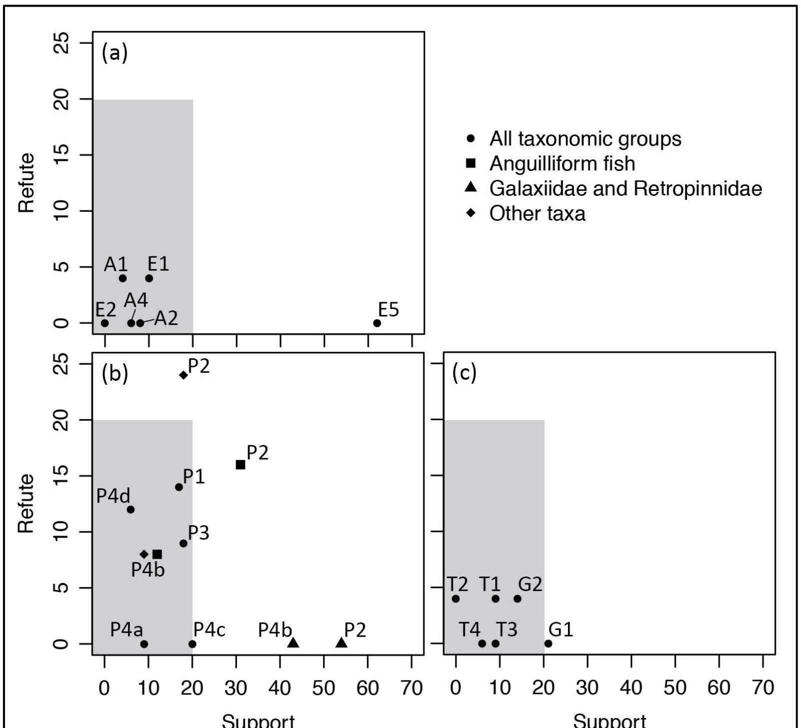

Figure 3. Summary weight of evidence results for hypotheses with effects relating to attraction and entrance efficiency (a), passage efficiency (b), and guidance efficiency and turbine mortality (c). Grey areas delineate 'insufficient evidence' outcome (see Figure 2).

4 DISCUSSION

Workers in the field of fish passage have consistently bemoaned the disproportionate focus of fishway research and design on large, relatively strong swimming species native to the Northern Hemisphere (Quirós, 1989; Roscoe and Hinch, 2010; Makrakis et al., 2011; Duarte et al., 2012; Katopodis and Williams, 2012).

Despite this, there have been no previous attempts to synthesise the evidence for fishway design criteria specifically relating to non-sport species. The large proportion of 'insufficient evidence' results returned here supports the contention that non-sport fish passage is an under-researched area.

4.1 Evidence for downstream fishway design

We found a particular deficiency in evidence relating to downstream passage, echoing several previous commentaries highlighting the disproportionate focus on upstream migration in the wider fish passage literature (Kemp and O'Hanley, 2010; Pompeu et al., 2012; Baumgartner et al., 2014). This disproportionate effort risks the creation of ecological traps upstream of barriers (Pelicice and Agostinho, 2008; Agostinho et al., 2011) and eventually local extinction.

Though we were able to support hypothesis G1, that a qualitative change in screen type would affect guidance efficiency, the four evidence items included evaluated the performance of three different screen types: Baker and Aldridge (2010) evaluated the effect of modification to a physical screen on three species native to New Zealand (in both anguilliform and Galaxiidae groups); Johnson and Miehls (2013) tested the response of *Petromyzon marinus* Petromyzontidae to two different electrical screens; and Piper et al. (2015) focused on hydrodynamic screening of migrant *A. anguilla*. The effectiveness of screens is related to many factors that are highly species- and site-specific (Katopodis, 2005), making the definition of general design criteria challenging.

The only evidence for the effectiveness of bypass types (hypothesis G2) and mortality due to blade strike (T2, T3), shear and turbulence (T4) during turbine entrainment was limited to a single species, *A. anguilla*. Evidence for the effect of pressure fluctuations on mortality due to barotrauma came from just two studies investigating a total of four species; *Entosphenus tridentatus* Petromyzontidae and *Lampetra richardonii* Petromyzontidae in Colotelo et al. (2012) and *Astyanax bimaculatus* Characidae and *Leporinus reinhardtii* Anostomidae in Pompeu et al. (2009). However, it could be misleading to include lamprey (e.g. *E. tridentatus*, *L. richardonii*) together with other species as evidence for this hypothesis. This is because the lack of a swim bladder in lamprey appears to render them insusceptible to barotrauma (Colotelo et al., 2012).

4.2 Evidence for upstream fishway design

We found that factors affecting attraction and entrance efficiency have been poorly researched for all taxonomic groups representative of the temperate south. The exception to this was in the case of hypothesis E5, demonstrating that the occurrence of drops between the downstream water surface and the upstream bed level would constitute poor fishway design. The general lack of evidence for attraction efficiency hypotheses is of major concern as poor attraction is one of the primary reasons for fishway failure worldwide (Larinier and Marmulla, 2004). Bunt et al. (2012) describe attraction and entrance failure mechanisms as: poor entrance location; insufficient discharge relative to competing flow; and excessive turbulence and velocities. We did not find sufficient evidence to evaluate hypotheses for any of these causes.

Causes relating to passage efficiency had comparatively more evidence. However, several design criteria relating to upstream passage are still not sufficiently researched to reach any general conclusions. For example, evidence for hypothesis P1, that a change in fishway type would affect passage efficiency, included studies on a range of fishway types (Foulds and Lucas, 2013; Matondo et al., 2015; Stuart et al., 2008; Noonan et al., 2012; Newbold et al., 2014). Mean velocity or fishway slope (hypothesis P2) was by far the most well researched design criterion, with a total of 20 individual evidence items. We found support for the hypothesis that the passage of anguilliform and galaxiid species is improved as mean velocity or longitudinal slope is decreased. For other species there was a greater weight of evidence for the opposite effect. We found that there was insufficient evidence to support hypothesis P3, that passage efficiency would increase with decreasing fishway length. Furthermore, the evidence contributing to this hypothesis came from two very different contexts: ramps up to 6 m long (Baker, 2014) and full-scale fishways (Noonan et al., 2012).

Turbulence (P4a) and the installation of baffles (P4b) have often been included in the design criteria for fishways due to swimming energetics (Feurich et al., 2012; Bretón et al., 2013; Baki et al., 2014a; 2014b). However, we found insufficient evidence for the benefits of these design criteria. The exception to this was for the response of galaxiids to baffle design, which was among our most strongly supported hypotheses. Several studies support the installation of complex baffle arrangements and rough substrates to improve the passage of galaxiid and related species (*e.g.* Baker and Boubée, 2006; MacDonald and Davies, 2007; Mallen-Cooper et al., 2008). Turbulence is a complex phenomenon that can be described in a variety of ways, including intensity, periodicity, orientation and scale (Lacey et al., 2012). The elucidation of relationships between fish swimming performance and turbulence, especially in the context of fishway design, remains a major challenge (Wilkes et al., 2013).

We were able to support hypothesis P4c, that a qualitative change in flow regime affects passage efficiency. However, the three studies that contributed to this evidence suggested opposite effects for two species, *A. anguilla* (Piper et al., 2012) and *Squalius pyrenaicus* (Branco et al., 2013a; 2013b). This conflicting evidence points to fundamental differences in the behaviour of eels and other species around barriers. A key characteristic of several species of the temperate south is their ability to climb vertical surfaces (e.g. *Galaxias fasciatus*, *Gobiomorphus huttoni*, *Anguilla dieffenbachii*). We therefore tested hypothesis P4d, that the presence and type of climbing substrate would affect passage efficiency. However, we found only one study evaluating this hypothesis (David & Hamer, 2012), which reported an increase in passage when mussel spat ropes were installed at a perched culvert entrance, and for only one of three climbing species native to New Zealand.

 ©2017, IAHR. Used with permission / ISSN 1562-6865 (Online) - ISSN 1063-7710 (Print)

5 CONCLUSIONS

There is currently very little evidence to support the design of effective fishways for non-sport fish native to the temperate south. More research is urgently required in areas relating to attraction, entrance and guidance efficiency and turbine entrainment, but with more robust experimental designs that allow findings to be transferred beyond the system being studied. The most urgent needs are for research into effective design of downstream passage facilities, otherwise there is a risk that resources used to construct effective upstream fishways are wasted when downstream migrants suffer high levels of mortality. There is currently a lack of empirical data to support fishway design in the temperate south, a geographic context that includes areas presently experiencing rapid hydropower development. This justifies the combination of available data, modelling outputs and expert judgement for informing fishway design decisions until sufficient empirical evidence can be collected.

ACKNOWLEDGEMENTS

This work was funded by the European Commission Marie Sklodowska-Curie action, 'Knowledge Exchange for Efficient Passage of Fish in the Southern Hemisphere' (RISE-2015-690857-KEEPFISH).

REFERENCES

Agostinho, C. S., Pelicice, F. M., Marques, E. E., Soares, A. B. & de Almeida, D. A. A. (2011). All that goes up must come down? Absence of Downstream Passage through a Fish Ladder in a large Amazonian River. *Hydrobiologia*, 675(1), 1-12.

Bahadori, A., Zahedi, G. & Zendehboudi, S. (2013). An overview of Australia's Hydropower Energy: Status and Future Prospects. *Renewable and Sustainable Energy Reviews*, 20, 565-569.

Baker, C.F. (2014). Effect of Ramp Length and Slope on the Efficacy of a Baffled Fish Pass. *Journal of Fish Biology,* 84(2), 491-502.

Baker, C. & Aldridge, B. (2010). Huntly Power Station - 2010 Fisheries Monitoring Report. *NIWA Client Report HAM2010-109 September 2010*, 212 pp.

Baker, C.F. & Boubée, J.A.T. (2006). Upstream Passage of Inanga Galaxias Maculatus and Redfin Bullies *Gobiomorphus Huttoni* over Artificial Ramps. *Journal of Fish Biology,* 69(3), 668-681.

Baki, A.B.M., Zhu, D.Z. & Rajaratnam, N. (2014a). Mean Flow Characteristics in a Rock-Ramp-Type Fish Pass. *Journal of Hydraulic Engineering,* 140(2), 156-168.

Baki, A.B.M., Zhu, D.Z. & Rajaratnam, N. (2014b). Turbulence Characteristics in a Rock-Ramp-Type Fish Pass. *Journal of Hydraulic Engineering,* 141(2), 04014075.

Barletta, M., Jaureguizar, A. J., Baigun, C., Fontoura, N.F., Agostinho, A.A. & Almeida-Val, V.M.F. (2010). Fish and Aquatic Habitat Conservation in South America: A Continental Overview with Emphasis on Neotropical Systems. *Journal of Fish Biology*, 76, 2118-2176.

Baumgartner, L., Zampatti, B., Jones, M., Stuart, I. & Mallen-Cooper, M. (2014). Fish Passage in the Murray-Darling Basin, Australia: Not just an Upstream Battle. *Ecological Restoration and Management*, 15(S1), 28-39.

Branco, P., Santos, J.M., Katopodis, C., Pinheiro, A. & Ferreira, M.T. (2013a). Effect of Flow Regime Hydraulics on Passage Performance of Iberian Chub (*Squalius Pyrenaicus*) (Günther, 1868) In an Experimental Pool-and-Weir Fishway. *Hydrobiologia*, 714(1), 145-154.

Branco, P., Santos, J.M., Katopodis, C., Pinheiro, A. & Ferreira, M.T. (2013b). Pool-Type Fishways: Two Different Morpho-Ecological Cyprinid Species Facing Plunging and Streaming Flows. *PloS one,* 8(5), e65089.

Bretón, F., Baki, A.B.M., Link, O., Zhu, D.Z. & Rajaratnam, N. (2013). Flow in Nature-Like Fishway and its Relation to Fish Behaviour. *Canadian Journal of Civil Engineering,* 40(6), 567-573.

Brown, R.S., Colotelo, A.H., Pflugrath, B.D., Boys, C.A., Baumgartner, L.J., Deng, Z.D. & Silva, L.G.M. (2014). Understanding Barotrauma in Fish Passing Hydro Structures: A Global Strategy for Sustainable Development of Water Resources. *Fisheries,* 39(3), 108-122.

Bunt, C.M., Castro-Santos, T. & Haro, A. (2012). Performance of Fish Passage Structures at Upstream Barriers to Migration. River *Research and Applications,* 28(4), 457-478.

Buysse, D., Mouton, A.M., Stevens, M., den Neucker, T. & Coeck, J. (2013). Mortality of European Eel after

Colotelo, A.H., Pflugrath, B.D., Brown, R.S., Brauner, C.J., Mueller, R.P., Carlson, T. J. & Trumbo, B. A. (2012). The Effect of Rapid and Sustained Decompression on Barotrauma in Juvenile Brook Lamprey and Pacific Lamprey: Implications for Passage at Hydroelectric Facilities. *Fisheries Research,* 129, 17-20.

Cooke, S.J. & Hinch, S.G. (2013). Improving the Reliability of Fishway Attraction and Passage Efficiency Estimates to Inform Fishway Engineering, Science And Practice. *Ecological Engineering*, 58, 123-132.

Coutant, C.C. & Whitney, R.R. (2000). Fish Behavior in Relation to Passage through Hydropower Turbines: A Review. *Transactions of the American Fisheries Society,* 129(2), 351-380.

David, B.O. & Hamer, M.P. (2012). Remediation of a Perched Stream Culvert with Ropes Improves Fish Passage. *Marine and Freshwater Research,* 63(5), 440-449.

Duarte, B.A.D.F. & Ramos, I.C.R. (2012). Reynolds Shear-Stress And Velocity: Positive Biological Response of Neotropical Fishes to Hydraulic Parameters in a Vertical Slot Fishway. *Neotropical Ichthyology,* 10(4), 813-819.
East, A.E., Pess, G.R., Bountry, J.A., Magirl, C.S., Ritchie, A.C., Logan, J.B. & Randle, T.J (2015). Large-Scale Dam Removal on the Elwha River, Washington, USA: River Channel and Floodplain Geomorphic Change. *Geomorphology,* 228, 765-786.
Feurich, R., Boubée, J. & Olsen, N.R.B. (2012) Improvement of Fish Passage in Culverts using CFD. *Ecological Engineering*, 47, 1-8.
Foulds, W.L. & Lucas, M.C. (2013). Extreme Inefficiency of Two Conventional, Technical Fishways used by European River Lamprey (*Lampetra Fluviatilis*). *Ecological Engineering,* 58, 423-433.
Goodman, J. M., Dunn, N. R., Ravenscroft, P. J., Allibone, R. M., Boubee, J. A., David, B. O. & Rolfe, J. R. (2014). Conservation Status of New Zealand Freshwater Fish, 2013. *New Zealand Threat Classification Series*, 7, 12.
Goodwin, P., Jorde, K., Meier, C. & Parra, O. (2006) Minimizing Environmental Impacts of Hydropower Development: Transferring Lessons from Past Projects to a Proposed Strategy for Chile. *Journal of Hydroinformatics,* 8(4), 253-269.
Greenhalgh, T. & Peacock, R. (2005). Effectiveness and Efficiency of Search Methods in Systematic Reviews of Complex Evidence: Audit of Primary Sources. *British Medical Journal,* 331(7524), 1064-1065.
Hicks, B., Roper, M., Ito, T. and Campbell, D. (2008). Passage of Inanga (Galaxias Maculatus) over Artificial Ramps as a Means to Restoring Upstream Access to Stream Habitat. *Centre for Biological and Ecological Research Contract Report,* 89, 20.
Johnson, N.S. & Miehls, S. (2013). Guiding Out-Migrating Juvenile Sea Lamprey (*Petromyzon Marinus*) with Pulsed Direct Current. *River research and applications,* 30(9), 1146-1156.
Katopodis, C. (2005). Developing a Toolkit for Fish Passage, Ecological Flow Management and Fish Habitat Works*. Journal of Hydraulic Research,* 43(5), 451-467.
Katopodis, C. & Williams, J.G. (2012). The Development of Fish Passage Research in a Historical Context. *Ecological Engineering,* 48, 8-18.
Kemp, P.S. & O'Hanley, J.R. (2010) Procedures for Evaluating and Prioritising the Removal of Fish Passage Barriers: A Synthesis. *Fisheries Management and Ecology,* 17(4), 297-322.
Larinier, M. & Marmulla, G. (2004). Fish Passes: Types, Principles and Geographical Distribution - An Overview. *Second International Symposium on the Management of Large Rivers for Fisheries*, 2, 183-206.
Larinier, M. (2008). Fish Passage Experience at Small-Scale Hydro-Electric Power Plants in France. *Hydrobiologia*, 609(1), 97-108.
Lauder, G.V. (2015). Fish Locomotion: Recent Advances and New Directions. *Annual Review of Marine Science,* 7, 521-545.
Liberati, A., Altman, D.G., Tetzlaff, J., Mulrow, C., Gøtzsche, P.C., Ioannidis, J.P. & Clarke, M.(2009). The PRISMA Statement for Reporting Systematic Reviews and Meta-Analyses of Studies That Evaluate Health Care Interventions: Explanation and Elaboration. *Annals of internal medicine,* 151(4), W-65.
Link, O. & Habit, E. (2015). Requirements and Boundary Conditions for Fish Passes of Non-Sport Fish Species based on Chilean Experiences. *Reviews in Environmental Science and Biotechnology,* 14(1), 9-21.
MacDonald, J.I. & Davies, P.E. (2007). Improving the Upstream Passage of Two Galaxiid Fish Species through a Pipe Culvert. *Fisheries Management and Ecology,* 14(3), 221-230.
Makrakis, S., Miranda, L.E., Gomes, L.C., Makrakis, M.C. & Junior, H.M.F. (2011). Ascent of Neotropical Migratory Fish in the Itaipu Reservoir Fish Pass. *River Research and Applications,* 27(4), 511-519.
Mallen-Cooper, M., Zampatti, B.P., Stuart, I.G. & Baumgartner, L.J. (2008). Innovative Fishways-Manipulating Turbulence in the Vertical-Slot Design to Improve Performance and Reduce Cost. *A report to the Murray Darling Basin Commission, Fishway Consulting Services, Sydney*, 19.
Matondo, B.N., Dierckx, A., Benitez, J.P. & Ovidio, M. (2015). Does Yellow Eel Prefer Old Pool and Weir or New Vertical Slot Fish Pass During Their Upstream Migration?. *International Conference on Engineering and Ecohydrology for Fish Passage*, Groningen, June 2015.
McKay, S.K., Schramski, J.R., Conyngham, J.N. & Fischenich, J.C. (2013). Assessing Upstream Fish Passage Connectivity with Network Analysis. *Ecological Applications*, 23(6), 1396-1409.
Moser, M.L., Matter, A.L., Stuehrenberg, L.C. & Bjornn, T.C. (2002). Use of an Extensive Radio Receiver Network to Document Pacific Lamprey (*Lampetra Tridentata*) Entrance Efficiency at Fishways in the Lower Columbia River, USA. *Aquatic Telemetry,* 165, 45-53.
Nakagawa, S. & Poulin, R. (2012). Meta-Analytic Insights into Evolutionary Ecology: An Introduction and Synthesis. *Evolutionary Ecology,* 26(5), 1085-1099.
Newbold, L.R., Karageorgopoulos, P. & Kemp, P.S. (2014). Corner and Sloped Culvert Baffles Improve the Upstream Passage of Adult European Eels (*Anguilla Anguilla*). *Ecological Engineering,* 73, 752-759.
Noonan, M.J., Grant, J.W. and Jackson, C.D. (2012). A Quantitative Assessment of Fish Passage Efficiency. *Fish and Fisheries,* 13(4), 450-464.

 ©2017, IAHR. Used with permission / ISSN 1562-6865 (Online) - ISSN 1063-7710 (Print)

Norris, R.H., Webb, J.A., Nichols, S.J., Stewardson, M.J. & Harrison, E.T. (2012). Analyzing Cause and Effect in Environmental Assessments: Using Weighted Evidence From The Literature. *Freshwater Science*, 31, 5–21.

Pelicice, F.M. & Agostinho, A.A. (2008). Fish Passage Facilities as Ecological Traps in Large Neotropical Rivers. *Conservation Biology,* 22, 180-188.

Piper, A.T., Manes, C., Siniscalchi, F., Marion, A., Wright, R.M. & Kemp, P S. (2015). Response of Seaward-Migrating European Eel (*Anguilla Anguilla*) to Manipulated Flow Fields. *Proceedings of the Royal Society of Biology,* 282(1811), 20151098).

Piper, A.T., Wright, R.M. & Kemp, P.S. (2012). The Influence of Attraction Flow on Upstream Passage of European Eel (*Anguilla Anguilla*) At Intertidal Barriers. *Ecological Engineering,* 44, 329-336.

Pompeu, P.D.S., Horta, L.F.M. & Martinez, C.B. (2009) Evaluation of the effects of pressure gradients on four Brazilian freshwater fish species. *Brazilian Archives of Biology and Technology* 52(1), 111-118.

Pompeu, P.S., Agostinho, A.A. & Pelicice, F.M. (2012). Existing and Future Challenges: The Concept of Successful Fish Passage in South America. *River Research and Applications,* 28(4), 504-512.

Pracheil, B.M., DeRolph, C.R., Schramm, M.P. & Bevelhimer, M.S. (2016). A Fish-Eye View of Riverine Hydropower Systems: The Current Understanding of the Biological Response to Turbine Passage. *Reviews in Fish Biology and Fisheries,* 26(2), 153-167.

Pringle, C.M., Freeman, M.C. & Freeman, B.J. (2000). Regional Effects of Hydrlogic Alterations on Riverine Macrobiota in the New World: Tropical-Temperate Comparisons. *BioScience,* 50(9), 807-823.

Quirós R. (1989). *Structures Assisting The Migrations Of Non-Salmonid Fish: Latin America*. *COPESCAL Technical Paper, No. 5*, United Nations, Rome, 44 pp.

Roscoe, D.W. & Hinch, S.G. (2010). Effectiveness Monitoring of Fish Passage Facilities: Historical Trends, Geographic Patterns and Future Directions. *Fish and Fisheries,* 11(1), 12-33.

Stuart, I.G., Baumgartner, L.J. & Zampatti, B.P. (2008). Lock Gates Improve Passage of Small-Bodied Fish and Crustaceans in a Low Gradient Vertical-Slot Fishway. *Fisheries Management and Ecology*, 15(3), 241-248.

Tummers, J.S., Winter, E., Silva, S., O'Brien, P., Jang, M.H. & Lucas, M.C. (2015). Tricky Little Lampreys! Efficacy of an Unmodified and Modified Super-Active Baffle Fish Pass for European River Lamprey (*Lampetra Fluviatilis*). *International Conference on Engineering and Ecohydrology for Fish Passage*, Groningen.

Webb, J. A., Miller, K.A. de Little, S.C., Stewardson, M.J., Nichols, S.J. & Wealands, S.R. (2015). An Online Database and Desktop Assessment Software to Simplify Systematic Reviews in Environmental Science. *Environmental Modelling and Software,* 64, 72-79.

Webb, J.A., Miller, K.A., King, E.L., de Little, S., Stewardson, M.J., Zimmerman, J.K.H. & Poff, N.L. (2013). Squeezing the Most Out of Existing Literature: A Systematic Re-Analysis of Published Evidence on Ecological Responses to Altered Flows. *Freshwater Biology,* 58, 2439-2451.

Wilkes, M.A., Maddock, I., Visser, F. & Acreman, M.C. (2013). Incorporating Hydrodynamics into Ecohydraulics: The Role of Turbulence in the Swimming Performance and Habitat Selection of Stream-Dwelling Fish. *Ecohydraulics: An Integrated Approach*, 7-30.

Zarfl, C., Lumsdon, A.E., Berlekamp, J., Tydecks, L. & Tockner, K. (2015). A Global Boom in Hydropower Dam Construction. *Aquatic Sciences*, 77(1), 161-170.

Proceedings of the 37th IAHR World Congress
August 13 – 18, 2017, Kuala Lumpur, Malaysia

THE EFFECT OF HYDRODYNAMIC CONDITION ON THE MORPHOLOGY, HYDRONAMICS AND PHOTOSYNTHESIS OF FOUR SUBMERGED PLANTS

YI MIN ZHANG(1), FEI YANG(2), MENG JIE MA(3), YUE XIANG GAO(4) ,LONG MIAN WANG(5) MING KONG(6) & YUEING ZHU(7)

(1,2,4,5,6,7) Nanjing Institute of Environmental Sciences of MEP, Najing, China,
zhangymzym@163.com
(3) School of Environmnent and Safety, University of Changzhou, Changzhou, China

ABSTRACT

Morphological traits (plant height and average biomass), hydrodynamic performance (drag, drag coefficient (Cd) and E-value) and photosynthetic fluorescence characteristics (Fv/Fm and rapid light curves) of various initial densities of four canopy-former species (Hydrilla verticillata, Potamogeton malaianus, Myriophyllum spicatum and Potamogeton crispus) were studied under different flow velocities. The results demonstrated that the largest average plant height and biomass appeared in 0.05m/s and decreased significantly with increasing flow velocity when the velocity is more than 0.05m/s ($P<0.05$). The drag exerted on plants also increased with increasing velocity ($P<0.05$). The value of Cd and E-value of four submerged plants were significantly different ($P<0.05$), which presented P. crispus < M. spicatum < P. malaianus < H. verticillata. The Fv/Fm and RLCs in the 0.05m/s were higher than 0m/s and 0.1m/s-0.3m/s had a negative impact on Fv/Fm and RLCs. It was evident from this study that high flow velocity inhibited the normal growth of all four plants, while low velocity did not harm them. M. spicatum was found to possess high adaptability to cope with this mechanical stress, which was the preferred species for the aquatic plant recovery. Moreover, faced with high velocity, the negative effect of water movement on plants could be reduced by increasing initial planting densities.

Keywords: Submerged macrophyte; flow velocity; morphological traits; hydrodynamic performance; photosynthetic fluorescence characteristics.

1 INTRODUCTION

Some of the important influences on morphology and physiology traits of aquatic rooted plants are wind (Wang et al., 2015), water movement (Geest et al., 2005) and mechanical stress stimulation (Blanchette, 1997). Terrestrial herbaceous plants (Wang et al., 2015), trees (Ge et al., 2013; Zhu et al. 2012), algae (Hun, 2013; Stewart, 2003) and aquatic moss (Biehle, 1998) have been studied extensively. However, there have been few studies with the morphological changes of submerged macrophyte in response to water movement. It was found that aquatic vegetation cannot successfully restored from many ecological restoration engineering practices in the field, which was related to hydrodynamic condition (wind, flow velocity, turbulence, change of water level (Geest et al., 2005) and others). Velocity was the most basic and intuitive parameter in the hydrodynamic condition (Champika et al., 2013). Velocity was a ubiquitous environmental factor for submerged macrophyte and had positive or negative influence for plant growth and survival. As a result, it is important for the choice of species in vegetation restoration projects and aquatic ecosystem management to know of the relationship between flow velocity and aquatic plants. Therefore, morphological traits (plant height and average biomass), hydrodynamic performance (drag, drag coefficient (Cd) and E-value) and photosynthetic fluorescence characteristics (maximum quantum yield (Fv/Fm) and rapid light curves(RLCs)) of various initial densities of four canopy-former species under different flow velocities (0.05m/s, 0.1m/s, 0.2m/s, 0.3m/s) were studied. The aim of this paper is to determine: (i) Morphological change of four submersed plants in response to velocity, (ii) interactions between drag and velocities and reconfiguration capacities of these four plants exposed to flow movement, which provide evidence for choice of species in vegetation restoration projects.

2 MATERIALS AND METHODS

2.1 Plant material

H. verticillate, P. malaianus, M. spicatum and P. crispus were all collected in Gaoyou Aquatic Plant Cultivation Base. The plant samples without damages, plant diseases or insect pests were selected and transferred to plastic air filled bags which were then transported to the laboratory. At the laboratory, these four submersed macrophytes were carefully washed in tap water to remove attached algae and sediments. These plants were cut and caulosomes of them were selected respectively as experimental materials.

 ©2017, IAHR. Used with permission / ISSN 1562-6865 (Online) - ISSN 1063-7710 (Print)

2.2 Experimental design

The experimental system construction: tiled the substrate sludge into the experimental small flower pot, of which the upper caliber is 16cm, lower caliber is 10cm, height is 12.5cm and bottom thickness is 10cm. After paving the substratum, the pot was placed into an annular flume of size 4.5m×1.4m×1.2m（Figure 1）and were poured slowly into tap water along the groove wall, the water depth should be 1m. After 7 days, four species of 3, 6, 9 and 15 plants were grown with cuttage, which were the same as 150/m^2, 300/m^2, 450/m^2 and 750/m^2. The flow velocities were set to 3.8Hz, 6.5Hz, 12.3Hz and 16.2Hz by adjusting the motor frequency, and the corresponding flow velocities were 0.05m/s, 0.1m/s, 0.20m/s and 0.3m/s respectively.

Experiments were carried out during the plant growth period. The tests were divided into two stages, H. verticillate, P. malaianus and M. spicatum tests were conducted from April 20, 2016 to August 20, 2016, and the average indoor temperature was controlled at 30±2℃; stage of P. crisps test was conducted from September 10, 2015 to January 10, 2016, and the temperature was controlled at 15±2℃.

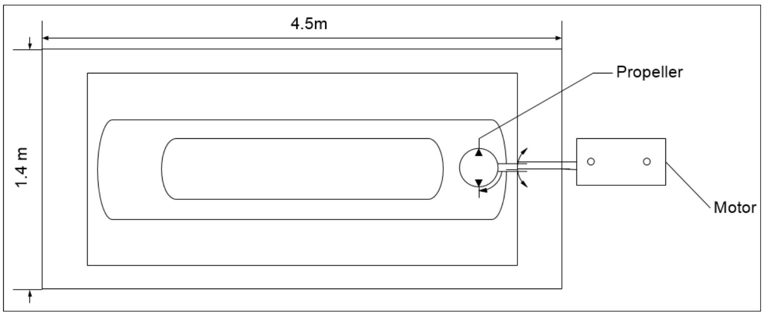

Figure 1. Diagram of annular flume

2.3 Test indexes and methods

2.3.1 Growth morphological characteristics measurement

At the end of the experiment, (the experimental period of each flow velocity is one month), all plants were harvested and the following growth traits were determined: (1) plant height (cm), were measured individually with the aid of a ruler; (2) plant biomass (g).

2.3.2 Hydrodynamic performance of plants

The determination of the drag of plants at different flow velocities were accomplished by means of device improved by Sagnes (Sagnes et al., 2000) (Figure 2). The plants were tied to an L shaped right-angled bar. 5cm long horizontal section of lower part of the right angled bar was placed parallel to the direction of water flow, near the bottom of the flume. The plant was fixed at the end of the horizontal part of the right angled bar.

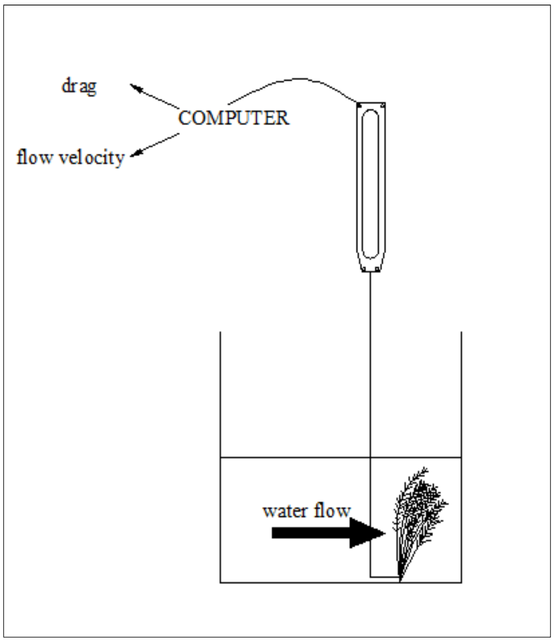

Figure 2. Device of measurement of drag

Plant adaptive hydrodynamic capacity was analyzed by quantitative measures (drag coefficient and E-value) of the relative change of the relationship between the force and the plant reconfiguration. Drag coefficient (Cd) refers to the relation of tension with respect to the velocity of flow and leaf area exposed to the flow; it is considered as a non-dimensional standard variable for the evaluation of capacities of different plant morphologies to withstand water flow. Cd (Vogel, 1984) is calculated by the following Eq.[1].

$$Cd=2F/\rho SU^2 \tag{1}$$

Where, F is the drag exerted on the plant (mN), ρ is the water density (kg/ m³), S is the leaf area (m^2) and U is the flow velocity (m/s).

E-value is a measurement of plant reconfiguration ability in increased flow velocity. It indicates that the drag varies with change in flow velocity, but is independent of the absolute value of drag. The lower the E-value, the better the plant reconfiguration ability. E-value is the slope of log (F/U2) against log U. Therefore, Cd and U was fitted using Eq. [2] and E-value is equal to exponent b in Eq.[2].

$$Cd=aU^b \tag{2}$$

2.3.3 Photosynthetic fluorescence characteristics

Since the beginning of the experiment, Chlorophyll parameter was determined on the 20th day using DIVING-PAM (German WAIZ) at normal position. (1) Fv/Fm: the determination was conducted from 6.30 to 7.30, and after dark adaptation for the leaves lasting 10 min, opened and modulated measuring light (0.15 $\mu mol\cdot m^{-2}\cdot s^{-1}$), and acquired initial fluorescence yield F0, then the saturation pulsed was started (1 000$\mu mol\cdot m^{-2}\cdot s^{-1}$) and acquired Fm, repeating 3 times for every group.

With reference to Fm and F0, Fv /Fm of PSⅡcould be calculated: Fv /Fm = (Fm－F0)/Fm. (2) Rapid light curves: determination was conducted from 10.30 to 11.30 in the morning, and the actinic light intensity gradient were 0,39,102,192,325,485,664,979,1 324$\mu mol\cdot m^{-2}\cdot s^{-1}$, and every actinic light of each tensity should shine for 10s, with interval 20s between every other group. With reference to (Fm－Fo)/Fm' of PSⅡand photosynthetically active radiation, ETR was calculated: ETR = (Fm－Fo) /Fm'× PAR×0.84×0.5; At last, RLCs of ETR mean value was drawn.The fitting method of rapid RLRCs adopts least square method, and that of RLCs adopts the equation proposed by Platt (Platt et al., 1980), Ralph (Ralph et al., 2005), shown as follows:

$$rETR = rETR_m\left(1 - e^{\frac{-\alpha\cdot PAR}{rETR_m}}\right)\cdot e^{\frac{-\beta\cdot PAR}{rETR_m}} \tag{3}$$

Where, rETRm is the maximum potential relative electron transfer rate when there is no light suppression; α is the initial slope of rETR-PAR curve, reflecting plant utilization of light energy; β is the light inhibition parameter.

3 RESULTS AND ANALYSES

3.1 Morphology

As observed from Figure 3, low velocity (0.05 m/s) had a positive effect on the average plant height of four kinds of submerged plants. However, when flow velocity is more than 0.05m/s, plant height decreased significantly with increasing flow velocity ($P<0.05$). Compared with 0m/s, height of H.verticillata, P. malaianus, M. spicatum and P. crispus under 0.3m/s decreased by 79.9%, 75.93%, 43.07% and 61.69% respectively.

The influence of initial density is not significant on the average plant height of H. verticillata and P. crispus ($P=0.137$). However, plant height of P. malaianus and M. spicatum was sensitive to initial density. Influence degree of flow velocity on four submerged plants: H.verticillata > P. malaianus > P. crispus > M. spicatum.

The effect of flow on biomass of four kinds of submerged macrophytes was similar to the impact of flow on plant height. When the velocity is over 0.05m/s, compared to static state, the biomass of single plant of H. verticillata, P. malaianus and P. crispus were significantly restrained($P<0.05$) (Figure 4).

However, a density of 15plants/pot of M. spicatum did not have a significant difference in terms of biomass of single plant at 0.1m/s compared with that at 0m/s($P=0.083$). With the increase of flow velocity, reduction degree of four submerged plants showed a tendency of H.verticillata > P. malaianus > P. crispus > M. spicatum. The influence of initial density on biomass of single plant of H. verticillata and P. crispus and that on plant height were similar, both increasing with increase in density.

 ©2017, IAHR. Used with permission / ISSN 1562-6865 (Online) - ISSN 1063-7710 (Print)

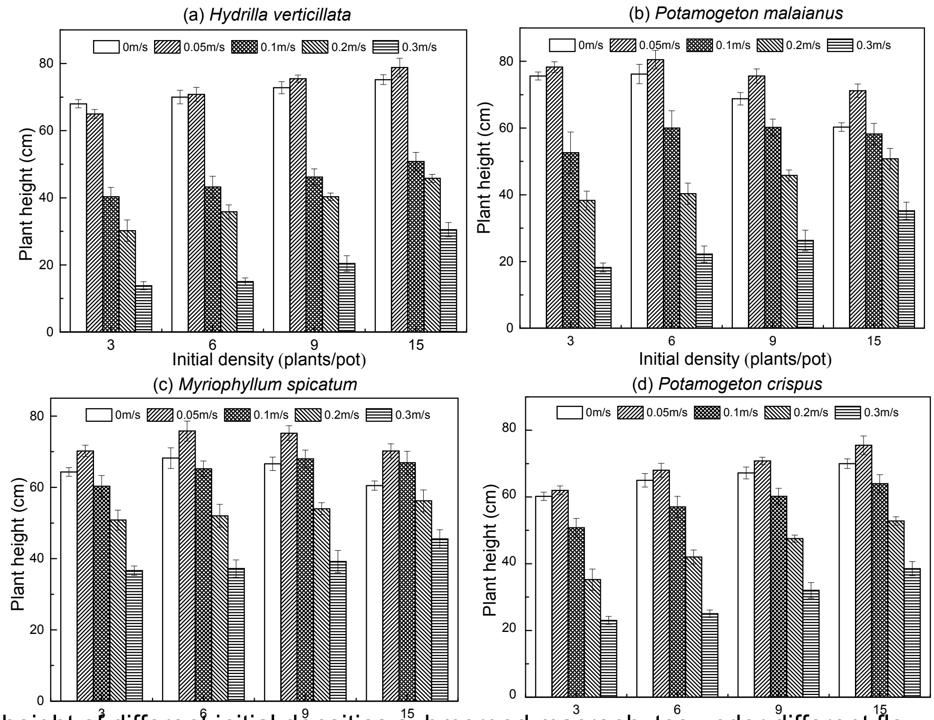

Figure 3. The plant height of different initial densities submerged macrophytes under different flow velocities

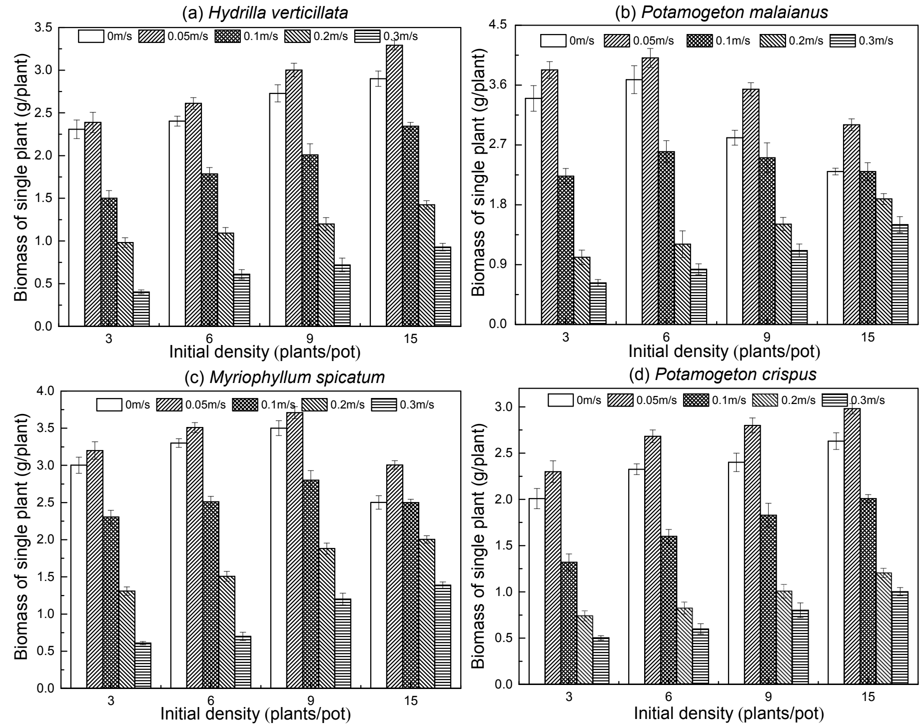

Figure 4. The biomass of different initial densities submerged macrophytes under different flow velocities

3.2 Hydrodynamic performance

For the four submerged plants, drags exerted on a single plant were significantly different under different flow velocities ($P<0.05$), showing a trend: P. crispus > M. spicatum > P.malaianus > H. verticillata (Figure 5). The drags exerted on the four plants increased exponentially with speed increase; the drags were fitted and showed that it basically accorded with the $F=aU^b$, and the range of fitting correlation coefficient R^2 was from 0.935 to 0.996 (Table 3). From Table 3, it could also be observed that drags reduced with increase of initial planting density, while under low flow velocity (0.05m/s 和 0.1m/s), the initial density had no significant effect on the drags exerted on plant ($P=0.086$); with increasing flow velocity, plants of different densities differ greatly in drags exerted ($P<0.05$) .

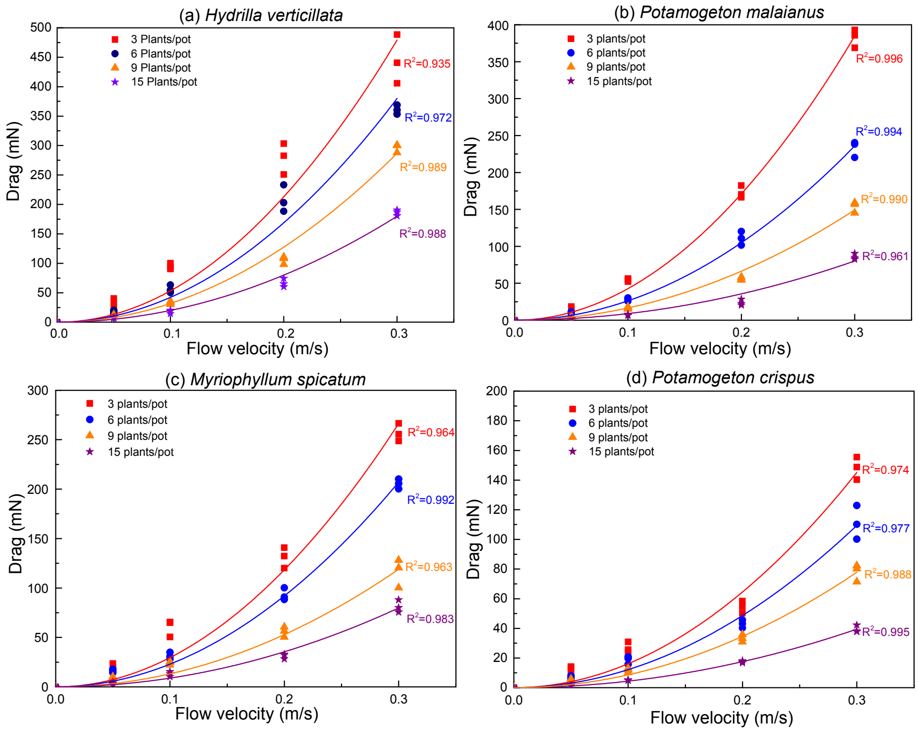

Figure 5. The Drag of different initial densities submerged macrophytes under different flow velocities

The equation $Cd=2F/\rho*u^2*S$ is used to calculate Cd of plants under different flow velocities and initial planting densities (Figure 6). As can be seen from Table 1, Cd of four submerged plants had significant difference, showing a trend: H. verticillata > P. malaianus > M. spicatum > P. crispus. It also presented that Cd reduced with increasing flow velocity. Compared to that at velocity of 0.05m/s, plant Cd decreases 20.42%, 28.56%,48.40% and 60.17% respectively at 0.3m/s. Initial planting density has significant influence on Cd, and Cd under various densities showed a trend: 3 plants/pot > 6 plants/pot > 9 plants/pot > 15 plants/pot.

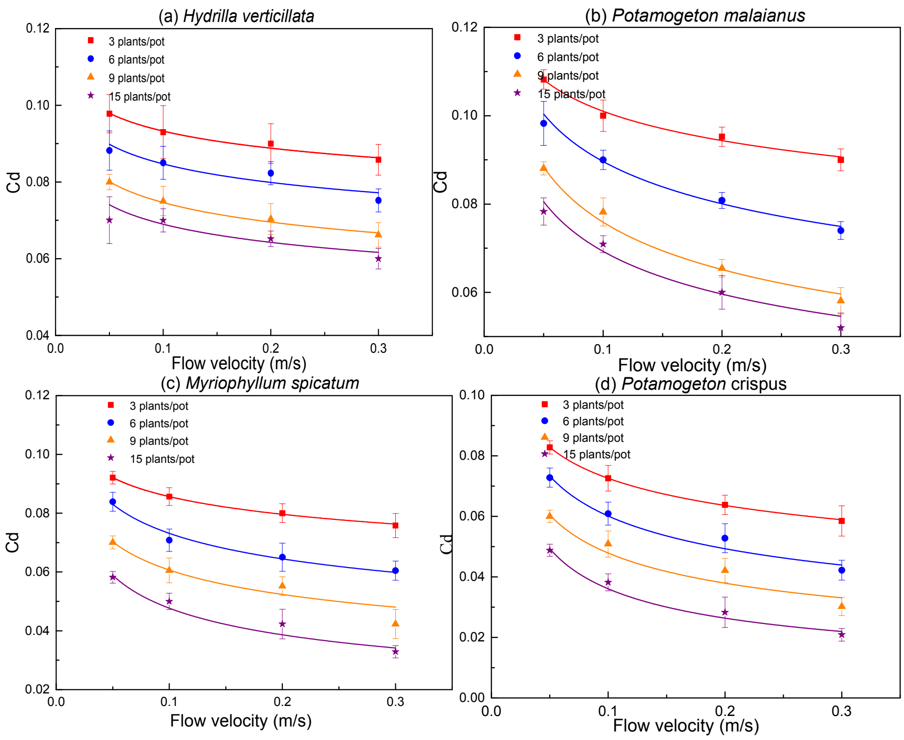

Figure 6. The Cd of different initial densities submerged macrophytes under different flow velocities

 ©2017, IAHR. Used with permission / ISSN 1562-6865 (Online) - ISSN 1063-7710 (Print)

Table 1. The E-value of different initial densities submerged macrophytes

Species	Initial planting density (plants/pot)	E-values	Correlation coefficient R^2
H. verticillata	3	-0.0705	0.960
	6	-0.0847	0.597
	9	-0.0965[c]	0.705
	15	-0.1025[c]	0.833
P.malaianus	3	-0.0983	0.986
	6	-0.1620	0.977
	9	-0.2172	0.932
	15	-0.2198	0.990
M. spicatum	3	-0.1056	0.891
	6	-0.1824	0.952
	9	-0.2123	0.905
	15	-0.2839	0.967
P. crispus	3	-0.1903	0.996
	6	-0.2859	0.969
	9	-0.3363	0.940
	15	-0.4512	0.831

E-value was acquired by fitting the formula $Cd=aU^b$ (Table 2). The four submerged plants had significant differences on E-value ($P<0.05$), presenting P. crispus < M. spicatum < P. malaianus < H. verticillata, which indicated that the reconfiguration ability of P. crispus in the face of water movement was better than the others, and H. verticillata had a relatively bad reconfiguration ability. E-Value of the four plants gradually reduced as initial density increases ($P=0.062$).

3.3 Photosynthetic fluorescence characteristics

As shown from Figure 7, water velocity had significant influence on Fv/Fm ($P<0.05$), while initial density did not have evident influence ($P=0.233$). Fv/Fm of H.verticillata, P. malaianus and P.crispus at 0.05m/s were higher than that of static state, and Fv/Fm reduced significantly as flow velocity increases, when the velocity is over 0.05m/s. Fv/Fm of M. spicatum at 0.1m/s is still higher than that of control group (0m/s), which is not restrained significantly.

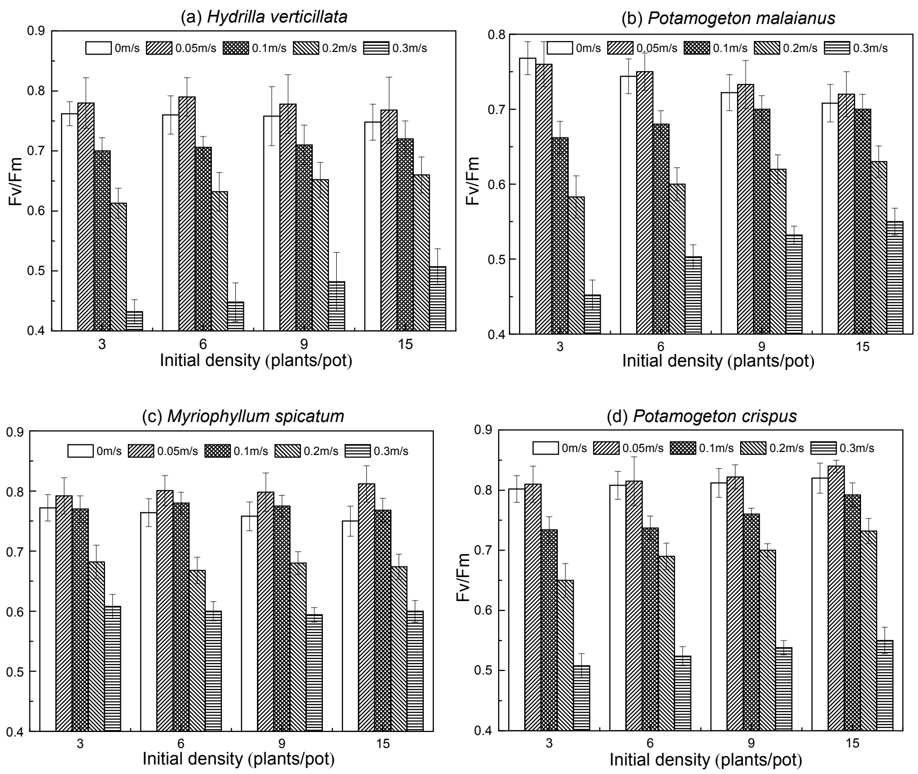

Figure 7. The Fv/Fm of different initial densities submerged macrophytes under different flow velocities

Table 2. Parameter values of RLCS of submerged macrophytes

Species	Flow velocity	Maximum relative transfer rate (rETRm/μmol m^{-2} s^{-1})	α	Half saturated light intensity (E_k/μmol m^{-2} s^{-1})
	0	28.325 ± 1.663	0.203±0.004	88.967 ± 3.220^{a}
	0.05	32.822± 1.587	0.228±0.017	93.212 ± 5.668^{a}
H. verticillata	0.1	20.525± 1.117	0.142±0.025	78.455 ± 3.074^{b}
	0.2	16.008± 0.587	0.098±0.008	64.233 ± 3.424^{c}
	0.3	10.726± 1.027	0.066±0.008	50.414 ± 1.706
	0	18.020± 2.002	0.289±0.010	80.383 ± 2.120
	0.05	13.332± 1.288	0.256±0.022	72.323 ± 2.244
P. malaianus	0.1	11.820± 1.353	0.200±0.020	65.618 ± 1.736
	0.2	9.216± 1.235	0.126±0.005	53.921 ± 1.446
	0.3	6.663± 0.283	0.076±0.005	40.290 ± 1.209
	0	28.828± 1.287	0.302±0.016	98.288 ± 2.238
	0.05	35.420± 2.882	0.389±0.028	105.525 ± 3.020
M. spicatum	0.1	30.002±3.008	0.307±0.020	100.202 ± 2.524
	0.2	20.516± 2.227	0.255±0.012	85.626 ± 2.002
	0.3	13.452± 1.322	0.128±0.009	70.233 ± 1.005
	0	21.033± 1.747	0.261±0.030	86.233 ± 2.006
	0.05	24.820± 2.200	0.338±0.026	90.181 ± 1.946
P. crispus	0.1	15.220± 1.352	0.225±0.020	70.244 ± 2.606
	0.2	10.750± 1.087	0.138±0.015	60.118 ± 1.826
	0.3	6.583± 0.887	0.082±0.012	48.292 ± 1.002

RLCS of submerged plants took on significant change under four different flow velocities (Figure 8). A series of parameters reflecting the photosynthetic capacity were acquired by curve fitting (Table 2). Except P. malaianus, the maximum rETRm, α and Ek of other three types of plants appeared at 0.05m/s and rETRm, α and Ek decreased significantly with increasing velocity (0.1-0.3m/s) ($P<0.05$). However, the rETRm、α and Ek of P. malaianus all reduced significantly as flow velocity increases. ($P<0.05$).

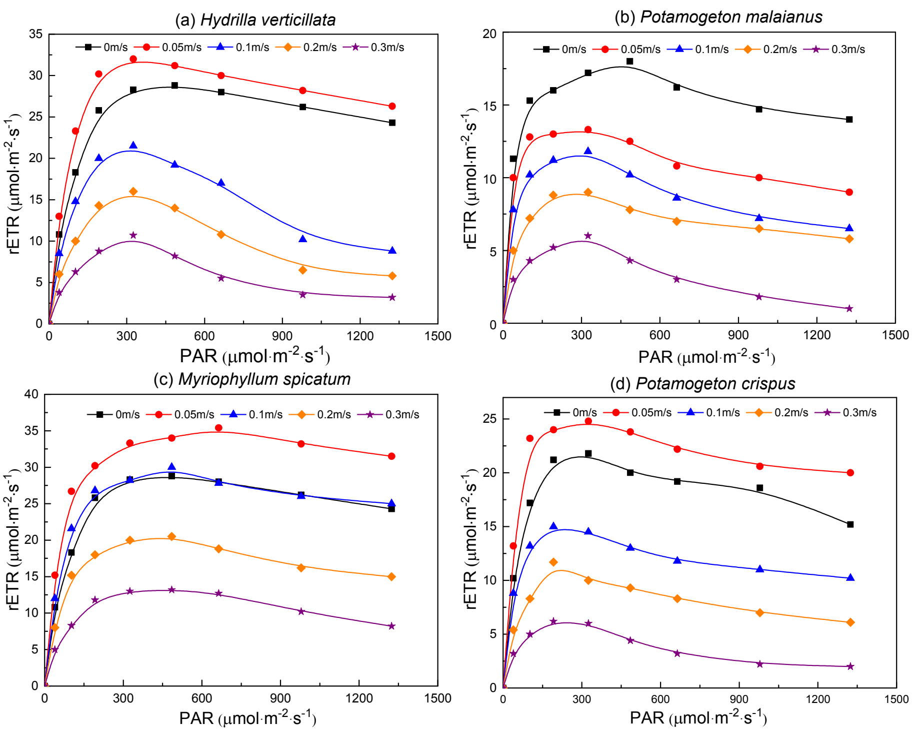

Figure 8. The RLCs of submerged macrophytes under different flow velocities

4 DISCUSSION

Aquatic plant growth depends on a series of environmental factors and biological factors, including the hydrological factor (Riis et al., 2003), the use of light, radiation (Wang et al., 2015), substrate (Li et al., 2015) and periphyton (Reid et al., 2007), etc. For shallow rivers and lakes, among these factors, hydrological factor has long been considered as an important factor influencing aquatic plant survival and species diversity (Riis et al., 2008; Biggs et al., 1996). Madsen (Madsen et al., 2001) pointed out that normally the richness and

 ©2017, IAHR. Used with permission / ISSN 1562-6865 (Online) - ISSN 1063-7710 (Print)

diversity of plants are stimulated to grow under low and medium flow velocities, while high velocity restrains plant growth. Biggs (Biggs et al., 2005) carried out a further discussion on this relationship in 2005, reckoning that shear stress is related to long period water movement with high intensity, and mass transport process is influenced by water movement with low intensity and high frequency. In the research, 0.05m/s favored the growth of these four species since low velocity made the boundary layer thickness of them on the surface thinning, which increases CO_2 and nutrient flux (Stewart et al., 2003); However, stretch and drag exerted on plants produced by shear stress generated by high velocity may lead to breakage of leaf, stem and reduction of plant height and biomass (Schutten et al., 2005; Koch, 2001). The value of Cd and E-value differed significantly among these four submerged macrophytes ($P<0.05$), which presented P. crispus < M. spicatum < P. malaianus < H. verticillata. It indicated that reconfiguration of P. crispus was better than the other three species in the face of water movement, while plasticity of H. verticillata was relatively poor, which may be related to the lignin content. The degree of lignification of stems of H. verticillata and P. malaianus were relatively high, which made them vulnerable (Jonas et al., 2010).

The Fv/Fm and RLCs in the 0.05m/s were higher than 0m/s because 0.05m/s was advantageous to photosynthesis by thinning boundary layer thickness on the surface and increasing the CO_2 and nutrient flux to the photosynthetic organ (Riis et al., 2008). However, 0.1m/s-0.3m/s had a negative impact on Fv/Fm and RLCs as a result of reduction of transparency of water caused by sediment suspension induced by high flow rate (Wang et al., 2016; Li et al., 2015; Madsen et al., 2001). Studies have shown that the synthesis of photosynthetic pigments of P. malaianus leaves is greatly influenced by light intensity, and the plant is not suitable to live in water with low transparency. There were also researches which reported that under environments of 100% natural light with attached algae, the physiological activity of M. spicatum is restrained, while water environments with 10% natural light and without attached algae are contribution to physiological metabolism (Song et al., 2015). This explains why the lowering speed of P. malaianus plant height and biomass with increase in flow velocityis higher than that of M. spicatum.

5 CONCLUSION

It was evident that high flow velocity inhibited the normal growth of all four plants, while lower velocity did not harm them and was in favor of growth. M. spicatum were found to possess high adaptability to cope with this mechanical stress, which was the preferred species for the aquatic plant recovery. Moreover, faced with high velocity, the negative effect of water movement on plants could be reduced by increasing initial planting densities.

ACKNOWLEDGEMENTS

This study was financially supported by the National Major Science and Technology Program for Water Pollution Control and Treatment of China (2012ZX07101-007).

.

REFERENCES

Biggs, B.J.F. (1996). Hydraulic Habitat of Plants in Streams. *River Research and Applications*, 12, 131-144.

Blanchette, C.A. (1997). Size and Survival of Intertidal in Respones to Wave Action: A Case Study with Fucus Gardneri. *Ecology*, 78, 1563-1578.

Biehle, G., Speck, T. & Spatz, H.C. (1998). Hydrodynamics and Biomechanics of the Submerged Water Moss Fontinalis Antipyretica: A Comparison of Specimens from Habitats with Different Flow Velocities. *Botanica Acta,* 111, 42-50.

Biggs, B.J.F., Nikora, V.I. & Snelder, T.H. (2005). Linking Scales of Flow Variability to Lotic Ecosystem Structure and Function. *River Research and Applications*, 21, 283-298.

Champika, E., Takashi, A. & Kiyoshi, K. (2013). Water Movement Induced Variations in Growth Regulation and Metabolism of Freshwater Macrophyte Vallisneria Spiralis L.In Early Growth Stages. *Hydrobiologia*, 709, 173-182.

Ge, R.L., Si, Q. & Liu, J.Y. (2013). Branches Tensile Mechanical Characteristics and the Influencing Factors of Six Plant Species in Inner Mongolia. *Journal of Desert Research*, 33(5), 1333-1339.

Geest, G., Wolters, H., Roozen, F. & Coops, H. (2005). Water Level Fluctuations Affect Macrophyte Richness in Floodplain Lakes. *Hydrobiologia*, 539(1), 239-248.

Hun, K.B. (2013). The Effect of River Flow Retardation on Algal Growth. *Natural Resources and Conservation*, 1(2), 30-34.

Jonas, S., Kris, B., Hans, B., Tomasz, O., Patrick, M. & Eric, S. (2010). Silica Uptake in Aquatic and Wetland Macrophytes: A Strategic Choice between Silica, Lignin and Cellulose. *New Phytologist*, 186, 385-391.

Koch, E. (2001). Beyond Light: Physical, Geological, and Geochemical Parameters as Possible Submerged Aquatic Vegetation Habitat Requirements. *Estuaries*, 24(1), 1-17.

Li, F., Zhu, L., Xie Y., Li, J., Chen, X., Deng, Z. & Pan, B. (2015). Colonization by Fragments of the Submerged Macrophyte Myriophyllum Spicatum under Different Sediment Type and Density Conditions. *Scientific Reports*, 2, 1-7.

Madsen, J.D., Chambers, P.A., James, W.F., Koch, E.W. & Westlake, D.F. (2001). The Interaction between Water Movement, Sediment Dynamics and Submersed Macrophytes. *Hydrobiologia*, 444, 71 -84.

Platt, T., Gallegos, C.L. & Harrison, W.G. (1980). Photo inhibition of Photosynthesis in Natural Assemblages of Marine Phytoplankton. *Journal of Marine Research,* 38, 687-701.

Ralph, P.J. & Gademann, R. (2005). Rapid Light Curves: A Powerful Tool Toassess Photosynthetic Activity. Aquatic Botany, 82, 222-237.

Riis, T. & Biggs B.J.F. (2003). Hydrologic and Hudraulic Control of Macrophyte Establishment and Performance In Streams. Limnol.Oceanogr, 48, 1488-1497.

Riis, T., Suren, A.M., Clausen, B. & Sand J.K. (2008). Vegetation and Flow Regime in Lowland Streams. *Freshwater Biology*, 53(8), 1531-1543.

Reid, R., Greenberg, M., Lorincz, A., Jenson, A.B., Husain, M., Zado, B., White, T. & Daoud, Y. (2007). Macrophyte-Phytoplankton Interactions: The Relative Importance of Allelopathy versus Other Factors. *Ecological Modelling*, 204(1), 85-92.

Sagnes, P., Champagne, J.Y. & Morel, R. (2000). Shifts in Drag and Swimming Potential during Grayling Ontogenesis: Relations with Habitat Use. *Journal of Fish Biology*, 7, 52-68.

Sara, P., Gudrun, B. & Pierre, S. (2005). Adaptation to Incresing Hydraulic Stress: Morphology, Hydrodynami Cs and Fitness of Two Higher Aquatic Plant Speices. *Journal of Experimental Botany*, 56(412), 777-786.

Schutten, J., Dainty, J. & Davy, AJ. (2005). Root Anchorage and Its Significance for Submerged Plants in Shallow Lakes. *Journal of Ecology*, 93, 556-571.

Stewart, H.L. & Carpenter, R.C. (2003). The Effect of Morphology and Water Flow on Photosynthesis of Marine Macroalgae. *Ecology*, 84(11), 2999-3012.

Song, Y. Z., Kong, F., Wang, M. & Zhang, Y.N. (2015). Effects of Light Intensity and Epiphytic Algae on Physiological Parameters of Myriophyllum Spicatum. *Journal of Agricultural Environmental Science*, 34(2), 233-239.

Vogel, S. (1984). Drag and Flexibility in Sessile Organisms. American Zoologist, 24, 37-44.

Wang, L., Dai, Y.X., Fan, X.L., Zhang, Y.X., Huang, P. & Wang, X.C. (2015). Effect of Wind on Hydraulic Properties and Growth of Artemisia Annua Linn. *Acta Ecologica Sinica*, 35(15), 4454-4461.

Wang, J.Q., Song, Y.Z. & Xue, Y. (2015). Effects of Ultraviolet Radiation on Rapid Light-Response Curves of Potamogeton Crispus. *Journal of Lake Sciences*, 27(3), 451-458.

Wang, P., Zhang, Q., Xu, Y.S. & Yu, H.F. (2016). Effects of Water Level Fluctuation on the Growth of Submerged Macrophyte Communities. *Flora-Morphology, Distribution, Functional Ecology of Plants*, 223, 83-89.

Zhu, G., Li, W., Zhang, M., Ni, L. & Wang, S. (2012). Adaptation of Submerged Macrophyte to both Water Depth and Flood Intensity as Revealed By Their Mechanical Resistance. *Hydrobiologia*, 696, 77-93.

 ©2017, IAHR. Used with permission / ISSN 1562-6865 (Online) - ISSN 1063-7710 (Print)

A STUDY ON CRITICAL HYDRODYNAMIC CONDITIONS FOR INDUCING SPAWNING BEHAVIOR OF FOUR MAJOR CHINESE CARPS

LEI TANG[(1)], YU QING LIN[(2)], QIU WEN CHEN[(3)], WEI JIANG[(4)] & YU XIN ZHANG[(5)]

[(1,2,3,5)] Center for Eco-Environmental Research, Nanjing Hydraulic Research Institute, Nanjing, China
tangleiNHRI@126.com; linyuqing820918@hotmail.com; qwchen@nhri.cn; Zhangx321@hotmail.com
[(4)] Institute of Chinese Sturgeon, Three Gorges Corporation, Yichang, China
106635291@QQ.com

ABSTRACT

The Three Gorges Reservoir is a key project in the middle reach of Yangtze River, impoundment of the reservoir has changed hydrological regime in downstream area, and also affected the natural reproduction of four major Chinese carps, leading to a deep recession in population. In this paper, a research about hydrodynamic spawning cues for four major Chinese carps was undertaken as follows: firstly, the amount of eggs of four major Chinese carps in the Yanzhiba spawning ground of the Yangtze River have been monitored daily during spawning seasons from 2012 to 2014. Then, flow conditions of the spawning ground at the monitoring periods were simulated through a two-dimension hydrodynamic model, which has been validated by measured hydrological data. Finally, relationships between the quantity of eggs of four major Chinese carps and flow conditions were compared. The results showed that both velocity and rise rate of velocity acted as crucial hydrodynamic factors, which obviously affected the spawning success by four major Chinese carps. Furthermore, the suitable velocity for stimulating spawning behavior was between 1.31 to 1.48 m/s, too small or too large velocity was not benefit for spawning success, the same suitable velocity rise rate for spawning appeared to range from 0.013 to 0.023 (m/s)/d. This paper could not only offer important basis to spawning ground restoration work of four major Chinese carps but also provide reasonable guidance for the eco-regulation of Three Gorges Reservoir.

Keywords: Four major Chinese carps; spawning behavior; fish egg quantity; flow velocity; velocity rise rate.

1 INTRODUCTION

Reservoirs and dams could adjust the water resource configuration and relieve the tension between supply and demand of the water resource in some degree, which not only play an important role in the management of flood control but also provide guarantee for social sustainable development (Li et al., 2015; Li et al., 2012; Yi et al., 2010a). However, large reservoirs will inevitably cut off the natural connect between the rivers, blocking the migration of the nutrient and changing the water temperature that aquatic organism live on. Meanwhile, since the reservoirs should satisfy the demand of flood control, electricity generation and water supply, seasonal changing discharge was replaced by uniform release, which has resulted in a destruction for the fish spawning habitat and generated a bad effect on their natural reproduction (Wang and Xia, 2009; Yi et al., 2010b).

Fish spawning habitat is always characterized by unique hydrodynamic condition (Yao and Rutschmann, 2015). The study on the hydrodynamic characteristics of fish spawning habitats started at 1980s. (Sempeski and Gaudin, 1995) reported that mean velocities observed on grayling spawning sites did not differ apparently between rivers or years. Moreover, spawners before spawning activities were found in a resting pool characterized by slow-flowing water (mainly<20 cm s^{-1}), it could be considered that current velocity was a significant factor to describe grayling spawning ground. (Moir et al., 1998) have shown that hydraulic variables including (depth, velocity and Froude number) appeared as a significant influence on spawning habitat for Atlantic salmon; (Crowder and Diplas, 2002) used two-dimensional hydraulic model to reproduce flow patterns based on detailed channel geometry and suggested that vorticity and circulation could be used as means to evaluate the spatial flows occurring within different regions of stream habitat; (Yang et al., 2008) analyzed the flow field characteristics in Chinese sturgeons' spawning ground by calculating the density of vorticity, kinetic energy gradient and its growth rate, the results showed that density of vorticity was the most sensitive variable to describe egg density of Chinese sturgeons in unit suitable area. Most studies on characteristics of spawning habitat only developed from some descriptions of hydraulic factors. However, the corresponding relationship between fish spawning behaviors and related hydrodynamic factors was seldom involved. The way to which how to find the hydraulic cues for fish spawning has become a problem that needs to be solved for the restoration and protection of fish spawning habitat.

Grass carp (Ctenop haryngodon idellus), black carp (Mylopharyngodon piceus), silver carp (Hypophthalmichthys molitrix) and bighead carp (Aristichthys nobilis) are known as four major Chinese carps (Chinese carps for short). The Yangtze River is a natural resources reservoir for Chinese carps, where fish fry

©2017, IAHR. Used with permission / ISSN 1562-6865 (Online) - ISSN 1063-7710 (Print)

production takes 70% of national total output. At present, Three Gorges Dam across the Yangtze River has cut off the breeding migration course of Chinese carps, leading to a sharp decrease of spawning habitats and fish resources (Li et al., 2006). To restore the natural spawning habitats of Chinese carps and recover the population quantity, a large number of scholars have studied on hydrodynamic factors characterized by Chinese carps spawning site (Liu et al.,2004; Liu et al., 1997; Yi et al., 2010a). However, research on hydrodynamic cues for initiating the spawning behavior has not been undertaken and quantization of flow pattern required by spawning requirement is not clear, which could not provide reasonable reference for eco-operation.

This study analyzed the impact of two sensitive factors (mean velocity and velocity rise rate) on the natural reproduction for Chinese carps, and then established appropriate scope of velocity and velocity rise rate satisfying the spawning requirement of Chinese carps.

2 STUDY SITE DESCRIPTION

The Yangtze River is the biggest river in China, originating from Tanggula Mountains in Tibetan Plateau, running through 11 provinces and cities including Qinghai Province, Tibet, Sichuan Province, Yunnan Province and others, and finally falling into the East China Sea at Shanghai (See Fig. 1).

Yanzhiba spawning ground (Fig. 1) is located at the upstream of Yidu city with a length of 10km, which has representative landform and hydrodynamic characteristic here. The width of water surface does not change sharply with the stream. At dry season, the width is about 800-100m and 820-1300m at wet season. The composition of riverbed is mainly made up of sand. The stream gradient is small, water fronts at both sides basically are smooth, and many cross sections are “U” shapes. Longitudinally, deep pools and shallow areas appear alternately and flow velocity here is fast which can provide necessary flow stimulation for the spawning of Chinese carps.

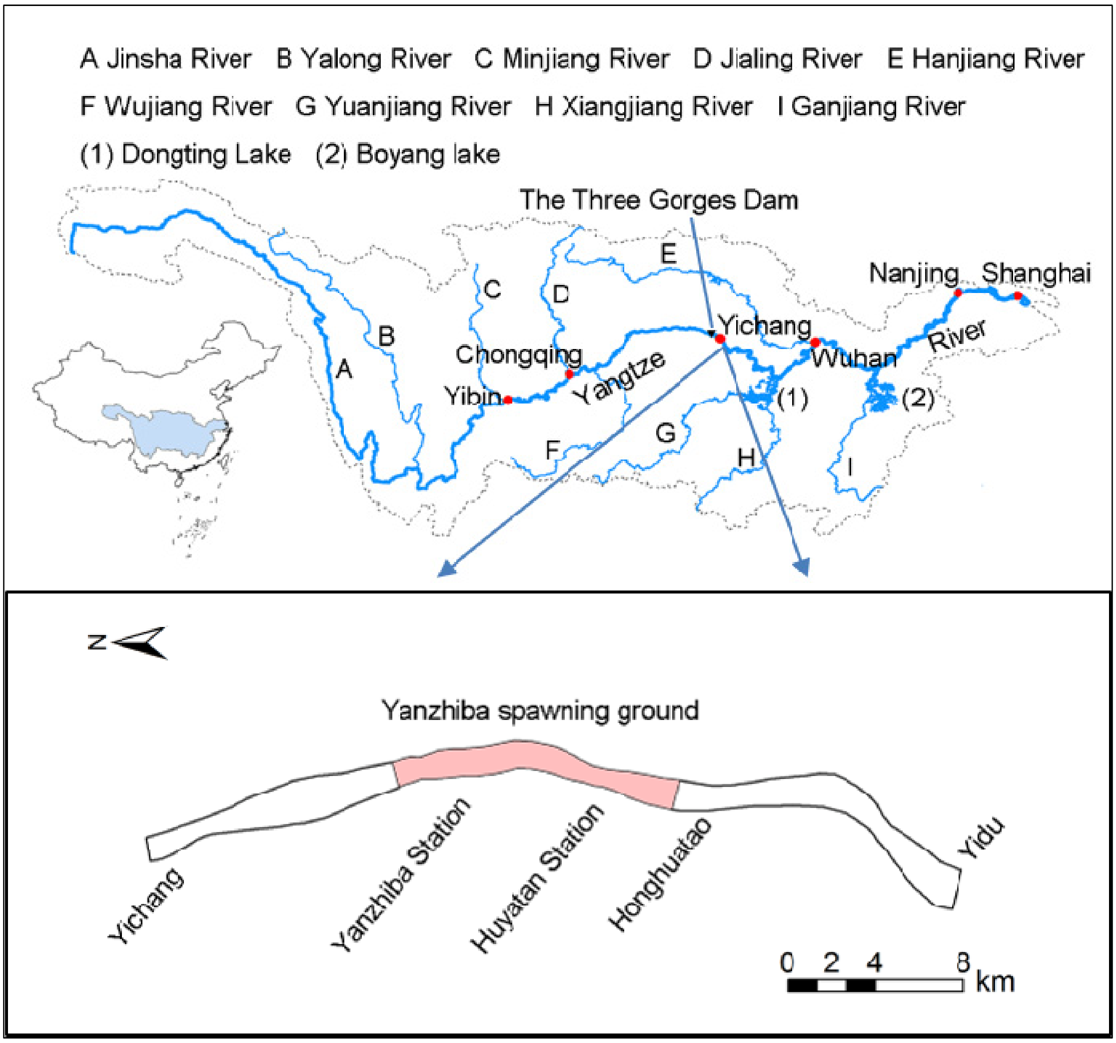

Figure 1. The location of Yangtze River and the Yanzhiba spawning ground.

 ©2017, IAHR. Used with permission / ISSN 1562-6865 (Online) - ISSN 1063-7710 (Print)

3 METHODS

3.1 Field monitoring

From the year of 2012-2014, the amount of eggs of Chinese carps in Yanzhiba spawning ground was daily monitored and the natural reproduction data of Chinese carps was acquired. Field monitoring was usually conducted from mid May to early July, since this period is just the time for natural reproduction. Chinese carps' eggs belongs to pelagic egg which is a little heavier than water, the fertilization eggs will suspend on the water surface after a period of water absorption. Field monitoring was carried out in Yidu section, 15km to the downstream of spawning ground. At the sampling section, 5 sampling sites were arranged equidistantly from left bank to right bank. During the monitoring periods, eggs were collected twice a day and each sampling collection continued for 1 hour, one was between 8:00 am and 9:00 am, the other was between 16:00 pm to 17:00 pm. A conical net and a collection box were used to gather the eggs. Meanwhile, flow velocity was recorded by current meter fixed on net opening. Sampling eggs were firstly sorted out primarily at field monitoring section, then we took Chinese carps' eggs back for further cultivation and identification, and calculated the drifting density (D) of Chinese carps' eggs that is the average of the total amount of eggs' densities in every sampling sites. The calculation formula is as below:

$$D = \sum_{i=1}^{n} d_i / n \qquad [1]$$

where, D represents eggs density in the monitoring section, ind/1000m^3; d_i is the eggs' density in the sampling site (i), ind/1000m^3; n is the amount of sampling sites.

3.2 Mathematical model

This study mainly focused on the hydraulic cues for the spawning behavior of Chinese carps. Therefore, we established a two-dimensional hydrodynamic model and performed a simulation of the flow condition for spawning site so as to obtain the temporal and spatial variation of the hydrodynamic factors during the spawning dates. The governing equation of the simulation is as follows:

$$\frac{\partial h}{\partial t} + \frac{\partial (hu)}{\partial x} + \frac{\partial (hv)}{\partial y} = Q_a \qquad [2]$$

$$\frac{\partial u}{\partial t} + u\frac{\partial u}{\partial x} + v\frac{\partial u}{\partial y} = -\frac{1}{\rho_0}\frac{\partial p}{\partial x} + fv + \upsilon\left(\frac{\partial^2 u}{\partial x^2} + \frac{\partial^2 u}{\partial y^2}\right) + \frac{1}{\rho_0 H}\tau_x \qquad [3]$$

$$\frac{\partial v}{\partial t} + u\frac{\partial v}{\partial x} + v\frac{\partial v}{\partial y} = -\frac{1}{\rho_0}\frac{\partial p}{\partial y} - fu + \upsilon\left(\frac{\partial^2 v}{\partial x^2} + \frac{\partial^2 v}{\partial y^2}\right) + \frac{1}{\rho_0 H}\tau_y \qquad [4]$$

where, Q_a is the term accounting for local water sink or source, m/s; h is the depth of water, m; u and v account for the velocity on directions of x and y, m/s; υ is the horizontal viscosity coefficient, m^2/s; f is Coriolis force coefficient; τ_x, τ_y account for the shearing strength at bottom, N/m.

We verified the accuracy of the model by using measured data from the Yanzhiba and Huyatan Hydrologic Station (See Fig. 1). The comparison between measured and computed values of daily mean water level in May, 2014 is shown as Fig.2. The result indicated that the measured and computed values were highly consistent, which could show that the hydrodynamic model was a rational design, and the parameter was accurate.

4 RESULT AND DISCUSSION

4.1 The relationship between average velocity and fish eggs density

Fig.3 shows that the reproductive activities of Chinese carps mainly focused on the velocity between 0.99 to 1.83m/s, and no fish eggs appeared outside this scope. In nature, Chinese carps always prefer to spawn in a high flow condition. By targeting spawning efforts to times with high velocity, they will be able to maximize the chances that make the offspring to survive under a favorable environmental condition. Furthermore, the eggs are more likely to remain suspended in a high flow condition, thus reducing the potential mortality from settling and providing more opportunity for embryo development. Therefore, a high velocity may be more likely to favor the spawning strategy of Chinese carps. However, over-high velocity magnitude will result in higher turbulent intensity, which is not good for sperm-egg interaction and limit the success of fertilization. In summary, neither too slow nor too high velocity condition would be able to fit the spawning requirement of Chinese carps.

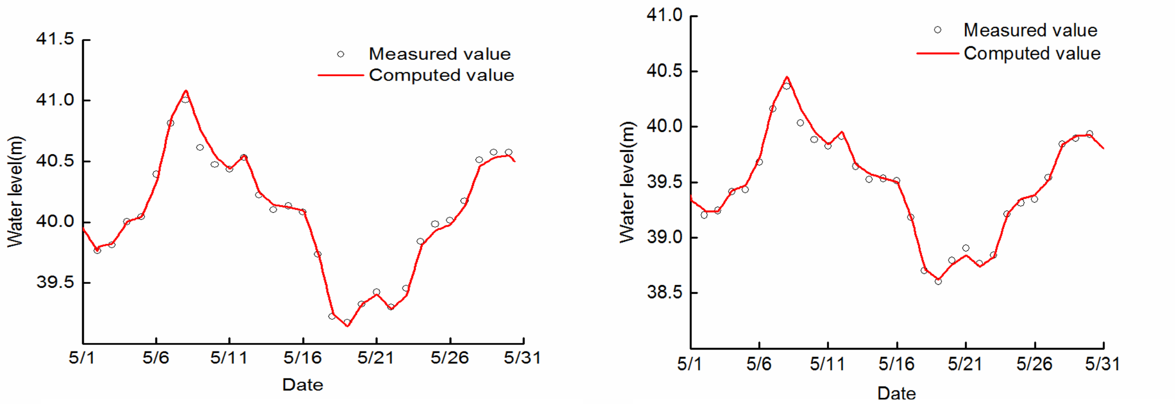

(b) Measured value and computed value for mean water level in Yanzhiba Station.

(a) Measured value and computed value for mean water level in Huyatan Station.

Figure 2. Comparison for measured value and computed value for water level in May, 2014.

The variation trend of fish eggs density in Fig.3 shows that when the average velocity value was between 1.31 to 1.48 m/s, the fish eggs per unit area would reach to a relatively higher level, indicating that the appropriate velocity scope for the spawning behavior was 1.31-1.48m/s, in accordance with previous studies. Moreover, it could be seen that the spawning peak occurred at the time when velocity reached 1.4m/s, which might be the most suitable magnitude for initiating spawning behaviors.

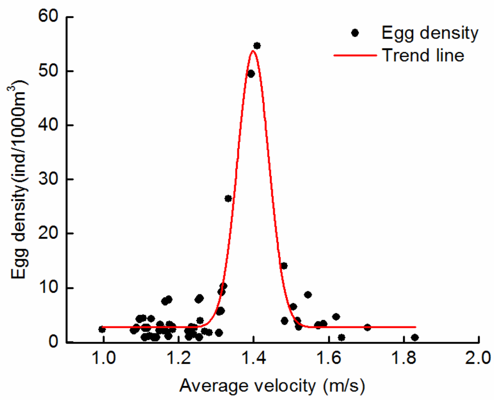

Figure 3. The relationship between egg density and the average velocity.

4.2 The relationship between egg density and velocity rise rate

An increasing discharge is often thought as another driving factor for Chinese spawning activities. On the one hand, a rising rate in velocity may aid the fish in locating their migration route and spawning ground. On the other hand, spawning activities always occurred after a rising flow pattern, for which accelerated gonad mature of adult fish and brought them into spawning condition. The relationship between egg density and velocity rise rate is as shown in Fig.4, which significantly shows that eggs density firstly raised and then dropped with the increasing of velocity rise rate, mass spawning events occurred when diurnal velocity rise rate was between 0 to 0.23 (m/s)/d, which could be considered as a suitable range for Chinese carps spawning. The most appropriate velocity rise rate for spawning activities might be ranging from 0.013 to 0.023 (m/s) /d, during which the spawning peaks occurred. In addition, velocity rise rate is not always the bigger the better, overlarge rising rate of the velocity was more likely to create higher turbulent flow pattern which would limit the mating ability for Chinese carps.

 ©2017, IAHR. Used with permission / ISSN 1562-6865 (Online) - ISSN 1063-7710 (Print)

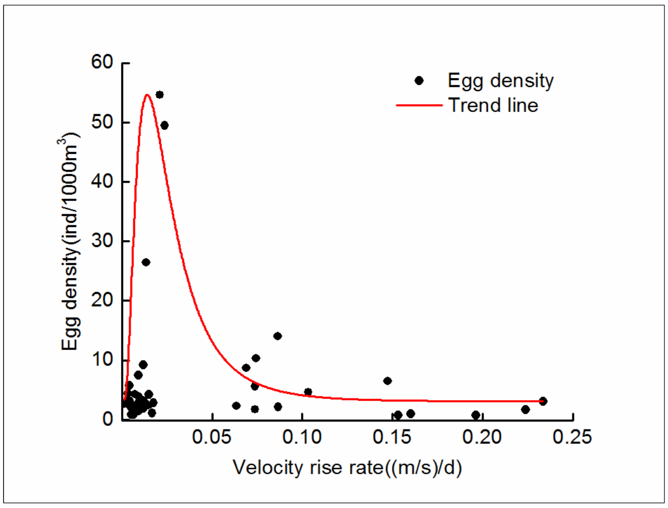

Figure 4. The relationship between egg density and velocity rise rate

5 CONCLUSION

From this paper, it could be concluded that the velocity and velocity rise rate in spawning ground have great impact on the natural reproduction of Chinese carp. The suitable velocity to initiate spawning behavior ranged from 1.31 to 1.48 m/s, and the same suitable velocity rise rate range was 0.013 to 0.023 (m/s) /d. The study in this paper may provide reasonable reference for eco-regulation of the Three Gorges Reservoir. Additionally, it can also be used to other rivers where Chinese carps spawning habitat need to be improved.

ACKNOWLEDGEMENTS

This study was supported by the Eco-Environmental Research Center of Nanjing Hydraulic Research Institute. We also gratefully acknowledge the contributions by Institute of Chinese sturgeon.

REFERENCES

Crowder, D. W. & Diplas, P. (2002). Vorticity and Circulation: Spatial Metrics for Evaluating Flow Complexity in Stream Habitats. *Canadian Journal of Fisheries and Aquatic Sciences*, 59(4), 633-645.

Li, C., Peng, J. & Liao, W. (2006). Study on the Eco-Hydrological Factors and Flow Regime Requirement on Spawning of Four Major Chinese Carps in the Middle Reaches of Yangtze River. *Journal of China Institute of Water Resources and Hydropower Research*, 3, 001.

Li, R., Chen, Q., Tonina, D. & Cai, D. (2015). Effects of Upstream Reservoir Regulation on the Hydrological Regime and Fish Habitats of the Lijiang River, China. *Ecological Engineering*, 76, 75-83.

Li, Z., Dai, H. & Mao, J. (2012). Short-term Effects of Flow and Sediment on Chinese Sturgeon Spawning. *Procedia Engineering*, 28, 555-559.

Liu, S. P., Qiu, S. L., Chen, D. Q. & Huang, M. G. (1997). Protection and Rational Utilization of the Germplasm Resources of the Four Major Chinese Carps in the Yangtze River System. *Resources and Environment in the Yangtze Valley*, 6(2), 127-131.

Liu, S., Chen, D., Duan, X., Qiu, S. & Huang, M. (2004). Monitoring of the Four Famous Chinese Carps Resources in the Middle and Upper Reaches of the Yangtze River. *Resources and Environment in the Yangtze Basin*, 13(2), 183-186.

Moir, H. J., Soulsby, C. & Youngson, A. (1998). Hydraulic and Sedimentary Characteristics of Habitat Utilized by Atlantic Salmon for Spawning in the Girnock Burn, Scotland. *Fisheries Management and Ecology*, 5(3), 241-254.

Sempeski, P. & Gaudin, P. (1995). Habitat Selection by Grayling—I. Spawning Habitats. *Journal of Fish Biology*, 47(2), 256-265.

Wang, Y. & Xia, Z. (2009). Assessing Spawning Ground Hydraulic Suitability for Chinese Sturgeon (Acipenser Sinensis) from Horizontal Mean Vorticity in Yangtze River. *Ecological Modelling*, 220(11), 1443-1448.

Yang, Y., Yan, Z. & Chang, J. (2008). Hydrodynamic Characteristics of Chinese Sturgeon Spawning Ground in Yangtze River. *Journal of Hydrodynamics*, 20(2), 225-230.

Yao, W. & Rutschmann, P. (2015). Three High Flow Experiment Releases from Glen Canyon Dam on Rainbow Trout and Flannelmouth Sucker Habitat in Colorado River. *Ecological Engineering*, 75, 278-290.

Yi, Y., Wang, Z. & Yang, Z. (2010a). Impact of the Gezhouba and Three Gorges Dams on habitat suitability of carps in the Yangtze River. *Journal of Hydrology*, 387(3), 283-291.

Yi, Y., Wang, Z. & Yang, Z. (2010b). Two-Dimensional Habitat Modeling of Chinese Sturgeon Spawning Sites. *Ecological Modelling*, 221(5), 864-875.

Proceedings of the 37th IAHR World Congress
August 13 – 18, 2017, Kuala Lumpur, Malaysia

EXPERIMENTAL STUDY ON THE IMPACT OF HYDRAULIC CHARACTERISTIC ON THE DISSIPATION PROCESS OF SUPERSATURATED TOTAL DISSOLVED GAS

CHENJUN ZENG [1], QIUWEN CHEN [2], JIN ZHANG [3], YUQING LIN [4] & XIA HU [5]

[1,2,3,4] Center for Eco-environmental Research, Nanjing Hydraulic Research Institute, Nanjing, China
[1] College of Hydrodynamic and Ecology Engineering, Nanchang Institute of Technology, Nanchang, China
[5] School of Civil Engineering and Architecture, Nanchang University, Nanchang, China
zcjling@163.com; qwchen@nhri.cn; zhangjin@nhri.cn; yqlin@nhri.cn; zhx0406@163.com

ABSTRACT

Dam discharge is the main source for total dissolved gas (TDG) supersaturation, which may cause fishes to suffer from gas bubble disease, especially when the dissipation process of supersaturated TDG is slow. Hydraulic characteristics are important factors in the dissipation process of supersaturated TDG, the quantitative relationship between the dissipation process and hydraulic characteristic has not been previously clarified. This paper aimed to study the impacts of hydraulic characteristic on supersaturated TDG dissipation process in different conditions by using annular flume. Through a series of experiments, an equation describing the relationship between Reynolds number and dissipation coefficient was established in this study. The results showed that the supersaturated TDG dissipation coefficient increased with the Reynolds number and the flow velocity under the same water depth. When the TDG saturation was higher than 112%, the dissipation rate increased with the flow velocity. The dissipation of supersaturated TDG was dominated by the release of gas molecules which filled in the water molecule gaps in this period. When the TDG saturation was decreased down to 112%～110% or even lower, the dissipation rate appeared stable, in this situation, the dissipation of supersaturated TDG was dominated by the release of compounds which are formed by gas molecules and water molecule.

Keywords: Total dissolved gas; supersaturation; dissipation coefficient; hydraulic characteristic.

1 INTRODUCTION

Total dissolved gas (TDG) supersaturation is an issue associated with dams and has been a water quality issue since the late 1960s. Spillway discharges from hydropower dams, thermal discharge from power plants and photosynthesis have been identified as main sources of supersaturated TDG in the rivers (Tan et al., 2006), which frequently causes a supersaturation level above 140% (Feng et al., 2010). The supersaturated TDG is then dissipated and released to the atmosphere while transported with flow to downstream rivers, but the dissipation process is relatively slow that it may last for tens or hundreds of kilometers. Field observations have been conducted previously to study on TDG dissipation process in the downstream of spillways, and have indicated that, the dissipation rate of TDG saturation is 5% per 100km decreasing along the mid-Yangtze River downstream of the Three Gorges Dam (Feng et al., 2010), and TDG saturation degree in 10kms downstream of Tongjiezi Hydropower Station is still remained as 130% (Qu et al., 2011a). Such high TDG saturation degree may cause gas bubble disease in fish and roe (Tan et al., 2006; Johnson et al., 2007), even may threaten fish survival and reproduction.

Dissipation process is affected by many factors. IIHR have already developed series of numerical models to predict the distribution of TDG in downstream rivers (Huang, 2002; Politano et al., 2004; Weber et al., 2004). One dimensional longitudinal dissipation model of TDG has been developed by US Army Corps of Engineers (USACE, 2005). Politano used two-phase flow models to simulate TDG dissipation process (Politano et al., 2009). Sichuan University has conducted several field observations, by using the methods of experiments, numerical simulation and theoretical analysis, the dissipation rules of TDG in both Three Gorges Dam and Ertan Hydropower Station were studied, results showed that water depth, temperature, wind speed, turbulence intensity and others, were all the factors that influenced dissipation process of supersaturated TDG (Feng et al., 2010; Qu et al., 2011a; 2011b; Feng et al., 2012; Feng et al., 2014; Li et al., 2015; Huang et al., 2016). The dissipation coefficient decreased with the water depth, increased with water temperature and wind speed. Hydraulic characteristics are important factors that influence TDG dissipation, but a more practical equation for describing the quantitative relationship between hydraulic characteristics with dissipation coefficient is still missing. In this study, an annular flume model is constructed to simulate ideal watercourse, a serial of tests was carried out to study the quantitative relationship between hydraulic characteristic with dissipation coefficient.

 ©2017, IAHR. Used with permission / ISSN 1562-6865 (Online) - ISSN 1063-7710 (Print)

2 MODEL DESIGN AND TESTING PROGRAM

2.1 Test Device and Measure System

The experimental device was composed of an annular flume, nylon propeller, transmission shaft, motor and others. The annular flume was made of organic glass, straight line flume was 1.68m long, curved flume's inner radius was 0.3m and its outer radius was 0.6m. The diagram of experimental device is shown in Figure 1.

The TDG supersaturation generating device was composed of a pressure pot, an air compressor, an air inlet pipe, a water inlet pipe, a water outlet pipe and rotor flowmeters, as shown in Figure 2. The volume of pressure pot was 40L, the maximum pressure was 0.15MPa, the pressure of air compressor was 0.2MPa, gas inlet flow rate was 4 L/min, water inlet and outlet flow rate were 5 L/min.

The TDG pressure in water was measured by using a Hydrolab MS5 Water Quality Multiprobes which is made by the Hach Company, the device was arranged in measuring point A. The probe's measurement range was between 400mmHg～1300 mmHg, the measuring accuracy was about ± 0.1%, and the resolution was about 1.0mmHg. The flow velocity was measured by using a rotational flow velocity instrument, with a measuring accuracy of 0.1cm/s. After measuring the velocity of points A, B, C and D, the flow mean velocity was derived by calculating the average value.

At the beginning of the experiment, supersaturated water was generated from the TDG supersaturation generating device and then was drained into the annular flume up to the target water depth. Motor and propeller were operated to push the water flowing. TDG pressure and mean flow velocity were measured.

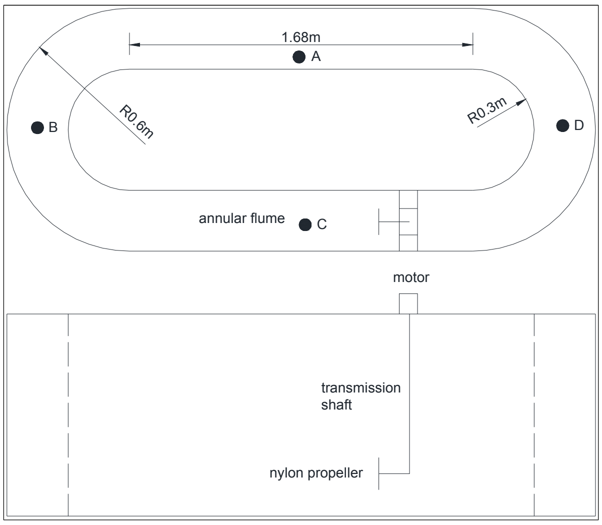

Figure 1. Sketch of the Experimental Device.

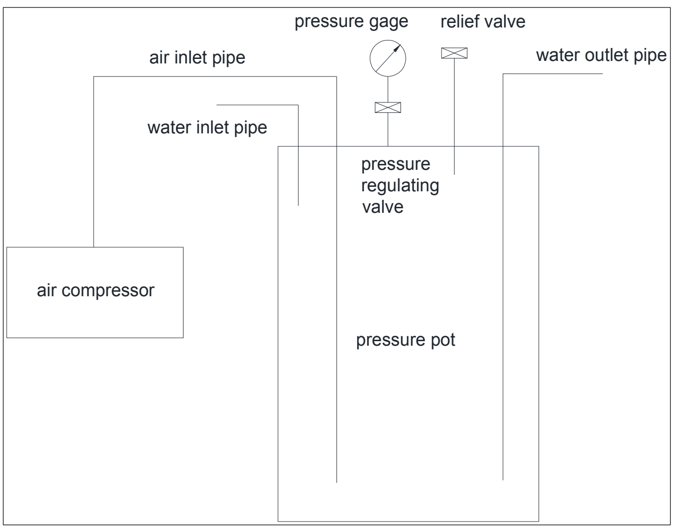

Figure 2. Sketch of the TDG Generation Component.

2.2 Experiment Condition

The dissipation rates of supersaturated TDG under different conditions of flow velocities and water depths (H) were mainly measured. Flow velocity was controlled by motor speed (n). Experiment conditions and their mean flow velocity (v) are shown in Table 1.

Table 1. Experiment Conditions.

Case NO.	Motor Speed n (r/min)	Water Depth H (m)	Flow Velocity v (m/s)
25a	700	0.25	0.17
25b	1000	0.25	0.31
25c	1300	0.25	0.45
30a	700	0.30	0.15
30b	1000	0.30	0.19
30c	1300	0.30	0.25
35a	700	0.35	0.13
35b	1000	0.35	0.15
35c	1300	0.35	0.21

3 EXPERIMENT RESULTS AND ANALYSIS

3.1 Relationship analysis between the TDG dissipation rate and flow velocity

The TDG saturation degree with different flow velocity conditions were monitored. The measured time evolution of supersaturated TDG is shown in Figure 3. When water depth was 0.25m, flow velocities were 0.17m/s, 0.31m/s and 0.45m/s, time consuming for TDG saturation decreasing from 125% to 110% was 4.0h, 2.7h and 2.2h respectively; when water depth was 0.30m, flow velocities were 0.15m/s, 0.19m/s and 0.25m/s, time consuming for TDG saturation decreasing from 122% to 110% was 4.3h, 3.4h and 3.1h respectively; when water depth was 0.35m, flow velocities were 0.13m/s, 0.15m/s and 0.21m/s, time consuming for TDG saturation decreasing from 137% to 115% was 5.2h, 4.1h and 3.4h respectively. The results showed that, under the same water depth, the lower the flow velocity was, the slower the dissipation process of TDG.

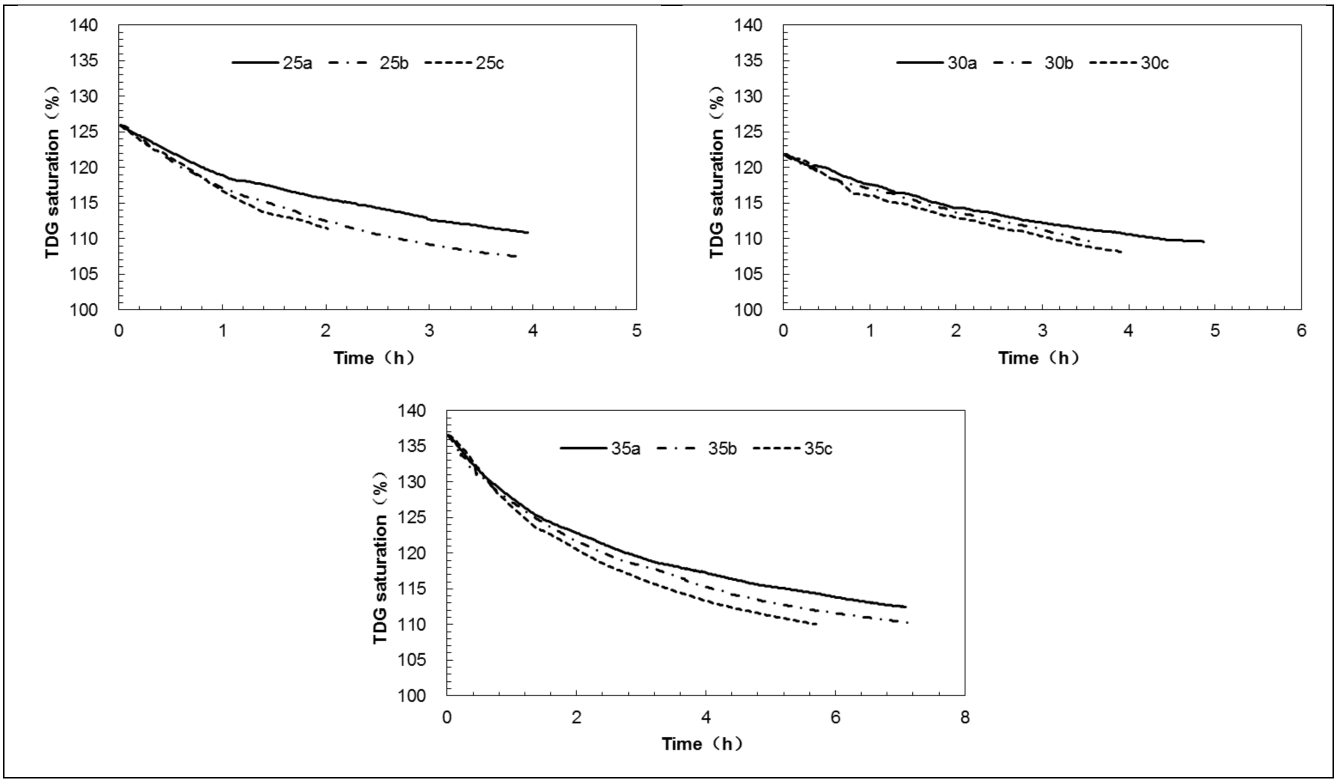

Figure 3. TDG Dissipation Processes at Same Water Depth and Different Flow Velocities.

In order to analyze the TDG dissipation characteristic, a new parameter which is named as dissipation rate (v_G) was defined in this study to describe the changing speed of TDG saturation, its physical interpretation was TDG saturation variation per unit time:

$$v_G = \frac{dG}{dt} \quad [1]$$

where dG is TDG saturation variation (%), and dt is the time TDG saturation variation spend (h).

On the basis of Eq. (1), when TDG saturation were near, the dissipation rates with different TDG saturation degrees of 120%, 112% and 110% were computed and the results are shown in Table 2. The

 ©2017, IAHR. Used with permission / ISSN 1562-6865 (Online) - ISSN 1063-7710 (Print)

results indicated that, under the same water depth, dissipation rate increased with flow velocity while TDG saturation was near 120%. Dissipation rates became approximately equal while TDG saturation was 112% to 110%, despite flow velocities and the water depths were not the same. There are two paths for gas dissipating in water (Ma et al., 1996), one is through the release of gas molecules which filled in the water molecule gaps, and another one is through the release of gas molecules which are held together with water molecules by hydrogen bonding. From the analysis, it was showed that, when the TDG saturation was higher than 112%, the dissipation of supersaturated TDG was dominated by the release of gas molecules which filled in the water molecule gaps. Although, when the TDG saturation decreased to 112%～110% or even lower, the dissipation of supersaturated TDG was dominated by the release of compounds which formed by gas molecules and water molecules.

Table 2. Dissipation Rates of Supersaturated TDG.

TDG Saturation G (%)	Dissipation Rate v_G (%/h)								
	25a	25b	25c	30a	30b	30c	35a	35b	35c
120	6.37	7.96	10.33	6.12	6.37	8.75	3.17	4.00	4.79
112	2.38	4.00	3.17	3.17	2.38	3.35	1.58	2.38	1.58
110	1.58	3.17	3.17	2.38	1.58	2.56	1.58	1.58	1.58

3.2 Relationship analysis between the dissipation coefficient and hydraulic characteristic

TDG dissipation processes satisfied the first-order kinetic equation (USACE, 2005):

$$\frac{d\left(G-G_{eq}\right)}{dt}=k_T\left(G-G_{eq}\right) \quad [2]$$

where, G is TDG saturation (%), G_{eq} is TDG saturation of at the local atmospheric pressure and temperature (%), usually taking 100%, k_T is dissipation coefficient (h^{-1}), and t is dissipation time (h).

Through integrating Eq.2,

$$G-G_{eq}=\left(G_0-G_{eq}\right)e^{-k_T t} \quad [3]$$

where, G_0 is TDG saturation (%).

Eq.3 is used to formulate the dissipation process, and fitting equations are shown in Figure 4, the TDG dissipation coefficients obtained in different flow velocity conditions are summarized in Table 3. As shown, all of the correlation coefficients (R^2) were greater than 0.96, which indicated that the formulating process with Eq.3 appeared satisfying. The results showed that, the maximum dissipation coefficient was $0.441h^{-1}$, which was derived in the case of NO. 25c, and the minimum dissipation coefficient was $0.142h^{-1}$, which was derived in the case of NO. 35a. Dissipation coefficient increased obviously as Reynolds number increased; when linear equation was used to formulate the relationship between Reynolds number and dissipation coefficient, as shown in Figure 5, the correlation coefficient (R^2) was 0.9734, and the fitting equation of dissipation coefficient and Reynolds number is:

$$k_T=0.00001R_e+0.0426 \quad [4]$$

where, R_e is Reynolds number.

Table 3. Dissipation Coefficients of Supersaturated TDG.

Case NO.	Dissipation Coefficient k_T (h^{-1})	Flow Velocity v (m/s)	Water Depth H (m)	Reynolds Number R_e	Correlation Coefficient R^2
25a	0.217	0.17	0.25	13597	0.9801
25b	0.323	0.31	0.25	22185	0.9935
25c	0.411	0.45	0.25	32204	0.9946
30a	0.172	0.15	0.30	9924	0.9917
30b	0.229	0.19	0.30	14504	0.9850
30c	0.257	0.25	0.30	19084	0.9933
35a	0.142	0.13	0.35	8015	0.9687
35b	0.172	0.15	0.35	12023	0.9790
35c	0.224	0.21	0.35	16832	0.9866

©2017, IAHR. Used with permission / ISSN 1562-6865 (Online) - ISSN 1063-7710 (Print)

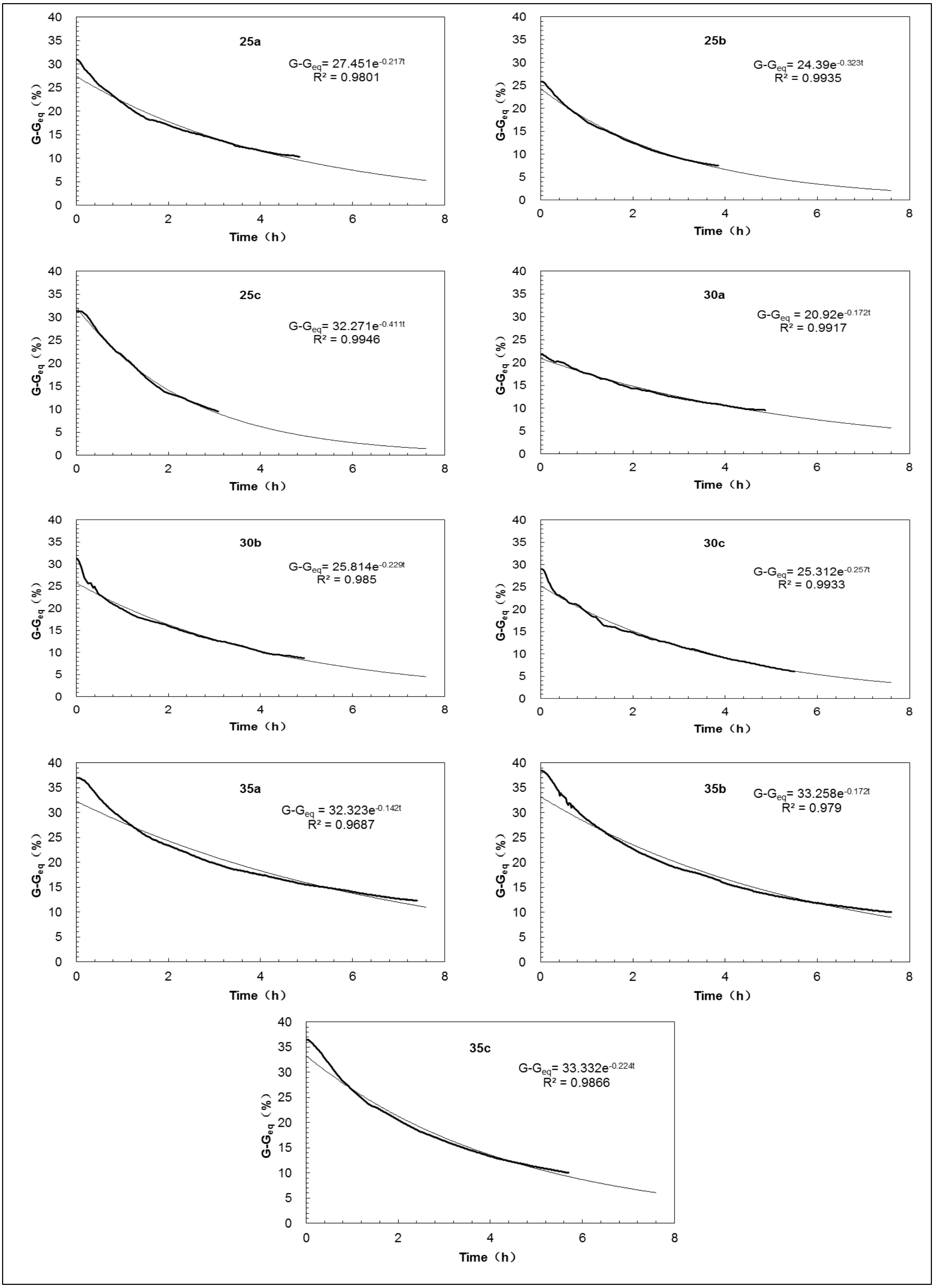

Figure 4 TDG Dissipation Processes and Fitting Curves at Different Cases.

 ©2017, IAHR. Used with permission / ISSN 1562-6865 (Online) - ISSN 1063-7710 (Print)

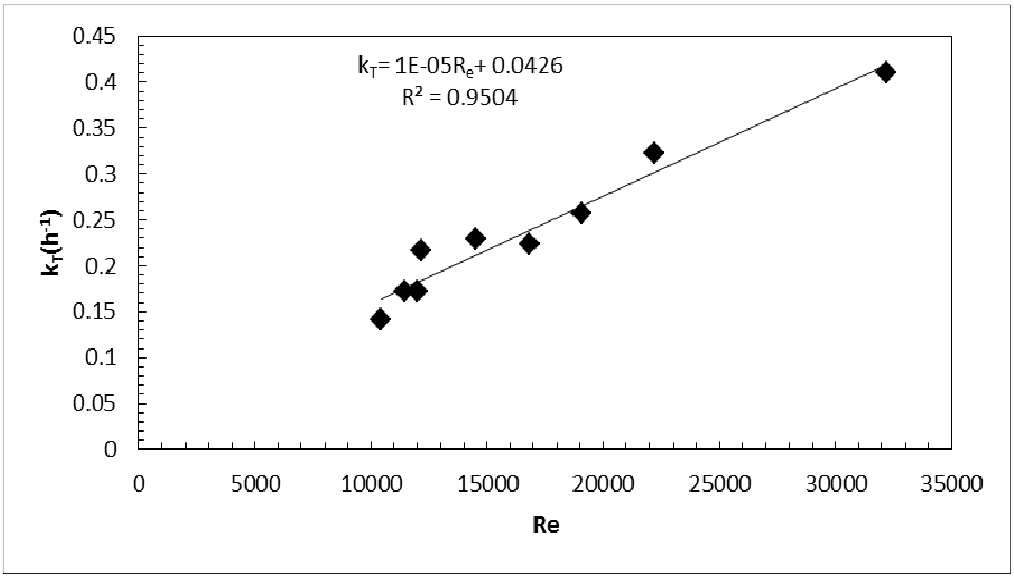

Figure 5. Relationship between Reynolds Number and Dissipation Coefficient.

4 CONCLUSIONS

This research carried out an experimental study on the relationship between hydraulic characteristics and TDG dissipation process with annular flume. The experimental results showed that the dissipation coefficient increased with Reynolds number and flow velocity, the quantitative relationship between Reynolds number and dissipation coefficient was developed, the dissipation rate increased with flow velocity while TDG saturation was above 120%, or was stable while TDG saturation was below 110%. The results were of great importance to scientific basis for the prediction of TDG dissipation process. However, the condition of natural river course is so complex that deeper researches are needed to be carried out on TDG dissipation rules in the future.

ACKNOWLEDGEMENTS

The research reported herein was funded by Major Project of the National Natural Science Foundation of China (NO. 2016YFC0502205) and Postdoctoral Foundation of Jiangsu Province (NO. 08BS915002).

REFERENCES

Feng, J.J., Li, R., Li, K.F., Li, J., & Qu, L., (2010). Study on Release Process of Supersaturated Total Dissolved Gas Downstream of High Dam. *Journal of Hydraulic Engineering*, 29(1), 7-12.

Feng, J.J., Li, R., Tang, C.Y. & Yong, X.D. (2012). Experimental Study on The Sediment Effect on Releasing Process of Supersaturated Total Dissolved Gas. *Advances in Water Science*, 23(5), 702-708.

Feng, J.J., Li, R., Ma Q. & Wang L.L. (2014). Dissipation Coefficient of Supersaturated Total Dissolved Gas in a One-dimensional Longitudinal Model. *Journal of Central South University*, 21, 1995-2003.

Huang, H. (2002). Numerical Modeling of TDG Downstream of a Spillway. *Ph.D. Dissertation*, IIHR, the University of Iowa.

Huang, J., Li, R., Feng, J., Xu, W. & Wang, L. (2016). Relationship Investigation Between the Dissipation Process of Supersaturated Total Dissolved gas and Wind Effect. *Ecological Engineering*, 95, 430-437.

Johnson, E.L., Clabough, T.S., Peery, C.A., Bennett, D.H., Bjornn, T.C., Caudill, C.C., & Richmond M.C. (2007). Estimating Adult Chinook Salmon Exposure to Dissolved Gas Supersaturation Downstream of Hydroelectric Dams Using Telemetry and Hydrodynamic Models. *River. Research and Application*, 23(9), 963–978.

Li, R., Gualtieri, P., Feng, J.J. & Gualtieri, C. (2015). A Dimensional Analysis of Supersaturated Total Dissolved Gas Dissipation. *E-proceedings of the 36th IAHR World Congress*, 1-8.

Ma, Y.G., Ba, P. & Yu, G.Z. (1996). Progress of Theoretical Studies on Gas Liquid Mass Transfer. *Chemical Engineering*, 24 (6), 7-10.

Politano, M., Carrica, P.M., Turan, C. & Weber, L. (2004). Prediction of the Total Dissolved Gas Downstream of Spillways Using a Two-phase Flow Model, *World Water & Environmental Resources Congress*, ASCE, Utah, 1-10.

Politano, M., Carrica, P. & Weber, L. (2009). A Multiphase Model for the Hydrodynamics and Total Dissolved Gas in Tailraces. *International Journal of Multiphase Flow*, 35, 1036-1050.

Qu, L., Li, R., Li, J., Li, K.F. & Deng, Y. (2011a). Field Observation of Total Dissolved Gas Supersaturation of High-dams. *Science China Technological Sciences*, 54(1), 156-162.

Qu, L., Li, R., Li, J., Li, K.F. & Wang, L. (2011b). Experimental Study on Total Dissolved Gas Supersaturation in Water. *Water Science and Engineering*, 4(4), 396-404.
Tan, D.C., Ni, Z.H., Zheng, Y.H., Li, L.Y. & Li, Y.F. (2006). Dissolved Gas Supersaturation Downstream of Dam and Its Effects on Fish. *Freshwater Fisheries*, 36(3), 56-59.
US Army Corps of Engineers. (2005). *Technical analysis of TDG processes*. Washington D C: US Army Corps of Engineers, Northwest Division, Environmental Resources and Fish Planning Offices.
Weber, L.J., Huang, H., Lai, Y. & McCoy, A. (2004). Modeling Total Dissolved Gas Production and Transport Downstream of Spillways: Three-Dimensional Development and Applications, *International Journal of River Basin Management*, 2(3), 157-167.

 ©2017, IAHR. Used with permission / ISSN 1562-6865 (Online) - ISSN 1063-7710 (Print)

SYDNEY DESALINATION SEAWATER CONCENTRATE OUTFALL LABORATORY AND FIELD INVESTIGATIONS

BRETT M. MILLER[1] & GRANLEY P. SMITH [2]

[1,2] Water Research Laboratory, School of Civil and Environmental Engineering
UNSW Sydney, Australia
b.miller@wrl.unsw.edu.au; g.smith@wrl.unsw.edu.au

ABSTRACT

Physical modelling was undertaken as part of the diffuser design of the Sydney Desalination Plant seawater concentrate outfall. Subsequent to the construction, dye dispersion trials were undertaken with the desalination plant operating at full capacity. This paper presents the results and comparison of laboratory and field methodologies, with particular attention to interacting jets. The field observations show how actual conditions can vary from laboratory conditions, but also provide reassurance that the laboratory and numerical predictions are slightly conservative. Both results demonstrate how interacting jets reduce the mixing in the near field.

Keywords: Dense jets; field trials; physical modelling; plumes; rhodamine.

1 INTRODUCTION

The Sydney Desalination Plant is located at Kurnell towards the southern end of the Sydney coastline. A subsurface tunnel delivers seawater concentrate (brine) to two risers each 25m apart, located approximately 500m offshore in approximately 25m of water (Figure 1). The risers are located on a gradually sloping rocky seabed. Each riser cap is 7m diameter, with four 370mm diameter nozzles angled upwards at 60 degrees from the horizontal.

When the plant is producing 250 ML/day of potable water, the brine discharge is 4.0 $m^3.s^{-1}$ with salinity typically between 58 ppt and 62 ppt. The exit velocity is approximately 4.8 $m.s^{-1}$ and the receiving water salinity is approximately 35 ppt.

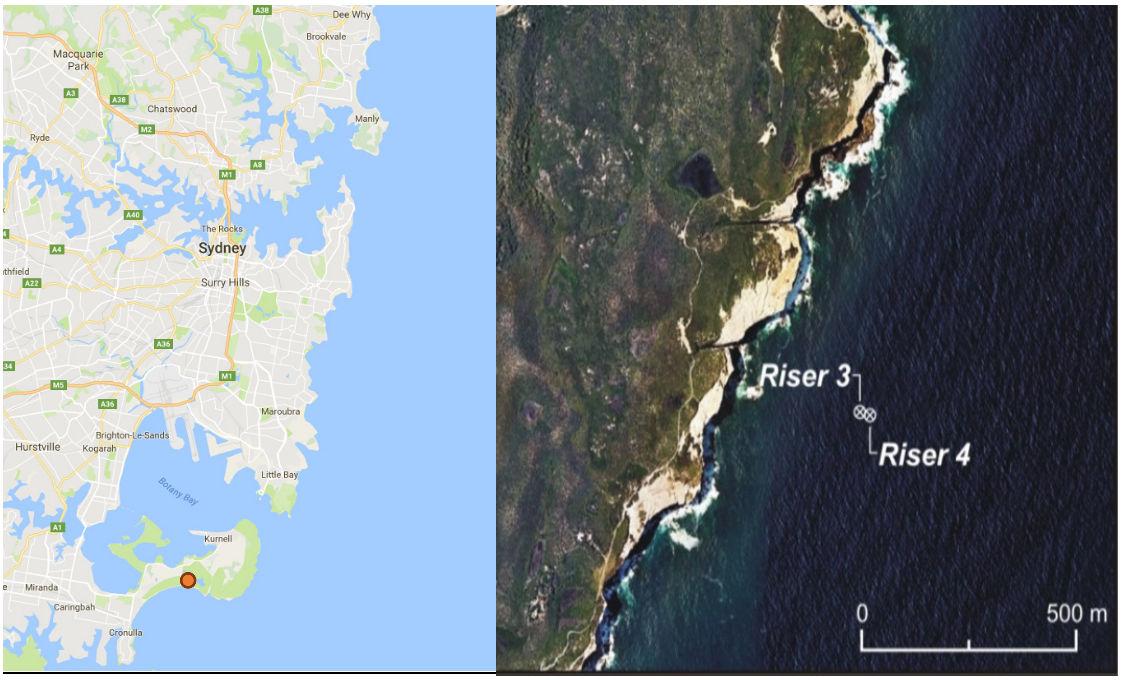

Figure 1. Location of the Sydney Desalination Outfall Risers.

The performance criteria were that (i) there was no visual evidence of the plume on the sea surface by ensuring that the maximum plume rise height should be at least 2m below the water surface, (ii) at the impact point where the plume returns to the sea bed, salinity must be within 1ppt of background and the dilution must be at least 30 times (as determined by eco-toxicity testing of other chemicals in the brine stream). Figure 2 presents the height of rise and the distance to the impact point on a photograph taken during laboratory testing.

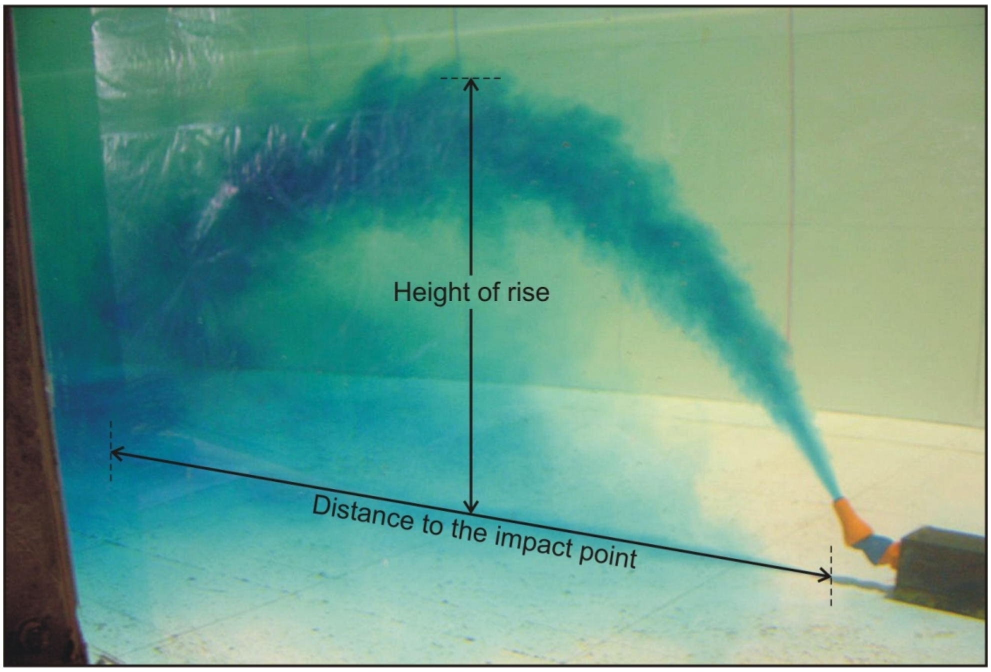

Figure 2. Height of Rise and Distance to the Impact Point

The port densimetric Froude number is defined as:

$$F = \frac{u}{\sqrt{g'.d}}$$

where

$$g' = g\left(\frac{\rho - \rho_o}{\rho_o}\right)$$

with

ρ being the density of the brine
ρ_o being the density of the seawater
u being the discharge velocity
d being the diameter of the port

Roberts, et al. (1999) reported that the impact point dilution was 1.6 x F, the distance to the impact point was 2.4 x F x d, and that the height of rise was 2.2 x F x d.

2 LABORATORY TESTING

Laboratory testing (**Figure 3**) was undertaken in a 4.5m x 4.5m x 0.6m tank. The purpose of the modelling was to verify empirical relationships on brine dispersion in jets and to assess the decrease in dilution when neighboring jets interact.

The receiving water tank was filled with freshwater and brine was discharged from a head tank into the receiving water tank through valves and rotameters. The modified gravity (g_0') in the model was kept the same as the modified gravity in the prototype so that the density difference between the seawater concentrate and the receiving waters in the ocean were the same as in the physical modelling experiments ($\Delta_r = 1$). The model scale was approximately 60:1 such that the Reynolds number in the jets was maintained above 4000.

Dilutions were measured as the ratio of initial and observed conductivity. Twelve single microelectrodes consisted of two small probes and a cylindrical body of 30 mm length and 4 mm diameter, hence minimizing the potential for disruption to flow. The electrodes were mounted in two array frames of six electrodes. Each array was mounted on a brass base, which was heavy enough to ensure that the arrays did not move during the experiments. Individual electrodes were then mounted on aluminum tabs with the electrode sensors offset from the brass base. The electrodes were set in line and horizontally spaced at 50 mm, which is equivalent to 3 m at prototype scale. Sensors were set to be 8 mm above the model floor, which is equivalent to 0.5 m above the prototype sea bed. The arrays were designed to allow measurement of EC both longitudinally and laterally through the plume at the point of impact.

Electrical conductivity was related to density through chemistry laboratory tests. Dilutions were calculated on the basis of density. The brine was also colored by dye so that video could be recorded both in plan and elevation.

 ©2017, IAHR. Used with permission / ISSN 1562-6865 (Online) - ISSN 1063-7710 (Print)

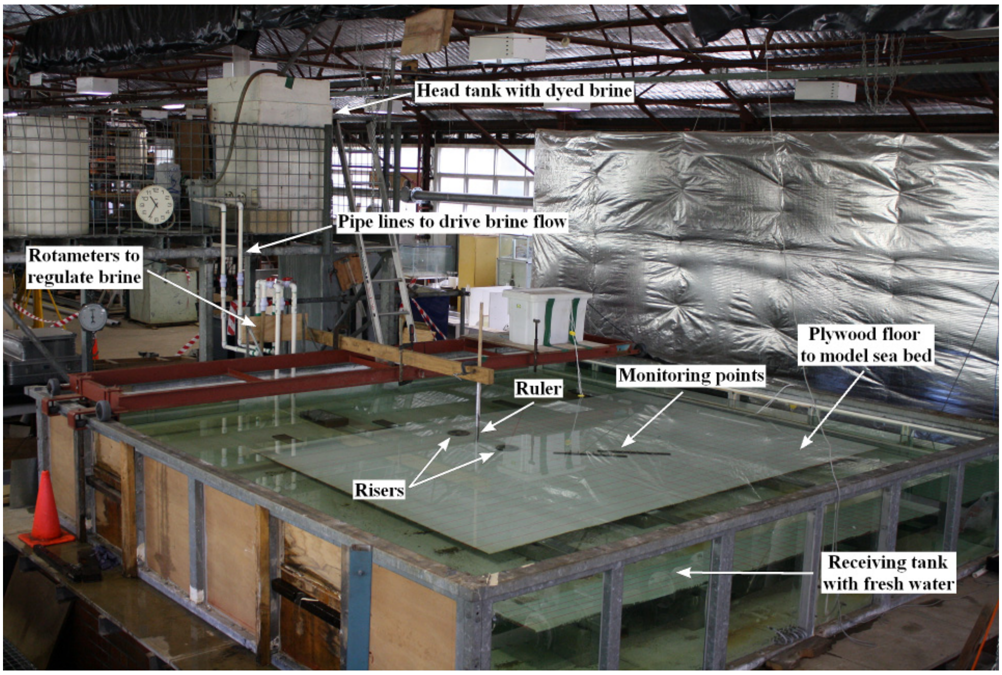

Figure 3. Laboratory Testing Facility.

Many tests were undertaken and are reported in Miller et al. (2009). Table 1 presents the various rates, sizes and parameters from the configuration that was finally constructed (prototype) and the scaled model. Tests were run three times and the results were compiled.

Table 1. Prototype and Model Parameters for Testing that Matched the Final Constructed Outfall

	Prototype	*Units*	Model	*Units*
Scale	1		59.68	
Number of risers tested	2		2	
Number of nozzles per riser	4		4	
Nozzle diameter	370	*mm*	6.2	*mm*
Nozzle angle	60	*degrees*	60	*degrees*
Volume	16688	*m3/h*	10.1	*L/min*
Water Depth above Seabed	25	*m*	419	*mm*
Salinity of Brine	62	*ppt*		
Density Brine	1046.4	*kg/m3*	1018.7	*kg/m3*
Nozzle exit velocity	5.4	*m/s*	0.70	*m/s*
Density	1026.2	*kg/m3*	999	*kg/m3*
Density Difference	20.2	*kg/m3*	19.7	*kg/m3*
Modified Gravity	0.2		0.2	
Port Froude Number	20.1		20.1	
Reynolds Number	2.00E+06		4.33E+03	

The inner jets, being those from each riser that interacted (Figure 4), achieved a substantially lower dilution than individual, outer jets. The test results are presented at prototype scale in Figure 5. The impact point shown on Figure 5 represents the best interpretation of where the centre of the plume touched down on the bed of the tank. Roberts (1999) relationships predict an impact point dilution of 32 at a distance of 17m which fits well with these observations, albeit with a slightly different interpretation of the impact point.

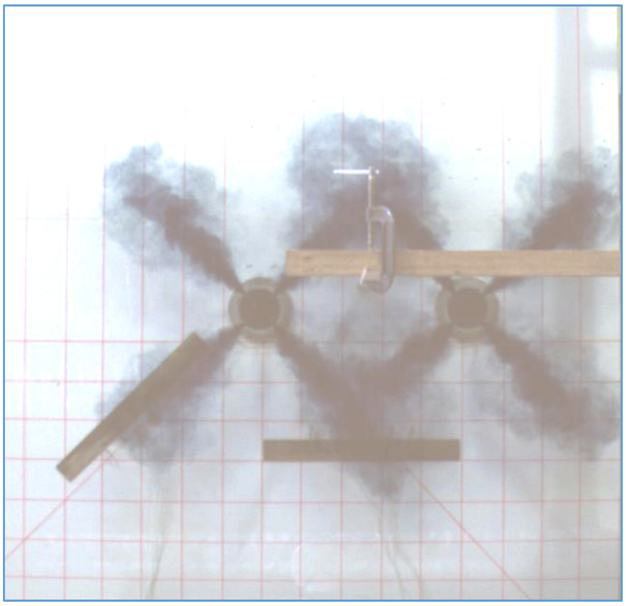

Figure 4. Overhead photograph of laboratory testing of the two risers, showing the four outer jets being separated and the four inner jets interacting.

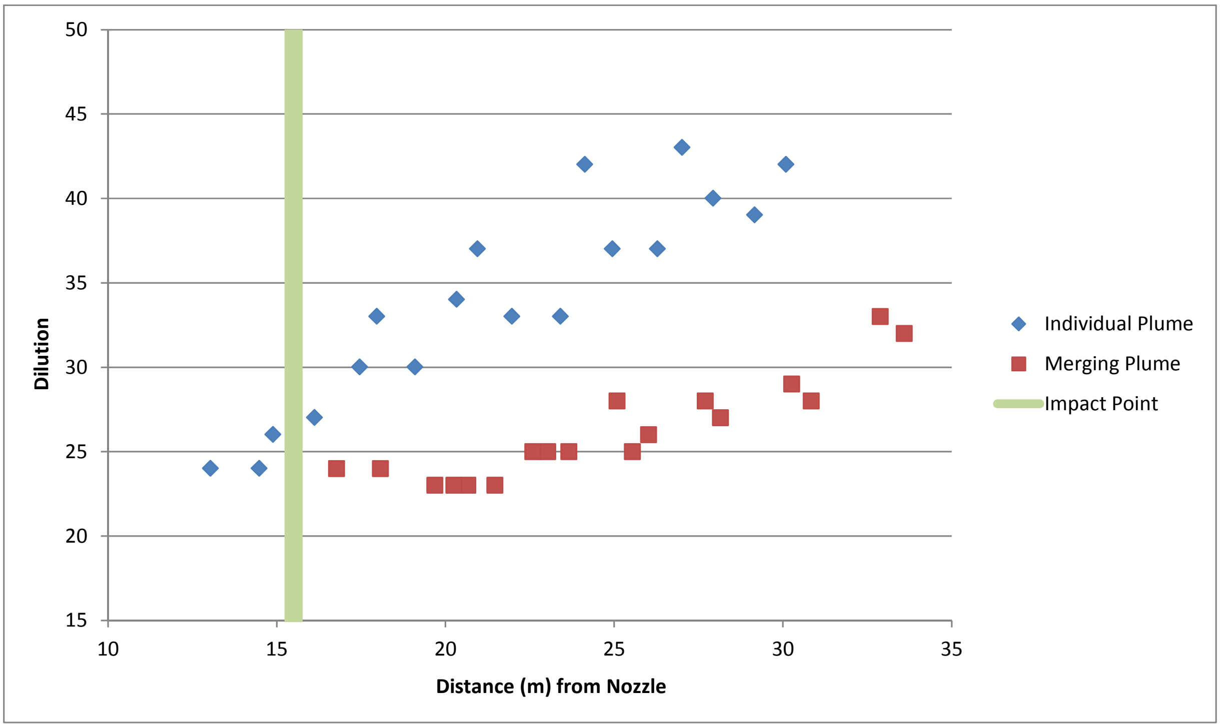

Figure 5. Results of laboratory testing showing the decrease in dilution from merging plumes.

3 FIELD DYE DISPERSION TESTS

Rhodamine WT (a fluorescent tracer dye) was injected into the drop structure chamber at the Sydney Desalination Plant at a known rate and concentration. The dye tracer concentration was then measured throughout the receiving waters using calibrated fluorimeters. Measurement of the plume in the near vicinity of the outfall risers very close to the bed from surface deployed instruments was considered too difficult. Rather, divers were used to swim the instruments directly into and around the outfall diffuser jets. This allowed for direct and targeted measurement of the plume dilution at the plume impact point and into the far-field. Rhodamine WT was used as it is not naturally occurring and provides greater accuracy than simply measuring salinity. Experimental dye concentrations of 0 – 5 ppb can be detected with an accuracy of 0.01 ppb.

The main vessel was a large barge with a qualified commercial dive team on board. This vessel was moored between the two risers to enable a stable point to conduct the diving. The diver was cabled back to the surface so that engineers on board could see measurements and video in real time from helmet mounted video equipment and a WetLabs ECO fluorometer attached to the Buoyancy Control Device (BCD). The diver was directed by engineers to make direct and targeted measurements of the plume rise height and plume

 ©2017, IAHR. Used with permission / ISSN 1562-6865 (Online) - ISSN 1063-7710 (Print)

impact point by swimming into and around the plume jets. The diver's location at each measurement point was noted using a distance tagged grid line attached to the outfall diffuser along with a diver recorded compass bearing and a digital depth gauge. Plume measurements by the diver were focussed on the near-field around the plume impact point. The diver also obtained grab samples as a secondary means to confirm dilution. **Figure 6** shows the diver equipment and the dyed brine leaving an outfall port.

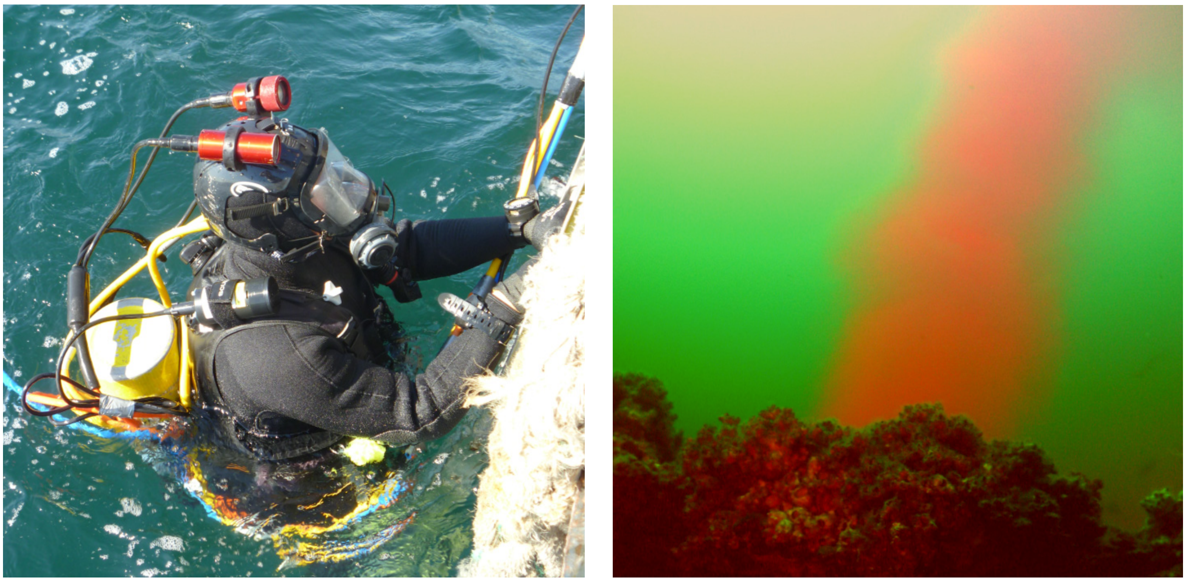

Figure 6. A diver with camera on head and fluorimeter on shoulder. Dye coloured brine jet.

Field work was undertaken on the 29^{th} and 30^{th} March 2011. As expected, results were not identical on both days due to slightly different conditions. Due to space limitations, only a subset of the results that demonstrate the effects of merging versus individual plumes are presented here, but the full results can be found in Smith et al. (2011).

During testing on Day 1, outfall discharge was constant at 4.00 m^3/s, 24.1°C and 57.9ppt. Rhodamine WT was injected into the outfall flow at a rate of 7.1 L/h, providing an active Rhodamine WT concentration in the seawater concentrate flow of 98 ppb. Discharge was maintained for approximately three hours. Calm offshore winds prevailed and wave conditions were slight. Ocean currents at the site were measured as being between 0.16 m/s and 0.30 m/s in a south-westerly direction. There was negligible stratification of temperature or salinity throughout the 25m of water column and the water temperature was 22.7°C and salinity was 35.0 ppt.

Figure 7 shows a schematic of the locations where measurements were taken. The Day 1 experiment concentrated on the southern (downstream) jets from "Riser 3". The South-Westerly (SW) jet acts independently whereas the South-Easterly (SE) jet interacts with the neighboring plume from "Riser 4". The impact of the northward (upstream) jets being turned back onto the downstream jets would have had some influence on the observations but the effect was not significant. Note that risers 1 and 2 were not constructed.

Profile plots showing mean concentrations of Rhodamine WT along the South Westerly (SW) and the South Easterly (SE) alignments are shown in Figure 9 and Figure 8 respectively. These figures show mean measured concentration values plotted at the measured distance and depth relative to the riser nozzle, which is represented on the bottom left of the figure. These figures also show an envelope of the 30 times dilution (calculated as the discharge concentration (98ppb) divided observed concentration) which were interpreted based on the recorded values and the plume behaviour observed during the experiment. Solid lines on the contour envelope represent sections of the contour that were directly interpreted from the measured data. Dashed lines on sections of the contour envelope represent sections of the envelope that were inferred on the basis of nearby concentration measurements and the observations of the divers and the engineers during the experiment.

It is clear from the results that a great deal of variability was observed in concentrations near the seabed. The South Westerly (SW) plume had an area where there was less than 22 times dilution whereas the South Easterly (SE) plume had no such area. The reason for this was unclear, however, it might be attributed to the SW plume being oriented up-slope, the interaction with the northbound plumes or simply the variability underneath the arc of the plume jet. For both the (SW) individual and the (SE) merging jets, the distance to the impact point was between 35 and 45m which were greater than either the empirical relationships or laboratory test results. The distance to the impact point was attributed to the mean ocean current of 0.23 $m.s^{-1}$. However, under these conditions, there was no noticeable difference between the merging plumes dilution and the individual plume dilutions.

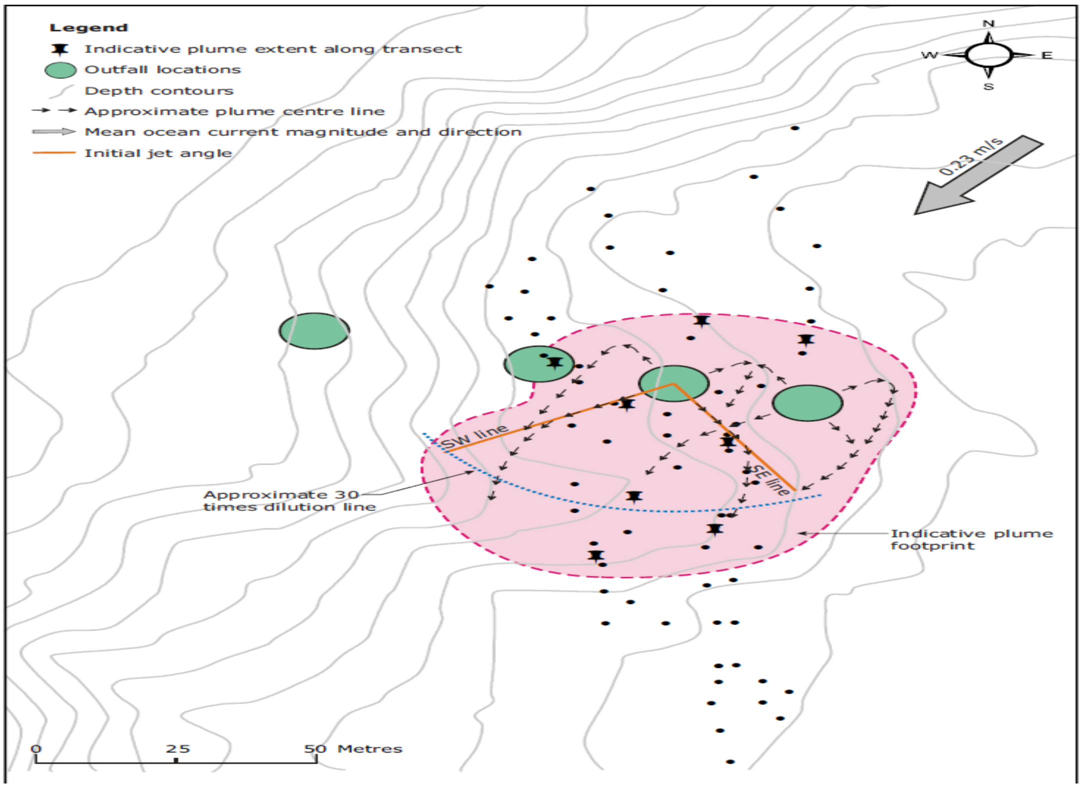

Figure 7. Schematic showing the SE measurement line (plume merges with the next riser) and the SW measurement line (independent plume) along with indicative plume footprint and plume lines.

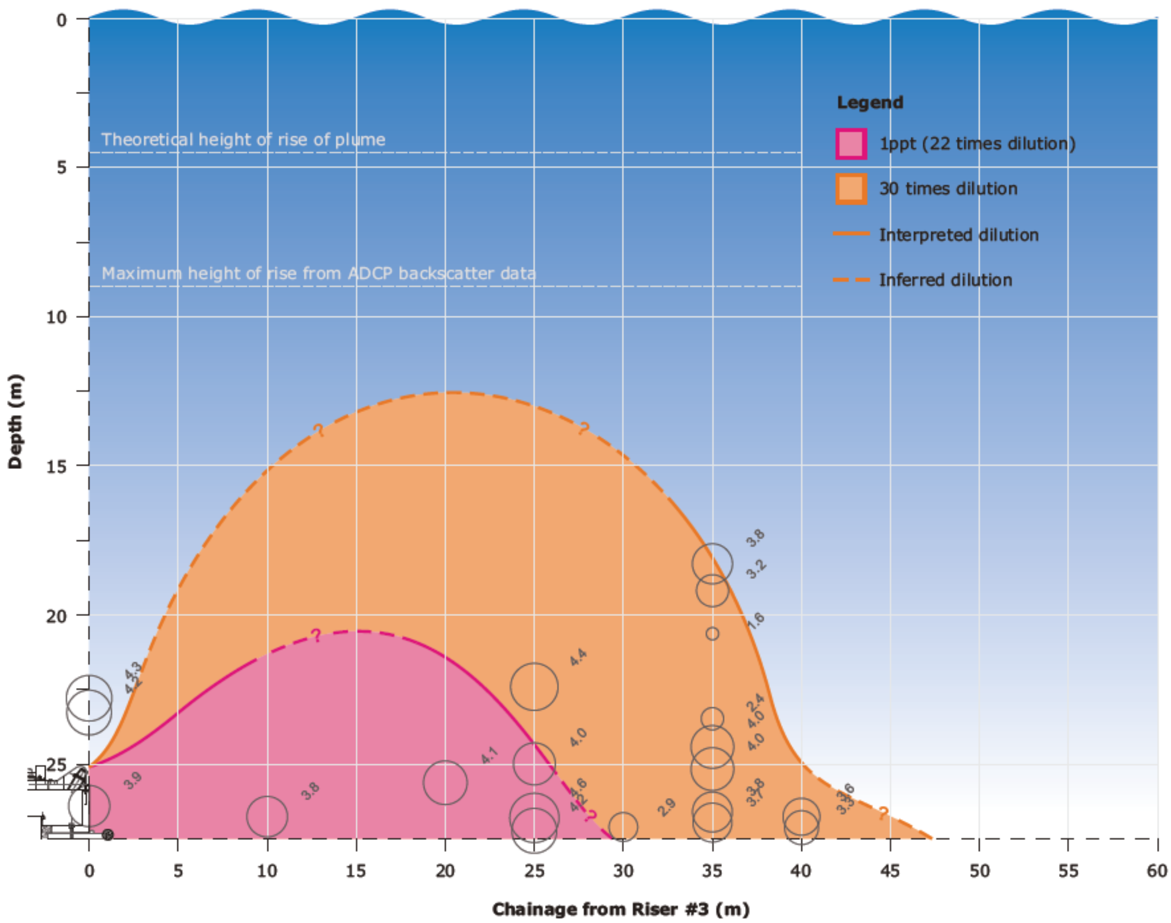

Figure 8. (SW) Plume Concentrations. Dilutions can be calculated by dividing 98 by the concentration.

©2017, IAHR. Used with permission / ISSN 1562-6865 (Online) - ISSN 1063-7710 (Print)

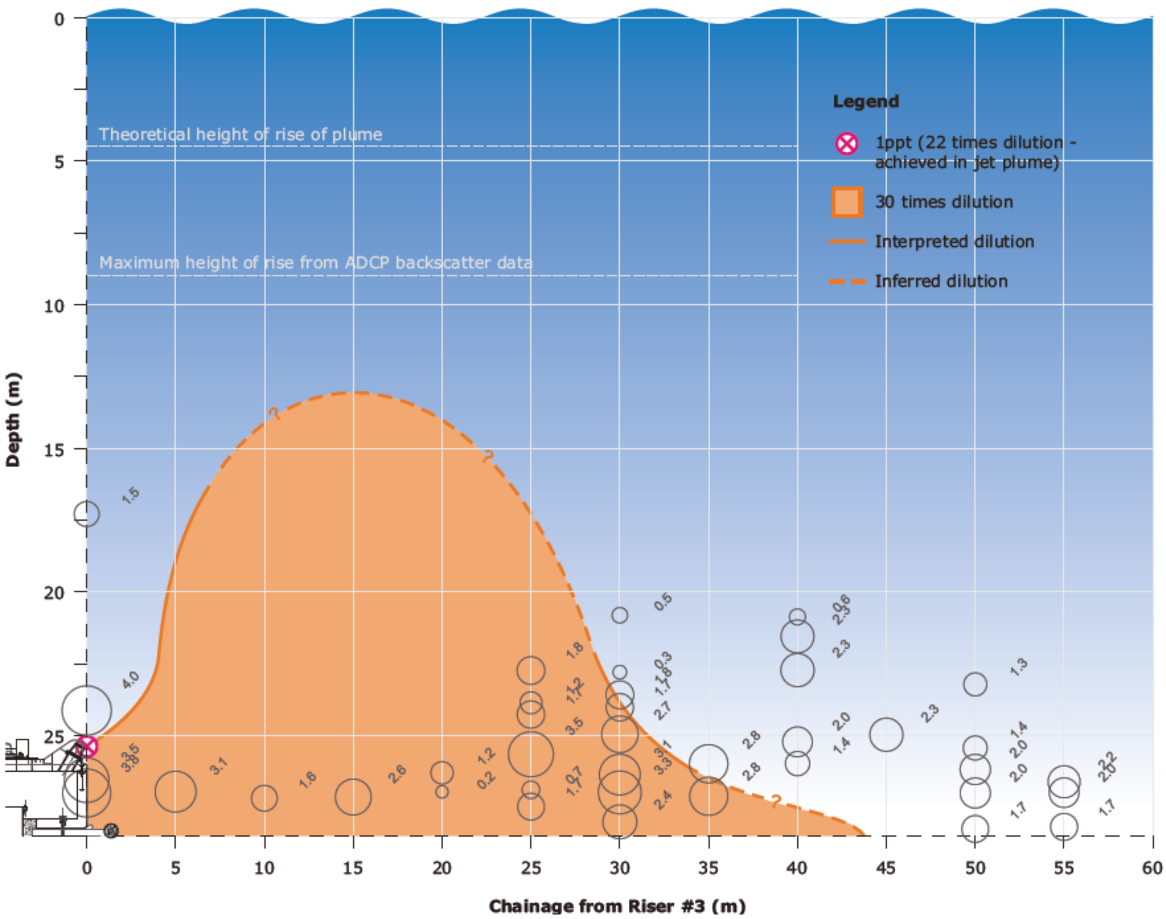

Figure 9. (SE) Plume Concentrations. Dilutions can be calculated by dividing 98 by the concentration.

4 CONCLUSION

Physical modelling and field observations were compared for the same diffuser configuration, flow and brine densities. The physical modelling was under quiescent conditions whereas the field experiment was undertaken with currents of approximately 0.23 $m.s^{-1}$. The physical modelling predicted the impact zone to be 16m from the diffuser with a dilution of 27 times whereas the field observations indicated that the impact point was approximately 30m from the diffuser but with dilutions of approximately 30 times. All observed field dilutions including those before and after the impact point were greater than the physical model predicted impact dilution.

In the ocean with a receiving current, bed forms and overall greater variability, the current was observed to have a strong influence on the position of the plume, but a lesser impact on the dilution. However, field observations did not exhibit the substantial reduction in dilution from a merging jet compared to an individual jet. As such, we can conclude that the laboratory testing is conservative and further fieldwork on merging plumes may allow for outfall risers to be placed closer together.

REFERENCES

Miller, B.M. Smith, G.P. & Tarrade, L. (2009). *Physical Modelling of Sydney's Desalination Outfall at 250ML/day Operation with Two Risers,* WRL Technical Report No 2009/15.

Smith G.P., Miller B.M., Ruprecht J.E. & Flocard F. (2011), *Dye Tracer Testing of The Sydney Desalination Plant Outfall: 29th and 30th March 2011,* WRL Technical Report No 2009/15.

Roberts, J W, Ferrier, A & Daviero, G (1997), *Mixing in Inclined Dense Jets.* Journal of Hydraulic Engineering. 123(8), 693-699.